NAM

Development of Version 2 GMPEs for Response Spectral Accelerations and Significant Durations from Induced Earthquakes in the Groningen Field

Julian J Bommer, Bernard Dost, Benjamin Edwards, Adrian Rodriguez-Marek, Pauline P Kruiver, Piet Meijers, Michail Ntinalexis & Peter J Stafford

Datum November 2015

Editors Jan van Elk & Dirk Doornhof

General Introduction

The hazard due to induced earthquakes is presented by the ground motion to which buildings and people are subjected. Therefore the prediction of ground motion resulting from earthquakes in the Groningen area induced by the production of gas is critical.

This research was started in 2012 and is continuing with ever more ground motion data from Groningen earthquakes being collected. The GMPE methodology is therefore updated regularly and progress is documented accordingly. In the Technical Addendum to Winningsplan 2013, a Ground Motion Prediction methodology based on a catalogue of tectonic earthquakes in southern Europe was presented. In order not to understate possible ground motions a conservative approach was used as a starting point. Generally speaking by gathering more and better data, predicted ground motions are inherently more likely to be adjusted downwards than upwards in the future.

In an earlier report "Development of GMPEs for Response Spectral Accelerations and for Strong-Motion Durations (Version 1)" the May 2015 status of this research was documented. This current document presents version 2 of the of the GMPE methodology of November 2015. The report describes an update of the Ground Motion Prediction methodology tailored to the Groningen situation. This update has in general led to a downward adjustment of assessed ground motions for larger earthquakes, resulting in a reduction of the assessed hazard.

A further update of the GMPE is in preparation to be reported mid-2016. This will in more detail include the results of measurements of the site response carried out in 2015.

NAM has assembled a team of experts in the field of GMPE to prepare a methodology for assessing ground motions, due to the induced earthquakes in the Groningen area. This team is led by Julian Bommer and consists of academics from various universities and knowledge institutes.

Main members of this team are:

External Expert	Affiliation	Main Expertise Area
Julian Bommer	Independent Consultant, London	Ground Motion Prediction and Site Response
Ben Edwards	University Liverpool	Ground Motion Prediction
Michail Ntinalexis	Independent Consultant	Ground Motion Prediction
Barbara Polidoro	Independent Consultant, London	Ground Motion Prediction
Adrian Rodriguez - Marek	Virginia Tech, USA	Site Response Assessment
Peter Stafford	Imperial College London	Ground Motion Prediction
Sinan Akkar	Bogazici, University Istanbul	Ground Motion Prediction
Pauline Kruiver	Deltares	Site Response Assessment
Piet Meijers	Deltares	Site Response Assessment

The research was done in close cooperation with experts from KNMI. Valuable comments from Bernard Dost (KNMI) have been incorporated in this report.

The studies into the ground motion prediction methodology were reviewed by a team of academics and experts from various universities. The team consisted of the following experts.

External Expert	Affiliation	Main Expertise Area
Gail Atkinson	Western University, Ontario, Canada	Ground Motion Prediction
Hilmar Bungum	NORSAR, Norway	Ground Motion Prediction
Fabrice Cotton	GFZ Potsdam, Germany	Ground Motion Prediction
John Douglas	University of Strathclyde, UK	Ground Motion Prediction
Jonathan Stewart	UCLA, California, USA	Ground Motion Prediction
Ivan Wong	AECOM, Oakland, USA	Ground Motion Prediction
Bob Youngs	AMEC, Oakland, USA	Ground Motion Prediction

The team met in October 2015 in London to discuss progress and further development of the GMPE methodology.

Reports describing progress of Ground Motion Prediction Methodology:

1 NAM, Technical Addendum Winningsplan 2013 – November 2013.
2 Julian Bommer and GMPE Team, Development of GMPEs for Response Spectral Accelerations and for Strong-Motion Durations (Version 1), May 2015
3 Julian Bommer and GMPE Team, Development of Version 2 GMPEs for Response Spectral Accelerations and Significant Durations from Induced Earthquakes in the Groningen Field, November 2015

Reports describing studies supporting the Ground Motion Prediction Methodology:

1 Deltares, Geological schematisation of the shallow subsurface of Groningen. For site response to earthquakes for the Groningen gas field (three documents).
2 Erik Meijles (Rijksuniversiteit Groningen), De ondergrond van Groningen: een geologische geschiedenis.

These reports are also available at the study reports page ('onderzoeksrapporten') of the website www.namplatform.nl.

NAM

Title	**Development of Version 2 GMPEs for Response Spectral Accelerations and Significant Durations from Induced Earthquakes in the Groningen Field**		**Date**	November 2015
			Initiator	NAM
Author(s)	Julian J Bommer, Bernard Dost, Benjamin Edwards, Adrian Rodriguez-Marek, Pauline P Kruiver, Piet Meijers, Michail Ntinalexis & Peter J Stafford	**Editors**	Jan van Elk & Dirk Doornhof	
Organisation	Various universities and knowledge institutes	**Organisation**	NAM	
Place in the Study and Data Acquisition Plan	Study Theme: Ground Motion Prediction Comment: The prediction of Ground Motion is central to the hazard assessment. This report describes an update of the Ground Motion Prediction methodology (version 2) for the Groningen situation.			
Directliy linked research	(1) Hazard Assessment. (2) Fragility assessment of buildings in the Groningen region.			
Used data	Accelerograms from the accelerometers placed in the Groningen field. P- and S-wave velocity model sub-surface Groningen. Description of the shallow geology of Groningen.			
Associated organisation	Imperial College (London), Deltares, KNMI & Virginia Tech (USA).			
Assurance	Assurance team has met in London in October 2015. Recommendations of the assurance team have been included in this report.			

Groningen Seismic Hazard and Risk Assessment Model

Development of Version 2 GMPEs for Response Spectral Accelerations and Significant Durations from Induced Earthquakes in the Groningen Field

Julian J Bommer[1], **Bernard Dost**[2], **Benjamin Edwards**[1], **,Pauline P Kruiver**[3], **Piet Meijers**[3], **Michail Ntinalexis**[1], **Barbara Polidoro**[1], **Adrian Rodriguez-Marek**[1] **& Peter J Stafford**[1]

1. Independent consultant, 2. Royal Netherlands Meteorological Institute (KNMI), 3. Deltares

Version 2

29 October 2015

Table of Contents

Executive Summary i

Acknowledgements xi

1. INTRODUCTION 1

1.1. Purpose and applications of the GMPEs 1
1.2. Overview of Groningen GMPE development process 2
1.3. GMPE requirements for fragility functions and risk calculations 6
1.4. Overview of report 12

2. OVERVIEW of V2 GMPEs 14

2.1. Functional form of the GMPEs and explanatory variables 14
2.2. Overview of derivation process 17
2.3. Definition of reference rock horizon 19
2.4. Spatial correlation of ground motions 23

3. GRONINGEN GROUND-MOTION DATABASES 25

3.1. Groningen ground-motion recording networks 25
3.2. Strong-motion database for Groningen 28
3.3. Additional small-magnitude events for inversions 34

4. CHARACTERISATION of RECORDING STATIONS 36

4.1. Site kappa values for recording stations 36
4.2. Preliminary station profiles for site response analyses 40
4.3. Site response analyses and linear amplification factors for stations 46
4.4. *In situ* measurements of shear-wave velocities 48

5. INVERSION of GROUND MOTIONS for SOURCE, PATH and REFERENCE ROCK PARAMETERS 50

5.1. Fourier amplitude spectra at the reference rock horizon 50
5.2. Overview of inversion process for source, path and reference rock parameters 50
5.3. Geometrical spreading function from full waveform simulations 52
5.4. Inversions for source, path and reference rock parameters 54

6. EQUATIONS for GROUND MOTIONS at REFERENCE ROCK HORIZON 68

6.1. Input parameters for stochastic simulations 68
6.2. Predicted accelerations at reference rock horizon 71
6.3. Functional form for reference rock GMPE 75
6.4. Regression analyses 79
6.5. Residual analyses 97
6.6. Ground-motion model for reference rock horizon 103

7. SITE RESPONSE MODEL 106

7.1. Shallow V_S profiles 106
7.2. Extension of V_S profiles to reference rock horizon 108
7.3. Layering model and layer-to-layer correlations 112
7.4. Mass densities 114
7.5. Modulus reduction and damping curves 115
7.6. Modulus reduction and damping curves for peats 118
7.7. Randomisations 122

8. SITE RESPONSE ANALYSES 124

8.1. Choice of analysis procedure 124
8.2. Input motions at reference rock horizon 147
8.3. Amplification factors and variability 151

9. ZONIFICATION for SITE AMPLIFICATION FUNCTIONS 154

9.1. Criteria for zonification 154
9.2. Zonification of the study area 156
9.3. Zone amplification factors 161
9.4. Comparison with amplification factors for recording stations 180

10. SIGMA MODEL 183

10.1. Elements of the sigma model for surface motions 183
10.2. Component-to-component variability 188
10.3. Sigma corrections for point-source approximation 190
10.4. Tau and ϕ_{ss} model 195
10.5. Site-to-site variability model 200

11. APPLICATION and EXTENSION of the GMPEs for Sa(T) 203

11.1. Model for predicting surface response spectra 203
11.2. Comparisons with V1 GMPE predictions 209
11.3. Period-to-period correlations 344
11.4. Vertical-to-horizontal ratios 345

12. GMPE for DURATION 359

12.1. Durations of Groningen ground motions 359
12.2. Existing duration GMPEs 367
12.3. Exploratory analyses 377
12.4. Exploration of model options 383
12.5. Development of the adjusted functional form 389
12.6. Version 2 GMPEs for duration 392
12.7. Correlation of residuals of duration and acceleration 398

13. REFINEMENTS and IMPROVEMENT of the GMPEs 400

13.1. Expansion of the ground-motion database 400
13.2. Use of measured V_S profiles at recording stations 404
13.3. Use of borehole recordings 405
13.4. New duration definition and consistent duration predictions 405
13.5. Summary of sensitivity analyses and potential refinements 407

References 414

APPENDIX I Kappa determinations for recording stations 425

APPENDIX II Station V_S, density and damping profiles 434

APPENDIX III Transfer functions for recording stations 463

APPENDIX IV Linear amplification functions for Sa(T) at recording stations 472

APPENDIX V Spectral fits for corner frequency and stress drop 479

Executive Summary

The V2 ground-motion prediction equations (GMPEs) for the Groningen field predict response spectral accelerations across the gas field and within the 5 km buffer area surrounding the field that collectively form the region for the seismic hazard and risk assessment. The ground-motion model comprises GMPEs for the prediction of accelerations at the base of the Upper North Sea formation (NU_B), which is the reference rock horizon, and a zonation in which non-linear site amplification factors are defined relative to the motions at the NU_B level. The model also includes equations for the prediction of the significant duration of the ground shaking, conditional on the spectral acceleration.

The first element of the GMPEs predicts median values of geometric mean horizontal response spectral accelerations, Sa, (in units of cm/s^2) at 16 oscillator periods, T. The functional form of the equations for motions at the NU_B reference rock horizon is:

$$\ln[Sa_{\mu}(T)] = c_1 + c_2 M + c_3 (M - 4.5)^2 + g(R) \qquad M \le 4.5 \qquad \text{(ES.1a)}$$

$$\ln[Sa_{\nu}(T)] = c_1 + c_2 M + c_{3a} (M - 4.5)^2 + g(R) \qquad M > 4.5 \qquad \text{(ES.1b)}$$

The distance, R (km), is defined as a function of epicentral distance, R_{epi}, and a magnitude-dependent near-source distance saturation term:

$$R = \sqrt{R_{epi}^2 + h(M)^2} \qquad \text{(ES.2)}$$

and the near-source saturation term is given by the following equation in all cases:

$$h(M) = \exp(0.423318M - 0.608279) \qquad \text{(ES.3)}$$

The distance-dependent terms are segmented into four ranges of R:

$$g(R) = c_4 \ln(R) \qquad R \le r_a \qquad \text{(ES.4a)}$$

$$g(R) = c_4 \ln(r_a) + c_{4a} \ln\left(\frac{R}{r_a}\right) \qquad r_a < R \le r_b \qquad \text{(ES.4b)}$$

$$g(R) = c_4 \ln(r_a) + c_{4a} \ln\left(\frac{r_b}{r_a}\right) + c_{4b} \ln\left(\frac{R}{r_b}\right) \qquad r_b < R \le r_c \qquad \text{(ES.4c)}$$

$$g(R) = c_4 \ln(r_a) + c_{4a} \ln\left(\frac{r_b}{r_a}\right) + c_{4b} \ln\left(\frac{r_c}{r_b}\right) + c_{4c} \ln\left(\frac{R}{r_c}\right) \qquad R > r_c \qquad \text{(ES.4d)}$$

The distances defining the different segments are as follows:

$$r_a = \sqrt{7^2 - 3^2} \qquad \text{(ES.5a)}$$

$$r_b = \sqrt{12^2 - 3^2} \quad \text{(ES.5b)}$$

$$r_c = \sqrt{25^2 - 3^2} \quad \text{(ES.5c)}$$

There are three versions of the median model—lower, central and upper—corresponding to three different models for the median stress drop. The coefficients of Eqs.(ES.1) and (ES.4) are listed in Tables ES.1-ES.3, and also provided electronically in the supplementary Excel file: **V2_GMPEs_*date*.xlsx**.

Using Eqs.(ES.1) to (ES.5) the median spectral acceleration, Sa_μ, at each of the 16 target periods can be calculated, using the coefficients in Tables ES.1 to ES.3. The complete calculation of the spectral accelerations at the NU_B reference rock horizon also requires sampling the aleatory variability, which has several elements; the equation is shown here without the (T) indicating response period since all elements of the model are defined period-by-period:

$$\ln(Sa_{NU\_B,arb}) = \ln(Sa_\mu) + \varepsilon_E\tau + \varepsilon_S(\phi_{SS} + \delta\phi) + \varepsilon_C\sigma_{C2C} \quad \text{(ES.6)}$$

$$\ln(Sa_{NU\_B,GM}) = \ln(Sa_\mu) + \varepsilon_E\tau + \varepsilon_S(\phi_{SS} + \delta\phi) \quad \text{(ES.7)}$$

where $Sa_{NU\_B,arb}$ and $Sa_{NU\_B,GM}$ are the arbitrary and geometric mean components of horizontal motion, to be used in the risk and the hazard calculations respectively; ε_E is a random sample from the normal distribution for each earthquake, ε_S is a random sample from the normal distribution for each site, and ε_C is a random sample from the normal distribution for each location; it is assumed that ε_S and ε_C are entirely uncorrelated. The values of τ, ϕ_{SS}, and σ_{C2C} are in Table ES.4.

Table ES.1. Coefficients of the lower model

T (s)	c_1	c_2	c_3	c_{3a}	c_4	c_{4a}	c_{4b}	c_{4c}
0.01	0.109814	1.18928	-0.2262	-0.09761	-1.76074	-0.40011	-2.3041	-1.81431
0.1	0.946105	1.131886	-0.1465	-0.08741	-1.80353	-0.53834	-2.5332	-2.06718
0.2	1.395916	1.017826	-0.24373	-0.04957	-1.51587	-0.47299	-2.37385	-2.12964
0.3	1.209262	1.014554	-0.36141	-0.04434	-1.3983	-0.40524	-2.23346	-1.89373
0.4	0.957899	1.050353	-0.44786	-0.05556	-1.32835	-0.36476	-2.15757	-1.74098
0.5	0.461128	1.117279	-0.50058	-0.07867	-1.28697	-0.33453	-2.10876	-1.63472
0.6	-0.26982	1.208317	-0.52492	-0.11009	-1.26841	-0.30779	-2.07409	-1.55541
0.7	-0.99959	1.314239	-0.53294	-0.14737	-1.26257	-0.28292	-2.04768	-1.49273
0.85	-1.94632	1.470465	-0.5266	-0.20257	-1.26476	-0.25247	-2.01997	-1.42568
1	-2.85758	1.629383	-0.50131	-0.25731	-1.2813	-0.22642	-2.00093	-1.37589
1.5	-5.12076	2.071045	-0.39885	-0.40282	-1.31893	-0.17606	-1.96296	-1.27436
2	-6.79118	2.379842	-0.29235	-0.48582	-1.35857	-0.15524	-1.94786	-1.22371
2.5	-8.06116	2.562726	-0.19956	-0.50607	-1.44554	-0.14964	-1.95333	-1.2064
3	-8.99662	2.70147	-0.13234	-0.50813	-1.49057	-0.15149	-1.95771	-1.19703
4	-10.2997	2.895223	-0.0429	-0.49008	-1.50244	-0.15662	-1.95938	-1.18789
5	-11.1275	3.00163	0.008789	-0.45468	-1.4759	-0.15965	-1.95566	-1.18621

Table ES.2. Coefficients of the central model

T (s)	c_1	c_2	c_3	c_{3a}	c_4	c_{4a}	c_{4b}	c_{4c}
0.01	0.490759	1.289798	-0.26723	-0.11245	-1.82121	-0.42537	-2.34672	-1.88538
0.1	1.516608	1.189682	-0.18504	-0.08694	-1.84137	-0.56502	-2.57456	-2.16914
0.2	1.980877	1.058019	-0.34117	-0.045	-1.51518	-0.49349	-2.38909	-2.17046
0.3	1.531262	1.105582	-0.46354	-0.06252	-1.39508	-0.41835	-2.24683	-1.91583
0.4	0.972248	1.202062	-0.53114	-0.0998	-1.32534	-0.37184	-2.16988	-1.75591
0.5	0.194881	1.32448	-0.55637	-0.14527	-1.2869	-0.33669	-2.12089	-1.64709
0.6	-0.76825	1.461856	-0.55119	-0.19356	-1.27536	-0.30585	-2.08673	-1.56741
0.7	-1.69932	1.608117	-0.52966	-0.24393	-1.27881	-0.27743	-2.06094	-1.50456
0.85	-2.87048	1.808749	-0.48682	-0.31096	-1.29416	-0.24341	-2.03361	-1.43685
1	-3.92479	1.994758	-0.43355	-0.36884	-1.32276	-0.21625	-2.01476	-1.38699
1.5	-6.38636	2.464976	-0.28091	-0.49898	-1.38146	-0.16927	-1.97542	-1.284
2	-7.95338	2.739589	-0.16998	-0.54476	-1.42915	-0.15626	-1.96009	-1.23455
2.5	-8.91454	2.848895	-0.10561	-0.51852	-1.52008	-0.16125	-1.96734	-1.22251
3	-9.58158	2.922099	-0.06568	-0.48143	-1.56462	-0.17006	-1.97334	-1.21692
4	-10.4741	3.014683	-0.01932	-0.40673	-1.57522	-0.17991	-1.97779	-1.21252
5	-11.0116	3.050216	0.001003	-0.33716	-1.54808	-0.1818	-1.97617	-1.21403

Table ES.3. Coefficients of the higher model

T (s)	c_1	c_2	c_3	c_{3a}	c_4	c_{4a}	c_{4b}	c_{4c}
0.01	-0.25612	1.609903	-0.28536	-0.22324	-1.8288	-0.45491	-2.38222	-1.93922
0.1	0.976817	1.470684	-0.23334	-0.18656	-1.84069	-0.59382	-2.61349	-2.24319
0.2	1.262278	1.374449	-0.37738	-0.16481	-1.51082	-0.50315	-2.40895	-2.20521
0.3	0.517515	1.479449	-0.46186	-0.20465	-1.39345	-0.42009	-2.26459	-1.93394
0.4	-0.29847	1.624274	-0.49279	-0.25809	-1.32512	-0.36896	-2.18582	-1.76771
0.5	-1.26553	1.780391	-0.48785	-0.31169	-1.28771	-0.33159	-2.13536	-1.65678
0.6	-2.35046	1.937092	-0.4599	-0.36059	-1.27775	-0.30004	-2.10018	-1.5769
0.7	-3.36234	2.094027	-0.42015	-0.40667	-1.28347	-0.27197	-2.07315	-1.51393
0.85	-4.59102	2.298136	-0.35903	-0.46202	-1.30236	-0.23922	-2.04384	-1.44572
1	-5.63322	2.47352	-0.29714	-0.50205	-1.33458	-0.21468	-2.02319	-1.39578
1.5	-7.89705	2.879205	-0.14464	-0.56702	-1.40062	-0.17668	-1.97891	-1.29118
2	-9.14424	3.070818	-0.0601	-0.55399	-1.45198	-0.17212	-1.96241	-1.24231
2.5	-9.75364	3.09789	-0.03488	-0.48498	-1.5446	-0.18739	-1.97259	-1.2345
3	-10.145	3.105677	-0.02626	-0.41758	-1.58858	-0.20205	-1.98173	-1.23247
4	-10.6554	3.106824	-0.02324	-0.30727	-1.59865	-0.21391	-1.99146	-1.23281
5	-10.965	3.088108	-0.02927	-0.22469	-1.57129	-0.21323	-1.9933	-1.23771

Table ES.4. Elements of aleatory variability in Eqs.(ES.6) and (ES.7)

Period (seconds)	τ			ϕ_{SS}			σ_{C2C}
	Lower	Central	Upper	Lower	Central	Upper	
0.01	0.3185	0.2758	0.2012	0.38	0.45	0.52	0.267
0.1	0.3353	0.2778	0.2075	0.38	0.45	0.52	0.240
0.2	0.3597	0.2913	0.2422	0.38	0.45	0.52	0.277
0.3	0.3804	0.3204	0.3001	0.38	0.45	0.52	0.321
0.4	0.3960	0.3561	0.3548	0.38	0.45	0.52	0.293
0.5	0.4075	0.3874	0.3935	0.38	0.45	0.52	0.309
0.6	0.4160	0.4103	0.4182	0.38	0.45	0.52	0.303
0.7	0.4225	0.4257	0.4336	0.38	0.45	0.52	0.319
0.85	0.4295	0.4397	0.4469	0.38	0.45	0.52	0.331
1.0	0.4344	0.4474	0.4540	0.38	0.45	0.52	0.342
1.5	0.4432	0.4568	0.4628	0.38	0.45	0.52	0.416
2.0	0.4472	0.4591	0.4651	0.38	0.45	0.52	0.416
2.5	0.4493	0.4600	0.4659	0.38	0.45	0.52	0.416
3.0	0.4506	0.4604	0.4663	0.38	0.45	0.52	0.416
4.0	0.4521	0.4607	0.4666	0.38	0.45	0.52	0.416
5.0	0.4528	0.4608	0.4667	0.38	0.45	0.52	0.416

The term $\delta\phi$ in Eqs.(ES.6) and (ES.7) is defined by the following series of equations:

$$\delta\phi = SF.\frac{\varphi(z)}{\sigma_Z} \qquad M \geq 4 \qquad \text{and} \quad R_{epi} > 0 \qquad \text{(ES.8a)}$$

$$\delta\phi = 0 \qquad M < 4 \qquad \text{or} \quad R_{epi} = 0 \qquad \text{(ES.8b)}$$

where SF is the magnitude-dependent scaling factor, expressed as follows:

$$SF = \beta_1(M-4) + \beta_2(M-4)^2 \qquad \text{(ES.9)}$$

and $\varphi[\ ]$ is the normal probability density function, which is given by the following expression:

$$\varphi(z) = \frac{1}{\sqrt{2\pi}}\exp\left(\frac{-z^2}{2}\right) \qquad \text{(ES.10)}$$

The argument of this expression is given by:

$$z = \frac{\ln(R_{epi}) - \mu_Z}{\sigma_Z} \qquad \text{(ES.11)}$$

and the parameters of this expression are given by:

$$\mu_Z = \beta_3 + \beta_4(M-6.75) + \beta_5(M-6.75)^2 \qquad \text{(ES.12)}$$

$$\sigma_Z = \beta_6 \qquad \text{(ES.13)}$$

The coefficients of these equations are provided in Tables ES.5 and ES.6.

Table ES.5. Coefficients of Eqs.(ES.9)

Period (s)	β_1	β_2
0.01	0.20370	0.07357
0.1	0.20117	0.09277
0.2	0.20280	0.08043
0.3	0.20486	0.06478
0.4	0.20671	0.05081
0.5	0.20751	0.04468
0.6	0.20847	0.03742
0.7	0.20939	0.03044
0.85	0.21039	0.02286
1.0	0.21102	0.01808
1.5	0.21208	0.01001
2.0	0.21273	0.00508
2.5	0.213084	0.00243
3.0	0.21325	0.00117
4.0	0.21370	-0.00228
5.0	0.21416	-0.00573

Table ES.6. Coefficients of Eqs.(ES.12) and (ES.13)

β_3	β_4	β_5	β_6
3.394377	0.710239	0.0909	1.03011

The complete model for the NU_B motions is as defined in Eqs.(ES.1) to (ES.5) and (ES.6) and (ES.7), depending on whether being applied to risk or hazard calculations; the three branches of the logic-tree for the NU_B motions are defined by the combinations and weights indicated in Table ES.7.

Table ES.7. Ground-motion logic-tree branches for NU_B motions

Model	**Median Coefficients**	τ	ϕ_{SS}	**Weight**
Lower	Table ES.1	Table ES.4 (lower)	Table ES.4 (lower)	0.2
Central	Table ES.2	Table ES.4 (central)	Table ES.4 (central)	0.5
Upper	Table ES.3	Table ES.4 (upper)	Table ES.4 (upper)	0.3

The coefficients of the median equations and all the components of the variability model at the NU_B horizon are presented in the Excel file **V2_GMPEs_*date*.xlsx**.

At any given location, the surface motions are given by the following equation when calculating seismic risk:

$$\ln(Sa_{arb}) = \{\ln(Sa_{\mu}) + \varepsilon_E\tau + \varepsilon_S(\phi_{SS} + \delta\phi) + \varepsilon_C\sigma_{C2C}\} + \ln(AF_j) + \varepsilon_Z\phi_{S2Sj} \qquad \text{(ES.14)}$$

and this equation when calculating seismic hazard:

$$\ln(Sa_{GM}) = \{\ln(Sa_{\mu}) + \varepsilon_E\tau + \varepsilon_S(\phi_{SS} + \delta\phi)\} + \ln(AF_j) + \varepsilon_Z\phi_{S2Sj} \qquad \text{(ES.15)}$$

where AF_j is the amplification function for spectral acceleration at the target period in the j^{th} zone; ϕ_{S2Sj} is the site-to-site variability in the j^{th} zone, and ε_Z is a random sample from the normal distribution. The field is divided into 167 zones, and each of the 140,821 grid squares of 100 m x 100 m is assigned to one of these zones. The zonations are provided in the Excel file **V2_Site Response Zonations_*date*.xlsx**, which contains the following information: (X,Y) coordinates, in the Dutch RD system, of the centre of the grid square and the zone identifier (4 digit integer). For each zone and each response period, the amplification factor is given by the following equation:

$$\ln(AF) = f_1 + f_2 \ln\left(\frac{Sa_{NU\_B,g} + f_3}{f_3}\right) \qquad \text{(ES.16)}$$

where $Sa_{NU\_B,g}$ is obtained from Eq.(ES.6) or (ES.7) but expressed here in units of *g*, the acceleration due to gravity (9.807 m/s^2), rather than cm/s^2. The surface acceleration then

requires the addition of the random sample from the site-to-site variability, ϕ_{S2S}. For each zone and each response period, the value of this sigma component is defined as a function of the value of Sa_{NU_B}, as illustrated in Figure ES.1. If the resulting value is ever smaller than 0.2, it should be constrained to this minimum value.

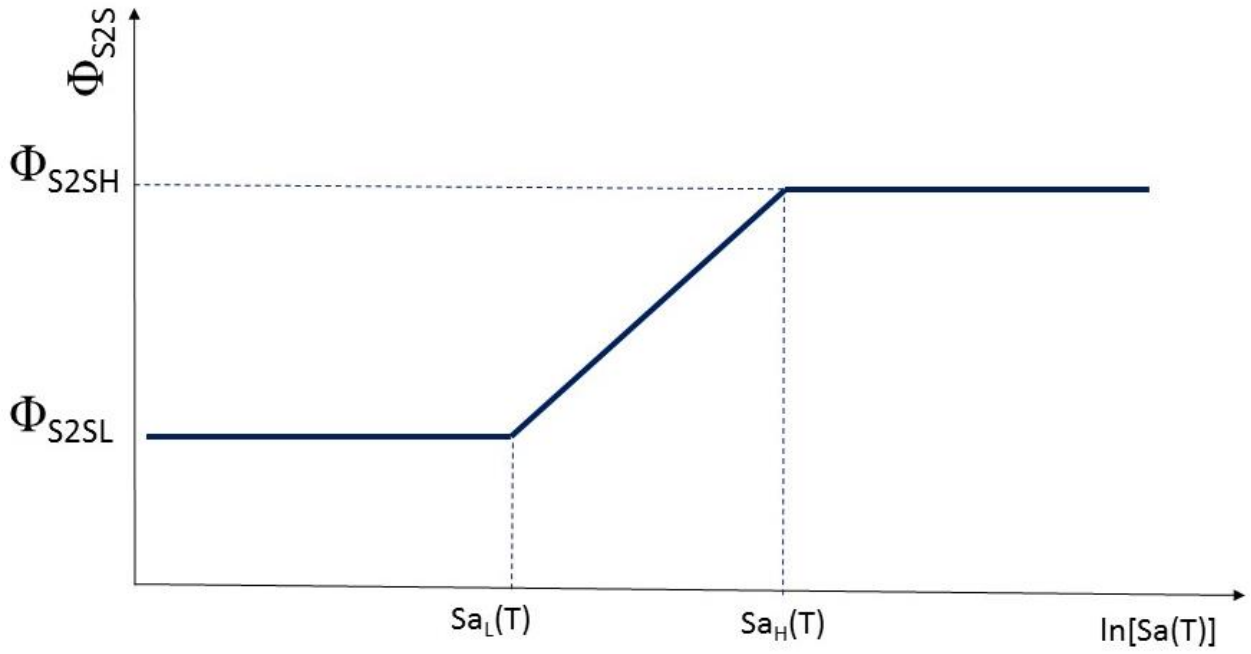

Figure ES.1. Schematic illustration of the parameters defining ϕ_{S2S}, in which the subscript L and H indicate the low and high values; the acceleration on the x-axis is the spectral acceleration obtained applying Eq.(ES.6) or (ES.7) at the same response period for which the surface motion is required

The amplification factors are subject to both upper and lower limits, AF_{max} and AF_{min}, and should be constrained to the specified values if they exceed them. The coefficients f_1, f_2 and f_3 of Eq.(ES.16) for the 2,672 combinations of site amplification zone and response period are listed in the Excel file **V2_Site Amp Functions_*date*.xlsx** .The file also provides the values of AF_{max} and AF_{min}, and the four values defining the site-to-site variability, as illustrated in Figure ES.1: Sa_L, ϕ_{S2SL}, Sa_H, ϕ_{S2SH}; as noted earlier, $\phi_{S2S} \geq 0.2$.

The calculated values of AF using Eq.(ES.16), the tabulated coefficients and the sampling of ϕ_{S2S} are then applied to the spectral acceleration at the reference rock horizon, Sa_{NU_B}, as calculated from Eq.(ES.6) or (ES.7).

For the risk calculations, values of Sa(T) calculated at a given location for different periods, T, must account for the period-to-period correlations of the residuals. The correlation coefficients, which should be applied to all the components of variability, are provided in Table ES.8 and also in the Excel file **V2_Period2Period correlations_*date*.xlxs**. In the table below the values are provided only for periods up to 4 seconds; at 5 seconds, the same

coefficients are assumed to apply as at 4 seconds; the complete set of values is provided in the Excel file.

Table ES.8. Period-to-period correlation matrix for residuals of spectral accelerations

T (s)	0.01	0.1	0.2	0.3	0.4	0.5	0.6	0.7	0.85	1	1.5	2	2.5	3	4
0.01	1.000	0.935	0.897	0.831	0.774	0.721	0.670	0.633	0.587	0.542	0.468	0.460	0.441	0.409	0.328
0.1	0.935	1.000	0.864	0.730	0.647	0.572	0.510	0.468	0.421	0.379	0.318	0.321	0.306	0.286	0.246
0.2	0.897	0.864	1.000	0.883	0.789	0.709	0.637	0.587	0.524	0.472	0.373	0.355	0.337	0.321	0.267
0.3	0.831	0.730	0.883	1.000	0.922	0.841	0.773	0.721	0.661	0.607	0.485	0.453	0.431	0.400	0.307
0.4	0.774	0.647	0.789	0.922	1.000	0.937	0.871	0.821	0.761	0.706	0.575	0.529	0.505	0.467	0.355
0.5	0.721	0.572	0.709	0.841	0.937	1.000	0.954	0.905	0.845	0.793	0.665	0.615	0.592	0.547	0.425
0.6	0.670	0.510	0.637	0.773	0.871	0.954	1.000	0.964	0.912	0.863	0.738	0.684	0.657	0.603	0.493
0.7	0.633	0.468	0.587	0.721	0.821	0.905	0.964	1.000	0.957	0.908	0.786	0.725	0.696	0.632	0.517
0.85	0.587	0.421	0.524	0.661	0.761	0.845	0.912	0.957	1.000	0.966	0.847	0.786	0.753	0.694	0.576
1	0.542	0.379	0.472	0.607	0.706	0.793	0.863	0.908	0.966	1.000	0.905	0.843	0.811	0.752	0.635
1.5	0.468	0.318	0.373	0.485	0.575	0.665	0.738	0.786	0.847	0.905	1.000	0.941	0.907	0.855	0.735
2	0.460	0.321	0.355	0.453	0.529	0.615	0.684	0.725	0.786	0.843	0.941	1.000	0.968	0.914	0.799
2.5	0.441	0.306	0.337	0.431	0.505	0.592	0.657	0.696	0.753	0.811	0.907	0.968	1.000	0.958	0.863
3	0.409	0.286	0.321	0.400	0.467	0.547	0.603	0.632	0.694	0.752	0.855	0.914	0.958	1.000	0.931
4	0.328	0.246	0.267	0.307	0.355	0.425	0.493	0.517	0.576	0.635	0.735	0.799	0.863	0.931	1.000

The median duration of the motion, $D_{S5\text{-}75}$ (in seconds), is predicted by the following equations:

$$\ln(D_{S5-75}) = \ln[F_E(M,\Delta\sigma)] + F_P(R_{epi}) + F_S(V_{S30}) \qquad \text{(ES.17)}$$

The first term is given by the following expression, in which $\gamma = \Delta\sigma/100$, where the stress parameter, $\Delta\sigma$, is expressed in bar:

$$F_E = \max[0.014374\gamma^{\frac{-1}{3}}\exp(0.85093M), 1.0] \qquad \text{(ES.18)}$$

Eq.(ES.18) should be evaluated using three different values of the stress parameter to yield three different models for the duration, as per Table ES.9.

Table ES.9. Stress parameters for duration models in Eq.(ES.18)

Model	$\Delta\sigma$ **(bar)**		
Lower	10		
Central	30		
Upper	M = 2.5, 30	linear interpolation of log($\Delta\sigma$)	M ≥ 4.5, 100

The path scaling is defined by:

$$F_P = 0.72985\ln\sqrt{R_{epi}^2 + 1.706^2} - 0.38985 \qquad \text{(ES.19)}$$

Finally, the site term is:

$$F_S = -0.2246 \ln\left[\frac{\min(V_{S30}, V_1)}{V_{ref}}\right] \quad \text{(ES.20)}$$

where V_1 is 600 m/s, V_{ref} is 368.2 m/s, and V_{S30} is the representative value of the average 30-m shear-wave velocity in each zone, given in Excel file **V2_Vs30 zonation_*date*.xlsx**.

The inter-event standard deviation of the duration model is 0.2 and the intra-event standard deviation is 0.6136, and a total sigma, therefore, of 0.6454. The total epsilon sampled for the duration should be conditional on the total epsilon sampled for the spectral acceleration using the correlation coefficients in Tables ES.10; these correlation coefficients are also provided in the Excel file **V2_GMPEs_*date*.xlsx**. The epsilon to be sampled on the duration is simply the total epsilon on the spectral accdeleration multiplied by the corresponding value from Table ES.10.

Table ES.10. Correlation coefficients for total residuals of duration and Sa(T)

T [s]	**0.01**	**0.1**	**0.2**	**0.3**	**0.4**	**0.5**	**0.6**	**0.7**	**0.85**	**1**	**1.5**	**2**	**2.5**	**3**	**4**	**5**
ρ	-0.45	-0.39	-0.39	-0.39	-0.33	-0.28	-0.24	-0.21	-0.17	-0.13	-0.05	-0.01	0.02	0.05	0.09	0.12

Acknowledgements

First and foremost, our thanks to Jan van Elk who, with assistance from Dirk Doornhof, has provided clear leadership, helpful guidance and continuous support for the work presented herein. Jan provided the conditions that enabled this study to be carried out in a timely fashion by a multi-disciplinary team distributed over several locations. Assistance provided by Jeroen Uilenreef at NAM has also been very useful in several situations.

We are also indebted to Helen Crowley, who is leading the development of the fragility functions for the Groningen risk study, for her very helpful inputs and clear communication regarding the required ground motion and hazard inputs for the fragility derivation and the risk calculations. Similarly, we have benefited from feedback, questions and checks from Stephen Bourne and Steve Oates, who implement the ground-motion and fragility models into their hazard and risk calculation engines. Discussions with Helen, Stephen and Steve, and also with Rui Pinho (the fifth member of the core Hazard & Risk Assessment Team, together with the lead author of this report) from the very beginning of the project have always been constructive, stimulating and informative, and these exchanges of ideas have added great value to the work.

In the development of the V2 GMPEs, the most significant development has been the incorporation of a field-wide model for non-linear site response and many individuals have contributed significantly to this work. Specific mention is due to members of the team at Deltares: Marco de Kleine for descriptions of the surface geology at the recording stations; Ger de Lange and Renée de Bruijn for information regarding the field geology and advice on appropriate geotechnical properties for the Groningen soils; Pim Witlox, Bruno Zuada Coelho, Jonathan Nuttal and Tommer Vermaas for programming STRATA and for running enormous numbers of site response analyses; and Veronique Marges for generating maps and for numerous GIS operations. The Deltares team members also express thanks to Mandy Korff for her role as the liaison with NAM. A great deal of assistance with the site response modelling and analyses was also provided by Ashly Cabas and Julia Baaklini of Virgnia Tech and by Gonzalo Montalva of Universidad de Concepción, Chile. We also gratefully acknowledge the helpful responses from Albert Kottke to various queries regarding STRATA and the helpful discussions with Ellen Rathje at an early stage of the V2 model development. The development of the site response models for the Groningen field also benefited from several discussions with Russell Green at Virginia Tech.

Ewoud van Dedem also played a key role in building the sub-surface velocity model for the field together with Remco Romijn from NAM whose contributions on the deeper velocity model were of critical importance. Remco also played a central role in the selection of the base of the Upper North Sea formation as the reference rock horizon for the site response calculations. We are also grateful to Thomas Piesold from Shell and to Jesper Spetzler from KNMI for help with obtaining coordinates for recent earthquake epicentres and for recording stations in the expanded networks.

The V2 GMPE development work has also benefited from waveform modelling results provided by Ewoud van Dedem of Shell, supported by Sara Minisini and Alexander Droujinine and building on earlier work by Diego di Lazzari, also all at Shell. The ongoing interactions with Ewoud and Sara regarding the influence of the velocity structure of the field on the propagation of seismic waves from the reservoir to the ground surface continue to be valuable and to provide valuable insights. In this regard we have also benefited from discussions with colleagues at ExxonMobil who are performing their own waveform simulations for the Groningen field and the mutual exchange of results with the ExxonMobil Upstream Research team—including Erika Biediger, Will Burnett, Grant Gist, Paul Hector, Darren Pais, Joe Reilly and Ward Turner—as well as their earthquake engineering consultant Ron Hamburger, has proven helpful.

A very special note of gratitude is due to members of the independent review panel established for the development of the Groningen GMPE and site response model. Constructive and useful feedback on the V1 model and the proposed approach for the development of the V2 models was provided by Hilmar Bungum, John Douglas, Jonathan Stewart and Ivan Wong. We are also grateful to Trevor Allen and Bob Darragh for very helpful feedback on the V1 model that they provided in their capacity as peer reviewers for the *Bulletin of the Seismological Society of America*. Our thanks also to Jonathan Stewart for making available the draft version of his new duration prediction equation. John Douglas also sent detailed review comments on the first draft of this report that helped us to improve the presentation and correct several errors.

The full review panel (Gail Atkinson, Hilmar Bungum, Fabrice Cotton, John Douglas, Jonathan Stewart, Ivan Wong and Bob Youngs) participated in a workshop held in London on 27-28 October 2015 to discuss the V2 GMPE and provide potential improvements. The open and constructive discussions at that meeting, and the many suggestions, insights and recommendations made by the panel members during that meeting have greatly enriched our ideas for improving the model. The closing section of the final chapter of the report captures many of the ideas provided by the panel members for further development of the model. We are very grateful to have received this feedback from such an eminent group of experts in this field.

The work presented herein has been presented at different stages in numerous meetings with the Groningen Scientific Advisory Committee (SAC), chaired by Lucia van Geuns, and the Dutch State Supervision of Mines (SodM), as well as observers and advisors to these two bodies. Feedback and questions at these meetings have helped us to develop our justifications for the modelling choices made and to explain and justify our results. We note in particular the comments from Stefan Baisch, Hans de Waal, Hein Haak, Iunio Iervolino, Dirk Kraaijpoel, Annemarie Muntemdam-Bos, Raphael Steenbergen, Karin van Thiennen-Visser, Brecht Wassing and Stefan Wiemer.

1. INTRODUCTION

Gas production in the Groningen field in the northern Netherlands is inducing earthquakes, the largest of which to date was the magnitude 3.6 Huizinge event of August 2012. In response to the induced seismicity, NAM is developing a comprehensive seismic hazard and risk model for the region—which comprises the entire gas field plus a 5 km buffer zone onshore—in order to ascertain the threat to local inhabitants and to design, where necessary, appropriate remedial measures to reduce the risk to acceptable levels.

1.1. Purpose and applications of the GMPEs

The primary objective of the NAM study is currently the development of a risk model that characterises the threat from induced earthquakes to the exposed population in terms of the probabilities of earthquake-induced damage to buildings leading to injury or death. This requires comprehensive modelling of the sequence of steps from production-induced compaction of the gas reservoir through to estimated damage levels in the exposed buildings and the consequent effects on their inhabitants. In broad terms, the risk model, spanning the entire process from production scenarios to casualty estimates, may be viewed as illustrated in Figure 1.1. The first part of the model predicts possible seismicity patterns in terms of the expected numbers and locations of earthquakes of different magnitudes in a given production period. The impact of these potential earthquakes on people is estimated via a model that combines the exposure model (in effect, a database of the building stock), fragility functions for each building type that define the probability of reaching or exceeding a defined damage state under different levels of shaking, and casualty functions that specify the probability of injury to inhabitants within a building experiencing that damage state. The seismicity model is linked to the fragility-casualty models via a ground-motion prediction equation (GMPE), which predicts distributions of specified ground-motion parameters as a function of parameters such as earthquake magnitude, the distance from the earthquake source to the site, and the dynamic characteristics of the site itself. The GMPE links the seismicity and fragility models in the calculation of risk by providing estimates at the location of each exposure element as a result of each earthquake simulated by the seismicity model.

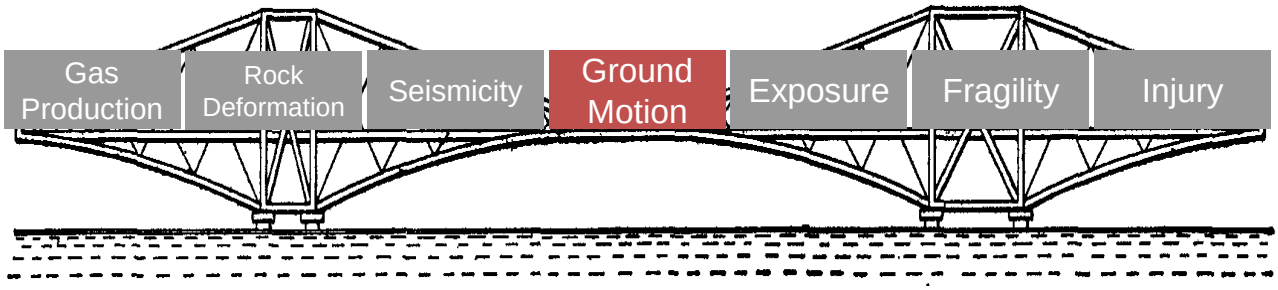

Figure 1.1. Schematic illustration of the full risk calculation process from gas production causing compaction of the field to building damage leading to casualties (*image courtesy of Jan van Elk*)

As the link between the two models, the GMPE must be consistent and compatible with the parameterisation of the seismicity model, which is discussed in Section 2.1. Similarly, the GMPE needs to provide outputs that are consistent with the definitions of the fragility functions, as discussed below in Section 1.3.

The primary purpose of the GMPEs is therefore to serve as the linking element between the seismicity and fragility models in the calculation of risk in the Groningen field. However, the GMPEs will also be used in combination with the seismicity model to generate estimates of the seismic hazard in terms of ground-motion parameters with a specified annual probability of exceedance (for a given production period). Such hazard estimates can be displayed in the form of contour maps for a given ground-motion parameter—such as peak ground acceleration (PGA)—or as acceleration response spectra at specified locations. Such representations of the ground shaking hazard may be useful for the purpose of calibration of seismic design codes such as the draft NPR 9998 (NEN, 2015) which has been produced to guide earthquake-resistant design for structures in the Groningen region. In general, representations of the seismic hazard may be useful for defining seismic actions to be considered in the design of new constructions or the retrofit of existing buildings, although it is more logical to base these directly on risk calculations (*e.g*., Bommer *et al*., 2005; Crowley *et al*., 2012). Such considerations are implicit in the derivation of the seismic design loads and performance requirements in the NPR 9998 document, but in the long-run it is expected that the seismic risk model will allow iterative modelling to directly determine appropriate strengthening levels for existing buildings. In summary, the hazard outputs are viewed as a beneficial by-product of the seismic risk model, but the primary focus—which therefore dictates the requirements of the GMPEs—is the calculation of risk.

1.2. Overview of the GMPE development process

The GMPEs presented in this report are developed for the Version 2 seismic hazard and risk model. The development of seismic hazard models for the Groningen field began following the 2012 Huizinge earthquake and a preliminary model was produced for the Winningsplan submitted in late 2013 (Bourne *et al*., 2014; Bourne *et al*., 2015). One of the outcomes of that application for a continued gas production license was the development of a comprehensive probabilistic risk assessment as part of the next Winningsplan due for submission on 1st July 2016. The work on extending the initial seismic hazard model to a full probabilistic risk model began in April 2014 with snapshots of the model presented for review and evaluation at six-monthly intervals. The first complete risk model—dubbed Version 0, or V0—was presented in October 2014, and this was superseded in April 2015 by the V1 model. The current work is focused on the V2 seismic risk model, which will be presented in October 2015 and which is expected to be the basis for the 2016 Winningsplan. The changes and improvements in the models from V0 to V1 were substantial and potentially even greater modifications will be implemented in the V2 model. Refinements to the V2 model will be made between November 2015 and early 2016, in the light of feedback and sensitivity analyses, but given the time required to prepare the Winningsplan submission, it is not envisaged that a substantially different V3 model will be produced in April 2016. This situation has made it very important to identify the most important requirements for the V2 GMPEs.

For the 2013 Winningsplan, GMPEs were developed for the prediction of PGA and peak ground velocity (PGV) as a result of induced earthquakes in the Groningen field. The equations were modified versions of the GMPEs derived using strong-motion data from Europe, the Mediterranean and the Middle East by Akkar *et al*. (2014a), hereafter ASB14. The equations using hypocentral distance, R_{hyp}, were selected, and applied with an assumed field-wide 30-metre shear-wave velocity, V_{S30}, of 200 m/s and the assumption of normal faulting. The coefficients of the equations were modified below a certain magnitude—**M**4.2 for PGA, **M**3.8 for PGV—to fit the peak motions from 40 accelerograms obtained from 8 earthquakes by the KNMI network. The aleatory variability for the small-magnitude extension, represented by the standard deviation (sigma) of the residuals, was assumed to be the same as that associated with the original equations. These preliminary GMPEs are described as part of the 2013 hazard model in Bourne *et al*. (2015). For the Version 0 hazard and risk model, an additional 14 records were available from the **M**3.0 Leermens earthquake of February 2014. A very simple residual analysis suggested that the additional data did not warrant a modification of the 2013 GMPE, for which reason it was decided to retain those PGA and PGV equations for the Version 0 hazard and risk models (Bommer & Dost, 2014). The residual analyses did show, however, that the models did not fit the data well at short epicentral distances, which was concluded to be a consequence of the functional form of the ASB14 equation and specifically the use of a fixed value for the near-source saturation term at all magnitudes. The addition of the Leermens records expanded the available dataset but not sufficiently to allow direct calculation of the aleatory variability.

V0 GMPE

The V0 GMPEs were calibrated to local recordings of ground motion in the small-magnitude range and followed patterns inferred from recordings of tectonic earthquakes in the larger magnitude range, without any confirmation of the applicability of the latter to Groningen. Moreover, the equations were only developed for PGA and PGV, and were associated with the large sigma values obtained from regression analysis using a heterogeneous database from Europe and the Middle East. One potential merit of the V0 GMPEs was the inclusion of site amplification terms based on the time-averaged shear-wave velocity over the uppermost 30 m at the site (V_{S30}) and the inclusion of non-linear soil response in these terms. However, the equations were applied with a constant value of V_{S30} (200 m/s) over the entire field, which therefore ignored any spatial variation in the ground conditions; although subsequent work has suggested that 200 m/s was a good estimate of the average value for the study area the actual values vary considerably (Kruiver *et al*., 2015). In addition to these shortcomings, the non-linear site amplification functions were empirically derived from ground-motion recordings in Japan and Europe (Sandıkkaya *et al*., 2013) without any calibration to Groningen conditions. Another important feature of the V0 GMPEs was that they only considered epistemic uncertainty in the ground-motion predictions, which will inevitably be large for magnitudes above the largest recorded event of **M**3.6, in a very crude manner. Rather than providing best estimate predictions accompanied by alternative models to capture the range of uncertainty, single equations were produced for PGA and PGV. Consequently, these tended towards being conservative estimates—both in terms of median predictions and sigma values—by adopting models derived from recordings of tectonic earthquakes.

V1 GMPE

The V1 GMPEs addressed several of the shortcomings in the V0 equations, while consciously leaving one specific feature (the site amplification functions) to be improved in the V2 development stage when the required field information would become available. The most fundamental difference with regards to the V0 model was that rather than extrapolate a GMPE derived from tectonic earthquakes to match local recordings in the small-magnitude range, a model calibrated to the Groningen database—which was expanded relative to that used in adjusting the V0 equations—was extrapolated to larger magnitudes. The Groningen database was used to constrain both the median predictions and estimates of the sigma model, and three alternative models were generated to capture the epistemic uncertainty, which grows with increasing earthquake magnitude and hence greater extrapolation from the data (Figure 1.2). The V1 GMPEs were produced for PGA and for response spectral ordinates at a few oscillator periods (0.2, 0.5, 1.0 and 2.0 seconds) as required for the fragility functions. While a positive development, the limited number of response periods for which the full GMPEs were developed imposed two limitations on the development of the V1 fragility functions, the first being that all building typologies needed to be represented by one of the five selected periods (with PGA assumed equal to the spectral acceleration at 0.01 seconds), which in some cases represented a poor approximation to the dynamic characteristics of the buildings. The second limitation, directly related to the first, was that response spectral shape became an important parameter, requiring formulation of the fragility functions to include magnitude as a surrogate for this feature of the ground motions. This in turn precluded the explicit modelling of the influence of duration on the structural response, even though it is expected to be an important factor in the damage experienced by unreinforced masonry buildings (*e.g*., Bommer *et al*., 2004). The V1 GMPEs are documented in detail in Bommer *et al*. (2015a) and summarised in Bommer *et al*. (2016).

The most important weakness of the V1 GMPEs relates to the modelling of site response. Rather than using an assumed value of a proxy such as V_{S30} and imported site amplification functions, a network-average site amplification term was derived from the recordings and then used in forward modelling to generate the predictive equations. One shortcoming of this approach is that it assumes that the sampling of the dynamic characteristics at the recording station locations is a reasonable approximation to the average amplification functions across the entire field. To some extent this is likely to be a conservative assumption since most of the records were obtained by instruments located in the north of the gas field where softer soils are encountered than in the south. However, the model is limited in not capturing the spatial variation of ground conditions. The most serious deficiency in the model, however, is the failure to account for non-linear site response. Given the weak levels of motion recorded to date, it is likely that the inferred amplification function is a reasonable estimate of the average linear site response term across the recording network. However, when extrapolated to larger magnitudes, the soils would be expected to respond non-linearly to the higher amplitudes of acceleration propagating upwards from the underlying rock, leading to reduced surface accelerations. Consequently, it can be assumed with confidence that the V1 GMPEs are conservative when applied for larger magnitudes and short distances, especially the upper branch (Figure 1.2).

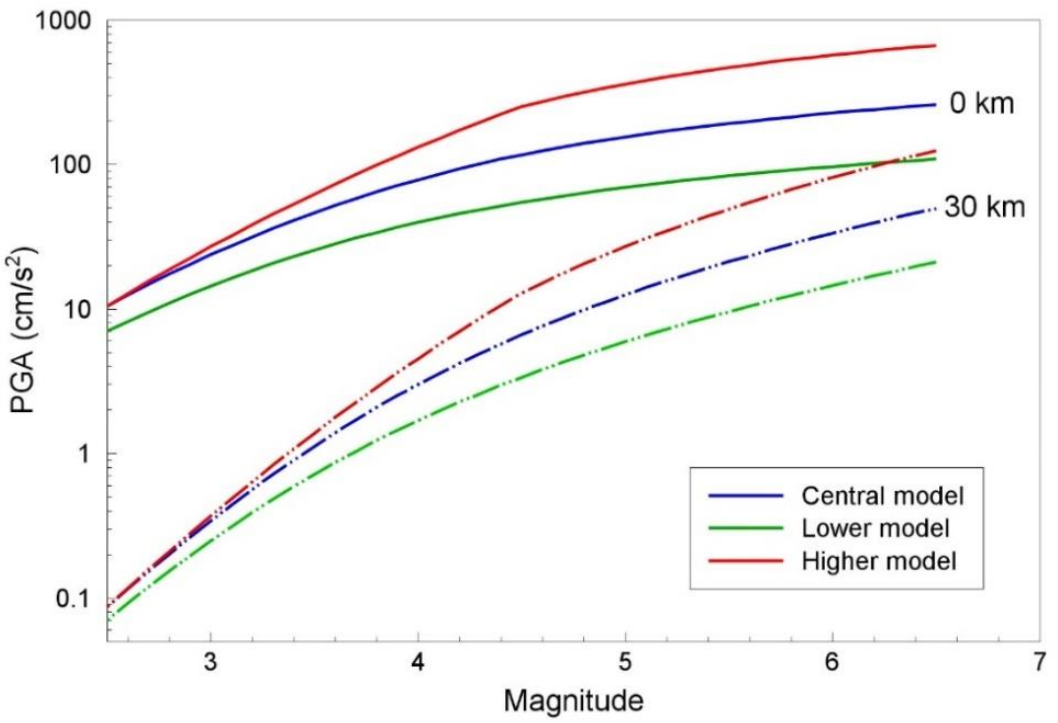

Figure 1.2. Median PGA predictions from V1 GMPEs as a function of magnitude at two distances

V2 GMPE

The single most important feature of the V2 GMPE development with respect to the V1 equations is the explicit inclusion of field-specific non-linear site amplification functions. Other improvements embodied in the V2 GMPEs include the generation of predictive equations for a much larger number of response periods, as discussed in the next section. Table 1.1 summarises the developmental stages with regards to the GMPEs for horizontal spectral accelerations.

Table 1.1. Key features of the three phases of Groningen GMPE development

GMPE Feature	Version 0	Version 1	Version 2
Predicted parameters	PGA, PGV	Sa(T) for 5 periods	Sa(T) for 16 periods
Sigma model	Adopted from ASB14	Groningen-specific	Groningen-specific
Epistemic uncertainty	Single model	Three alternatives	Three alternatives
Site classification	V_{S30} = 200 m/s	Field-wide constant	Zonation based on amplification factors
Site amplification	ASB14 model	Network average, linear extrapolation	Groningen-specific, non-linear soil response
Period-to-period correlations	n/a	Used Akkar *et al*. (2014b)	Uses Akkar *et al*. (2014b)
Components	Horizontal geometric mean	Horizontal geometric mean	Horizontal geometric mean and arbitrary; component-to-component ratios

1.3. GMPE requirements for fragility functions and risk calculations

Structural sensitivity analyses conducted for the early development of the V2 fragility functions explored which intensity measures (IMs) would be efficient predictors of the maximum displacement experienced by typical structures in the Groningen field, a response parameter that in turn can be related to damage. The spectral acceleration at the fundamental vibration period of the structure was found to be an efficient IM, in terms of being able to predict the maximum displacement of the structures with low dispersion. Additional analyses were conducted to establish whether this IM was also sufficient with respect to magnitude, distance and a measure of ground-motion duration; sufficiency would imply that including additional parameters would have no effect in terms of reducing the dispersion in the predictions. The spectral acceleration, Sa(T), was found to be sufficient with respect to magnitude but not with respect to distance or duration, the latter being measured using the significant duration definition and the interval of 5-75% of the total Arias intensity, I_A, which is referred to hereafter as $D_{S5\text{-}75}$. Consequently, the fragility functions will be based on Sa(T) with the possibility of slightly improved constraint by extending this to a vector prediction of Sa(T) and $D_{S5\text{-}75}$.

For the primary IM of Sa(T), there are two decisions to be made. The first regards the appropriate range of response periods to be covered by the equations and an appropriate sampling within this range, the second the component definition. Regarding the first issue, whereas the greatest flexibility for the development and application of the fragility functions would be provided by generating the GMPEs for Sa(T) at a large number of response periods, there are issues of computational effort—with regards to the GMPE derivation and to the execution of the risk calculations—that make it advantageous to limit the numbers of response periods explicitly modelled. Figure 1.3 shows a histogram of yield periods of vibration for the Groningen building typologies; this information is indicative since the capacity curves for the buildings are subject to updating as the structural modelling work proceeds, but it nonetheless gives a useful indication of the periods that should be covered. The final range needs to account for the fact that at some stage it may be desirable to estimate risk in terms of lower (pre-collapse) damage states, which would point to shorter response periods, and the fact that those implied in the final fragility functions might be slightly larger than these yield periods (to account for period elongation after damage).

The motivation for increasing the number of oscillator periods is primarily to provide greater flexibility for the derivation of the fragility functions but also to allow generation of complete response spectral shapes. For the latter, GMPEs often provide coefficients and sigmas at a large number of response periods—often sampled at regular intervals in log-space—to provide smooth spectral shapes; for example, Akkar *et al.* (2014a) provided equations at 62 oscillator periods between 0.01 and 4.0 seconds (in the electronic supplement; a subset of 18 of these were presented in the paper itself). The sampling of periods in log-space tends to be particularly dense at shorter periods, which allows for clear definition of the spectral peak and the shape of the spectra at high oscillator frequencies. For the Groningen risk model, we do not necessarily require such dense sampling for two reasons: one is that short periods (< 0.15 s) are of little relevance to the structural response of buildings in the

Groningen region, and the second is that the very soft soil conditions across most of the field lead to spectral shapes that peak at longer periods (> 0.2 s).

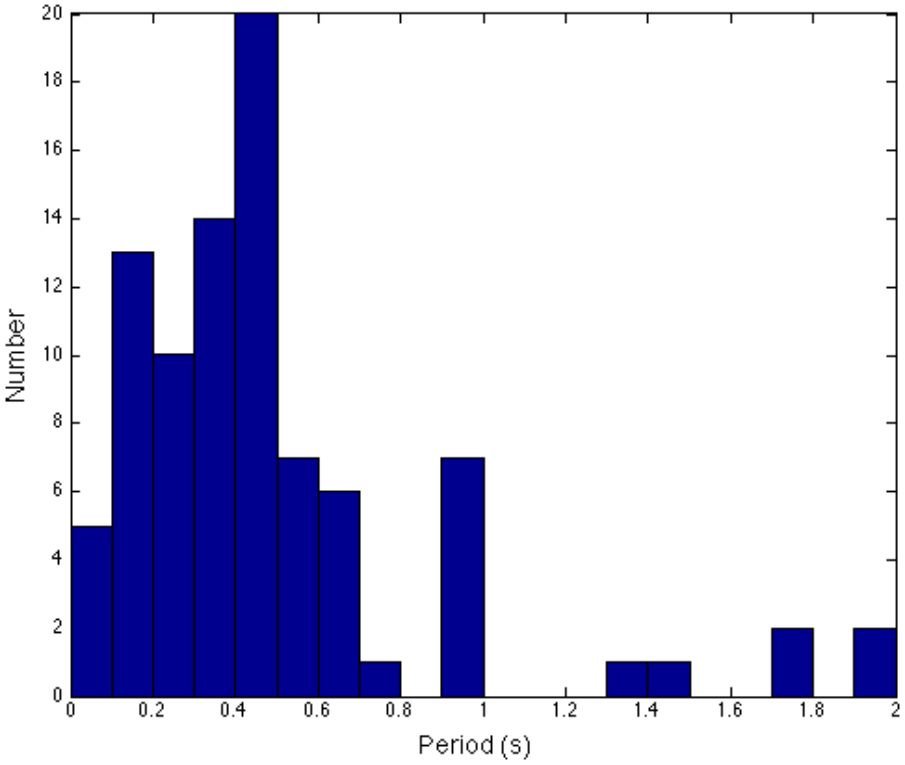

Figure 1.3. Histogram of yield vibration periods for the 89 building typologies defined for the Groningen exposure database (*image courtesy of Helen Crowley*)

There are, however, two considerations when selecting target response periods for the models. In addition to the final surface predictions that will be used to link the hazard model to the fragility functions, there is the intermediate step of the reference rock motions, which correspond to a much stiffer horizon at which the spectral peak is likely to occur at much shorter periods (where the influence of the kappa parameter—which is effectively a high-frequency filter, as explained in Sections 4.1 and 5.2—is most pronounced). For this reason, two sets of target periods are defined, one for the simulations at the reference rock horizon (see Section 2.3) and another for the final predictions at the ground surface, with the latter being a subset of the former. The inclusion of additional periods in the rock simulations is not onerous in terms of computational expense and this expanded list of target periods means that the information will be available if it is subsequently found that there are gaps to fill in the surface predictions. Table 1.2 summarises the proposed 71 target periods, with those highlighted in bold being the subset of 16 for which full surface predictions will be generated.

The second key decision required with respect to the modelling of the horizontal response spectral acceleration is the component definition to be employed. For the V1 GMPEs, the definition used was simply the geometric mean of the two horizontal components, which is the most widely-used definition, although there are several subtle variations of this definition (Boore *et al*., 2006; Boore, 2010).

Table 1.2. Target response periods for reference rock simulations and for development of full GMPEs for surface motions (highlighted, bold)

Period (s)	Frequency (Hz)	Period (s)	Frequency (Hz)
0.01	**100.000**	0.75	1.333
0.02	50.000	0.8	1.250
0.03	33.333	**0.85**	**1.176**
0.04	25.000	0.9	1.111
0.05	20.000	0.95	1.053
0.075	13.333	**1**	**1.000**
0.1	**10.000**	1.1	0.909
0.11	9.091	1.2	0.833
0.12	8.333	1.3	0.769
0.13	7.692	1.4	0.714
0.14	7.143	**1.5**	**0.667**
0.15	6.667	1.6	0.625
0.16	6.250	1.7	0.588
0.17	5.882	1.8	0.556
0.18	5.556	1.9	0.526
0.19	5.263	**2**	**0.500**
0.2	**5.000**	2.1	0.476
0.22	4.545	2.2	0.455
0.24	4.167	2.3	0.435
0.26	3.846	2.4	0.417
0.28	3.571	**2.5**	**0.400**
0.3	**3.333**	2.6	0.385
0.32	3.125	2.7	0.370
0.34	2.941	2.8	0.357
0.36	2.778	2.9	0.345
0.38	2.632	**3**	**0.333**
0.4	**2.500**	3.2	0.313
0.42	2.381	3.4	0.294
0.44	2.273	3.6	0.278
0.46	2.174	3.8	0.263
0.48	2.083	**4**	**0.250**
0.5	**2.000**	4.25	0.235
0.55	1.818	4.5	0.222
0.6	**1.667**	4.75	0.211
0.65	1.538	**5**	**0.200**
0.7	**1.429**		

For derivation of the V2 fragility functions, however, there may be advantages in adopting the arbitrary component of motion. This issue has been considered in detail by Dr Helen Crowley—who leads the fragility development work—and discussed with the GMPE development team; in the following text we briefly summarise these considerations and the final decisions in this regard.

The first point to note is that, provided consistent definitions are used for the hazard and fragility, the probabilistic risk assessment should be the same regardless of the definition of spectral acceleration, with an increased dispersion either being estimated on the side of the

hazard (when the arbitrary component definition is used) or on the side of the fragility (when the geometric mean is used). The drawback of the latter is that more dynamic analyses are required to predict the dispersion with a given level of confidence, although this should not necessarily restrict the choice of spectral acceleration to the arbitrary component, given the simplicity of the structural models currently being used. The V2 fragility models for the building typologies in Groningen will be developed through non-linear dynamic analyses of equivalent single-degree-of-freedom (SDOF) systems. Given that a number of the typologies have very different stiffness and strength in their two orthogonal axes, SDOF systems for each direction will be calibrated, and fragility functions in each direction of the building will be developed.

In order to develop the V2 fragility functions in terms of the geometric mean spectral acceleration at a given period of vibration, it would be necessary to associate the nonlinear response of the SDOF (*e.g.*, drift) obtained from a single component of the ground motion against the geometric mean spectral acceleration of the two components of ground motion. As noted above, this will result in higher dispersion in the response, given the spectral acceleration at the selected period of vibration (which is the selected IM), as the response will be plotted using the geometric mean response spectrum of the two components, rather than the IM from the response spectrum of the component used in the analysis. In this case, the risk engine would need to estimate the geometric mean significant duration and the geometric mean spectral acceleration for the period of vibration defined in each direction of the building using period-to-period correlation of the geometric mean residuals, and the probability of collapse would be defined by the direction with the highest probability of collapse.

Figure 1.4 shows an example of typical response spectra of two components of ground motion, and the geometric mean response spectrum. As can been seen in this figure, the spectra of the two horizontal components cross at various periods across the spectrum. The recordings from the Groningen field to date, however, show a strong polarization, as shown in Figure 1.5. In order to ensure that this polarization is accounted for when modelling the response of the SDOF systems, modifications to the records selected for the dynamic analyses would probably need to be made, to ensure that the component-to-component ratios are consistent with those found in the Groningen field.

In order to develop the V2 fragility functions in terms of the arbitrary component of hazard, the nonlinear response of the SDOF (*e.g.*, drift) obtained from a single component of the ground motion would be plotted against the spectral acceleration at the given period of vibration for that component. The risk engine would need to estimate the arbitrary component spectral acceleration for the period of vibration defined in each direction of the building, as well as the arbitrary component significant duration, and the probability of collapse (for the structure) would be defined by the direction with the highest probability of collapse. The period-to-period correlation of the residuals of the two horizontal components of ground motion would be needed to estimate the demand in each direction of the building (*e.g.*, Baker & Cornell, 2006a).

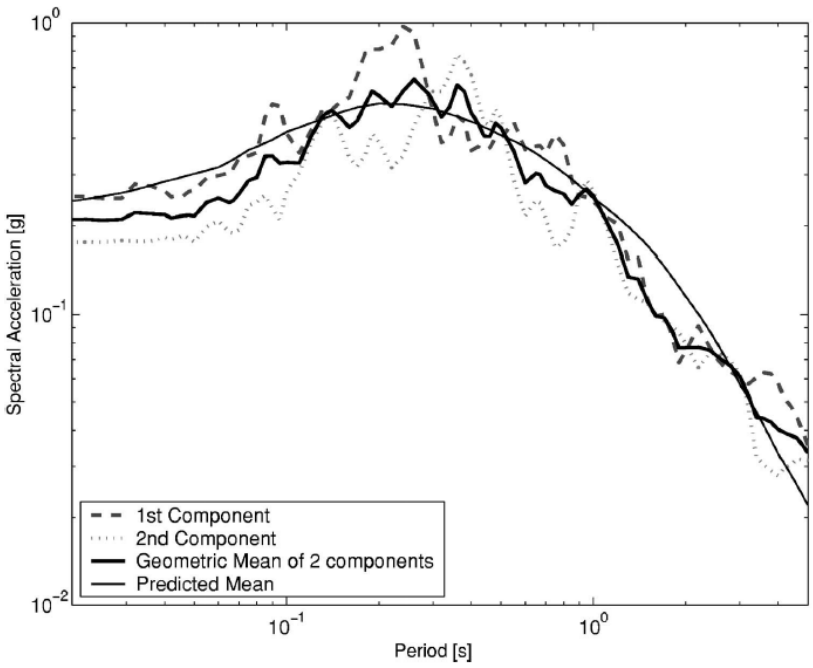

Figure 1.4. Response spectra for two horizontal components of ground motion (*dashed and dotted line*), the geometric mean of the response spectra (*bold line*) and the predicted mean from a GMPE (*thin line*) (Baker & Cornell, 2006a)

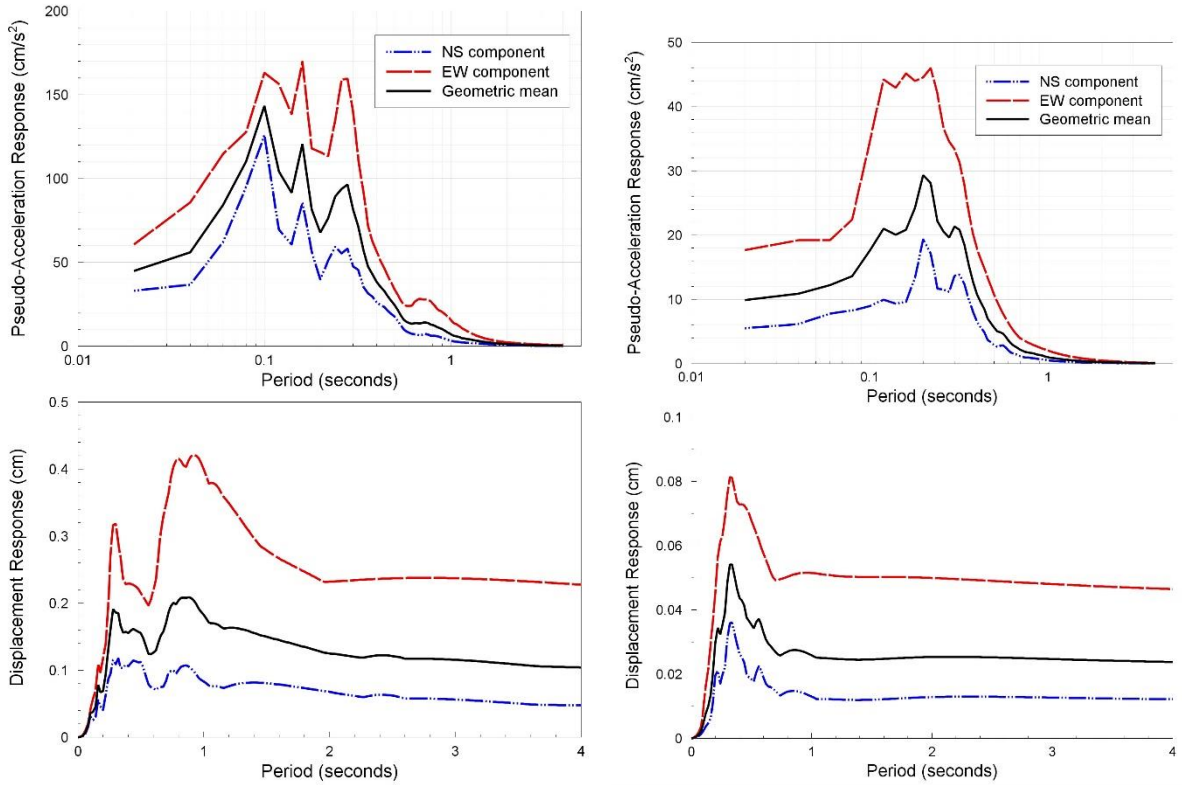

Figure 1.5. Example response spectra from the Groningen field, illustrating the strong polarisation in the horizontal components. *Upper*: pseudo-acceleration response spectra; *lower*: displacement response spectra

Defining the V2 hazard in terms of the geometric mean component would have the advantage that estimates of the hazard for the Groningen field would be directly comparable with previous models. However, the records used for the development of fragility functions may need modification to ensure that their component-to-component ratios are consistent with those found in the Groningen field. Furthermore, there is uncertainty regarding the physical meaning of the geometric mean significant duration.

The use of an arbitrary component GMPE for the V2 hazard assessment would appear to lead to higher levels of hazard as compared to previous models (V0 and V1), due to the increased aleatory variability in the GMPE. Although comparison of the models would not be valid, as the component of spectral acceleration would have changed from V0/V1 to V2, such comparisons would undoubtedly be made nonetheless without attention to appropriate caveats. For this reason it would be prudent to continue to develop a GMPE in terms of the geometric mean spectral acceleration, for the hazard assessment.

For the development of fragility functions, the use of the arbitrary component spectral acceleration has the advantage that fewer non-linear dynamic analyses are needed to predict the dispersion with a given level of confidence. Furthermore, the component-to-component ratios would not need to be explicitly considered when selecting the records.

Hence, for the V2 hazard and risk assessment it was decided that a GMPE for geometric mean spectral acceleration would be developed for the hazard model, whilst GMPEs for arbitrary component spectral acceleration, together with a model of the correlation of the residuals between two horizontal components in perpendicular directions, would be developed for the risk model. In essence, the only difference between the geometric mean and the arbitrary components is in the sigma values, with the median predictions expected to be identical. Therefore, in developing the sigma model (Chapter 9) the component-to-component variability is also required.

As noted above, period-to-period correlations are also required. For the V1 fragility and risk calculations, the model of Akkar *et al*. (2014b) derived from European strong-motion data was used; in the long-run, a Groningen-specific model is preferred but for the V2 model we retained the same correlations proposed by Akkar *et al*. (2014b), as discussed in Section 11.3..

Although it is not envisaged that the vertical components of motion will be explicitly included in the fragility functions or the risk calculations, it is believed that some of the structural typologies encountered in the Groningen field may be sensitive to vertical motions. For this reason, structural modelling may require definition of the vertical response spectrum and to this end a Groningen-specific model for the vertical-to-horizontal response spectral ratios is developed (Section 11.4).

As noted previously, the fragility functions are likely to be defined in terms of both spectral acceleration, Sa(T), and the significant duration, $D_{S5\text{-}75}$, which then requires the vector prediction of these two parameters. In essence, this means developing a model for the

prediction of durations conditional on the predictions of Sa(T), which is also addressed in this report.

1.4. Overview of the report

From the discussions in the previous sections it may be concluded that the basic requirement for the V2 hazard and risk model is a suite of GMPEs for the prediction of both the geometric mean and arbitrary component of 5%-damped response spectral acceleration at 16 oscillator periods (Table 1.2). The GMPEs should be well calibrated to the seismological, geological and geotechnical conditions encountered in the Groningen field, and most specifically they should reflect the non-linear dynamic response of near-surface layers across the study area. An overview of how the basic models are developed is given in Chapter 2, which focuses in particular on the scheme for predicting motions at a reference rock horizon and then transferring these rock motions to the ground surface via non-linear site amplification factors. Chapter 2 also includes a brief discussion of the issue of spatial correlation of ground motions.

Chapter 3 then describes the characteristics of the Groningen ground-motion databases used in the derivation of the V2 GMPEs. Chapter 4 discusses the dynamic characterisation of the recording station sites and the development of linear site amplification factors that are used to translate the surface motions to the reference rock horizon. Chapter 5 describes the inversion of the motions at the rock horizon to estimate source and path parameters for Groningen, together with a field-wide amplification factor for the reference rock elevation. In Chapter 6, the parameters obtained from the inversions are applied in stochastic simulations to generate spectral accelerations at the rock horizon, to which functional forms are fitted in order to obtain parametric GMPEs for the median motions at this level. The residuals of the recorded motions deconvolved to the reference rock horizon are calculated to inform the development of the sigma model (Chapter 10).

Chapters 7 to 9 are focused on the development of the non-linear site amplification factors that are applied in conjunction with the rock GMPEs to obtain median ground-motion predictions at the surface. Chapter 7 describes the development of layer models for the profiles from the reference rock horizon to the ground surface across the entire field, and Chapter 8 describes the site response analyses performed using these profiles. Chapter 9 explains the aggregation of the calculated site amplification factors into zones for which a single representative site amplification function may be adopted.

Chapter 10 explains the development of the sigma model for the GMPEs at the ground surface, for both the geometric mean and arbitrary components of motion. Chapter 11 then summarises the current models and compares the predictions with those from the V1 GMPEs. Chapter 11 also discusses additional features required for various applications, including period-to-period correlation functions and vertical-to-horizontal response spectral ratios.
Chapter 12 describes the derivation of improved GMPE for the significant duration of ground shaking in the field. Through the development of a correlation function between the residuals

of duration and of spectral accelerations, a vector model is developed through which the duration conditioned on the spectral acceleration is predicted.

Chapter 13 discusses potential improvements to the ground-motion model that will be explored prior to finalisation of the models for the 2016 Winningsplan. These improvements include expected enhancements to come from expanding the ground-motion database, incorporating the measured V_S profiles at the recording stations, and potentially also the use of borehole recordings for partial verification of the site response models. The exploration of a more appropriate definition of duration for the Groningen motions and the use of consistent predictions of duration in all elements of the hazard and risk modelling are also discussed. Chapter 13 concludes with a list of planned sensitivity studies and potential refinements to the preliminary V2 GMPEs for spectral accelerations presented herein.

In addition to the 13 chapters presenting the derivation of the V2 GMPEs for response spectral accelerations and durations, there are several appendices, most of which contain plots related to different elements of the model development process. In order to avoid an excessively large report, detailed documentation on various aspects of the work is provided in supplementary reports that are referenced in this report. Although this report is intended to provide sufficient information to serve as a stand-alone narration of how the V2 GMPEs were developed and their characteristics, additional detail can be found in these supplementary reports and papers, which are listed here for convenience:

- Overview paper on the seismic hazard model developed for the 2013 Winningsplan, which also includes the V0 GMPE (Bourne *et al*., 2015)
- Report on the derivation of the V1 GMPEs (Bommer *et al*., 2015a)
- Summary paper on V1 GMPEs (Bommer *et al*., 2016)
- Deltares report on Groningen geological model for site response (Kruiver *et al*., 2015)
- Summary report on selection of record processing procedures for accelerograms of Groningen earthquakes (Ntinalexis *et al*., 2015a)
- Comprehensive report on V2 ground motion database (Ntinalexis *et al*., 2015b)

Additionally, there are a number of electronic supplements containing the coefficients of equations and coordinates of the field zonation required for the full implementation of the model. These electronic supplements are identified in the Executive Summary.

2. OVERVIEW of V2 GMPEs

This Chapter provides a general overview of the V2 GMPEs for response spectral accelerations, including the form of the equations and the procedure established for their derivation, details of which are provided in subsequent chapters. The chapter closes with a brief discussion of the choice not to model spatial correlations in the current phase of development of the hazard and risk models.

2.1. Functional form of the GMPEs and explanatory variables

The V1 GMPEs were derived as a function of only moment magnitude, **M**, and epicentral distance, R_{epi}. There was no explicit term for site response since the model was calibrated to an assumed field-wide linear amplification function (Bommer *et al*., 2015a). There was no motivation to include any other terms in the equations since none of the other parameters commonly used in modern GMPEs could be defined in a way that would be expected to refine the predictions. In terms of style-of-faulting, for example, it is known that ruptures in the Groningen field may be pure normal, strike-slip or an oblique combination of these mechanisms, but fault plane solutions are not available for most of the earthquakes in the database. Including a parameter such as depth-to-top-rupture, Z_{TOR}, would not improve the predictive power of the model since all earthquakes are assumed to occur within the gas reservoir at a depth of about 3 km (although it must be recognised that there is no clear model regarding the expected geometry and vertical extent of the fault ruptures associated with larger earthquakes).

The most significant difference in the V2 GMPE development is the inclusion of spatially-varying non-linear site amplifications to be applied to motions predicted at a reference rock horizon. The equations for predicting motions at the reference rock horizon will also be calibrated to a single field-wide amplification factor corresponding to the path from the gas reservoir to that elevation. Consequently these equations are expected to have a very similar functional form as the V1 GMPEs and be functions only of magnitude and distance. However, there are three potential improvements to the formulation of the GMPE for median predictions that are explored in the V2 development:

1. The adoption of a segmented geometrical spreading model rather than a single function applicable over the full range of distances, in order to capture more faithfully the patterns resulting from the velocity structure above the reservoir and particularly the presence of the high-velocity Zechstein salt layer and even higher velocity anhydrite layers within the Zechstein. The form of the geometrical spreading function will be informed by full waveform simulations (Section 5.3).
2. The inclusion of an explicit term to represent the anelastic attenuation in this very low-Q environment; this was not done in the V1 GMPEs for simplicity and also because of the relatively short distances over which the equations are applied. If the segmented geometrical spreading function discussed in the previous point is adopted then an

option will be to add an anelastic attenuation term that applies only in conjunction with the more distant spreading function.

3. The use of a distance metric defined relative to extended fault ruptures rather than to point sources. As part of the V1 development work, GMPEs were derived as functions of both R_{epi} and R_{JB} (the latter being the horizontal distance to the closest point on the surface projection of the fault rupture) and sensitivity analyses were performed on calculated risk using the R_{epi}-based GMPE in conjunction with a source model defining hypocentres and the R_{JB}-based GMPE in conjunction with a source model assigning earthquakes to ruptures on mapped faults. At short distances and especially for larger magnitudes, the R_{JB}-based model predicts lower median values and has a lower sigma value but the highest motions affect a larger area than in the case of the point sources. The former effect was found to be dominant, with the R_{JB}-based model yielding lower estimates of both local personal risk (LPR) and group risk (GR) for Groningen, as shown in Figures 2.1 and 2.2 respectively. Given the higher predicted median values and higher sigmas associated with the R_{epi}-based model, higher LPR estimates were to be expected. For the GR metric, the fact that the extended ruptures associated with larger earthquakes lead to larger areas of strong shaking (and hence more buildings being shaken) turns out to be a lesser effect than that of the lower predicted motions. At the same time it should be noted that for both LPR and GR the differences were not very large even though the calculations were performed using a single estimate of the maximum magnitude (Mmax) of 6.5; as this abrupt cut-off is replaced by a distribution of potential Mmax values, including lower estimates of the upper limit on earthquake size, it can be expected that the differences in risk estimates using the two approaches will be reduced. The final choice is to use only R_{epi} at this stage, based on balancing the computational efficiency of the R_{epi}-based model that comes at the expense of slightly conservative estimates with the increased accuracy obtained with R_{JB}-based model that is computationally more demanding. This may be re-visited for subsequent sensitivity analyses and refinements, but for the initial development of the V2 GMPEs we proceed with epicentral distance knowing that it is not leading to underestimation of the risk in terms of either of the metrics in consideration.

The final form and parameterisation of the reference rock GMPE is presented in Section 6.3. If we designated the predicted spectral acceleration at a given period as Sa(T) and the corresponding median value at the reference rock horizon as Sa_{ref}(T), then the general form of the GMPE can be written as follows:

$$\ln[Sa(T)] = \{\ln[Sa_{ref}(T)] + \delta B + \delta WS\} + \ln[AF_j(T)] + \delta S2S_j \qquad (2.1)$$

where $AF_j(T)$ is the median amplification function for the spectral acceleration at period T for the j^{h} zone, and $\delta S2S_j$ is the variability of the zone-specific amplification function. In terms of the variability in the predictions, the term δB is the earthquake-to-earthquake residual (*i.e.*, a random sample from the distribution of between-event variability) and δWS is randomly sampled from the distribution of single-station within-event variability.

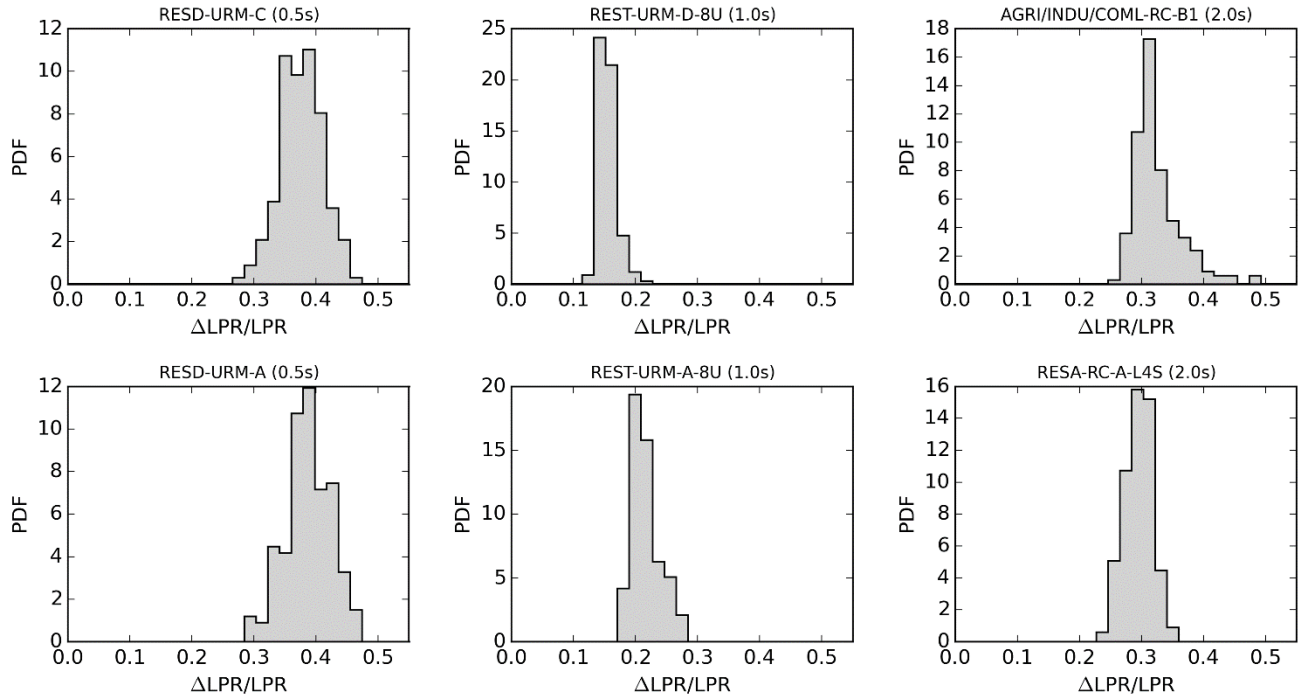

Figure 2.1. Histograms of the differences in calculated results of local personal risk (LPR) using point-source and extended-source simulations for the earthquakes in the risk model, for 6 representative buildings (the natural periods of which are indicated in parentheses) from the exposure database (*Courtesy of Stephen Bourne and Helen Crowley*)

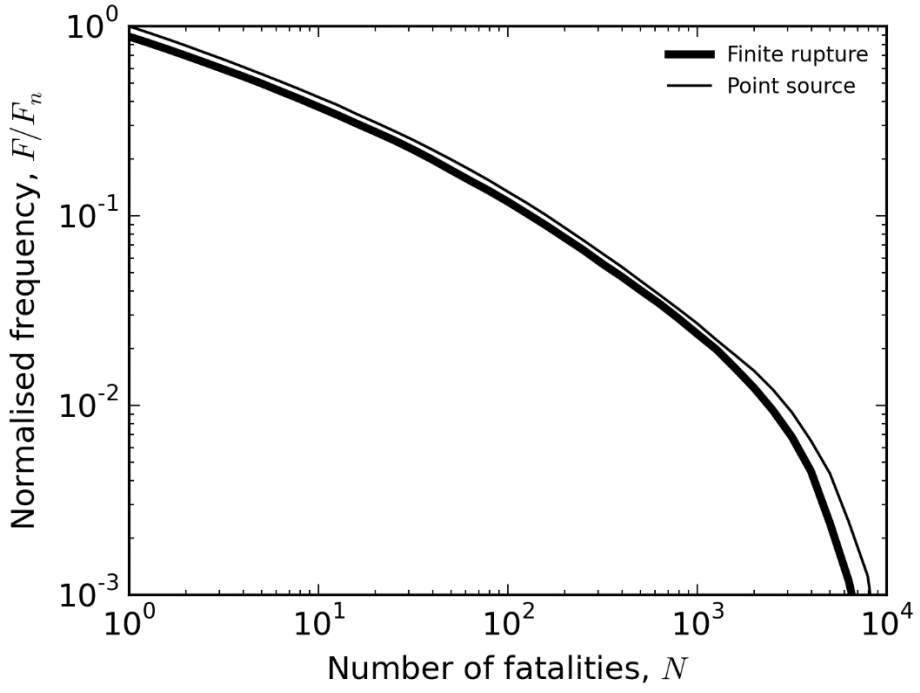

Figure 2.2. Comparison of normalised group risk (GR) calculated over the field for the 6 building classes shown in Figure 2.1 (*Courtesy of Stephen Bourne and Helen Crowley*)

In Eq.(2.1) both δB and δWS are assumed to be zero-mean Gaussian random variables with standard deviation τ and Φ_{ss}, respectively. These two components of variability will have distributions that are constant across the field. The term $\delta S2S_j$ is the randomly sampled

residual from the site-to-site variability for zone *j*, which is assumed to be a zero-mean Gaussian random variable with standard deviation Φ_{S2Sj}; for more background on these terms and the decomposition of the ground-motion variability, see Al Atik *et al*. (2010) and Rodriguez-Marek *et al*. (2014). The full development of the variability model is discussed in detail in Chapter 10, but herein some general comments on the formulation in Eq.(2.1) are appropriate.

As noted previously, the ultimate objective is to develop GMPEs that include non-linear site amplification functions for the Groningen field. The aim is to condition the functions at each response period on the spectral acceleration at the same period in the underlying reference rock, which is preferable to the more widely-used approach of conditioning the non-linear response on PGA, as recommended by Bazzurro & Cornell (2004a) and implemented by Chiou & Youngs (2008). While it is tempting to integrate fully probabilistic site response into the hazard and risk calculations following the method of Bazzurro & Cornell (2004b), especially in view of the relatively simple (but computationally intense) implementation of this approach within a Monte Carlo framework, this is more appropriate for site-specific studies (*e.g*., Rodriguez-Marek *et al*., 2014). It may also be noted in Eq.(2.1) that the intention is to condition the non-linear site response not on the median prediction of the $Sa_{ref}(T)$ but on the actual predicted value resulting from the sampling of the between-event variability and the single-station within-event variability.

The formulation in Eq.(2.1) requires the study region to be divided into a number of zones, within each of which a unique set of non-linear site amplification functions—for the 16 selected response periods—is assumed to be representative. The definition of these zones is described in Chapter 9. The degree of variation of the site amplification functions across an individual zone is reflected in the assigned value of the term $\delta S2S_j$.

2.2. Overview of derivation process

Figure 2.3 provides an overview of the process followed to define the V2 GMPEs in the form of a flowchart. There are two starting points indicated at the top left-hand corner and top centre of the figure, which are parallel activities. One of these is the development of a field-wide layer model for site response analyses to estimate the amplification factors due to the profile above the reference rock horizon (which is indicated as NU_B; see next section). The development of these site response models is described in Chapter 6.

The second starting point is the compilation of the ground-motion database for the Groningen field, which is the focus of Chapter 3. Following down the central portion of the diagram, these records are used to infer site kappa values at the recording station locations. Chapter 4 describes the development of linear site amplification functions for the recording stations using available V_S information and assigning damping values that are consistent with a reasonable estimate of the kappa value in the underlying reference rock. Linear amplification factors suffice at this stage because the surface recordings to which they will be applied to deconvolve the motions to the rock horizon are rather weak (the highest recorded PGA value is 0.08*g*). Amplification factors are derived both in terms of Fourier amplitude spectra (FAS)

and acceleration response spectra. The former are applied to the surface motions to obtain acceleration FAS at the reference rock horizon, which—as described in Chapter 5—are inverted to obtain estimates of source, path and site parameters for the Groningen earthquakes. The source parameters include the Brune stress parameter and the seismic moment, although the latter can be independently constrained from magnitude estimates provided by KNMI. The path parameters are the geometric spreading model—which will be at least partially constrained by finite difference simulations, as noted earlier—and the attenuation parameter Q. The site terms are a site kappa value for the reference rock and a field-wide amplification factor.

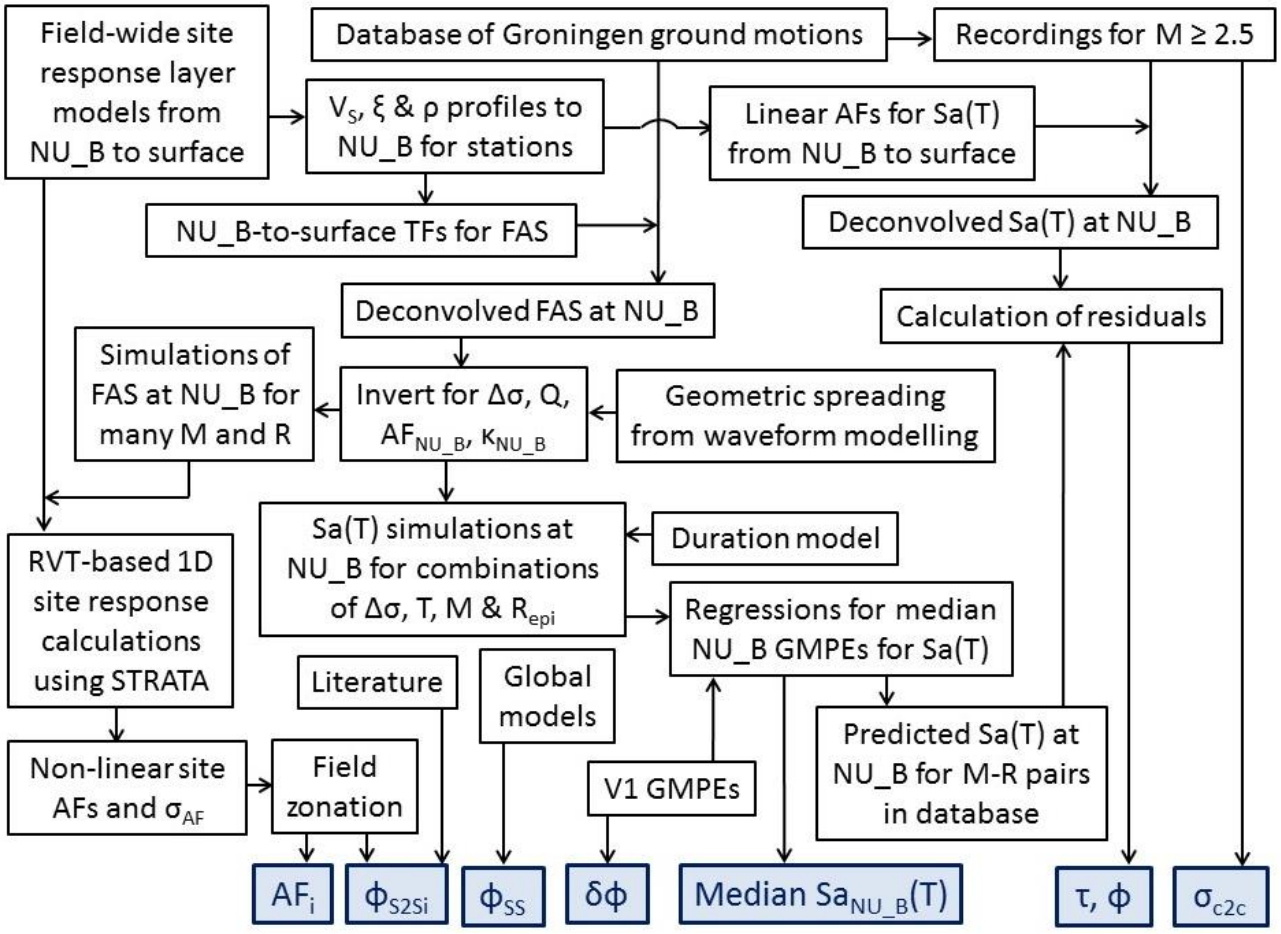

Figure 2.3. Flowchart illustrating the procedure used to generate the V2 GMPEs for horizontal spectral accelerations; the blue boxes at the foot of the figure indicate the outputs of the process that are the elements of the V2 ground-motion model. TF is Transfer Function, AF is Amplification Function; Δσ is stress drop, M is magnitude, R_{epi} is epicentral distance, T is period and Sa(T) is spectral acceleration.

Optimal values of inverted parameters are then used to perform stochastic simulations of the motions, expressed in terms of both FAS of acceleration and response spectra, at the reference rock horizon. For the response spectra simulations estimates of the signal duration are also required. As for the V1 GMPEs, multiple values of the Brune stress parameter will be applied in these forward simulations to generate multiple models in order to capture the

inevitable epistemic uncertainty associated with the predictions at larger magnitudes. The simulations for response spectral accelerations and the fitting of suitable functional forms to these values to obtain the median GMPEs for the reference rock horizon are described in Chapter 6. As indicated by the upwards arrow from the box “V1 GMPEs”, some of the parameters of the rock equations may be adopted directly from the V1 models, in which they were constrained by direct regression analyses (Bommer *et al*., 2015a,b).

The two parallel activities of building a site response model (Chapter 7) and developing GMPEs for the reference rock horizon (Chapter 3 to 6) come together in Chapter 8, which corresponds to the bottom left-hand corner of the flowchart. The site response analyses are performed using an RVT-based implementation of the 1D equivalent linear approach, for reasons that are explained in detail in Section 8.1. One of the advantages that this approach provides is that the input rock motions can be directly generated in the form of FAS that are also used in the stochastic simulations (Section 8.2). These analyses result in non-linear site amplification functions, which are coalesced into zones to which a representative function is assigned; this aggregation procedure is described in Chapter 9. The remainder of the flowchart corresponds to calculating the variability terms, from both the residuals of recorded surface motions and from the site amplification factors, which are used to construct the sigma models (Chapter 10).

2.3. Definition of the reference rock horizon

The first step in developing a model as described by Eq.(2.1) is to define the reference rock horizon that will be treated as the top of the elastic half-space for the site response calculations. The general geological profile across the field is illustrated in Figure 2.4. The gas reservoir is comprised of the Rotliegend sandstone layer which has a thickness varying from about 130 to 300 m, underlain by hard Carboniferous rock. Immediately above the reservoir is the Zechstein salt layer, with a very high-velocity basal anhydrite (Tenboer). The Zechstein is overlain by a layer of Cretaceous chalk. The uppermost part of the field is comprised of Cenozoic and younger deposits, including the North Sea formation that is mainly claystone.

In general, the criteria for selecting a reference rock horizon are related to the required properties corresponding to the assumption of an elastic half-space below that horizon. The key criteria are that the layer should be sufficiently stiff to behave linearly under the envisaged levels of acceleration and also that it should be an absorbing boundary, which means that downward propagating waves (reflected from the free surface) are not reflected back up towards the surface. There are also practical considerations for this particular application, for which some degree of simplification is desirable in view of the large numbers of site response calculations that are required to obtain amplification functions over the entire study area (which extends for about 50 km in the north-south direction and 35 km in the east-west direction). A reference rock horizon is sought that is therefore sufficiently deep to capture the most important site response effects, and below which there is limited lateral structural variability, while avoiding the need to conduct site response analyses for very deep profiles.

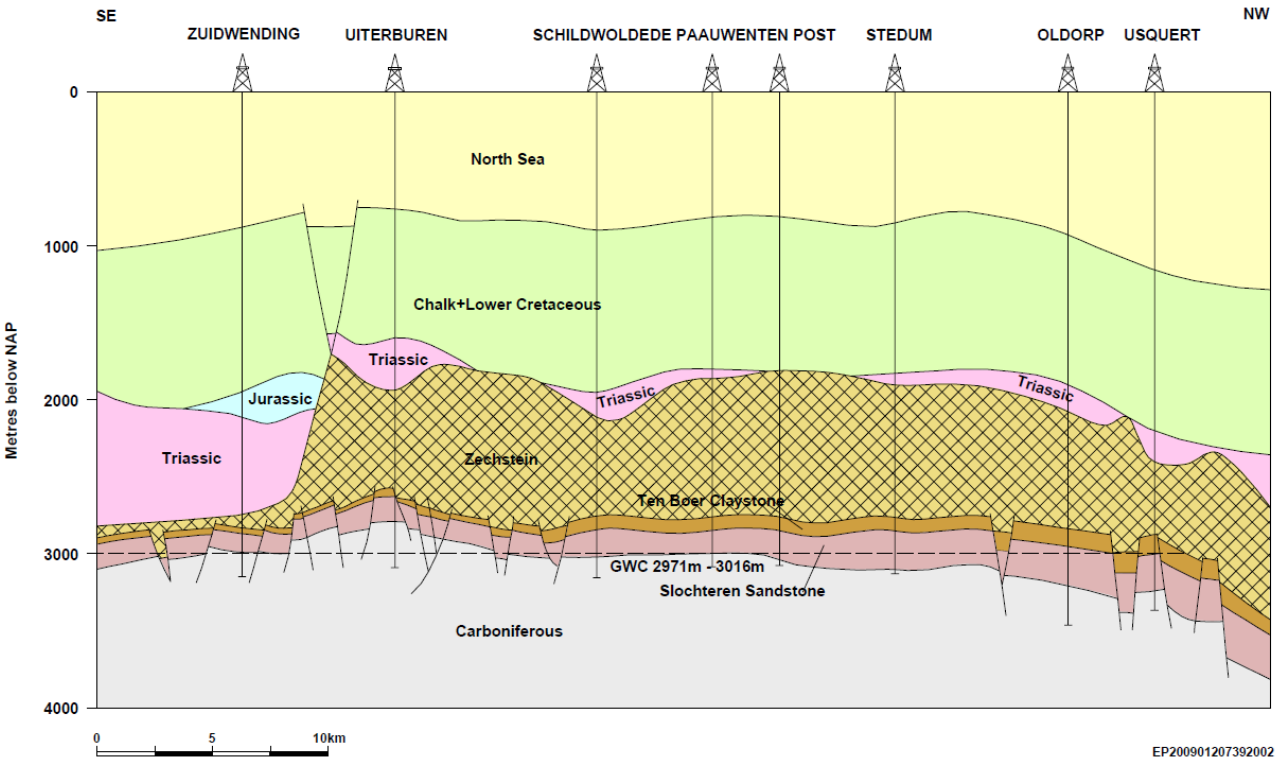

Figure 2.4. Simplified geological profile of the Groningen field (Source: NAM)

To inform the final decision, V_S profiles extending down to the reservoir from the surface, obtained from two deep boreholes, were examined (Figure 2.5) as well as the field-wide deep velocity model developed by NAM. Two horizons are indicated on the figure, the base of the North Sea Supergroup Formation (NS_B) and the base of the Upper North Sea Formation (NU_B), located at depths of about 800 m and 350 m respectively. The NS_B horizon is a very clear impedance contrast and it would therefore appear to be a logical choice for the top of the elastic half-space. However, it is also the case that the profile across the field between the NU_B and NS_B horizons is fairly uniform, which means that an additional ~400 m would be included in the site response analyses that would not produce significant differences in the resulting surface motions from one location to another. In view of this, the NU_B horizon is to be preferred. In Figure 2.5, it may be noted that there is an apparent impedance contrast approximately 100 m below the NU_B horizon, which corresponds to the Brussels Sands. While this would seem a more logical location, the location of this horizon is not clearly mapped across the entire field, which would lead to additional uncertainty if it were used as the reference rock horizon. In contrast, the NU_B horizon is well constrained throughout the entire study area (Figure 2.6). Therefore, the NU_B horizon is chosen as the reference rock horizon.

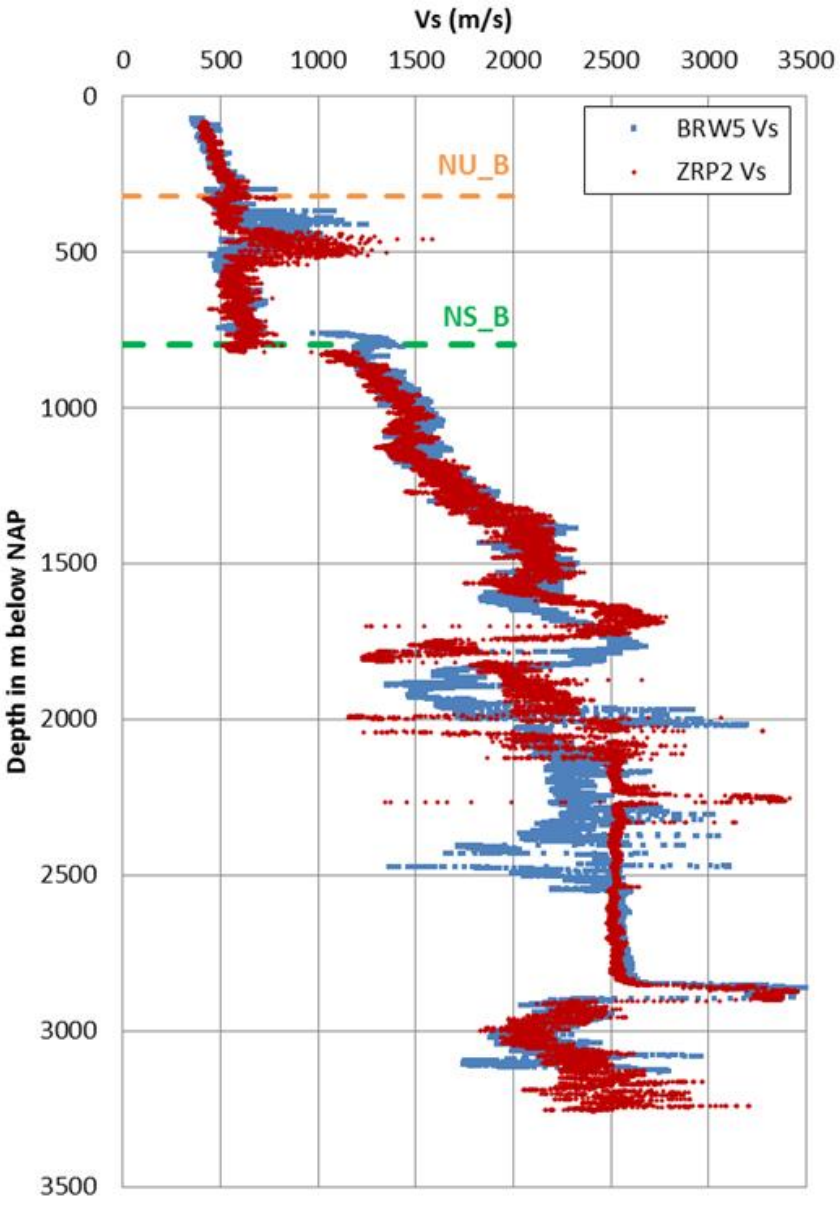

Figure 2.5. Shear-wave velocity profiles from two deep borehole logs, indicating the location of the base of both the North Sea Supergroup Formation (NS_B) and the Upper North Sea Formation (NU_B) formations (*Source: NAM database*)

Over most of the field the NU_B horizon is encountered at a depth of about 350 m; it is at appreciably greater depths to the northwest of the area, but since some of these areas are offshore (as are the slightly deeper areas to the north and east of the study area) they are of little consequence. To the south there are small areas in which the NU_B horizon is much closer to the surface but these areas are a very small proportion of the entire study region.

The choice of the NU_B horizon as the top of the elastic half-space implies that waves that are reflected from the impedance boundary at the NS_B boundary are ignored. An important point to emphasise is that selection of the NU_B horizon as the reference rock level does not mean that the influence of deeper impedance contrasts is being entirely ignored. The inversions of the recorded motions are expected to capture such effects if they are sufficiently influential to manifest in the surface motions. Where these contrasts are persistent across

the entire field—or at least across the area covered by the recording networks—they will manifest in the average field-wide NU_B amplification factor obtained from the inversions. Where deep impedance contrasts may be more localised, they would be expected to influence the estimation of sigma, although it is noted that this will not account for such local variations that are outside the area covered by the recording network.

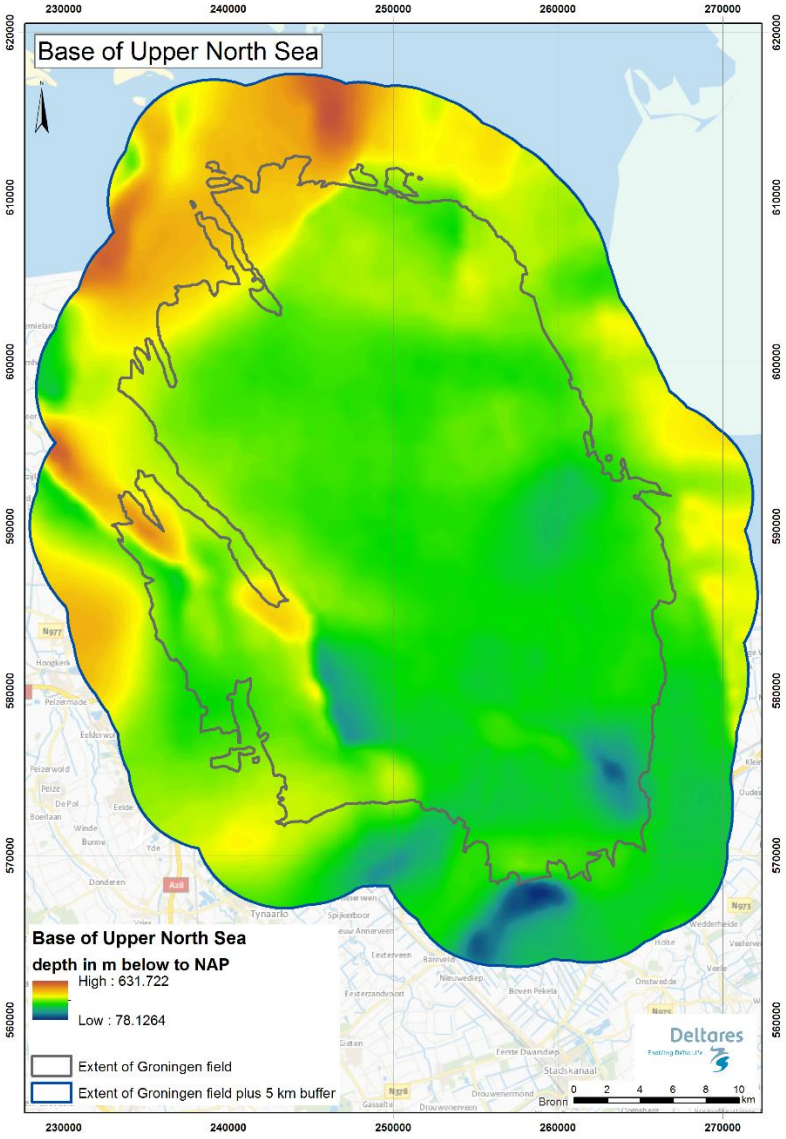

Figure 2.6. Maps of the study are showing the depth to the NU_B horizon (*figure prepared by Deltares using data from NAM database*).

The dynamic properties assigned to the elastic half-space are a shear-wave velocity, V_S, of 639 m/s and a damping (which exerts very little influence on the outcome of site response analyses) of 0.3%, having been chosen to be consistent with the Q value (Q=150) determined from accelerograph data and used for the V1 GMPE simulations.

2.4. Spatial correlation of ground motions

The preceding sections of this chapter, together with Section 1.3, have provided an overview of all the elements that are included in the V2 GMPEs. To close these introductory chapters, we briefly explain why a choice was made not to include a function for the spatial correlations of ground motions for implementation of the V2 risk calculations.

Several studies have noted that the variability of ground-motion amplitudes at closely-spaced accelerograph stations is lower than that expected from empirical GMPEs, indicating that there is a degree of spatial correlation in the seismic shaking (*e.g.*, Boore *et al.*, 2003; Wang & Takada, 2005; Jayaram & Baker, 2009; Goda & Atkinson, 2010; Esposito & Iervolino, 2011). Examples of spatial correlation functions for PGA are shown in Figure 2.7.

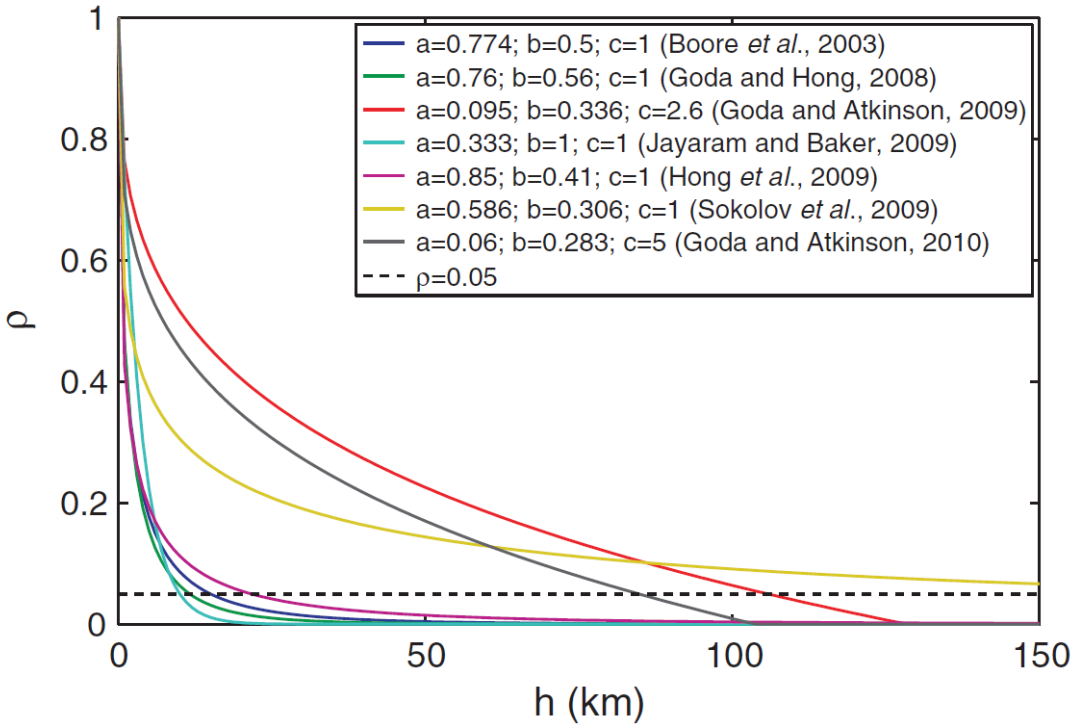

Figure 2.7. Comparison of published correlation functions for PGA as a function of separation distance, *h*; the dashed black line represents the correlation coefficient of 0.05, which may be considered as the level at which all correlation is effectively lost (Esposito & Iervolino, 2011)

The considerable variation among these models suggest that there is still a degree of uncertainty regarding the spatial correlation lengths or that these lengths are influenced by local factors; the latter interpretation would lead us to conclude that a Groningen-specific correlation model would be needed rather than simply adopting one or more of the existing relationships. Regardless of the specific model for the variation of the correlation coefficient with separation distance, the effect of the spatial correlation of ground motions is to produce pockets of higher and lower motions rather than simply random variations that would result from simply sampling the within-event variability of the GMPE. In terms of group risk (GR), these spatial concentrations of elevated ground motion can result in higher estimates of

losses in risk modelling for geographically-distributed exposure when these coincide with concentrations of weak buildings (*e.g*., Crowley *et al.,* 2008). However, local personal risk (LPR), which reflects the risk at a single location, should not be affected by spatial correlations of ground motions. Since the primary risk metric being considered for the Groningen field is LPR, the decision to not model spatial correlation is relatively unimportant. However, since there is also an interest in GR estimates, it will need to be borne in mind that the absence of a spatial correlation model may lead to some underestimation of this metric.

In the Version 0 and Version 1 risk models, the exposure is grouped into 3 x 3 km squares and the ground-motion amplitudes calculated at the centre of each square applied to all buildings within the grid cell. This is a computational convenience, since sensitivity analyses showed that using a smaller grid size (such as 1 x 1 km) resulted in a tremendous computational penalty, while the coarser grid does not result in great loss of accuracy, consistent with findings from other studies (*e.g*., Bal *et al*., 2010). The assumption of uniform motions across each grid cell also conveniently serves as a surrogate for including spatial correlation. However, it must be recognised that the correlation lengths vary with spectral response period (*e.g*., Esposito & Iervolino, 2012), so the approximation becomes even cruder when spectral ordinates at multiple oscillator frequencies are being considered. For the V2 risk model, the uniform grid will be replaced by an uneven grid related to the site amplification zones, and prior to the definition of these zones—which will be determined primarily on the basis of limiting the within-zone variation in the site amplification functions across the full period range—it is not possible to make a judgement regarding the need for refinement in the definition of spatial correlation. Moreover, any spatial correlation model should presumably account for both spatial correlation of the motions at the NU_B horizon and spatial correlation of the site profiles and their corresponding amplification functions.

3. GRONINGEN GROUND-MOTION DATABASES

The most valuable resource used for the derivation of GMPEs for a given region is a database of accelerograph recordings from local networks. The Groningen seismic hazard and risk modelling project is in a privileged position in this regard, with excellent networks now in operation in the gas field and a growing database of ground-motion records. In this chapter we provide a brief overview of the existing and forthcoming networks of recording instruments, identifying those from which records are being used in the derivation of the V2 equations. The characteristics of the current database are then summarised, followed by an overview of the additional recordings from smaller-magnitude events that were added for inversions to estimate source, path and site parameters.

3.1. Strong-motion networks in the Groningen field

The existing and planned strong-motion recording networks in the Groningen field were discussed in the V1 GMPE report (Bommer *et al*., 2015a). The network that has provided the majority of the recordings in the current database are the digital accelerographs that have been operated by KNMI in the field for many years. The network was expanded and upgraded between 2013 and 2014, and now consists of 18 instruments, all installed at the ground surface (Figure 3.1).

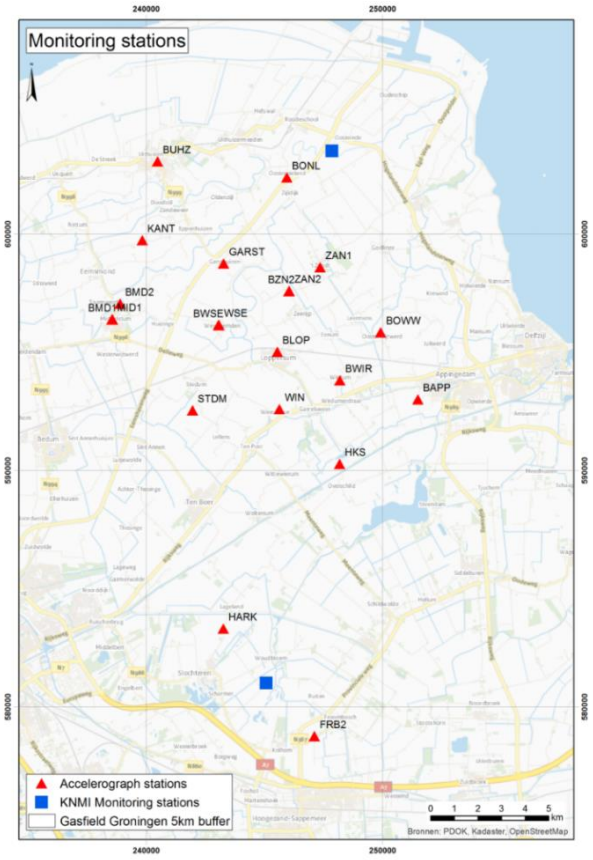

Figure 3.1. Locations of KNMI accelerographs (*red triangles*) in the Groningen field.

As part of the response to the Groningen earthquakes, NAM is installing 70 new 200-metre boreholes instrumented with geophones (Figure 3.2). The 70 geophone-instrumented boreholes, some of which have already been installed, will all be accompanied by an accelerograph at the surface, all operated by KNMI. A large number of these boreholes have now been installed and are operational, and the current database includes recordings from some of the surface accelerographs.

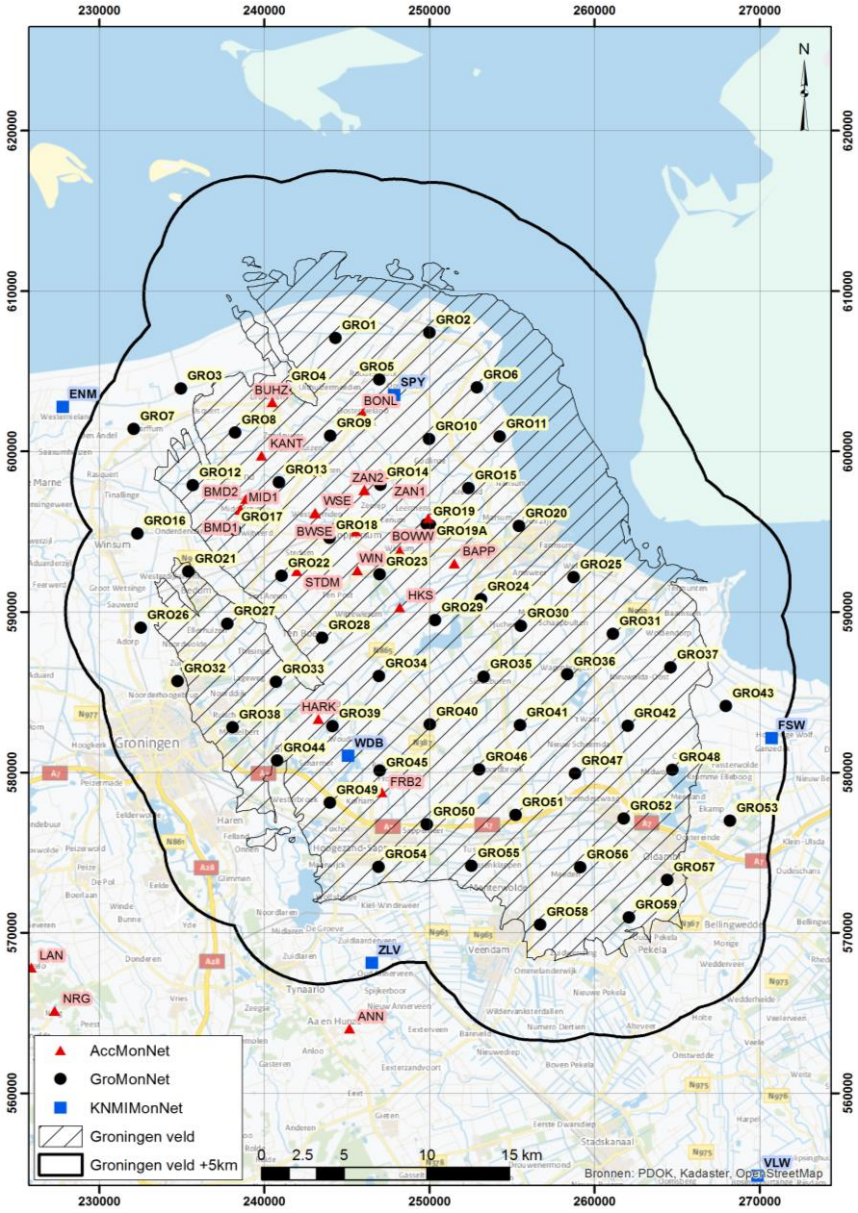

Figure 3.2. Locations of 59 (of 70) instrumented boreholes and co-located accelerographs (*black circles*) being installed by NAM. Also shown are the KNMI accelerographs (*red triangles*) and five 200-m boreholes installed with geophones that KNMI has operated for many years (*blue squares*).

There are two other accelerograph networks operating in the Groningen field. An additional 60 accelerographs have been installed (in clusters of three instruments at each of 20 locations) on the key facilities of the NAM gas production network in the field. The purpose of the NAM accelerograph is to allow safe shut-down of the facilities if accelerations in excess

of specific thresholds are exceeded, but the records obtained by these instruments will also be made available and are likely to be added to database used for derivation of the GMPEs, provided that the records are not excessively contaminated by the influence of the gas production plant and equipment at the sites. The records obtained to date are being evaluated—and compared to those from the other networks during the same events—with a view to their subsequent incorporation into the database (Section 13.1). If the records are judged to be usable for ground-motion prediction purposes, it will be necessary to expand the current programme of field measurements being conducted by Deltares (Section 4.5) to also incorporate these recording locations.

A fourth network consists of some ~300 accelerographs that have been installed by TNO, under contract to NAM, in some public buildings and private homes. The latter instruments were installed in homes selected by requests made in response to an open invitation by NAM. The spread and density of this network is such that it could provide invaluable information for the refinement of the ground-motion model. To date the records obtained from these instruments have not been incorporated into the database because of concerns regarding their installation. The digital accelerographs have been mounted on small steel brackets and in many instances the brackets have then been affixed to walls several centimetres above the floor, which means that contamination of the records by the building response is very likely. Comparisons of recorded PGA values from these instruments with those from the KNMI accelerographs obtained in two earthquakes suggested that the former were generally somewhat higher, although the number of records in the latter database may be insufficient to draw such conclusions with confidence. If the trend is genuine, it might indicate amplification of the ground shaking due to structural response. Another possibility that has been suggested is that the network may be inherently 'biased'—perhaps to locations with softer ground conditions—because residents who feel the shaking episodes more clearly may have been more motivated to make a request for an instrument to be installed in their abode (John Douglas, *personal communication*, 2015). Investigations are ongoing to document the installation details of each instrument and examine the recordings for evidence of structural influence. Additionally, experiments are being planned that will involve the installation of free-field instruments on small concrete slabs adjacent to some of the instrumented buildings in order to identify the extent of the influence of the building response on the recorded motion (Kees Tanis, *personal communication*, 2015). As for the instruments installed at the NAM facilities, for any TNO-installed station assessed to be producing usable records, it will ultimately be necessary to perform in situ measurements for the location-specific V_S profiles (Section 4.5).

Other instruments that are either operational in the field or in the process of installation include KNMI velocity recorders in shallow boreholes, the geophones in the 70 new 200-m boreholes and the geophones installed at reservoir depth in two deep boreholes being installed by NAM. All of these data will be examined and incorporated where appropriate for subsequent refinements of the model—in particular the borehole geophones may be very useful for calibrating the site response model—but for the development of the initial V2 GMPE only records from surface accelerographs are being considered.

3.2. Strong-motion database for Groningen

For the V1 GMPEs, records were selected from events of magnitude 2.5 and greater for which the accelerograms were judged, on the basis of visual inspection, to have acceptably high signal-to-noise ratios. The records were adjusted using linear or polynomial baselines, as needed, after truncation of the pre-event memory, and used to generate response spectral ordinates at periods up to 2 seconds. The total dataset consisted of 85 recordings from 12 earthquakes.

For the V2 GMPEs, the database has been considerably expanded through the addition of four more recent earthquakes, two of which had lower magnitudes (Figure 3.3). With the expansion of the recording networks, the number of records being obtained from each earthquake has increased appreciably (Table 3.1): the first eight events produced an average of 5 records each whereas the most recent eight events have yielded more than 2.5 times as many records. With the expansion of the recording networks, this trend can be expected to continue and increase, which is very promising for future refinements of the model (as discussed in Section 13.1).

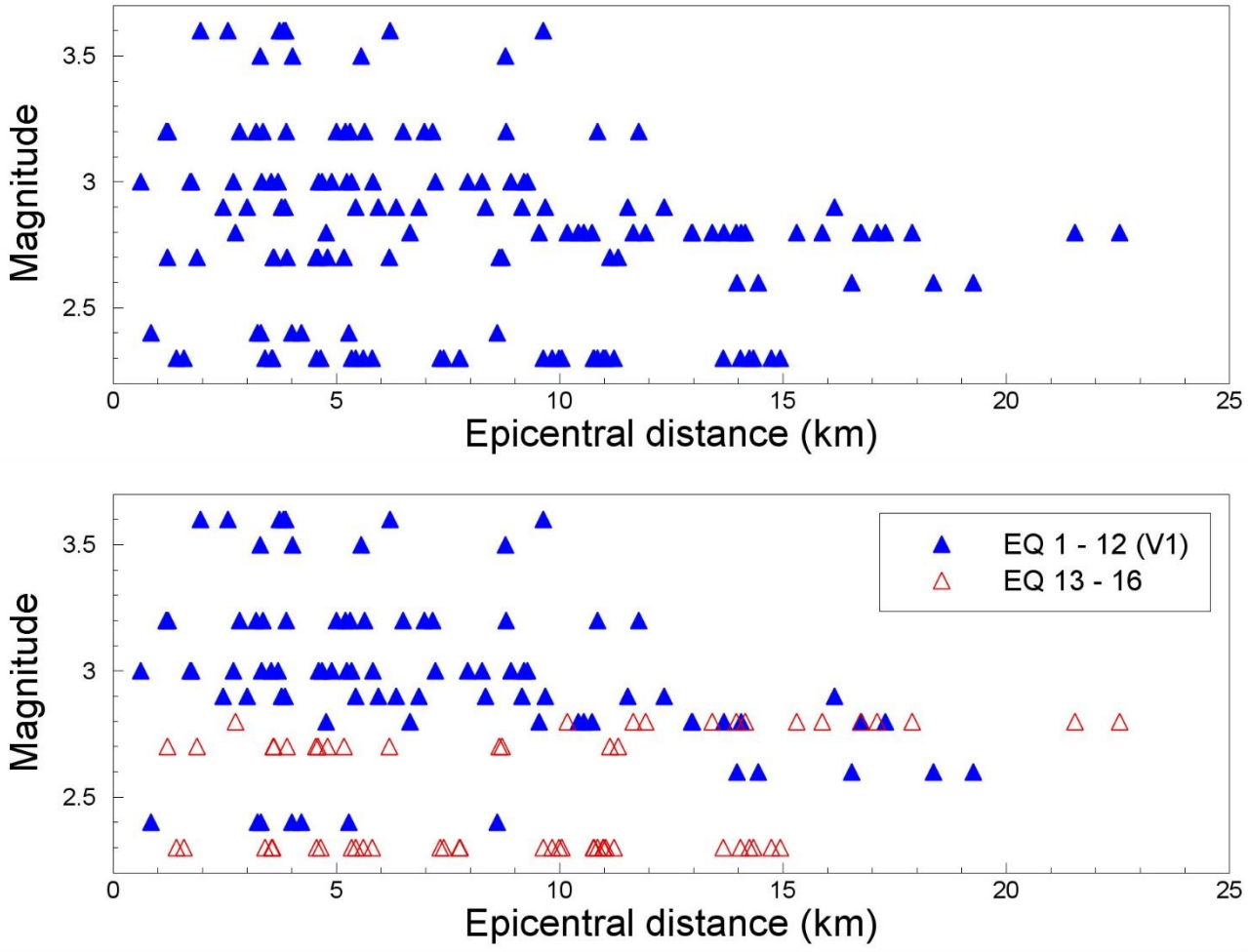

Figure 3.3. Magnitude-distance distribution of the V2 database. The lower plot distinguishes the data from the 12 earthquakes in the V1 database (*blue triangles*) and the additional recordings added to the V2 database (*red triangles*)

Table 3.1. Numbers and features of records from each earthquake

EQ ID	Date			M	Recs	Min. R_{epi} (km)	Max. R_{epi} (km)	Max. PGA (g)	Max. PGV (cm/s)
	Y	M	D						
01	2006	VIII	8	3.5	4	3.31	8.79	0.050	1.25
02	2008	X	30	3.2	6	1.20	5.32	0.035	1.44
03	2009	V	8	3.0	5	0.63	7.95	0.023	0.62
04	2011	I	19	2.4	4	3.24	5.29	0.007	0.18
05	2011	VI	27	3.2	8	1.21	11.78	0.027	1.21
06	2012	VIII	16	3.6	7	1.97	9.64	0.084	3.51
07	2013	I	19	2.4	3	0.85	8.61	0.016	0.57
08	2013	II	7	3.2	3	1.23	5.64	0.031	1.44
09	2014	II	13	3.0	14	1.76	9.30	0.070	1.62
10	2014	IX	1	2.6	5	13.99	19.27	0.0003	0.02
11	2014	IX	30	2.8	12	4.79	17.30	0.002	0.11
12	2014	XI	5	2.9	14	2.46	16.17	0.077	1.78
13	2014	XII	30	2.8	14	2.73	22.54	0.017	0.35
14	2015	I	6	2.7	14	1.22	11.32	0.013	0.43
15	2015	II	25	2.3	17	1.59	14.94	0.039	0.36
16	2015	III	24	2.3	16	1.41	14.74	0.008	0.18

The locations of the recording stations and the earthquake epicentres are shown in Figure 3.4. As for the V1 database, recordings from the FRB2/BFB2 station have been excluded because of a strong and as-yet unexplained high-frequency content throughout the entire signal (Bommer *et al*., 2015a).

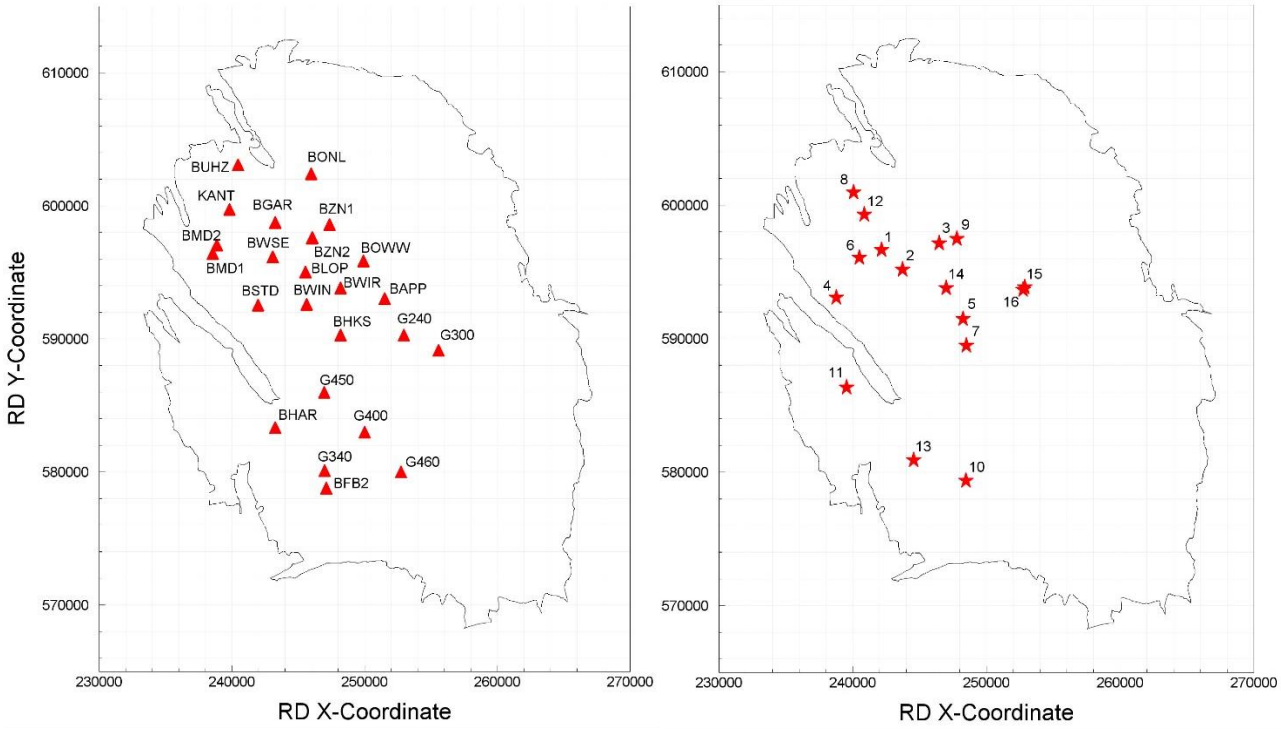

Figure 3.4. Location of the accelerograph stations (*left*) and the epicentres of the earthquakes in the current database (*right*); earthquake ID numbers as in Table 3.1

Epicentral distances are calculated using the station coordinates and epicentral locations provided by KNMI, and all focal depths are assumed to be equal to 3 km (*i.e*., all earthquakes

are assumed to be located within the gas reservoir). As for the V1 GMPE, it is assumed that local magnitudes calculated by KNMI are equivalent to moment magnitudes (*i.e.*, M_L = **M**). Since only local data are being used in the derivation of the GMPEs and since the same assumption is invoked for the earthquake catalogue used to define the seismicity model, the question of the magnitude scales is not critical in terms of internal consistency of the models. However, it is recognised that the issue does need to be addressed in depth and the true nature of the relationship between local and moment magnitudes for Groningen does need to be resolved. With this in mind, a separate and parallel study of this specific topic is being undertaken (Dost *et al*., 2015).

An important point to note here is that from V1 to V2, the values of six earthquake magnitudes have been updated (in Figure 3.3 and Table 3.1 the updated values are used). The changes apply to six of the first eight earthquakes, which was the database used to derive the V0 GMPE (Bourne *et al*., 2015). On inspection, it transpired that these magnitudes were early estimates of M obtained by KNMI and their use was inconsistent with the adoption of the same ML values used for the earthquake catalogue. The resulting changes varied from +0.1 to -0.4, with an average change of -0.1 over the six earthquakes. Figure 3.5 shows the changes to the magnitude-distance distribution as a result of these corrections.

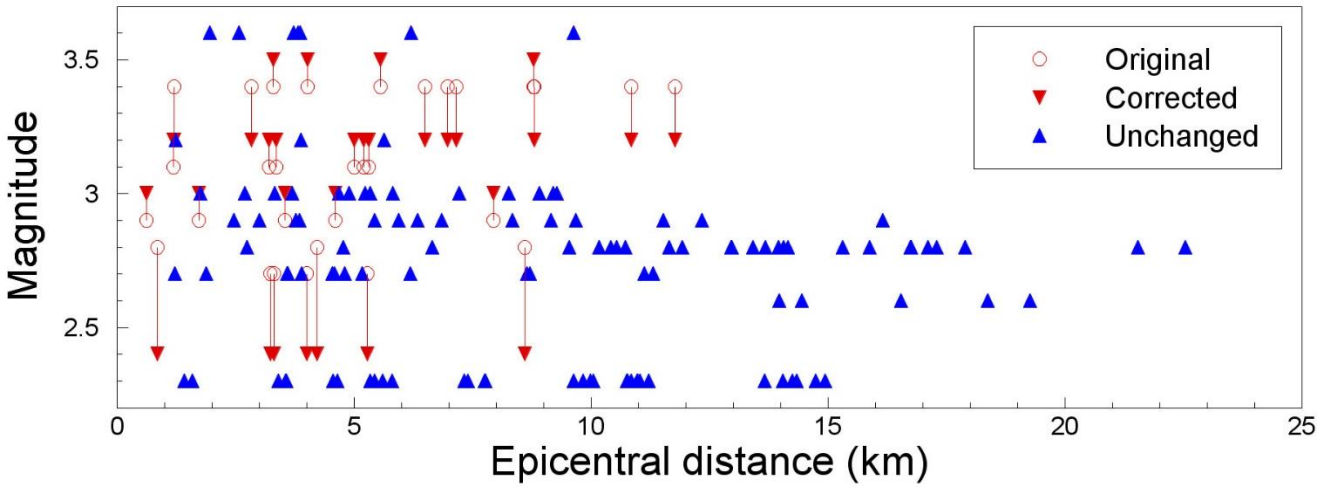

Figure 3.5. Magnitude-distance distribution of the V2 database (*solid triangles*); the circles show the values from the V1 database that were corrected in this update.

The final database consists of 146 records from 16 earthquakes. Among the criteria that Bommer *et al.* (2010) put forward for basic acceptability of empirical GMPEs was the specification that the database should include at least 10 earthquakes for each unit of magnitude covered and 100 records per 100 km of distance covered. In the magnitude range from 2.3 to 3.6, the database now includes 11.4 records per magnitude unit, which is therefore acceptable (although, of course, this does not allow for extrapolation to larger magnitudes if this were done empirically). In terms of distance, the criterion proposed by Bommer *et al*. (2010) is satisfied and exceeded by a factor of more than 6. Since some of the coefficients of the model are constrained by direct empirical regression (see Chapter 6),

these indicators are useful although it is clear that the constraint on earthquake-to-earthquake variability may not be as robust as would be desired.

A very important improvement of the V2 database with regard to that used to derive the V1 GMPEs is that the records have been uniformly processed with individually selected high-pass filter parameters to remove long-period noise. Full details of the record processing is presented in a separate report (Ntinalexis *et al*., 2015a) and the filter parameters are summarised in the database report (Ntinalexis *et al*., 2015b) but a brief summary is given here for completeness. The records were processed using an 8-order acausal Butterworth filter with the cut-off selected on the basis of deviation of Fourier amplitude spectrum (FAS) of acceleration of the record from an ideal f^2 trend. Signal-to-noise ratios from the FAS were also explored using the pre-event memory as the noise model but the very low amplitude of many of the records made it very difficult to clearly distinguish a pre-event memory from the signal. The same filter was applied to both horizontal components on each recording to allow for the possibility of vector resolution and other such operations on the processed accelerograms (Boore & Bommer, 2005). The maximum usable period was then defined as 0.9 of the long-period cut-off, confirmed as appropriate by comparison between the acceleration response spectra of filtered and unfiltered records, and also consistent with the recommendations of Akkar & Bommer (2006) for digital accelerograms. However, the filter cut-offs that were applied were less severe than might be expected for such small-magnitude recordings, suggesting that the recording are of very high quality (see Fig. 2 of Akkar & Bommer, 2006). The consequence of the filtering is that the number of spectral accelerations available for analyses decreases with increasing oscillator period (Figures 3.6 and 3.7). Up to 0.5 seconds, the full dataset is retained and even up to 0.85 seconds only 8 records (5% of the data) drop out because of the usable period range. Thereafter, however, the rate of attrition increases sharply and at 1 second only 78% of the records are retained and at 1.5 seconds this is reduced to 42%. For response periods of 3 seconds and greater there are no usable records at all (Figure 3.7). For response periods beyond 1 second, the data are unlikely to be sufficient to serve as a basis for constraining the aleatory variability (sigma) and other features of the ground-motion model, which means that there will be additional uncertainty associated with the predictions for longer periods.

In terms of the amplitudes of the motion, the largest recorded PGA is still the 0.084*g* value obtained in the 2012 **M** 3.6 Huizinge earthquake (Table 3.1); the same record produced the maximum recorded PGV of 3.5 cm/s. The geometric mean values of PGA of the entire database are plotted against distance in Figure 3.8. General trends of increasing acceleration with increasing magnitude and decreasing distance can be observed, as would be expected. A noteworthy observation is that less than 30 records (*i.e*., about 20% of the dataset) have geometric mean PGA values greater than 0.01*g*. Similar plots are shown for response spectral accelerations at different oscillator periods in Figure 3.9 but without any grouping by magnitude range.

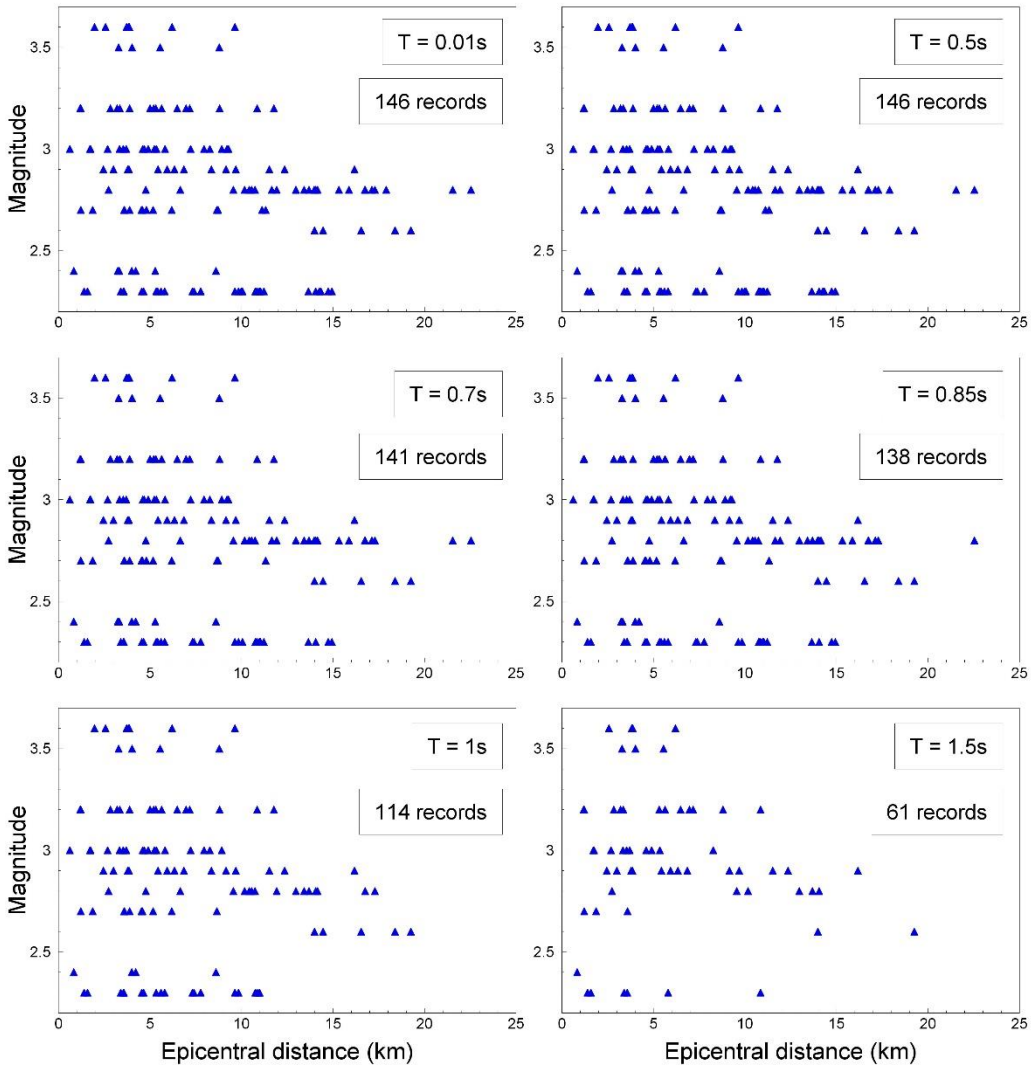

Figure 3.6. Magnitude-distance distribution of the spectral acceleration as a function of oscillator period as a result of the application of high-pass filters to the recordings

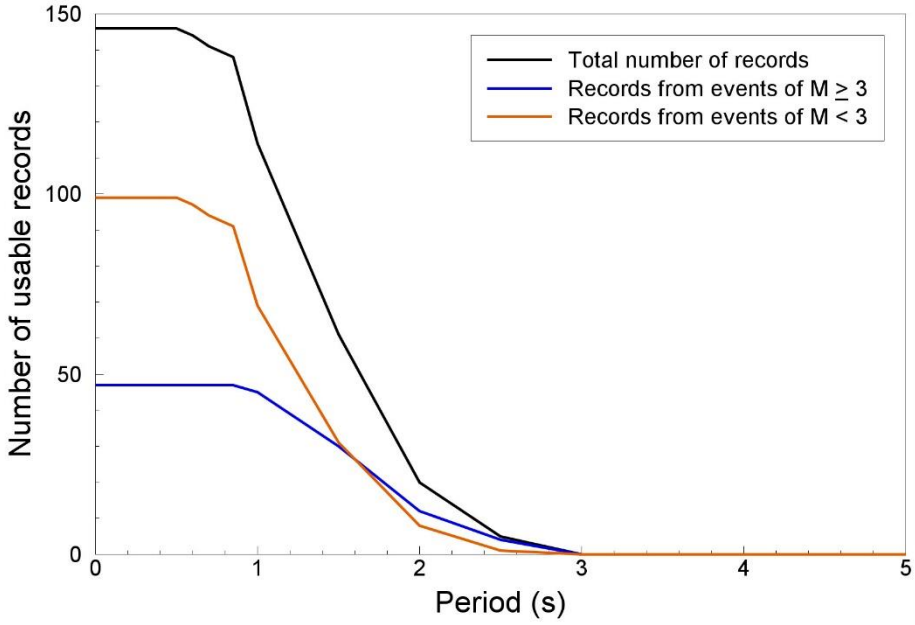

Figure 3.7. Number of usable records as a function of oscillator period, showing the total number and those corresponding to different earthquake magnitude ranges

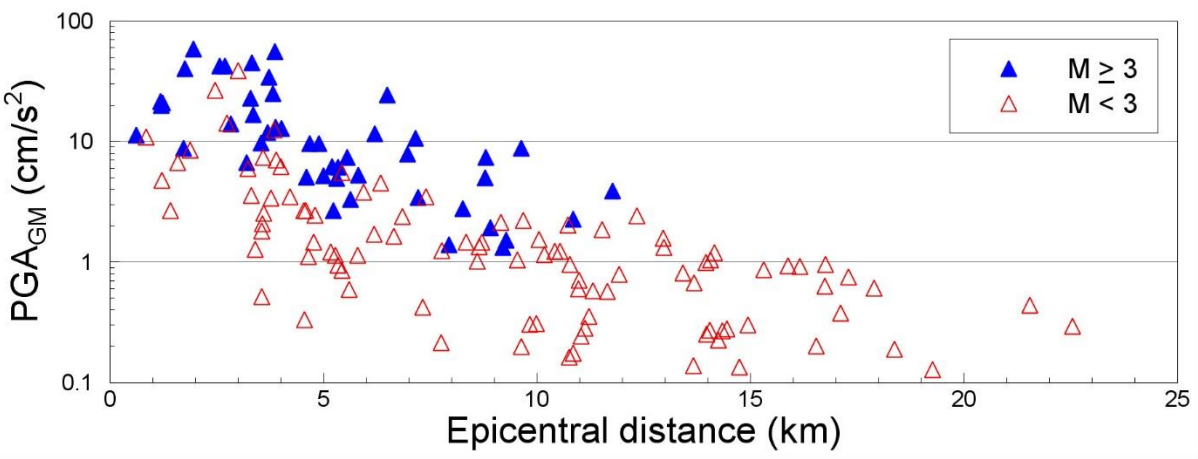

Figure 3.8. Geometric mean values of PGA against epicentral distance

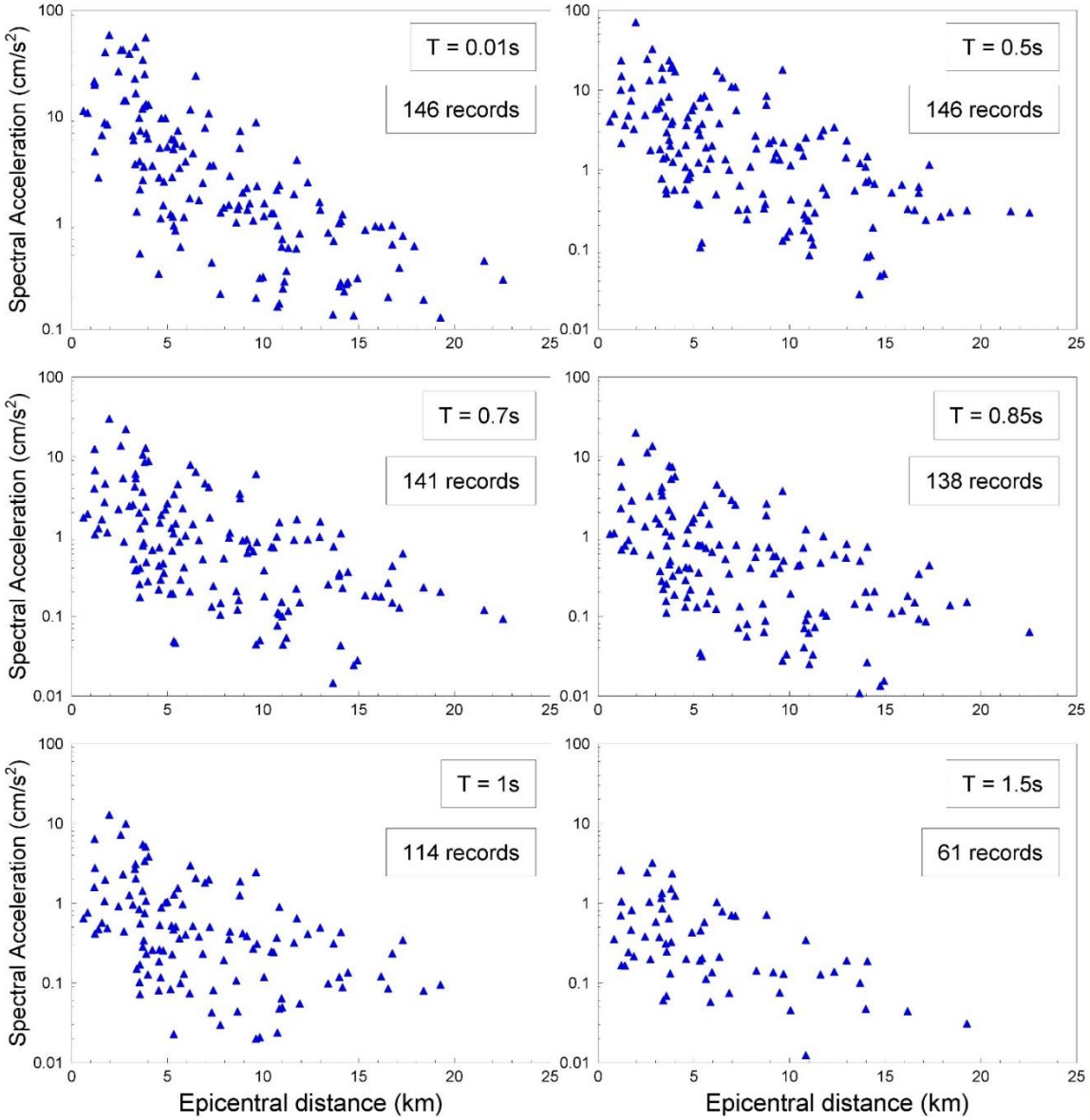

Figure 3.9. Geometric mean values of spectral accelerations at different oscillator periods plotted against epicentral distance; only the usable records are plotted at each period

3.3. Additional small-magnitude events for inversions

The database of 146 records from 16 earthquakes presented above is the compilation of accelerograms considered for direct use in the regressions to constrain elements of the GMPEs (Chapter 6) and also for the estimation of elements of the aleatory variability (Chapter 10). It is noted that for the V1 GMPE, a lower magnitude limit of **M** 2.5 was considered (since smaller events did not contribute to the hazard or risk estimates) and if this same limit applies for the V2 GMPE then the database is reduced to 106 records from 12 earthquakes, since the two most recent events are smaller than the lower limit (Table 3.1). For the inversions to estimate the source, path and site parameters, however, provided the records have acceptable signal-to-noise there is no need to impose a lower magnitude limit. With this mind, additional recordings were included in the database for the inversions, and the characteristics of these additional recordings are summarised in Table 3.2.

Table 3.2. Numbers and features of records from each additional earthquake in the expanded database used for the inversions of Fourier amplitude spectra

EQ ID	Date			M	Recs	Min. R_{epi} (km)	Max. R_{epi} (km)	Max. PGA (g)	Max. PGV1 (cm/s)
	Y	M	D						
A01	2013	IX	04	2.8	1	4.1	4.1	0.0260	0.4142
A02	2013	XI	26	2.0	9	1.5	13.7	0.0143	0.1988
A03	2014	III	11	2.3	6	10.8	18.2	0.0006	0.0176
A04	2014	III	18	2.1	10	4.1	16.7	0.0035	0.0524
A05	2014	VII	02	2.1	2	11.6	18.2	0.0007	0.0877
A06	2014	VIII	09	2.0	8	1.1	12.9	0.0344	0.3660
A07	2015	V	27	2.0	6	0.5	12	0.0086	0.1458
A08	2015	VII	07	2.1	10	6.4	14.9	0.0058	0.0960

The additional data comprises a total of 52 recordings from 8 additional earthquakes, after removing those considered to have insufficiently good signal-to-noise ratios; amongst these, 12 had only a single horizontal component considered usable. The additional data bring the total database for the inversions up to 198 records from 24 earthquakes with magnitudes between 2.0 and 3.6. However, whereas records from the FRB2/BFB2 station were excluded from the analyses of residuals and empirical regressions, the application of high-frequency filters allowed the use of these records for inversions, which added another 5 records from the main database. In summary, a database of 203 records from 24 earthquakes with magnitudes from 2.0 to 3.6 was assembled for the V2 inversions, which is a considerable improvement from the database of 85 records from 12 earthquakes with magnitudes from 2.6 to 3.6 used for the V1 inversions.

Most of the additional records are from smaller earthquakes than the lower limit in the main database (Figure 3.10), with one important exception: a single recording (at station BWSE) of a magnitude 2.8 earthquake on 4 September 2013. In fact, there are a few records from this event, which will be added to the database for the next iteration of the model (this information came to light when the analysis to develop the V2 models was already advanced; the event occurred at the time of the network upgrade and of the 5 stations recording the

earthquake, only BWSE was fitted with new sensors and loggers and streaming in real-time). The expansion of the database is discussed in Section 13.1 of the report.

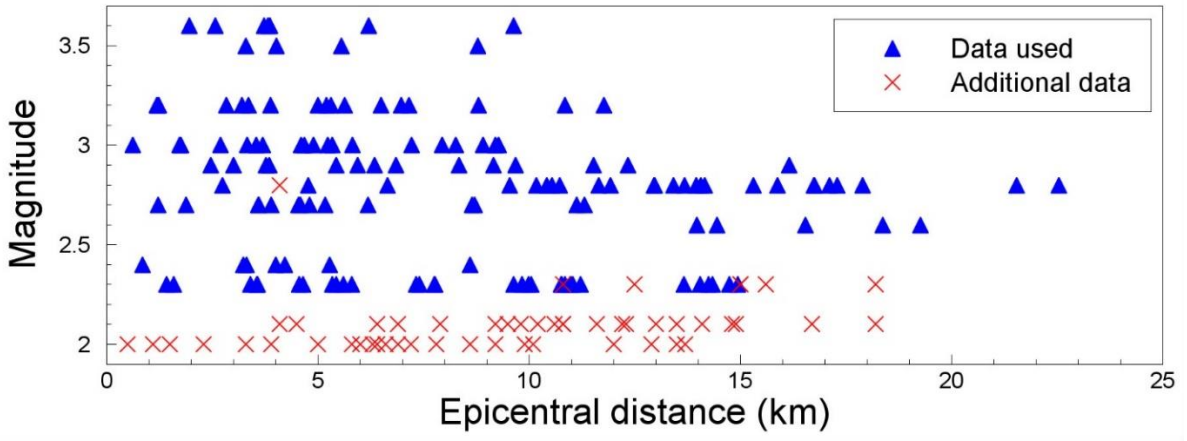

Figure 3.10. Magnitude-distance distribution of the total database used for the inversions; the additional records to the database assembled for the regressions are shown as red crosses

As can be appreciated from Table 3.2, the additional records are generally rather weak and consequently their usable period range was found to be rather limited. Adopting the filter cut-offs applied to process these records and the same criterion to define the maximum usable period as adopted for the main database (see Section 3.2), the number of usable horizontal components from these additional records as a function of oscillator period is shown in Figure 3.11; the rate of drop-off is even higher than that shown in Figure 3.7, which is consistent with the smaller magnitudes.

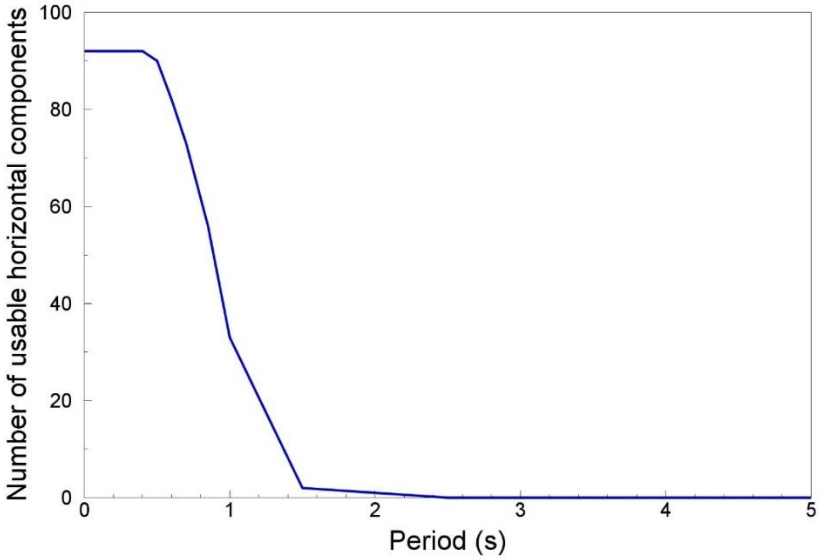

Figure 3.11. Number of usable horizontal components as a function of oscillator period for the additional recordings (red crosses in Figure 3.10)

4. CHARACTERISATION of RECORDING STATIONS

In accordance with the decision to develop ground-motion predictions at the NU_B horizon and to then combine these with site amplification factors, the first stage of the work is to transform the surface recordings to the NU_B horizon. For this purpose, site amplification factors at each of the recording stations, defined relative to the NU_B horizon, are required.

4.1. Site kappa values for recording stations

Following the approach of Anderson & Hough (1984), the slope of the high-frequency decay ($-\pi\kappa$) of log-Fourier amplitude spectra of acceleration (FAS) is determined for each of the recordings with a sufficient signal-to-noise ratio (SNR). κ is measured directly from the recorded FAS by fitting a line with gradient equal to $-\pi\kappa$ to the high-frequency part of the log-FAS. The frequency range over which the slope is measured is from f_1 (lying above the source corner frequency) to f_2, which should lie below the frequency at which the noise floor begins (a SNR of 3.5 is used to define f_2).

The decay of the high frequency FAS has, in the past, been attributed to both source, and path and site effects, but the majority of studies find dominant effects related to the path and site, with κ increasing with distance from the source. This has been interpreted as related to Q, where attenuation acting along the whole path length contributes to the loss of high frequency energy, such that:

$$\kappa = \int_{r=0}^{R} \frac{1}{\beta(r)Q(r)}\,dr \qquad (4.1)$$

where $\beta(r)$ and $Q(r)$ are the shear wave velocity and Q at given points along the propagation path, respectively. From borehole analyses *(e.g.,* Abercrombie & Leary, 1993) it is apparent that the bulk of this observed high-frequency decay is due to attenuation (Q) in the uppermost layers of rock and soil. Since the near surface is (i) significantly more heterogeneous than the deeper layers and (ii) the time spent in the near surface is significantly shorter we can separate path and site components in Eq. (4.1):

$$\kappa = \frac{R}{\beta Q} + \kappa_0 \qquad (4.2)$$

where β and Q are the average shear wave velocity and attenuation along the path (excluding the uppermost layers) and κ_0 is the path-independent site specific attenuation attributed to the uppermost layers. Conceptually this defines a layer-over-half-space model, with the layer depth, H, not explicitly defined. The component of κ that increases with distance from the source is attributed to Q in the half-space, while the 'zero-distance' part κ_0 is attributed to propagation in the upper layers, where body wave paths are mostly vertical due to the velocity reduction. Consistent with its implementation in forward simulations (SMSIM; Boore,

2005a), and Eqs. (4.1) and (4.2) for short path lengths, the distance used in Eq. (4.2) is hypocentral distance. This is different to the distance used by Anderson & Hough (1984), which was epicentral distance.

The minimum frequency used to measure the slope of the FAS of acceleration (f_1) was calculated based on the expected source-corner frequency for a 5 MPa earthquake according to the model of Brune (1970). f_1 is set to 10 Hz for earthquakes with **M** ≥ 2.7, and 15 Hz for events with 2.5 ≤ **M** < 2.7. Events with **M** < 2.5 were not used, as the remaining frequency bandwidth (*e.g.*, with f_1 set to 20 Hz) was found to be insufficient to reliably measure κ. The upper frequency (f_2) is record-specific and is defined as the highest frequency at which the signal-plus-noise-to-noise ratio exceeds 2.5 (equivalent to a SNR of 1.5). An example of the κ fits is shown in Figure 4.1; the full set of plots for all the recordings is presented in Appendix I.

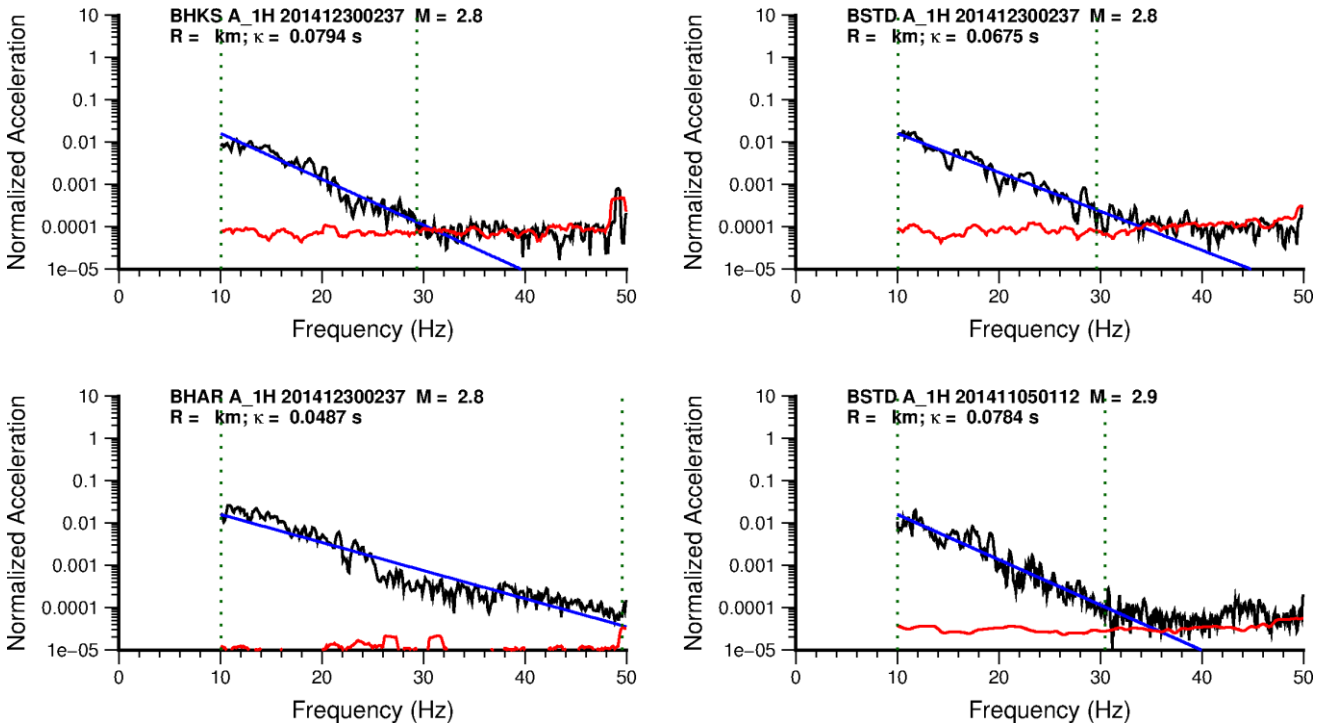

Figure 4.1. Example of $-\pi\kappa$ fits (*blue*) to the FAS of acceleration (*black*) for stations BHKS, BHAR and BSTD. Noise FAS estimates are shown in red, with the fitting limits f_1 and f_2 indicated by dotted vertical lines.

After determining κ for all records with suitable SNR κ_0 values for each station are determined by separating the path (Q) and site-specific components (κ_0) in Eq. (4.2). Different approaches can be used to effectively decouple the path and site components. In Anderson & Hough (1984) this was performed individually for each station, effectively providing a unique Q for each station (although they did not state Q explicitly). For our purpose we require a field-wide average Q for use in the simulations for response spectral ordinates. Two approaches are used here, the first is to use an iterative approach—where we can take advantage of an outlier-resistant approach (minimisation of the misfit modulus,

L1)—with an initial regression using all stations for a common Q and record-average κ_0. Subsequent station-by-station regressions are performed using this Q as a priori, searching only for the best fitting site-specific κ_0.The second approach is to solve simultaneously for Q and site specific κ_0 using a least-squares minimisation. The latter (matrix) approach avoids issues related to uneven data sampling.

Using all available data, the L1 solution for Q was 250 using an average shear-wave velocity of 2.6 km/s. For the purpose of comparison Q was 185 using a more common average crustal shear-wave velocity of 3.5 km/s. A bootstrapping procedure was used to estimate the uncertainty, resampling the data 1000 times with random selection (with repetition) in each sub-sample. The resulting Q values span the range 113 to no attenuation (infinite Q), with a mean value of 262 and lower and upper limits of the standard-deviation at 188 and 543 respectively. Using the mean value from the bootstrap analyses, site specific κ_0 were obtained for 25 stations (Figure 4.2). Using the matrix approach, a Q value of 273 was found, with standard-error spanning limits 220 to 359. The κ_0 values, along with standard errors, obtained for the sites using this method are shown in Table 4.1.

Table 4.1. Estimates of κ_0 for Groningen accelerograph stations

Station	Matrix κ_0 (s)	Std. Error (s)	Iterative κ_0 (s)	Std. Error (s)	No. Records
BAPP	0.0660	0.0091	0.0663	0.0132	2
BFB2	0.0390	0.0095	0.0394	0.0051	2
BGAR	0.0650	0.0075	0.0654	0.0036	4
BHAR	0.0477	0.0075	0.0480	0.0028	3
BHKS	0.0646	0.0124	0.0649	--	1
BLOP	0.0455	0.0064	0.0459	0.0033	5
BMD2	0.0483	0.0077	0.0487	0.0077	3
BONL	0.0536	0.0079	0.0540	0.0043	3
BOWW	0.0638	0.0067	0.0642	0.0050	5
BSTD	0.0561	0.0068	0.0564	0.0059	4
BUHZ	0.0583	0.0088	0.0585	0.0164	2
BWIN	0.0591	0.0091	0.0595	0.0023	2
BWIR	0.0334	0.0078	0.0338	0.0040	3
BWSE	0.0469	0.0092	0.0473	0.0030	2
BZN2	0.0542	0.0066	0.0545	0.0050	5
GARST	0.0607	0.0063	0.0609	0.0043	4
HKS	0.0580	0.0059	0.0583	0.0044	5
KANT	0.0712	0.0085	0.0713	0.0007	2
MID1	0.0648	0.0086	0.0650	0.0118	2
MID3	0.0662	0.0071	0.0664	0.0085	3
STDM	0.0710	0.0120	0.0712	--	1
WIN	0.0436	0.0062	0.0437	0.0055	4
WSE	0.0578	0.0085	0.0579	0.0036	2
ZAN1	0.0495	0.0063	0.0497	0.0089	4
ZAN2	0.0621	0.0071	0.0623	0.0148	3
Average	**0.0562**	**0.0080**	**0.0565**	**0.0058**	**44**

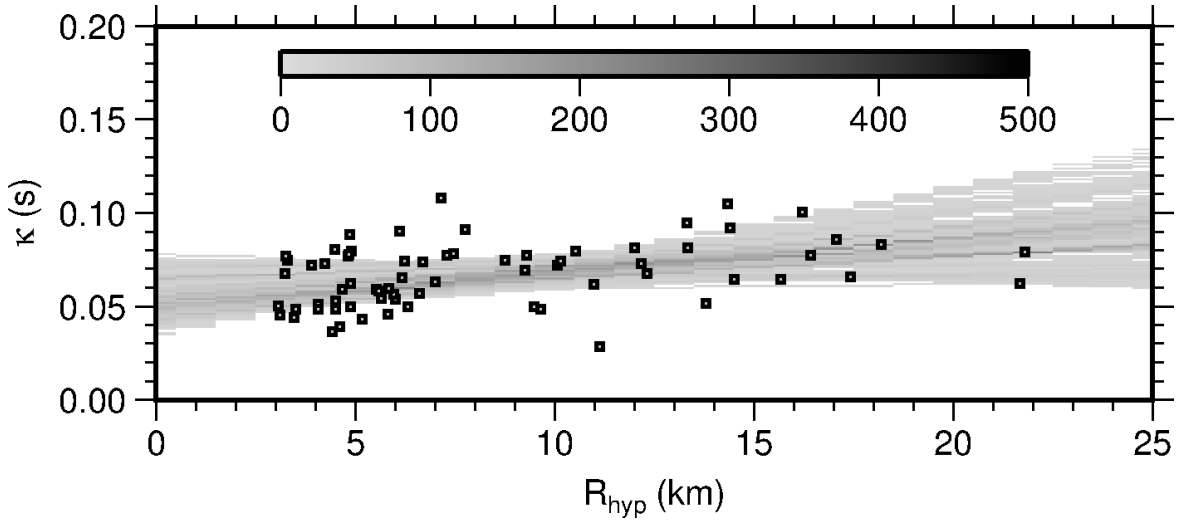

Figure 4.2. Bootstrap results of fitting Q and record-average κ_0

A comparison between the κ_0 values found for the V2 GMPE and those values found for the V1 GMPE (the site-specific versions of which were not directly used; Bommer *et al*., 2015a) is shown in Figure 4.3. On average, the κ_0 values are slightly higher (~0.005 s) in this version, owing to the slightly higher Q used. The scatter highlights the uncertainty of the values, which are based on few recordings and should not be over-interpreted.

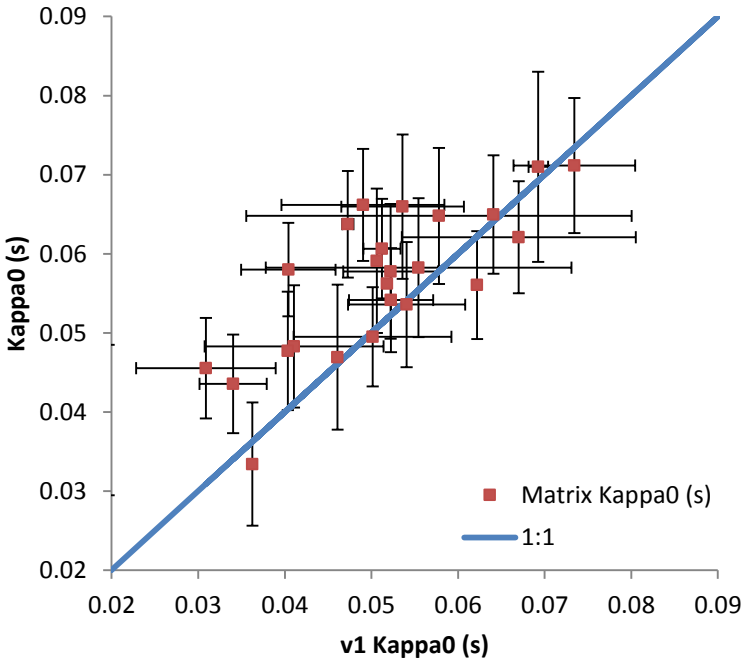

Figure 4.3. Comparison of κ_0 obtained for the expanded Version 2 dataset compared to the values found for the Version 1 GPME dataset; error bars indicate standard errors

4.2. Preliminary stations profiles for site response analyses

In order to deconvolve the motions recorded at the surface down to the NU_B horizon, it was necessary to calculate the transfer functions at the location of each recording station. This required profiles of V_S, density and damping at each of the locations to be generated, but since only linear response is expected for the motions in the current database, modulus reduction and damping curves (against shear strain) are not required. The profiles developed for all of the station sites are presented in Appendix II, each plot showing the full profile down to the NU_B horizon and also the uppermost 50 m on separate plots in order to allow the near-surface details to be appreciated. The profiles from all the sites over the full depth are shown together in Figure 4.4. The plots confirm the consistency of the profile at greater depths, apart from the depth at which the NU_B is encountered (See Figure 2.6), and also the considerably variability of the near-surface profiles. The latter feature justifies the need for location-specific site amplification factors rather than the network-average factors implicit in the V1 GMPE. Moreover, these profiles indicate that there is likely to be even greater lateral variation over the entire study area, which further reinforces the need to model the site amplification functions at different locations.

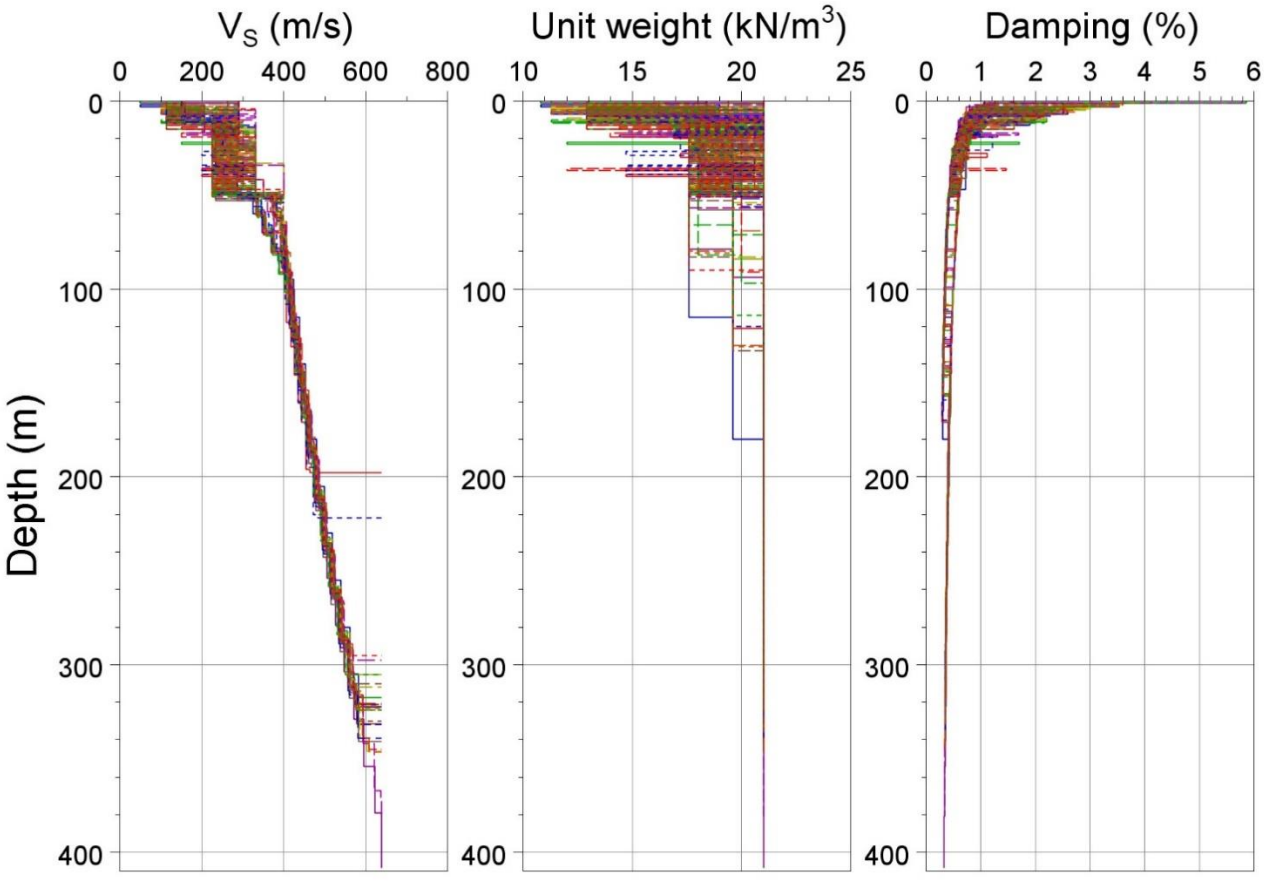

Figure 4.4. Profiles of shear-wave velocity, unit weight and density at the KNMI accelerograph stations; for the plots at individual stations see Appendix II

The profiles were developed by Deltares using the field-wide models that have been developed as part of the Groningen seismic hazard and risk assessment project (Kruiver *et al*., 2015). Brief explanations regarding the sources of information for the three sets of profiles are given below. Greater details regarding many aspects of the profile construction are provided in Chapter 7, where the development of such profiles for non-linear site response analyses over the entire field is described.

Shear-wave velocity, V_S

The V_S profiles are a combination of three models of V_S of varying depth ranges. The shallow depth range from the surface to NAP-50 m consists of V_S values assigned to vertical sections through the GeoTOP model of stratigraphic units and lithological class (Section 7.1). The V_S values are based on the average V_S measured in the Groningen SCPT (seismic CPT) dataset for each combination of stratigraphical unit and lithological class. The intermediate depth range, from NAP-50 m to approximately NAP-120 m, is based on the reinterpretation of the ground-roll signal from Shell's legacy data of land seismic surveys (Section 7.2). Between a depth of approximately NAP-70 m and the reference baserock horizon NU_B, the V_S is derived from the improved time-to-depth (T2D) model from the seismic imaging of the reservoir (Section 7.2).

Density or Unit Weight

The assignment of unit weight is based on representative values for lithostratigraphical units derived from CPTs using Lunne *et al*. (1997). For the Formations of Oosterhout and Breda, present at deeper depth ranges, the density is taken to be constant, consistent with the borehole logs from two NAM boreholes BRW5 and ZRP2 (see Section 7.4).

Damping

Small strain damping (D_{min}) is derived using Darendeli's 2001 equation for D_{min} for clay and sand (Section 7.5) and the newly derived equations for damping for peat (Section 7.6). D_{min} is dependent on loading frequency and number of cycles of loading; default values were used for frequency (1Hz) and for the number of cycles (10). Other input parameters for the small strain damping equations are unit weight, over-consolidation ratio (OCR) and plasticity index (Ip). For each layer, these values were automatically estimated combining geological layering model (Kruiver *et al*., 2015) with representative values derived from CPTs (Lunne *et al*., 1997; Skempton & Henkel, 1953; Sorensen & Okkels, 2013) and expert geotechnical judgement.

The kappa measured at the stations (Section 4.1) reflects the combined effect of attenuation below the NU_B horizon and the attenuation of the material above the NU_B horizon, which results from the combined effect of material attenuation (due to D_{min}) and the effects of wave scattering. We can evaluate these effects by looking at the high frequency slope of the amplification factors at the station (Section 4.3); for simplicity we denote this contribution to

kappa, κ_{TF}. These damping values are shown in Figure 4.5. As expected, these values are lower than the kappa values measured at the stations (Section 4.1).

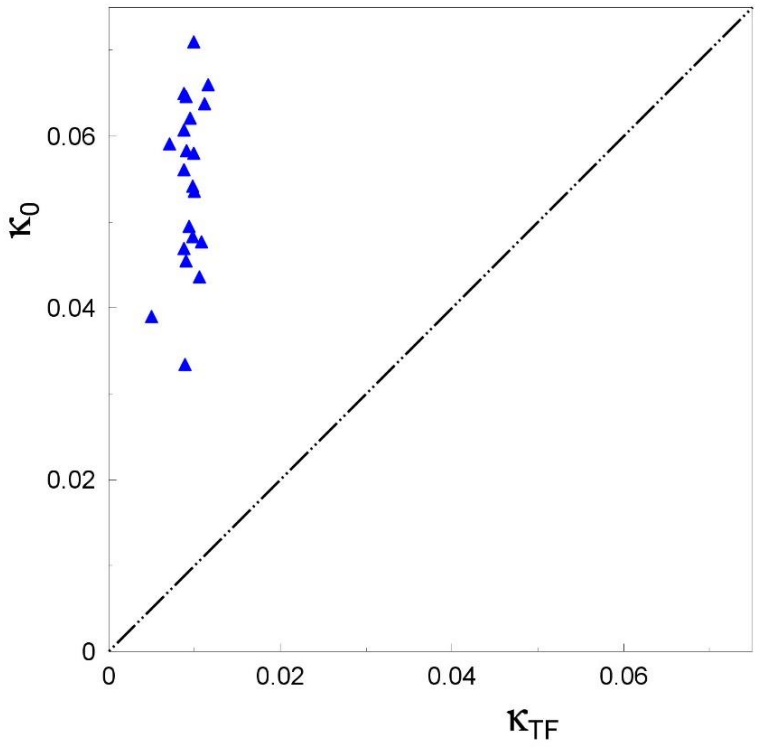

Figure 4.5. Comparison of κ_0 obtained from the expanded Version 2 dataset compared with the contribution to kappa at the stations estimated from 1D site response through the material above NU_B (κ_{TF})

Surface Geology and V_{S30} at the Stations

Figure 4.6 shows the locations of the recording stations superimposed on the general geological map of the Groningen field from Kruiver *et al*. (2015). Table 4.2 summarises the surface geology at each station, inferred from this map, together with the V_{S30} values calculated from the profiles in Appendix II. In general, the stations with lower V_{S30} values are found in the north of the field, where Holocene deposits of clays and peats are encountered, whereas the higher V_{S30} values are encountered to the south where Pleistocene deposits—mainly sands—predominate. Over the network of stations, the V_{S30} values calculated from the preliminary profiles range from 180 m/s to 277 m/s, with an average value of 212 m/s and median value of 200 m/s. These values are broadly consistent with those determined for the entire field (Kruiver *et al*., 2015). There are two important conclusions that can be drawn from these results, the first being that although the range of V_{S30} values may only be 100 m/s, in terms of relative changes from one location to another the spatial variation is appreciable. Secondly, in most site classification schemes the entire study area would be denoted as ‘soft soil’ and therefore significant site effects may be expected.

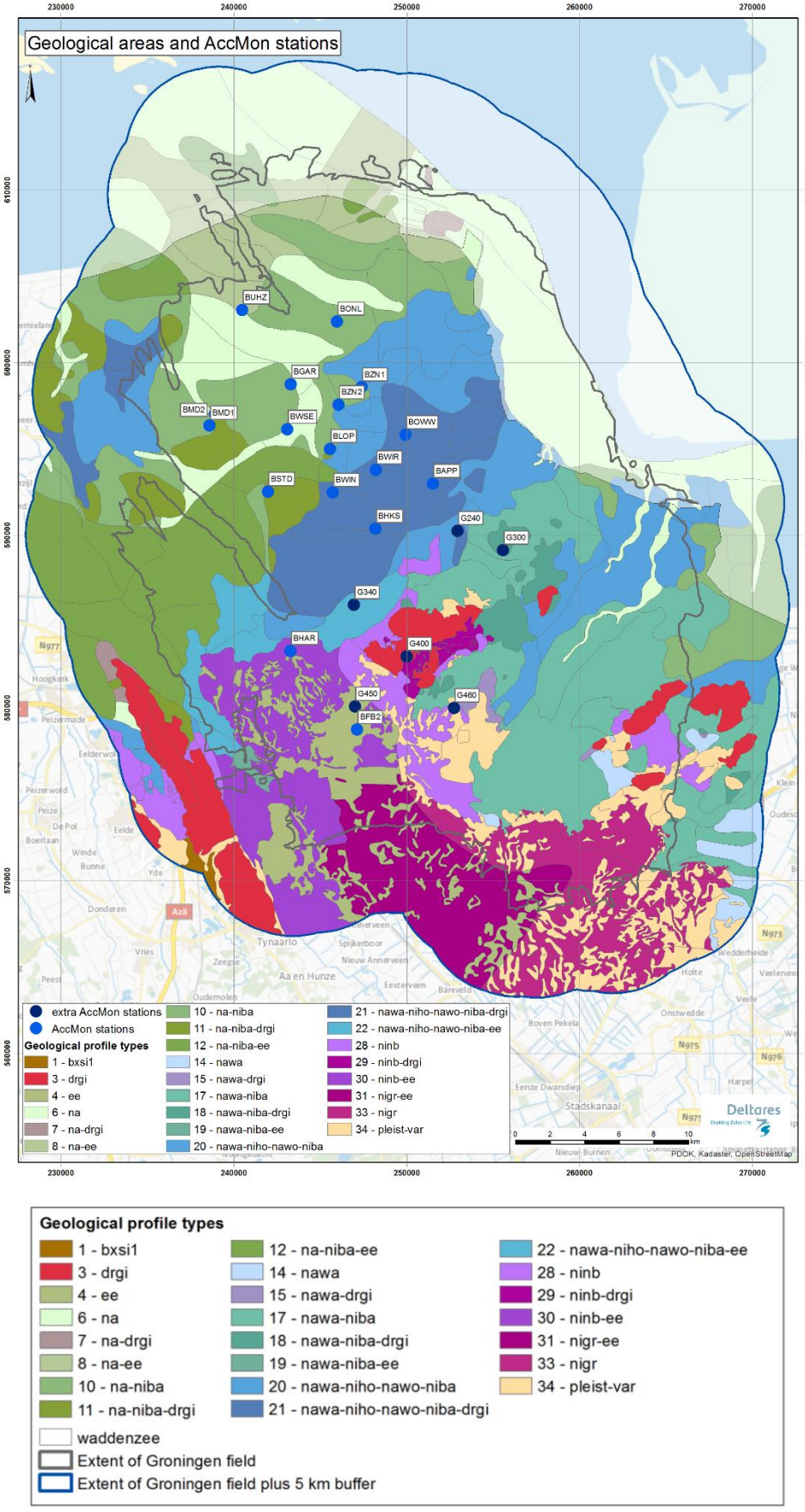

Figure 4.6. Geological map of the Groningen area from Kruiver *et al.* (2015) showing the locations of the recording stations

Table 4.2. Geological descriptions and calculated V_{S30} values of recording station sites

Station Code	V_{S30} (m/s)	Geological description of near-surface profile at station
BAPP	180	The location is situated in a non-erosive area. The Holocene deposits consist of clay with a peat layer in between at a depth of 1 metre. The basal peat is present in this area. Top of the Pleistocene is found at a depth of ± 5 metres with a slope to the east to 6 metres. Glacial till is present. The location is situated in the middle of a Peelo valley with a depth of 180 metres.
BMD1	180	The location is situated in a non-erosive area bordering a small erosive valley in the north at a distance of 700 metres with a depth up to 15 metres. Pleistocene is covered by Holocene deposits with a thickness of ± 10 metres. The deposits can be divided in a coverage layer of clay with a thickness of ± 3 metres on a sandy layer. The basal peat and older clay has remained untouched and present.
BOWW	184	The location is situated in a non-erosive area. The top of the Pleistocene is situated at a depth of 8 to 10 metres. The Holocene deposits consist of a clay layer with a peat layer in between at a depth of ± 2.5 metres. Basal peat is present in this area. To the east at a distance of 500 metres is a small erosive valley with clay on top of boulder clay from the formation of Drente. The top of the boulder clay is found at a depth of 10 metres. The location is situated on the bottom of a Peelo valley with a depth of 100 metres.
BONL	186	The location is situated on a NW – SE running ridge with a width of 1500 metres and sided with Holocene erosion valleys with a depth up to ± 25 metres. The Pleistocene is covered with ± 14 metres of Holocene deposits mostly consisting of sand with clay layers. The base of the Holocene consists of basal peat or humid clay and therefore the top of the Pleistocene is not eroded.
BZN2	186	The location is situated in a non-erosive area bordering an erosive valley in the West. The Pleistocene is covered with Holocene deposits consisting mostly of sand that is part of an erosive system but at the base older clay and basic peat has remained untouched. Thickness of the Holocene is up to ± 12 metres. The location is situated outside the Peelo valleys.
BZN1	189	The location is situated in a non-erosive area. The Pleistocene is covered with Holocene deposits consisting mostly of sand that is part of an erosive system but at the base older clay and the basal peat has remained untouched. Thickness of the Holocene is up to ± 12 metres. The location is situated outside the Peelo valleys.
BGAR	193	The location is situated on the edge of a non-erosive area bordering an erosive valley in the east. The Pleistocene is covered with ± 14 metres of Holocene deposits consisting of sands and clay. The base of the Holocene consists of Basic peat or humid clay and therefore the top of the Pleistocene is not eroded.
BWSE	194	The location is situated in a narrow Holocene erosive valley with a width of ± 800 metres. The depth of the valley is 12 metres southwest of the location and deepening up to ± 20 metres to the northeast. The Holocene fill of the valley is in the southwest in majority clay and to the northeast a mix of sand and clay. In the non-erosive surrounding area, the basal peat is found on the top of the Pleistocene. The accelerograph is positioned either within our just outside this Holocene valley. The site is position outside of the Peelo valley.
KANT	196	The location is situated in an erosive area within distance of 750 metres from a non-erosive area in the southeast. The Holocene deposit consist of clay with an erosive sand base on top of a thin Pleistocene sand layer. Underneath 'Pot clay' (Peelo formation) can be found.The location is situated in an erosive area within distance of 750 metres from a non-erosive area in the southeast. The Holocene deposit consists of clay with an erosive sand base on top of a thin Pleistocene sand layer. Underneath 'Pot clay' (Peelo formation) can be found. Top of the Pleistocene at the location is found at a depth of ± 20 metres. In the southeast the top Pleistocene depth is ±10 metres with a slope to the north and the northeast to 25 metres.
BMD2	198	The location is situated in a non-erosive area bordering a small erosive valley in the West at a distance of 100 metres with a depth up to 15 metres. Pleistocene is covered by Holocene deposits with a thickness of ± 10 metres. The deposits can be divided in a coverage layer of clay with a thickness of ± 3 metres on a sandy layer. The basal peat and older Clay has remained untouched and present.

Table 4.2. *Continued*.

Station Code	V_{S30} (m/s)	Geological description of near-surface profile at station
BWIN	198	The location is situated in a non-erosive area. The top of the Pleistocene is situated at a depth of 6 to 7 metres. The Holocene deposits consist of a clay layer with a peat layer in between, at a depth of ± 3 metres. The basal peat is present in this area as is the glacial till. The location is situated on the bottom of a Peelo valley with a depth of 135 metres.
BSTD	199	The location is situated in a non-erosive area. The top of the Pleistocene is situated at a depth of ± 9 metres. The Holocene deposits are clay layers. The basal peat is present in this area. Possibly part of the survey line is positioned on an small erosive channel. The location is situated on the declining slope of a Peelo valley that reaches from 40 metres at the location up to the maximum depth of 136 metres in the centre over a distance of 2.5 kilometres to the east.
BLOP	202	The location is situated in an erosive area with clay on top of the Pleistocene. The top of the Pleistocene is situated at a depth of ± 10 metres. The Holocene deposits consist mainly of Clay. To the south east at a distance of 500 metres a thin layer of basic peat covers the Pleistocene. The location is situated on a declining slope of a Peelo valley that reaches from 70 metres at the location up to the maximum depth of 115 metres in the centre over a distance of 2 kilometres to the southeast.
BWIR	203	The location is situated in a non-erosive area. The top of the Pleistocene is situated at a depth of 6 to 7 metres. The Holocene deposits consist of a clay layer with a peat layer in between at a depth of ± 3 metres. The basal peat is present in this area as is the glacial till. The location is situated on a declining slope of a Peelo valley that reaches from 109 metres at the location up to the maximum depth of 115 metres in the centre over a distance of 0.5 kilometre to the northwest.
BUHZ	203	The location is situated in an erosional valley bordered in the east by a non-erosive area. Eem deposists (sand) are present. Pleistocene is covered with erosive Holocene deposits consisting of fine sand. Thickness of the Holocene differs from 14 metres in the east of the line up to 30 metres to the west in the centre of the erosive channel. The site is position outside of the Peelo valley.
BHKS	215	The location is situated in a non-erosive area. The Holocene deposit consists of clay with a peat layer in between at the depth of 0.5 meter. Basic peat is present in this area. Top of the Pleistocene is found at a depth of ± 5 metres. Eem deposits (sands) are present. Glacial Till (Boulder clay) is present. At a distance of 1 kilometre to the west of the line an erosive valley with a depth of ± 8 meter can be found oriented towards the northeast. Here the Holocene clay layer is present on the Pleistocene that consists of boulder clay or cover sand. The location is situated on a flat part of a Peelo valley between two deeper valleys, the base of the valley varies from 63 metres at the accelerograph station up to the maximum depth of 174 metres in the centre of the valley over a distance of 1.5 kilometre to the southwest.
G340	219	Location is situated in a non-erosive area. The Pleistocene is covered with ± 4 meter of Holocene deposits consisting mainly of peat The pleistocene consists of a thick layer of cover sand (Boxtel Formation) with a thickness up to 7 mtr. At the location Eemian is found consisting of loam and medium coarse sand upon 'pot clay' of the Peelo formation at a depth of 14mtr. The location is situated on a Peelo valley with a depth of 105 meter, the maximum depth of the valley is 175 meter in the centre.
BHAR	221	The location is situated in a non-erosive area. The Holocene clay has not been deposited only a peat layer is found on top of the Pleistocene. The peat layer has a thickness of 40 cm. To the north the peat layers thickens up to 1 metre. Eem deposists (sand) are present. The location is situated on the end of a declining slope of a Peelo valley that reaches from 70 metres at the location up to the maximum depth of 106 metres in the centre over a distance of 1.3 kilometres to the northwest.
G240	238	Location is situated in a non-erosive area. Pleistocene is covered with ± 4 meter of Holocene deposits consisting of clay upon the Basal peat. Top of the Pleistocene is therefore not eroded A thin layer of boulder clay is found in the vicinity of the location, but is not wide spread. The Peelo formation is found at a depth of 5 to 6 metres, main lithology is medium fine sands At a distance of 2000 metres to the west a deep NW-SW running Peelo valley can be found with a depth of ± 170 m.

Table 4.2. *Continued*.

Station Code	V_{S30} (m/s)	Geological description of near-surface profile at station
G400	244	The location is situated in a non-erosive area. The thickness of the Holocene is very limited (0-2 metres). The top of the Pleistocene consists of cover sands which overlie a thin layer of glacial till (1-2 metres). The site is situated at a flank of a Peelo valley, a thick layer of 'pot klei' could be is present.
G460	256	The location is situated in a non-erosive area. To the north a small incised Holocene valley is present. The thickness of the Holocene is very limited (0-2 metres). The top of the Pleistocene consists of a thick payer of cover sands. The site is situated ion the flank or just outside a Peelo valley. The Peelo Formation consists probably of fine to coarse sand and clay layers.
G450	258	The location is situated in a non-erosive area. The thickness of the Holocene is very limited (0-2 metres). The top of the Pleistocene consists of a thick payer of cover sands which overlie clay and sand layers belonging to the (lacustrine) Eem formation . The site is situated in the centre of a Peelo valley (south end of a north-south valley). The valley fill consists probably of fine to coarse sand.
BFB2	273	The location is situated in an area with cover sand (Boxtel Formation) at the surface. There are no Holocene deposits present. Locally some thin peat layers can be found at or near the surface. Eem deposits (sand and clay) are present. The location is situated on a declining slope of a Peelo valley that reaches from 78 metres at the location up to a maximum depth of 100 metres in the centre of the valley, over a distance of 1 kilometre to the southwest.
G300	277	Location is situated in a non-erosive area. The Pleistocene is covered with ± 4 metres of Holocene deposits consisting of clay upon the Basal peat. The Peelo formation has an almost horizontal top. There might be a thin layer glacial till present. The Peelo formation is found at a depth of 5 to 6 metres, main lithology is medium fine sands. The top of the Peelo formation can consist of clay.

4.3. Site response analyses and linear amplification factors for stations

In order to apply the procedure illustrated in Figure 2.3 to develop the GMPE for rock motions at the NU_B horizon, it is necessary to transform the surface recordings to that level. For different elements of the model-building process, both the Fourier amplitude spectra (FAS) of acceleration and acceleration response spectra are required at the NU_B horizon, so amplification factors are required in both domains. The methodology applied to calculate these amplification factors is 1D linear analysis using the random vibration theory (RVT) approach as implemented in the program STRATA (see Section 8.1). As noted in the previous section, due to the low amplitudes of the recorded motions only linear response is expected hence the only input needed are the profiles described in Section 4.2, together with the properties of the elastic half-space starting at the NU_B horizon (namely, V_S = 639 m/s, unit weight = 20.05 kN/m^3).

The input motions at the NU_B horizon, which are required for the computation of the amplification functions for response spectra, are obtained from point-source simulations using the parameters used to generate the motions for the generation of the NU_B motions subsequently used to derive the GMPE (see Section 6.1) for a range of scenarios reflecting the ranges covered by the recordings: **M** 2.0 to 3.6, and distances from 0 to 20 km.

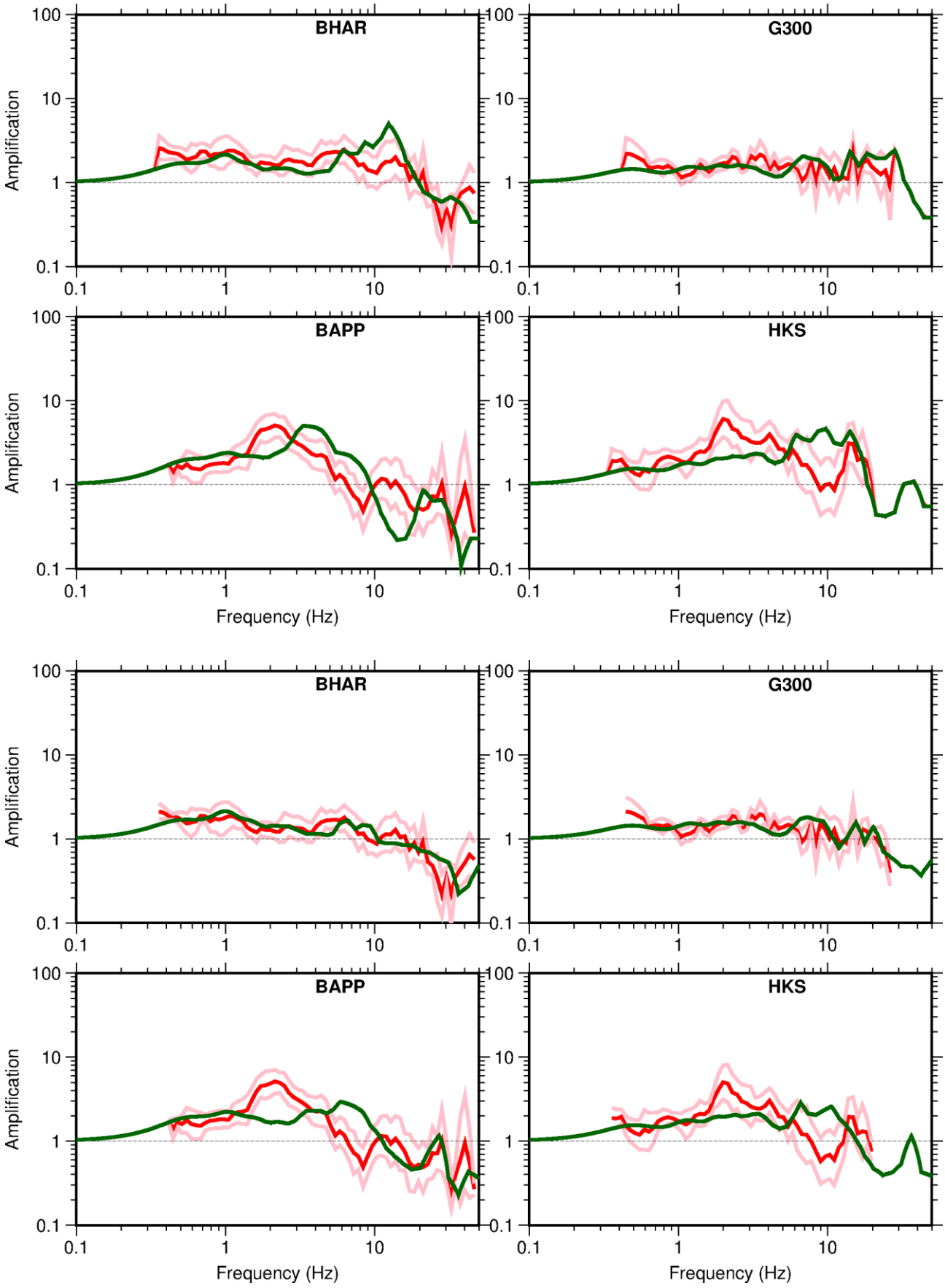

Figure 4.7. Comparison of empirical transfer functions (*red*), shown +/- one standard deviation, with computed transfer functions (*green*) for sites with (*upper block*) and without (*lower block*) a top-most soft soil layer

The analytical transfer functions computed with STRATA are smoothed using a Konno-Ohmachi filter (Konno & Ohmachi, 1998) with the *b*-parameter set equal to 40. The computed and smoothed FAS amplification factors, or transfer functions, are shown in Appendix III, and the response spectra amplification factors in Appendix IV. At a few recording stations, the inferred V_S profiles include a shallow (1-3 m) low-V_S layer that resulted in high-frequency resonances; these layers were typically soft clays or peats. These high-frequency resonances were not observed in the preliminary inversions conducted on the recorded data (Figure 4.7). A decision was therefore taken to compute the site response for these stations using a profile that did not include the shallow low-V_S layers. Figure 4.7 also includes the comparison of the computed transfer functions with those estimated from the inversion for profiles where the uppermost layers were removed. The comparison clearly shows that the transfer functions obtained using the modified profiles fit the recorded data much better. Table 4.3 lists the stations where the profiles assembled using the geological model of Kruiver *et al*. (2015) were modified.

Table 4.3. Station for which the V_S profiles were modified

Station	Modification
BHAR	Remove top 1 m peat layer
G240	Remove top 2 m of soft clay
G300	Remove top 1 m peat layer
G340	Remove top 3 m (2 m clay layer, 1m Peat layer)
HARK	Remove top 1 m peat layer
HKS	Remove top 1 m peat layer
BAPP	Remove top 3 m (2 m clay layer, 1m Peat layer)

4.4. *In situ* measurements of shear-wave velocities

In order to develop a GMPE including field-specific site response characteristics it is clearly very important to have the best possible dynamic characterisation of the locations at which the ground-motion recordings have been obtained. In this chapter we have presented station characteristics as inferred from the recordings themselves, in terms of kappa, but the site amplification functions have been calculated using profiles developed from a field-wide model in which near-surface velocities are assigned based on lithology. Recognising the need to have reliably measured shear-wave velocity profiles at the recording stations, NAM commissioned Deltares to conduct *in situ* measurements at the locations of the KNMI accelerograph stations (Figure 3.1) with a view to extending these subsequently to the new accelerographs being co-located with the 200-m geophone boreholes (Figure 3.2).

The proposed campaign of *in situ* measurements envisaged applying a wide range of techniques at the first few stations in order to test and calibrate the different approaches in order to select those most suitable for general application across the networks. The multiple measurement approach was also designed to provide insight into the inherent uncertainty in the resulting V_S profiles and, to some extent, the degree of lateral heterogeneity at each site. The techniques envisaged included seismic CPT (with differing offsets), active MASW (with multiple sources), passive MASW, cross-hole measurements and PS suspension logging.

Four of the accelerograph stations were identified as good candidates for the pilot measurements using the full range of techniques based on sampling different surface geological characteristics (Figure 4.6): BHAR, BOWW, BWIN, and BZN2.

Unfortunately, there were numerous and serious delays in obtaining access to many of the sites that were selected for the pilot studies with the consequence that measurements were not conducted in time for the interpreted profiles to be used in the initial development of the V2 GMPE. For this reason, the profiles presented in Section 4.2 were generated and employed, with a view to re-evaluating these profiles, and the resulting models, in the subsequent revision and refinement of the V2 model. The use of the measured profiles in these refinements is discussed in Section 13.2.

5. INVERSIONS of GROUND MOTIONS for SOURCE, PATH and REFERENCE ROCK PARAMETRES

In view of the limited magnitude range of the earthquakes currently represented in the Groningen ground-motion database—with an upper limit of **M** 3.6—one of the key challenges in developing the GMPEs for the hazard and risk models is the extrapolation to the largest magnitude currently considered, **M** 6.5. As for the V1 GMPEs, this extrapolation is performed using point-source simulations based on seismological theory. In order to perform these simulations, estimates of the source, path and site parametres that define the Fourier amplitude spectra (FAS) of the motion are required. This chapter presents the inversion of the FAS of the Groningen ground-motion recordings to obtain estimates of these source, path and site parameters.

5.1. Fourier amplitude spectra at the reference rock horizon

In order to develop a stochastic ground-motion simulation model at the reference rock horizon (the base of the Upper North Sea group, NU_B; Section 2.3) we require source, path and reference rock parameters at that horizon. The database of recorded surface motions are therefore first deconvolved with the response of the overlying material. Since the recordings are weak-motion—and therefore not expected to exhibit non-linear amplification effects—we use linear site amplification (as presented in Section 4.3). This provides a fully consistent approach as the same amplification functions (albeit with non-linear effects at high ground-motion levels) are used to transform the reference horizon GMPE back to the surface during hazard calculations.

Fitting source, path and site parameters for developing a stochastic simulation model requires only the FAS. Therefore, the phase information is not required and the deconvolution simply involves dividing the FAS of recordings at the surface by the linear FAS amplification functions (Section 4.3; Appendix III).

5.2. Overview of inversion process for source, path and reference rock parametres

The FAS of the 16 Groningen earthquake recordings (Section 3.2) and an additional 8 smaller magnitude earthquake recordings (Section 3.3), deconvolved to the NU_B horizon, are used to determine the source, path and reference rock parameters. Initially the FAS are fit in the log-linear acceleration-frequency domain to estimate the slope of the high-frequency decay: kappa (κ) (Anderson & Hough, 1984). Values of κ were measured using only the high frequency information (f > 10 Hz) for some recordings, as described in Section 4.1, in order to define the site-specific component (κ_0), however it is not possible to use the Anderson & Hough (1984) approach for noisy recordings, and those of smaller earthquakes. Record-specific κ values were therefore estimated for all FAS using a broadband fit to extend the usable frequency range to lower frequencies (*e.g.*, Scherbaum, 1990). The approach we are using is detailed in Edwards *et al*. (2011); essentially it fits the FAS with an earthquake far-

field point-source model Brune (1970, 1971), defined by its source-corner frequency (f_0) and long-period spectral displacement plateau (related to the seismic moment, M_0), along with the κ parameter to account for attenuation. The FAS for an acceleration recording is given by:

$$\Omega_{ij}(f) = 4\pi^2 f^2 \hat{\Omega}_0 E_i(f, f_{0i}) B_{ij}(f, \kappa) T_j(f) \quad (5.1)$$

where *f* is the frequency and *i* and *j* represent the i^{th} source and j^{th} station respectively. $\hat{\Omega}_0$, the far-field spectral displacement plateau is a frequency independent factor that is dependent on the seismic moment (M_0), average amplification, geometrical spreading and radiation pattern effects. $E_i(f,f_0)$ is the normalised Brune (1970, 1971) source model with a defining corner-frequency f_{0i}:

$$E_i(f, f_{0i}) = \frac{1}{\left(1 + \left(\frac{f}{f_{0i}}\right)^2\right)} \quad (5.2)$$

$B_{ij}(f,\kappa)$ is the attenuation along the path:

$$B_{ij}(f, \kappa) = e^{-\pi f \kappa} \quad (5.3)$$

The site amplification function, $T_j(f)$, reflects the amplification between the source and NU_B horizon, in addition to any effects not accounted for through the deconvolution described in Section 5.1 (*e.g.*, reflections).

Frequencies up to 50 Hz are considered in the fitting, with the bandwidth defined based on the measured signal exceeding the pre-event noise by a factor 3 (*i.e.,* signal-plus-noise to noise ratio > 3, SNR > 2). A least-squares minimisation is performed to find the best fitting event-specific f_0 and record specific long-period spectral plateau and κ. Then, using the high-frequency decay term, κ, defined in the previous step the FAS are refit in log-log space (again with a least-squares minimisation) to more robustly determine the record-specific long-period spectral displacement plateau and the event-specific source corner-frequencies.

The stress parameter is obtained from the source corner frequency and the seismic moment using the Brune (1970, 1971) and Eshelby (1957) models:

$$\Delta\sigma = f_0^3 M_0 / (0.4906\beta)^3 \quad (5.4)$$

Where M_0 (in SI units) is given by (Hanks & Kanamori, 1979):

$$M_0 = 10^{1.5M + 9.05} \quad (5.5)$$

The shear wave velocity at the source, β = 2.0km/s, while the moment magnitudes are based on magnitudes provided by KNMI, invoking the assumption **M** = M_L. The far-field spectral displacement plateau is next inverted to provide values of average site amplification and geometrical decay as a function of distance using the approach detailed in Edwards *et al.* (2008).

5.3. Geometrical spreading function from full waveform simulations

In the V1 GMPEs, it was observed that the residual misfit followed a characteristic pattern with distance, indicating changes in the rate of decay. Such behaviour has previously been observed at regional scales, and is attributed to the Moho bounce effect: strong reflections from the Mohorovičoć discontinuity leading to increased amplitudes (and an apparent decrease in the rate of decay) somewhere between 50 and 120 km from the source. In order to explore if this effect—albeit on a smaller scale—was present in Groningen, full waveform simulations have been undertaken at Shell. These simulations have the potential to inform the inversion for source, path and site parameters. Since such inversions are known to suffer from parameter trade-offs, fixing terms in the inversion leads to increasingly robust results.

A range of simulations have been performed using the Shell WFD simulation code with progressively more complex velocity models, and using a variety of source mechanisms and distributions. For the source model, a wavelet was created that is consistent with the seismological model described in the previous section—termed the Brune wavelet—a time-domain wavelet with frequency characteristics of the Brune earthquake source model (Eq. 5.2). Three characteristic wavelets were used: f_0=0.4 Hz (equivalent to **M** 5.0 for a stress drop of Δσ = 30 bars, and β=2 km/s), f_0=2.3 Hz (**M** 3.5) and f_0=4 Hz (**M** 3.0). From initial testing in layered media, with velocities similar to those seen in the field, it was obvious that a change in the rate of geometrical decay should occur with increasing distance from the source (consistent with the residual analysis of the V1 GMPEs). In order to define a model for this behaviour, the most complex—and realistic—simulations were performed over 16000 s at 16 ms intervals, with ‘recordings’ made at 350 m depth (close to the NU_B) and at 200 m intervals in the horizontal *x* and *y* directions. The 3D Groningen velocity model was used (Figure 5.1). Source mechanisms were averaged over a range of strikes (130° to 150° and 310° to 350°, in 10° steps), dips (60° to 90° in 10° steps) and rakes (-100° to -80° in 10° steps). While it was shown that the source location made a small difference to the observed ground-motion, it was decided to place the source in the centre of the field to maximise the observed distances and range of azimuths.

For each of the source mechanism scenarios, the average ground-motion field in terms of geometrical mean horizontal PGV, normalised to the peak PGV, was plotted against hypocentral distance (Figure 5.2). It was clear that a three-segment geometrical decay function, with constant rates of decay over each segment, was appropriate and this was fit for each source mechanism. Based on the observations over numerous simulations, distances of 3, 7 and 12 km were selected as the hinge-points. Averaging the rates of decay between those distances the following values were determined:

- R = 3-7 km: $R^{-2.3 \pm 0.2}$
- R = 7-12 km: $R^{1.4 \pm 0.5}$
- R = 12-25 km: $R^{-1.9 \pm 0.4}$

The rates of decay did depend on the selected hinge-points, particularly for the smaller magnitudes (higher frequency) wavelets. Consequently, the hinge-distances and the decay rates must be taken as a coupled model. While significant variations were observed depending on source mechanism, the developed GMPE is independent of source mechanism (with earthquakes represented as hypocentres), it is therefore necessary to provide a model, as above, averaged over a realistic range of possible sources.

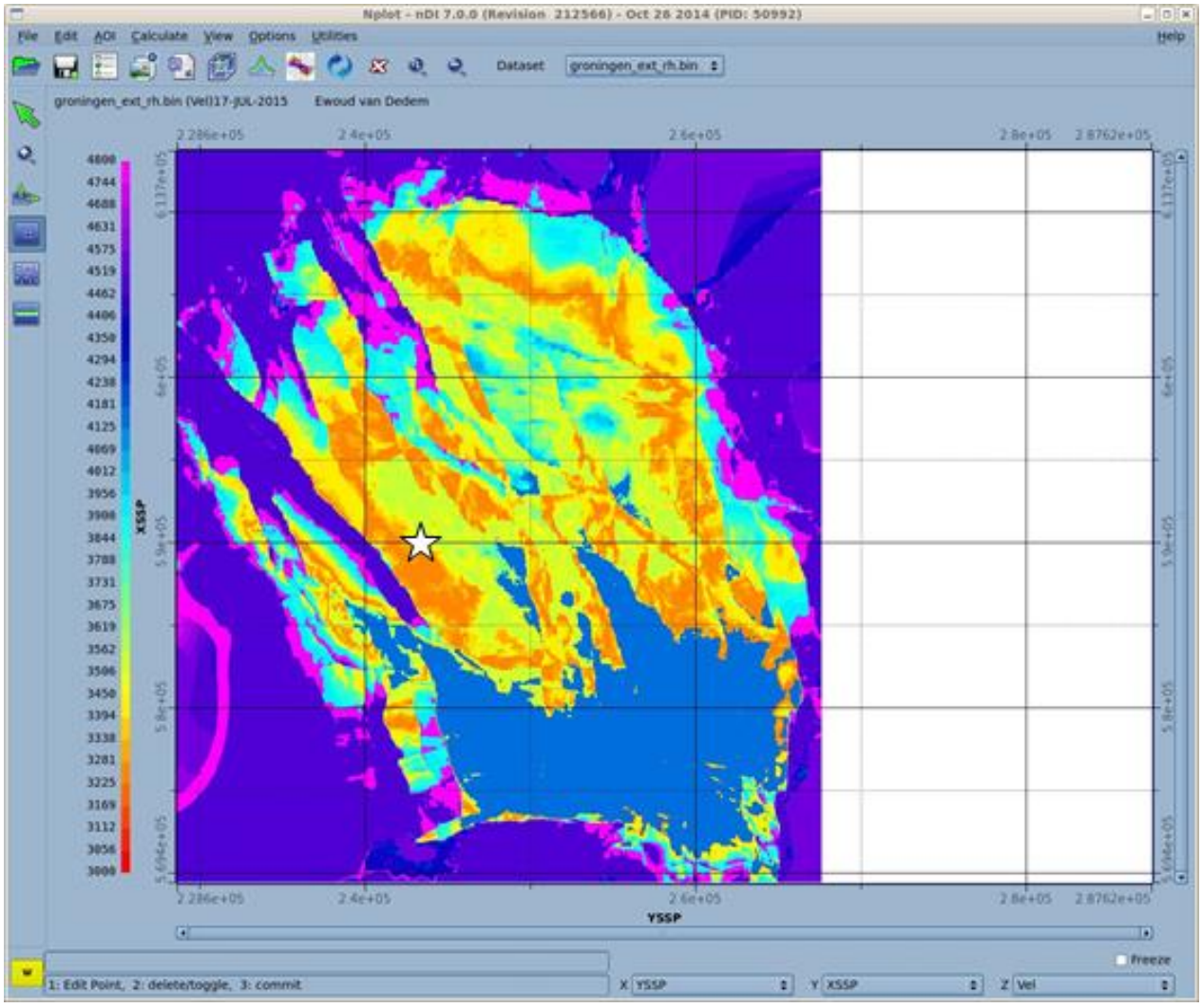

Figure 5.1. Screenshot of velocity model and source location used in full waveform simulations (*Courtesy of Ewoud van Dedem*)

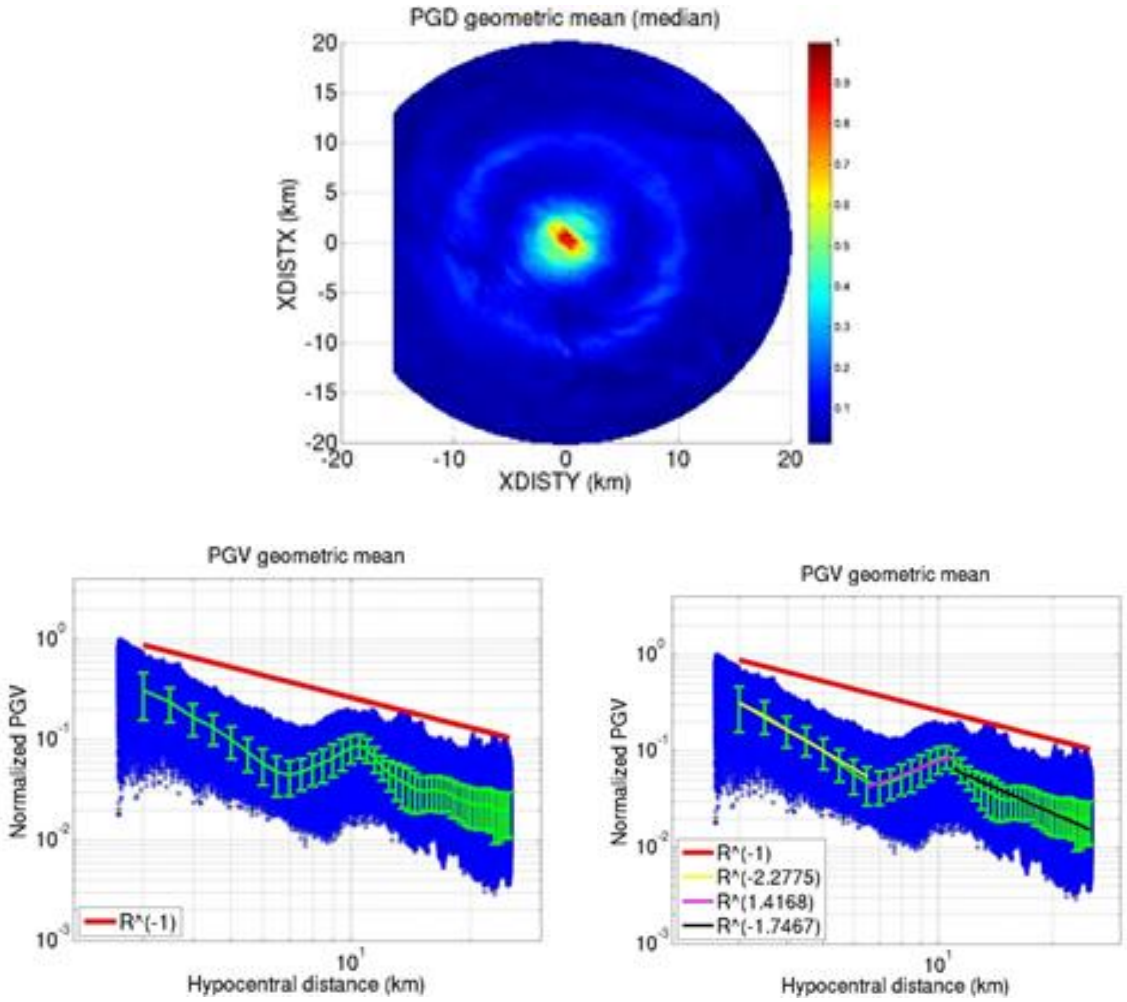

Figure 5.2. *Top*: Example of normalised ground-motion field; *Bottom*: PGV values plotted against hypocentral distance (*left*) with binned mean values every 500m, with 1/R decay (*red line*) indicated for reference; in the right-hand panel a 3-segment geometrical spreading model is fit to the binned data (*Courtesy of Ewoud van Dedem*)

5.4. Inversions for source, path and reference rock parametres

The spectral fitting of Groningen FAS, corrected to the NU_B, led to estimates of the stress parameter that were not substantially different to those determined in the V1 GPMEs (Figure 5.3). However, due to a decrease in the shear-wave velocity assumed at the source (2 km/s as opposed to 2.6 km/s) from improved knowledge of the velocity structure, the values were systematically higher. It should be noted, however, that since both stress-parameter estimates and the source-region velocity will be updated in the simulations, this will not result in a change in the simulated ground-motion levels (*i.e*., the FAS corner frequencies remain the same). A magnitude dependence is observed in the relationship between stress parameter versus magnitude plot (Figure 5.4). However, due to the limited number of earthquakes, the wide scatter, and the difficulty in extrapolating a magnitude-dependent stress-parameter, it is still recommended to use a constant stress parameter that is suitable for the larger magnitudes (*i.e*., 3 to 3.6).

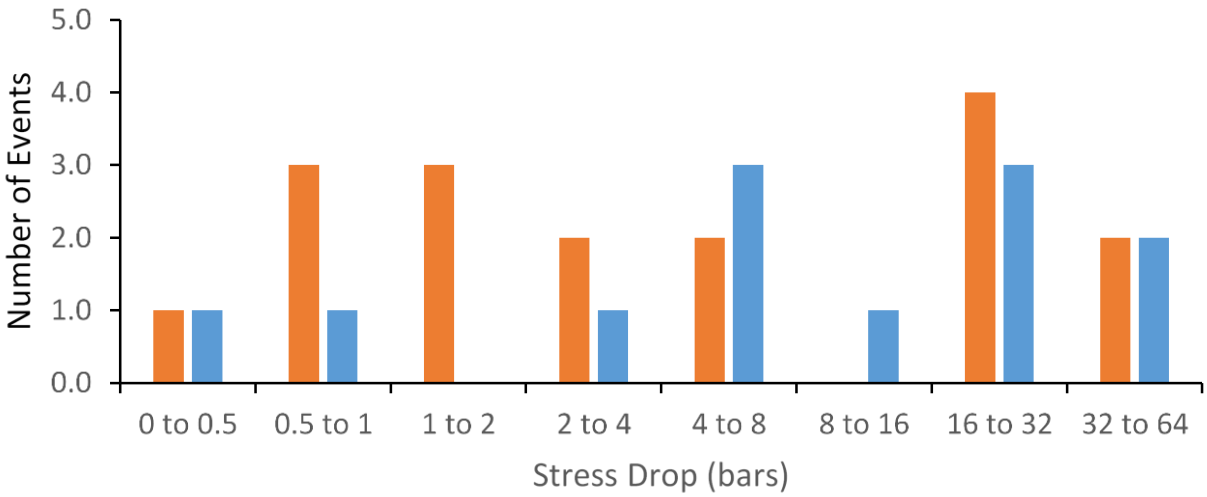

Figure 5.3. Comparison of stress parametres computed for the V2 data (*orange*) compared to those obtained for V1 (*blue*)

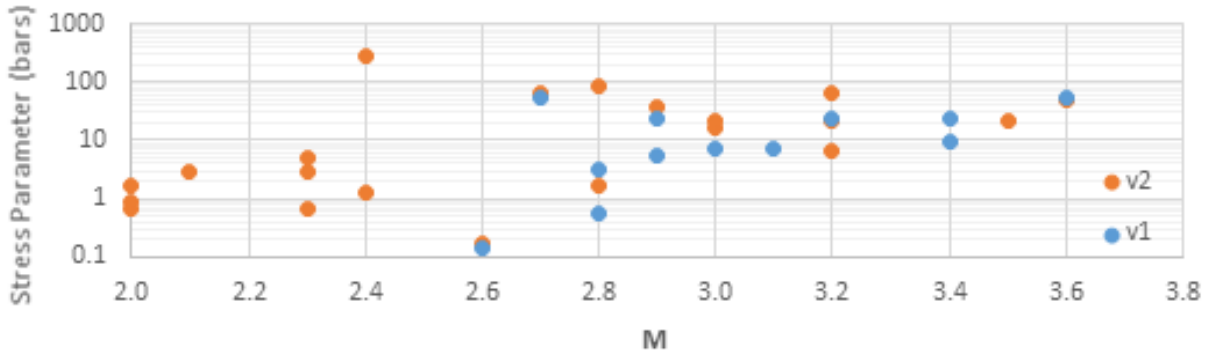

Figure 5.4. Best-fitting stress parameter for Groningen earthquakes: from V1 (*blue*) and the current version (*orange*)

As seen in Section 4.1 (Figure 4.2) there is a large uncertainty in the Q value obtained from the record-specific κ terms. A Q value of 380 is obtained for an average shear-wave velocity of 2.6 km/s (equivalent to 280 at 3.5 km/s). This is higher than previously obtained (both from V1 and from the high-frequency analysis in Section 4.1). Testing the Q value used in V1 of the model (Q = 150 at 3.5 km/s or Q = 202 at 2.6 km/s), we can see no discernible trend in the residual misfit (Figure 5.5), so there is no strong reason to change this value based on the new data—but it should be noted that it is still highly uncertain due to the limited distance range to the data used. As seen in Figure 5.6, the κ_0 values computed at the NU_B (allowing for the field-wide average Q) are mostly lower than those calculated at the surface (Section 4.1). This is consistent with the equivalent kappa, κ_{TF}, calculated between the NU_B and surface in Section 4.3 (Figure 4.4).

Figure 5.7 shows typical surface FAS fits using the record specific long-period displacement plateau; event-specific source corner frequency and site-specific amplification computed using the NU_B corrected FAS, and applying the NU_B to surface amplification function (Section 4.3). The plots of the fits for all of the NU_B adjusted FAS are presented in Appendix V.

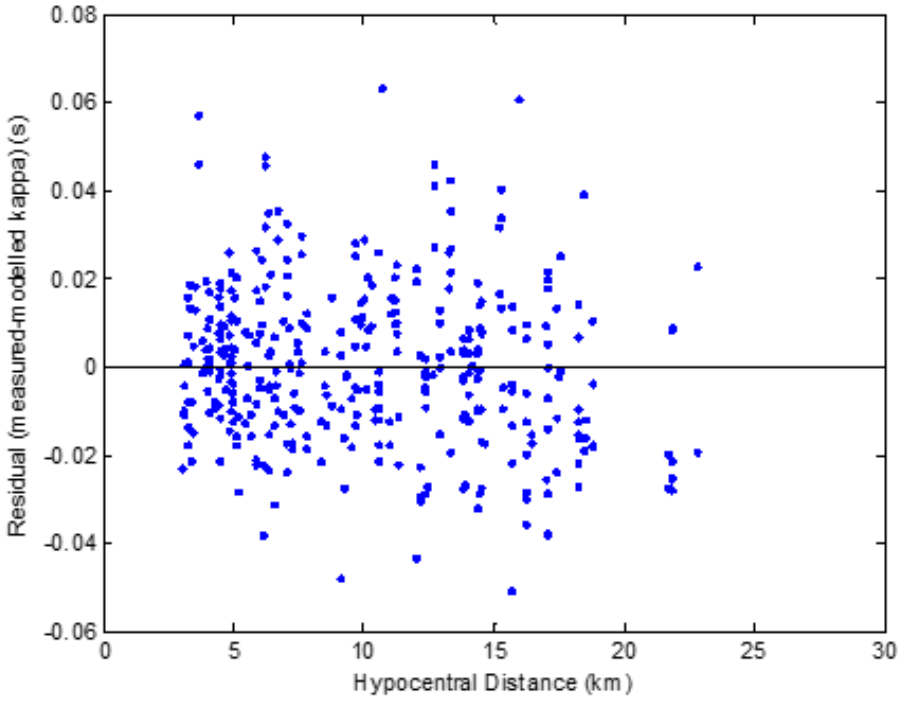

Figure 5.5. Residual misfit of the κ values as a function of distance using the V1 Q model (Q = 202, average velocity 2.6 km/s)

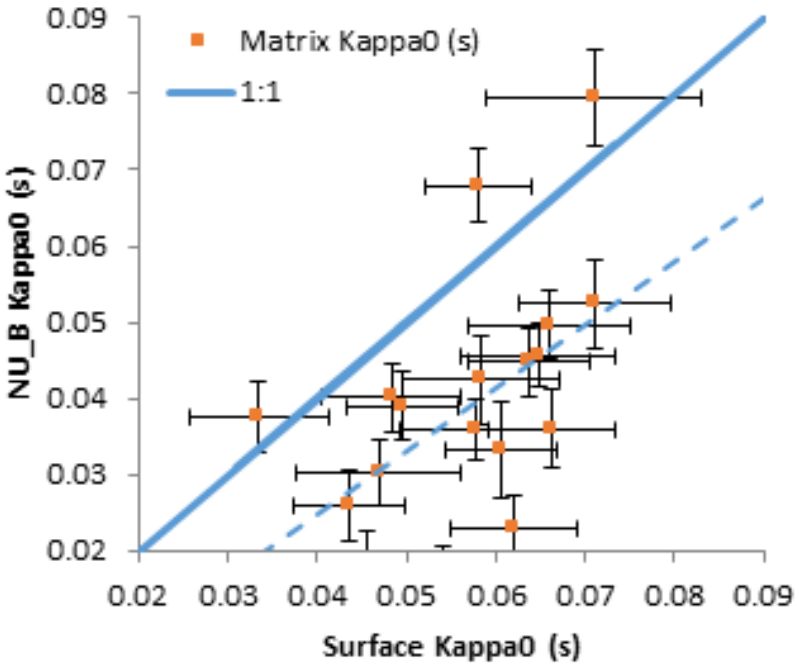

Figure 5.6. Comparison of κ_0 values computed at the surface (Section 4.1) and κ_0 values computed at the NU_B horizon

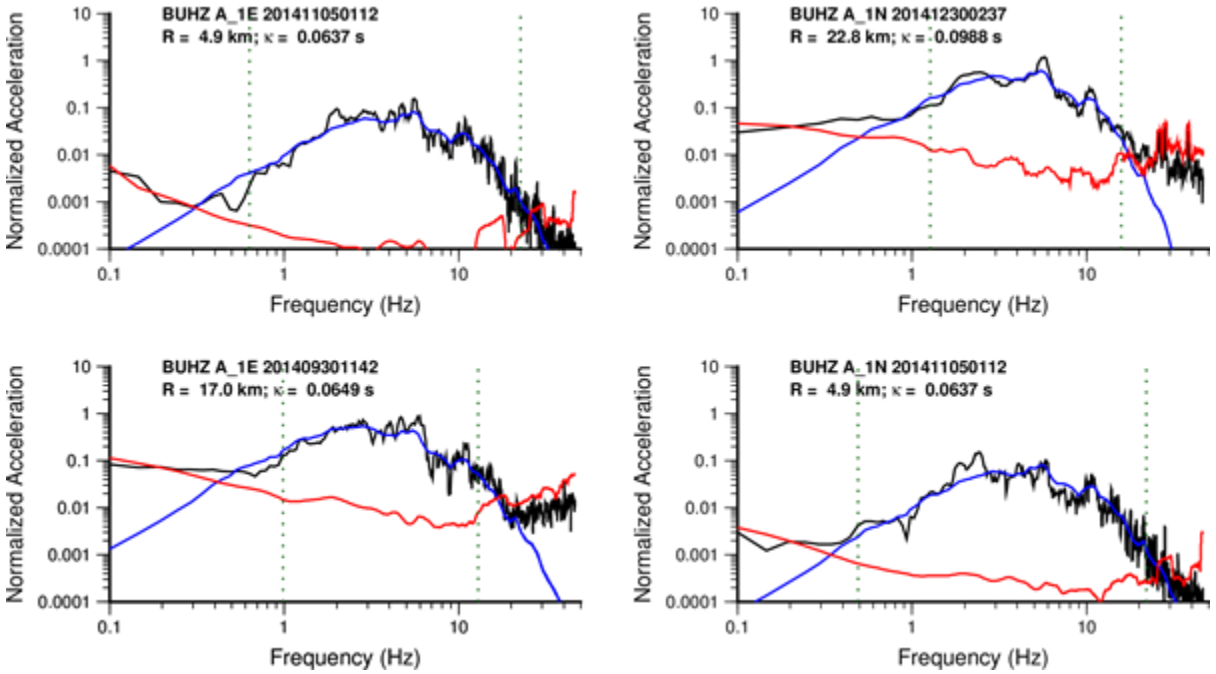

Figure 5.7. Example of spectral fits to the surface Groningen FAS. *Black*: signal FAS; *red*: noise FAS; *blue*: model (NU_B record specific long-period displacement plateau; NU_B event-specific source corner frequency; NU_B site-specific amplification and the NU_B to surface amplification from Section 4.3). The vertical lines indicate the fitting bandwidth

Using the long-period displacement plateau of the NU_B-corrected FAS, the geometrical decay function was inverted for along with average site amplification, fixing the moment magnitudes as in the database. The hinge points of the geometrical spreading function were selected to coincide with the distances observed during the full waveform simulations (Section 5.2): 7 km and 12 km. We assume that below 3 km (the minimum observed hypocentral distance), the decay is constant. The geometrical spreading rates determined using this model were much lower than observed in the simulations (Section 5.2) and are more consistent with the expectations of close to 1/R decay for a homogeneous medium (as used in the V1 GMPEs). Nevertheless, the shape of the decay is very similar to that observed during the simulations (Figure 5.8), indicating that the velocity structure has a strong impact on the recorded amplitudes as a function of distance. The decay rates observed were: $R^{-1.07}$ up to 7km, $R^{-0.074}$ from 7 to 12 km, and $R^{-1.91}$ beyond 12 km (although there are no data beyond around 30 km so we assume R^{-1} beyond 25 km, the limit of the full waveform analyses).

Comparing the empirically derived amplification at the surface with the NU_B to surface amplification (Section 4.3), in Figure 5.9 we see a good match in most cases, indicating that most amplification occurs above the NU_B. Some strong differences remain (e.*g.,* BAPP) which may indicate inaccuracies in the station V_S profiles derived at some sites. The source to NU_B amplification functions are shown in Figure 5.10 along with the NU_B to surface amplification functions (Section 4.3).

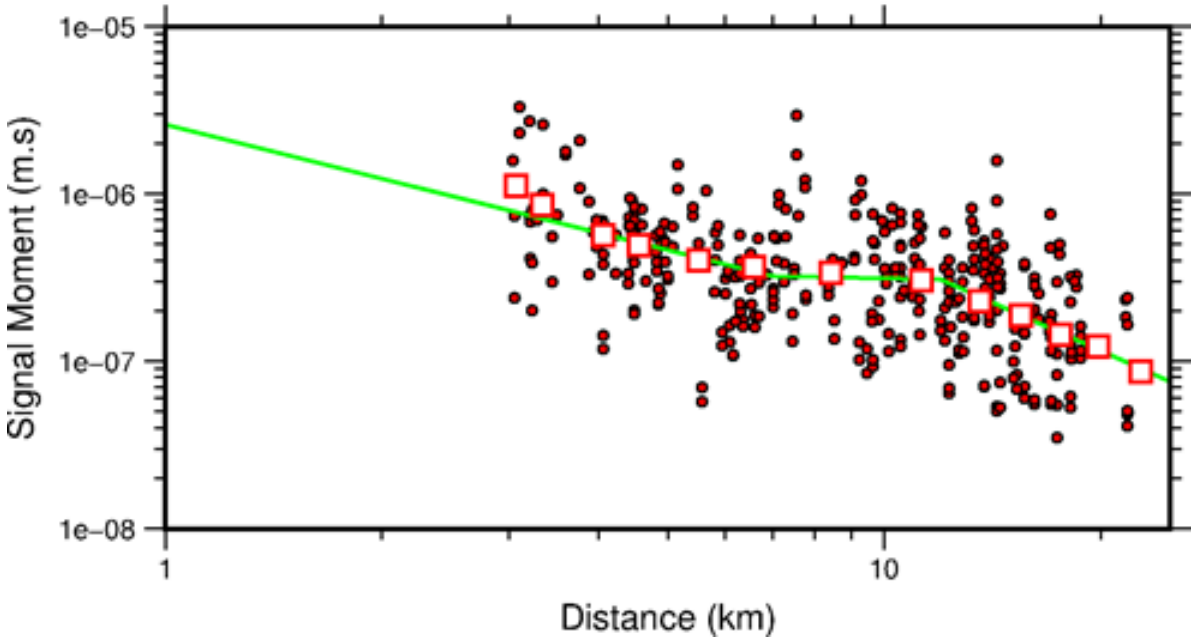

Figure 5.8. Signal moment (long-period spectral plateau) plotted against distance, along with binned mean values (*squares*) and the best fitting geometrical spreading model (*green*)

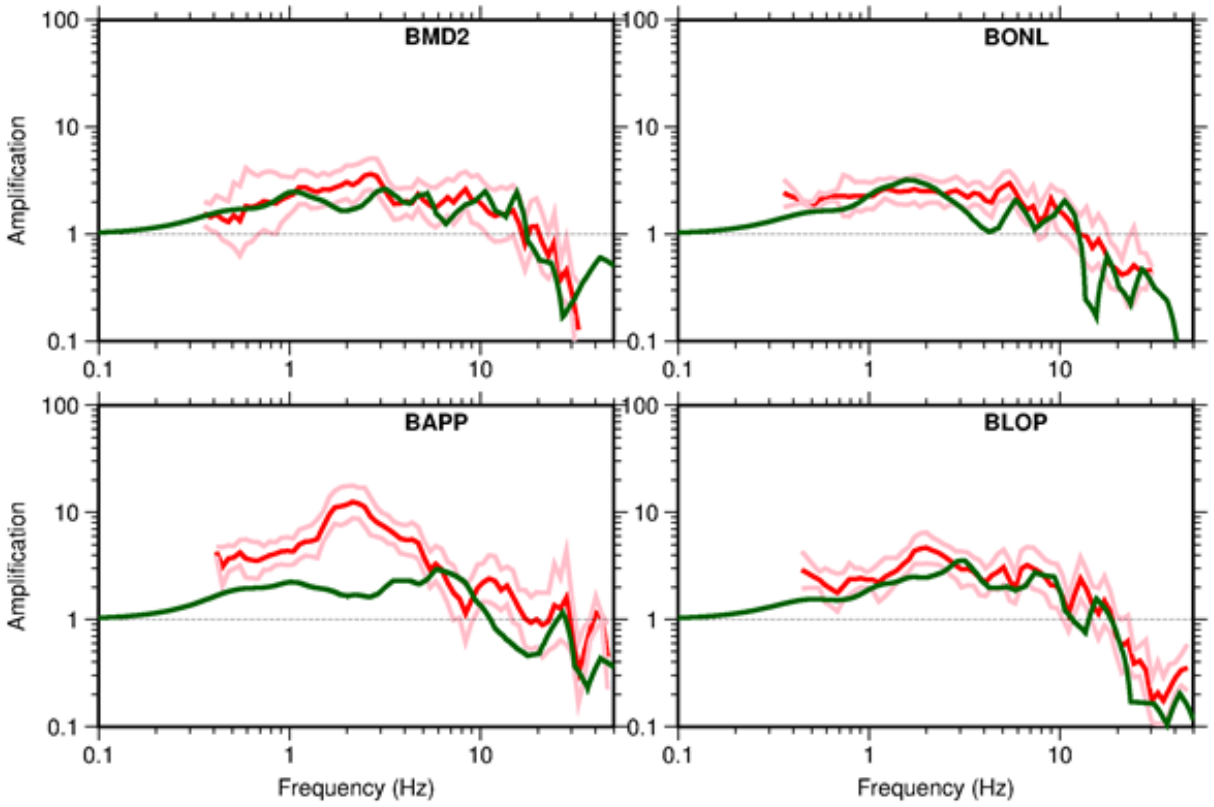

Figure 5.9. Comparison of inverted surface amplification (*red*) and standard deviation (*pink*) along with the NU_B to surface amplification (*green*) as presented in Section 4.3

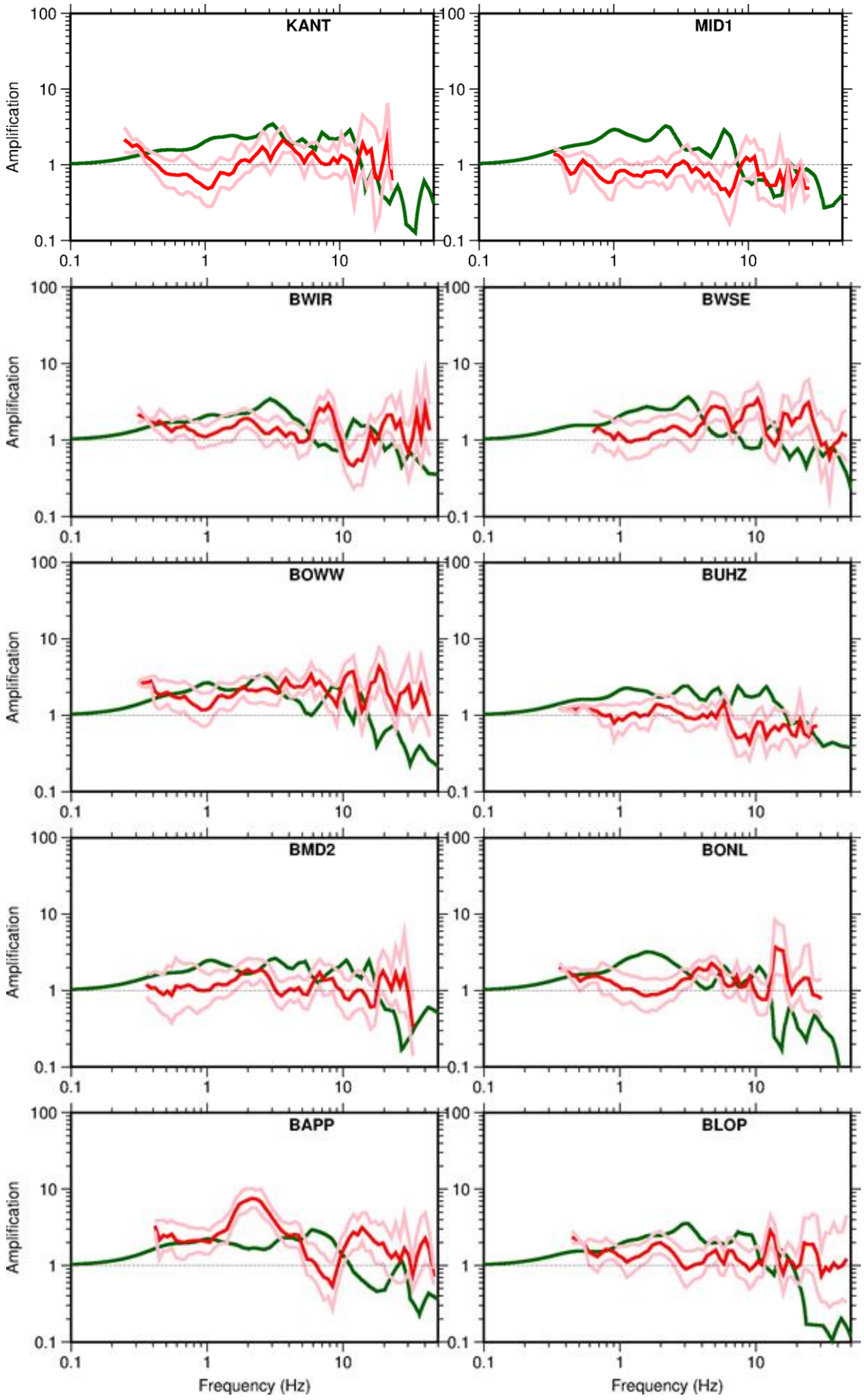

Figure 5.10. Source to NU_B amplification function (*red*) and standard deviation (*pink*) shown along with the NU_B to surface amplification functions (*green*)

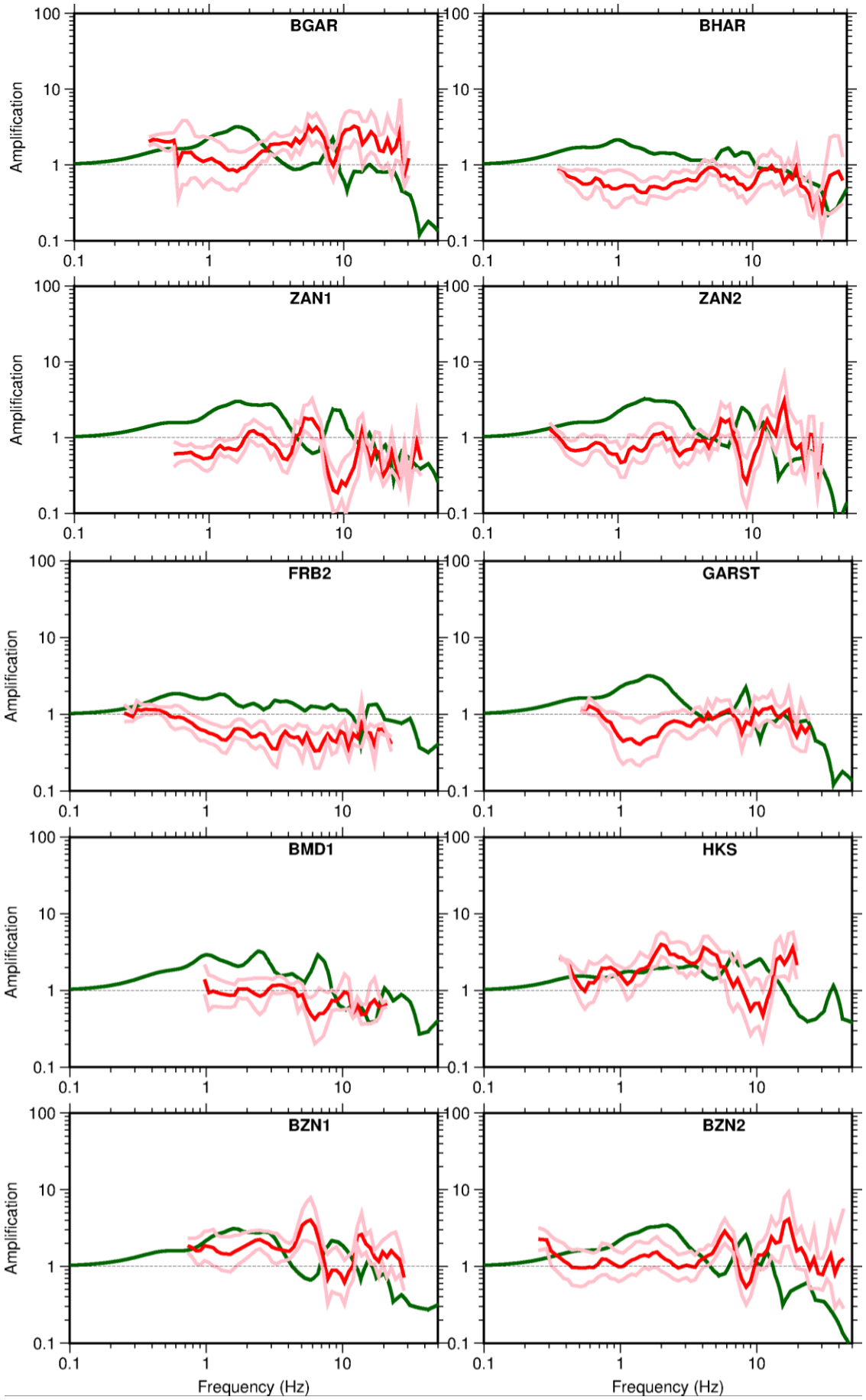

Figure 5.10. *Continued*

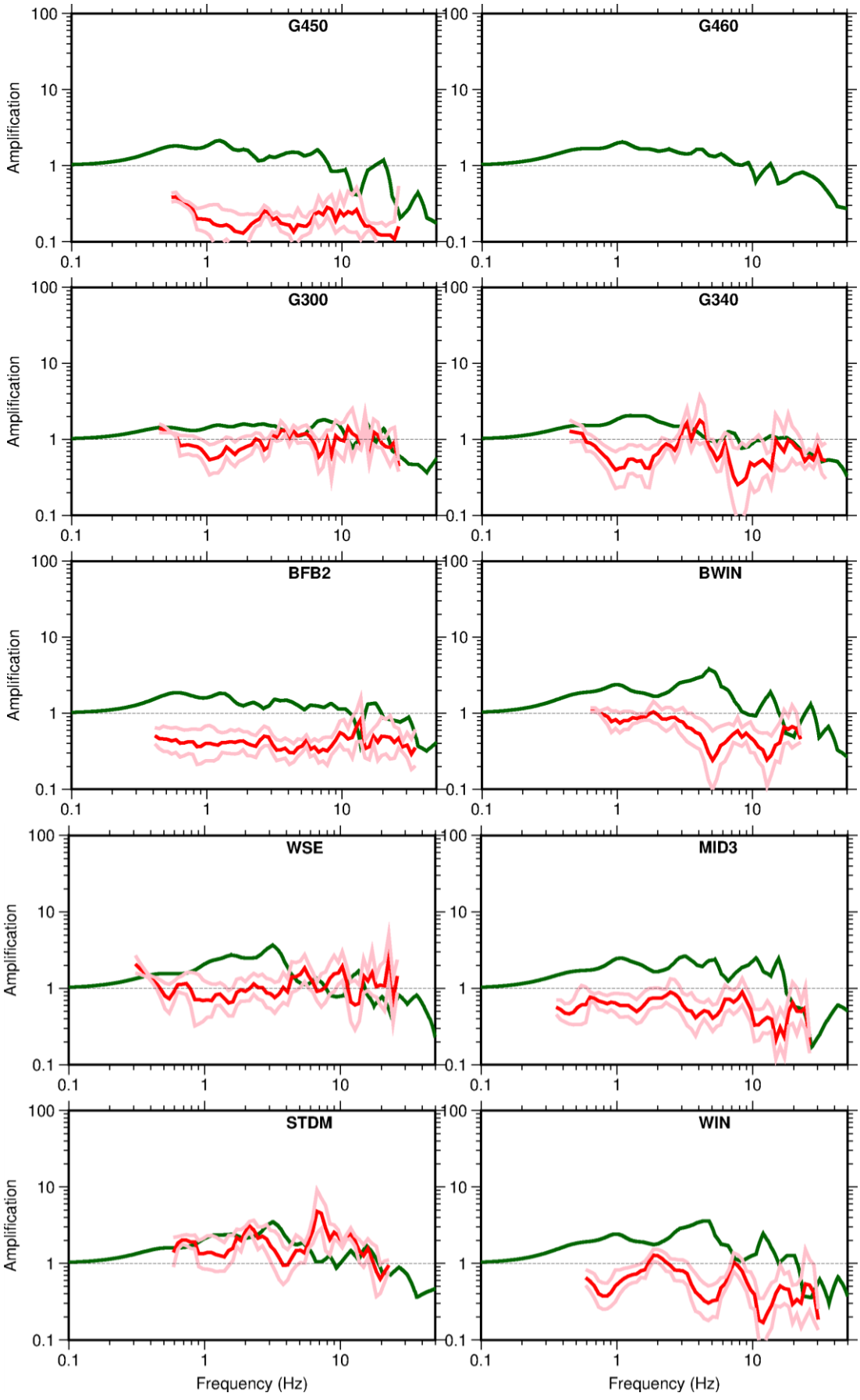

Figure 5.10. *Continued*

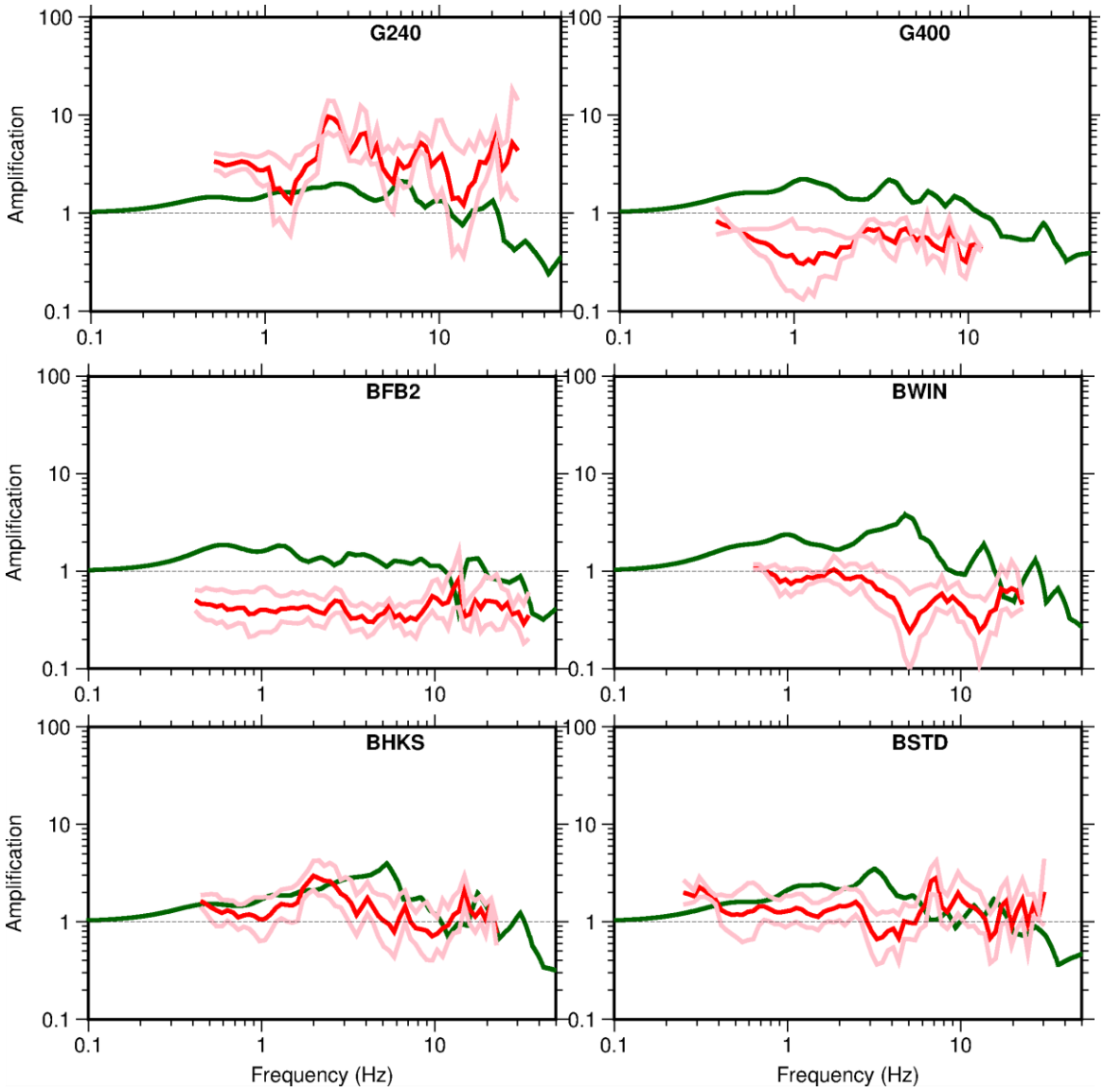

Figure 5.10. *Continued*

In order to define a field average amplification at the NU_B level, the (geometric) average of all sites was computed. However, because of the limited range of usable frequencies of the field recordings (see Figure 3.7) this amplification function is not constrained by the data for frequencies below 0.6 Hz. This is important because of the major impedance constrast associated with the base of the North Sea formation (NS_B) at a depth of about 800 m, some 400 m below the reference rock NU_B horizon (Figure 2.5). This lower horizon could potentially affect ground motions at the surface because of the strong impedance contrast for two reasons: (1) some energy will be trapped above this horizon (which is not captured by the AF computed from NU_B to the surface); and (2) there may be resonances that develop in the entire profile from NS_B to the surface. Moreover, we already had insight to effects of the NS_B impedance contrast manifesting at periods beyond the limits of the data—or rather at periods where the number of usable recordings is too small to be reliable—from a site-specific hazard assessment conducted for the Groninger Forum site in the city of Groningen (Bommer *et al*., 2015b).

In the Forum study, which included site response analyses for the layers above the NU_B, motions at the NU_B horizon were generated using the V1 simulations but replacing the generic field-wide surface amplification function with a calculated amplification function for the V_S profile from the reservoir to the NU_B level (Figure 5.11). The amplification function showed a distinct peak at about 0.3 Hz (Figure 5.12), which also showed up clearly in the response spectra at the NU_B and surface horizons (Figure 5.13).

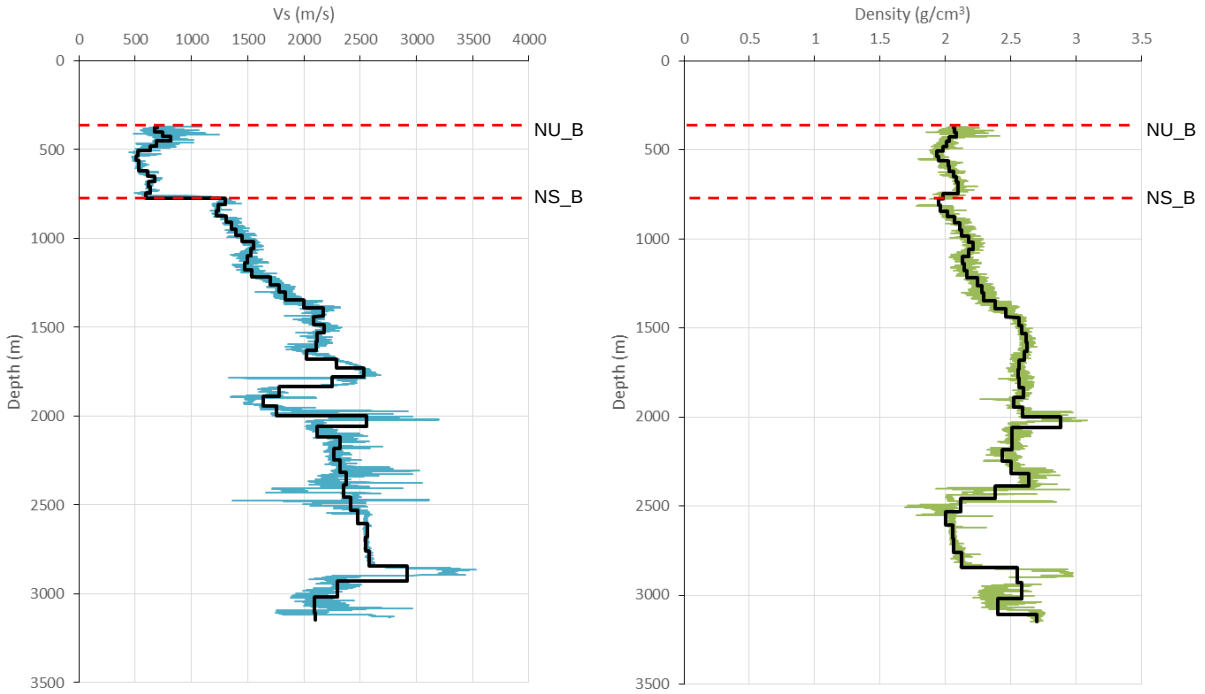

Figure 5.11. Measured velocity (*left*) and density (*right*) profiles from the BRW5 log; the stepped black lines show the layer model developed for the simulation of the motions in the Groningen Forum site-specific study

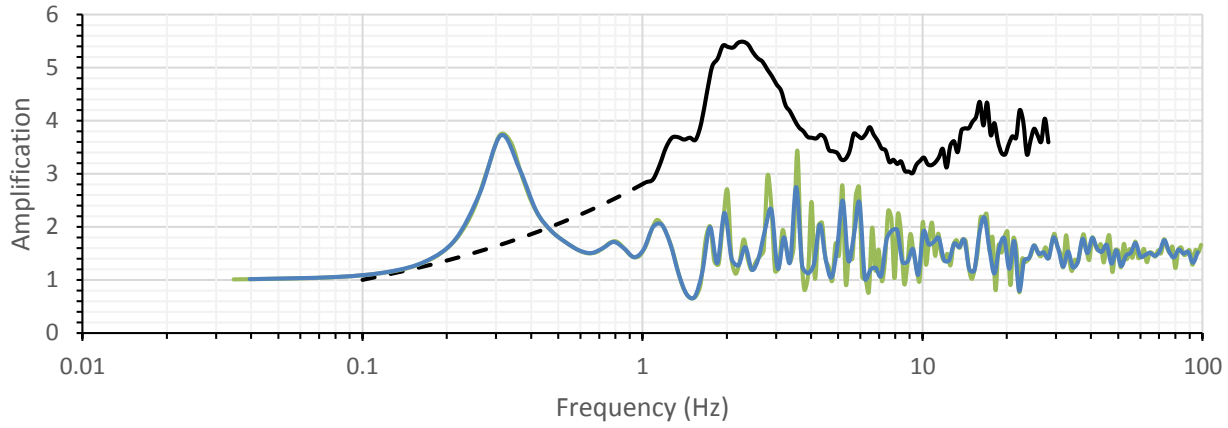

Figure 5.12. 1D-SH amplification calculated between 3 km depth and the NU_B interface (370 m) as an outcrop for the Groningen Forum study. The green line shows the smoothed values down-sampled to 200 points, while the blue shows the smoothed values down-sampled to 120 points (as used in the simulations). For reference the black line shows the amplification used for the surface motions predicted in the V1 GMPE (*solid*: inverted, *dashed*: extrapolated)

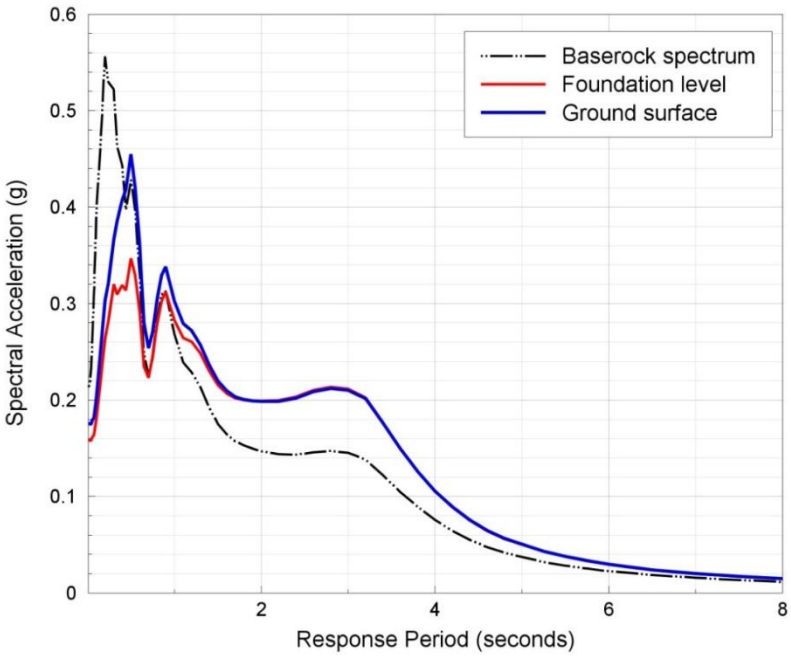

Figure 5.13. Final response spectra proposed for the design of the Forum, in which the amplification effect of the NS_B horizon at a ~3 seconds is clearly visible

The period at which the NS_B amplification manifests and the sharpness of the spectral peak it produces are exaggerated by the fact that the amplification function shown in Figure 5.12 was calculated treating the NU_B as an outcrop (and thereby decoupling the effect of the overlying layers to broaden the frequency range and reduce the amplification peak). However, even taking account of these factors, the effects of the NS_B impedance contrast are expected to manifest at periods beyond the period range where most of the records are usable. Therefore, in order to ensure that the effect is captured in the V2 GMPEs, an adjustment to the empirical amplification function obtained in the inversions was derived. Figure 5.14 shows the difference in the calculated transfer functions between NS_B and the surface (labelled 'Full Column') and NU_B and the surface (labelled 'Above NU_B only').

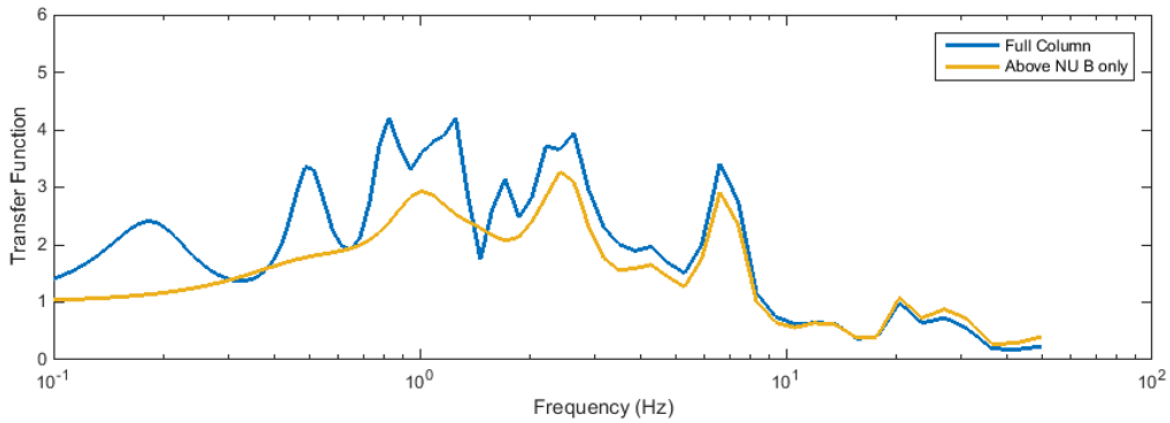

Figure 5.14. Site response for station BMD1 considering the full column above NS_B (labelled 'Full Column') and only the profile above the reference horizon NU_B

In Figure 5.14 the impedance effects are seen as higher values of the TF for all frequencies lower than about 10 Hz, whereas the additional damping due to the material between NU_B and NS_B is seen at high frequencies. At low frequencies (below about 0.7 Hz) the first two resonant modes of the full column are seen. These resonances are not seen for the analysis that considers only the material above NU_B. At intermediate frequencies (between about 0.7 Hz and 2 Hz) there is coupling between the site response above and below NU_B.

To account for the "Full column" effects, a correction factor is proposed. This correction factor only acts at low frequencies where the data are not available for empirical constraint. At higher frequencies, the effect of the deeper impedance contrast is captured by the field-wide site amplification term obtained in the inversions. The correction factors for each station are computed as follows:

- The "Full Column" transfer function is computed and smoothed with a Konno-Ohmachi filter (Konno & Ohmachi, 1998) with the *b* parameter set to 40 (Transfer function for a column from NS_B to the surface); this is labeled TF_{Full}
- The correction factor is defined as the ratio of TF_{Full} over the AF for each station as defined in Section 4.3

An implicit assumption in the derivation of the proposed correction is that the effects of the deeper impedance contrast are uniform across all the stations in the network, which is consistent with the adoption of the NU_B horizon at the reference rock elevation.

Figure 5.15 shows the correction factors (CF) computed for a subset of stations.

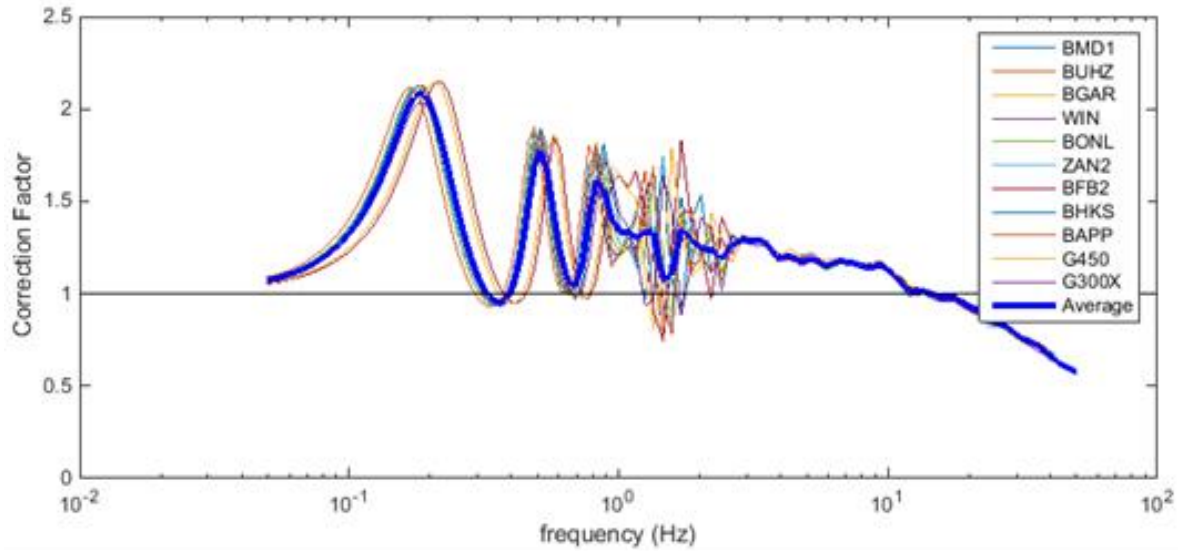

Figure 5.15. Correction factors for a subset of stations; the thick blue line is the average of the individual station factors

A number of important observations can be made on Figure 5.15. The CF are fairly uniform below about 0.7 Hz (which coincides with the range of frequencies not covered by the surface instruments as a result of the filters applied to those portions of the recordings with excessive noise). The CF are actually constant for frequencies above 3 Hz, but between about 0.7 Hz and 3 Hz the CF show appreciable station-to-station variability. Based on these observations, we conclude that applying the correction factor below about 0.7 Hz is a valid way of incorporating the effects of the NS_B boundary for these frequencies (as noted before, the effects of the NS_B boundary at higher frequencies are captured by the empirically-determined site amplification factor).

The proposed correction for the field is obtained as follows (Figure 5.16): At frequencies below 0.6 Hz, the average correction factor for the set of stations shown in Figure 5.15 is used; at frequencies above 0.6 Hz, a second-order polynomial is fit to the average amplification factor. The two functions described above are parsed and a smoothing filter (Konno-Ohmachi filter; Konno & Ohmachi, 1998) is used to smooth the transition between the high- and low-frequency portions. In order to avoid under-predicting ground motions, the trough between the first and second mode peaks is reduced by averaging the smooth polynomial fit and the average correction factor.

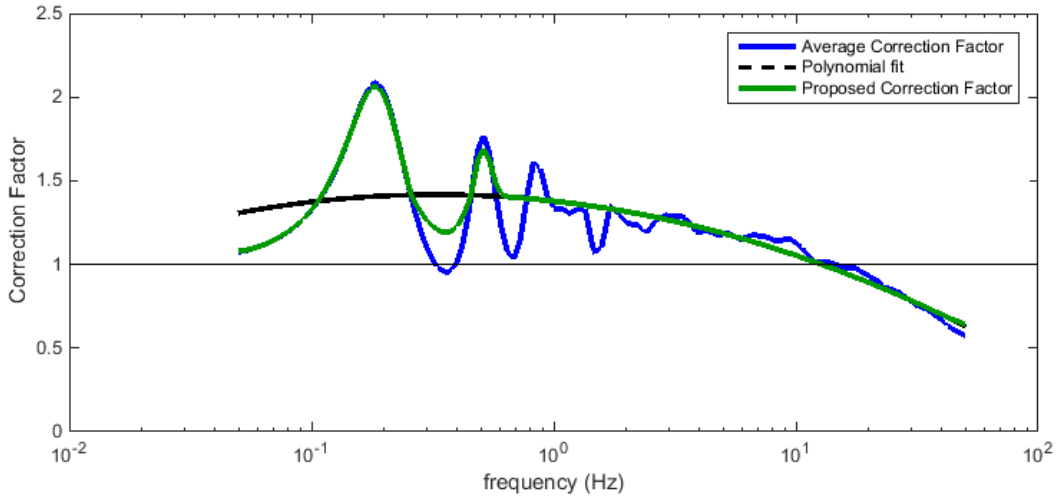

Figure 5.16. Proposed correction factor for the NS_B impedance contrast amplification effect

This amplification correction factor is then parsed with the field-wide site amplification function at NU_B as obtained from the inversions. The theoretical amplification between the source and NU_B (accounting for down-going reflections) as computed above is applied to lower frequencies, whereas the empirical site term is retained at high frequencies. The two functions (empirical for $f > 0.6$ Hz and theoretical for $f < 0.6$ Hz) are then combined (Figure 5.17) by altering the absolute level of the empirical amplification (which is rather poorly constrained in the inversions) to be consistent with the theoretical function. A scaling factor of 1.2 was therefore applied to the empirical model.

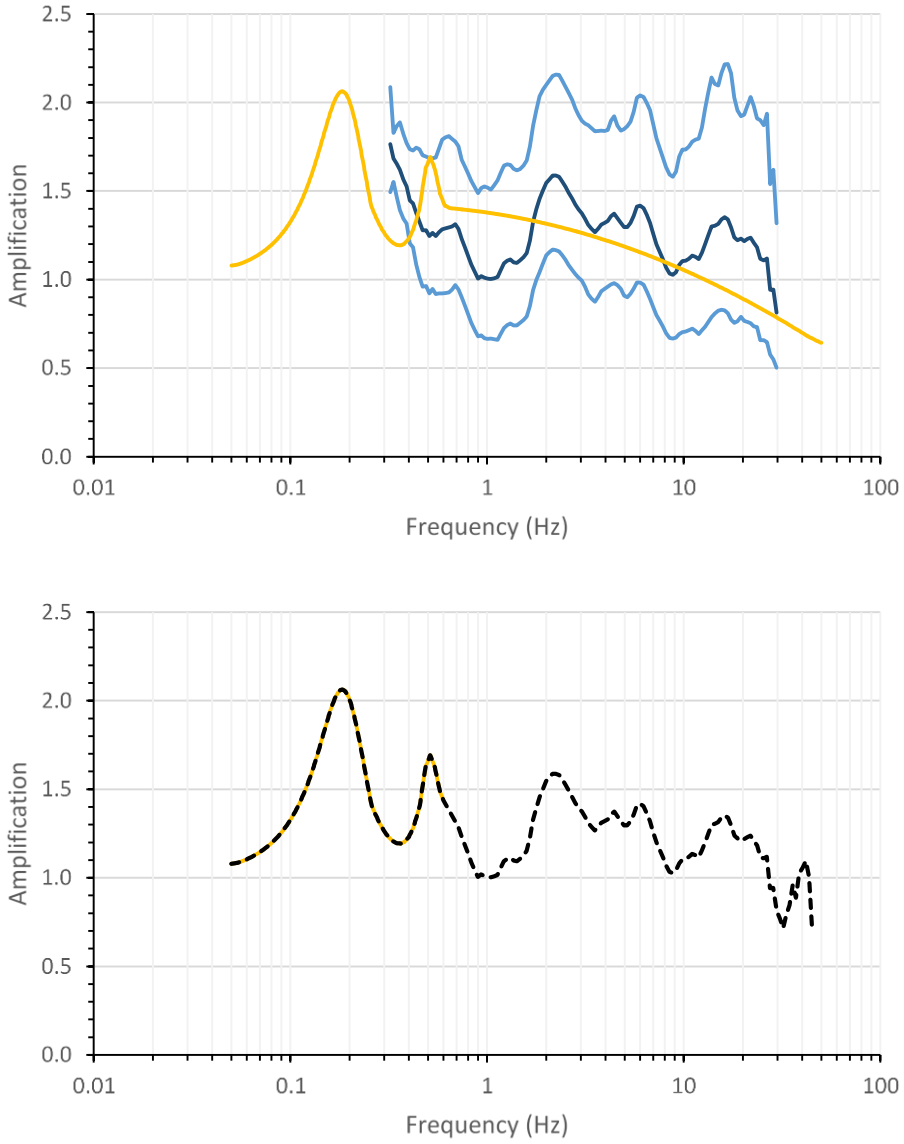

Figure 5.17. *Top panel*: field average amplification (*blue*) and standard deviation (*light blue*) along with the theoretical source to NU_B amplification (*yellow*) smoothed after the first two fundamental peaks. *Bottom panel*: combined NU_B amplification model for use in the simulations

6. EQUATIONS for GROUND MOTIONS at REFERENCE ROCK HORIZON

This chapter describes the derivation of the basic equations for predicting response spectral accelerations at the NU_B horizon, which is the first part of the V2 GMPE as defined in Eq.(2.1). The median motions are obtained primarily from stochastic simulations using the results of the inversions described in the previous chapter, as summarised in Section 6.1. The results of the simulations are described briefly in Section 6.2, after which the appropriate functional form for the parametric form of the GMPEs is discussed in Section 6.3. The results of regression analyses on the simulations to fit the functional form are presented in Section 6.4. Sections 6.5 and 6.6 are concerned with the calculation of the residuals of the recordings, including their transformation to the NU_B horizon. The predictions obtained with the reference rock GMPEs are briefly presented and discussed in Section 6.7.

6.1. Input parameters for stochastic simulations

The inversions discussed in Section 5.4 yield a range of possible combinations of source, path and site parameters that are consistent with the recorded data (after its translation from the surface to the NU_B horizon using the transfer functions from Section 4.3). While there is therefore an estimate of the mean value of each of the parameters obtained from the inversion, what is sought is the combination that when used in point-source stochastic simulations yields predicted spectral ordinates that best reproduce the recordings. Based on the initial observations (Section 5.4) we defined 76 possible models based on the combination of: κ_0 values of 0.03, 0.035, 0.04, 0.045, 0.05, and 0.055 s; and Brune stress parameter, $\sigma\Delta$, of 1, 3, 10, 20, 30, 40, 50, 60, 70, 80, 90, 100, 125, 150, 200 and 300 bar (Figure 6.1). Only the 1, 3, 10, 30 and 100 bar stress-parameter models used the lower range of κ_0, the rest used 0.04 to 0.055s. All simulations used the geometrical spreading model determined in Section 5.3 and a Q values of 150 (as in V1). Site specific NU_B to surface amplification functions (Section 4.3) were used in addition to the average source to NU_B amplification, with the long-period adjustment described in Section 5.4. The simulations were compared to the recorded response spectra at the surface (individual horizontal components) at PGA, 0.2, 0.5, 1.0 and 1.5 s. The average misfit (data minus prediction in natural log units) and misfit variance at each period was averaged (using root-mean-square to penalise either over- or under-estimation) leading to a single measure of misfit bias and sigma for each combination of simulation parameters (Figure 6.2).

The best fitting model for the motions at the NU_B horizon is found to have the following parameter combination based on the smallest RMS average misfit (bias) and sigma: site kappa, κ_0 = 0.05 s and stress drop parameter, $\Delta\sigma$ = 30 bar. The stress parameter value is the same as determined for the V1 model, but the site kappa value is, understandably, smaller (the V1 value was 0.06 s) given that the V2 model is referenced to the NU_B reference rock horizon rather than to the ground surface.

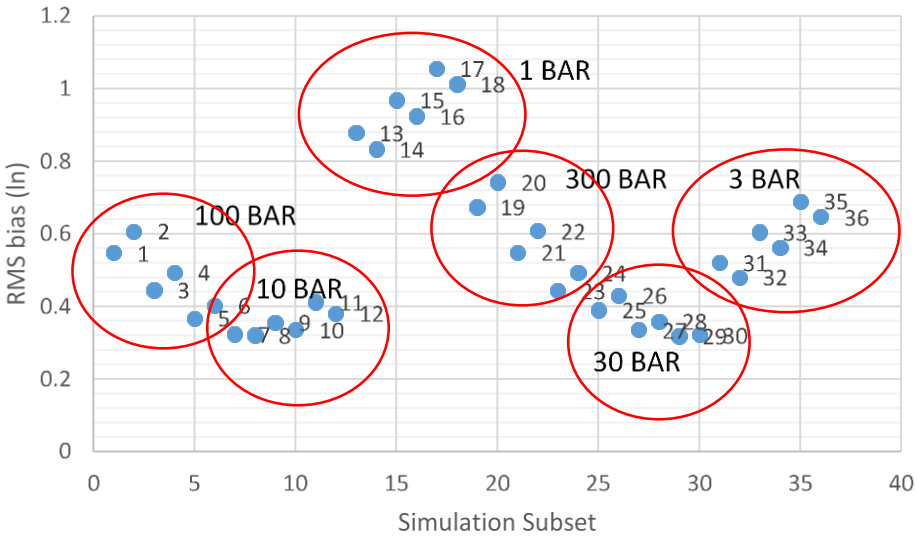

Figure 6.1. Examples of RMS bias calculated for different sets of simulations

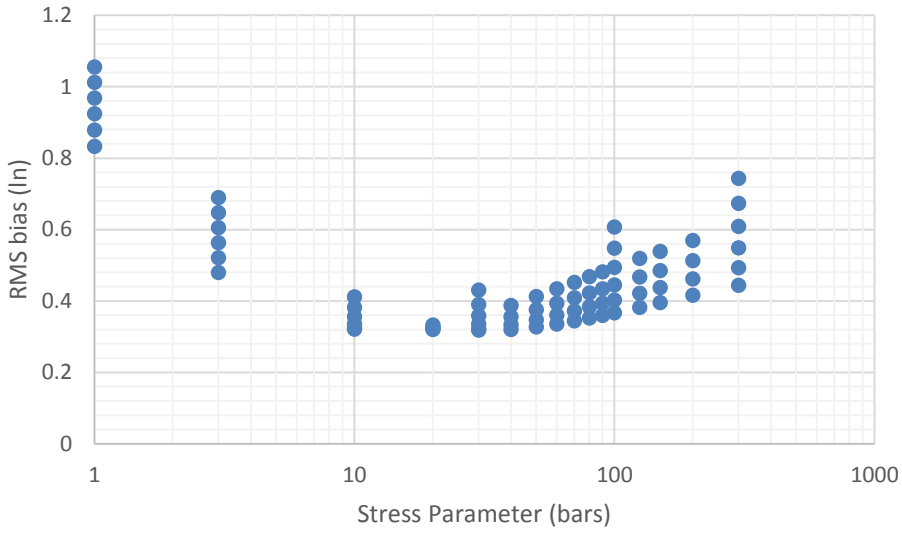

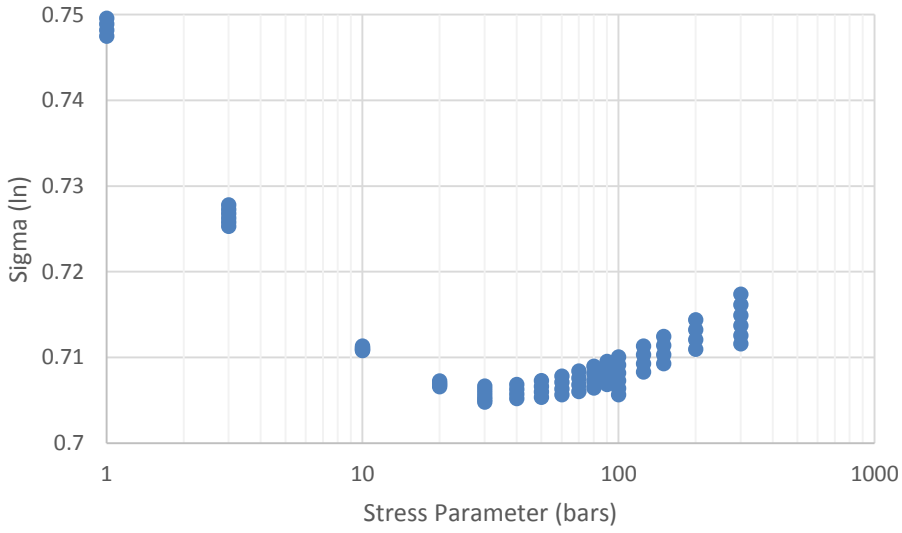

Figure 6.2. RMS bias (*upper*) and sigma (*lower*) with respect to the recordings as a function of Δσ

As for the V1 model, for the forward simulations it was decided to use alternative values of the stress parameter to reflect the considerable epistemic uncertainty associated with extrapolation to much larger magnitudes. We found no compelling reason to adopt different models from the V1 GMPE, namely a central branch with a stress parameter of 30 bars, a lower branch corresponding to 10 bars and an upper branch—reflecting the possibility of the motions being similar to those from normal tectonic earthquakes—with a stress drop rising from 30 bars at **M** 2.5 to 100 bars at **M** 4.5 and then remaining constant (Figure 6.3).

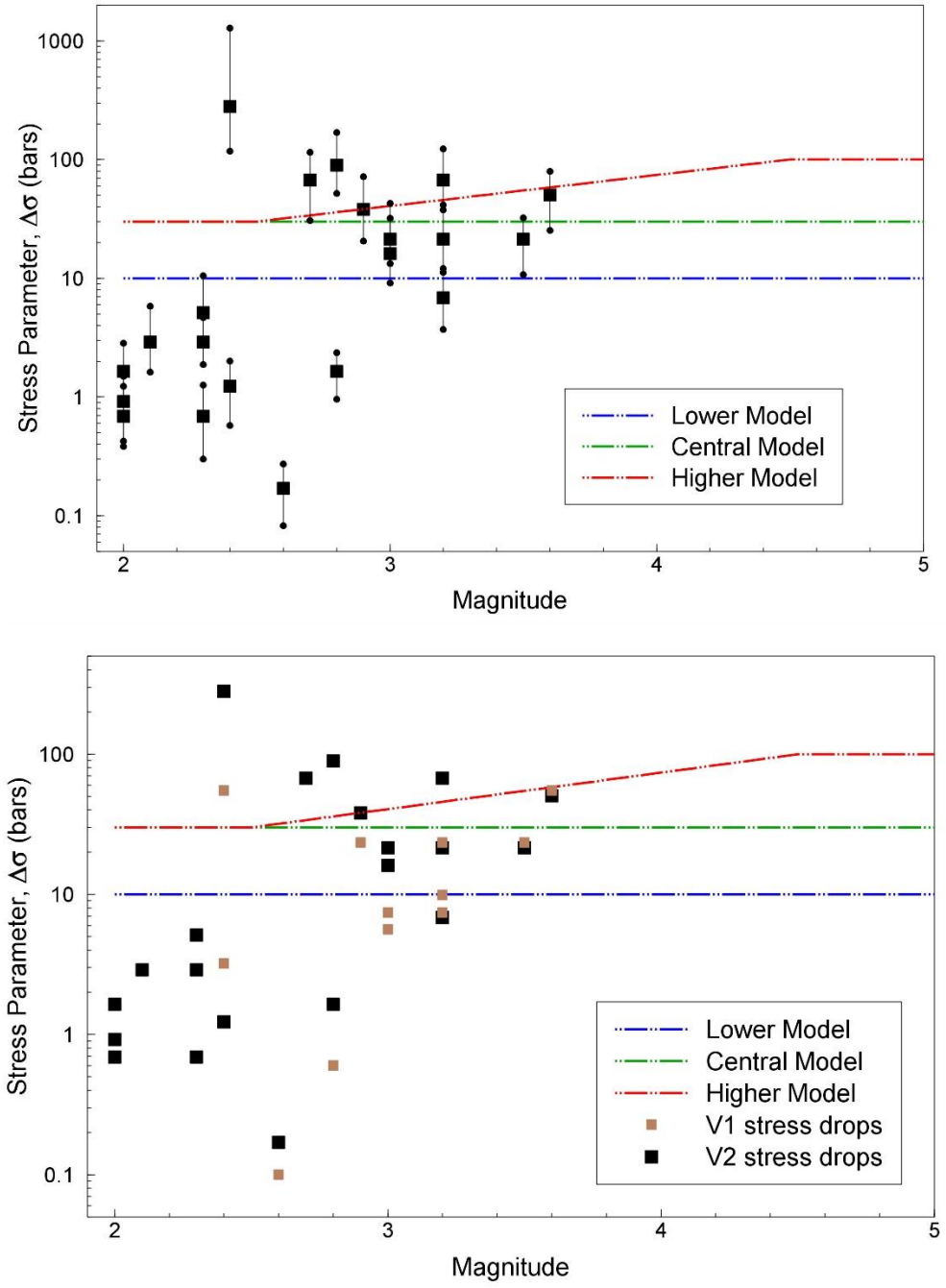

Figure 6.3. *Upper*: Estimates of stress drop together with confidence intervals as a function of magnitude, together with the three models adopted for the simulations; *Lower*: comparison of V1 and V2 stress drops, with corrected magnitudes

Table 6.1 summarises the full set of inputs to the simulations used to generate the motions at the NU_B reference for the derivation of the median GMPE.

Table 6.1. Parameter values used in simulations for NU_B motions

Parameter	Symbol (units)	Value(s)	Notes
Density	ρ (g/cm^3)	2.6	
Shear-wave velocity	β (km/s)	2	
Horizontal partition		0.707	
Radiation coefficient	θ	0.55	
Free surface	F	2	
Source type		Brune ω^{-2}	
Source depth	Z (km)	3	
Stress parameter (Lower, Central, Upper)	Δσ [**M** = 2.5] (bars)	10, 30, 30	Linear interpolation of log(Δσ) with **M** for Upper model
	Δσ [**M** = 4.5] (bars)	10, 30, 100	
Near-source saturation	c_5	0.4233	Section 6.3
h(**M**)=exp(c_5**M**+c_6)	c_6	-0.6083	
Geometrical spreading distances	R1, R2, R3 (km)	7, 12, 25	
Geometrical decay rates	λ1, λ2, λ3, λ4	-1.07, -0.074, -1.91, -1.00	
Path attenuation	Q	150	
Site attenuation	κ_0 (s)	0.05	
Source duration	T_S (s)	$1/0.4906\beta(\Delta\sigma/M_0)^{1/3}$	
Path duration	T_P [R (km), T_P (s)]	0.0, 0.0	Boore & Thompson (2014)
		7, 2.4	
		45, 8.4	
		125, 10.9	
Site amplification	A(f)	NU_B model	Section 5.4
Oscillator correction for T_{rms}			Liu & Pezeshk (1999)

6.2. Predicted accelerations at reference rock horizon

Using the parameter suites summarised in Table 6.1, point-source stochastic simulations were performed for spectral accelerations at the target oscillator periods using SMSIM (Boore, 2005a). For each oscillator period and for each stress parameter—corresponding to lower, central or upper model—simulations were performed for magnitudes from **M** 1.0 to 6.5 in increments of 0.1 units, and for each magnitude at 45 epicentral distances sampled logarithmically between 0 and 60 km. The patterns displayed by these simulated spectral accelerations concord with expectations in terms of the scaling with magnitude and stress drop, and especially the divergence between the three models with increasing magnitude that correctly reflects the greater epistemic uncertainty with increasing separation from the range covered by the data. Figures 6.4 to 6.9 show the predicted accelerations at different oscillator periods from the three models as a function of magnitude, for sites a 0 and 30 km epicentral distance.

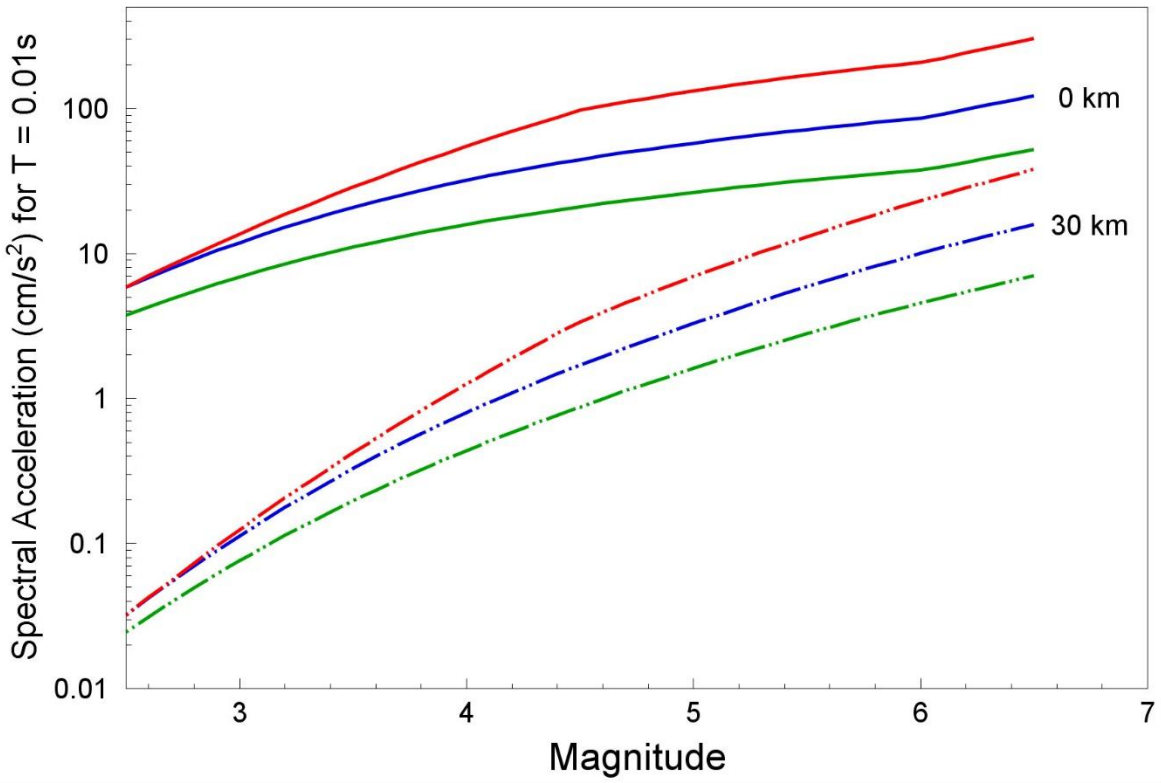

Figure 6.4. Spectral accelerations at 0.01 s from point-source stochastic simulations for lower (*green*), central (*blue*) and upper (*red*) models at epicentral distances of 0 and 30 km as a function of magnitude

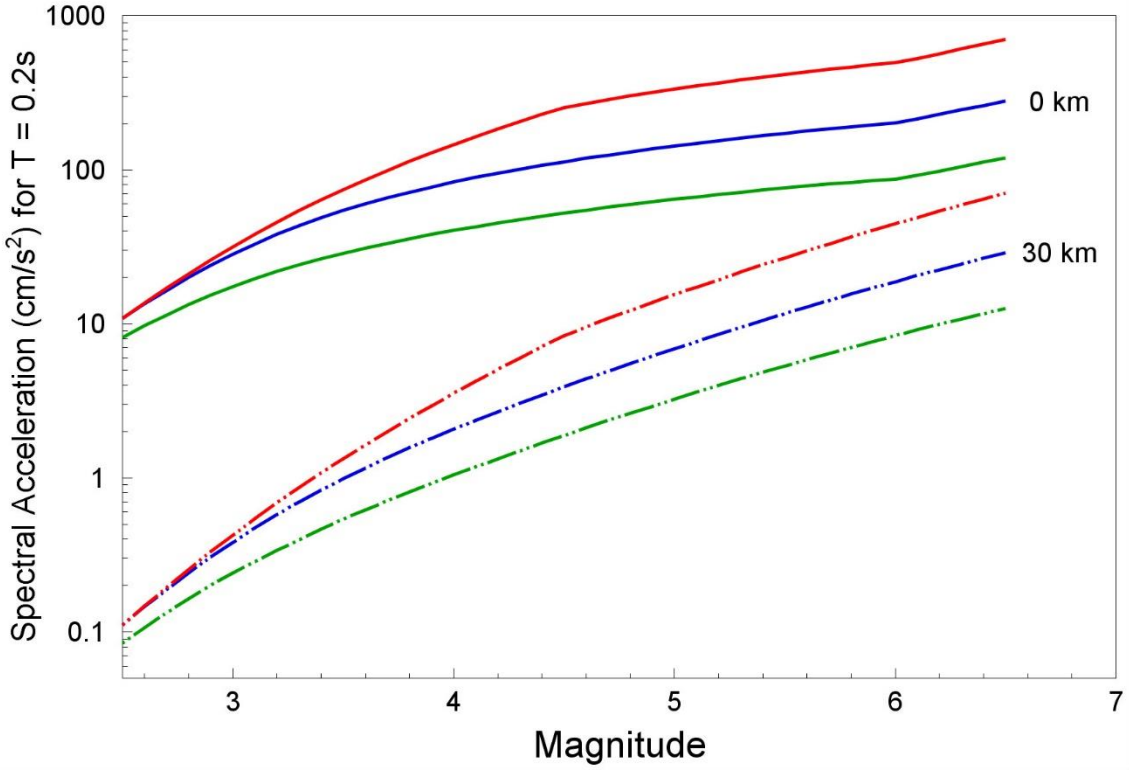

Figure 6.5. Spectral accelerations at 0.2 s from point-source stochastic simulations for lower (*green*), central (*blue*) and upper (*red*) models at epicentral distances of 0 and 30 km as a function of magnitude

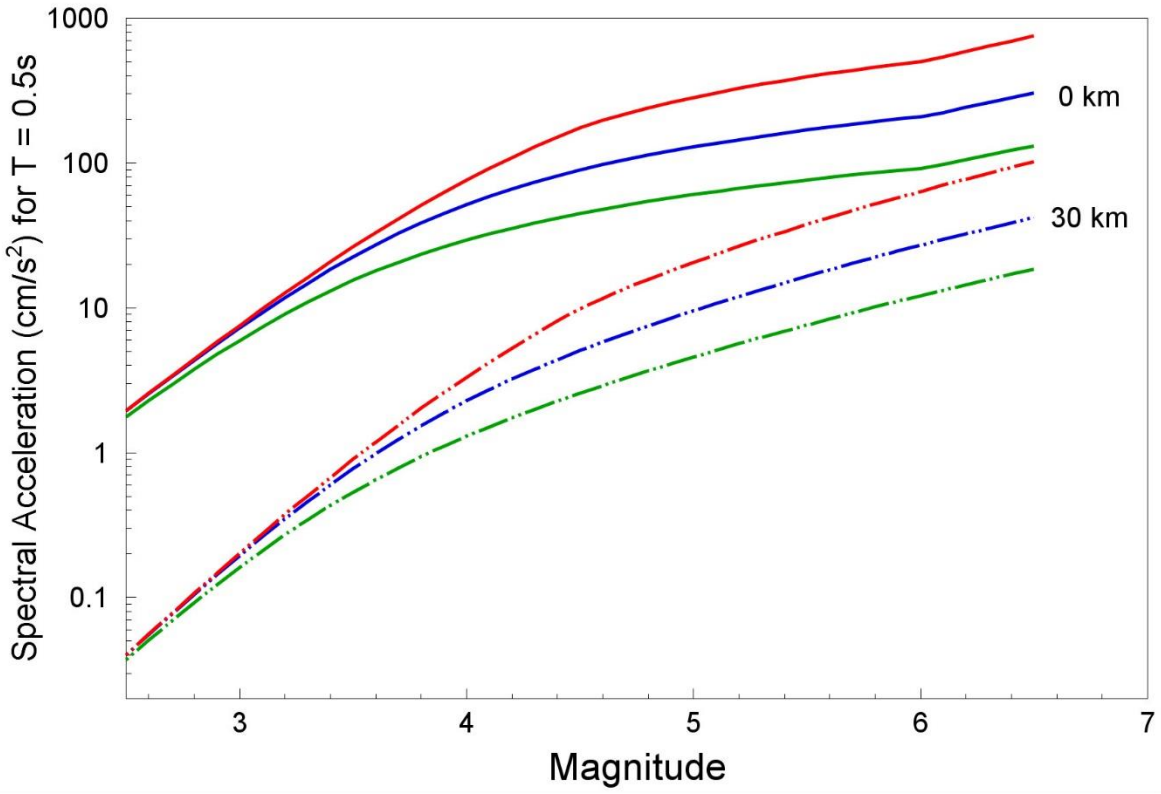

Figure 6.6. Spectral accelerations at 0.5 s from point-source stochastic simulations for lower (*green*), central (*blue*) and upper (*red*) models at epicentral distances of 0 and 30 km as a function of magnitude

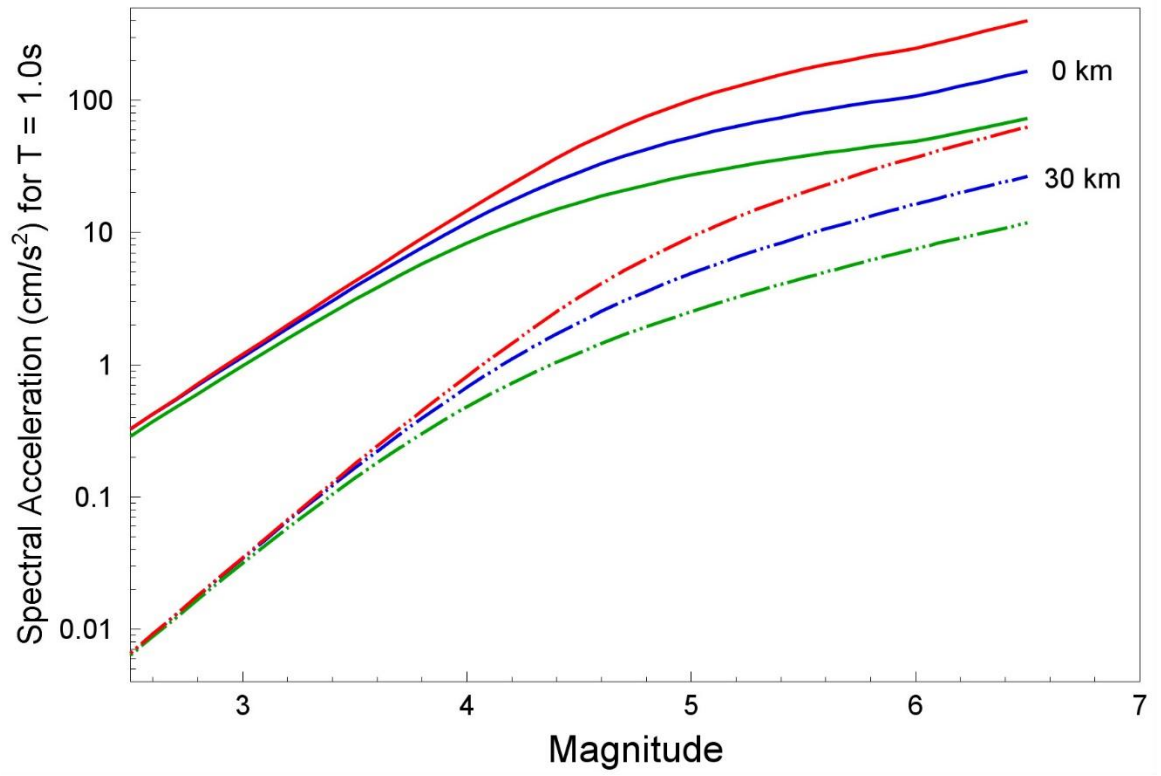

Figure 6.7. Spectral accelerations at 1.0 s from point-source stochastic simulations for lower (*green*), central (*blue*) and upper (*red*) models at epicentral distances of 0 and 30 km as a function of magnitude

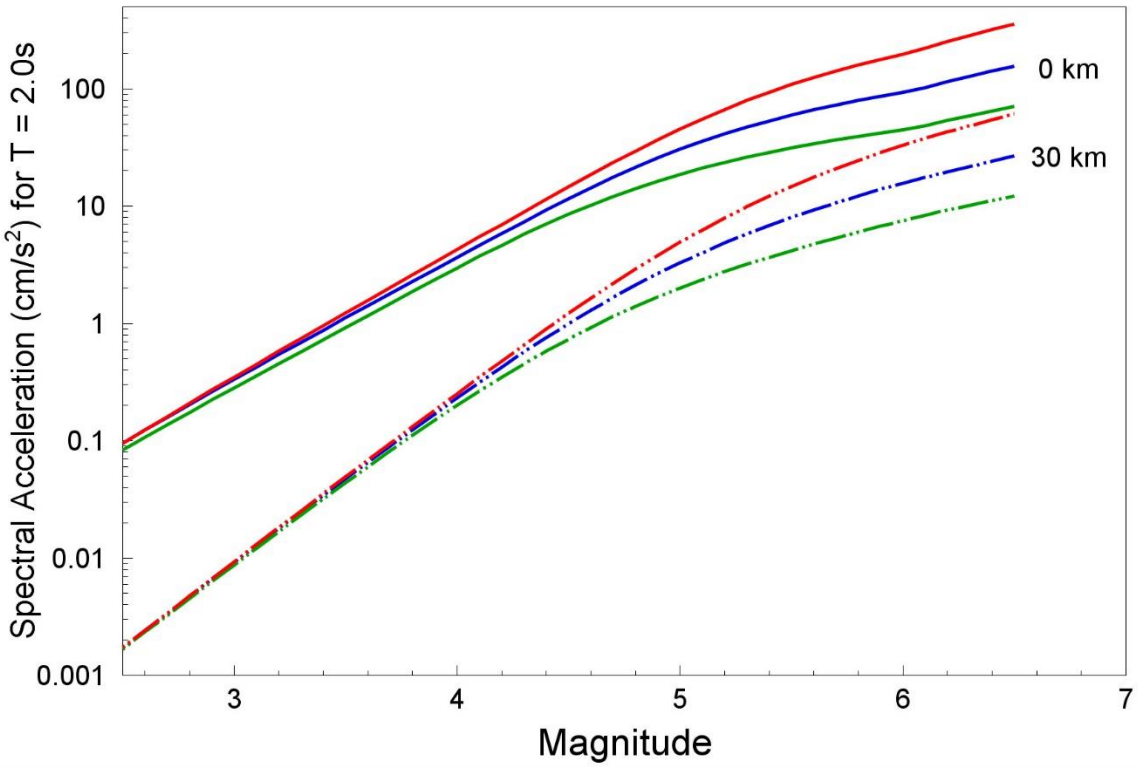

Figure 6.8. Spectral accelerations at 2.0 s from point-source stochastic simulations for lower (*green*), central (*blue*) and upper (*red*) models at epicentral distances of 0 and 30 km as a function of magnitude

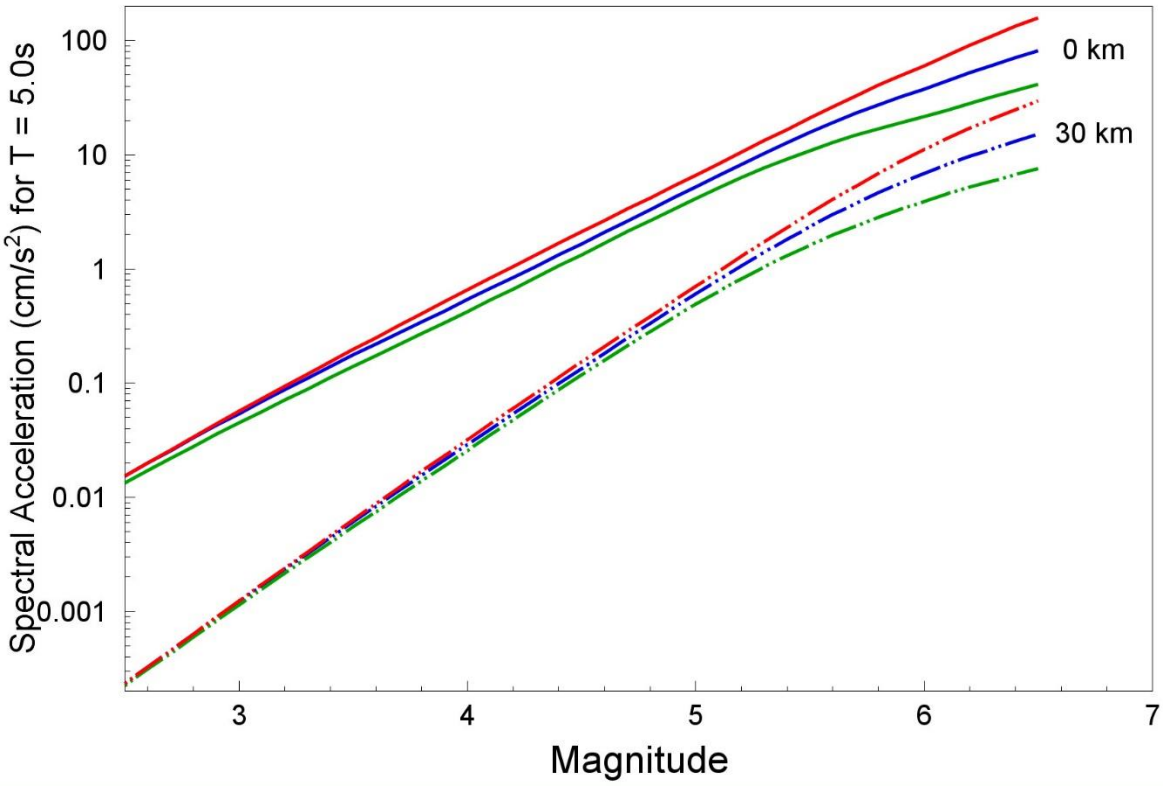

Figure 6.9. Spectral accelerations at 5.0 s from point-source stochastic simulations for lower (*green*), central (*blue*) and upper (*red*) models at epicentral distances of 0 and 30 km as a function of magnitude

One feature of these plots is worthy of comment before closing this section, namely the apparent change in scaling at larger magnitudes (**M** > ~6) seen at shorter distances. The effect is most pronounced for the spectral accelerations at shorter response periods. This arises from the inclusion of a near-source distance saturation term, which is itself dependent on magnitude. The simulations are expressed in terms of epicentral distance, R_{epi}, for consistency with the chosen parameterisation of the GMPEs (Section 2.1), but in reality they are based on an effective distance, R_{eff}, given by:

$$R_{eff} = \sqrt{R_{epi}^2 + h(M)^2} \tag{6.1}$$

where the near-source saturation term is as defined in the V1 model (which is discussed in more detail in Section 6.3 below):

$$h(M) = \exp(0.423318M - 0.608279) \tag{6.2}$$

An important difference with the V1 model, however, is that the geometric spreading is no longer a continuous function of distance but rather is segmented, with breaks at hypocentral distances, R_{hyp}, of 7 km and 12 km, as discussed in Section 5.3. At a magnitude of **M** 5.8, the effective distance reaches the value of 7 km at which the first scaling break occurs, hence the apparent overall magnitude scaling changes because Eqs.(6.1) and (6.2) result in a change of the distance scaling (even for R_{epi} equal to zero).

6.3. Functional form for reference rock GMPE

For the V1 GMPEs, a functional form was chosen that was able to provide a good fit to the simulations over the range of magnitudes from **M** 2.5 to **M** 6.5. There was a conscious decision not to develop equations applicable to smaller magnitudes since this would have required an additional break in magnitude scaling to capture the influence of kappa (*e.g.*, Douglas & Jousset, 2011; Baltay & Hanks, 2014). Given the null contributions of smaller earthquakes to all relevant estimates of both hazard and risk, the lower magnitude limit is maintained. Even though the unique value of M_{max} equal to 6.5 is being replaced in V2 by a distribution of possible maximum magnitudes, the equations are still required to be applicable to the upper limit of **M** 6.5.

The functional form adopted for the V1 GMPEs had the following form:

$$\ln(Y) = c_1 + c_2 M + c_3 (M - 4.5)^2 + c_4 \ln\sqrt{R_{epi}^2 + [\exp(c_5 M + c_6)]^2} \qquad M \le 4.5 \tag{6.3a}$$

$$\ln(Y) = c_1 + c_2 M + c_{3a} (M - 4.5)^2 + c_4 \ln\sqrt{R_{epi}^2 + [\exp(c_5 M + c_6)]^2} \qquad M > 4.5 \tag{6.3b}$$

where *ln*(Y) is the acceleration in cm/s^2. The only feature of the model that was found to be potentially wanting in the derivation of the V1 GMPEs was the absence of a term to represent the effects of anelastic attenuation, which resulted in some misfit of the simulated motions at

greater distances. Even though the distances of interest to the hazard and risk calculations are limited (~50 km), the low Q values obtained for these shallow-focus earthquakes do result in an appreciable attenuation effect within the dimensions of the field. Another consideration in adapting the functional form to the V2 equations is the fact that the new simulations, informed by the waveform modelling using finite difference simulations (Section 5.3), have a segmented geometric spreading function. However, before considering the segmentation of the functional form and the possible inclusion of additional terms for anelastic attenuation, a decision was made regarding the near-source saturation term, as represented by the term with the coefficients c_5 and c_6. The first step was to check the influence of the revision of magnitudes (see Section 3.2) on this term, which was found to be negligible (Figure 6.10).

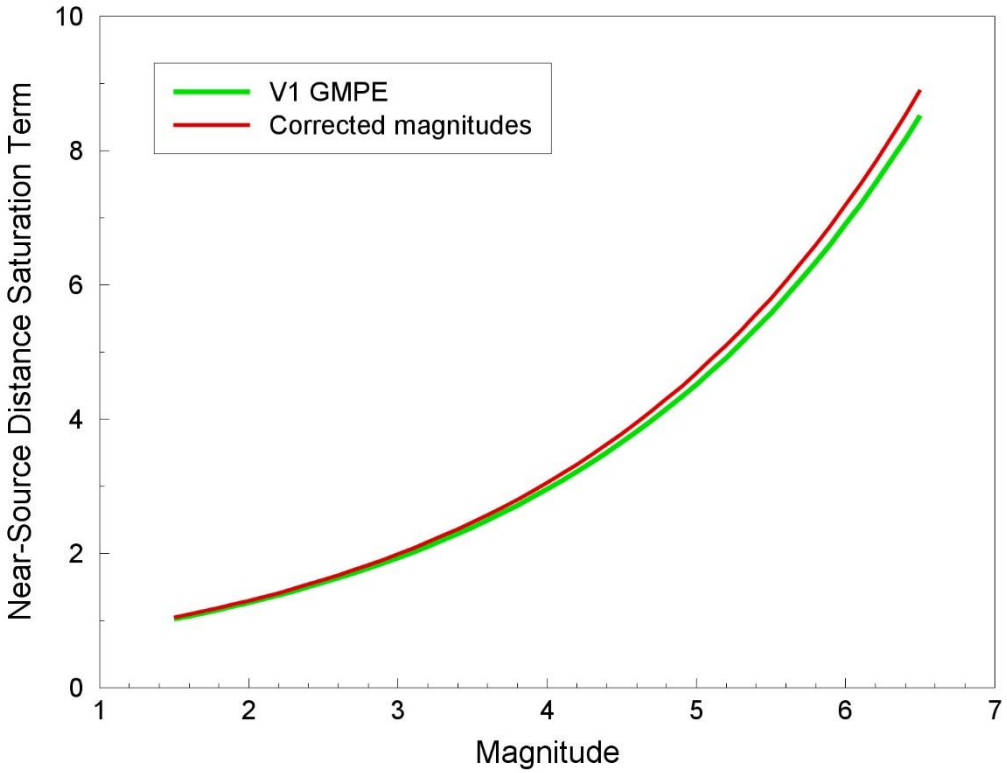

Figure 6.10. Near-source distance saturation term as determined for the V1 GMPEs (*green*) and as obtained with the corrected magnitudes (*red*)

This observation led us to conclude that it was appropriate to retain the same value of these coefficients as found in the derivation of the V1 model. This decision is to some extent vindicated by the plot in Figure 6.11 which compares this saturation term with that obtained by Yenier & Atkinson (2014) for earthquakes of **M** 6 and greater. This latter term was adopted for the GMPE derived by Atkinson (2015) that was intended specifically for application to small-magnitude induced earthquakes but derived using data from the NGA-West2 database, which are sparse at very short distances. Atkinson (2015) imposed a minimum value of 1 km for the saturation term, which applies to magnitudes of **M** 4 and lower. Recognising that larger saturation terms could be reconciled with her data, Atkinson (2015) also considered an alternative model having a value three times greater at **M** 4 and converging to the values proposed by Yenier & Atkinson (2014) for larger earthquakes. As

can be seen in Figure 6.11, the alternative model considered by Atkinson (2015)—albeit to be used in conjunction with R_{hyp} than with R_{epi}—is almost identical to the V1 model for magnitudes up to about 5.8.

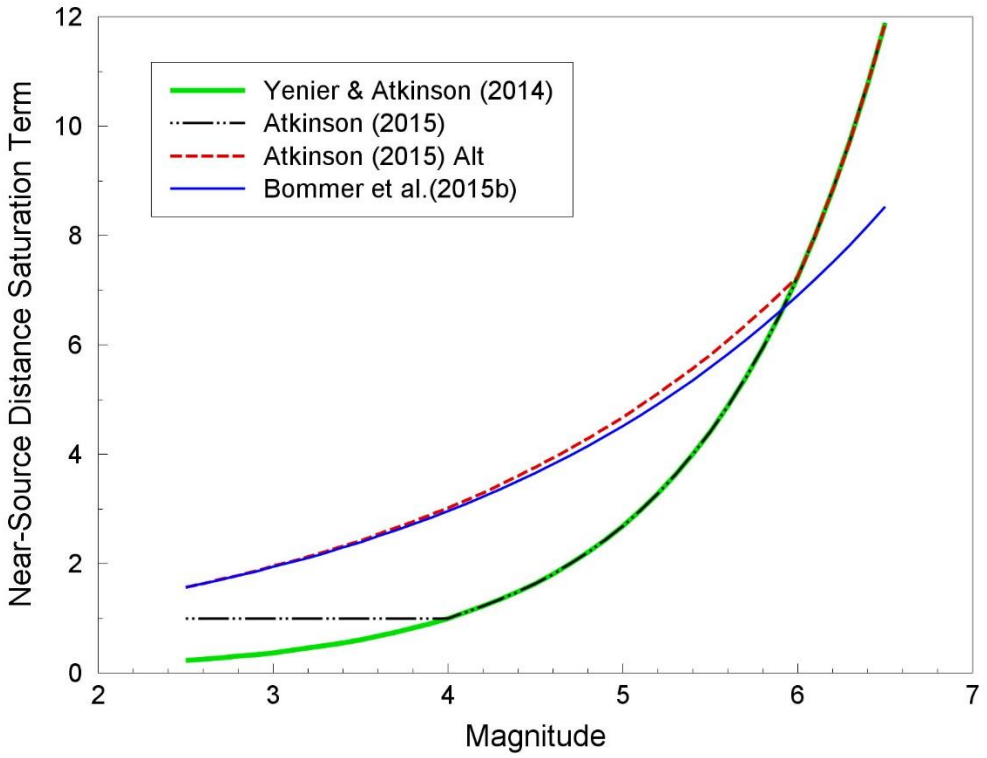

Figure 6.11. Comparison of the V1 near-source distance saturation term with those proposed in other studies

The near-source distance saturation term from V1 was therefore retained for V2 model, and the effective distance thus defined as in Eq.(6.1):

$$R = \sqrt{R_{epi}^2 + h(M)^2} \tag{6.4}$$

where the near-source saturation term is as in Eq.(6.2), repeated here for ease of reference:

$$h(M) = \exp(0.423318M - 0.608279) \tag{6.5}$$

Using the same functional form as for the V1 GMPEs was found to produce a relatively poor fit to the simulations for the simple reason that it was unable to capture the changes in geometrical spreading with distance. To address this shortcoming, the functional form was modified to accommodate the changes in distance-dependence that occur at R_{hyp} values of 7 km and 12 km. As noted in Section 5.3, the spreading terms constrained by the waveform modelling only extend to hypocentral distances of 25 km, beyond which 1/R spreading was imposed rather than extrapolating the more rapid decay rate from the finite difference

simulations. Therefore, to accommodate all of these changes in spreading rates, the equation was defined in four segments:

$$g(R) = c_4 \ln(R) \qquad R \le r_a \qquad (6.6a)$$

$$g(R) = c_4 \ln(r_a) + c_{4a} \ln\left(\frac{R}{r_a}\right) \qquad r_a < R \le r_b \qquad (6.6b)$$

$$g(R) = c_4 \ln(r_a) + c_{4a} \ln\left(\frac{r_b}{r_a}\right) + c_{4b} \ln\left(\frac{R}{r_b}\right) \qquad r_b < R \le r_c \qquad (6.6c)$$

$$g(R) = c_4 \ln(r_a) + c_{4a} \ln\left(\frac{r_b}{r_a}\right) + c_{4b} \ln\left(\frac{r_c}{r_b}\right) + c_{4c} \ln\left(\frac{R}{r_c}\right) \qquad R > r_c \qquad (6.6d)$$

The distances demarking the different segments of attenuation are obtained from the hypocentral distances defined from the finite difference waveform simulations and the constant focal depth of 3 km:

$$r_a = \sqrt{7^2 - 3^2} \qquad (6.7a)$$

$$r_b = \sqrt{12^2 - 3^2} \qquad (6.7b)$$

$$r_c = \sqrt{25^2 - 3^2} \qquad (6.7c)$$

The segmented spreading terms are then incorporated into the same model as used in V1—as in Eq.(6.3)—replacing the single geometric spreading term in the previous equations:

$$\ln(Y) = c_1 + c_2 M + c_3 (M - 4.5)^2 + g(R) \qquad M \le 4.5 \qquad (6.8a)$$

$$\ln(Y) = c_1 + c_2 M + c_{3a} (M - 4.5)^2 + g(R) \qquad M > 4.5 \qquad (6.8b)$$

The final question to be addressed in defining the functional form was whether to include an additional term to capture the effects the anelastic attenuation separately, as noted earlier. Such a term would only have a pronounced influence at longer distances (> 30 km) and all hazard and risk disaggregation results to date have indicated that contributions from such distant scenarios are very small. Moreover, there are no data available at such distances and the simulations for distances beyond 25 km are based on an assumed decay rate. A term could be added to the GMPE to explicitly reflect the influence of the low Q used in the simulations, but it would not serve to necessarily make the model more realistic. The absence of an explicit term to capture the effect of Q does not, of course, mean that anelastic attenuation is omitted from the parameterised equations since the effect will influence the coefficients on the geometric spreading terms. In the V1 model, using a single geometric spreading term over all distances, resulted in slight over-prediction of the simulated motions at greater distances but some mild under-prediction at intermediate distances (Figure 6.12).

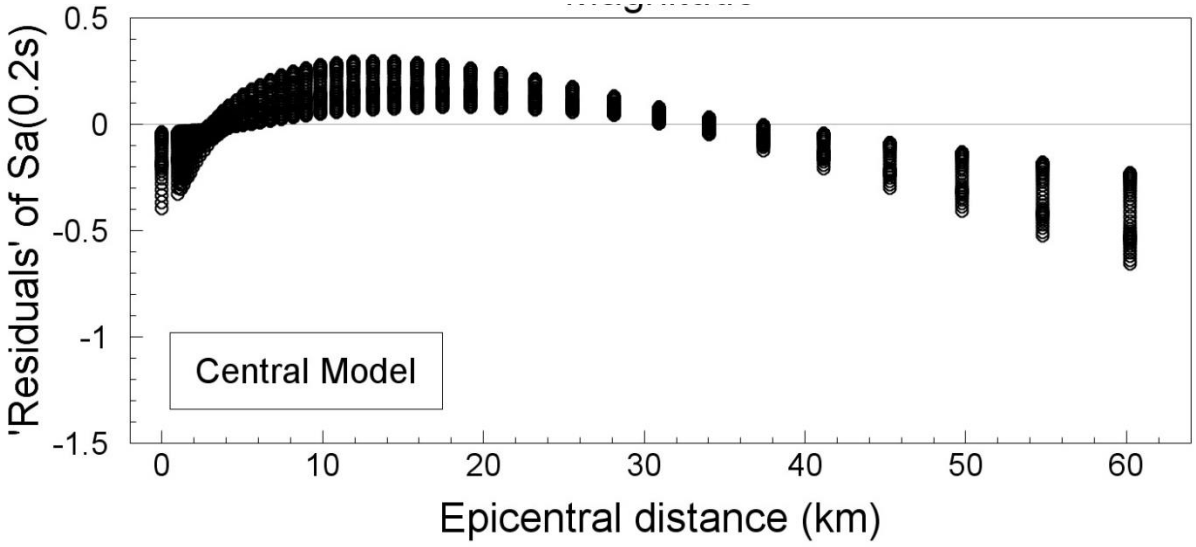

Figure 6.12. Example of the fit of the V1 GMPE to the stochastic simulations at shorter periods where the influence of anelastic attenuation leads to slight over-prediction at longer distances and some under-prediction at intermediate distances (5-20 km)

This feature would tend to motivate for the inclusion of an explicit anelastic term but now that the geometric spreading is segmented, the same effect is not expected to occur. The only consequence of not including an anelastic term in the V2 model will be a mild over-prediction of the amplitudes predicted by the stochastic simulations beyond 25 km, which are themselves poorly constrained. Therefore, to avoid unnecessary complexity, the functional form chosen for the V2 GMPEs was as summarised in Eqs.(6.4)-(6.8).

6.4. Regression analyses

As for the V1 GMPEs, the regression analyses were performed to estimate the values of the coefficients of Eqs.(6.6) and (6.8) by fitting the functional form to the outputs from the stochastic simulations using the parameter combinations summarised in Table 6.1. The coefficients for the three models that correspond to the three different values for the stress parameter are presented in Tables 6.2 to 6.4, and the ‘residuals’ of the simulated motions with respect to the regression equations are shown in Figures 6.13 to 6.30. The figures show a generally very good fit to the simulations, the only significant divergence being seen at greater distances for the spectral accelerations at short oscillator periods, which is most likely the result of not fully capturing the anelastic attenuation. Figures 6.31 to 6.42 show comparison of the median predictions at six response periods with simulations as a function of magnitude for four different epicentral distances, all of which confirm the good fit of the regressions to the simulated motions.

Table 6.2. Coefficients of the lower model

T (s)	c_1	c_2	c_3	c_{3a}	c_4	c_{4a}	c_{4b}	c_{4c}
0.01	0.109814	1.18928	-0.2262	-0.09761	-1.76074	-0.40011	-2.3041	-1.81431
0.1	0.946105	1.131886	-0.1465	-0.08741	-1.80353	-0.53834	-2.5332	-2.06718
0.2	1.395916	1.017826	-0.24373	-0.04957	-1.51587	-0.47299	-2.37385	-2.12964
0.3	1.209262	1.014554	-0.36141	-0.04434	-1.3983	-0.40524	-2.23346	-1.89373
0.4	0.957899	1.050353	-0.44786	-0.05556	-1.32835	-0.36476	-2.15757	-1.74098
0.5	0.461128	1.117279	-0.50058	-0.07867	-1.28697	-0.33453	-2.10876	-1.63472
0.6	-0.26982	1.208317	-0.52492	-0.11009	-1.26841	-0.30779	-2.07409	-1.55541
0.7	-0.99959	1.314239	-0.53294	-0.14737	-1.26257	-0.28292	-2.04768	-1.49273
0.85	-1.94632	1.470465	-0.5266	-0.20257	-1.26476	-0.25247	-2.01997	-1.42568
1	-2.85758	1.629383	-0.50131	-0.25731	-1.2813	-0.22642	-2.00093	-1.37589
1.5	-5.12076	2.071045	-0.39885	-0.40282	-1.31893	-0.17606	-1.96296	-1.27436
2	-6.79118	2.379842	-0.29235	-0.48582	-1.35857	-0.15524	-1.94786	-1.22371
2.5	-8.06116	2.562726	-0.19956	-0.50607	-1.44554	-0.14964	-1.95333	-1.2064
3	-8.99662	2.70147	-0.13234	-0.50813	-1.49057	-0.15149	-1.95771	-1.19703
4	-10.2997	2.895223	-0.0429	-0.49008	-1.50244	-0.15662	-1.95938	-1.18789
5	-11.1275	3.00163	0.008789	-0.45468	-1.4759	-0.15965	-1.95566	-1.18621

Table 6.3. Coefficients of the central model

T (s)	c_1	c_2	c_3	c_{3a}	c_4	c_{4a}	c_{4b}	c_{4c}
0.01	0.490759	1.289798	-0.26723	-0.11245	-1.82121	-0.42537	-2.34672	-1.88538
0.1	1.516608	1.189682	-0.18504	-0.08694	-1.84137	-0.56502	-2.57456	-2.16914
0.2	1.980877	1.058019	-0.34117	-0.045	-1.51518	-0.49349	-2.38909	-2.17046
0.3	1.531262	1.105582	-0.46354	-0.06252	-1.39508	-0.41835	-2.24683	-1.91583
0.4	0.972248	1.202062	-0.53114	-0.0998	-1.32534	-0.37184	-2.16988	-1.75591
0.5	0.194881	1.32448	-0.55637	-0.14527	-1.2869	-0.33669	-2.12089	-1.64709
0.6	-0.76825	1.461856	-0.55119	-0.19356	-1.27536	-0.30585	-2.08673	-1.56741
0.7	-1.69932	1.608117	-0.52966	-0.24393	-1.27881	-0.27743	-2.06094	-1.50456
0.85	-2.87048	1.808749	-0.48682	-0.31096	-1.29416	-0.24341	-2.03361	-1.43685
1	-3.92479	1.994758	-0.43355	-0.36884	-1.32276	-0.21625	-2.01476	-1.38699
1.5	-6.38636	2.464976	-0.28091	-0.49898	-1.38146	-0.16927	-1.97542	-1.284
2	-7.95338	2.739589	-0.16998	-0.54476	-1.42915	-0.15626	-1.96009	-1.23455
2.5	-8.91454	2.848895	-0.10561	-0.51852	-1.52008	-0.16125	-1.96734	-1.22251
3	-9.58158	2.922099	-0.06568	-0.48143	-1.56462	-0.17006	-1.97334	-1.21692
4	-10.4741	3.014683	-0.01932	-0.40673	-1.57522	-0.17991	-1.97779	-1.21252
5	-11.0116	3.050216	0.001003	-0.33716	-1.54808	-0.1818	-1.97617	-1.21403

Table 6.4. Coefficients of the higher model

T (s)	c_1	c_2	c_3	c_{3a}	c_4	c_{4a}	c_{4b}	c_{4c}
0.01	-0.25612	1.609903	-0.28536	-0.22324	-1.8288	-0.45491	-2.38222	-1.93922
0.1	0.976817	1.470684	-0.23334	-0.18656	-1.84069	-0.59382	-2.61349	-2.24319
0.2	1.262278	1.374449	-0.37738	-0.16481	-1.51082	-0.50315	-2.40895	-2.20521
0.3	0.517515	1.479449	-0.46186	-0.20465	-1.39345	-0.42009	-2.26459	-1.93394
0.4	-0.29847	1.624274	-0.49279	-0.25809	-1.32512	-0.36896	-2.18582	-1.76771
0.5	-1.26553	1.780391	-0.48785	-0.31169	-1.28771	-0.33159	-2.13536	-1.65678
0.6	-2.35046	1.937092	-0.4599	-0.36059	-1.27775	-0.30004	-2.10018	-1.5769
0.7	-3.36234	2.094027	-0.42015	-0.40667	-1.28347	-0.27197	-2.07315	-1.51393
0.85	-4.59102	2.298136	-0.35903	-0.46202	-1.30236	-0.23922	-2.04384	-1.44572
1	-5.63322	2.47352	-0.29714	-0.50205	-1.33458	-0.21468	-2.02319	-1.39578
1.5	-7.89705	2.879205	-0.14464	-0.56702	-1.40062	-0.17668	-1.97891	-1.29118
2	-9.14424	3.070818	-0.0601	-0.55399	-1.45198	-0.17212	-1.96241	-1.24231
2.5	-9.75364	3.09789	-0.03488	-0.48498	-1.5446	-0.18739	-1.97259	-1.2345
3	-10.145	3.105677	-0.02626	-0.41758	-1.58858	-0.20205	-1.98173	-1.23247
4	-10.6554	3.106824	-0.02324	-0.30727	-1.59865	-0.21391	-1.99146	-1.23281
5	-10.965	3.088108	-0.02927	-0.22469	-1.57129	-0.21323	-1.9933	-1.23771

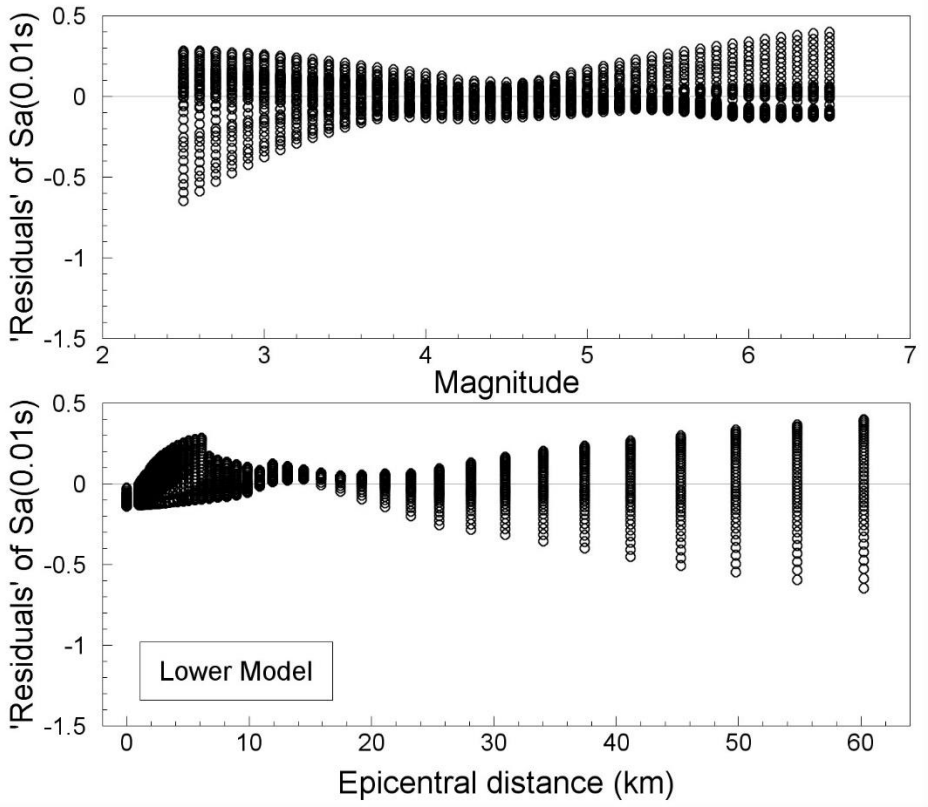

Figure 6.13. Total 'residuals' of spectral accelerations at 0.01 s with respect to the median predictions from the lower NU_B GMPE

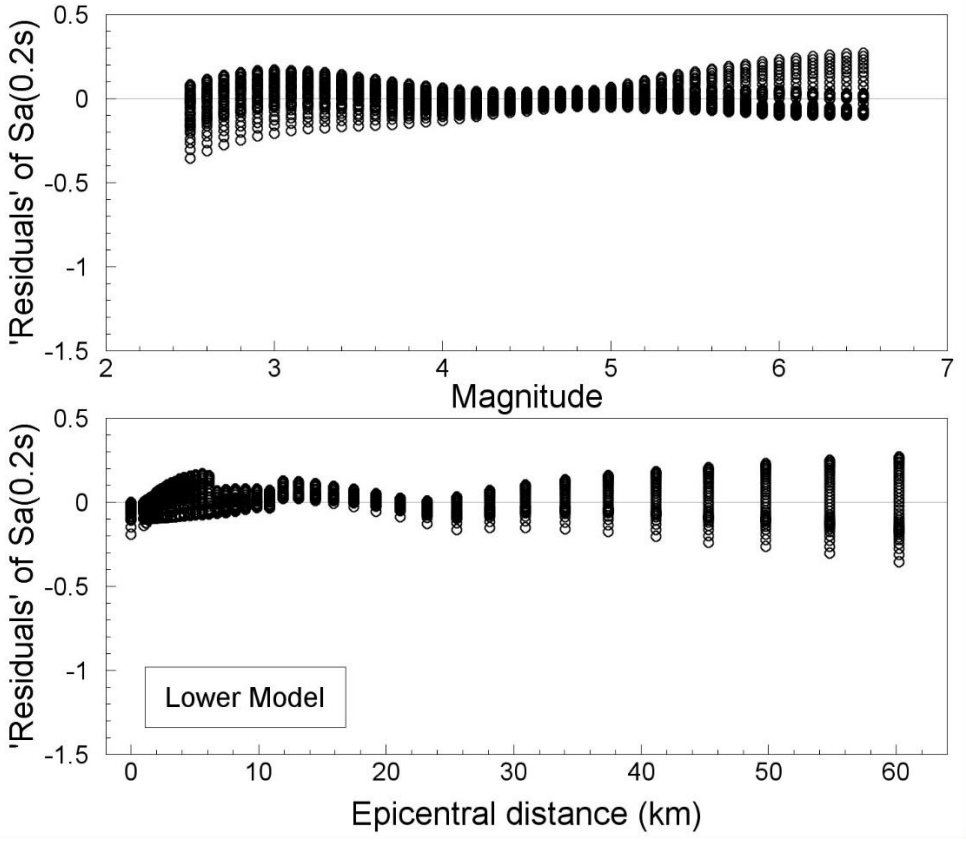

Figure 6.14. Total 'residuals' of spectral accelerations at 0.2 s with respect to the median predictions from the lower NU_B GMPE

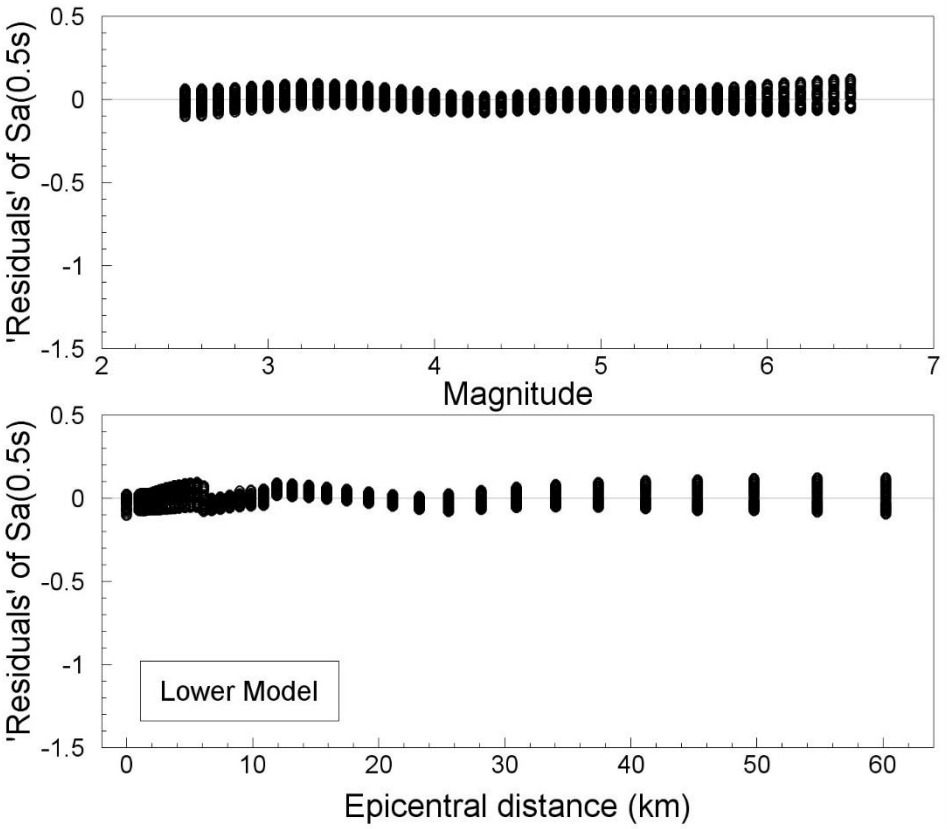

Figure 6.15. Total 'residuals' of spectral accelerations at 0.5 s with respect to the median predictions from the lower NU_B GMPE

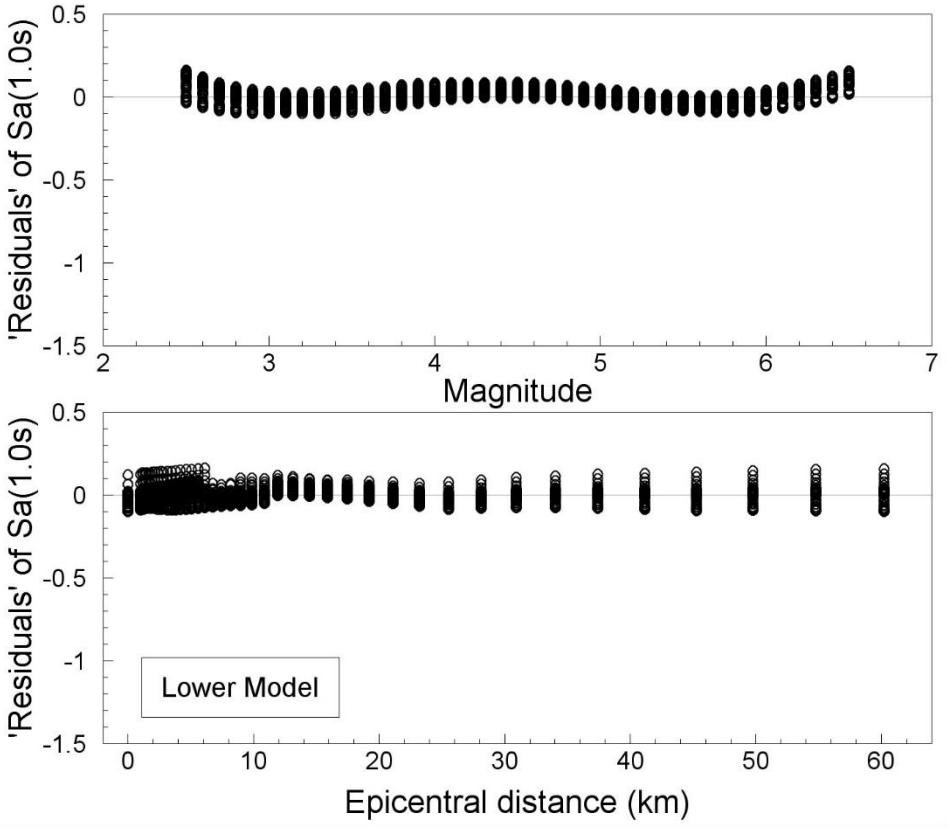

Figure 6.16. Total 'residuals' of spectral accelerations at 1.0 s with respect to the median predictions from the lower NU_B GMPE

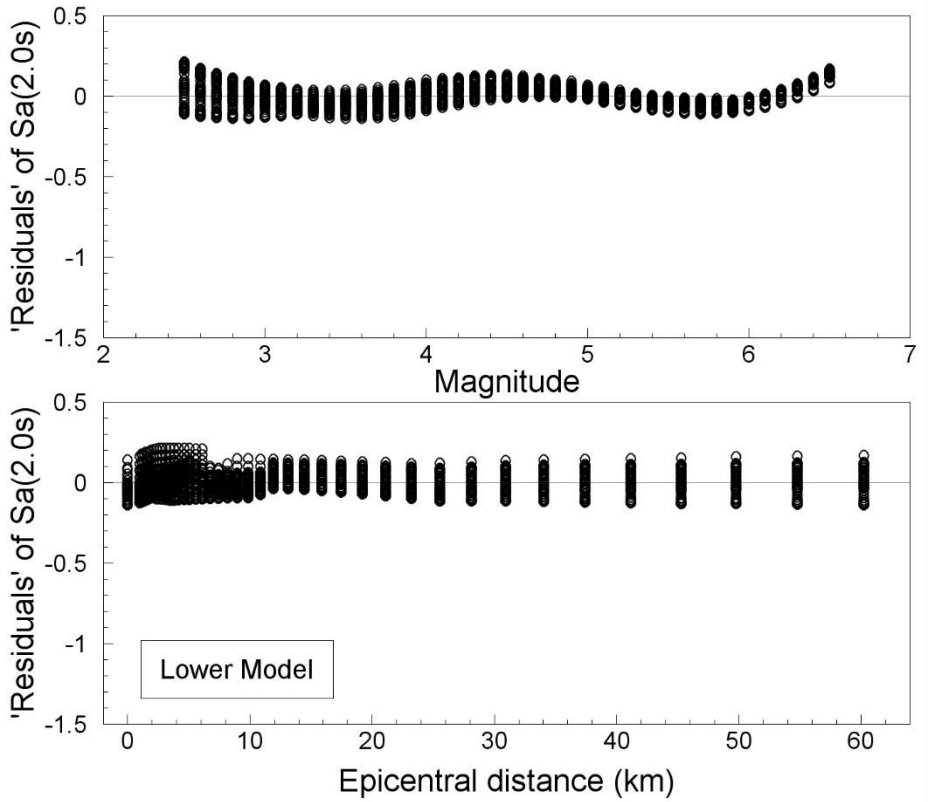

Figure 6.17. Total 'residuals' of spectral accelerations at 2.0 s with respect to the median predictions from the lower NU_B GMPE

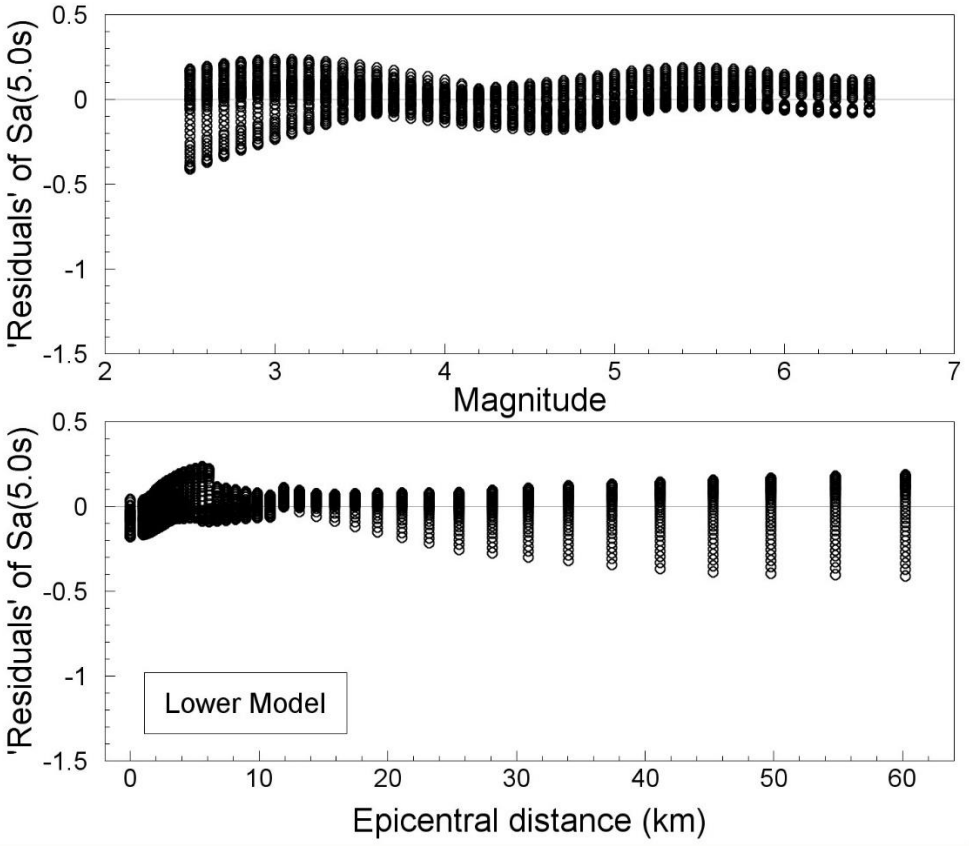

Figure 6.18. Total 'residuals' of spectral accelerations at 5.0 s with respect to the median predictions from the lower NU_B GMPE

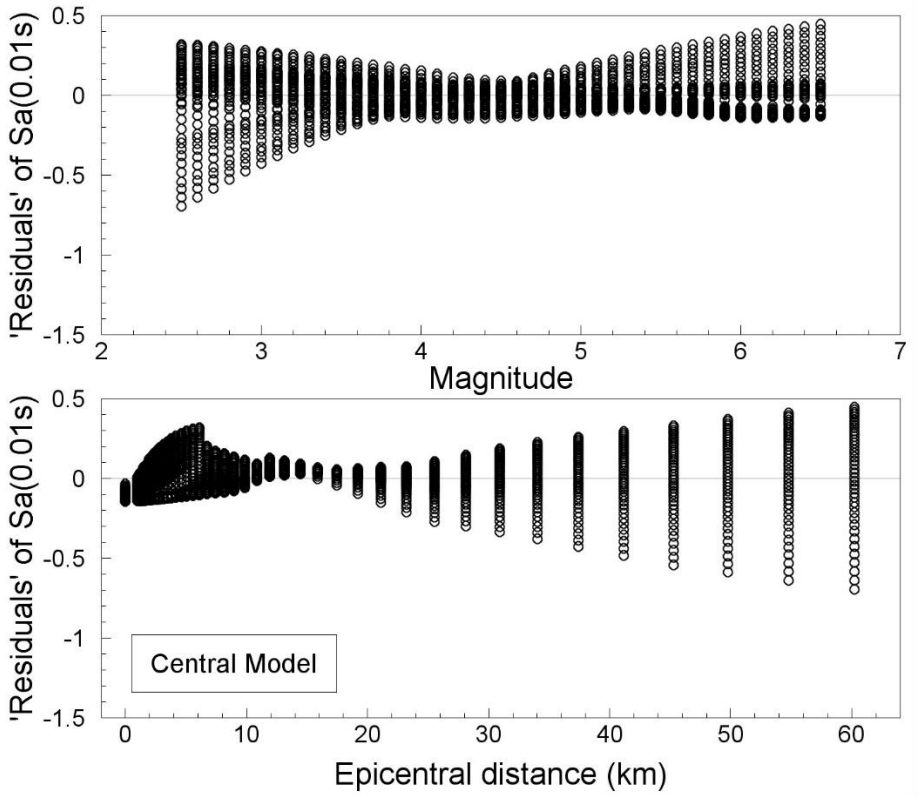

Figure 6.19. Total 'residuals' of spectral accelerations at 0.01 s with respect to the median predictions from the central NU_B GMPE

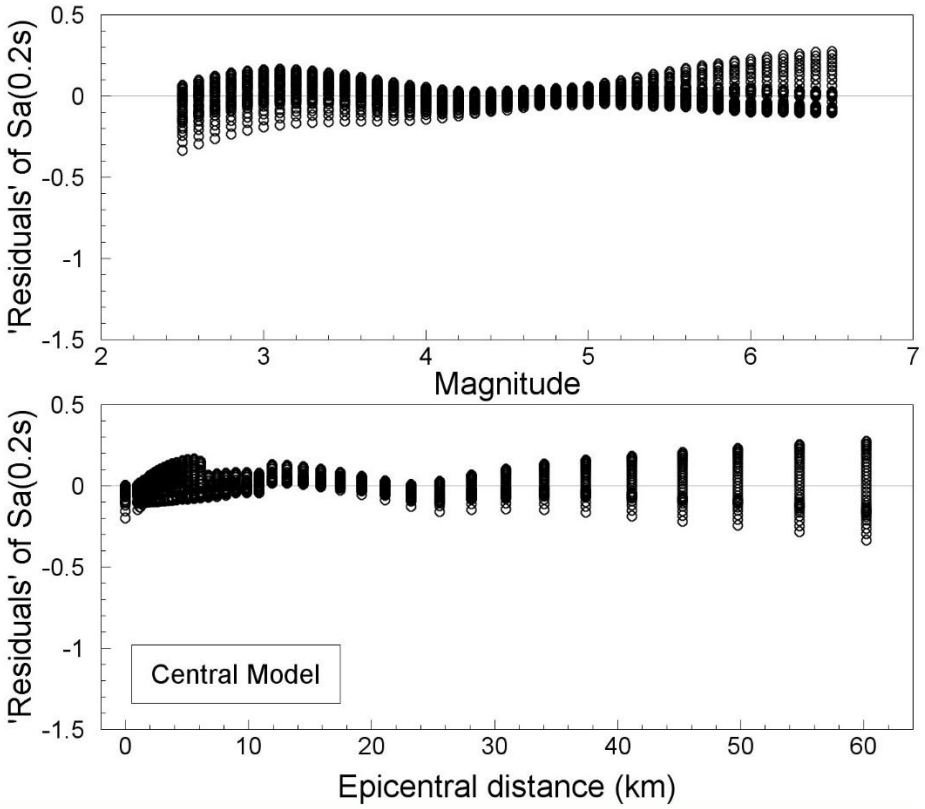

Figure 6.20. Total 'residuals' of spectral accelerations at 0.2 s with respect to the median predictions from the central NU_B GMPE

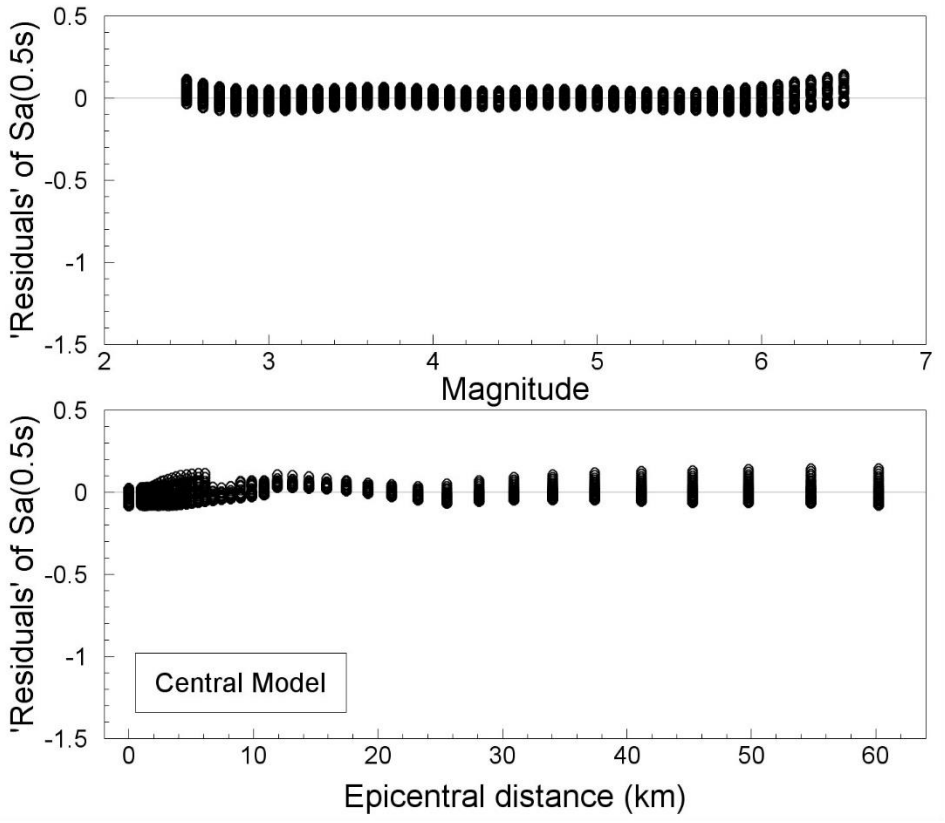

Figure 6.21. Total 'residuals' of spectral accelerations at 0.5 s with respect to the median predictions from the central NU_B GMPE

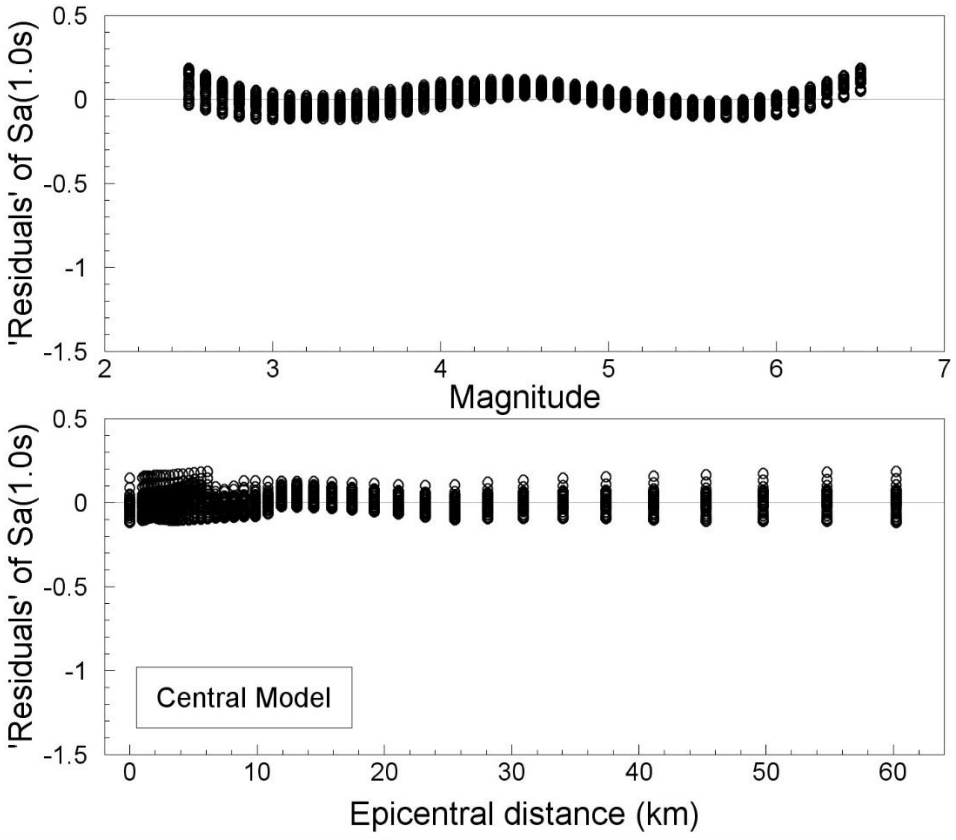

Figure 6.22. Total 'residuals' of spectral accelerations at 1.0 s with respect to the median predictions from the central NU_B GMPE

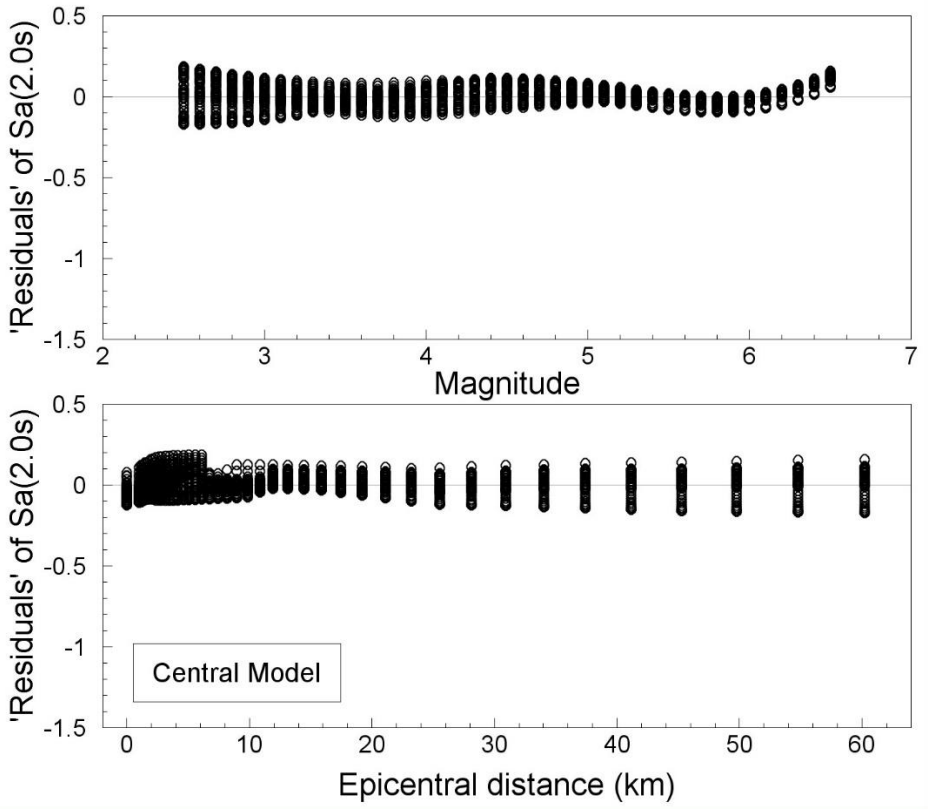

Figure 6.23. Total 'residuals' of spectral accelerations at 2.0 s with respect to the median predictions from the central NU_B GMPE

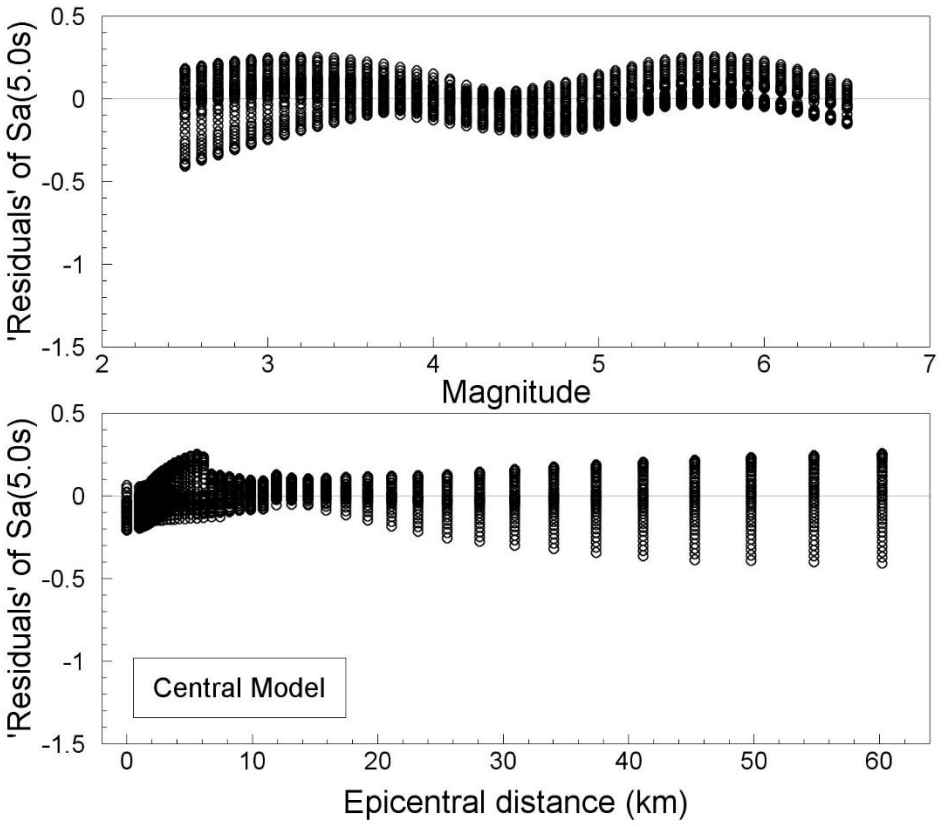

Figure 6.24. Total 'residuals' of spectral accelerations at 5.0 s with respect to the median predictions from the central NU_B GMPE

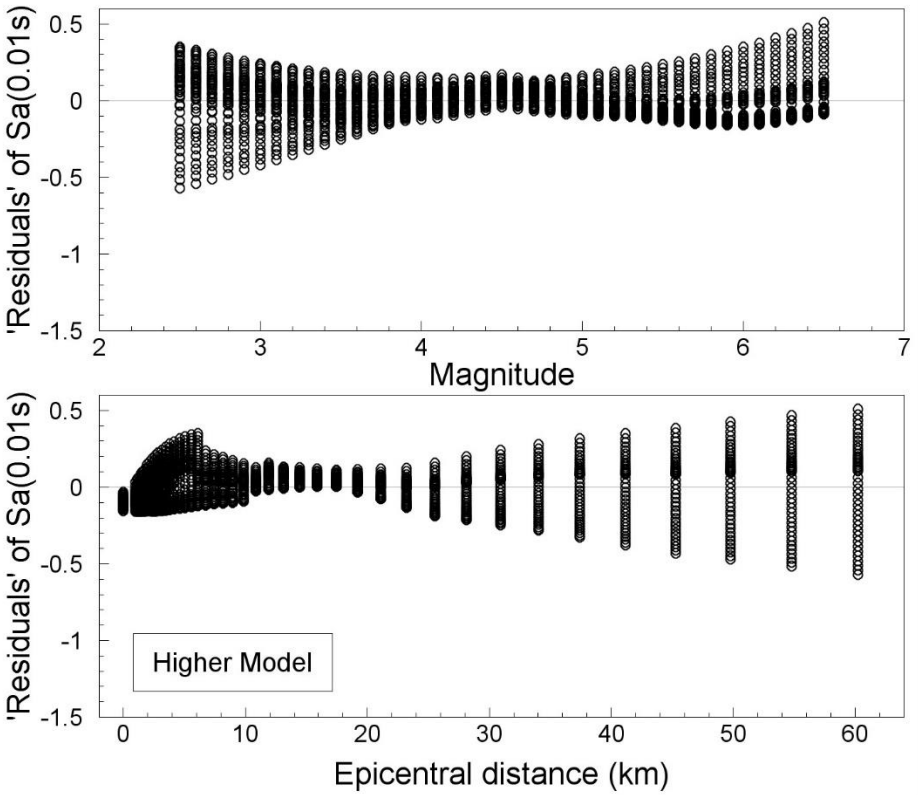

Figure 6.25. Total 'residuals' of spectral accelerations at 0.01 s with respect to the median predictions from the upper NU_B GMPE

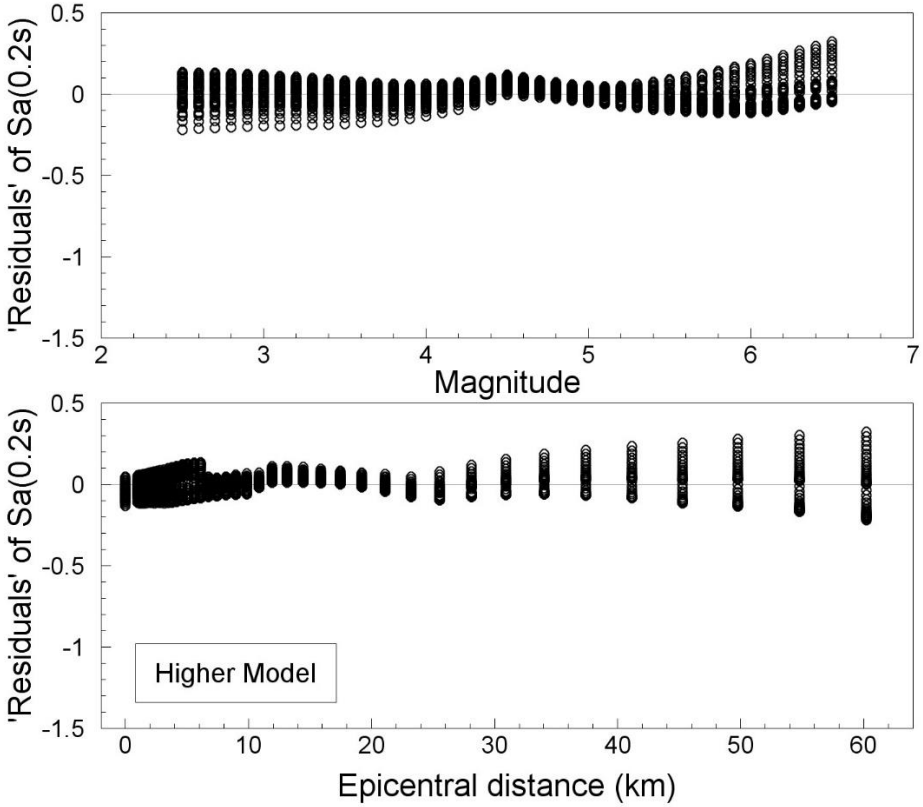

Figure 6.26. Total 'residuals' of spectral accelerations at 0.2 s with respect to the median predictions from the upper NU_B GMPE

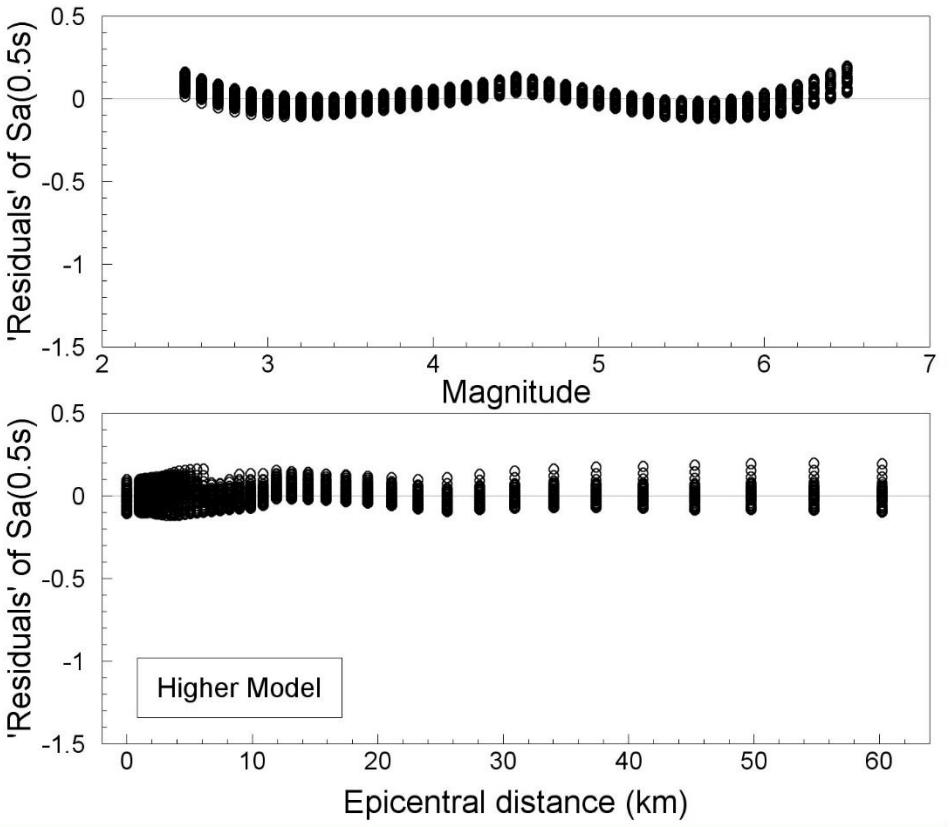

Figure 6.27. Total 'residuals' of spectral accelerations at 0.5 s with respect to the median predictions from the upper NU_B GMPE

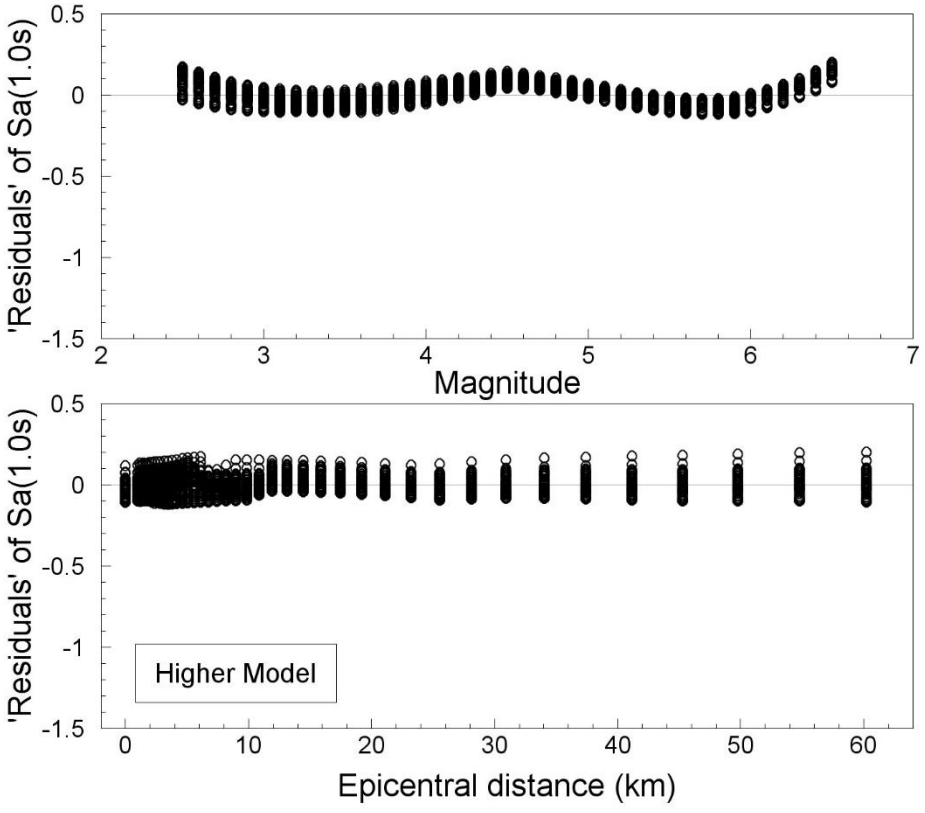

Figure 6.28. Total 'residuals' of spectral accelerations at 1.0 s with respect to the median predictions from the upper NU_B GMPE

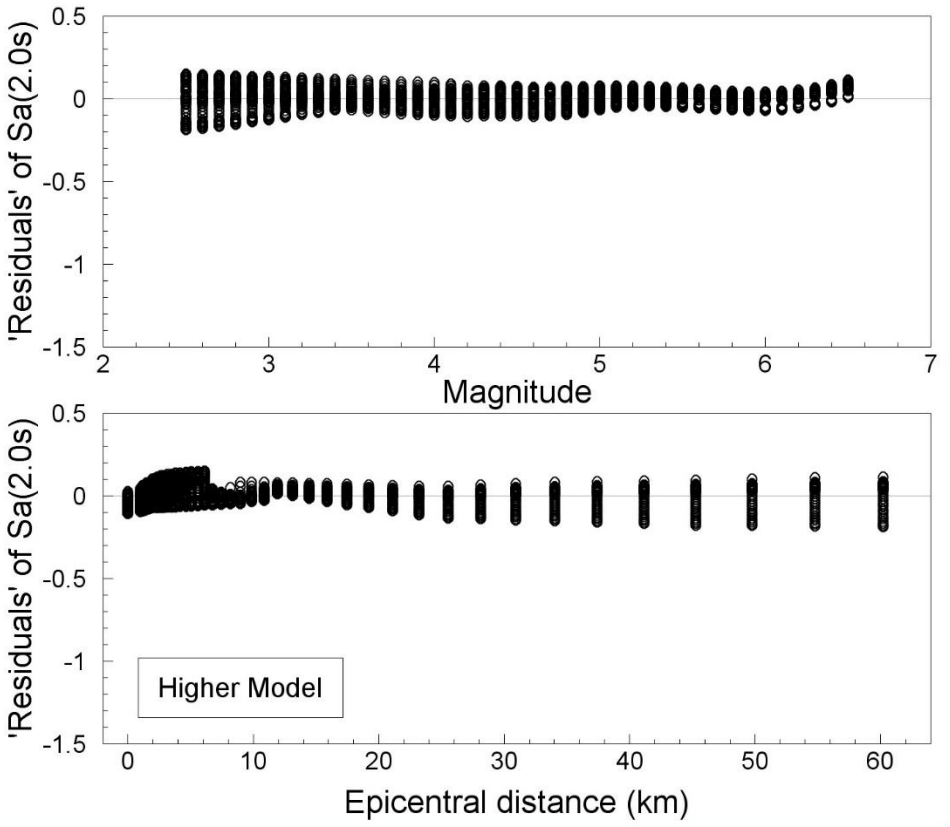

Figure 6.29. Total 'residuals' of spectral accelerations at 2.0 s with respect to the median predictions from the upper NU_B GMPE

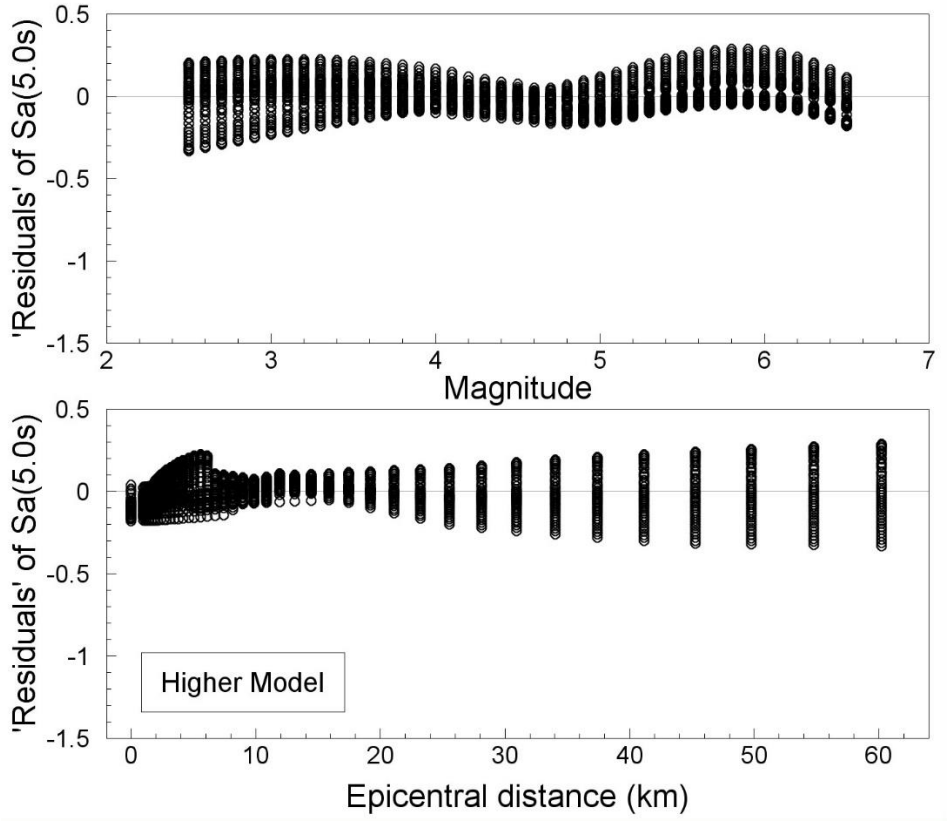

Figure 6.30. Total 'residuals' of spectral accelerations at 5.0 s with respect to the median predictions from the upper NU_B GMPE

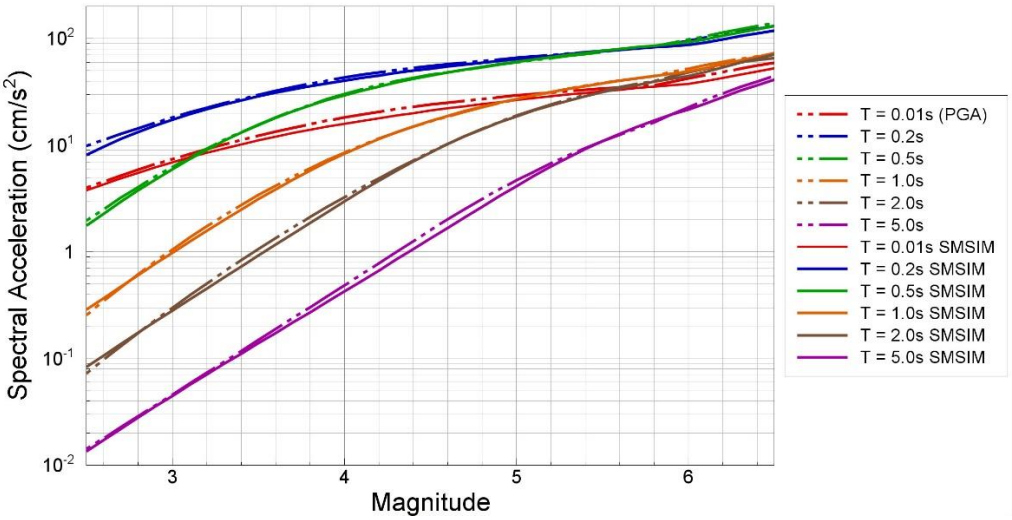

Figure 6.31. Comparison of simulations and median predictions from the parameter equation for the lower model for 6 response periods at 0 km epicentral distance

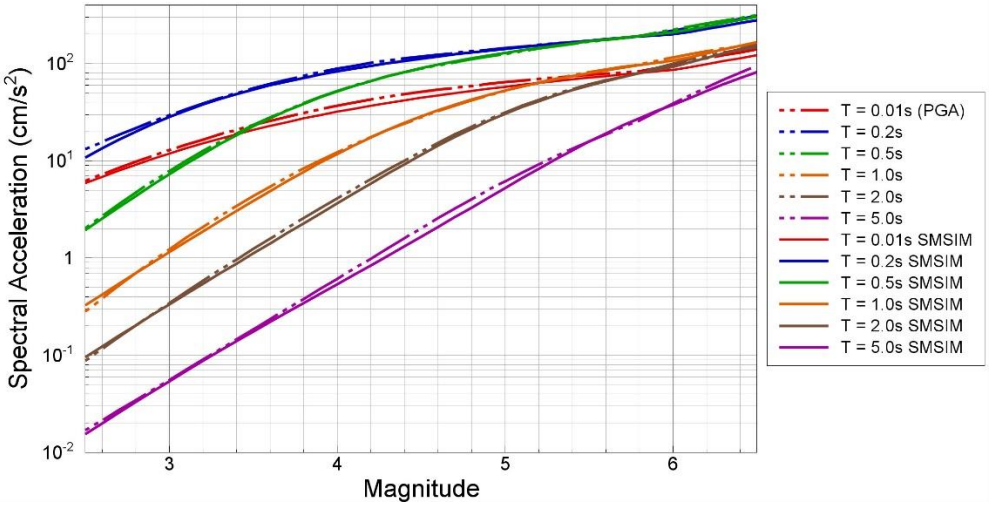

Figure 6.32. Comparison of simulations and median predictions from the parameter equation for the central model for 6 response periods at 0 km epicentral distance

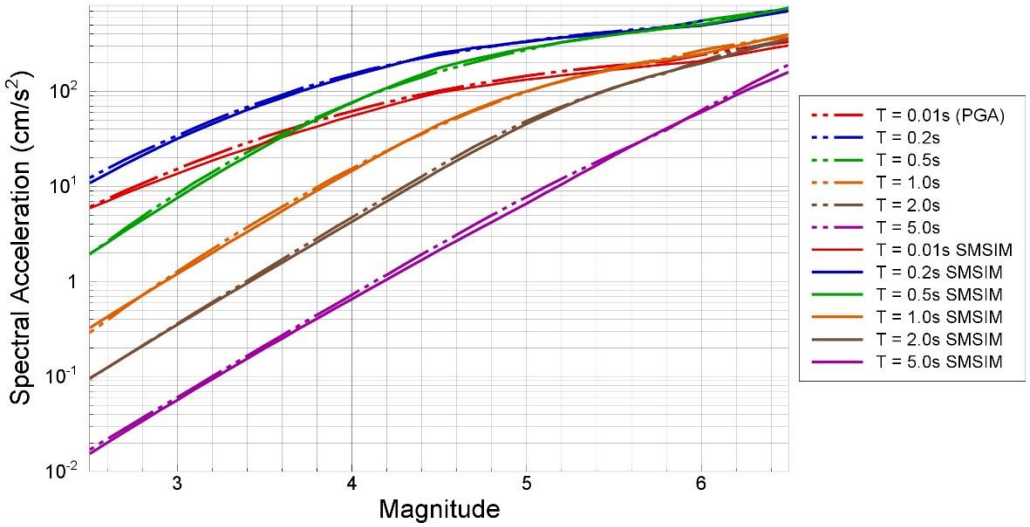

Figure 6.33. Comparison of simulations and median predictions from the parameter equation for the upper model for 6 response periods at 0 km epicentral distance

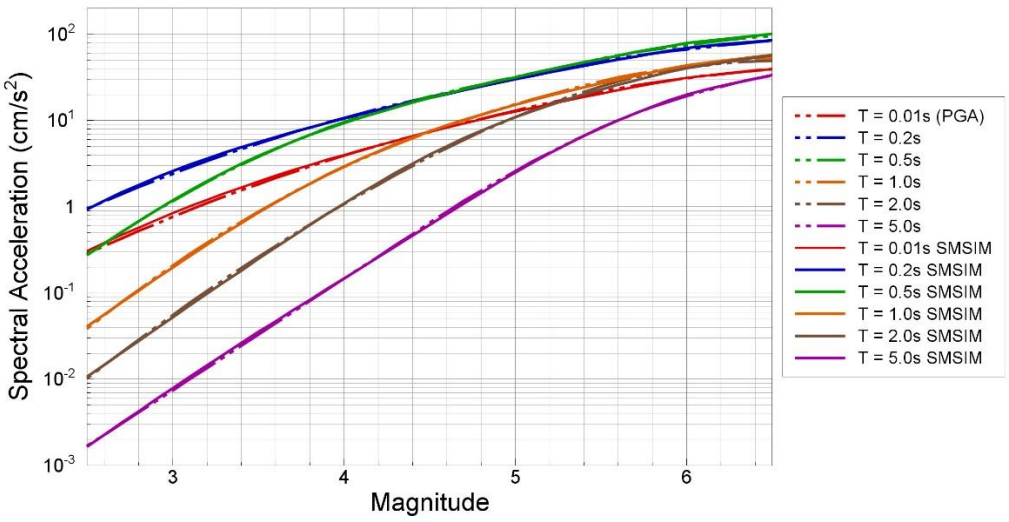

Figure 6.34. Comparison of simulations and median predictions from the parameter equation for the lower model for 6 response periods at 10 km epicentral distance

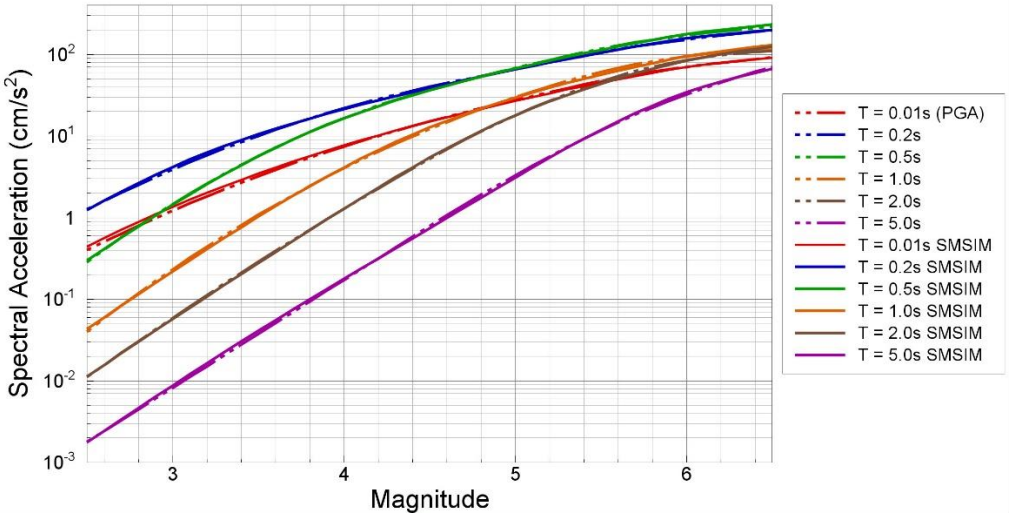

Figure 6.35. Comparison of simulations and median predictions from the parameter equation for the central model for 6 response periods at 10 km epicentral distance

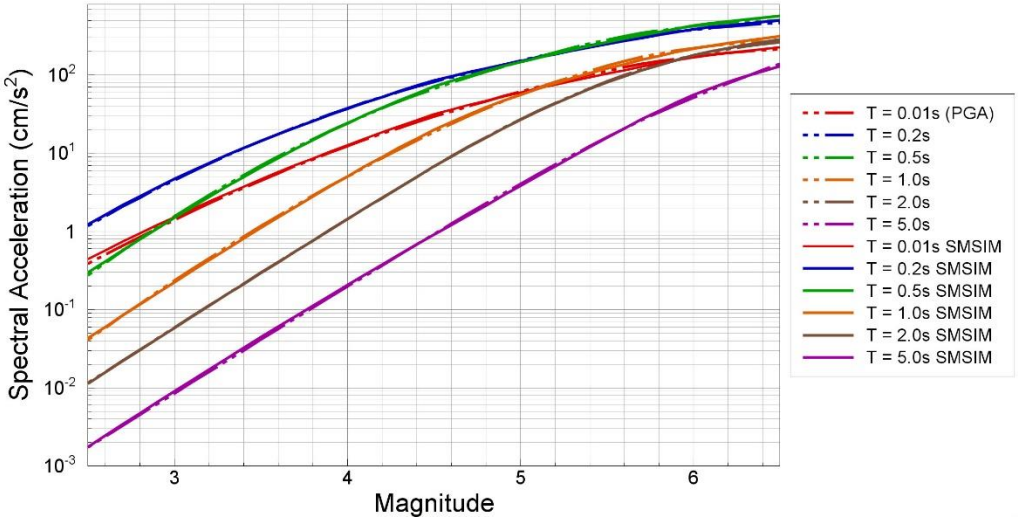

Figure 6.36. Comparison of simulations and median predictions from the parameter equation for the upper model for 6 response periods at 10 km epicentral distance

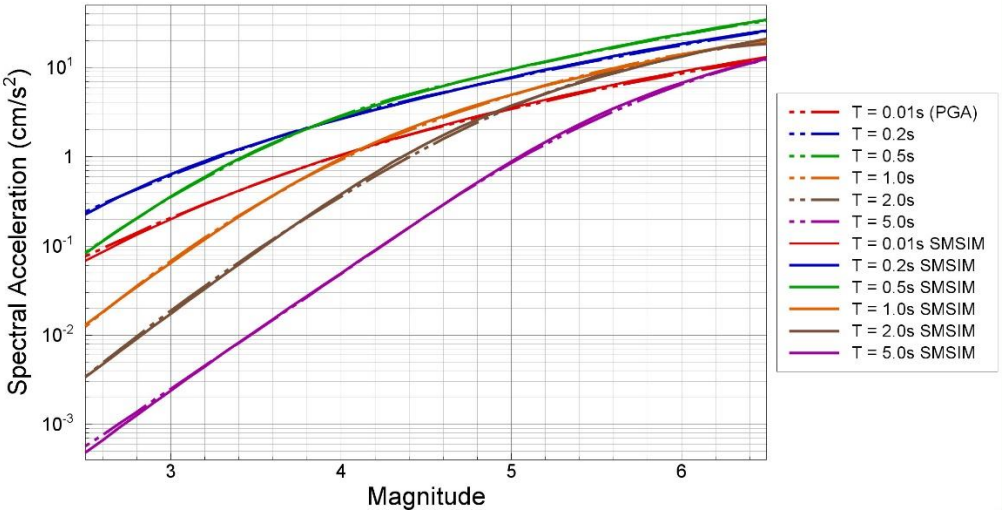

Figure 6.37. Comparison of simulations and median predictions from the parameter equation for the lower model for 6 response periods at 20 km epicentral distance

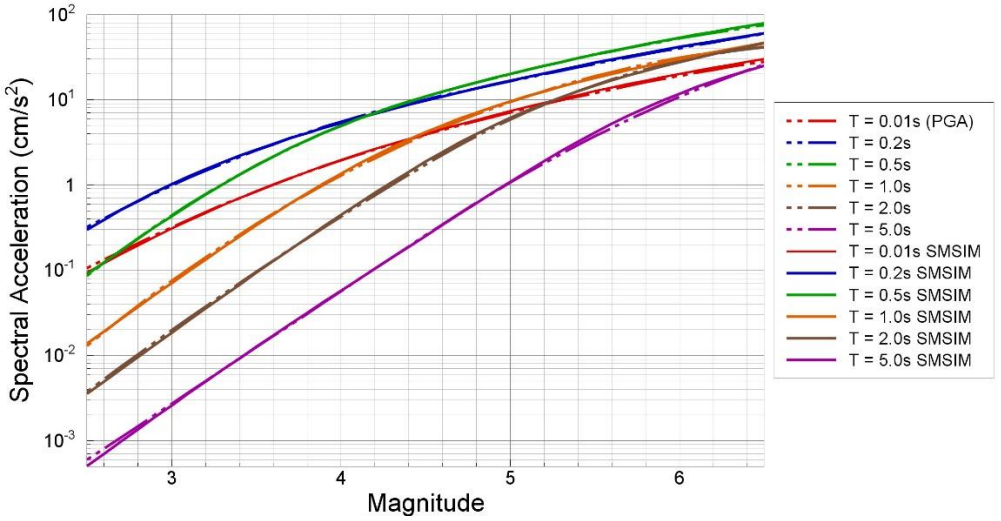

Figure 6.38. Comparison of simulations and median predictions from the parameter equation for the central model for 6 response periods at 20 km epicentral distance

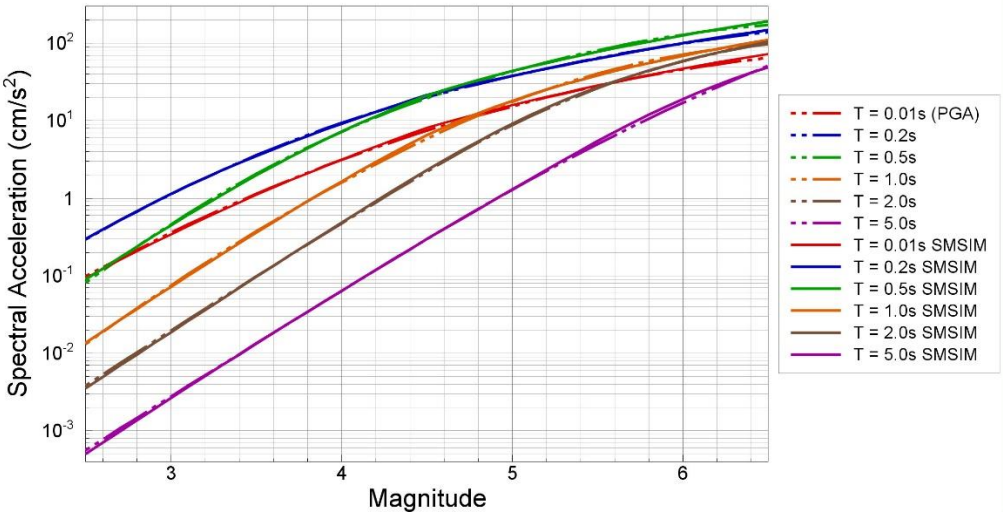

Figure 6.39. Comparison of simulations and median predictions from the parameter equation for the upper model for 6 response periods at 20 km epicentral distance

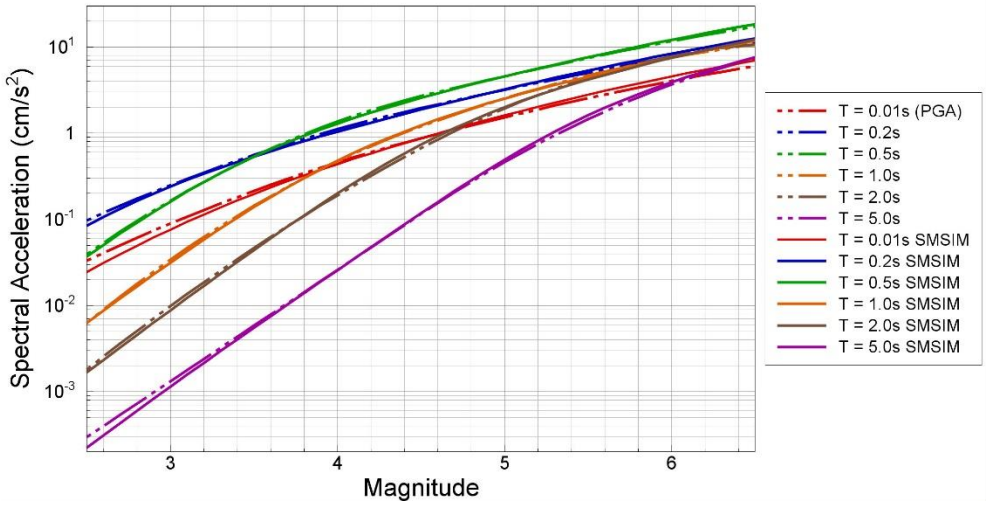

Figure 6.40. Comparison of simulations and median predictions from the parameter equation for the lower model for 6 response periods at 30 km epicentral distance

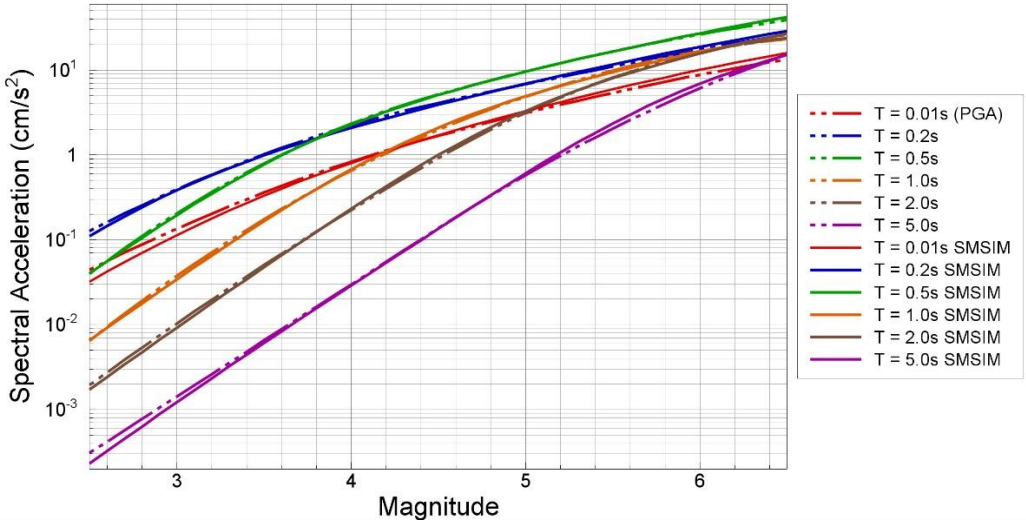

Figure 6.41. Comparison of simulations and median predictions from the parameter equation for the central model for 6 response periods at 30 km epicentral distance

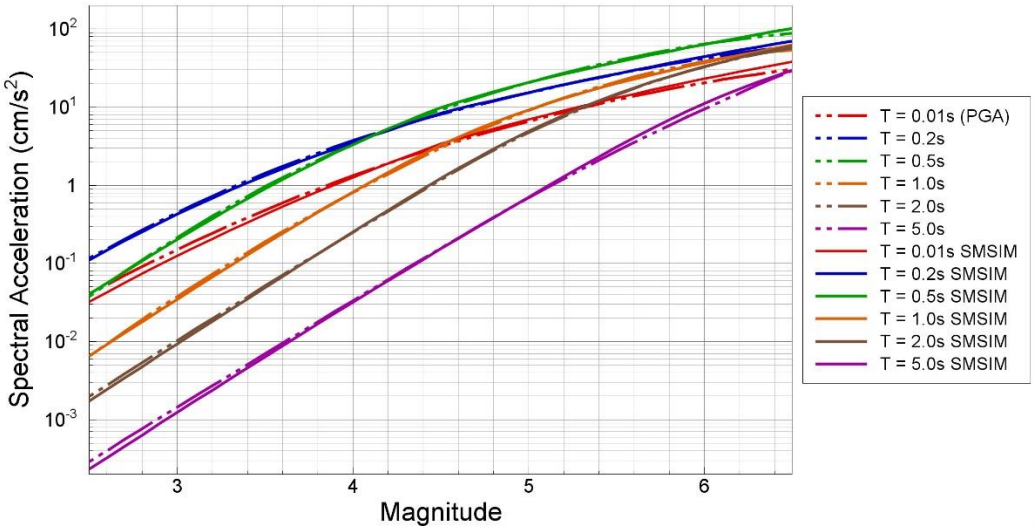

Figure 6.42. Comparison of simulations and median predictions from the parameter equation for the upper model for 6 response periods at 30 km epicentral distance

In closing this section, Figures 6.43 to 6.50 compare the simulated and predicted response spectral ordinates at the NU_B horizon for several combinations of magnitude and distance, which also confirm the generally very good level of agreement between the stochastic simulations and the predictions from the parametric equations obtained from the regressions. These plots also provide insight into the shape of the predicted spectra at the NU_B reference rock horizon, including the expected tendency for the spectral peak to occur at longer periods for larger magnitudes. The amplified motions at periods on the order of 2 seconds, due to the impedance contrast at the NS_B horizon (Section 5.4) are also clearly visible, particularly for larger magnitude motions.

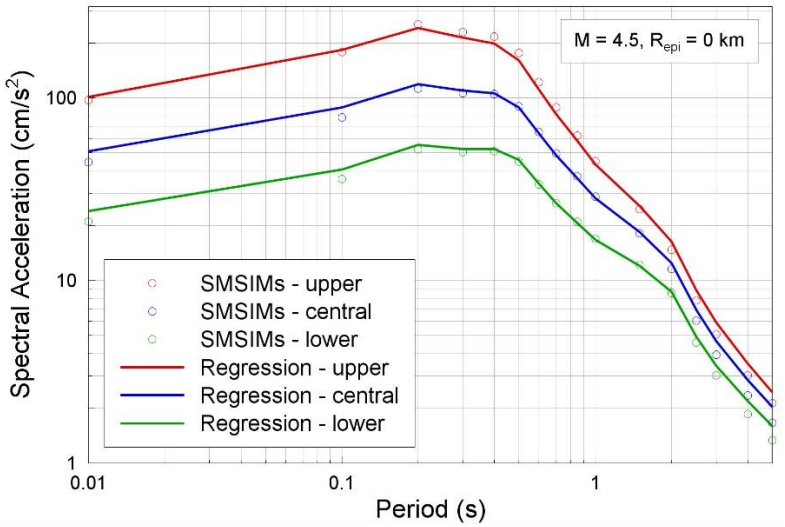

Figure 6.43. Comparison of simulated and predicted response spectra at NU_B due to a magnitude **M** 4.5 earthquake at an epicentral distance of 0 km

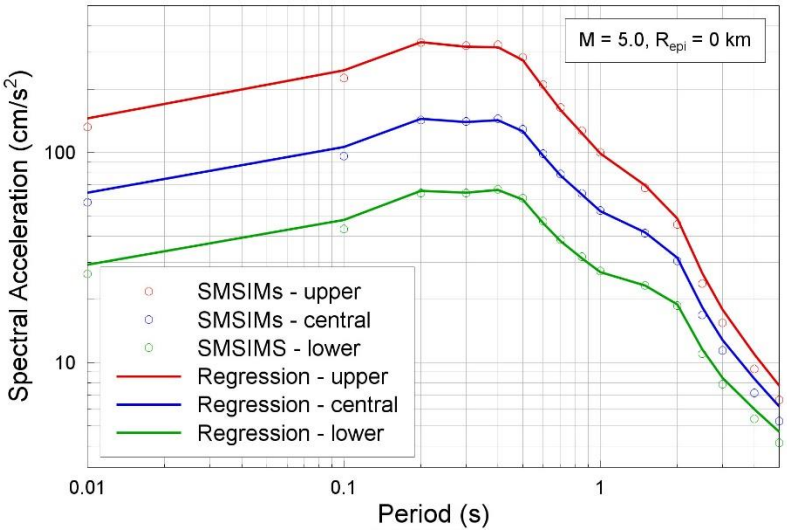

Figure 6.44. Comparison of simulated and predicted response spectra at NU_B due to a magnitude **M** 5.0 earthquake at an epicentral distance of 0 km

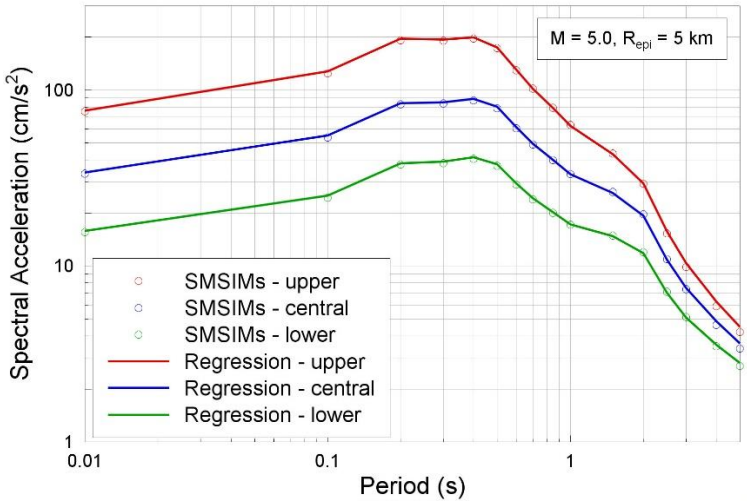

Figure 6.45. Comparison of simulated and predicted response spectra at NU_B due to a magnitude **M** 5.0 earthquake at an epicentral distance of 5 km

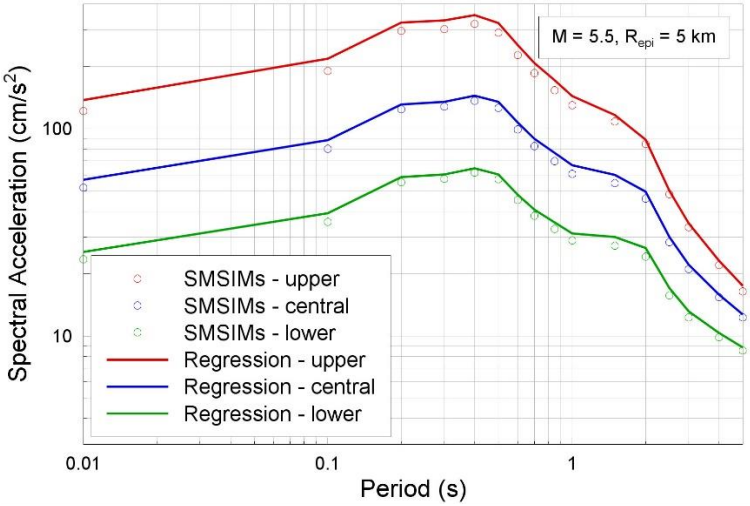

Figure 6.46. Comparison of simulated and predicted response spectra at NU_B due to a magnitude **M** 5.5 earthquake at an epicentral distance of 5 km

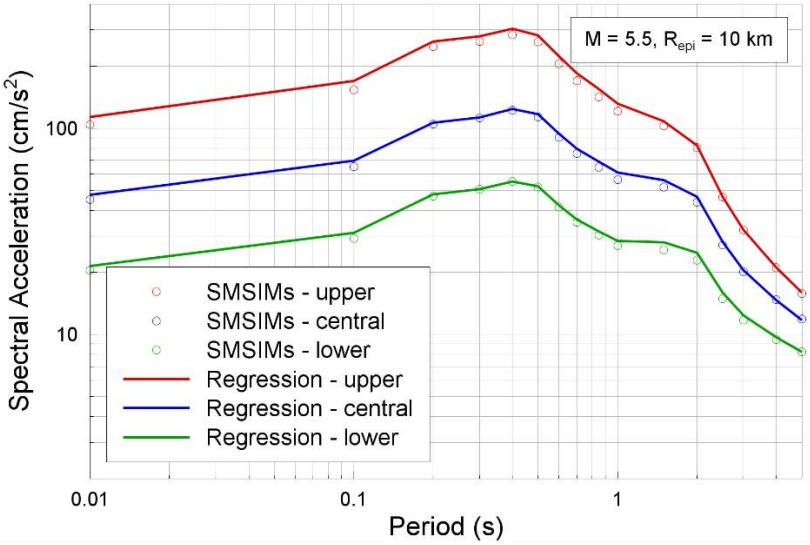

Figure 6.47. Comparison of simulated and predicted response spectra at NU_B due to a magnitude **M** 5.5 earthquake at an epicentral distance of 10 km

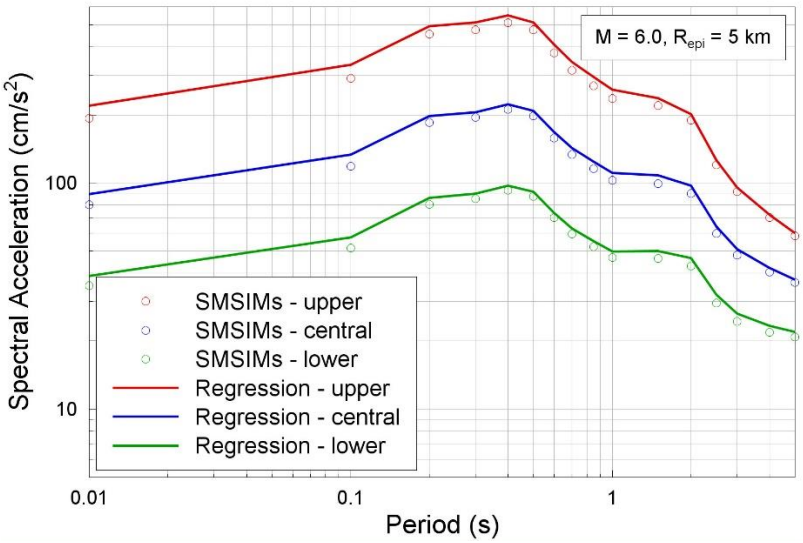

Figure 6.48. Comparison of simulated and predicted response spectra at NU_B due to a magnitude **M** 6.0 earthquake at an epicentral distance of 5 km

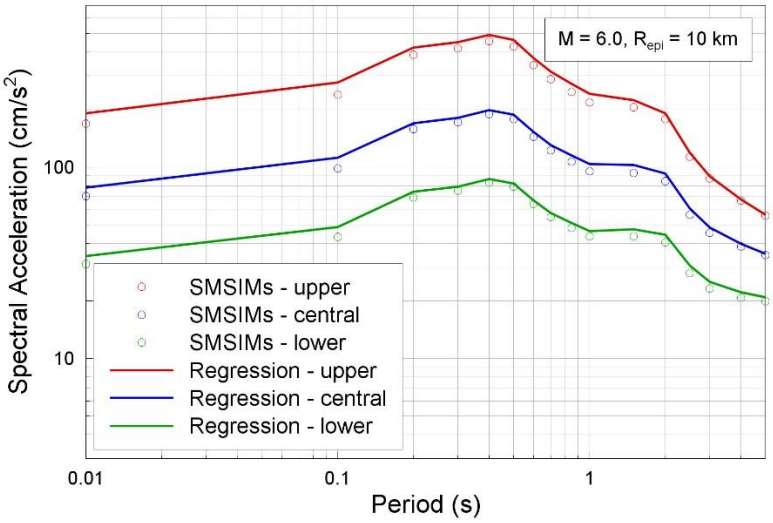

Figure 6.49. Comparison of simulated and predicted response spectra at NU_B due to a magnitude **M** 6.0 earthquake at an epicentral distance of 10 km

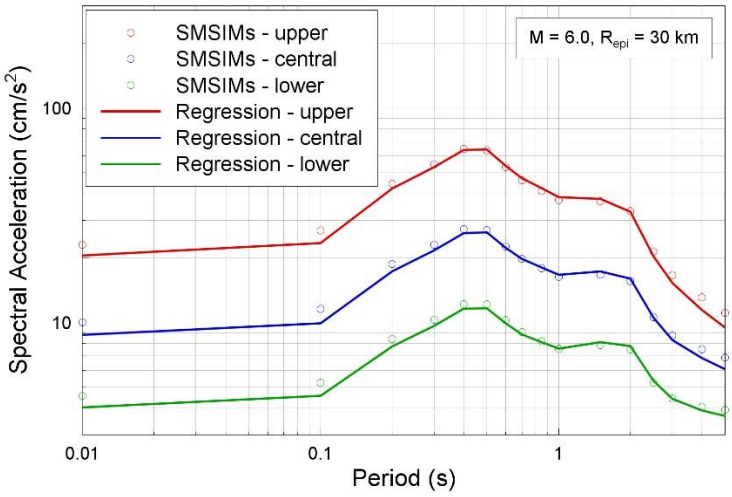

Figure 6.50. Comparison of simulated and predicted response spectra at NU_B due to a magnitude **M** 6.0 earthquake at an epicentral distance of 50 km

6.5. Residual analyses

As for the V1 GMPEs, the first stage in building the sigma models that complete the predictive equations together with the coefficients for median predictions presented in the previous section, is to calculate the residuals of the recorded motions with respect to the predictions from the central model. The difference in this case is that the residuals are calculated for motions recorded at the surface with respect to predictions at the NU_B reference rock horizon. Therefore, the usable response spectral ordinates of the surface recordings (Section 3.2) were first deconvolved to the NU_B horizon using the response spectral amplification factors derived for each recording station (Section 4.3, Appendix IV). The residuals are then calculated as the difference between the observed and predicted values in natural log units, which is also equivalent to the natural logarithm of the ratios of observed to predicted motions.

The number of records, even at shorter response periods, available for these calculations is not much greater than those available for the V1 model. A database of almost 200 records from 24 earthquakes with magnitudes from 2.0 to 3.6 was assembled for the V2 inversions, which is a considerable improvement from the database of 85 records from 12 earthquakes with magnitudes from 2.6 to 3.6 used for the V1 inversions. However, as far as the 'strong-motion' database to be used directly in the regressions and the estimation of sigma components is concerned, since the model is once limited to magnitude 2.5 and greater, then—taking into account the corrections of some magnitudes—the V2 database is only increased to 106 records from 12 earthquakes. Therefore, similar caveats as applied to the variability calculated for the V1 model, are relevant here, which means that the between-event variability estimates in particular must be interpreted with some caution.

The first observation made from the random effects regression to calculate the residuals is that the central model is not unbiased with respect to the recordings, which manifests primarily in the event-terms (also referred to as inter-event or between-event residuals). The biases are then calculated using a mixed effects regression, which in effect removes an average offset from all the residuals, the effect of which manifests almost entirely—but not quite exclusively—in changes to the inter-event residuals and hence to the inter-event variability. The biases are illustrated in Figure 6.51 for all three models corresponding the three selected values of the stress parameter. A positive value of the bias factor means that the model is underestimating the data and a negative bias factor indicates over-prediction. The degree of disagreement between the models and the data is perhaps surprising, especially in view of the relatively good fit obtained for the central V1 model. However, there are several reasons why this misfit may manifest in the V2 models. Firstly, for the V1 models, the data used for the inversions and for the calculation of residuals were identical, whereas in the V2 model development a much larger database was employed for the inversions, including recordings from many smaller earthquakes (Section 3.3). Even in the selection of the optimal parameter combinations to be used for the simulations, the full database of stronger motions—including recordings from two earthquakes of **M** 2.4 and another two of **M** 2.3, which are not considered in the residual calculations—was employed (Section 3.2).

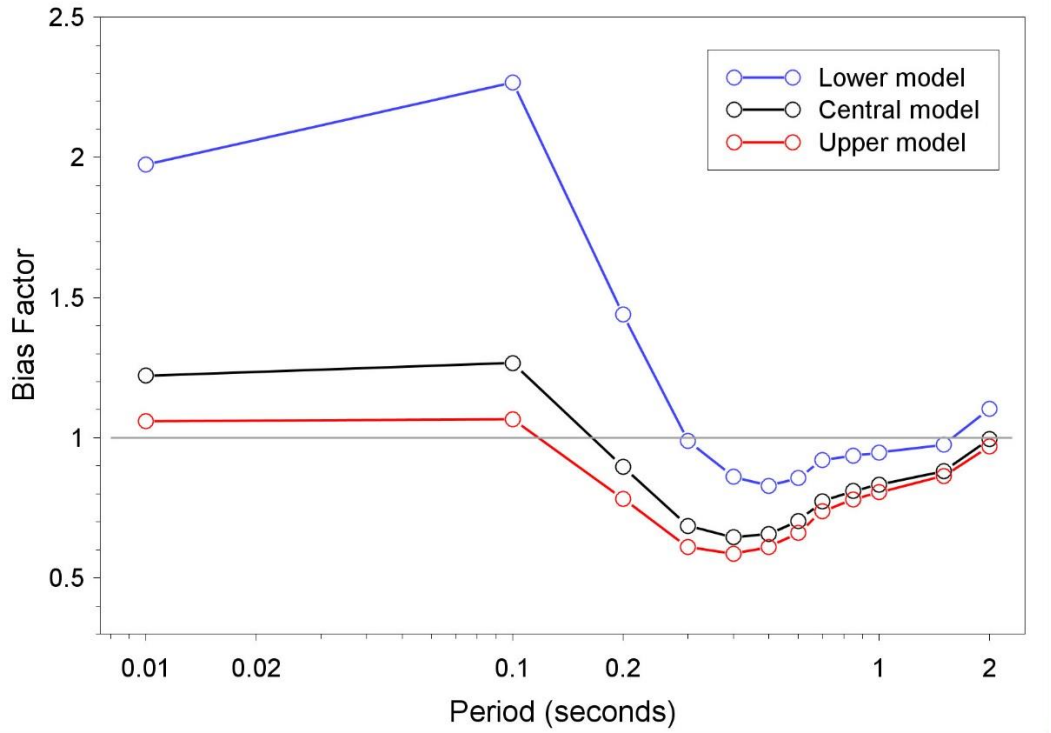

Figure 6.51. Bias factors for the three median NU_B GMPEs with respect to the deconvolved ground-motion recordings from earthquakes of **M** ≥ 2.5

Perhaps even more importantly, whereas for V1 the inversions were performed for the FAS of the surface recordings and the residuals were also calculated at the surface, in V2 the model is developed at the NU_B horizon some 350 m below the ground surface at which the records are obtained. Although the simulations were compared to the surface motions to optimise the combination of source, path and site parameters (Section 6.1), in effect the process has involved calculating the response spectral ordinates at the NU_B horizon in two different ways, one using the transfer functions for FAS (Section 4.3, Appendix III) and the other using the amplification functions for response spectral ordinates (Section 4.3, Appendix IV). Although these might be expected to yield very similar results, some cases of divergence have been found. To illustrate this point, Figure 6.52 shows ratios between the response spectral ordinates obtained by application of the amplification factors to the surface response spectra and those obtained by applying the transfer functions to the surface FAS. In the latter case, the phase spectra of the surface motions are retained and the inverse Fourier transform applied at the NU_B to generate accelerograms from which the response spectral ordinates are then obtained. The ratios are only calculated for the usable period range of each record. While it can be seen that the average ratio is close to unity, except at very short periods where the response spectra obtained from the FAS are consistently higher, there are a number of cases where the ratios are significantly different from unity. The largest outlier in the period range of greatest interest to the risk calculations (highlighted in pink in the figure), is the EW component of the MID1 recording of event #6 (the 2012 Huizinge earthquake, which at **M** 3.6 is the largest earthquake to have occurred in the field to date) obtained at 2 km from the epicentre; the NS component of this same record has the largest PGA value recorded at date at 0.08*g*. The EW component also has an appreciable PGA—in relative

terms for the Groningen database—at about 0.04*g*. This component is one of those with very short duration, with a 5-75% AI significant duration (see Section 12.1) of 0.7 seconds.

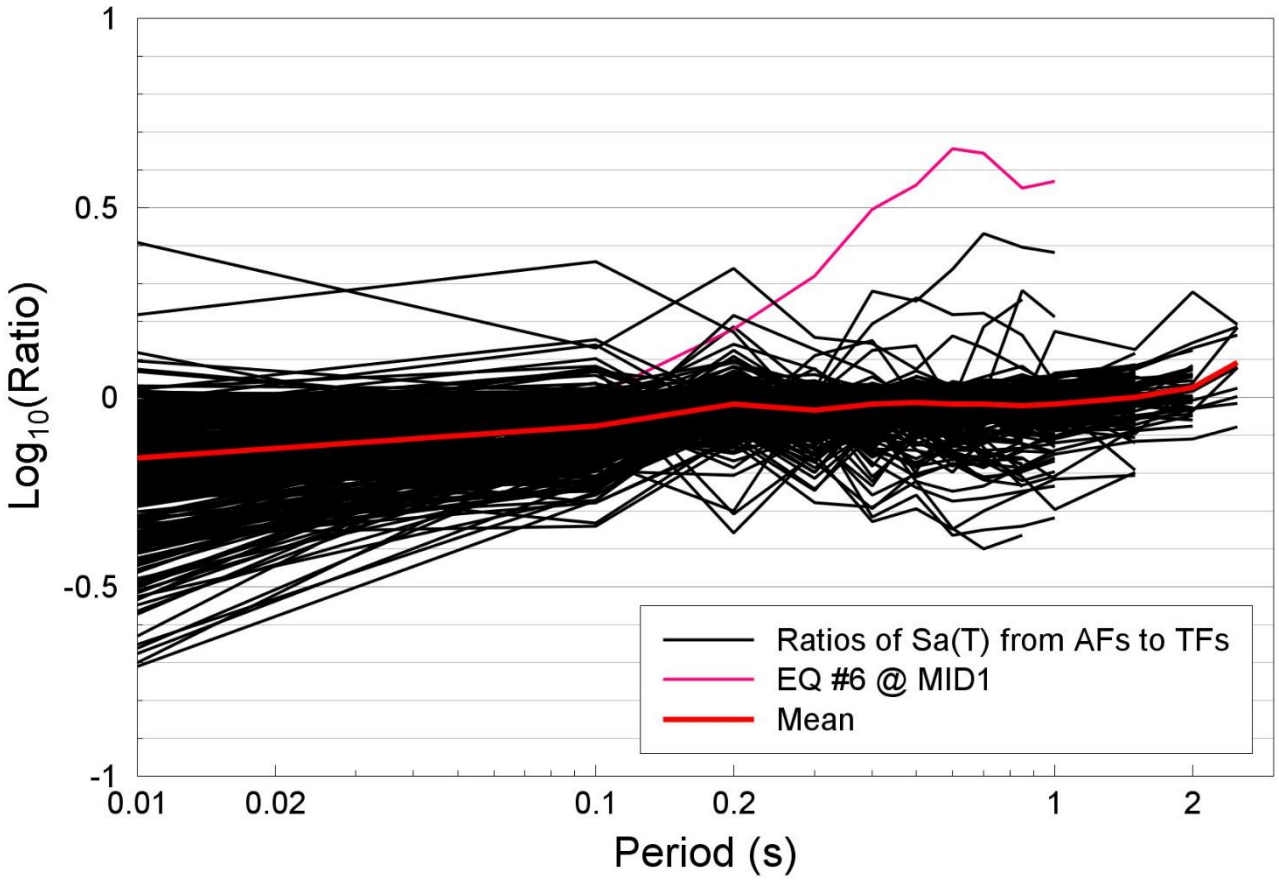

Figure 6.52. Ratios of response spectral ordinates, per horizontal component, estimated at the NU_B using amplification factors to those obtained from transfer functions for FAS. The thick red line indicates the average ratio, the pink line the highest outlier that is discussed in the text

Possible features of these recordings that might have contributed to these deviations—which could perhaps be related to the very short durations given the role of that parameter in generating response spectra from FAS—are being explored. For now, it is noted that this may be a possible contributing factor to the observed bias in the models, in particular the fairly consistent underestimation of the data at very short periods.

An additional issue to be considered is the factor of 1.2 applied to amplification function from the reservoir to the NU_B horizon obtained in the inversions that was applied to facilitate the merging of this amplification function with the long-period adjustment for the impedance contrast at the NS_B horizon (Section 5.4). Moreover, the functional forms of the parameterised equations were fitted to simulated motions over a wide range of magnitudes (Section 6.3) and were not particularly focused on the magnitude range of the recorded motions, which has very little impact on the hazard and risk estimates.

In the range of periods of most building typologies in the field (Figure 1.3) the central and upper models appear to be positively biased with regard to the recordings, meaning that the

observed motions are being over-predicted. This is obviously of much less concern than if there was appreciable under-estimation and it is also not clear if the predictions would also be biased at larger magnitudes. In view of these considerations, for this preliminary version of the V2 GMPEs, we do not make any adjustment to the equations to attempt to remove the bias. However, the bias clearly does influence the calculation of the variability from the residuals as can be appreciated from Figures 6.53 and 6.54 which show the inter-event and intra-event residuals of the data with respect to the central prediction equations. From these plots—particular Figures 6.53 and 6.54 that correspond to the central model—that the bias mainly influences the inter-event residuals. This is also confirmed by the calculated inter-event and intra-event variability for each of the three models (Table 6.5) in which it can be clearly seen that the removal of the bias impacts mainly on the inter-event variability. Note that although the variability components at a period of 2.5 seconds are shown in the figures, these values are completely unreliable because of the very small number of events and recordings usable at this response period.

For the V2 model, the within-event sigma values and the total sigmas obtained from the residuals are of less interest than in the development of the V1 model, since the within-event variability at the NU_B rock horizon must, by necessity, be single-station sigma (see Section 10.4). Nonetheless, it is interesting to compare the within-event variability estimates to ascertain if the more complex geometric spreading model and the removal of local site effects has resulted in reduced spatial variability, which does not appear to be the case (Figure 6.55). The between-event variability obtained from the residuals of the central V2 GMPE, apart from an unexplained dip at 0.2 seconds, seem to be in reasonable agreement with the values assigned to central V1 model at shorter response periods, but are greater at long periods—even exceeding the values assigned to the upper V1 model, which were adopted from the GMPE of Akkar *et al*. (2014a) for tectonic earthquakes in Europe and the Middle East. However, the values at the highest periods should be interpreted with great caution given the very small number of earthquakes on which they are based (Table 6.5).

Table 6.5. Variability estimates for the central NU_B GMPE

Period (secs)	No. EQs	No. Recs	Original Values			Without Bias		
			τ	ϕ	σ	τ	ϕ	σ
0.01	12	106	0.3249	0.5864	0.6704	0.261	0.5886	0.6439
0.1	12	106	0.3719	0.6815	0.7764	0.2856	0.6852	0.7423
0.2	12	106	0.1936	0.6747	0.7019	0.1877	0.6738	0.6995
0.3	12	106	0.4925	0.5035	0.7043	0.3414	0.5023	0.6073
0.4	12	106	0.5547	0.4571	0.7187	0.3575	0.4565	0.5798
0.5	12	106	0.5351	0.4938	0.7281	0.3484	0.4932	0.6039
0.6	12	105	0.5173	0.4809	0.7063	0.4013	0.4804	0.626
0.7	12	104	0.5006	0.4386	0.6655	0.4549	0.4383	0.6317
0.85	12	103	0.4847	0.4159	0.6387	0.4609	0.4157	0.6206
1.0	12	90	0.4701	0.4331	0.6391	0.4598	0.4325	0.6313
1.5	12	54	0.4145	0.4154	0.5868	0.4259	0.4139	0.5939
2.0	8	19	0.4922	0.2627	0.5579	0.5325	0.2623	0.5937
2.5	4	5	0.4545	0.3946	0.6019	0	0.271	0.271

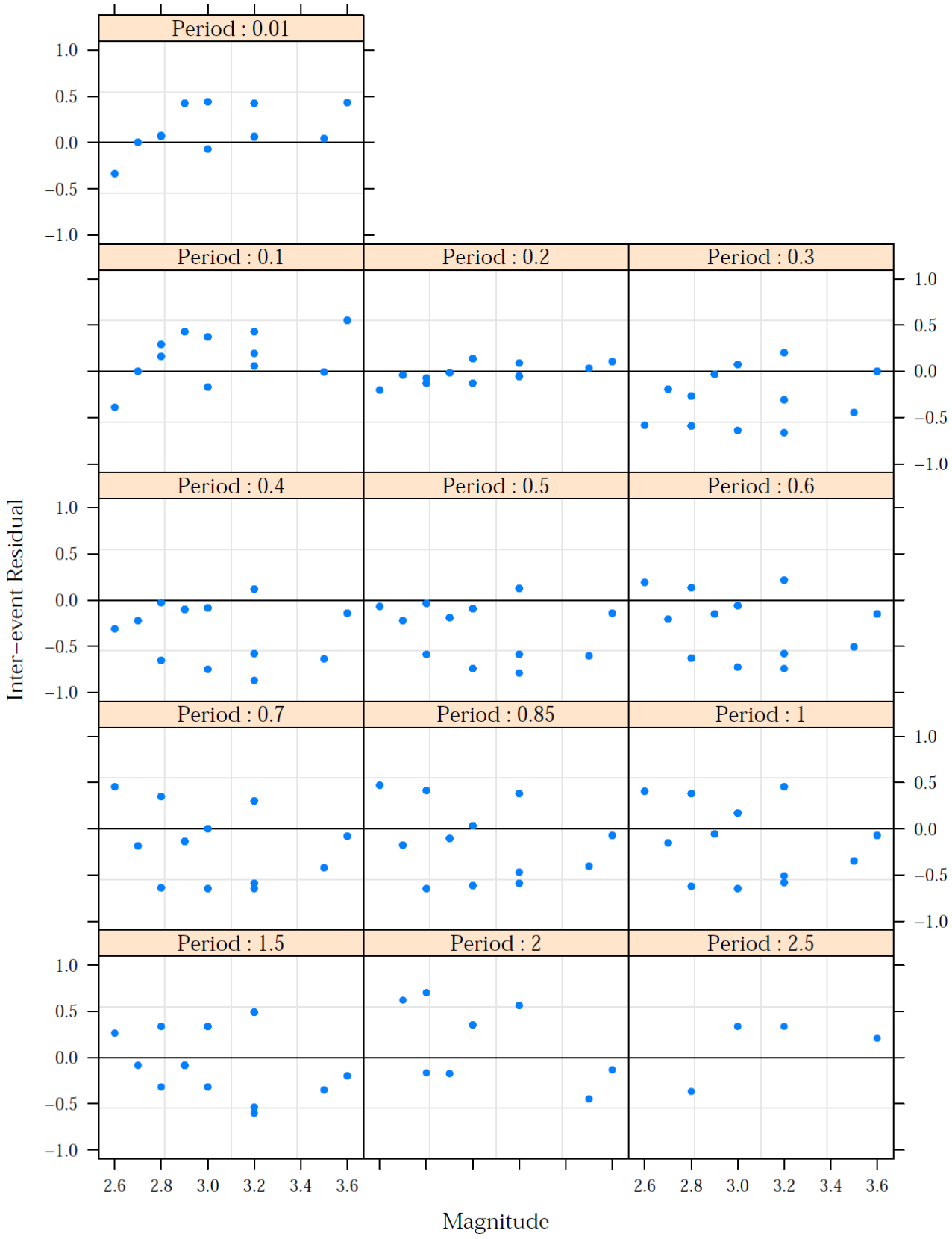

Figure 6.53. Between-event residuals with respect to the central NU_B GMPE

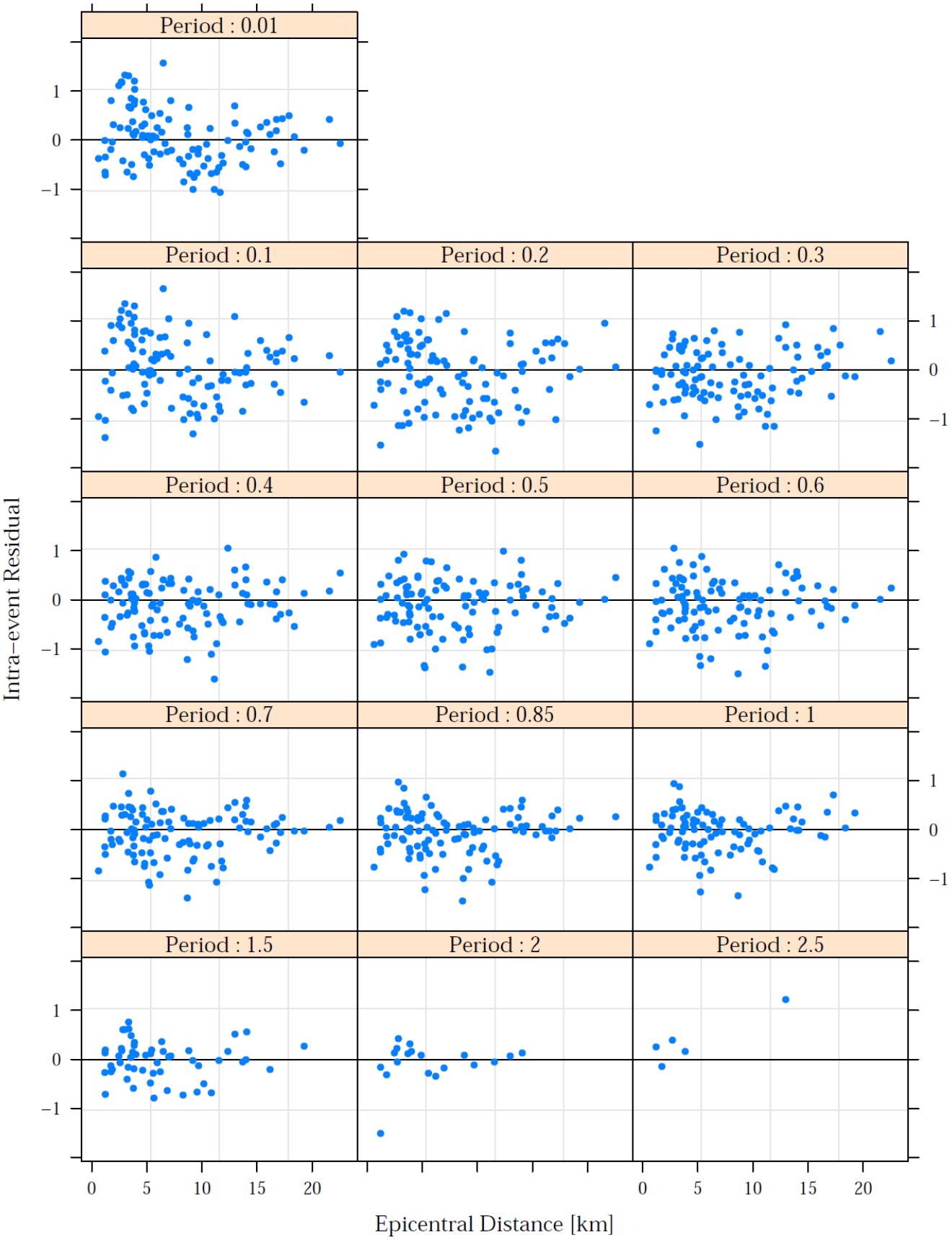

Figure 6.54. Within-event residuals with respect to the central NU_B GMPE

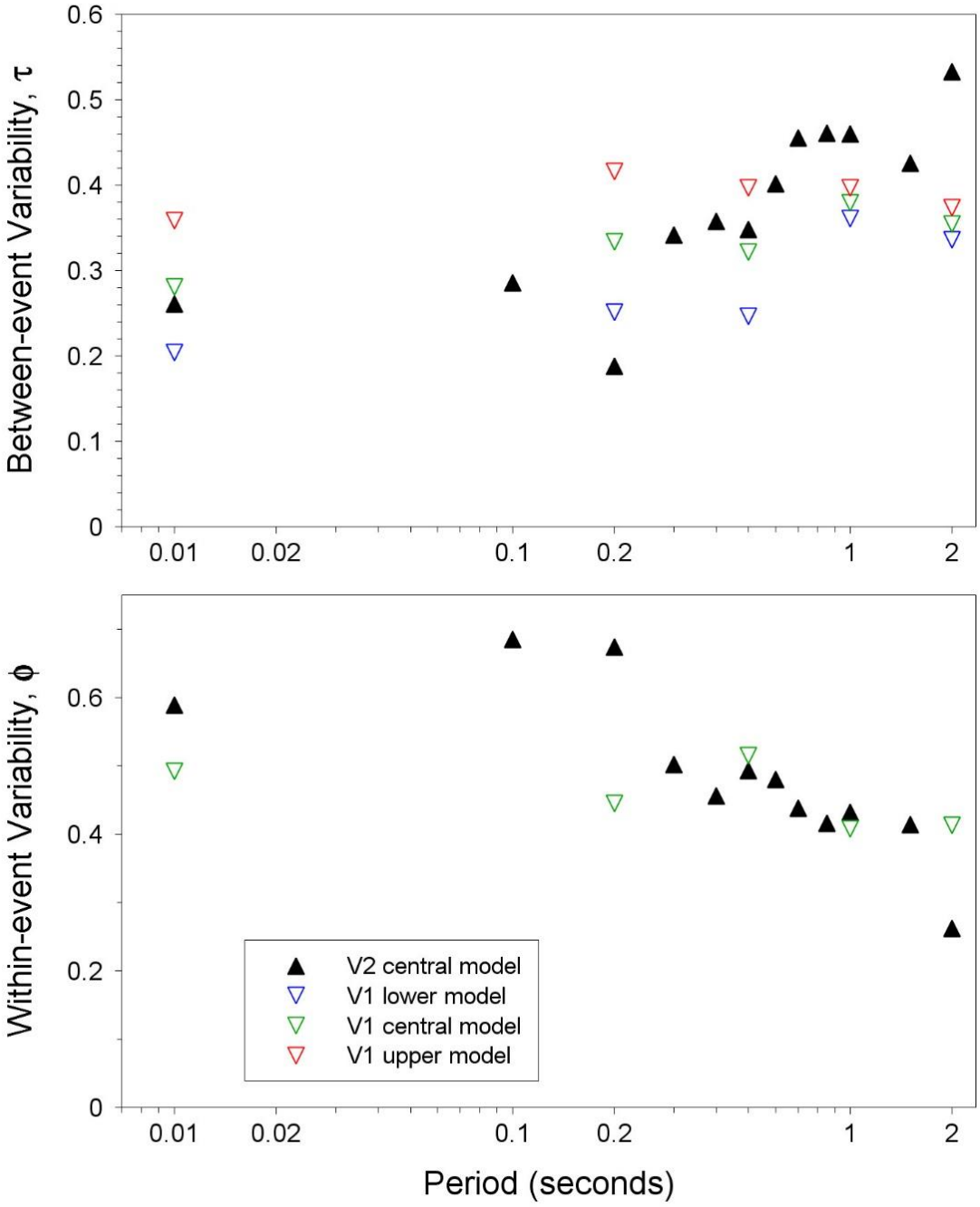

Figure 6.55. Comparison of between-event (*upper*) and within-event (*lower*) variability from the V1 and V2 GMPEs

6.6. Ground-motion model for reference rock horizon

The ground-motion model for predicting median spectral accelerations at the 16 selected target oscillator periods is fully defined by Eqs.(6.4) to (6.8) with the coefficients in Tables 6.2, 6.3 and 6.4 for the lower, central and upper models respectively. Figure 6.56 shows the predicted median values of spectral acceleration at all 16 target periods as a function of epicentral distances for various magnitudes.

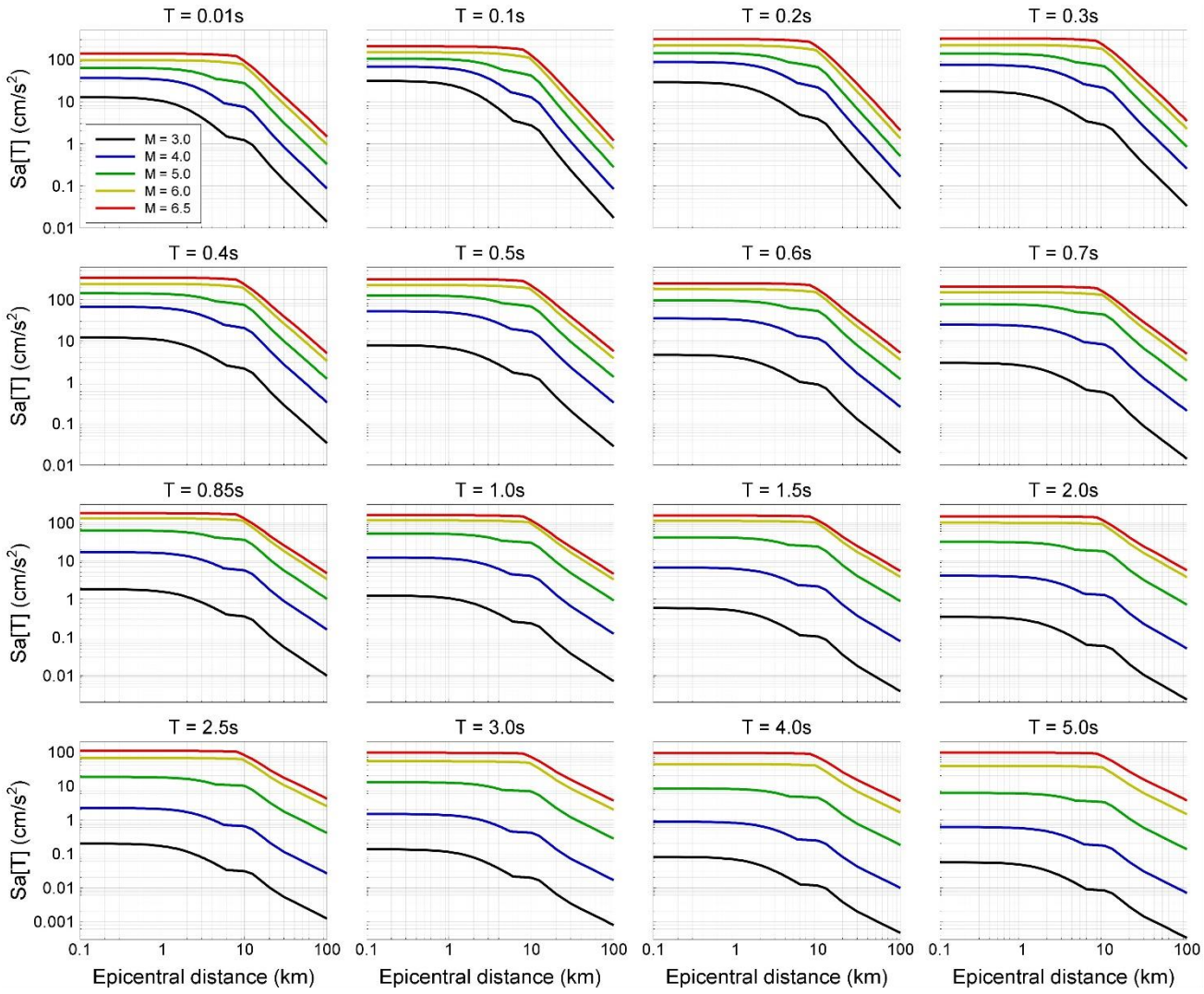

Figure 6.56. Median predictions of spectral accelerations from the central model for the NU_B reference rock horizon as a function of epicentral distance for a range of magnitudes

The complete model requires the terms defining the variability associated with these median predictions, for which the values inferred from the residuals presented in the previous section do not suffice for a number of reasons. Most importantly, as has already been stated, because the site-to-site variability in the site amplification functions is to be fully accounted for in the predictions of the surface motions, this variability must not be included at the rock horizon to avoid double counting. Therefore, the within-event variability at the rock horizon will be selected to represent single-station sigma, whereas the final choice for the between-event component of the variability will be informed by the residual analyses presented in the preceding section. The final selections are discussed in Section 10.4. Additional elements of the variability in the reference rock motion arise because of (1) the need to include the component-to-component variability (Section 10.2) because the risk calculations will be performed used the arbitrary component of motion, as discussed in Section 1.3, and (2) the need to correct for the underestimation of within-event variability as a result of using a distance metric based on a point representation of the earthquake source (Section 10.3).

As in the V1 model, there will inevitably be uncertainty in the sigma model just as there is in the median predictions. Rather than having de-coupled branches for median predictions and for sigma, which would result in at least 9 branches for the reference rock GMPE, the plan is to once again pair median and sigma models to maintain a small number of logic-tree branches, in the interests of computational efficiency. Although conservative, for the preliminary V2 model we follow the practice established in V1 of coupling the highest median model with the largest sigma model and the lowest medians with the smallest sigma.

The final step is then to assign weights to these branches. In the V1 model, we chose branch weights of 0.2 on the lower branch, 0.5 on the central branch, and 0.3 on the upper branch. This could be considered somewhat conservative, especially given the coupling of high medians with large sigmas, for which reason consideration could be given to assigning equal weights (of 0.25) to the upper and lower branches, especially in view of the growing body of evidence to support lower stress drops for shallow earthquakes (Bommer *et al*., 2015a,b). The final logic-tree formulation is discussed in Section 11.1.

7. SITE RESPONSE MODEL

This chapter presents the development of the site response model to be used in site response analyses. The model includes the definition of shear-wave velocity (V_S) and mass density profiles for the Groningen site, and the modulus reduction and damping versus shear strain (MRD) for the soil types found at the Groningen site. The site response analyses are described in Chapter 8.

7.1. Shallow V_S profiles

The shallow V_S profile was built from the GeoTOP model described in Kruiver *et al.* (2015). This model assigns a lithostraphical unit and a lithological class to each voxel in the Groningen area. In general, V_S depends on both lithostratigraphy and lithology. Values of V_S can be assigned to geological formations present in the area of interest from published values of measured V_S in the Netherlands (*e.g.,* Wassing *et al.*, 2003). In some cases, this assignment can be extended to lithological classes. Additionally, there are 60 seismic cone penetration tests (SCPTs) in the Groningen region that allow for determination of representative V_S values that are specific to this region. The SCPTs typically reach to a depth of approximately 30 m below the surface.

In deriving representative values for V_S for combinations of lithostratigraphical units (*e.g.,* "Formation Naaldwijk") and lithoclasses (*e.g.,* "clay"), all SCPTs logs were classified. This means that for each V_S value in the SCPT, the lithostratigraphical unit and lithoclass were determined by a geotechnical engineer. This resulted in distributions of V_S values for each combination of lithostratigraphy and lithoclass represented by the SCPTs. Examples of the distributions are given in Figure 7.1. The distributions are characterized by the average and standard deviation of the natural logarithm of V_S, $\ln V_S$.

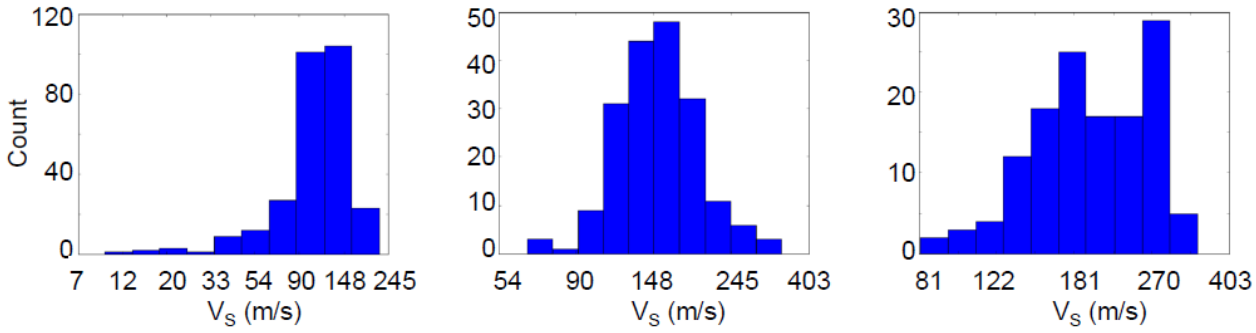

Figure 7.1. Examples of V_S distributions for the combination of lithostratigraphical unit "Naaldwijk Formation" and the lithoclass "Clay" (*left*), "Clayey sand and sandy clay" (centre) and "Fine sand" (*right*). Note that the V_S values are given on a logarithmic scale

Sixteen combinations of lithostratigraphical unit and lithoclass were represented in the current SCPT dataset (Table 7.1). For the combinations that were not represented in the

SCPT data set, either average values for V_S of similar lithostratigraphy and lithoclass or values from Wassing *et al.* (2003) were adopted. In some cases, an estimate based on expert judgement was necessary. When the lithostratigraphy/lithoclass combination was not represented in the SCPTs, the standard deviation was based on the coefficient of variance of 0.037 (on a logarithmic scale), which is the average for the 16 combinations that were represented.

Table 7.1. Values of mean $\ln V_S$ and standard deviation of $\ln V_S$ for the lithostratigraphical units and lithoclasses in the GeoTOP model, as defined by the SCPT dataset for Groningen

Litho-stratigraphical unit	Lithological class	Mean $\ln(V_S)$	Standard deviation $\ln(V_S)$	Number of obs.	Coefficient of variance (lognormal)
Boxtel	Clayey sand and sandy clay	5.40726	0.16770	44	0.03101
Boxtel	Fine sand	5.54527	0.20986	239	0.03784
Boxtel	Medium sand	5.66405	0.10608	43	0.01873
Drenthe	Fine sand	5.65246	0.08843	9	0.01565
Drenthe	Medium sand	5.70146	0.07074	10	0.01241
Drenthe-Gieten	Clayey sand and sandy clay	5.42551	0.22052	20	0.04064
Eem	Clayey sand and sandy clay	5.52305	0.09965	21	0.01804
Eem	Fine sand	5.54544	0.07379	25	0.01331
Naaldwijk	Clay	4.65501	0.44690	283	0.09600
Naaldwijk	Clayey sand and sandy clay	5.02699	0.26078	188	0.05188
Naaldwijk	Fine sand	5.28690	0.29967	132	0.05668
Peelo	Clay	5.39551	0.19933	338	0.03694
Peelo	Clayey sand and sandy clay	5.43863	0.18006	23	0.03311
Peelo	Fine sand	5.64246	0.15808	231	0.02802
Peelo	Medium sand	5.79386	0.11375	41	0.01963

A log-normal distribution was assumed for V_S. The parameters in Table 7.1 were used to assign randomly selected V_S values to the voxel stacks from GeoTOP. For a voxel containing, for example, “Naaldwijk Formation” and lithoclass “clay”, a V_S value was randomly selected from the V_S distribution belonging to Naaldwijk clay (average $\ln V_S$ is 4.65501, and the standard deviation is 0.44690). Although the V_S distributions are derived from SCPTs reaching to a depth of 30 m below the surface, the relations have been used to assign V_S values for the entire GeoTOP depth range (down to NAP-50 m). The correlations between V_S values in two consecutive layers were also taken into account in assigning V_S values to the voxel stack. These correlations are described in section 7.3.

An alternative to using the measured SCPTs to obtain the distribution parameters for Groningen soil types would be to use generic relations between cone resistance q_c from CPT and V_S (*e.g.,* Andrus *et al.*, 2007 and references therein). The large database of SCPTs and CPTs for Groningen also offers the opportunity to derive Groningen-specific relations between q_c, V_S and lithology. This alternative would allow for the inclusion of depth dependency of V_S, which has not been taken into account in the current V_S relations for Groningen. Derivation of V_S relations based on both SCPTs and CPTs will be undertaken in

future updates of the model, benefiting also from the recently measured SCPTs at the recording stations.

7.2. Extension of V_S profiles to reference rock horizon

Information on the V_S distribution at depths larger than the range of direct measurements using SCPT comes from indirect measurements. Large seismic survey campaigns were conducted by NAM/Shell around 1988 for imaging purposes. Two legacy datasets were reinterpreted to extend the V_S distributions to depths beyond those measured by the SCPT: ground roll data (MEIDAS) and the Time-to-Depth model (T2D).

MEIDAS near surface V_S model

Ground roll refers to surface waves present in seismic records. For the imaging of deep reflectors associated with the reservoir, the ground roll is normally regarded as noise and removed from the data. For other purposes, this ground roll can be useful data. For the Groningen project, Ewoud van Dedem from Shell has reprocessed the ground roll and guided waves in the data to derive V_S and V_P values using the Modal Elastic Inversion method (MEIDAS). MEIDAS is an approximate elastic full waveform inversion method in which the elastic wavefield is approximated by focusing on waves that propagate laterally through the shallow surface (*i.e.*, the ground roll), its higher modes, and guided waves. A limited number of horizontally propagating modes, characterized by lateral propagation properties and depth dependent amplitude properties, are taken into account to represent the near-surface elastic wavefield (see also Ernst, 2013).

The seismic data acquisition was designed for deep imaging of the Groningen reservoir and therefore receiver arrays were used to attenuate undesired noise, such as the ground roll. The receiver arrays were designed to distort and attenuate ground roll with wavelengths smaller than 80 m, effectively restricting the temporal frequency bandwidth that can be used for the inversion. Because of the acquisition setup and the frequencies present in the data, the depth range for which the near surface model obtained from the MEIDAS inversions is considered to be reliable is from approximately 30 to 120 m below the surface. Additionally, there are several areas of limited size with large misfits between the ground roll data and the final V_S model. These misfits are due to different seismic sources being used in cities (vibroseis) and lakes (air guns) from the other regions (mostly buried dynamite sources).

The V_S model from the inversion of the ground roll yielded depth slices of V_S at 10 m depth intervals. An example of a depth slice is shown in Figure 7.2, in this case for NAP-65 m. It shows distinct zones of relatively high and relatively low V_S values in patterns that resemble geological features, such as buried channels. Generally, the uncertainty in V_S values in the resulting V_S model is estimated to be 5 to 10%.

The MEIDAS V_S model has a slightly smaller geographical extent than the entire area of interest (Figure 7.2). Outside of the extent of the MEIDAS model, the average V_S value is used for each depth interval.

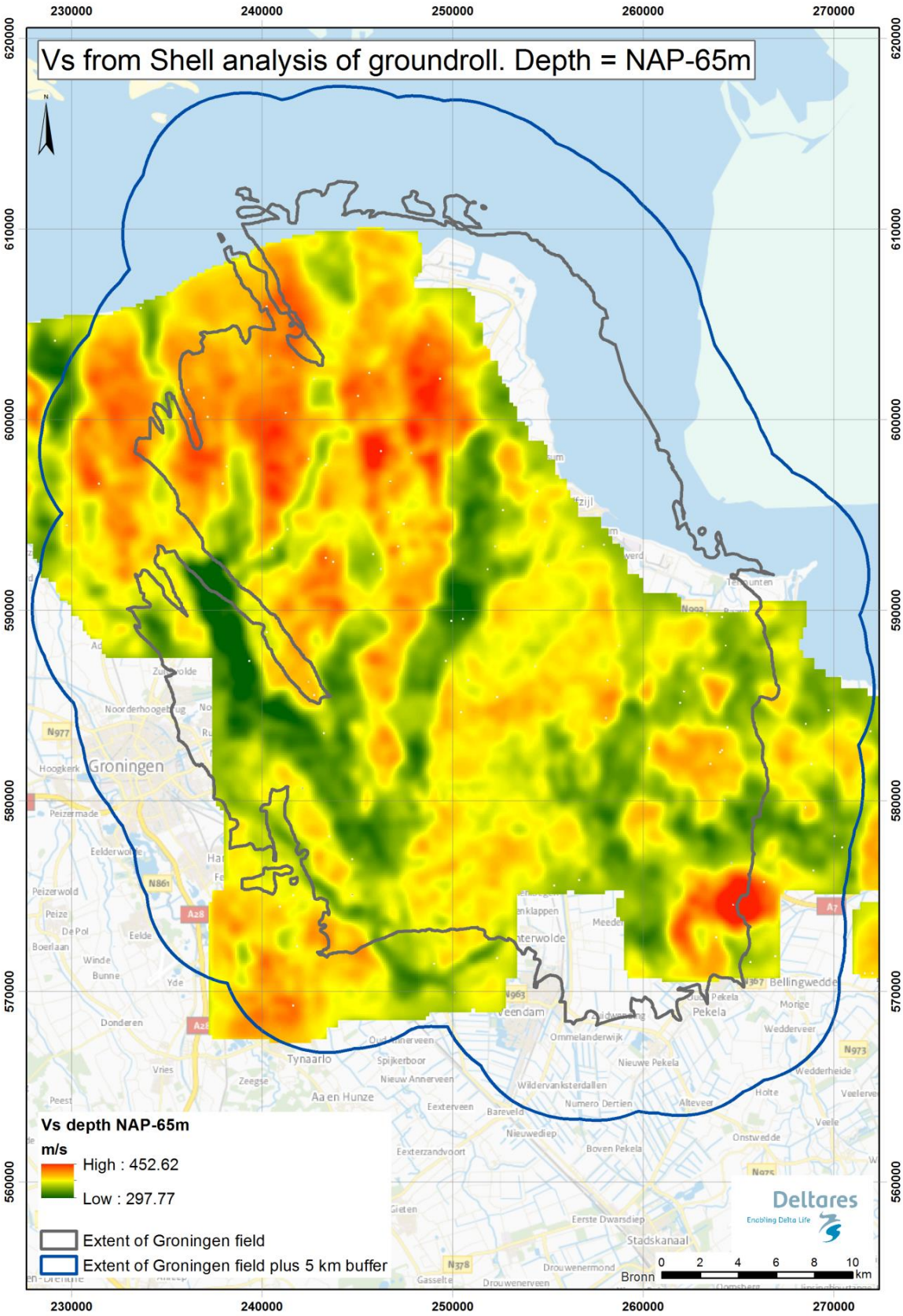

Figure 7.2. Depth slice at NAP-65 m through the MEIDAS V_S model (*data from Shell, courtesy Ewoud van Dedem*)

Improved T2D model of reflection seismicity

Shell has a seismic model developed to image the Groningen reservoir, updated in the 2012 Groningen Field Review (GFR). The model to convert travel times of seismic waves (measured) to depth (important for reservoir imaging) is the T2D model (Figure 7.3). In the T2D model, the entire North Sea Group has one interval velocity for V_P (homogeneous red colour in Figure 7.3). Remco Romjin from NAM recently reinterpreted the data to improve this model and to derive depth and location dependent V_P and V_S relations for the Upper and for the Lower North Sea Group separately.

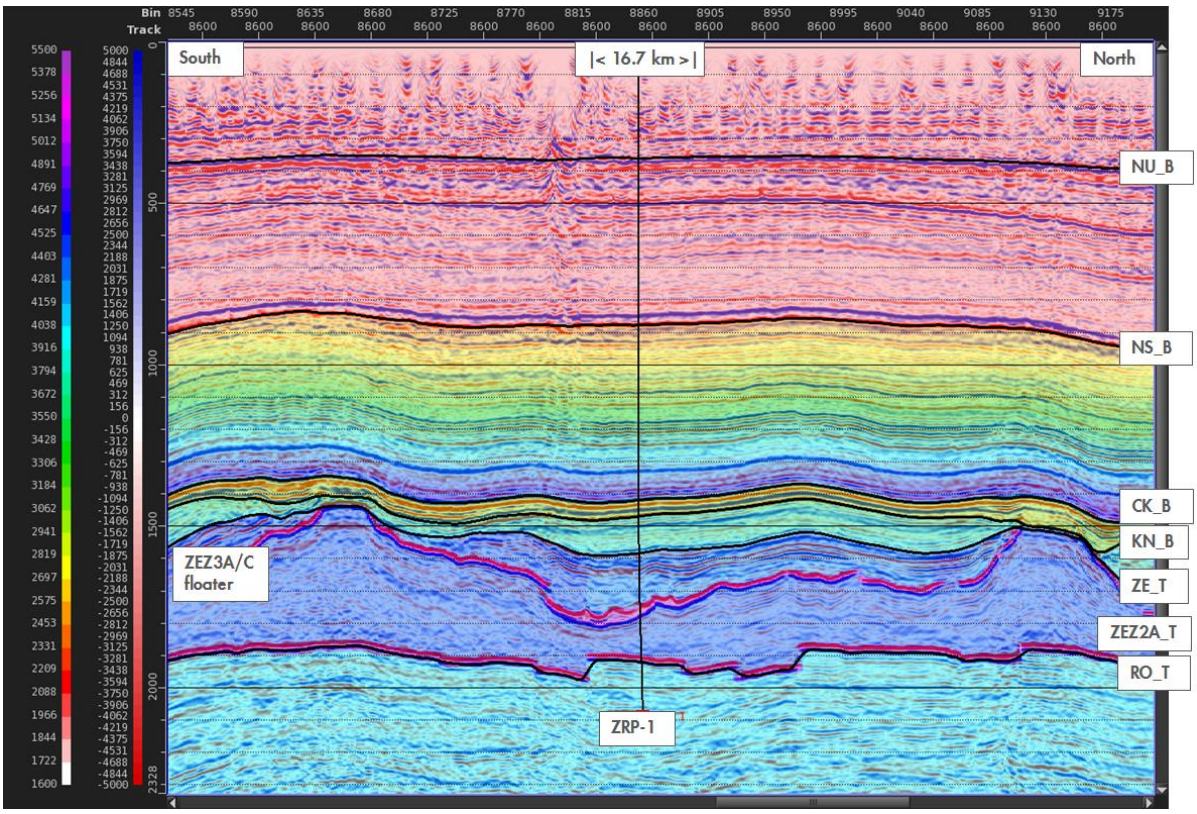

Figure 7.3. T2D model from Shell's 2012 GFR. This snapshot shows the V_P distribution near the well ZRP-1. The base of the Upper North Sea is indicated by NU_B; the base of the Lower North Sea is indicated by NS_B

In the original T2D model, for each location a constant interval velocity from the surface to the base of the Lower North Sea Group (NS_B) was defined. However, two wells with both V_P and V_S measurements, Zeerijp 2 (ZRP2) and Borgsweer-5 (BRW5) show that the velocity profiles from surface to NS_B are not constant but vary with depth and, in particular for the Upper North Sea, the velocities increase with depth (Figure 2.5).

For the derivation of the improved velocity relation for V_S for the North Sea Group we split the group in two depth ranges (Figure 7.4):

- An Upper part, from the surface to the base of the Upper North Sea (NU_B). In this depth range, V_P is assumed to vary linearly with depth V_S varies with depth according to:

$$V_p(z) = V_{0,P} + kz \qquad (7.1)$$

where $V_{0,P}$ is the intersect at the surface and z is the depth. A value of k=0.5 was selected because it fits well the data while preventing a velocity reversal at the intersection with NU_B. The well log data was also used to fit a linear relationship to the V_P/V_S data (Figure 7.5). This relationship, coupled with Eq.(7.1), give the following relationship:

$$V_S(z) = \frac{V_{0,P} + 0.5z}{-0.0047z + 4.7819} \qquad (7.2)$$

This relationship proposes a nearly linear change of V_S with depth.

- A lower part, from the base of the Upper North Sea (NU_B) to the base of the Lower North Sea (NS_B). In this depth range, the constant interval velocity V_{int} is laterally varying. For the purpose of assigning a constant V_S to the bedrock in the site response calculations, we adopt the median V_{int} of the improved model (V_S value of 639 m/s).

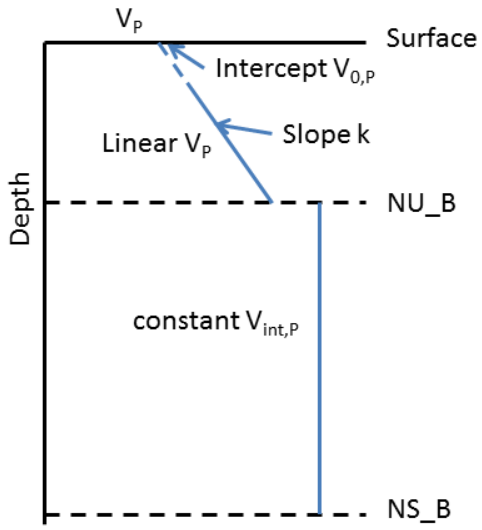

Figure 7.4. Schematic representation of the improved seismic velocity model for the North Sea Group. Note that the value of the intercept V_0 and the constant V_{int} vary with location

The V_S and V_P measurements at the two wells (ZRP2 and BRW5) are made only below the depth of the conductor at the well (approx. 70 m depth). Hence, the range over which V_P, V_S and the V_P/V_S ratio relation is valid, is roughly from 70 m depth down to the NU_B horizon. Figure 7.5 shows a comparison of the measured V_S values at the BRW5 well with the proposed model.

The uncertainty in V_S values is estimated from the difference in measured V_S at the two wells and the V_S calculated from Equation 7.1. Overall, the uncertainty in the V_S values for the extended depth range from MEIDAS depths to NU_B is considered to be approximately 10%.

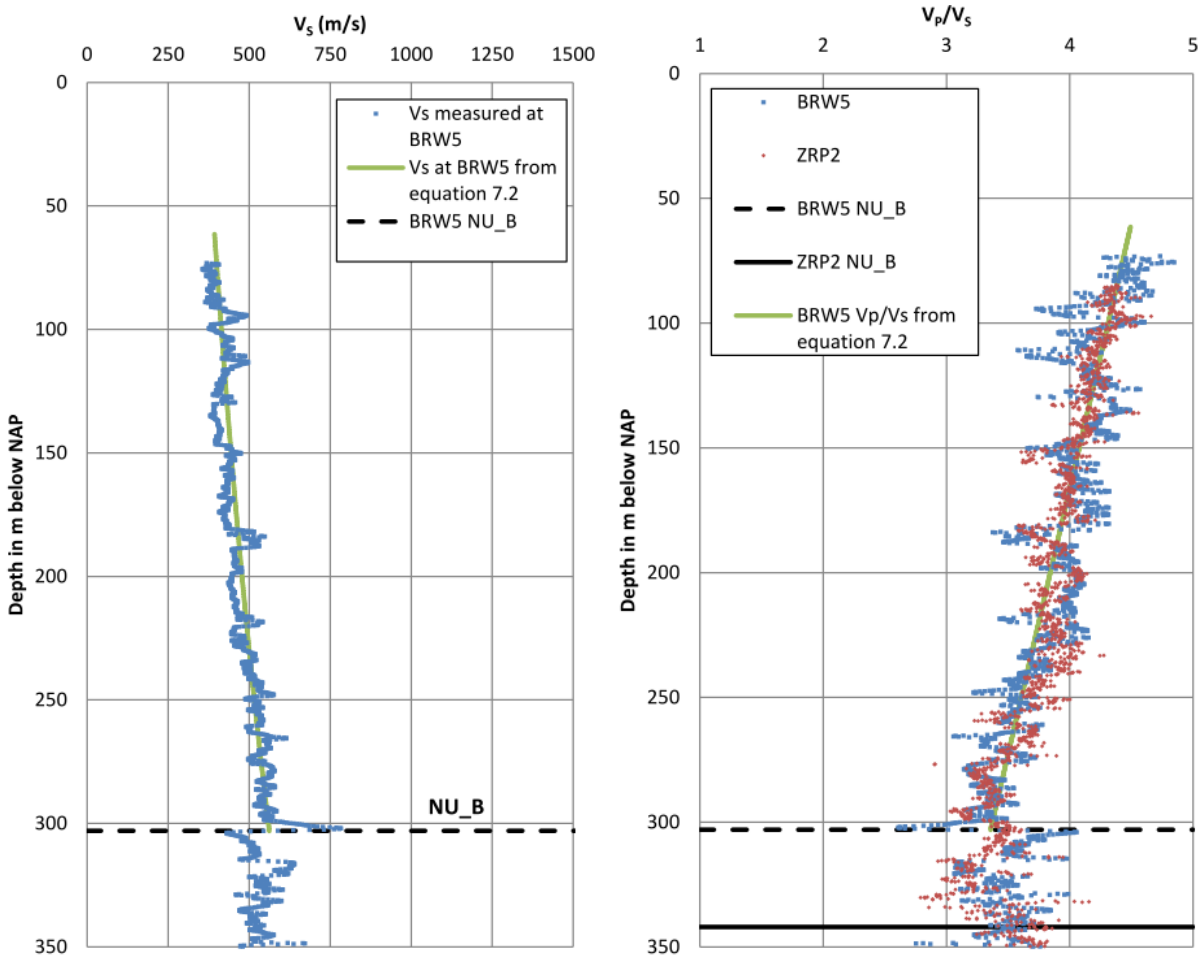

Figure 7.5. *Left*: V_S measured at well BRW5 (*blue dots*) compared to the linear relation for V_S according to Equation 7.2 at the location of the well. *Right*: Ratio of measured V_P over V_S values

7.3. Layering model and layer-to-layer correlations

The main input data for the STRATA calculations are the thickness, mass density, and V_S of each layer. The V_S and density values are assumed to be constant for each layer. In addition, for each soil type modulus reduction and damping versus strain curves must be defined (section 7.4 and 7.5).

The thickness and the depth of the layers are based on the geological model (Kruiver *et al.*, 2015). The voxel stacks of the GeoTOP model define the vertical succession in terms of lithostratigraphy and lithoclass for each x-y coordinate to a depth of NAP-50 m. The layering in terms of lithostratigraphy and lithoclass for each x-y coordinate for the depth range below NAP-50 m is defined by the simulations for the subsurface geological areas. (Figure 6.8 of Kruiver *et al.*, 2015). For each subsurface geological area, the simulations are randomly distributed over the coordinates in that area such that they are in agreement with the

probabilities of encountering the scenarios. For example, for one subsurface geological zone with two scenarios with probabilities 0.6 and 0.4, 60% of the voxel stacks receive the layering from the first simulation and 40% of the voxel stacks receive the layering of the second simulation. The maximum thickness for each layer is 10 m for the depth range of the MEIDAS model and 25 m for the T2D model. For example, a layer between 65 and 100 m of the Urk Formation in the MEIDAS depth range will be split into 4 layers: three layers of 10 m and one layer of 5 m. A layer between 200 and 244 m of the Oosterhout Formation in the T2D depth range will be split into two layers: one of 25 m and one of 19 m.

To obtain the full stack at one x-y coordinate, the GeoTOP voxel stack layers are combined with the scenario-based layers based on that coordinate. For the GeoTOP depth range, each layer is assigned a random value from the V_S distribution based on the lithostratigraphical unit and lithoclass of the voxel. However, layers with the same combination of lithostratigraphy and lithoclass (unit) all get the same V_S value within one voxel stack. This means that there is full vertical correlation between units. For a different combination of lithostratigraphy and lithoclass within the same voxel stack, a new random value is drawn from the V_S distribution. This means that there is no vertical correlation between units. This is illustrated in Figure 7.6.

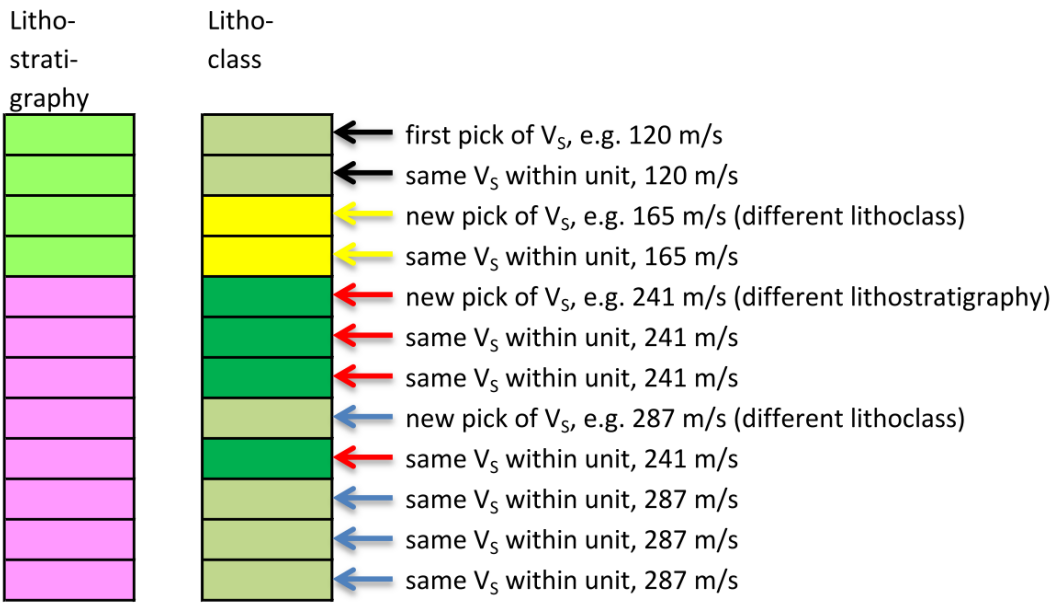

Figure 7.6. Example of correlation of V_S within and between units in a GeoTOP voxel stack. Each box represents a GeoTOP voxel of 0.5 m thickness

Alternatively, the Toro (1995) model can be used to compute the vertical correlation between layers. This model postulates a correlation between two layers that is a function of the separation between layers and the depth of the layer. In the application to the Groningen field the simpler model was selected because of insufficient data to fully determine the site-specific parameters of the correlation model. Moreover, this simpler model respects the geo-statistical model already build into the GeoTOP database.

For the depth range below NAP-50 m, V_S profiles are defined by the MEIDAS and the T2D models. The transition between the MEIDAS and the T2D model is taken at a depth such that no velocity reversal occurs (*i.e.*, no decrease of V_S as depth increases). In some cases, the T2D model is extrapolated to depths shallower than NAP-70 m, although the T2D model is not necessarily valid at these depths. The transition between the two models is illustrated in Figure 7.7.

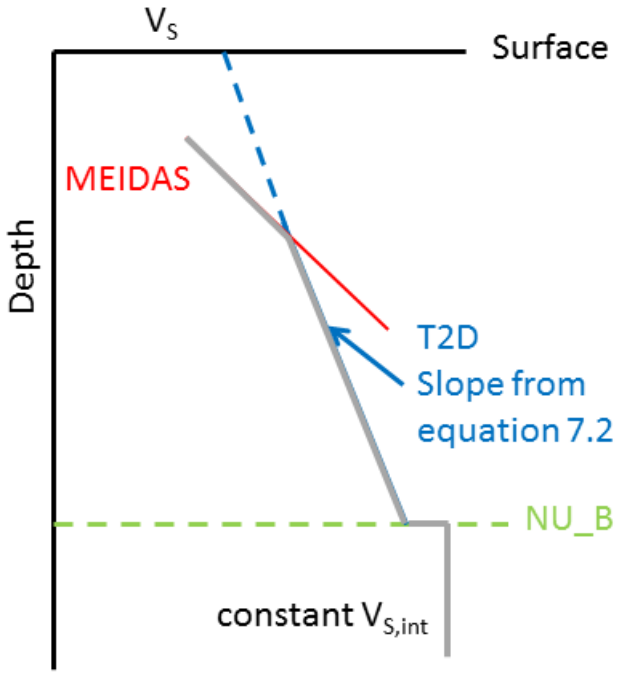

Figure 7.7. Transition of V_S between the MEIDAS and T2D depth range.

7.4. Mass densities

One of the parameters in STRATA is unit weight. For the shallow depth range down to approximately 30 m below the surface, the unit weights were estimated from a subset of 31 CPTs that were classified in terms of lithostratigraphical unit and lithological class. All cone tip resistance values from the CPTs from one combination of lithostratigraphical unit and lithoclass were assembled and converted to unit weight using Lunne *et al.*, (1997). The average unit weight was calculated. For units that were not represented in the CPTs, a value for unit weight from a comparable geological unit was taken. Depth dependency of unit weight has been investigated for the shallow depth range. The data were inconclusive to derive a depth relation. Therefore, no depth dependency was implemented for unit weight. For the deeper geological units, a constant value of 21 kN/m^3 was determined for unit weight. This is slightly higher than the average density measured in the well logs ZRP2 and BRW5 (Figure 7.8).

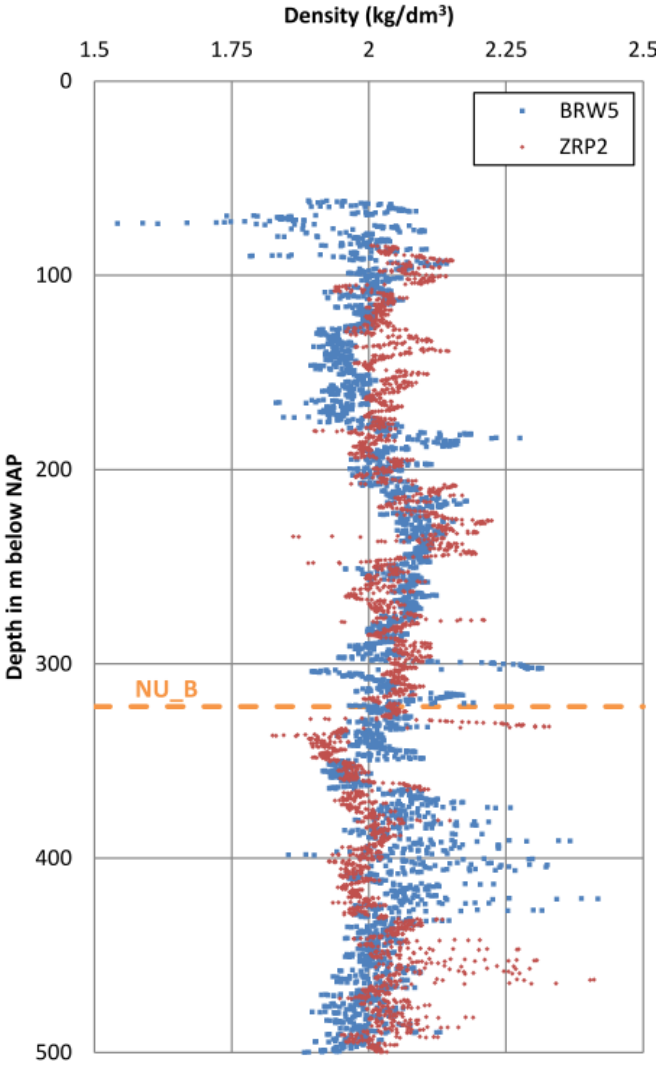

Figure 7.8. Density profiles from two deep borehole logs (*Source: NAM database*)

7.5. Modulus reduction and damping curves

The shear modulus reduction and damping (MRD) versus strain curves of Darendeli (2001) were used to model the nonlinear behaviour of Groningen soils. These curves are based on large numbers of measurements for both sands and clays of varying plasticity and over-consolidation ratios. These curves are widely used in equivalent site response analyses.

The general form of the Darendeli (2001) curves is described below. The shear modulus reduction curve is a hyperbolic model given by:

$$\frac{G}{G_{\max}} = \frac{1}{1+(\gamma/\gamma_r)^a} \qquad (7.3)$$

where γ is the shear strain amplitude, γ_r is the reference shear strain amplitude (shear strain amplitude at which the value of $G/G_{max} = 0.5$) and *a* is a parameter describing the curvature of the shear modulus reduction curve. The damping values, D, are given by:

$$D = F \times D_{Masing} + D_{\min} \tag{7.4}$$

where F is a multiplication factor (defined below) that is used to modulate the Masing damping at large strains to prevent overdamping, D_{Masing} is the damping that results from applying the Masing rule, and D_{min} is the damping at small shear strain amplitudes. D_{Masing} is given by:

$$D_{Masing} = c_1 D_{Masing,a=1} + c_2 D^2_{Masing,a=1} + c_3 D^3_{Masing,a=1} \tag{7.5}$$

where the parameters c_1, c_2 and c_3 are fit parameters and $D_{Masing,a=1}$ is the value of D_{Masing} when the parameter a is equal to 1. Darendeli (2001) derives equations for the coefficients c_1, c_2 and c_3 a function of the parameter a:

$$\begin{aligned} c_1 &= -1.1143a^2 + 1.8618a + 0.2523 \\ c_2 &= 0.0805a^2 - 0.071a - 0.0095 \\ c_3 &= -0.0005a^2 + 0.0002a + 0.0003 \end{aligned} \tag{7.6}$$

The parameter $D_{Masing,a=1}$ has a closed form solution that is given by:

$$D_{Masing,a=1} = \frac{100}{\pi}\left[4\frac{\gamma - \gamma_r \ln\left(\frac{\gamma+\gamma_r}{\gamma_r}\right)}{\frac{\gamma^2}{\gamma+\gamma_r}} - 2\right] \tag{7.7}$$

The multiplication factor F in the Darendeli (2001) model is given by:

$$F = b\left(\frac{G}{G_{\max}}\right)^p \tag{7.8}$$

where b and p are parameters that control the shape of the function. To simplify the model a fixed value of p=0.1 is used by Darendeli (2001).

Equations 7.3 through 7.8 result in a 4-parameter model (G_{max}, γ_r, a and b). Darendeli (2001) fits the model parameters to various soils and obtains correlations for these parameters as a function of the mean effective stress (σ') normalized by the atmospheric pressure (p_a = 100 kPa), plasticity index (I_p), over-consolidation ratio (OCR), number of cycles of loading (N) and loading frequency f. The resulting expressions are given by:

$$\gamma_r = (0.0352 + 0.001 I_p OCR^{0.32463})(\sigma' / p_a)^{0.34834} \tag{7.9}$$

$$a = 0.919 \tag{7.10}$$

$$D_{\min} = (0.8005 + 0.0129 I_p OCR^{-0.1069})(\sigma' / p_a)^{-0.2889}(1 + 0.2919 \ln(f)) \quad (7.11)$$

$$b = 0.6329 - 0.0057 \ln(N) \quad (7.12)$$

Default values recommended by Darendeli (2001) for N (N=10) and f (f=1 Hz) were used. No laboratory tests for OCR and I_p were available at the time of starting the site response calculations. Therefore, representative values for geological units were derived in a manner similar to the derivation of unit weights (*i.e.*, based on a subset of geologically classified CPTs). The overconsolidation ratio OCR was estimated for clay from the normalized total cone resistance following Lunne *et al.*, (1997):

$$OCR = k\left(\frac{q_t - \sigma_{v0}}{\sigma'_{v0}}\right) \quad (7.13)$$

where σ_{vo} and σ'_{vo} are the total and the mean vertical effective stresses, respectively, and k is a parameter that is set to 0.3. Note that since I_p=0 for sands, the OCR is not needed in Equations 7.9 and 7.11. If a sufficiently large number of OCR values was available for a combination of lithostratigraphical unit and lithoclass, then the depth-dependency of OCR was computed; otherwise, a constant OCR value was used.

The plasticity index I_p was estimated using Skempton & Henkel (1953):

$$\frac{s_u}{\sigma'_{v0}} = 0.11 + 0.37\left(\frac{I_p}{100}\right) \quad (7.14)$$

in which the undrained shear strength s_u was derived from the normalized cone resistance, according to:

$$s_u = \frac{q_c - \sigma_{v0}}{N_k} \quad (7.15)$$

using N_k = 15 as recommended by Robertson (1990). For geological units not represented by the CPTs, such as Pleistocene, glacial and Tertiary clays, the I_p values were estimated from Sorensen & Okkels (2013).

The Darendeli (2001) model implies a large stress-strain behaviour that is not necessarily compatible with the shear strength of the soil. For this reason, a model to impose a limiting shear strength at large strains was implemented. We used the Yee *et al.* (2013) model with a parameter γ_l equal to 0.3%. Additionally, the undrained shear strength s_u estimated from Equation 7.15 was increased by 30% to account for rate effects (Lefebvre & LeBoeuf, 1987; Stewart *et al.* 2014). Limiting shear strengths were implemented for clay, clayey sand and sandy clay and for peat. No limiting strength was used for sand layers because of the higher strengths for sand and the lower strains typically observed in the analyses.

7.6. Modulus reduction and damping curves for peats

Empirical modulus reduction and damping curves specifically derived for peat are rather limited in literature. However, preliminary studies indicated that peats have a strong influence on site response, as expected due to their low stiffness. For this reason, a particular effort was directed at obtaining representative MRD curves for peat. In the absence of curves derived from tests on Groningen peats, which are planned for the near future, we developed a model based on published worldwide data. In order to be consistent with the sand and clay curves, we adopt a formulation similar to the Darendeli (2001) model.

The available test data on peat in the literature are summarised in Table 7.2. Because of the lack of data, only confining stress dependency was modelled. The influence of overconsolidation ratio (OCR), number of cycle (N), frequency of loading (*f*) and organic content (OC) was ignored.

Table 7.2. Summary of available data for constraining the peat MRD model

Reference	Location	Consolidation stress [kPa]	Organic content [%] (a)	Ash content [%] (a)	Density [ton/m^3](b)	Remarks
Seed & Iddriss (1970)	Union Bay [USA]	Unknown	Unknown	Unknown	1.003 – 1.058	Damping curve not measured. Index properties from Kramer (1996)
Kramer (1996, 2000)	Mercer Slough [USA]	1,5		19.7 – 27.4	1.0 – 1.04	
		12,5		19.7 – 27.4		
		19		19.7 – 27.4		
Stokoe *et al.* (1994)	Queensboro bridge [USA]	114		37-65		Data from Kramer (2000) and Boulanger *et al.,* 1997)
Boulanger *et al.* (1997)	Sherman Island [USA]	132/200		36-65	11.1 – 11.8	
Wehling *et al.* (2001)	Sherman Island [USA]	78		48-68	1.06 – 1.23	
		45				
		12				
Kishida *et al.* (2009a)	Montezuma Slough [USA]	17	42		1.06 – 1.33	
		35	44			
		51	23			
		67	15			
Kishida *et al.* (2009a)	Clifton Court [USA]	55 - 69	14-35		1.19-1.46	
Zwanenburg (2005)	Breukelen [Netherlands]	10 30/55		44.7	1.04	damping curve not measured
Tokimatsu & Sekiguchi (2006a,b and 2007)	Ojiya P-1 [Japan], Ojiya P-2	Not reported	Not reported	Not reported	Not reported	
Kallioglou *et al.* (2009)	Greece	370/400		38 / 52	1.33/1.43	Peat from two locations in Greece, sampling depth 35 m 85 m

Notes: (a) Either the organic content or the ash content is reported in this table, depending on the parameter used in the original publication; (b) Either the mass or the density is reported in this table, depending on the parameter used in the original publication

In the Darendeli (2001) formulation, the parameter *a* determines the curvature of the shear modulus reduction curve. For sands and clays, Darendeli (2001) used a constant value of 0.919. For peats, the parameter *a* is estimated from reported modulus reduction curves in the references listed in Table 7.2. The resulting values for *a* are shown in Figure 7.9. The data point from the Queensboro bridge peat is outside the range of the other soils and it is considered to be an outlier. For the other data points, the correlation between *a* and consolidation stress is weak, hence we conclude that the stress dependency of the parameter *a* is negligible. The average value of *a* for the peats that were studied is 0.776. This value is adopted for our model.

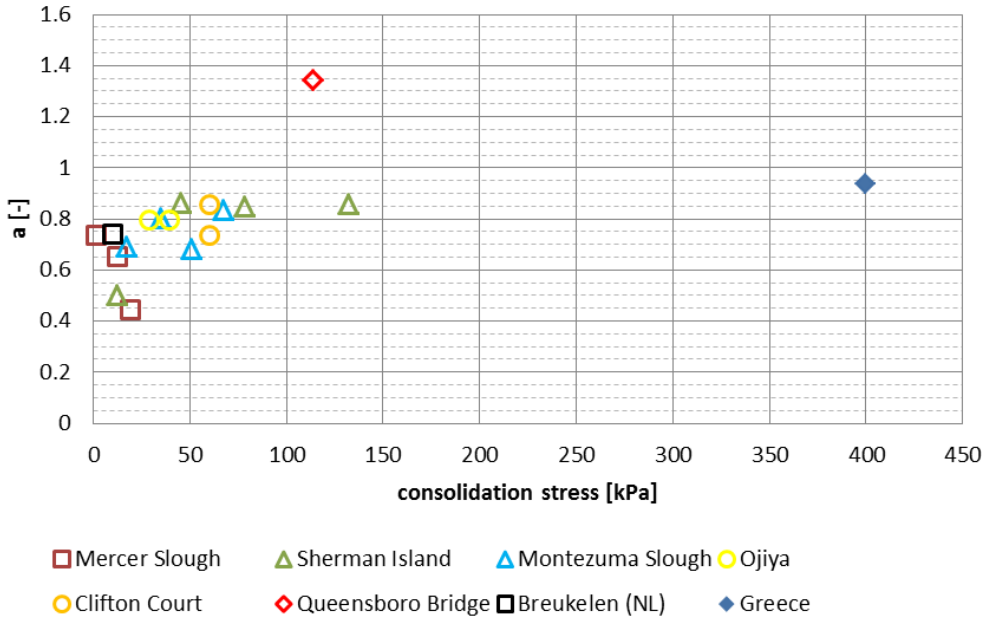

Figure 7.9. Value of *a* as function of the consolidation stress for soils in Table 7.2

For the reference shear strain amplitude γ_r, we use the power function proposed by Darendeli (2001):

$$\gamma_r = a'(\sigma' / p_a)^{b'} \qquad (7.16)$$

where *a'* and *b'* are model parameters. Figure 7.10 shows the relation between γ_r and consolidation stress for all data points. Again, the data from the Queensboro Bridge soils seems to be an outlier. Moreover, one data point from Ojiya and two from Montezuma Slough seem to be outside the general trend. The data were fitted for *a'* and *b* using a non-linear least square method for two options. The resulting values are:

- Considering all data points, except Queensboro Bridge: a' = 1.175 % and b' = 0.319.
- Ignoring all points with γ_r > 1.5 (excluding 4 data points): a' = 0.995 % and b' = 0.674

The Darendeli (2001) curve with PI = 100 and OCR = 1 is often selected as an alternative curve for peats. For comparison, this curve is shown in Figure 7.10 as well. It is clear that the

Darendeli (2001) curve is not suitable to describe the behaviour of peat. Ignoring the four possible outliers gives a better overall fit of the data points, especially at lower consolidation stresses. Therefore, the expression for the reference strain γ_r and the consolidation stress results in:

$$\gamma_r = 0.995(\sigma' / p_a)^{0.694} \qquad (7.17)$$

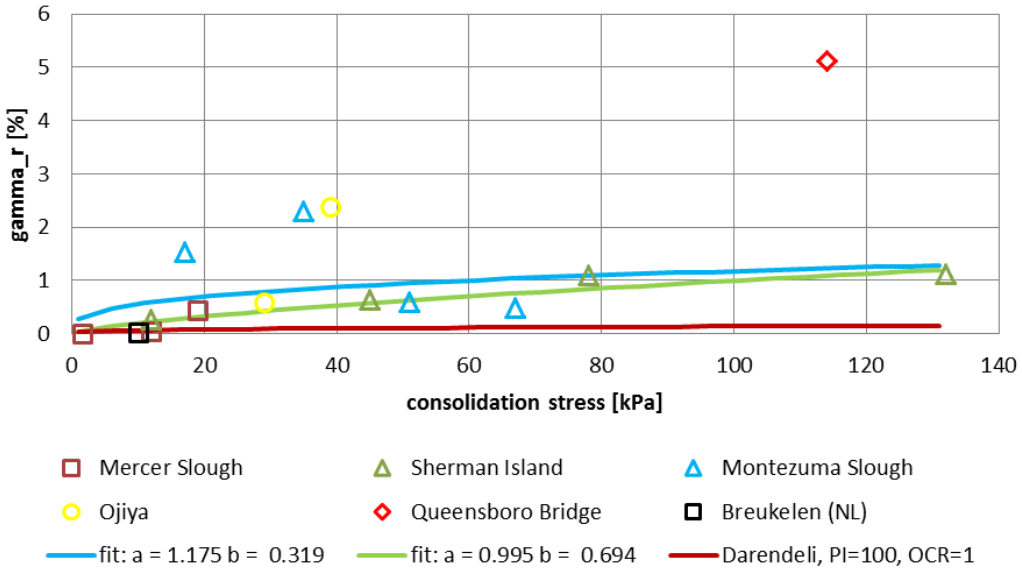

Figure 7.10. Results for curve fitting for γ_r. *Blue curve*: all data points except Queensboro Bridge; *green curve*: all data points, except the four outliers; *red curve*: Darendeli (2001) with PI=100 and OCR =1 (shown for comparison)

The damping at small shear strains, D_{min}, for the soils in Table 7.2 varies with the consolidation stress (Figure 7.11). Since the Darendeli (2001) curve for D_{min} for I_p = 100 and an OCR of 1 fits the data points well, we adopt for D_{min} the Darendeli (2001) formulation:

$$D_{min} = 2.512(\sigma' / p_a)^{-0.2889} \qquad (7.18)$$

Two other parameters that describe the damping curves according to Darendeli (2001) are the multiplication factor F, which is a function of parameters *b* and *p* (Equation 7.8). Darendeli (2001) used a value of *p*=1, which is also adopted for the peat model. Figure 7.12 shows the values of b as a function of consolidation stress. The Queensboro Bridge data point is again considered to be an outlier. In the Darendeli formulation, parameter b is a constant, which is independent of consolidation stress. The average value for b for the literature data set, excluding the Queensboro Bridge data point, is 0.712 with a standard deviation of 0.216.

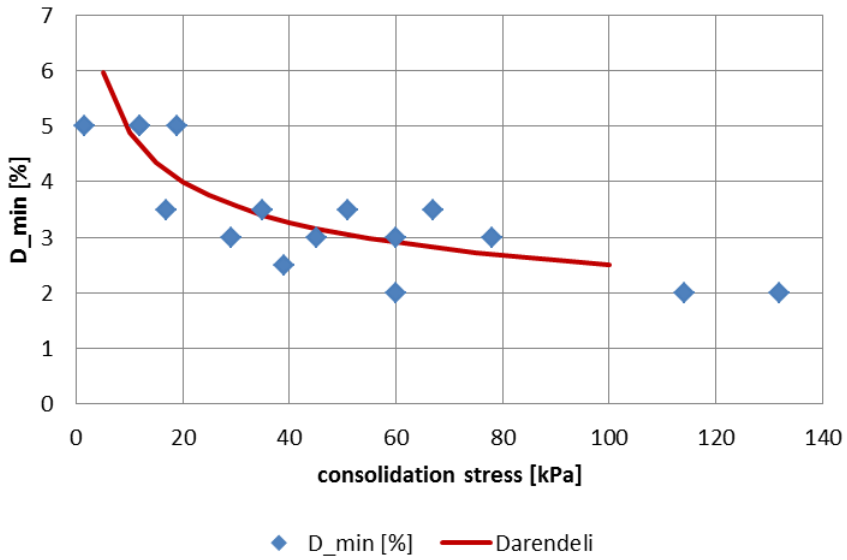

Figure 7.11. Minimum damping D_{min} as function of the consolidation stress for the soils in Table 7.2 (blue symbols). The Darendeli curve for Ip = 100 and OCR =1 is shown in red

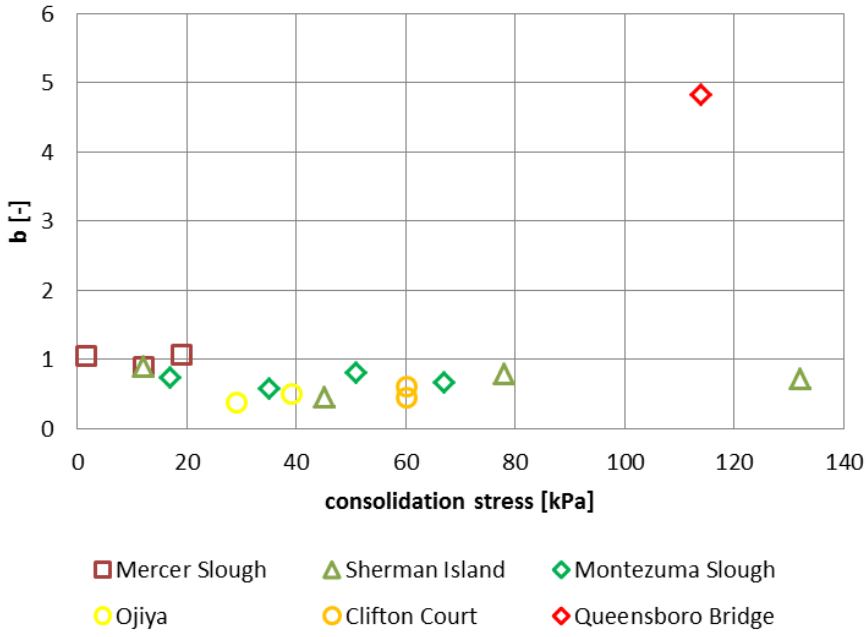

Figure 7.12. Value of *b* as function of the consolidation stress for the literature data set

In summary, the following peat-specific parameters are defined for peats as input in the Darendeli (2001) model:

- For shear modulus reduction curves (Equation 7.3):
  - $\gamma_r = 0.995(\sigma' / p_a)^{0.694}$ (replaced Equation 7.9)
  - $a = 0.776$ (replaces Equation 7.10)

- For damping (equations 7.4 and 7.8):
  - $D_{\min} = 2.512(\sigma' / p_a)^{-0/2889}$ (replaces Equation 7.11)
  - $b = 0.712$ (replaces Equation 7.12)

Kishida *et al.* (2009b) published a model for the MRD curves for peats in the Sacramento River delta. A comparison of the proposed MRD curves for Peat with those of Kishida *et al.* (2009b) are shown in Figure 7.13. Note that the model proposed for this study has a stronger dependence on confining stress. This dependence was noted by various other studies (e.g., Kramer, 2000). On the other hand, the proposed model does not have dependency on organic content.

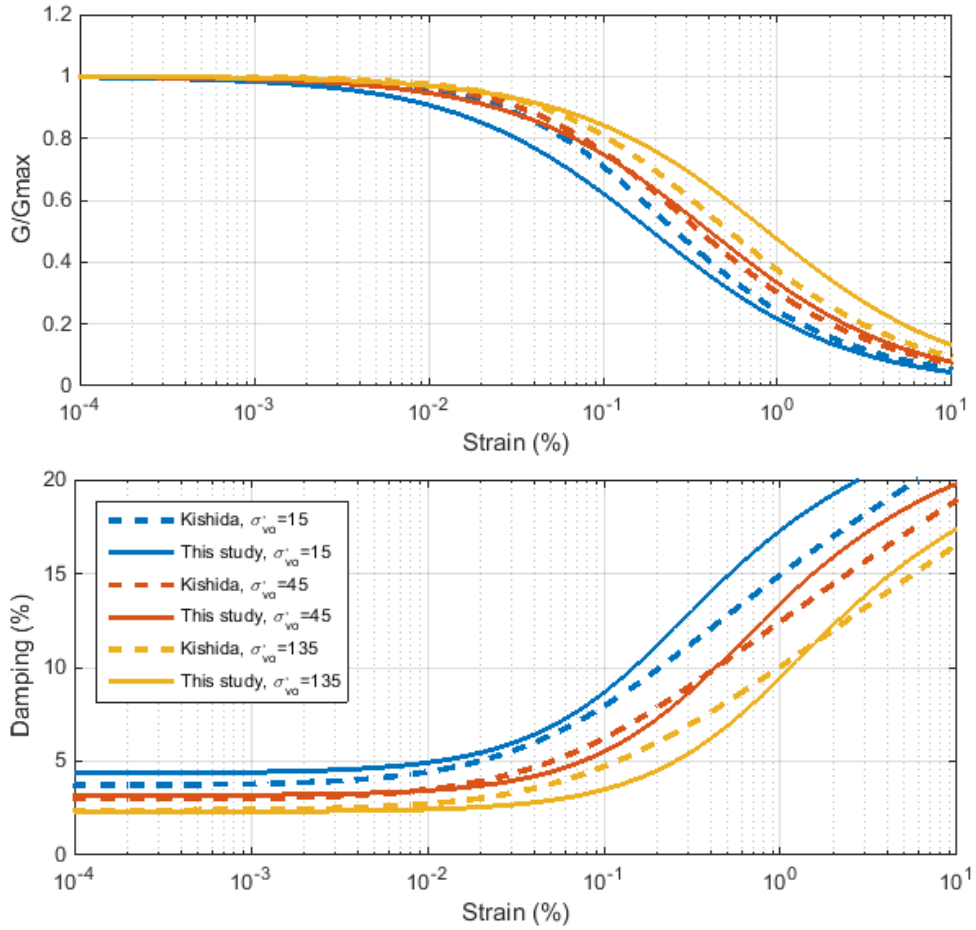

Figure 7.13. Comparison of MRD curves obtained from the proposed model and the model by Kishida *et al.* (2009b) for different vertical effective stresses. Curves for Kishida *et al.* (2009b) are shown for an organic content of 15%

7.7. Randomisations

Potentially, all variables that are input in the site response calculations can be randomized. However, for each added parameter to a randomization process, the calculation time increases exponentially. Therefore, the parameters chosen for randomization need to be selected carefully. Moreover, the amount of information on the variability of the parameter

dictates the possibility to randomize the parameter. Figure 7.14 illustrates how the general level of knowledge varies with depth.

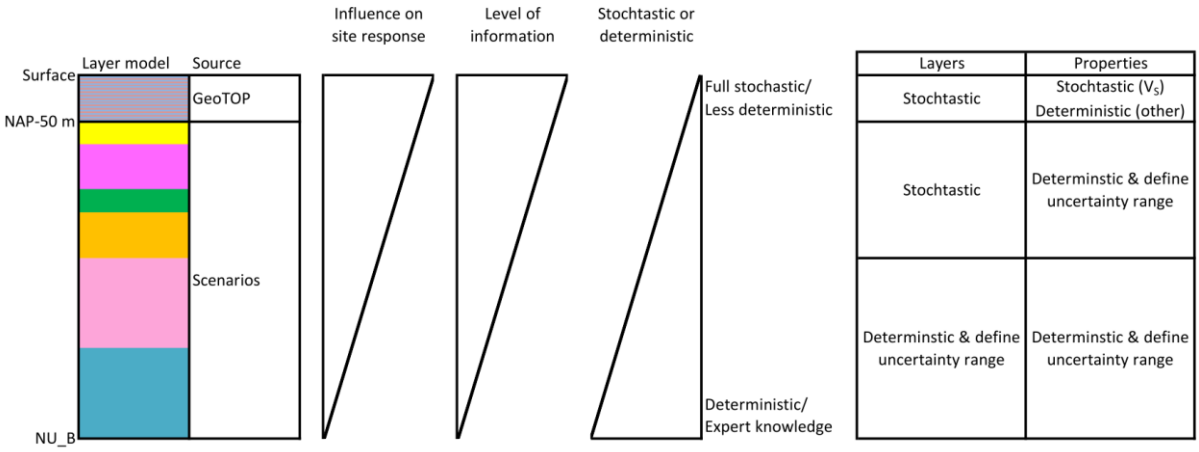

Figure 7.14. Site layer and property model with the coupling of depth ranges of the geological models (GeoTOP and scenarios, Kruiver *et al.*, 2015) to the reference baserock horizon (NU_B). The level of information decreases with depth, as does the influence of the deeper layers on the site response

The following randomisations were implemented in the site response calculations:

- The variability of lithostratigraphy and lithoclass is represented by the distribution of voxel stacks of GeoTOP within one geological zone for depth range from the surface to NAP-50 m.
- The variability of lithostratigraphy in the depth range between NAP-50 m and NU_B is taken into account by the probabilities of the scenarios.
- Randomisation of V_S is applied only for the GeoTOP depth range, taking into account full vertical correlation within units and no correlation between units and using the V_S distributions described in section 7.1. Below NAP-50 m, the MEIDAS and T2D velocities are taken as provided by NAM and Shell. No uncertainties were implemented in this depth range.
- Randomisation of input signals: The input motions were ranked according to their PGA and split into 5 classes of increasing PGA. For each layer file, one input signal was randomly selected from each class.

No randomisation was applied to unit weight, OCR and I_p. For these parameters, average values were used for each combination of lithostratigraphy and lithoclass. Uncertainty in the MRD curves was also not taken into account in the site response analyses. Uncertainty in MRD curves is, however, taken into account in the proposed model for uncertainty of the amplification factors (Chapter 9).

8. SITE RESPONSE ANALYSES

This chapter follows directly from the construction of the site profile models developed for site response analyses presented in Chapter 7, and focuses on how the site response analyses have been conducted to obtain the site amplification functions for the Groningen field. The chapter begins with a discussion of the choices that were made for how the site response analyses were to be performed in terms of methodological approach. The next section describes the generation of the dynamic inputs at the elastic half-space used in the analyses, and the final section then discusses the interpretation of the site response analysis results in the form of non-linear amplification factors and their associated variability.

8.1. Choice of analysis procedure

The site response analyses for the Groningen project will be conducted assuming one-dimensional (1-D) wave propagation. Non-linear soil behaviour will be modelled using an equivalent linear approach (EQL). In the EQL approach a single strain level for each soil layer is used to select strain-compatible values of shear-moduli and damping. These strains are proportional to the maximum strains, which in turn depend on the input motion. Generally, multiple input motions are necessary to capture the potential variability of maximum strain. Alternatively, Random Vibration Theory (RVT) can be used to obtain statistical estimates of maximum strains (Rathje & Ozbey, 2006). An additional advantage of RVT is that it can also be used to estimate peak time domain parameters from the predicted Fourier amplitude spectra at the surface. For these reasons, a much smaller set of input motions is needed to fully capture the effects of input motion variability on the variability of site amplification.

For the Groningen project, site response analyses will be conducted using the software STRATA (Kottke & Rathje, 2008) with the RVT option. The remainder of this section presents a review of relevant literature aimed at justifying this choice and at evaluating the possible bias resulting from this choice.

Comparison of EQL and fully non-linear analyses

EQL methods use a constant value of soil properties (shear moduli and damping) in each soil layer. This constant value is obtained by assuming a level of strain for each layer and is used in a closed-form solution of the 1-D wave propagation equation in elastic media. An iterative procedure using the soil's Modulus Reduction and Damping (MRD) curves is applied until the computed strains are equal to the assumed strains. On the other hand, non-linear (NL) site response analyses solves for the wave propagation equation using time-stepping methods where the soil properties vary with time. The soil properties can modulate with time as the severity of shaking changes (Stewart *et al*., 2014). This approach allows for more realistic modelling of the non-linear response of the soil, especially for high-intensity input motions (Kottke, 2010).

The EQL approach is easy to use and implement and is computationally inexpensive, but it involves a larger set of approximation to soil behaviour than non-linear analyses (Hashash & Park, 2002). Discrepancies between NL and EQL site response analyses (SRA) are typically associated with large shear strains over some depth interval in the profile (Stewart *et al*., 2014). Some authors have found that NL analyses are required when shear strains exceed 0.5-1.0% (Stewart *et al.*, 2014) while other studies suggest a smaller threshold: 0.1-0.4% (Kaklamanos *et al.*, 2013). In addition to its computational efficiency, an additional advantage of EQL is that the input parameters are generally easier to develop than those needed for NL analyses. For this reason, an issue that is commonly faced during SRA is whether EQL analyses are sufficient or whether more costly NL analyses are required (Stewart *et al*., 2014).

Validation studies using vertical array data have shown general consistency between EQL and NL predictions of site response (*e.g*., Stewart *et al*., 2008; Kwok *et al*., 2008; Assimaki & Li, 2012; Kaklamanos *et al*., 2013). Stewart *et al.* (2014), in an extensive review article, indicate that a limitation of these studies is that they involve relatively modest levels of shear strain. Stewart *et al.* (2014) propose that more meaningful insight into the differences between EQL and NL ground motion predictions can be made when the analyses are performed for relatively strong shaking levels that induce large strains. However, care must be taken when comparing model assumptions to make sure errors in the specification of soil properties do not obscure the results.

Other researchers have also provided insights on the relationships between EQL and NL SRA by comparing NL, EQL, and linear numerical evaluations of site responses with linear empirical evaluations. For instance, Assimaki & Li (2012) found that the intensity of non-linear effects at a given site during a specific ground motion is a function of the time-average shear-wave velocity in the upper 30 m of the site (V_{S30}) and the amplitude at the fundamental resonance, and the characteristics of the incident-motion parameter. Régnier *et al*. (2013), using empirical data from the Kiban-Kyoshin (KiK-net) Japanese database and a statistical analysis showed that, regardless of the site, the probability that there is a significant departure from linear site response is greater than 20% for PGA values recorded at the downhole station between 30 to 75 cm/s^2.

The differences in predictions between EQL and NL analyses are primarily due to overdamping in EQL and to an overprediction of amplification at resonant frequencies due to the assumed linearity in the EQL computations. Overdamping occurs in soft soils subjected to high intensity motions because the damping levels used in the EQL analyses are those that are compatible with strain levels that occur only during a short time interval in the strain time history, yet the same damping level applies for the entire duration of the time history (Stewart *et al*., 2014). Because damping affects more the high frequencies, this effect can cause an under-prediction of high frequency motions in EQL. On the other hand, EQL analyses may over-predict the amplitude of site response at resonance frequencies. This occurs because the EQL analyses assume time-invariant soil properties, which results in the constructive interference of trapped waves that leads to resonance. The change of soil properties with time that occurs in NL prevents the constructive interference from fully developing (Rathje & Kottke, 2011).

Another common source of discrepancies between EQL and NL analyses are due to the difference in predicted soil behaviour between the two types of analyses. The NL approach relies on a backbone shear stress-shear strain curve and Masing unloading/reloading rules to define the hysteretic response of the soil under cyclic loading. A common backbone curve is the MKZ model (Matasovic & Vucetic,1993), which is a modified hyperbola. To relate a non-linear stress-strain model to measured modulus reduction and damping curves, a non-linear backbone curve and its associated hysteresis loops at different strain levels are converted into equivalent G/Gmax and D curves. The non-linear fitting parameters are selected such that the equivalent modulus reduction and damping curves from the non-linear model match those specified for the soil (Kottke, 2010). Figure 8.1 shows a comparison of damping curves from the empirical model of Darendeli (2001) with those from the MKZ model. While the MKZ curves show favourable agreement at smaller strains, they deviate from the empirical curves at larger strains, with the NL model implying larger damping levels. This issue is common with NL models and is caused by the shape of the modified hyperbolic stress-strain curve at large strains and the use of the Masing rules to generate the hysteresis loops (Kottke, 2010). Improvements to these formulations have been proposed by Phillips & Hashash (2009).

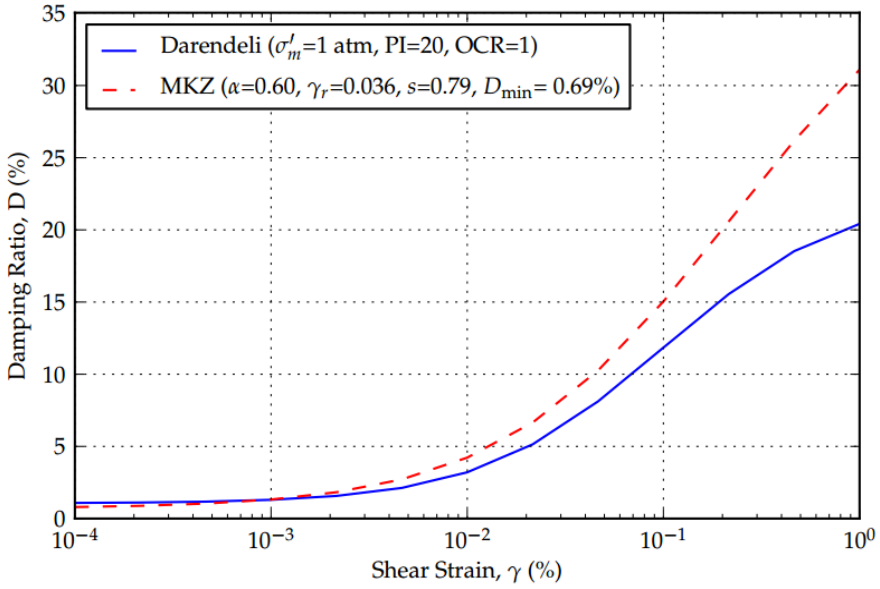

Figure 8.1. Differences in damping curves as obtained from the Darendeli (2001) and MKZ models (Kottke, 2010).

Additional differences between EQL and NL analyses can result from the numerical integration schemes implemented in NL analyses. DEEPSOIL, which is a site response program capable of conducting NL SRA, solves the equation of motion by means of the Newmark β method in time domain (Hashash *et al*., 2015). The model assumes that the acceleration within a time step is a constant, mean value. This time stepping method is unconditionally stable (Chopra, 2007), which is beneficial for multi-degree-of-freedom systems. However, numerical errors can produce inaccuracy in the solution in particular for

the high-frequency response (Hashash *et al*., 2015). These errors can cause frequency shortening and amplitude decay (Chopra, 2007; Kottke, 2010).

Kottke (2010) investigates these errors by considering linear-elastic (with frequency-independent damping) and NL site response results presented as the ratio of the Fourier amplitude spectrum (FAS) of the surface motion to the FAS of the input motion, which represents the equivalent transfer function for the selected sites. The amplitude of the transfer functions corresponding to the Sylmar County Hospital (SCH) parking lot site (located in San Fernando, CA) and the Calvert Cliffs (CC) site (in Maryland) for the closed form solution in the frequency domain and for three different motions used in the "linear-elastic", time-domain analysis are shown in Figure 8.2. For the time-domain analyses, the peaks at high frequencies shift towards lower frequencies, which represents frequency shortening, and the amplitudes of the peaks decrease, which represents amplitude decay. The frequency shortening and amplitude decay are more significant for motions with larger time steps (Δt).

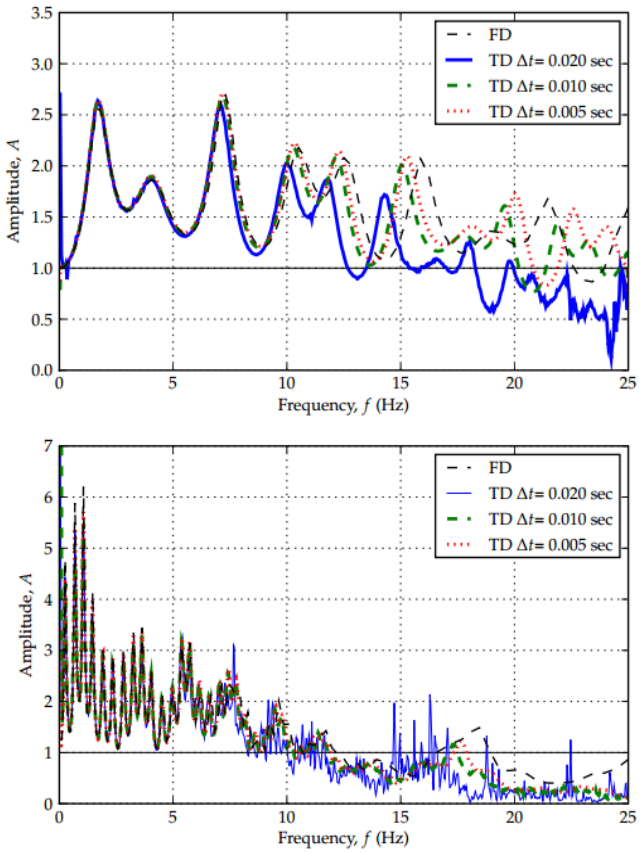

Figure 8.2. Amplitude of the transfer function computed for the SCH and CC sites using Linear Elastic time-domain (TD) and frequency-domain (FD) methods (Kottke, 2010)

The frequency shortening and amplitude decay shown in Figure 8.2 was found to affect spectral ratios at high frequencies (Kottke, 2010). For both sites investigated by Kottke (2010), the spectral ratios from the time domain analysis with frequency independent

damping are 5 to 15% smaller than the frequency domain results at frequencies above 10 Hz.

Kottke (2010) investigation focused on linear-elastic time-domain analyses versus EQL SRA elucidated two important effects that cause an underestimation of the site response at high frequencies for time domain methods. First, frequency-dependent viscous damping in NL formulations can significantly underestimate the site response at high frequencies. The frequency-independent Rayleigh damping formulation of Phillips & Hashash (2009) has been found to reduce this underestimation (Hashash *et al*., 2010), but at the expense of computational effort. Additionally, numerical errors introduced by the time-stepping integration used in time-domain analysis influence the site response at frequencies greater than about 10 Hz as shown in Figure 8.2 (Kottke, 2010).

Results from a survey conducted by Matasovic & Hashash (NCHRP, 2012) showed that there was a consensus amongst practitioners that a NL SRA is to be used when computed shear strain exceeds 1%, although this threshold was deemed as too high. These authors also indicated that only considering ground motion intensity measures cannot be sufficient to assess soil non-linearity given that strain levels in soft soil deposits can be quite high even when subjected to low intensity ground motions (Kim *et al*., 2013).

Kaklamanos *et al.* (2013) identified critical parameters that most significantly contribute to uncertainty in estimations of site response by performing linear and equivalent linear SRA using the KiK-Net downhole array data in Japan. Thresholds for selecting among linear, EQL and NL SRA were provided with respect to the maximum shear strain in the soil profile, the observed peak ground acceleration at the ground surface, and the predominant spectral period of the surface ground motion. The aforementioned parameters were found to be the best predictors of conditions where the evaluated site response models become inaccurate (Kaklamanos *et al*., 2013). The peak shear strains beyond which linear analyses become inaccurate in predicting surface pseudo-spectral accelerations are a function of vibration period and are between 0.01% and 0.1% for periods <0.5 s, whereas EQL SRA were found to become inaccurate at peak strains of ~0.4% over the aforementioned period range.

The proposed thresholds at which linear and EQL models should be used are presented in Figure 8.3. According to Kaklamanos *et al*. (2013), by using the statistically significant data set of 3720 ground motions at 100 sites, the breakpoint in the slope of the intra-site residuals versus the maximum shear strain (γ_{max}) or observed peak ground acceleration (PGA_{obs}) can be used to quantify the critical values of γ_{max} at which the linear and EQL site response estimates are no longer reliable.

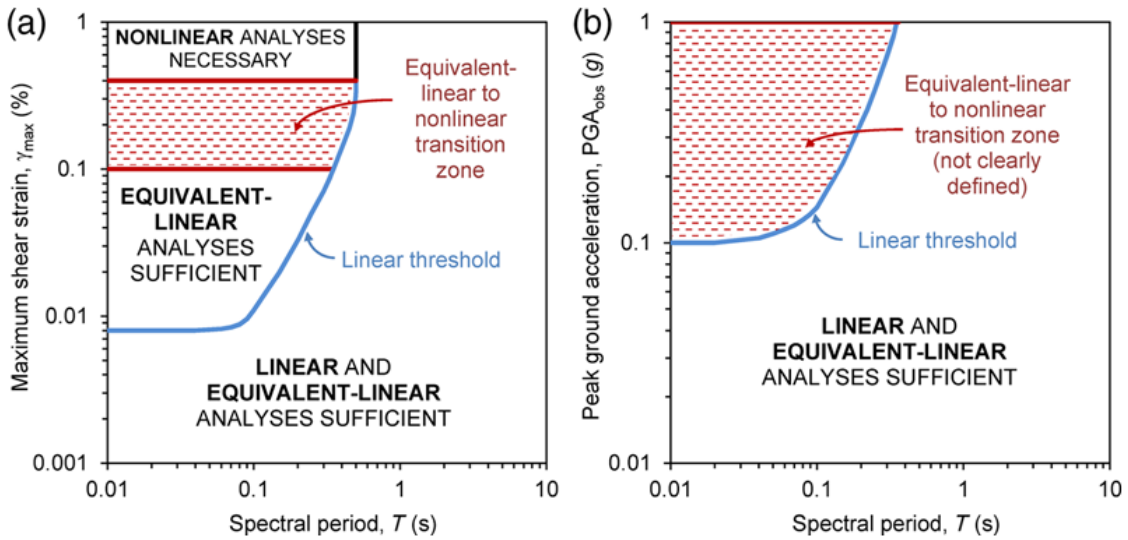

Figure 8.3. Approximate ranges of applicability of linear, EQL and NL SRA (Kaklamanos *et al*., 2013).

Kim *et al.* (2013) computed the ratio of amplification factors resulting from EQL and NL SRA (what they refer to as Sa^{EL}/Sa^{NL}) to develop a model for quantifying the differences between both approaches. Site response simulations were conducted for 510 incident motions and 24 sites. Then, regressions of Sa^{EL}/Sa^{NL} against several ground motion and site parameters were conducted to test their predictive capabilities. The estimated strain (γ_{est}), defined as the ratio of the peak ground velocity (PGV) and V_{s30} was found to correlate the best with relative differences between Sa^{EL} and Sa^{NL} (Kim *et al*., 2013). A similar framework to the one previously presented by Kaklamanos *et al.* 2013 (shown in Figure 8.3) was then developed to more clearly identify the conditions leading to different site estimates from EQL and NL SRA. Values of Sa^{EL}/Sa^{NL} equal to 0.7, 0.8, and 0.9 are presented in Figure 8.4 where γ_{est} and period are set up as the y- and x-axes respectively.

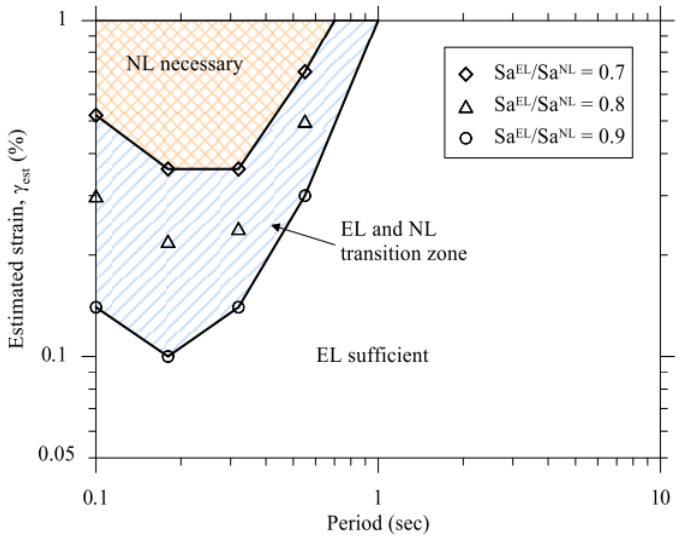

Figure 8.4. Guideline for a threshold between equivalent-linear (EL) and non-linear (NL) site response analysis in terms of estimated strain, γ_{est}, and period (after Kim *et al*., 2013).

A more recent study (Kim *et al*., 2015) has expanded the work of Kim *et al.* (2013) using preferred analysis protocols regarding the input motion selection process and specification of non-linear soil properties (Stewart *et al*., 2014). Site profiles and recorded ground motions from Western US (WUS) and Central and Eastern US (EUS) were used by Kim *et al.* (2014) to conduct 13,296 site response analyses using EQL and NL models as implemented in the site response program DEEPSOIL (Hashash *et al*., 2015).

Sa^{EL}/Sa^{NL} values were computed and plotted against the shear strain index, I_γ (*i.e*., same as the estimated strain, γ_{est}, defined by Kim *et al*., 2013) to investigate trends in the observed mismatch between EQL and NL SRA. Results for the WUS in terms of response spectra and FAS are presented in Figure 8.5.

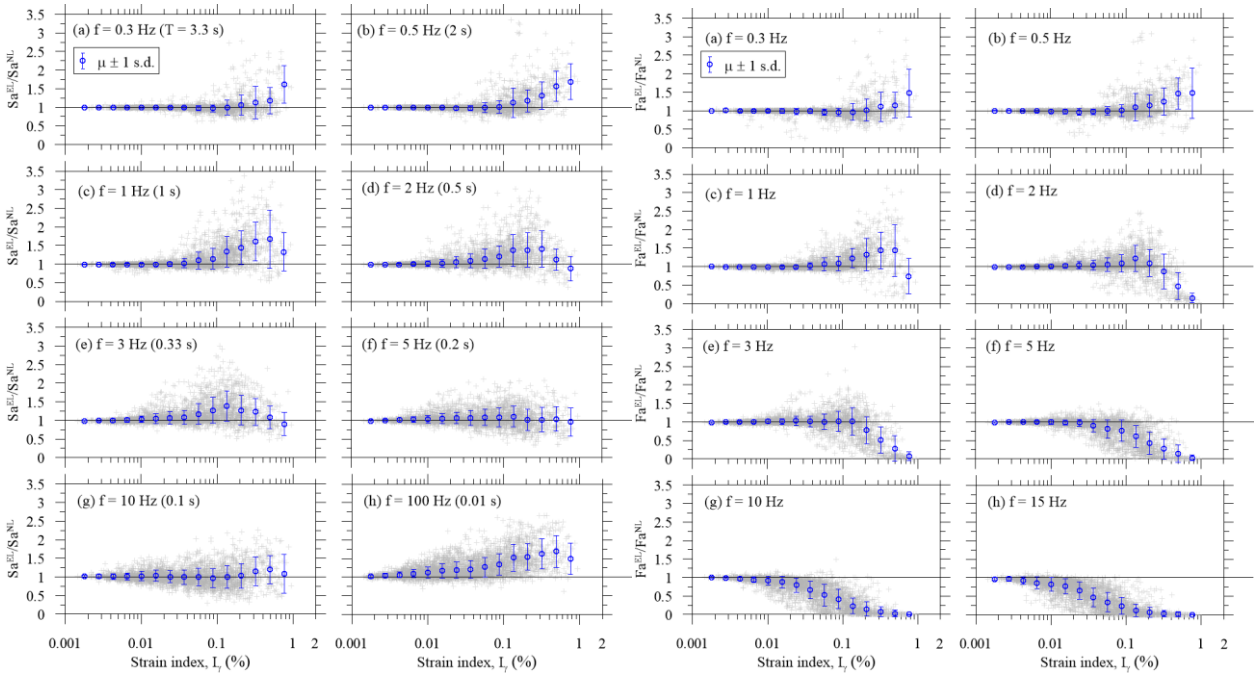

Figure 8.5. Ratio of Sa^{EL}/Sa^{NL} (*left*) and Fa^{EL}/ Fa^{NL} (*right*) for WUS in terms of I_γ (Kim *et al*., 2015)

EQL analyses seem to provide higher predictions of spectral accelerations at the frequencies considered for most of the I_γ values. At lower I_γ values, the Sa^{EL}/Sa^{NL} and Fa^{EL}/Fa^{NL} ratios are close to the unity for all frequencies but deviate from it for I_γ>0.1%. According to Kim *et al*. (2015), the decrease of Fa^{EL}/Fa^{NL} at higher frequencies (*i.e*., $f \geq 2$ Hz) responds to the over-damping from EQL analyses and its decrease as I_γ values increase is caused by increasingly smaller strains as frequency increases. Results corresponding to the CEUS are generally similar to the ones presented in Figure 8.5. Kim *et al*. (2015) summarised their findings in Figure 8.6, which compares trends of mean values of the aforementioned ratios against the I_γ for both WUS and CEUS.

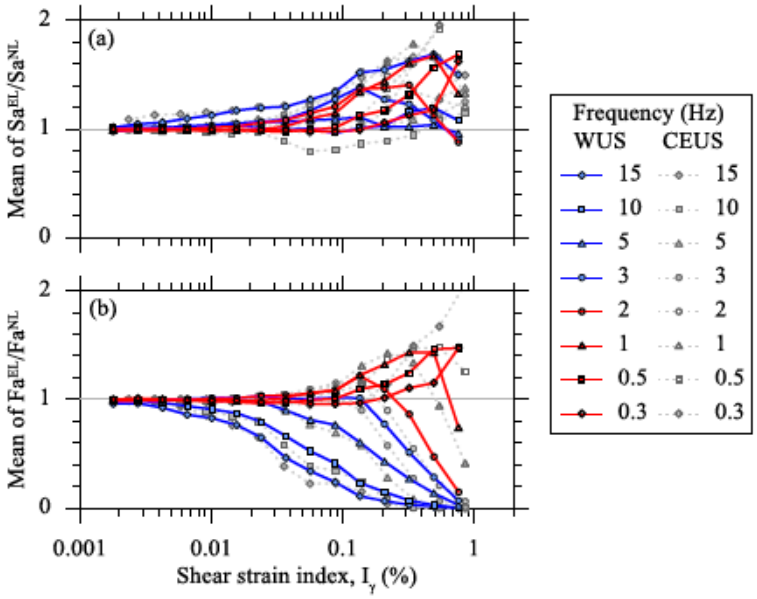

Figure 8.6. Comparison of Sa^{EL}/Sa^{NL} and Fa^{EL}/Fa^{NL} for WUS and CEUS versus I_γ (Kim *et al.*, 2015).

Mean values of Sa^{EL}/Sa^{NL} for the WUS and CEUS are generally similar (within a range of 1 to 2) although there are some differences. Likewise, for both the WUS and CEUS cases, the mean values of Fa^{EL}/Fa^{NL} start to deviate from unity at I_γ of around 0.1 %, but for frequencies greater than 5 Hz, they start to deviate from unity at lower values of I_γ (Kim *et al.* 2015). Considering this similarity in trends for WUS and CEUS conditions, Kim *et al.* (2015) proposed frequency-dependent threshold values of I_γ to identify conditions where EQL and NL SRA differ by amounts exceeding 20% (Figure 8.7):

$$I_\gamma = 0.12 f^{-0.6}. \tag{8.1}$$

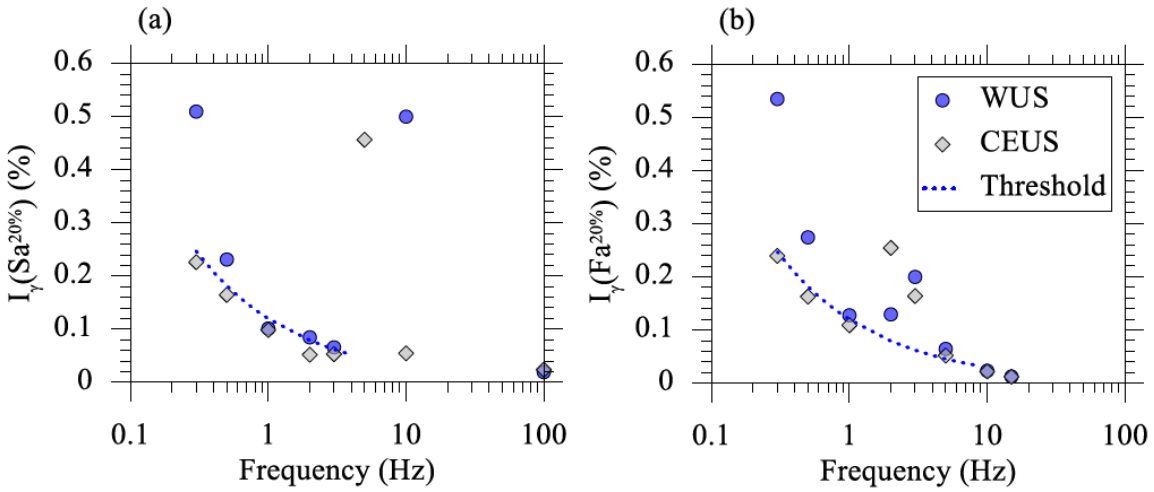

Figure 8.7. Shear strain index, I_γ, at which the EL response differs than the NL response by 20% for (A) Spectral accelerations and (B) Fourier amplitudes (Kim *et al.*, 2015).

Finally, an important contribution from this study is presented in Figure 8.8 where recommendations from previous studies for thresholds at which EQL SRA are no longer reliable are compared. The idea was to provide recommendations to identify “a priori” those conditions for which EQL and NL differ significantly.

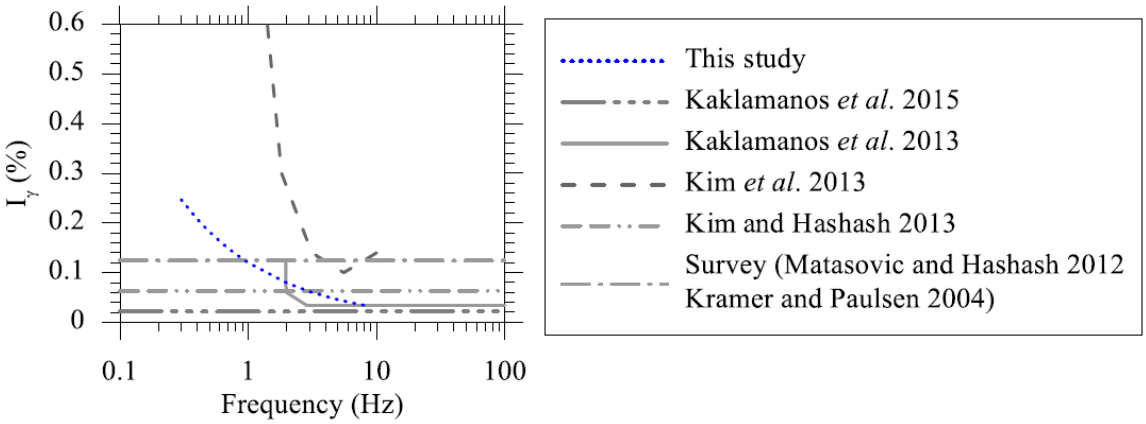

Figure 8.8. Comparison of threshold values of I_γ with those by Kim *et al.* (2013) and those converted from maximum shear strains (Kramer & Paulsen, 2004; Matasovic & Hashash, 2012; Kaklamanos *et al*., 2013; Kim & Hashash, 2013; Kaklamanos *et al*., 2015).

The most relevant conclusions to the Groningen project of the Kim *et al.* (2015) study are:

- Near the resonant site frequency, EQL ordinates exceed NL due to EQL forming a more strongly resonant response that is associated with the time-invariant soil properties.
- At high frequencies, EQL ordinates are lower than NL due to EQL over-damping. These differences are more distinct for Fourier amplitudes ratios than for spectral acceleration ratios.

Based on these conclusions (e.g., Figures 8.5 and 8.6), it is clear that when using response spectra, EQL analyses predict on average higher response than NL analyses at all frequencies, despite the fact that in some cases EQL results in over-damping at high frequencies (Stewart *et al*., 2014; Kwok *et al*., 2008). While this is true of the average response, in particular cases the amplification factors at intermediate periods (approximately between 0.1 and 0.6 seconds) might be larger for NL than for EQL analyses (Stewart & Kwok, 2008; Kottke, 2010). A reason why EQL analyses are higher than NL analyses for high frequency could be due to the phase incoherence that is introduced at high frequencies (Kottke, 2010), or to the fact that softened soil properties are used throughout the entire time history in EQL analyses. An alternative explanation is that the spectral acceleration values at high oscillator frequencies are controlled by Fourier Amplitudes at much lower frequencies. At these lower frequencies, EQL analyses are not affected as much by over-damping effects.

Various other studies have looked at the bias of EQL and NL analyses with respect to recorded data. Kaklamanos *et al*. (2015) used various site response analyses methods on six KiK-net array sites. They concluded that there is a large improvement in going from linear to EQL methods, but only a slight improvement at strains above 0.05% when going from EQL

to NL analyses. Kwok *et al.* (2008) did blind predictions of site response at the Turkey Flat vertical array in California using six different site response codes: SHAKE04 (Youngs, 2004); D-MOD_2 (Matasovic, 2006); DEEPSOIL (Hashash *et al.,* 2015); TESS (Pyke, 2000); OpenSees (McKenna & Fenves, 2001); and SUMDES (Li *et al*., 1992). Acceleration response spectra and comparisons with observed data (released after the predictions were made) are presented in Figure 8.9. Kwok *et al*. (2008) indicated that at periods well beyond the elongated site period at the site (*i.e*., 0.19-0.2 s), the predictions match the surface recordings well and are very similar to each other (which is expected considering that the computed site effect at such periods is negligible because of nearly rigid body motion. At shorter periods, the simulations generally under-predict the surface recorded motions (especially in the EW direction) and the simulation results demonstrate significant code-to-code variability. Predictions from the EQL analysis resulted in the lowest residuals. Theoretical amplification factors and observed amplification factors from recordings were also provided as a function of base motion acceleration (PGAr) in Figure 8.10 for comparison purposes. Even though for most events the site amplification is under-predicted by the models, EQL analyses seem to provide more conservative predictions than DEEPSOIL.

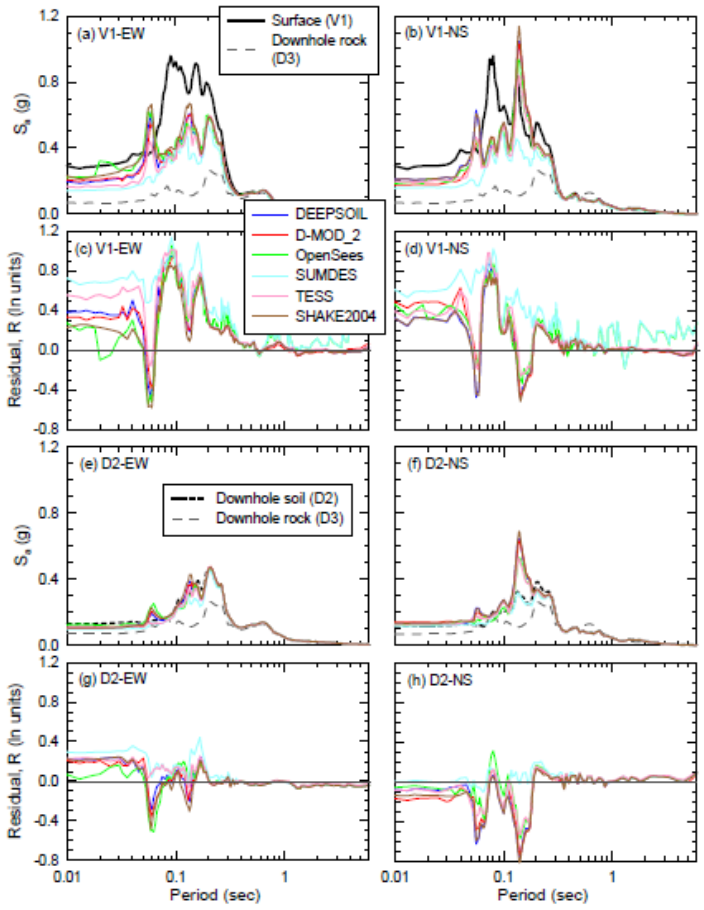

Figure 8.9. Acceleration response spectra for data and simulation results for two horizontal directions and two elevations (V1 = ground surface; D2 = 10 m depth) (Kwok *et al*., 2008)).

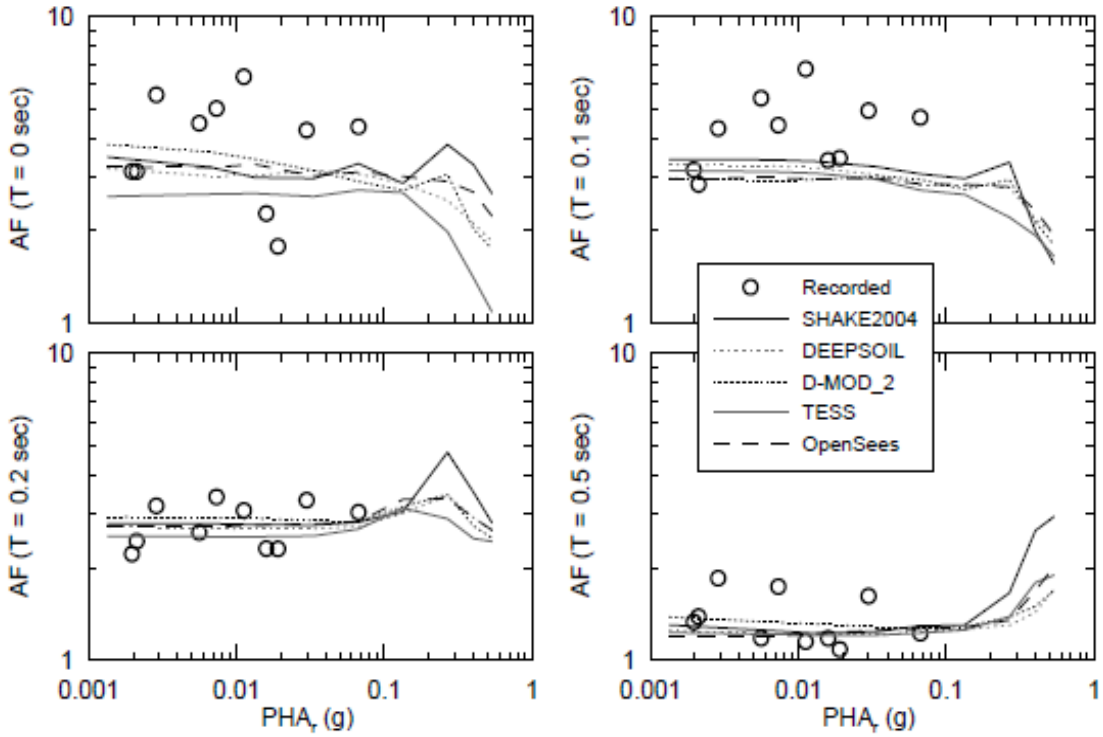

Figure 8.10. Theoretical and observed AFs at Turkey Flat site (Kwok *et al.*, 2008)

The impact of EQL and NL SRA on AF was also studied by Papaspiliou *et al.* (2012) in the context of investigating the sensitivity of hazard estimates to site response. The site program SHAKE91 was used to conduct EQL SRA while NL analyses were performed by means of DMOD2000. A sandy and a clayey site with similar V_{S30} values were used for this study. The median site amplification functions for all sets of analyses considered by Papaspiliou *et al*. (2012) for the sandy site, SCH (*i.e*., Sylmar County Hospital) are shown in Figure 8.11. EQL SRA seem to provide a conservative estimation of AF for short periods. Similar results were obtained for the clayey site. Details on the different assumptions (*i.e*., parameter selection) behind each EQL and NL analysis performed can be found in Table 1 in Papaspiliou *et al*. (2012).

Differences between Time-series EQL and RVT analyses

Kottke & Rathje (2013) compared site amplification values resulting from time series and RVT site response analyses by using the site response program STRATA (Kottke & Rathje, 2008). Stochastic simulations were used in order to ensure consistency between the ground motions needed for the time series (TS) type of analysis and the Fourier amplitude spectrum (FAS) required for the RVT approach. The program SMSIM (Boore, 2005) was used to generate a FAS based on a seismological model which was then used to generate 100 input-time series for TS site-response analysis and the FAS required as input into RVT site-response analysis (Kottke & Rathje, 2013). The parameter α_{AF} introduced by Kottke & Rathje (2013) to quantify the differences between the RVT and TS results is defined as the ratio of the AF ($S_{a,surface}$ / $S_{a,\ rock}$) from RVT (*i.e*., AF_{RVT}) to the median TS AF (*i.e*., AF_{TS}).

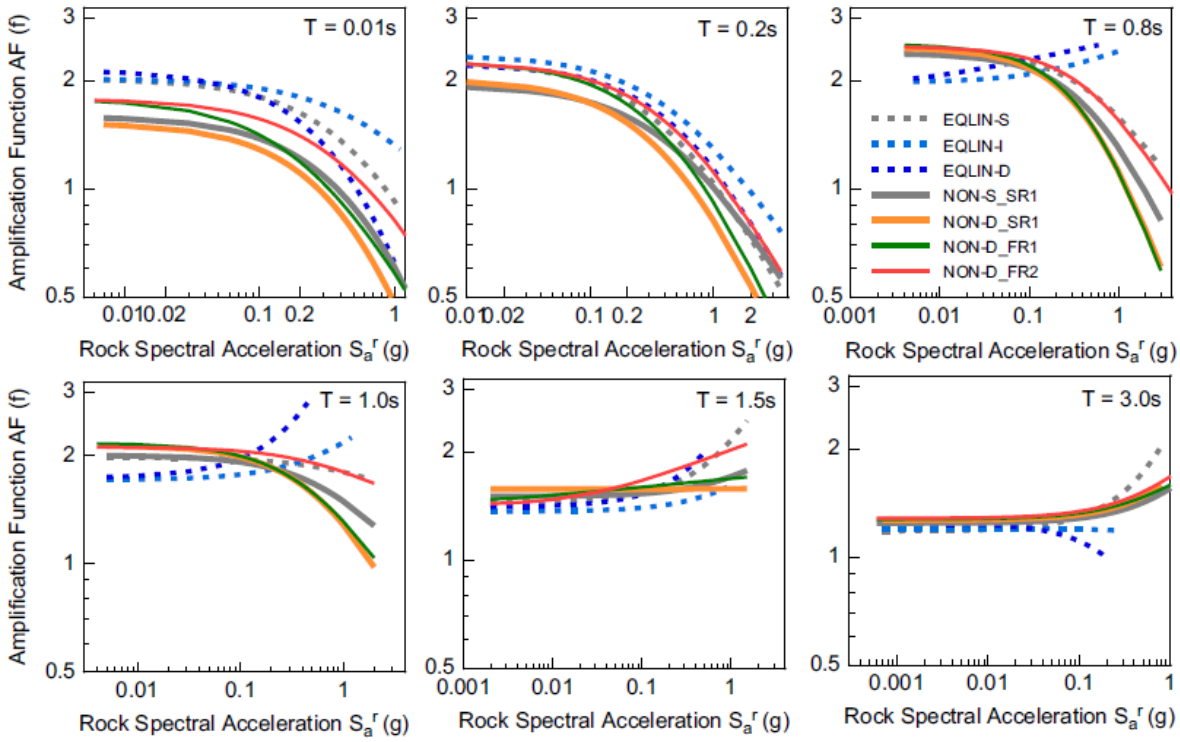

Figure 8.11. Median amplification functions for Sylmar County Hospital (SCH) (Papaspiliou *et al*., 2012).

First, comparisons were conducted for linear-elastic conditions. TS and RVT amplification factors (AF) for one of the sites under study (*i.e*., Sylmar County Hospital, SCH) turned out to be very similar. The value of α_{AF} varied between 0.95 and 1.1 across frequencies, with the maximum taking place at the fundamental frequency of the site (*i.e*., 1.7 Hz). Analogously, AF were computed for a second site (the Calvert Cliffs, CC) and the corresponding results for both sites are presented in Figure 8.12. Unlike SCH, CC did show significant differences between the median TS and RVT results, especially at the site's fundamental frequency (*i.e*., 0.25 Hz).

These findings demonstrated a site-dependency for the compatibility between TS and RVT results. A parametric study to further investigate this issue revealed that "*the maximum* α_{AF} *always occurs at the site frequency and that it increases as the site frequency decreases (i.e., soil thickness,* H_{soil}*, increases and/or* V_S *decreases) and as* $V_{S,rock}$ *increases*" (Kottke & Rathje, 2013). AF computed using RVT were found to be 20-50% larger than the AF resulting from TS analyses, while the potential under prediction can reach between 10% and 20%. The variation of the duration of the time series due to the response of the site was identified as a potential cause for the observed disagreement, given that the RVT site response does not account for it (*i.e*., the duration of the input ground motion is the one used in RVT calculations for surface response spectrum computation).

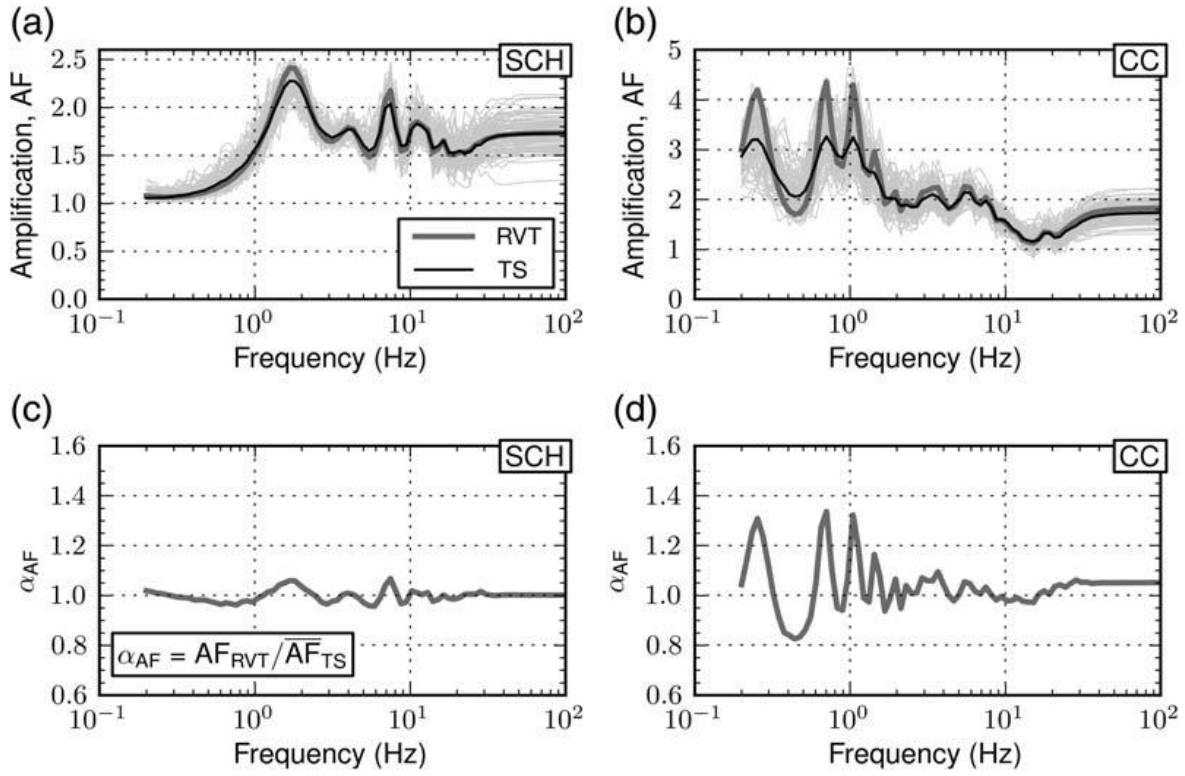

Figure 8.12. Amplification factors for TS and RVT analyses and α_{AF} for SCH and CC sites (Kottke & Rathje, 2013).

The influence of site property variations on RVT versus TS comparisons was also tested. It is well-known that introducing variability on the Vs profiles reduces the peaks in the average site amplification transfer function. This effect proved to be even more significant for RVT analyses conducted using the site response program Strata and its built-in Monte Carlo simulations as shown in Figure 8.13. For the CC site, the over prediction by RVT analyses (linear-elastic with no duration correction) at the first-mode frequency is reduced from 30% to 15% (for 100 V_S-profiles realizations with a σ_{lnVs}=0.2). Consequently, a better agreement between TS and RVT analyses can be achieved if velocity variations are modelled in the site response analyses; and the agreement improves with increasing levels of variability. Nevertheless, even including variability leads to differences as large as 10-20% between RVT and TS methods (Kottke & Rathje, 2013).

Furthermore, Kottke & Rathje (2013) indicate that varying V_S-profiles introduces more variability in RVT-based AF than the ones obtained by TS analyses that also account for variability in V_S: "*If one is considering only the median-site amplification, then this difference in variability is not important and using Monte Carlo simulations to improve the performance of RVT site-response analysis may be a viable option. However, the increase in variability in the RVT amplification factors will influence a soil-specific seismic-hazard curve that incorporates site-specific site amplification and its variability*" (Kottke & Rathje, 2013; Pehlivan *et al*., 2012).

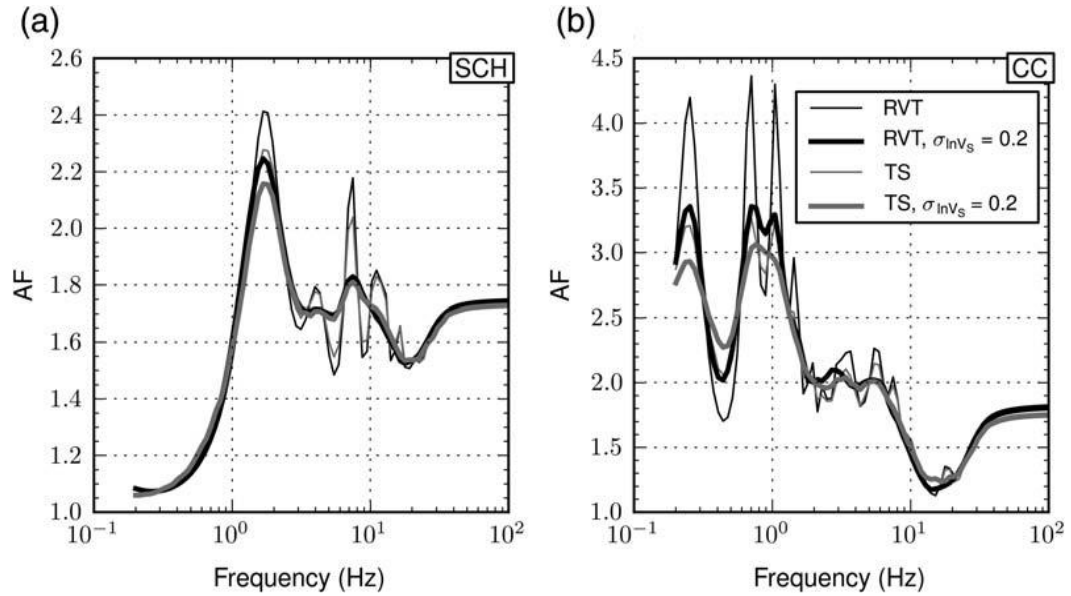

Figure 8.13. Influence of V_S variability on the site amplification predicted by RVT and TS site-response analysis (Kottke & Rathje, 2013).

Kottke (2010) also used stochastically simulated ground motions and propagated them through the Turkey Flat site in California to compare RVT and TS linear-elastic (LE) analyses (Figure 8.14). The relative differences of the spectral accelerations (δ_{Sa}) and spectral ratios (δ_{SR}) where estimated as follows:

$$\delta_{S_a} = \frac{S_{a,RVT} - \tilde{S}_{a,TS}}{\tilde{S}_{a,TS}} \tag{8.2a}$$

$$\delta_{SR} = \frac{SR_{RVT} - \tilde{\tilde{S}}\tilde{\tilde{R}}_{TS}}{\tilde{\tilde{S}}\tilde{\tilde{R}}_{TS}} \tag{8.2b}$$

where S_{aTS} and SR_{TS} are the median spectral acceleration and median spectral ratio of the time series simulations. The relative difference in the surface response spectrum was as large as 10% while it only reached 5% in terms of relative difference in spectral ratios (Figure 8.14). Kottke (2010) attributed the difference on the surface response spectrum to the relative difference observed in the input response spectrum for the stochastic input motions (Figure 8.15).

Kottke (2010) also explained that due to RVT's smooth variations in the input FAS and lack of valleys or peaks within the width of the peak of the site's transfer function, it propagates the full strength of the transfer function to the surface and predicts a larger spectral ratio. Typical input ground motions for TS analyses will have some irregularities in the FAS across the peak in the transfer function (Figure 8.16). Hence, the median spectral ratio from a suite of time-series analyses will never be as large as calculated by RVT analyses.

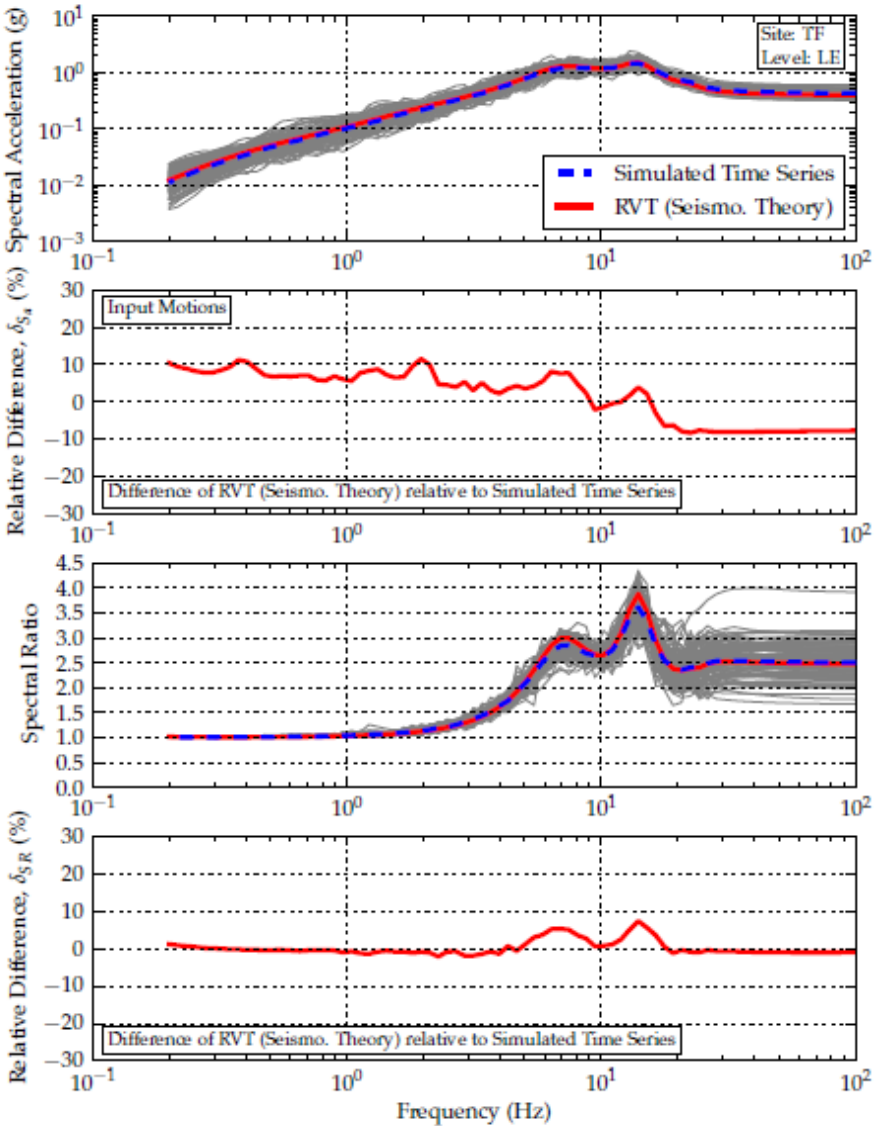

Figure 8.14. The response spectrum, spectral ratio, and relative difference for the Turkey Flat site computed with LE site response using simulated TS and an RVT motion defined by seismological theory (Kottke, 2010).

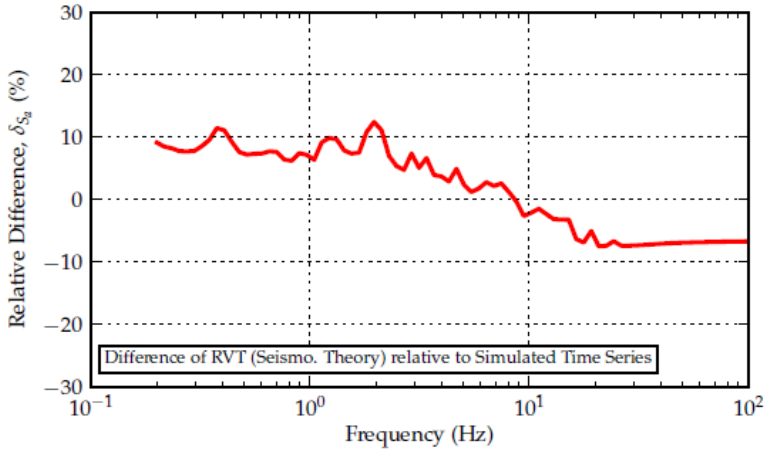

Figure 8.15. Relative difference of the input response spectrum for the stochastic input motions (Kottke 2010).

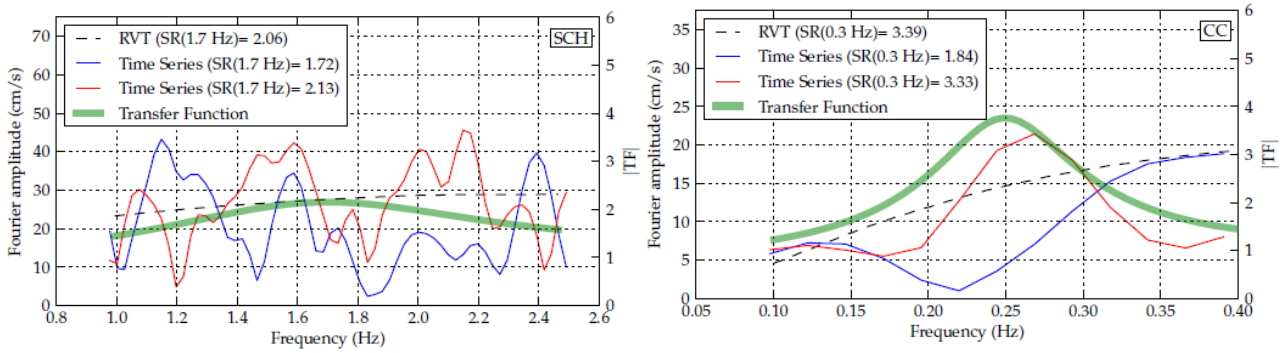

Figure 8.16. The input FAS for the time series with the largest and smallest spectral ratios for the SCH (*left*) and CC (*right*) site, along with the input FAS of the RVT analysis and the LE transfer function.

EQL site response analyses were also conducted to investigate the influence of input motion intensity and induced shear strains on the agreement between TS and RVT analyses. Input motions with median PGA of 0.17*g* and 0.4*g* were used. The comparison is presented in Figure 8.17 in terms of the parameter α_{AF}, however RVT results were not corrected for duration given that such correction was developed (and only applicable) to LE analyses (Kottke & Rathje, 2013).

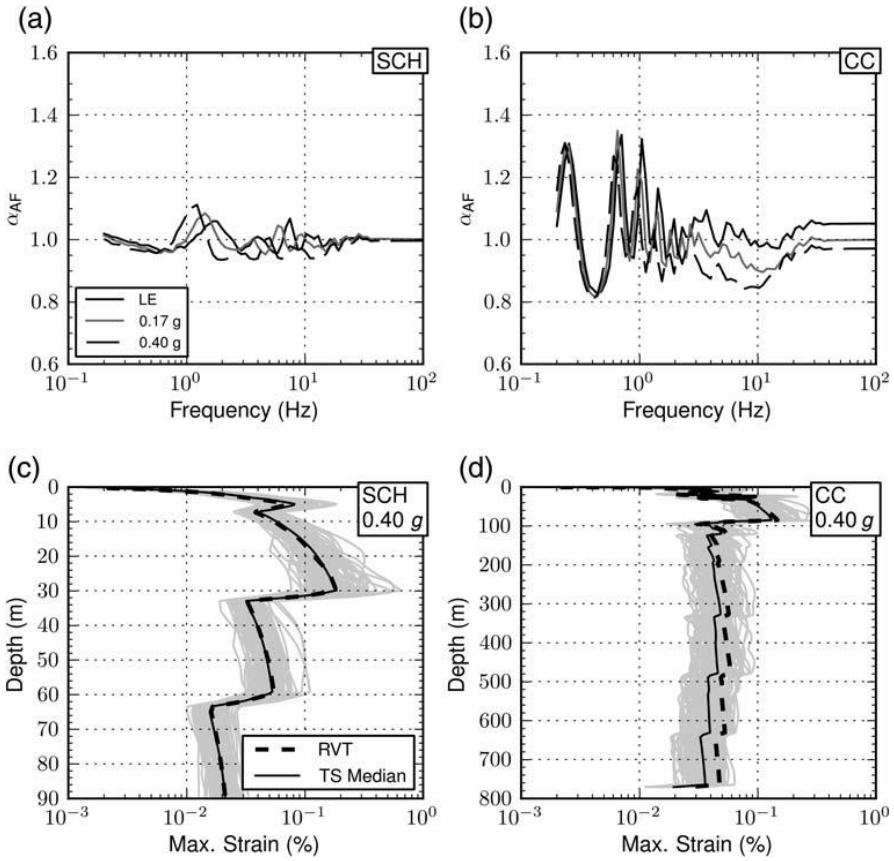

Figure 8.17. The influence of input motion intensity on α_{AF} (*a, b*); peak shear-strain profiles from RVT and TS analyses and an input PGA of 0.4*g* (*c, d*) (Kottke & Rathje, 2013).

Softening of strain-compatible properties at the SCH as the intensity of the input motion increases causes the site frequency to decrease and the peak α_{AF} to shift to lower frequencies. The resulting shear strains from both approaches at this site are very similar. In contrast, no significant changes in α_{AF} are observed at the CC site; probably because the large depth of the site controls the site frequency. However, the mismatch that takes place at frequencies higher than 3 Hz might be related to the larger shear strains predicted by the RVT EQL analyses. According to Kottke & Rathje (2013) "*while the levels of damping associated with the moderately larger strains are not significantly greater, when integrated over a very deep site they result in the smaller amplification factors at higher frequencies from RVT analysis*".

Kottke (2010) conducted similar analyses and found that differences in EQL site response as computed by means of RVT and TS analyses are influenced by both the site properties and the characteristics of the input ground motion. The major findings of his work are summarized below:

- The smooth shape of the RVT input FAS is more sensitive to the site transfer function than the irregular FAS of a time series, which results in larger amplification at the frequencies associated with peaks in the transfer function and less amplification at frequencies associated with troughs in the transfer function for RVT analyses. These differences are more important for sites with low natural frequencies and larger bedrock Vs (relative differences can be as high as 30%).
- The relative difference of RVT at the site frequency increases with increasing intensity because the RVT analysis does not take into account how individual motions strain a site differently (Figure 8.18).
- Sites in which RVT predicts significantly larger spectral ratios at the site frequency may induce larger strains that lead to smaller spectral ratio values for RVT at high frequencies (*i.e.*, RVT predicts larger strains and associated damping than the time-series analysis).

Pehlivan (2013) studied the effects of varying the Vs profiles on AF resulting from RVT and TS analyses. Figure 8.19 shows how much more significant incorporating Vs variability can be for RVT results in comparison with TS analyses. A comparison of AF obtained from TS and RVT analyses is shown in Figure 8.20, where as shown before, incorporating V_S variability improves the agreement between both approaches.

Analogously to the results presented in Figure 8.19, Pehlivan (2013) investigated the comparison between TS and RVT EQL site response analyses at a deep soil site—the previously mentioned CC site, also used by Kottke (2010) and Kottke & Rathje (2013)—but this time just for three periods (*i.e.*, PGA, 0.4 s and 1.6 s). Her findings are shown in Figure 8.21. The significantly larger AF from RVT-based analysis at the CC site for some periods has been reported previously by Kottke (2010) and Kottke & Rathje (2013). These authors suggested that the difference responds to changes in ground motion duration that are ignored in current implementations of RVT site response analysis. As also indicated by previous studies, an improved agreement can be achieved by incorporating V_S profile

variability into the site response analyses. In the example presented in Figure 10, the peak observed in the RVT analysis with σ_{lnVs}=0.2 is comparable with the peak observed in the TS analysis with σ_{lnVs}=0.0 (Pehlivan, 2013). As noted by Pehlivan (2013), not only the peak of the RVT results is reduced; as V_S variability is incorporated in TS, the peak in AF also diminishes. However, the reduction caused in RVT results is more pronounced, which leads to an improved match with TS AF.

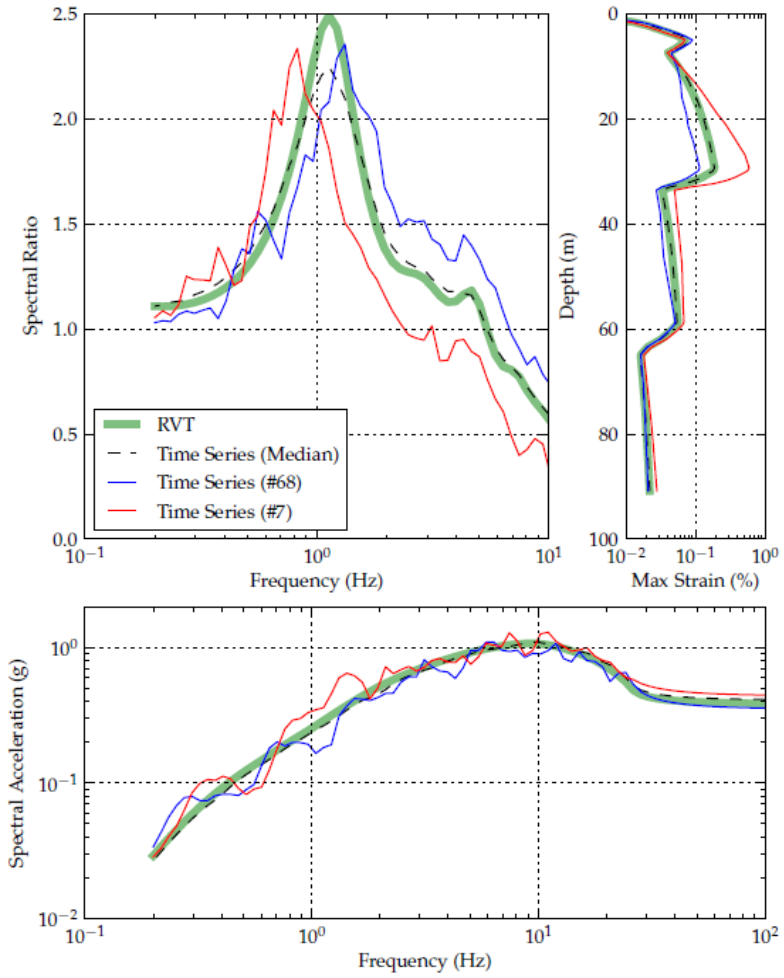

Figure 8.18. The spectral ratio and maximum strain profiles for selected motions propagated through the SCH site with an input PGA of 0.40*g* (Kottke, 2010).

An important reason for the differences in RVT and TS analyses is the effect of duration. An increase in duration for a given FAS results in a reduction in the root mean square acceleration (a_{rms}) as calculated by the RVT method (Kottke & Rathje, 2013):

$$a_{rms} = \sqrt{\frac{2}{D_{rms}} \int_0^\infty |A(f)|^2 \, df} = \sqrt{\frac{m_0}{D_{rms}}} \tag{8.3}$$

where *A(f)* is the Fourier amplitude at frequency f, m_0 is the zero-*th* moment of the FAS, and D_{rms} is taken as the ground motion duration (D_{gm}) when using RVT to compute PGA. An increase in a_{rms} leads to smaller PGA values and spectral acceleration that ultimately would

translate into smaller AF from RVT analyses. However, the impossibility of RVT analyses accounting for the increased duration of the time-series due to the response of the site has been found to be a potential cause for RVT-based AF being larger than TS-based AF (Kottke & Rathje, 2013).

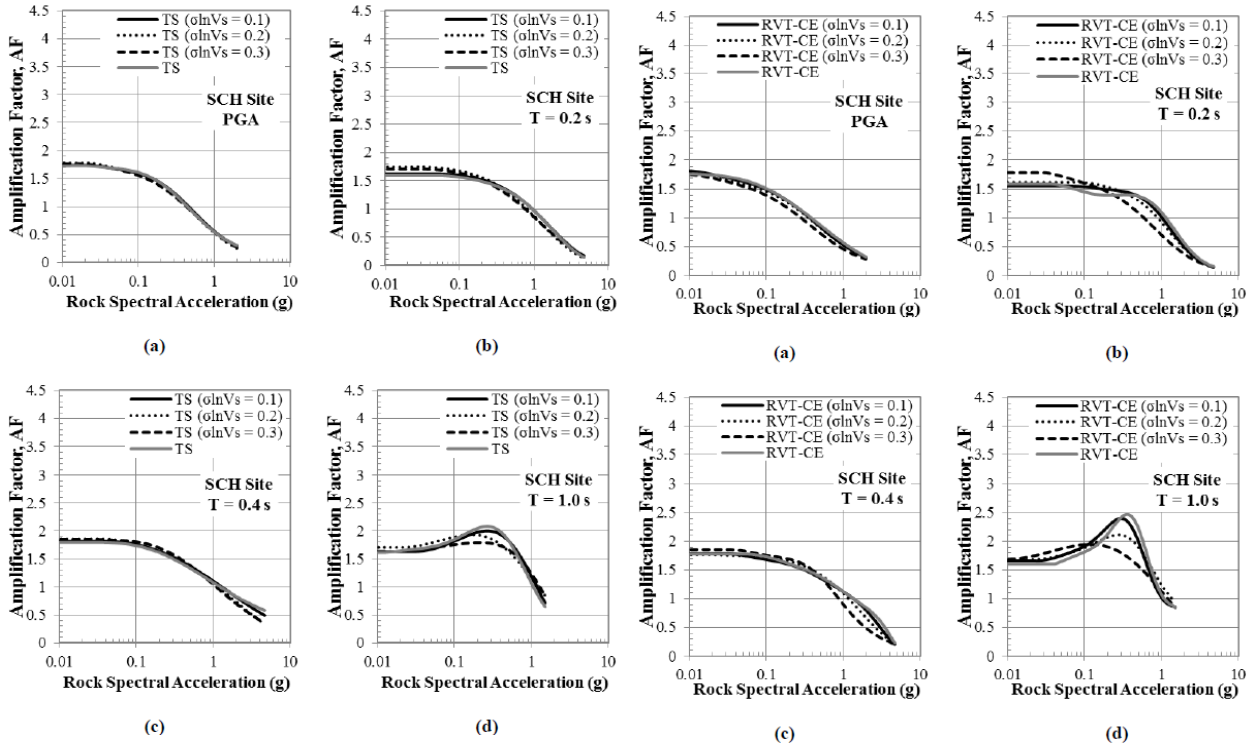

Figure 8.19. Comparison of functions of TS analyses (*left*) and RVT-CE (controlled earthquake, see Pehlivan, 2013) analyses (*right*) performed with sigmas of 0.1, 0.2, and 0.3, respectively at different periods: (a) PGA, (b) 0.2 s, (c)0.4 s, and (d) 1.0 s (Pehlivan, 2013)

The significant duration of input and surface motions (defined as the time interval between the occurrence of 5% and 75% of the Arias intensity of the acceleration time history) was computed for different site conditions and the resulting ratio is shown in Figure 8.22 versus oscillator frequency for comparison purposes. It was found that as the natural frequency of a site decreases, differences in duration of surface and input motions increase. However, the most significant variation in duration was observed when the bedrock V_S is larger because of the multi-reflections in the soil column due to stronger impedance contrasts (Kottke & Rathje, 2013). Moreover, similar shapes of the ratios provided in Figure 8.12, led the authors to suggest that it is the changes in duration that causes the over-prediction of RVT-based AF. A simple correction proposed by Kottke & Rathje (2013) to account for the variation in duration (*i.e.*, dividing AF by the square root of the duration ratio) has proved to reduce the resulting differences between TS and RVT analyses as seen in Figure 8.23.

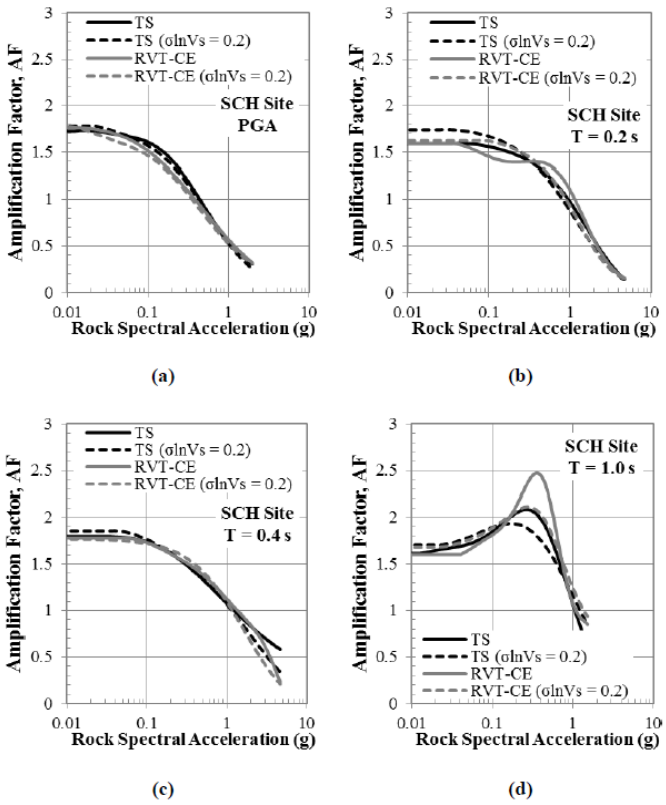

Figure 8.20. Comparison of functions predictions of TS and RVT-CE analyses performed with and without spatially varied V_S profiles (Pehlivan, 2013).

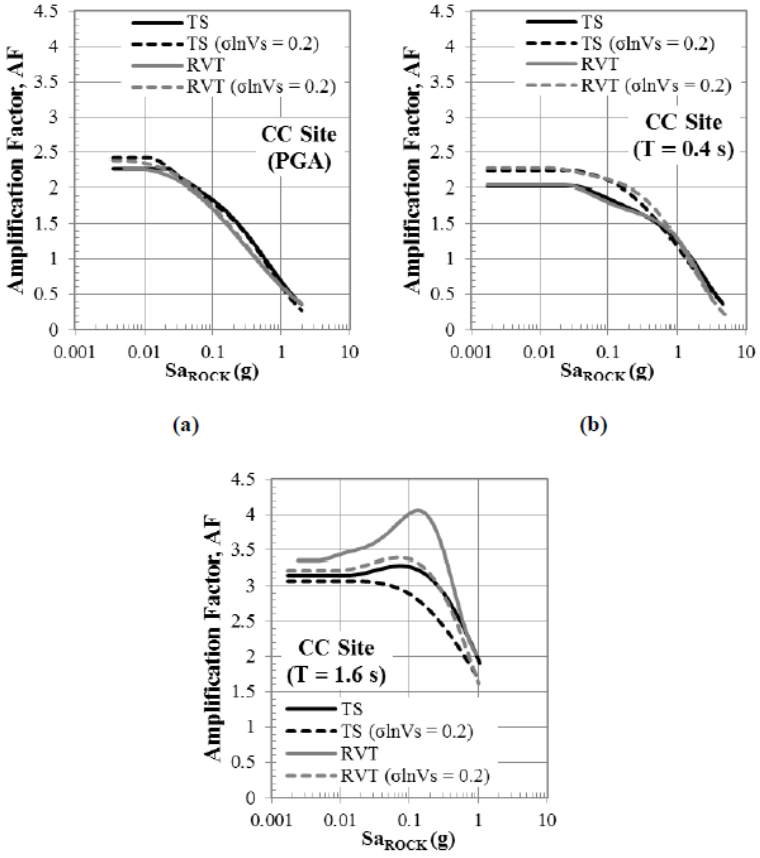

Figure 8.21. Comparison of functions predictions of TS and RVT analyses at the CC site (Pehlivan, 2013).

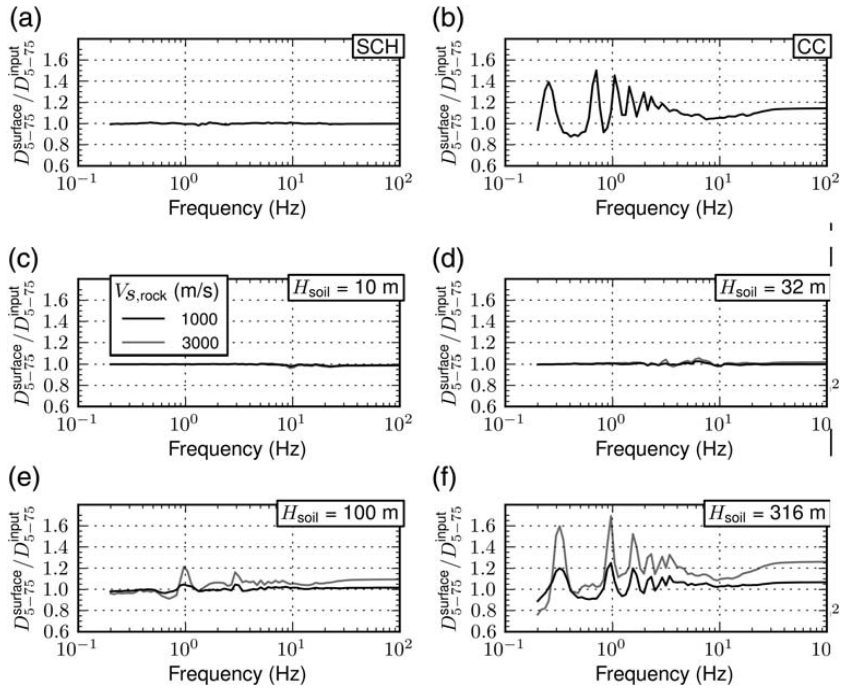

Figure 8.22. Ratio of the duration of the oscillator response of the surface motion to the duration of the oscillator response of the input motion (Kottke & Rathje, 2013).

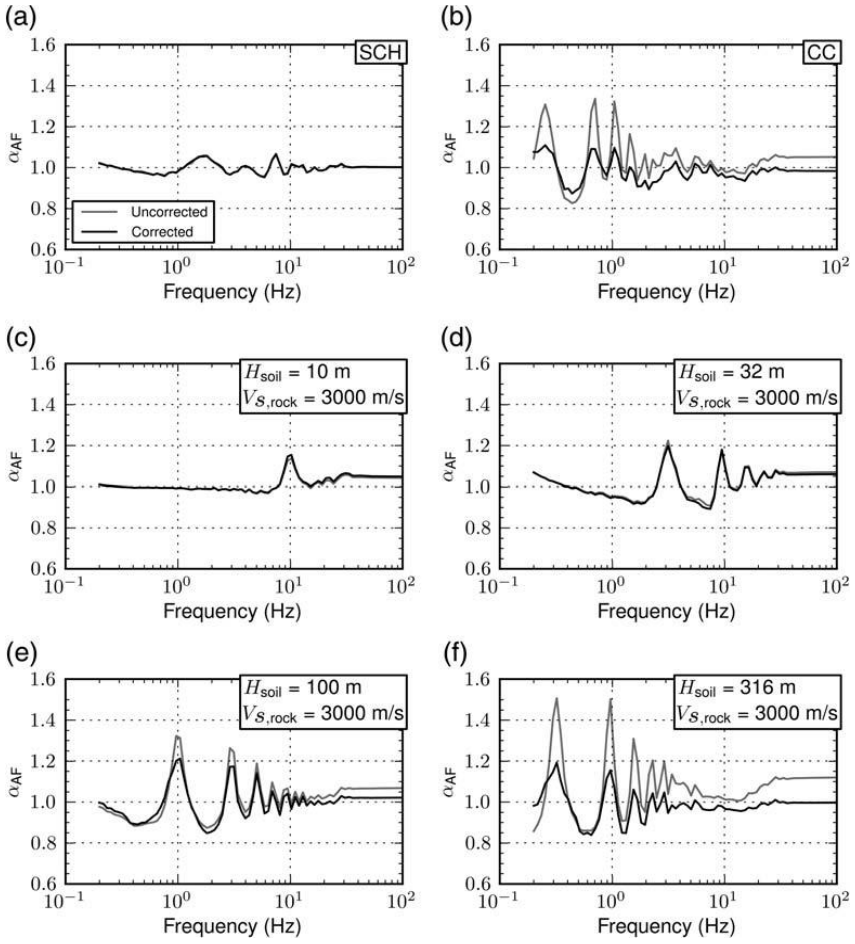

Figure 8.23. α_{AF} computed with the uncorrected RVT results and duration-corrected RVT results for each site analyzed (Kottke & Rathje, 2013).

It is important to note that the correction proposed by Kottke & Rathje (2013) is only theoretically applicable to linear-elastic conditions and it is based on duration estimates from TS analyses. However, these authors cite previous studies (*e.g*., Boore & Joyner, 1984; Liu & Pezeshk, 1999; Boore & Thompson, 2012) that have developed similar correction factors but in terms of spectral amplitudes computed directly from RVT and TS analyses.

The increase in duration due to the single-degree-of-freedom oscillator response must be included in the RVT calculations to obtain response spectra. Details on how to make this correction are provided in Kottke & Rathje (2013). Boore & Joyner (1984) investigated this phenomenon first when assessing RVT for use in stochastic ground-motion simulations. They noted that the increase in the duration of shaking due to the oscillator response must be taken into account in the rms calculation. They also showed that if this effect is considered RVT ground-motion simulations do not match time-domain ground-motion simulations (Rathje & Kottke, 2014).

The effect of the duration of shaking on the dynamic response of soils has been identified in other studies (*e.g*., Bommer *et al.* 2009). Rathje & Kottke (2014) used data from Grazier (2014) to show that the significant duration of recordings at the bedrock and at the surface differ and they show that this has an effect on comparisons between TS and RVT analyses (Figures 8.24 and 8.25).This change in duration is missing in current implementations of RVT analysis. This duration has an impact not only on the computation of the a_{rms} (Eq.8.3), but also on the estimate of peak strains. As Rathje & Kottke (2014) explain: "*The integral in Equation (1) essentially represents the energy associated with the FAS, and D_{rms} represents the duration over which that energy is distributed. Thus, a signal with the same energy and a shorter duration will generate a larger value of a_{rms}*".

Even though the input FAS are exactly the same for TS and RVT analyses, the response spectra differ because the duration for the RVT analysis is assigned independently of the FAS. The RVT surface-response spectrum was computed using the duration of the input ground motion and as seen in Figure 8.24c the RVT surface-response spectrum is larger than the TS surface-response spectrum at most periods. Particularly, RVT-based AF are 10-25% larger than TS-based AF at short periods, and 2 to 2.5 times larger than TS results at the fundamental modes of the site (Rathje & Kottke, 2014).

If D_{gm} is prescribed as 2.3 s (which is the significant duration of the surface motion according to TS analysis) for the RVT calculation of the surface-response spectrum, the agreement between RVT and TS surface-response spectra improves at periods less than about 0.15 s (Figure 8.25). Across all periods, the RVT response spectrum is reduced, on average, by 20% when the increased duration is used (Rathje & Kottke, 2014). Remaining differences at longer periods are most likely due to "the RVT oscillator duration correction not accurately modelling the increase in duration at oscillator frequencies associated with peaks in the FAS. The oscillator duration corrections that have been proposed in the literature (*e.g*., Boore & Joyner, 1984; Liu & Pezeshk, 1999; Boore & Thompson, 2012) are all based on ground-motion simulations that use smooth, seismological FAS with no local site amplification" (Rathje & Kottke, 2014).

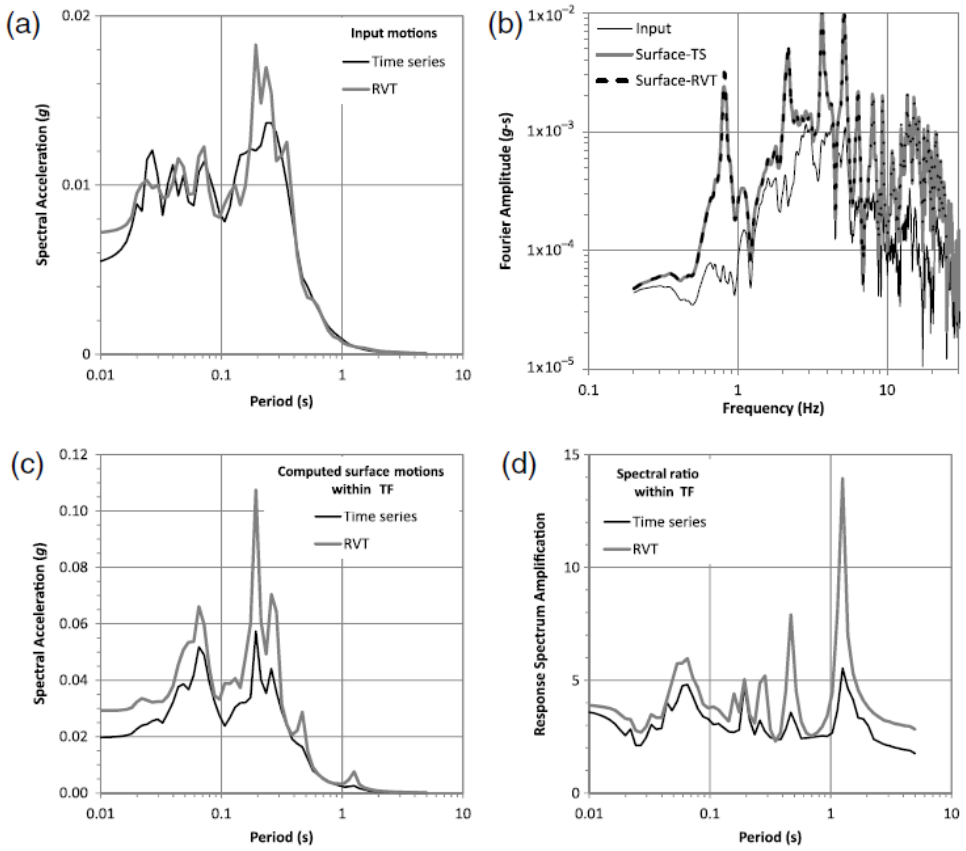

Figure 8.24. (a) Input-response spectra, (b) Fourier amplitude spectra, (c) surface-response spectra, and (d) response-spectrum amplification computed by TS and RVT site-response analyses for the Treasure Island downhole array (Rathje & Kottke, 2014).

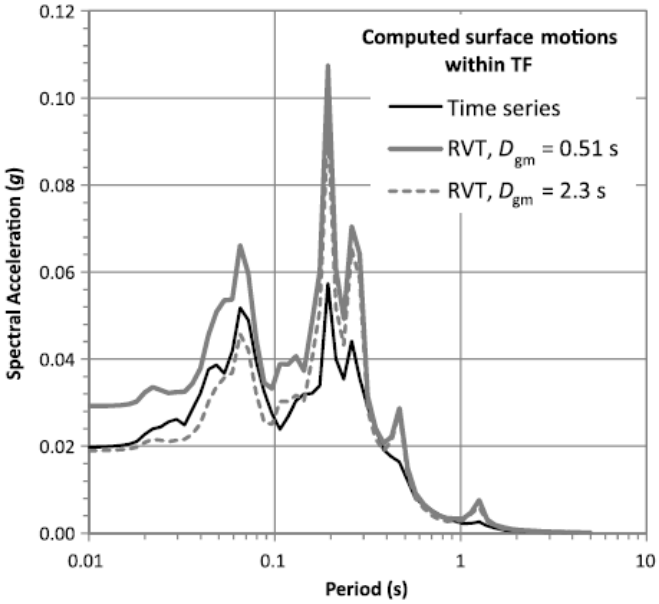

Figure 8.25. Influence of the duration of the input ground motion on computed surface-response spectrum from RVT (Rathje & Kottke, 2014).

Summary of Observations

The literature review presented in this section indicates that the choice of RVT-based EQL is justified insofar as it produces overall similar results to more elaborate non-linear time-domain analyses. An important consideration when selecting an analysis method is the possibility of model bias. The papers reviewed indicate that in general the selected analyses methods are likely to lead to positive biases in the prediction of amplification factors: RVT-based analyses are shown to consistently predict higher AFs than time series analyses, and the study of Kim *et al.* (2015) indicates that for spectral accelerations, EQL predictions of the AF are generally larger than those of NL. While other studies indicate that this is not the case in an intermediate period range, the possible under-predictions in this intermediate period range are balanced by the over-predictions due to the choice of RVT-based analyses.

8.2. Input motions at reference rock

Since the site response calculations were performed using the RVT approach in the STRATA software, the dynamic inputs at the elastic half-space need to be defined in the form of Fourier amplitude spectra (FAS) of acceleration. The STRATA program includes the facility to generate the FAS from a response spectra defined at the reference rock horizon. However, since the ground-motions at the NU_B horizon in this application are being predicted using stochastic simulations (Section 6.2), it was much more efficient to simply generate the required inputs directly as FAS using the same source, path and site simulation parameters as used for the derivation of the reference rock GMPE (Section 6.1). As for the generation of response spectral ordinates for the derivation of the GMPEs, the simulations were performed using the SMSIM software (Boore, 2005a).

A large number of reference rock motions was generated in order to capture the range of potential input motions to the layers above the NU_B horizon that could be expected from potential earthquakes in the Groningen field. The same three stress drop values that defined the lower, central and upper models for the reference rock motions—namely 10, 30 and 100 bar—were adopted, and for each stress parameter value the FAS were generated for 36 different combinations of magnitude and distance. Three magnitudes were considered (**M** 4, 5 and 6) that represent the main contributors to the hazard and risk estimates in the field. For each stress parameter and magnitude combination, the FAS were estimated at the epicentre and at an additional 11 log-spaced distances from 1 km to 57.7 km. The resulting 108 FAS were then ranked in terms of their intensity (based on the spectral amplitudes at 0.01 second) from the weakest to the strongest and then grouped into five sets of 21 or 22 spectra each (Figure 8.26). The purpose of this grouping was to ensure an adequate range of intensity in the reference rock motions used for each site response analysis in order to estimate both the linear and non-linear amplification factors. This was achieved by using five dynamic inputs for each site response analysis, each randomly chosen from one of the groups (Figure 8.27).

Checks were made that the sampling of the input motions had been sufficiently random to include all of the motions rather than repeatedly using the same FAS in any given site response analysis. This was considered to be important since apart from magnitude, stress parameter and distance, all other parameters used in the stochastic simulations were held constant in all cases. The overall sampling was very uniform with each of the signals used approximately the same number of times over the entire field (Figure 8.28). Checks were also made for the sampling in individual geological zones: Figure 8.29 shows the sampling in four different zones. Zone 3103 is a small zone that was ultimately combined with other zones (Chapter 9). Zone 2019 is a large zone and the signals were sampled evenly, with an average use of each one 35 times and a standard deviation of 6. Zone 1208 is another small zone and sampling of signals was less even; on average each signal is sampled almost 5 times (standard deviation of 2). Zone 0801 is another large zone, comparable to zone 2019, and on average each signal was sampled 38 times, also with a standard deviation of 6. Based on these checks it was concluded that the selection of the NU_B motions for input to the site response analyses was sufficiently random.

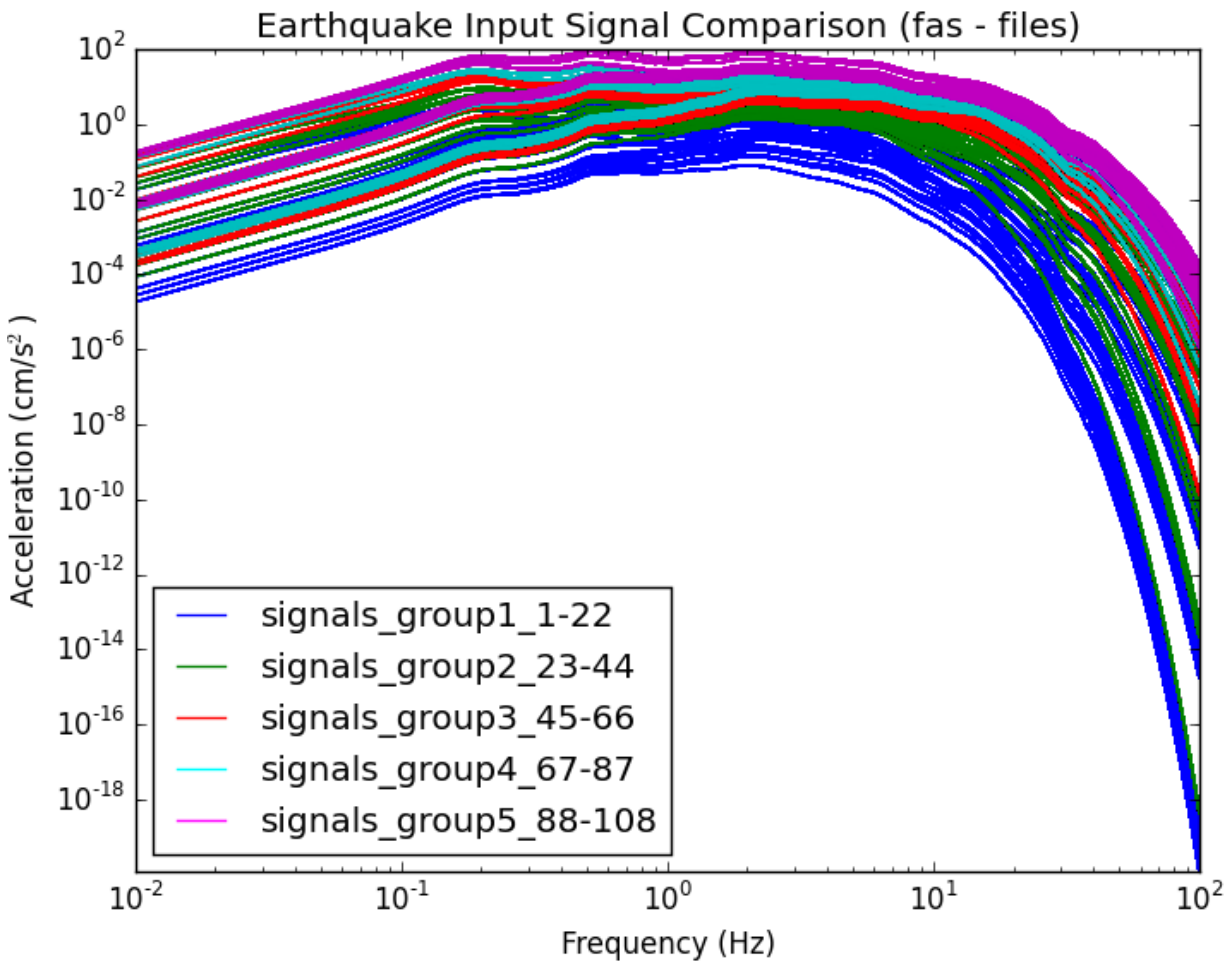

Figure 8.26. FAS generated at the NU_B horizon for use in RVT-based site response analyses

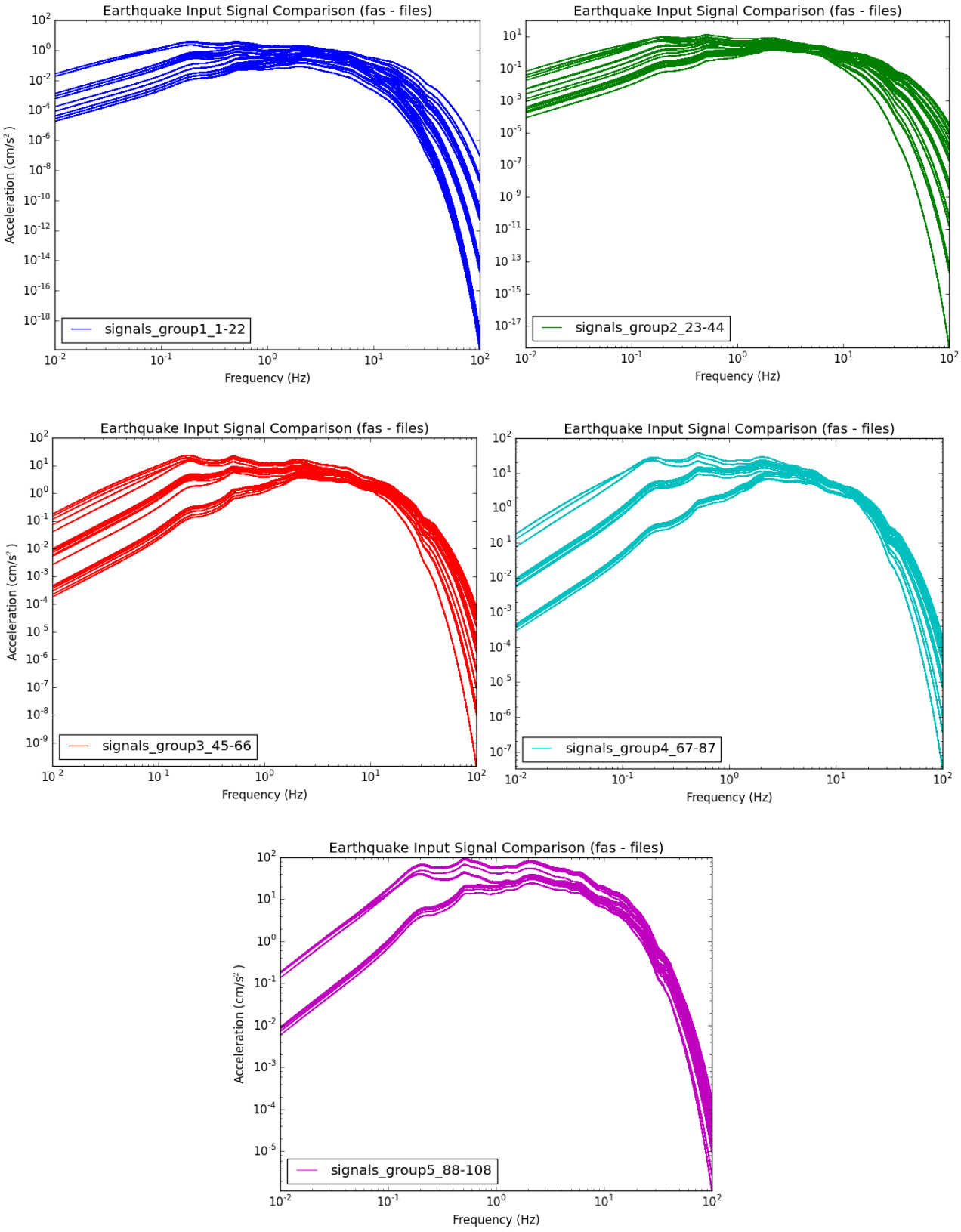

Figure 8.27. FAS generated at the NU_B horizon for use in RVT-based site response analyses shown in groups based on amplitude

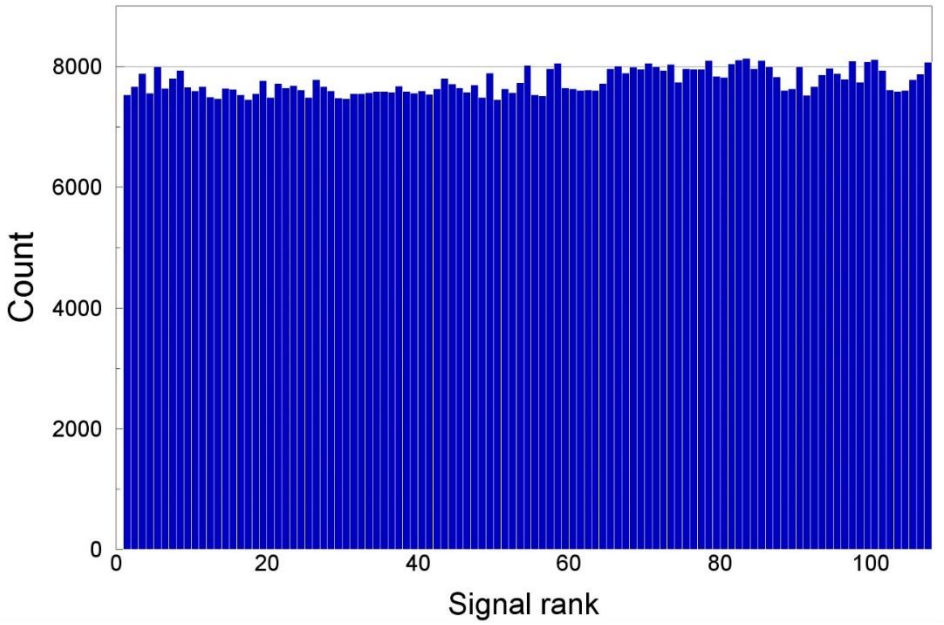

Figure 8.28. Sampling of the 108 NU_B FAS in the site response analyses over the whole field

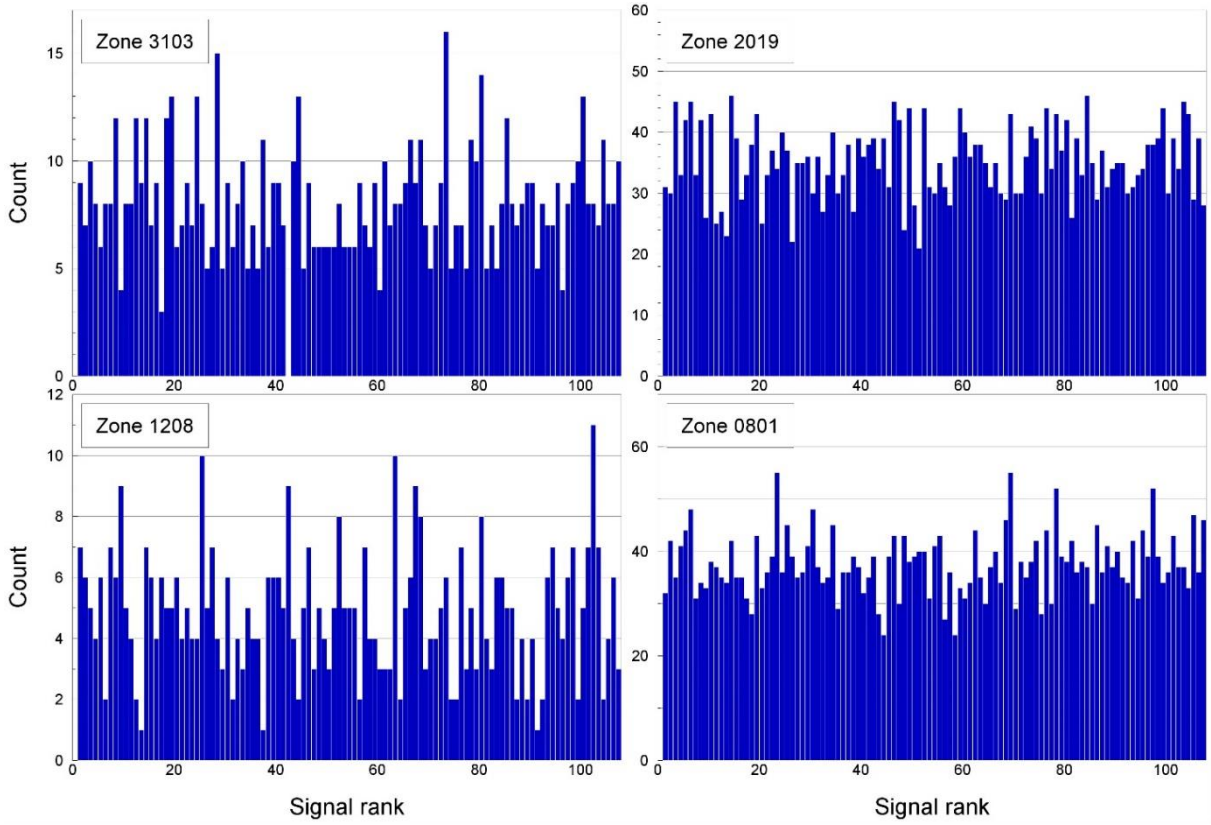

Figure 8.29. Sampling of the 108 NU_B FAS in the site response analyses for four of the geological zones

The required inputs to the STRATA analyses are both an FAS and an estimate of the duration, for which the significant duration corresponding to 5-75% of the total Arias intensity is used. The durations are modelled using the equation of Boore & Thompson (2014) and

the averages reported for 200 time-histories randomly generated for each FAS. The resulting durations are shown in Figure 8.30.

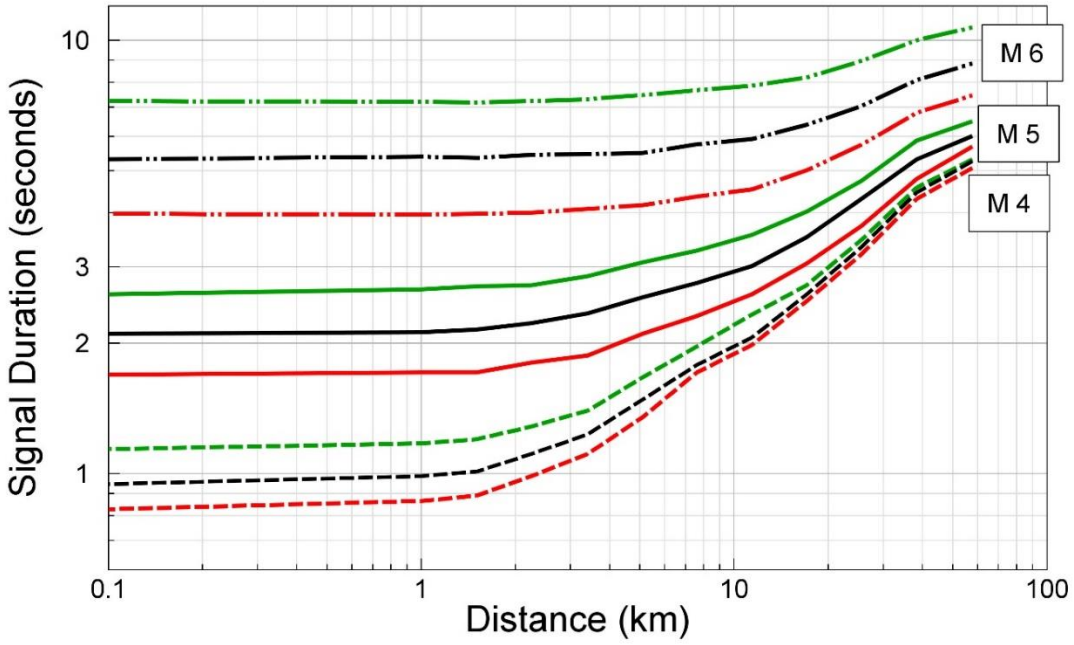

Figure 8.30. Durations provided with FAS for the inputs to STRATA

8.3. Amplification factors and variability

The spectral amplification functions (AF) were calculated using STRATA with the RVT option. Both motions at NU_B and at the surface are defined as outcrop motions (option 2A in STRATA). The input motions are entered into STRATA as Fourier Amplitude Spectra with a corresponding duration, as explained in the previous section. For each response period, the Sa_{rock} is computed for each input signal at NU_B. Five randomised input signals are used for each layer file, hence rendering five AF data points per layer file. For each zone, all AF values were plotted versus Sa_{rock} for each of the 16 required periods.

The amplification functions (AF) were found to be strongly nonlinear, as would be expected for soft soil profiles. The model proposed by Stewart *et al*. (2014) was used to fit the AF as a function of the input spectral acceleration:

$$\ln(AF) = f_1 + f_2 \left(\frac{Sa_{NU\_B} + f_3}{f_3} \right) + \varepsilon \sigma_{\ln AF} \qquad (8.4)$$

where f_1, f_2, and f_3 are parameters, Sa_{NU_B} is the baserock acceleration at NU_B (in units of *g*), ε is a standard normal random variable and σ_{lnAF} is a parameter that represents the standard deviation of the data with respect to the median prediction of the model. As will be explained later, this values is allowed to vary with Sa_{NU_B} (*i.e*., a heteroskedastic model). The parameters were determined for each period through regression analyses using Maximum

Likelihood regression (Benjamin & Cornell, 1970). Analogous to the Groninger Forum study (Bommer *et al*., 2015b), the parameter f_3 has been fixed to a value of 0.5. This value was seen to result in good fits for the Groningen sites.

An example of the AF values and the fit for zone 1208 is provided in Figure 8.31. Each point represents one STRATA calculation. For zone 1208, approximately 500 calculations were performed. The median fit through the data points for each period is represented by the black line. The median plus/minus one standard deviation are shown as the dashed lines. From the example it is clear that the AFs are highly non-linear. There is a marked transition in the effects of non-linearity at periods around 1.0 to 1.5 s. The parameter f_2 is always negative for periods smaller or equal to 1.0 s, which implies that for larger Sa_{rock}, the AF values decrease. For periods of 1.5 s, f_2 is either positive or negative. For periods equal or larger than 2.0 s, f_2 is generally positive, indicating that soil non-linearity leads to an increase in AF at larger Sa_{rock}.

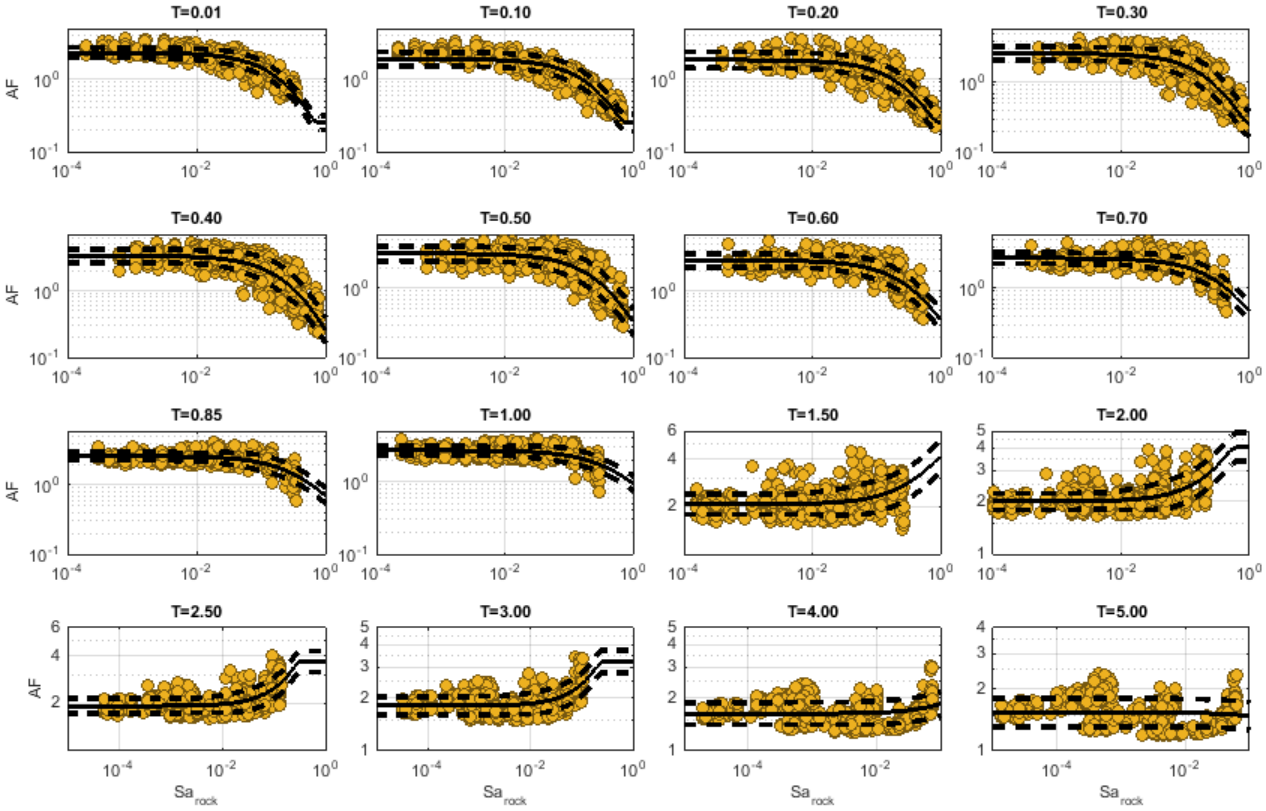

Figure 8.31. Amplification factors (AF) for zone 1208 for all periods. The fit through the data is represented by the black line. The dashed line indicates a one standard deviation band; Sa_{rock} has units of *g*.

In order to avoid unrealistic AF values outside the range of Sa_{rock} represented by the input motions, for each zone and each period a minimum and a maximum median AF is imposed. The minimum AF is equal to 0.25. This value is also a conservative choice that limits the reduction in ground motions resulting from the extreme nonlinear behaviour in soil layers that yield under the applied loading. The minimum AF is relevant for periods ≤ 1.0 s (*e.g*., periods of 0.01 and 0.1 s in Figure 8.31). The maximum AF is conservatively set to the predicted 98th

percentile AF at the maximum Sa_{rock} according to Eq.(8.4), that is the median plus two standard deviations. The maximum AF is relevant for periods ≥ 1.5 seconds (e.*g.,* periods of 2.0, 2.5 and 3.0 s in Figure 8.31)

The residuals between the computed AF values and the median values predicted by Eq.(8.4) are shown in Figure 8.32. The plus/minus one standard deviation (σ_{lnAF}) are shown by the dashed lines. Especially at smaller periods, the standard deviation varies with Sa_{rock} (*i.e.*, an heteroskedastic model). The variation of σ_{lnAF} with Sa_{rock} was modelled by a tri-linear function: a constant value a constant value σ_1 below $Sa_{rock,low}$, a constant value σ_2 above $Sa_{rock,high}$ and a linear increase in between these two Sa_{rock} cut-off points (see Section 10.5).

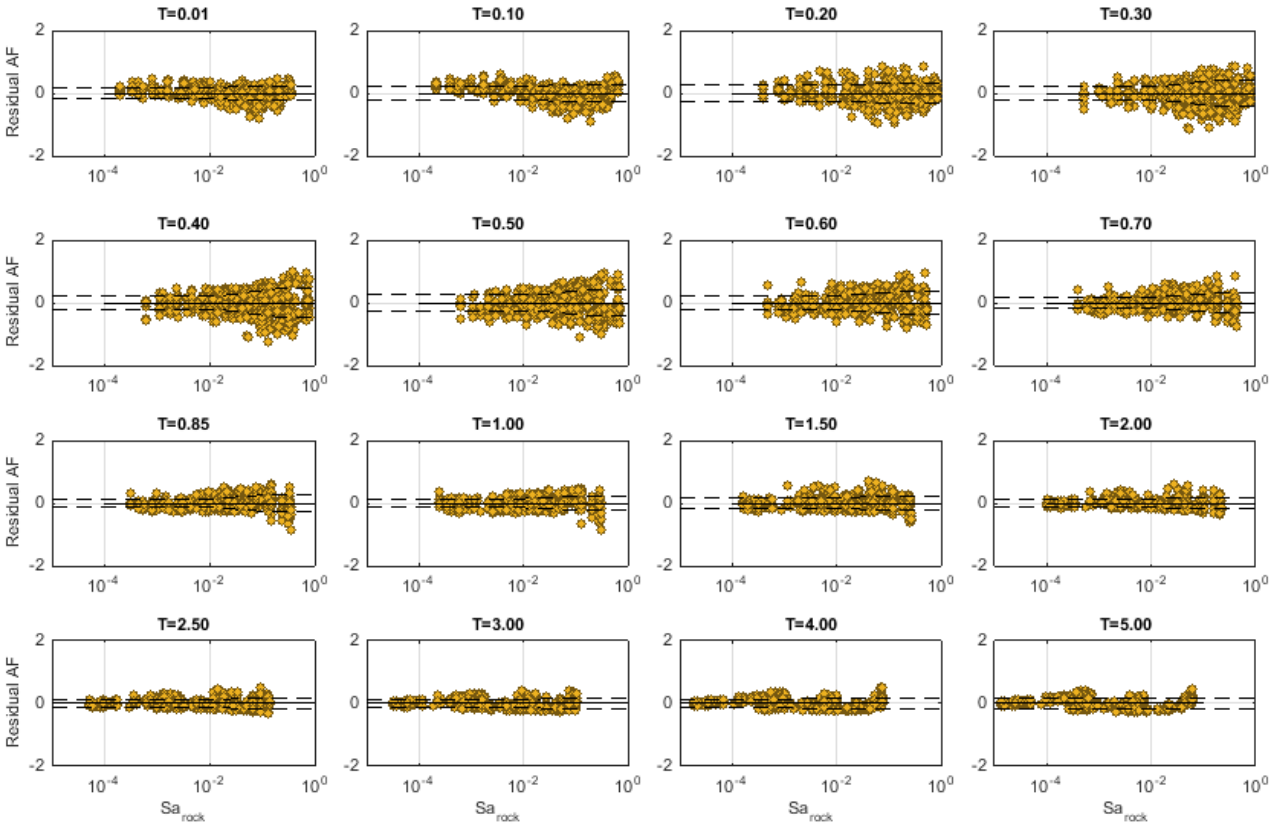

Figure 8.33. Residuals for the amplification factors for zone 1208 for all 16 target response periods; the standard deviation is heteroskedastic; Sa_{rock} has units of *g.*

The standard deviations obtained from Eq.(8.4) represent the uncertainty in the soil profile model at each voxel stack (Chapter 7) and the spatial variability across a zone. In addition, these standard deviations also include the effects of motion-to-motion variability because the AF were fit using a set of 100 input motions. The standard deviations, however, do not include the effects of the variability of modulus reduction and damping (MRD). The effects of MRD uncertainty on the AF were obtained from a review of relevant literature and for a pilot study conducted at the Groninger Forum site (Bommer *et al.,* 2015b). The final uncertainty model is presented in Section 9.3.

9. ZONIFICATION for SITE AMPLIFICATION FUNCTIONS

As has been noted several times, the most important enhancement in the V2 GMPEs compared with the earlier ground motion models for the Groningen field is the inclusion of site-specific non-linear amplification factors (AF). This approach required the development of GMPEs to predict motions at the NU_B reference rock horizon, which were broadly similar in their functional form to the V1 equations (Chapter 6). To develop a model of field-wide AFs to transfer these rock motions to the ground surface first required the development of layer models of velocity, density and damping, in addition to the selection of appropriate modulus reductions and damping curves for the different layers (Chapter 7). The model for the reference rock motions was then used to generate dynamic inputs at the NU_B horizon and these were used to run very large numbers of site response analyses for profiles covering the entire field. The output from these analyses was used to derive equations for non-linear AFs for the spectral acceleration at each of the 16 target periods (Chapter 8).

In this chapter, the zonification of the field is described whereby areas to which a common suite of AFs can be assigned are grouped into a single zone. The chapter begins with a description of the criteria adopted for grouping individual locations into zones (Section 9.1). The application of these criteria to the site response analyses results, leading to the definition of 167 zones across the study area, is the descried in Section 9.2. The final zone AF and their uncertainty are described in Section 9.3. Finally, Section 9.4 compares the computed AFs with the AF used at the stations for the inversion analyses, and also presents the V_{S30} characteristics of each of the zones.

9.1. Criteria for zonification

The starting point for the zonification for site response analyses is the geological model for the shallow depth range from Kruiver *et al.*, 2015 (Figure 9.1). The Groningen field, including a 5 km buffer, was divided into 256 geological zones. A geological zone is defined as a zone with distinct mappable geology as expressed by one or several characteristic sequence of deposits. The mappability depends on the quality and distribution of subsurface information and the associated uncertainties in the composition of each geological unit. Therefore, in some cases, a geological zone is homogeneous and contains one main characteristic sequence of deposits. In some other cases, however, the subsurface is more heterogeneous and the geological zone contains several characteristic sequences of deposits. For heterogeneous zones, smaller subdivisions were not feasible, because there is either lack of data to support a higher level of detail, or the geological zones would become too small to be of use in the hazard and risk analysis.

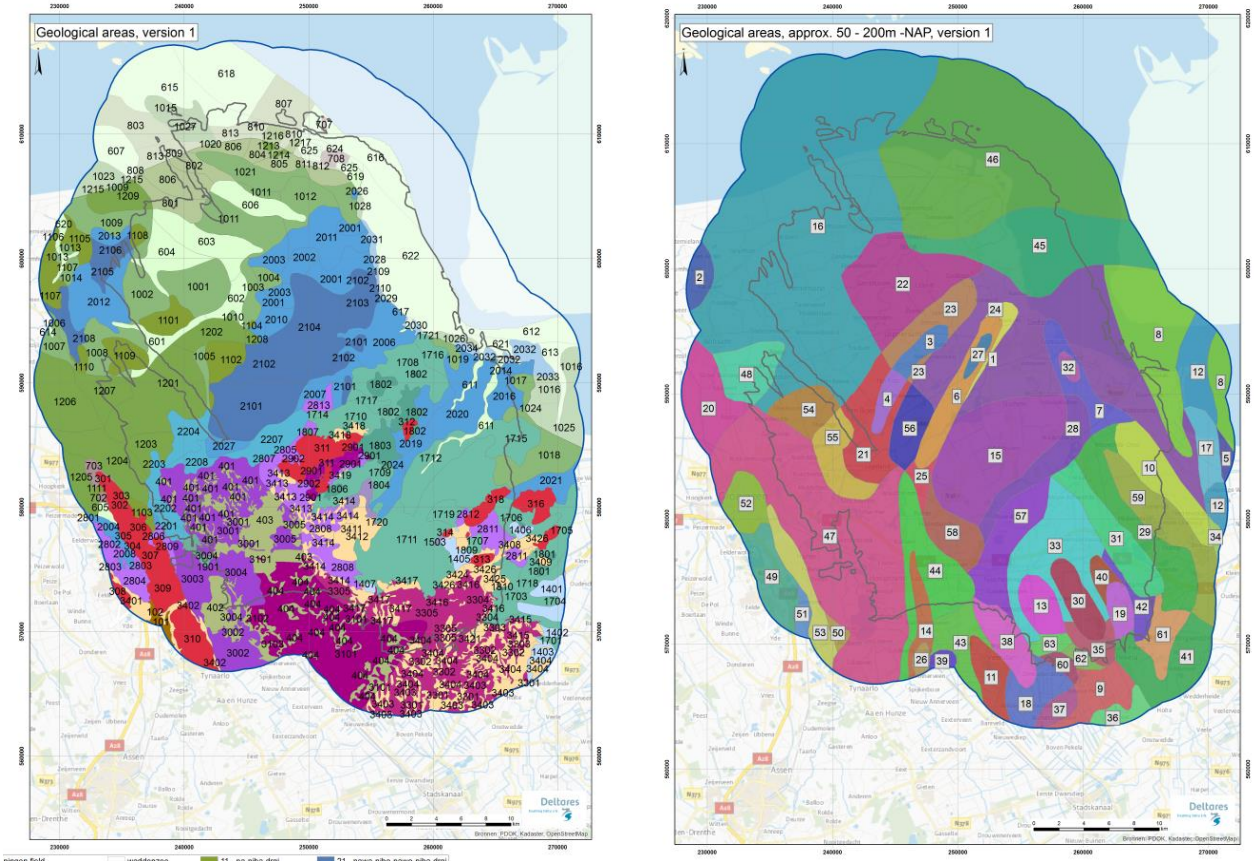

Figure 9.1. Geological zones for Version 1 of the geological model for site response for Groningen (Kruiver *et al.*, 2015). *Left*: depth range from surface to NAP-50 m; for legend see Figure 4.5. *Right*: for depth range below NAP-50 m, arbitrary colours

The geological zones were based on various sources of data including the beta version of GeoTOP, drillings and CPTs from the Dino database, additional CPTs from two companies (Fugro and Wiertsema and Partners), the digital elevation model AHN, the Digital Geological Model (DGM), the REgional Geohydrological Information System (REGIS II), and paleogeographical maps. The GeoTOP depth range is from the surface to NAP-50 m. Therefore, Version 1 of the geological model (V1) of Kruiver *et al.* (2015) consists of two depth ranges: surface to NAP-50 m (Figure 9.1, left) and NAP-50 m to NU_B (Figure 9.1, right). The shallow depth range model (surface to NAP-50 m) has been used as a basis for the zonification for site amplification because soft layers in the shallow subsurface have the largest effect on site response.

Several modification to the zonification of the V1 geological model were made. The general criteria was to eliminate smaller zones by merging them with larger zones provided that the amplification factors were sufficiently similar. This zonification approach is described in the next section. The objective, originally, was to optimise the grouping of voxel stacks into zones in order to minimise ϕ_{S2S} within a zone, while avoiding over-discretisation of the field. The practical application was slightly different but broadly consistent with this goal.

9.2. Zonification of the study area

The first modification of the geological zones in V1 of the geological model is to merge very small zones with adjacent bigger zones. In V1 the smallest zones consist of only 5 to 50 voxel stacks, corresponding to 5-50 hectares. Even with 5 signals per voxel stack, no representative spectral ratios can be determined for these very small zones. Moreover, very small zones are not practical in the hazard and risk analysis, which has a spatial aggregation level of several square kilometres. The decision to merge two or more zones is based on the comparison between the median and uncertainty of the amplification factors (Eq. 8.4) of the individual zones and the merged zone. If the median of the zones was not significantly different, then the merge proceeded. If the uncertainty in the AF (σ_{lnAF}) was significantly different between the two zones, then the merge proceeded only if the smaller zone had a smaller uncertainty. This was done to prevent under-estimation of the hazard in the smaller zone.

An example of the merge of a small zone (3419) and an adjacent large zone (2810) into a combined zone (2820) is shown in Figure 9.2.

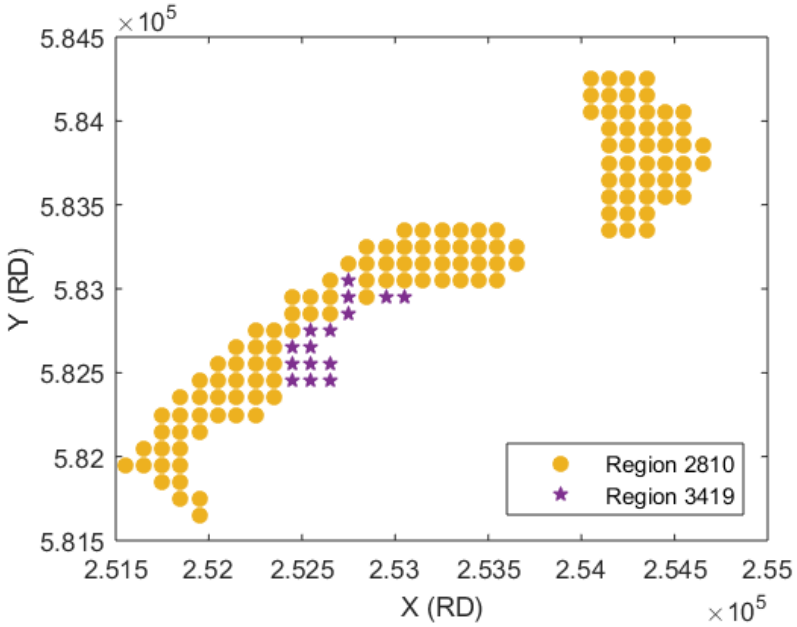

Figure 9.2. Geographical distribution of voxel stacks of the small zone (3419) and the adjacent larger zone (2810); the location of the zones within the Groningen field is shown in Figure 9.6

Figure 9.2 shows the geographical distribution of the voxel stacks for both zones. Figure 9.3 shows the AF and their uncertainty for selected periods. For most of the periods (4 selected periods are shown in Figure 9.3), the predicted AFs of the large zone (orange line) and of the combined zone (black line) are nearly identical. This is expected because the larger zone has a larger amount of data and these control the regression. However, the predicted AF of the individual zones are also similar to the combined AF. The σ_{lnAF} of the small area generally

has slightly lower values. However, this might be the result of a poor constraint of σ_{lnAF} due to the insufficient number of voxel stacks in the small zone. Therefore, in the case of (nearly) identical fits for the large and the combined zone, we have merged the small and the large zone into one. In that case, the new zone received a new code, corresponding to the main geological succession in the merged zone. Based on the comparative analysis of the fits, all geological zones in V1 that were smaller than 50 hectares (~ 50 voxel stacks) were merged with one of their adjacent zones.

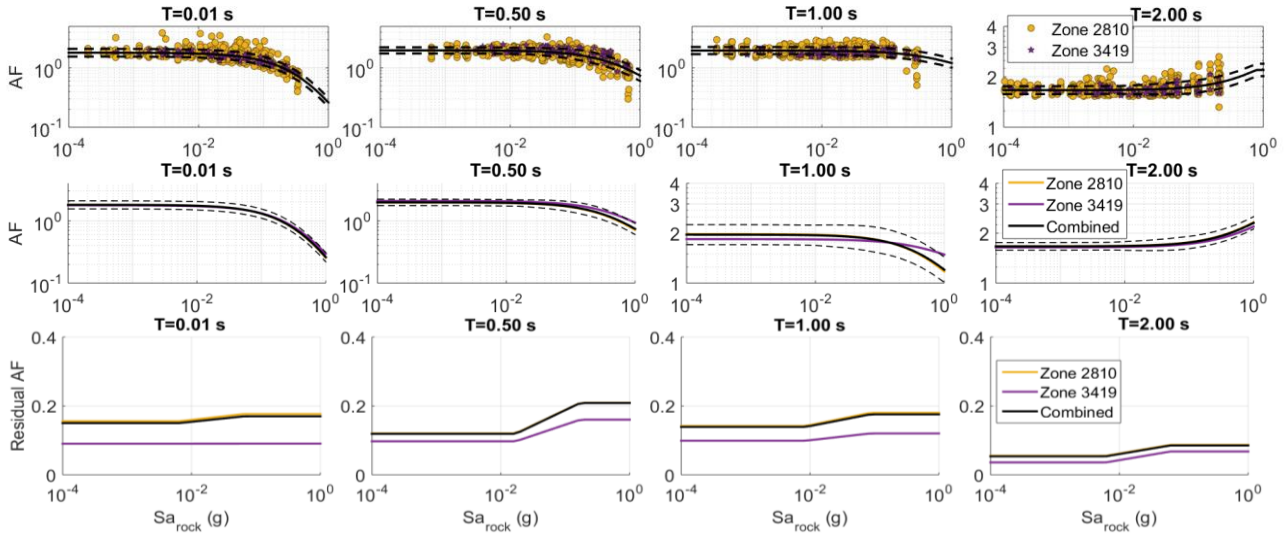

Figure 9.3. Example of merging AF results for small zone 3419, the adjacent large zone 2810 and the combined zone 2820 for periods (*l to r*) T = 0.01, 0.5, 1.0 and 2.0 s for the calculated amplification factor values (*top*), the resulting fit (*middle*) and the variability of the residuals (*bottom*)

The second modification of the geological zones in V1 of the geological model is related to the zones in the south of the Groningen region. In V1 there are patchy zones embedded in larger zones (Figure 9.1). In the south, the Pleistocene deposits reach, in some places, the current land surface. The topographical depressions were filled-in with peat and brook deposits. The patches are areas where no peat has accumulated, because these areas were elevated with respect to the surrounding land. The patches form a different geological zone than the surrounding region. Multipart polygons with irregular shapes and relatively small size, however, are difficult to deal with in the hazard and risk analysis. We therefore investigated the possibility of combining the patches with the zone they are embedded in.

An example of the comparison of the fit for one of the patchy zones embedded into a surrounding zone is given below. The geographical distribution of the voxel stacks is shown in Figure 9.4. The difference between the patches and the surrounding areas lies in the absence or the presence of peat. Therefore, we expect that there would be a difference in amplification factors. The AF are shown in Figure 9.5. Note, however, that the scatter of AF values within the zones (Figure 9.5, top panels), is larger than the scatter between the zones. The resulting fit through the AF data points is identical for the individual zones and for the combined zones (Figure 9.5, middle panel). Additionally, the σ_{lnAF} is nearly identical for most periods. In this example, the zones were merged into a new zone 3311.

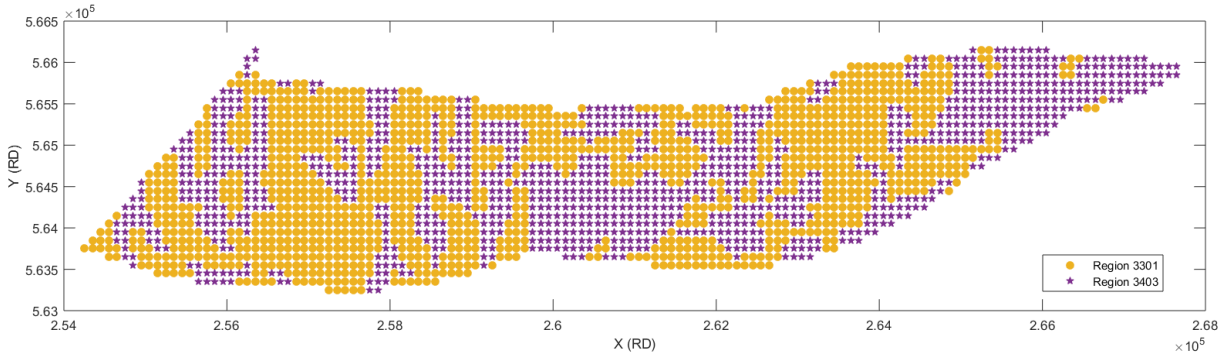

Figure 9.4. Geographical distribution of voxel stacks of the geographical mixed zones 3301 and 3403; the location of the zones within the Groningen region is shown in Figure 9.6

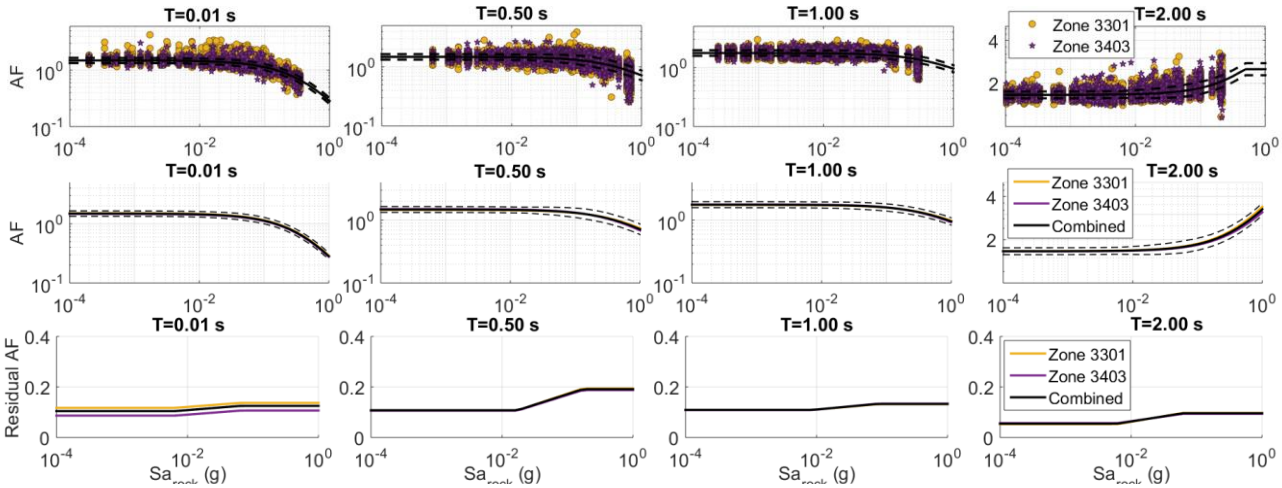

Figure 9.5. Example of merging AF results for geographically mixed zones 3301 and 3403 and the combined zone 3311 for periods (*l to r*) T = 0.01, 0.5, 1.0 and 2.0 s for the calculated amplification factor values (*top*), the resulting fit (*middle*) and the standard deviation of the residuals (*bottom*)

All zones in the south were analysed by comparing fits of individual zones and several combinations of combined zones. In case of identical or nearly identical fits (differences for only one or two periods), the zones were merged. In some cases, the fit of the combined zone (as evaluated by σ_{lnAF}) was worse than the fits of the individual zones (*e.g.,* for zones 3411 and 3412). In that case, they were kept as separate zones. The resulting zonation for the south part of Groningen is shown in Figure 9.6 (bottom panel).

The third modification to the V1 zonation model is to exclude geological zones that are situated in the Wadden Sea. Although large parts of the Wadden Sea become dry twice a day due to tides, there are no buildings situated on the mudflats. Therefore, Wadden Sea zones are not included in the current version (V2) of the geological zonation. The resulting V2 of the geological zones used for zonation of the spectral amplification functions is shown in Figure 9.7.

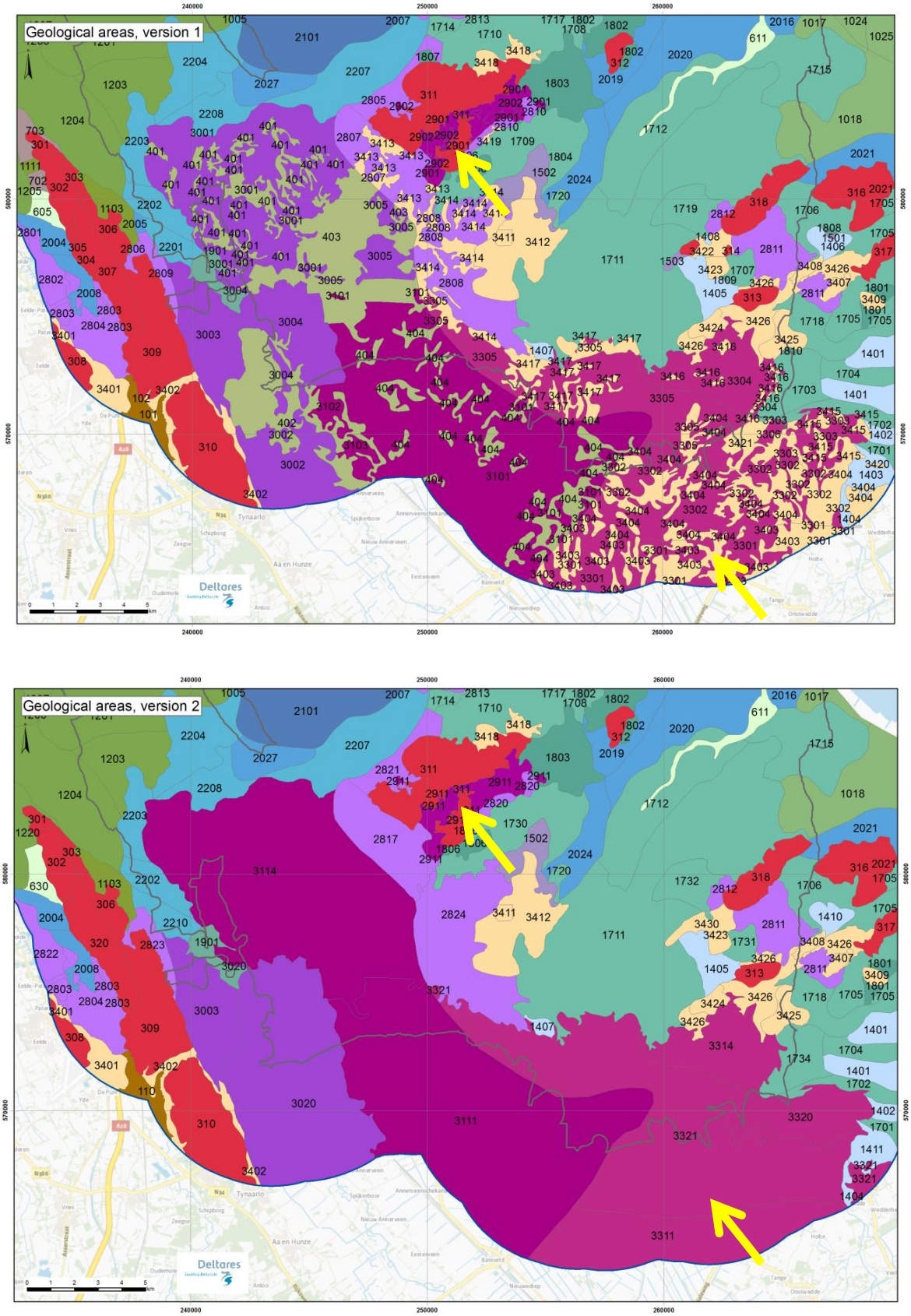

Figure 9.6. Zoom of geological zones of V1 before merging (*top*) and of the current zonation after merging (V2, *bottom*). The examples in Figure 9.2 and 9.4 are indicated by the yellow arrows; for legend, see Figure 4.5

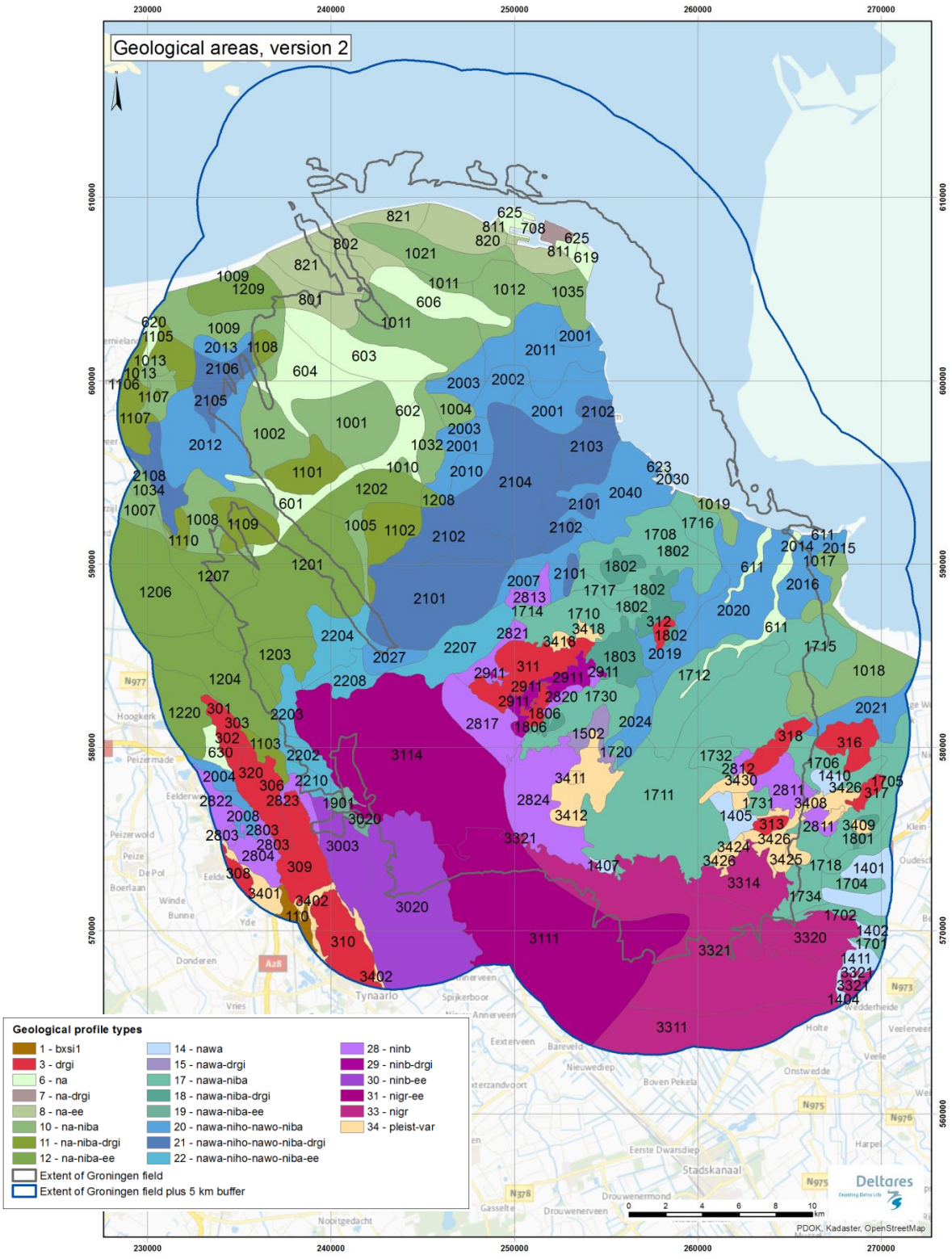

Figure 9.7. Version 2 of the geological zonation, used for the site amplification functions in GMPE V2

There are 167 zones defined in the V2 zonation of the field compared to the 256 zones in the original geological zonation (V1) of the field. A table in digital format is provided containing the zone assigned to each coordinate (see Executive Summary).

9.3. Zone amplification factors

The amplification factors for the zones were computed from the site response analyses described in Section 8.3. The V_S profile for each voxel stack was randomized using the model described in Chapter 7. A single randomisation per voxel stack was used, and all the voxel stacks within a zone were grouped to compute the amplification factors for the zone. The alternative (*i.e.*, to generate multiple randomization for each voxel-stack within a zone) resulted in a much larger number of site response analyses without much difference in the resulting factors. The computed AF at each period were fit using Eq.(8.4), and maximum and minimum limits on the AF were imposed, as described in Section 8.3. The zone amplification functions for the entire study area are shown in Figure 9.8. Observe that these functions are highly non-linear. For the Groningen profiles, the nonlinearity implies a reduction in AF for shorter periods but an increase in the AFs at longer periods. This increase is expected as the resonant period of the sites shifts to longer periods as the soil softens.

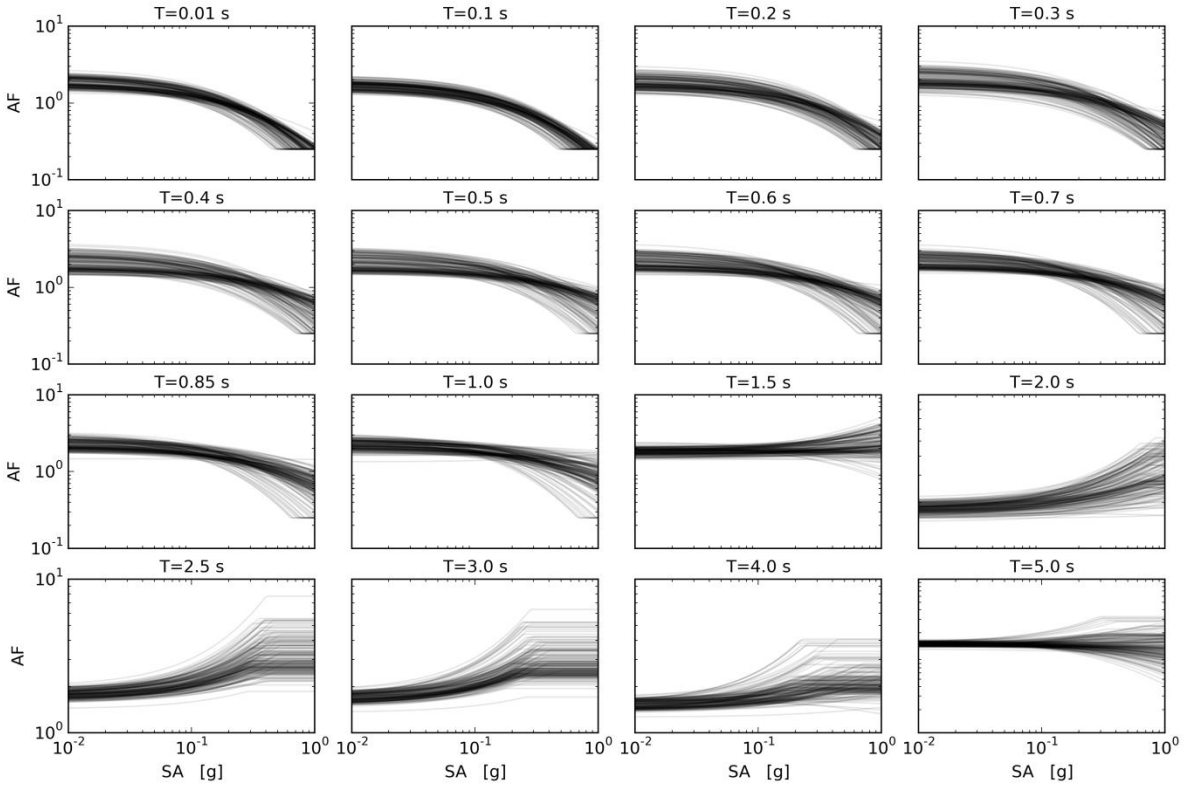

Figure 9.8. Fitted AF functions for all zones for all periods; note that y-axes are not the same in all cases and labels on left-hand side do not always apply (*courtesy of Stephen Bourne*)

The standard deviations of the amplification factors obtained from Eq. (8.4) (*i.e.*, σ_{lnAF}) were fitted to an heteroskedastic tri-linear model (see bottom panels of Figures 9.3 and 9.5) given by:

$$\sigma_{\ln AF} = \sigma_{\ln AF,1} \qquad Sa_{NU\_B} < Sa_{rock,low} \qquad (9.1a)$$

$$\sigma_{\ln AF} = (\sigma_{\ln AF,2} - \sigma_{\ln AF,1})\left(\frac{\ln(Sa_{NU\_B}) - \ln(Sa_{rock,low})}{\ln(Sa_{rock,high}) - \ln(Sa_{rock,low})}\right) \qquad Sa_{rock,low} \le Sa_{NU\_B} \le Sa_{rock,high} \qquad (9.1b)$$

$$\sigma_{\ln AF} = \sigma_{\ln AF,2} \qquad Sa_{NU\_B} > Sa_{rock,high} \qquad (9.1c)$$

where $\sigma_{lnAF,1}$, $\sigma_{lnAF,2}$, $Sa_{rock,low}$ and $Sa_{rock,high}$ are model parameters, and Sa_{NUB} is the predicted spectral acceleration at the reference rock (Section 6.6). The period dependence of all the parameters in Eq.(9.1) was omitted for clarity. The parameters for Equation 8.4, including the uncertainty parameters $\sigma_{lnAF,1}$, $\sigma_{lnAF,2}$ in Eq. (9.1), were computed using Maximum Likelihood regression. However, $Sa_{rock,high}$ and $Sa_{rock,low}$ could not be constrained in the regression and were determined from visual inspection. To maintain consistency across periods, $Sa_{rock,low}$ was obtained from the predictions of the GMPE at the reference rock (Section 6.6) for a scenario with **M** 5 and R_{epi} 15 km. $Sa_{rock,high}$ was set equal to $Sa_{rock,low}$ multiplied by 10.

As indicated in Section 8.3, the standard deviations obtained from Eq.(8.4) and given in Eq.(9.1) represent the effect of uncertainty in the soil profile model at each voxel stack (Chapter 7) and the spatial variability across voxel stacks in a zone. In addition, the σ_{lnAF} also includes the effects of motion-to-motion variability. These standard deviations are the basis for the uncertainty in the site response within a zone, ϕ_{S2S}. The subscript "S2S" implies that this uncertainty component represents the "site-to-site" variability for all sites within a given zone. The following issues, which were not taken into account in σ_{lnAF}, were considered when modifying these values to obtain the ϕ_{S2S} model:

- Modelling error
- Empirical bounds
- Contribution to uncertainty in AF due to MRD uncertainty

Modelling error can result from limitations of the adopted site response procedure. If the modelling procedure is likely to produce a bias in the results, this bias needs to be accounted for. One possible approach is to inflate the σ_{lnAF} to account for the bias. The literature review presented in Section 8.1 indicated that, in general, the EQL procedure has positive bias in computed spectral accelerations with respect to more accurate NL procedures. Similarly, the RVT procedure also produces positive bias with respect to time series analyses. For these reasons, it was considered that the selected RVT based EQL analyses results in conservative biases and no modelling error was added to σ_{lnAF}.

Empirical bounds to computed site response uncertainty may be necessary because the one-dimensional site response analyses predict no site effects at periods longer than the first-mode period of the site. However, empirical evidence shows that the site-to-site variability at long periods does not decrease significantly with V_{S30}. Similar to other projects (*e.g.*, Bommer *et al.*, 2015d), the minimum level of epistemic uncertainty on the site term was selected based

on the site-to-site variability at borehole stations in the KiK-net array (Rodriguez-Marek *et al.,* 2014). This variability is 0.2. The site conditions at borehole stations in the KiK-net array are relatively uniform and the site-to-site variability does not show dependency on site properties. For these stations, site response would predict almost no site-to-site variability, hence the measured 0.2 value is considered an empirical lower bound to ϕ_{S2S}. This value was selected as the lower bound for ϕ_{S2S} for applications in the Groningen region.

The additional uncertainty in the amplification factors needed to account for the epistemic uncertainty in MRD was obtained from a pilot study conducted at the Forum site (Bommer *et al.,* 2015b). The contributions to AF uncertainty from both V_S uncertainty and MRD uncertainty are shown in Figure 9.9. Note that the contribution to AF uncertainty at short periods is larger for MRD variability than for V_S variability. This trend reverses at longer periods. Other studies performed similar analyses to evaluate the contribution to AF variability from V_S and MRD. Kwok *et al.* (2008) and Li & Assimaki (2010) concluded that MRD uncertainty has a smaller contribution than V_S uncertainty to the total AF uncertainty. On the other hand, Rathje *et al.* (2010) observed similar contributions to AF uncertainty from V_S and MRD.

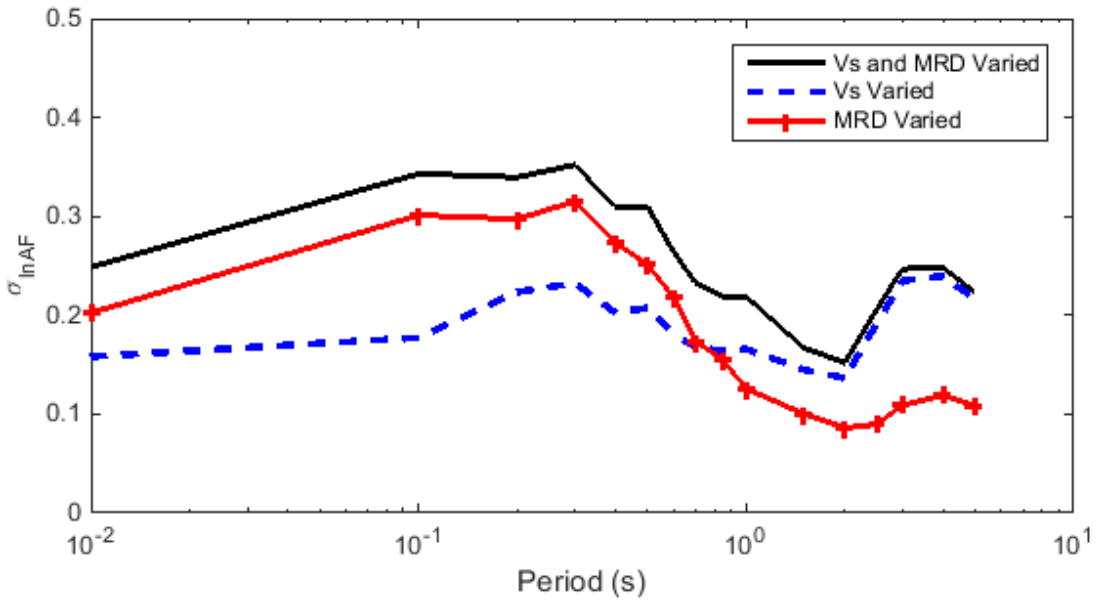

Figure 9.9. Contribution to AF variability from variability of V_S an MRD for the Groninger Forum site

The uncertainty in AF shown in Figure 9.9 corresponds to strong levels of shaking. For lower shaking intensity, it is expected that the uncertainty due to MRD curves would be lower. The final model for the contribution to AF uncertainty from MRD curves ($\sigma_{lnAF,MRD}$) is shown in Figure 9.10. In this figure, the black line corresponds to the contributions inferred from the Forum study (these values are slightly lower than those in Figure 9.9 to account for some negative correlation between the contribution from V_S and MRD variability). Note that the proposed model for High Intensity shaking envelopes the Forum results.

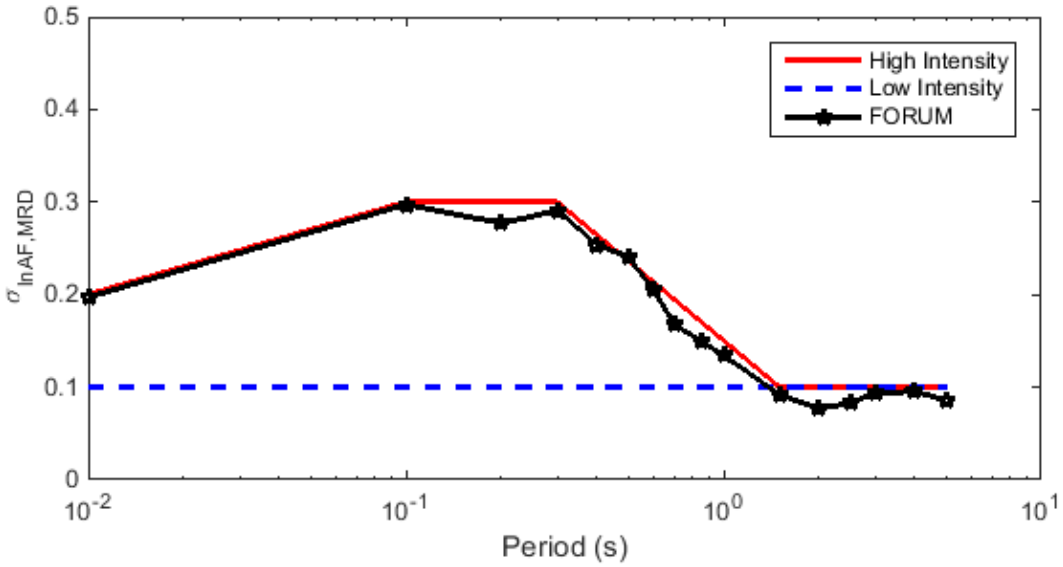

Figure 9.10. Model for the contribution to uncertainty of MRD variability

The final model for the site-to-site variability in the amplification factors is then given by:

$$\phi_{S2S} = \phi_{S2S,1} \qquad Sa_{NU\_B} < Sa_{rock,low} \qquad (9.2a)$$

$$\phi_{S2S} = (\phi_{S2S,2} - \phi_{S2S,1})\left(\frac{\ln(Sa_{NU\_B}) - \ln(Sa_{rock,low})}{\ln(Sa_{rock,high}) - \ln(Sa_{rock,low})}\right) \qquad Sa_{rock,low} \le Sa_{NU\_B} \le Sa_{rock,high} \qquad (9.2b)$$

$$\phi_{S2S} = \phi_{S2S,2} \qquad Sa_{NU\_B} > Sa_{rock,high} \qquad (9.2c)$$

where

$$\phi_{S2S,1} = \sqrt{(\sigma_{\ln AF,1})^2 + (\sigma_{\ln AF,MRD,low\_intensity})^2} \qquad (9.3a)$$

$$\phi_{S2S,2} = \sqrt{(\sigma_{\ln AF,2})^2 + (\sigma_{\ln AF,MRD,high\_intensity})^2} \qquad (9.3b)$$

where $\sigma_{lnAF,MRD}$ is the additional uncertainty due to MRD for low and high intensity given by the red line and blue lines in Figure 9.10, respectively; and σ_{lnAF} are obtained from Maximum Likelihood regression of Eq.(8.4) along with the uncertainty model in Eq.(9.1). In addition, a minimum value of ϕ_{S2S}=0.2 is imposed.

An example of the model fit for one individual zone (1208) was shown in Figure 8.32. The resulting values for the fit for the median model (f_1, f_2, f_3) and for the standard deviation model ($\phi_{s2s,1}$, $\phi_{s2s,2}$, $Sa_{rock,low}$, and $Sa_{rock,high}$) are listed in Table 9.1 for Zone 1208. The model for ϕ_{S2S} is shown in Figure 9.11 along with the residuals of the computed AFs. Note that the heteroskedasticity of the standard deviation is most pronounced for periods between T = 0.3 s and T = 0.85 s. A table in digital format is provided to the hazard and risk team containing

the fit parameters for all 167 geological zones of version V2 for all 16 periods (see Executive Summary).

Table 9.1. Example of the fit parameters and ϕ_{S2S} for zone 1208

Zone	T (s)	f_1	f_2	f_3	AF_{min}	AF_{max}	$\phi_{S2S,1}$	$\phi_{S2S,2}$	$Sa_{rock,low}$	$Sa_{rock,high}$
1208	0.01	0.8421	-2.6046	0.5	0.25	2.3189	0.2000	0.3006	0.0065	0.0650
1208	0.1	0.6416	-2.3279	0.5	0.25	1.8977	0.2416	0.4006	0.0090	0.0896
1208	0.2	0.6116	-2.0084	0.5	0.25	1.8404	0.2732	0.4438	0.0149	0.1487
1208	0.3	0.9645	-2.2973	0.5	0.25	2.6170	0.2453	0.5145	0.0164	0.1640
1208	0.4	1.2066	-2.3332	0.5	0.25	3.3323	0.2546	0.5197	0.0181	0.1815
1208	0.5	1.1532	-2.0644	0.5	0.25	3.1605	0.2640	0.4809	0.0171	0.1712
1208	0.6	1.0461	-1.8611	0.5	0.25	2.8414	0.2478	0.4053	0.0137	0.1370
1208	0.7	0.9973	-1.6053	0.5	0.25	2.7076	0.2113	0.3535	0.0115	0.1149
1208	0.85	0.9542	-1.1945	0.5	0.25	2.6316	0.2000	0.3087	0.0098	0.0983
1208	1	0.9934	-0.9510	0.5	0.25	3.0409	0.2000	0.2753	0.0085	0.0855
1208	1.5	0.7247	0.6391	0.5	0.25	4.6510	0.2000	0.2499	0.0076	0.0759
1208	2	0.6869	0.9613	0.5	0.25	4.4317	0.2000	0.2108	0.0062	0.0620
1208	2.5	0.6536	1.4060	0.5	0.25	3.8687	0.2000	0.2000	0.0037	0.0369
1208	3	0.5888	1.5427	0.5	0.25	3.3307	0.2000	0.2000	0.0027	0.0266
1208	4	0.4871	0.7088	0.5	0.25	2.4876	0.2000	0.2000	0.0019	0.0186
1208	5	0.4331	-0.2291	0.5	0.25	2.0362	0.2000	0.2000	0.0015	0.0147

Some more examples of the AF for various zones that have different levels of AF values are shown in Figures 9.12 through 9.14. Figure 9.12 shows the AF for Zone 309, which generally has low AF values. This region is located in the south and has a relatively high median V_{S30} (262 m/s). Figure 9.13 shows the results for Zone 601, which generally has intermediate AF values and also has an intermediate V_{S30} value (184 m/s). Figure 9.14 shows the results for Zone 1009 which has generally high AF values. The V_{S30} for this zone is 174 m/s.

The geographical distribution of the median AF and the ϕ_{S2S} for each zone are plotted in Figures 9.15 to 9.22 for four selected periods (0.01, 0.5, 1.0 and 2.0 s) and for selected combinations of **M** and R_{epi}. The magnitude-distance scenarios define the median spectral accelerations at the reference rock; these median values are multiplied by a factor that takes into account the possible deviations of the reference rock scenarios from their median values.

Figure 9.15 shows the AF for a **M** (4.0) and R_{epi} (50 km) scenario. This scenario leads to nearly linear site response at all periods. Figure 9.16 is plotted for an intermediate magnitude scenario (**M** 5.0 and R_{epi} 1 km). Figure 9.17 is for a large earthquake that generates strong motions at the reference rock (**M** 6.5, R_{epi} 1 km). Figure 9.18 is an example of a scenario that would generate very large reference rock motions (**M** 6.5 and R_{epi} 1 km: factor is 3.32). This factor corresponds approximately to a deviation of two epsilons considering a sigma of 0.6 at the reference rock level. In all cases, the median AF is shown. Figures 9.19 to 9.22 show the corresponding ϕ_{S2S} for these scenarios.

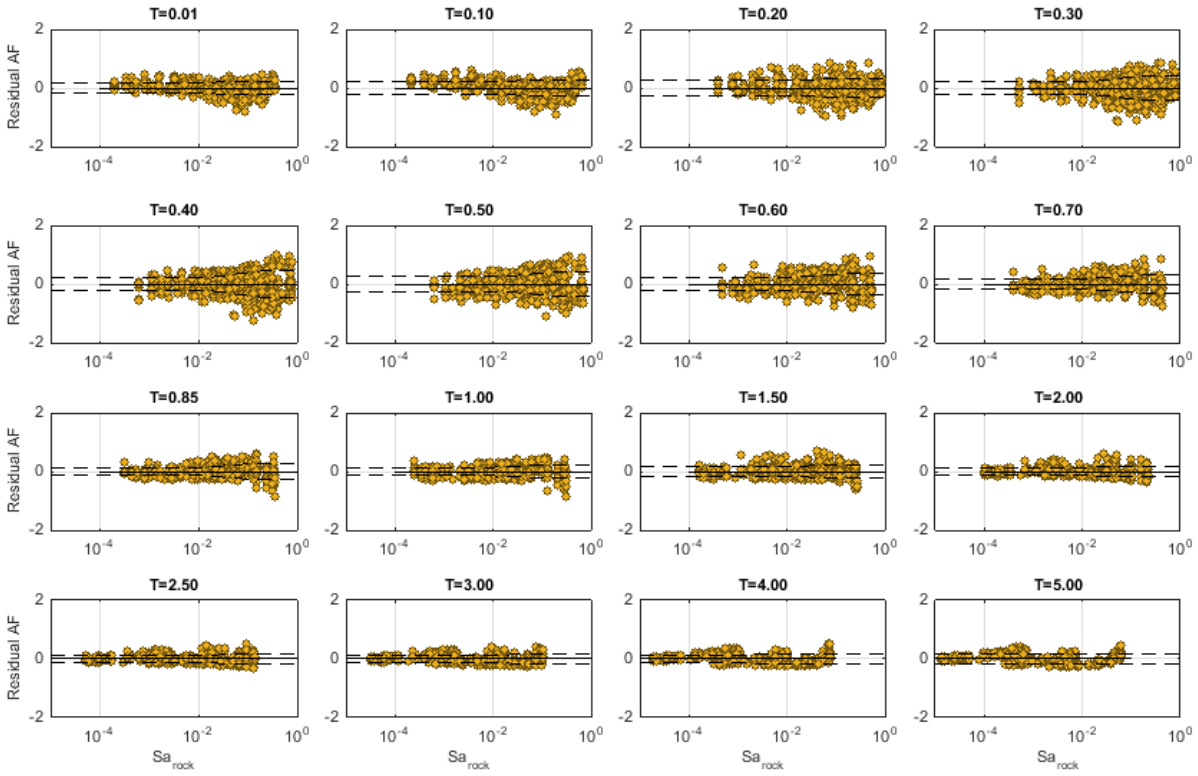

Figure 9.11. Residuals for the amplification factors for zone 1208 for all periods. The standard deviation is heteroskedastic

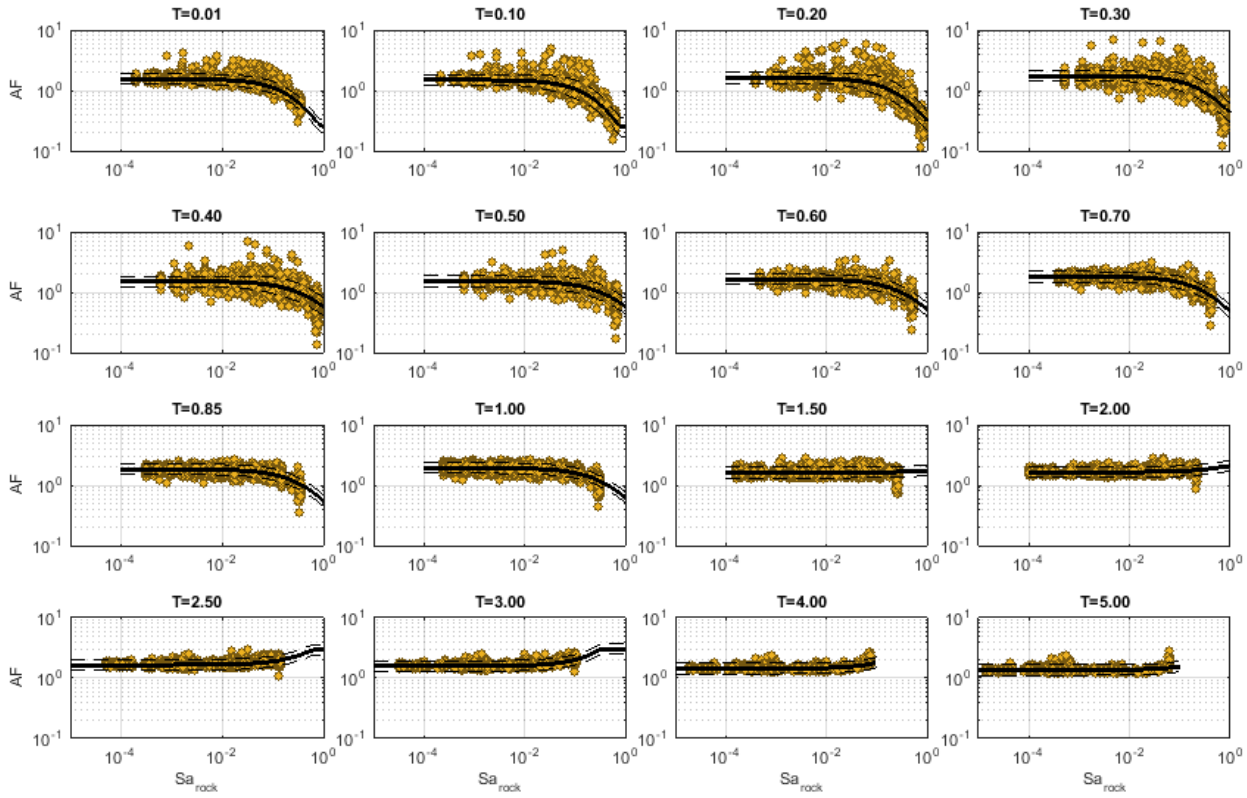

Figure 9.12. AF for Zone 309 (V_{S30} = 262 m/s), located in the south

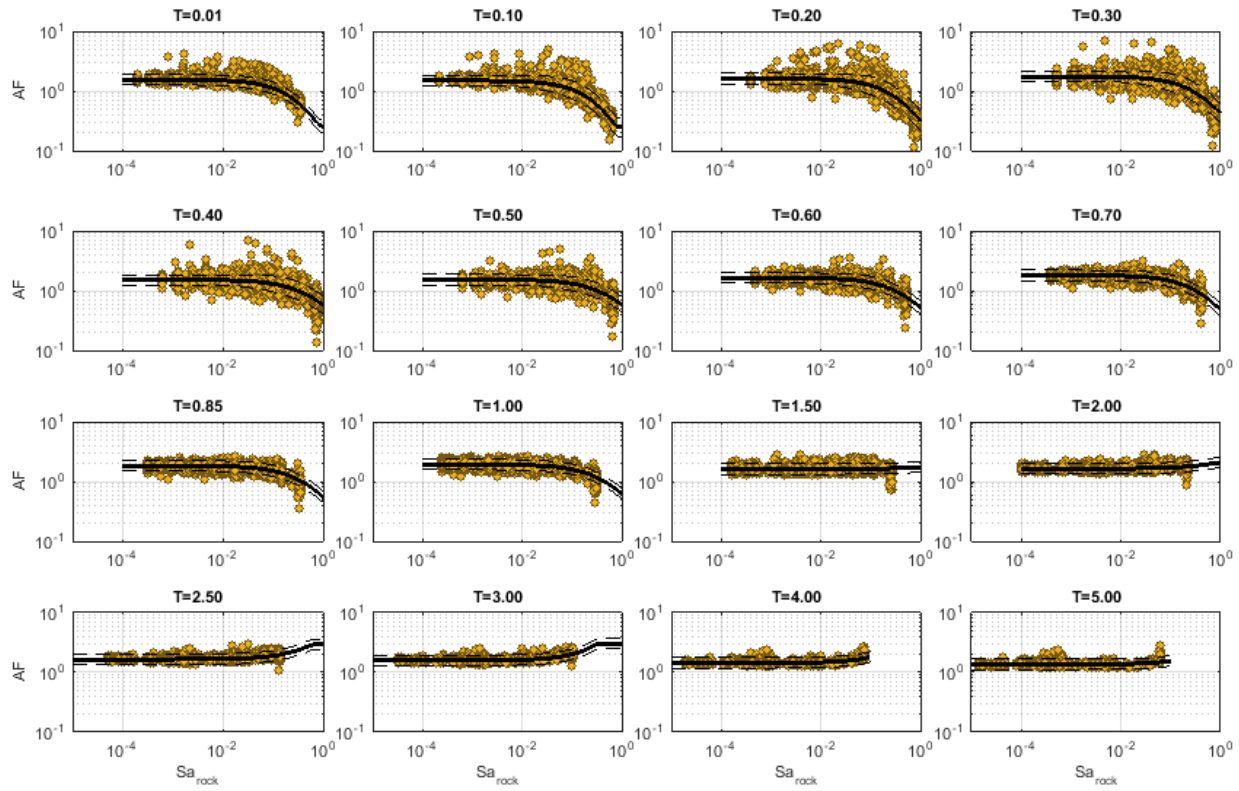

Figure 9.13. AF for Zone 601 (V_{S30} = 184 m/s), located in the centre

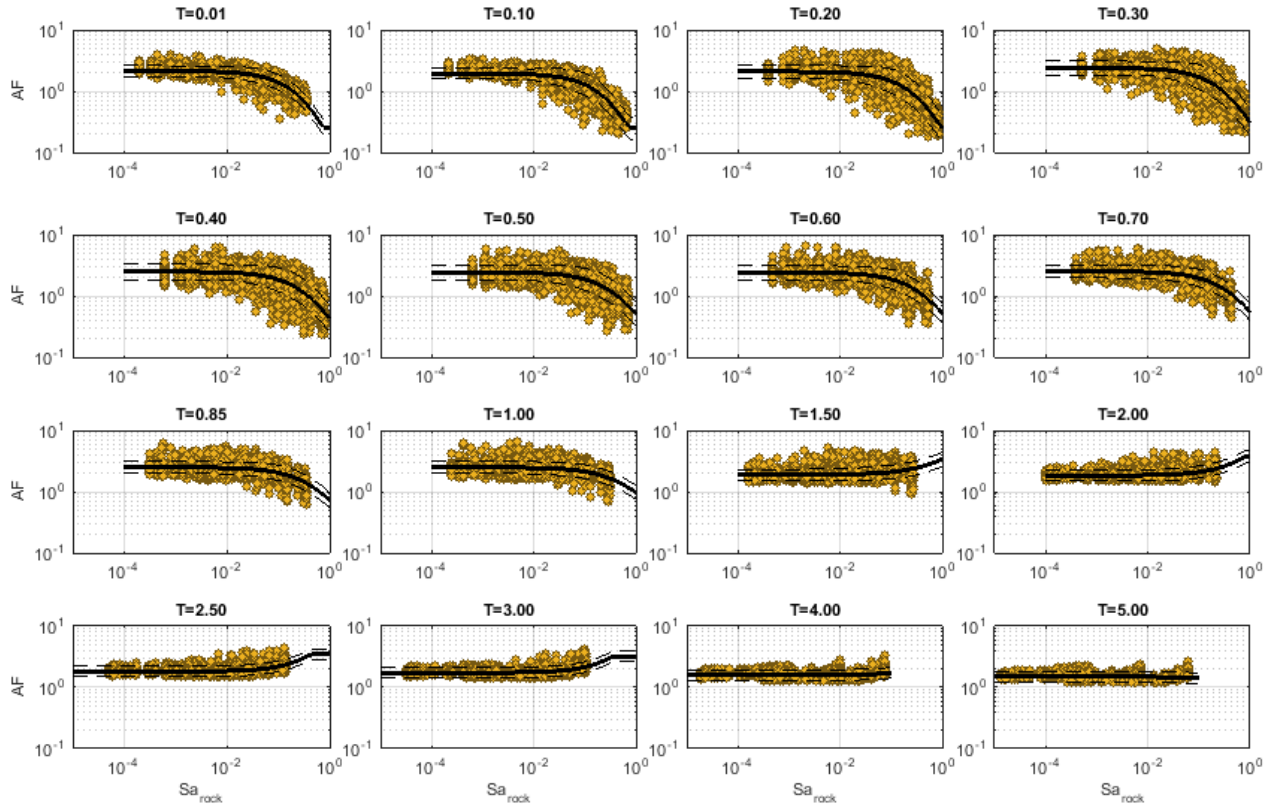

Figure 9.14. AF for Zone 1009 (V_{S30} = 174 m/s), located in the north-west

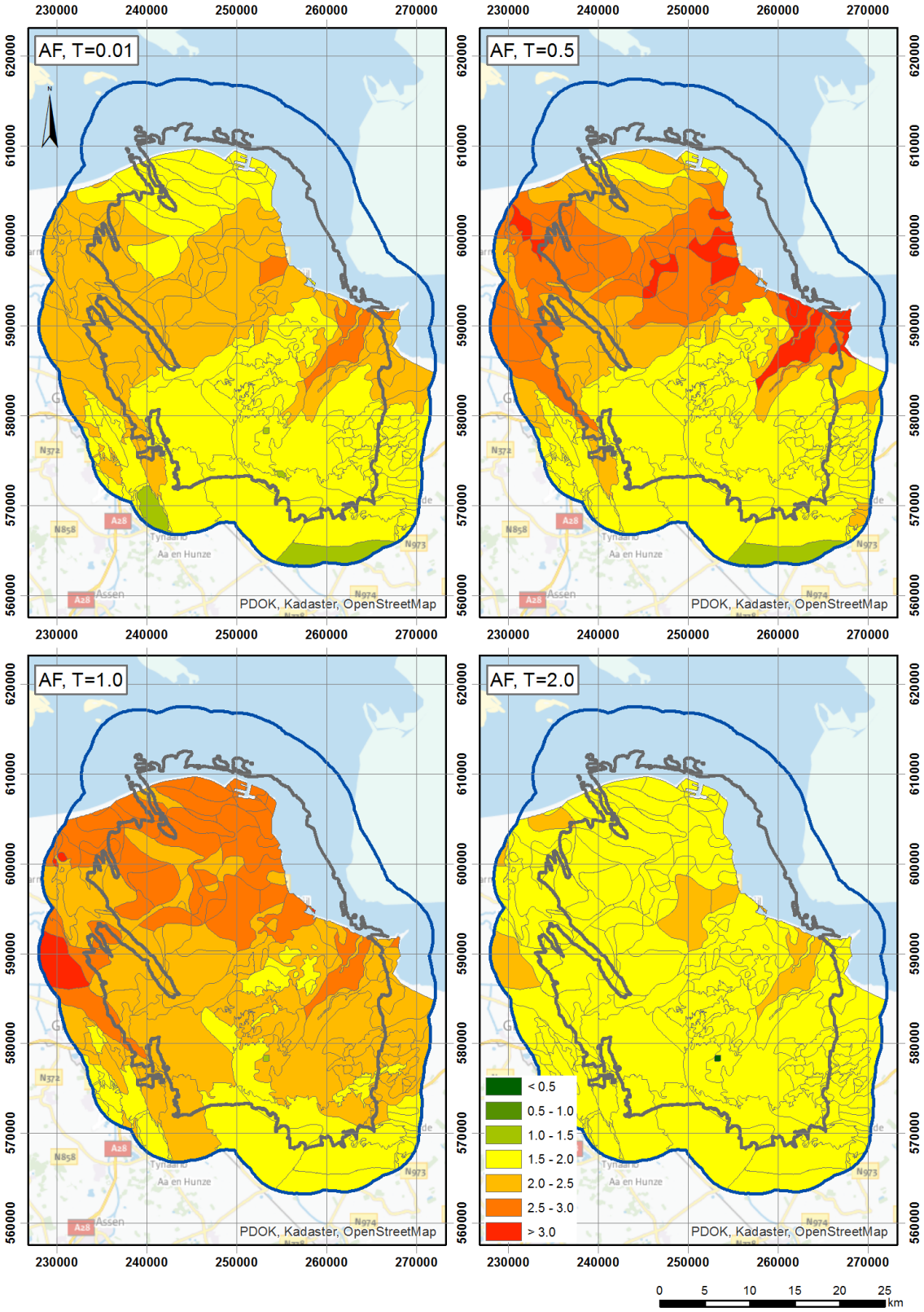

Figure 9.15. AF for the Groningen region for a scenario with **M** 4.0 and R_{epi} 50 km; NU_B acceleration factor = 1

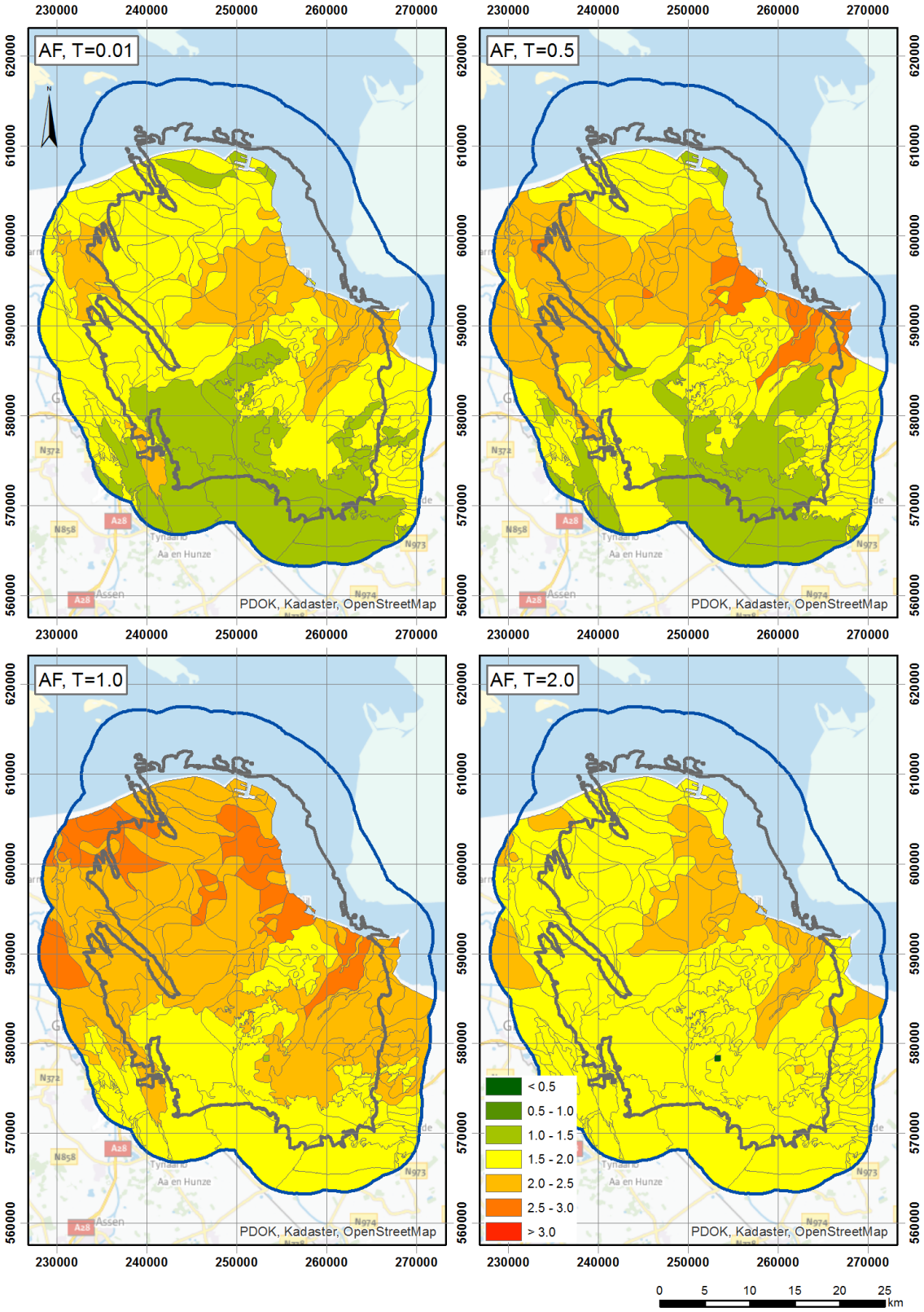

Figure 9.16. AF for the Groningen region for a scenario with **M** 5.0 and R_{epi} 1 km; NU_B acceleration factor = 1

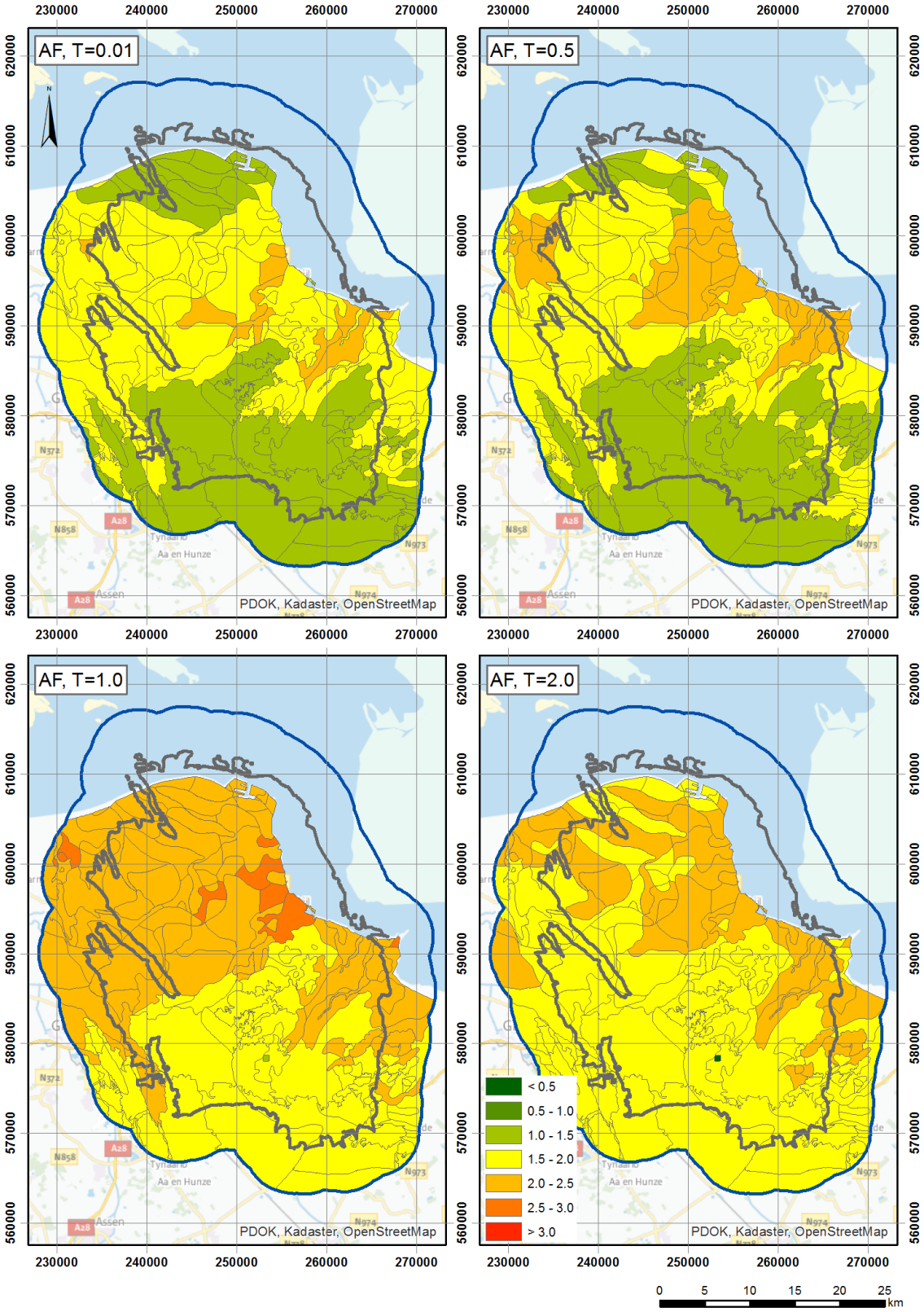

Figure 9.17. AF for the Groningen region for a scenario with **M** 6.5 and R_{epi} 1 km; NU_B acceleration factor = 1

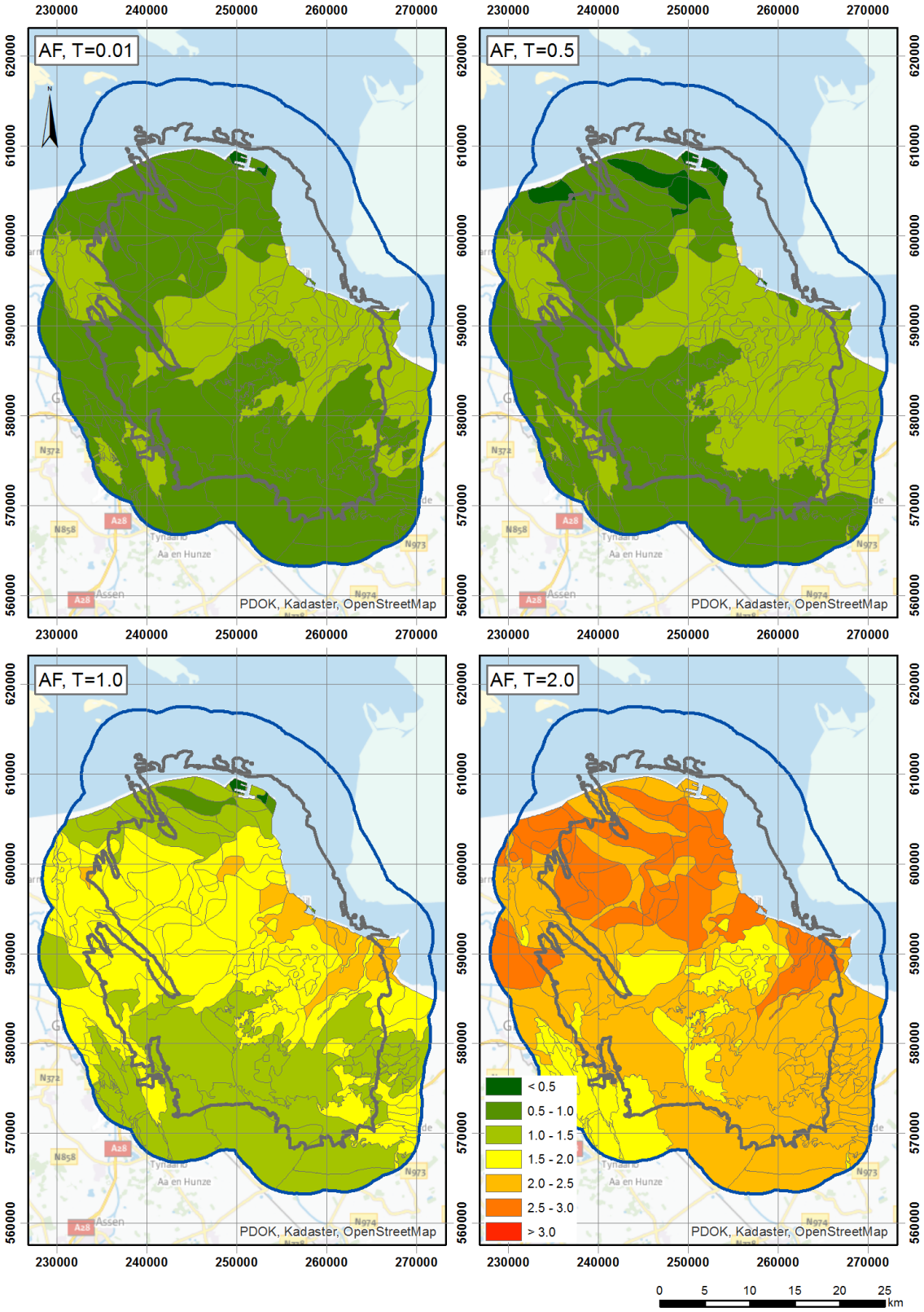

Figure 9.18. AF for the Groningen region for a scenario with **M**=6.5 and R_{epi}=1 km; NU_B acceleration factor = 3.32

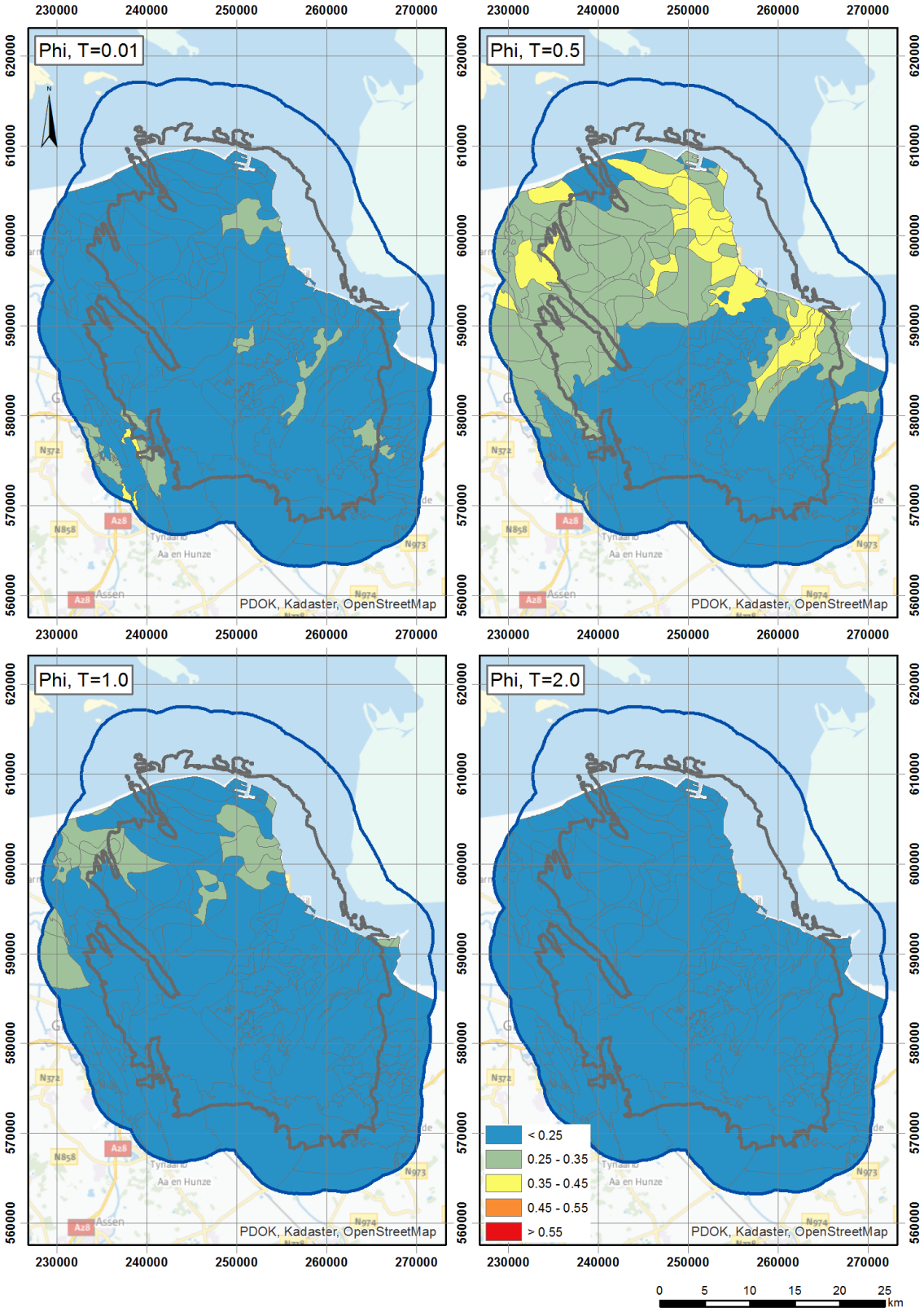

Figure 9.19. ϕ_{S2S} for the Groningen region for a scenario with **M** 4.0 and R_{epi} 50 km; NU_B acceleration factor = 1

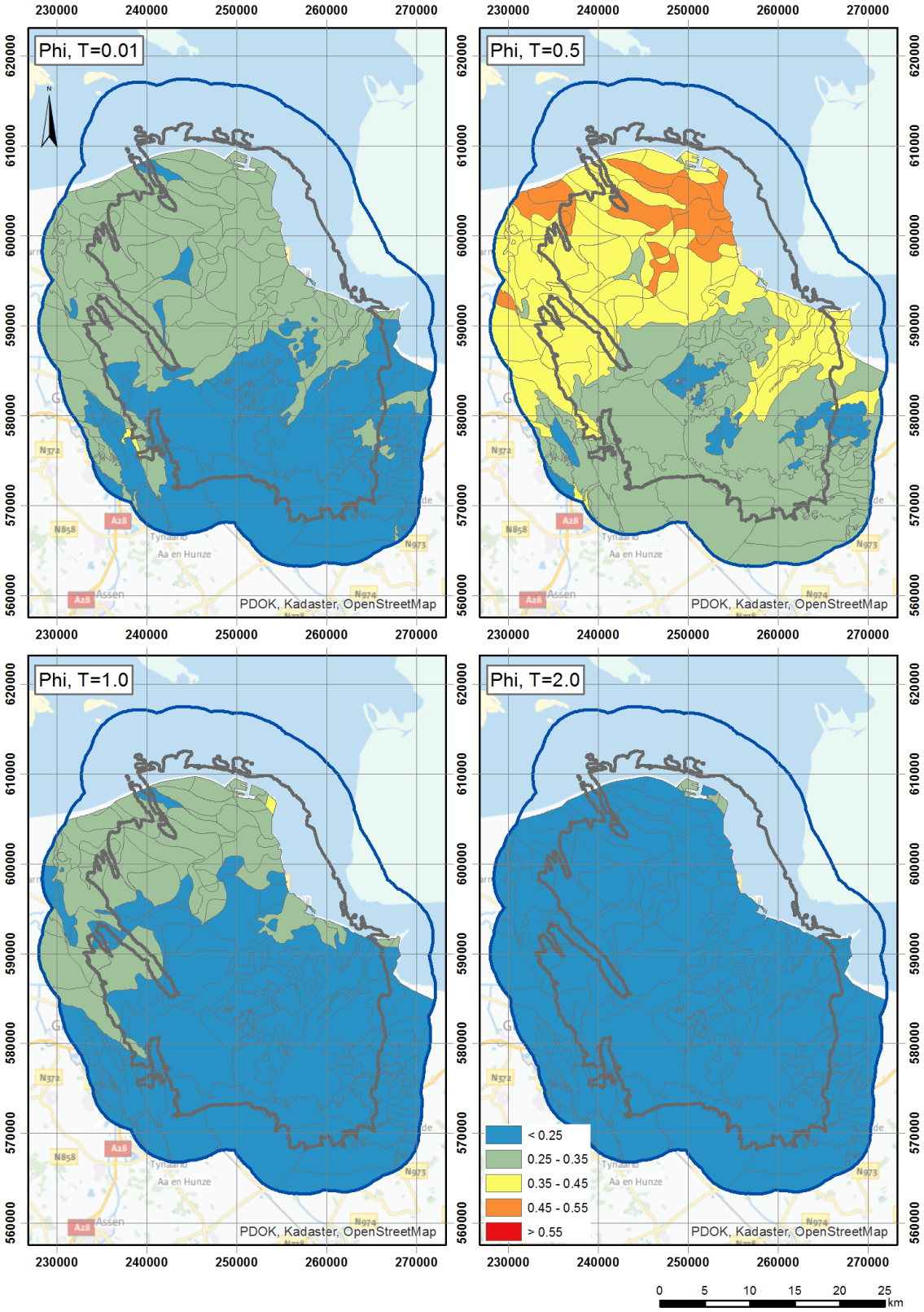

Figure 9.20. ϕ_{S2S} for the Groningen region for a scenario with **M** 5.0 and R_{epi} 1 km; NU_B acceleration factor = 1

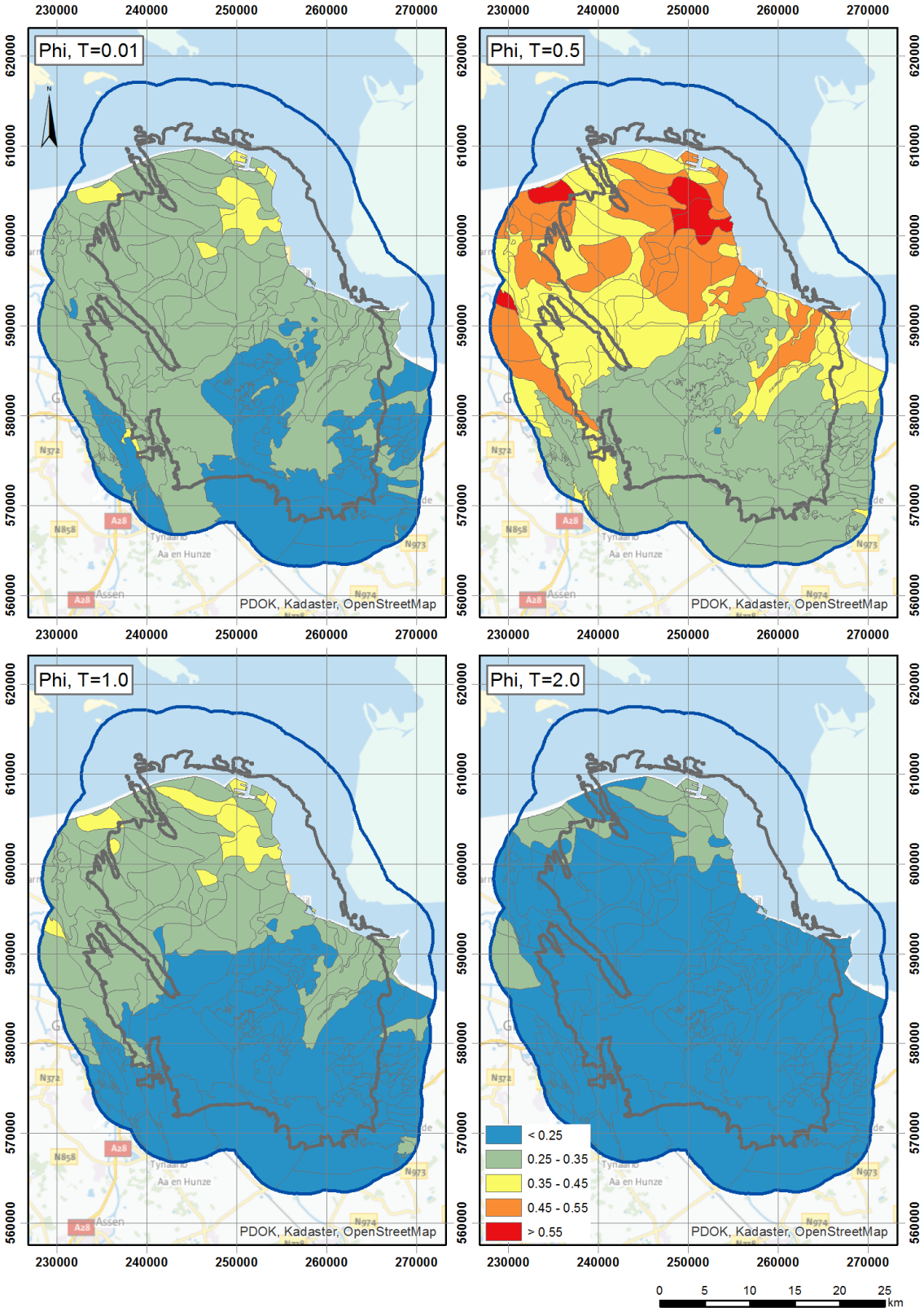

Figure 9.21. ϕ_{S2S} for the Groningen region for a scenario with **M** 6.5 and R_{epi} 1 km; NU_B acceleration factor = 1

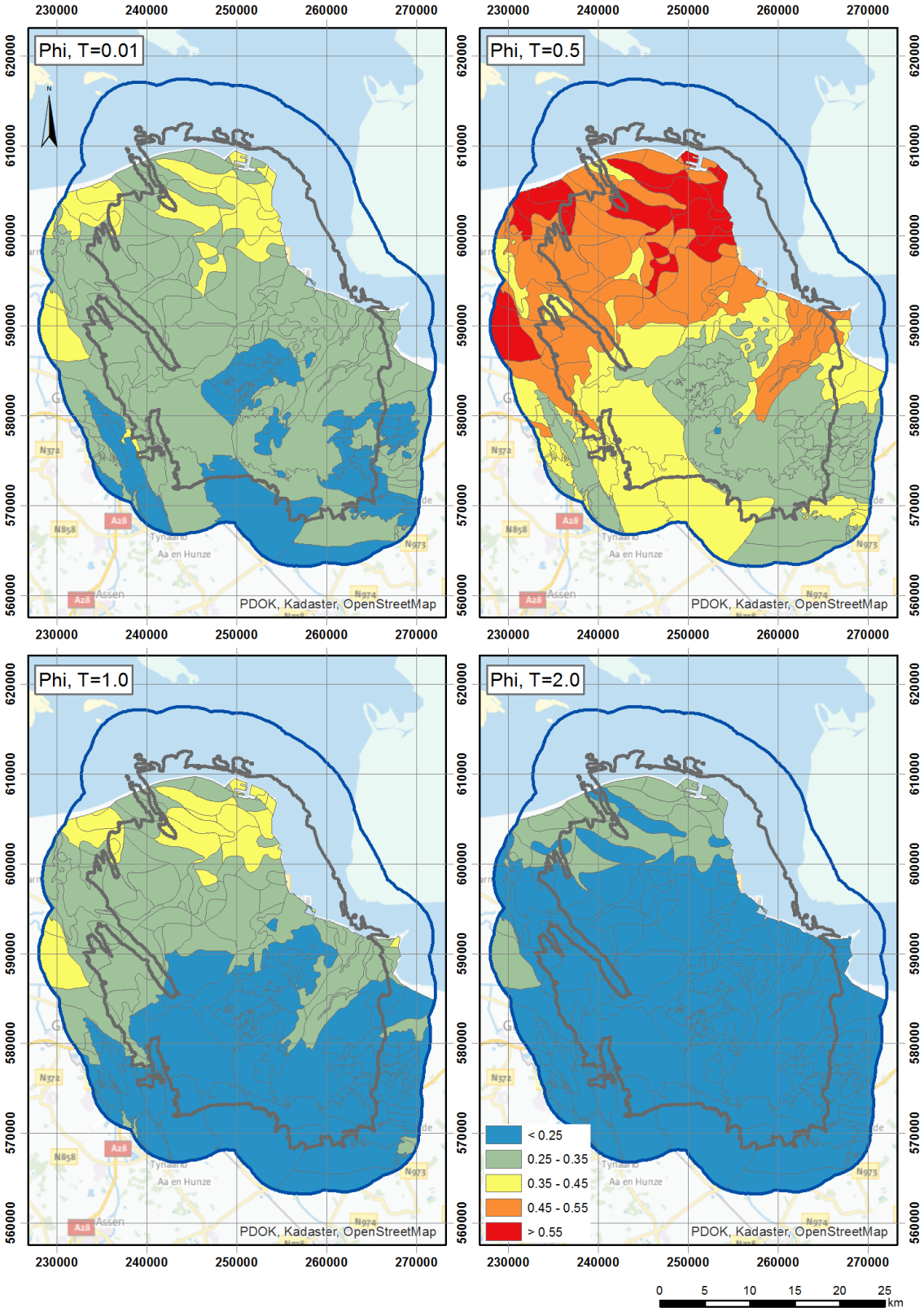

Figure 9.22. ϕ_{S2S} for the Groningen region for a scenario with **M** 6.5 and R_{epi} 1 km; NU_B acceleration factor = 3.32

Most modern GMPEs as well as building codes use V_{S30} as a proxy for the site response characteristics of any given location, the reason for which is primarily related to the relative abundance of this parameter (30 metres being the depth to which a borehole could be drilled in one day) rather than any compelling geophysical significance. For the spectral acceleration predictions, for which transportability has not been a consideration, the use of this rather crude parameter has been circumvented through the site response zonation. However, as is explained in Chapter 12, the duration GMPE—derived in a completely different way and defined directly at the ground surface rather than at the NU_B horizon for application of the AFs in each zone—does include this simplified parameter. Therefore, the implementation of the model requires a map of V_{S30} across the field, for which the preferred solution was to assign representative V_{S30} values to each of the site amplification zones. Based on the zonation proposed in Section 9.2 (Figure 9.7), median, average and standard deviations of V_{S30} for each zone were determined. The resulting V_{S30} maps are shown in Figure 9.23 (median V_{S30}), 9.24 (average V_{S30}) and 9.25 (standard deviation of V_{S30}). These maps may also prove useful for prioritisation schemes for building strengthening and improvements to the definition of seismic loads in the NEN-NPR draft seismic design code for the Groningen region (NEN, 2015).

For completeness, the V_{S30} values at the recording stations are reported in Table 9.2. Two V_{S30} values are reported: one set based on the zone where each station is located, and the other set calculated from the V_S profile at the station as inferred from the GeoTOP model. The latter values were originally reported in Table 4.2 in Chapter 4.

There is a distinct pattern in the distribution of V_{S30}, showing lower V_{S30} values in the north and higher V_{S30} values in the south. In the southern part, the high V_{S30} values reflect the presence of Pleistocene sediments at or near the surface. The Hondsrug is clearly recognisable as a high V_{S30} zone in the southwest, situated between the outline of the field and the 5 km buffer. East of the Hondsrug there is a channel infill with tidal deposits, resulting in a relatively low V_{S30} value. There is a sharp contrast in V_{S30} between the Hondsrug and the adjacent tidal deposits. This sharp contrast is expected because of depositional environment of a tidal zone next to a ridge structure. One small Holocene channel infill can be recognised in the east (geological area 1718). One large channel, with clayey infill, giving rise to low V_{S30} values is present in the east (geological area 2020). In the north and west, two sandier channel infills (geological area 802 and 1107+2108+1110) can be discerned in a more clayey environment.

The northern part generally shows lower V_{S30} values relative to the south. The resulting V_{S30} value is an interplay between the lithological infill and thickness of the Naaldwijk Formation, and the presence or absence and the thickness of peat layers. Generally, the Naaldwijk Formation is expected to be more sandy and consisting of a thicker layer to the north. Both aspects have counteracting effects on V_{S30}. Locally, the occurrence of shallow Pleistocene soils also increase the V_{S30}. In general, the difference between the median and the average V_{S30} is small. The standard deviation of V_{S30} varies geographically. The northern part consists of more heterogeneous tidal deposits of alternating peat and clay, giving rise to higher standard deviations of V_{S30}. The southern part, generally containing sandier deposits, shows lower standard deviations.

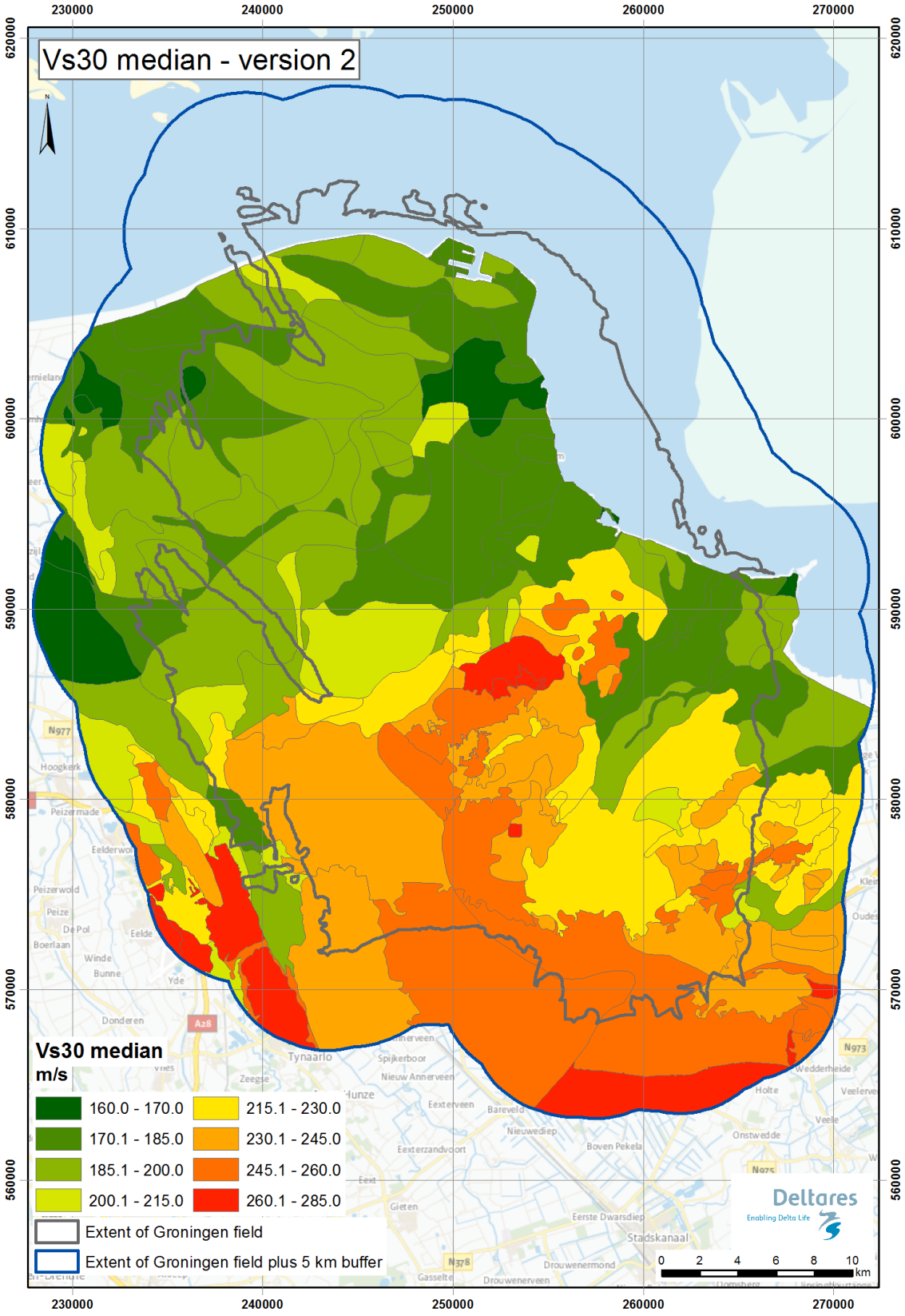

Figure 9.23. Median V_{S30} for the geological zonation V2. Updated V_{S30} map, following the methods described in Kruiver *et al.* (2015)

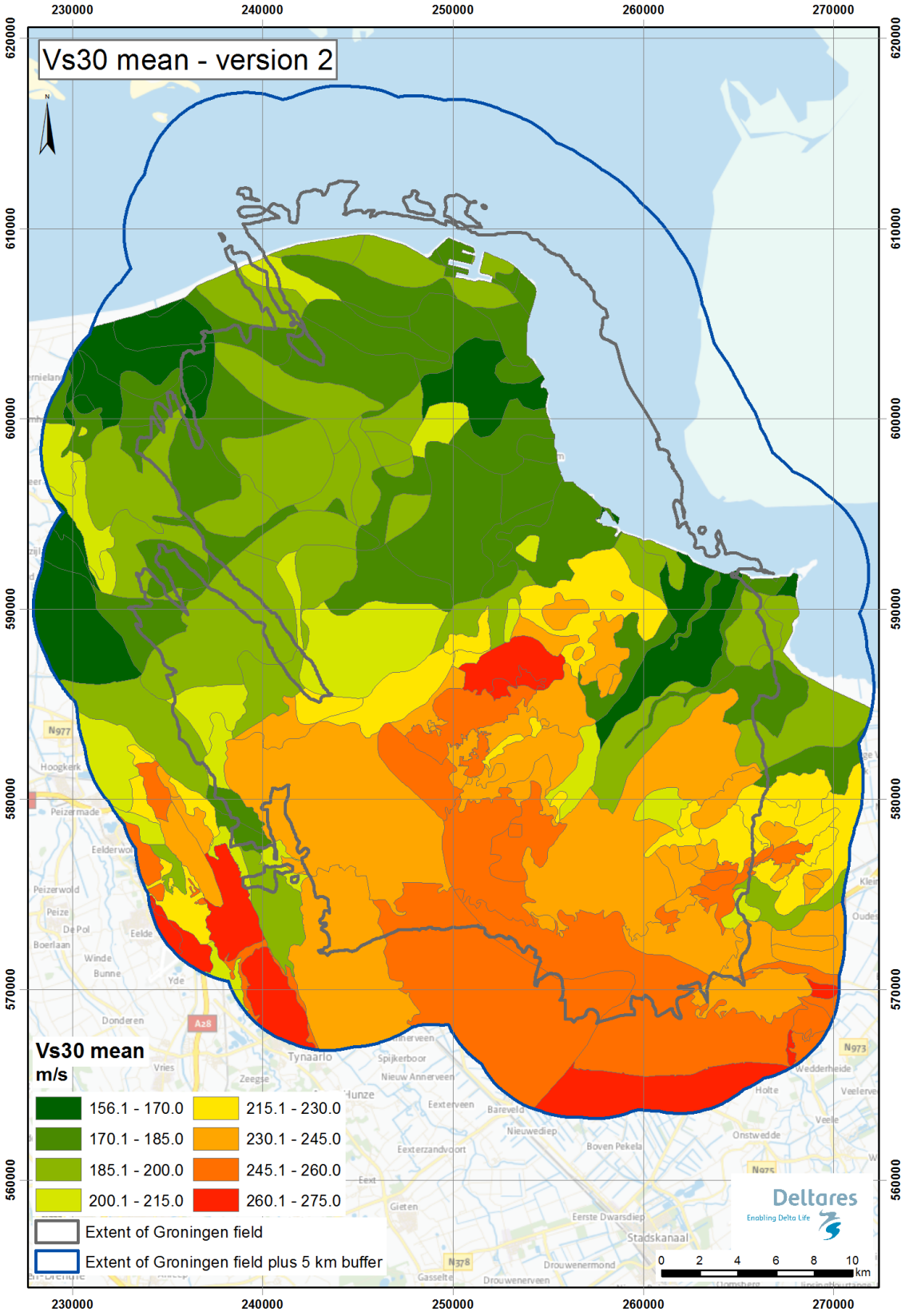

Figure 9.24. Average V_{S30} for the geological zonation V2. Updated V_{S30} map, following the methods described in Kruiver *et al.* (2015)

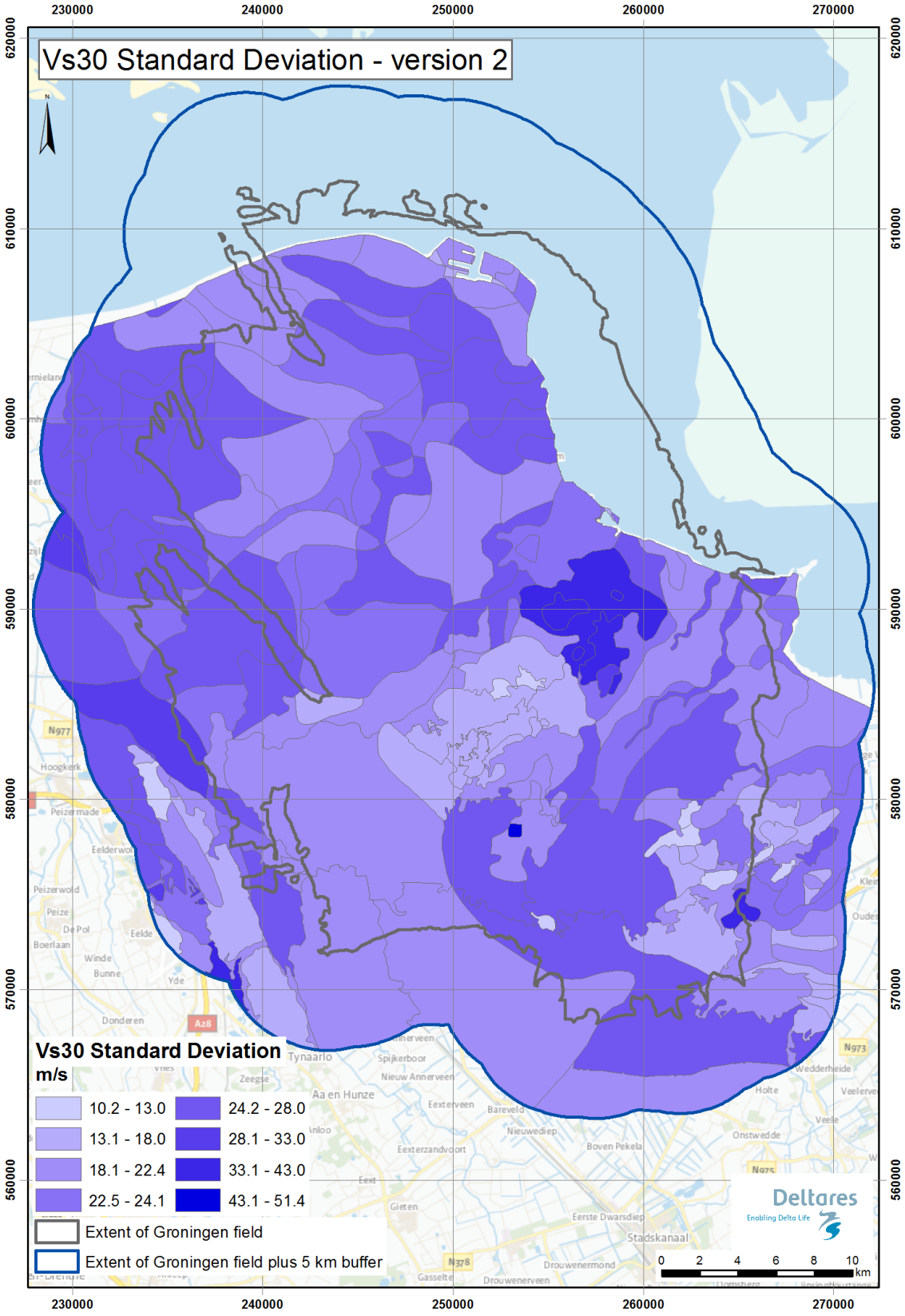

Figure 9.25. Standard deviation of V_{S30} for the geological zonation V2. Updated V_{S30} map, following the methods described in Kruiver *et al.* (2015)

Table 9.2. V_{S30} values at the recording stations.

Station	X (RD)	Y (RD)	Geological zone V2	Average V_{S30} from zone (m/s)	Median V_{S30} from zone (m/s)	Standard deviation of V_{S30} from zone (m/s)	V_{S30} calculated from V_S profile
BAPP	251515	593011	2104	178.0	179.6	22.1	179.7
BFB2	247128	578753	3114	238.3	240.0	21.5	272.9
BGAR	243289	598757	1001	188.0	190.7	22.2	193.0
BHAR	243266	583316	3114	238.3	240.0	21.5	221.4
BHKS	248207	590399	2102	183.4	184.4	24.4	214.8
BKAN	239844	599738	604	171.8	174.6	27.9	196.2
BLOP	245560	595020	1032	187.0	190.5	23.7	202.2
BMD1	238581	596379	1002	184.4	187.4	26.0	179.8
BMD2	238899	597051	1001	188.0	190.7	22.2	198.2
BONL	245966	602400	1011	182.1	185.4	22.9	185.7
BOWW	249933	595841	2104	178.0	179.6	22.1	184.3
BSTD	241967	592542	1102	188.0	189.9	22.9	199.4
BUHZ	240487	603067	801	177.6	179.9	19.8	203.4
BWIN	245723	592495	2102	183.4	184.4	24.4	198.2
BWIR	248213	593808	2104	178.0	179.6	22.1	202.6
BWSE	243091	596144	602	187.4	191.0	23.7	193.9
BZN1	247389	598590	1004	185.9	190.0	24.9	189.3
BZN2	246051	597580	1032	187.0	190.5	23.7	186.4
G240	252958	590272	2101	207.6	209.5	23.4	238.4
G300	255589	589141	1802	243.3	252.5	41.0	277.3
G340	246960	585982	2207	220.1	220.9	18.1	218.5
G400	250003	582993	311	249.9	249.0	17.0	244.0
G450	247006	580104	3114	238.3	240.0	21.5	258.1
G460	252738	580012	2824	253.7	254.0	24.6	255.6
HKS	248199	590274	2101	207.6	209.5	23.4	208.7
KANT	239844	599738	604	171.8	174.6	27.9	196.2
WIN	245644	592594	2102	183.4	184.4	24.4	191.6
ZAN1	247375	598600	1004	185.9	190.0	24.9	192.8
ZAN2	246063	597600	1032	187.0	190.5	23.7	188.0

9.4. Comparison with amplification factors for recording stations

In Section 4.3 the linear spectral amplifications for the recording stations were computed for use in the seismological inversions. In addition, the spectral amplifications for the 46 weakest signals from the input motion set described in Section 9.2 were determined with STRATA using the same layering file and V_S file as for the linear analysis. This was done as an internal check to ensure internal consistency of results. The input signals come from Group 1 and 2 from Figure 8.27 and have a maximum acceleration of 0.062*g*. The STRATA calculations were carried out on the original profiles, that is, without excluding peat layers as was done for the station amplification factors (code X in station name, see Section 4.3). The difference

in spectral amplification ratios is calculated as the relative difference between the linear amplification factor, AF_{lin}, and the amplification factor from STRATA, AF_{STRATA}:

$$\mathrm{Re}lative\_difference = \frac{AF_{lin} - AF_{STRATA}}{AF_{lin}} \qquad (9.4)$$

The results are summarised in Table 9.3 and shown as a histogram in Figure 9.26. Most of the differences are smaller than 20%. The distribution is slightly asymmetric, indicating that the AF values from the STRATA analyses using the original profiles are generally slightly larger than those from the linear analysis. For the linear range, the two methods compare well.

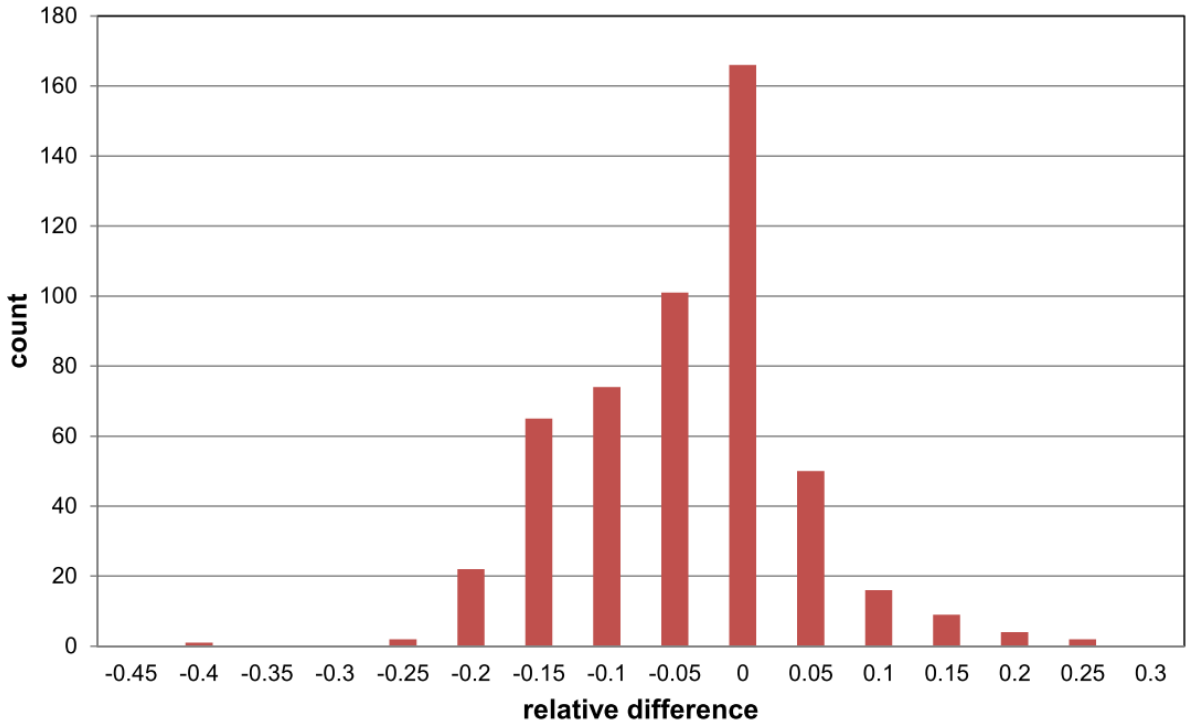

Figure 9.26. Distribution of relative differences between linear amplification factors and those from STRATA, results for all periods combined

Table 9.3. Relative difference between linear amplification factors and those from STRATA. Colour coding: difference < 20 % (*white*); between 20 and 30% (*peach*); > 30% (*red*)

Station	Periods (s)															
	0.01	0.1	0.2	0.3	0.4	0.5	0.6	0.7	0.8	1.0	1.5	2.0	2.5	3.0	4.0	5.0
BAPP	-0.04	-0.19	0.10	0.03	-0.02	-0.05	-0.04	-0.05	-0.02	-0.08	-0.05	-0.13	-0.22	-0.24	-0.22	-0.20
BFB2	-0.01	-0.06	0.01	0.00	-0.02	-0.03	0.00	-0.05	-0.06	-0.01	-0.06	-0.13	-0.14	-0.11	-0.08	-0.06
BGAR	-0.02	-0.11	-0.10	0.00	0.02	0.02	-0.02	-0.11	-0.06	-0.08	-0.05	-0.11	-0.18	-0.19	-0.17	-0.15
BHAR	0.05	0.14	-0.02	-0.02	-0.01	-0.02	-0.02	-0.01	-0.02	-0.03	-0.04	-0.04	-0.11	-0.13	-0.11	-0.09
BHKS	-0.01	-0.08	0.08	0.00	-0.03	-0.02	-0.06	-0.03	-0.06	-0.07	-0.05	-0.11	-0.18	-0.18	-0.17	-0.16
BLOP	-0.03	0.07	0.00	0.05	-0.01	-0.04	-0.06	-0.08	-0.06	-0.09	-0.05	-0.11	-0.19	-0.21	-0.20	-0.18
BMD1	-0.06	-0.24	-0.06	0.00	-0.02	-0.08	-0.03	-0.03	0.00	-0.06	-0.04	-0.10	-0.19	-0.21	-0.18	-0.16
BMD2	0.02	0.07	0.09	0.03	0.01	-0.04	-0.01	-0.03	0.01	-0.06	-0.03	-0.09	-0.16	-0.17	-0.15	-0.13
BONL	-0.05	-0.06	-0.08	0.01	0.01	0.00	-0.02	-0.12	-0.06	-0.08	-0.05	-0.11	-0.19	-0.21	-0.19	-0.18
BOWW	-0.04	0.04	-0.04	0.03	-0.01	-0.06	-0.04	-0.04	-0.01	-0.07	-0.04	-0.12	-0.20	-0.21	-0.19	-0.17
BSTD	-0.24	-0.45	-0.04	0.02	0.00	-0.01	-0.01	-0.04	-0.01	-0.02	0.12	0.10	0.10	0.13	0.18	0.21
BUHZ	0.00	0.02	0.08	0.04	-0.02	-0.04	-0.02	-0.06	-0.02	-0.05	-0.04	-0.08	-0.15	-0.17	-0.15	-0.14
BWIN	0.02	-0.12	0.17	0.00	0.02	-0.02	-0.02	-0.02	0.00	-0.07	-0.03	-0.10	-0.17	-0.18	-0.16	-0.14
BWIR	-0.08	-0.29	0.01	0.03	0.00	-0.04	-0.06	-0.05	-0.03	-0.08	-0.05	-0.11	-0.19	-0.20	-0.18	-0.16
BWSE	-0.08	-0.28	-0.08	0.08	-0.02	-0.05	-0.05	-0.11	-0.06	-0.08	-0.05	-0.11	-0.19	-0.21	-0.20	-0.18
BZN1	-0.05	0.03	-0.15	0.05	0.01	-0.03	-0.05	-0.11	-0.07	-0.08	-0.05	-0.12	-0.20	-0.21	-0.20	-0.18
BZN2	-0.08	-0.13	-0.16	0.00	0.00	-0.03	-0.05	-0.10	-0.07	-0.08	-0.06	-0.13	-0.21	-0.23	-0.21	-0.19
FRB2	-0.01	-0.06	0.01	0.00	-0.02	-0.03	0.00	-0.05	-0.06	-0.01	-0.06	-0.13	-0.14	-0.11	-0.08	-0.06
G240	-0.01	0.06	-0.01	-0.01	-0.04	-0.02	-0.06	-0.03	-0.07	-0.07	-0.03	-0.10	-0.14	-0.15	-0.13	-0.12
G300	-0.01	0.06	-0.04	-0.01	-0.04	-0.02	-0.05	-0.01	-0.07	-0.06	-0.03	-0.08	-0.12	-0.11	-0.09	-0.08
G340	0.06	0.19	-0.02	-0.01	0.00	-0.02	-0.02	-0.07	-0.02	-0.06	-0.03	-0.08	-0.14	-0.15	-0.13	-0.12
G400	-0.02	-0.04	-0.04	0.00	0.00	0.01	-0.03	-0.02	-0.01	-0.06	-0.03	-0.09	-0.14	-0.14	-0.11	-0.10
G450	-0.02	-0.12	-0.02	-0.03	0.03	-0.01	0.00	0.00	-0.06	-0.02	-0.05	-0.13	-0.14	-0.12	-0.09	-0.07
G460	-0.04	-0.10	-0.03	-0.03	-0.03	0.00	-0.04	0.01	-0.02	-0.06	-0.03	-0.10	-0.14	-0.13	-0.10	-0.08
GARST	-0.02	-0.11	-0.10	0.00	0.02	0.02	-0.02	-0.11	-0.06	-0.08	-0.05	-0.11	-0.18	-0.19	-0.17	-0.15
HARK	0.05	0.14	-0.02	-0.02	-0.01	-0.02	-0.02	-0.01	-0.02	-0.03	-0.04	-0.04	-0.11	-0.13	-0.11	-0.09
HKS	0.04	0.24	-0.02	0.00	-0.04	-0.02	-0.06	-0.02	-0.05	-0.07	-0.04	-0.10	-0.16	-0.17	-0.15	-0.14
KANT	0.04	0.18	0.14	0.11	0.14	0.06	0.00	-0.16	-0.18	-0.22	-0.11	-0.15	-0.21	-0.22	-0.20	-0.18
STDM	-0.05	-0.22	-0.01	0.06	0.00	-0.04	-0.04	-0.08	-0.04	-0.07	-0.05	-0.11	-0.18	-0.20	-0.18	-0.17
WIN	-0.01	-0.14	0.13	0.00	0.01	-0.03	-0.02	-0.03	0.00	-0.07	-0.04	-0.11	-0.18	-0.19	-0.17	-0.15
ZAN1	-0.05	0.07	-0.13	0.05	0.01	-0.03	-0.05	-0.11	-0.07	-0.08	-0.05	-0.12	-0.19	-0.21	-0.19	-0.18
ZAN2	-0.05	0.02	-0.11	0.02	0.01	-0.03	-0.04	-0.12	-0.08	-0.08	-0.06	-0.12	-0.20	-0.22	-0.21	-0.19

10. SIGMA MODEL

Ground-motion prediction equations (GMPEs) define distributions of the values of a specified ground-motion parameter for a given combination of magnitude, distance and site response. Since the residuals of the logarithmic values of ground-motion parameters with respect to the median predictions from GMPEs are generally found to follow to a Gaussian distribution, the distribution is defined by the standard deviation, sigma (σ). The value of sigma is just as important as the coefficients that define the median predictions and it can exert a very strong influence on estimates of seismic hazard and risk. This chapter describes the development of the complete sigma model for the V2 GMPEs, building on the calculated residuals of the recorded motions (Section 6.5) and the variability associated with the site amplification functions (Sections 8.3 and 9.3).

The chapter begins with an overview of all the components of ground-motion variability applicable to the Groningen ground-motion model for surface motions and a summary of the structure of the proposed sigma model. This is followed by descriptions of the derivations of two additional components of the variability that are required for the Groningen ground-motion model. The first is an estimate of the component-to-component variability for the horizontal ground motions, which is required in order to be able to transform predictions for the geometric mean component to the arbitrary horizontal component. This transformation is needed for the risk calculations, in order to be consistent with the treatment of the horizontal components of motion of the accelerograms used in the derivation of the fragility functions. The second component is a correction to the within-event variability for larger magnitudes due to the use of a point-source approximation that arises from adopting epicentral distance for these equations. The final two sections define the basic elements of the variability in the predicted motions at the reference rock horizon and the additional variability that is added at the ground surface to account for the site response. Since the site-to-site variability is explicitly accounted for in the surface predictions, the within-event variability in the reference rock horizons is necessarily single-station sigma.

10.1. Elements of sigma model for surface motions

The variability in ground-motion prediction equations is generally represented by a normal distribution of the logarithmic residuals, which can be represented by the standard deviation, σ (sigma). As was already manifest in the calculation of residuals at the NU_B horizon (Section 6.5) there is considerable scatter observed in the data with respect to the predictions of ground motions at the reference rock, which must be incorporated into the model. In order to develop the model for the variability associated with the predictions of the spectral accelerations at the ground surface, it is helpful to explore in a little detail the nature of this variability and its different components.

Residuals of ground-motion parameters are calculated as the logarithm of the recorded value minus the logarithm of the predicted median value, which can also be interpreted as the logarithm of the ratio of the observed to the predicted motion. A positive residual therefore

means that the median GMPE is under-estimating the observed amplitude of motion and a negative residual means that the motions are being over-predicted. The large scatter invariably observed in the residuals of ground motions is generally attributed to the fact that the GMPEs are very simple models to represent complex physical phenomena: even the most complex models in current use contain no parameters to model the influence of the heterogeneity of the fault rupture process in space and time, for example. Consequently, there is scatter in the residuals due to the effect of factors that are not included in the model; if this interpretation is valid then it might be more appropriate to refer to 'apparent randomness'. Some have argued that there may also be a genuinely random component of the ground-motion field generated by an earthquake, which could therefore never be removed regardless of the complexity of the predictive equations. The two arguments are, of course, not mutually exclusive and could both explain the origin of different parts of the variability.

Regardless of the exact nature of the variability, improvements in ground-motion modelling over the least two to three decades, in terms of expanded databases, greater numbers of explanatory variables and more sophisticated functional forms, have not led to any major reduction in the aleatory variability associated with ground-motion predictions (Strasser *et al*., 2009). Several studies have confirmed that the residuals are generally very well represented by a log-normal distribution, so for GMPEs predicting logarithmic values of spectral acceleration, the distribution of the residuals can be fully represented by the standard normal distribution with mean of zero and a standard deviation of sigma (σ). For a given suite of predictor variables, any ground-motion amplitude can be expressed as a combination of the median value and a normalised number of standard deviations, represented by epsilon (ε).

For the classification of residuals, we follow the notation of Al Atik *et al.* (2010). Total residuals (Δ_{es}) are defined as the difference between recorded ground motions and the values predicted by a GMPE (in natural log units). Total residuals are separated into a between-event term (δB_e) and a within event term (δW_{es}):

$$\Delta_{es} = \delta B_e + \delta W_{es} \tag{10.1}$$

where the subscripts denote an observation for event e at station s (Figure 10.1). The between-event and the within-event residuals have standard deviations τ and ϕ, respectively, and are assumed to be uncorrelated. Therefore, the total standard deviation is given by:

$$\sigma = \sqrt{\tau^2 + \phi^2} \tag{10.2}$$

If we assume that the variability is primarily due to the influence of factors that are either not included in the GMPE or else are crudely represented by the parameters in the equation, then the between-event variability may be assumed to be due to factors such as a stress drop as well as details of the rupture propagation (and in the case of Groningen, the mechanism of rupture), although it has been found that stress drop variability is much larger

than inter-event variability (Cotton *et al*., 2013). The within-event variability may be influenced by azimuthal variations, crustal heterogeneities, the deeper geological structure at the recording stations, and details of the near-surface velocity profiles not captured by V_{S30}.

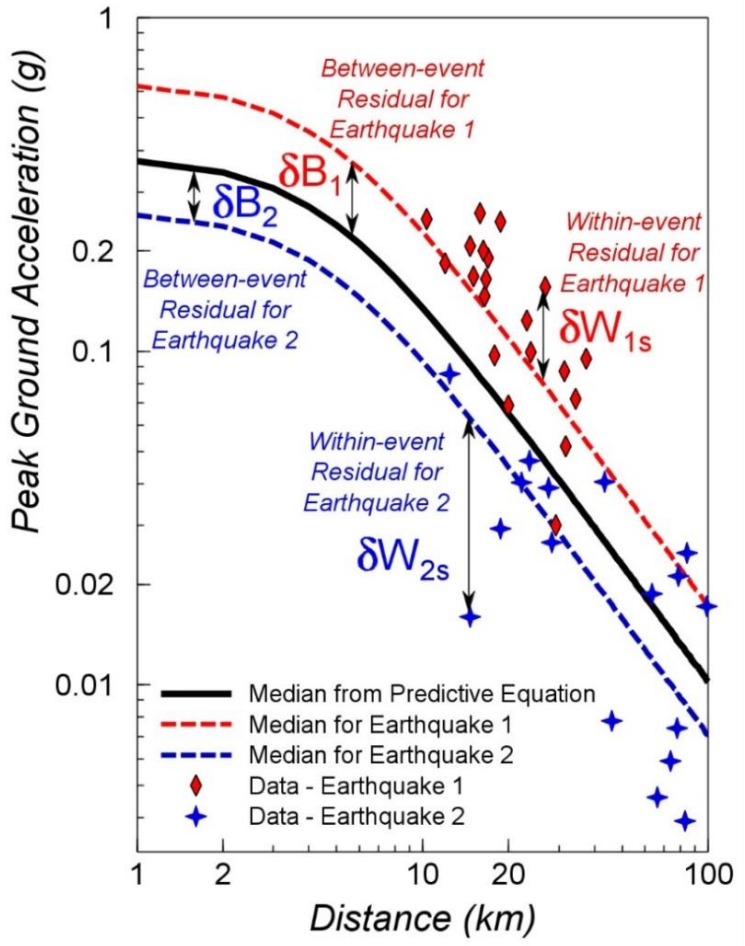

Figure 10.1. Illustration of the concepts of between-event and within-event residuals. The black curve represents the median predictions for an earthquake of magnitude M, whereas the blue and red dashed curves represent the median curves corresponding to two specific events of the same magnitude (Al Atik *et al*., 2010)

The within-event (or intra-event) residuals, which effectively represent the spatial variability of the ground motions, can in turn be separated into:

$$\delta W_{es} = \delta S2S_s + \delta WS_{es} \qquad (10.3)$$

where $\delta S2S_s$ represents the systematic deviation of the observed ground motion at site s (*e.g.*, the 'site term') from the median event-corrected ground motion predicted by the GMPE, and δWS_{es} is the site- and event-corrected residual. The standard deviation of the $\delta S2S_s$ and δWS_{es} terms are denoted by ϕ_{S2S} and ϕ_{ss}, respectively. Table 10.1 lists the components of the total residual, their respective standard deviations, and the terminology used for each standard deviation component.

Table 10.1. Terminology used for residual components and their standard deviations. $SD(\cdot)$ denotes the standard deviation operator

Residual Component	Residual Notation	Standard Deviation component	Definition of standard deviation component
Total residual	Δ_{es}	Total or ergodic standard deviation	$\sigma_{ergodic} = SD(\Delta_{\mathrm{es}})$
Event term	δB_e	Between-event (or inter-event) standard deviation (tau)	$\tau = SD(\delta B_e)$
Event-corrected residual	δW_{es}	Within-event (or intra-event) standard deviation (phi)	$\phi = SD(\delta W_{es})$
Site term	$\delta S2S_s$	Site-to-site variability	$\phi_{S2S} = SD(\delta S2S_s)$
Site- and event-corrected residual	δWS_{es}	Event-corrected single-station standard deviation (single-station phi)	$\phi_{ss} = SD(\delta WS_{es})$

The recognition of a repeatable site term—which is not random—being part of the model for the aleatory variability in the predictions challenges the ergodic assumption that is implicit in the derivation of empirical GMPEs. In applying a GMPE to the assessment of seismic hazard at a specific location, the interest is in the variation of motions at this site due to different earthquakes that could occur over time. Since it is rare to have recordings from the location under study, and even in the few cases where such recordings exist they will cover at most a few decades, PSHA generally invokes what is referred to as the ergodic assumption (Anderson & Brune, 1999). The ergodic assumption essentially states that variability over space can be used as a substitute for variation of time, and it is invoked in practice since the sigma values calculated from regression analyses to develop GMPEs represent the variability across many different sites (and sometimes many regions). Where there are multiple recordings from individual sites, they display lower variability than indicated by the sigma values of GMPEs (*e.g.*, Atkinson, 2006), the reason being that there are components of the behaviour at an individual site that are repeated in all cases and therefore do not contribute to variability. The effect is even more pronounced when there are multiple recordings from a single site of earthquakes associated with a single seismogenic source because in that case there are repeatable effects of both the path and the site.

If the repeatable contributions to the seismic motion at the site of interest can be modelled through an appropriate adjustment to the median predictions, then the sigma value can be reduced—to a value referred to as ‘single-station sigma’ (Atkinson, 2006)—by an amount that reflects the variability of the site term. The ergodic assumption effectively folds the epistemic uncertainty regarding individual site terms into the sigma value of the GMPE, representing it as aleatory variability:

$$\sigma_{ergodic} = \sqrt{\tau^2 + \phi_{ss}^2 + \phi_{S2S}^2} \tag{10.4}$$

If the site term is modelled explicitly and therefore the site-to-site component of the ground-motion variability is accounted for in the implementation of the GMPE into hazard calculations, a partially non-ergodic approach (also called a *single-station sigma* approach) may be invoked with a reduced variability. In this case, the standard deviation is known as the *single-station standard deviation* (Figure 10.2) and is given by:

$$\sigma_{ss} = \sqrt{\tau^2 + \phi_{ss}^2} \tag{10.5}$$

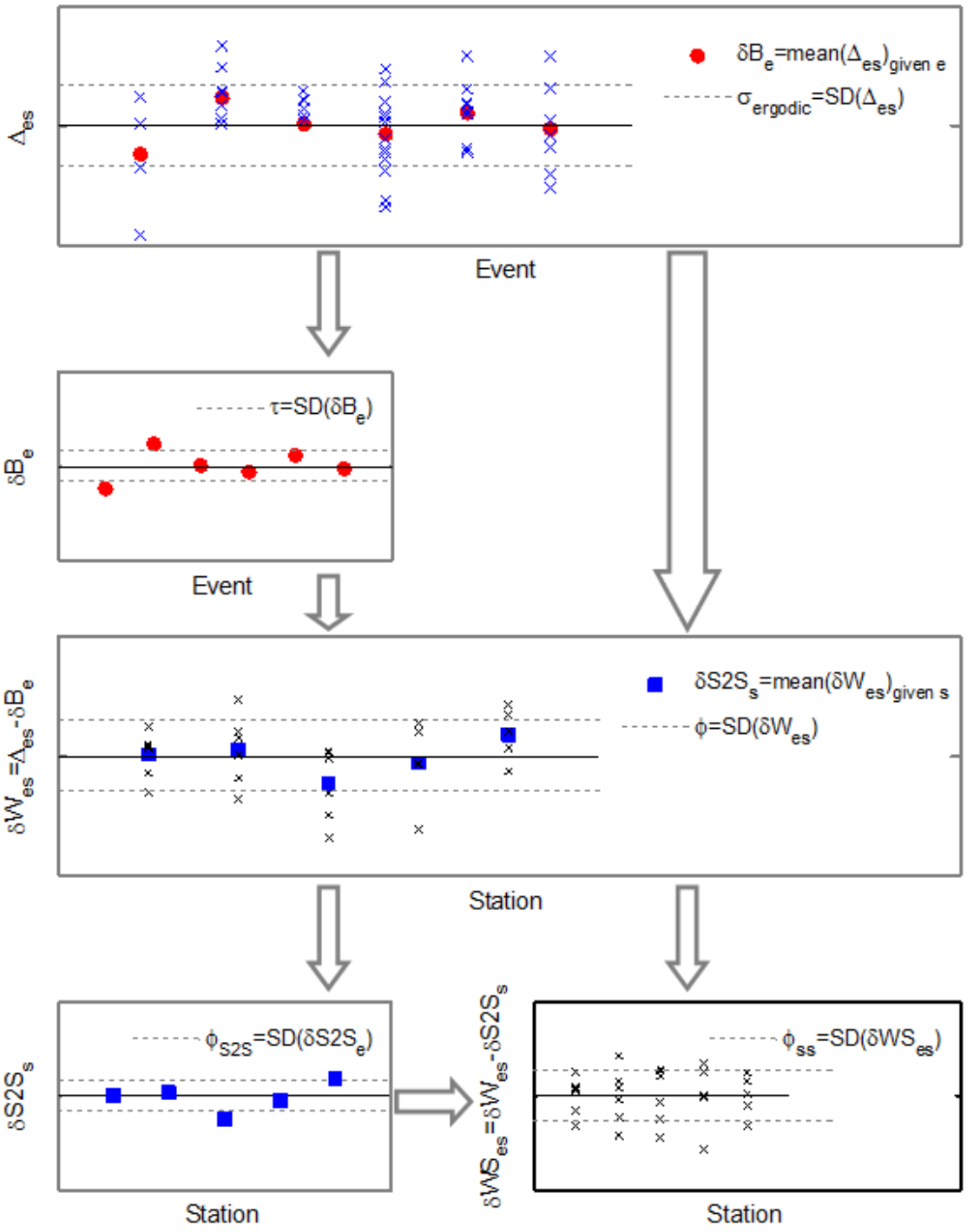

Figure 10.2. Schematic representation of the breakdown of residuals leading to the single-station phi (ϕ_{ss})

As is clear from the discussions of the non-linear site amplification factors and their associated variability in Section 8.3, and the zonation of the Groningen field with regard to site amplification effects presented in Chapter 9, the site-to-site variability in the estimation of surface motions in the Groningen field are being fully accounted for in the chosen formulation for the ground-motion prediction model. Therefore, it is essential to remove the site-to-site variability from the predictions of spectral accelerations at the reference rock horizon, since otherwise this element of the variability would be accounted for twice in the estimation of surface motions. This means that the within-event variability of the NU_B motions must be based on an estimate of ϕ_{SS}. In Section 10.4, the selection of the appropriate values for this parameter is discussed, together with the accompanying estimates of the between-event variability, τ. The specific model for ϕ_{S2S} is described in Section 10.5.

Before discussing these key elements of the variability in the ground-motion predictions at the reference rock horizon and at the ground surface, two other elements of the ground-motion variability are presented. The first is the component-to-component variability, required to transform the predictions of the geometric mean of the horizontal motions to the arbitrary component of horizontal motion, as required for the risk calculations (Section 1.3). The component-to-component variability is discussed in Section 10.2. In Section 10.3, the adjustment to the within-event variability required at larger magnitudes because of the use of a point-source based distance metric is presented. The complete sigma model for the V2 GMPEs for Groningen is presented in Section 11.1 in the context of the complete ground-motion model and the detailed guidance on its implementation.

10.2. Component-to-component variability

Consistent with the current global practice in seismic hazard modelling, the GMPEs have been derived in terms of the geometric mean of the two horizontal components. However, for the risk calculations, it is necessary to predict spectral accelerations corresponding to an arbitrarily-selected horizontal component, for consistency with the way the fragility functions have been derived (see Section 1.3). In terms of median predictions, no adjustment to the geometric mean component is required to transform these to the arbitrary component, an adjustment is needed to the sigma value in order to account for the component-to-component variability that is lost in the calculation of the geometric mean of each pair of horizontal components. The component-to-component variance is given by the following equation (Boore, 2005b):

$$\sigma_{C2C}^2 = \frac{1}{4N}\sum_{j=1}^{N}[\ln(Y_{1j}) - \ln(Y_{2j})]^2 \qquad (10.6)$$

where Y_1 and Y_2 are the spectral accelerations at period T from the two horizontal components of the j^{th} accelerogram, and N is the total number of records. Figure 10.3 shows the calculated values of the component-to-component variance for the Groningen ground-motion database, and also compares them with the values reported by Boore (2005b) and

by Campbell & Bozorgnia (2007). The first observation that can be made from this figure is that the component-to-component variability of the Groningen recordings seems to be exceptionally large, which is not particularly surprising given that it is known the recordings from the field show a very high degree of polarisation (see, for example, Figure 1.5). Another important observation is the erratic nature of the calculated values of component-to-component variability for the Groningen recordings at longer periods. The value at 2.5 seconds can be ignored since the number of usable records at this period is too small to allow a stable estimate but it is not clear if the values at 1.5 and 2.0 seconds are also too poorly constrained to be reliable. As the number of usable records decreases with increasing period, the proportion of stronger motions increases and since the polarisation is observed to be strongest for the higher-amplitude recordings (*e.g.*, Ntinalexis *et al.,* 2015b), this may be the explanation for the increase in component-to-component variability observed at longer periods.

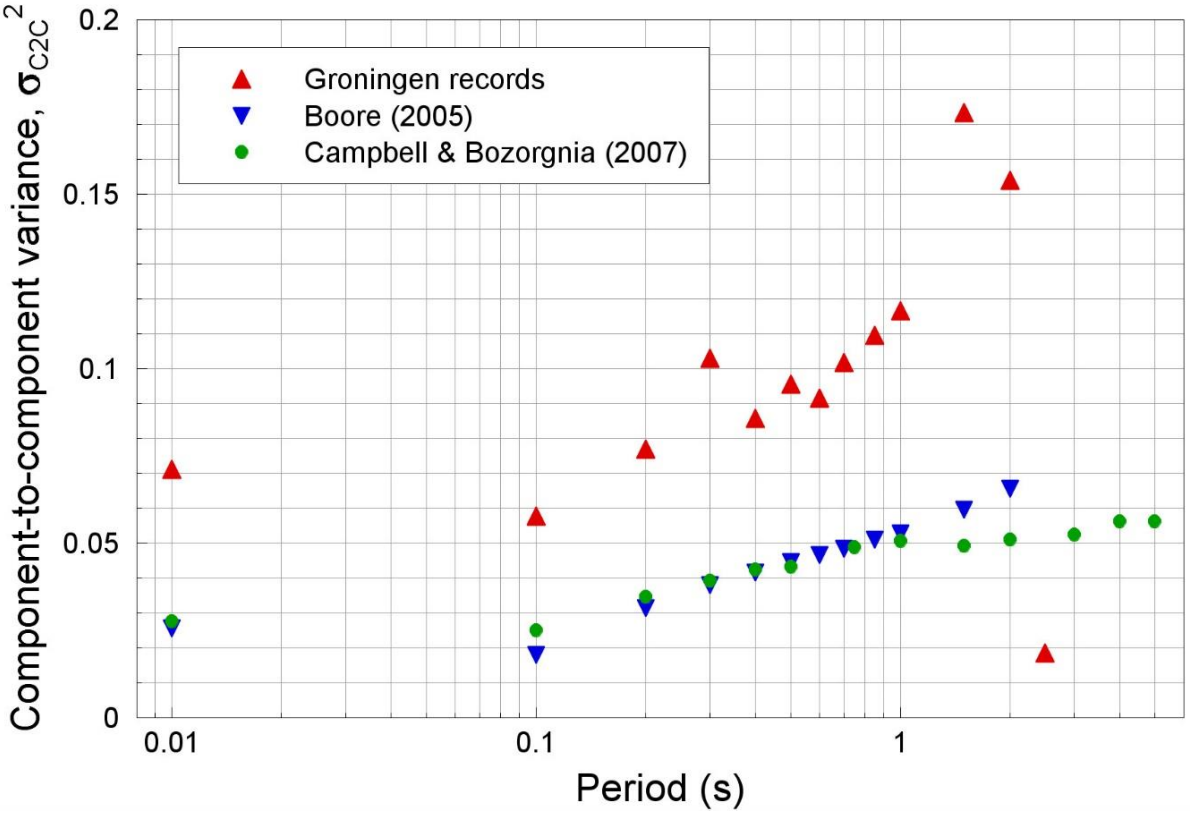

Figure 10.3. Component-to-component variance calculated for Groningen records and comparison with values from Boore (2005b) and from Campbell & Bozorgnia (2007)

Values for the component-to-component variability are required at all 16 target periods from 0.01 to 5.0 seconds. In view of the relatively constant values reported by Campbell & Bozorgnia (2007) at longer periods, we take the possibly conservative decision to apply the variability calculated for spectral accelerations at 1.5 seconds at all longer periods. The final values of σ_{C2C} are reported in Table 10.2.

Table 10.2. Component-to-component variability for Groningen motions

Period (seconds)	σ_{C2C}
0.01	0.267
0.1	0.240
0.2	0.277
0.3	0.321
0.4	0.293
0.5	0.309
0.6	0.303
0.7	0.319
0.85	0.331
1	0.342
1.5	0.416
2	0.416
2.5	0.416
3	0.416
4	0.416
5	0.416

10.3. Sigma corrections for point-source approximation

As explained in Section 2.1, the V2 GMPEs have been formulated in terms of epicentral distance, R_{epi}, following demonstration that while this brings very significant computational advantages over using a fault-based metric, such as R_{JB}—which requires each earthquake scenario to be modelled as an extended fault rupture in the hazard and risk calculations—it results in mild over-estimation of both of the relevant risk metrics. The use of the R_{epi} in combination with point-source (hypocentre) representations of the earthquake scenarios is internally consistent (*e.g.,* Bommer & Akkar, 2012) and, in light of the sensitivity analyses for risk calculations, defensible. However, it is acknowledged that the point-source approximation will lead to underestimation of the ground-motion variability for larger earthquakes having fault ruptures of several kilometres length, and an adjustment to the variability must be made to compensate for this feature.

The approach for developing such an adjustment was presented as part of the V1 GMPE (Bommer *et al*., 2015a,b) and the same approach is adopted herein. The calculation of the additional element of spatial variability arising from the geometry of the extended fault ruptures is inferred using the median predictions from the GMPEs of Akkar *et al.* (2014a) using R_{epi} and R_{JB}, fault dimensions inferred from the relationships of Wells & Coppersmith (1994), and dense networks of virtual receivers. While the applicability of the Wells & Coppersmith (1994) scaling relationships to shallow-focus induced earthquakes is not confirmed, there is no evidence at this time to suggest that any other available relationship (*e.g*., Clark *et al*., 2014; Leonard, 2014; Stafford, 2014) would be more apt for this application. Since this penalty is related to the geometry of the source and the spatial variation of ground motions, it is effectively a correction to the intra-event variability and is designated $\delta\phi$; the penalty is applied, by summing variances, to the intra-event variability inferred from the small-magnitude Groningen data, ϕ_{SM}, hence Eq.(10.2) becomes:

$$\sigma = \sqrt{\tau^2 + (\phi_{SM}^2 + \delta\phi^2)} \qquad (10.7)$$

The derivation of the sigma penalty is fully explained in Appendix II of the V1 GMPE report (Bommer *et al.,* 2015a), and is summarised here for completeness. The magnitude- and distance-dependent adjustment to the intra-event variability is defined as follows:

$$\delta\phi = SF.\frac{\varphi(z)}{\sigma_Z} \qquad M \geq 4 \qquad \text{and} \quad R_{epi} > 0 \qquad (10.8a)$$

$$\delta\phi = 0 \qquad M < 4 \qquad \text{or} \quad R_{epi} = 0 \qquad (10.8b)$$

where SF is the magnitude-dependent scaling factor, expressed as follows:

$$SF = \beta_1(M-4) + \beta_2(M-4)^2 \qquad (10.9)$$

and $\varphi[\ ]$ is the normal probability density function, which is given by the following expression:

$$\varphi(z) = \frac{1}{\sqrt{2\pi}}\exp\left(\frac{-z^2}{2}\right) \qquad (10.10)$$

The argument of this expression is given by:

$$z = \frac{\ln(R_{epi}) - \mu_Z}{\sigma_Z} \qquad (10.11)$$

and the parameters of this expression are given by:

$$\mu_Z = \beta_3 + \beta_4(M-6.75) + \beta_5(M-6.75)^2 \qquad (10.12)$$

$$\sigma_Z = \beta_6 \qquad (10.13)$$

The condition specified in Eq.(10.8) that the correction is only applied for earthquakes of magnitude 4 or greater since for smaller events the rupture dimensions may be assumed to be sufficiently small for the two distance metrics (R_{epi} and R_{JB}) to be considered equivalent and thus for no adjustment to the variability to be needed. The nature of this sigma adjustment as a function of magnitude and distance is illustrated in Figure 10.4.

The coefficients at the response periods common to the V1 model (0.01, 0.2, 0.5, 1.0 and 2.0 seconds) are slightly different from those obtained previously because of the fact that the coefficients are determined simultaneously at all periods; the influence of the number of periods considered on the values obtained for the coefficients has been observed in other ground-motion regressions (*e.g*., Boore *et al*., 2006).

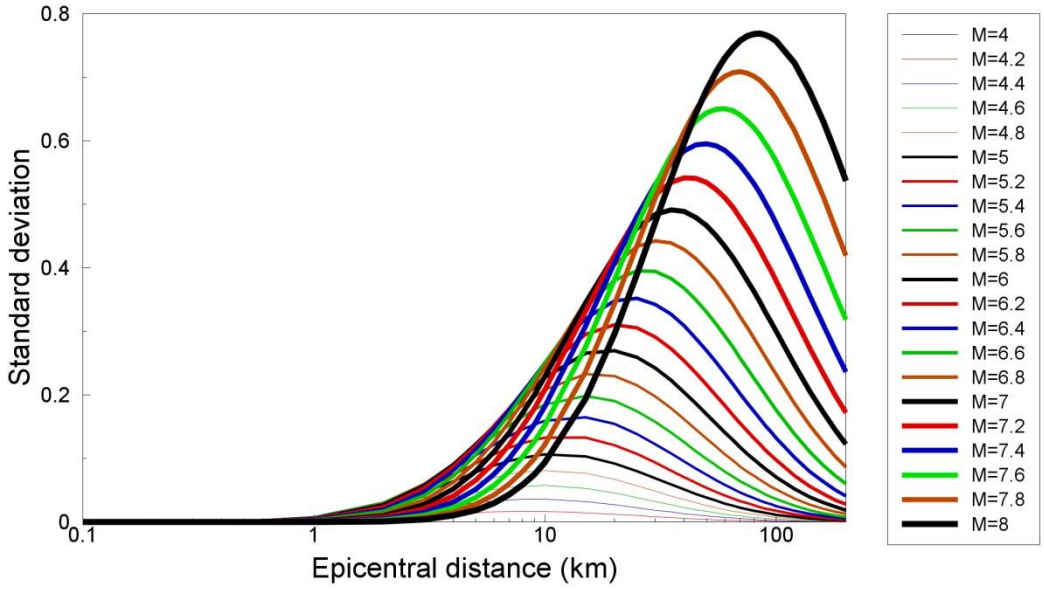

Figure 10.4. The values of the correction $\delta\phi$ for PGA predictions as a function of distance for a range of magnitude values

One issue that arises, however, is that the Akkar *et al.* (2014a) GMPEs do not include coefficients for spectral accelerations at all 16 of the target response periods. Specifically, the two periods not covered are 2.5 seconds and 5.0 seconds. The only coefficients of the equations that vary with response period are β_1 and β_2, since all the other coefficients are constant across the entire period range, hence only four coefficients in all are missing. The period of 2.5 s is simply omitted by Akkar *et al.* (2014a), who provide coefficients for spectral ordinates at 2.4 and 2.6 seconds. For this case, it is relatively straightforward to interpolate values of the missing coefficients against the logarithm of period using either a cubic spline, as suggested by Bommer *et al*. (2012), or a piece-wise cubic Hermite interpolating polynomial (PCHIP). The two approaches yield almost identical results for both β_1 and β_2. The great challenge is posed for the coefficients at 5 seconds, which is beyond the upper limit of 4 seconds covered by the Akkar *et al*. (2014a) model. Three options were considered to obtain the missing values of the two coefficients at this period:

- Maintaining the values at 4 seconds constant for higher periods
- Linear extrapolation against log(T) of the interval from 3 to 4 seconds
- Extrapolation against log(T) using the PCHIP

Figure 10.5 compares the second two approaches, and Figure 10.6 shows the results in terms of the resulting value of $\delta\phi$ for a moderately large earthquake at intermediate distance scenario for which the adjustment is expected to be large (Figure 10.4). From Figure 10.6 it can be appreciated that there is a pattern of decreasing values of $\delta\phi$ with increasing periods beyond 1 second, which would make the first option listed above—maintaining the coefficient at 4 seconds constant for higher periods—very pessimistic. At the same time, there is no strong basis for having greater confidence in either of the extrapolation schemes, which made us tend to opt for the simpler log-linear extrapolation. This option also yields

coefficients at 5 seconds that yield slightly higher estimates of the sigma adjustment at 5 seconds, which makes this a slightly more conservative option. The final coefficients period-dependent coefficients of Eq.(10.9) are listed in Table 10.3 and the period-independent of Eqs.(10.12) and (10.13) are listed in Table 10.4.

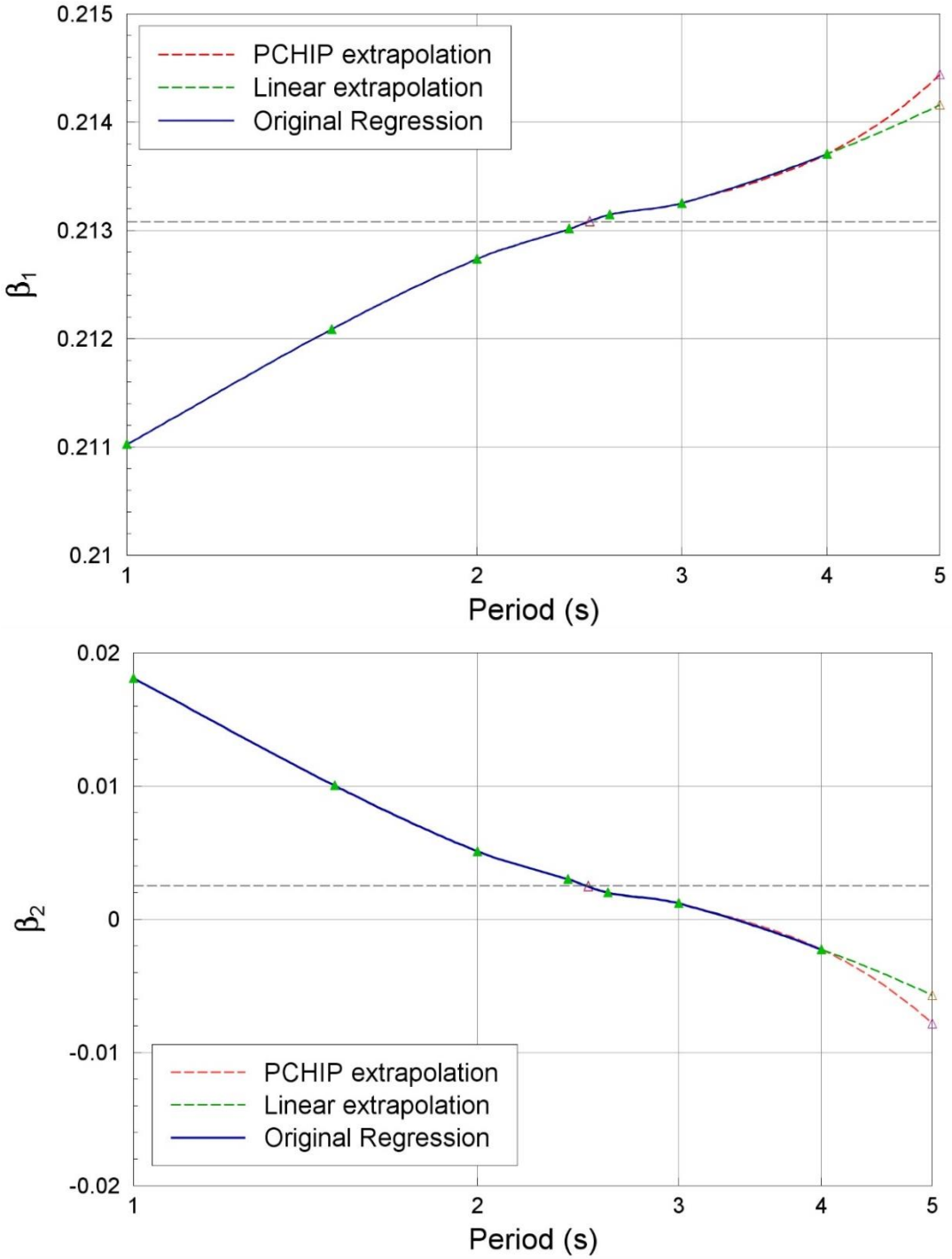

Figure 10.5. Coefficients β_1 (*upper*) and β_2 (*lower*) against period, indicating interpolated values at 2.5 s and options for extrapolation to 5 seconds

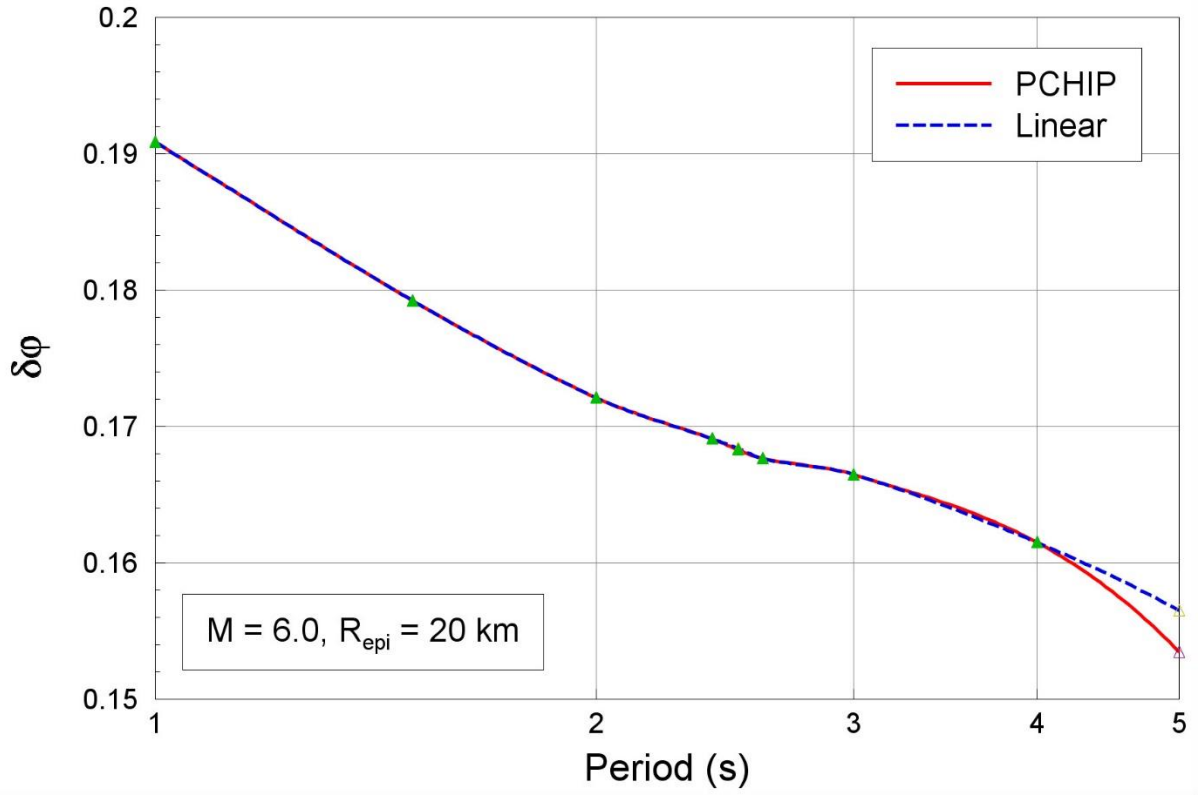

Figure 10.6. Sigma adjustments $\delta\phi$ for an earthquake of **M** 6.0 at an epicentral distance of 20 km, and comparison of values obtained at 5 seconds with different extrapolation schemes

Table 10.3. Coefficients of Eq.(10.9)

Period (s)	β_1	β_2
0.01	0.20370	0.07357
0.1	0.20117	0.09277
0.2	0.20280	0.08043
0.3	0.20486	0.06478
0.4	0.20671	0.05081
0.5	0.20751	0.04468
0.6	0.20847	0.03742
0.7	0.20939	0.03044
0.85	0.21039	0.02286
1.0	0.21102	0.01808
1.5	0.21208	0.01001
2.0	0.21273	0.00508
2.5	0.213084	0.002428
3.0	0.21325	0.00117
4.0	0.21370	-0.00228
5.0	0.21416	-0.00573

Table 10.4. Coefficients of Eqs.(10.12) and (10.13)

β_3	β_4	β_5	β_6
3.394377	0.710239	0.0909	1.03011

10.4. Tau and Φ_{SS} model

As explained in Section 10.1, the variability in the ground-motion predictions at the NU_B reference rock horizon must be expressed as single-station sigma, which was given in Eq.(10.5) and is repeated here for completeness and ease of reference:

$$\sigma_{ss} = \sqrt{\tau^2 + \phi_{ss}^2} \qquad (10.14)$$

The two elements required therefore are the between-event (earthquake-to-earthquake) variability and the single-station within-event variability.

Starting with the single-station within-event variability, one option is to estimate this from multiple recordings at individual recording locations. This option will be explored in the refinement of the V2 GMPE but since using such data requires a well-centred predictive model, it was decided not to explore this option while the model is still affected by an appreciable degree of bias with respect to the local recordings (Section 6.5) and the amplification functions to transform the surface motions to the reference rock horizon are based on inferred rather than measured velocity profiles (Chapter 4). Even though this option is to be explored, it may not yield robust results given that relatively few stations have multiple recordings to date. Moreover, while a locally-calibrated model might generally be preferred, it has been found from detailed analysis of datasets from various different regions that estimates of ϕ_{SS} are remarkably stable around the globe (*e.g*., Rodriguez-Marek *et al*., 2013). Therefore, it is defensible to adopt values estimated from such global datasets and for this purpose we decided to use the homoscedastic model—in other words, the model in which the value of this variability does not vary with magnitude—as defined in the PSHA project for the Thyspunt nuclear site in South Africa (Bommer *et al*., 2015d). The best estimate value for ϕ_{SS} is 0.45 with the epistemic uncertainty represented by upper and lower limits of 0.522 and 0.378 respectively (Rodriguez-Marek *et al*., 2014). In the Thyspunt project, these alternative estimates were assigned weights of 0.2, while a weight of 0.6 was placed on the central value. The preliminary branch weights assigned to the Groningen ground-motion logic-tree are slightly different from these values but sufficiently close to allow the same branches on ϕ_{SS} to be adopted: 0.38, 0.45, and 0.52. These values replace ϕ_{SM} in Eq.(10.7).

Turning now to the between-event variability, the between-event variability was estimated from the bias-adjusted residuals (see Section 6.5) for all three median models. In all cases, the value of τ at 0.2 seconds was found to be exceptionally low, for reasons that are not yet understood, whereas at other periods the values displayed a consistent pattern of relatively constant values at short periods and then rising to another plateau at longer periods (Figure 10.7). Up to a period of 1.5 seconds, all 12 earthquakes remained in the analyses (taking account of the usable period range of each record) but this number rapidly dropped off at longer periods. A functional form was fitted that defines two asymptotes (τ_1 at shorter periods, τ_2 at longer periods) and the transition between them, with two fitting options explored, one constraining the value of τ_2 to match the largest observed value.

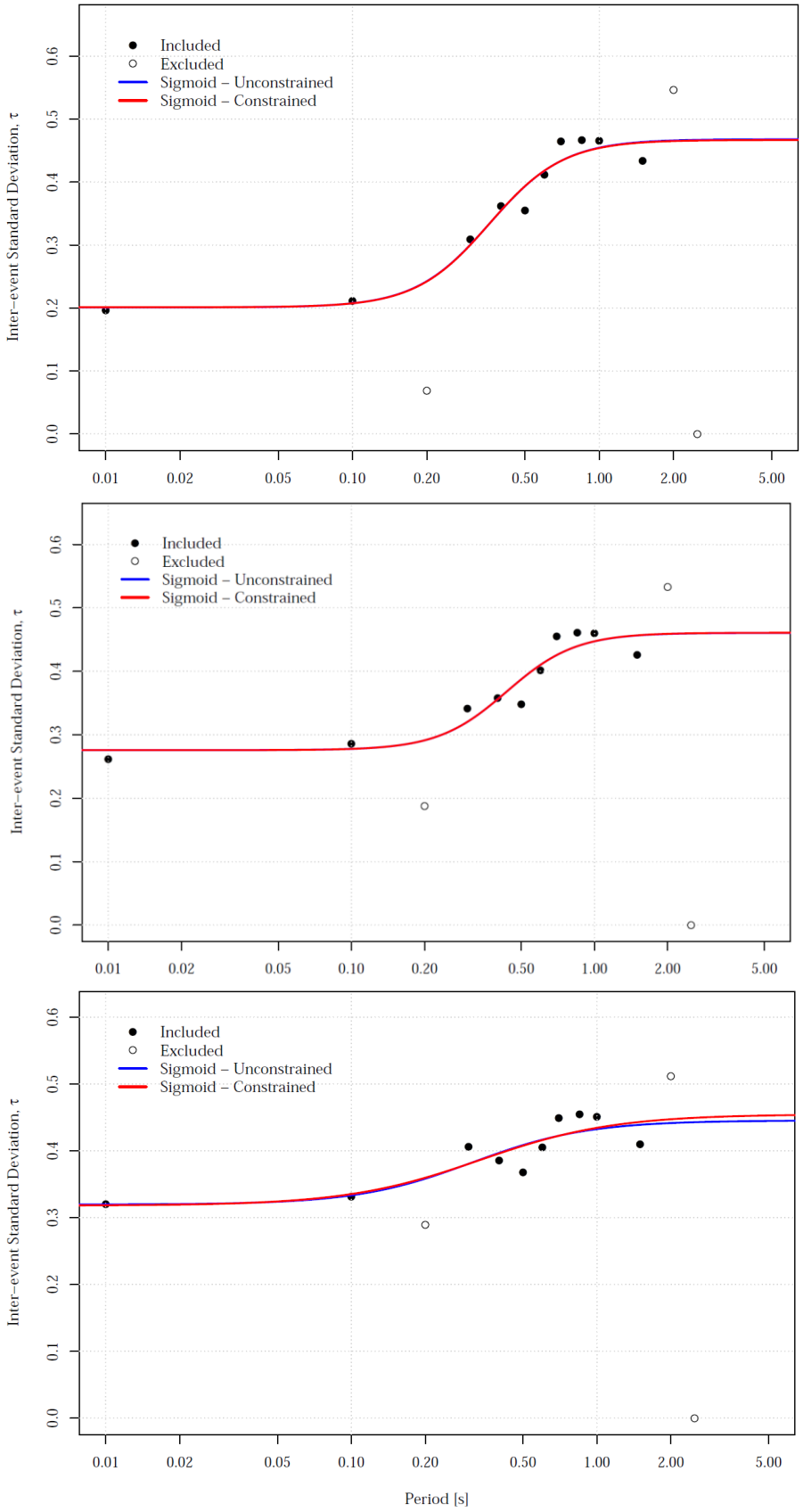

Figure 10.7. Calculated between-event standard deviations from the upper (*top*), central (*middle*) and lower (*bottom*) models after removal of the bias, and fitting of Eq.(10.15) with and without constraint to match the largest observed value

$$\tau = \tau_1 + \frac{\tau_2 - \tau_1}{1 + \exp[(\tau_3 - \ln T)/\tau_4]} \qquad (10.15)$$

The fitting is performed on the values at periods between 0.01 and 1.5 seconds but excluding the low values at 0.2 seconds. As can be appreciated from Figure 10.7, the constraint makes very little difference to the results but in the spirit of erring on the side of conservatism until stable reductions can be justified we opt to use those results. The coefficients of Eq.(10.15) from the three models are presented in Table 10.5 and the resulting values of τ at the 16 target periods in Table 10.6, including extrapolations to the periods beyond 1.5 seconds. The between-event variability values are paired with their corresponding median prediction, even though at shorter periods this means that the variability associated with the upper model is smaller than that associated with the lower model (Figure 10.8), which represents a move away from the deliberate conservatism of the V1 model.

Table 10.5. Coefficients of Eq.(10.15)

Coefficient	10 bar	30 bar	100 bar
τ_1	0.31797	0.27576	0.20119
τ_2	0.45464	0.46086	0.46686
τ_3	-1.09470	-0.82961	-1.02455
τ_4	0.62642	0.32617	0.34363

Table 10.6. Between-event standard deviations

Period (s)	Lower	Central	Upper
0.01	0.3185	0.2758	0.2012
0.1	0.3353	0.2778	0.2075
0.2	0.3597	0.2913	0.2422
0.3	0.3804	0.3204	0.3001
0.4	0.3960	0.3561	0.3548
0.5	0.4075	0.3874	0.3935
0.6	0.4160	0.4103	0.4182
0.7	0.4225	0.4257	0.4336
0.85	0.4295	0.4397	0.4469
1.0	0.4344	0.4474	0.4540
1.5	0.4432	0.4568	0.4628
2.0	0.4472	0.4591	0.4651
2.5	0.4493	0.4600	0.4659
3.0	0.4506	0.4604	0.4663
4.0	0.4521	0.4607	0.4666
5.0	0.4528	0.4608	0.4667

From Figure 10.8 it can be seen that the new τ values are smaller than those associated with the V1 model at short periods (T ≤ 0.2 s) and somewhat larger at longer periods, even though the upper value selected for the V1 model was based on the conservative assumption of equivalence with a model for tectonic earthquakes in a very broad regions. For completeness Figure 10.8 also compares the basic within-event sigmas—but without the $\delta\phi$

corrections (Section 10.3) since these are essentially the same—and here again we see lower values at short periods (T ≤ 0.5 s) and somewhat higher values at longer periods.

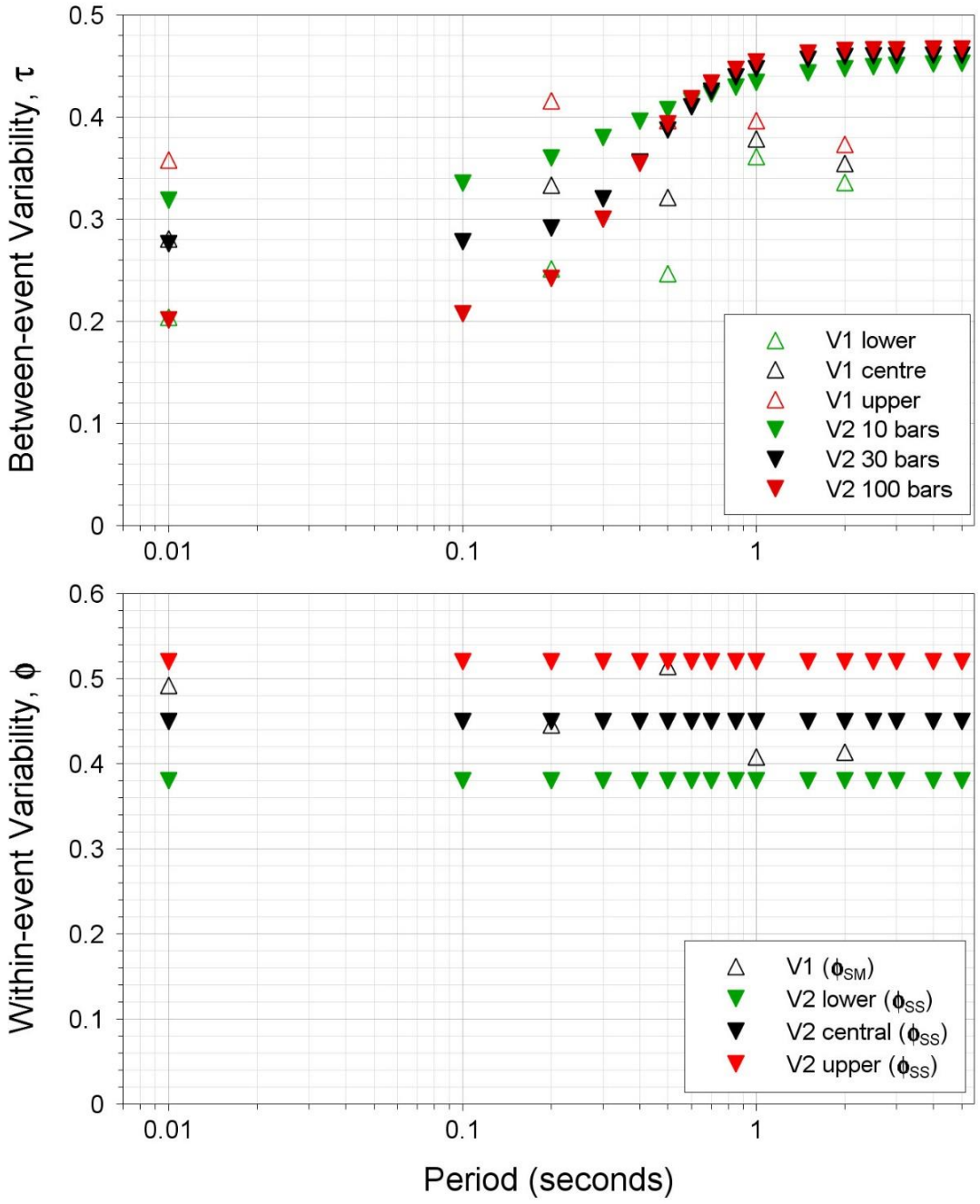

Figure 10.8. Comparison of between-event (*upper*) and within-event (*lower*) standard deviations from the V1 and V2 models, with the latter referenced to the NU_B rock horizon

Figure 10.9 compares the proposed model for within-event variability for the V2 GMPEs with those calculated from the residuals after removal of the bias (Section 6.5). It can be appreciated that at longer periods the adopted single-station within-event sigma model implies greater variability than that measured from the recordings but this does not hold at shorter periods (≤ 0.3 s). However, we still believe that the model is justified for predictions

over the full magnitude range because of the inclusion of site-to-site variability associated with the amplification factors.

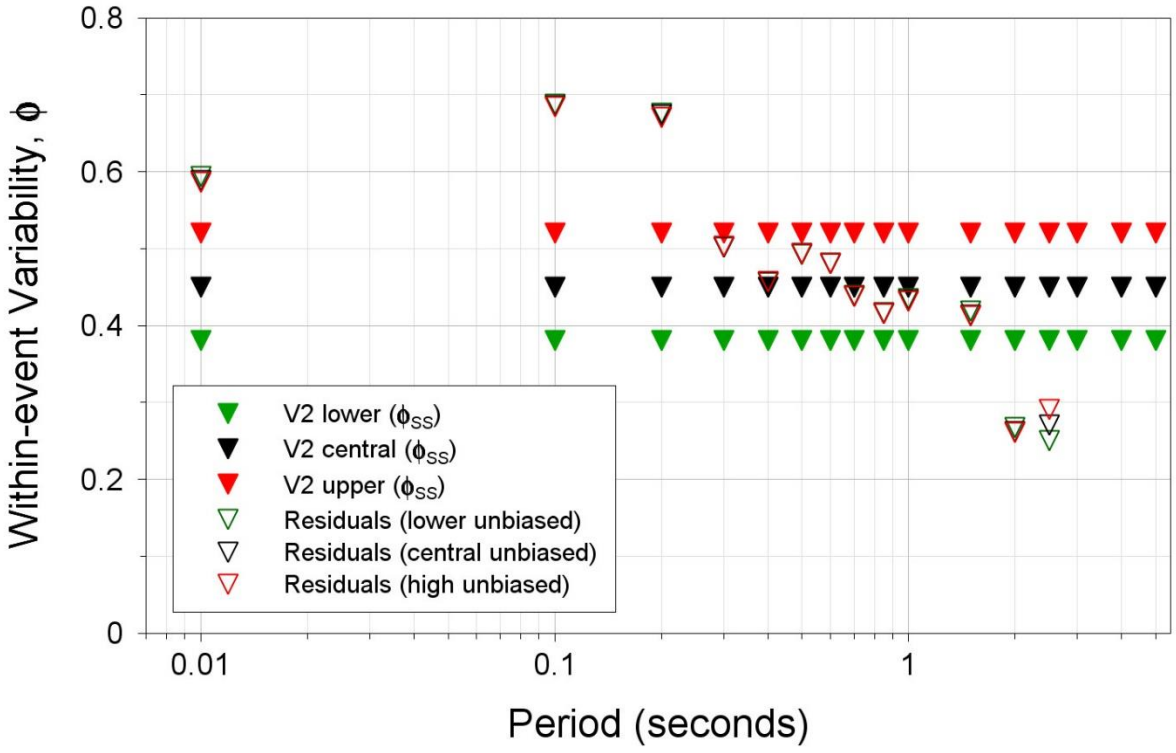

Figure 10.9. Comparison of the measured within-event standard deviations from V2 model and the assumed single-station within-event sigma adopted

Figure 10.10 shows the resulting values of total sigma (again without $\delta\phi$) from the V1 and V2 models, and for comparative purposes those from R_{hyp}-based GMPEs of Akkar *et al*. (2014a), which were the basis for the V0 model (Bourne *et al*., 2015). As would be expected from the preceding discussion, the values are lower at short periods, comparable at about 0.5 seconds, and somewhat larger at longer periods. However, over most of the period range from 0.01 to 3 seconds, the sigma values—at the baserock level—are appreciably smaller than those from GMPE of Akkar *et al.* (2014a) although it must be borne in mind that the V2 values plotted do not include the minor adjustment of $\delta\phi$ and also that the final sigma at the surface must also take account of the site-to-site variability, ϕ_{S2S}, which is discussed in the next section.

Given that all of the Groningen earthquakes occur within the gas reservoir and the seismic waves propagate to the NU_B horizon through very similar geological layers, we could assume an approximation to the condition of single-path, single-station sigma. For such a situation, sigma would be expected to be much smaller than the fully ergodic values that accompany GMPEs derived from large databases of recordings from tectonic earthquakes in very broad regions (*e.g*., Atkinson, 2006; Lin *et al*., 2011, Villani & Abrahamson, 2015). In this regard, we also note that the sigmas of the Akkar *et al.* (2014a) are amongst the largest

obtained in recent GMPEs hence we might expect a greater gap between the Groningen values and the ASB14 sigmas in Figure 10.9. Clearly there remains scope for exploring and possibly refining the model in order to reduce the aleatory variability in the prediction models.

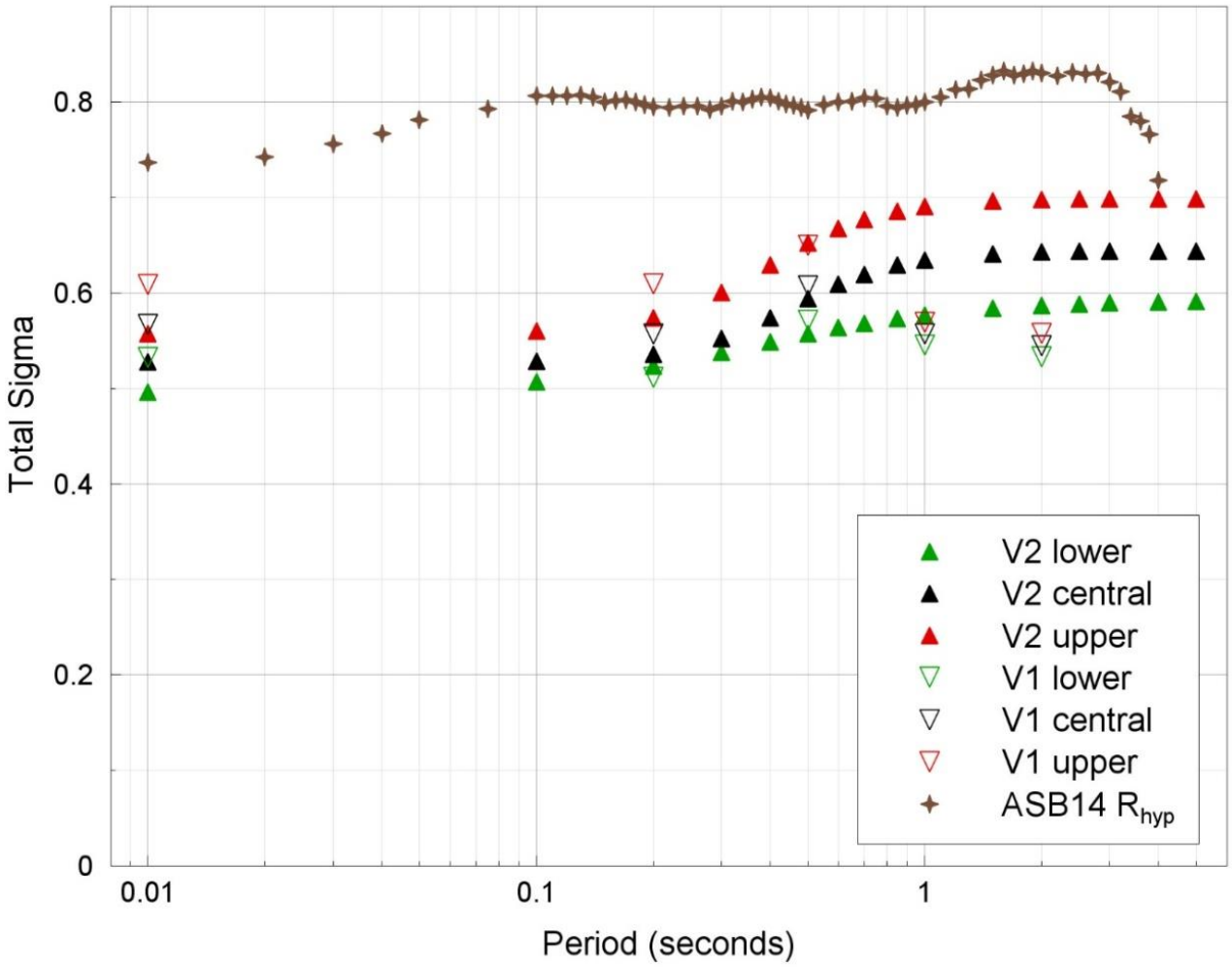

Figure 10.10. Comparison of total sigmas from the V1 and V2 models together with those from the R_{hyp} model of Akkar *et al.* (2014a)

10.5 Site-to-site variability model

The final component of the sigma model is the site-to-site variability, which was discussed in Section 8.3. Examples of this variability in the calculated site amplification factors for each zone were presented in Section 9.3. The variability is found to vary with the amplitude of the shaking in the reference rock, reflecting the greater variability invoked when the soil response becomes more non-linear. The variation of ϕ_{S2S} with reference rock acceleration is represented by the simple model illustrated in Figure 10.11. The model is defined by an upper and lower level of ϕ_{S2S} and the acceleration levels defining the transition from one level to

another. In the very small number of cases where the results indicate a reduction of ϕ_{S2S} with increasing acceleration, ϕ_{S2SH} was simply set equal to ϕ_{S2SL} .

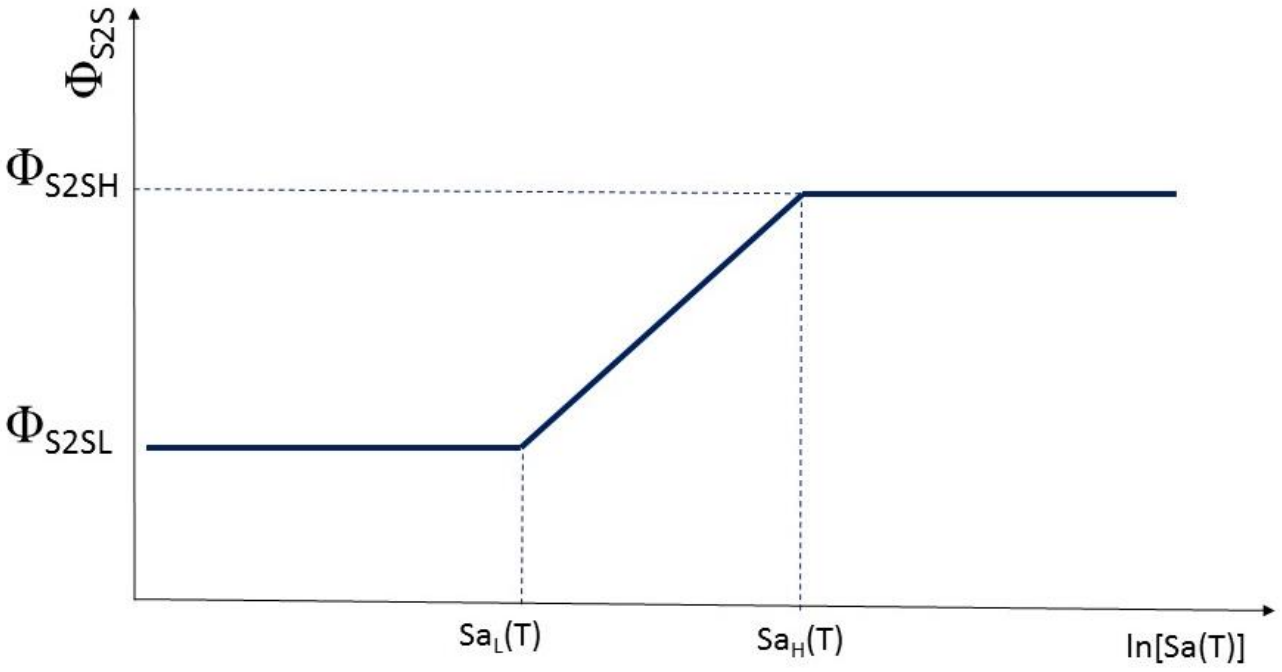

Figure 10.11. Schematic illustration of the parameters defining ϕ_{S2S} , in which the subscript L and H indicate the low and high values; the acceleration on the x-axis is the spectral acceleration at the NU_B horizon

On the basis of observations from borehole recordings in rock from Kik-Net, which therefore represent rather uniform linear site conditions, a minimum threshold of 0.2 for the site-to-site variability has been inferred (Rodriguez-Marek *et al*., 2011). This minimum value is imposed on the ϕ_{S2S} values for Groningen. Figure 10.12 illustrates the ϕ_{S2S} model at six response periods for one of the 167 site amplification zones (604), from which the heteroskedastic nature of the variability can be appreciated. In this example, the minimum value of 0.2 is imposed at the lower end for a period of 2 seconds, and over the entire range of reference rock accelerations for a period of 5 seconds.

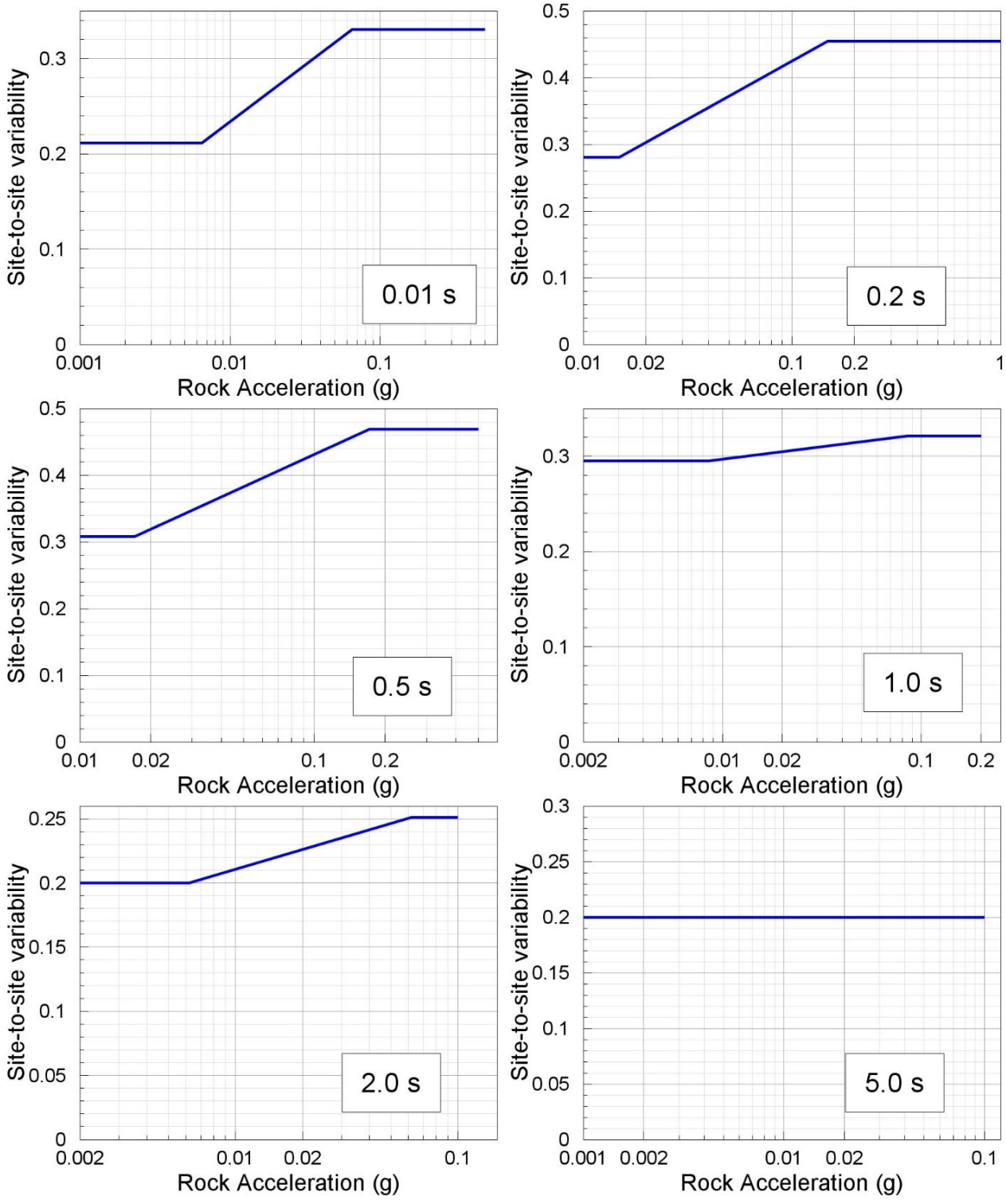

Figure 10.12. Values of ϕ_{S2S} at six response periods in Zone 604

11. APPLICATION and EXTENSION of the GMPEs for Sa(T)

This chapter summarises the final V2 GMPE for spectral accelerations at the ground surface across the field, including additional elements required for its application in the risk calculations and in structural analyses. The first section of the chapter describes the implementation of the basic model for predicting spectral accelerations at the ground surface. These predictions are compared with those from the V1 model in the second section. The third section summarises the adopted model for period-to-period correlations of residuals of spectral accelerations and the final section discusses suitable models for the ratio of vertical-to-horizontal spectral accelerations.

11.1. Model for predicting surface response spectra

The final model for estimating the spectral acceleration at any one of the 16 target oscillator periods at a specified location within the Groningen field as a result of a given earthquake—defined by its magnitude, **M**, and its distance from the site, R_{epi}, due to its location—is in reality rather simple since it is a function of only three variables: magnitude, distance and site response zone. However, the implementation of the model is a little complex because of the multiple components of variability included in the formulation of the model. The formulation of the model was expressed in the following way in Chapter 2:

$$\ln[Sa(T)] = \{\ln[Sa_{ref}(T)] + \delta B + \delta WS\} + \ln[AF_j(T)] + \delta S2S_j \qquad (11.1)$$

The calculation of the median value of the spectral acceleration at the NU_B reference rock horizon, $Sa_{ref}(T)$, for a given **M**-R_{epi} combination is performed using the equations and coefficients presented in Section 6.4. The actual spectral acceleration at the NU_B, however, used to obtain the non-linear amplification factor and to which this amplification factor is applied, requires both the median value of $Sa_{ref}(T)$ and an appropriate sampling of the associated variability (and in this regard a significant advantage of the Monte Carlo approach can be appreciated since it avoids the simplification of only conditioning the non-linear response on the median amplitudes of motion in the reference rock). The full formulation can therefore be expressed as a combination of the elements of the variability and random samples of these distributions; since every element of the model applies to a specific period, T, in order to make the equation simpler the specification (T) is removed:

$$\ln(Sa) = \{\ln(Sa_{ref}) + \varepsilon_E\tau + \varepsilon_S\sqrt{\phi_{SS}^2 + \delta\phi^2} + \varepsilon_C\sigma_{C2C}\} + \ln(AF_j) + \varepsilon_Z\phi_{S2Sj} \qquad (11.2)$$

Each of these variability terms is now briefly discussed, and the full procedure for the implementation is illustrated in Figure 11.1

Sa_{ref} is the median spectral acceleration predicted at the NU_B horizon using Eqs.(6.4) to (6.8) and the coefficients in Tables 6.2 to 6.4.

The next term $\varepsilon_E \tau$ is the between-event or inter-event residual, sampled for each earthquake in the synthetic catalogues and held constant for all sites for a given earthquake. The values of τ are given in Section 10.4 (Table 10.6).

The next terms in another log-normal distribution which is sampled using the random variable ε_S at each location at which the hazard is calculated. The log-normal distribution for the spatial variability is comprised of two parts: ϕ_{SS} is single-station sigma and takes a value of 0.38, 0.45 and 0.52 for the lower, central and upper models, respectively, at all oscillator periods; $\delta\phi$ is an adjustment made for the use of a point-source-based distance metric at larger magnitudes, and is defined in Section 10.3 by Eqs.(10.8) to (10.13) and the coefficients in Tables 10.3 and 10.4.

The next term is another log-normal distribution sampled randomly at each location by ε_C; the standard deviation σ_{C2C} represents the component-to-component variability, and the values are provided in Section 10.2 (Table 10.2). This term is included when calculating risk but should be set to zero when calculating the hazard, as explained in Section 1.3.

The three components of variability considered so far, ε_E, ε_S and ε_C are assumed to be completely uncorrelated. Adding these three components of variability to the median spectral acceleration yields the actual baserock acceleration for each earthquake-site combination considered in the Monte Carlo simulations.

The coordinates at which the calculations are being performed automatically define which of the 167 site amplification zones the site is located within. The coefficients of the equation for the median amplification factor, AF, as expressed in Eq.(8.4) can then be retrieved, and the amplification factor calculated for the spectral acceleration (expressed in units of *g*) at the NU_B horizon. A check must then be performed that AF is neither smaller than 0.25 nor larger the specified value of AF_{max}; if either condition is violated, AF is set to either AF_{min} or AF_{max}. The final value of AF is then multiplied by the spectral acceleration at the NU_B horizon. The final step is then to sample randomly (ε_Z) from one more log-normal distribution with standard deviation ϕ_{S2S}, which represents the site-to-site variability within the zone; $\phi_{S2S} \geq 0.2$. This variability term varies with the value of NU_B acceleration, as explained in Section 10.5. The product of the NU_B spectral acceleration and AF is then multiplied by the exponent of the value of $\varepsilon_Z \phi_{S2S}$ to obtain the final surface acceleration at that period. The calculation of the surface accelerations at other response periods at the same site needs to take account of the period-to-period correlation model in Section 11.3.

For those fragility functions defined in terms of spectral acceleration and duration, the median duration should be estimated using the model in Section 12.4 and the variability sampled conditional on the total ε sampled for the acceleration, using the correlation coefficients presented in Section 12.5.

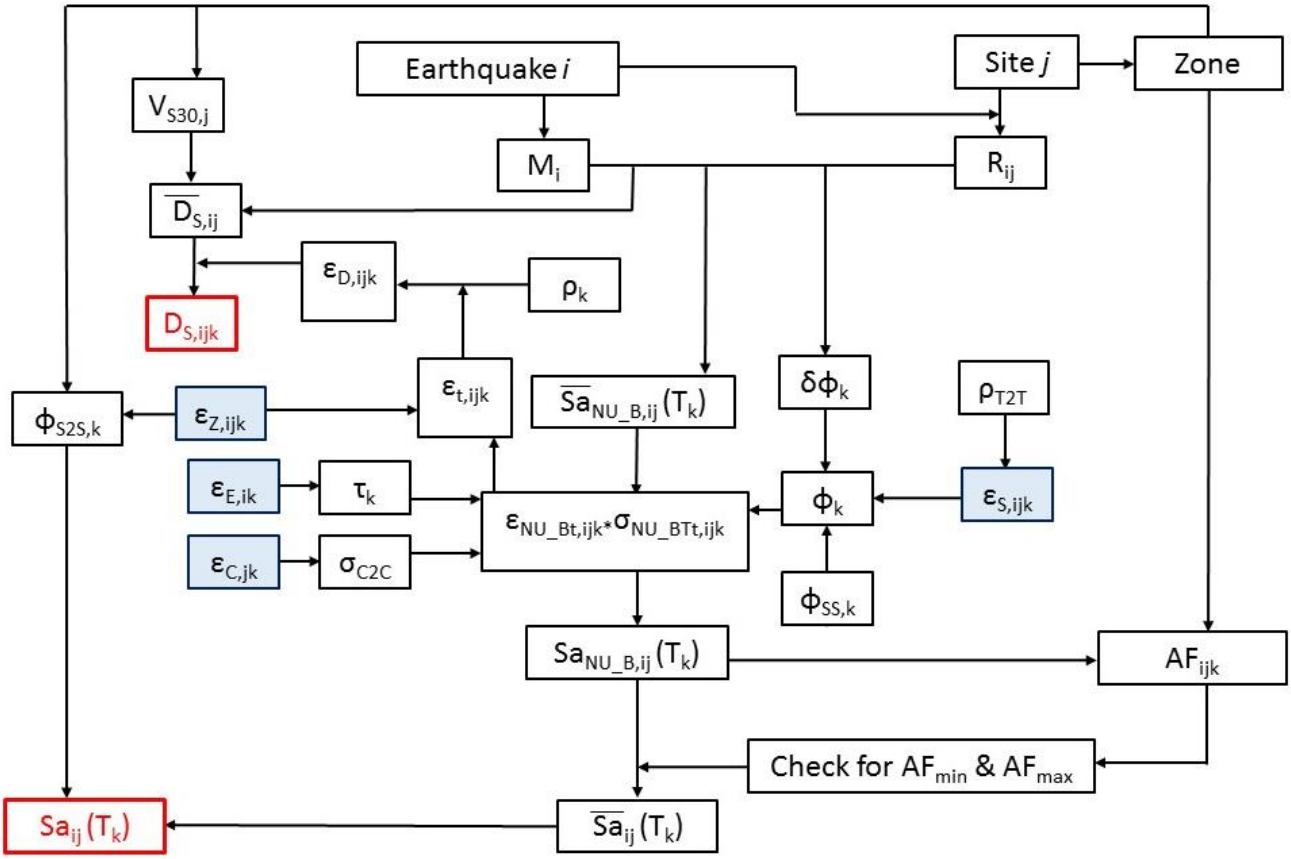

Figure 11.1. Flowchart illustrating implementation of the V2 GMPEs in the risk calculations. The subscript t refers to total, the subscript T to period, and the subscript C to component; for hazard, rather than risk, calculations, the component-to-component variability is ignored. The four boxes shaded in blue are the random samples from log-normal distributions and the two red boxes indicate the final outcomes: spectral acceleration at the ground surface at each period and the associated significant duration

Figure 11.1 inevitably is unable to illustrate the full complexity of the calculations, which are conducted at each site for 16 oscillator periods for one of the three branches of the ground-motion logic-tree. In practice, the calculations are performed using the coefficients and sigma models for all three branches and the weighted mean of the resulting motions (for hazard) or the weighted mean of the resulting damage levels (for risk) calculated using the branch weights of 0.2, 0.5 and 0.3 assigned to the lower, central and upper branches; as noted in Section 6.6, modified branch weights could be justified but we opt to retain them the same as in the V1 model for now. For each earthquake, a large number (several hundred) of sites across the study area are considered, and then for each catalogue the calculations are repeated for all of the earthquakes. However, the diagram does serve to illustrate the key steps of the implementation and the sampling of the different components of the variability, as well as the correlations that are currently considered between these random samples.

In order to test the performance of the final complete model with respect to the Groningen recordings, we calculate the predicted median motions for each of the records, using the AFs for the zone hosting each recording station (Section 9.3) rather than the station-specific AFs derived in Section 4.3. The total residuals are plotted against both magnitude and distance in Figures 11.2 to 11.5, for spectral accelerations up to 2 seconds; residuals are also calculated for Sa(2.5s) but there are too few usable data for these to be meaningful (Figure 11.6). The plots show that there is very considerable scatter in the residuals and there is generally a bias, sometimes associated with an apparent trend, particularly with magnitude. However, it is also the case the overall the model provides a reasonable fit to the data and the bias that does exist is in nearly all cases indicative of over-prediction, which is an acceptable situation for this preliminary version of the Groningen ground-motion model in its final form incorporating reference rock predictions combined with a field-wide zonation for non-linear site amplification factors. The fine-tuning that will now be performed, in particular incorporating improved site information at the recording stations (Section 13.2) in addition to many other refinements (Section 13.5), is expected to both remove much of the bias and also reduce the associated scatter. These results, however, are encouraging in terms of the preliminary version of the complete model.

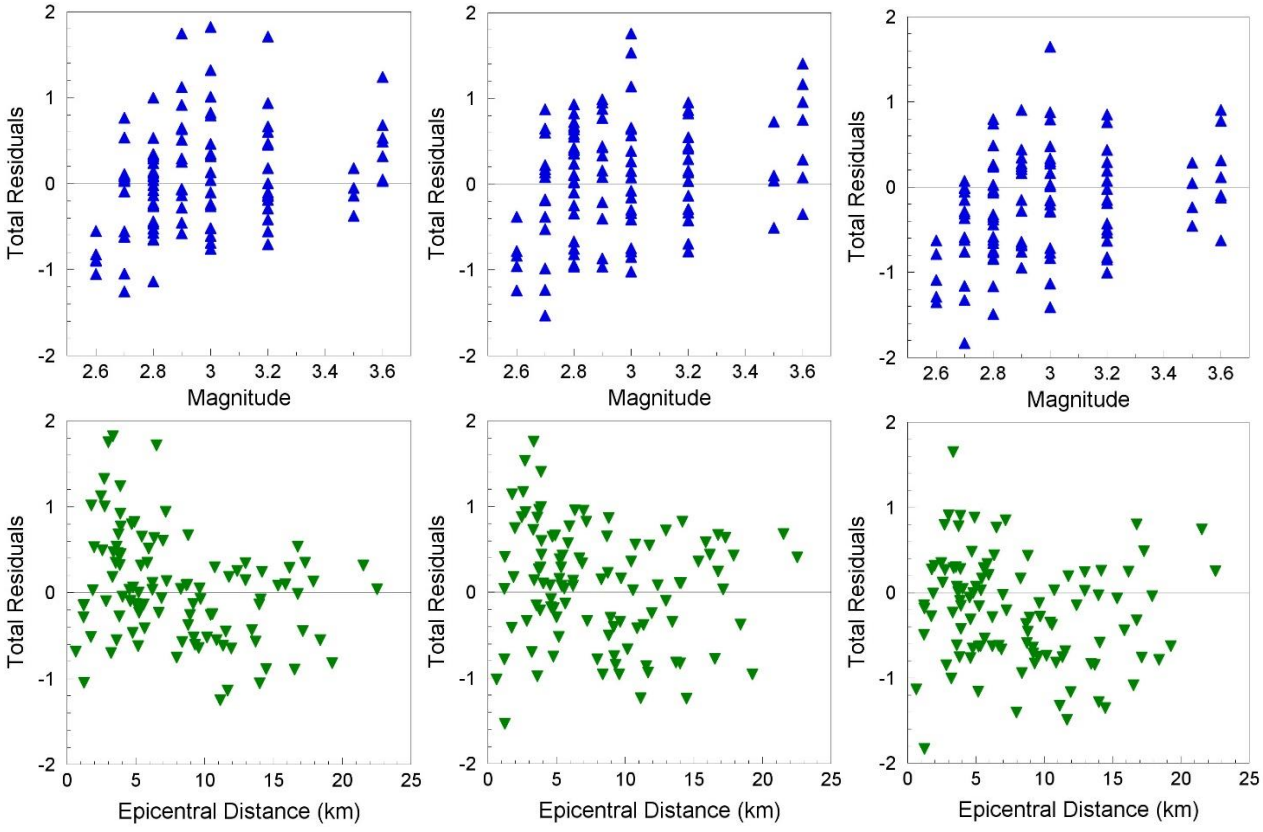

Figure 11.2. Total residuals of the surface motions with respect to the full V2 model for spectral accelerations at 0.01 s (*left*), 0.1 s (*centre*) and 0.2 s (*right*)

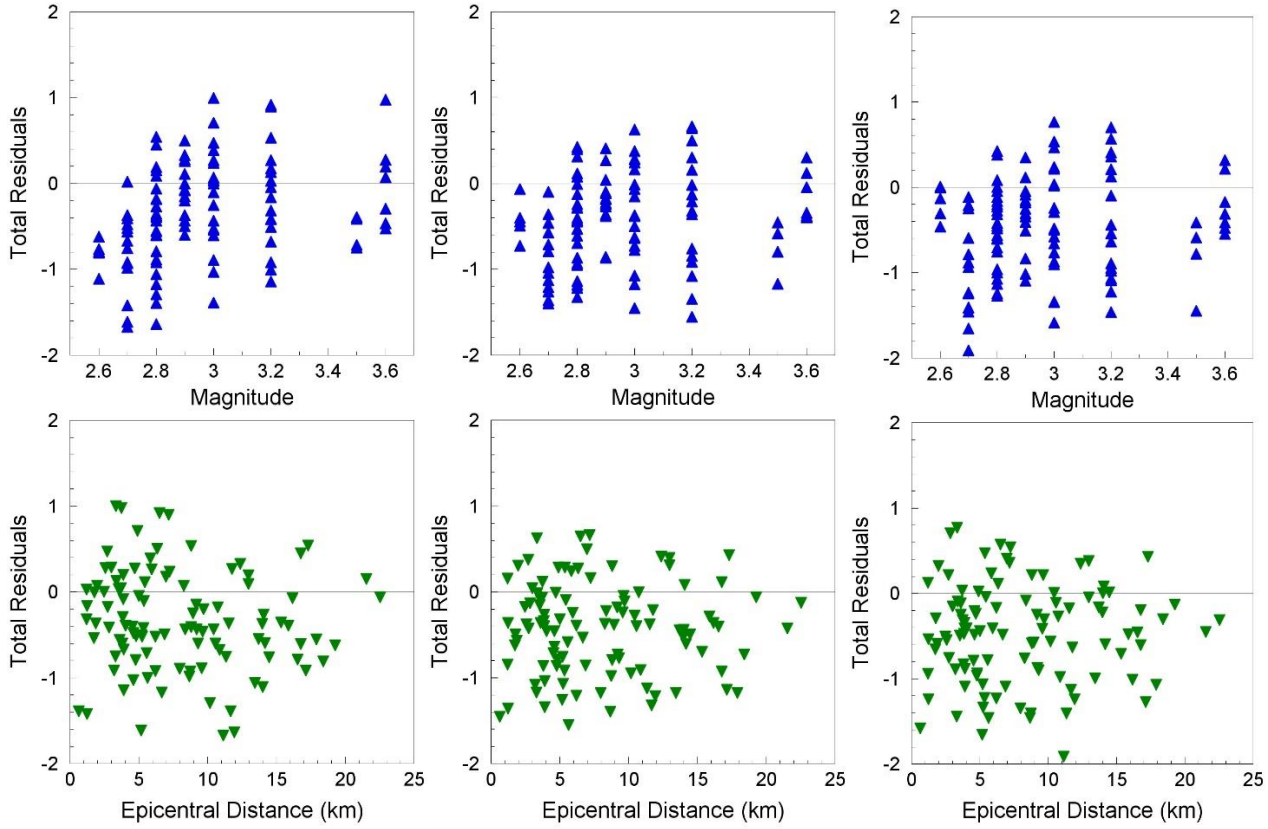

Figure 11.3. Total residuals of the surface motions with respect to the full V2 model for spectral accelerations at 0.3 s (*left*), 0.4 s (*centre*) and 0.5 s (*right*)

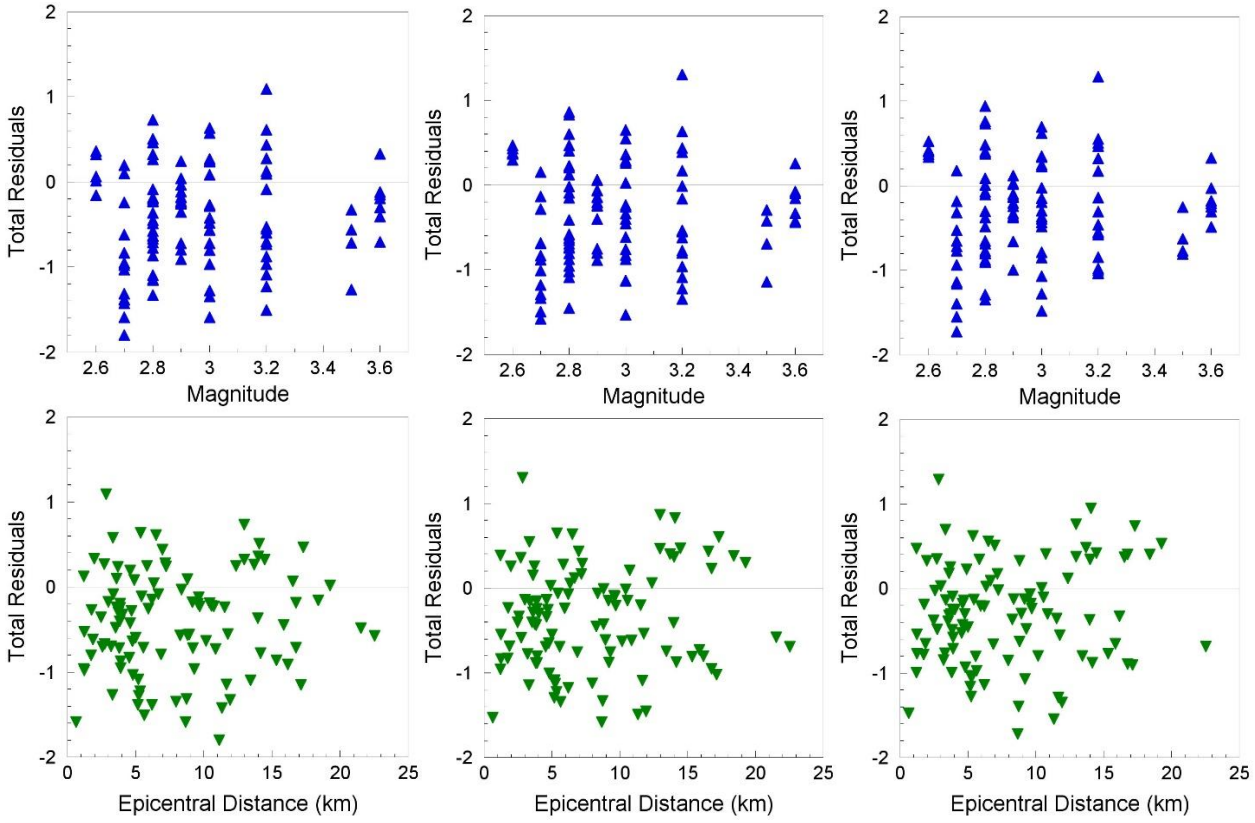

Figure 11.4. Total residuals of the surface motions with respect to the full V2 model for spectral accelerations at 0.6 s (*left*), 0.7 s (*centre*) and 0.85 s (*right*)

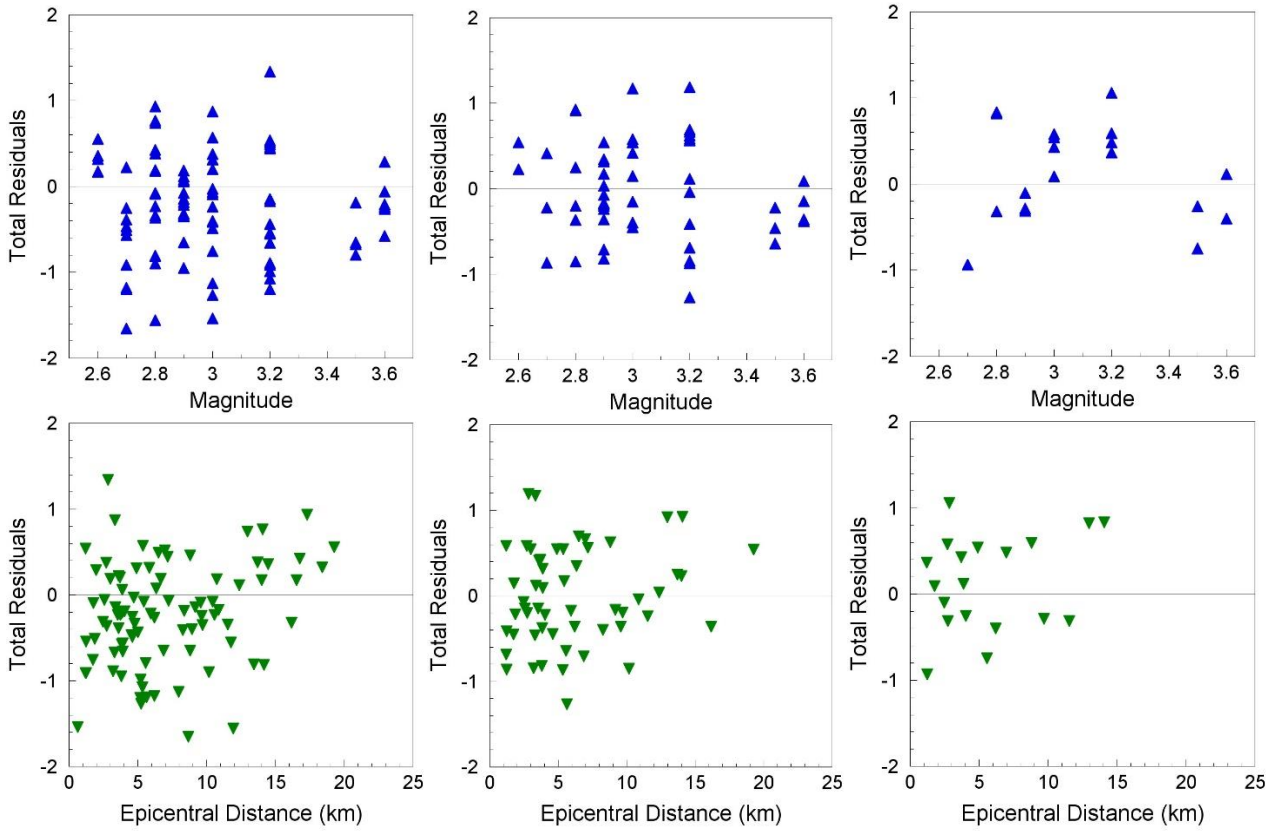

Figure 11.5. Total residuals of the surface motions with respect to the full V2 model for spectral accelerations at 1.0 s (*left*), 1.5 s (*centre*) and 2.0 s (*right*)

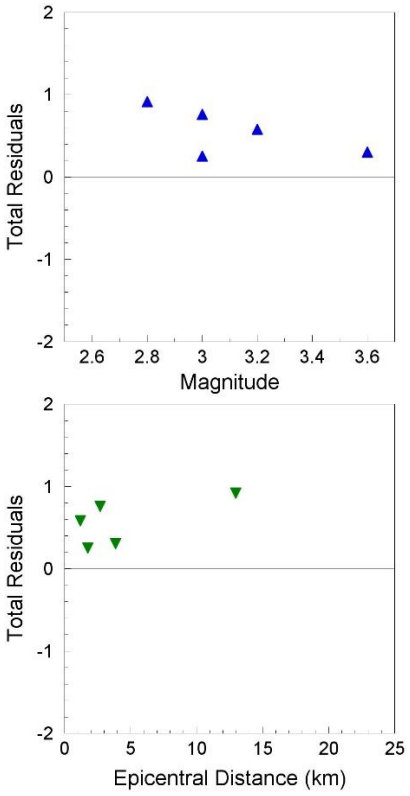

Figure 11.6. Total residuals of the surface motions with respect to the full V2 model for spectral accelerations at 2.5 s; there are insufficient usable records at this period for these results to be meaningful but they are shown for completeness

11.2. Comparison with V1 GMPE predictions

The new GMPEs presented in this report completely supersede the V1 equations issued, in their final form, in June 2015. Since the hazard and risk estimates will now be updated using these new models, it is useful to acquire some insight regarding how different the new predictions are from those obtained from the previous equations at the five oscillator periods common to both models. The focus in this section is on a comparison between the median predictions only since the nature of the aleatory variability model is quite different in the two models. As was illustrated in the previous chapter (Figures 10.8 and 10.9), the standard deviations associated with the baserock predictions in the V2 model are comparable, overall, with those in the V2 model for direct predictions at the surface. However, it must be remembered that in the V2 model there is an additional component of variability at the surface although since this is assumed to be completely uncorrelated with the variability in the reference rock motions, there will be cases where high positive epsilons at the NU_B will lead to greater non-linearity in the soil response, and this will then be combined with a negative epsilon for the site-to-site variability. Consequently, it is very difficult to predict general trends in terms of the influence of the sigma model on the final surface motions.

Even for the median motions, a complete comparison is cumbersome since the new non-linear site amplification factors are different in each of the 167 site response zones that has been defined, so only an illustrative sample of the zones can be shown. For this purpose we selected a total of nine zones:

- Zone 309 (SW of study area over the sand layers that underlie the city of Groningen) as an example of low amplification factors
- Zones 601 (NW of the field), 820 (northern limit of the field), 1705 (SE corner) and 2204 (middle of the field to the west side) as examples of intermediate amplification factors
- Zones 1009 (centre west) and 2011 (NE of field) as examples of high amplification factors

In Figures 11.7-11.76 the scaling of median motions from the V2 and V1 models with magnitude are compared at the five common response periods (0.01, 0.2, 0.5, 1 and 2 seconds) for epicentral distances of 0 and 10 km. In every case, the upper, central and lower models are compared. For the V2 model, in each case the motions at the NU_B reference rock are shown as well as the linearly amplified surface motions (neglecting the non-linear component of the site amplification factors), as well as the final surface motions invoking the non-linear response. This is done in order to illustrate the variation due to site response characteristics with respect to the assumed constant field-wide amplification function in the V1 GMPEs. Additionally, the difference between the two V2 curves for surface motions serves to illustrate the strength of the non-linearity in the soil response.

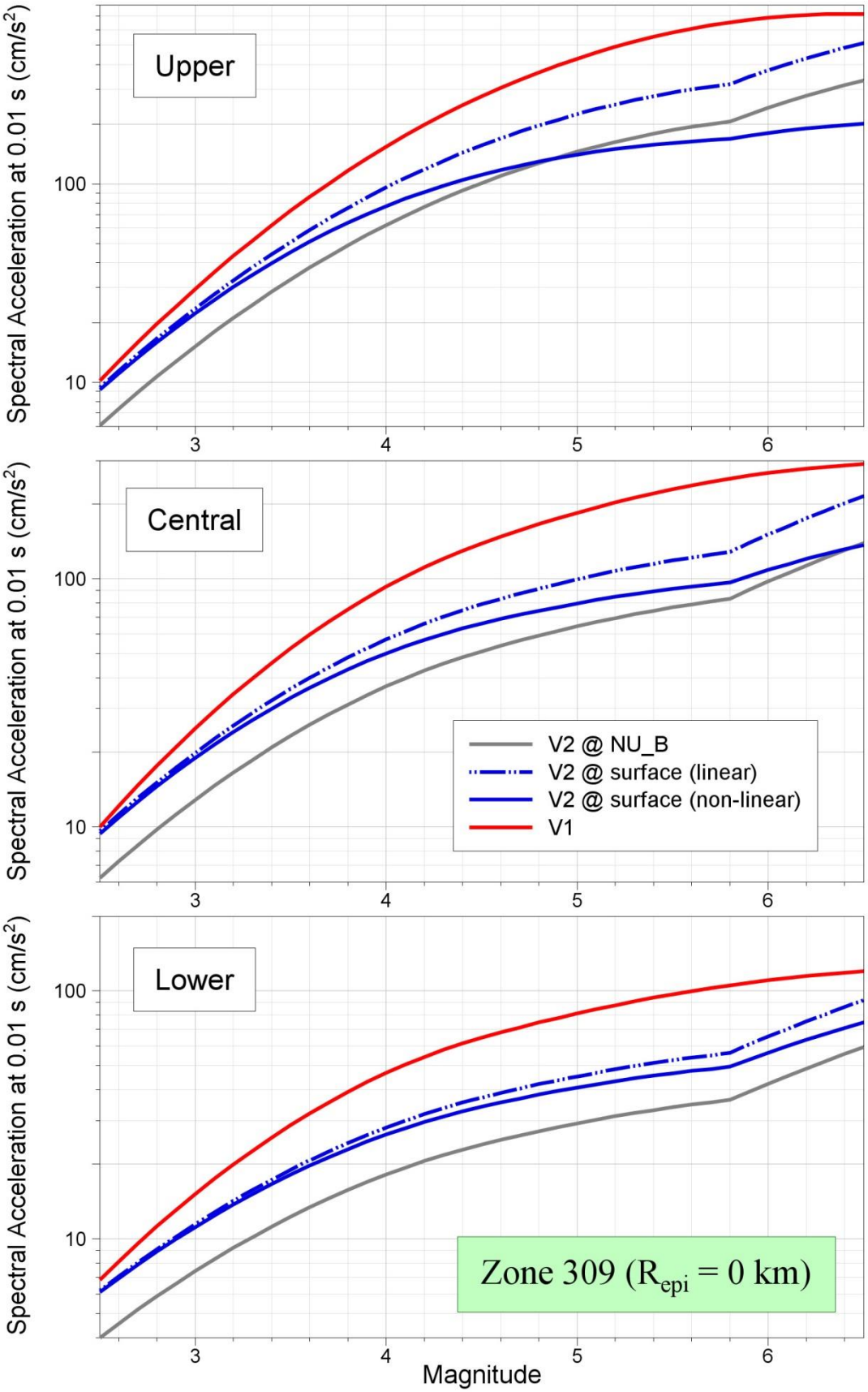

Figure 11.7. Comparison of median predictions of Sa(0.01) as a function of magnitude from the V1 and V2 models for Zone 309 and R_{epi} = 0 km

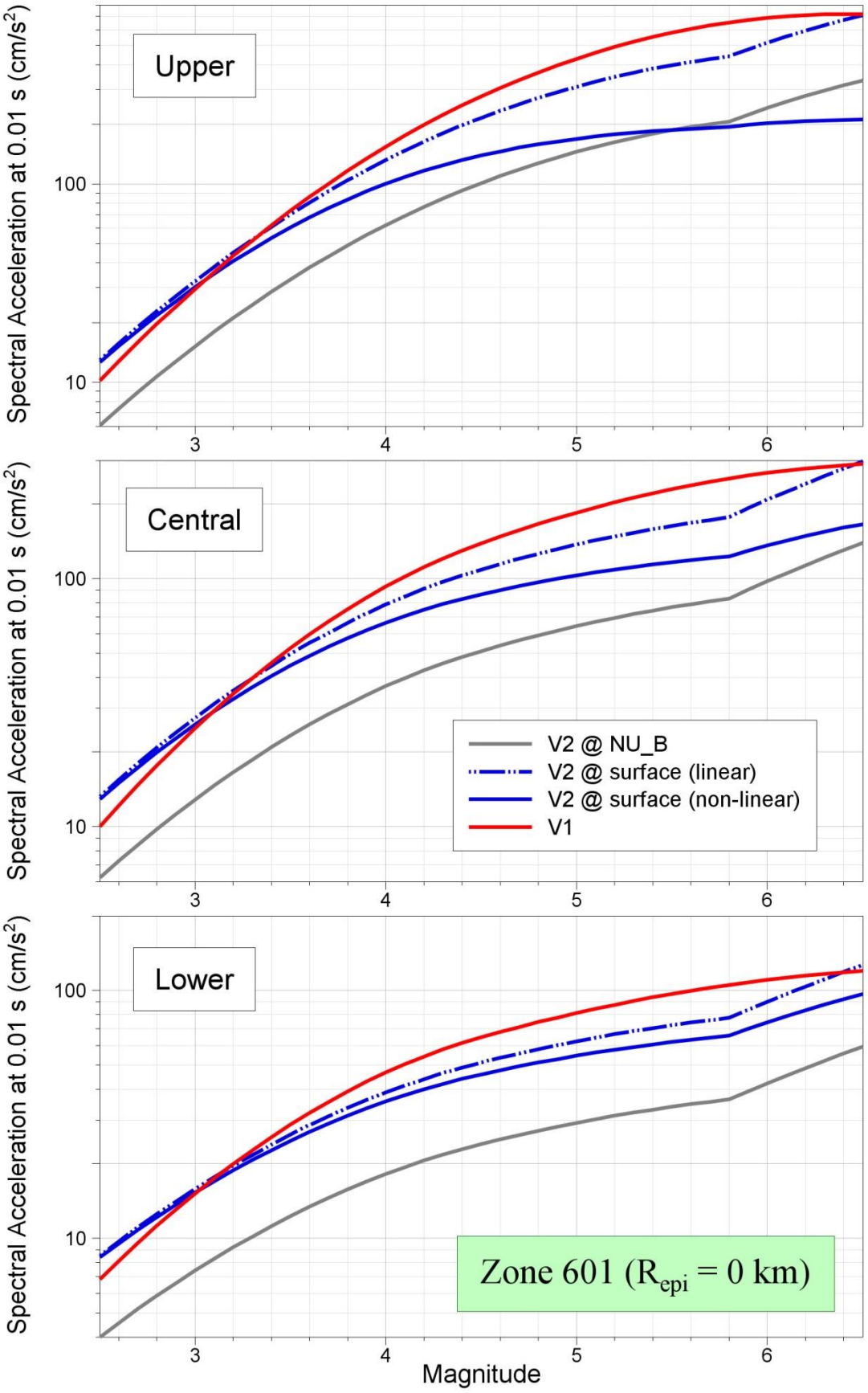

Figure 11.8. Comparison of median predictions of Sa(0.01) as a function of magnitude from the V1 and V2 models for Zone 601 and R_{epi} = 0 km

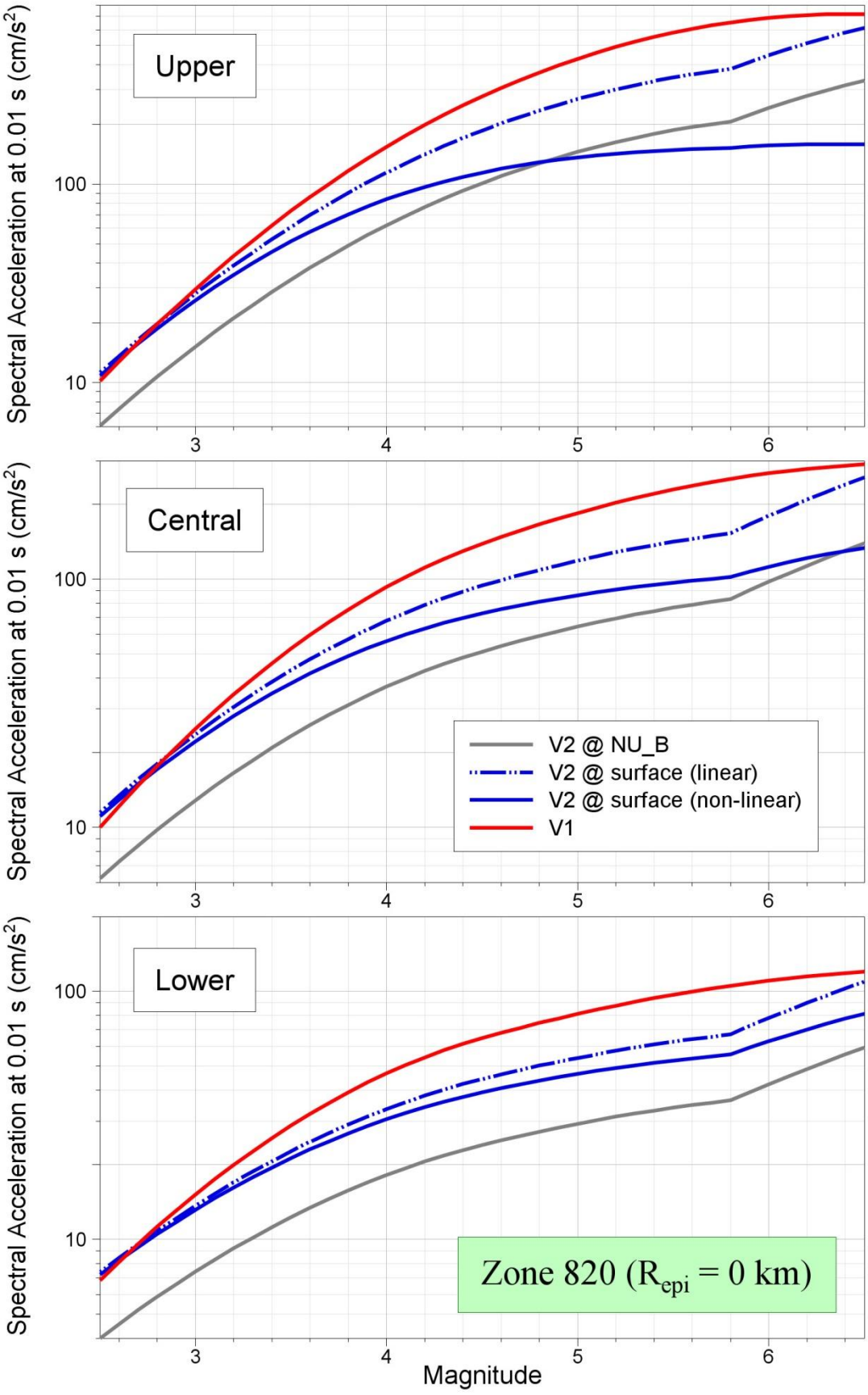

Figure 11.9. Comparison of median predictions of Sa(0.01) as a function of magnitude from the V1 and V2 models for Zone 820 and R_{epi} = 0 km

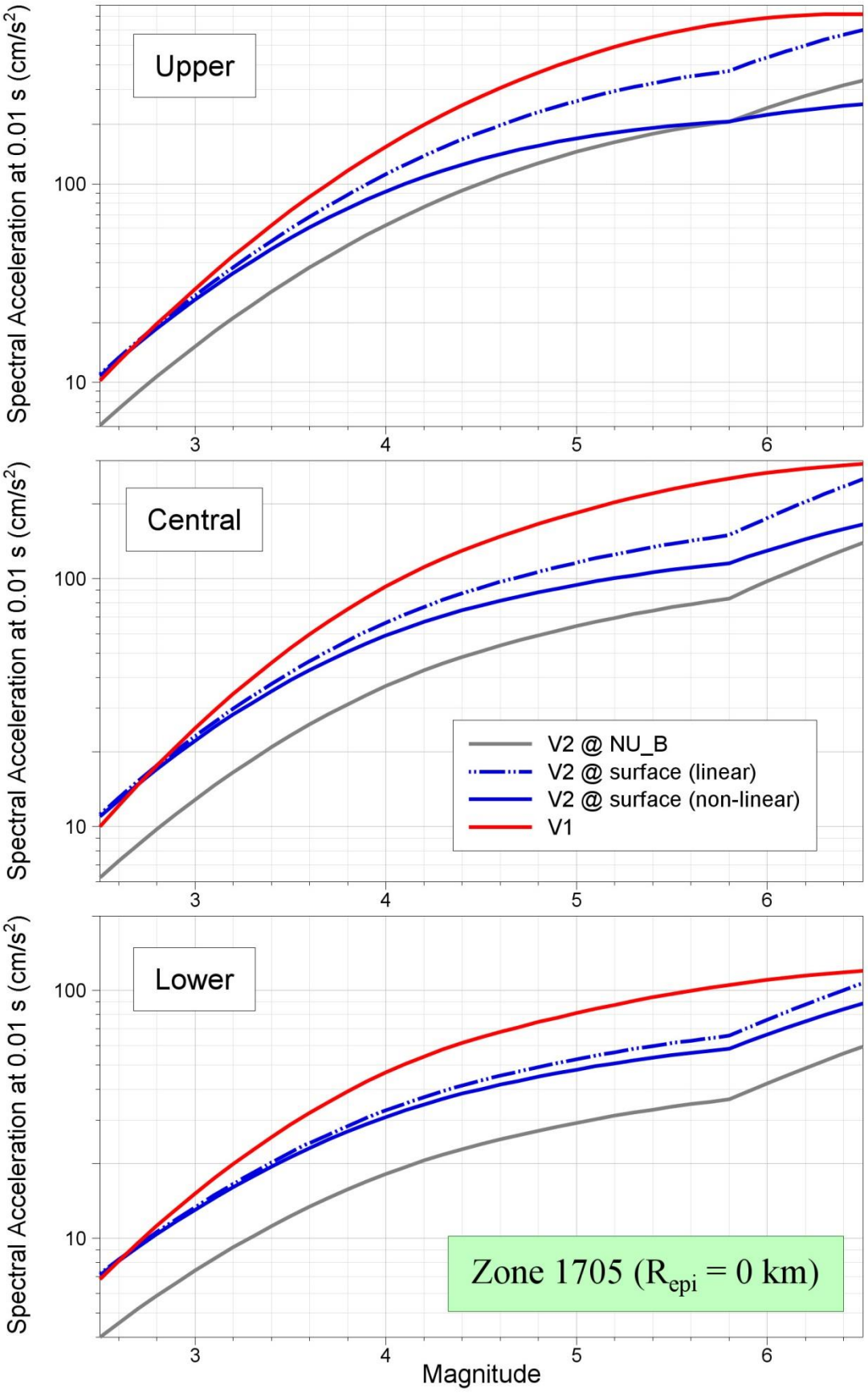

Figure 11.10. Comparison of median predictions of Sa(0.01) as a function of magnitude from the V1 and V2 models for Zone 1705 and R_{epi} = 0 km

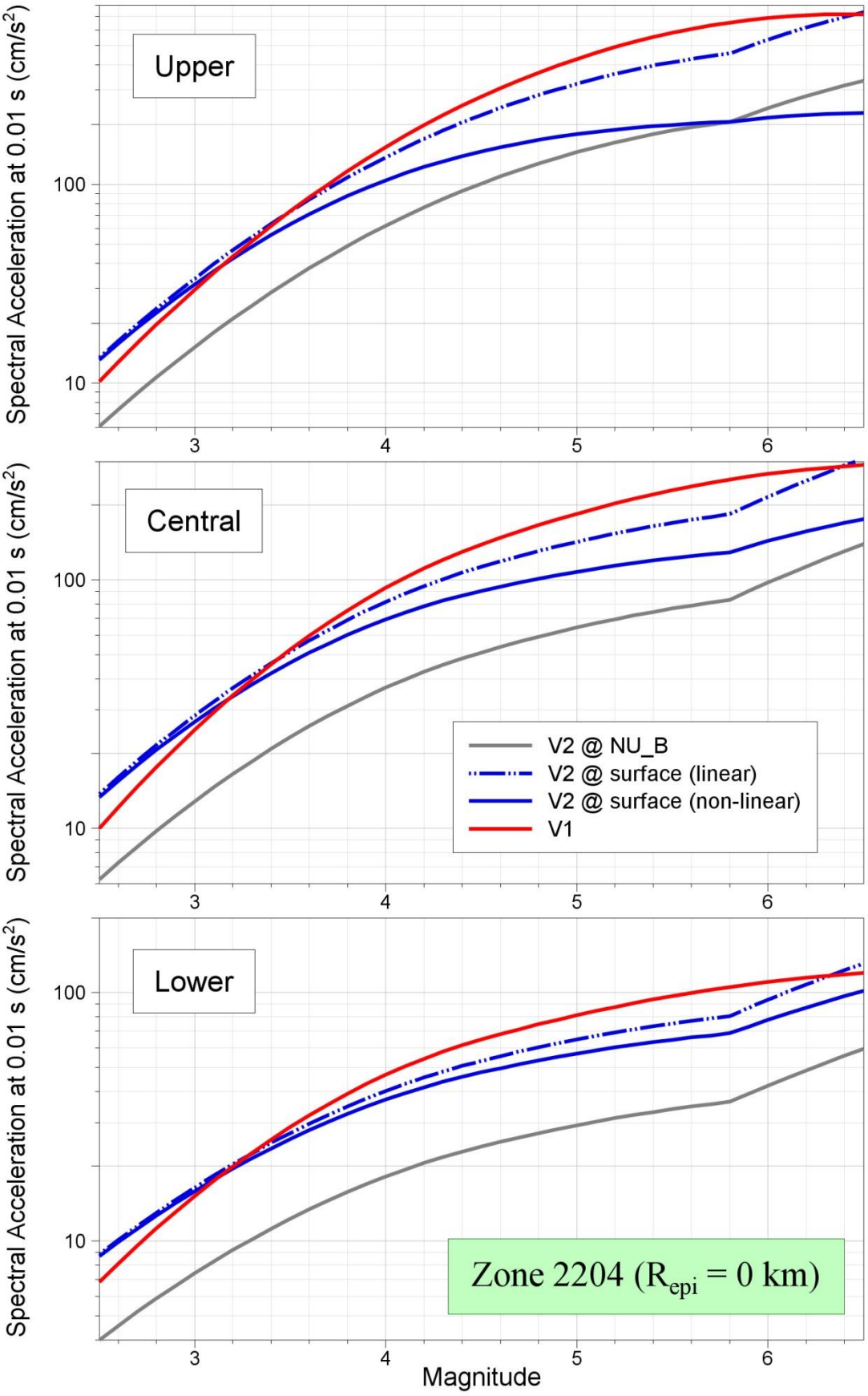

Figure 11.11. Comparison of median predictions of Sa(0.01) as a function of magnitude from the V1 and V2 models for Zone 2204 and R_{epi} = 0 km

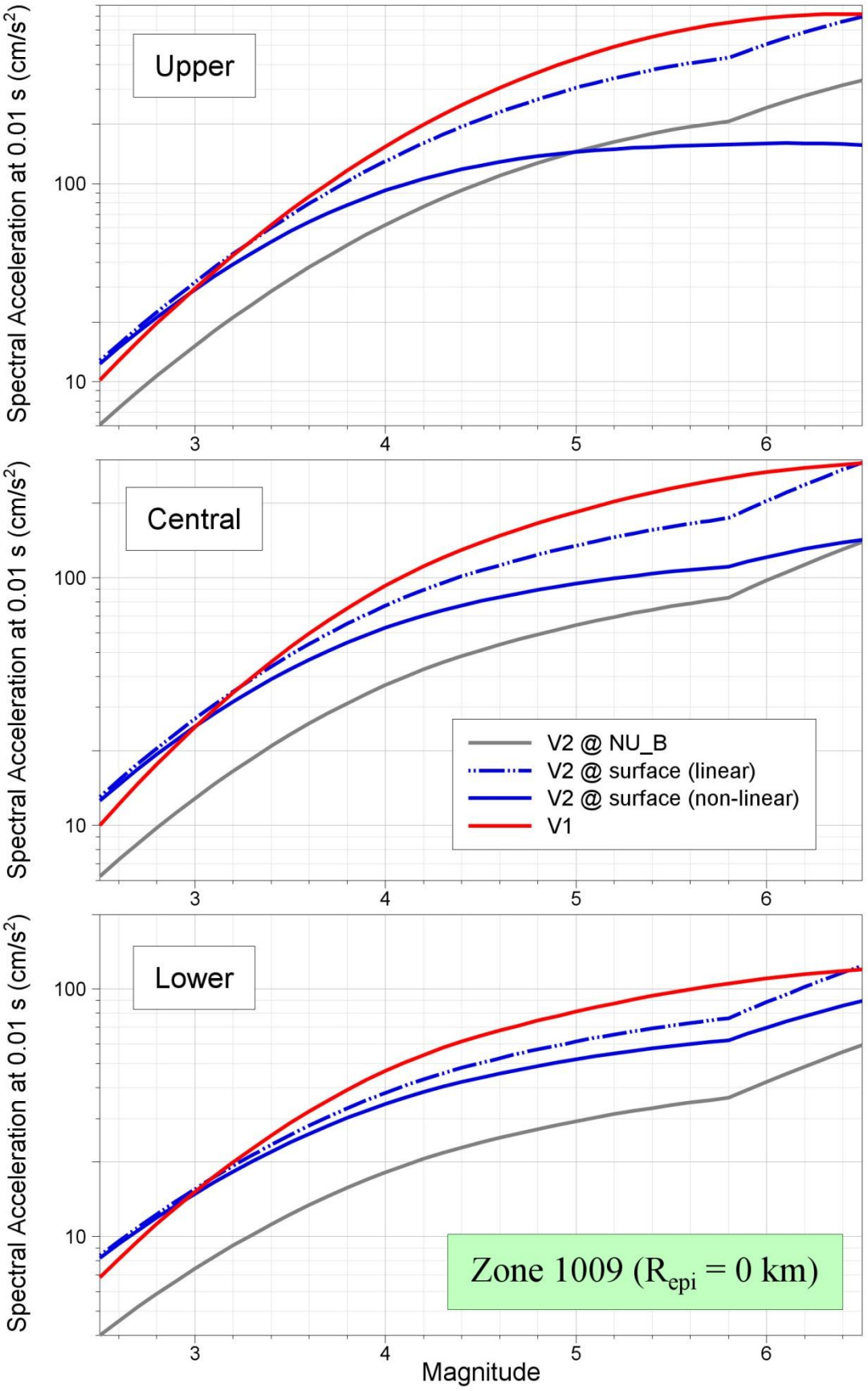

Figure 11.12. Comparison of median predictions of Sa(0.01) as a function of magnitude from the V1 and V2 models for Zone 1009 and R_{epi} = 0 km

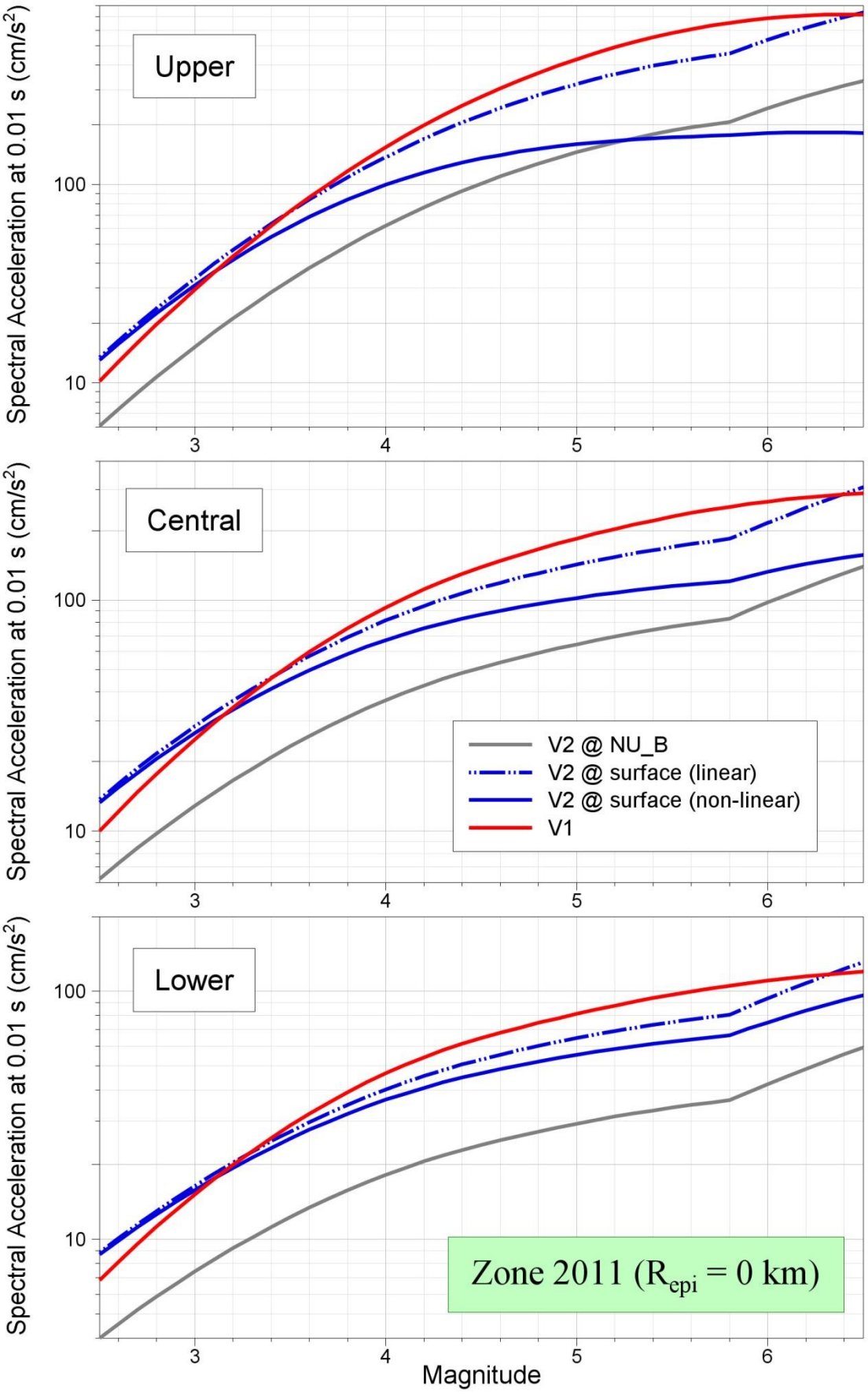

Figure 11.13. Comparison of median predictions of Sa(0.01) as a function of magnitude from the V1 and V2 models for Zone 2011 and R_{epi} = 0 km

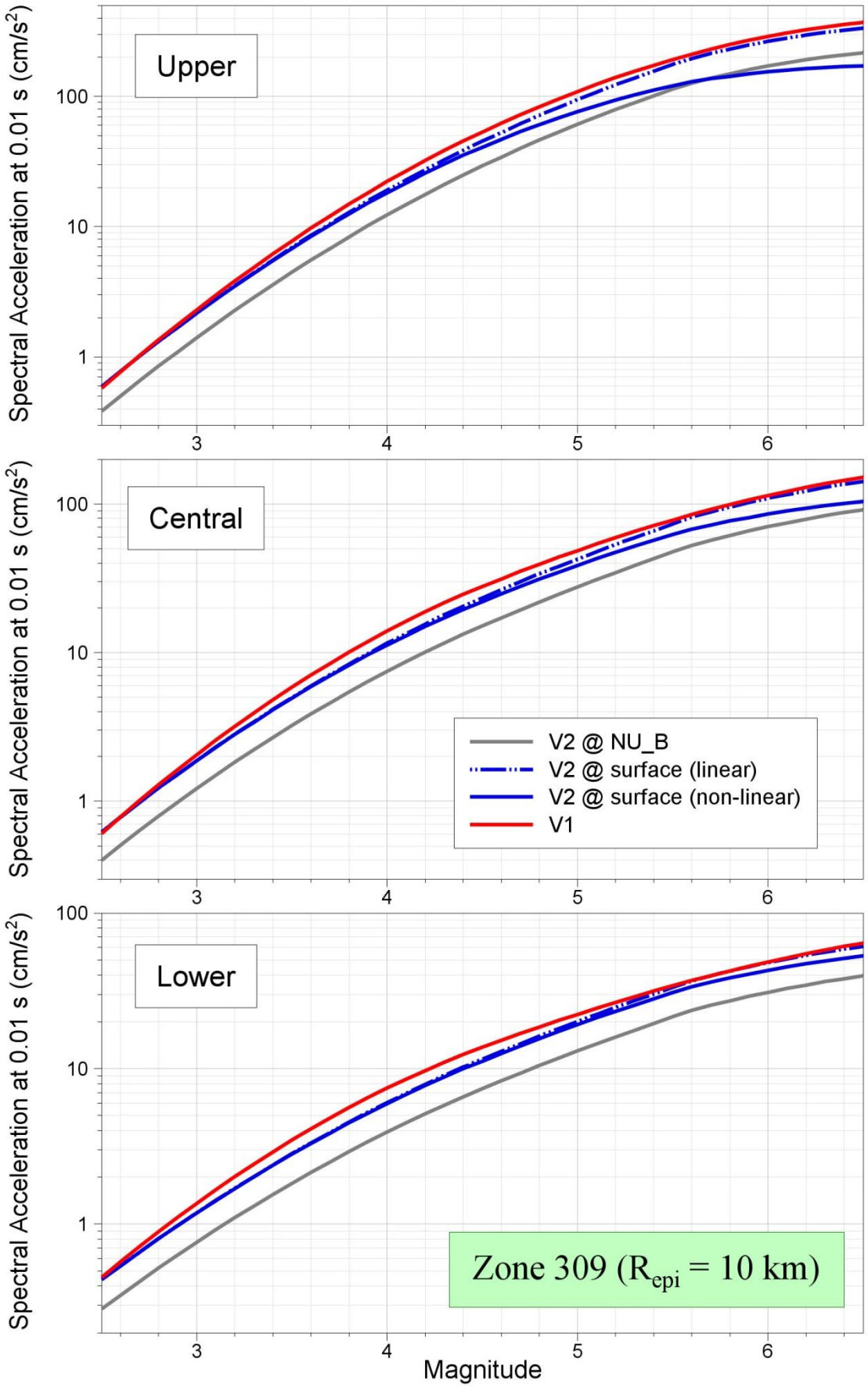

Figure 11.14. Comparison of median predictions of Sa(0.01) as a function of magnitude from the V1 and V2 models for Zone 309 and R_{epi} = 10 km

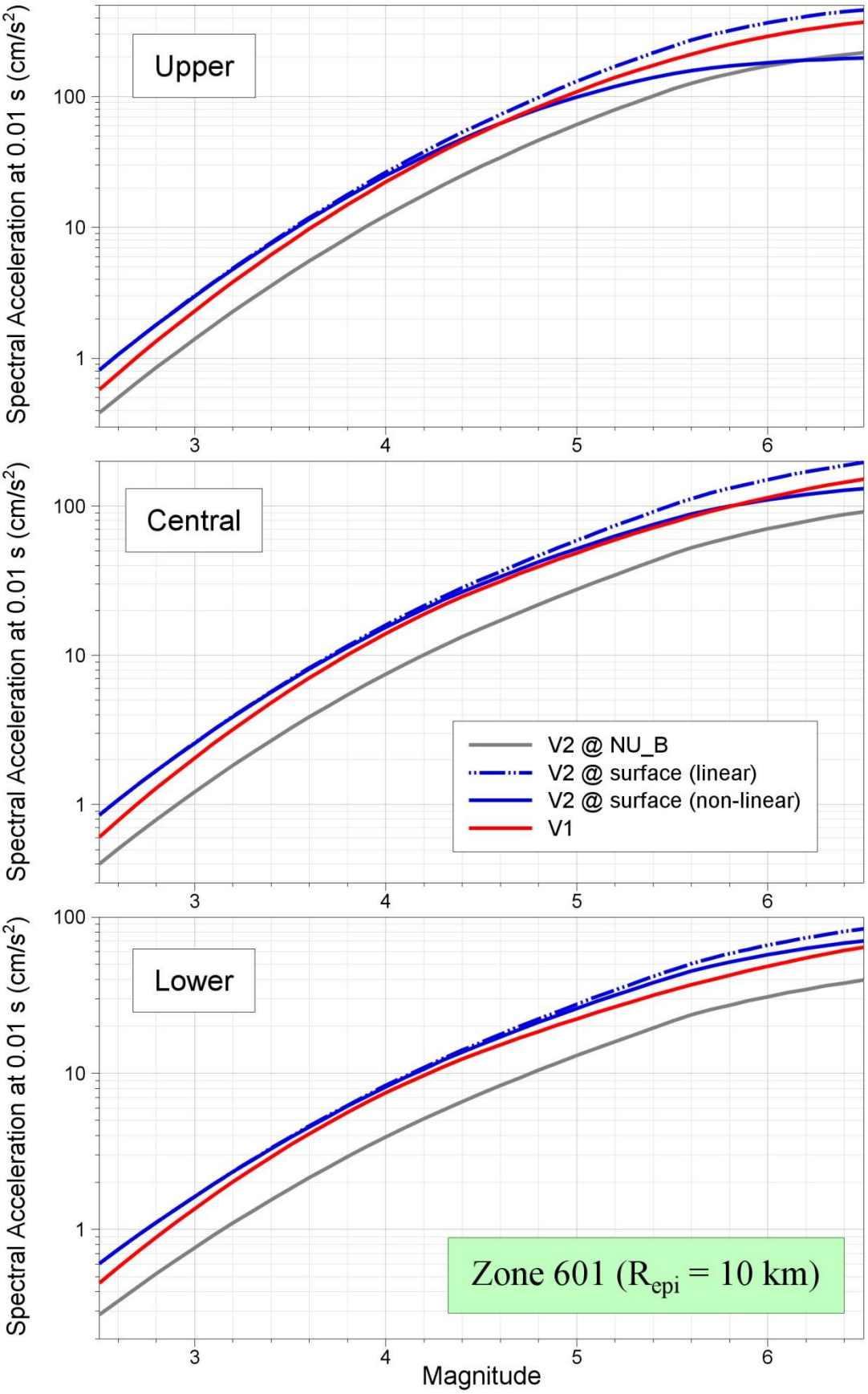

Figure 11.15. Comparison of median predictions of Sa(0.01) as a function of magnitude from the V1 and V2 models for Zone 601 and R_{epi} = 10 km

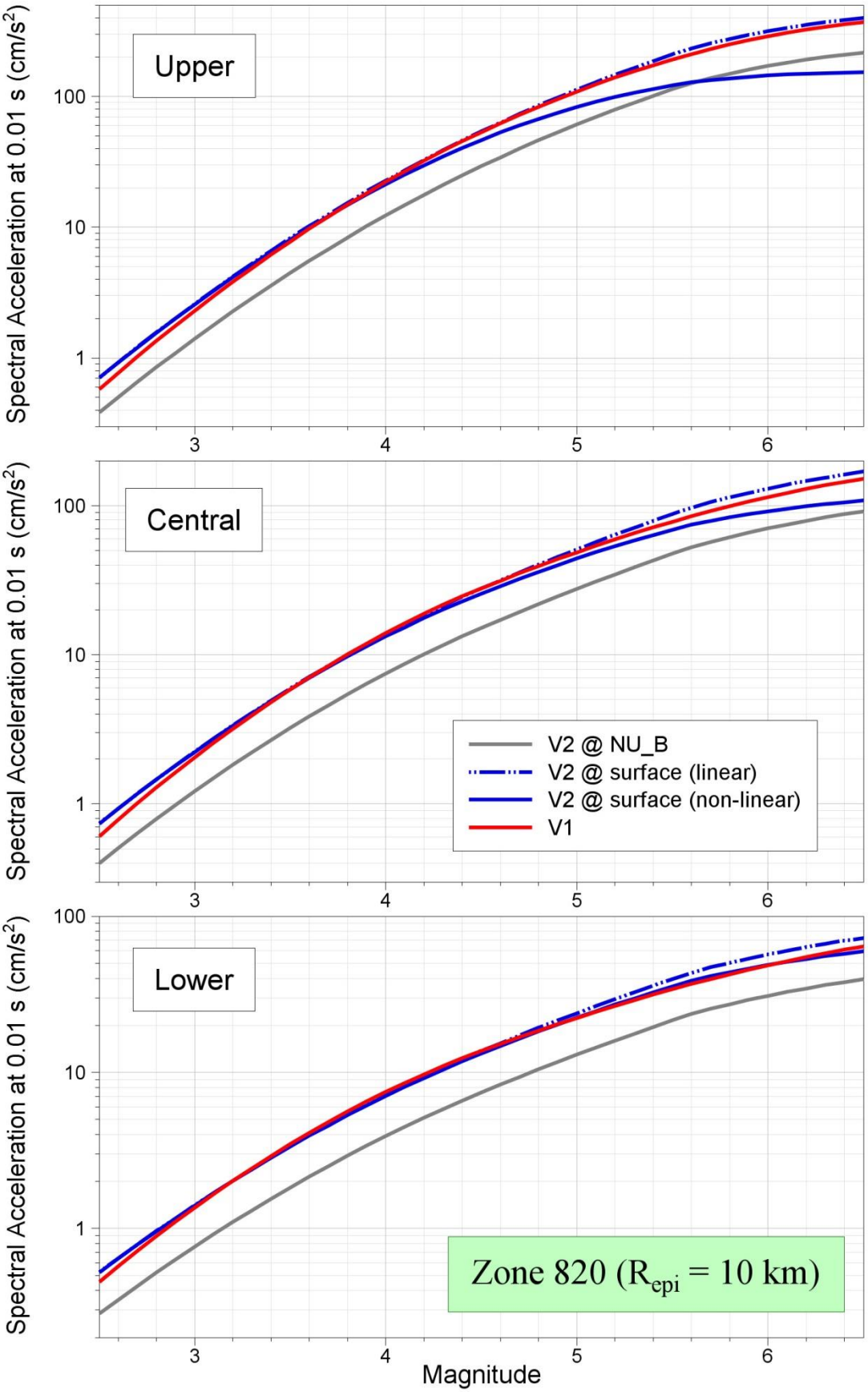

Figure 11.16. Comparison of median predictions of Sa(0.01) as a function of magnitude from the V1 and V2 models for Zone 820 and R_{epi} = 10 km

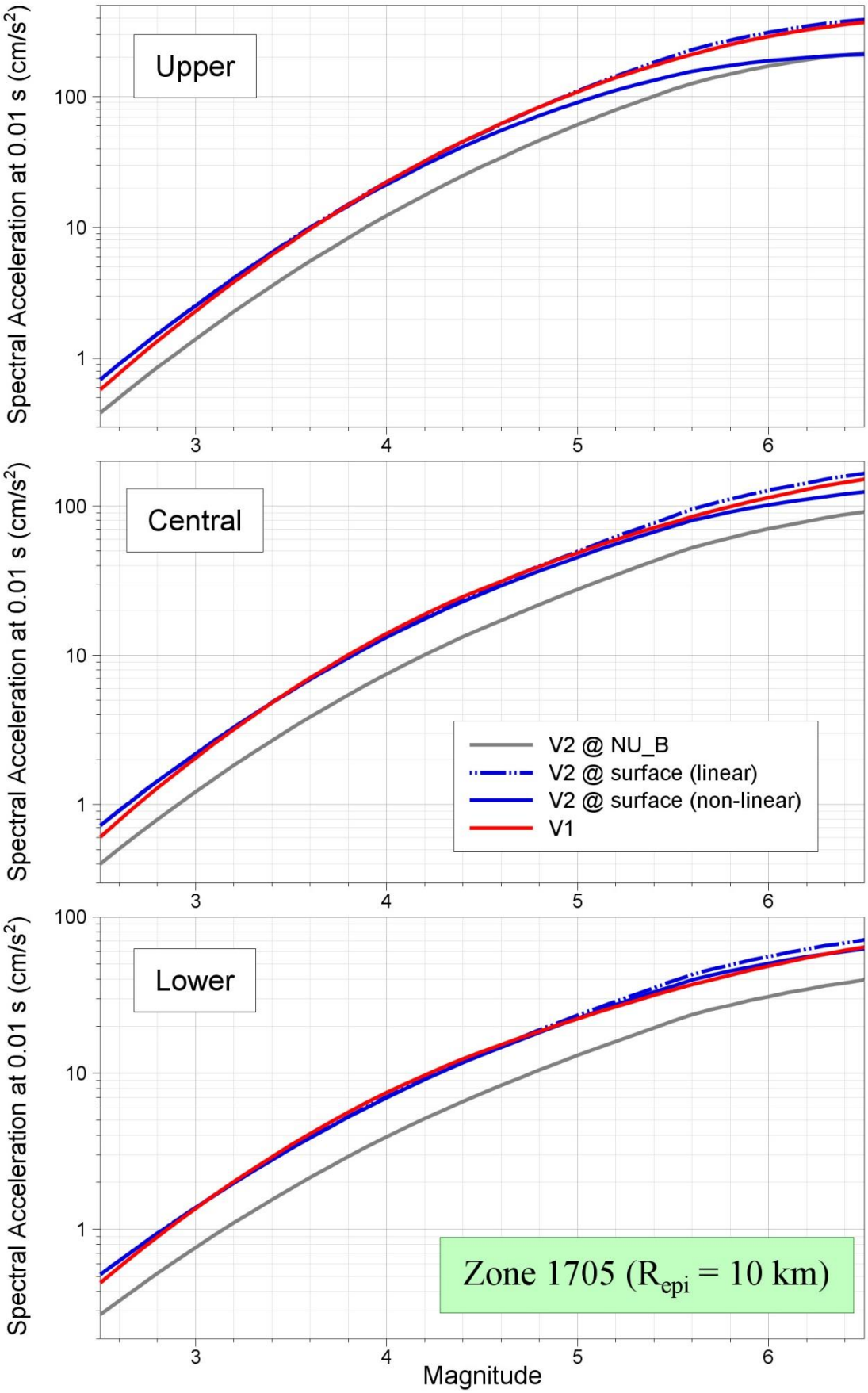

Figure 11.17. Comparison of median predictions of Sa(0.01) as a function of magnitude from the V1 and V2 models for Zone 1705 and R_{epi} = 10 km

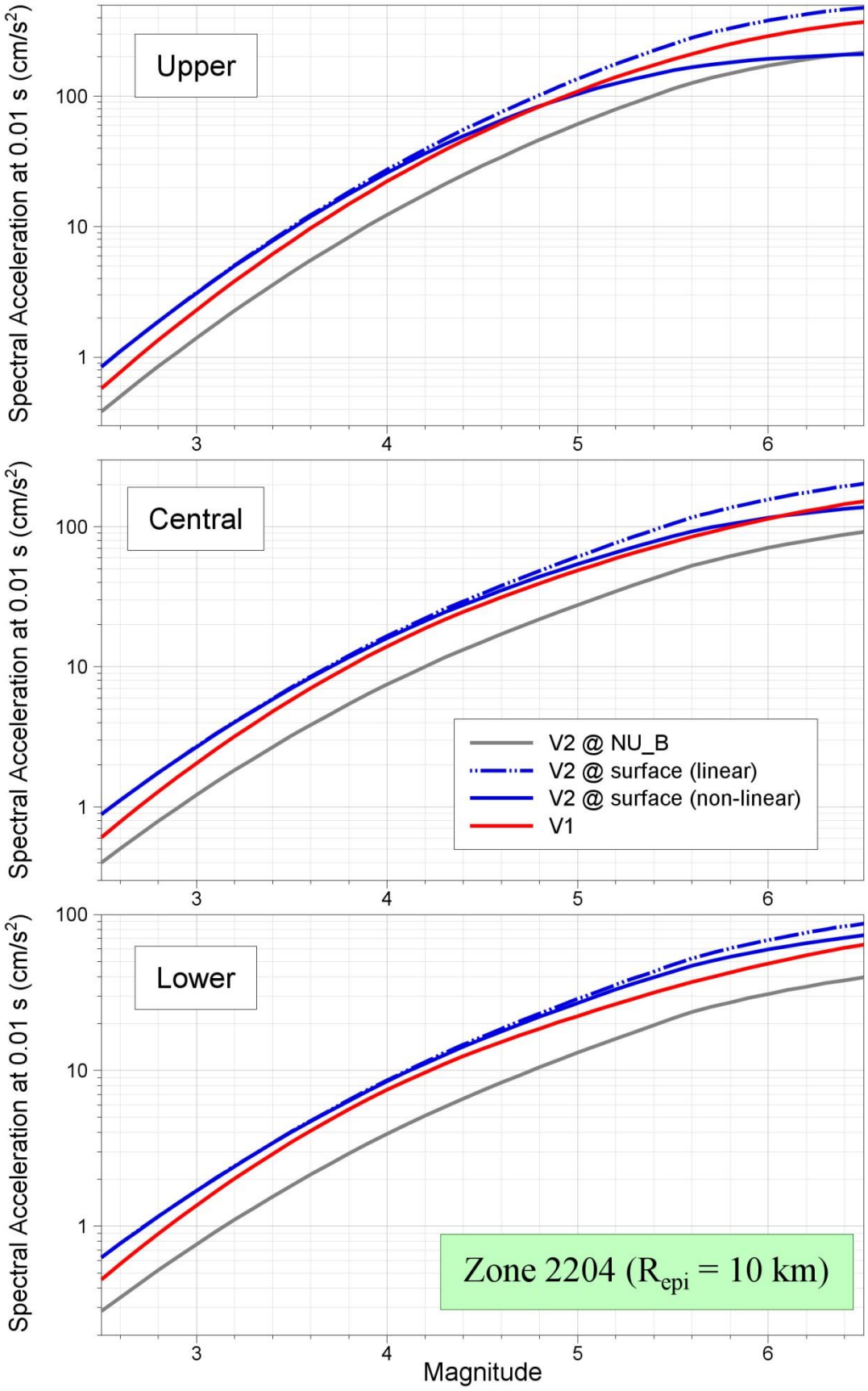

Figure 11.18. Comparison of median predictions of Sa(0.01) as a function of magnitude from the V1 and V2 models for Zone 2204 and R_{epi} = 10 km

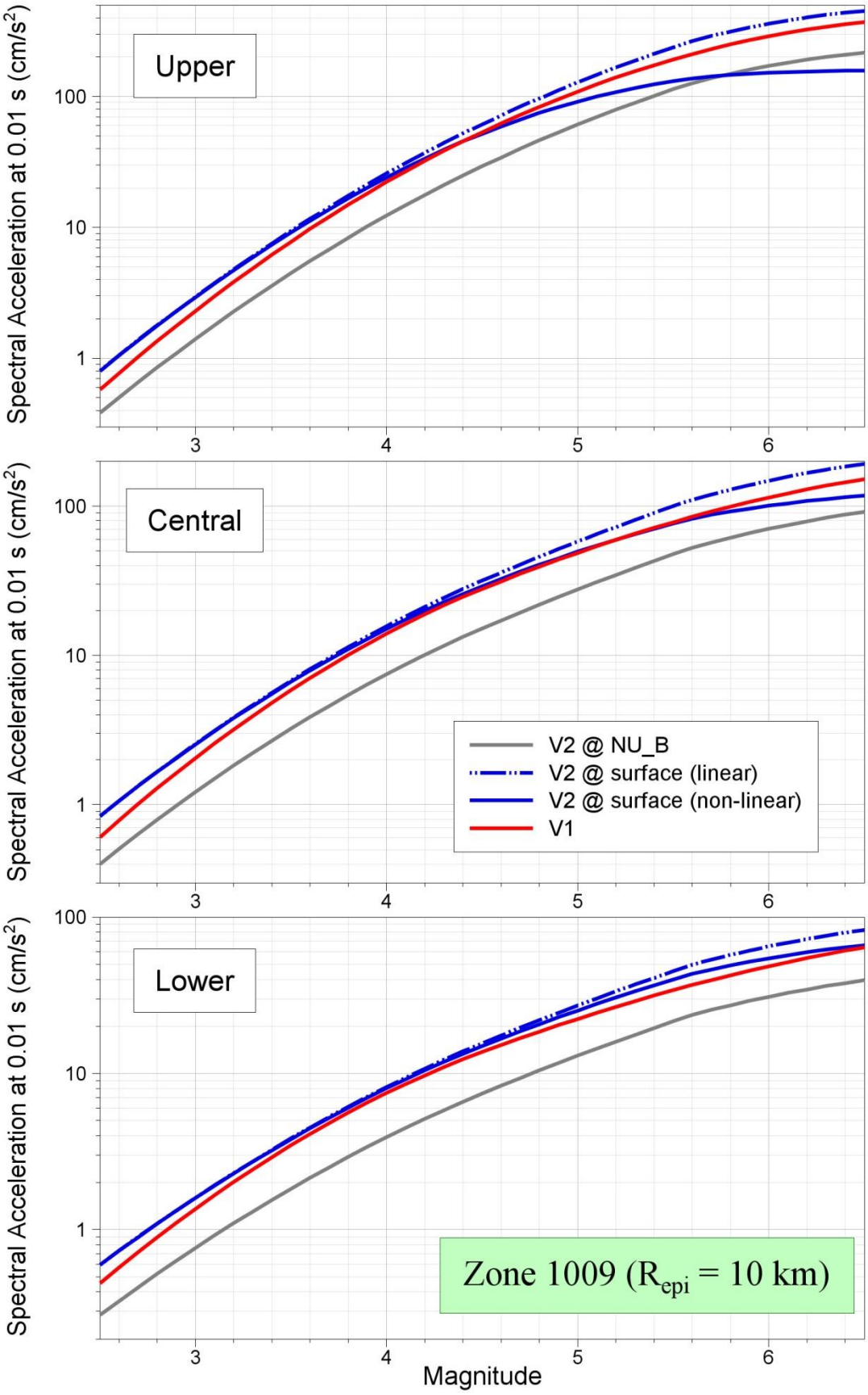

Figure 11.19. Comparison of median predictions of Sa(0.01) as a function of magnitude from the V1 and V2 models for Zone 1009 and R_{epi} = 10 km

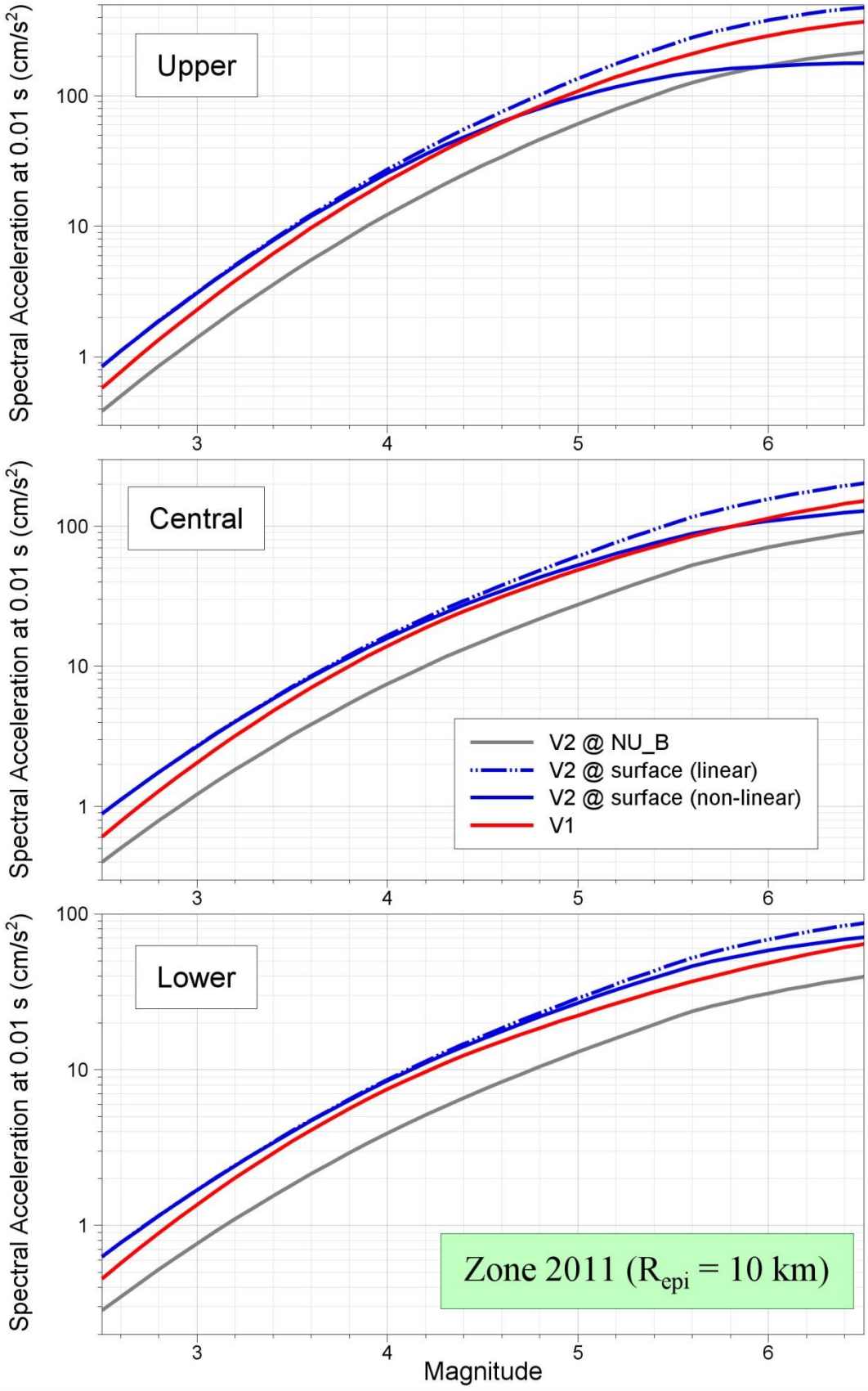

Figure 11.20. Comparison of median predictions of Sa(0.01) as a function of magnitude from the V1 and V2 models for Zone 2011 and R_{epi} = 10 km

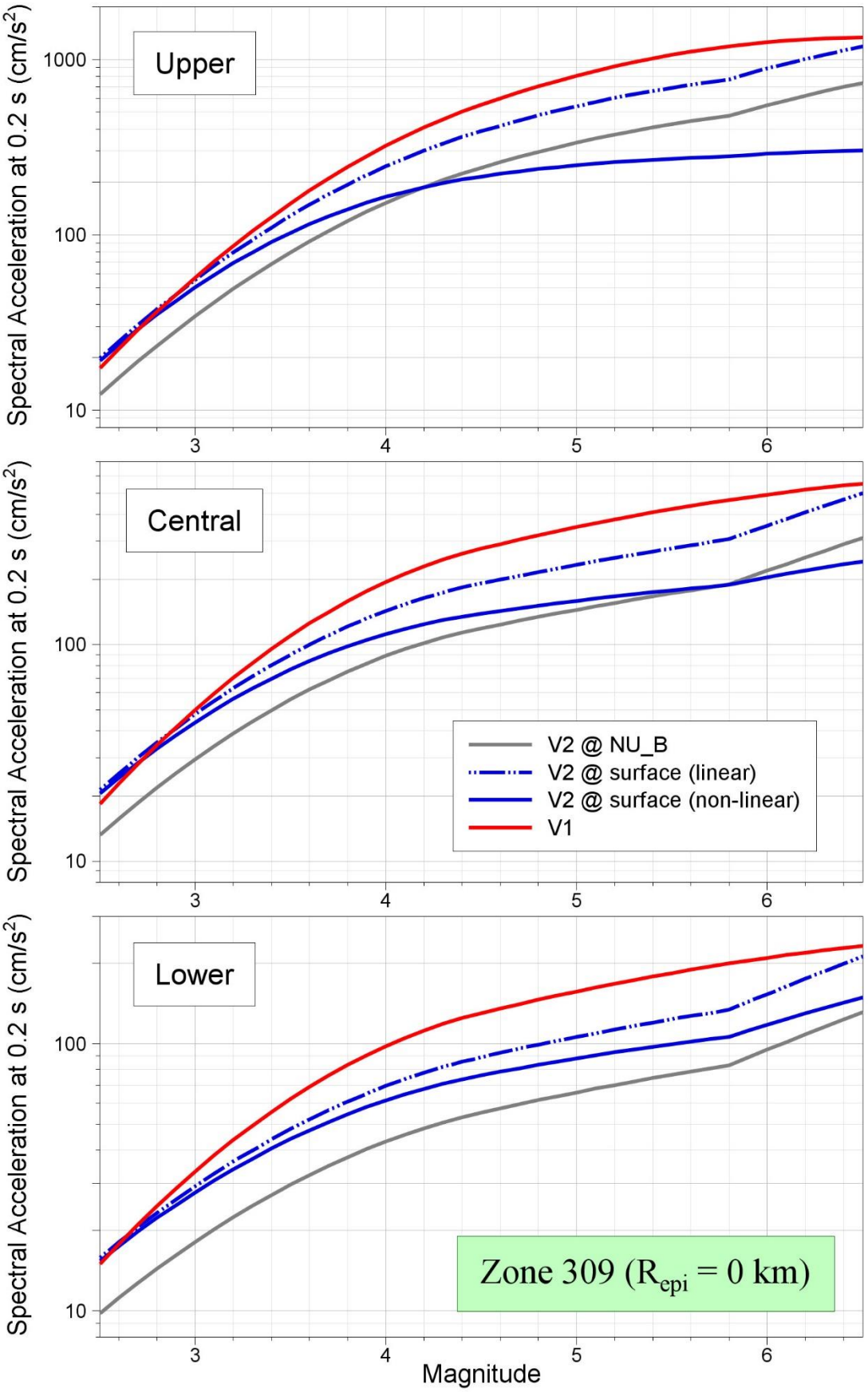

Figure 11.21. Comparison of median predictions of Sa(0.2) as a function of magnitude from the V1 and V2 models for Zone 309 and R_{epi} = 0 km

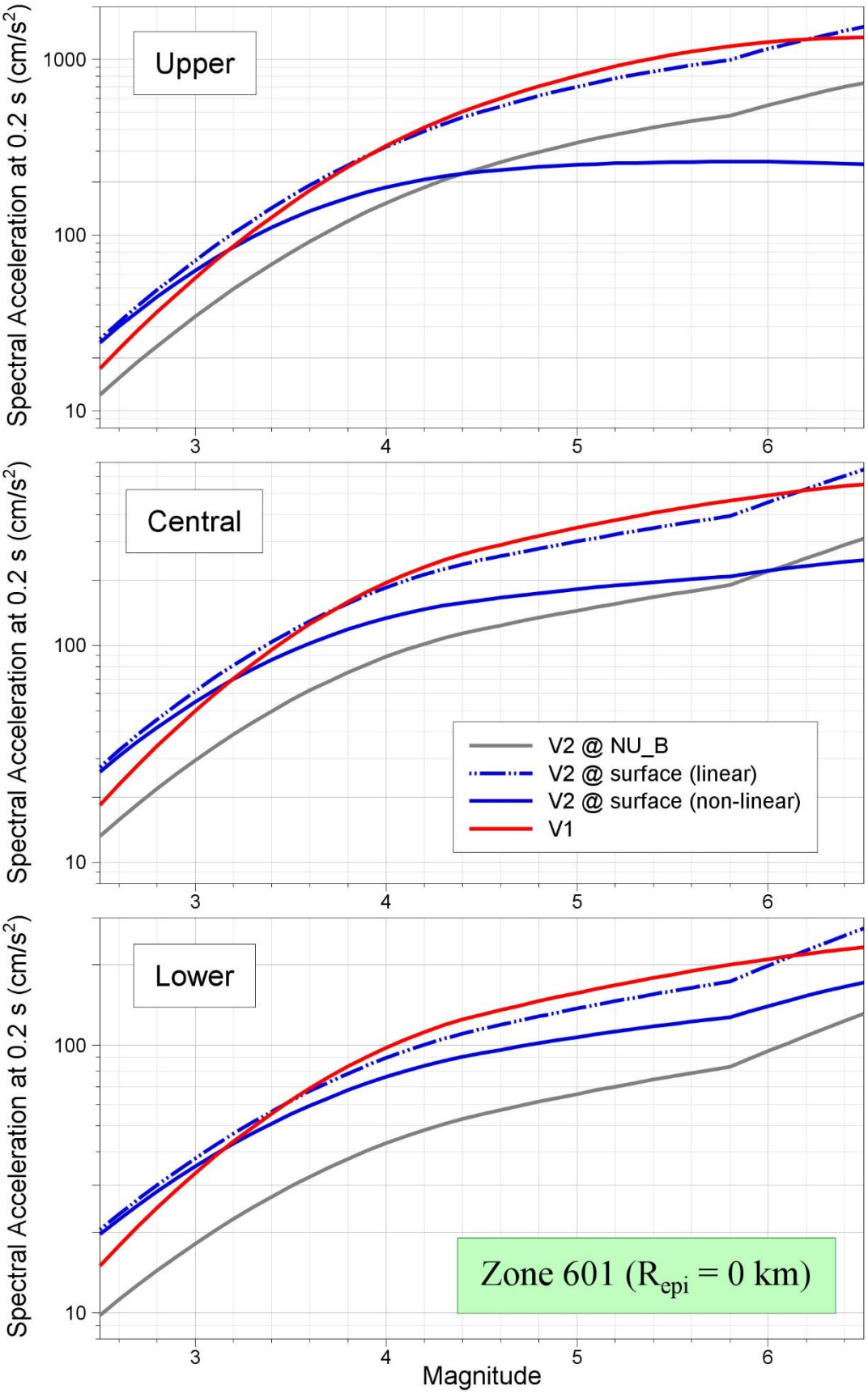

Figure 11.22. Comparison of median predictions of Sa(0.2) as a function of magnitude from the V1 and V2 models for Zone 601 and R_{epi} = 0 km

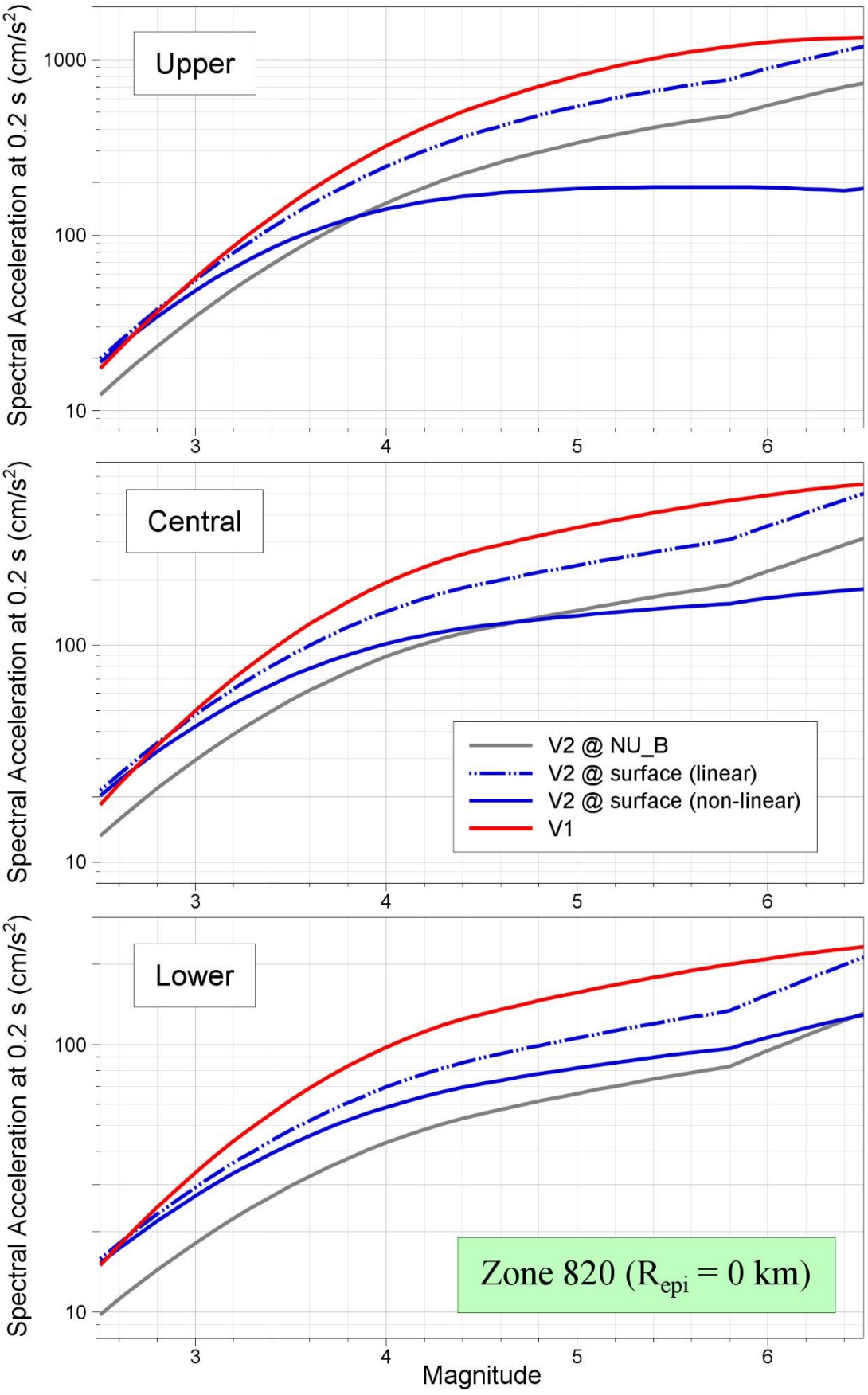

Figure 11.23. Comparison of median predictions of Sa(0.2) as a function of magnitude from the V1 and V2 models for Zone 820 and R_{epi} = 0 km

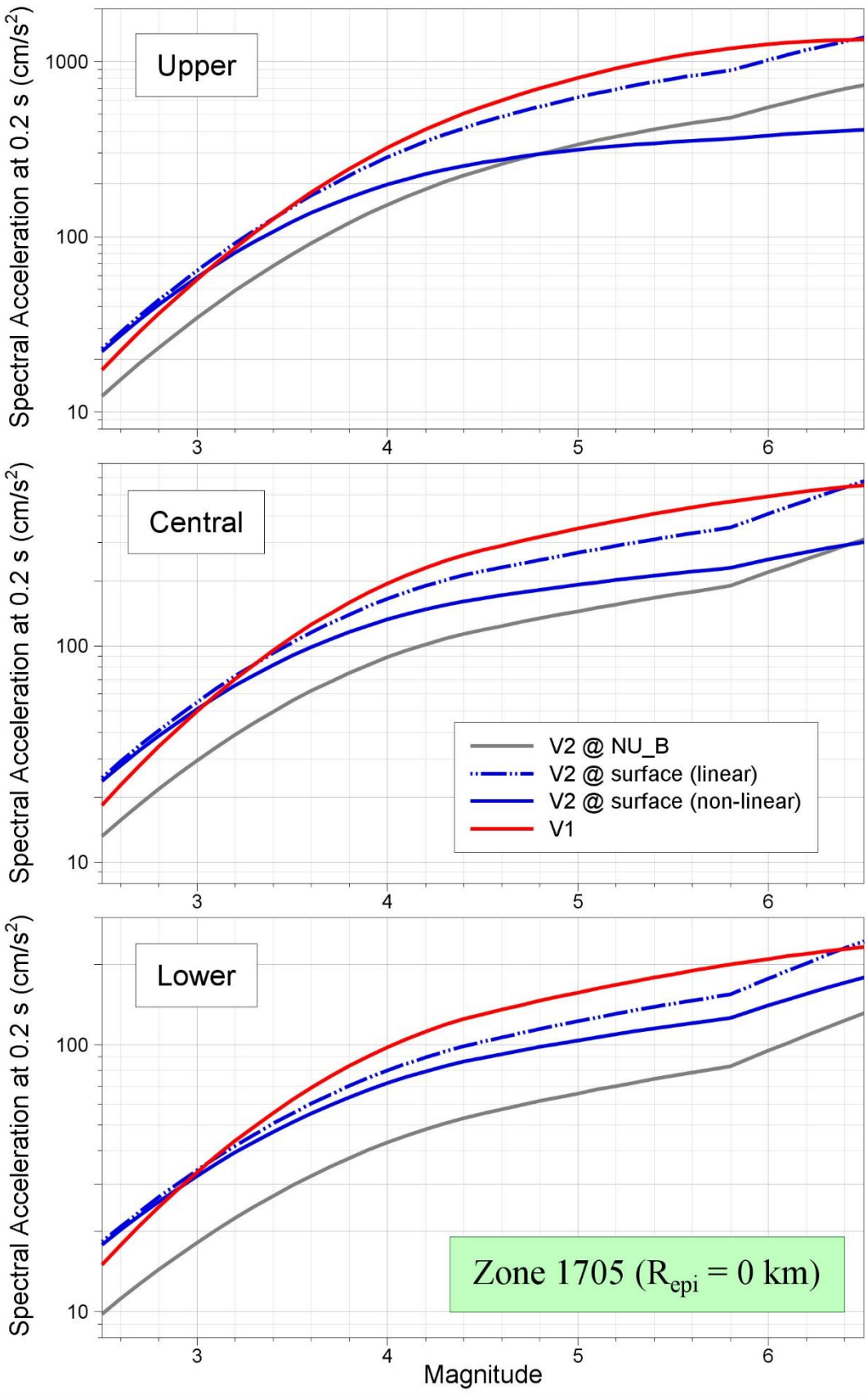

Figure 11.24. Comparison of median predictions of Sa(0.2) as a function of magnitude from the V1 and V2 models for Zone 1705 and R_{epi} = 0 km

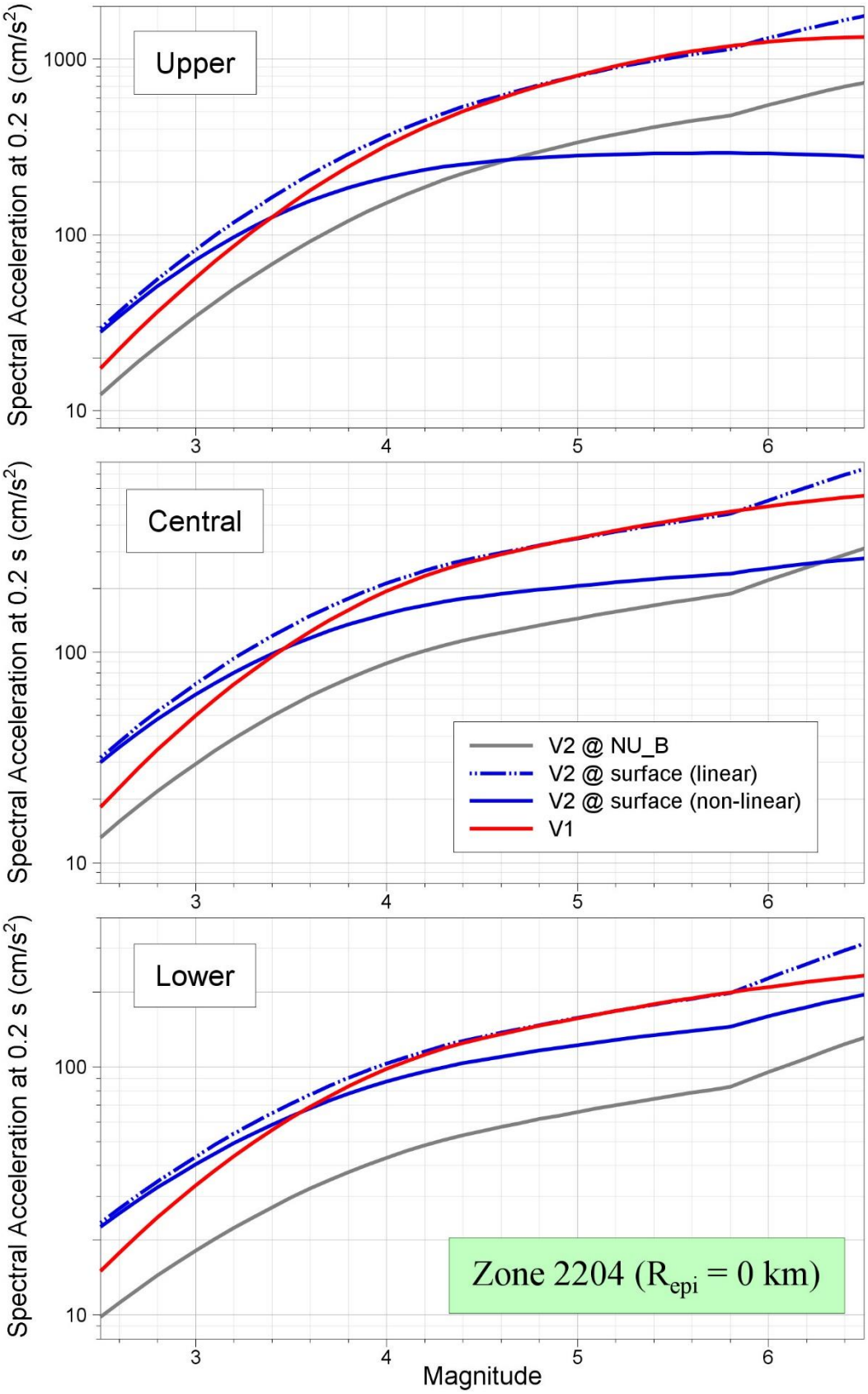

Figure 11.25. Comparison of median predictions of Sa(0.2) as a function of magnitude from the V1 and V2 models for Zone 2204 and R_{epi} = 0 km

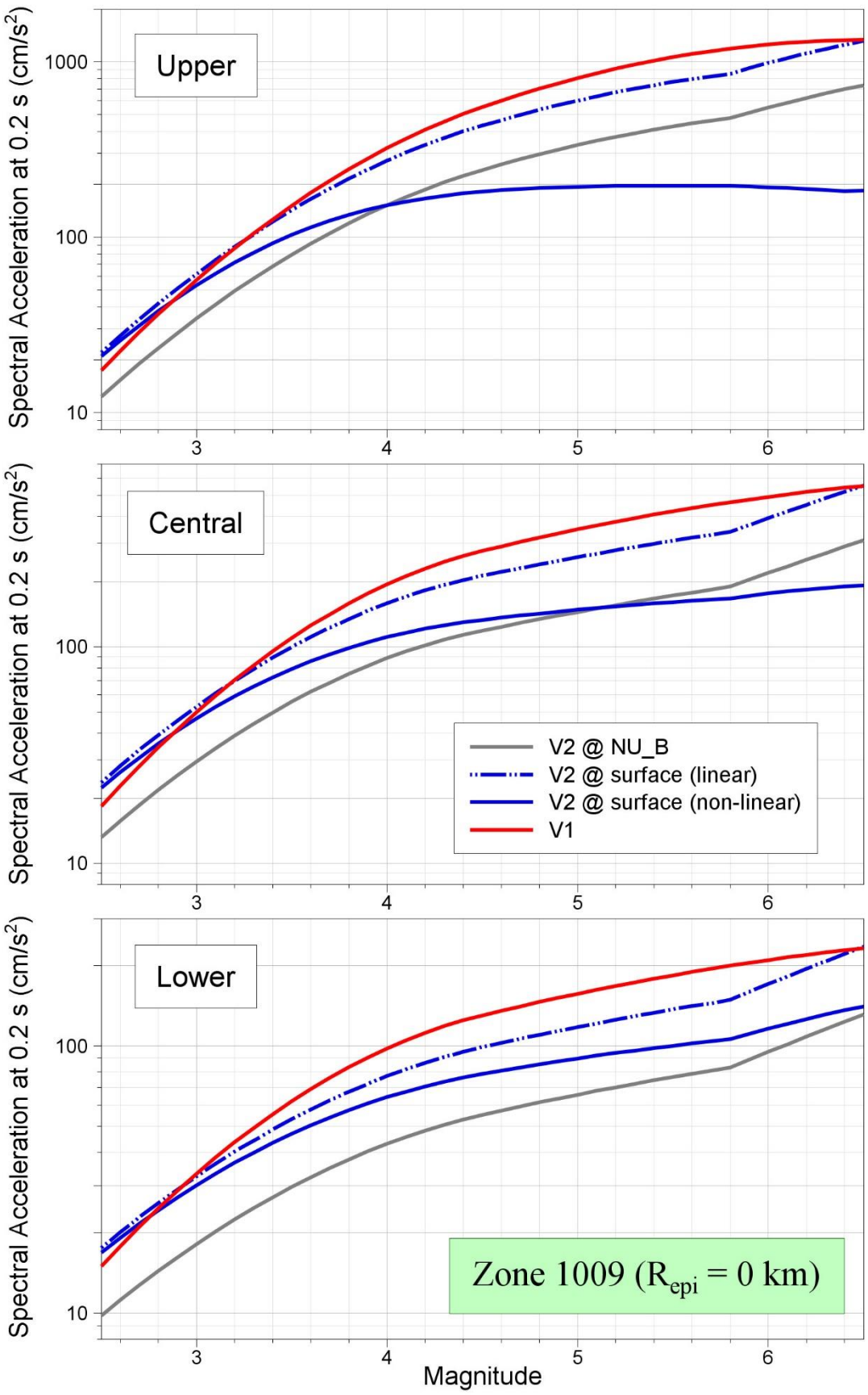

Figure 11.26. Comparison of median predictions of Sa(0.2) as a function of magnitude from the V1 and V2 models for Zone 1009 and R_{epi} = 0 km

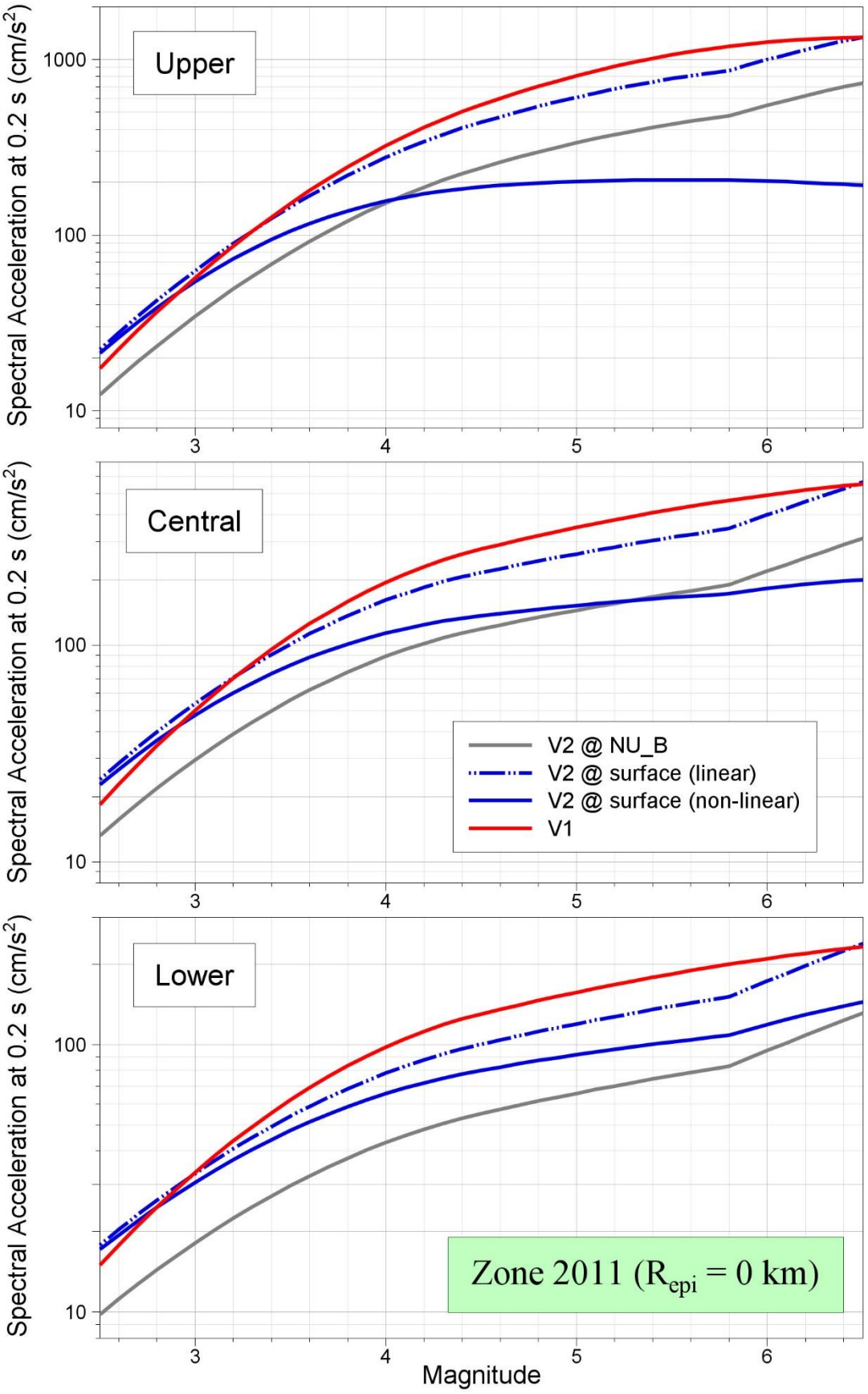

Figure 11.27. Comparison of median predictions of Sa(0.2) as a function of magnitude from the V1 and V2 models for Zone 2011 and R_{epi} = 0 km

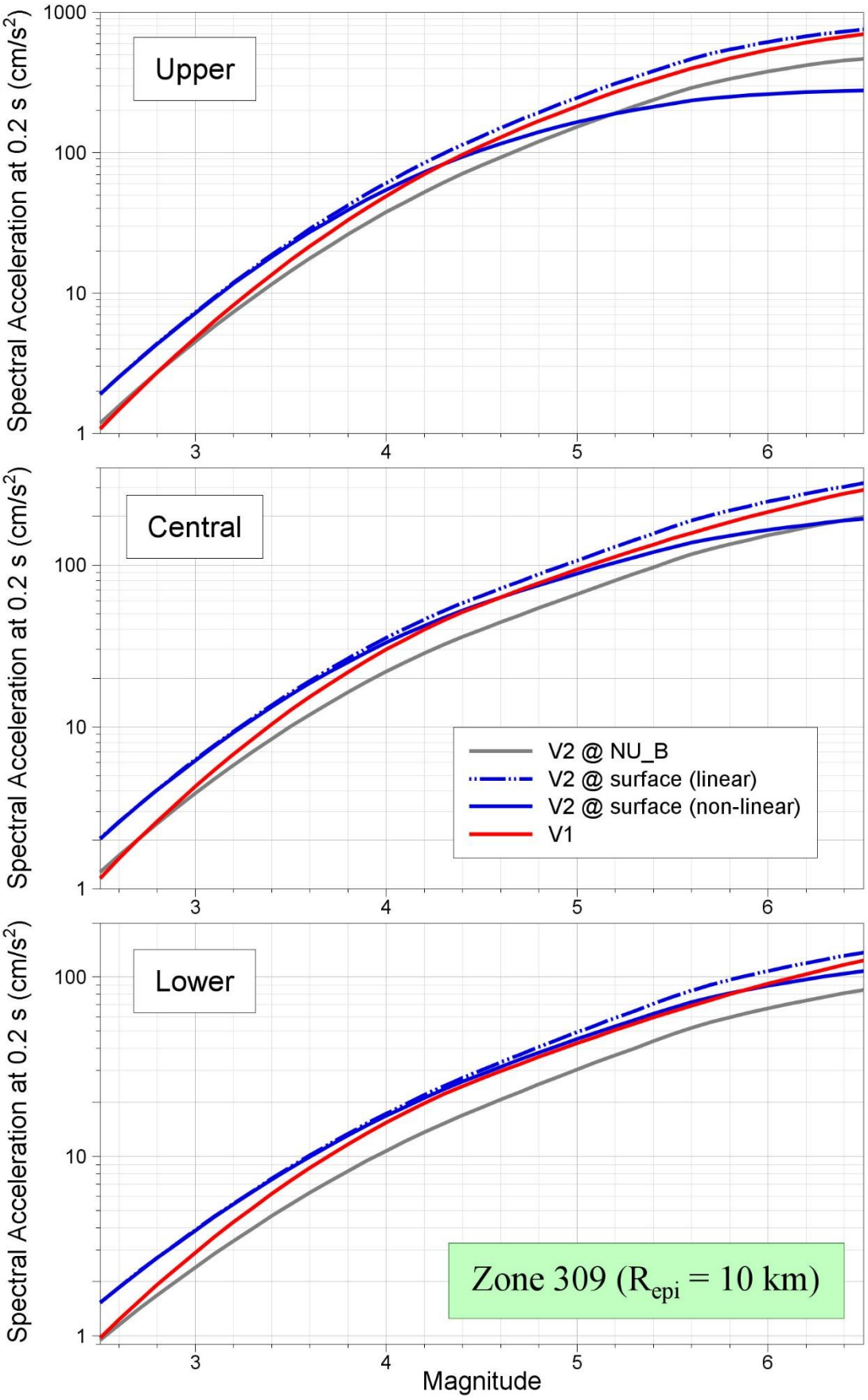

Figure 11.28. Comparison of median predictions of Sa(0.2) as a function of magnitude from the V1 and V2 models for Zone 309 and R_{epi} = 10 km

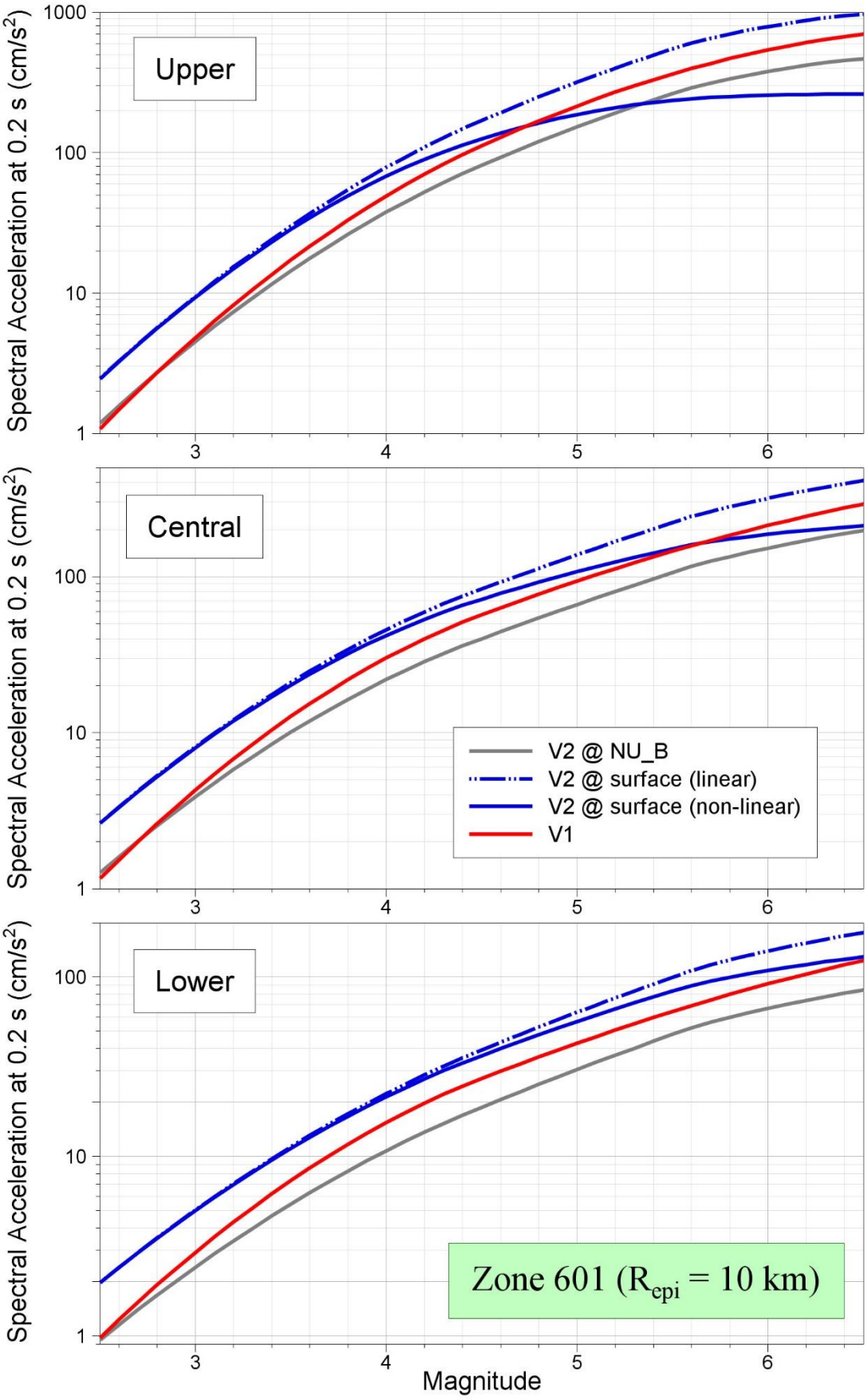

Figure 11.29. Comparison of median predictions of Sa(0.2) as a function of magnitude from the V1 and V2 models for Zone 601 and R_{epi} = 10 km

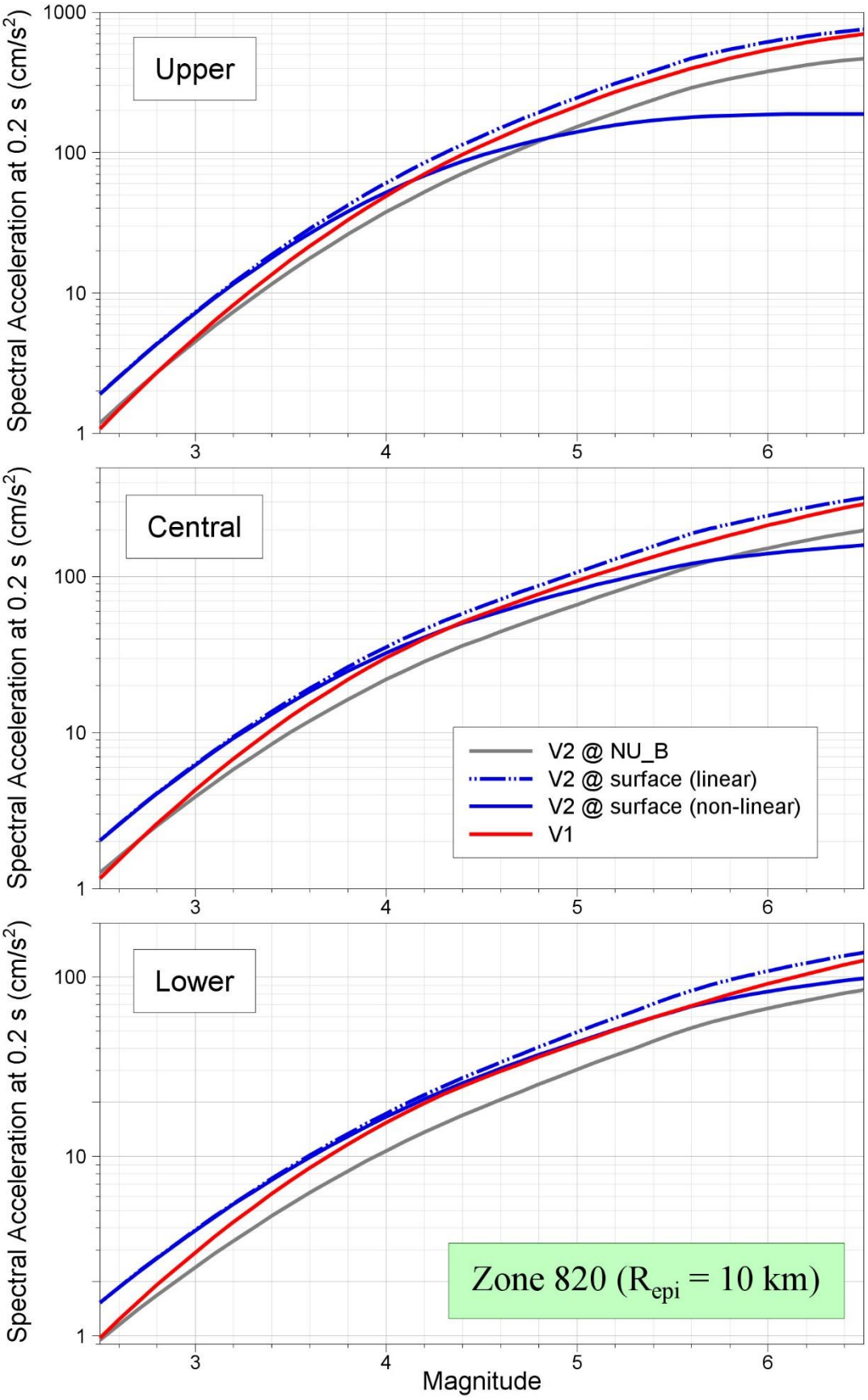

Figure 11.30. Comparison of median predictions of Sa(0.2) as a function of magnitude from the V1 and V2 models for Zone 820 and R_{epi} = 10 km

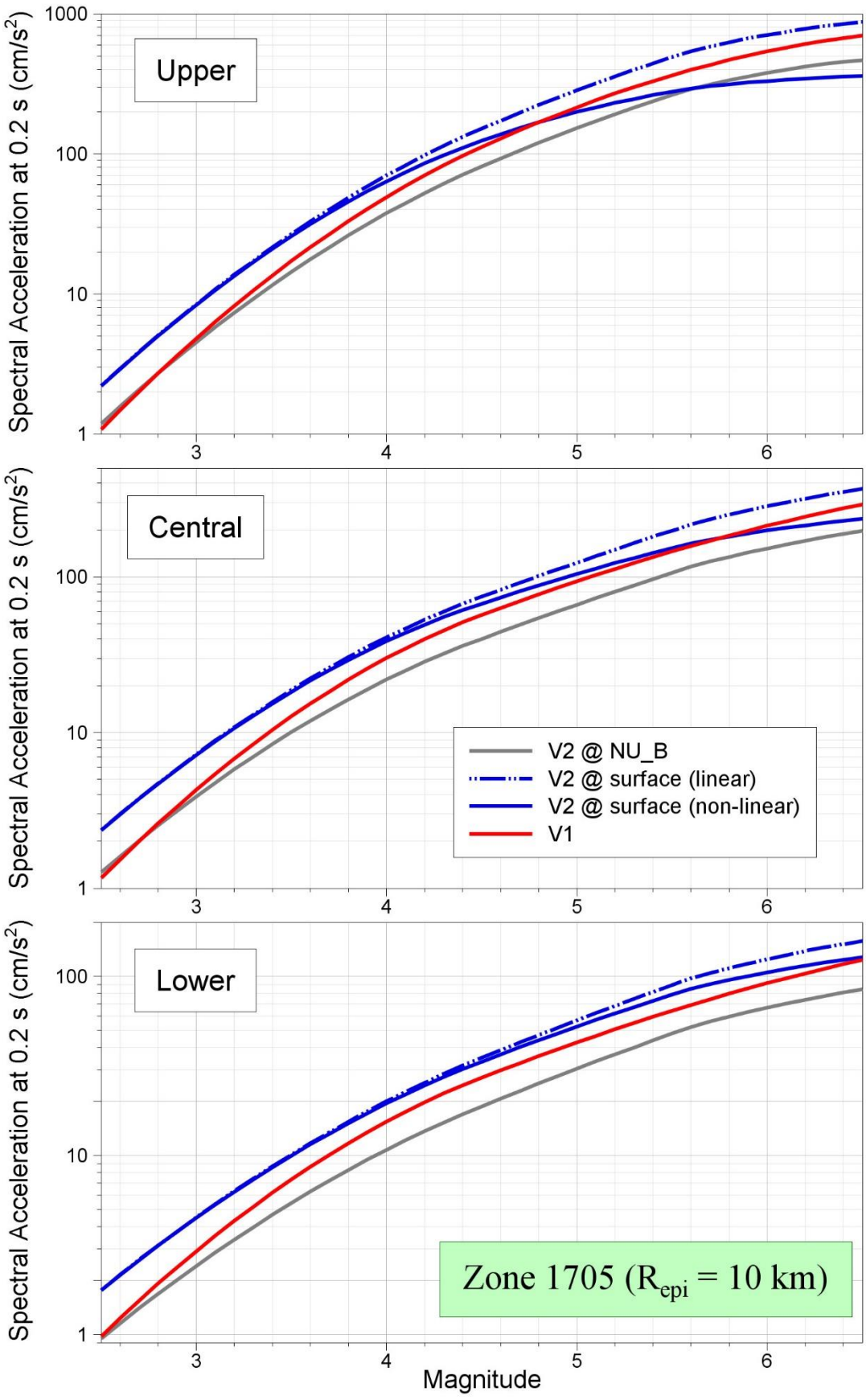

Figure 11.31. Comparison of median predictions of Sa(0.2) as a function of magnitude from the V1 and V2 models for Zone 1705 and R_{epi} = 10 km

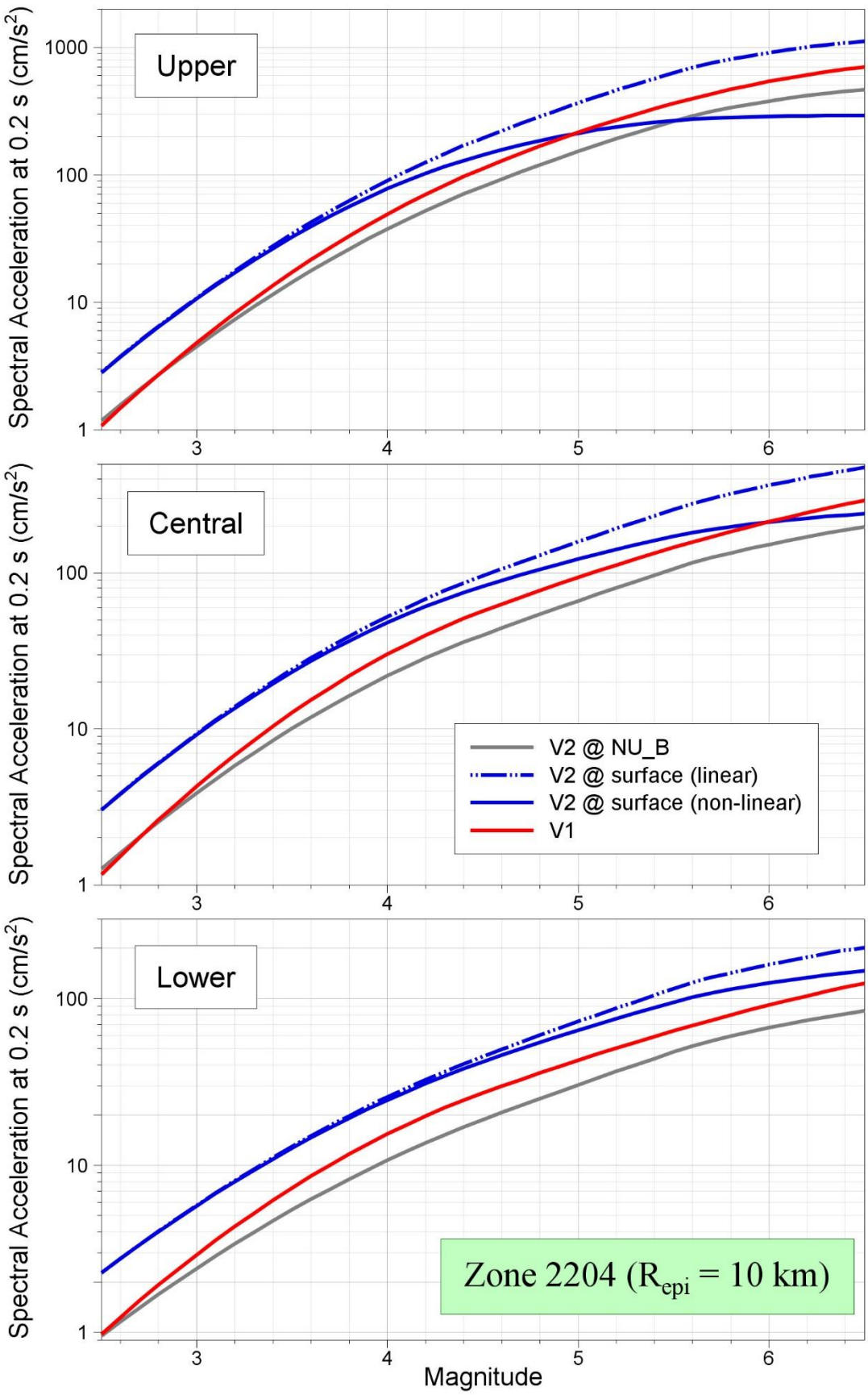

Figure 11.32. Comparison of median predictions of Sa(0.2) as a function of magnitude from the V1 and V2 models for Zone 2204 and R_{epi} = 10 km

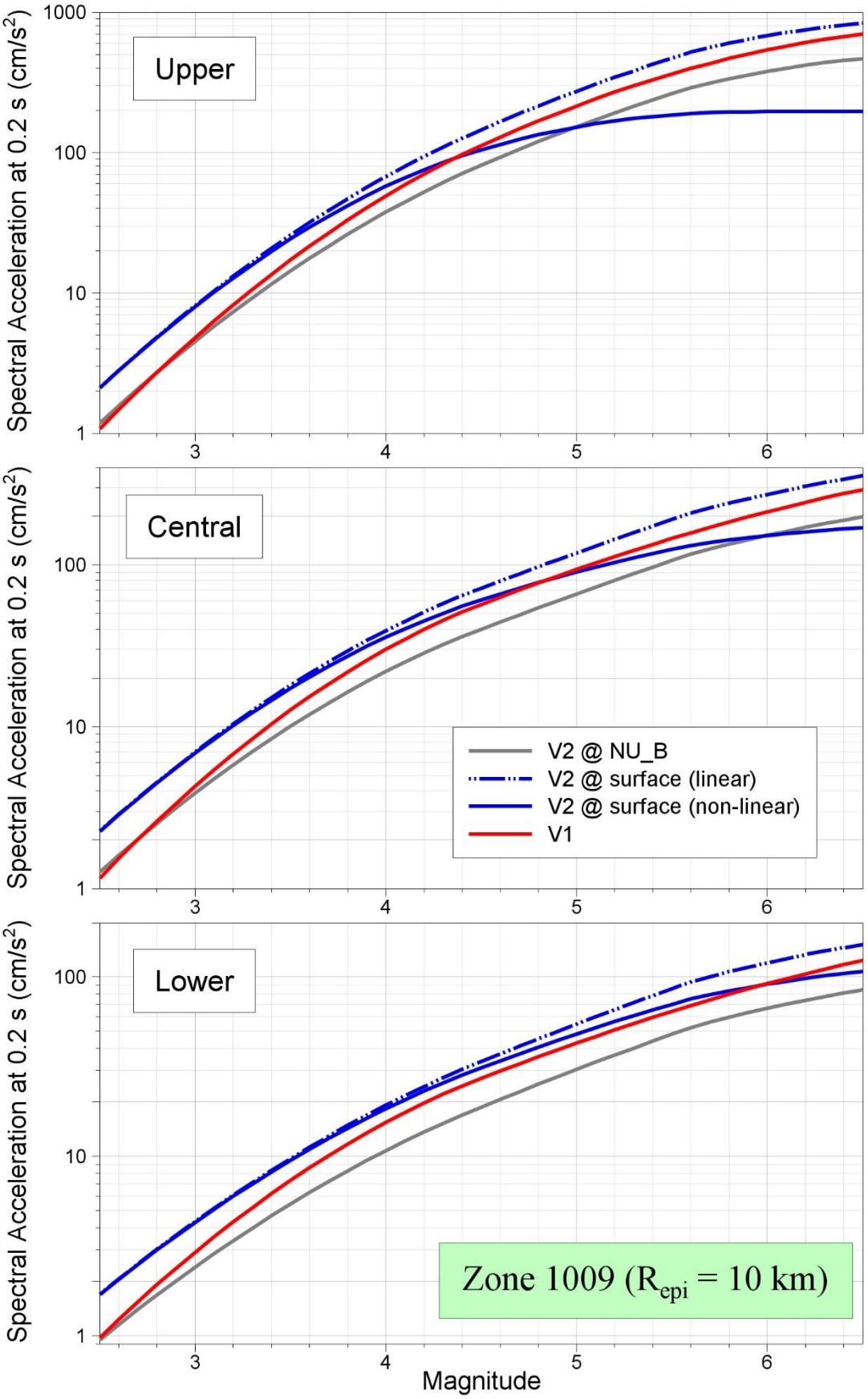

Figure 11.33. Comparison of median predictions of Sa(0.2) as a function of magnitude from the V1 and V2 models for Zone 1009 and R_{epi} = 10 km

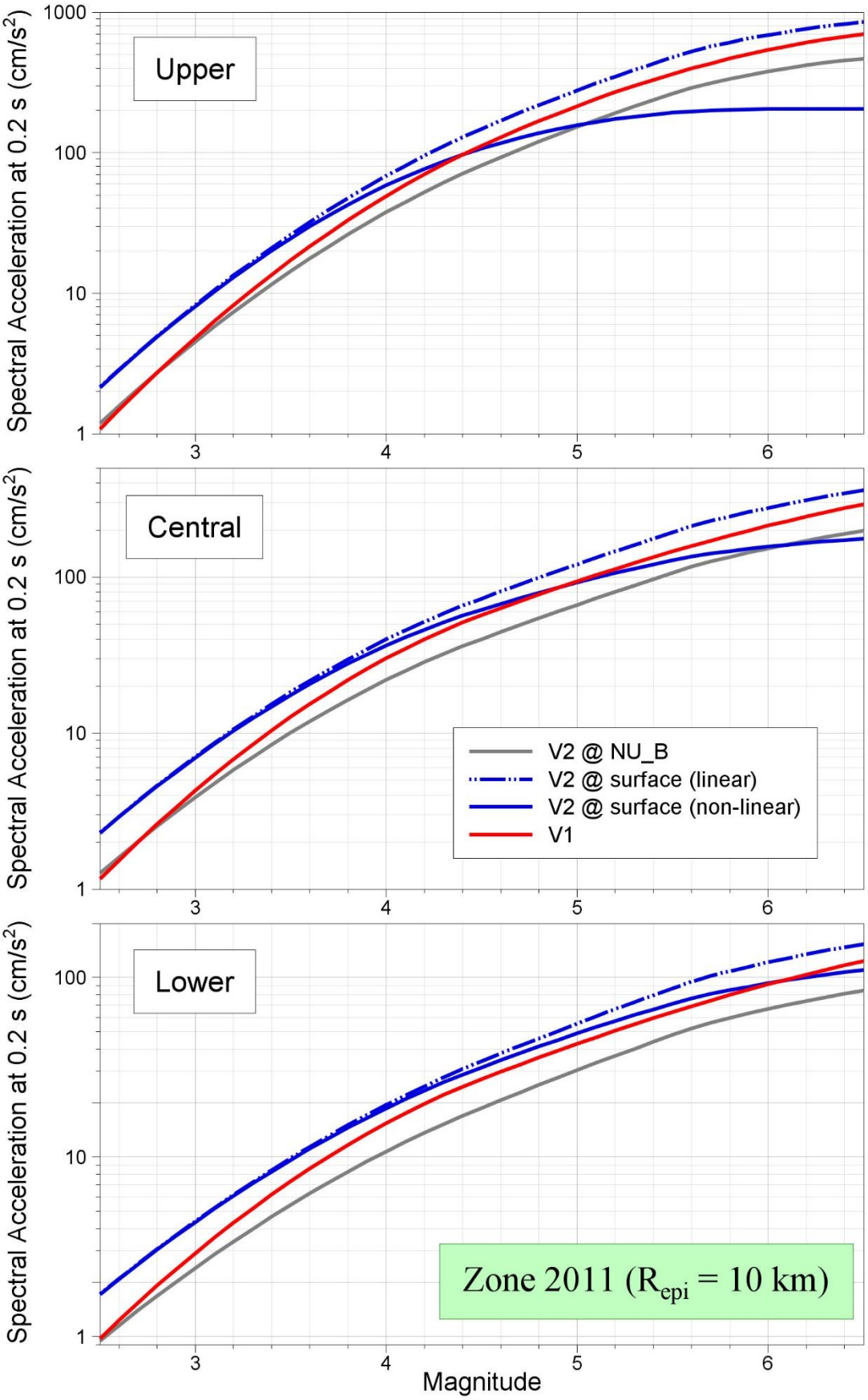

Figure 11.34. Comparison of median predictions of Sa(0.2) as a function of magnitude from the V1 and V2 models for Zone 2011 and R_{epi} = 0 km

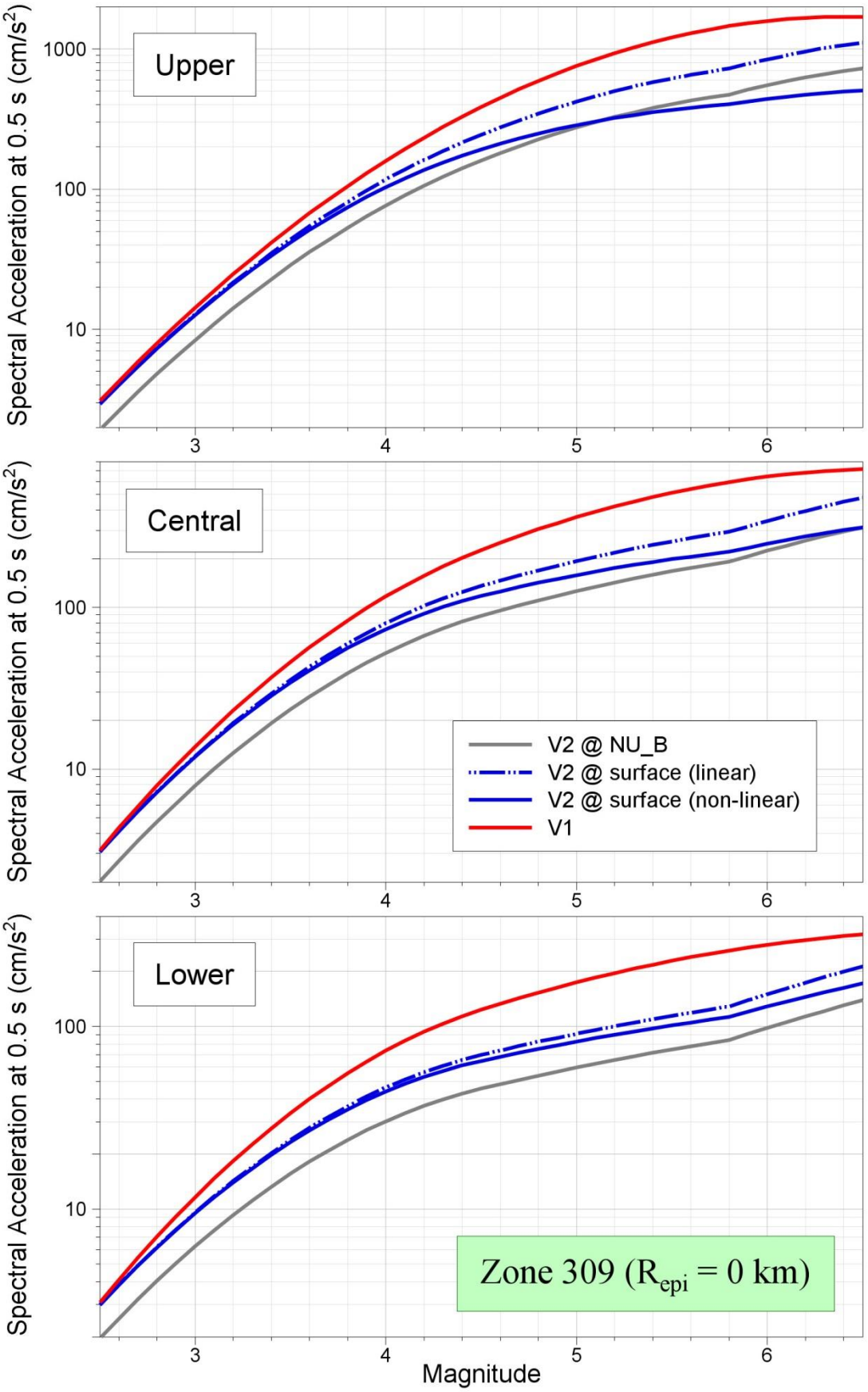

Figure 11.35. Comparison of median predictions of Sa(0.5) as a function of magnitude from the V1 and V2 models for Zone 309 and R_{epi} = 0 km

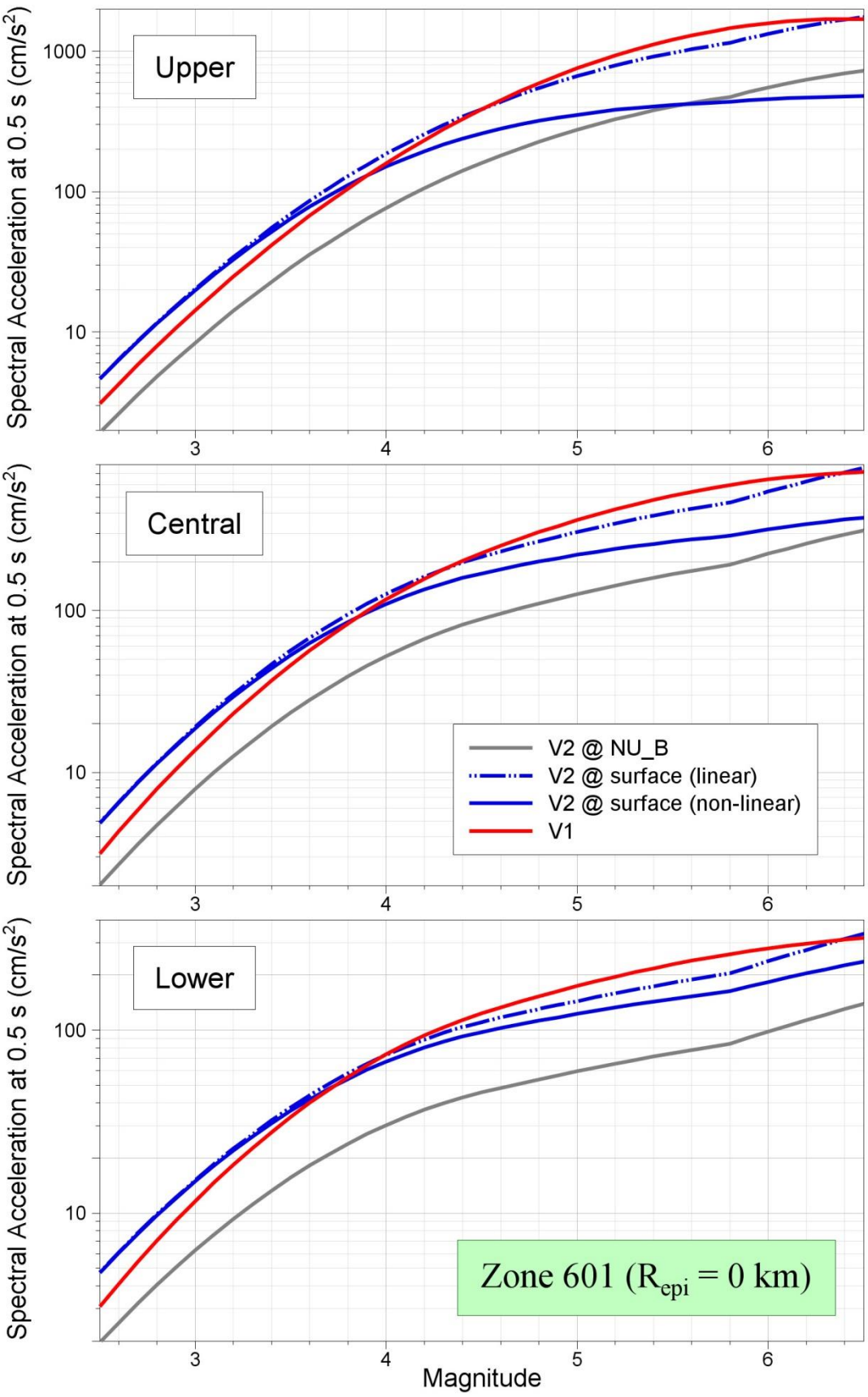

Figure 11.36. Comparison of median predictions of Sa(0.5) as a function of magnitude from the V1 and V2 models for Zone 601 and R_{epi} = 0 km

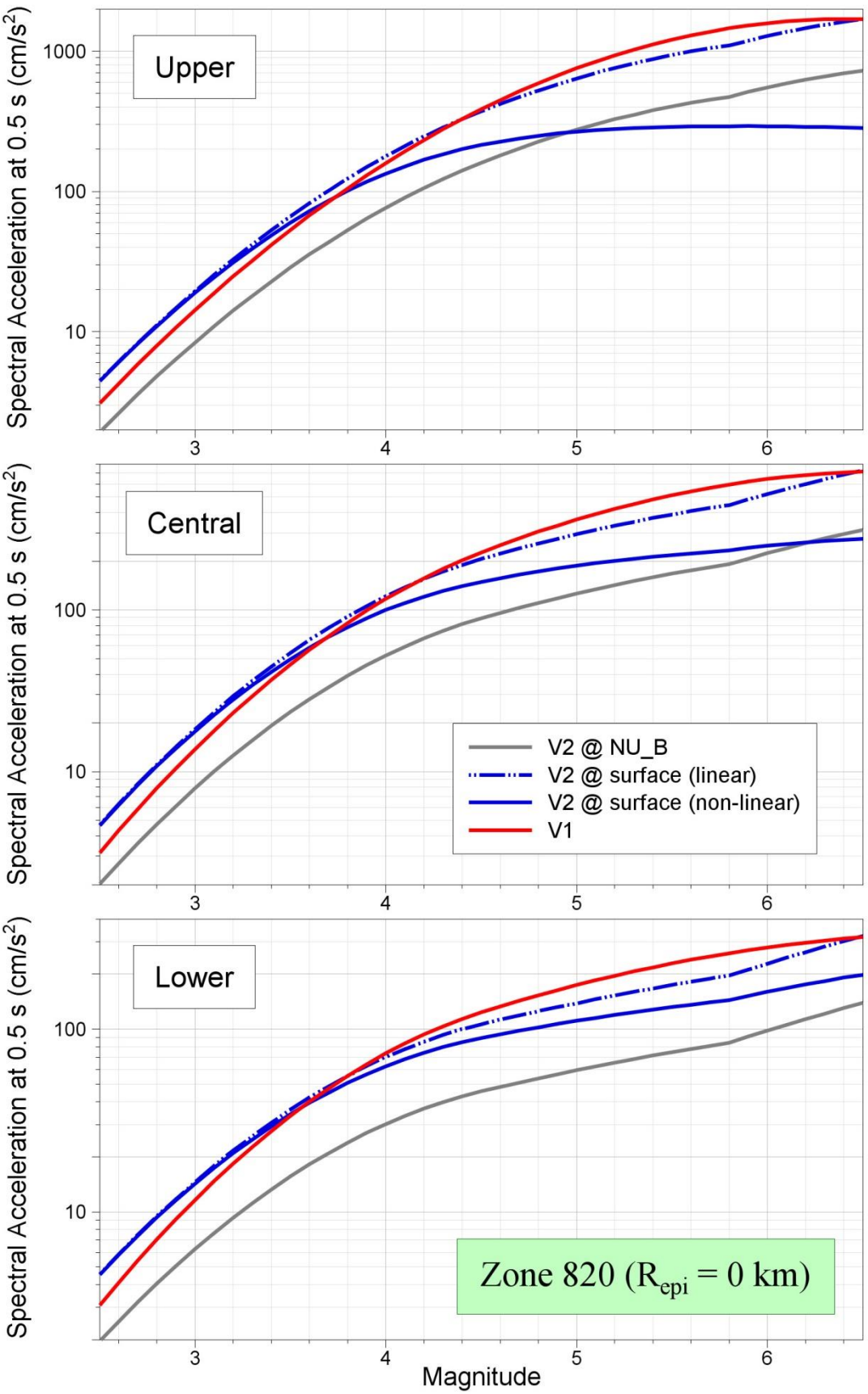

Figure 11.37. Comparison of median predictions of Sa(0.5) as a function of magnitude from the V1 and V2 models for Zone 820 and R_{epi} = 0 km

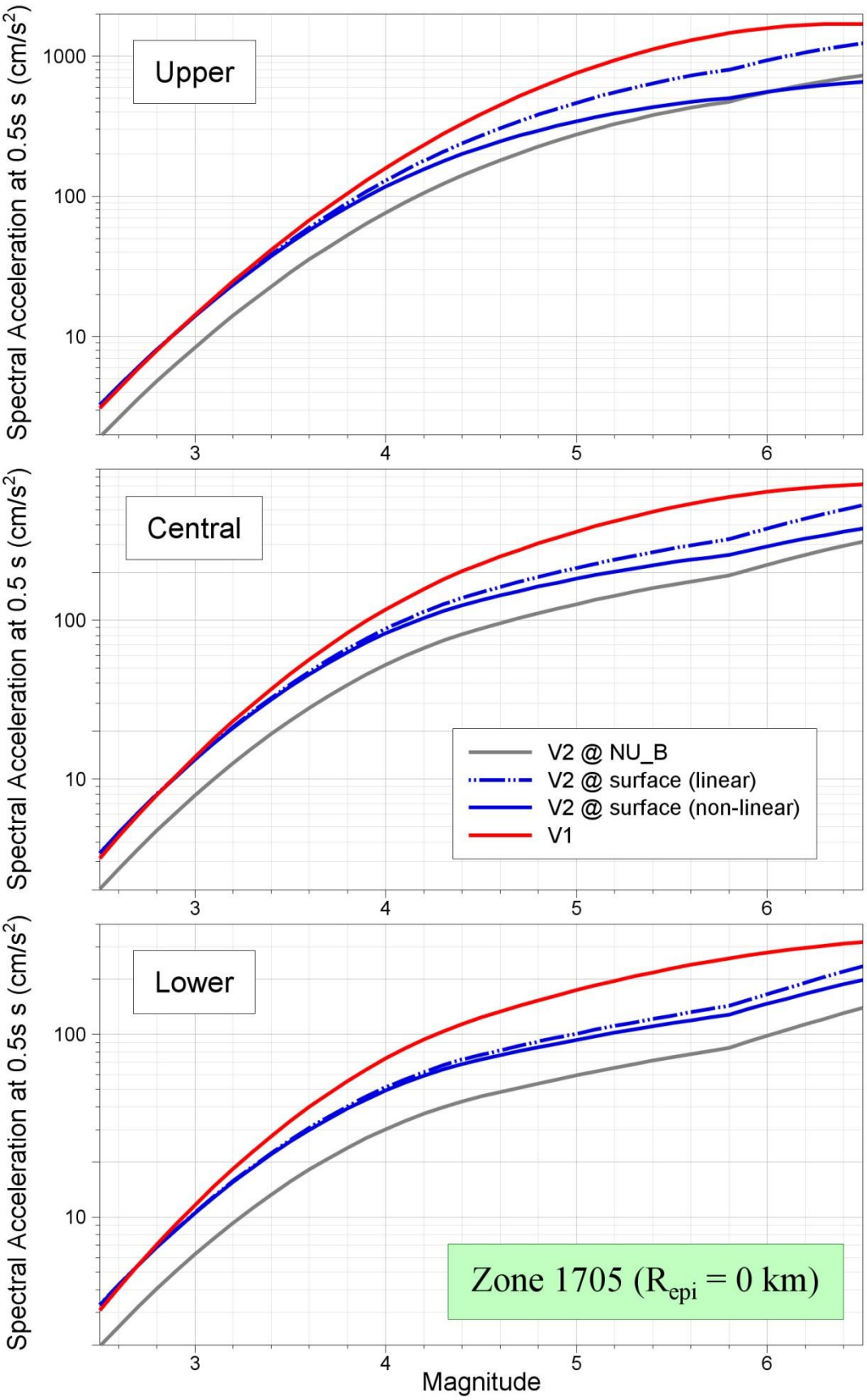

Figure 11.38. Comparison of median predictions of Sa(0.5) as a function of magnitude from the V1 and V2 models for Zone 1705 and R_{epi} = 0 km

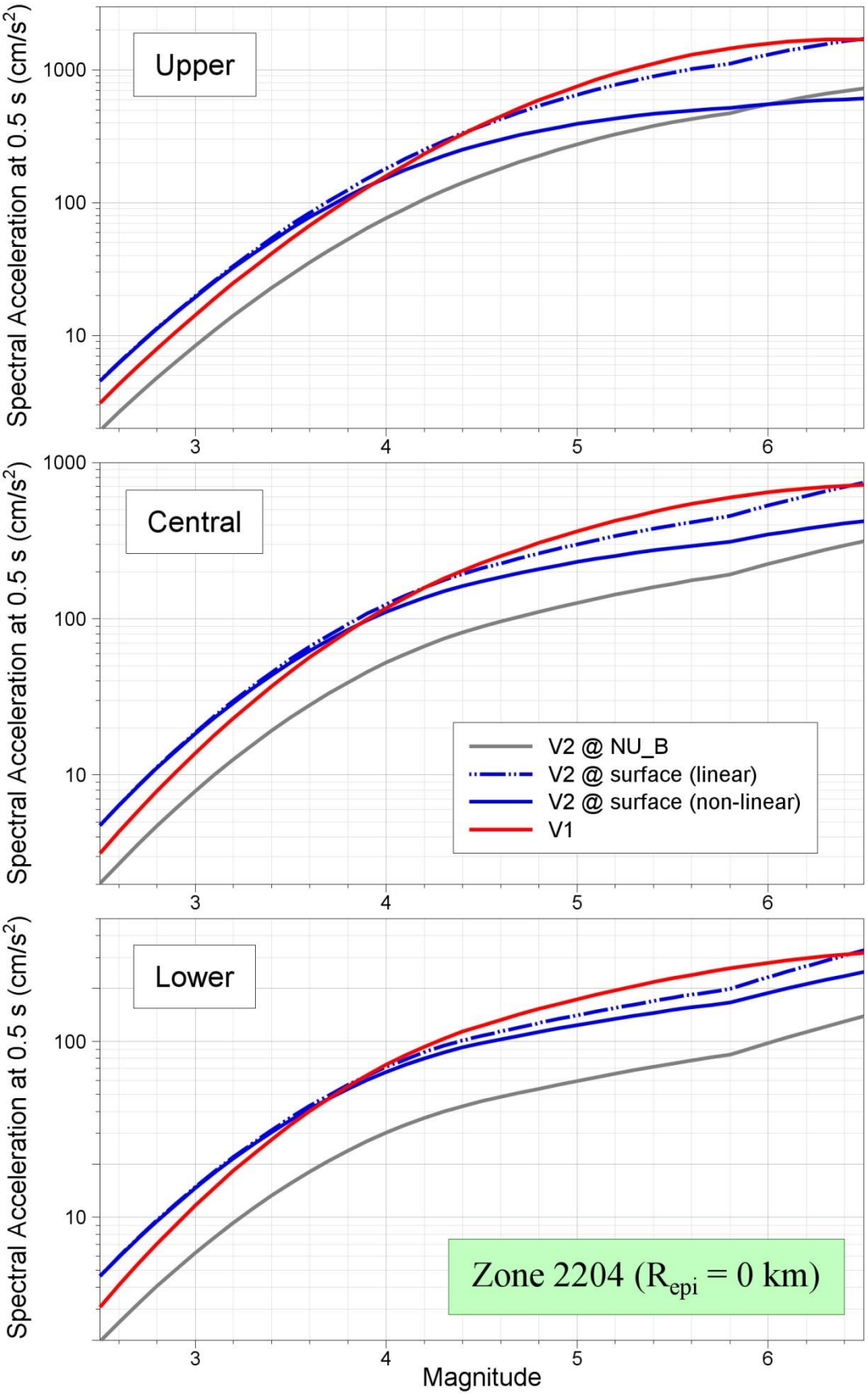

Figure 11.39. Comparison of median predictions of Sa(0.5) as a function of magnitude from the V1 and V2 models for Zone 2204 and R_{epi} = 0 km

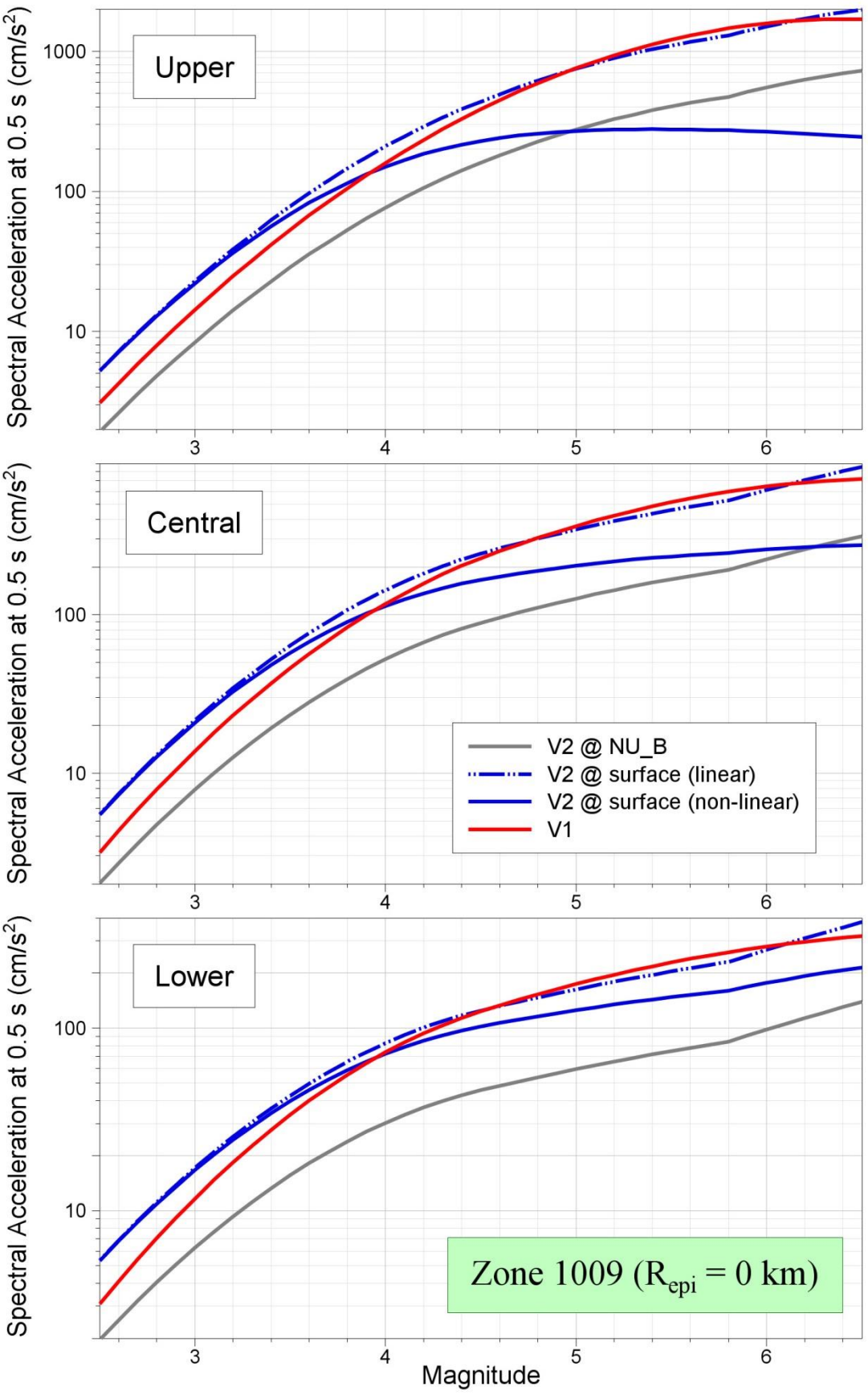

Figure 11.40. Comparison of median predictions of Sa(0.5) as a function of magnitude from the V1 and V2 models for Zone 1009 and R_{epi} = 0 km

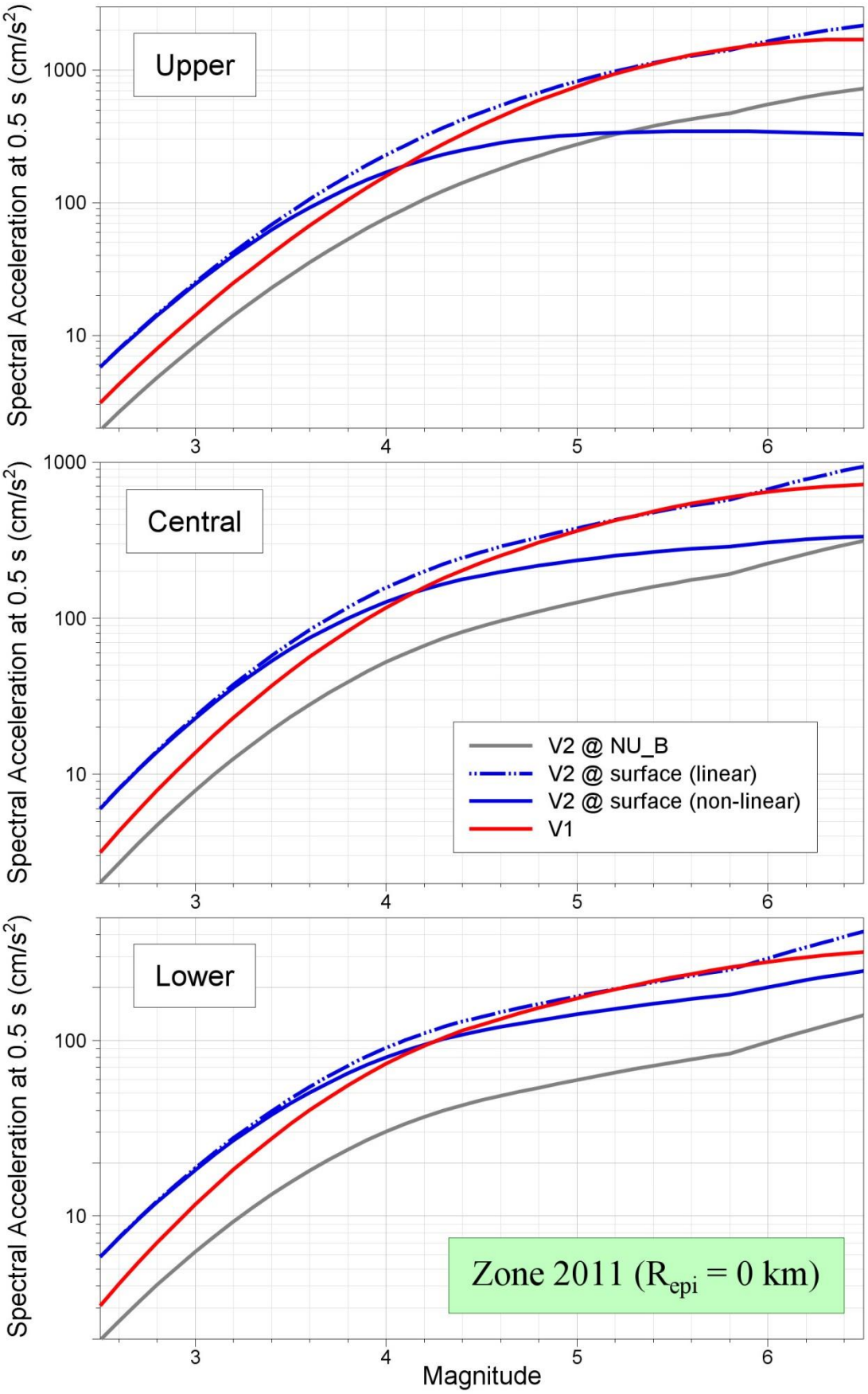

Figure 11.42. Comparison of median predictions of Sa(0.5) as a function of magnitude from the V1 and V2 models for Zone 2011 and R_{epi} = 0 km

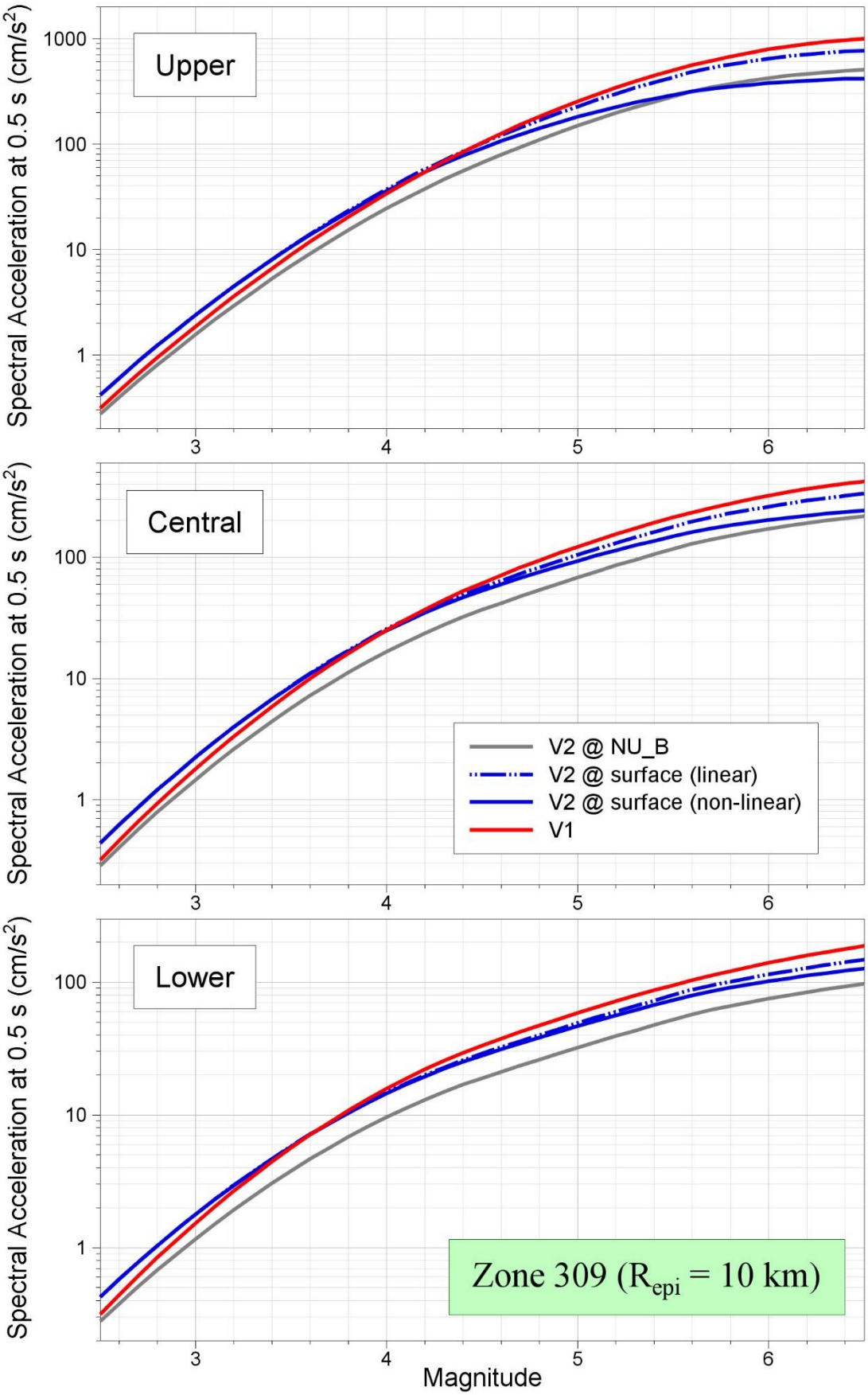

Figure 11.42. Comparison of median predictions of Sa(0.5) as a function of magnitude from the V1 and V2 models for Zone 309 and R_{epi} = 10 km

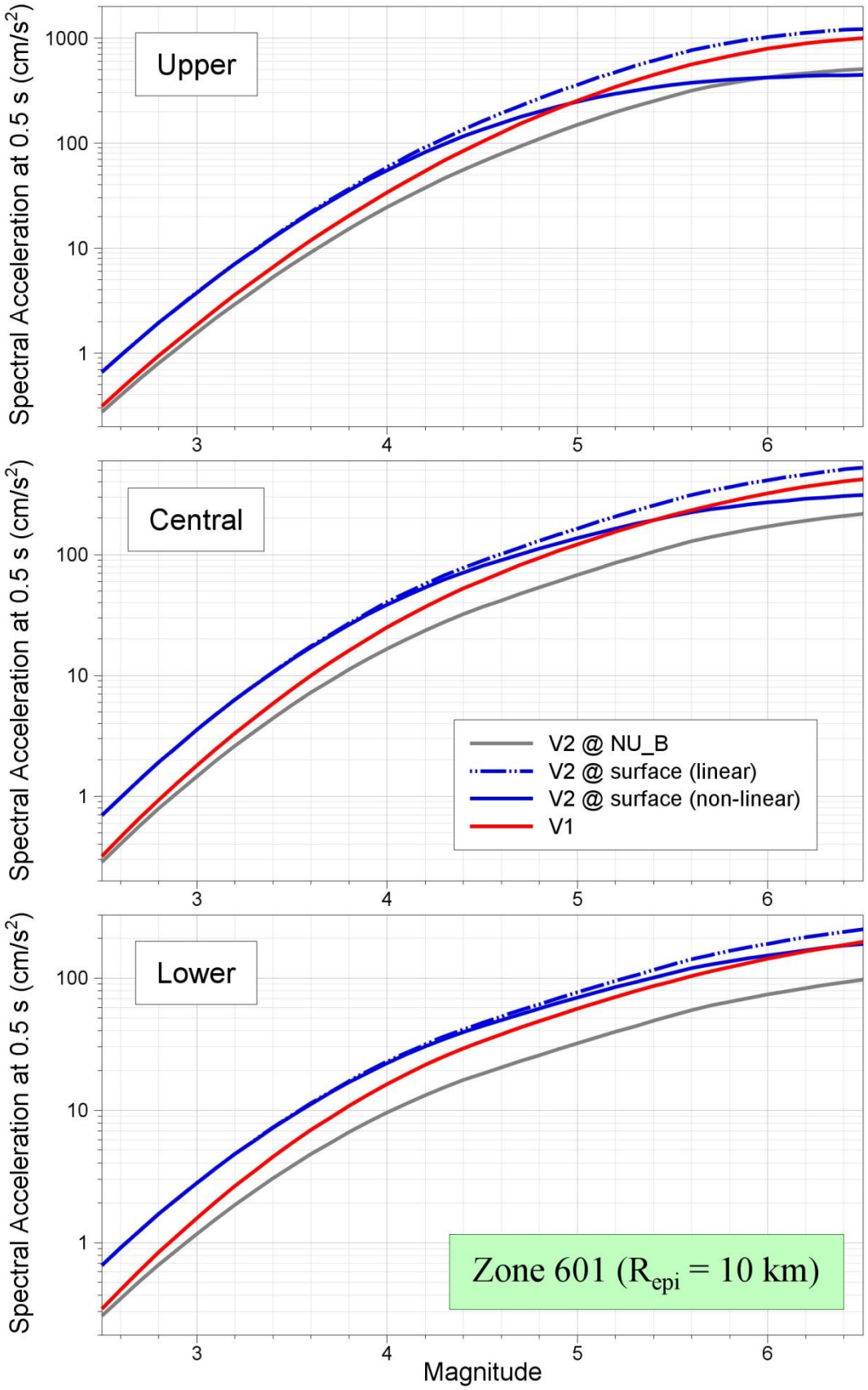

Figure 11.43. Comparison of median predictions of Sa(0.5) as a function of magnitude from the V1 and V2 models for Zone 601 and R_{epi} = 10 km

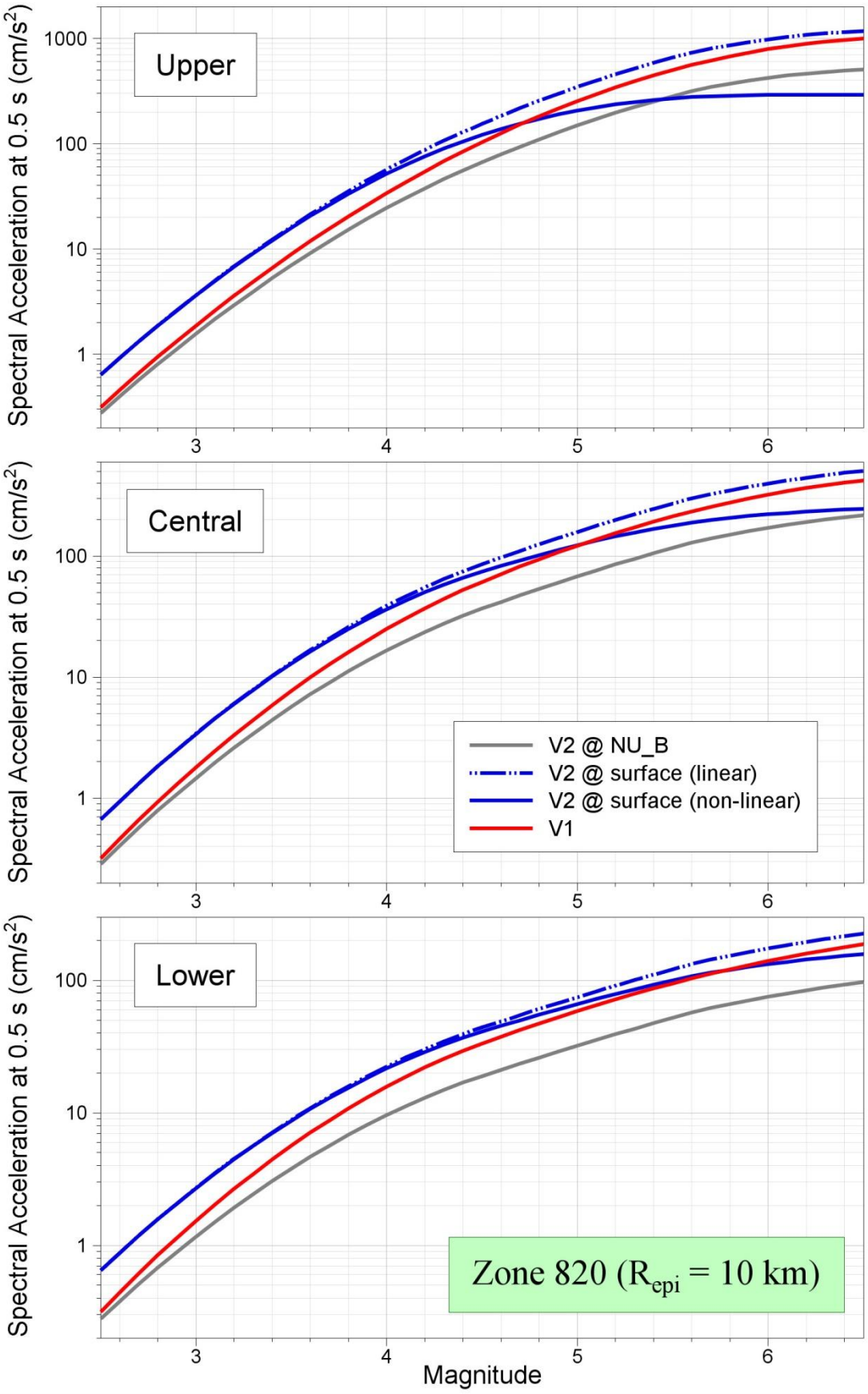

Figure 11.44. Comparison of median predictions of Sa(0.5) as a function of magnitude from the V1 and V2 models for Zone 820 and R_{epi} = 10 km

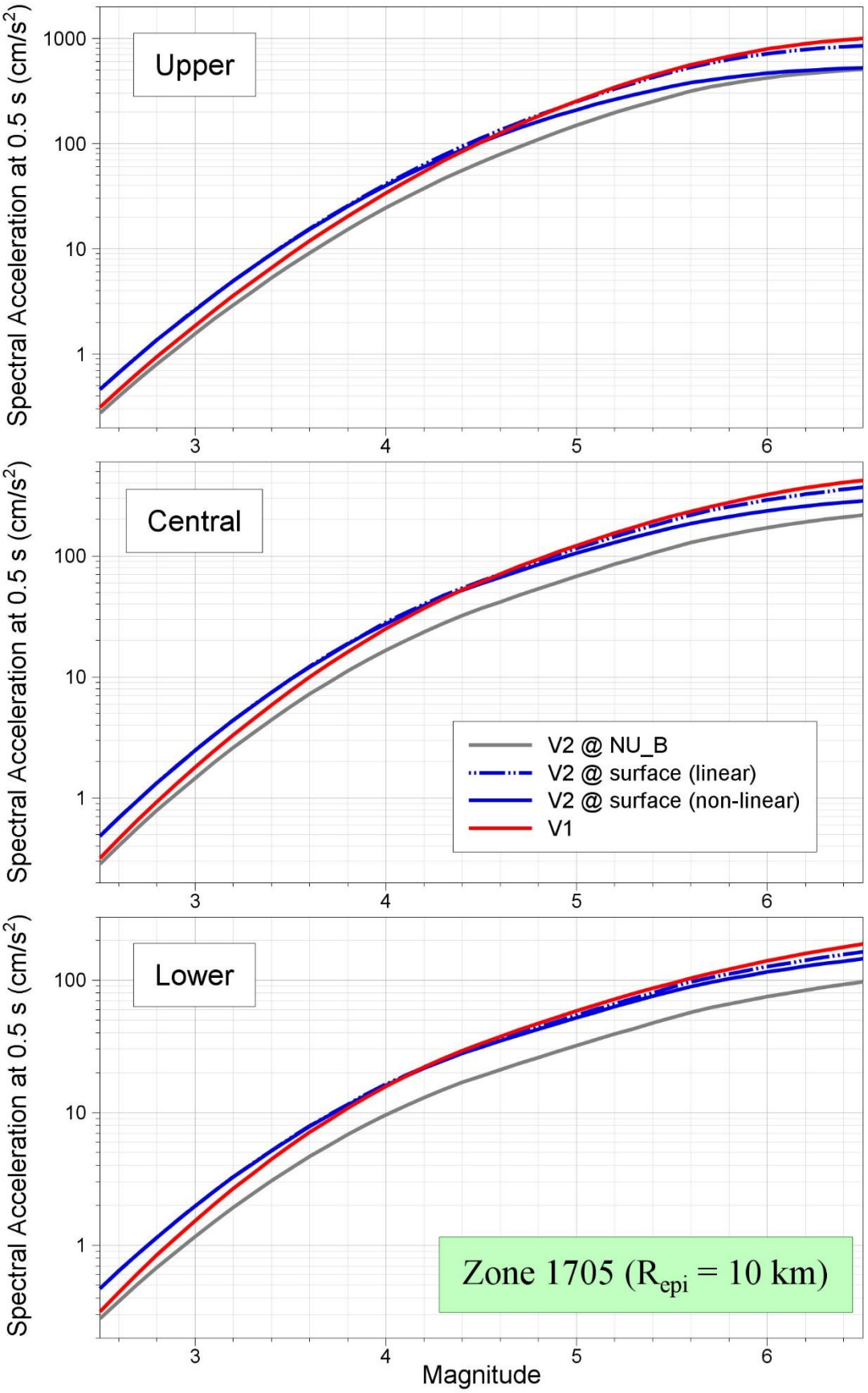

Figure 11.45. Comparison of median predictions of Sa(0.5) as a function of magnitude from the V1 and V2 models for Zone 1705 and R_{epi} = 10 km

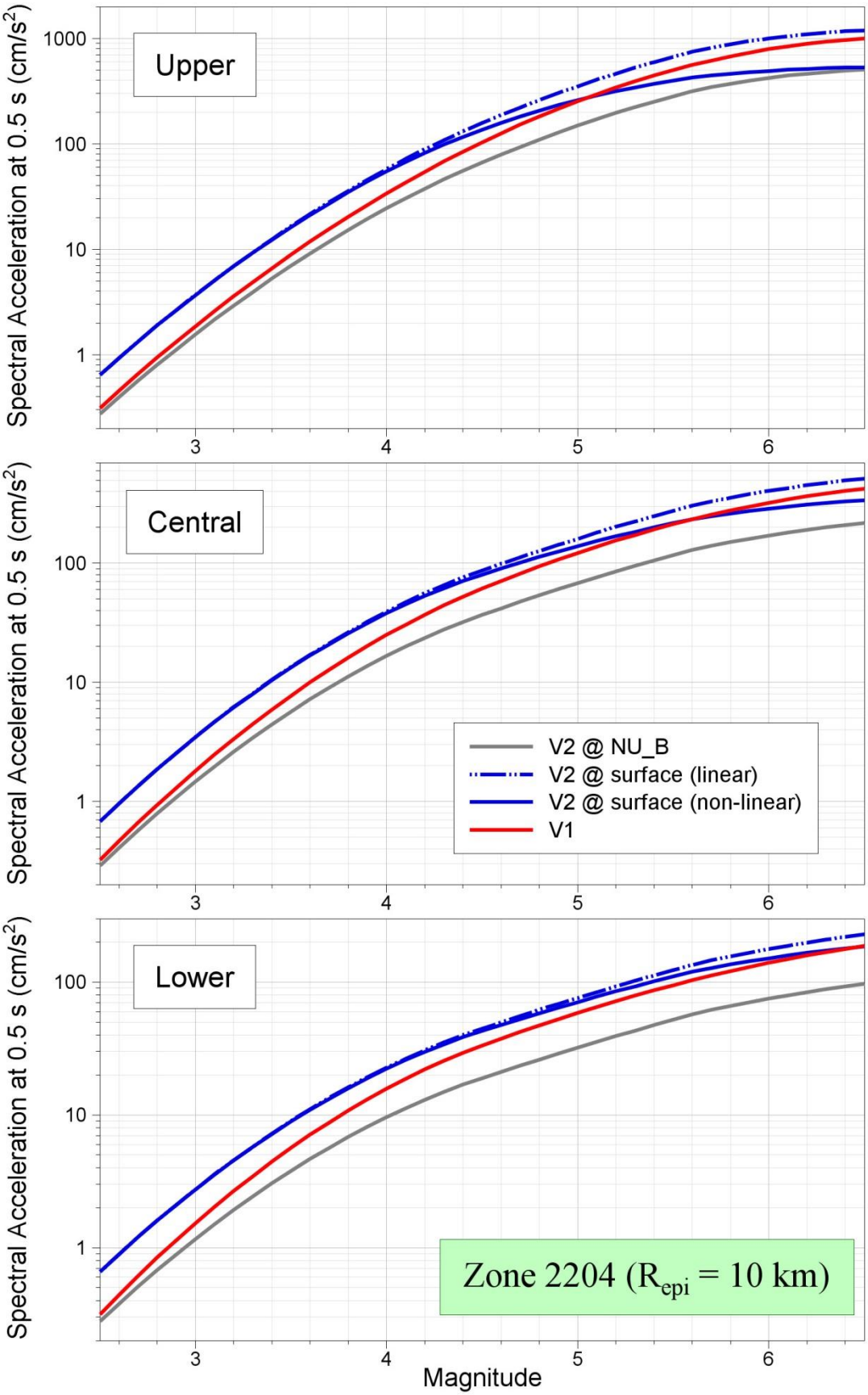

Figure 11.46. Comparison of median predictions of Sa(0.5) as a function of magnitude from the V1 and V2 models for Zone 2204 and R_{epi} = 10 km

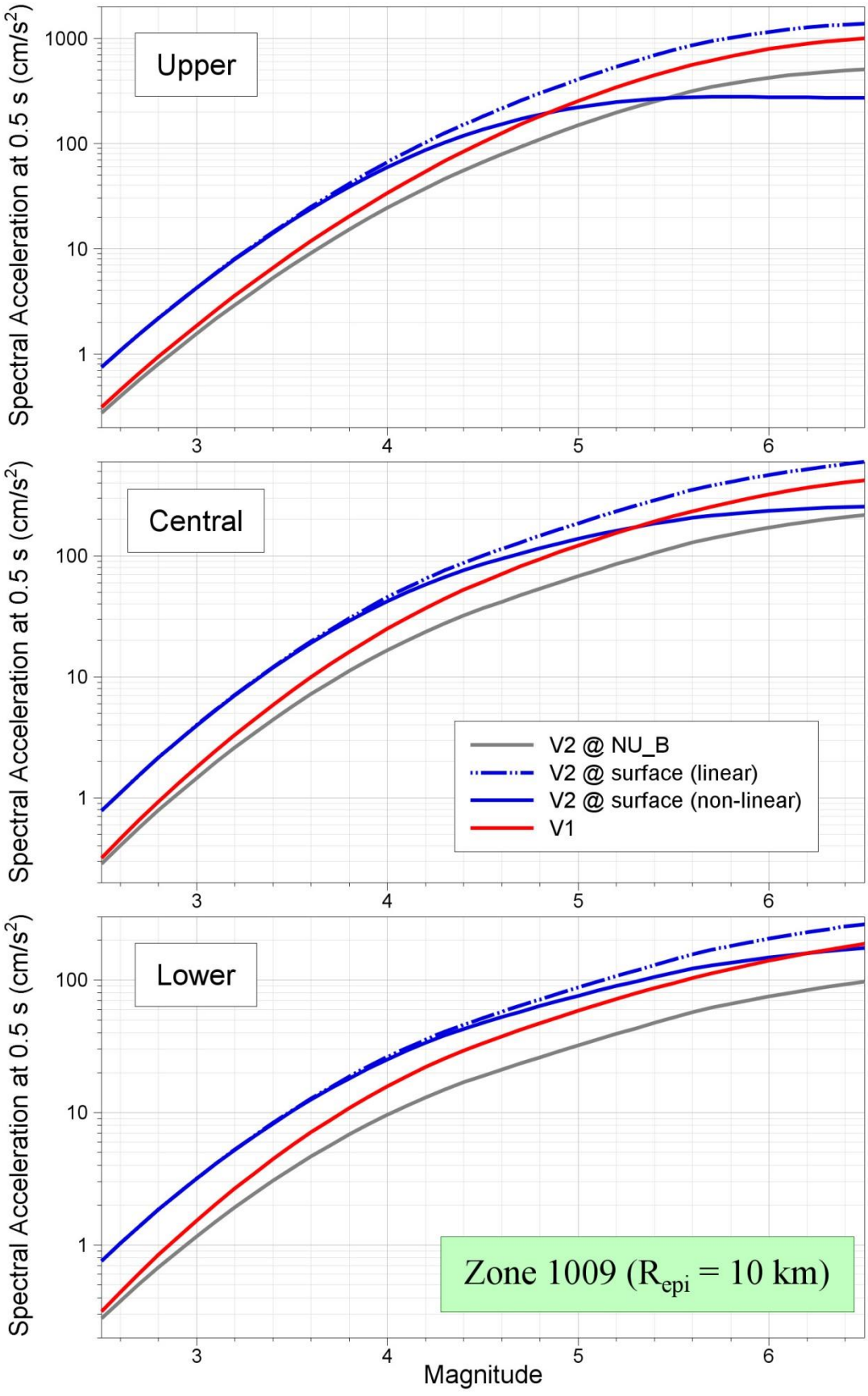

Figure 11.47. Comparison of median predictions of Sa(0.5) as a function of magnitude from the V1 and V2 models for Zone 1009 and R_{epi} = 10 km

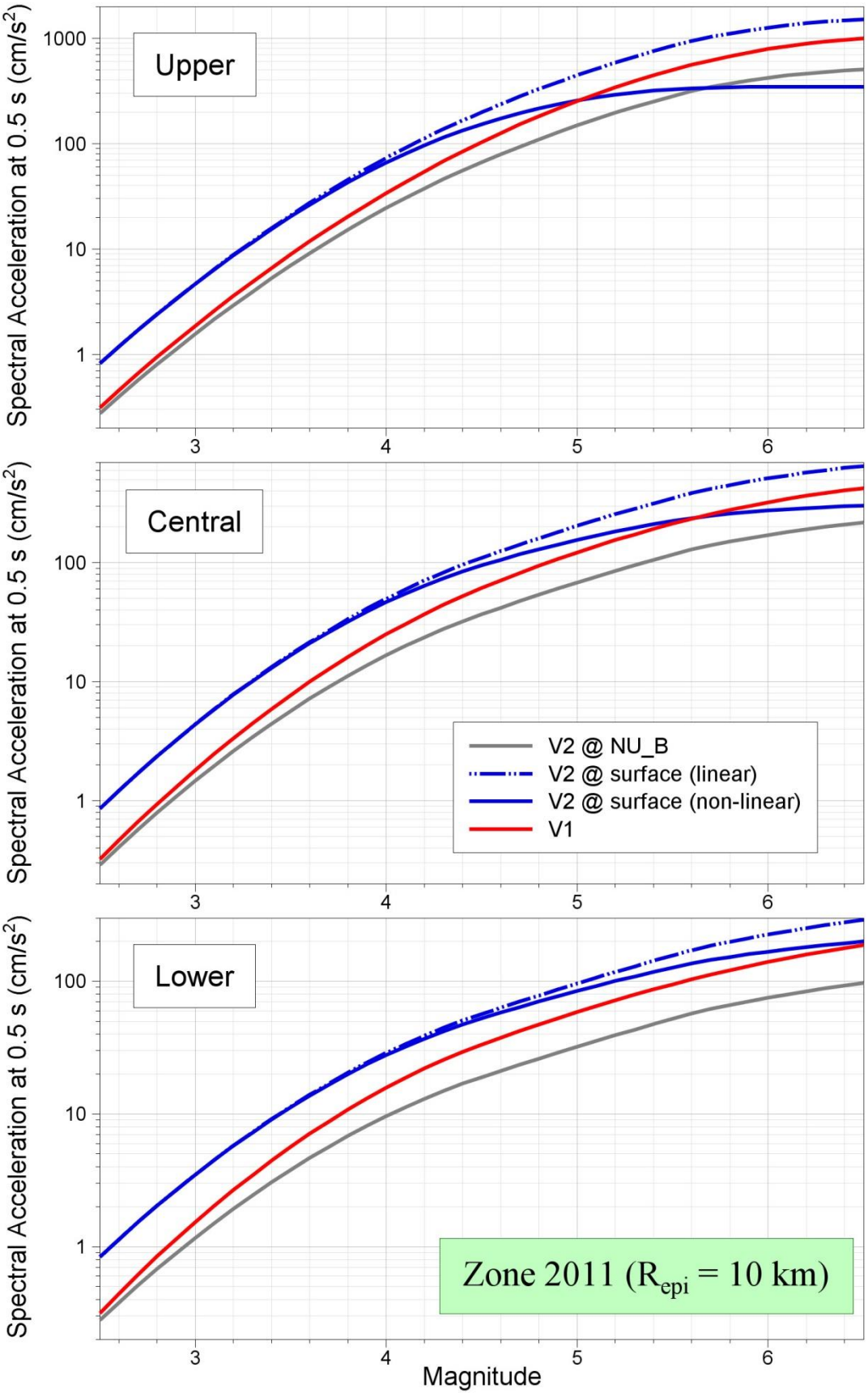

Figure 11.48. Comparison of median predictions of Sa(0.5) as a function of magnitude from the V1 and V2 models for Zone 2011 and R_{epi} = 10 km

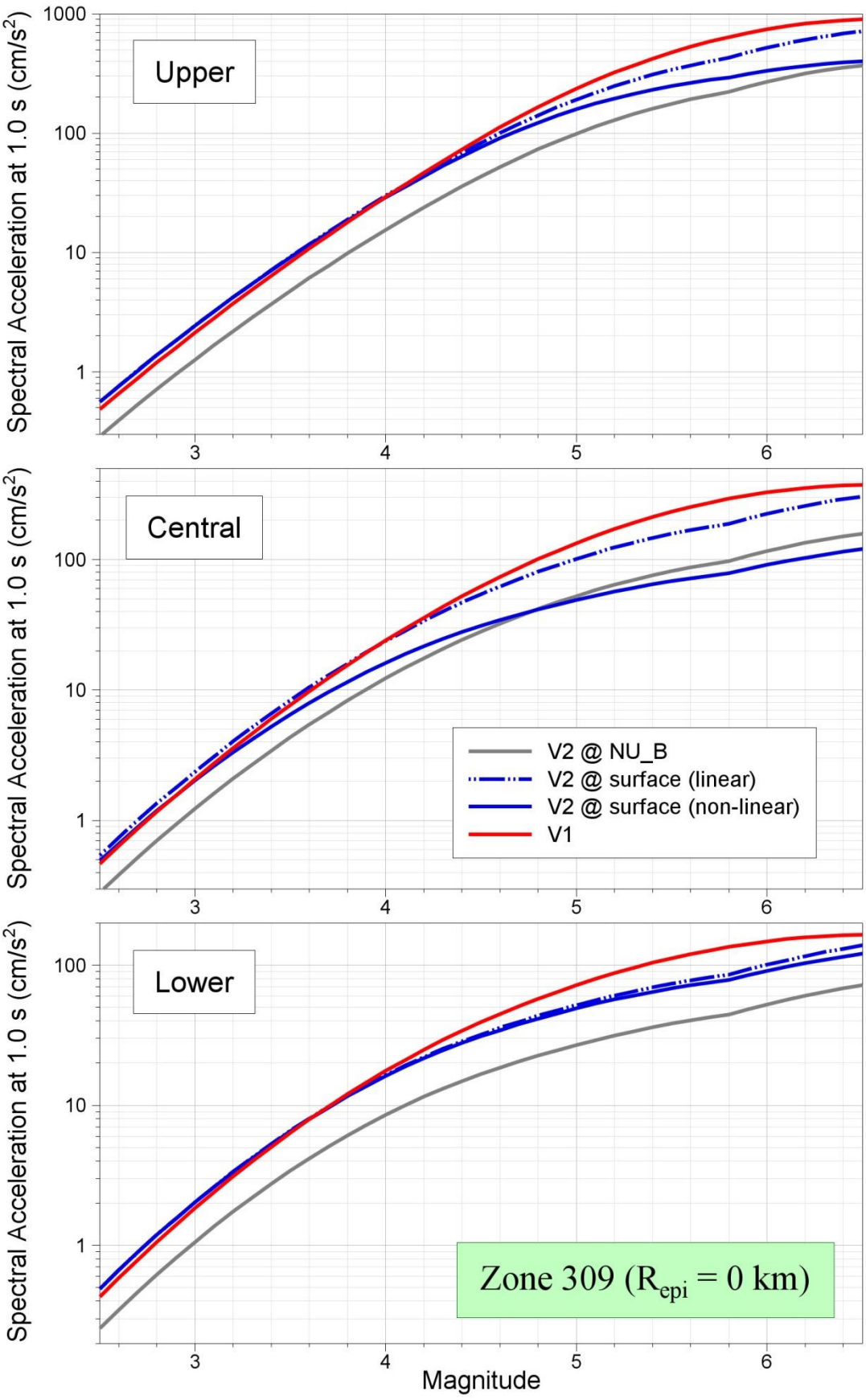

Figure 11.49. Comparison of median predictions of Sa(1.0) as a function of magnitude from the V1 and V2 models for Zone 309 and R_{epi} = 0 km

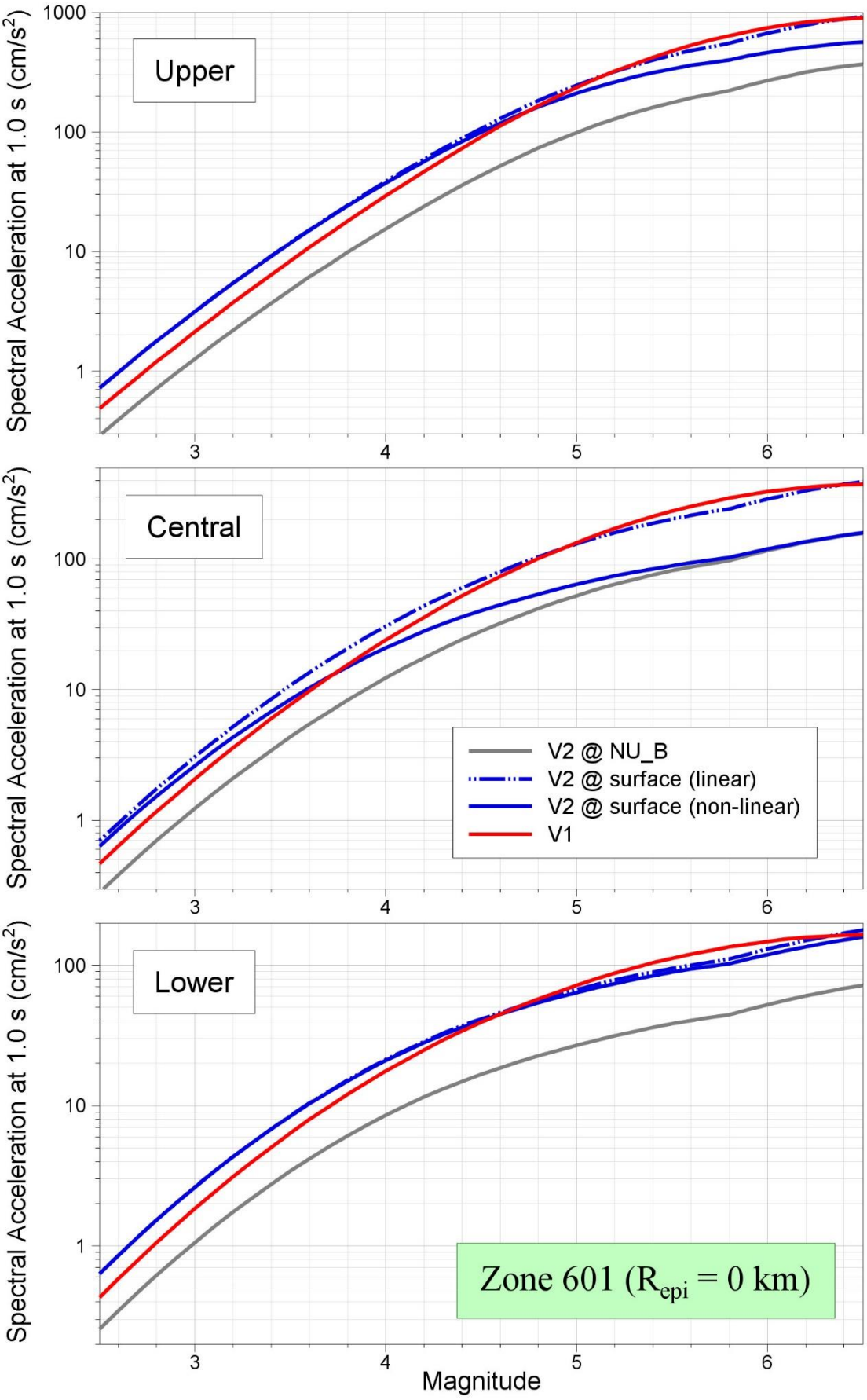

Figure 11.50. Comparison of median predictions of Sa(1.0) as a function of magnitude from the V1 and V2 models for Zone 601 and R_{epi} = 0 km

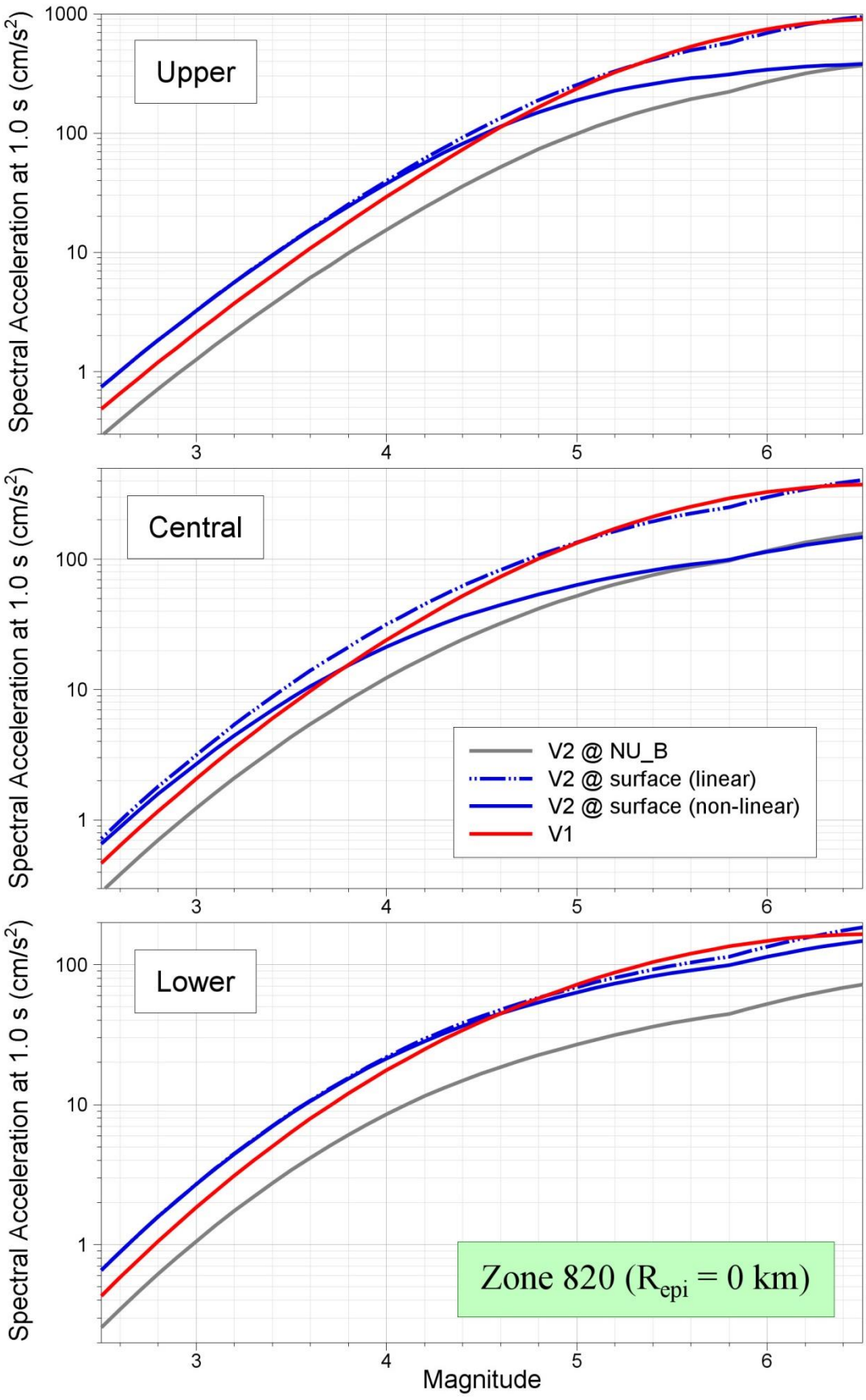

Figure 11.51. Comparison of median predictions of Sa(1.0) as a function of magnitude from the V1 and V2 models for Zone 820 and R_{epi} = 0 km

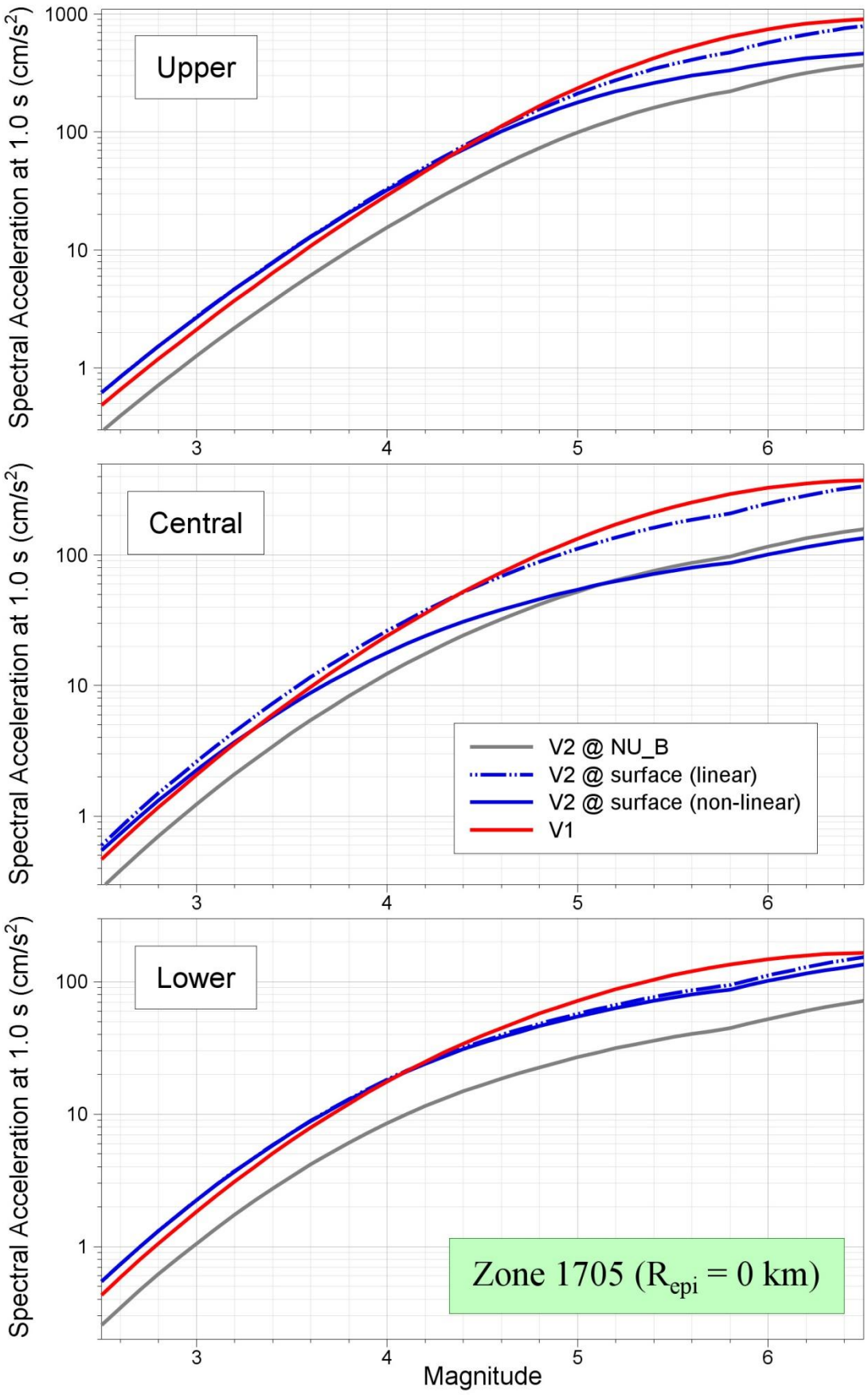

Figure 11.52. Comparison of median predictions of Sa(1.0) as a function of magnitude from the V1 and V2 models for Zone 1705 and R_{epi} = 0 km

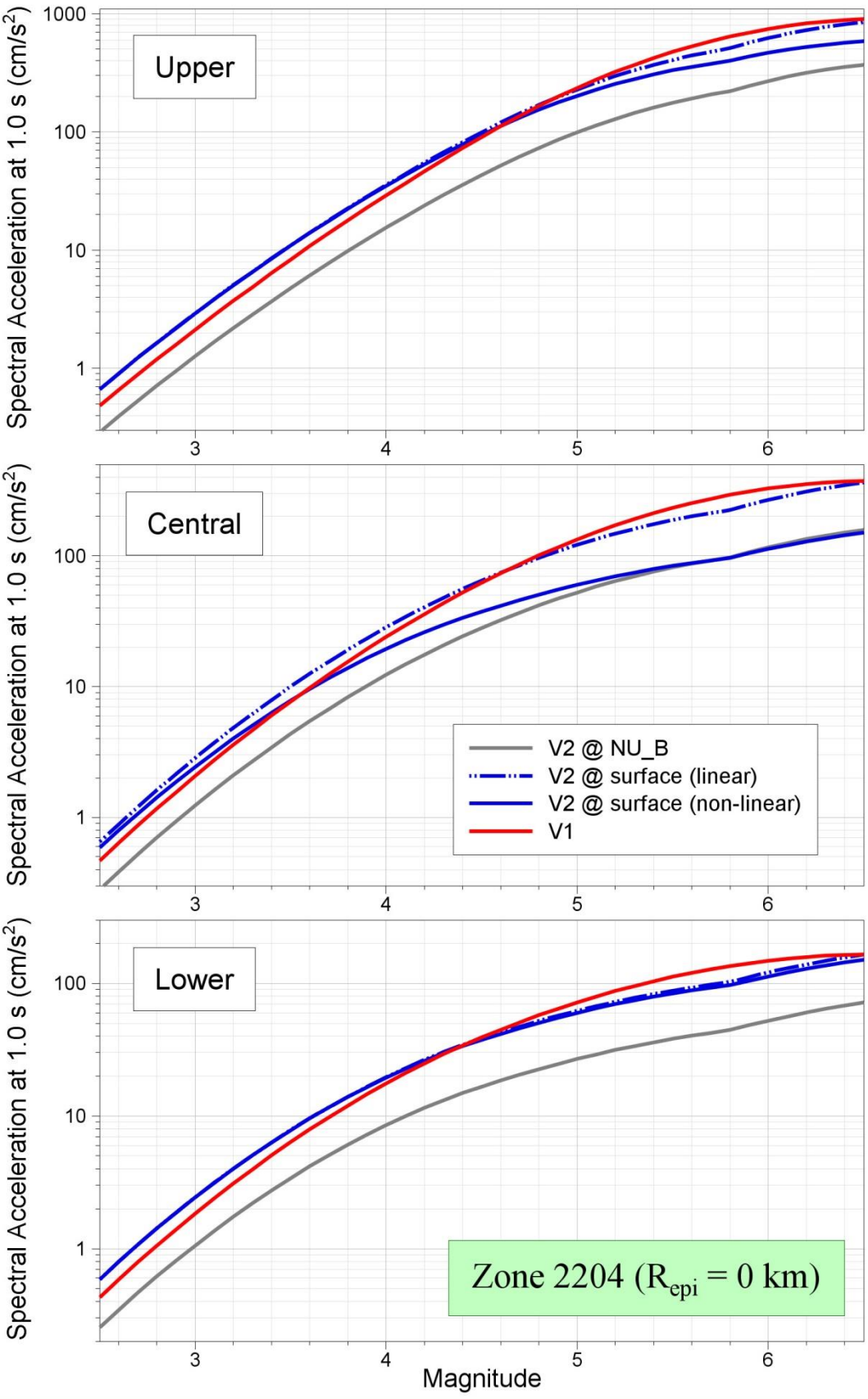

Figure 11.53. Comparison of median predictions of Sa(1.0) as a function of magnitude from the V1 and V2 models for Zone 2204 and R_{epi} = 0 km

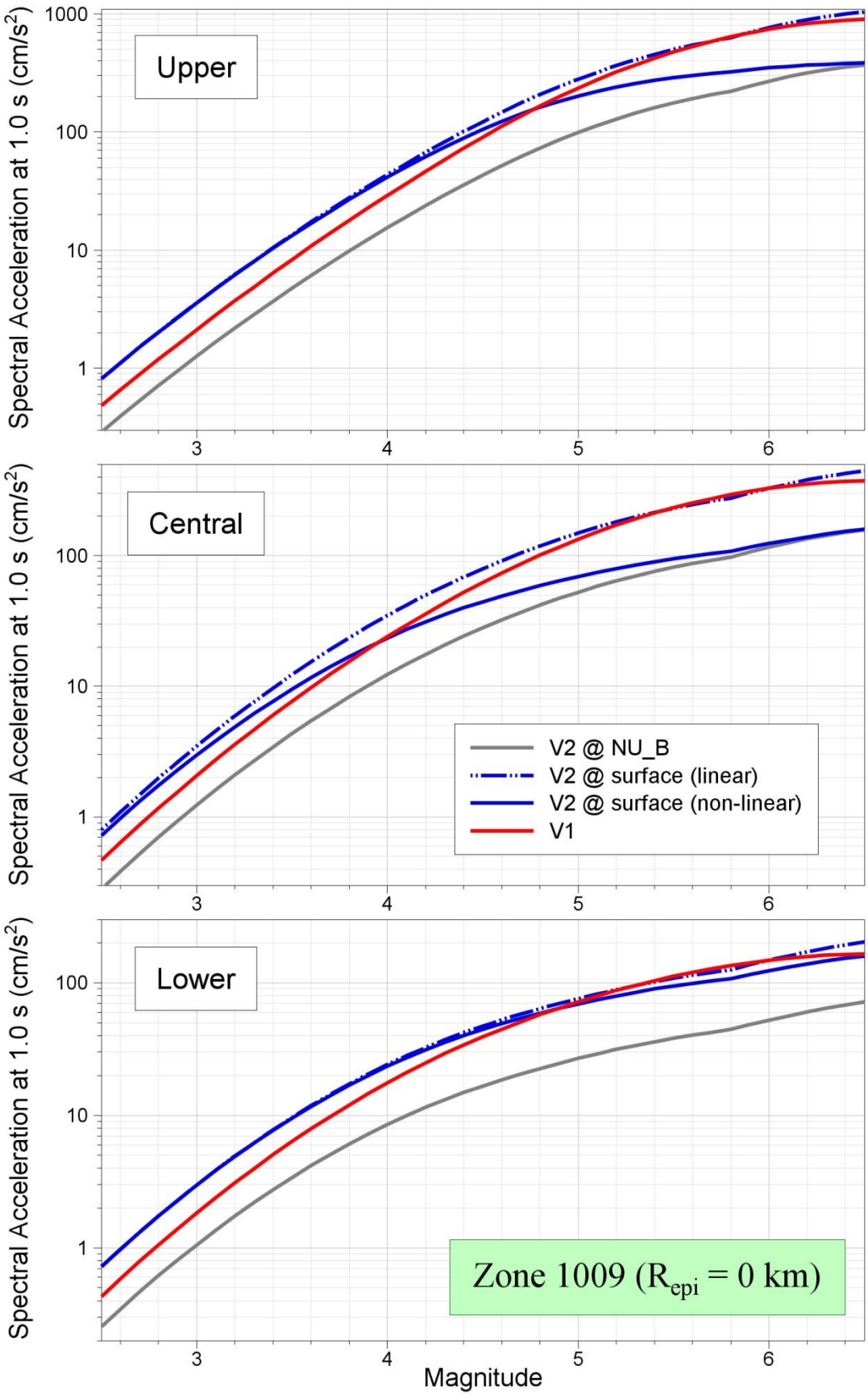

Figure 11.54. Comparison of median predictions of Sa(1.0) as a function of magnitude from the V1 and V2 models for Zone 1009 and R_{epi} = 0 km

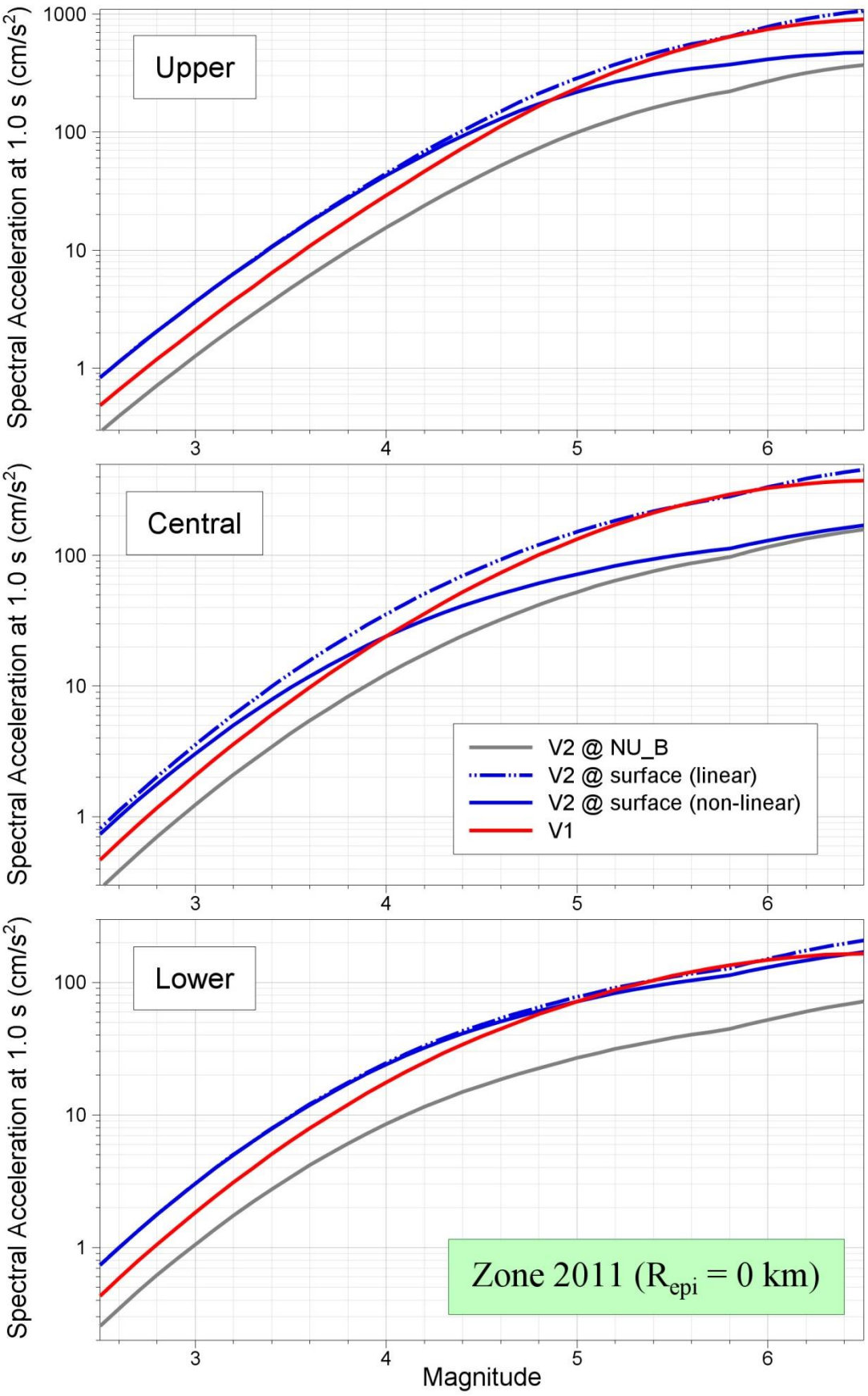

Figure 11.55. Comparison of median predictions of Sa(1.0) as a function of magnitude from the V1 and V2 models for Zone 2011 and R_{epi} = 0 km

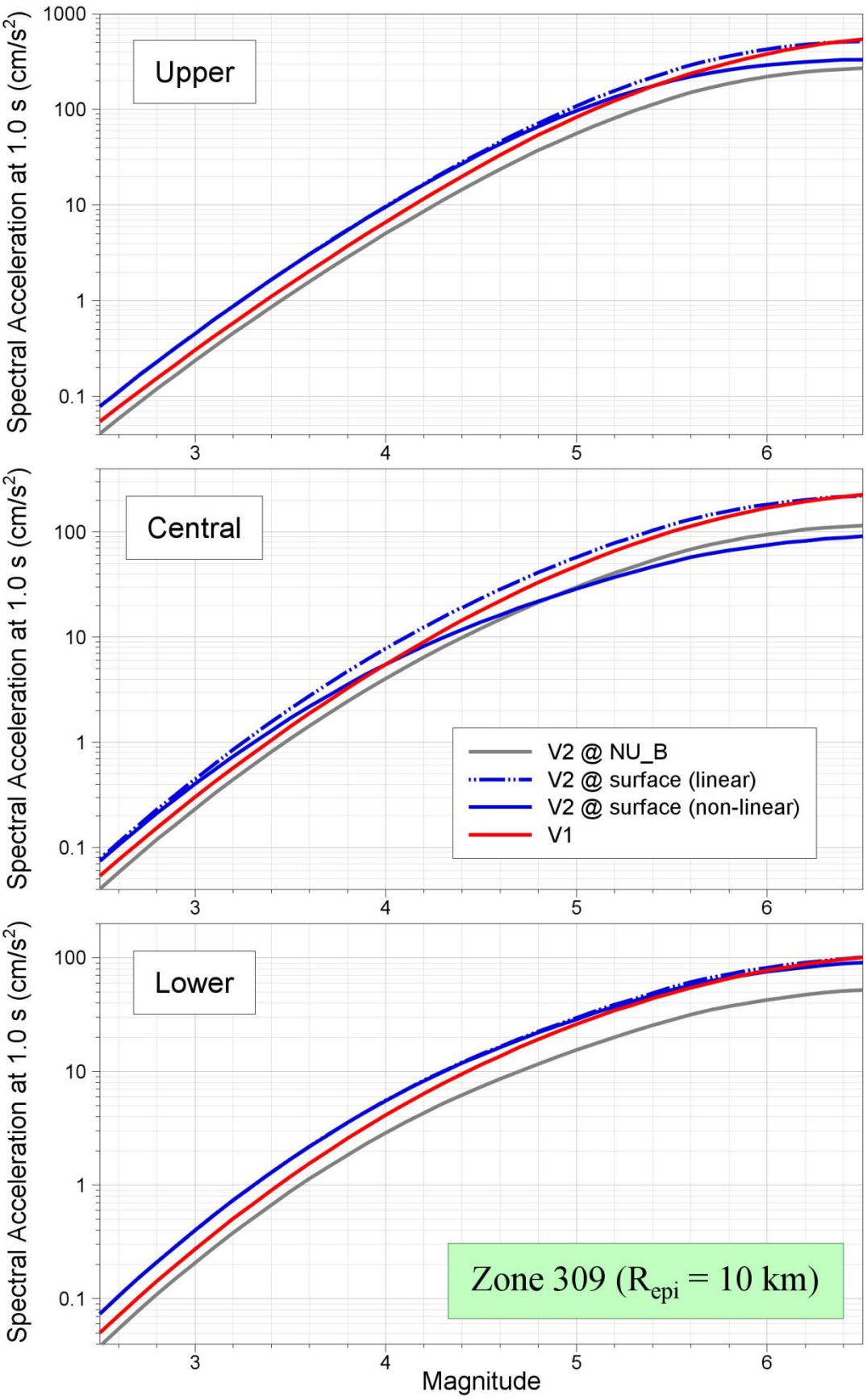

Figure 11.56. Comparison of median predictions of Sa(1.0) as a function of magnitude from the V1 and V2 models for Zone 309 and R_{epi} = 10 km

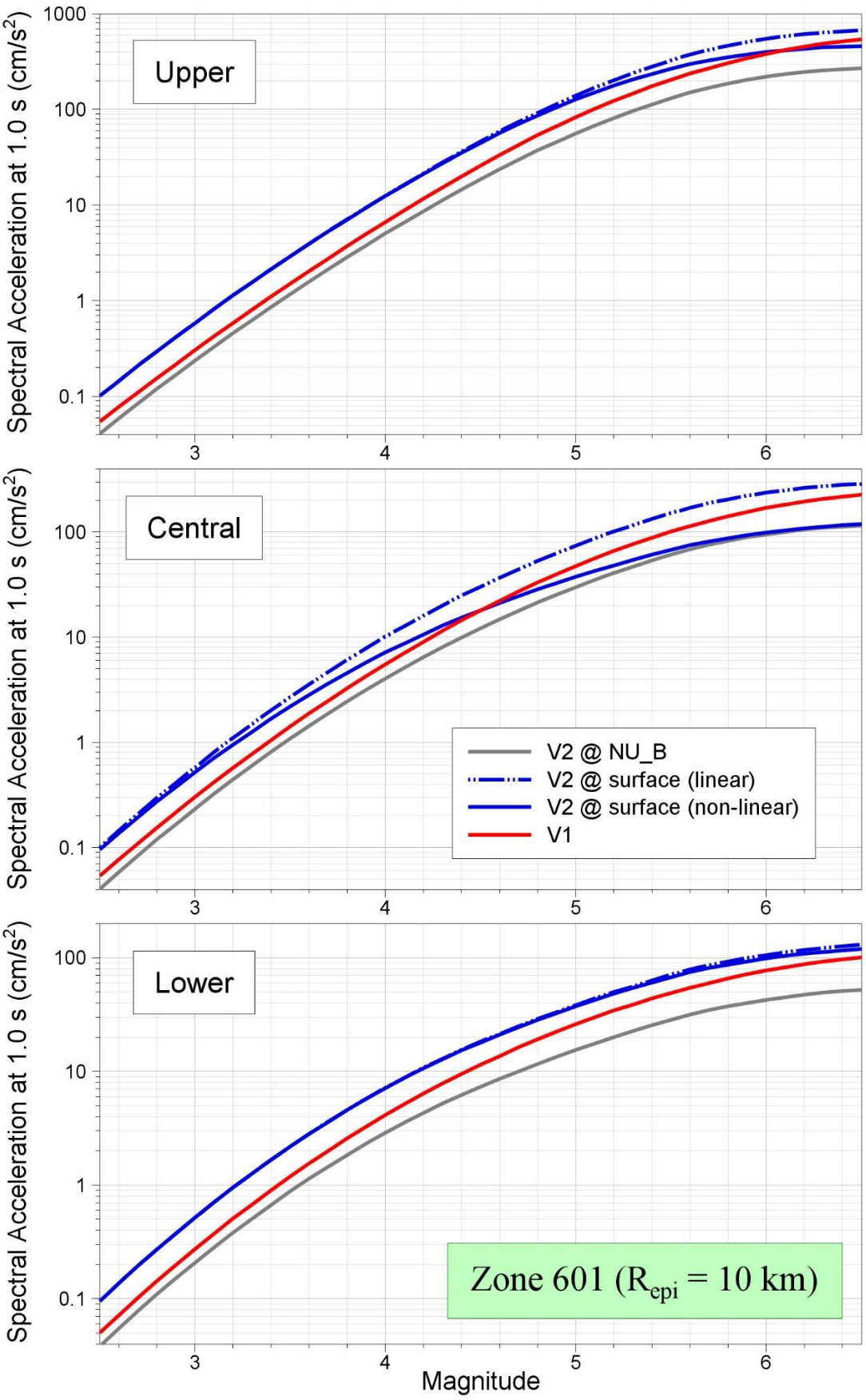

Figure 11.57. Comparison of median predictions of Sa(1.0) as a function of magnitude from the V1 and V2 models for Zone 601 and R_{epi} = 10 km

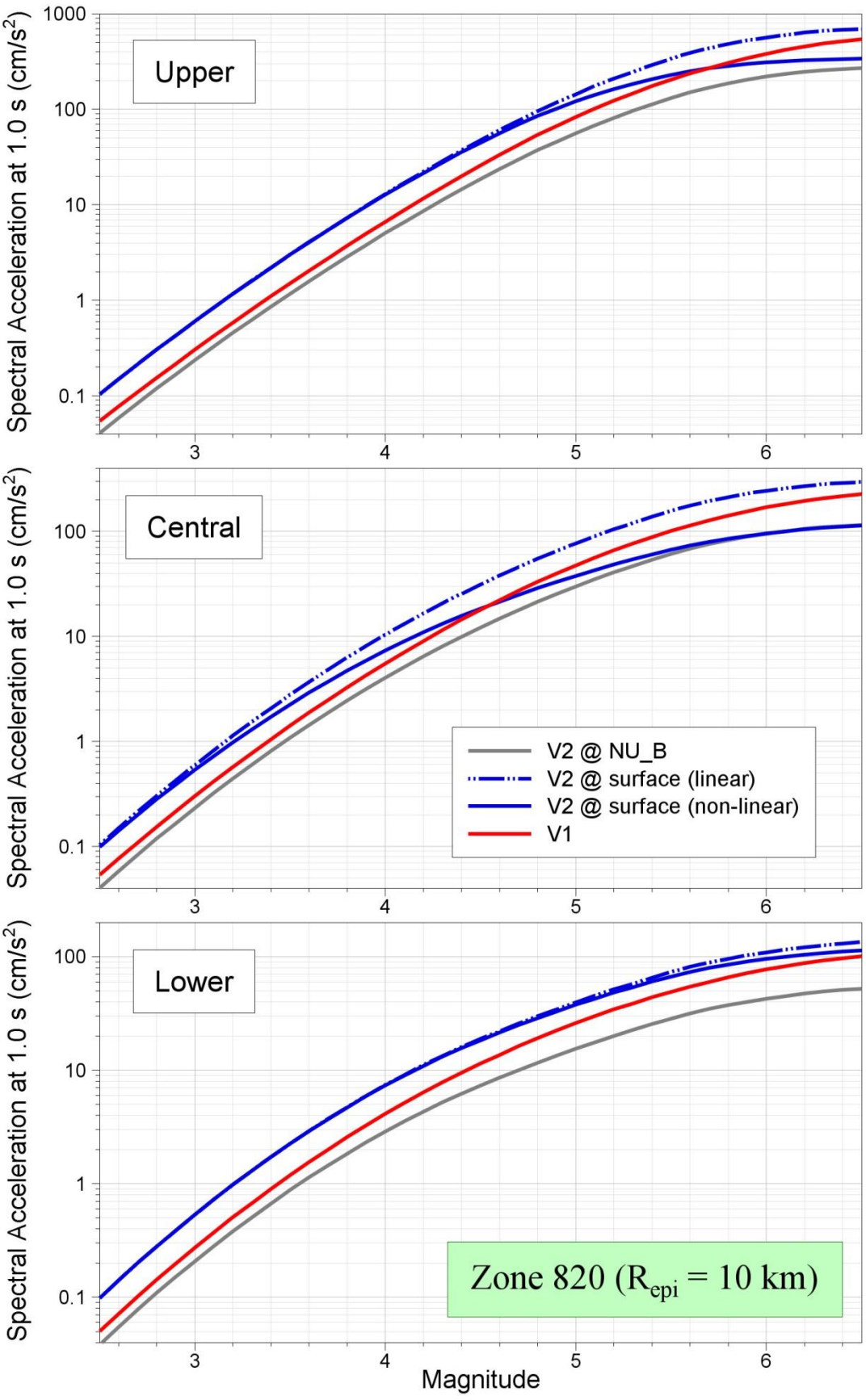

Figure 11.58. Comparison of median predictions of Sa(1.0) as a function of magnitude from the V1 and V2 models for Zone 820 and R_{epi} = 10 km

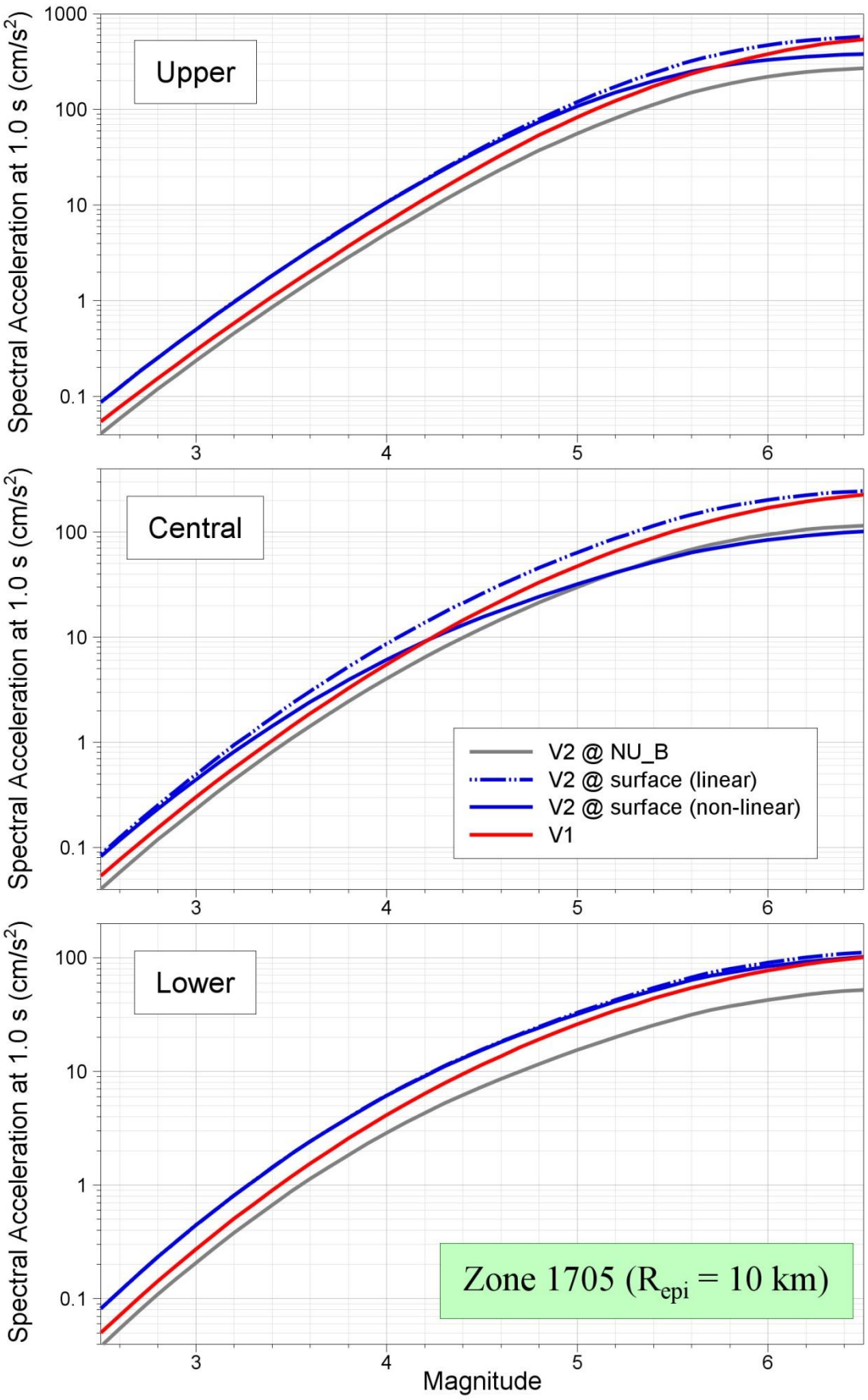

Figure 11.59. Comparison of median predictions of Sa(1.0) as a function of magnitude from the V1 and V2 models for Zone 1705 and R_{epi} = 10 km

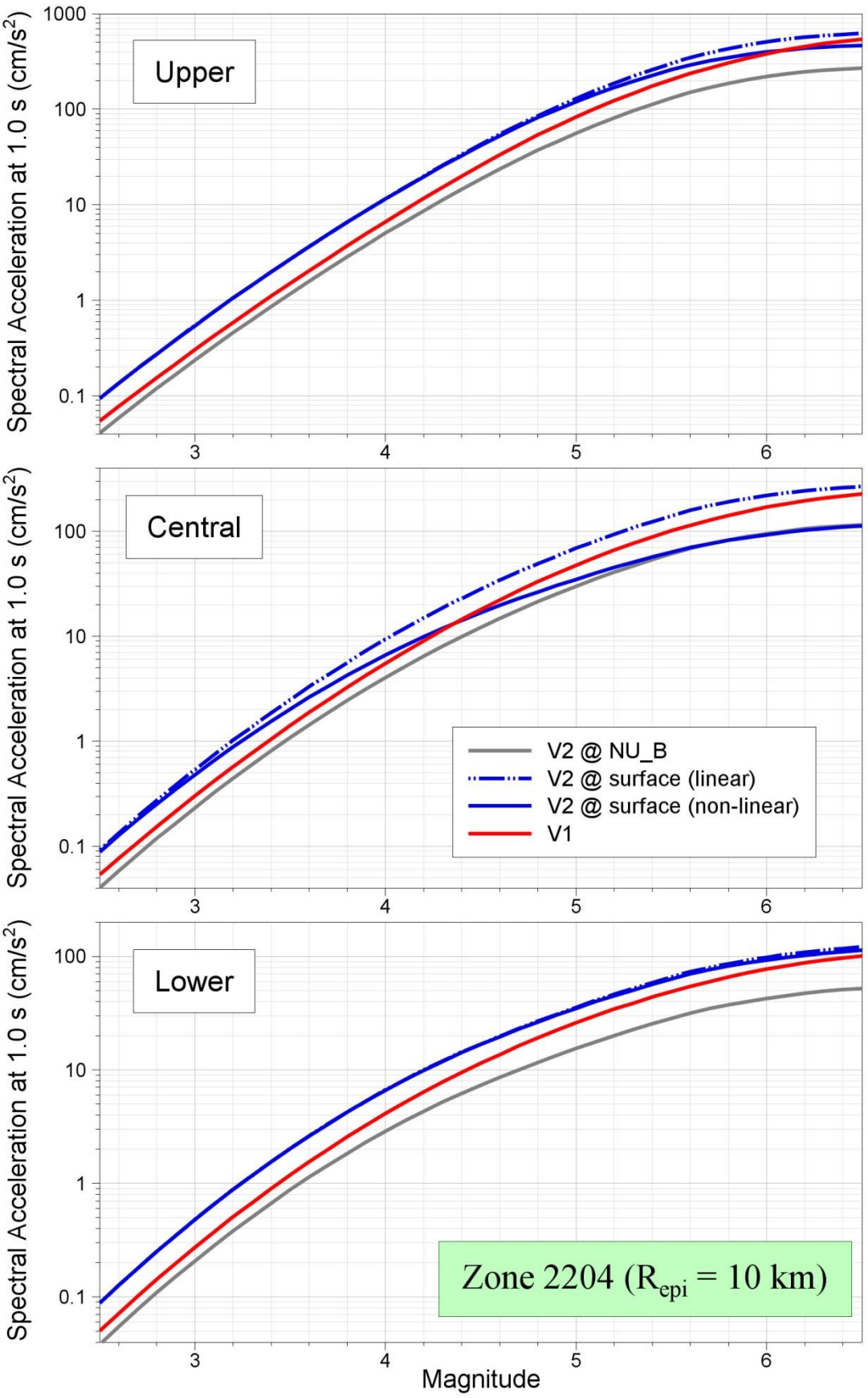

Figure 11.60. Comparison of median predictions of Sa(1.0) as a function of magnitude from the V1 and V2 models for Zone 2204 and R_{epi} = 10 km

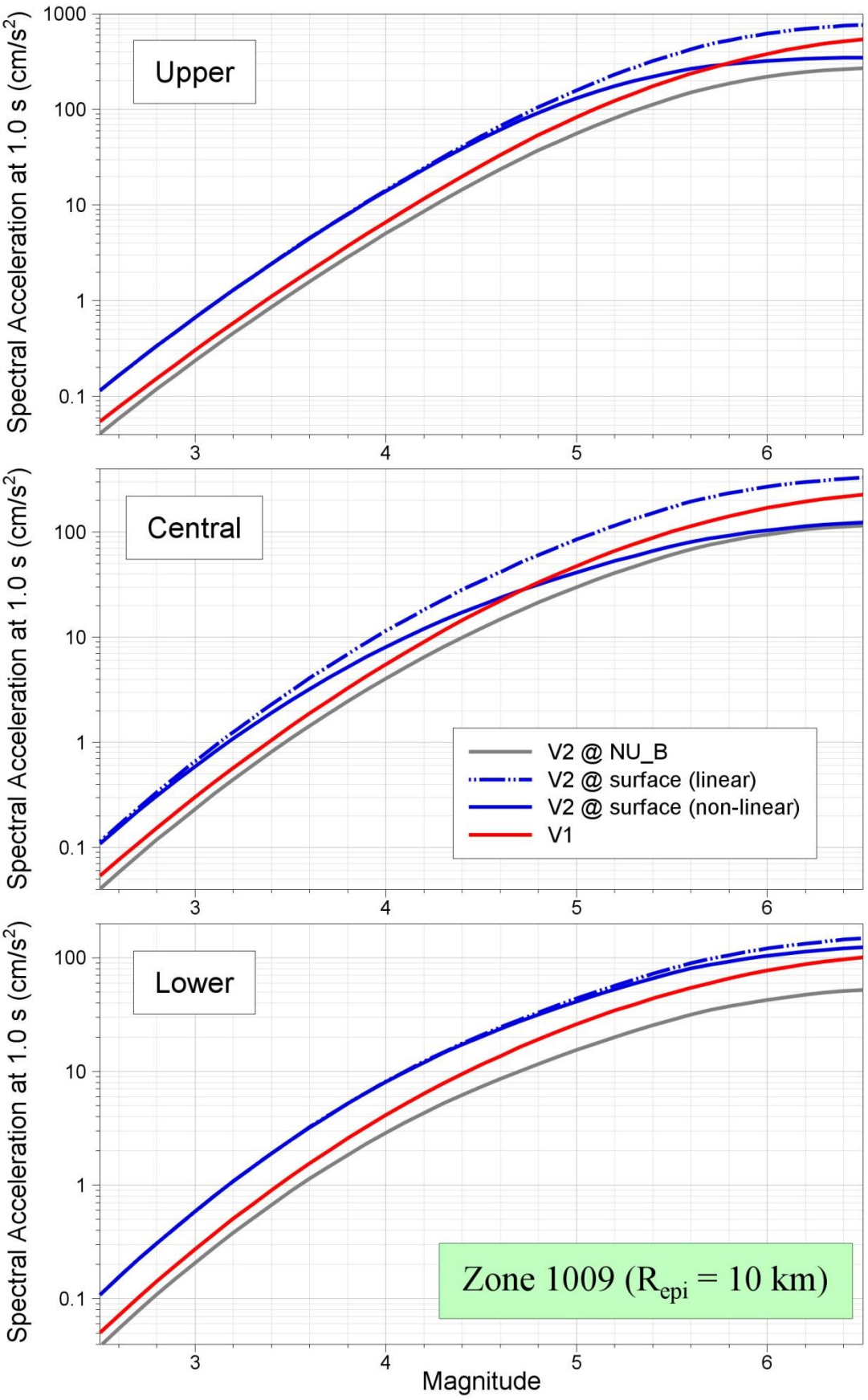

Figure 11.61. Comparison of median predictions of Sa(1.0) as a function of magnitude from the V1 and V2 models for Zone 1009 and R_{epi} = 10 km

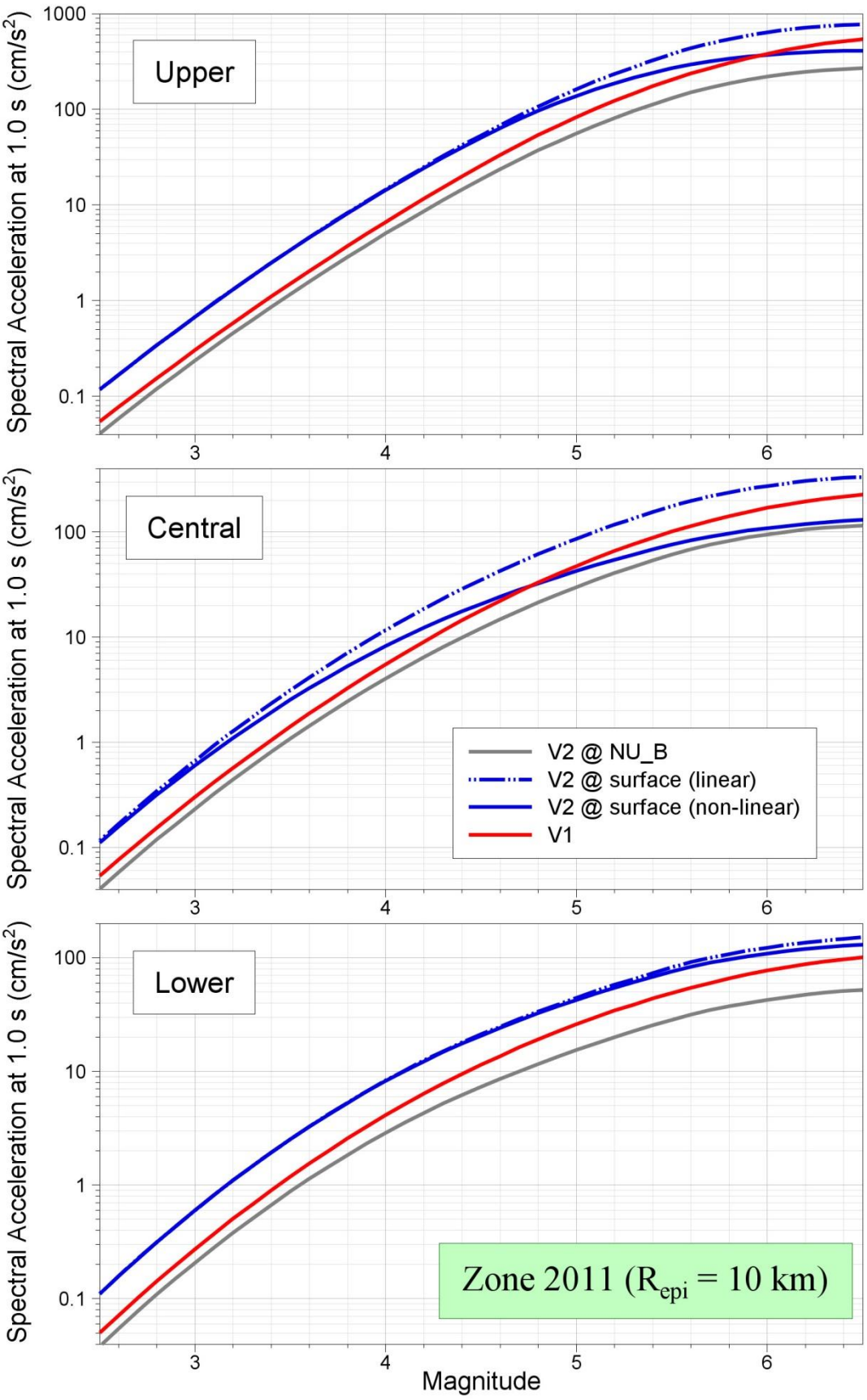

Figure 11.62. Comparison of median predictions of Sa(1.0) as a function of magnitude from the V1 and V2 models for Zone 2011 and R_{epi} = 10 km

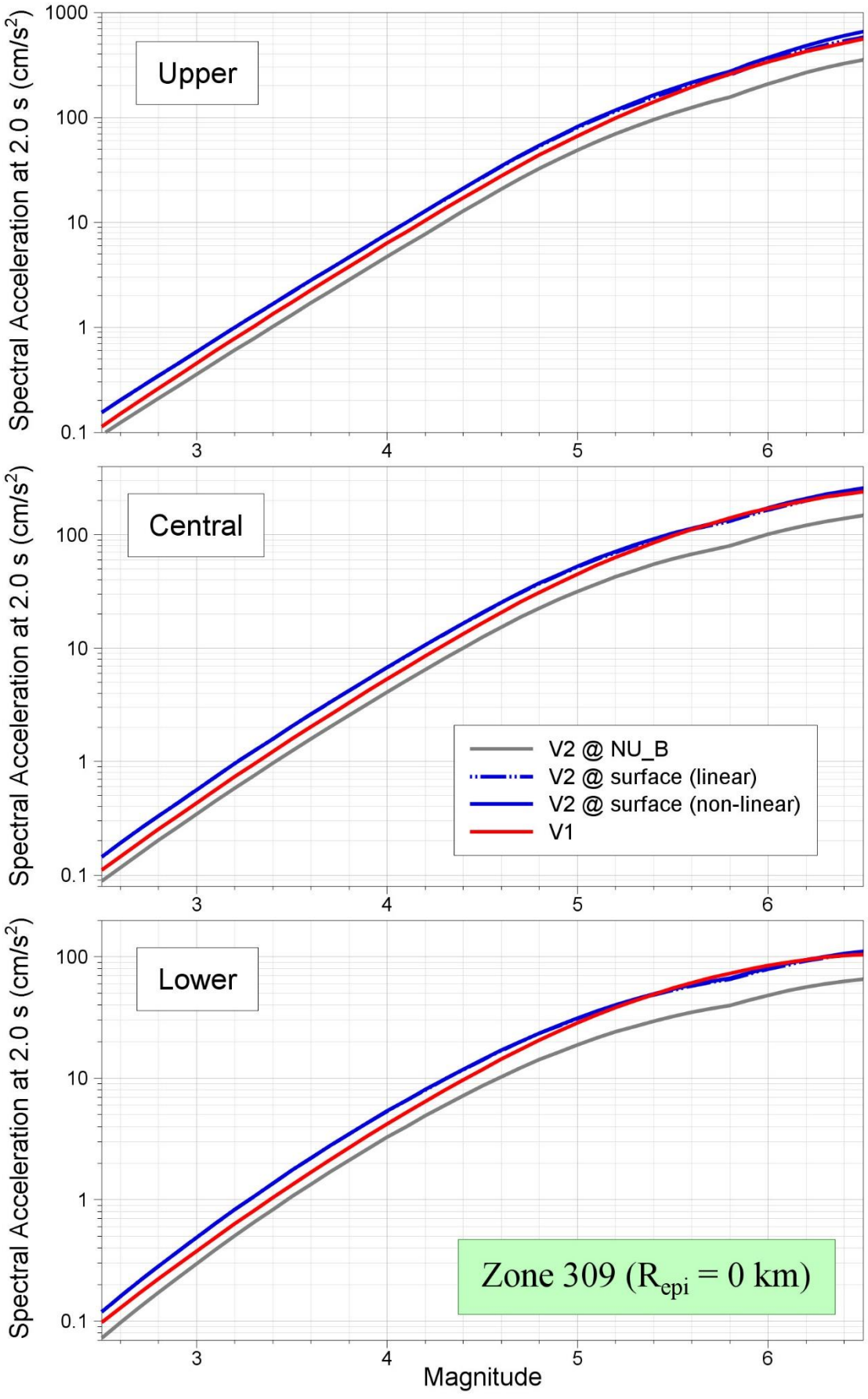

Figure 11.63. Comparison of median predictions of Sa(2.0) as a function of magnitude from the V1 and V2 models for Zone 309 and R_{epi} = 0 km

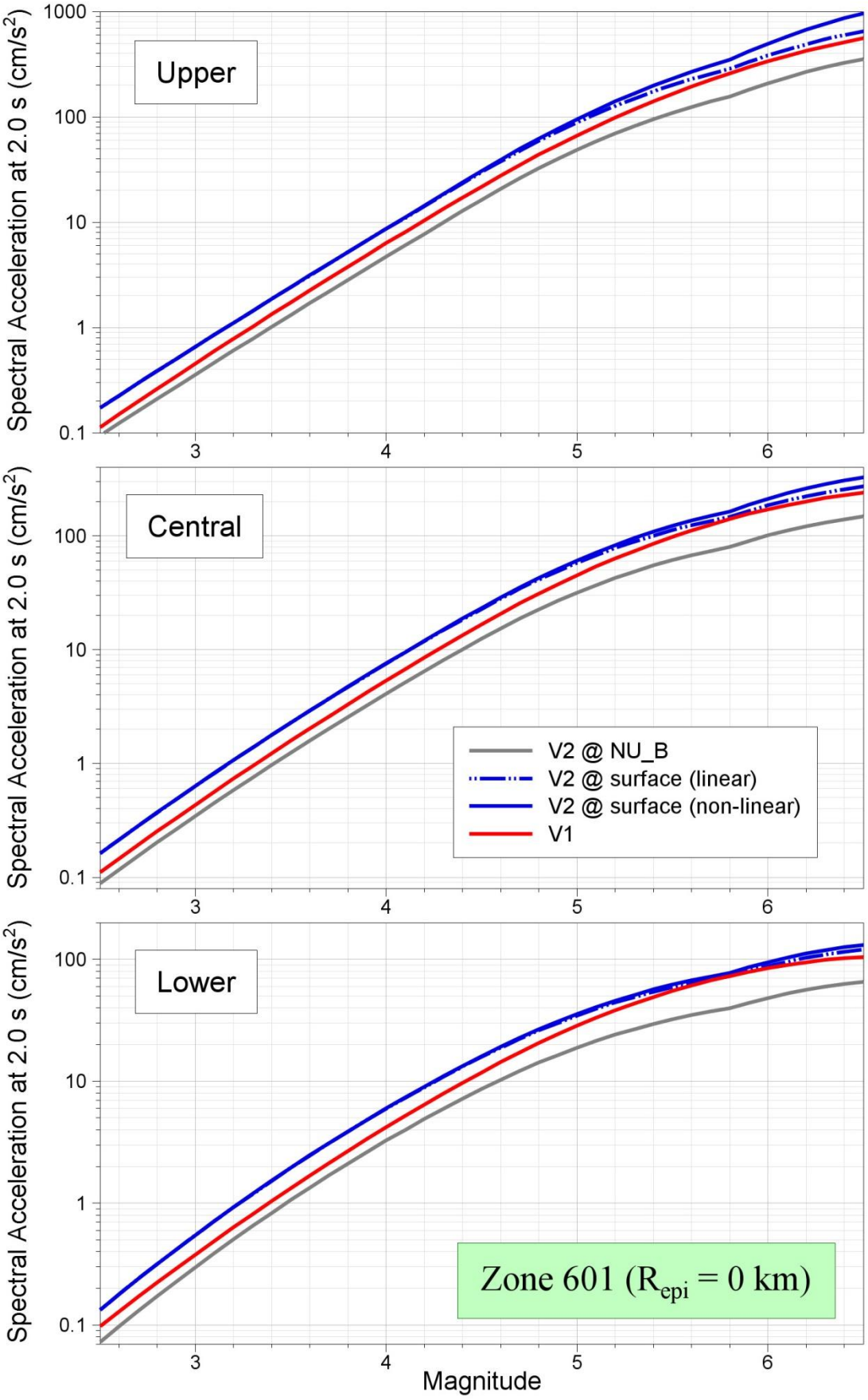

Figure 11.64. Comparison of median predictions of Sa(2.0) as a function of magnitude from the V1 and V2 models for Zone 601 and R_{epi} = 0 km

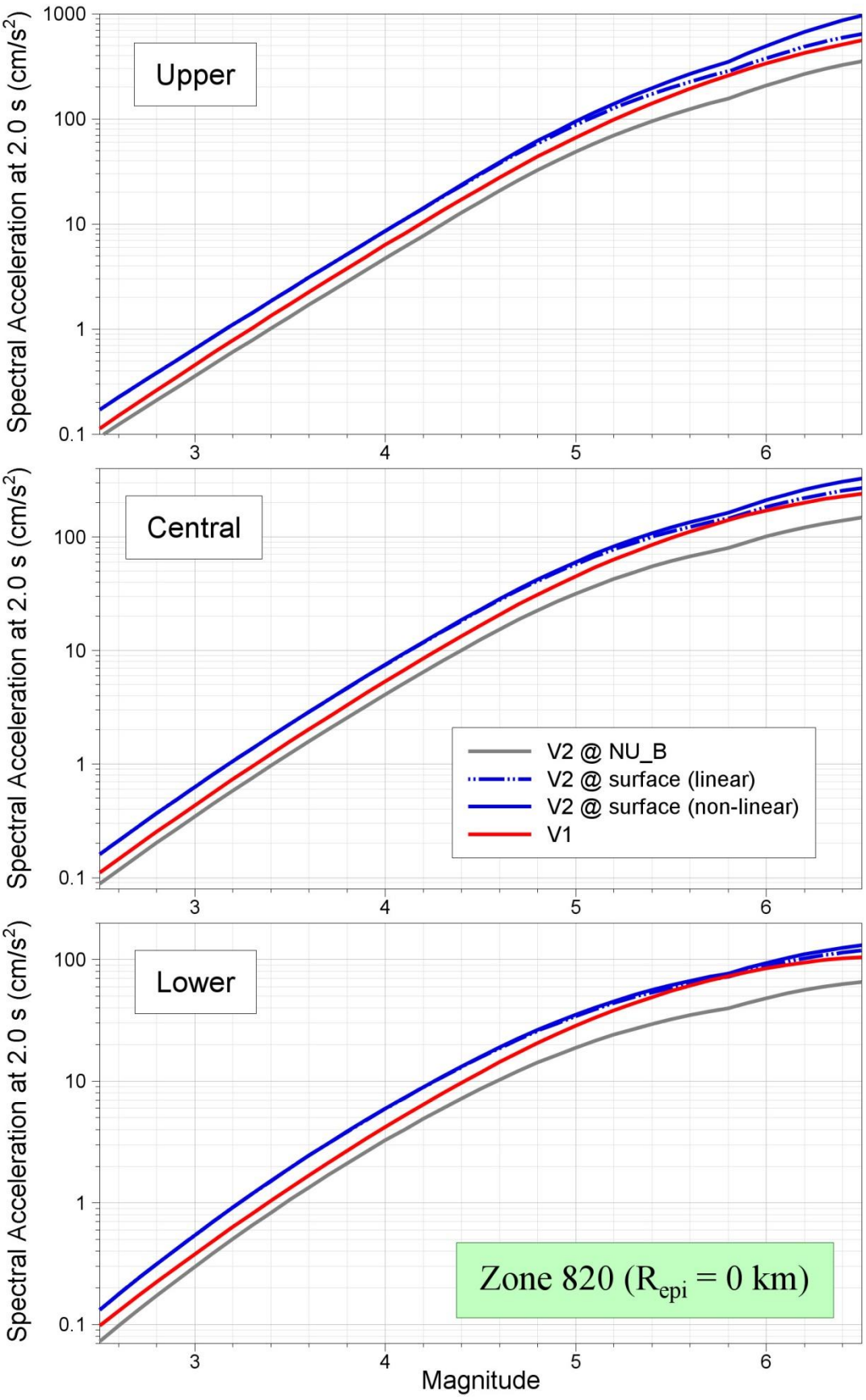

Figure 11.65. Comparison of median predictions of Sa(2.0) as a function of magnitude from the V1 and V2 models for Zone 820 and R_{epi} = 0 km

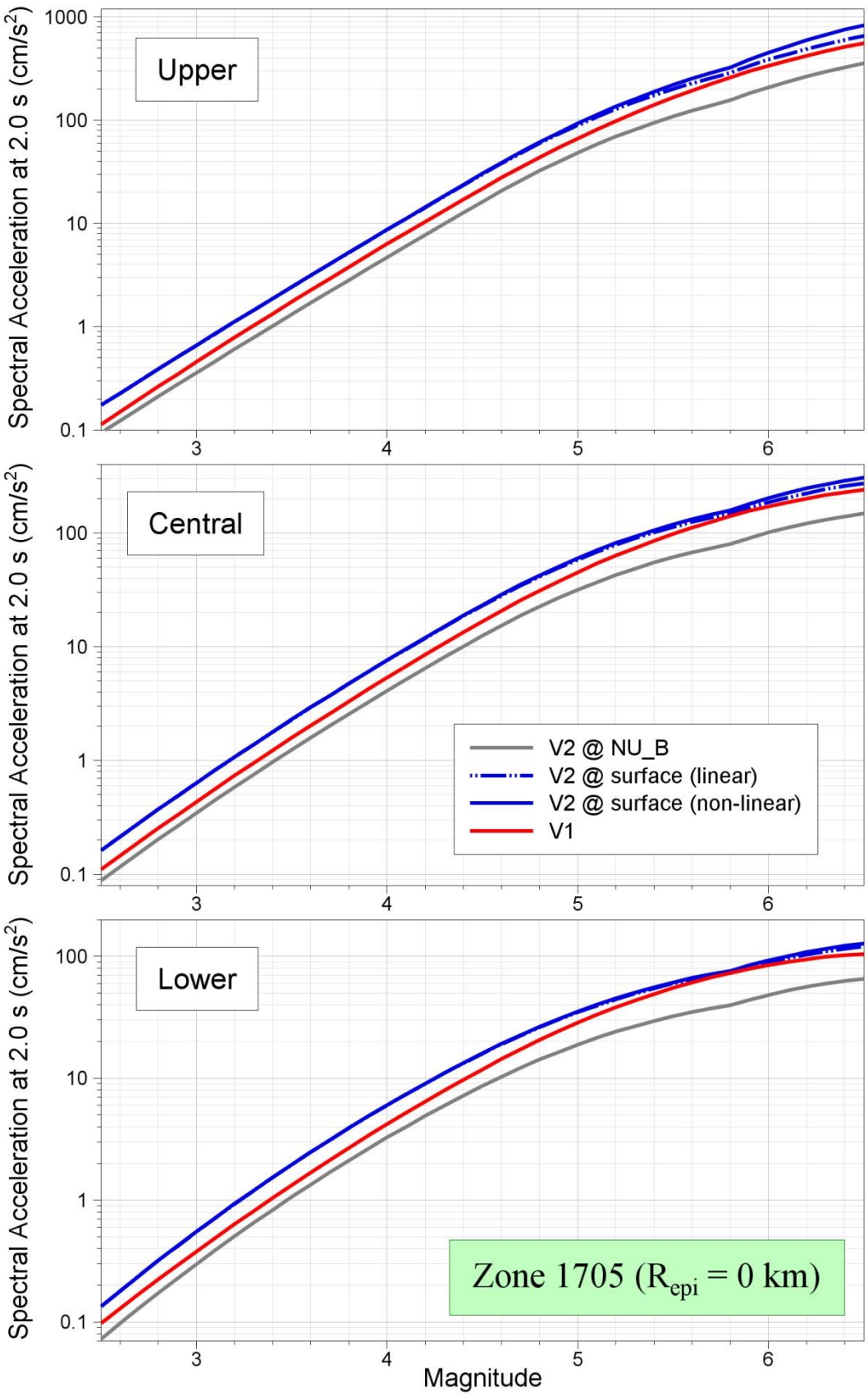

Figure 11.66. Comparison of median predictions of Sa(2.0) as a function of magnitude from the V1 and V2 models for Zone 1705 and R_{epi} = 0 km

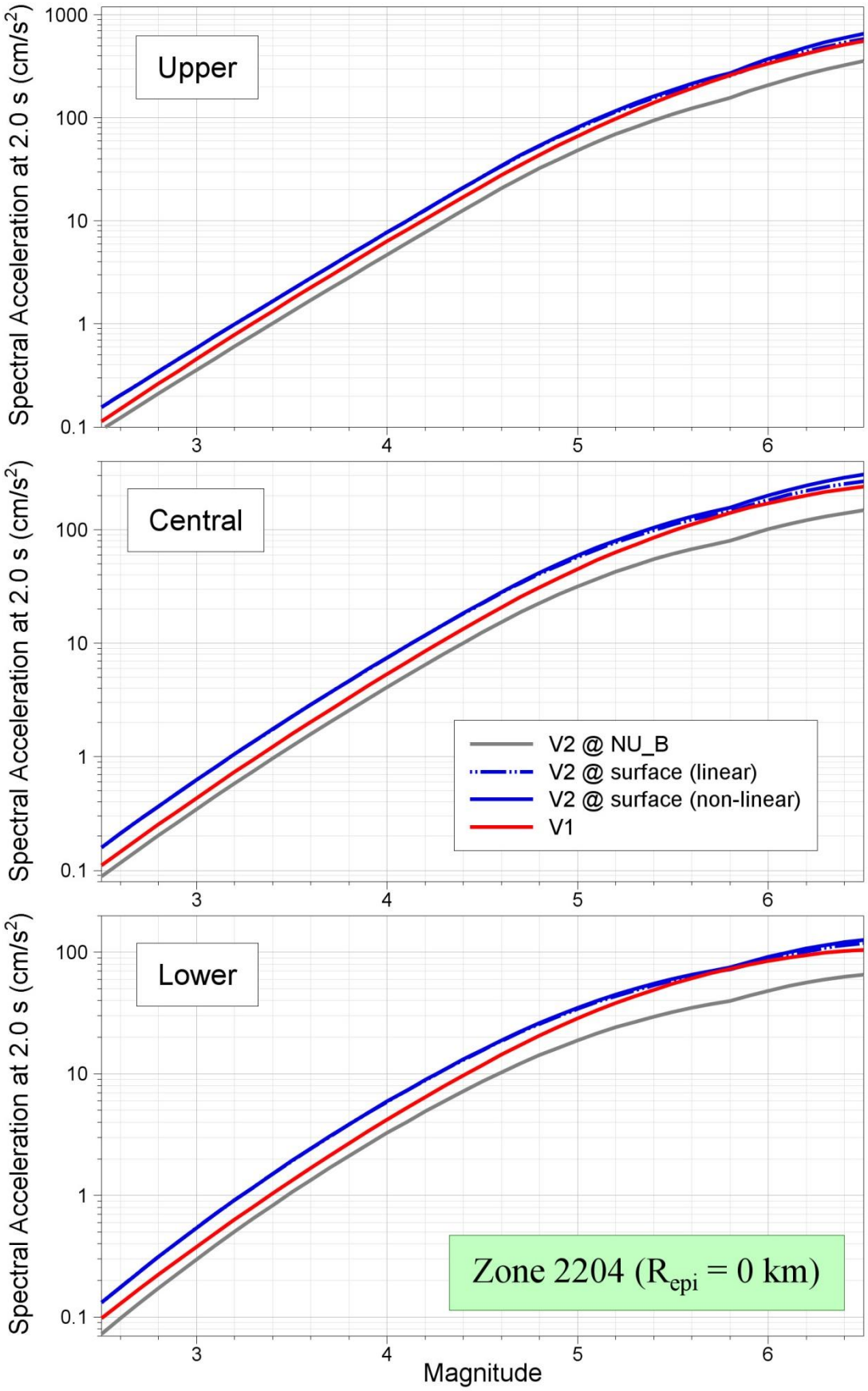

Figure 11.67. Comparison of median predictions of Sa(2.0) as a function of magnitude from the V1 and V2 models for Zone 2204 and R_{epi} = 0 km

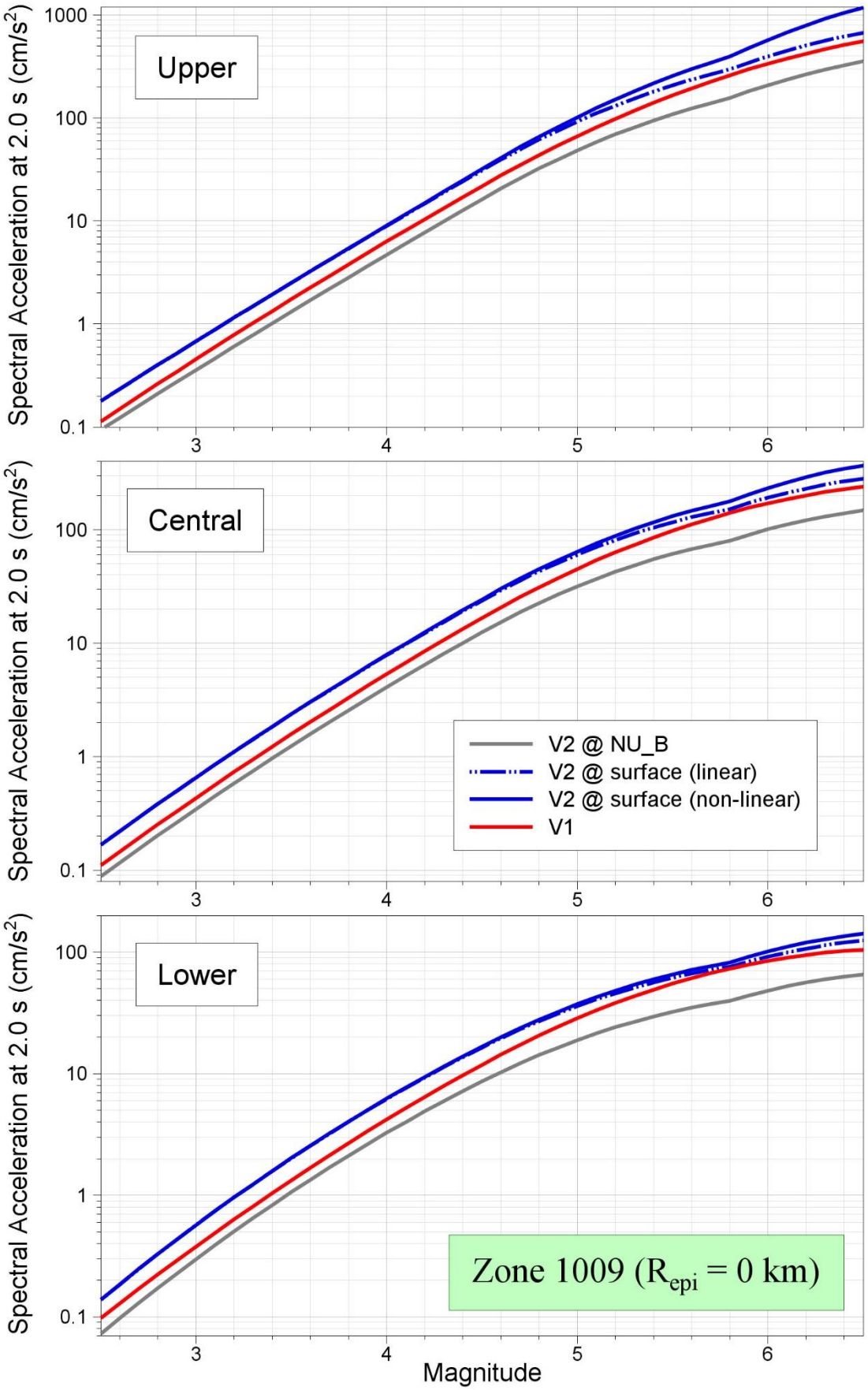

Figure 11.68. Comparison of median predictions of Sa(2.0) as a function of magnitude from the V1 and V2 models for Zone 1009 and R_{epi} = 0 km

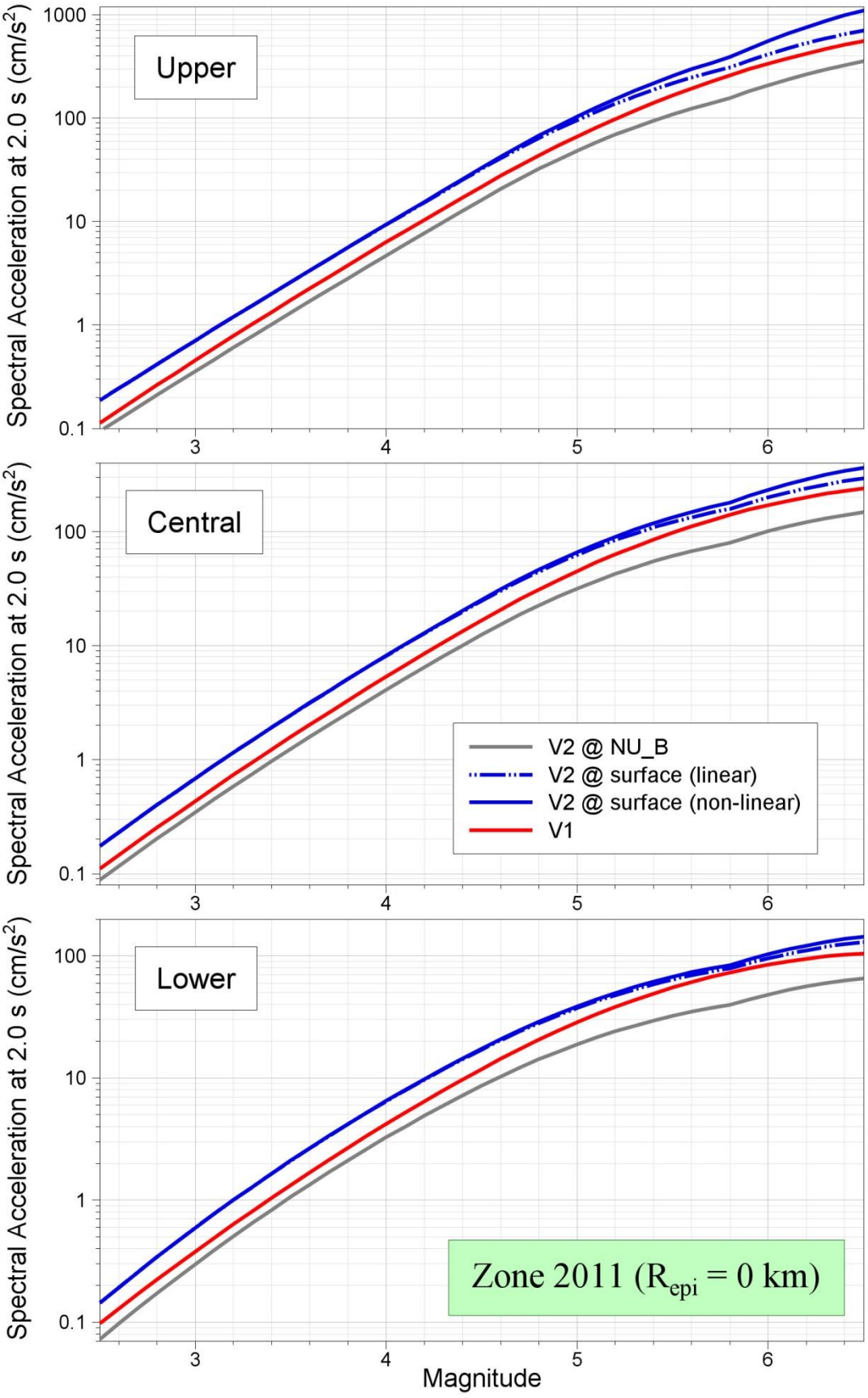

Figure 11.69. Comparison of median predictions of Sa(2.0) as a function of magnitude from the V1 and V2 models for Zone 2011 and R_{epi} = 0 km

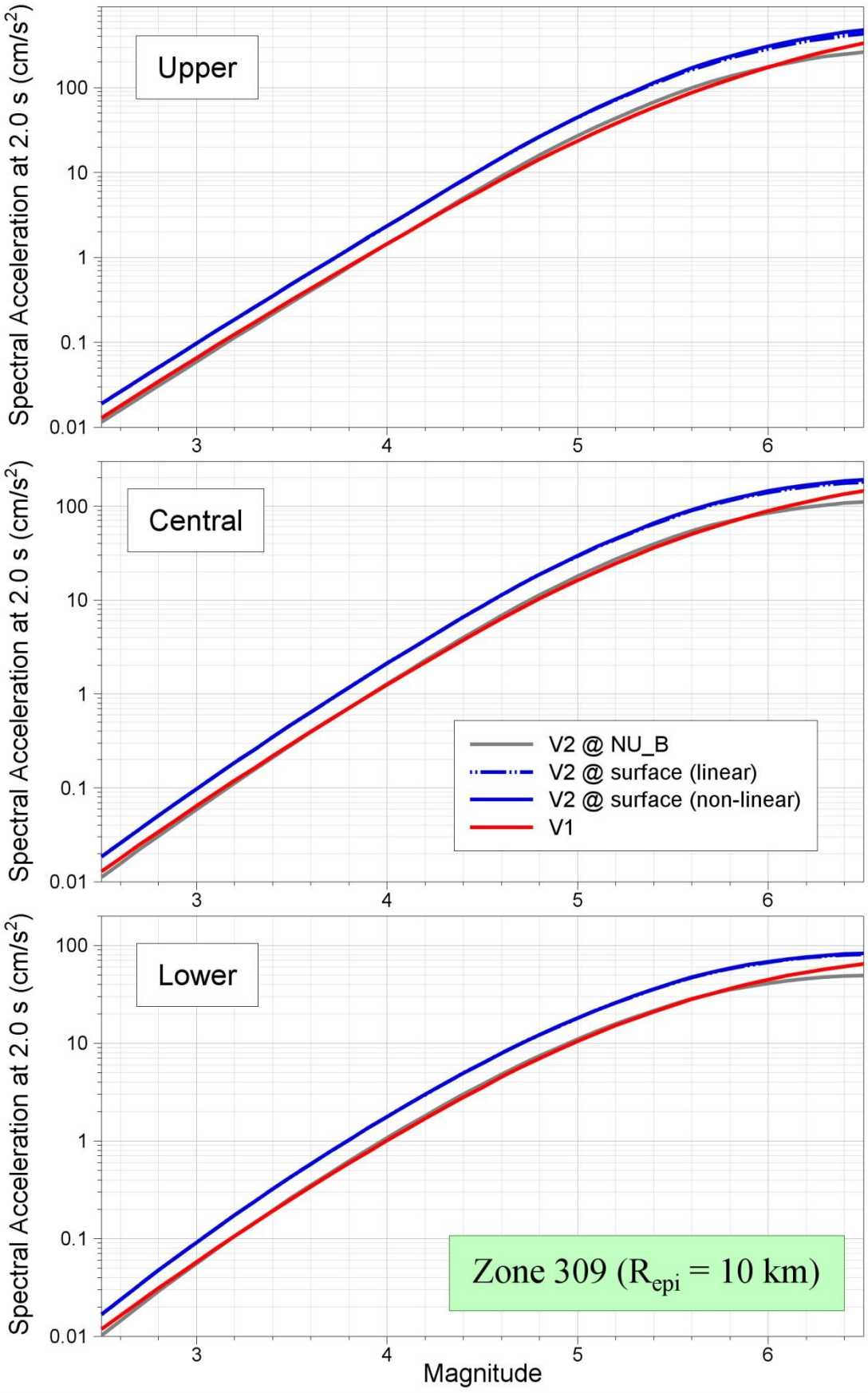

Figure 11.70. Comparison of median predictions of Sa(2.0) as a function of magnitude from the V1 and V2 models for Zone 309 and R_{epi} = 10 km

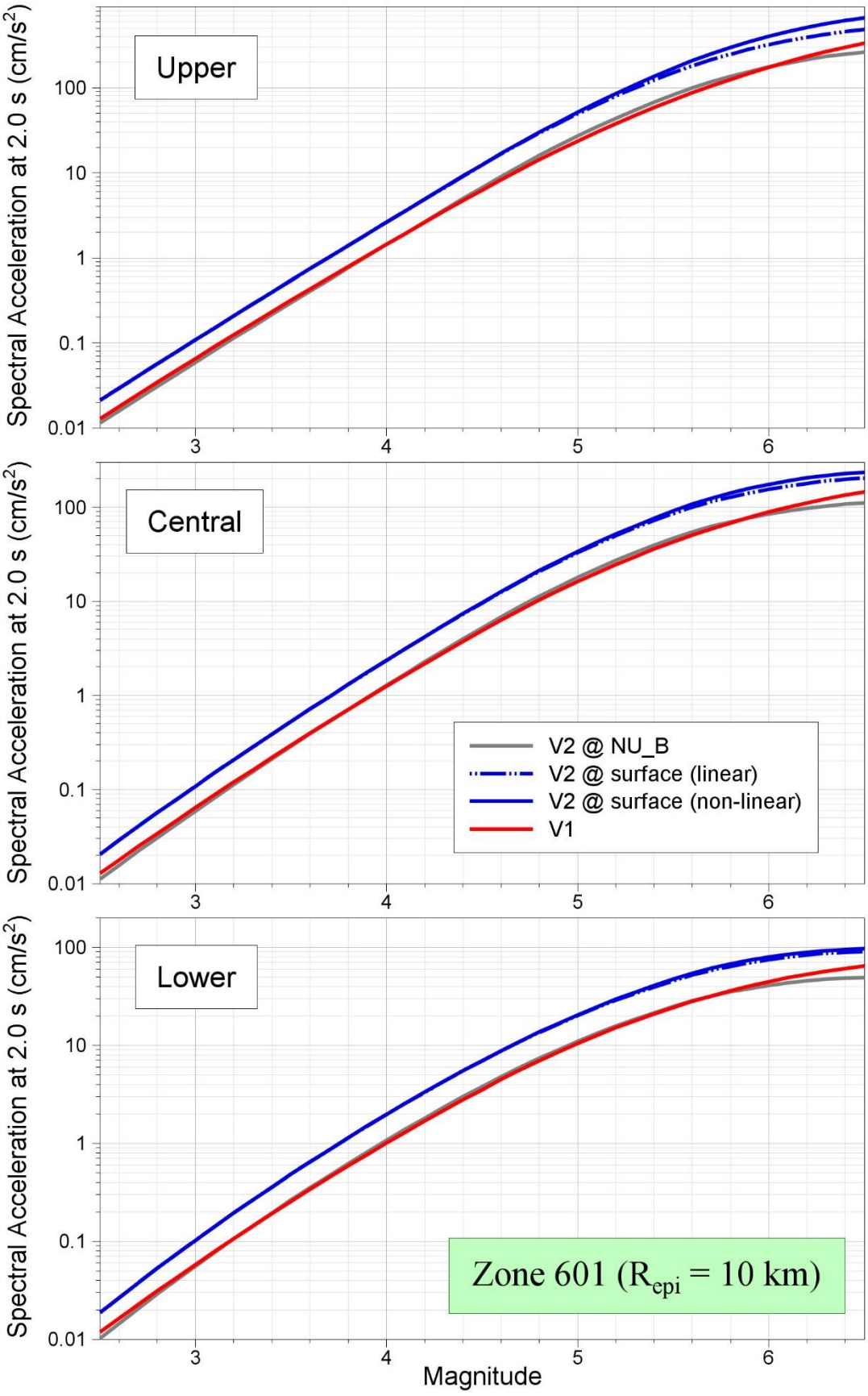

Figure 11.71. Comparison of median predictions of Sa(2.0) as a function of magnitude from the V1 and V2 models for Zone 601 and R_{epi} = 10 km

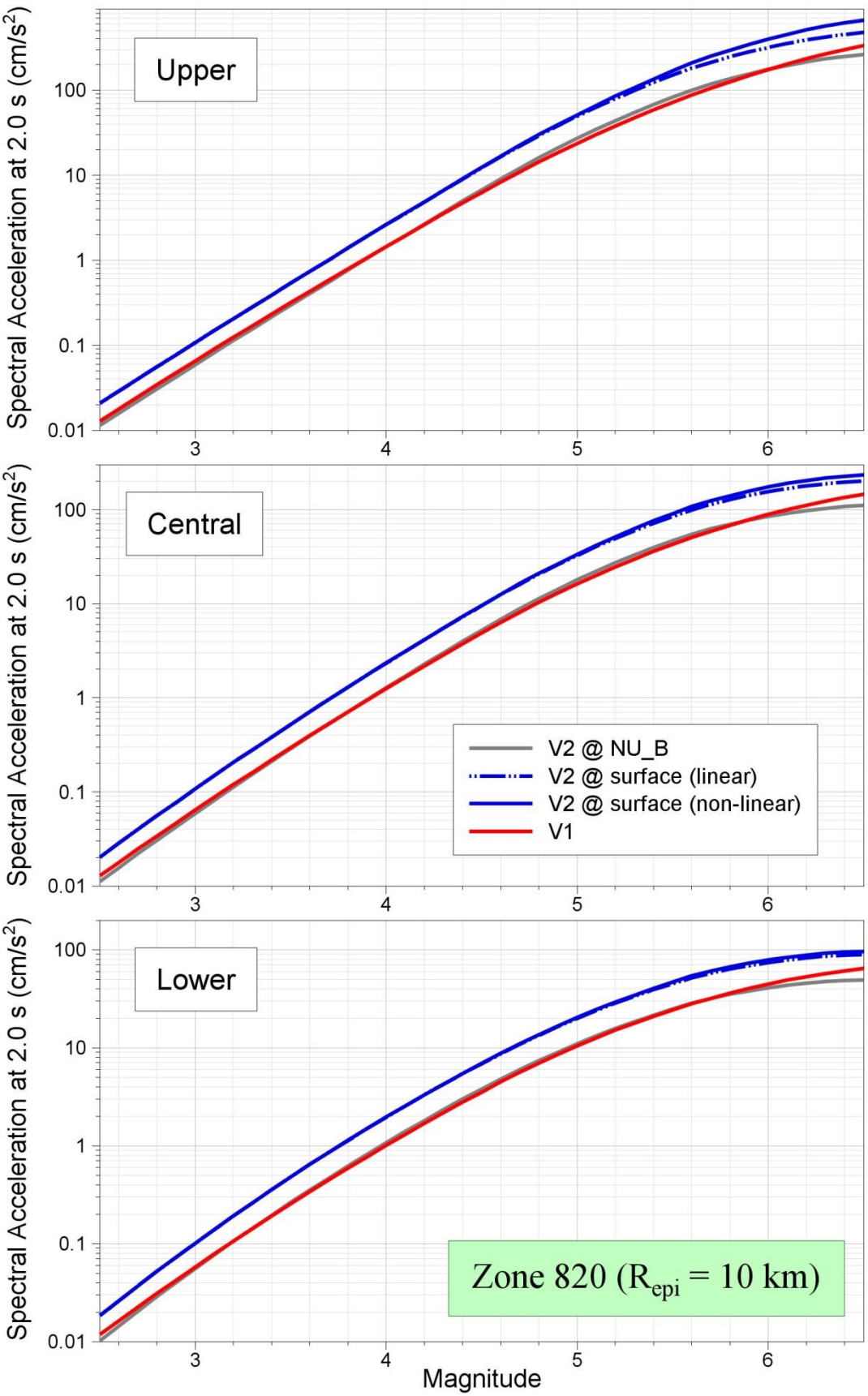

Figure 11.72. Comparison of median predictions of Sa(2.0) as a function of magnitude from the V1 and V2 models for Zone 820 and R_{epi} = 10 km

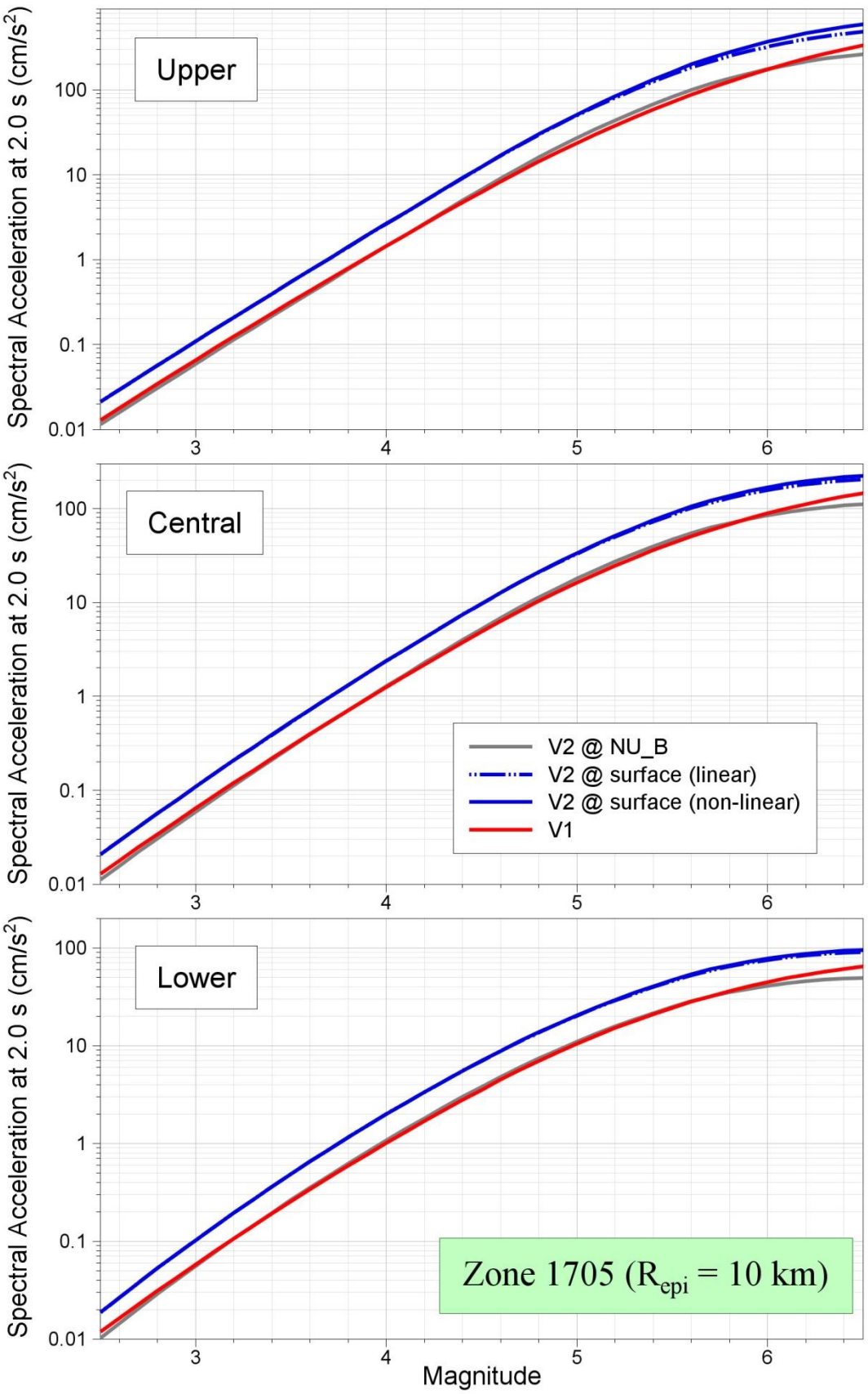

Figure 11.73. Comparison of median predictions of Sa(2.0) as a function of magnitude from the V1 and V2 models for Zone 1705 and R_{epi} = 10 km

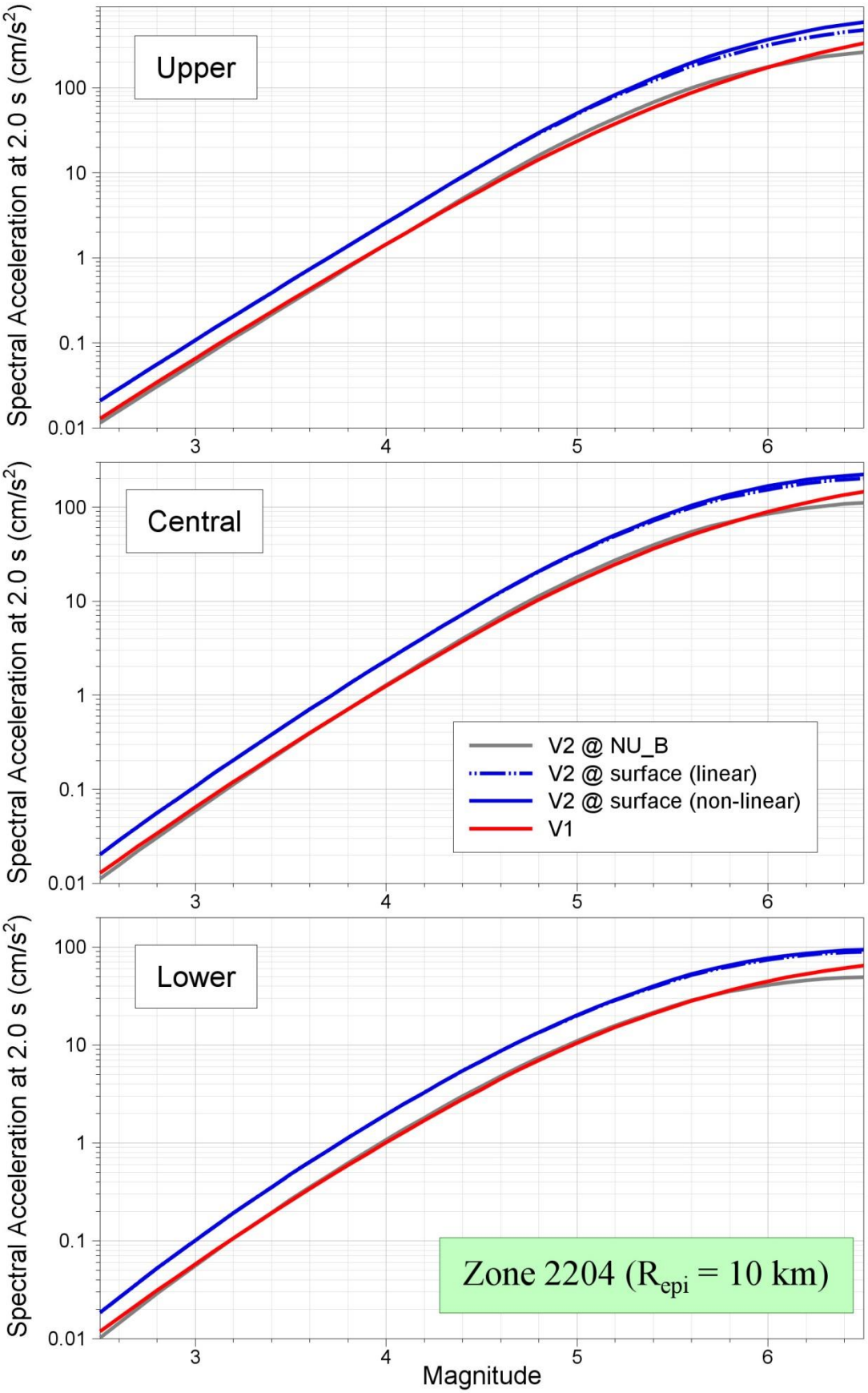

Figure 11.74. Comparison of median predictions of Sa(2.0) as a function of magnitude from the V1 and V2 models for Zone 2204 and R_{epi} = 10 km

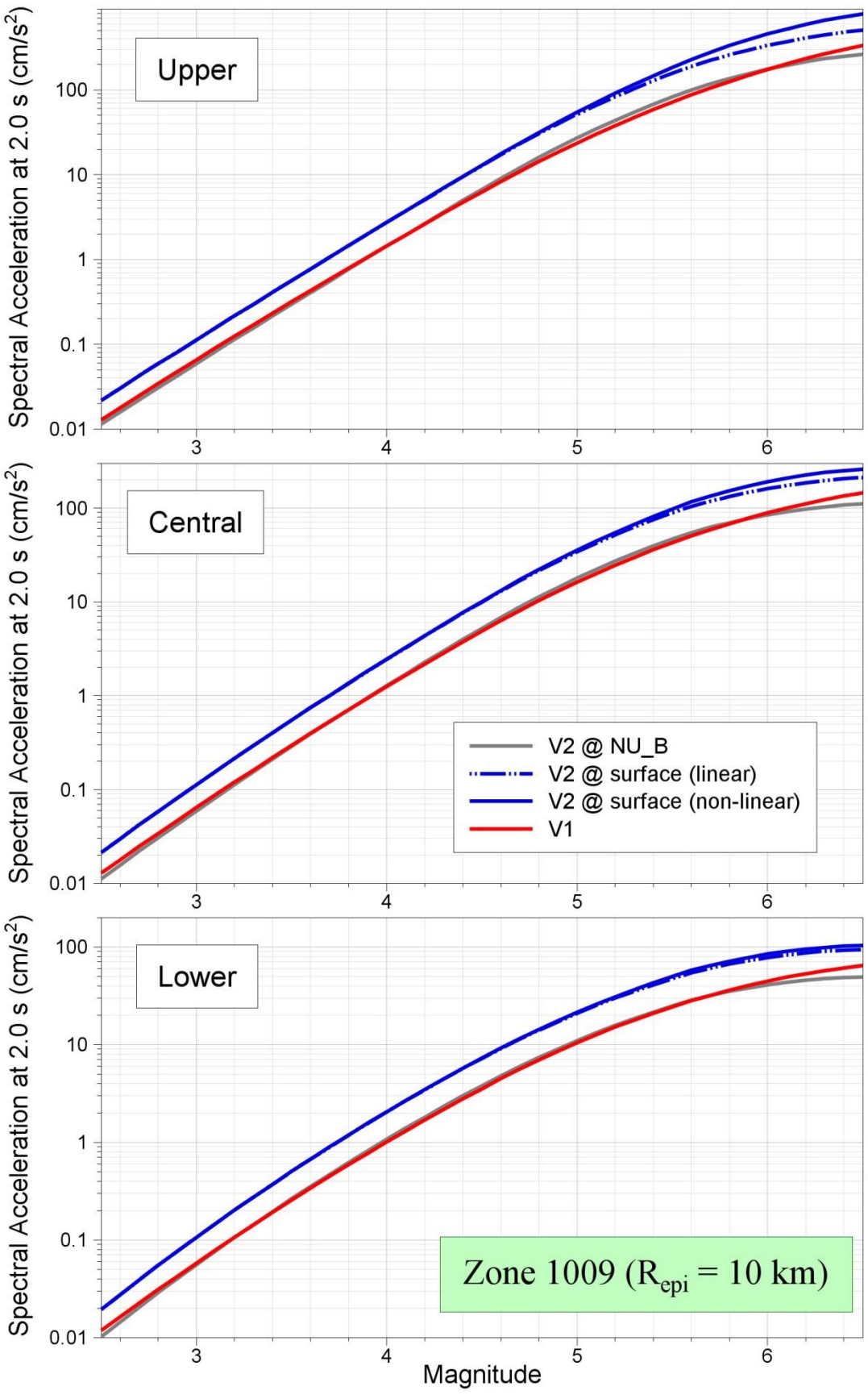

Figure 11.75. Comparison of median predictions of Sa(2.0) as a function of magnitude from the V1 and V2 models for Zone 1009 and R_{epi} = 10 km

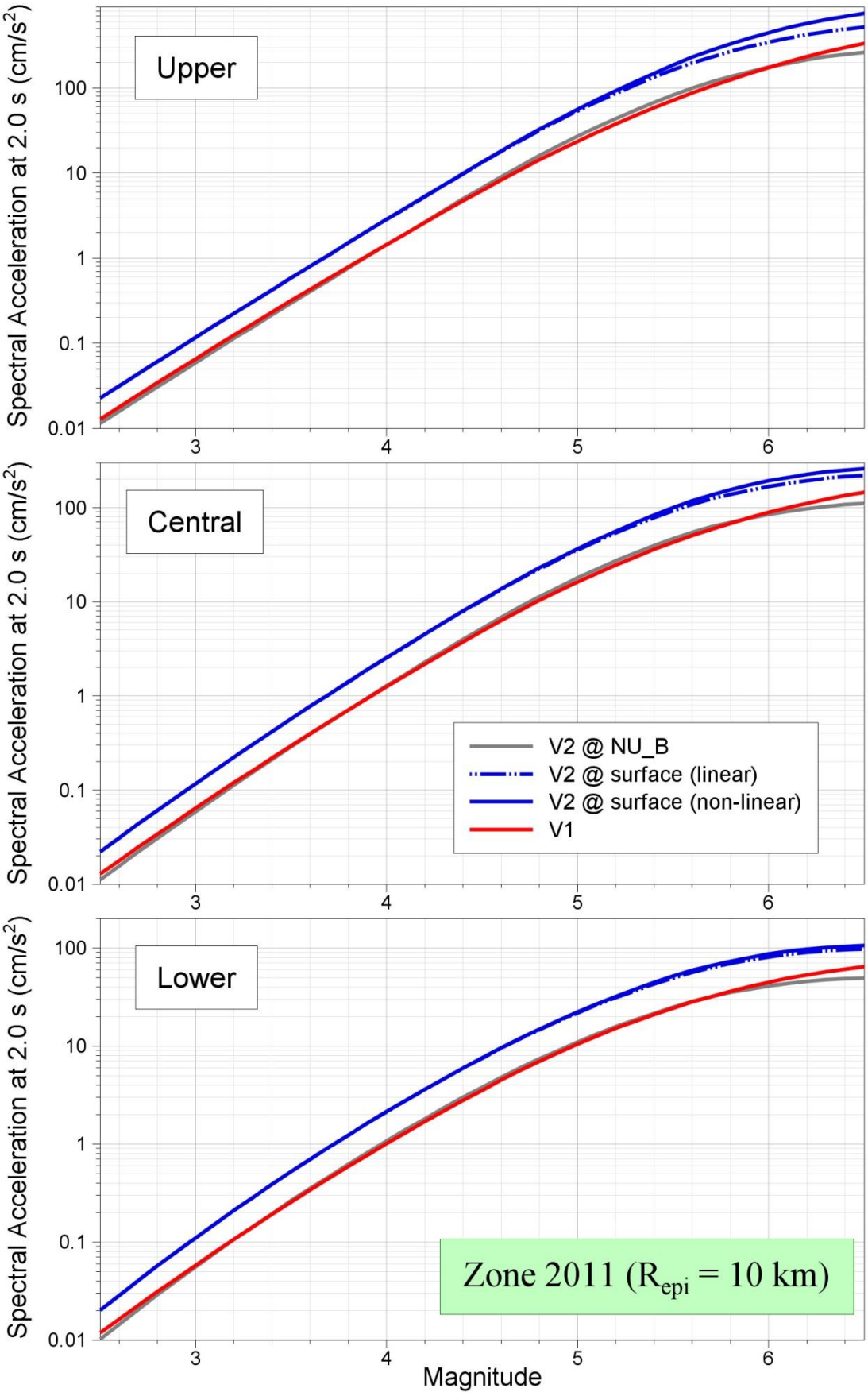

Figure 11.76. Comparison of median predictions of Sa(2.0) as a function of magnitude from the V1 and V2 models for Zone 2011 and R_{epi} = 10 km

A number of observations can be made from these comparative plots. The pattern for the shortest response period of 0.01 seconds is that the surface predictions from the V2 model are consistently lower than those obtained with the V1 model at short distances, except at the smallest magnitudes. At greater distance, the difference is smaller but at larger magnitudes the beneficial effect of the non-linear soil response is still to reduce the V2 predictions with respect to the former model. This is particularly pronounced, as would be expected, for the upper model that predicts the strongest accelerations at the reference rock level and therefore results in greater non-linearity in the overlying soil layers. A similar pattern is seen for spectral accelerations at 0.2 and 0.5 seconds for epicentral sites, but at 10 km from the source the V2 models predict higher motions than the V1 model for smaller magnitudes (M < ~4.5). For larger magnitudes, the influence of the non-linearity results in the predictions from the two models being similar or the V2 motions being slightly lower.

As the response period increases, the patterns change and the V2 model yields less favourable predictions than the V1 model. In the epicentral region this is true only for smaller magnitudes and for larger events the influence of the non-linear site response pushes the V2 predictions below those from the V1 models. At 10 km from the source, the rock motions become weaker meaning that the soil response becomes more linear and the V2 predictions are consistently greater than those from the V1 equations.

At an oscillator period of 2 seconds, the V2 predictions are always higher than those from the V1 model. This is partly to be expected since in most cases the non-linear site response functions at longer periods actually lead to amplification of the rock motions.

Another interesting observation that can be made is to look at any one set of plots for a given response period and epicentral distance, since in these cases both the V1 predictions and the V2 predictions at the NU_B horizon are constant across the sites. The variations in both the linear and non-linear surface predictions from the V2 models thus confirm how variable the site response characteristics are across the field. Such strong variations in site response characteristics were completely ignored in both the V0 and V1 models, and it is unlikely that they would be well captured using simple proxy parameters such as V_{S30}. We interpret this as vindication for the choice to develop a model that explicitly includes non-linear site amplification functions over the field calculated over the complete soil column.

The patterns discussed above are confirmed by the plots in Figures 11.77 to 11.139, which show predicted median response spectra in the same seven zones for nine combinations of magnitude (**M** 4, 5 and 6) and distance (R_{epi} 0, 5 and 15 km). As in the previous plots, the V2 predictions are plotted at the NU_B horizon and at the surface using both linear and non-linear site amplification factors. The predictions from the V1 model are again plotted for comparison. A notable features is how, in general, the spectral shape implied by the V1 predictions are similar to those from the V2 model with linear response. Another striking feature is how at shorter periods and particularly for the upper model, severe scenarios (large magnitude earthquakes at short distances) lead to surface motions considerably smaller than those at the NU_B horizon.

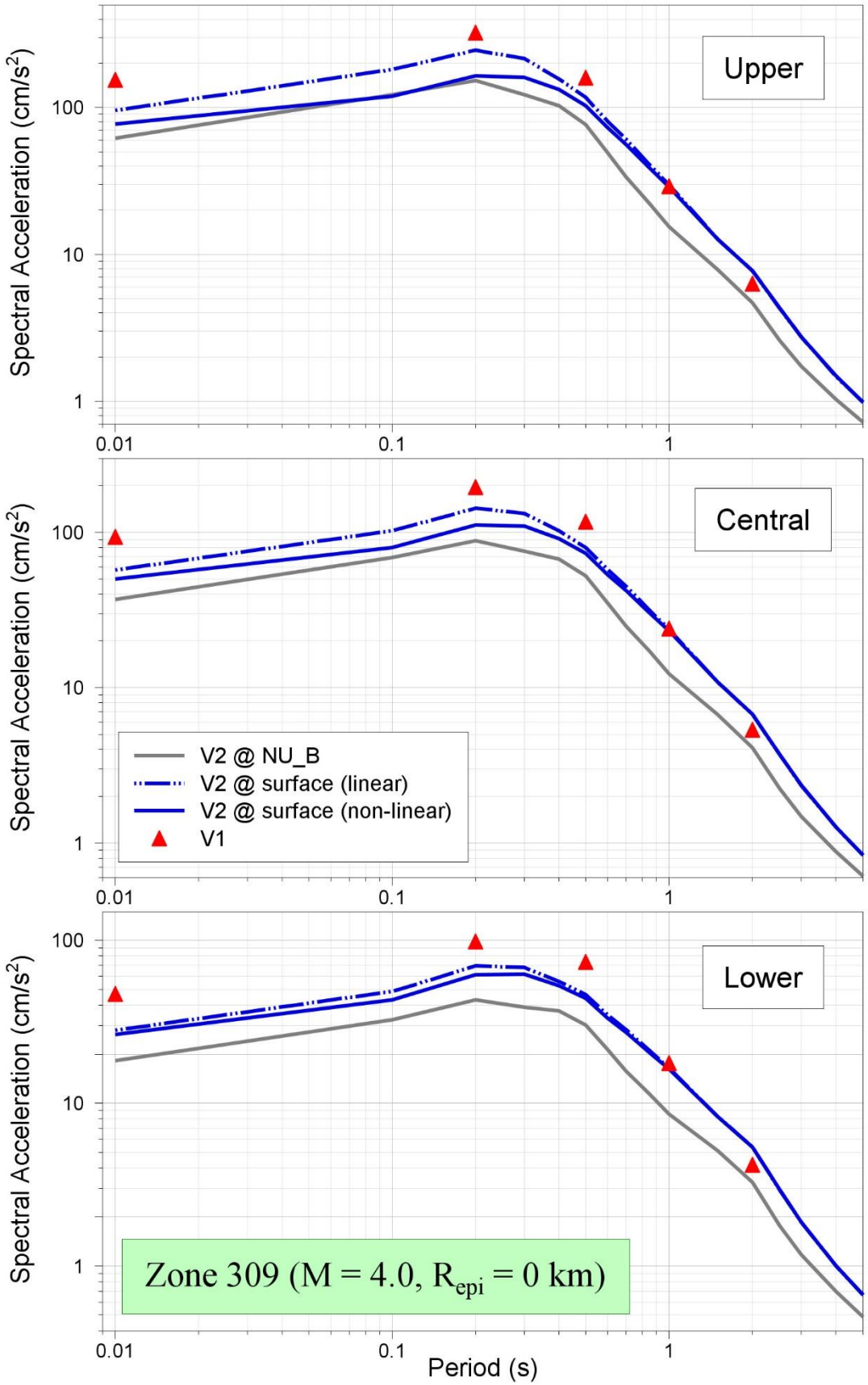

Figure 11.77. Comparison of median predicted response spectral accelerations from the V1 and V2 models for Zone 309 due to an earthquake of **M** 4 at R_{epi} = 0 km

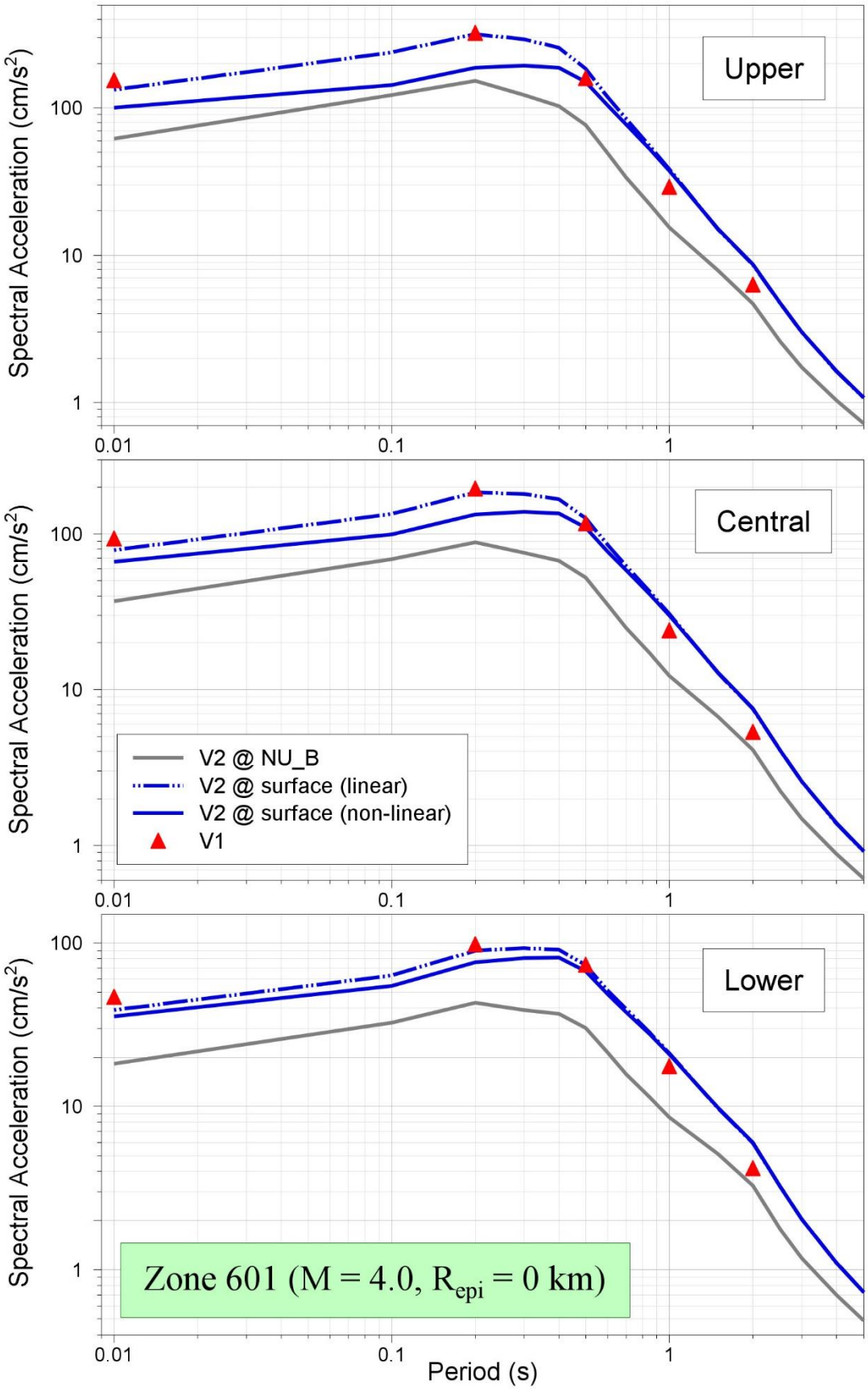

Figure 11.78. Comparison of median predicted response spectral accelerations from the V1 and V2 models for Zone 601 due to an earthquake of **M** 4 at R_{epi} = 0 km

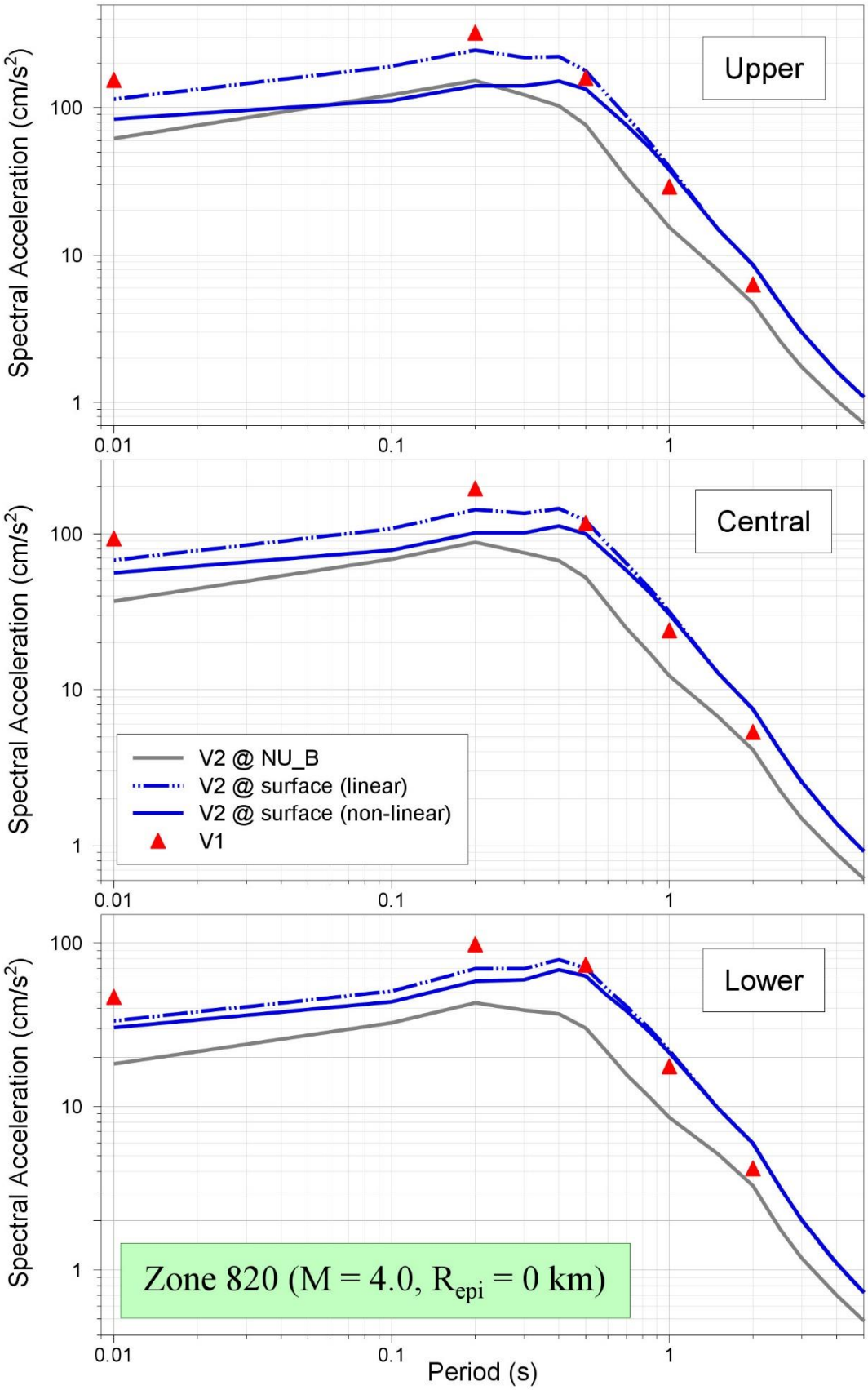

Figure 11.79. Comparison of median predicted response spectral accelerations from the V1 and V2 models for Zone 820 due to an earthquake of **M** 4 at R_{epi} = 0 km

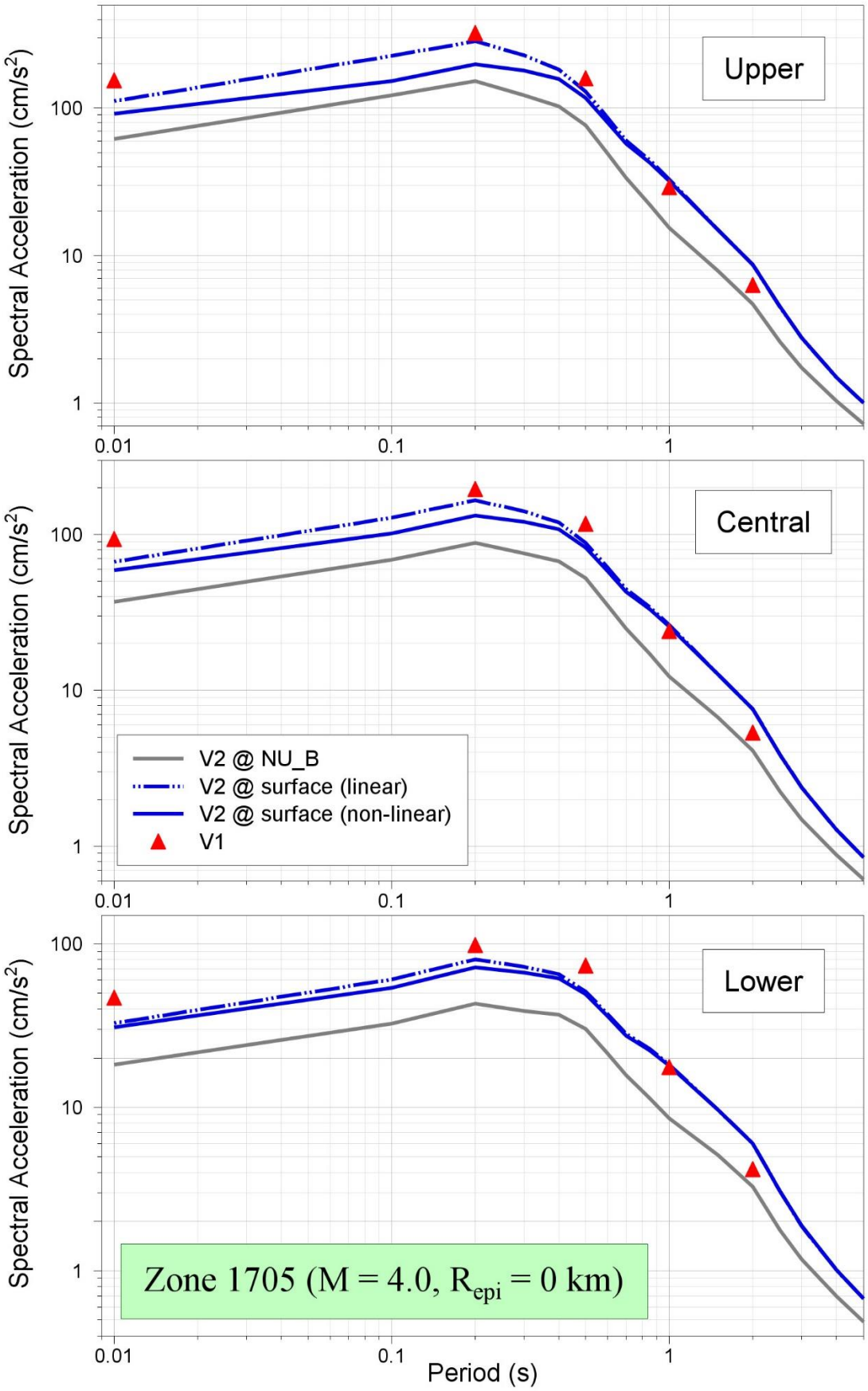

Figure 11.80. Comparison of median predicted response spectral accelerations from the V1 and V2 models for Zone 1705 due to an earthquake of **M** 4 at R_{epi} = 0 km

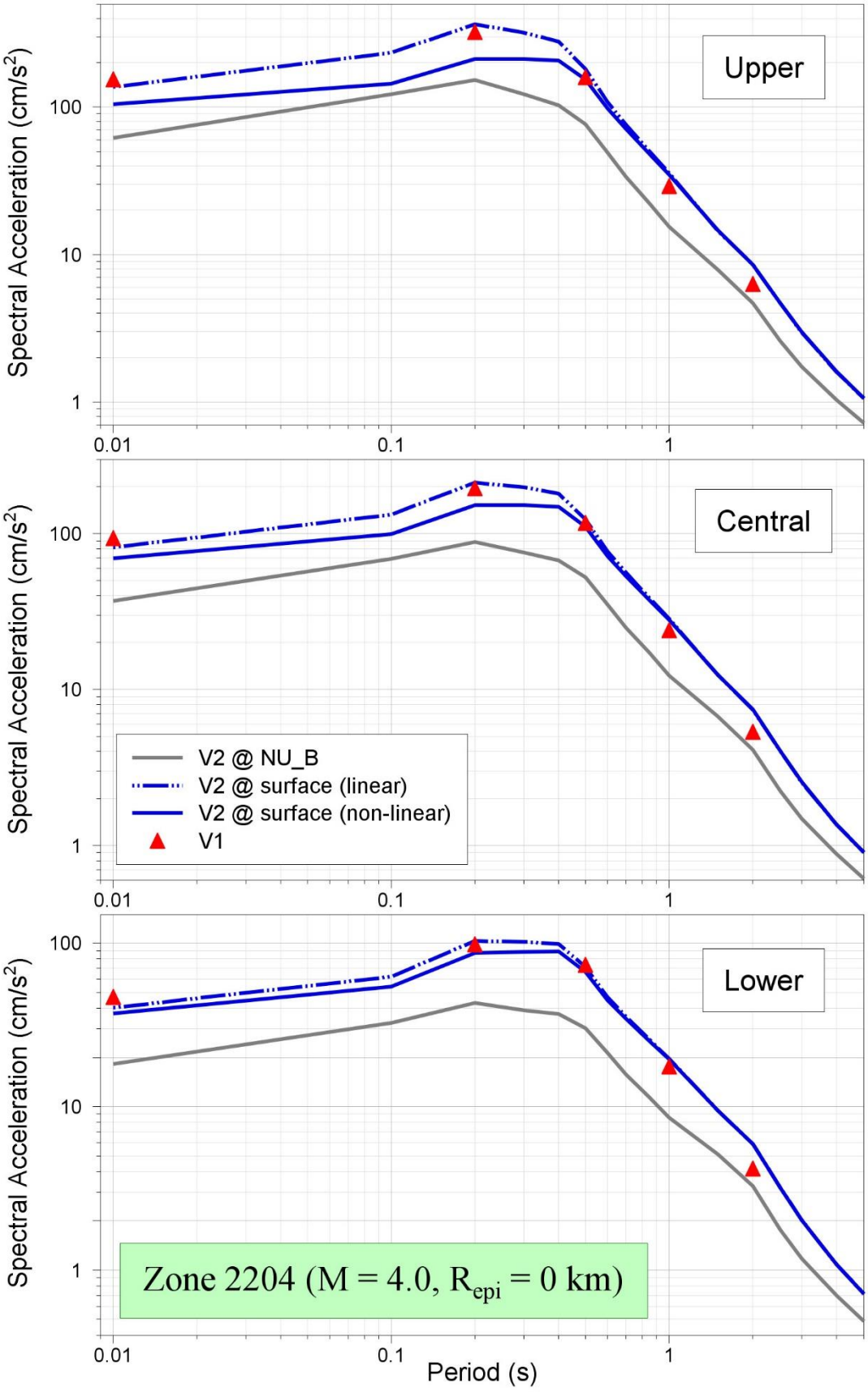

Figure 11.81. Comparison of median predicted response spectral accelerations from the V1 and V2 models for Zone 2204 due to an earthquake of **M** 4 at R_{epi} = 0 km

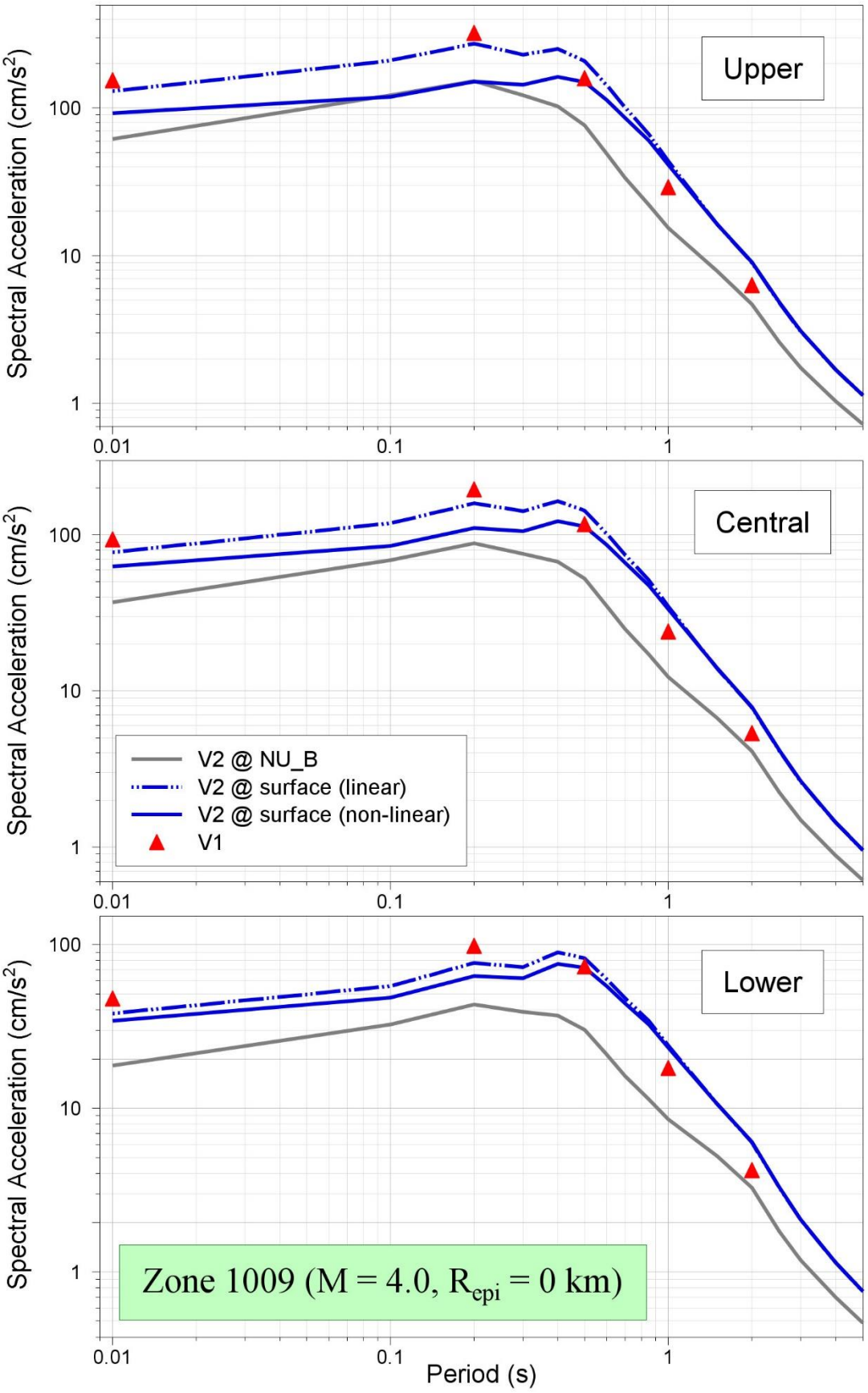

Figure 11.82. Comparison of median predicted response spectral accelerations from the V1 and V2 models for Zone 1009 due to an earthquake of **M** 4 at R_{epi} = 0 km

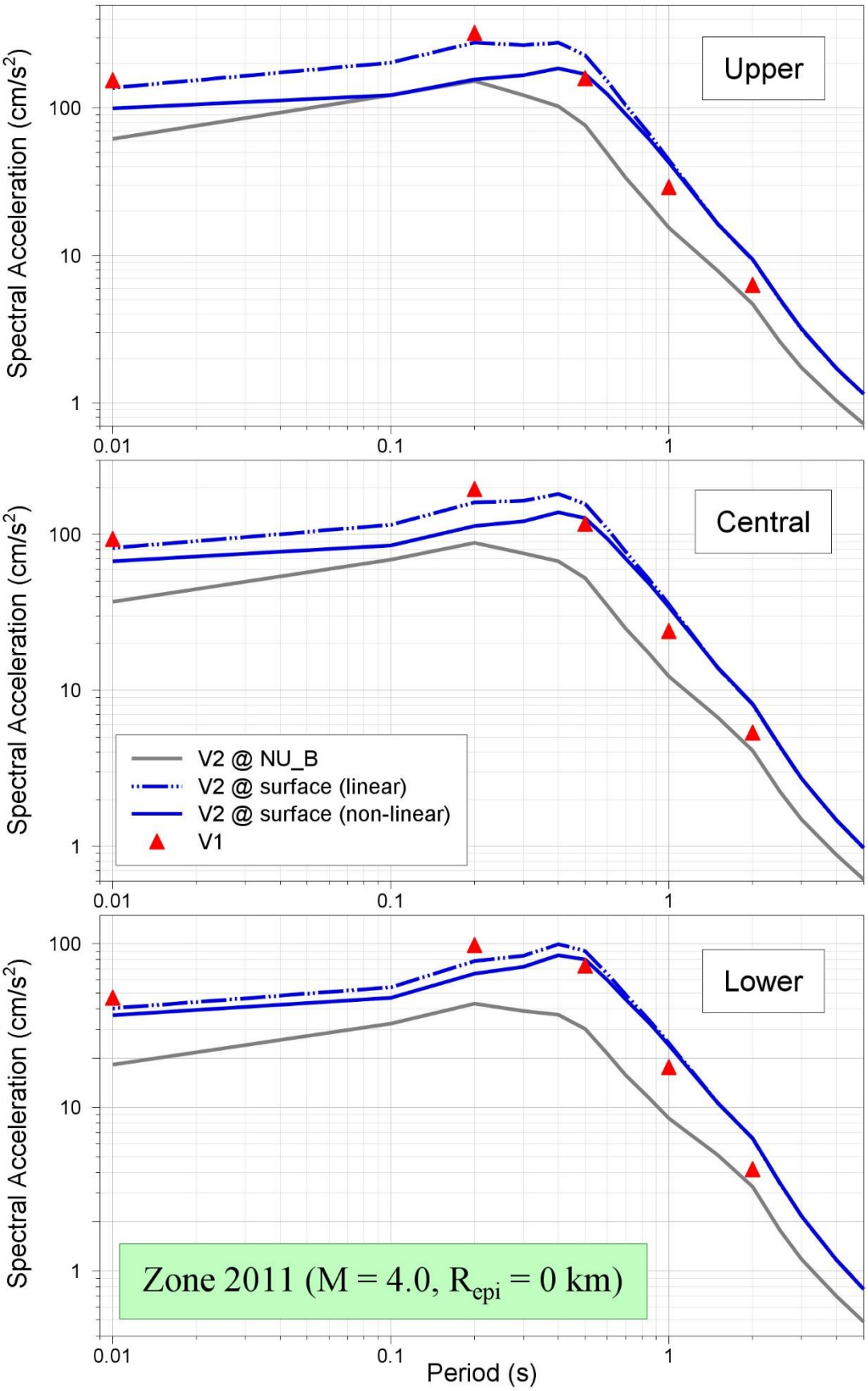

Figure 11.83. Comparison of median predicted response spectral accelerations from the V1 and V2 models for Zone 2011 due to an earthquake of **M** 4 at R_{epi} = 0 km

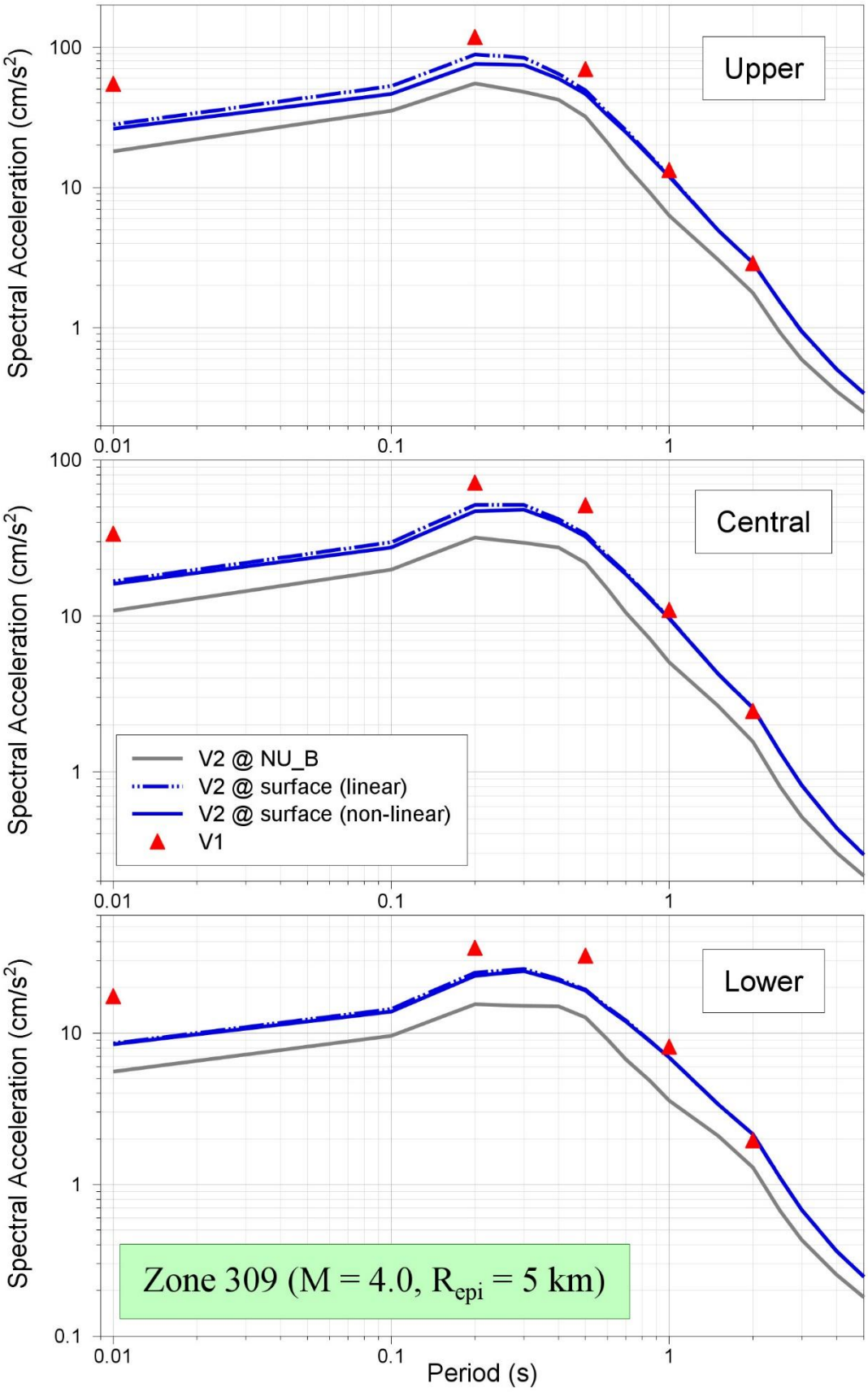

Figure 11.84. Comparison of median predicted response spectral accelerations from the V1 and V2 models for Zone 309 due to an earthquake of **M** 4 at R_{epi} = 5 km

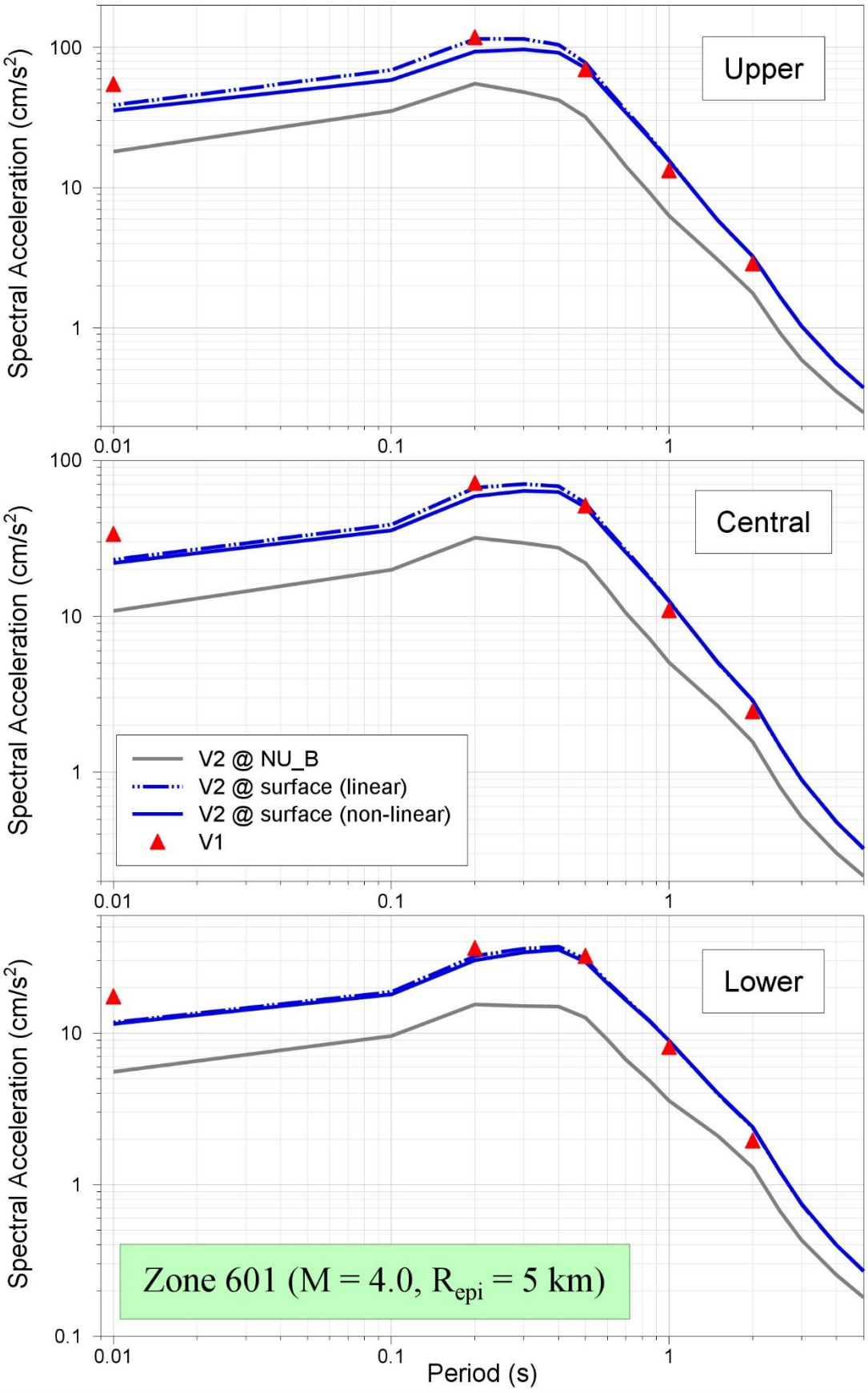

Figure 11.85. Comparison of median predicted response spectral accelerations from the V1 and V2 models for Zone 601 due to an earthquake of **M** 4 at R_{epi} = 5 km

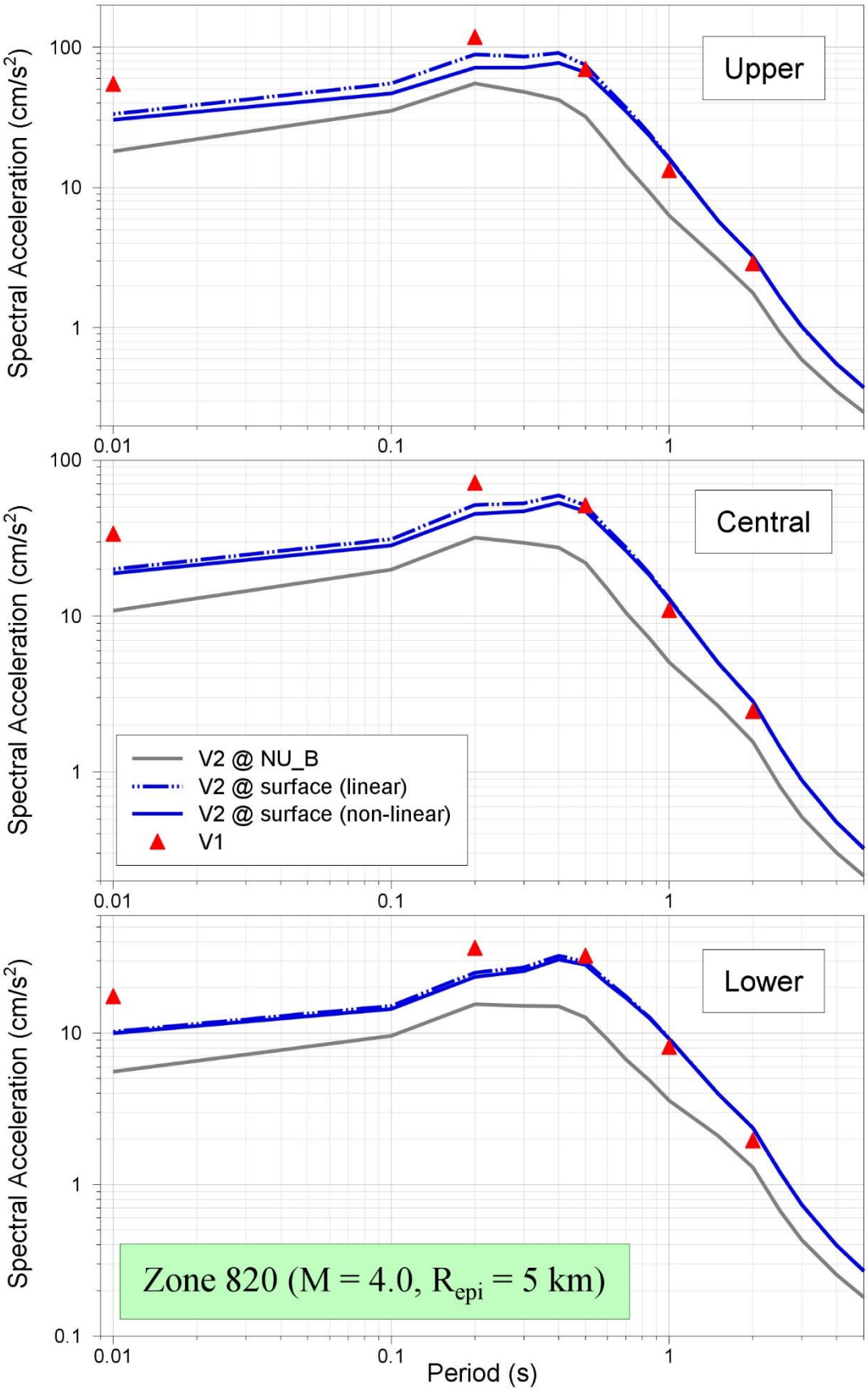

Figure 11.86. Comparison of median predicted response spectral accelerations from the V1 and V2 models for Zone 820 due to an earthquake of **M** 4 at R_{epi} = 5 km

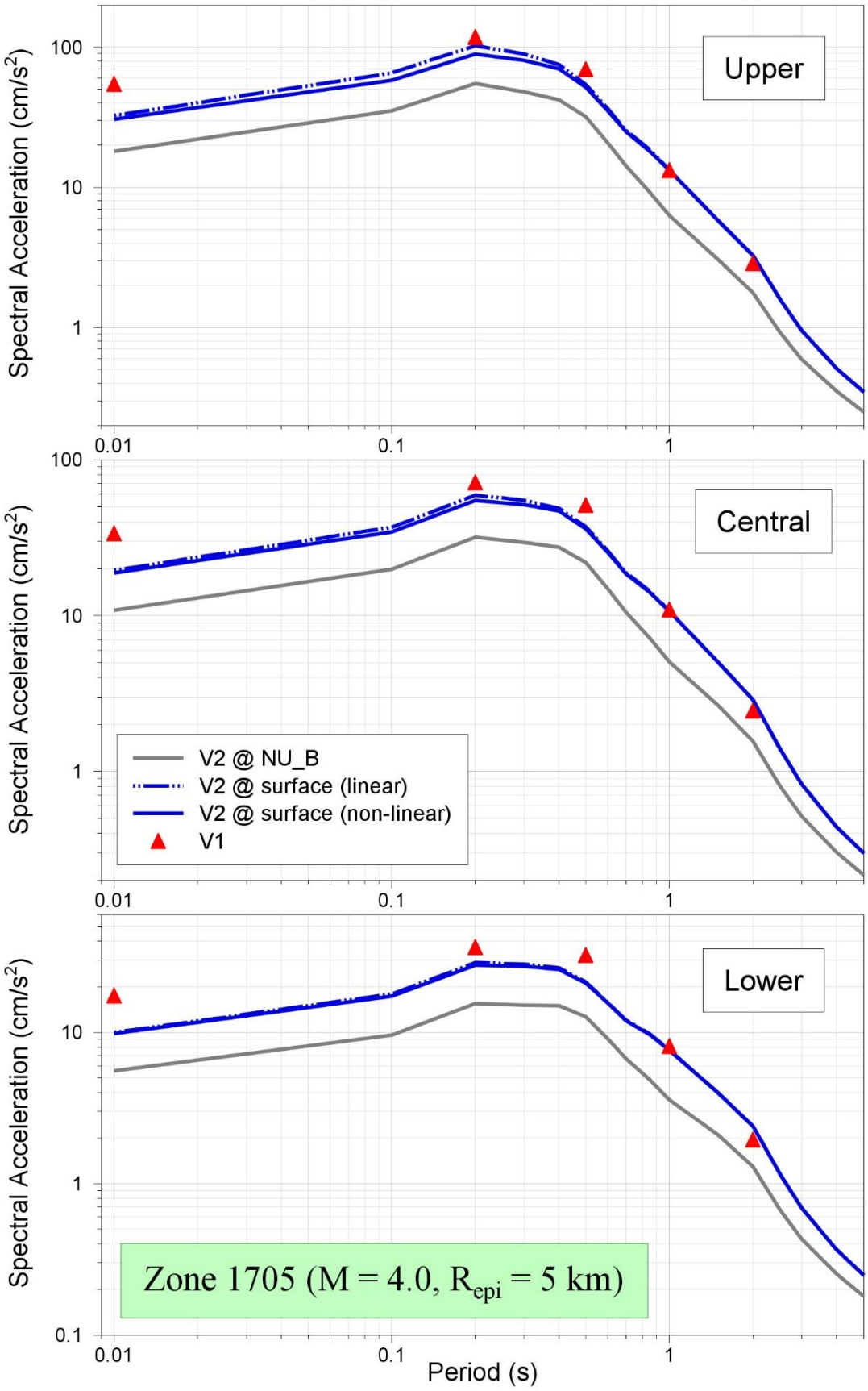

Figure 11.87. Comparison of median predicted response spectral accelerations from the V1 and V2 models for Zone 1705 due to an earthquake of **M** 4 at R_{epi} = 5 km

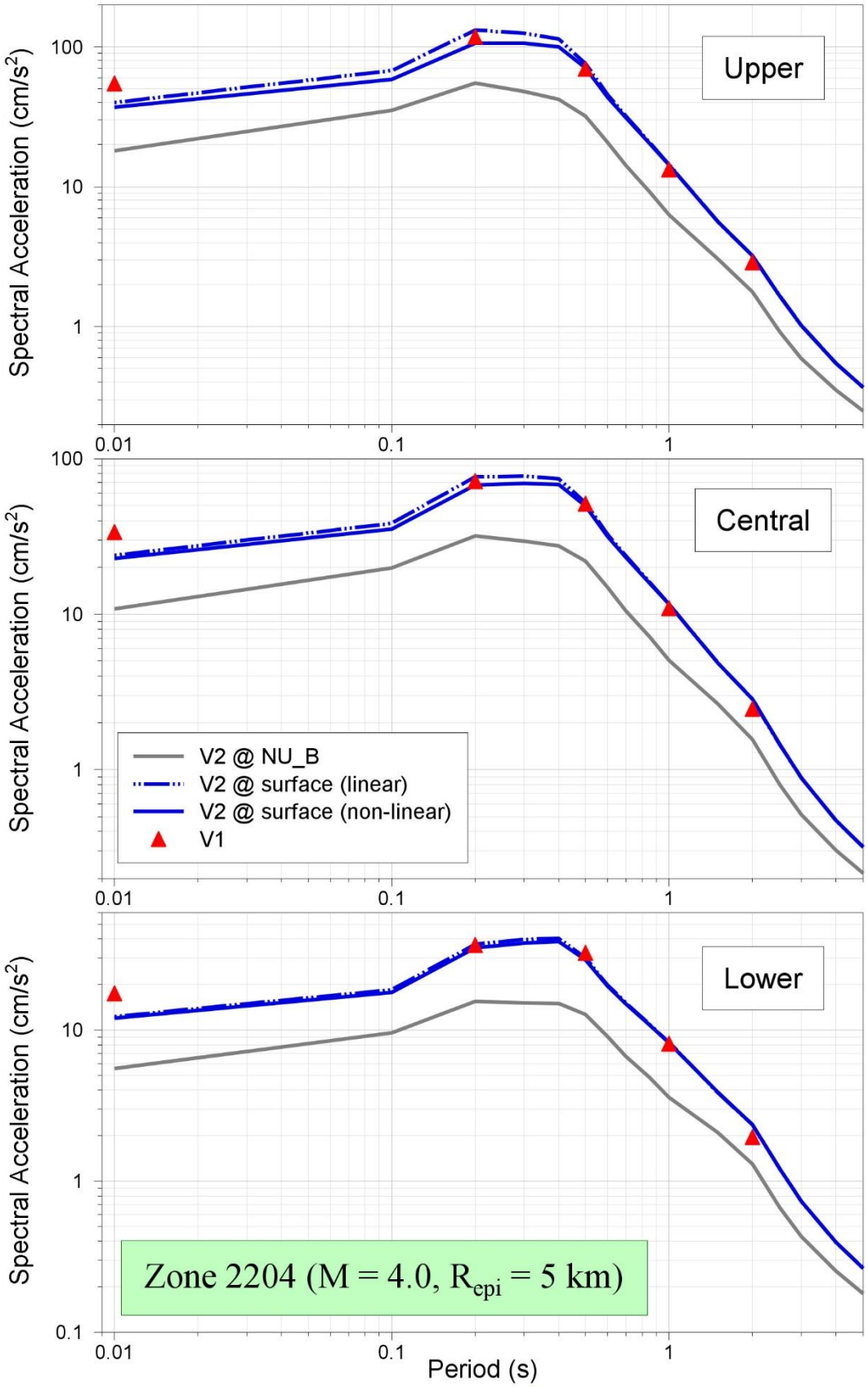

Figure 11.88. Comparison of median predicted response spectral accelerations from the V1 and V2 models for Zone 2204 due to an earthquake of **M** 4 at R_{epi} = 5 km

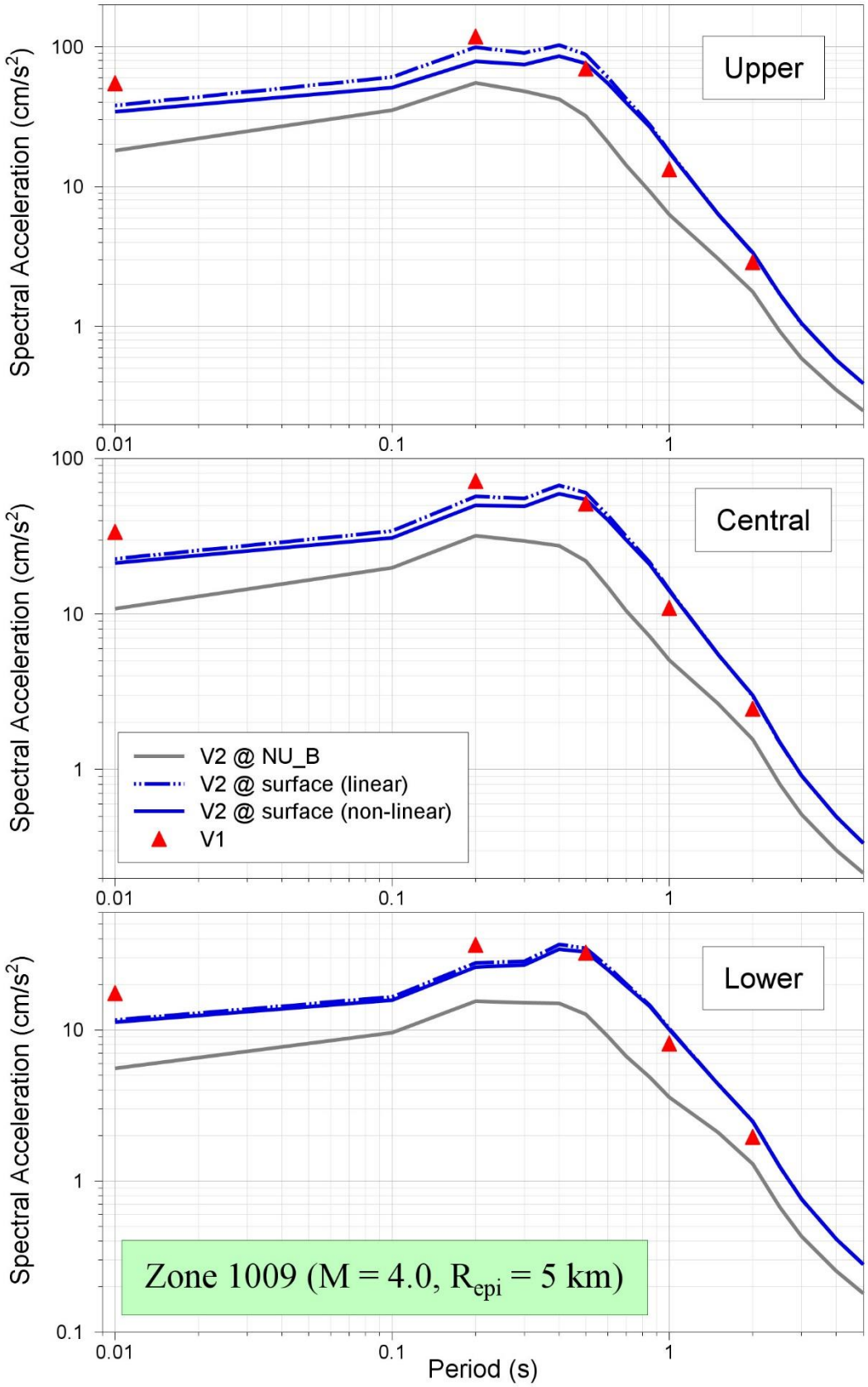

Figure 11.89. Comparison of median predicted response spectral accelerations from the V1 and V2 models for Zone 1009 due to an earthquake of **M** 4 at R_{epi} = 5 km

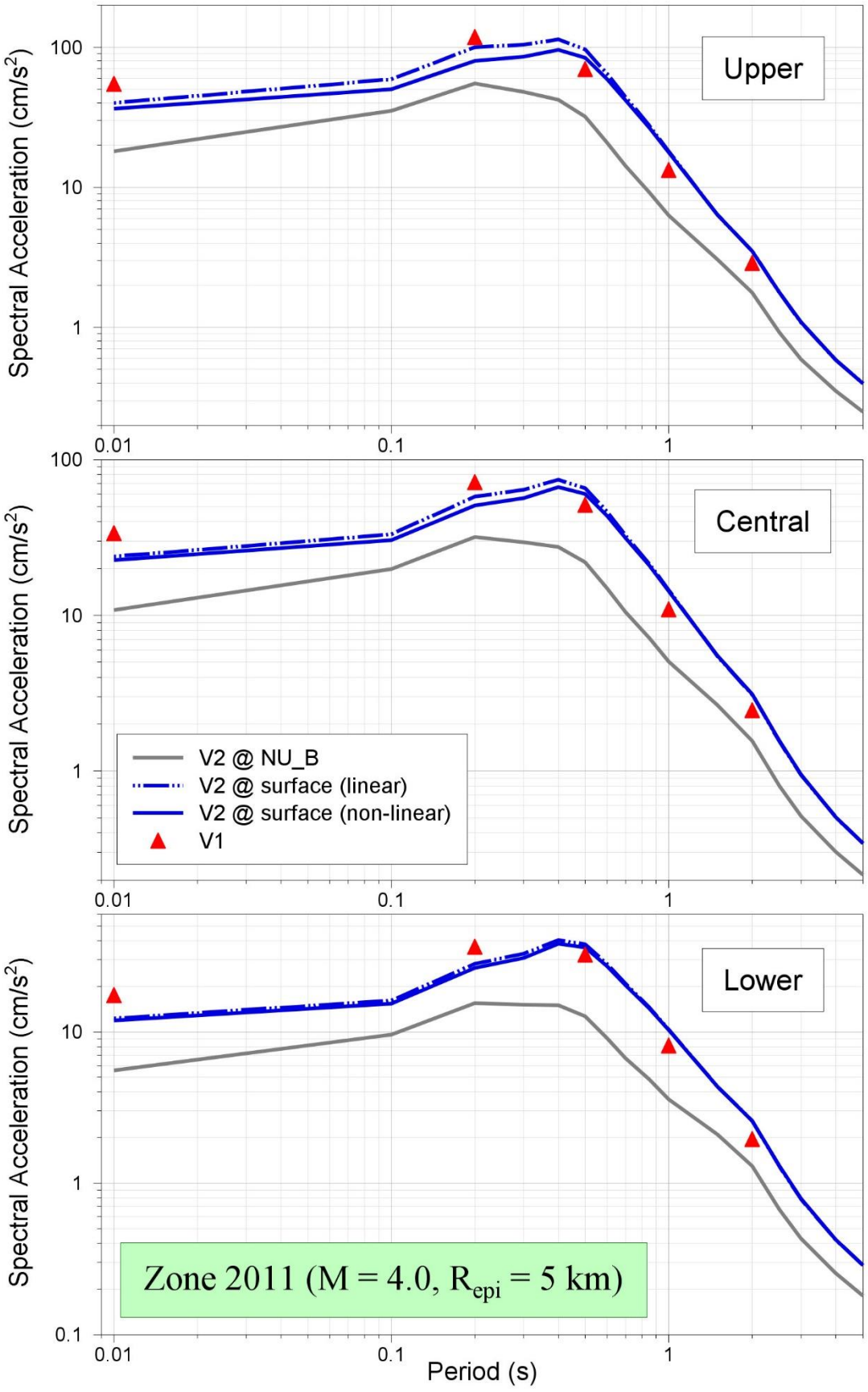

Figure 11.90. Comparison of median predicted response spectral accelerations from the V1 and V2 models for Zone 2011 due to an earthquake of **M** 4 at R_{epi} = 5 km

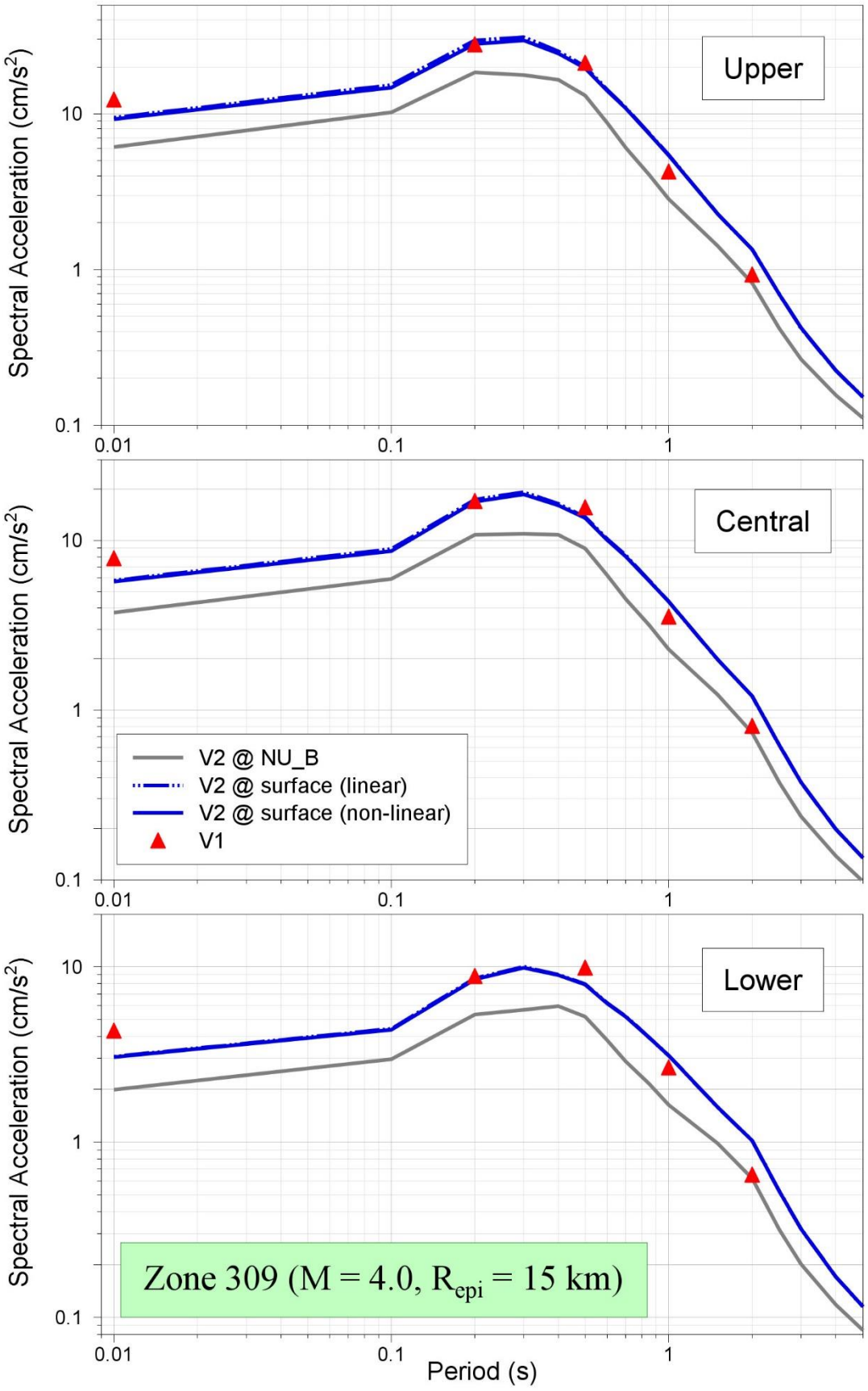

Figure 11.91. Comparison of median predicted response spectral accelerations from the V1 and V2 models for Zone 309 due to an earthquake of **M** 4 at R_{epi} = 15 km

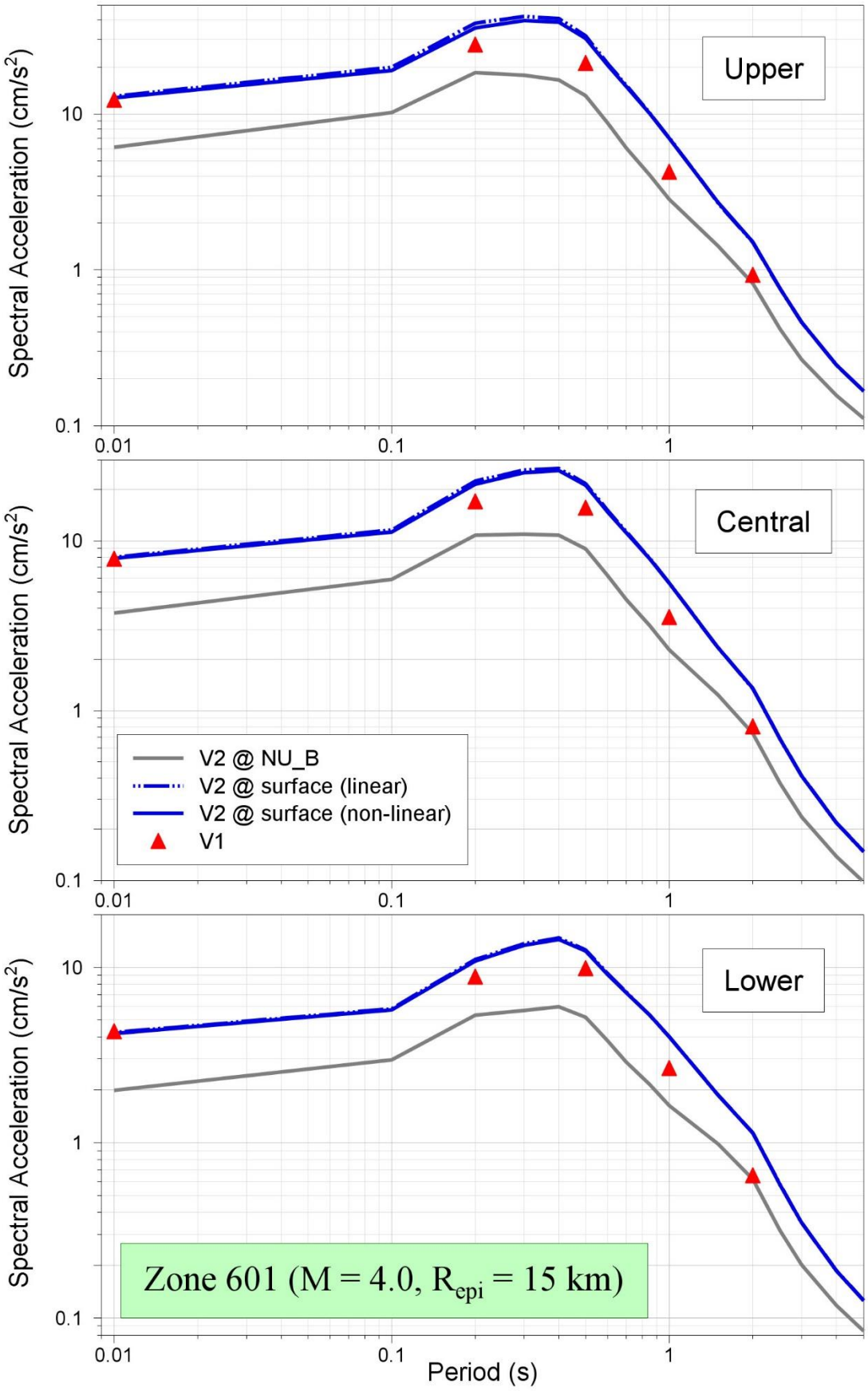

Figure 11.92. Comparison of median predicted response spectral accelerations from the V1 and V2 models for Zone 601 due to an earthquake of **M** 4 at R_{epi} = 15 km

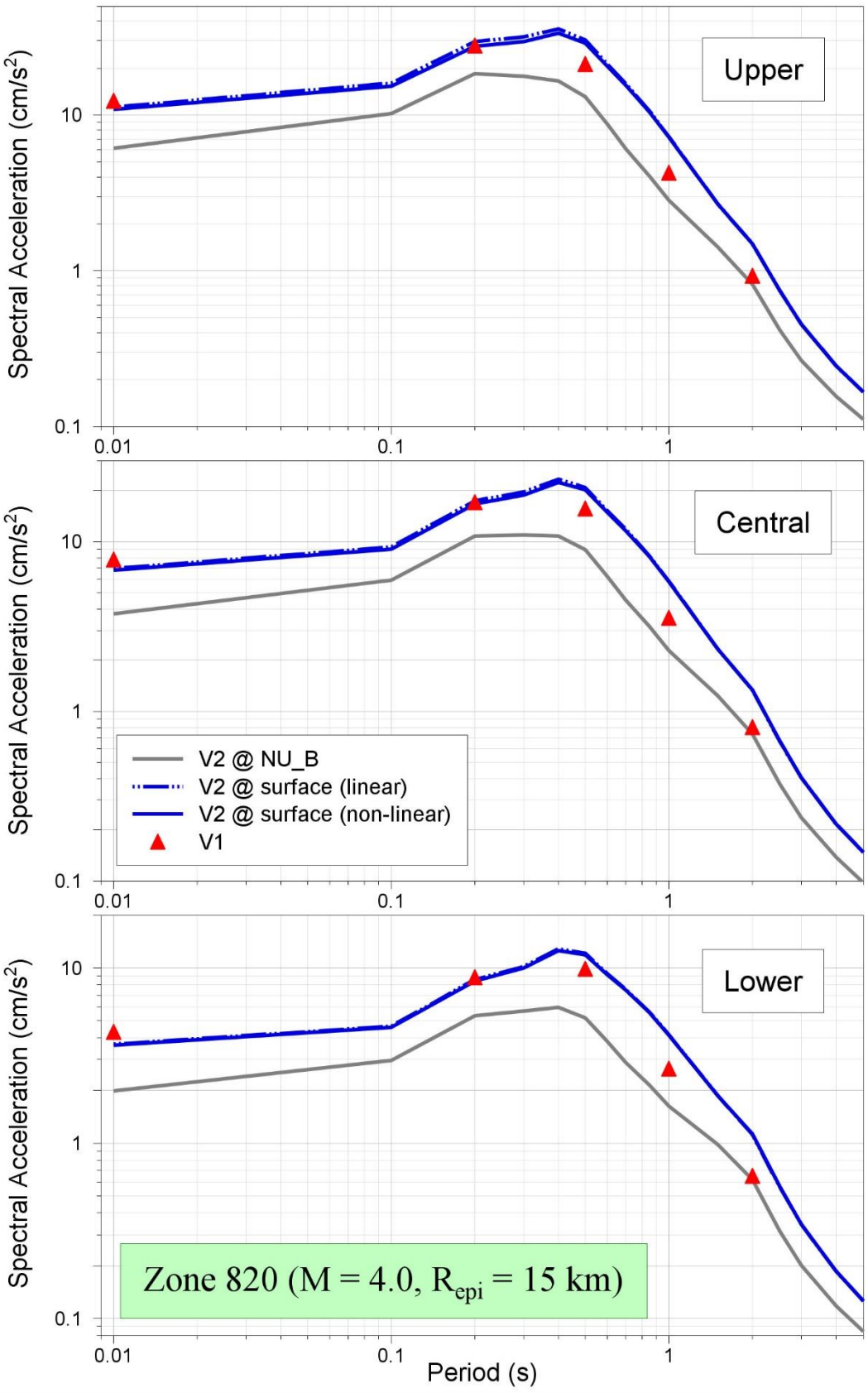

Figure 11.93. Comparison of median predicted response spectral accelerations from the V1 and V2 models for Zone 820 due to an earthquake of **M** 4 at R_{epi} = 15 km

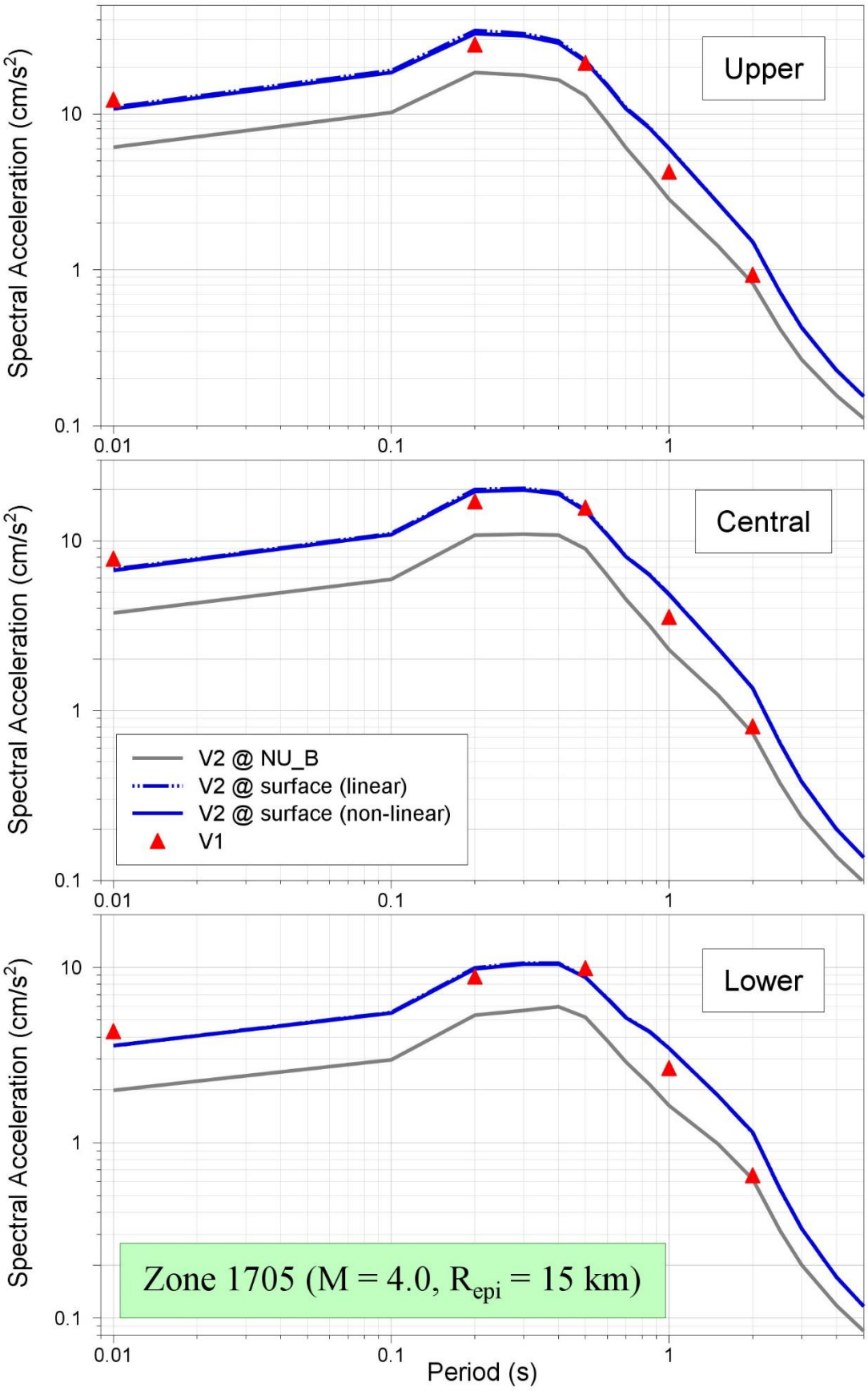

Figure 11.94. Comparison of median predicted response spectral accelerations from the V1 and V2 models for Zone 1705 due to an earthquake of **M** 4 at R_{epi} = 15 km

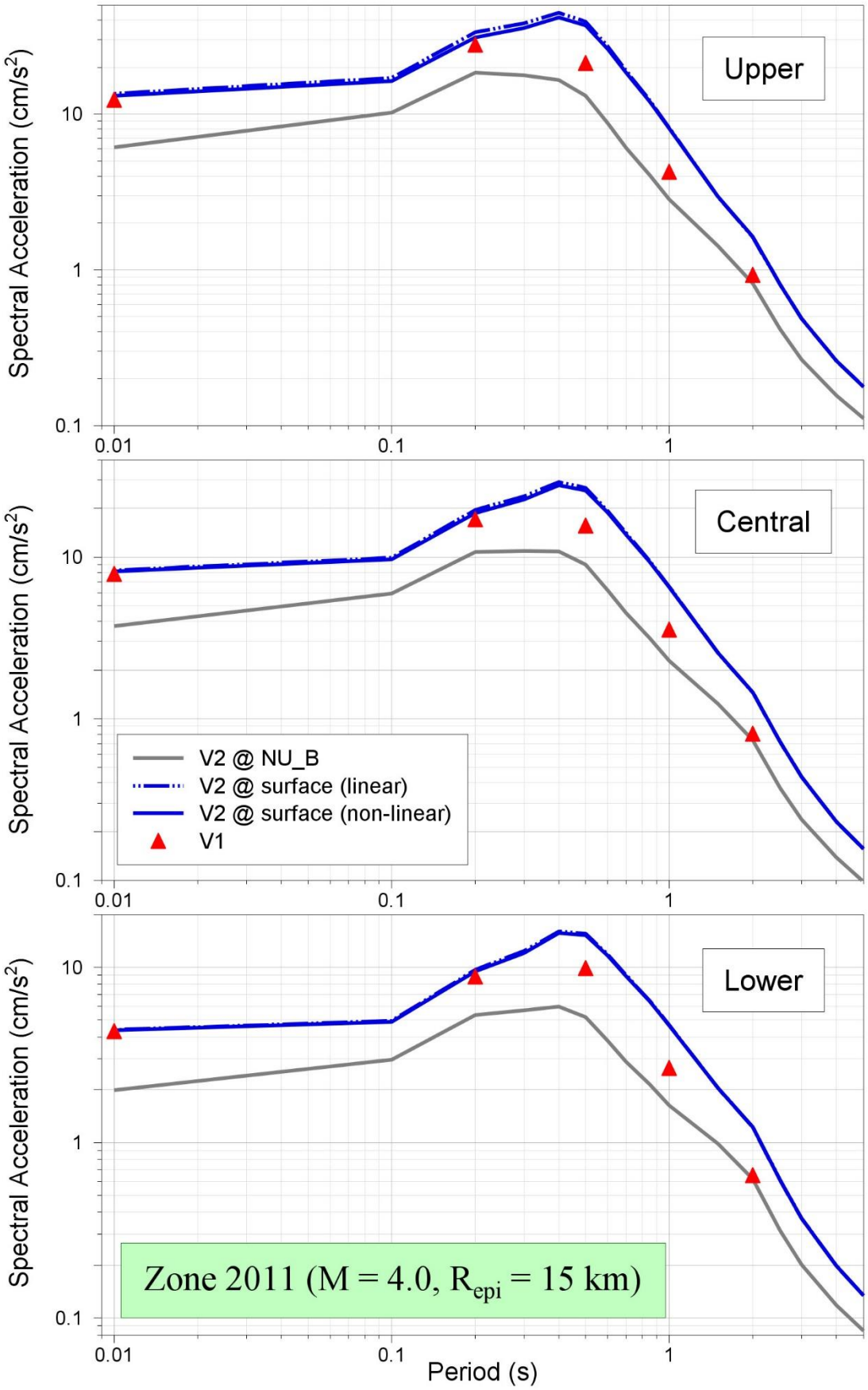

Figure 11.95. Comparison of median predicted response spectral accelerations from the V1 and V2 models for Zone 2204 due to an earthquake of **M** 4 at R_{epi} = 15 km

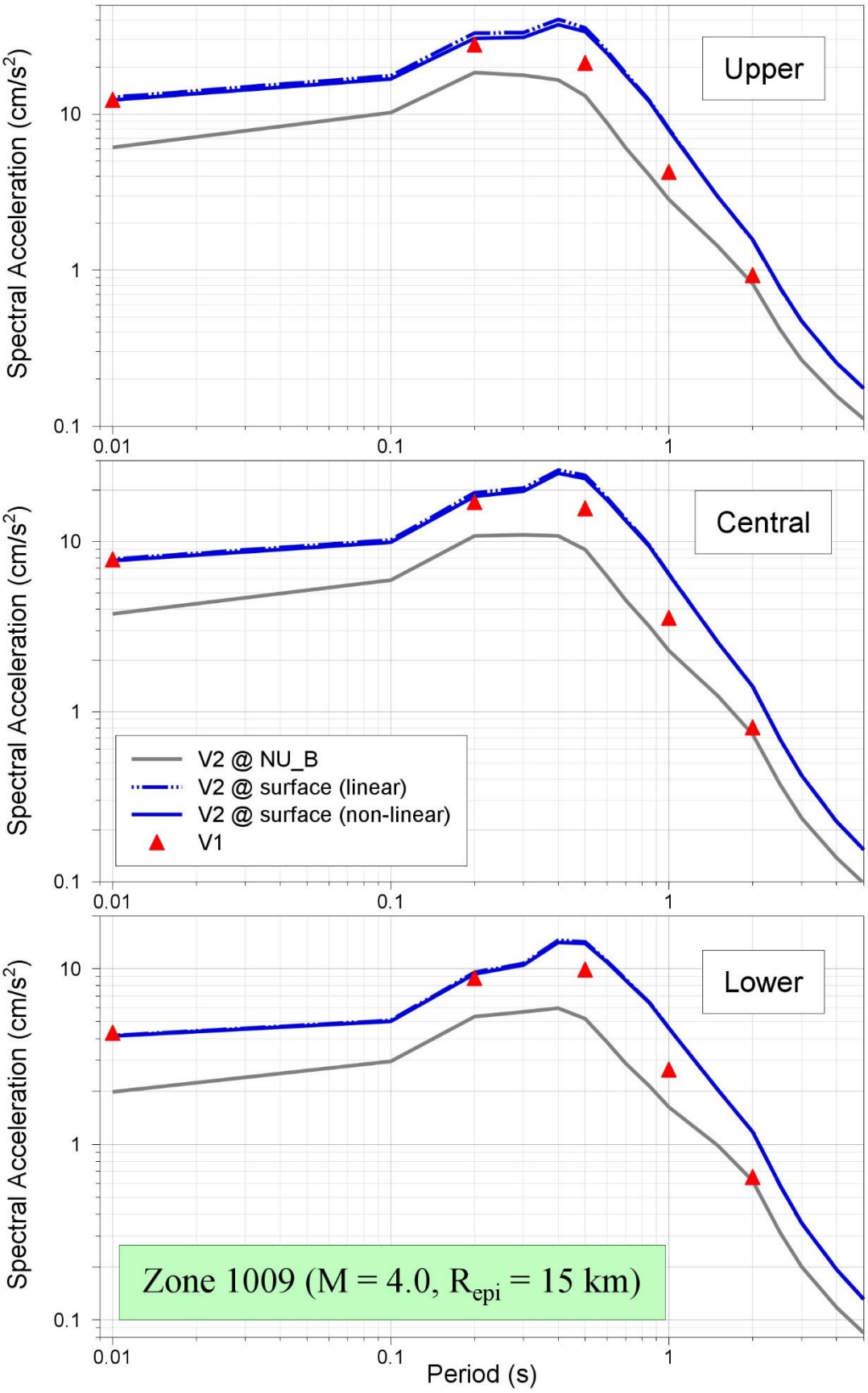

Figure 11.96. Comparison of median predicted response spectral accelerations from the V1 and V2 models for Zone 1009 due to an earthquake of **M** 4 at R_{epi} = 15 km

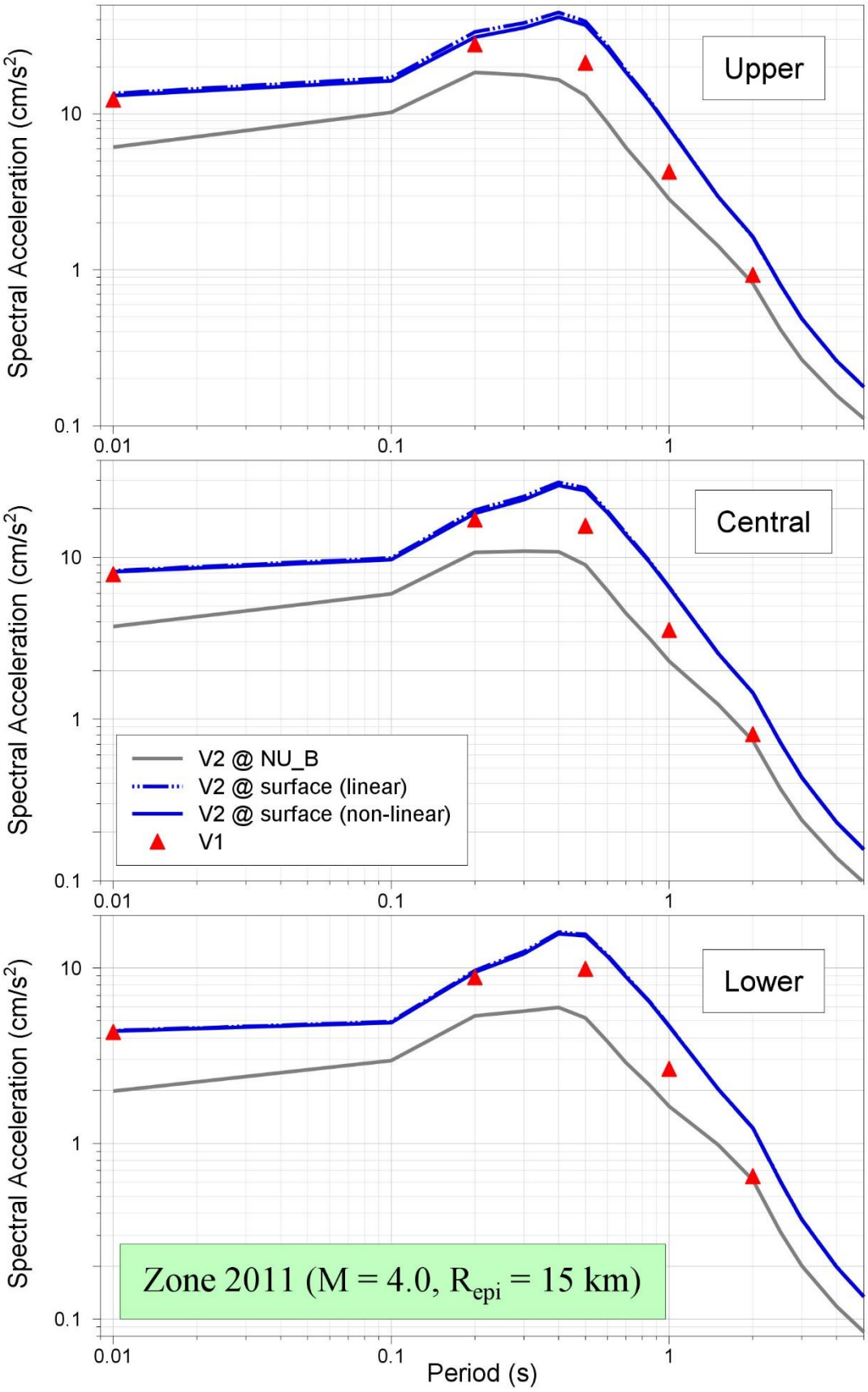

Figure 11.97. Comparison of median predicted response spectral accelerations from the V1 and V2 models for Zone 2011 due to an earthquake of **M** 4 at R_{epi} = 15 km

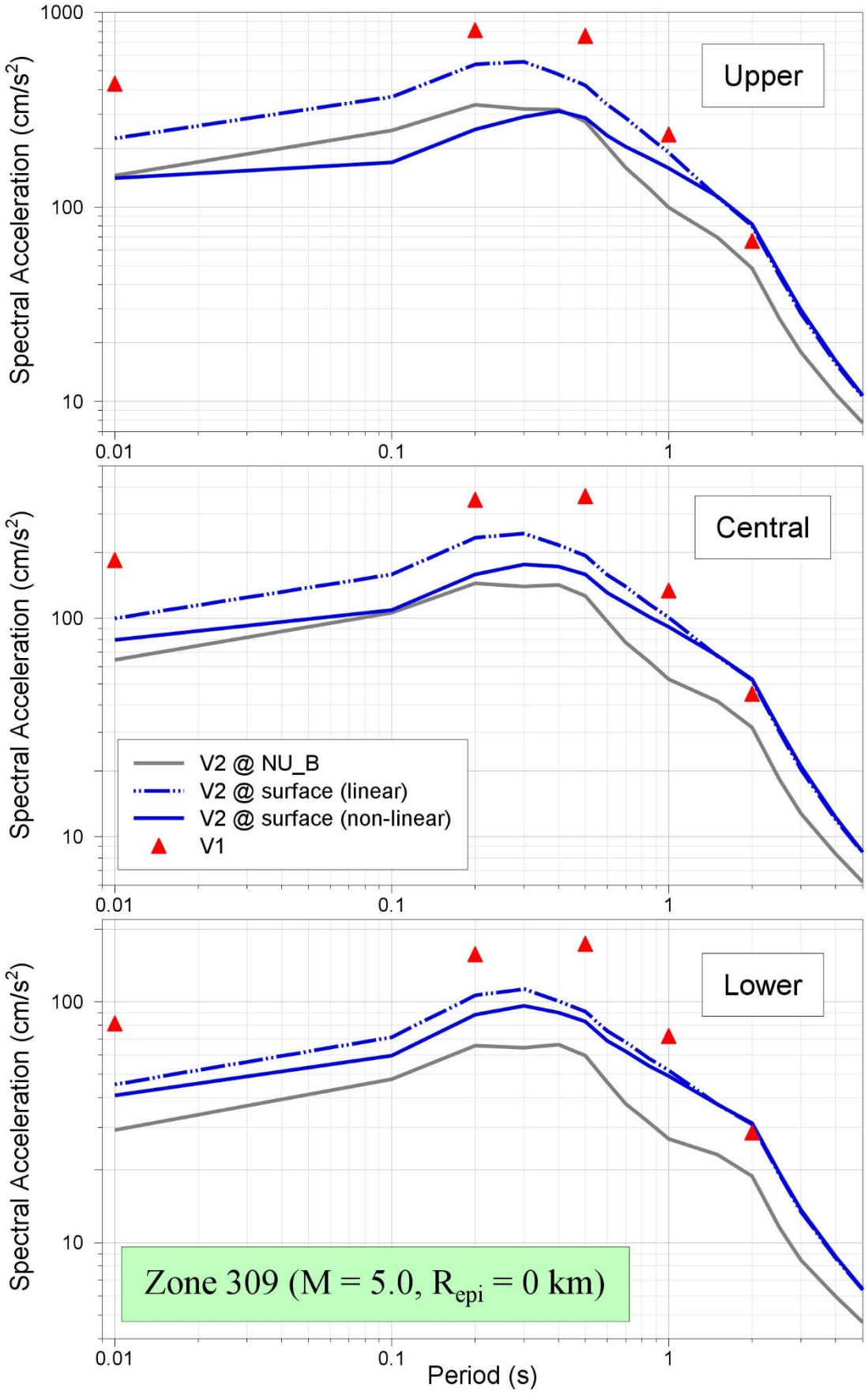

Figure 11.98. Comparison of median predicted response spectral accelerations from the V1 and V2 models for Zone 309 due to an earthquake of **M** 5 at R_{epi} = 0 km

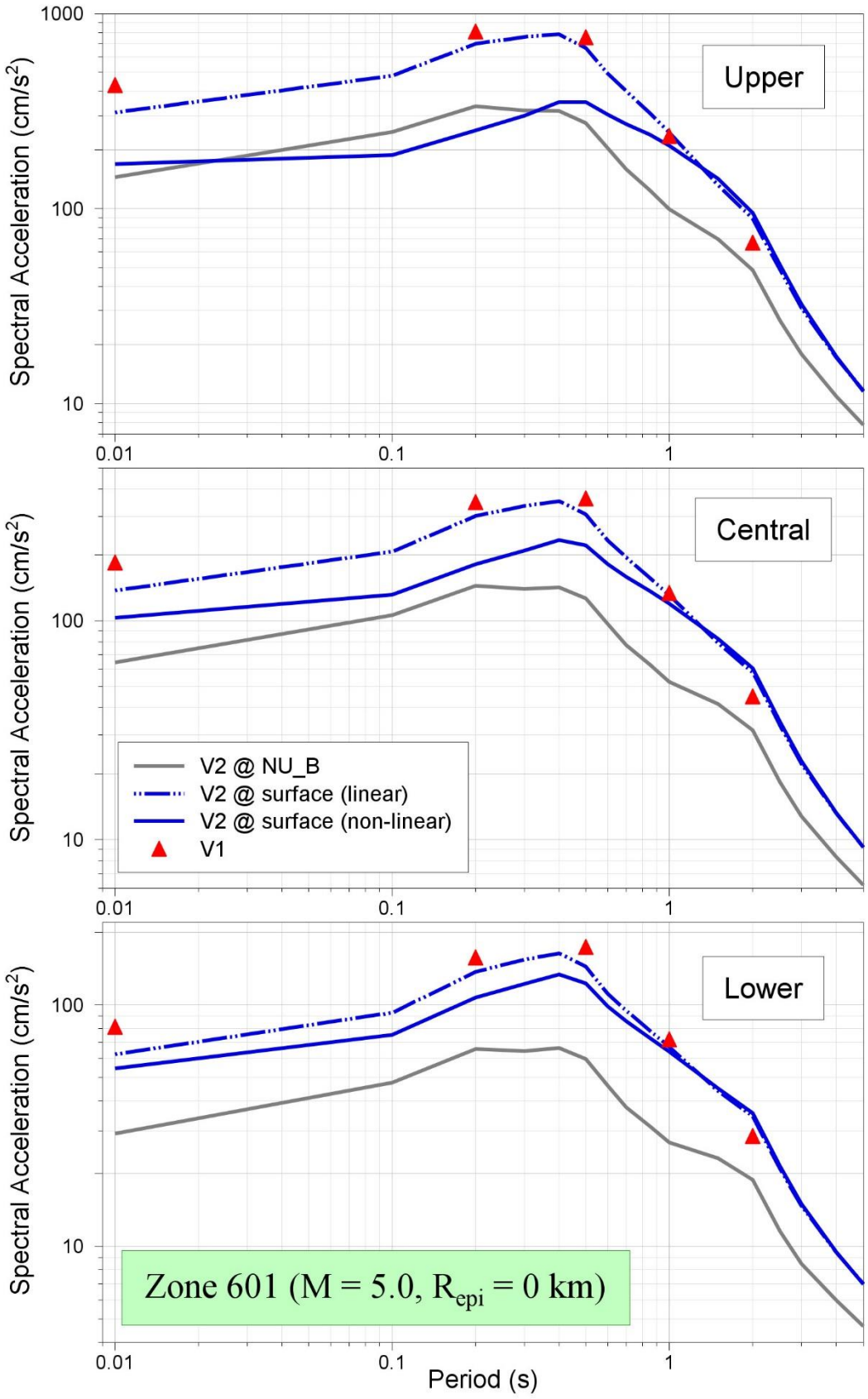

Figure 11.99. Comparison of median predicted response spectral accelerations from the V1 and V2 models for Zone 601 due to an earthquake of **M** 5 at R_{epi} = 0 km

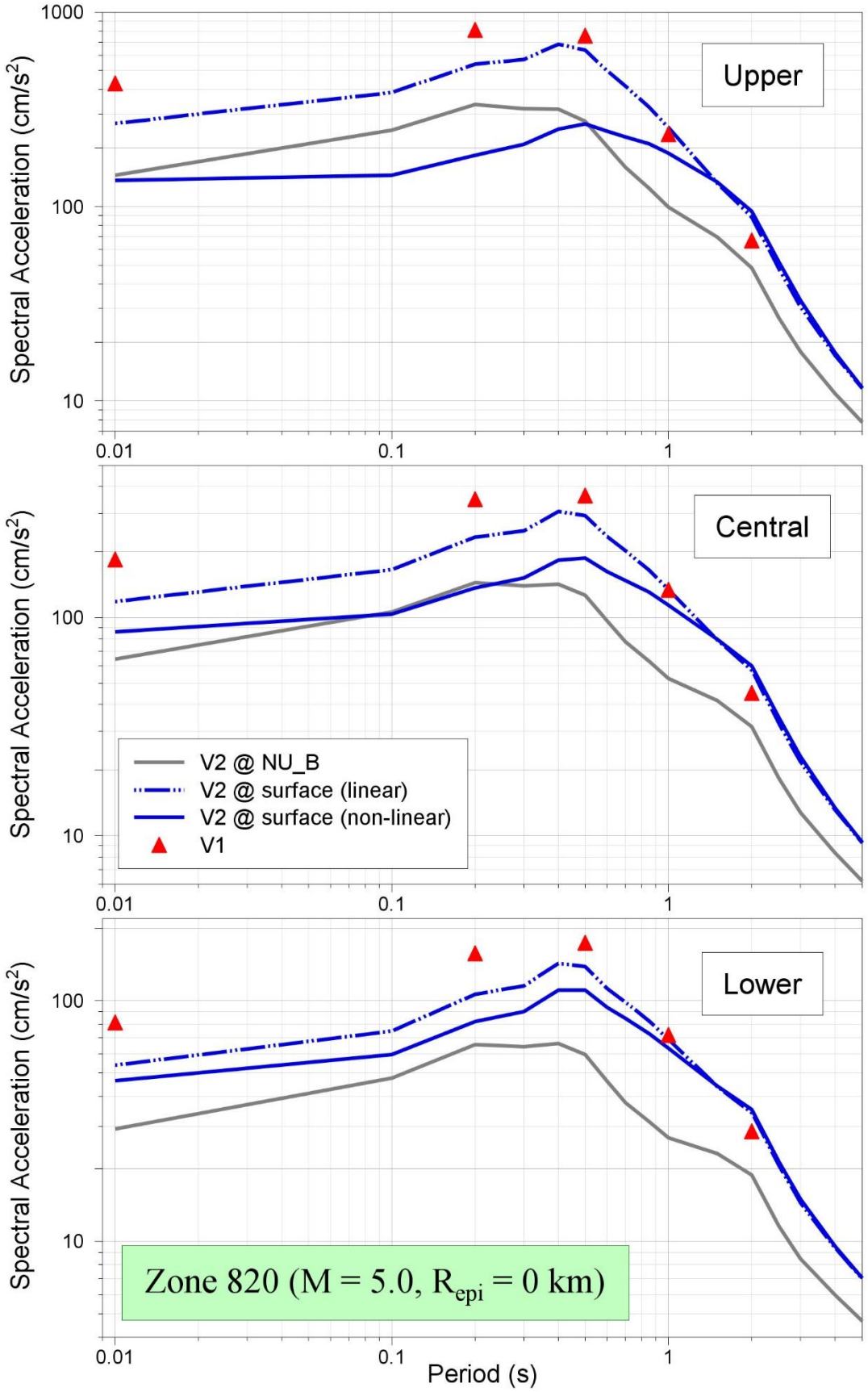

Figure 11.100. Comparison of median predicted response spectral accelerations from the V1 and V2 models for Zone 820 due to an earthquake of **M** 5 at R_{epi} = 0 km

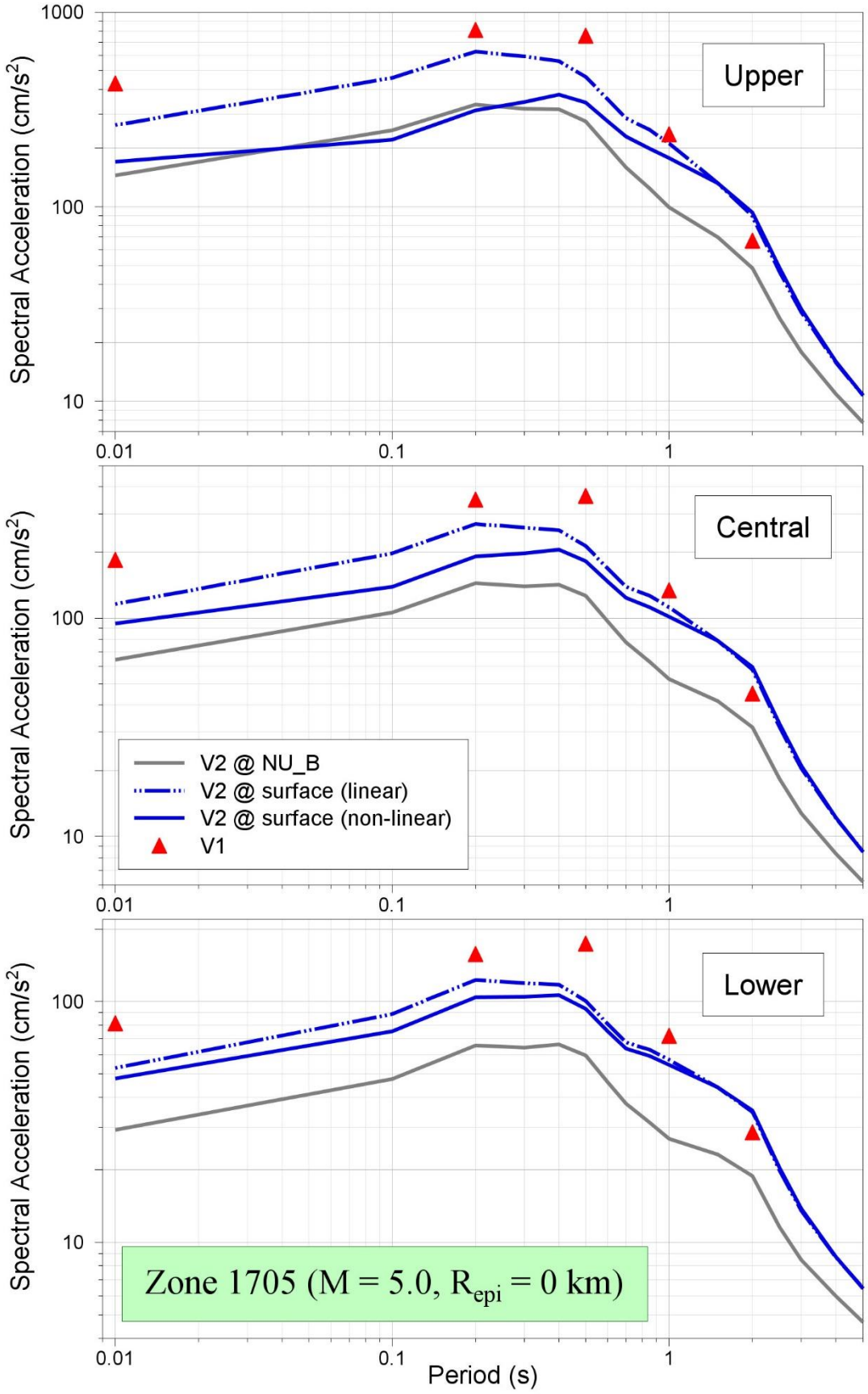

Figure 11.101. Comparison of median predicted response spectral accelerations from the V1 and V2 models for Zone 1705 due to an earthquake of **M** 5 at R_{epi} = 0 km

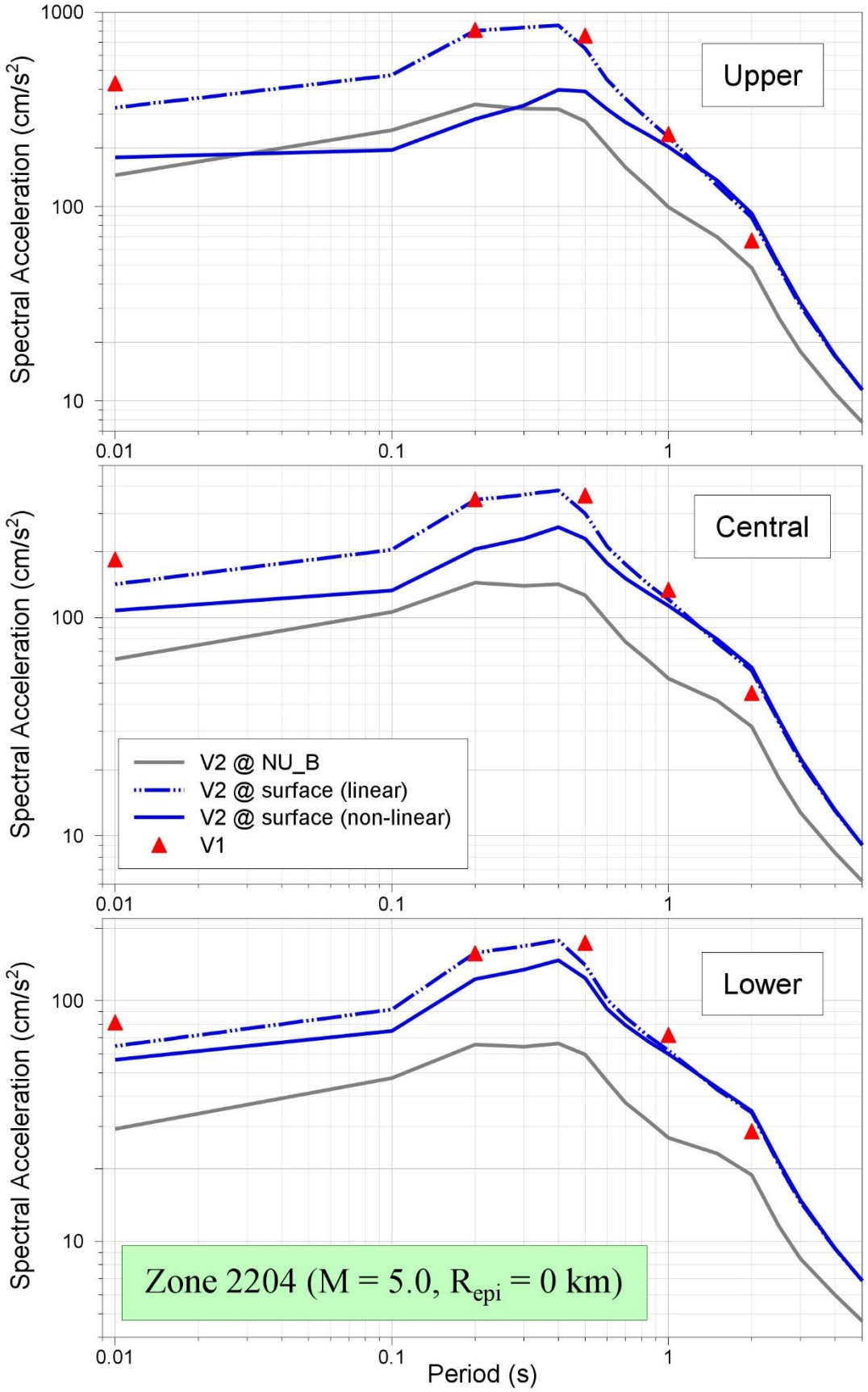

Figure 11.102. Comparison of median predicted response spectral accelerations from the V1 and V2 models for Zone 2204 due to an earthquake of **M** 5 at R_{epi} = 0 km

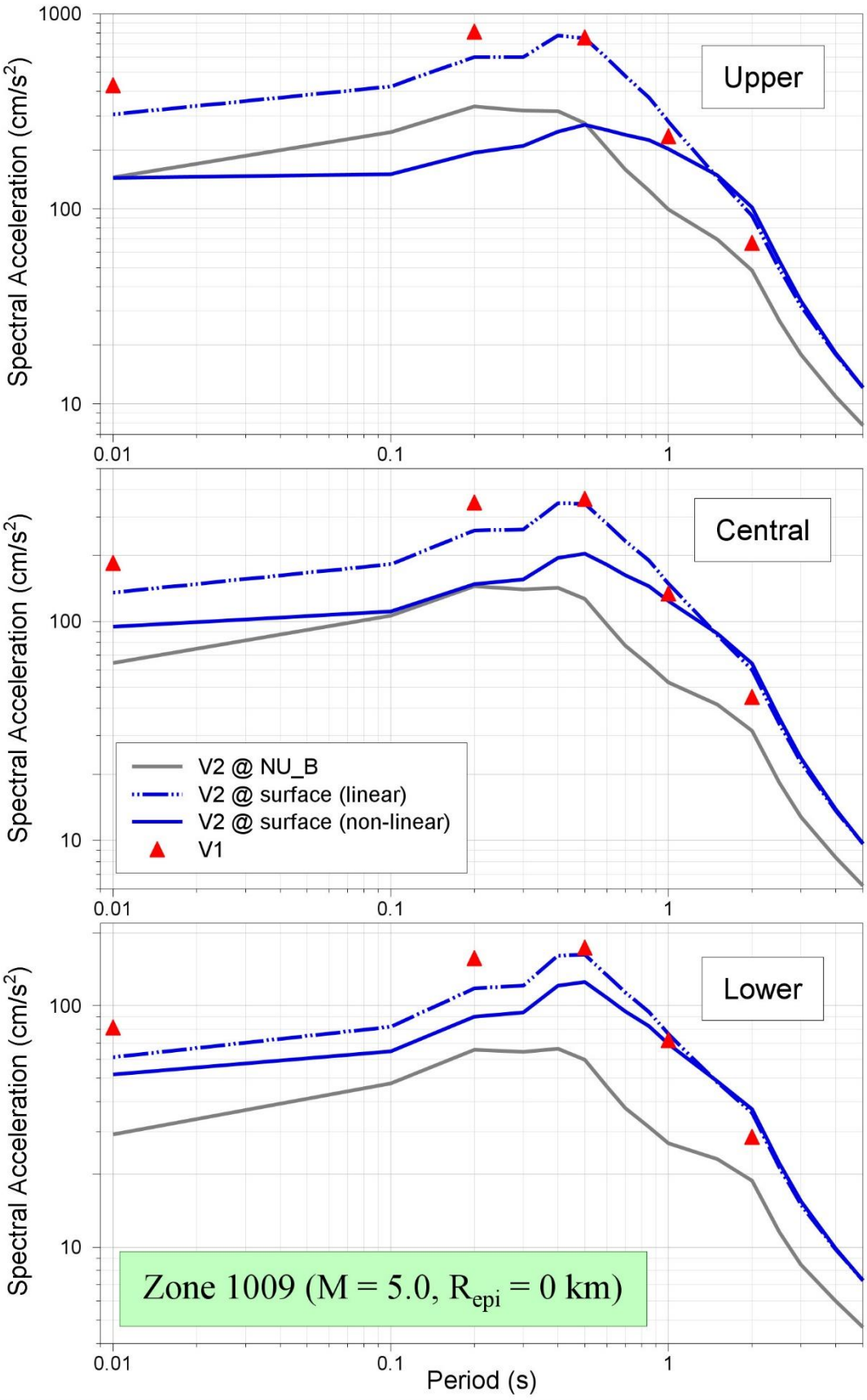

Figure 11.103. Comparison of median predicted response spectral accelerations from the V1 and V2 models for Zone 1009 due to an earthquake of **M** 5 at R_{epi} = 0 km

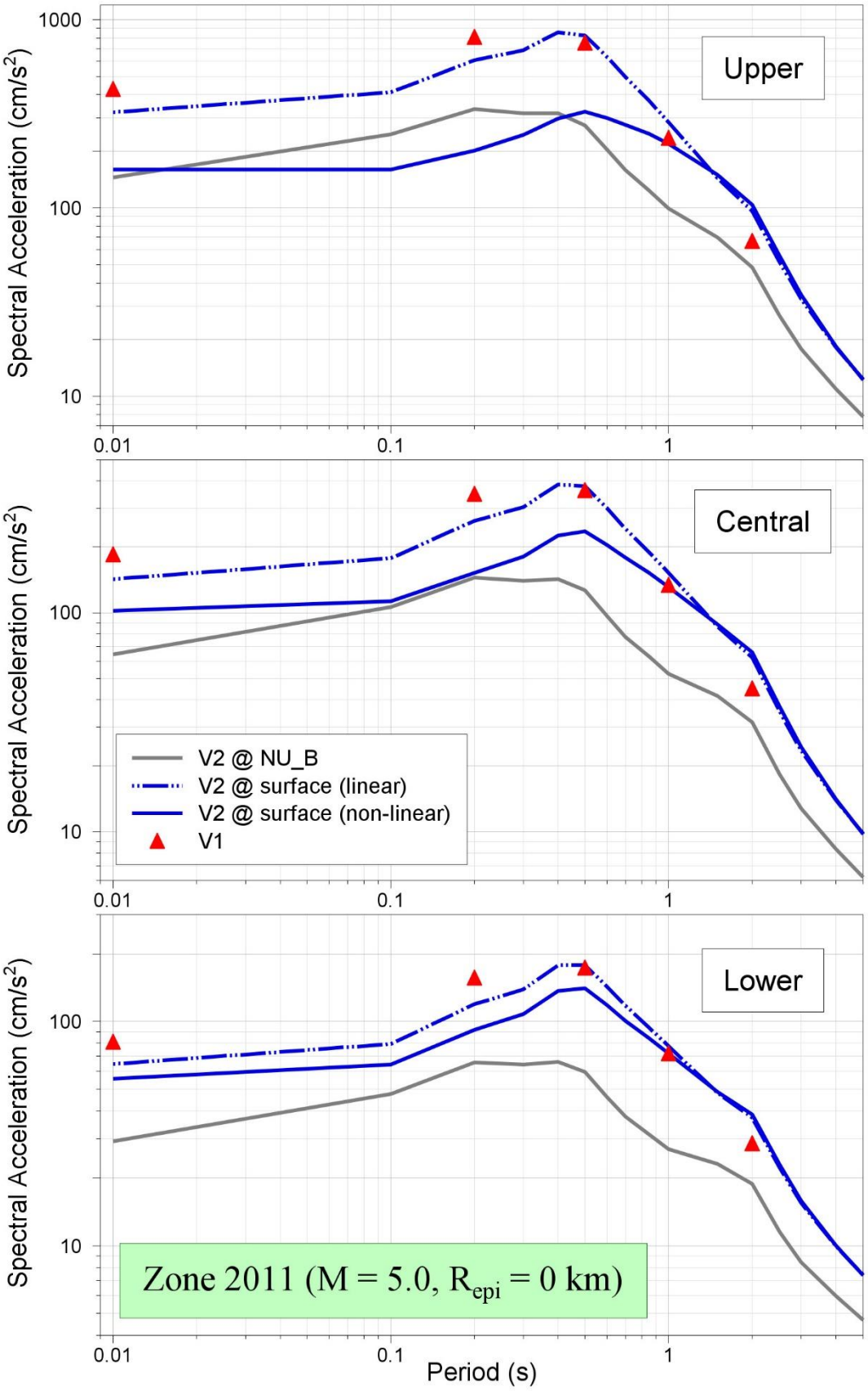

Figure 11.104. Comparison of median predicted response spectral accelerations from the V1 and V2 models for Zone 2011 due to an earthquake of **M** 5 at R_{epi} = 0 km

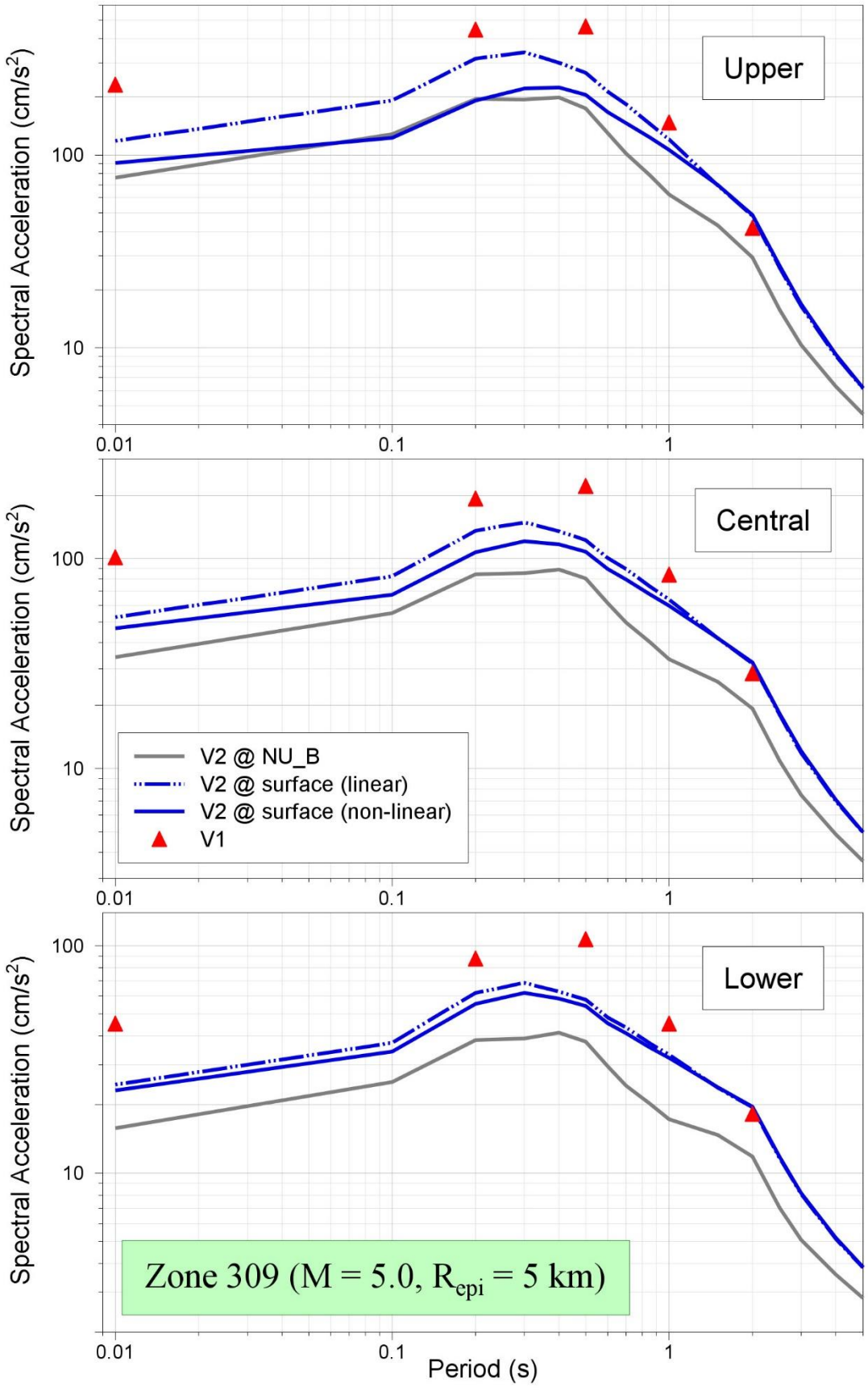

Figure 11.105. Comparison of median predicted response spectral accelerations from the V1 and V2 models for Zone 309 due to an earthquake of **M** 5 at R_{epi} = 5 km

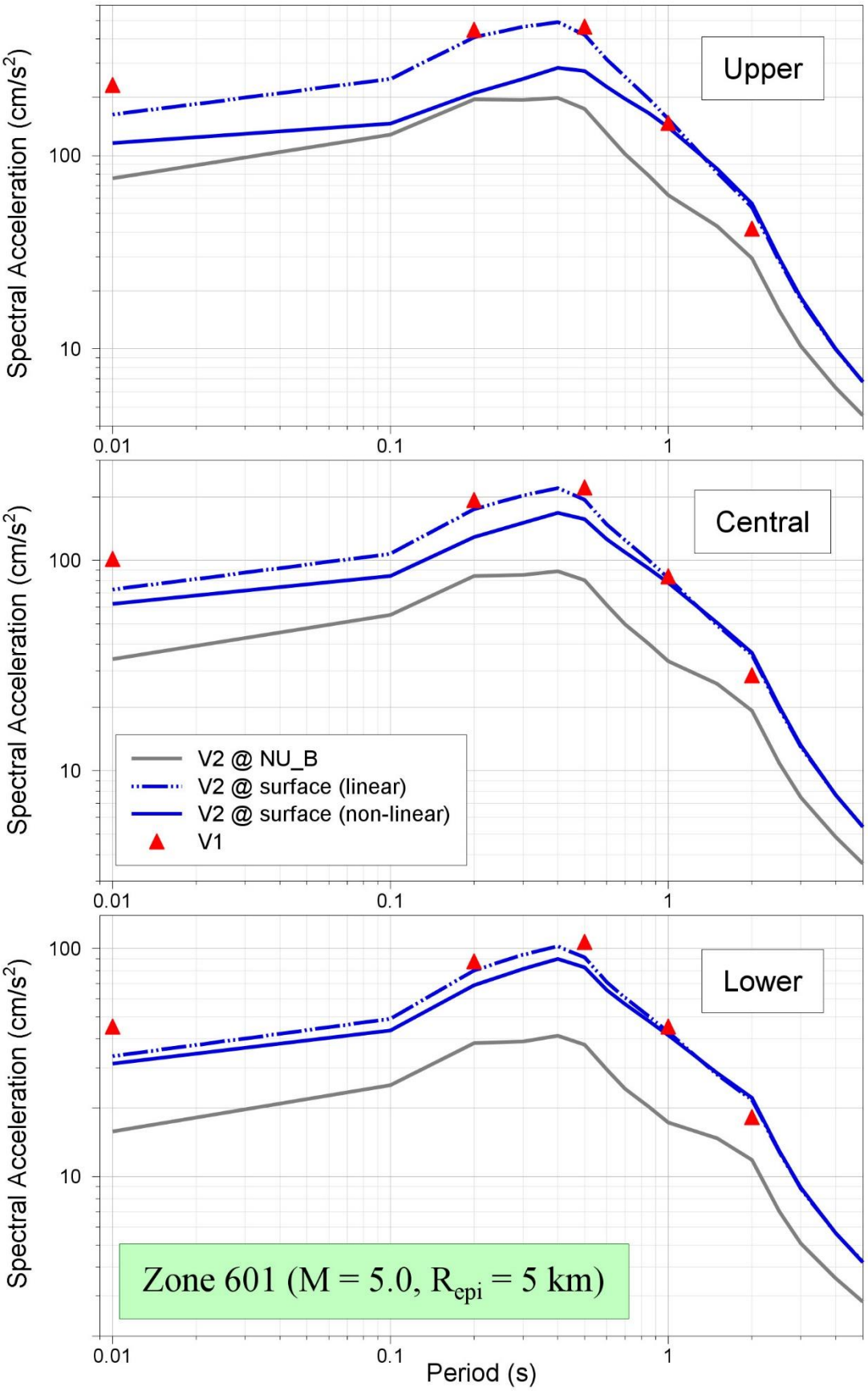

Figure 11.106. Comparison of median predicted response spectral accelerations from the V1 and V2 models for Zone 601 due to an earthquake of **M** 5 at R_{epi} = 5 km

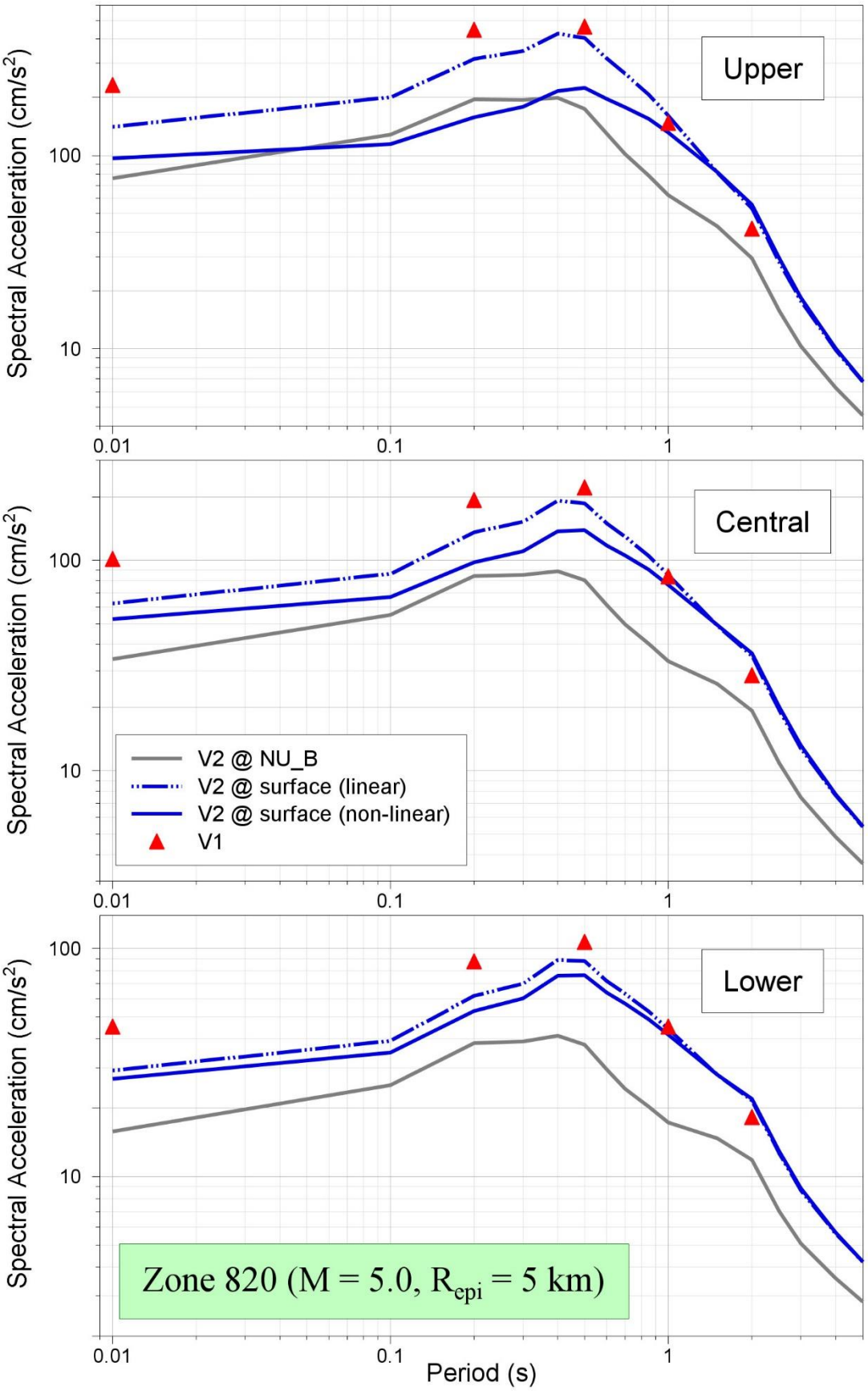

Figure 11.107. Comparison of median predicted response spectral accelerations from the V1 and V2 models for Zone 820 due to an earthquake of **M** 5 at R_{epi} = 5 km

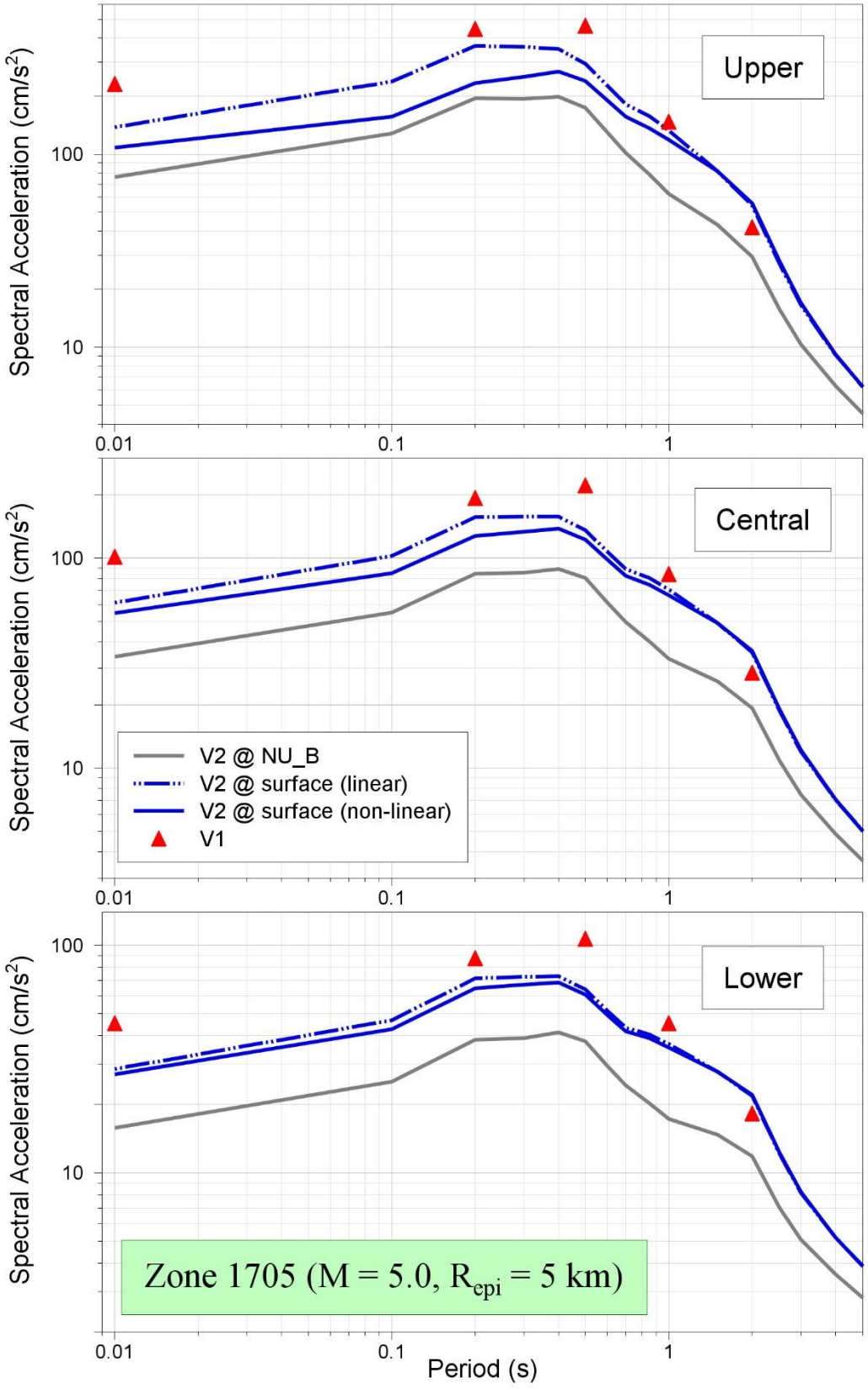

Figure 11.108. Comparison of median predicted response spectral accelerations from the V1 and V2 models for Zone 1705 due to an earthquake of **M** 5 at R_{epi} = 5 km

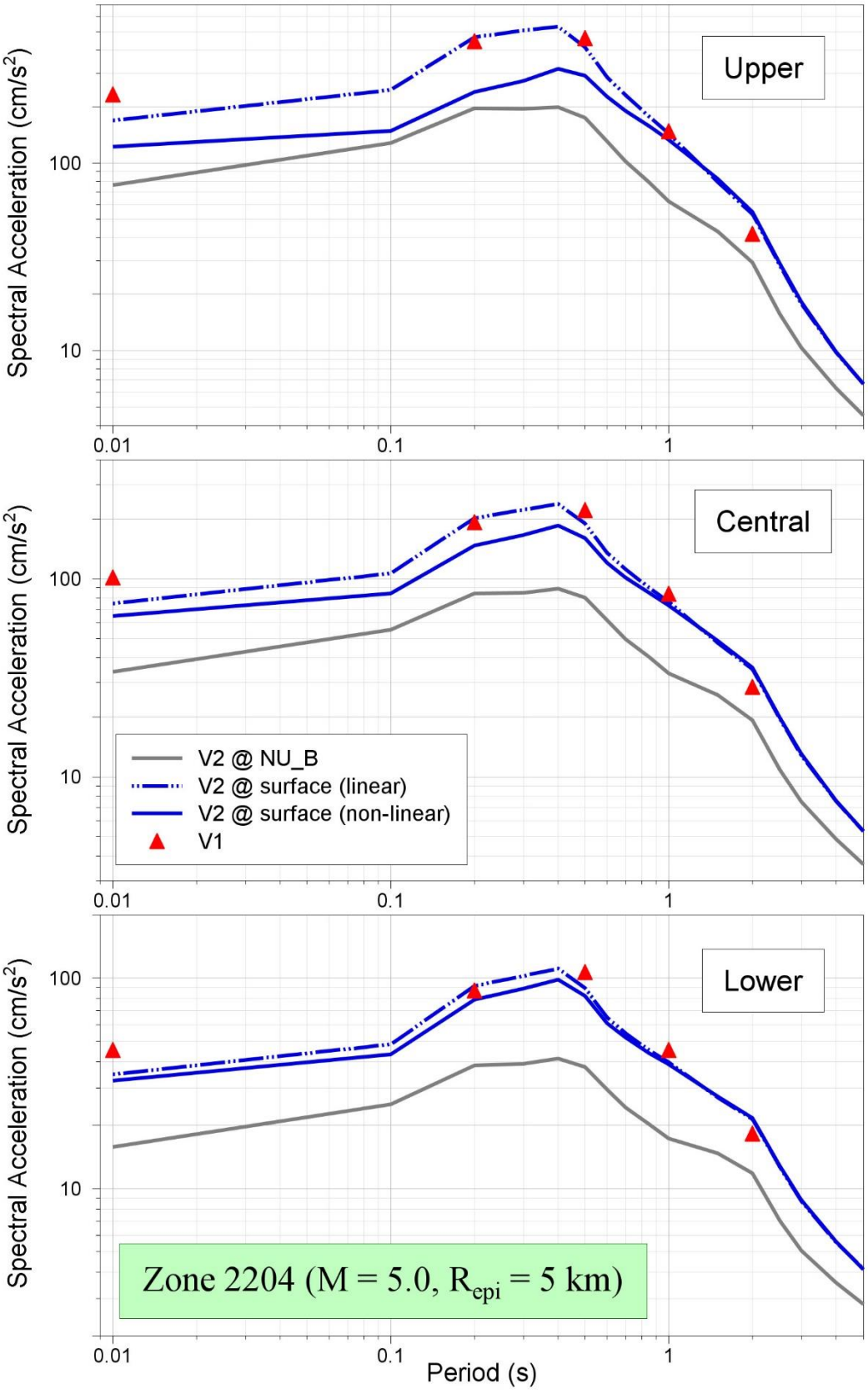

Figure 11.109. Comparison of median predicted response spectral accelerations from the V1 and V2 models for Zone 2204 due to an earthquake of **M** 5 at R_{epi} = 5 km

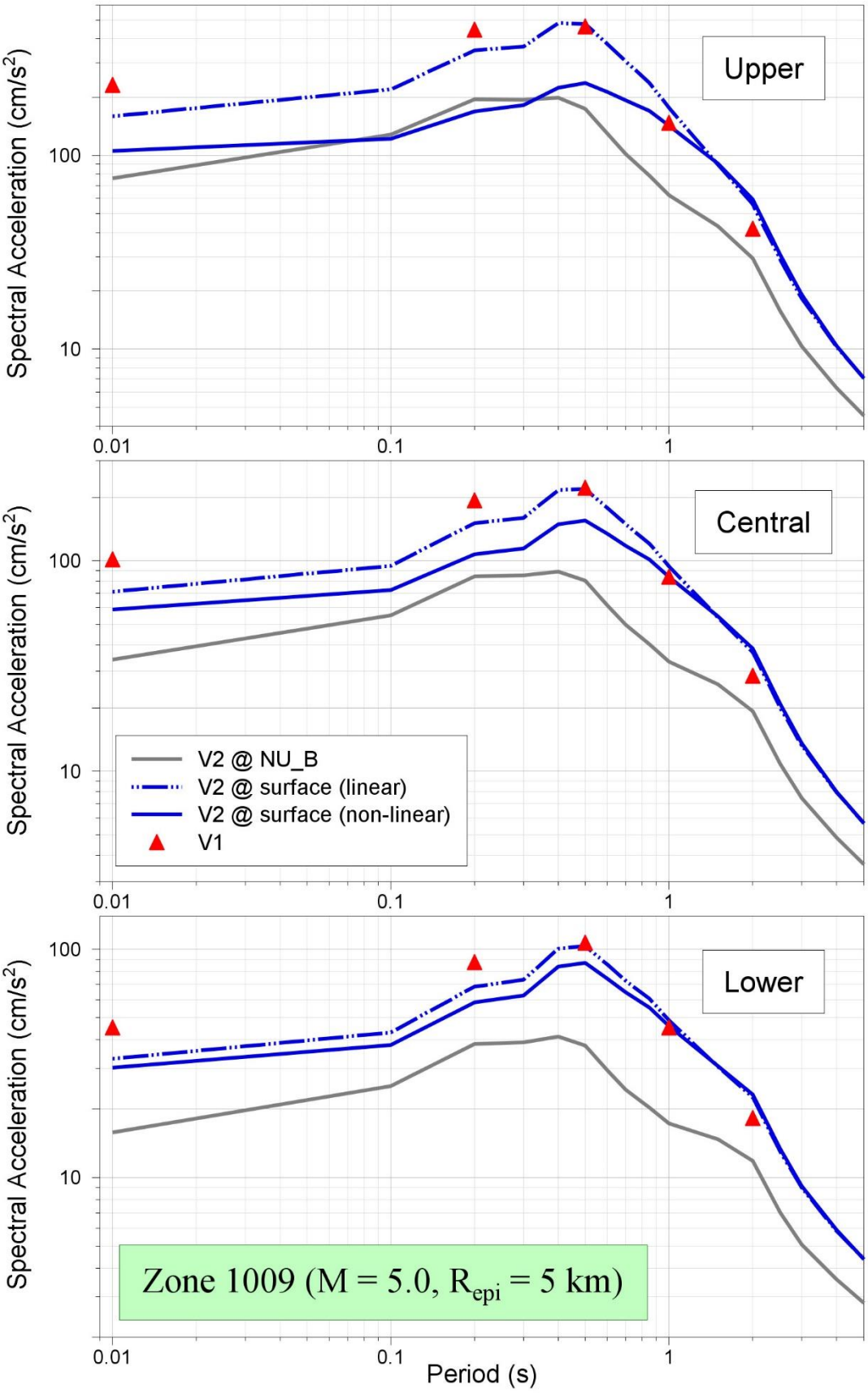

Figure 11.110. Comparison of median predicted response spectral accelerations from the V1 and V2 models for Zone 1009 due to an earthquake of **M** 5 at R_{epi} = 5 km

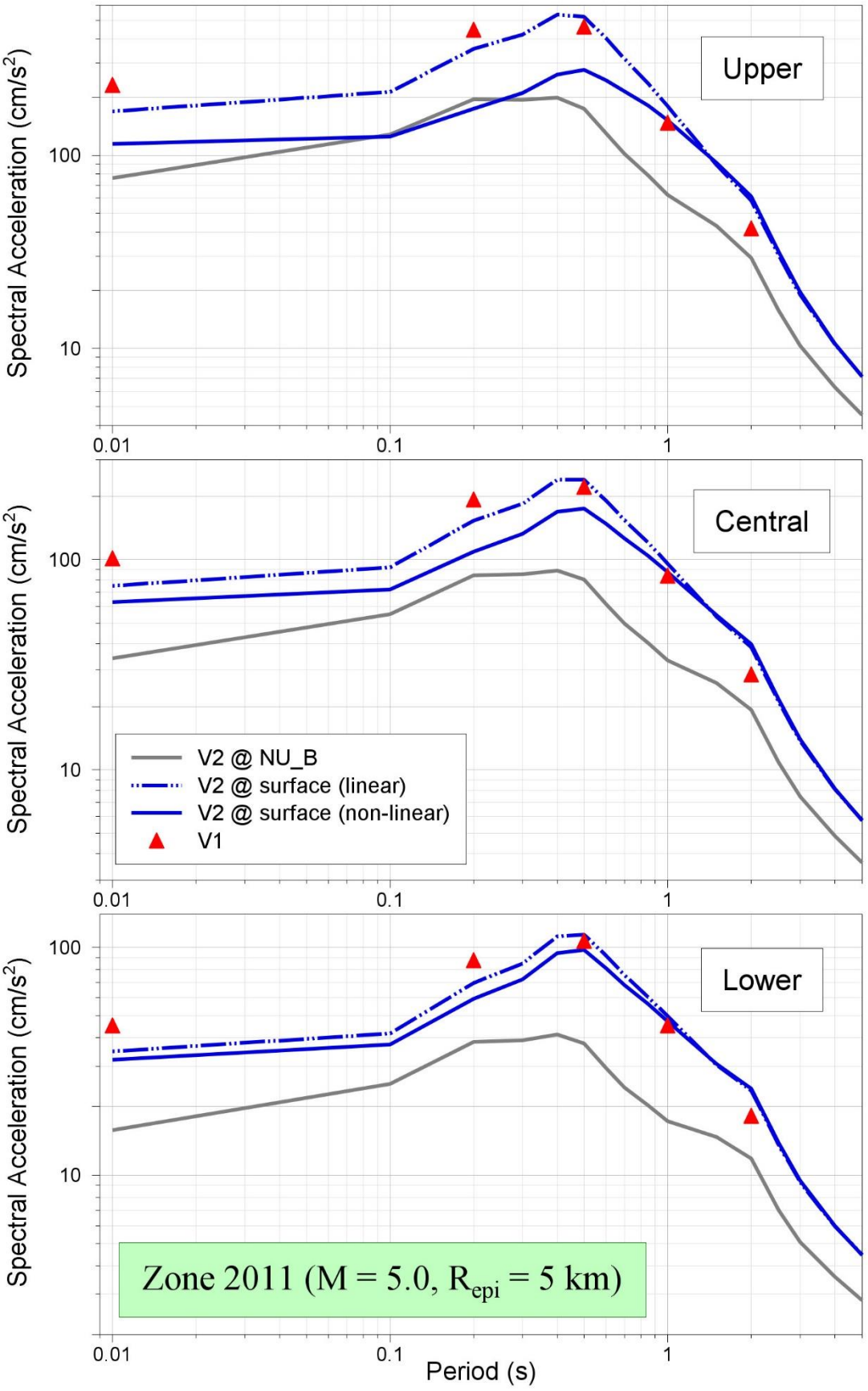

Figure 11.111. Comparison of median predicted response spectral accelerations from the V1 and V2 models for Zone 2011 due to an earthquake of **M** 5 at R_{epi} = 5 km

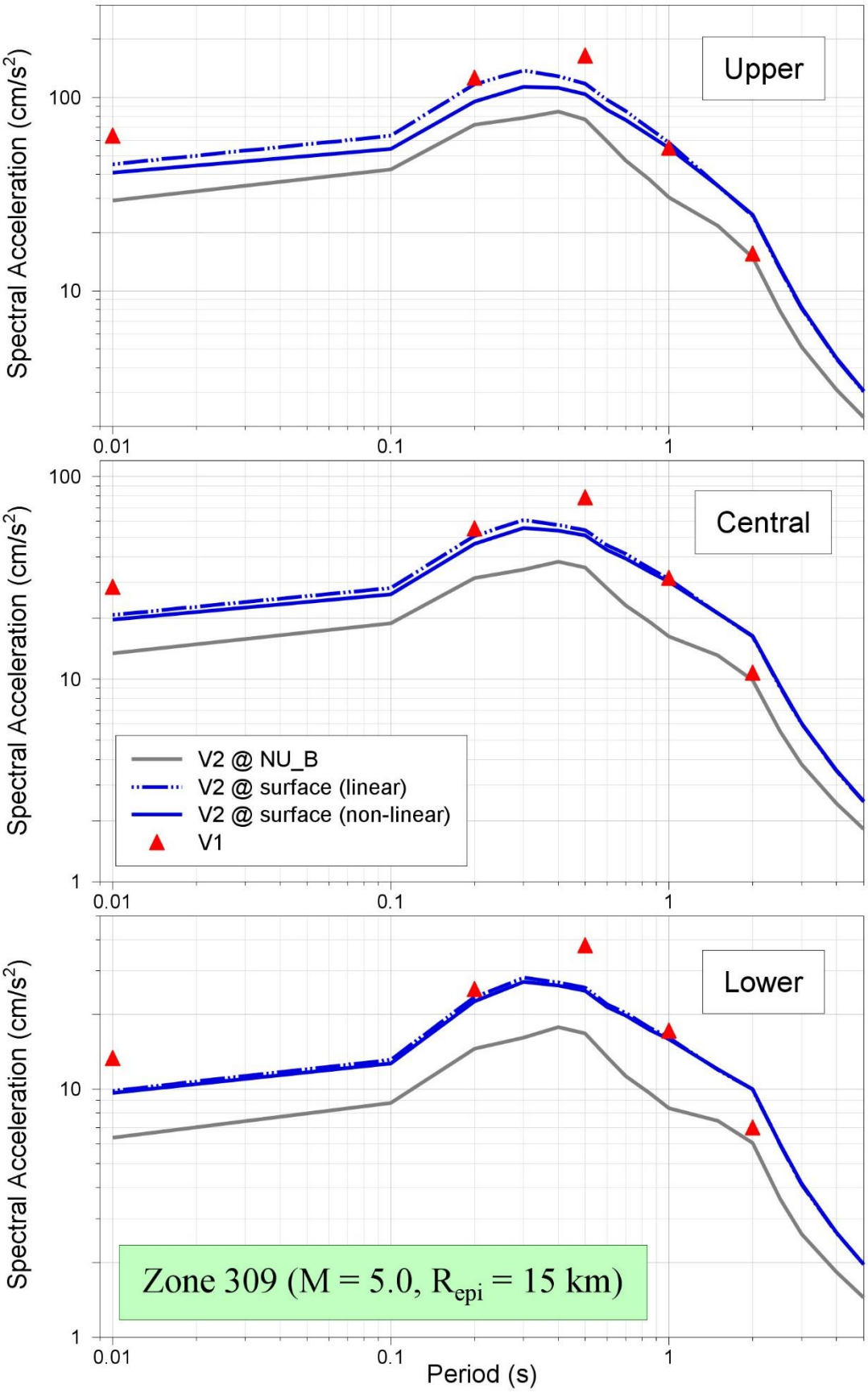

Figure 11.112. Comparison of median predicted response spectral accelerations from the V1 and V2 models for Zone 309 due to an earthquake of **M** 5 at R_{epi} = 15 km

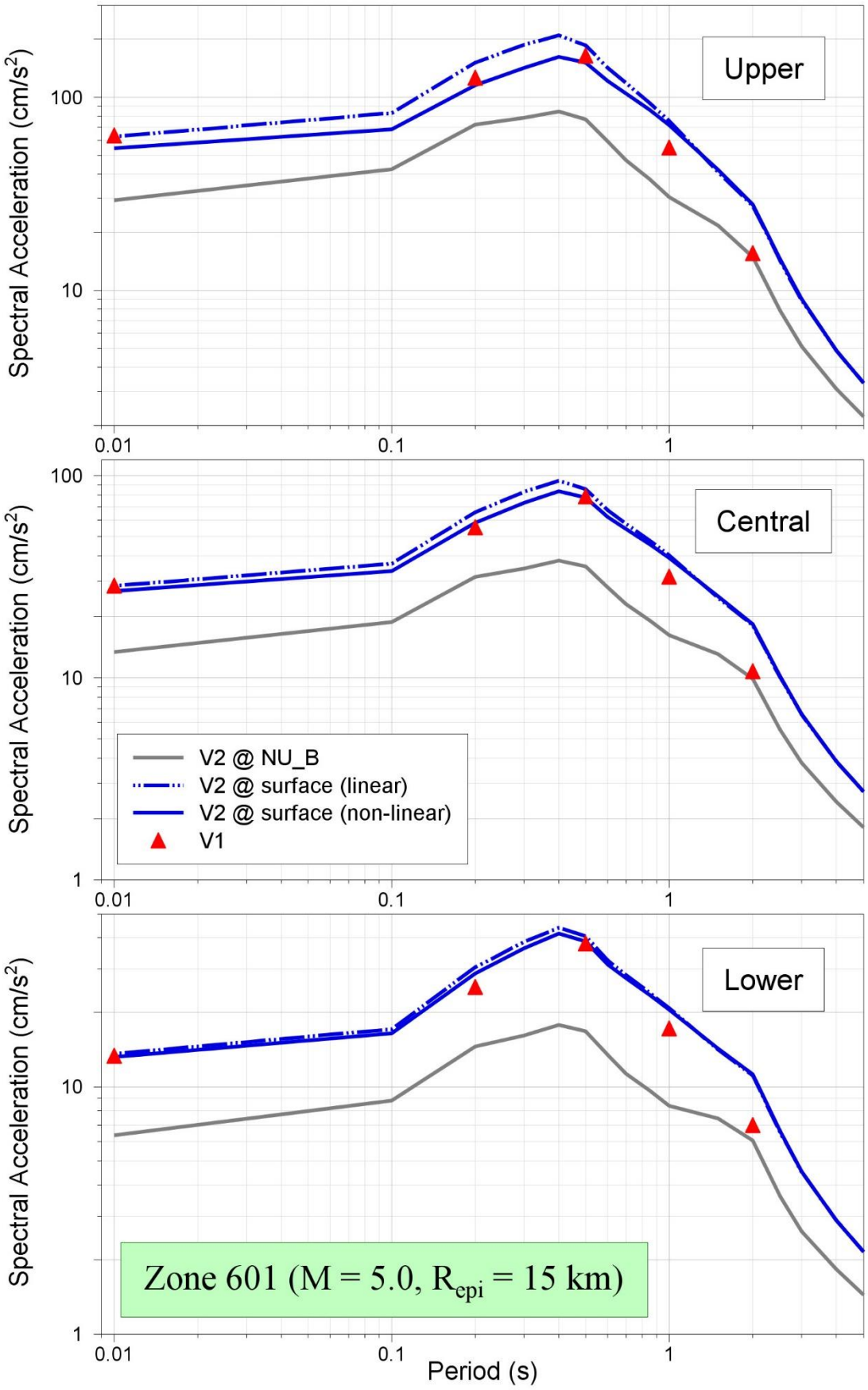

Figure 11.113. Comparison of median predicted response spectral accelerations from the V1 and V2 models for Zone 601 due to an earthquake of **M** 5 at R_{epi} = 15 km

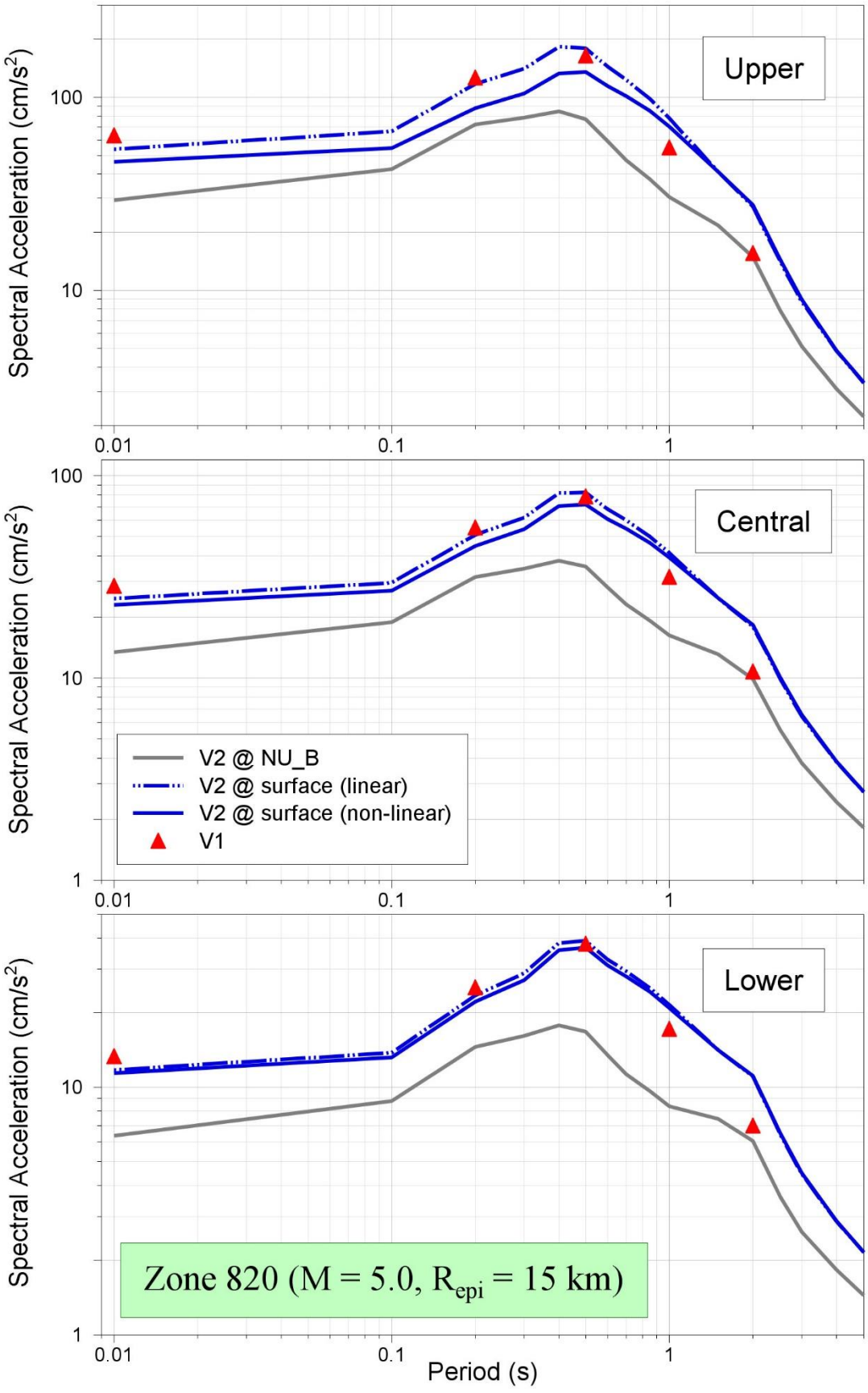

Figure 11.114. Comparison of median predicted response spectral accelerations from the V1 and V2 models for Zone 820 due to an earthquake of **M** 5 at R_{epi} = 15 km

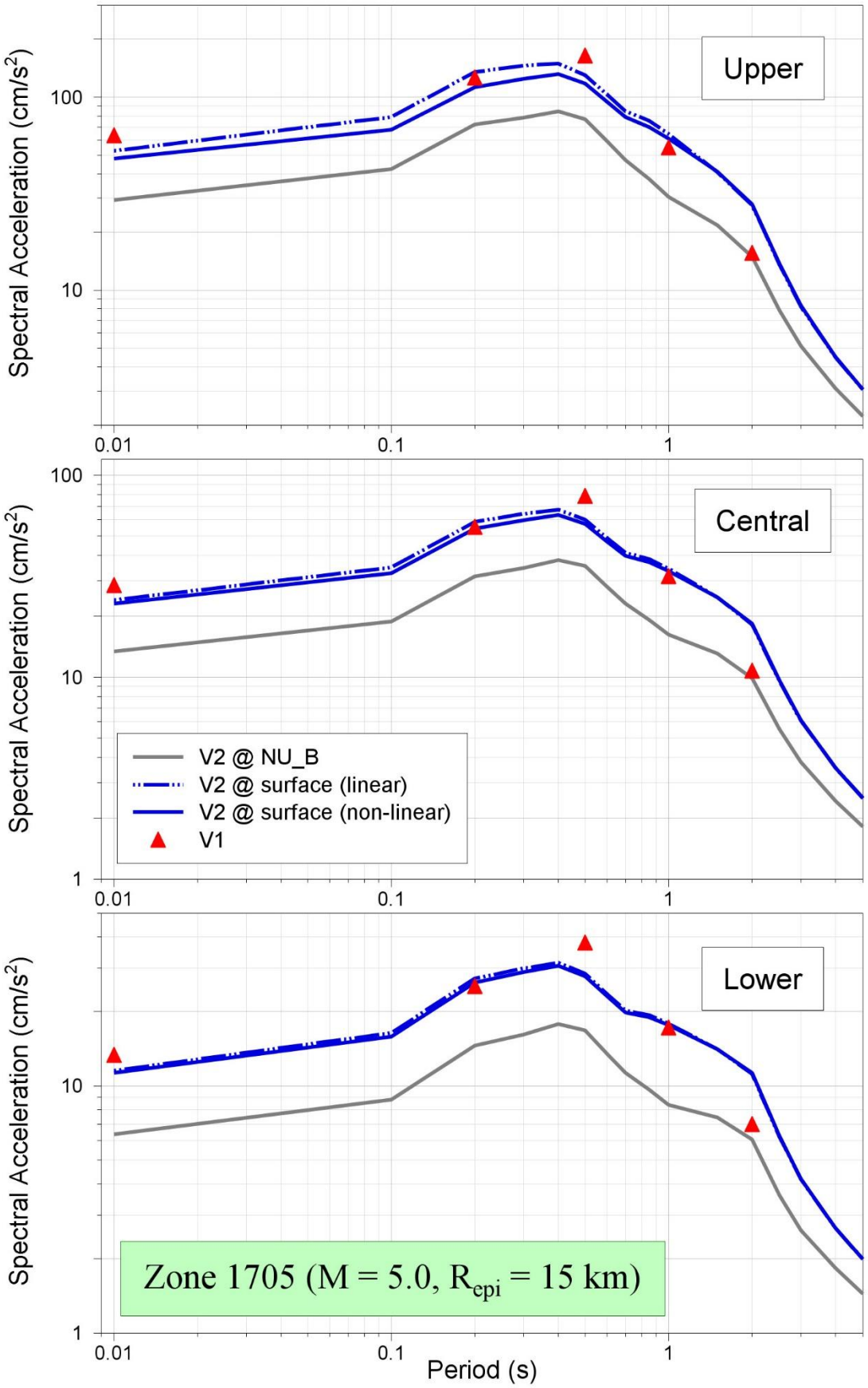

Figure 11.115. Comparison of median predicted response spectral accelerations from the V1 and V2 models for Zone 1705 due to an earthquake of **M** 5 at R_{epi} = 15 km

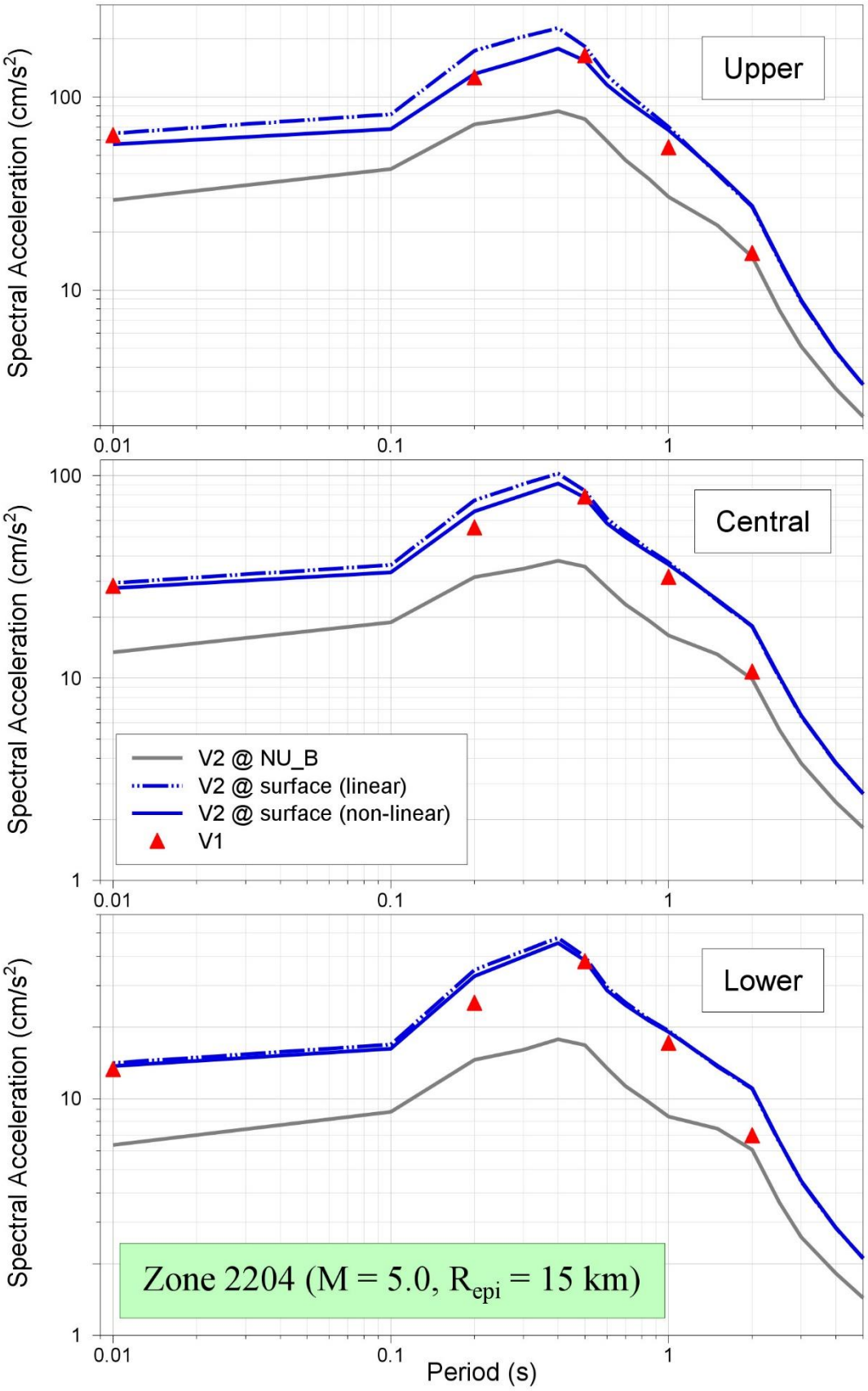

Figure 11.116. Comparison of median predicted response spectral accelerations from the V1 and V2 models for Zone 2204 due to an earthquake of **M** 5 at R_{epi} = 15 km

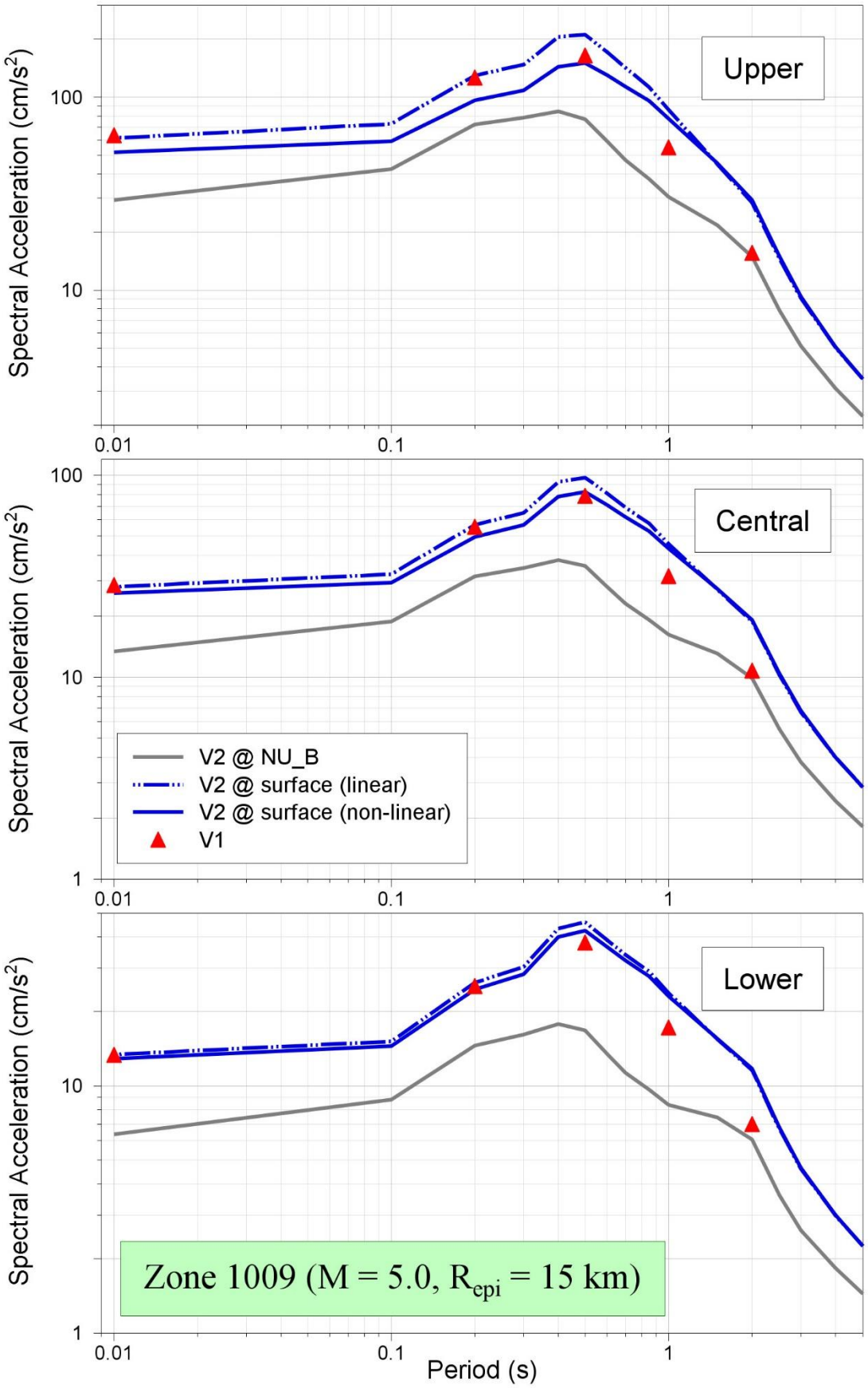

Figure 11.117. Comparison of median predicted response spectral accelerations from the V1 and V2 models for Zone 1009 due to an earthquake of **M** 5 at R_{epi} = 15 km

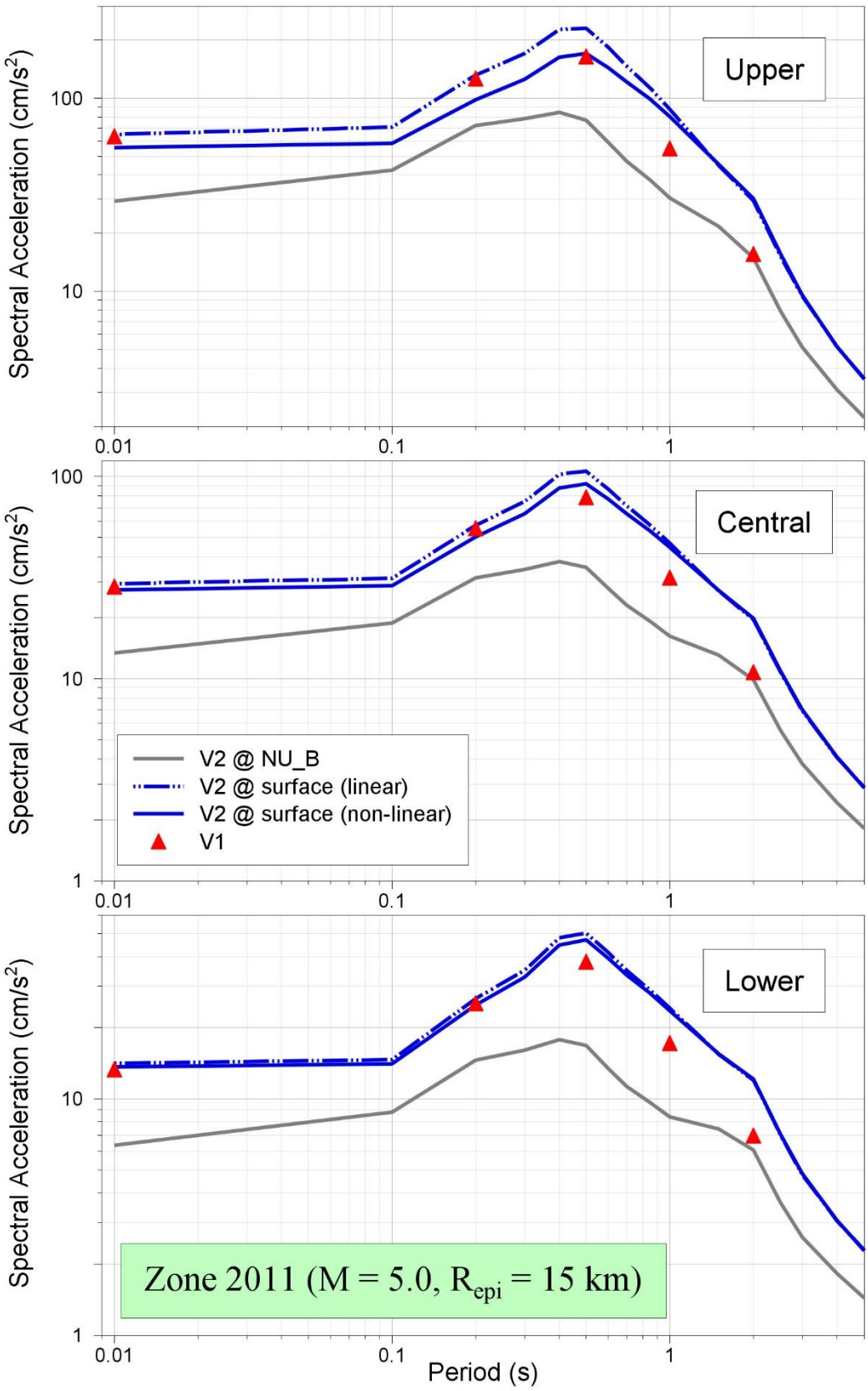

Figure 11.118. Comparison of median predicted response spectral accelerations from the V1 and V2 models for Zone 2011 due to an earthquake of **M** 5 at R_{epi} = 15 km

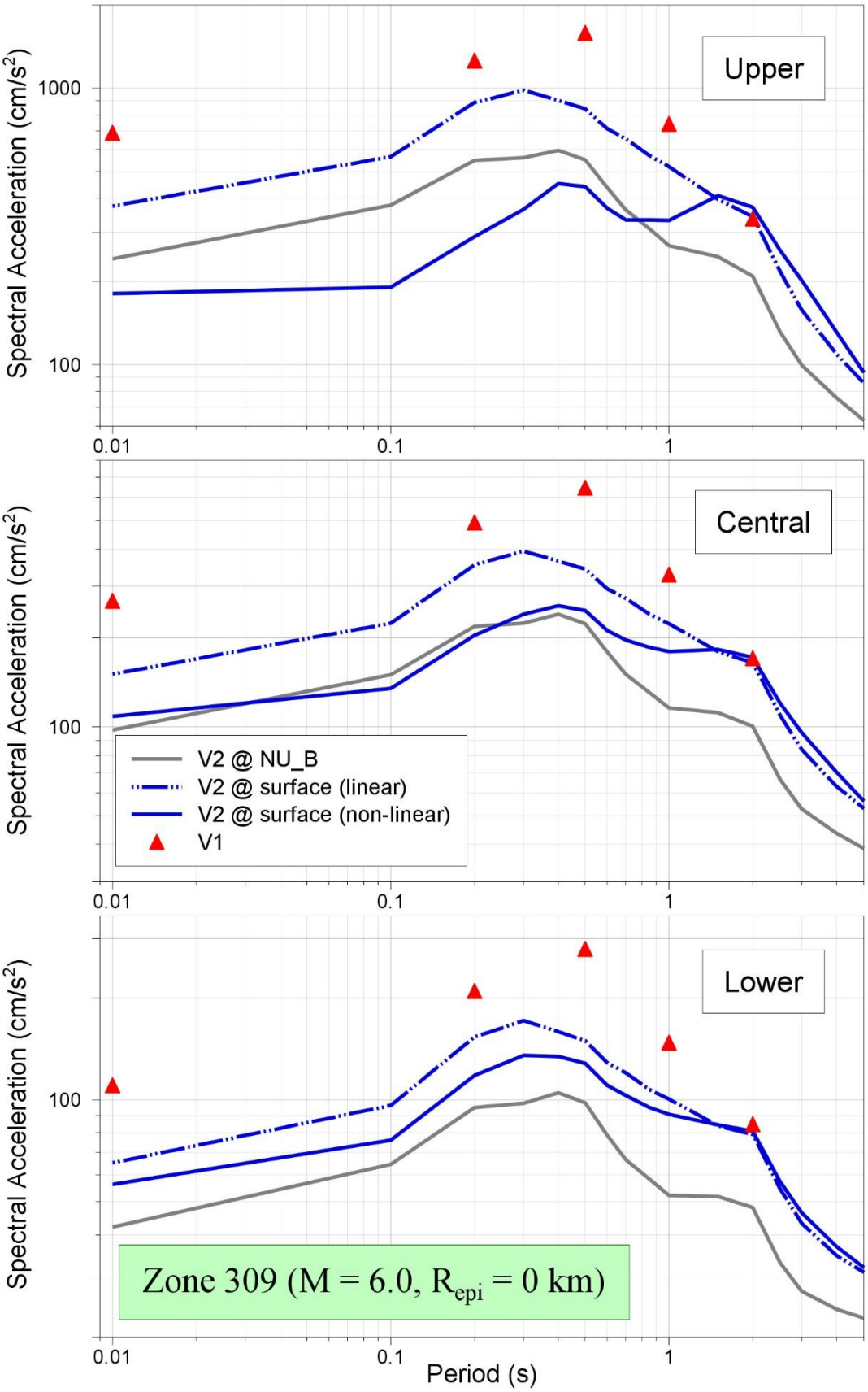

Figure 11.119. Comparison of median predicted response spectral accelerations from the V1 and V2 models for Zone 309 due to an earthquake of **M** 6 at R_{epi} = 0 km

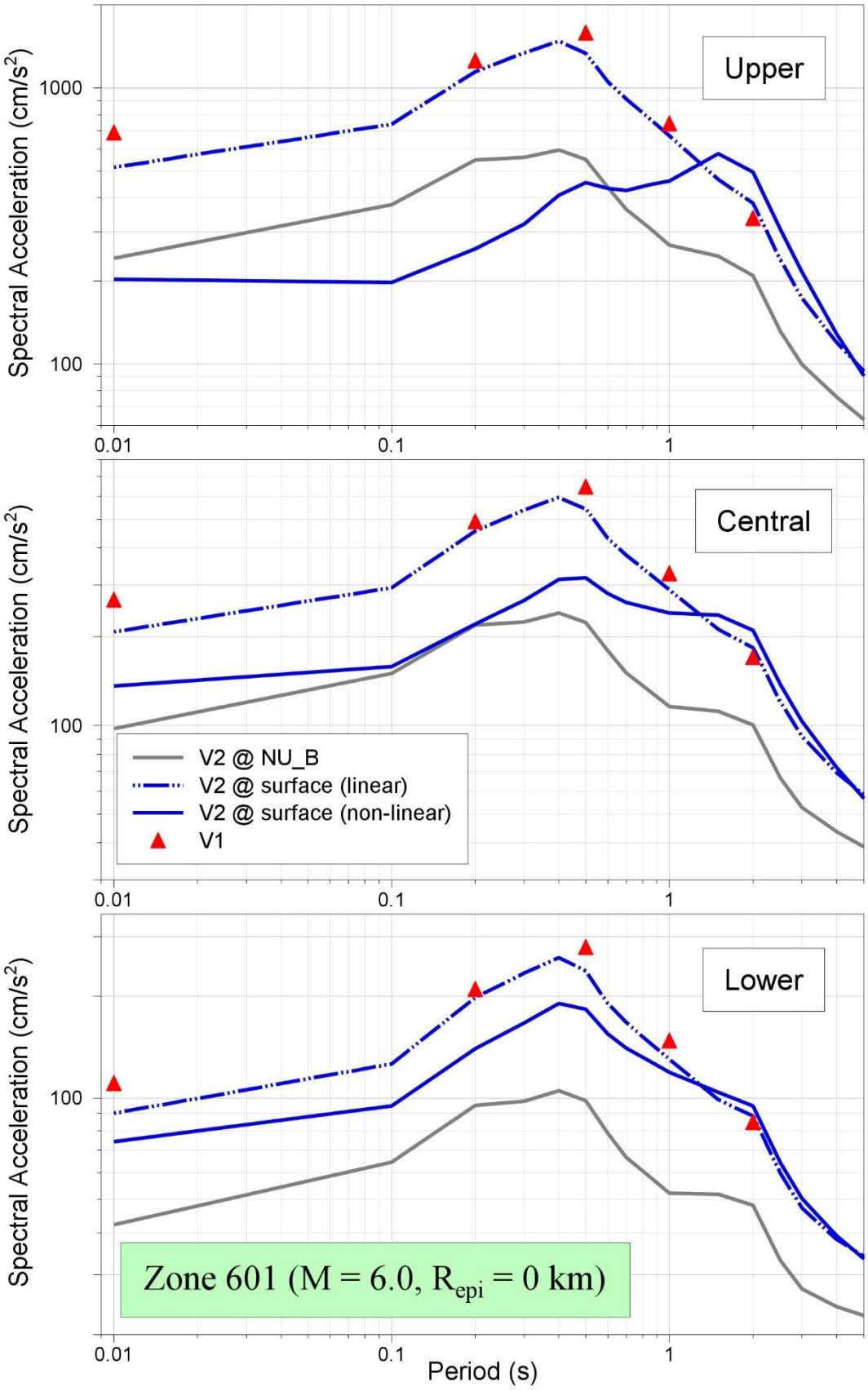

Figure 11.120. Comparison of median predicted response spectral accelerations from the V1 and V2 models for Zone 601 due to an earthquake of **M** 6 at R_{epi} = 0 km

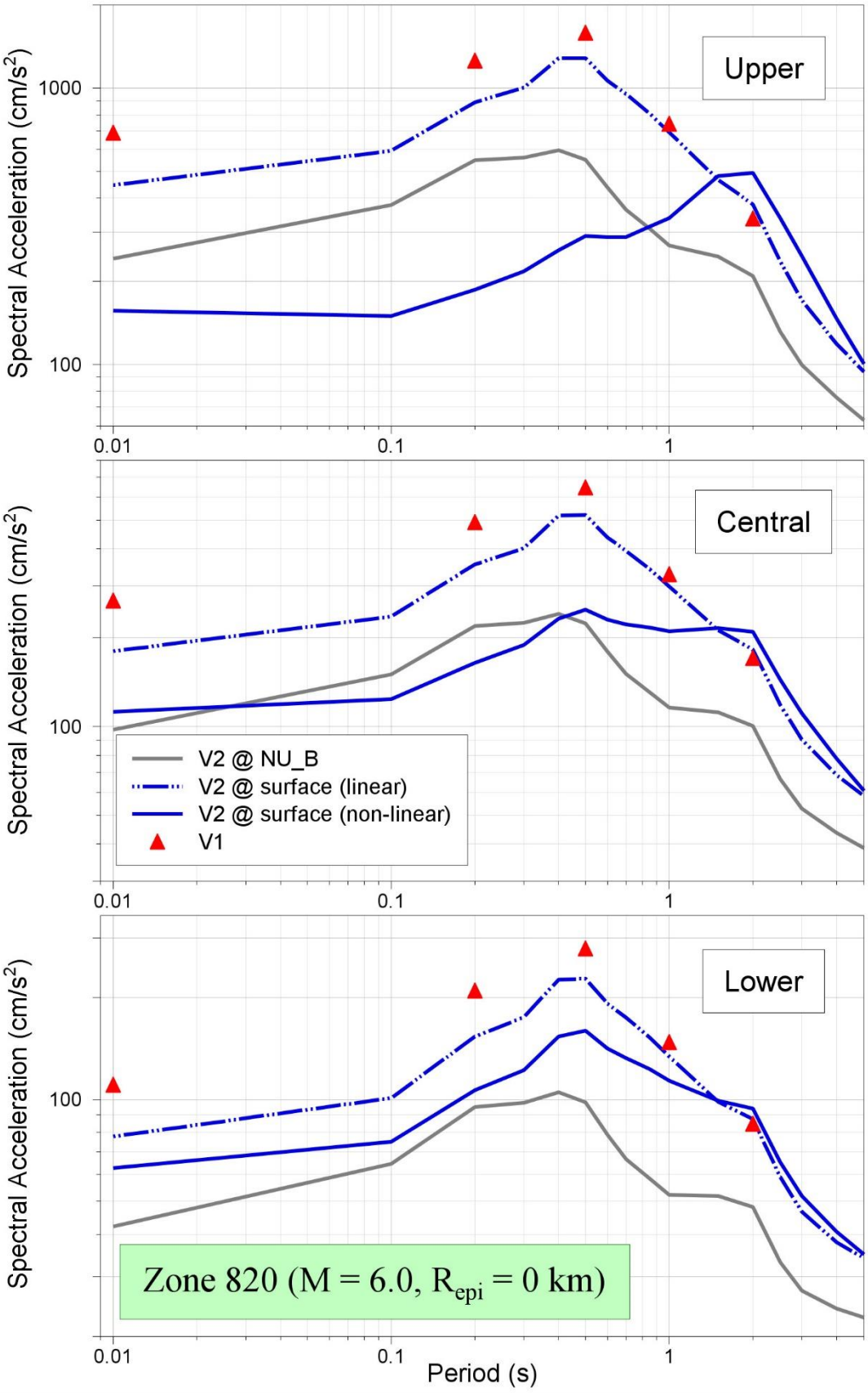

Figure 11.121. Comparison of median predicted response spectral accelerations from the V1 and V2 models for Zone 820 due to an earthquake of **M** 6 at R_{epi} = 0 km

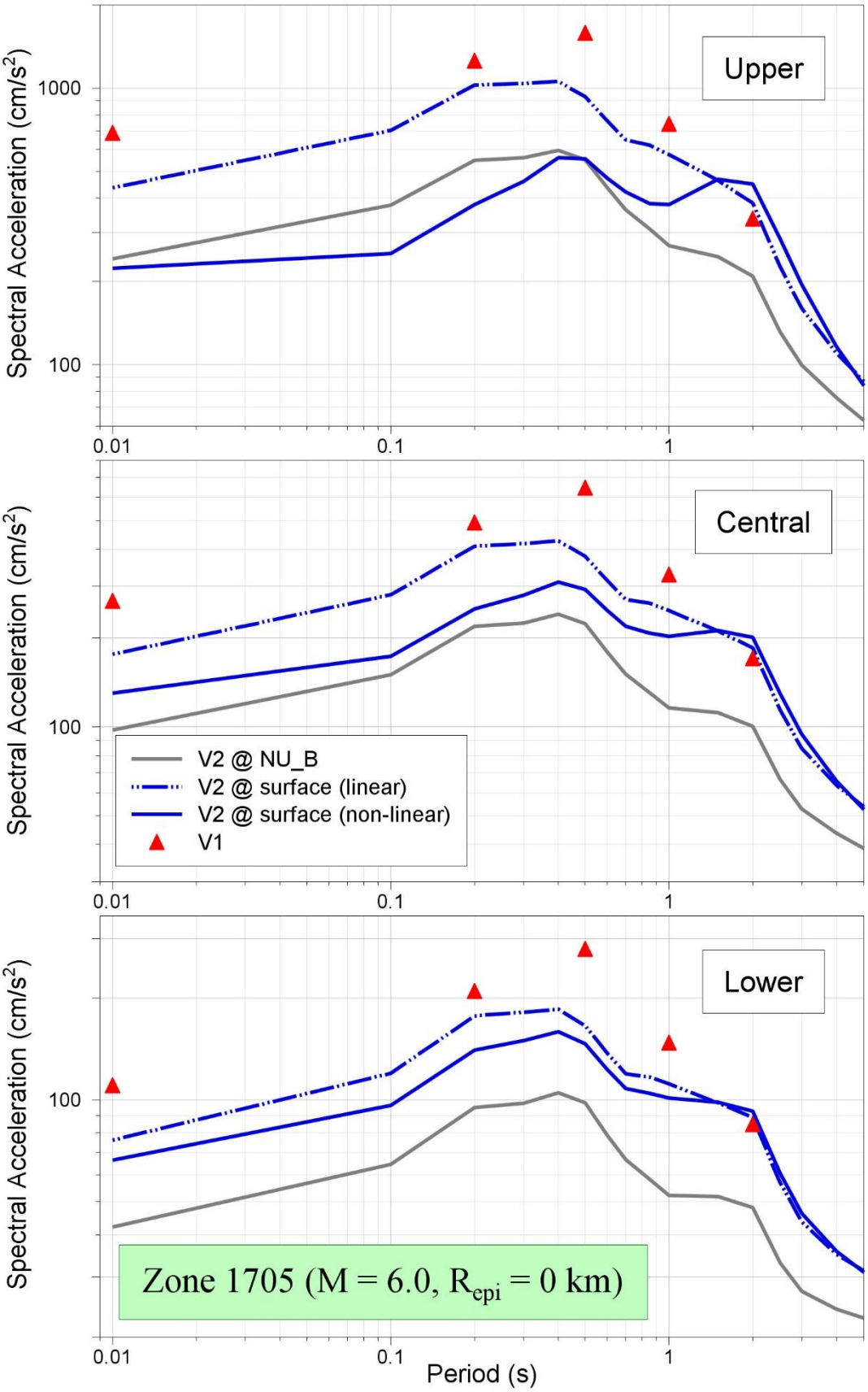

Figure 11.122. Comparison of median predicted response spectral accelerations from the V1 and V2 models for Zone 1705 due to an earthquake of **M** 6 at R_{epi} = 0 km

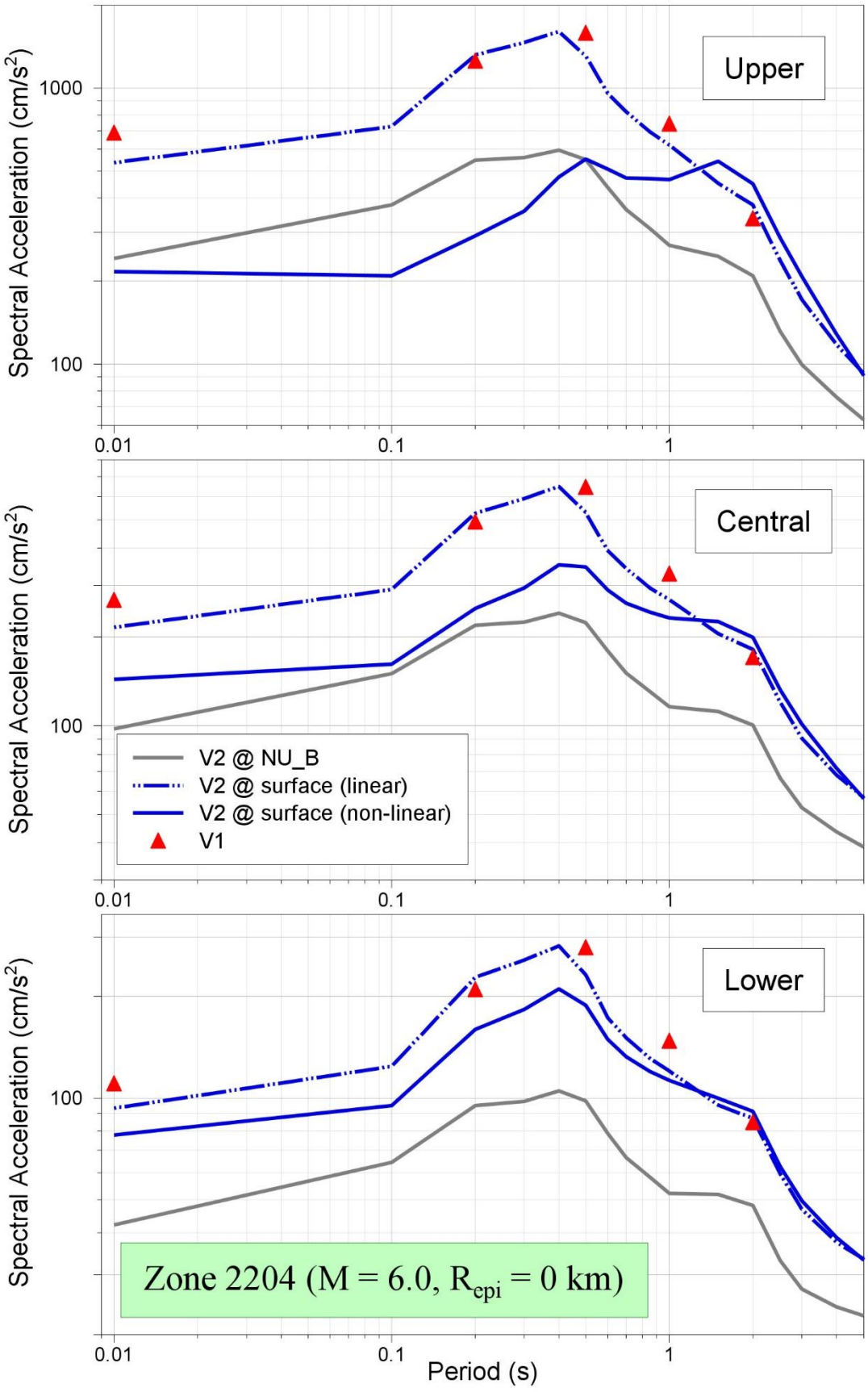

Figure 11.123. Comparison of median predicted response spectral accelerations from the V1 and V2 models for Zone 2204 due to an earthquake of **M** 6 at R_{epi} = 0 km

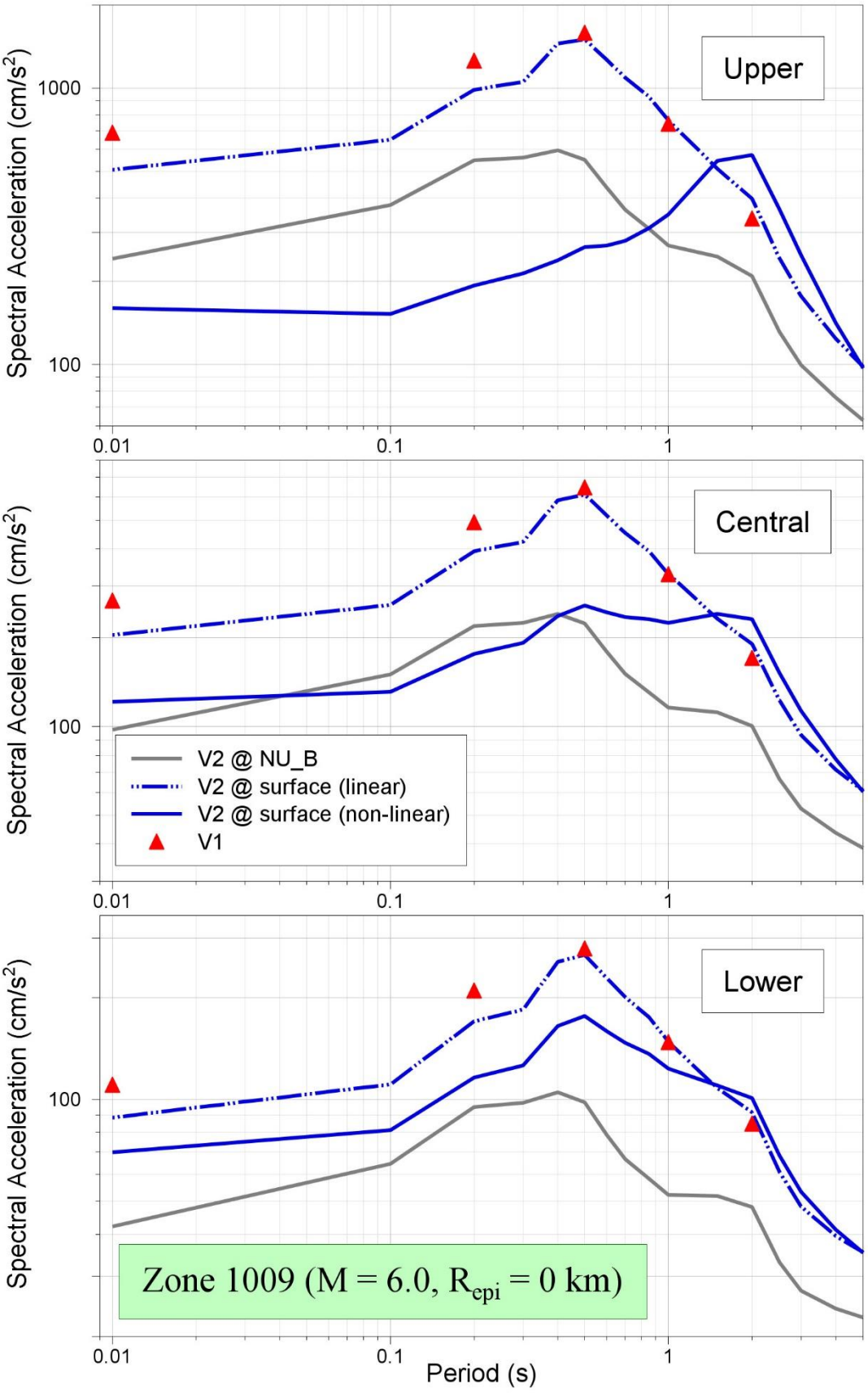

Figure 11.124. Comparison of median predicted response spectral accelerations from the V1 and V2 models for Zone 1009 due to an earthquake of **M** 6 at R_{epi} = 0 km

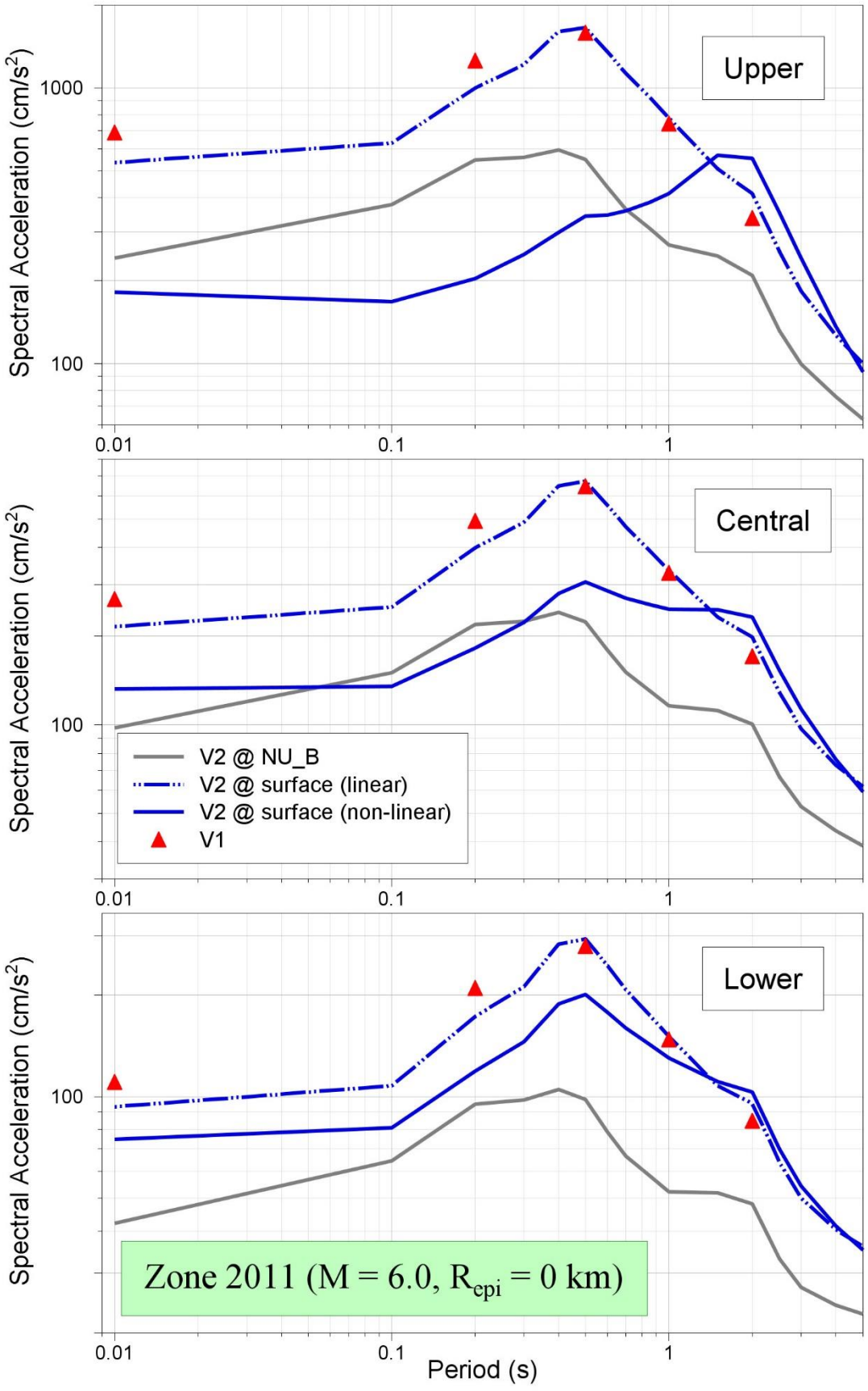

Figure 11.125. Comparison of median predicted response spectral accelerations from the V1 and V2 models for Zone 2011 due to an earthquake of **M** 6 at R_{epi} = 0 km

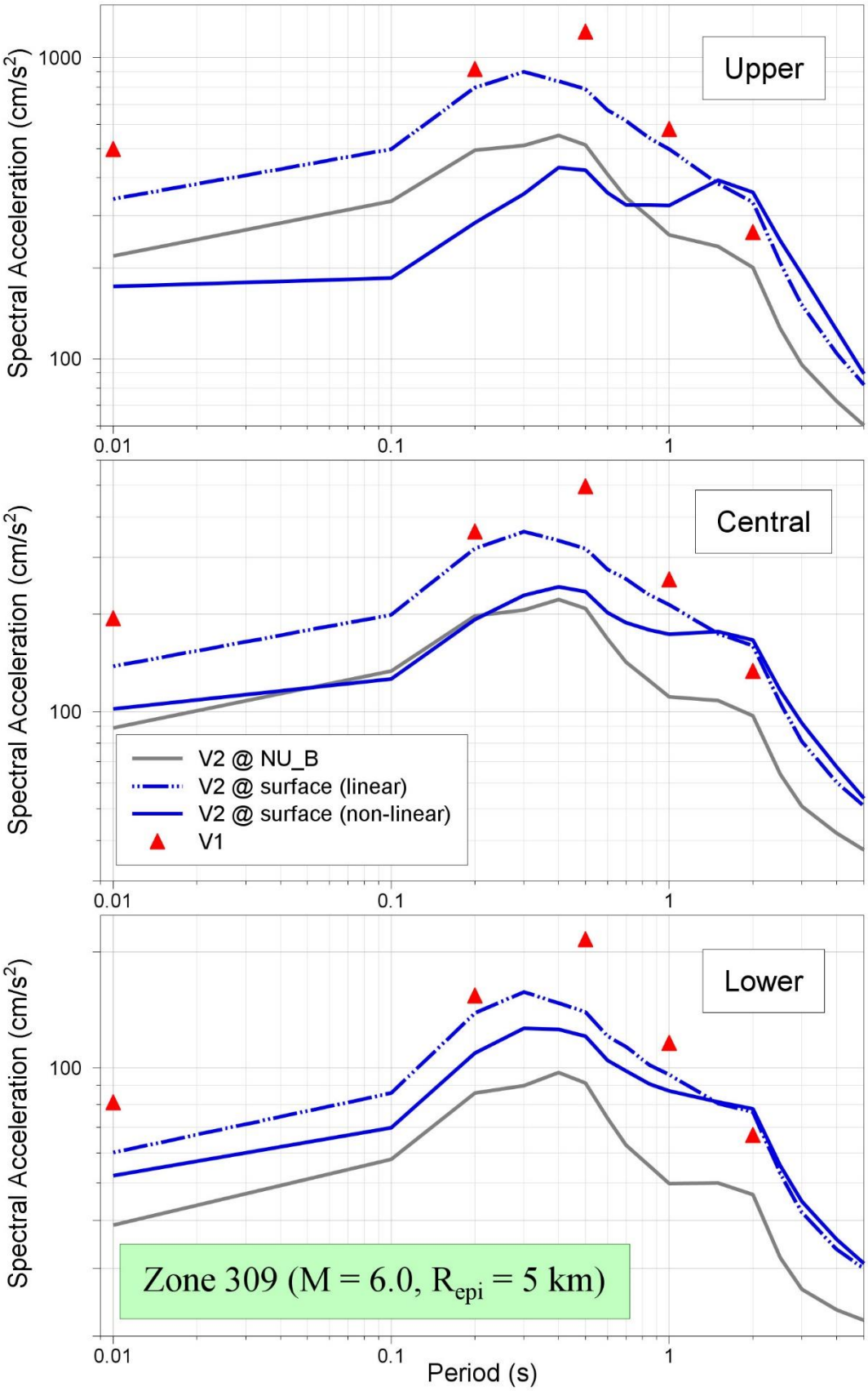

Figure 11.126. Comparison of median predicted response spectral accelerations from the V1 and V2 models for Zone 309 due to an earthquake of **M** 6 at R_{epi} = 5 km

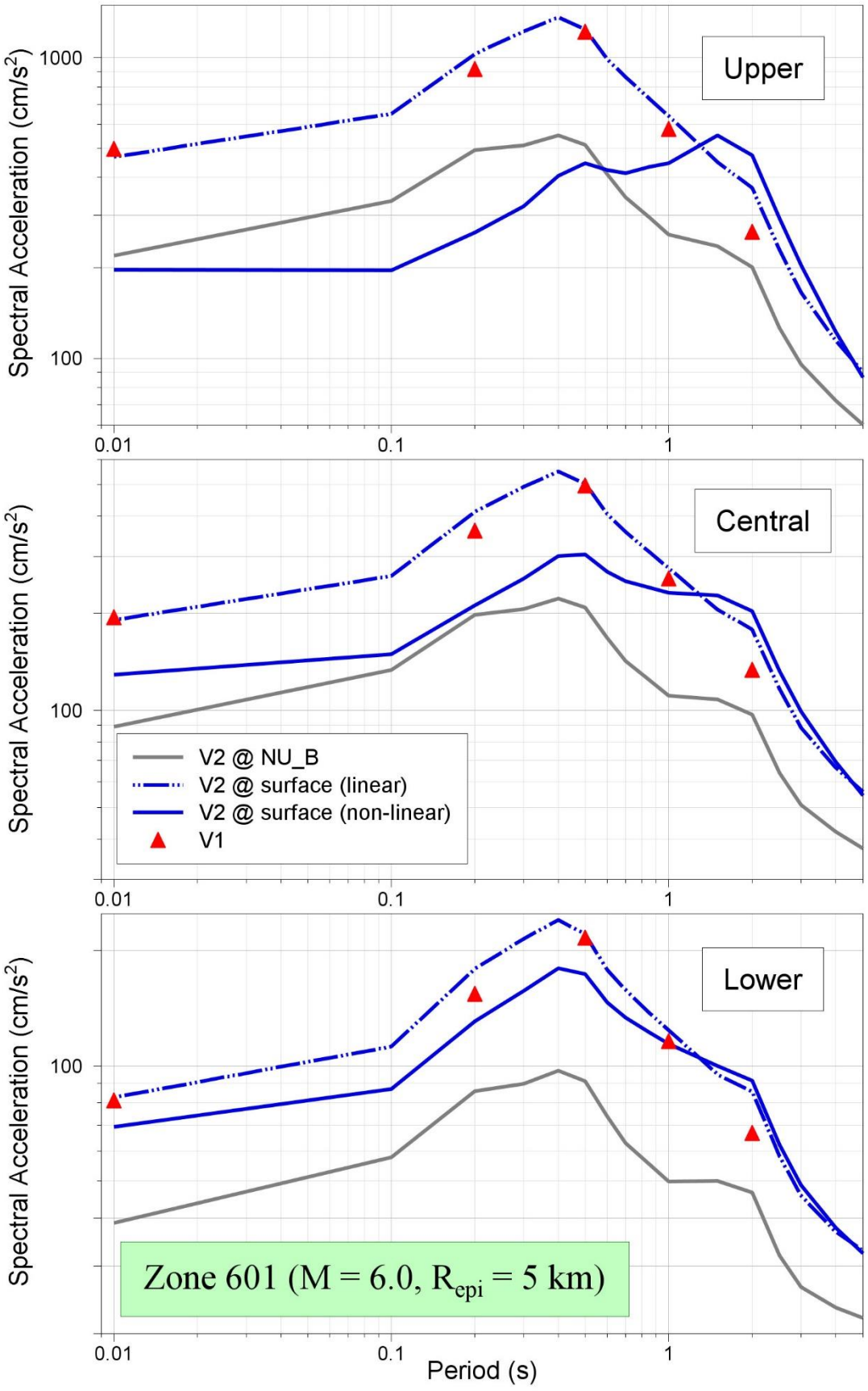

Figure 11.127. Comparison of median predicted response spectral accelerations from the V1 and V2 models for Zone 601 due to an earthquake of **M** 6 at R_{epi} = 5 km

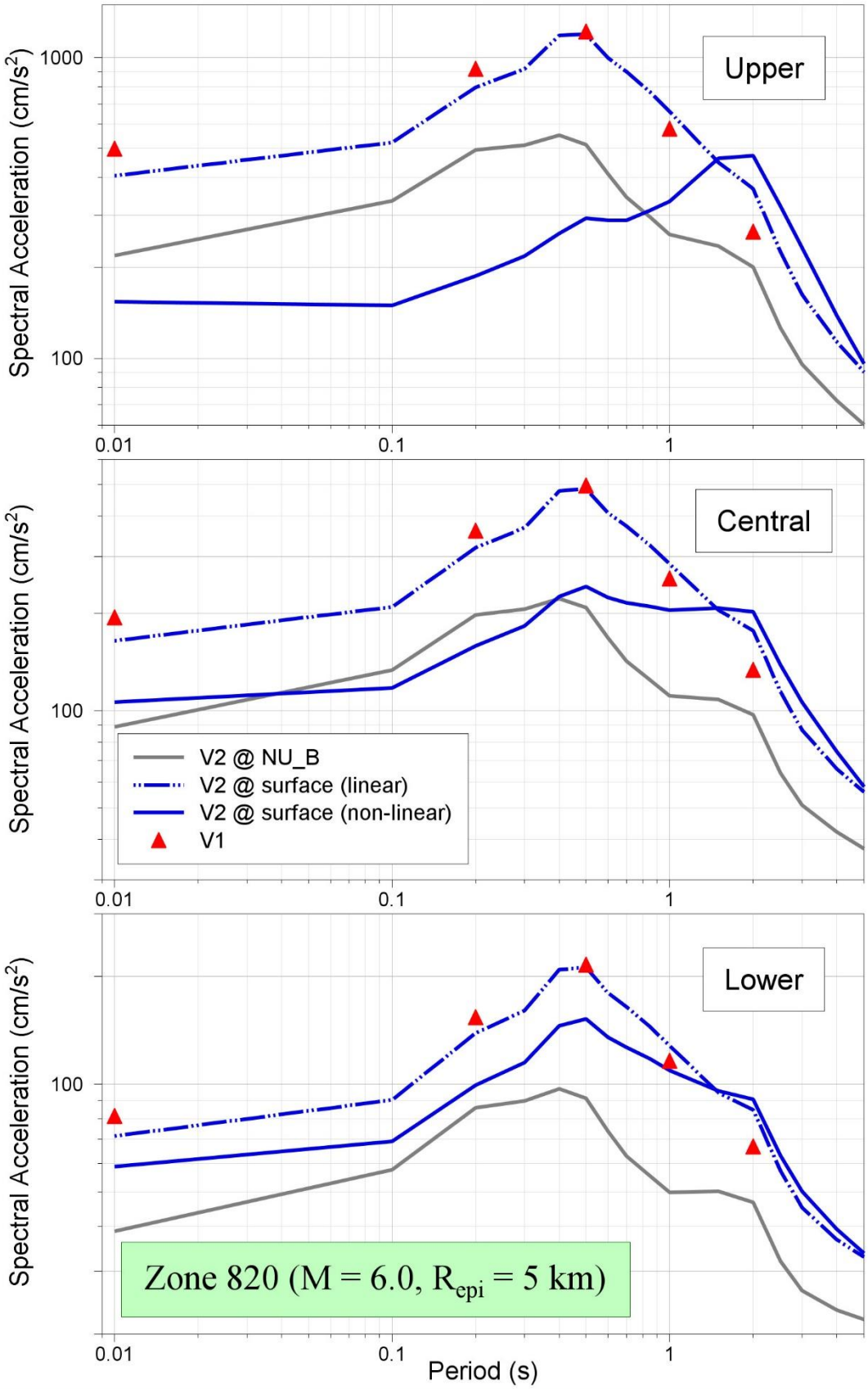

Figure 11.128. Comparison of median predicted response spectral accelerations from the V1 and V2 models for Zone 820 due to an earthquake of **M** 6 at R_{epi} = 5 km

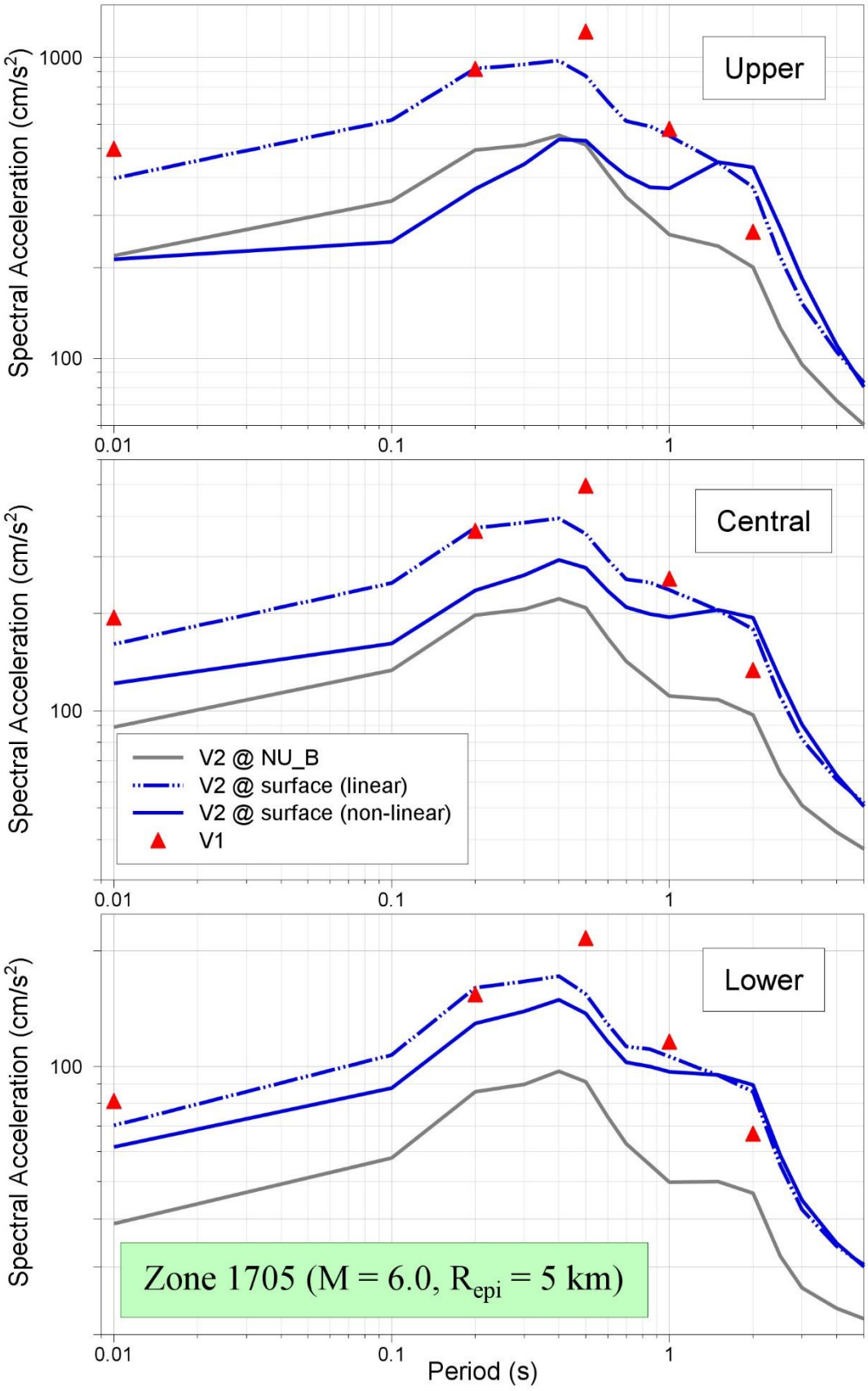

Figure 11.129. Comparison of median predicted response spectral accelerations from the V1 and V2 models for Zone 1705 due to an earthquake of **M** 6 at R_{epi} = 5 km

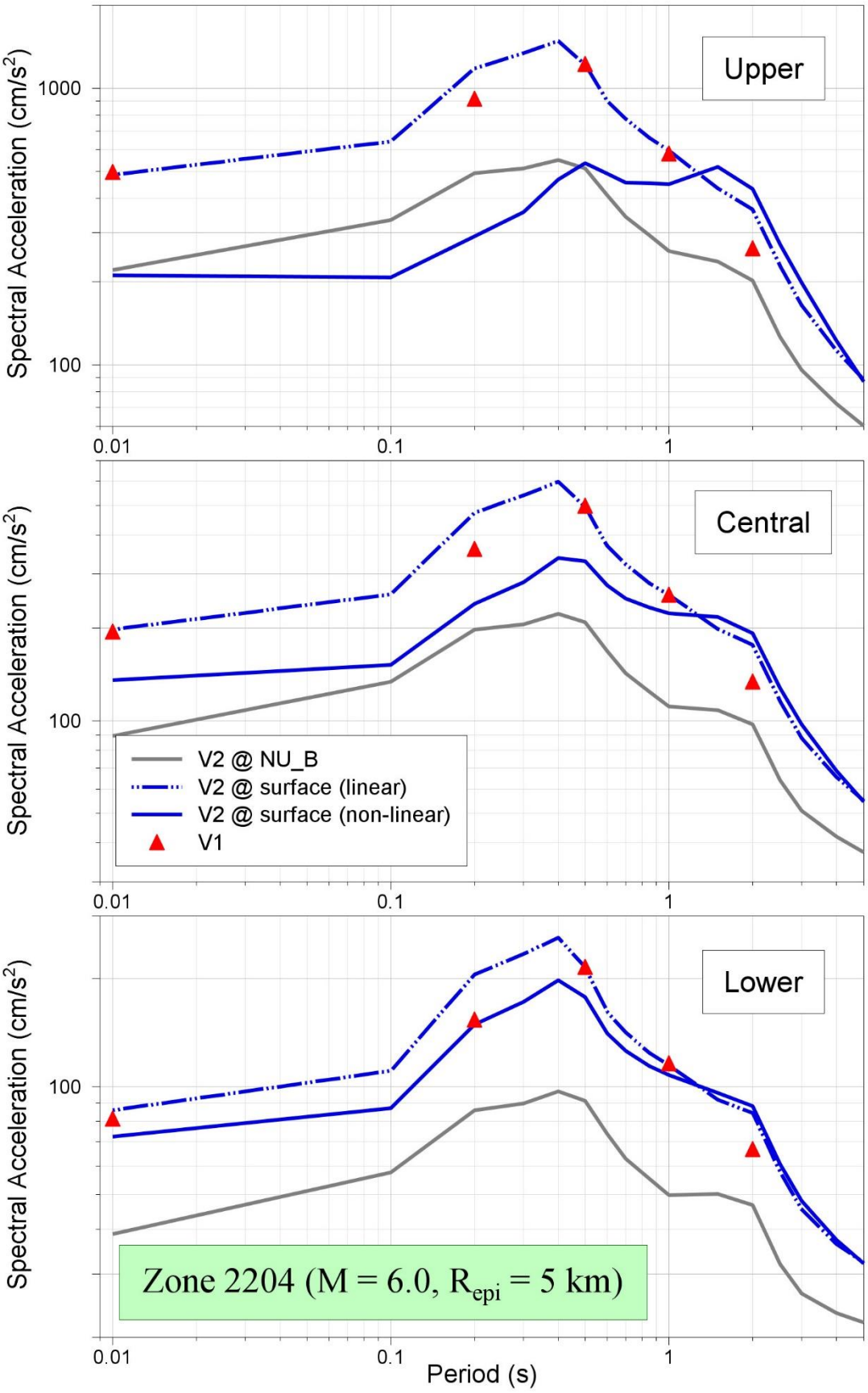

Figure 11.130. Comparison of median predicted response spectral accelerations from the V1 and V2 models for Zone 2204 due to an earthquake of **M** 6 at R_{epi} = 5 km

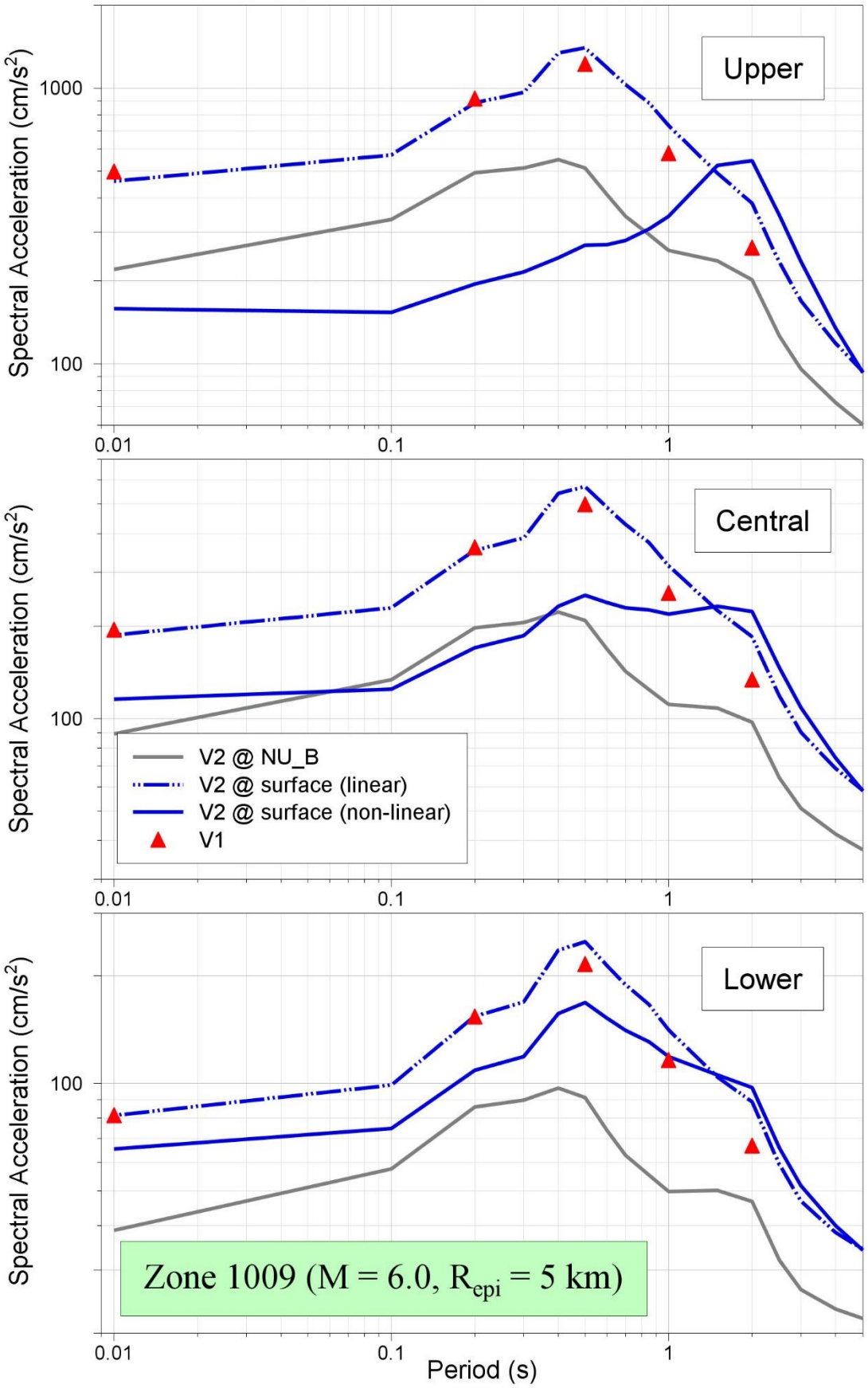

Figure 11.131. Comparison of median predicted response spectral accelerations from the V1 and V2 models for Zone 1009 due to an earthquake of **M** 6 at R_{epi} = 5 km

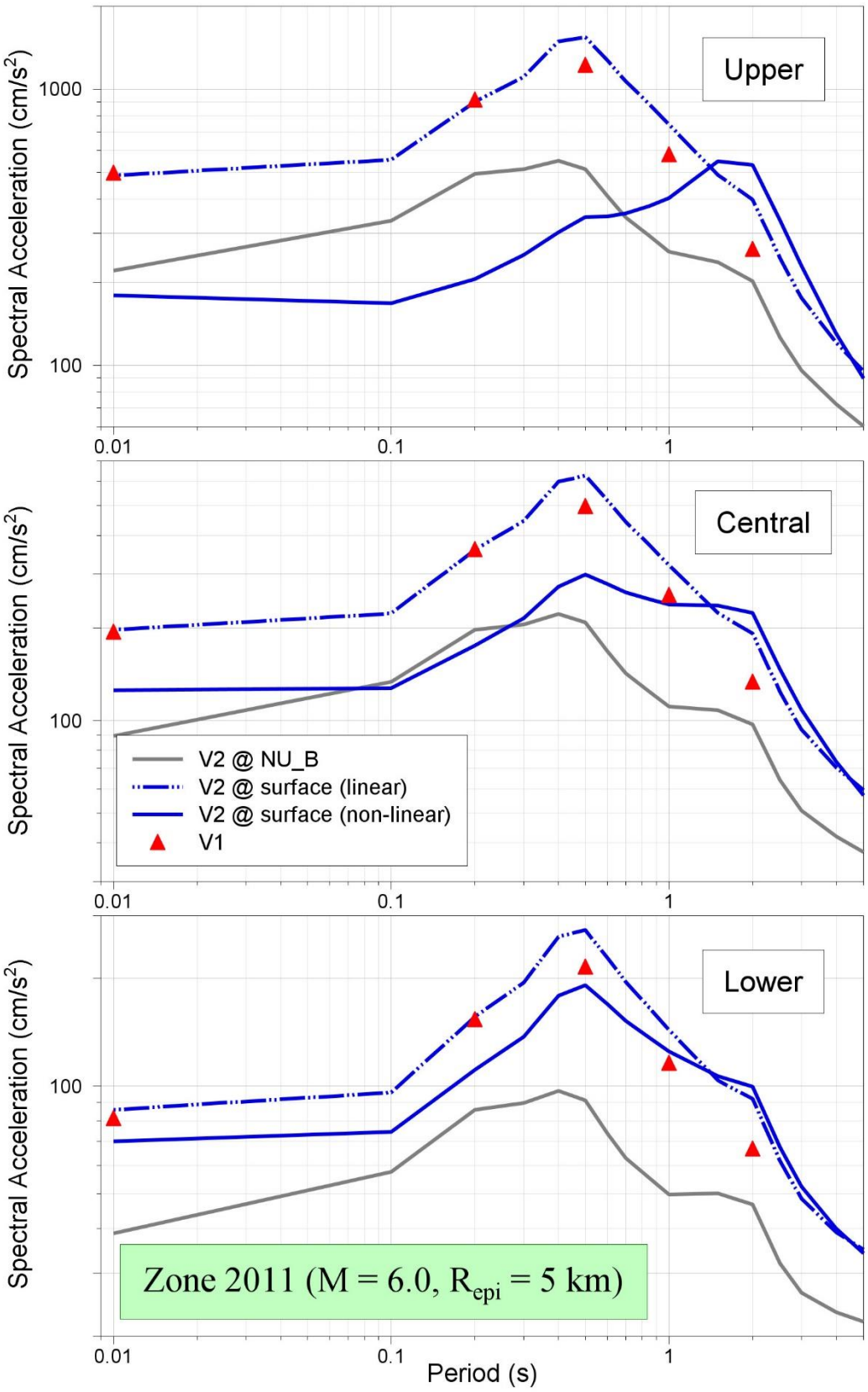

Figure 11.132. Comparison of median predicted response spectral accelerations from the V1 and V2 models for Zone 2011 due to an earthquake of **M** 6 at R_{epi} = 5 km

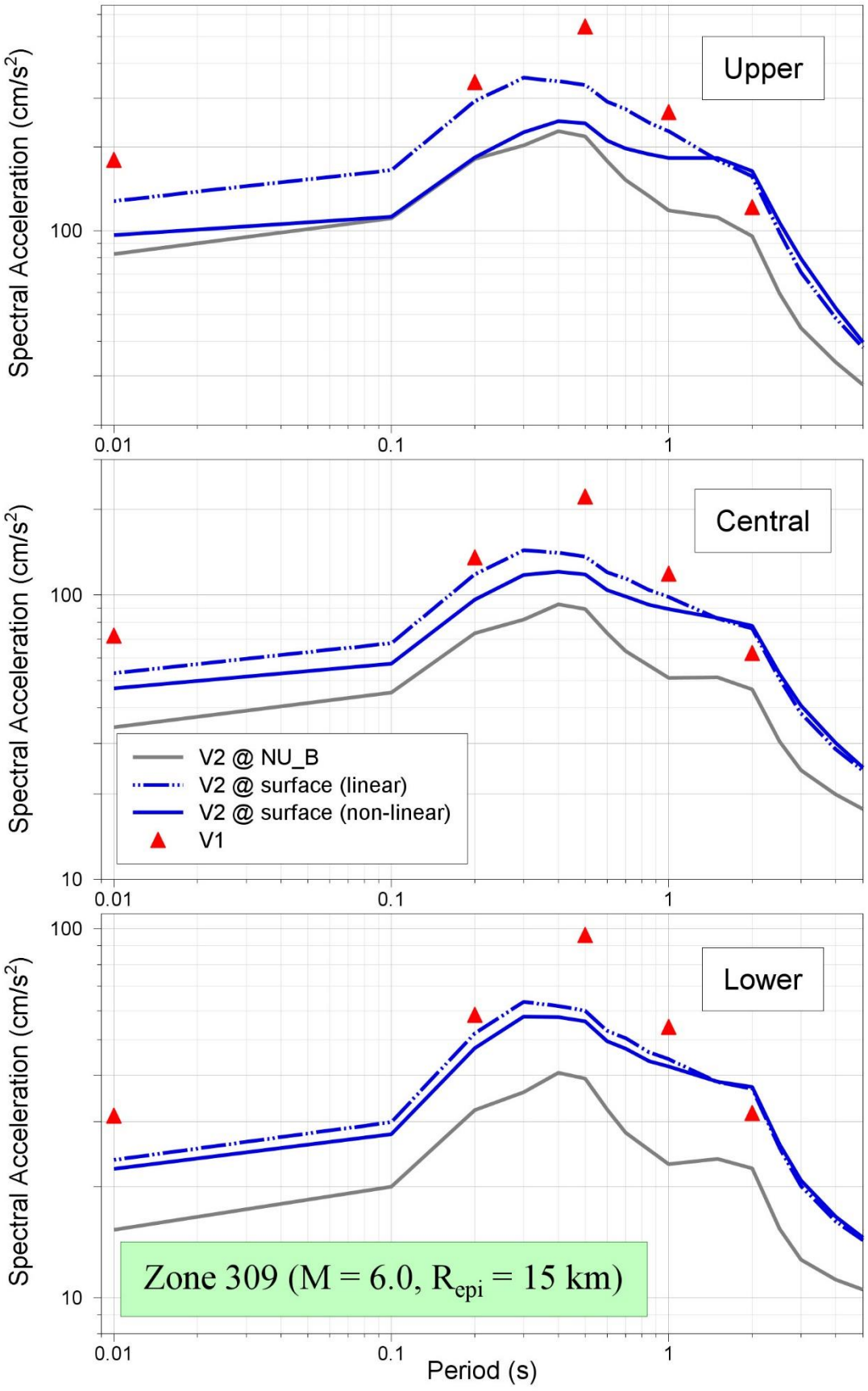

Figure 11.133. Comparison of median predicted response spectral accelerations from the V1 and V2 models for Zone 309 due to an earthquake of **M** 6 at R_{epi} = 15 km

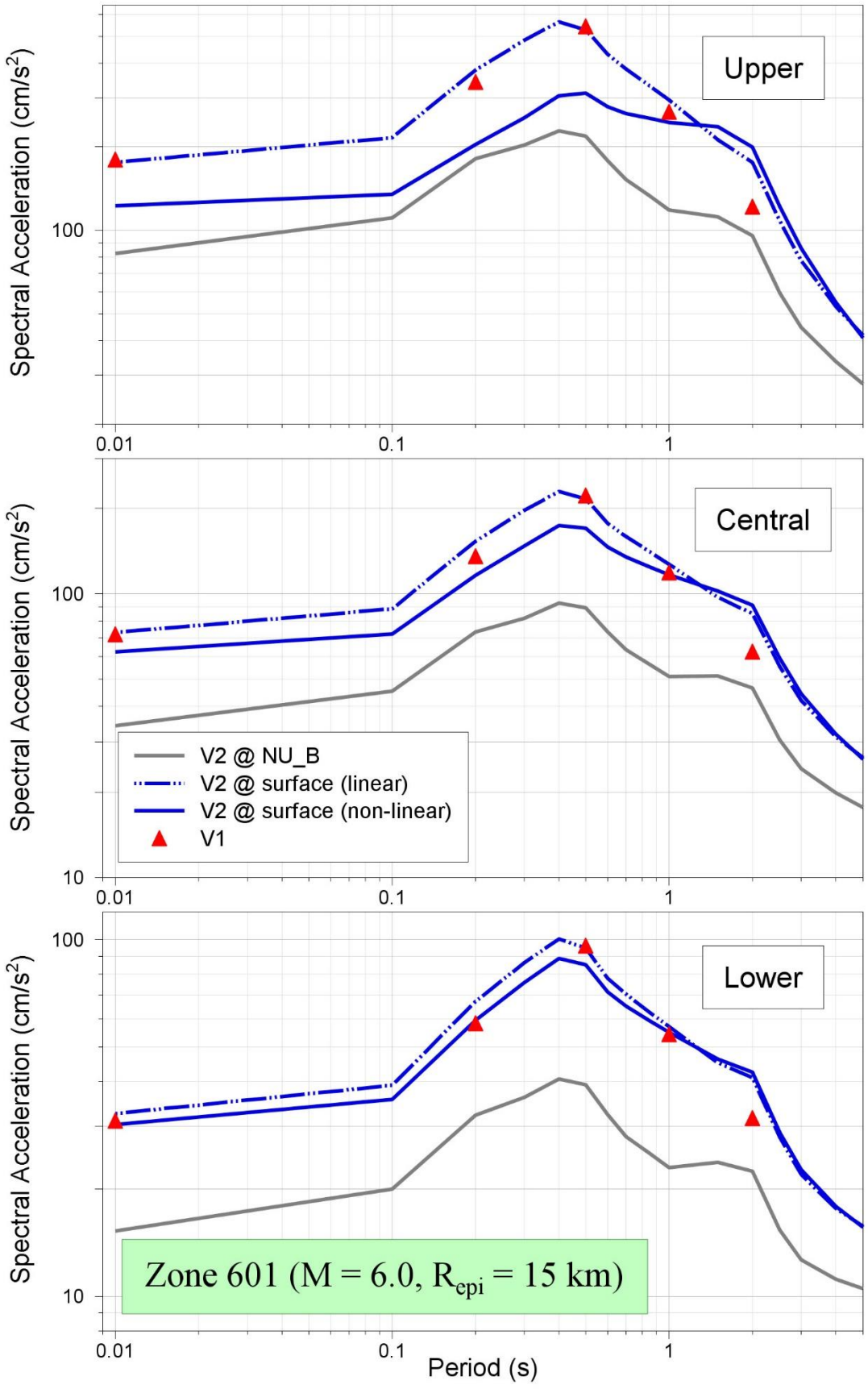

Figure 11.134. Comparison of median predicted response spectral accelerations from the V1 and V2 models for Zone 601 due to an earthquake of **M** 6 at R_{epi} = 15 km

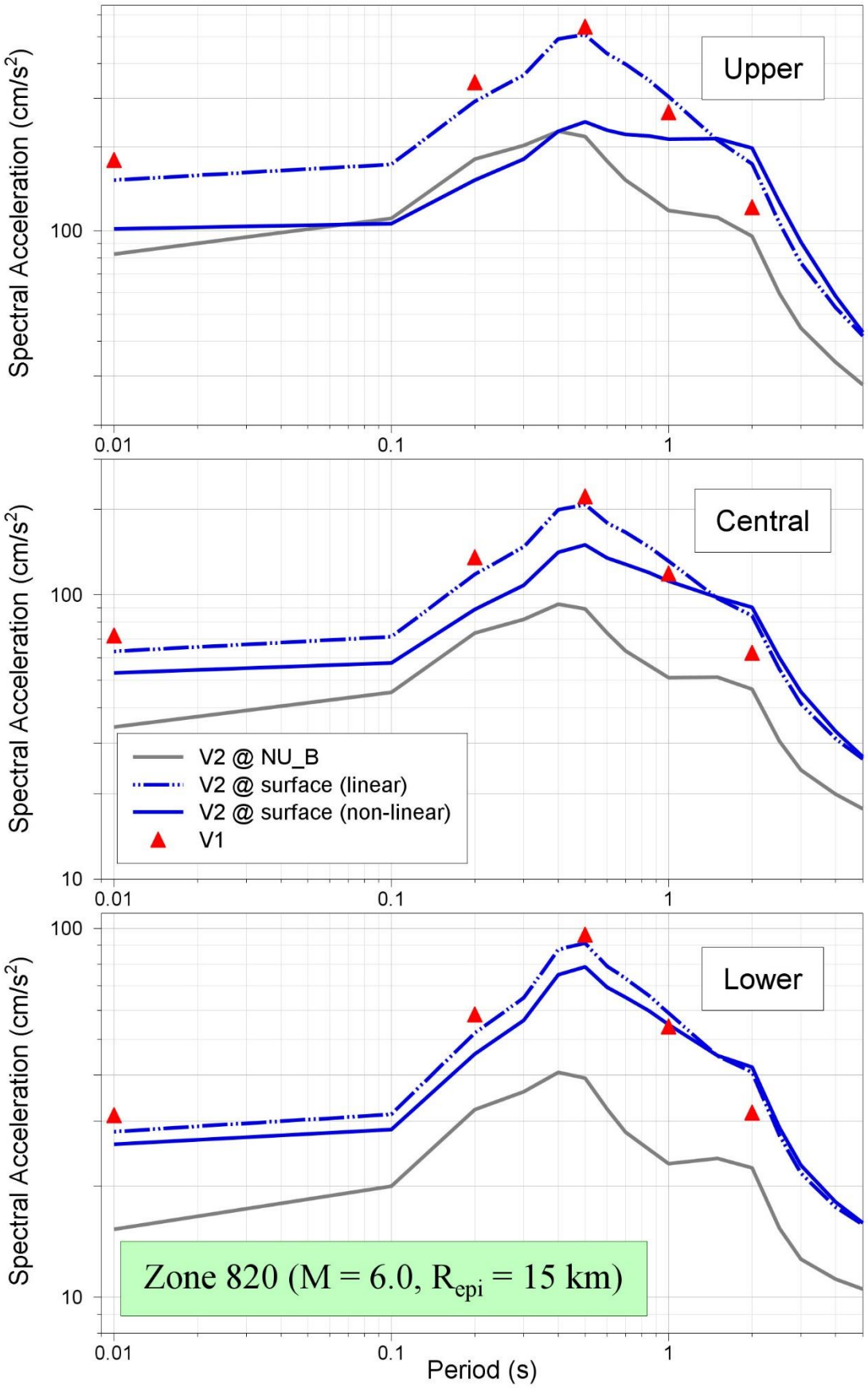

Figure 11.135. Comparison of median predicted response spectral accelerations from the V1 and V2 models for Zone 820 due to an earthquake of **M** 6 at R_{epi} = 15 km

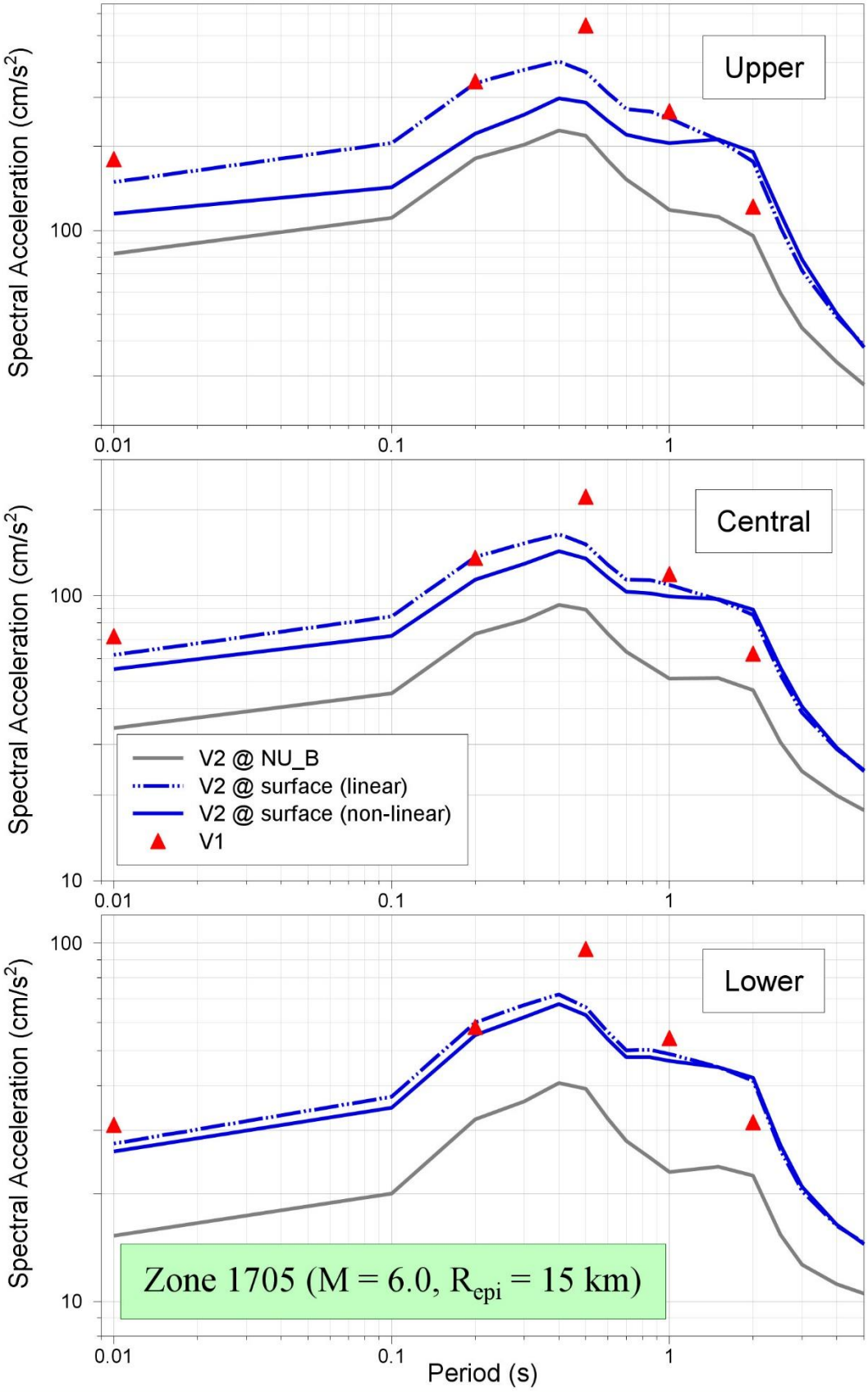

Figure 11.136. Comparison of median predicted response spectral accelerations from the V1 and V2 models for Zone 1705 due to an earthquake of **M** 6 at R_{epi} = 15 km

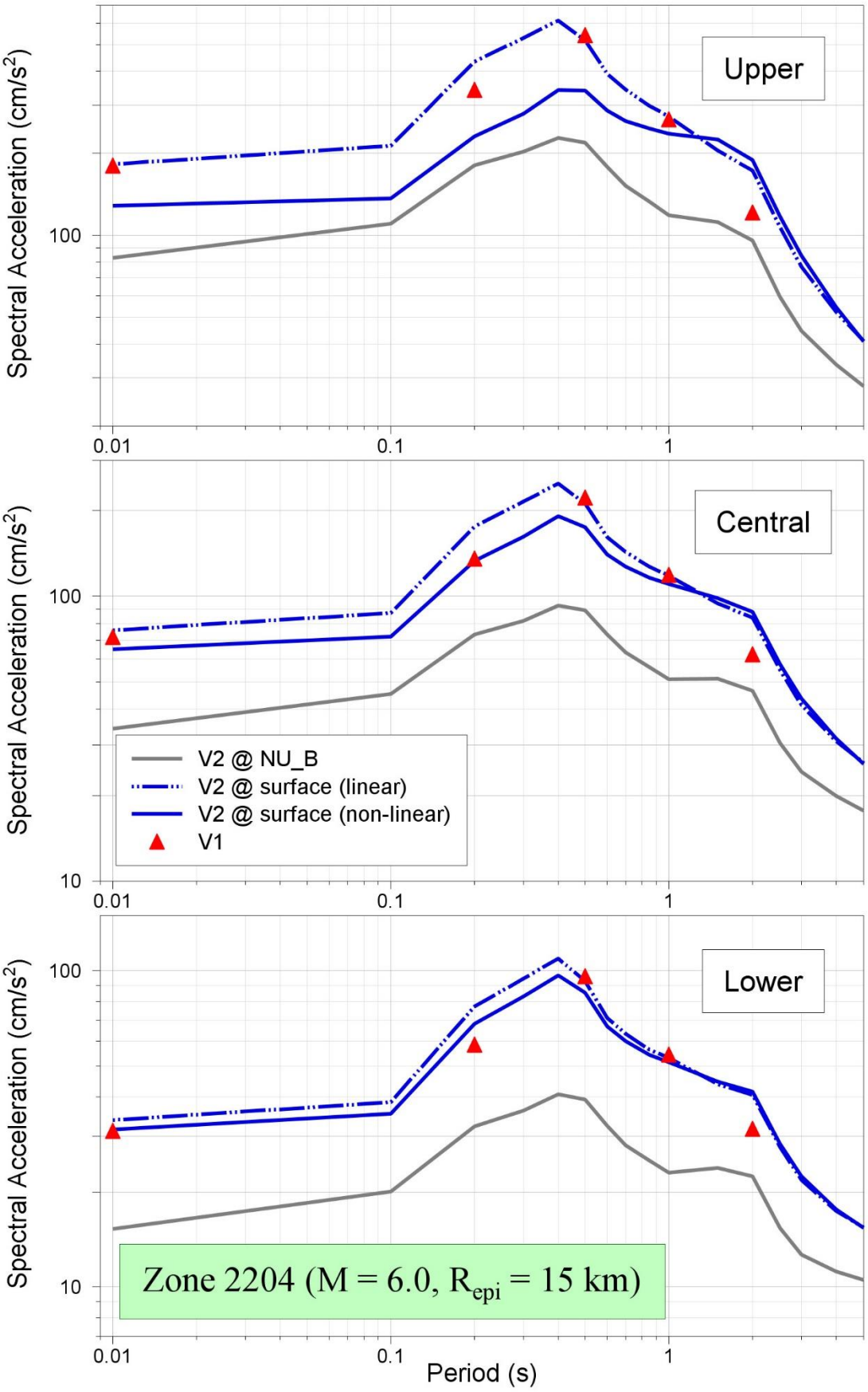

Figure 11.137. Comparison of median predicted response spectral accelerations from the V1 and V2 models for Zone 2204 due to an earthquake of **M** 6 at R_{epi} = 15 km

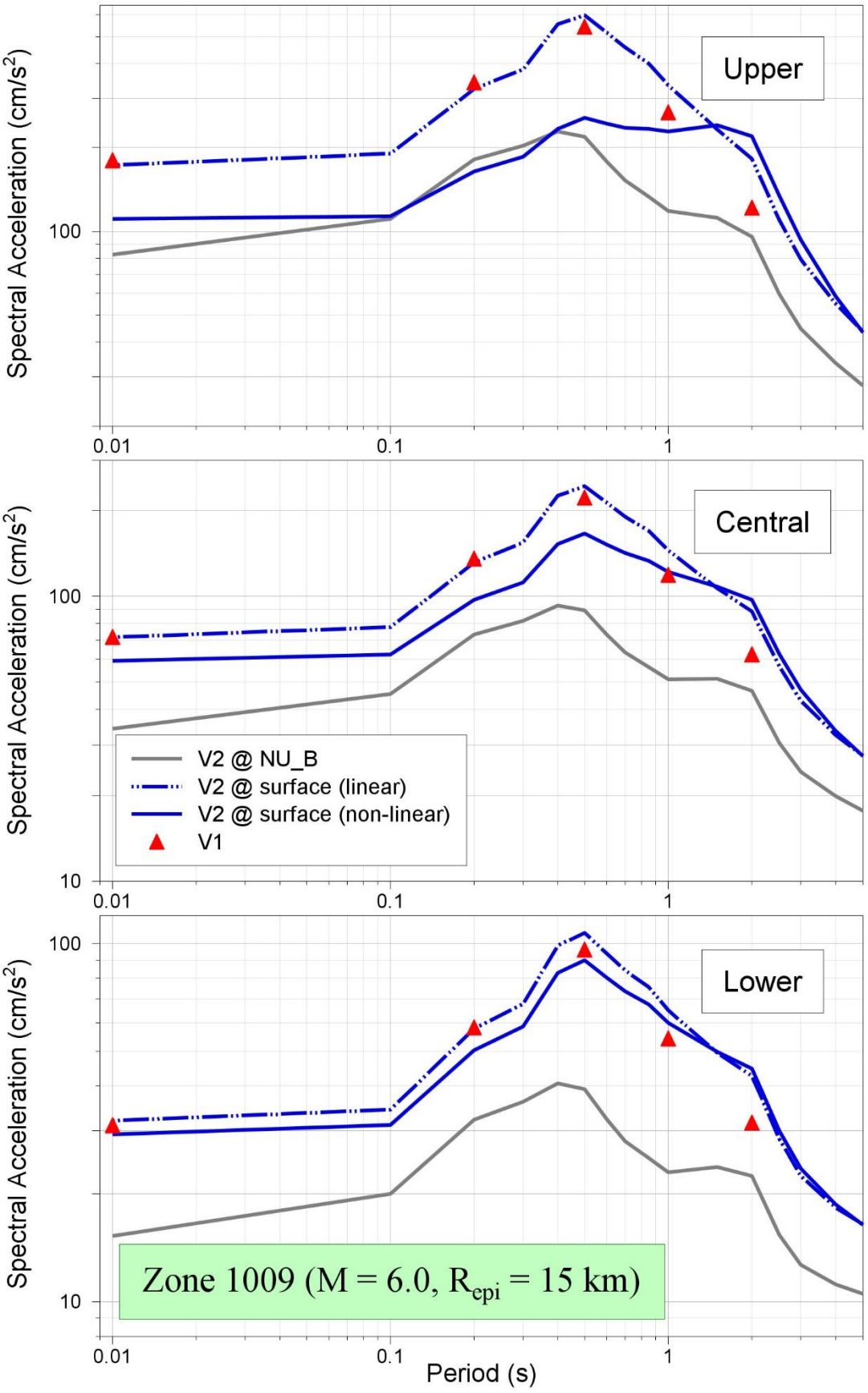

Figure 11.138. Comparison of median predicted response spectral accelerations from the V1 and V2 models for Zone 1009 due to an earthquake of **M** 6 at R_{epi} = 15 km

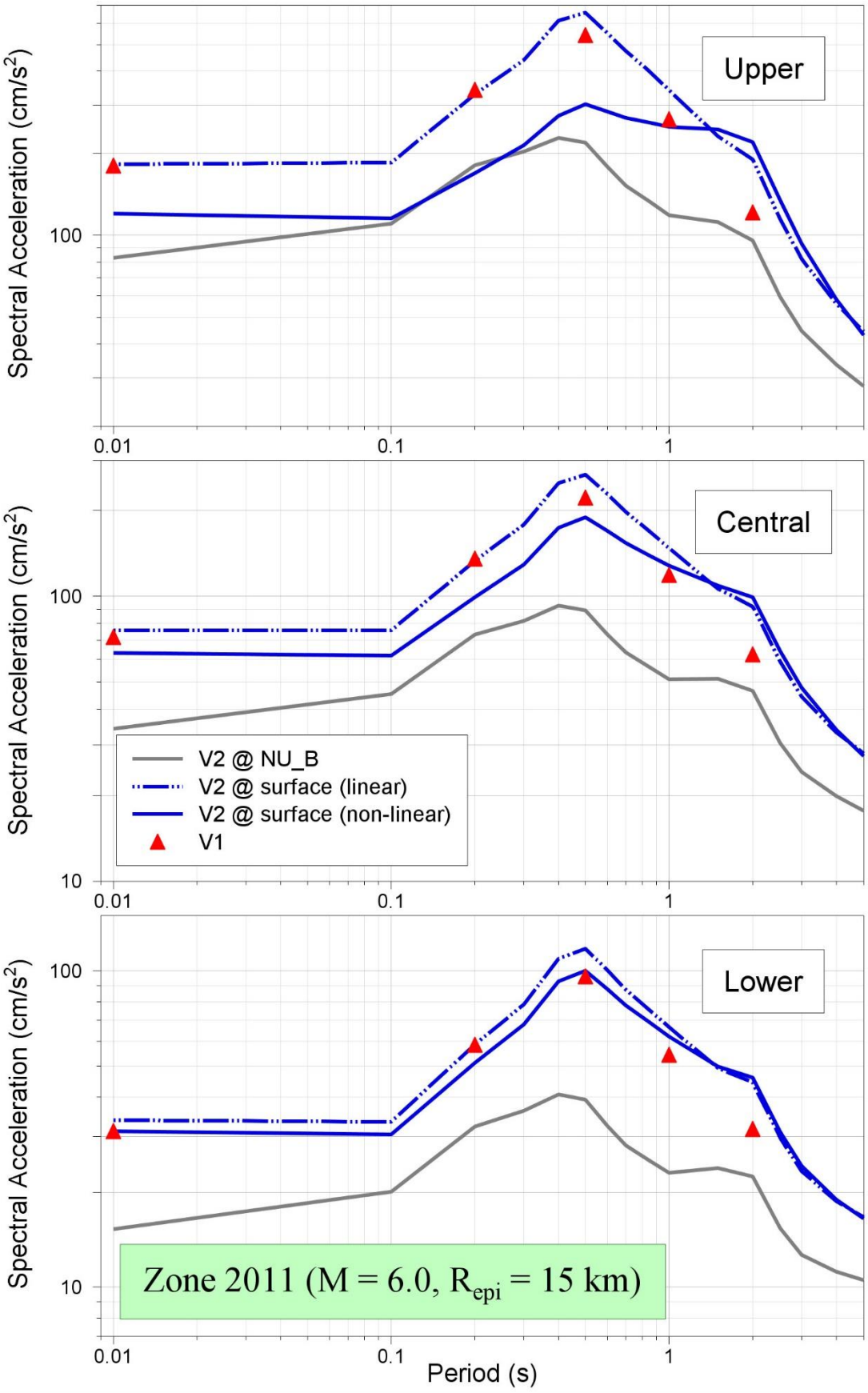

Figure 11.139. Comparison of median predicted response spectral accelerations from the V1 and V2 models for Zone 2011 due to an earthquake of **M** 6 at R_{epi} = 15 km

11.3. Period-to-period correlations

For the risk calculations, spectral ordinates at different response periods often need to be estimated at a single location in the Monte Carlo simulations. This requirement arises because there are building typologies with different characteristic vibration periods and some for which the buildings have different periods of vibration in the two orthogonal directions. Since the risk is being calculated for all buildings simultaneously, the spectral accelerations at each of the target response periods need to be estimated taking account of the correlation of the residuals at different periods. If the accelerations are calculated sampling the variability at each response period with the same epsilon values (*i.e*., the same number of standard deviations above or below the median predictions for the earthquake scenario in terms of magnitude and distance), this effectively treats the variability at all periods as being perfectly correlated. Various studies have shown that this is not the case and to avoid this unintended conservatism it has been proposed to generate response spectra taking account of the decreasing correlation with increasing separation of the periods (Baker & Cornell, 2006b). For this purpose, a model for the period-to-period correlation of residuals with respect to predicted median spectral accelerations is needed.

At this stage, rather than deriving a Groningen-specific model for this correlation matrix—which would be incomplete because of the maximum usable period limit of 1.5-2.0 seconds—it was decided to follow the same practice as used in the V1 risk model and adopt the correlation function from another study. For this purpose, we selected the model of Akkar *et al*. (2014b) derived from accelerograms of tectonic earthquakes in Europe and the Middle East and consistent with the GMPEs of Akkar *et al*. (2014a). The maximum response period for which this model provides coefficients is 4 seconds; for the additional target period considered in the V2 risk model of 5 seconds, the simple assumption is made that the values for 4 seconds can be maintained constant at longer periods. For completeness, the correlation matrix for total residuals of spectral accelerations at the first 15 target periods is presented in Table 11.1.

Table 11.1. Period-to-period correlation matrix for residuals of spectral accelerations at 15 target periods adopted from Akkar et al. (2014*b*)

T (s)	0.01	0.1	0.2	0.3	0.4	0.5	0.6	0.7	0.85	1	1.5	2	2.5	3	4
0.01	1.000	0.935	0.897	0.831	0.774	0.721	0.670	0.633	0.587	0.542	0.468	0.460	0.441	0.409	0.328
0.1	0.935	1.000	0.864	0.730	0.647	0.572	0.510	0.468	0.421	0.379	0.318	0.321	0.306	0.286	0.246
0.2	0.897	0.864	1.000	0.883	0.789	0.709	0.637	0.587	0.524	0.472	0.373	0.355	0.337	0.321	0.267
0.3	0.831	0.730	0.883	1.000	0.922	0.841	0.773	0.721	0.661	0.607	0.485	0.453	0.431	0.400	0.307
0.4	0.774	0.647	0.789	0.922	1.000	0.937	0.871	0.821	0.761	0.706	0.575	0.529	0.505	0.467	0.355
0.5	0.721	0.572	0.709	0.841	0.937	1.000	0.954	0.905	0.845	0.793	0.665	0.615	0.592	0.547	0.425
0.6	0.670	0.510	0.637	0.773	0.871	0.954	1.000	0.964	0.912	0.863	0.738	0.684	0.657	0.603	0.493
0.7	0.633	0.468	0.587	0.721	0.821	0.905	0.964	1.000	0.957	0.908	0.786	0.725	0.696	0.632	0.517
0.85	0.587	0.421	0.524	0.661	0.761	0.845	0.912	0.957	1.000	0.966	0.847	0.786	0.753	0.694	0.576
1	0.542	0.379	0.472	0.607	0.706	0.793	0.863	0.908	0.966	1.000	0.905	0.843	0.811	0.752	0.635
1.5	0.468	0.318	0.373	0.485	0.575	0.665	0.738	0.786	0.847	0.905	1.000	0.941	0.907	0.855	0.735
2	0.460	0.321	0.355	0.453	0.529	0.615	0.684	0.725	0.786	0.843	0.941	1.000	0.968	0.914	0.799
2.5	0.441	0.306	0.337	0.431	0.505	0.592	0.657	0.696	0.753	0.811	0.907	0.968	1.000	0.958	0.863
3	0.409	0.286	0.321	0.400	0.467	0.547	0.603	0.632	0.694	0.752	0.855	0.914	0.958	1.000	0.931
4	0.328	0.246	0.267	0.307	0.355	0.425	0.493	0.517	0.576	0.635	0.735	0.799	0.863	0.931	1.000

As noted in the previous section, these period-to-period correlations are applied to the full variability and therefore to all the variability components listed in Eq.(11.2). A pending exercise is to explore whether this correlation matrix is consistent with Groningen V2 GMPE and recordings (see Section 13.5).

11.4. Vertical-to-horizontal ratios

The fragility functions for the Groningen building stock are defined only in terms of horizontal ground motions but for the masonry and pre-cast concrete structures, it is thought that vertical motion may have a significant influence on the response. Therefore, three-dimensional dynamic input to the analyses of the structures will ultimately be required and to this end estimates are required of the vertical motions expected in the Groningen field. In order to ensure that the vertical components are appropriately selected and scaled, V/H response spectral ratios consistent with the seismicity and ground conditions need to be defined. Past practice has often defined the vertical spectrum as simply a scalar product—the factor usually being of the order of ⅔—of the horizontal spectrum, but it is now recognised that the V/H ratio varies with response period and that the vertical spectrum has a distinct shape. Moreover, it is recognised that the V/H ratio varies with magnitude, style-of-faulting, distance and site classification. Several of the ground-motion recordings from the Groningen field show high ratios of the vertical to horizontal (geometric mean) components of motion (Figure 11.140). If this pattern persists at large magnitudes, appreciable levels of vertical loading may be expected, for which reason a model for the vertical accelerations is important.

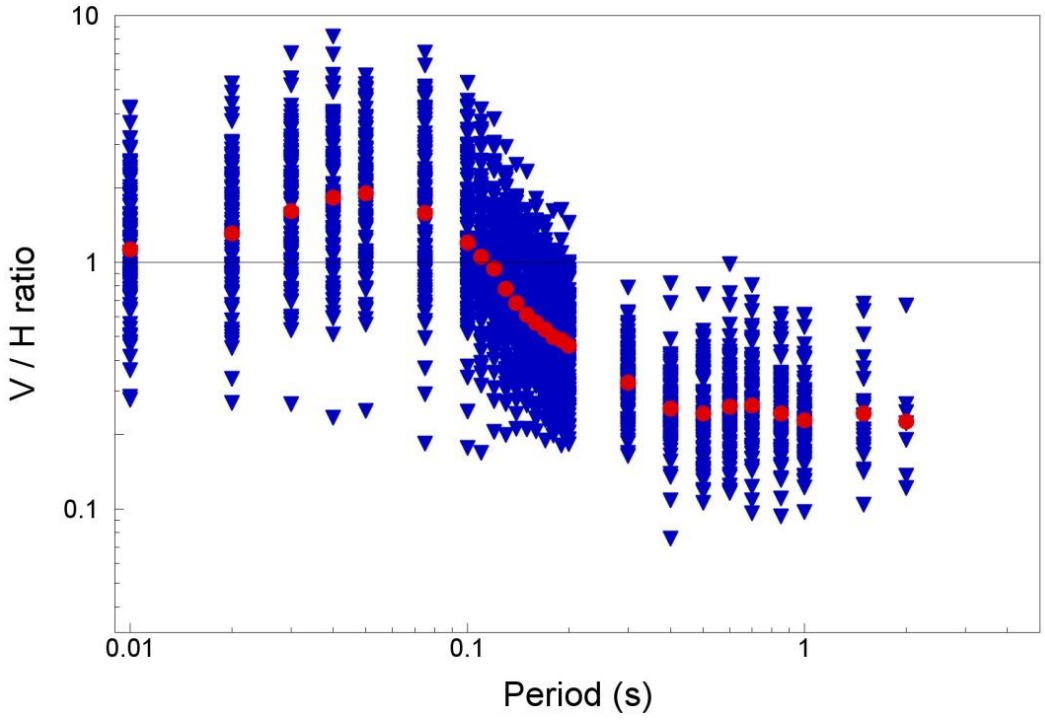

Figure 11.140. V/H rations of spectral accelerations from the Groningen recordings; the red dots show the average ratio at each oscillator period

The V/H ratios at a few selected periods are plotted as a function of magnitude and distance in Figures 11.141 to 11.143, from which no clear trend with magnitude can be discerned, although this is not unexpected given the very limited magnitude range covered by the recordings. There are also at best only weak trends with distance: at very short periods, there is a perceptible drop in the largest ratios with increasing distance but not definitive trend that can be seen through the complete dataset.

One option for estimating vertical accelerations is to develop GMPEs for the vertical component (*e.g.,* Campbell & Bozorgnia, 2003; Bozorgnia & Campbell, 2015; Stewart *et al.*, 2015) but conducting PSHA separately for the horizontal and vertical components of motion can lead to different dominant scenarios contributing to the hazard estimates in the two directions (*e.g*., Bommer et al., 2011). Our preferred approach for generating vertical response spectra is to apply vertical-to-horizontal (V/H) ratios to the horizontal response spectra defined at the ground surface. Given the very limited magnitude range covered by the Groningen recordings, it is unlikely that a usable V/H prediction model could be derived directly from the local data. Therefore, the approach adopted in the first instance is to explore the fit of existing models for the prediction of V/H ratios to the Groningen data, and if no model is found to be adequate in its original state, then the possibility of using the local recordings to adjust the equations will be explored.

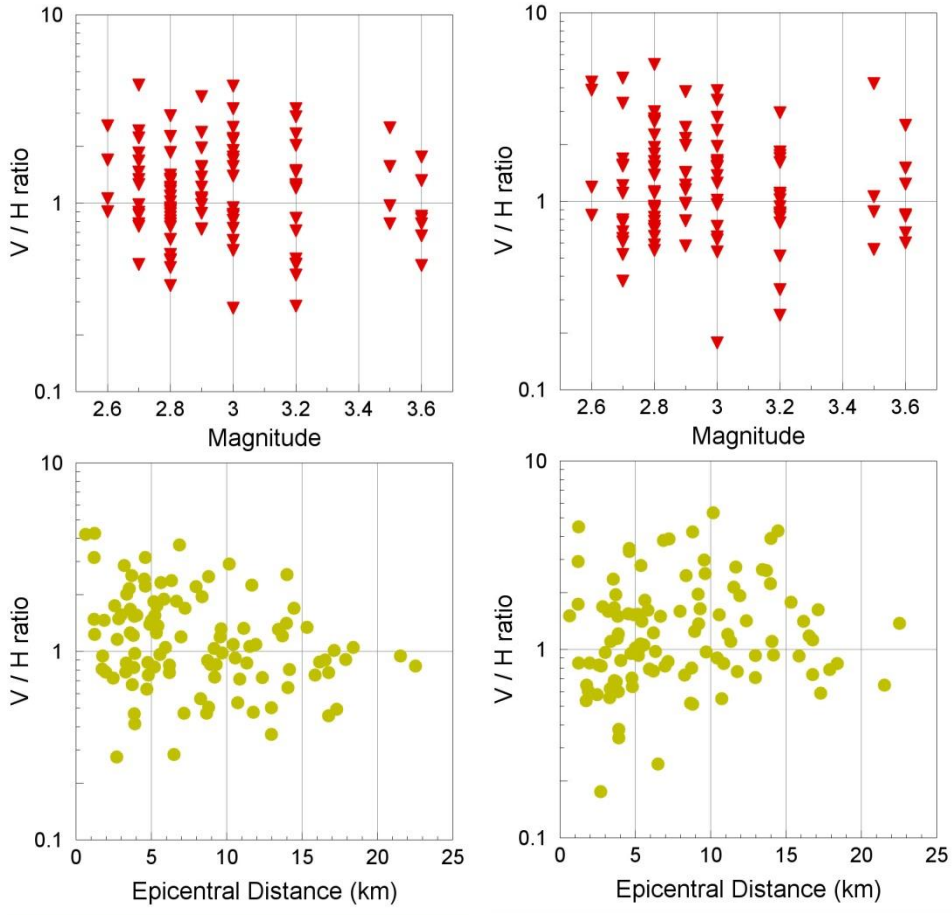

Figure 11.141. Vertical-to-horizontal component ratios against magnitude and distance for T = 0.01s (*left*) and T = 0.1s (*right)*.

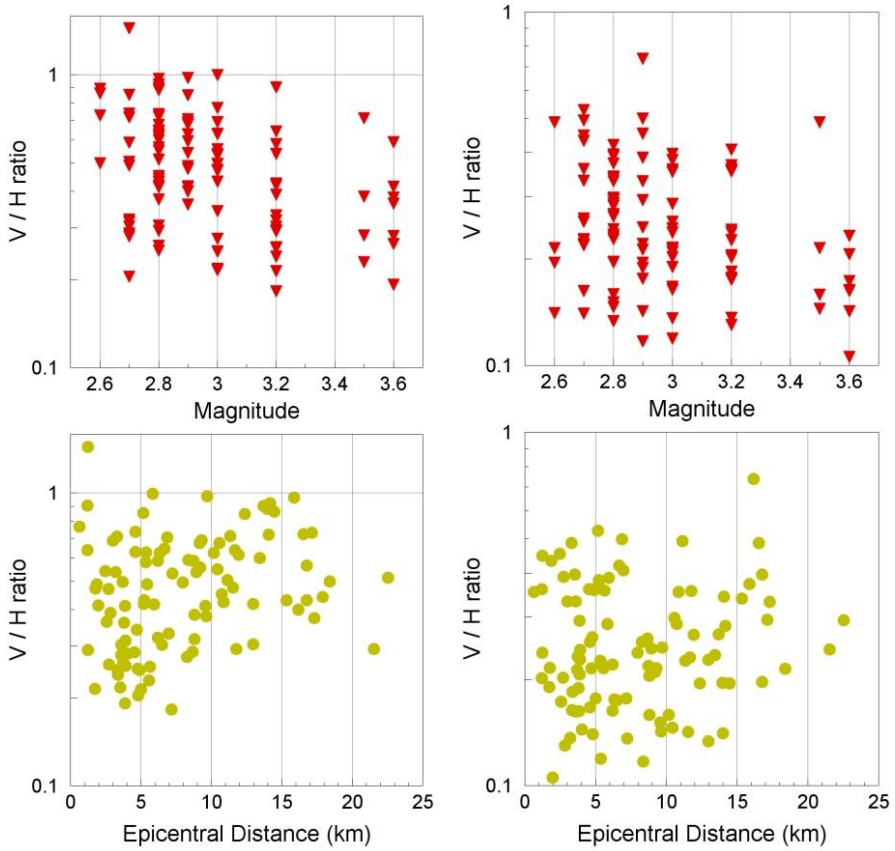

Figure 11.142. Vertical-to-horizontal component ratios against magnitude and distance for T = 0.2s (*left*) and T = 0.5s (*right)*.

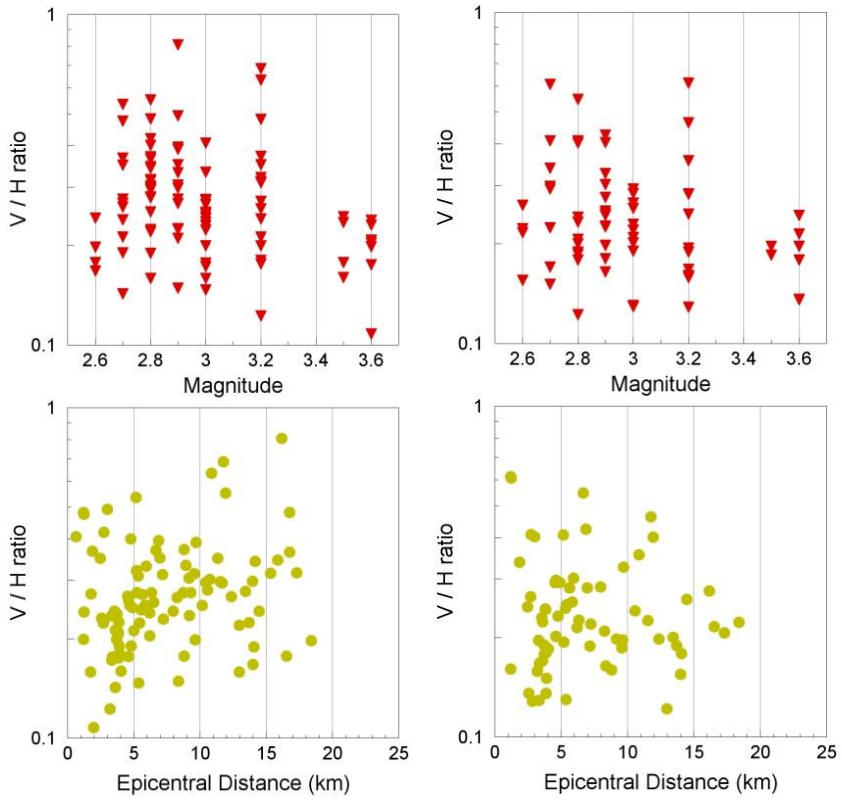

Figure 11.143. Vertical-to-horizontal component ratios against magnitude and distance for T = 0.7s (*left*) and T = 1s (*right)*.

There is a small number of published models for the prediction of V/H ratios of response spectral ordinates but we only consider two of these, namely the equations of Gülerce & Abrahamson (2011) and Akkar *et al*. (2014b), which have the merits of including V_{S30} as an explicit prediction parameter and also modelling non-linear site response. The residuals of the V/H ratio were calculated using these two models and while neither performed well enough to be adopted for the Groningen application, the performance of the Akkar *et al.* (2014b) model was better, particular at longer periods. The European model may, in any case, have been a preferred candidate given that it is applicable from magnitude **M** 4 whereas the model of Gülerce & Abrahamson (2011) is only applicable to earthquakes of magnitude 5 and greater.

The residuals calculated with Akkar *et al.* (2014b) equations are shown in Figures 11.144 to 11.152, with the standard deviations of the original GMPE. These are calculated using the R_{epi} values for each recordings as R_{JB} in the equations, and applying the V_{S30} values at the recording stations from Section 4.2. The predicted ratios are obtained as the average for those for normal and strike-slip earthquakes, since both styles of faulting are considered possible in the Groningen field. The residuals are shown as between-event residuals plotted against magnitude and within-event residuals plotted against epicentral distance. The general indication is gross under-estimation at shorter periods and mild over-estimation at longer periods. The most interesting features is that from periods of about 0.3-0.4 seconds, the event terms become very small and there is no discernible trend with magnitude, whereas at short periods there is a consistent positive offset in the event terns. Some trends with distance are visible in the residuals but these are not particularly pronounced.

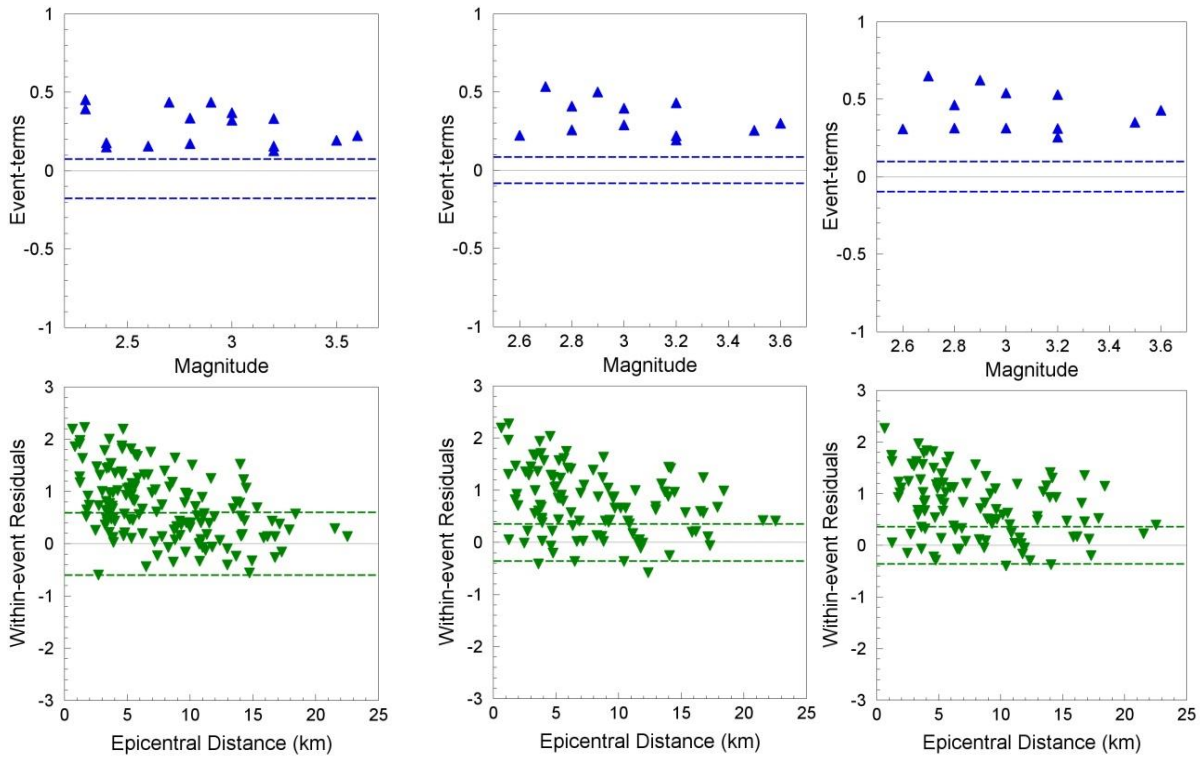

Figure 11.144. Residuals of V/H ratios of the Groningen database calculated with respect to the GMPEs of Akkar *et al.* (2014b) for periods of 0.01 s (*left*), 0.02 s (*centre*) and 0.03 s (*right*)

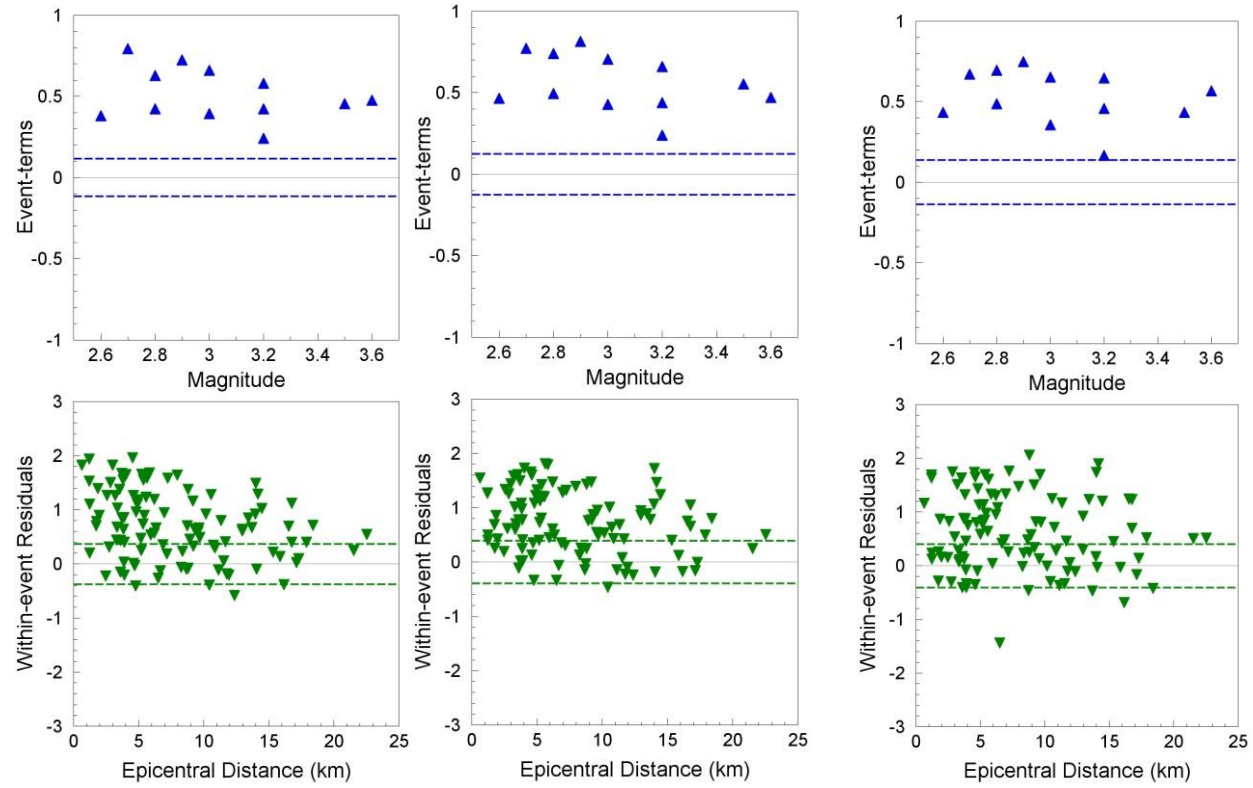

Figure 11.145. Residuals of V/H ratios of the Groningen database calculated with respect to the GMPEs of Akkar *et al.* (2014b) for periods of 0.04 s (*left*), 0.05 s (*centre*) and 0.075 s (*right*)

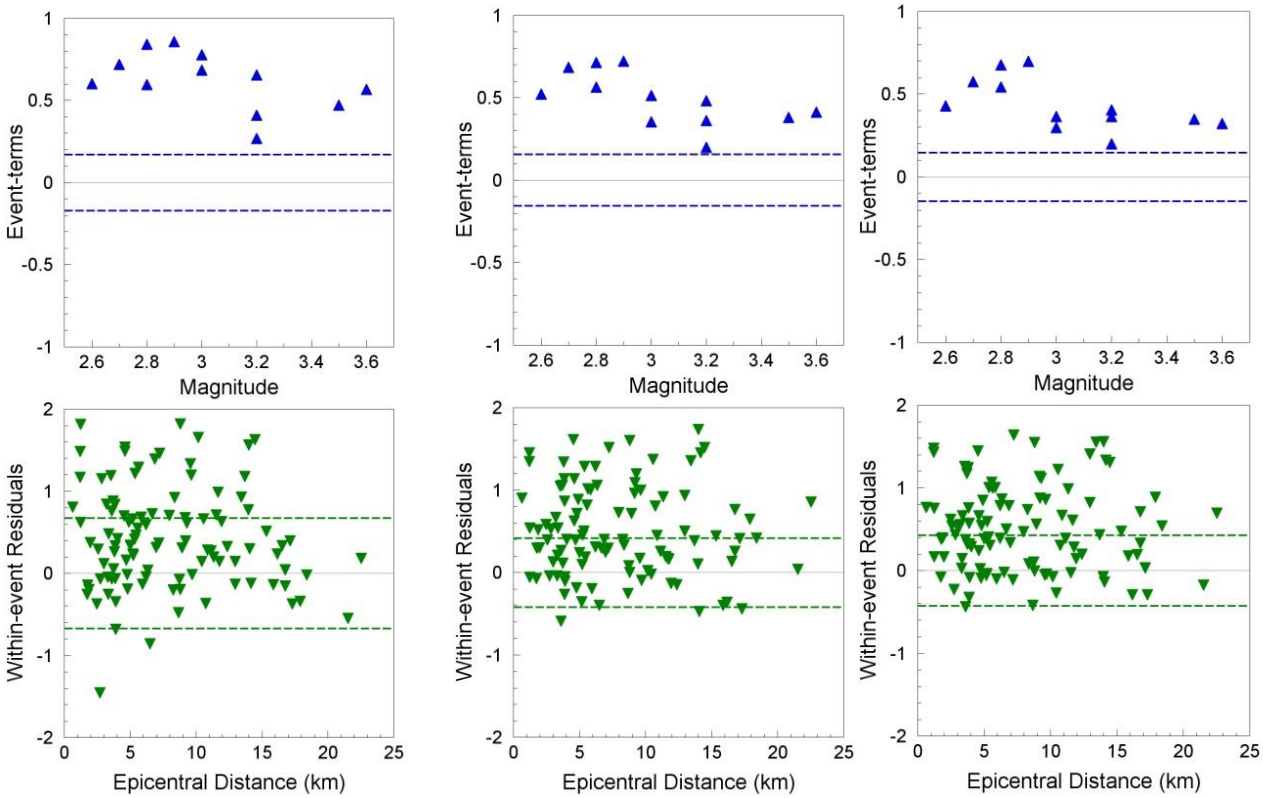

Figure 11.146. Residuals of V/H ratios of the Groningen database calculated with respect to the GMPEs of Akkar *et al.* (2014b) for periods of 0.10 s (*left*), 0.11 s (*centre*) and 0.12 s (*right*)

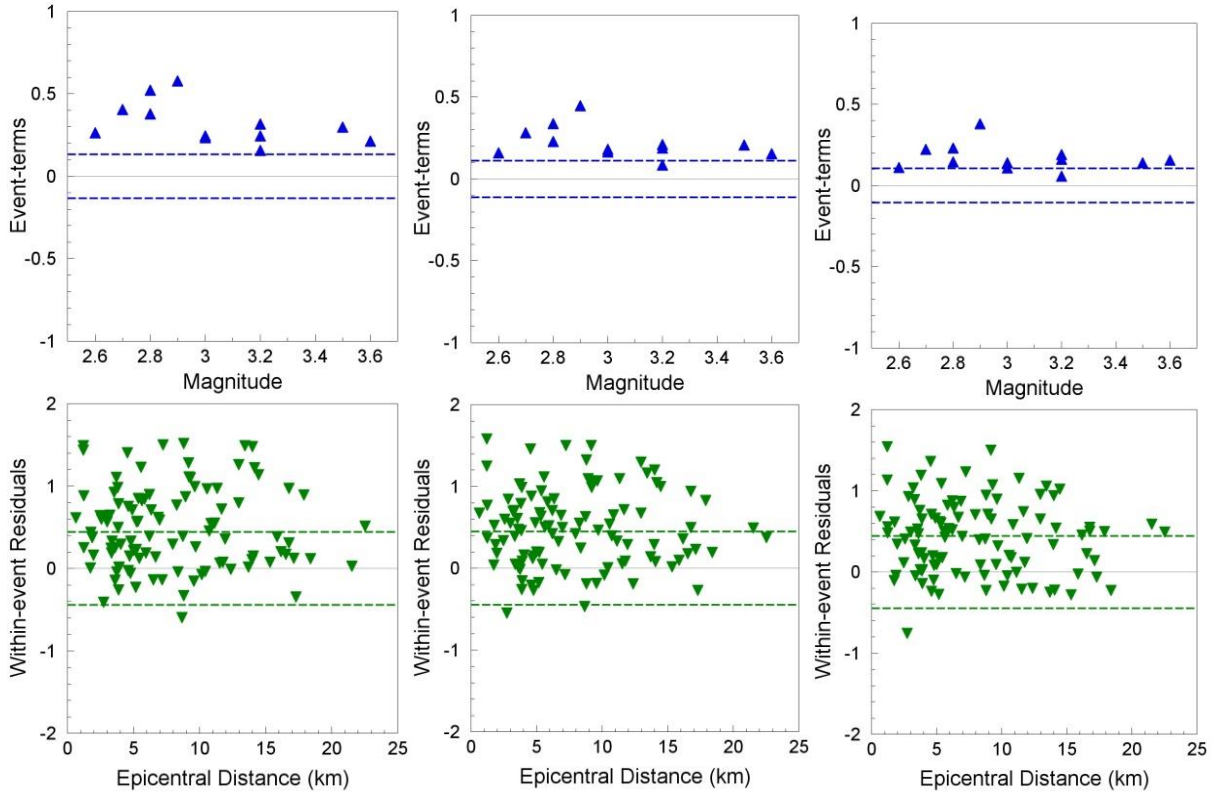

Figure 11.147. Residuals of V/H ratios of the Groningen database calculated with respect to the GMPEs of Akkar *et al.* (2014b) for periods of 0.13 s (*left*), 0.14 s (*centre*) and 0.15 s (*right*)

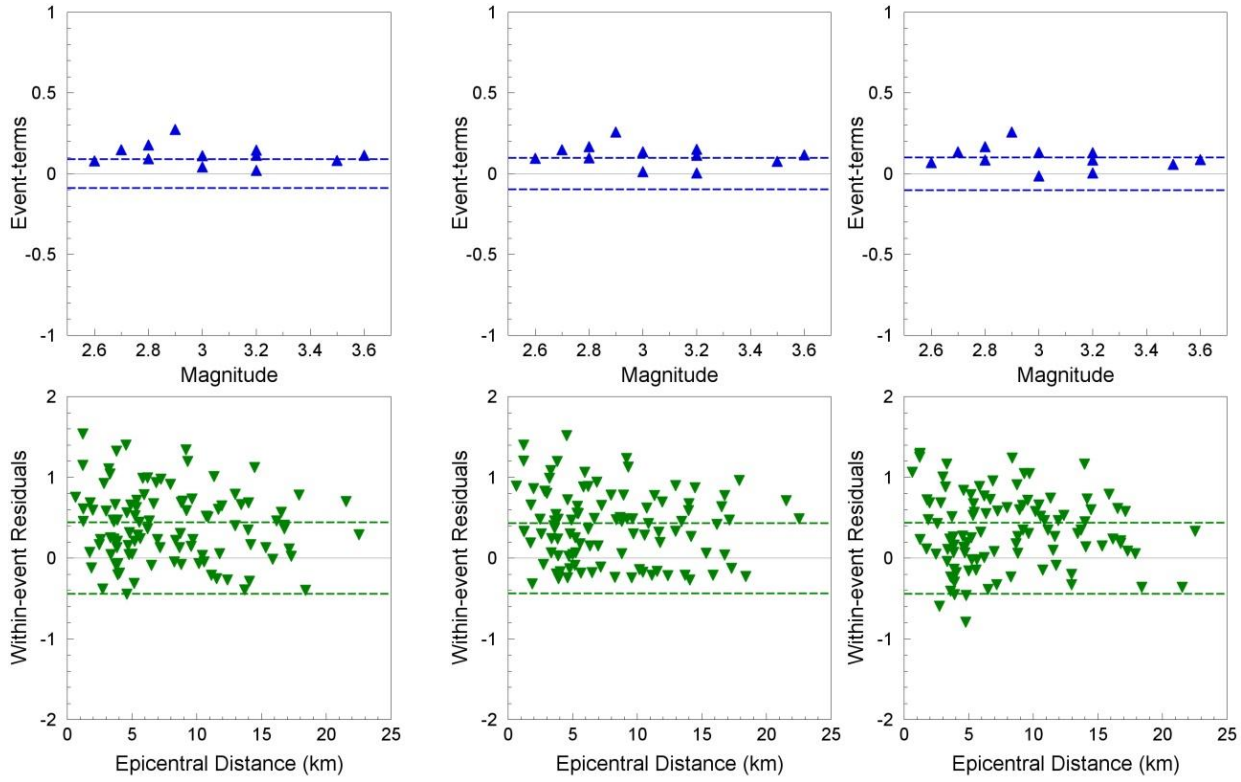

Figure 11.148. Residuals of V/H ratios of the Groningen database calculated with respect to the GMPEs of Akkar *et al.* (2014b) for periods of 0.16 s (*left*), 0.17 s (*centre*) and 0.18 s (*right*)

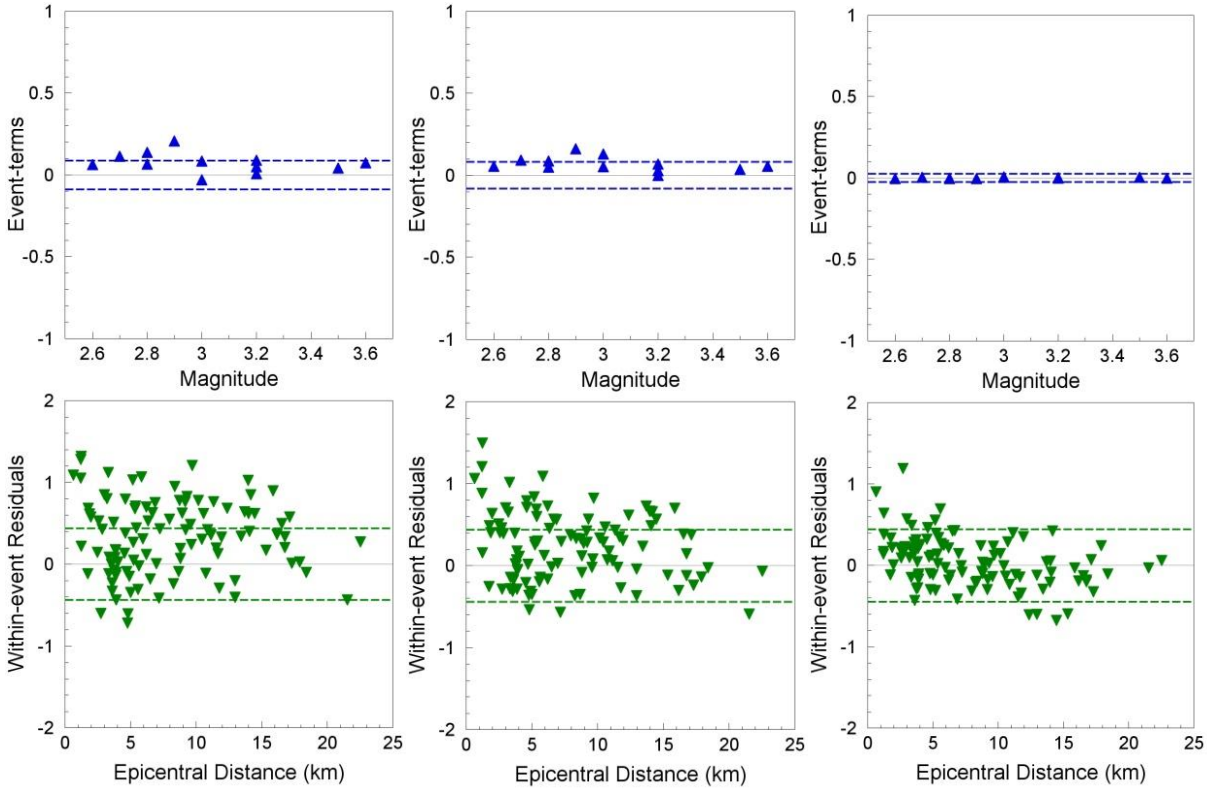

Figure 11.149. Residuals of V/H ratios of the Groningen database calculated with respect to the GMPEs of Akkar *et al.* (2014b) for periods of 0.19 s (*left*), 0.20 s (*centre*) and 0.30 s (*right*)

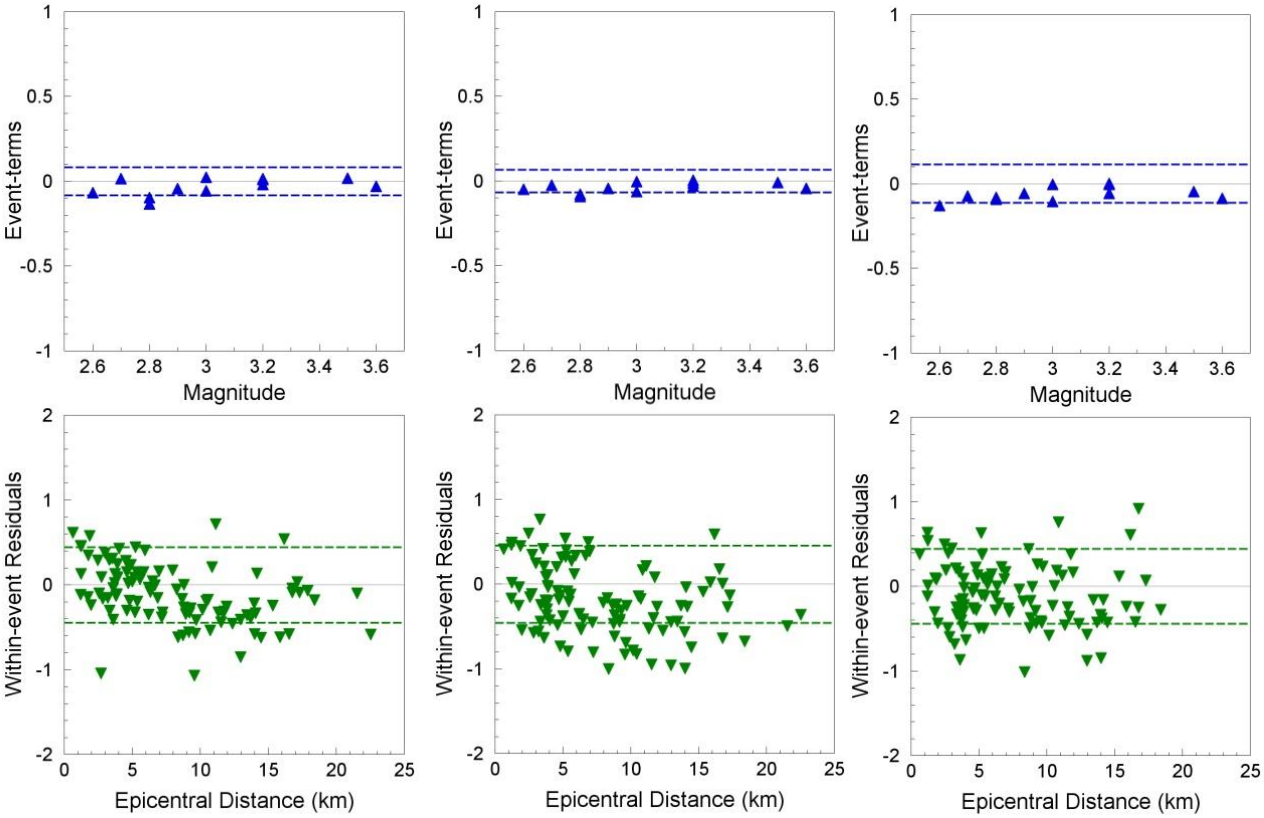

Figure 11.150. Residuals of V/H ratios of the Groningen database calculated with respect to the GMPEs of Akkar *et al.* (2014b) for periods of 0.4 s (*left*), 0.5 s (*centre*) and 0.6 s (*right*)

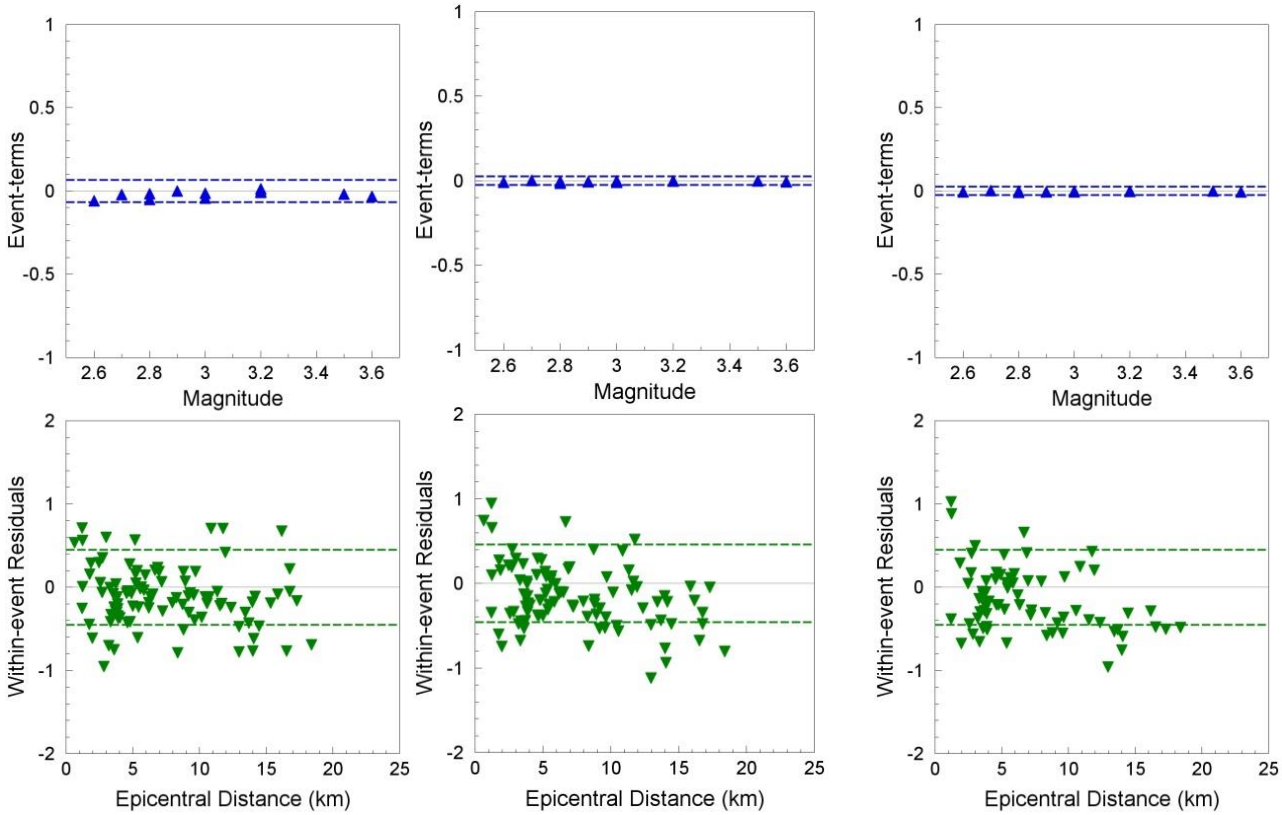

Figure 11.151. Residuals of V/H ratios of the Groningen database calculated with respect to the GMPEs of Akkar *et al.* (2014b) for periods of 0.7 s (*left*), 0.85 s (*centre*) and 1.0 s (*right*)

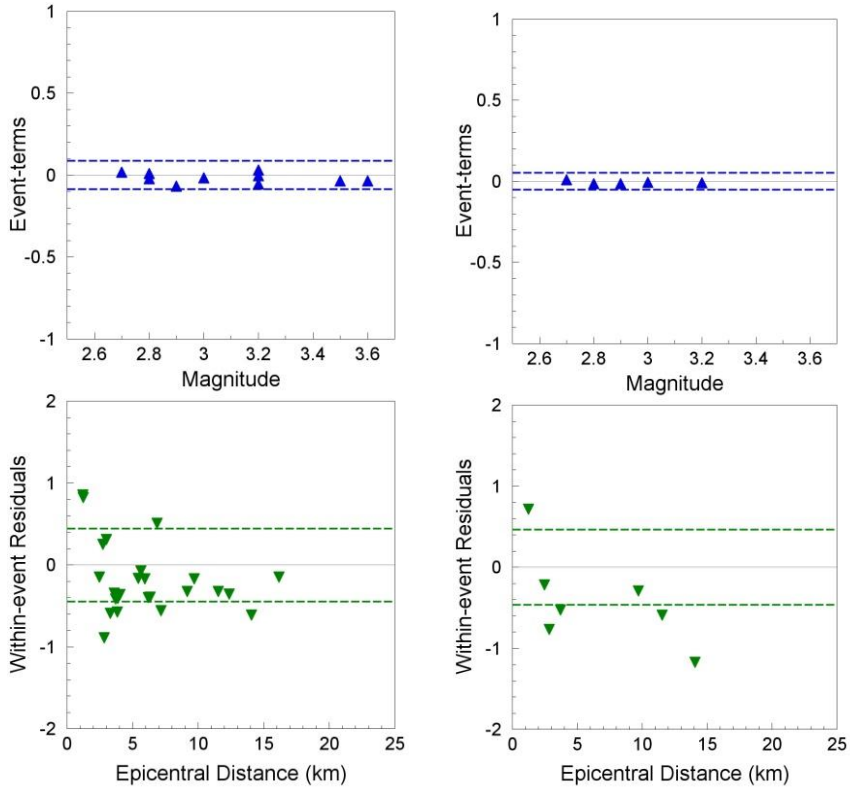

Figure 11.152. Residuals of V/H ratios of the Groningen database calculated with respect to the GMPEs of Akkar *et al.* (2014b) for periods of 1.5 s (*left*) and 2.0 s (*right*)

In view of these observations, it was decided to adjust the constant term in the Akkar *et al*. (2014b) equations in order to remove the bias with respect to the Groningen recordings in order to obtain a preliminary model for the field. The small negative bias at periods greater than 0.3 seconds was ignored and the adjustment was only made for response periods up to 0.2 seconds. Although the V2 GMPEs are only derived for 16 target periods, given the very different shape of vertical response spectra, it was decided to use all of the periods up to 0.2 seconds for which Akkar *et al*. (2014b) provide coefficients. The original and modified constants (a_1) in the predictive equation are listed in Table 11.2. Examples of the residuals obtained with the adjusted equation at short response periods are shown in Figures 11.153 and 11.154, from which it can be seen that the model provides a reasonable fit to the small-magnitude recordings from the field.

Table 11.2. Original and Groningen-adjusted constants in the Akkar *et al*. (2014b) GMPEs

T (s)	Original constant	Bias estimate	Adjusted constant
0.01	-0.54467	1.04056	0.49589
0.02	-0.46655	1.15641	0.68986
0.03	-0.25416	1.25664	1.00248
0.04	-0.03087	1.25108	1.22021
0.05	0.09261	1.34097	1.43358
0.075	-0.02755	1.15071	1.12316
0.1	-0.2157	1.09503	0.87933
0.11	-0.32916	1.01770	0.68854
0.12	-0.46642	0.97162	0.50520
0.13	-0.58641	0.83507	0.24866
0.14	-0.69689	0.72187	0.02498
0.15	-0.79732	0.60626	-0.19106
0.16	-0.86803	0.52804	-0.33999
0.17	-0.90007	0.45689	-0.44318
0.18	-0.94543	0.39352	-0.55191
0.19	-0.97616	0.36634	-0.60982
0.2	-1.02981	0.31300	-0.71681
0.3	-1.14208	0.05004	-1.14208
0.4	-1.09718	-0.12064	-1.09718
0.5	-1.0642	-0.23776	-1.0642
0.6	-1.03283	-0.17653	-1.03283
0.7	-0.9426	-0.14632	-0.9426
0.85	-0.8344	-0.16483	-0.8344
1	-0.73533	-0.16032	-0.73533
1.5	-0.70636	-0.20068	-0.70636

The variability of the Groningen data with respect to the adjusted Akkar *et al.* (2014b) equations at short periods is large (Figures 11.140-141), so the variability components were calculated following the same procedures used to calculate the bias and variability in the predictions at the NU_B horizon (Section 6.5). The between-event, within-event and total standard deviations are reported in Table 11.3 and compared with those from the original GMPEs of Akkar *et al*. (2014b).

Since the V2 GMPEs only define the horizontal response spectral ordinates at periods of 0.01, 0.1 and 0.2 seconds in the high-frequency range, the application of these ratios is not straightforward since it would first require some smoothed interpolation of the spectral ordinates at the intervening response periods. Beyond 0.2 seconds, it would be sufficient to apply the V/H ratios at the selected target periods for which the horizontal spectrum is

defined. For 2.5 seconds, coefficients need to be interpolated (using a cubic spline) since Akkar *et al.* (2014b) only provide coefficients at 2.4 and 2.6 seconds. For 5 seconds, it would be recommended to maintain the V/H ratios calculated for a period of 4 seconds, which is the upper limit covered by the Akkar *et al*. (2014b) model. The resulting median predictions of V/H ratios for various combinations of magnitude and distance are illustrated in Figures 11.155 and 11.156, and compared with those from the original GMPEs.

Table 11.3. Variability components of the original and Groningen-adjusted V/H GMPEs

T (s)	Akkar *et al*. (2014b)			Groningen-adjusted version		
	τ	ϕ	σ	τ	ϕ	σ
0.01	0.0747	0.3571	0.3648	0.27815	0.54861	0.615094
0.02	0.0844	0.3558	0.3657	0.2601	0.604	0.657623
0.03	0.0969	0.3613	0.3741	0.2911	0.5861	0.65441
0.04	0.1161	0.373	0.3907	0.1812	0.6289	0.654483
0.05	0.1259	0.3922	0.4119	0.2467	0.5698	0.620913
0.075	0.1377	0.405	0.4278	0.2321	0.7196	0.756105
0.1	0.1701	0.4103	0.4442	0.15319	0.6256	0.644083
0.11	0.1556	0.4196	0.4475	0.158	0.5646	0.586291
0.12	0.1473	0.4274	0.4521	0.3696	0.5223	0.639845
0.13	0.133	0.4418	0.4614	0.1787	0.505	0.535685
0.14	0.112	0.4481	0.4619	0.0669	0.4746	0.479292
0.15	0.1057	0.4455	0.4579	0.0769	0.4529	0.459382
0.16	0.089	0.4417	0.4506	0.0675	0.4407	0.445839
0.17	0.0975	0.436	0.4468	0.1026	0.4333	0.445282
0.18	0.1014	0.4397	0.4512	0.2207	0.4577	0.508132
0.19	0.0882	0.4377	0.4465	0.0854	0.4532	0.461176
0.2	0.0816	0.4404	0.4479	0.076479	0.42513	0.431954

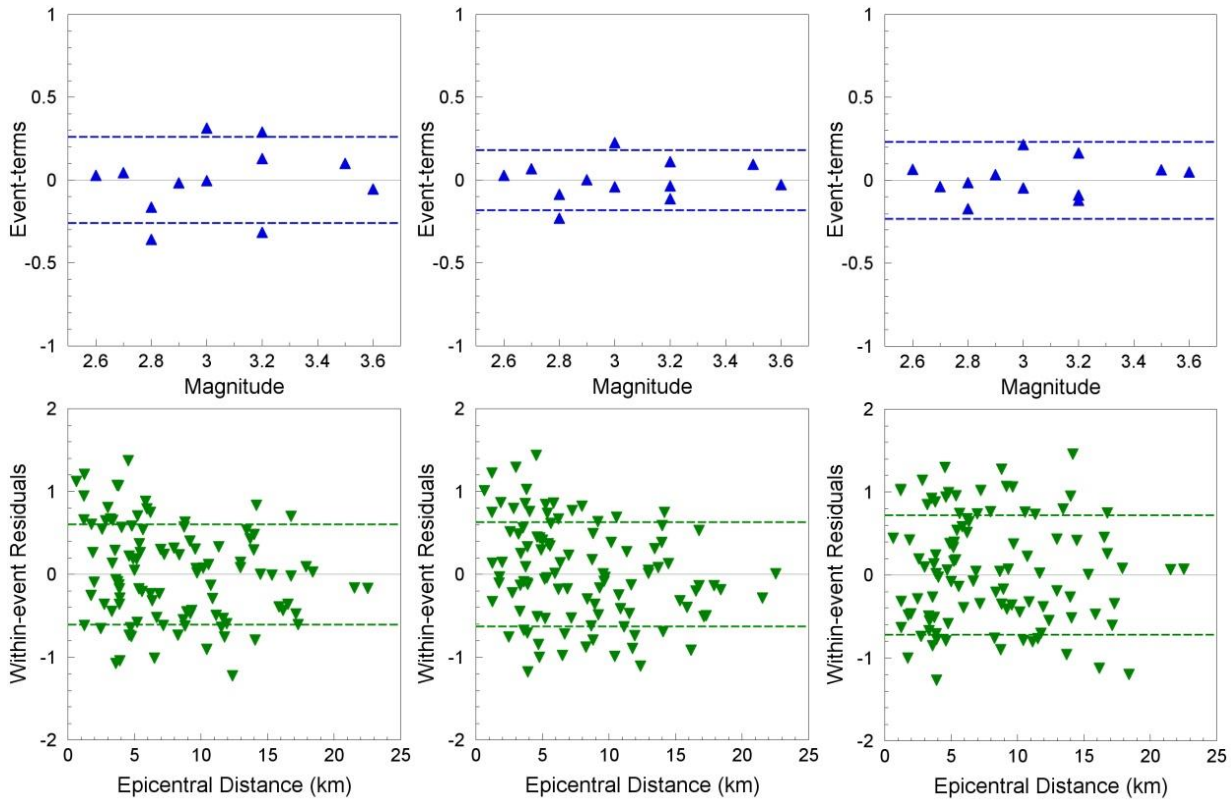

Figure 11.153. Residuals of V/H ratios of the Groningen database with respect to the adjusted GMPEs of Akkar *et al.* (2014b) for periods of 0.02 s (*left*), 0.04 s (*centre*) and 0.075 s (*right*)

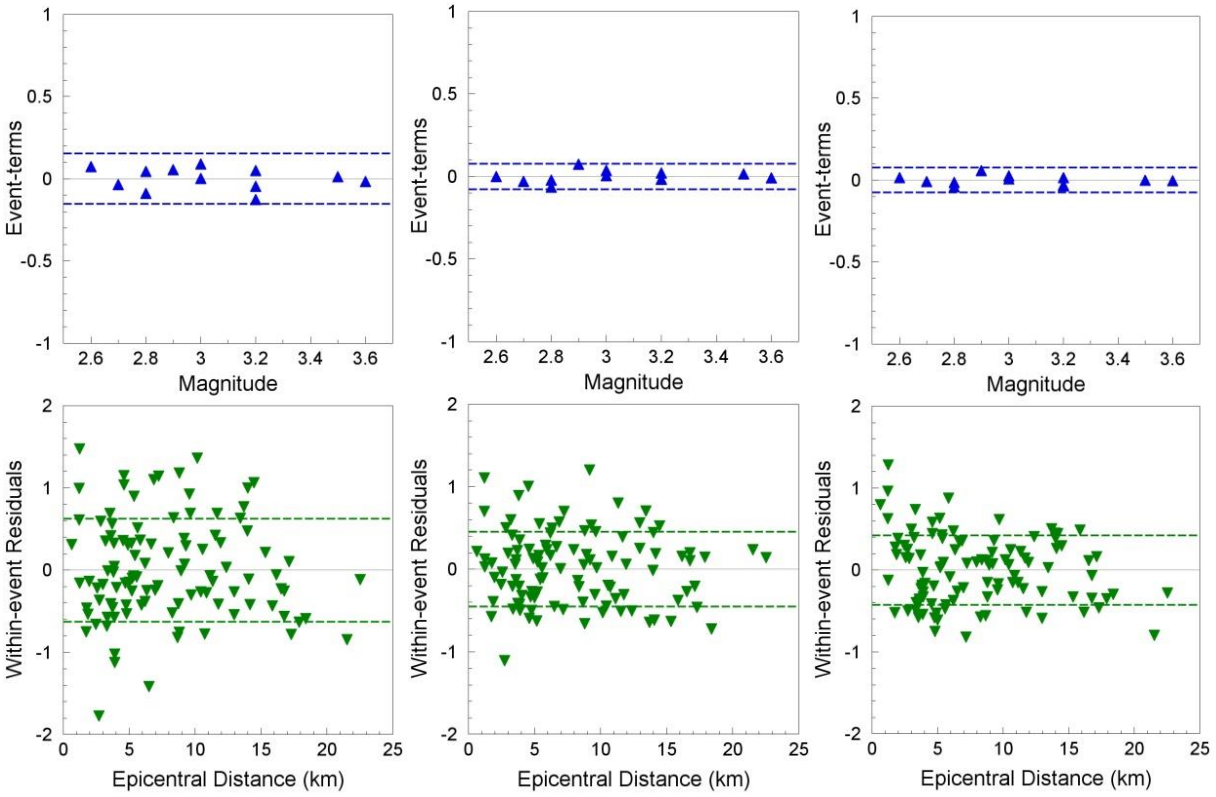

Figure 11.154. Residuals of V/H ratios of the Groningen database with respect to the adjustred GMPEs of Akkar *et al.* (2014b) for periods of 0.7 s (*left*), 0.85 s (*centre*) and 1.0 s (*right*)

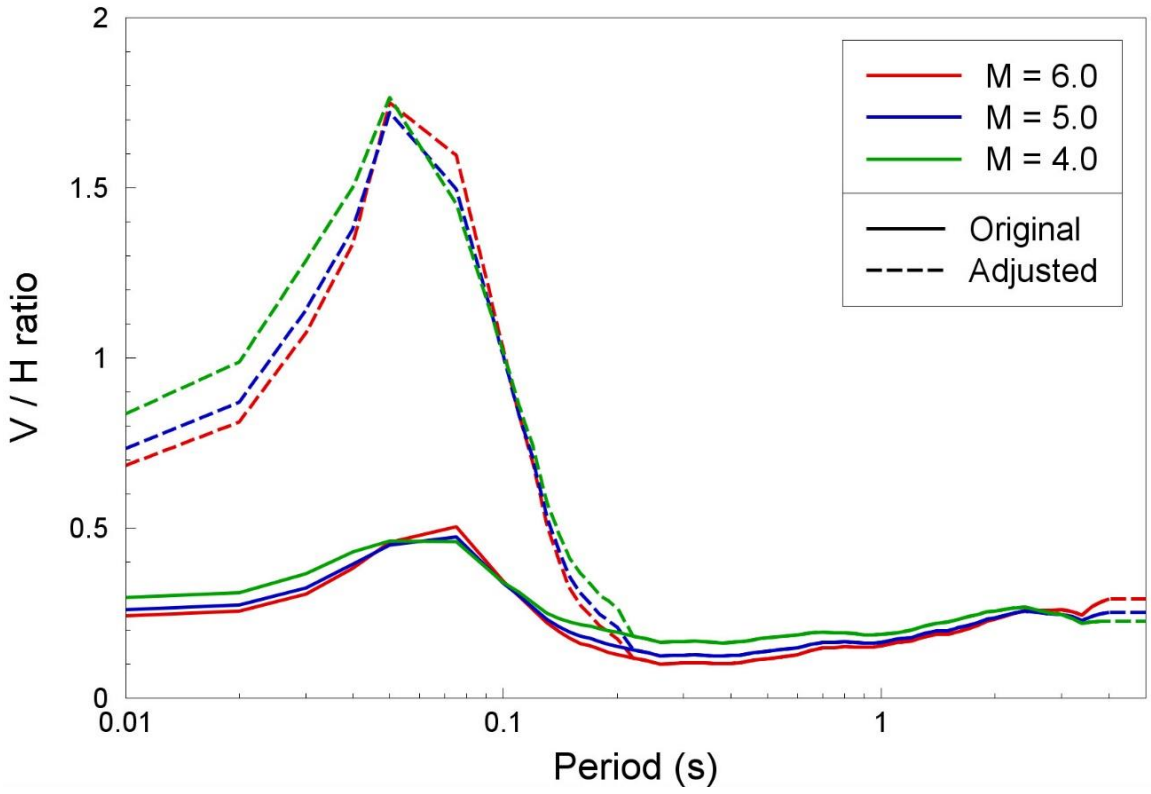

Figure 11.155. Predicted median V/H ratios from the original (*solid*) and Groningen-adjusted (*dashed*) equations of Akkar *et al.* (2014b) for R_{epi} = 0 km

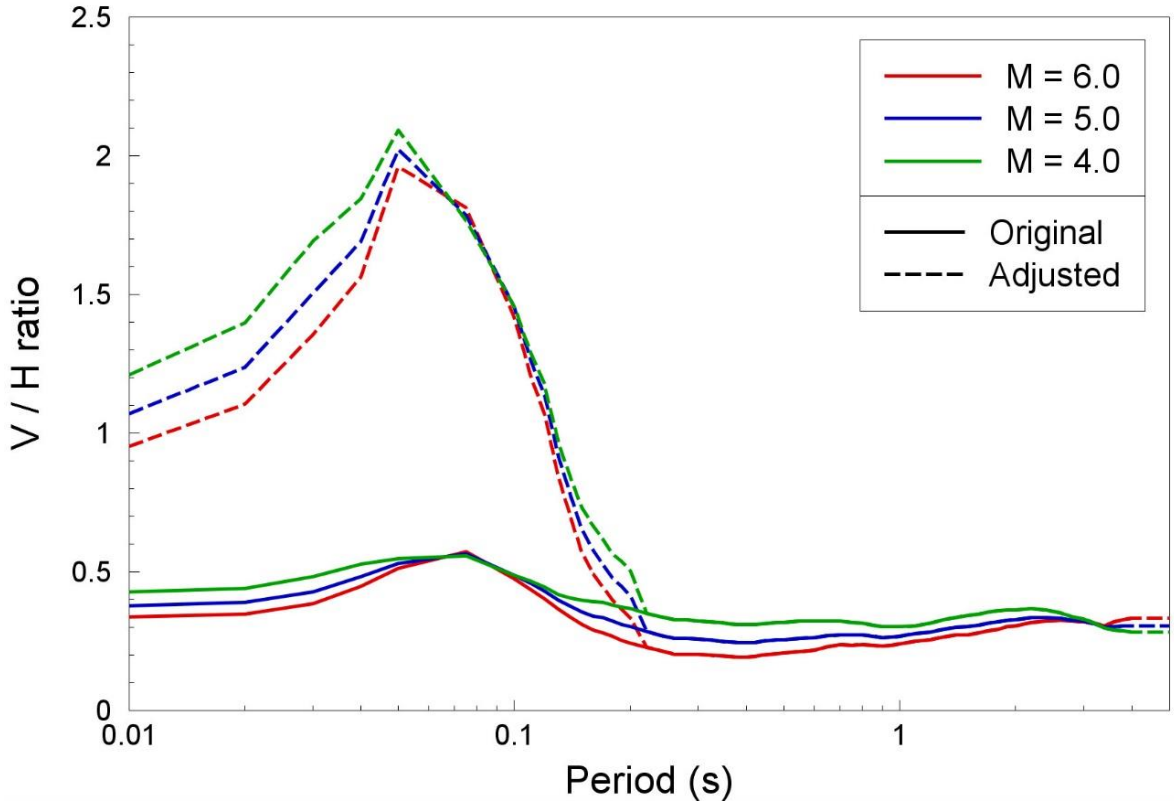

Figure 11.156. Predicted median V/H ratios from the original (*solid*) and Groningen-adjusted (*dashed*) equations of Akkar *et al.* (2014b) for R_{epi} = 20 km

The appearance of the modified model is clearly radically different from the original equations of Akkar *et al.* (2014b). However, the resulting predictions of the V/H ratios for response spectral ordinates are not inconsistent, at least at short distances, with those from the model of Gülerce & Abrahamson (2011). Figures 11.157 to 11.160 compare the V/H ratios from the original and Groningen-adjusted Akkar *et al.* (2014b) equations with those obtained from Gülerce & Abrahamson (2011) model at four different distances. For the latter model, the rupture distance is simply assumed equal to epicentral distance, V_{S30} is set to 200 m/s, and predicted ratios are shown as the average of those for strike-slip and normal-faulting earthquakes. In the short-period range, where the ratio peaks, the Gülerce & Abrahamson (2011) model predicts values that are comparable to those obtained with the Groningen-adjusted model at shorter distances. Farther away from the source, the Gülerce & Abrahamson (2011) predictions suggest that the Groningen-adjusted model is over-predicting the V/H ratios, which may indicate that the non-linear site response effect in the Akkar *et al*. (2014b) model is insufficiently sensitive to distance. While the derivation of this preliminary V/H model is somewhat crude, these comparisons indicate that it may be an acceptable first approximation, tending to be somewhat conservative in the range of short response periods likely to be of greatest relevance. For a special structure such as the Groninger Forum (Bommer et al., 2015c), with large diaphragms and dominated by more distant earthquakes that locations within the gas field, it may be appropriate to simply adopt the Gülerce & Abrahamson (2011) equations for transforming horizontal response spectra to the vertical component.

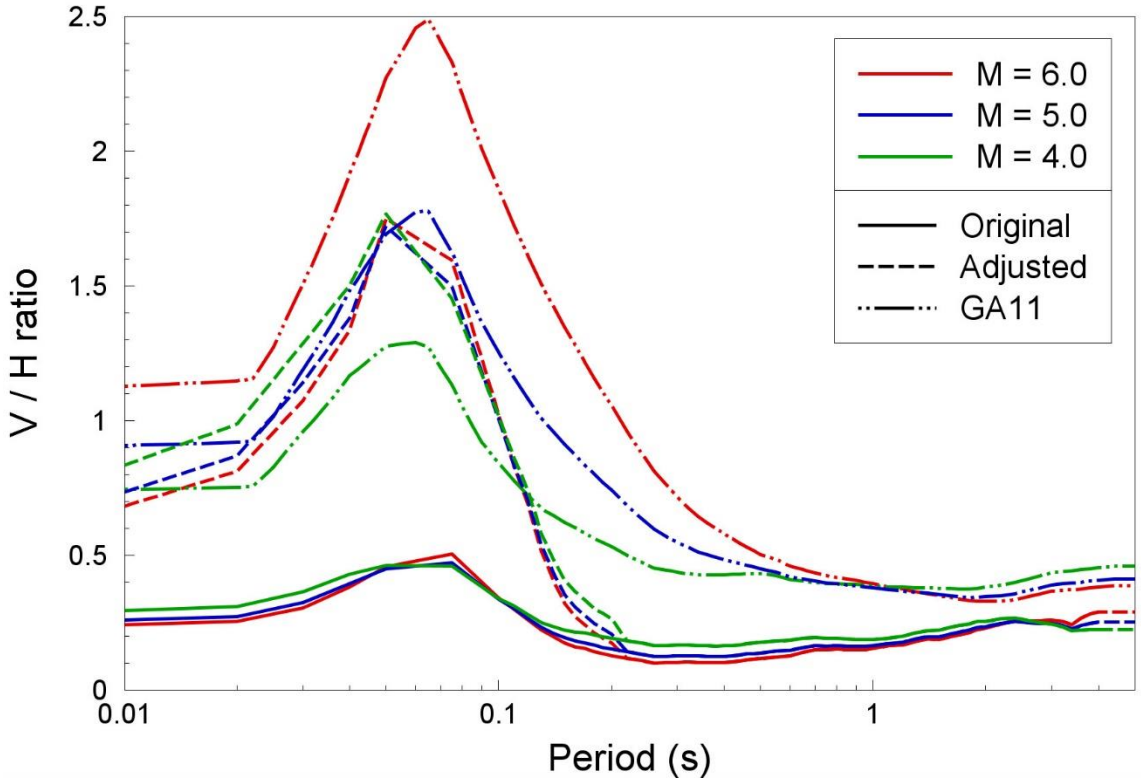

Figure 11.157. Predicted median V/H ratios from the original (*solid*) and Groningen-adjusted (*dashed*) equations of Akkar *et al.* (2014b) with those from the Gülerce & Abrahamson (2011) model (*dashed-dotted*) for R_{epi} = 0 km

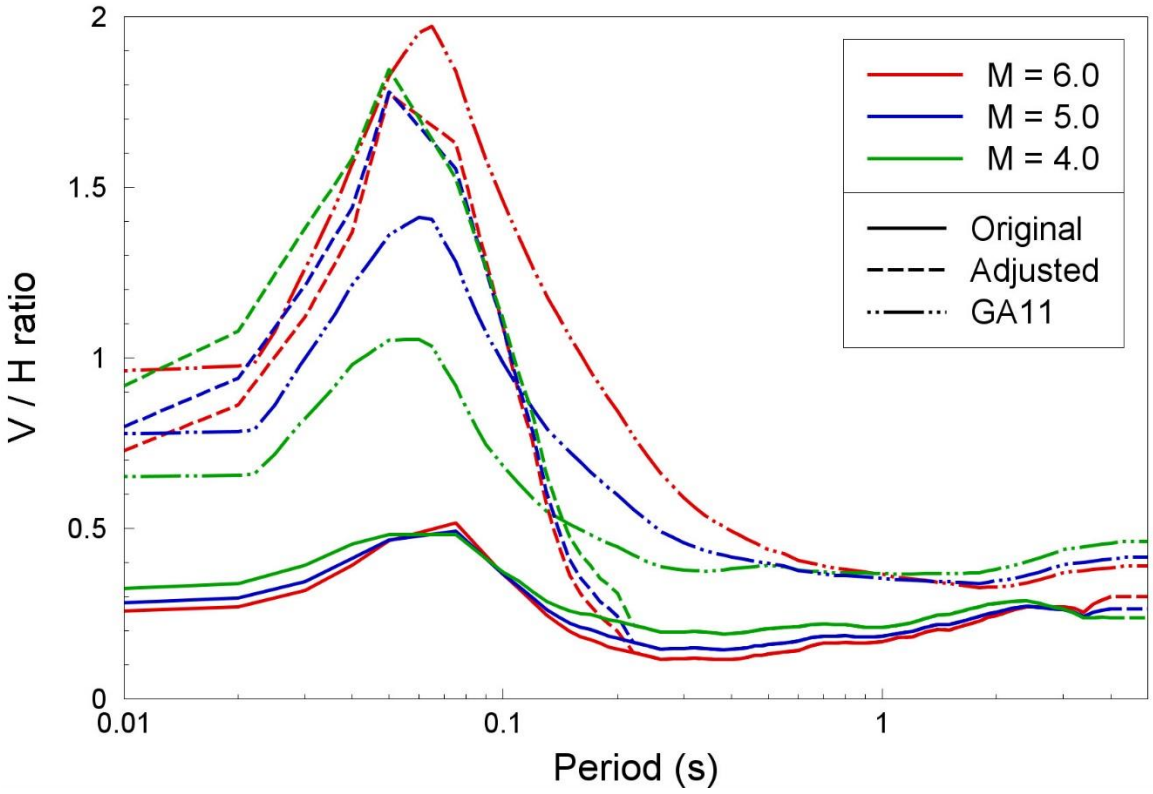

Figure 11.158. Predicted median V/H ratios from the original (*solid*) and Groningen-adjusted (*dashed*) equations of Akkar *et al.* (2014b) with those from the Gülerce & Abrahamson (2011) model (*dashed-dotted*) for R_{epi} = 5 km

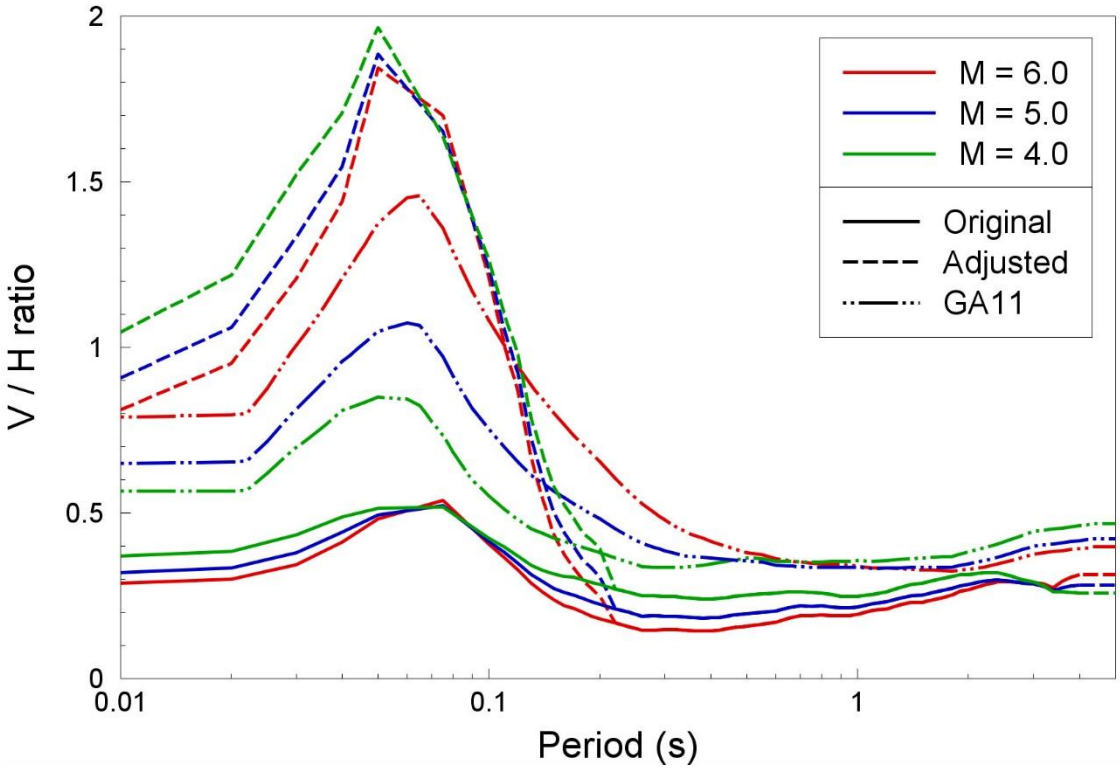

Figure 11.159. Predicted median V/H ratios from the original (*solid*) and Groningen-adjusted (*dashed*) equations of Akkar *et al.* (2014b) with those from the Gülerce & Abrahamson (2011) model (*dashed-dotted*) for R_{epi} = 10 km

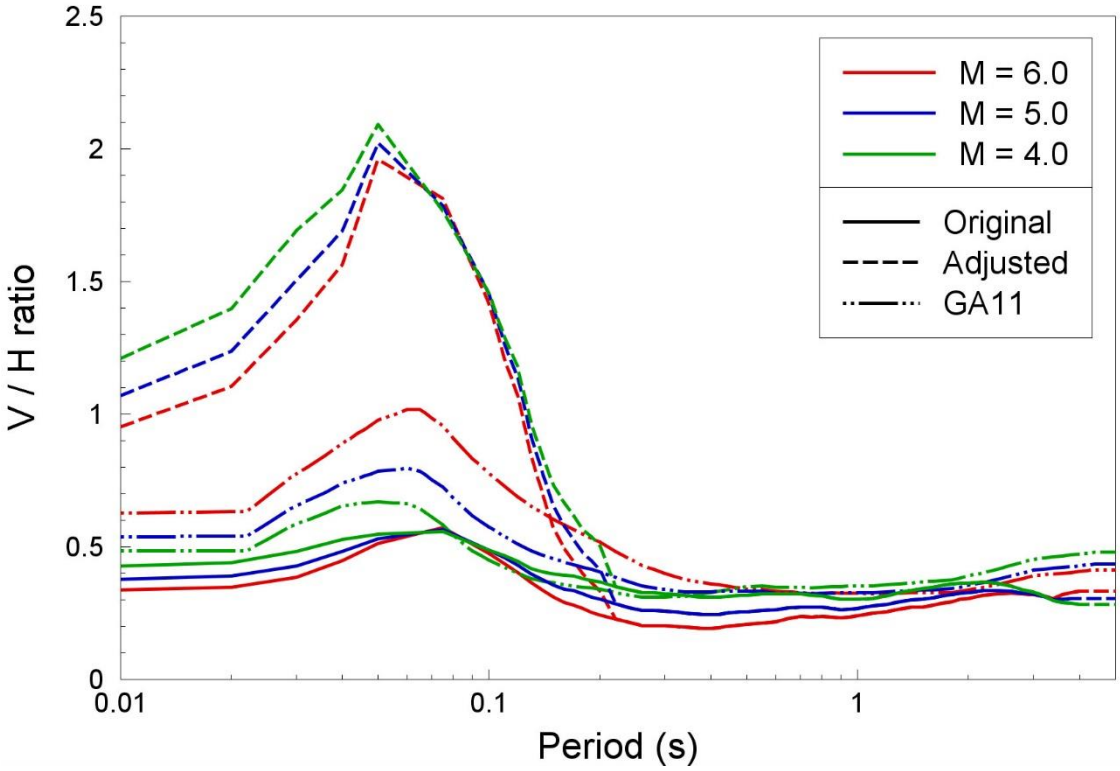

Figure 11.160. Predicted median V/H ratios from the original (*solid*) and Groningen-adjusted (*dashed*) equations of Akkar *et al.* (2014b) with those from the Gülerce & Abrahamson (2011) model (*dashed-dotted*) for R_{epi} = 20 km

12. GMPE for DURATION

The effect of the duration of ground shaking is generally not considered in structural design, other than with regard to its influence on scaling factors to adjust response spectral ordinates to alternative damping ratios (*e.g.*, Stafford *et al.*, 2008). However, the influence of duration has been recognised as being important in the seismic assessment of buildings (*e.g.*, Iervolino *et al.*, 2006; Chandramohan *et al.*, 2015), particularly those constructed from materials such as masonry that is prone to experience degradation of both strength and stiffness under dynamic loading (*e.g.*, Bommer *et al.*, 2004). For this reason, the development of the fragility functions for the buildings in the Groningen field aims to take account of the ground-motion duration, for which reason a predictive equation is required for the chosen definition of the ground-motion duration.

12.1 Durations of Groningen motions

A large number of definitions for the duration of earthquake-induced ground-shaking have been put forward in the technical literature, and application of these definitions to a given accelerogram can produce very different estimates of the duration of strong motion. Bommer & Martínez-Pereira (1999) classified all of the published definitions into three categories:

- Bracketed duration, D_B. This is defined as the interval between the first and last excursions of a specified threshold of acceleration.
- Uniform duration, D_U. This is defined as the sum of the intervals during which the acceleration is above a specified threshold.
- Significant duration, D_S. This is the interval over which some specified portion of the total energy in the record (usually calculated as the integral of the squared acceleration over time) is accumulated.

Each of the definitions can be applied to the actual ground motion or to the response of an oscillator, or other structure, to the ground motion. The definitions can also be applied with absolute or relative thresholds: for example, the bracketed duration can be defined by excursions of an acceleration level of, say, 0.1*g*, or of a fraction of the PGA.

Since duration has little significance in isolation, its influence is usually coupled with a measure of the amplitude of the motion, such as response spectral acceleration. This being the case, it makes more sense to then use definitions defined using relative measures, which will generally result in durations that increase with distance as well as with magnitude. The significant duration is the most widely-used definition, the original interval being that related to the accumulation from 5% to 95% of the total Arias intensity of the record (Trifunac & Brady, 1975). In more recent years, there has been a tendency to move towards using the interval from 5% to 75% of the total energy in the record, which is more likely to isolate the strongest portion of the record that generally corresponds to the arrival of shear waves. However, other variations have been proposed, such as the proposal by Boore & Thompson (2014) to use a duration that is equal to twice the interval between 20% and 80% of the total

energy being accumulated as a surrogate for the 5-95% definition with improved performance for smaller earthquakes. Figures 12.1-12.3 show correlations of different duration definitions computed for the whole Groningen database.

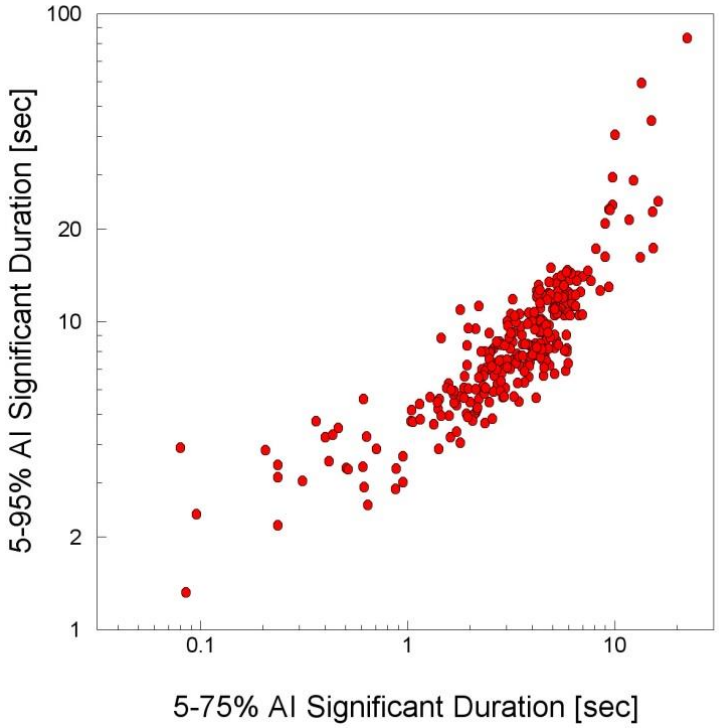

Figure 12.1. Correlation between D_{S5-75} and D_{S5-95}.

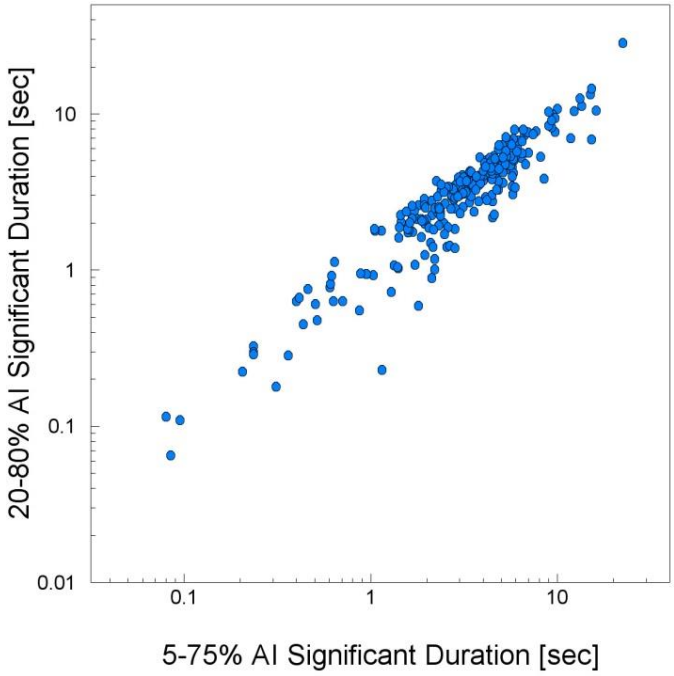

Figure 12.2. Correlation between D_{S5-75} and D_{S20-80}.

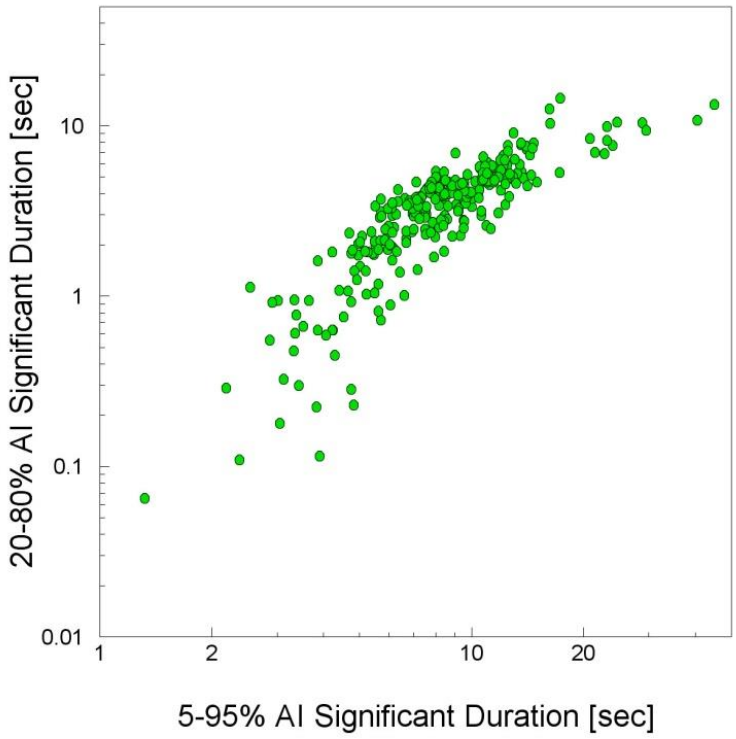

Figure 12.3. Correlation between D_{S5-95} and D_{S20-80}.

As D_{S5-75} is more likely than others to isolate the strongest part of the motion and more prediction equations have been developed for this measure than any other, it has been selected as the duration measure for which the V2 GMPE will be developed. Note that this same measure was used for the V1 GMPE also.

Figures 12.4-12.5 show two cases when the D_{S5-75} represents a good option in terms of isolating the strong portion of the accelerogram where the energy input rate is roughly constant (the steep portions of the Husid plots shown in these figures). Figure 12.6 instead shows the case when the D_{S5-75} definition can represent a quite good option for one component (*i.e.*, the EW component) but not for the other one (*i.e.*, the NS component) and finally Figures 12.7-12.12 show some cases where this measure does not capture the strong part of the shaking highlighting the fact that the D_{S5-75} definition does not always represent the best option.

For these reasons, work is underway to explore which definition will work best for the Groningen field and this exploration involves consideration of how efficient the duration measure is within the fragility component of the model as well as how well it describes characteristics of the accelerograms. Table 12.1 lists the characteristics of recordings shown in Figures 12.4-12.12.

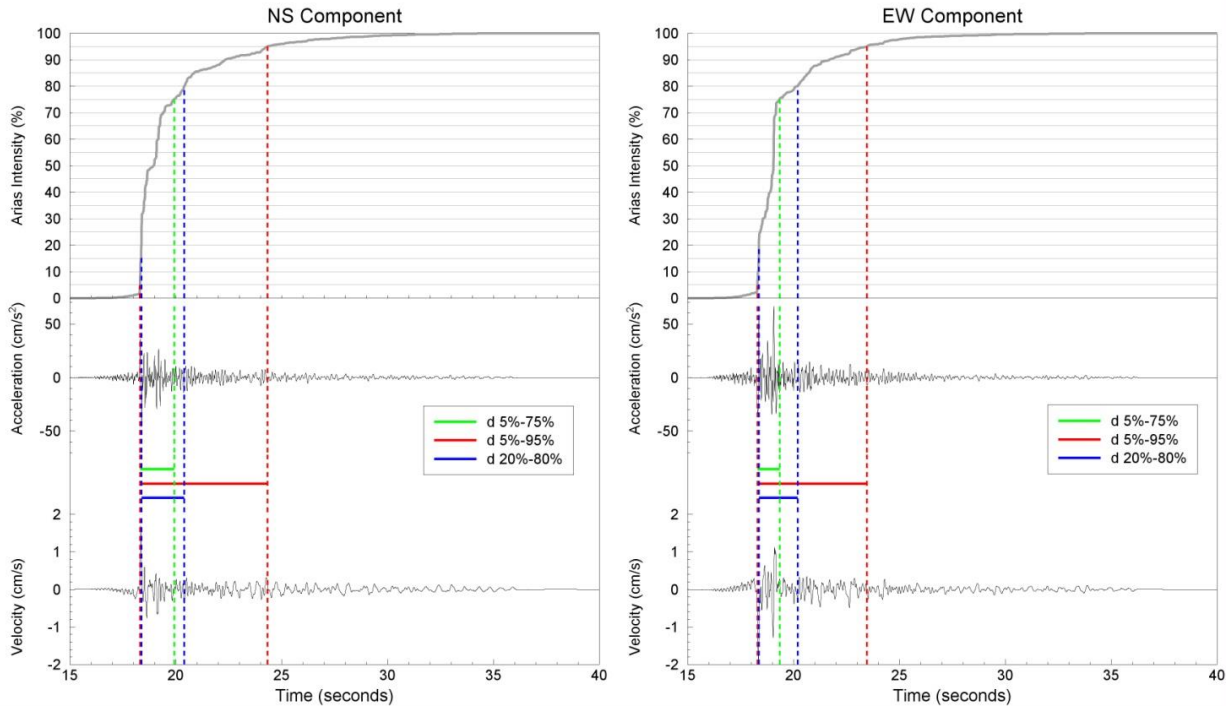

Figure 12.4. Normalised Husid plot, time-series and durations from the Groningen Earthquake 6 at GART showing the duration intervals defined by D_S with different starting and finishing percentages of the total Arias intensity.

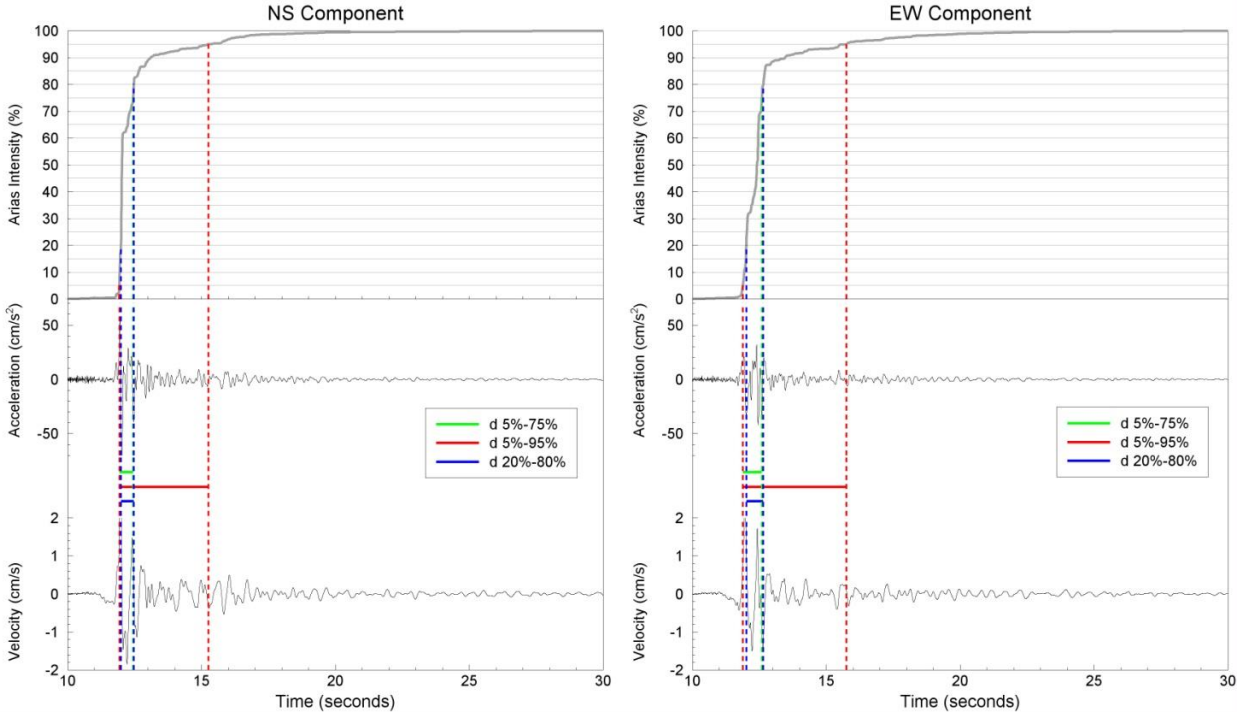

Figure 12.5. Normalised Husid plot, time-series and durations from the Groningen Earthquake 6 at MID1 showing the duration intervals defined by D_S with different starting and finishing percentages of the total Arias intensity.

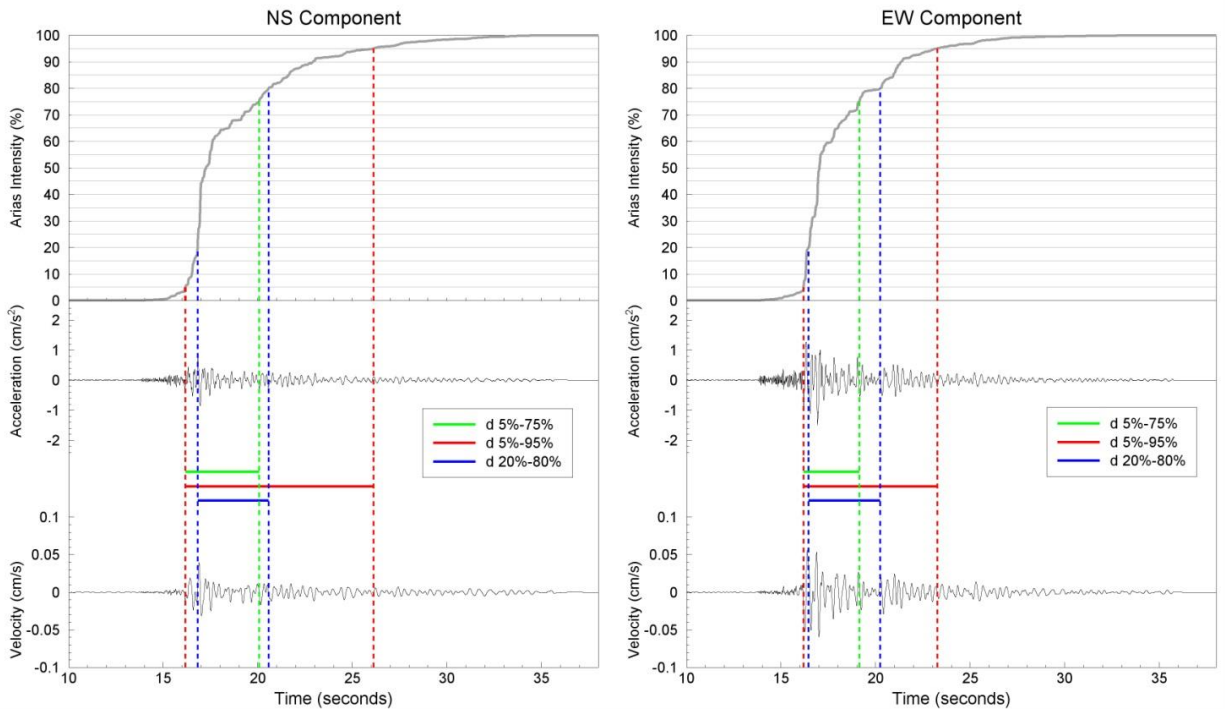

Figure 12.6. Normalised Husid plot, time-series and durations from the Groningen Earthquake 15 at BHKS showing the duration intervals defined by D_S with different starting and finishing percentages of the total Arias intensity.

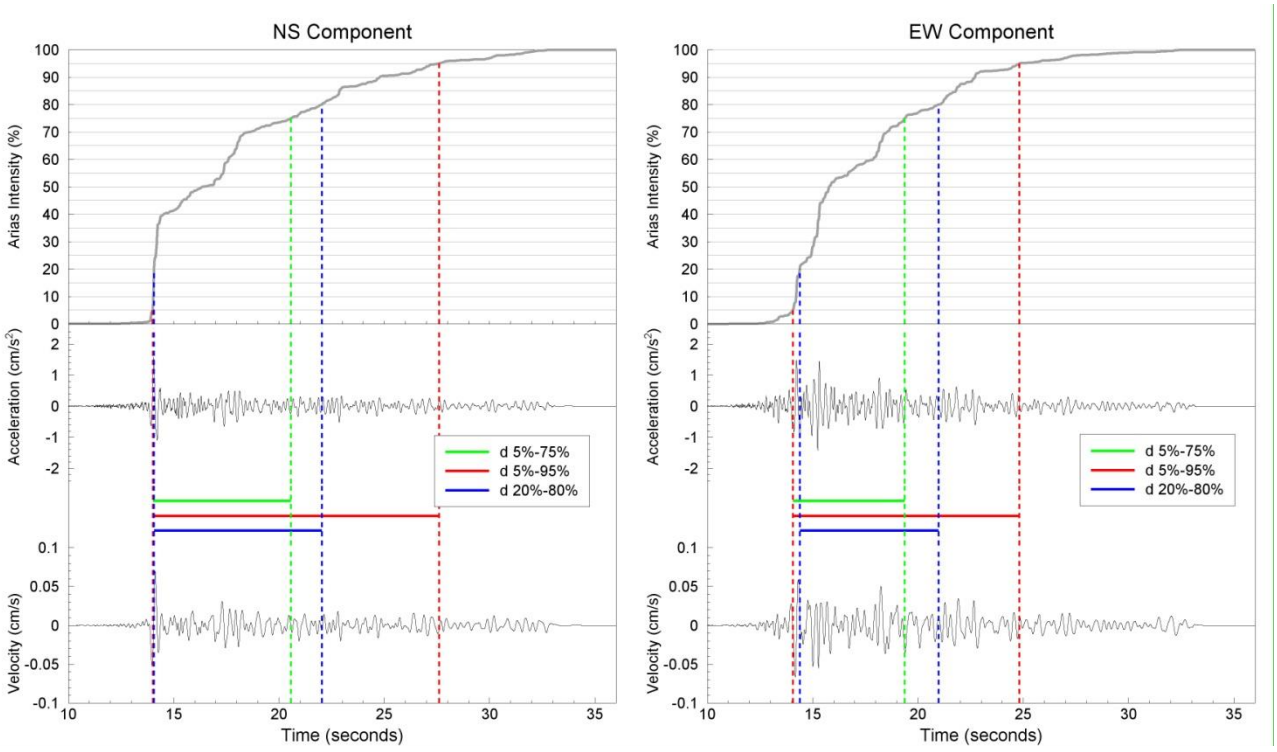

Figure 12.7. Normalised Husid plot, time-series and durations from the Groningen Earthquake 9 at BMD1 showing the duration intervals defined by D_S with different starting and finishing percentages of the total Arias intensity.

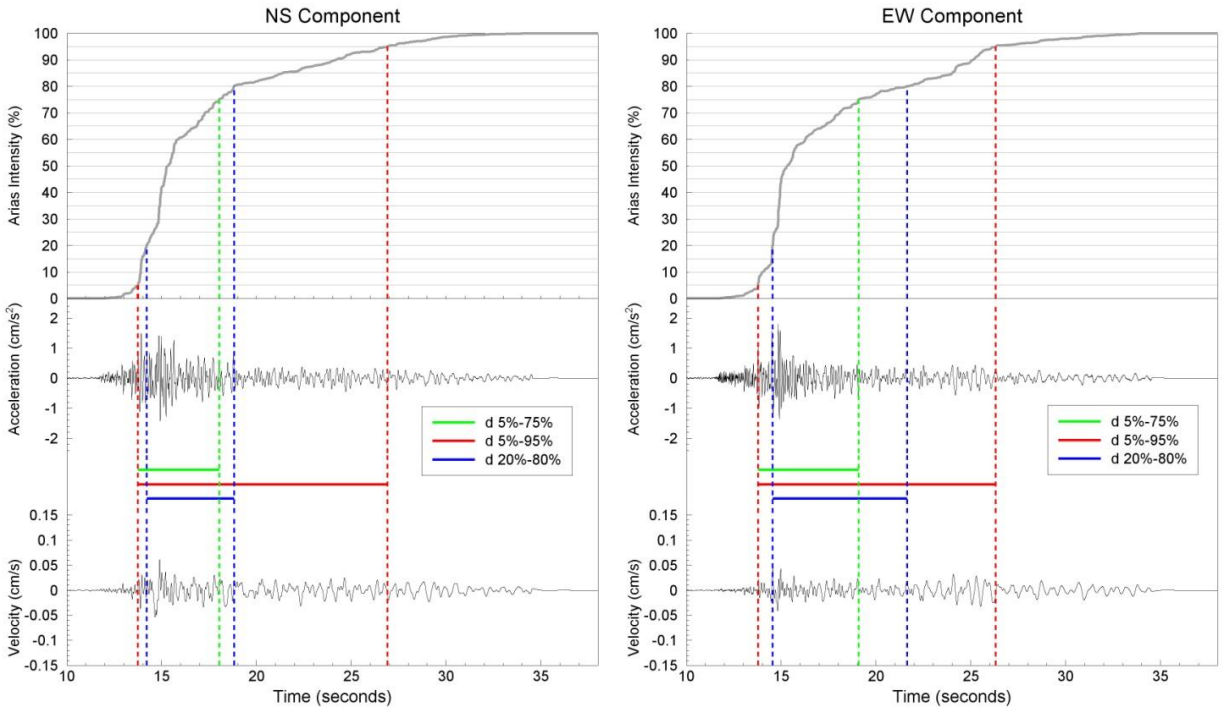

Figure 12.8. Normalised Husid plot, time-series and durations from the Groningen Earthquake 11 at BSTD showing the duration intervals defined by D_S with different starting and finishing percentages of the total Arias intensity.

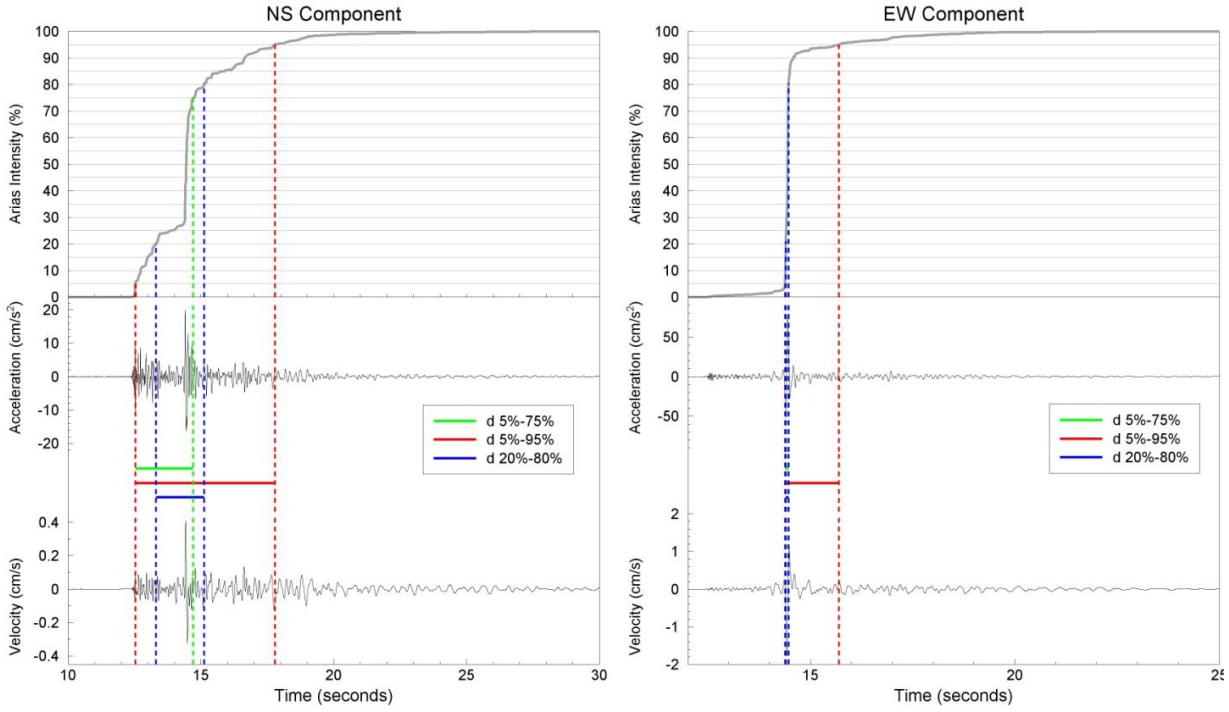

Figure 12.9. Normalised Husid plot, time-series and durations from the Groningen Earthquake 12 at BMD2 showing the duration intervals defined by D_S with different starting and finishing percentages of the total Arias intensity.

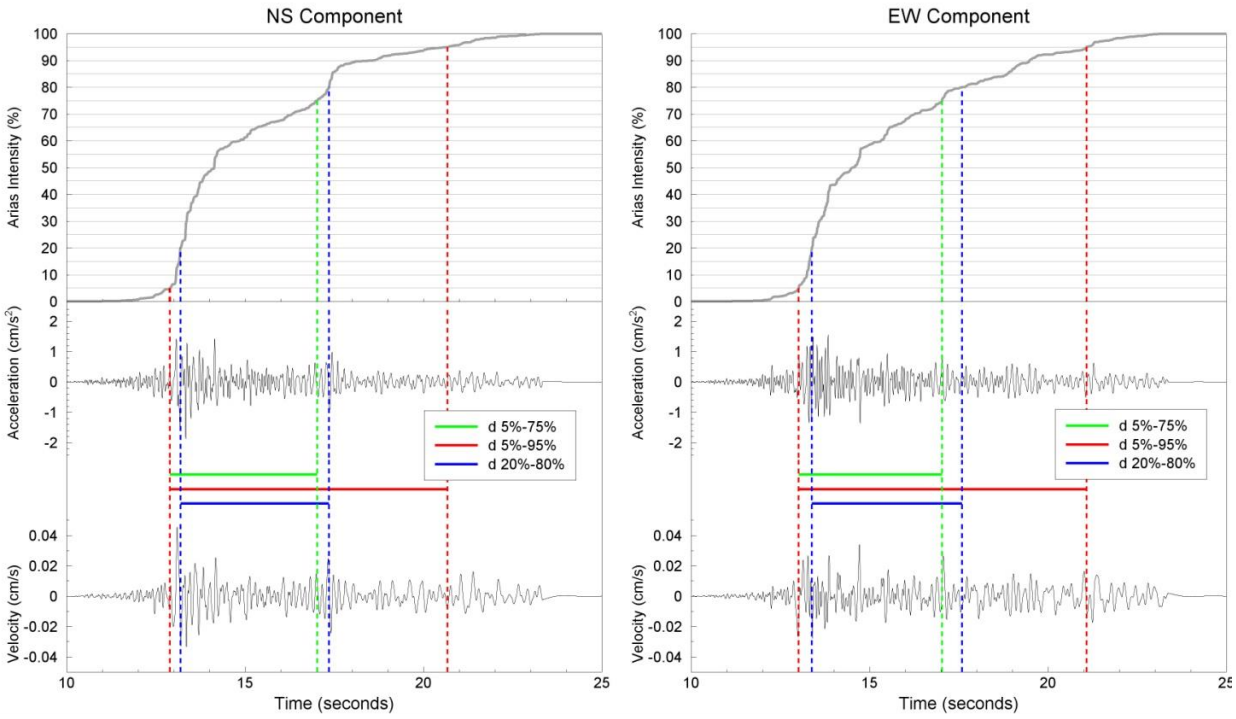

Figure 12.10. Normalised Husid plot, time-series and durations from the Groningen Earthquake 14 at BGAR showing the duration intervals defined by D_S with different starting and finishing percentages of the total Arias intensity.

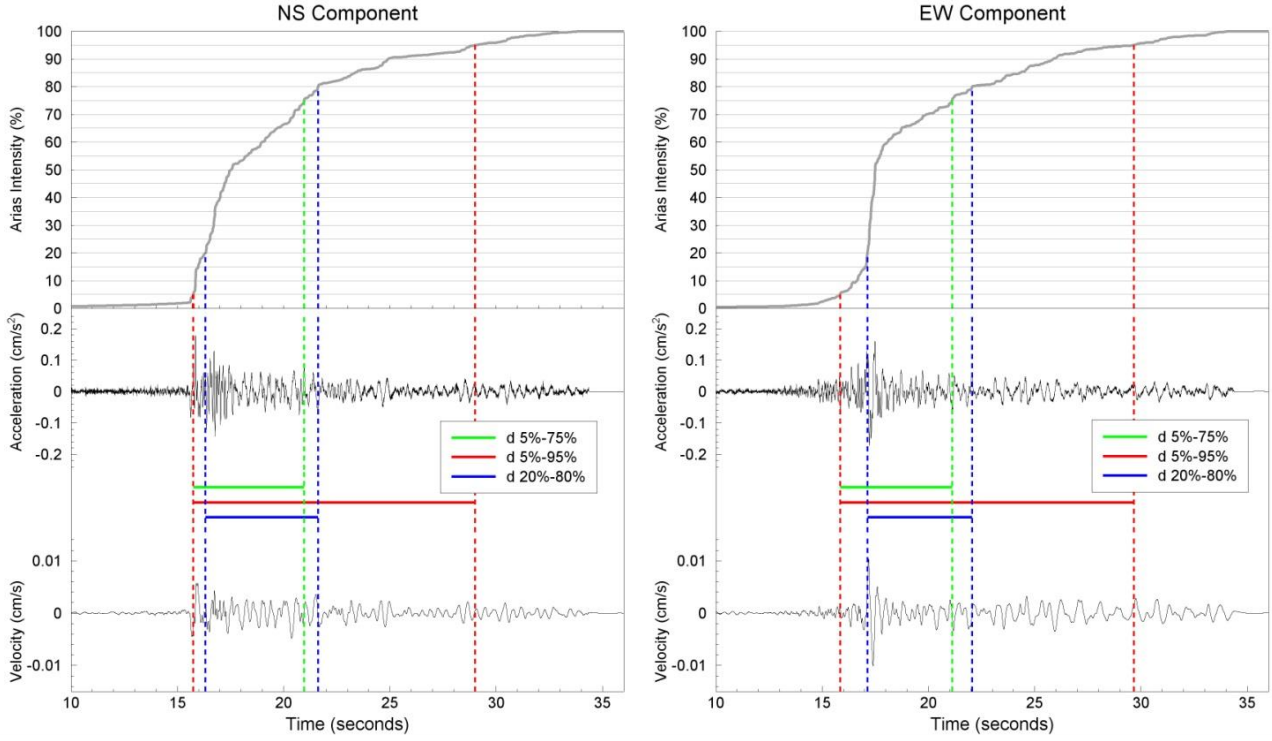

Figure 12.11. Normalised Husid plot, time-series and durations from the Groningen Earthquake 16 at BSTD showing the duration intervals defined by D_S with different starting and finishing percentages of the total Arias intensity.

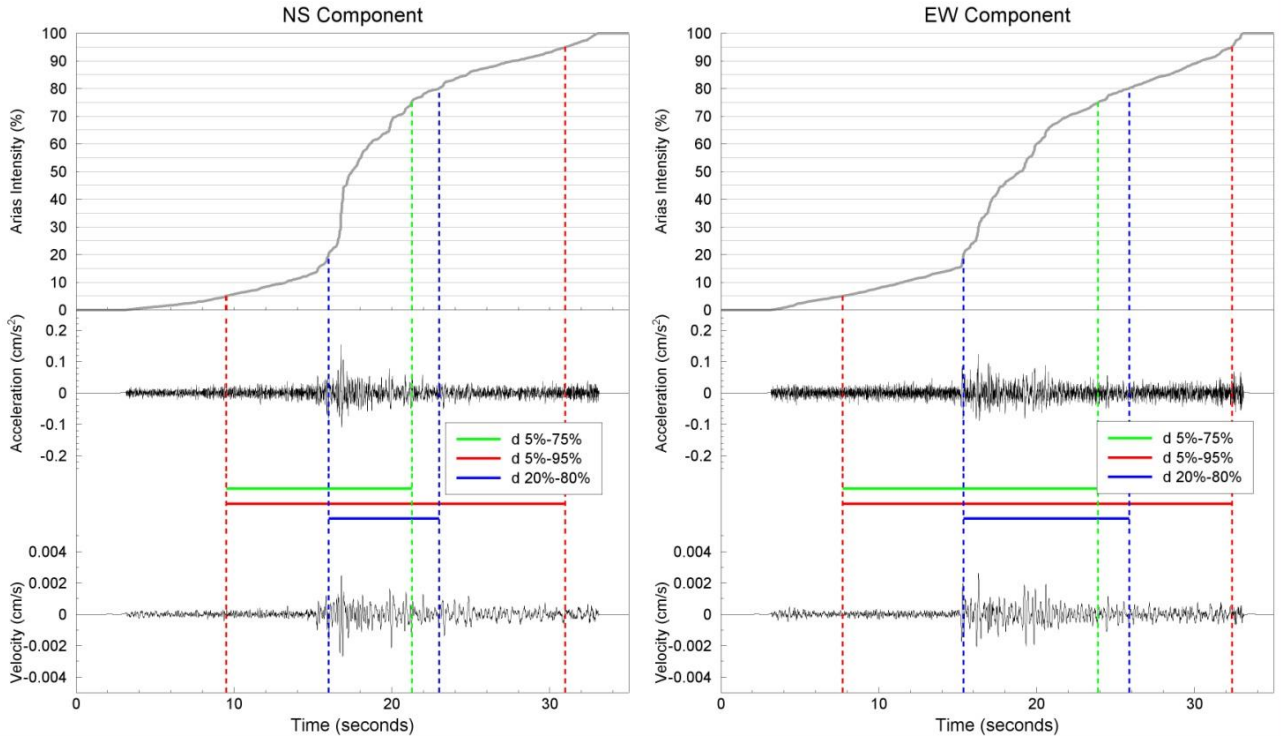

Figure 12.12. Normalised Husid plot, time-series and durations from the Groningen Earthquake 16 at G460 showing the duration intervals defined by D_S with different starting and finishing percentages of the total Arias intensity.

Table 12.1. Characteristics of Groningen recordings shown in Figures 12.4-12.12.

EQID	Date	STAT	M	R_{epi} (km)	COMP	D_{S5-75} (s)	D_{S5-95} (s)	D_{S20-80} (s)
6	2012_Aug_16	GART	3.6	3.9	NS	1.615	6.02	2.015
6	2012_Aug_16	GART	3.6	3.9	EW	1.045	5.17	1.835
6	2012_Aug_16	MID1	3.6	2.0	NS	0.515	3.32	0.48
6	2012_Aug_16	MID1	3.6	2.0	EW	0.705	3.86	0.635
9	2014_Feb_13	BMD1	3	9.3	NS	6.555	13.6	7.975
9	2014_Feb_13	BMD1	3	9.3	EW	5.305	10.76	6.595
11	2014_Sep_30	BSTD	2.8	6.7	NS	4.29	13.155	4.6
11	2014_Sep_30	BSTD	2.8	6.7	EW	5.31	12.53	7.1
12	2014_Nov_05	BMD2	2.9	3.0	NS	2.17	5.25	1.815
12	2014_Nov_05	BMD2	2.9	3.0	EW	0.085	1.32	0.065
14	2015_Jan_06	BGAR	2.7	6.2	NS	4.125	7.78	4.165
14	2015_Jan_06	BGAR	2.7	6.2	EW	4.015	8.065	4.21
15	2015_Feb_15	BHKS	2.3	5.8	NS	3.89	9.945	3.75
15	2015_Feb_15	BHKS	2.3	5.8	EW	2.945	7.065	3.785
16	2015_Feb_15	BSTD	2.3	10.9	NS	5.215	13.255	5.3
16	2015_Mar_24	BSTD	2.3	10.9	EW	5.27	13.82	4.93
16	2015_Mar_24	G460	2.3	13.7	NS	11.755	21.455	7
16	2015_Mar_24	G460	2.3	13.7	EW	16.175	24.655	10.49

An important issue when including the effects of duration in the risk assessment is to account for the inverse correlation between the duration of the shaking and the amplitude of the acceleration. As shown in Figure 12.13, for the 292 horizontal components in the current Groningen database, there is a clear pattern: components associated with higher peaks of acceleration (> 50 cm/s^2) are associated with durations of 1 second or shorter, whereas all the records with longer durations (longer than, say, 6 seconds) are associated with extremely low amplitudes (< 5 cm/s^2). The plot also shows that the former type of records (high PGA,

short duration) are typically obtained at epicentral distances of less than 4 km, whereas the long-duration, low-amplitude records are generally from recording stations at epicentral distances of at least 8 km. These observations are consistent with the current hypothesis that waves leaving the reservoir at take-off angles that are not nearly vertical are subjected to multiple refractions and reflections by the high-velocity Zechstein salt formation overlying the reservoir—and the even higher velocity anhydrite layers within the Zechstein—leading to signals outside the epicentral area being dominated by multiple indirect arrivals.

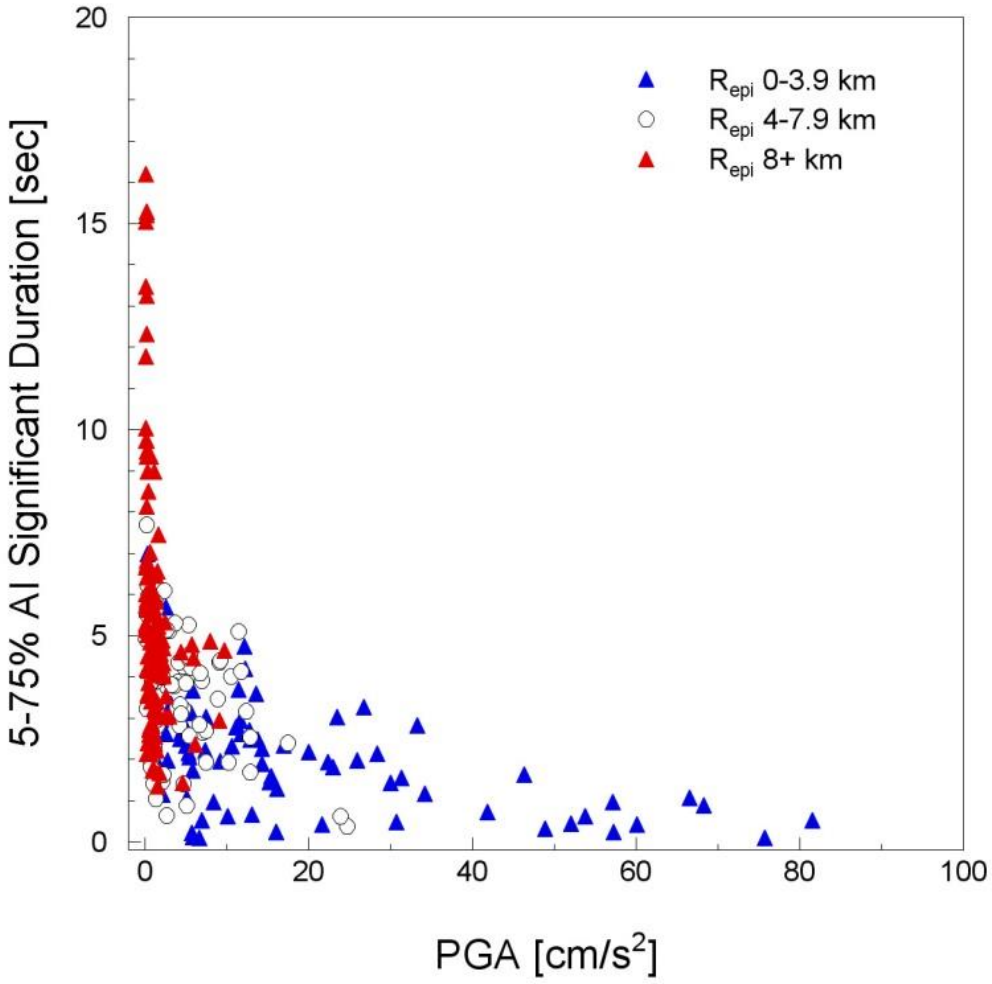

Figure 12.13. Relationship of D_{S5-75} and PGA values of Groningen events for different distance intervals

12.2 Existing duration GMPEs

As for PGA and the spectral acceleration ordinates, the current Groningen database is clearly insufficient to enable the derivation of GMPEs for duration that could be expected to provide reliable predictions over the full range of magnitudes of interest, namely from **M** 2.5 to 6.5. In this case, however, unlike for the prediction of spectral accelerations, stochastic simulations would not provide a useful tool for the extrapolation of predictions to larger

magnitudes for the simple reason that the simulations actually require an estimate of the ground-motion duration as an input (Bommer *et al.*, 2015a,b).

For the Version 1 GMPEs (Bommer *et al.*, 2015a,b), in order to produce a preliminary model, the most compromising approach was to adjust an existing GMPE for $D_{S5\text{-}75}$, derived from recordings of tectonic earthquakes, following a similar approach to what was done for the Version 0 GMPEs (Bommer & Dost, 2014). In particular, for the V1 model the two existing duration prediction equations of Bommer *et al.* (2009) and Kempton & Stewart (2006) were explored, with the former being adjusted in order to better fit the Groningen data (Bommer *et al.*, 2015a).

These two V1 candidate models should be regarded as first approximations to the solution of predicting durations. The main difference between them is that the modified Bommer *et al.* (2009) equation has a relatively strong distance dependence (out to 15 km) while the Kempton & Stewart (2006) model exhibits a stronger magnitude dependence (for large magnitude events). That said, a comparison of the two candidate models in terms of between-event and within-event residuals showed that the overall performance of these two candidates is similar in the region where we have data. However, the Kempton & Stewart (2006) model provides greater flexibility in terms of enabling physically-motivated adjustments to be made and it provides more meaningful predictions over a wide range of magnitudes and distances (specifically when extrapolating to the small magnitude range). Moreover, it leads to correlations with Sa that are broadly consistent with the Bradley (2011) model over the period range required, and for all these reasons this model was selected for use in the V1 risk model (Bommer *et al.*, 2015a).

For the V2 model, these two models have been further investigated, with additional considerations made in light of the availability of the average shear-wave velocity over the uppermost 30 m at each station, V_{S30} (m/sec). For the V1 model, all duration predictions were made assuming a field-wide constant value of V_{S30} equal to 200 m/s. Two additional, and very recent, GMPEs for duration (Lee & Green, 2014; Afshari & Stewart, 2015) have been considered as candidates for the V2 model. In the following, a brief description of each model and the parameter values adopted for the purpose of making comparisons is provided. Subsequently, the residuals of the Groningen durations calculated with respect to each GMPE are presented.

It should be noted that all of the above models represent the variation in the mean values of duration from earthquake-to-earthquake (*i.e.*, inter-event variability) and the variation in the data for a single earthquake (*i.e.*, intra-event variability) through the variances of random earthquake effects (inter-event residuals) and intra-event residuals respectively (Abrahamson & Youngs, 1992). The random effect for each earthquake (often referred to as the inter-event residual) is designated by η_i where the subscript i represents the i^{th} event in the database. The inter-event residuals can be thought of as the difference between the mean logarithmic duration for the i^{th} event and the mean logarithmic duration of an event having the same magnitude that is representative of the wider population (which in this case is assumed to be captured by the entire database). The model for the inter-event residuals assumes that these are normally distributed with a mean of zero and a variance of τ^2. The

intra-event error is designated by ε_{ij} where the subscripts *ij* indicate the j^{th} recording of the i^{th} event. The intra-event error is defined as the difference between the logarithmic duration value for the j^{th} record and the predicted median for the i^{th} event. The intra-event residuals are also considered to be normally distributed with a mean of zero and a variance of ϕ^2. The total variability of the duration model (σ_{tot}) is defined as the square root of the sum of the corresponding inter- and intra-event variances, as in Eq.(12.1).

$$\sigma_{tot} = \sqrt{\tau^2 + \phi^2} \tag{12.1}$$

The first model investigated is that proposed by Bommer *et al.* (2009). This model was calibrated using the records from the Next Generation of Attenuation (NGA) global database of accelerograms from shallow crustal earthquakes. The equation can be used to estimate ground-motion duration from shallow crustal earthquakes of magnitude between **M** 4.8 and 7.9 at distances up to 100 km from the source. Therefore, this model has been extrapolated down to lower magnitudes in order to make comparisons with the Groningen data.

The explanatory variables adopted in this model are the moment magnitude, **M**, the closest distance from the site to the fault rupture, R_{rup} (km), depth to the top of rupture, Z_{tor} (km) and the average shear-wave velocity over the uppermost 30 m at the site, V_{S30} (m/sec). The functional form adopted is given in Eq.(12.2).

$$\ln(D_{S5-75}) = c_0 + m_1 M + (r_1 + r_2 M)\ln(\sqrt{R_{rup} + h_1^2}) + v_1 \ln(V_{S30}) + z_1 Z_{tor} \tag{12.2}$$

For the small-magnitude earthquakes in the current database, it is reasonable to assume that R_{rup} and R_{hyp} are equivalent, hence the equation can be expressed in terms of R_{epi} and assuming a Z_{tor} = 3 km the model can be written as in Eq.(12.3).

$$\ln(D_{S5-75}) = -5.7864 + 1.2619M + (2.0063 - 0.252M)\ln(\sqrt{R_{epi}^2 + 14.4364}) - 0.29\ln(V_{S30}) \tag{12.3}$$

The total residuals of the Groningen records with respect to Eq.(12.3) are plotted in the left-hand panel of Figure 12.14, while the inter-event and intra-event residuals are plotted in the right-hand panels. The plot shows very large event terms for all of the earthquakes, reflecting a strong and consistent under-prediction of the durations by the GMPE.

The Kempton & Stewart (2006) model is based on recordings with magnitudes between **M** 5.0 and 7.6 while the close site-source distance ranges between 0 and 200 km, that is, also this model has been extrapolated to examine its compatibility with the Groningen data. Many of the records used by Kempton & Stewart (2006) are also common to the database used by Bommer *et al*. (2009) – albeit with different processing procedures having been applied to the records.

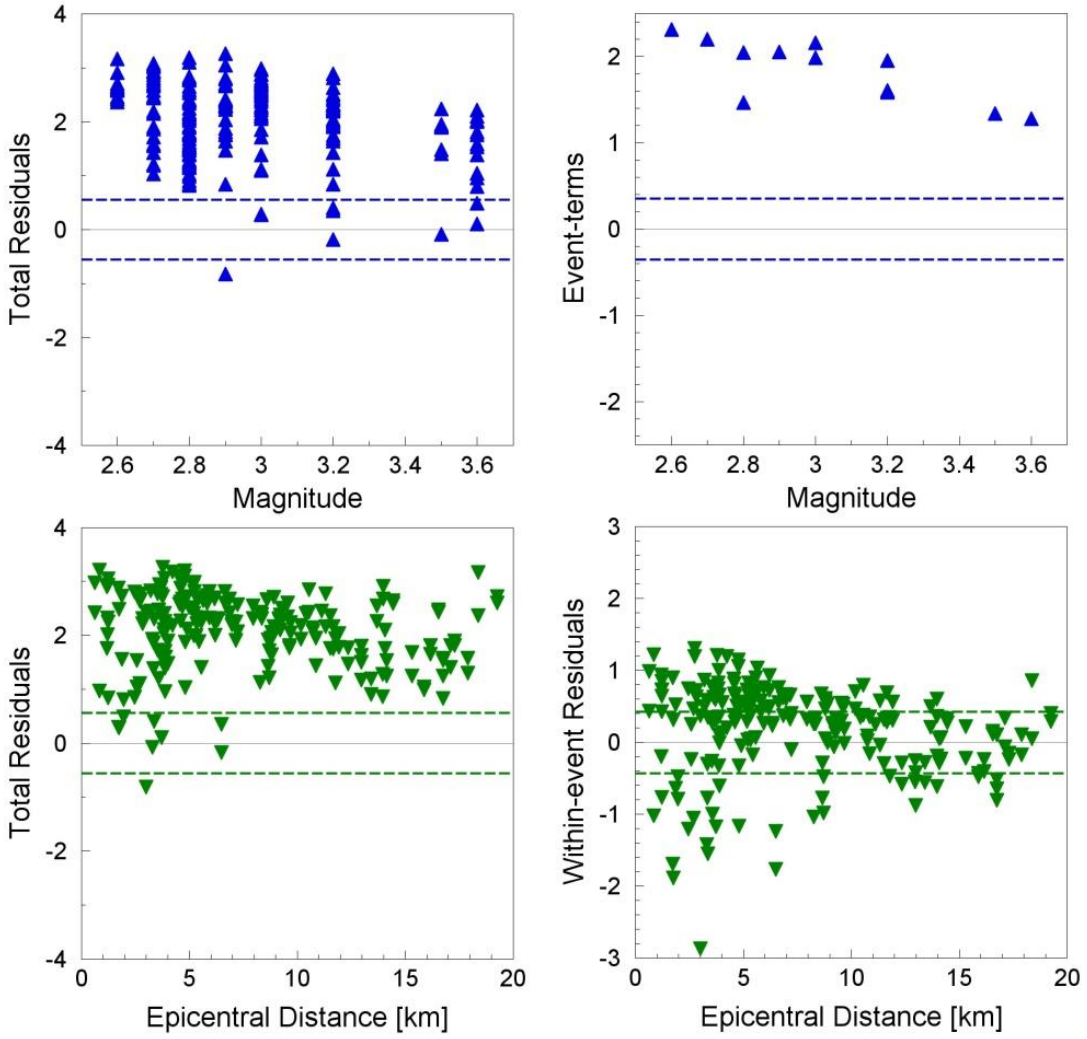

Figure 12.14. Total (*left*), between-event (*upper right*) and within-event (*lower right*) residuals of $D_{S5\text{-}75}$ durations of Groningen records with respect to the GMPE of Bommer *et al.* (2009). Dashed lines correspond to the total sigma (left) and the inter- and intra-event standard deviations (*right*).

For this GMPE, increases in significant duration associated with wave propagation and site effects (*i.e.* shear-wave velocity and basin effects) are taken as additive to the source term, $1/f_c(M_0,\Delta\sigma)$ (where f_c represents the corner frequency while M_0 and $\Delta\sigma$ the seismic moment and the stress drop respectively), Eq.(12.4). In the same equation, $f_1(r)$ represents the distance dependence while $f_2(s)$ represents the site dependence.

$$SD = \frac{1}{f_c(M_0,\Delta\sigma)} + f_1(r) + f_2(s) \qquad (12.4)$$

For the site response term, the authors provide three alternative basin-effect models, one for which the earthquake source is located within, or beneath, the basin (named “CBL” model) and another for which it is remote from the basin in which the site is located (“DBL” model). The third option is simply a generic option to account for deep soil effects without any particular information about the basin/source geometry. The general functional form is expressed in Eq.(12.5).

$$\ln(D_{S5-75})_{ij} = \ln\left[\frac{\left(\frac{\exp(b_1 + b_2(M_i - M^*))}{10^{1.5M_i+16.05}}\right)^{-1/3}}{4.9\cdot10^6\beta} + r_{ij}c_2 + (c_4 + c_5(V_{S30})_{ij}) + c_6 + c_7(z_{1.5})\right] \quad (12.5)$$

In this equation β is the shear-wave velocity in the source region in km/s. This functional form is used to predict different types of significant duration. However, for the case of the 5-75% significant duration the model can be simplified slightly as in this case the 'stress drop' term becomes magnitude independent. In addition, and again assuming for small-magnitude earthquakes that the R_{rup} distance metric is equivalent to R_{hyp} and considering the hypothesis of CBL model ($Z_{1.5}$ is assumed equal to 600m as considered the best option in Bommer *et. al*, 2015a), the equation becomes:

$$\ln(D_{S5-75}) = \ln\left[\frac{\left(\frac{\exp(6.02)}{10^{1.5M_i+16.05}}\right)^{-1/3}}{4.9\cdot10^6\beta} + 0.07\sqrt{R_{epi}^2 + 9} + (0.82 - 0.0013V_{S30}) + 1.46\right] \quad (12.6)$$

As an alternative, Eq.(12.7) illustrates the corresponding equation when no assumption is made about the basin/source geometry. This corresponds to the 'ALL' case presented by the authors. It should also be noted that this generic 'ALL' case provides predictions that are very similar to those arising from consideration of DBL basin effects.

$$\ln(D_{S5-75}) = \ln\left[\frac{\left(\frac{\exp(6.02)}{10^{1.5M_i+16.05}}\right)^{-1/3}}{4.9\cdot10^6\beta} + 0.07\sqrt{R_{epi}^2 + 9} + (0.82 - 0.0013V_{S30}) + 0.42\right] \quad (12.7)$$

Residuals of the Groningen durations with respect to Eq.(12.6-12.7) are illustrated in Figure 12.15 and 12.16 respectively, using the same format as for Figure 12.14.

Figure 12.15 shows that event-terms, within-event residuals and total residuals are smaller than Figure 12.14 and closer to the zero mean (suggesting a better fit of Groningen data with respect to the GMPE proposed by Bommer *et al.*, 2009), although the plots of the inter-event residuals with respect to magnitude show a weak negative trend (upper part of Figure 12.15) whereas plots with respect to epicentral distance show a weak positive trend (lower part of Figure 12.15). Similar observations can be made for Figure 12.16, although in this case the event-terms are consistently higher than those in Figure 12.15, implying a consistent under-prediction of the duration.

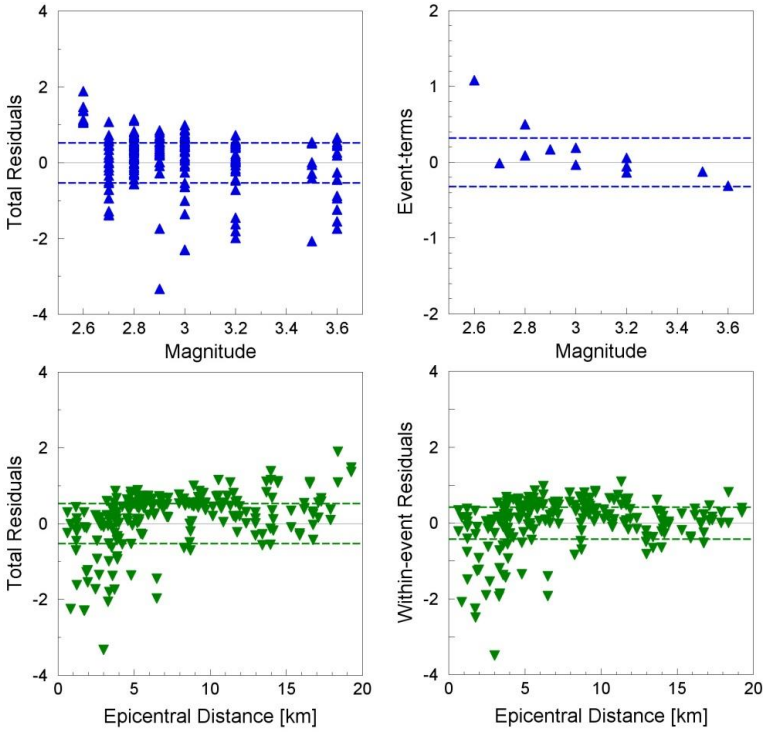

Figure 12.15. Total (*left*), between-event (*upper right*) and within-event (*lower right*) residuals of $D_{S5\text{-}75}$ durations of Groningen records with respect to the GMPE of Kempton & Stewart (2006) considering for the basin-effect the CBL model. Dashed lines correspond to the total sigma (left) and the inter- and intra-event standard deviations (*right*).

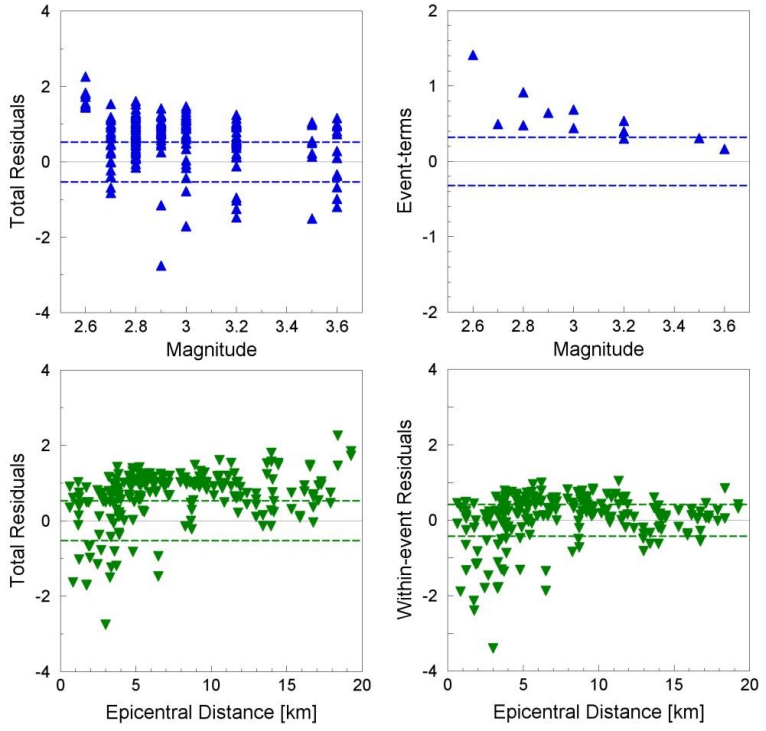

Figure 12.16. Total (*left*), between-event (*upper right*) and within-event (*lower right*) residuals of $D_{S5\text{-}75}$ durations of Groningen records with respect to the GMPE of Kempton & Stewart (2006) considering for the basin-effects the case “ALL”. Dashed lines correspond to the total sigma (left) and the inter- and intra-event standard deviations (*right*).

The model presented by Lee & Green (2014) is based on a dataset that encompasses magnitudes from **M** 4.5 to 7.6 and distances from 0.1 to 199 km and has the simple functional form shown in Equation 12.8.

$$\ln(D_{S5-75}) = \ln\{C_1 + C_2 \exp(M-6) + C_3 R_{rup} + [S_1 + S_2(M-6) + S_3 R_{rup}]S_S\} \quad (12.8)$$

In this equation, the parameters C_1 through C_3 and S_1 through S_3 are regression coefficients, M is the moment magnitude, R_{rup} is the closest distance to the fault rupture plane (km) and S_S is a binary number representing local site conditions: S_S=0 for rock sites and S_S=1 for soil sites.

The regression analyses were performed on the significant durations of the individual horizontal components of the data set. Coefficients are different for stable continental and active shallow crustal regions. Hence, considering the latter case and 'soil' site conditions, Equation 8 can be rewritten using specific numerical coefficients as in Eq.(12.9).

$$\ln(D_{S5-75}) = \ln\left(1.86\exp(M-6) + 0.06\sqrt{R_{epi}^2 + 9} + 0.22\right) \quad (12.9)$$

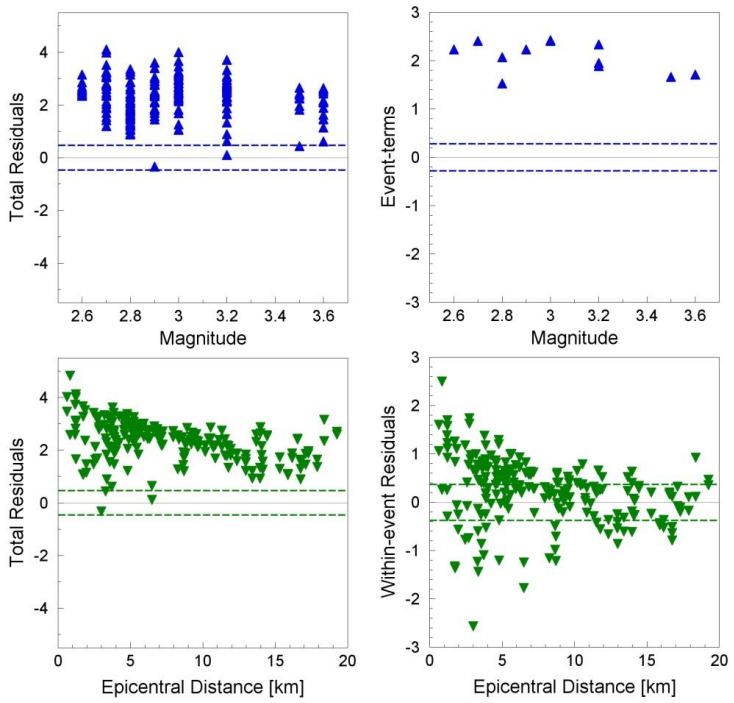

Figure 12.17. Total (*left*), between-event (*upper right*) and within-event (*lower right*) residuals of D_{S5-75} durations of Groningen records with respect to the GMPE of Lee & Green (2014). Dashed lines correspond to the total sigma (left) and the inter- and intra-event standard deviations (*right*).

The total residuals of the D_{S5-75} durations for the Groningen records with respect to Eq.(12.9) are plotted in the left-hand panel of Figure 12.17 while the inter-event and intra-event residuals are shown in the right-hand panel of the same figure. In Figure 12.17 very large values of event-terms and total residuals can be observed, implying a strong and consistent

under-prediction of the duration. It could be argued that there is a slight negative trend with respect to magnitude, but the overall bias overwhelms any trend that exists.

Finally, the model of Kempton & Stewart (2006) has been superseded (since the release of the V1 duration model, Bommer *et al.*, 2015a) by a new model by Afshari & Stewart (2015) that makes use of a much larger database of ground-motion recordings, with a particularly large increase in the coverage of the database at small magnitudes. Given that the Kempton & Stewart (2006) model was the preferred option for the V1 model, the new model superseding this is clearly a prime candidate whose performance must also be investigated.

The GMPE was derived using a global database for active crustal regions recently developed for the Next Generation Attenuation NGA-West2 project (Ancheta *et al.*, 2014). This database builds upon the NGA database considered by Bommer *et al*. (2009) and covers the magnitude range from **M** 3.0-7.9. The additions to the database used by Bommer *et al*. (2009) are not major for moderate to large magnitudes (say, above **M** 5.0), but are very significant for the smaller events. Like the model of Kempton & Stewart (2006), a distinguishing feature of this model relative to other recent duration GMPEs (*e.g.*, Bommer *et al.*, 2009) is that they consider the source and path contributions to duration as additive in arithmetic units (*e.g.*, seconds) and the source term is parameterized directly in terms of a 'stress parameter'. However, unlike the other studies, these authors combine significant durations from the two as-recorded horizontal components using the geometric mean for the purposes of developing their model.

The median prediction of the ground motion duration is expressed as in Eq.(12.10) with the terms F_E, F_P and F_S reflecting source, path and site terms, respectively.

$$\ln(D_{S5-75}) = \ln\left[F_E(M, sof) + F_P(R_{rup})\right] + F_S(V_{S30}, \delta z_1) \qquad (12.10)$$

The source scaling in the Afshari & Stewart (2015) model is defined by Eq.(12.11).

$$F_E(M, sof) = \begin{cases} 1/f_c & M > M_1 \\ b_0(sof) & M \le M_1 \end{cases} \qquad (12.11)$$

In this expression, the corner frequency is defined as in Eq.(12.12) where $M_0 10^{1.5M+16.05}$ and β = 3.2km/s.

$$f_c = 4.9 \times 10^6 \beta \left(\frac{\Delta\sigma}{M_0}\right)^{1/3} \qquad (12.12)$$

The stress parameter is defined as a function of magnitude (Eq.(12.13)) where b_1, b_2, b_3, and $\mathbf{M}_2$ are model parameters and **M*** is a reference magnitude (specified as 6).

$$\Delta\sigma = \begin{cases} \exp\left[b_1(mech) + b_2(M_2 - M^*)\right] & M \le M_2 \\ \exp\left[b_1(mech) + b_2(M_2 - M^*)\right] + b_3(M - M_2) & M > M_2 \end{cases} \qquad (12.13)$$

The path duration is linearly dependent on distance R_{rup}, but with different slopes for three R_{rup} intervals with changing slopes at R_1 and R_2 as in Eq.(12.14), where c_1 to c_3, R_1 and R_2 are model parameters.

$$F_P = \begin{cases} c_1 R_{rup} & R_{rup} \geq R_1 \\ c_1 R_1 + c_2 (R_{rup} - R_1) & R_1 < R_{rup} \leq R_2 \\ c_1 R_1 + c_2 (R_2 - R_1) + c_3 (R_{rup} - R_2) & R_{rup} > R_2 \end{cases} \quad (12.14)$$

The site term F_S is defined in Eq.(12.15-16) and accounts for both shallow and deep effects.

$$F_S = c_4 \ln\left(\frac{\min(V_{S30}, V_1)}{V_{ref}}\right) + F_{\delta Z_1} \quad (12.15)$$

Parameters c_4, c_5, V_{ref}, V_1, and $\delta z_{1,ref}$ are the model parameters set by regression or by visual inspection of the data. The term $F_{\delta z_1}$ captures the effects of the deeper velocity structure beneath the site, and is a function of the difference, δz_1, between the depth to a velocity horizon of 1.0 km/s at the site and a reference value representative of a particular region (*e.g.*, California).

$$F_{\delta Z_1} = c_5 \min(\delta z_1, \delta z_{1,ref}) \quad (12.16)$$

Considering the maximum values of magnitude and distance in the Groningen database, assuming unknown style-of-faulting and ignoring the extremely weak effects of sediment depth (by setting $\delta z_1 = 0$, each term of Eq.(12.10) can be evaluated and simplified into the forms shown in Eq.(12.17-19).

$$F_E = 1.28 \qquad (M < 5.35) \quad (12.17)$$

$$F_P = \begin{cases} 0.1159 R_{rup} & R_{rup} \leq 10km \\ 0.1159 R_{rup} + 0.1065(R_{rup} - 10) & 10 < R_{rup} \leq 50km \end{cases} \quad (12.18)$$

$$F_S = -0.2246 \ln\left(\frac{V_{S30}}{368.2}\right) \qquad (V_{s30} \leq 600 m/s) \quad (12.19)$$

The total, within-event and between-event residuals of Groningen duration for the Afshari & Stewart (2015) model are shown in Figure 12.18.

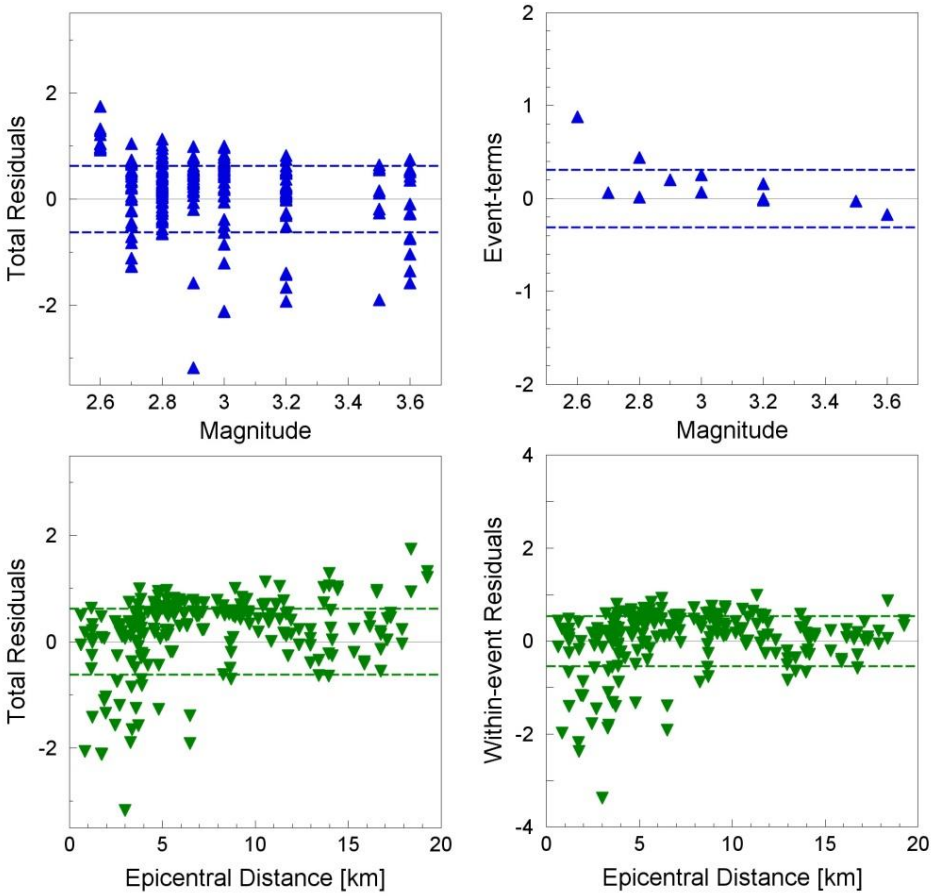

Figure 12.18. Total (*left*), between-event (*upper right*) and within-event (*lower right*) residuals of $D_{S5\text{-}75}$ of Groningen records with respect to the GMPE of Afshari & Stewart (2015). Dashed lines correspond to the total sigma (left) and the inter- and intra-event standard deviations (*right*).

Figure 12.18 shows that the model seems to fit the Groningen data reasonably well. The event-terms, within-event residuals and total residuals are relatively small and close to zero, when compared with the other candidates. However, the plots of the inter-event residuals against magnitude show a weak negative trend and a clear positive bias (upper part of Figure 12.18) while the plot of intra-event residuals with respect to epicentral distance shows clear issues at short distances (lower part of Figure 12.18). Table 12.2 shows the components of the standard deviations for total residuals (σ), event-terms (τ) and the within-event residuals (ϕ) published by each model investigated. On the basis of the investigations illustrated in this section, the Kempton & Stewart (2006) and the Afshari & Stewart (2015) warrant further consideration for the V2 model.

Table 12.2. Standard deviation components associated with duration prediction equations.

	Bommer *et al.* (2009)	**Kempton & Stewart (2006)**	**Lee & Green (2014)**	**Afshari & Stewart (2015)**
τ	0.3527	0.32	0.28	0.31
ϕ	0.4304	0.42	0.37	0.54
σ	0.5565	0.528	0.464	0.6227

12.3 Exploratory analyses

While the Kempton & Stewart (2006) model used as the V1 duration model and the more recent Afshari & Stewart (2015) model both show promise for use as the V2 model, the previous section has highlighted biases and trends in the residuals computed using these models in their unadjusted forms. In particular, since the V1 duration model adopted the Kempton & Stewart (2006) model, as a first step, some exploratory analyses have been carried out to identify adjustments that can be made to this model. As a first step, the distance scaling implied by the Groningen data is investigated given that trends that were observed for all models in the previous section. Hence, different functional forms, representing possible path scaling options, have been considered. The most promising functional forms obtained are reported in Table 12.3. In the same table for each model the total standard deviation of the residuals is also reported. Figures 12.19-12.22 (left panels) illustrate the Groningen data and the median predictions calculated for different magnitude values, while the right hand panels of the same figures show the total residuals of Groningen durations with respect to magnitude for each model.

Table 12.3. Regression models and standard deviation of residuals.

Model	Regression expression	σ_{tot}
#1	$\ln(D_{S5-75}) = b_1 + b_2 M + b_3 R_{epi}$	0.674
#2	$\ln(D_{S5-75}) = b_1 + b_2 M + b_3 \ln(R_{epi})$	0.649
#3	$\ln(D_{S5-75}) = b_1 + b_2 M + b_3 \ln(\sqrt{R_{epi}^{\ 2} + b_4})$	0.646
#4	$\ln(D_{S5-75}) = b_1 + b_2 M + b_3 \ln(R_{epi} + b_4)$	0.647

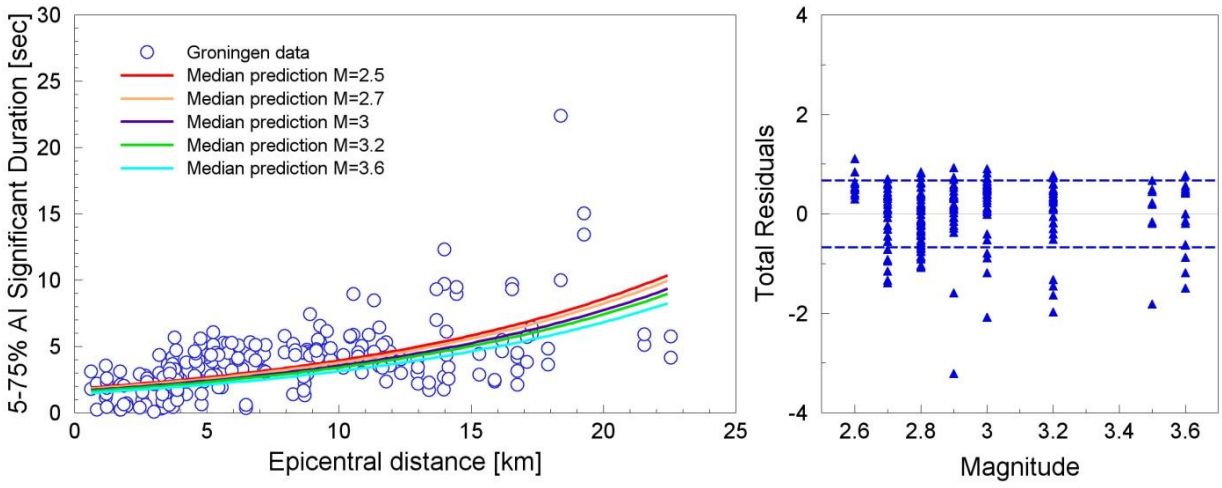

Figure 12.19. Groningen data, median prediction according to model #1 and total residuals of Groningen durations with respect to magnitude for the same model.

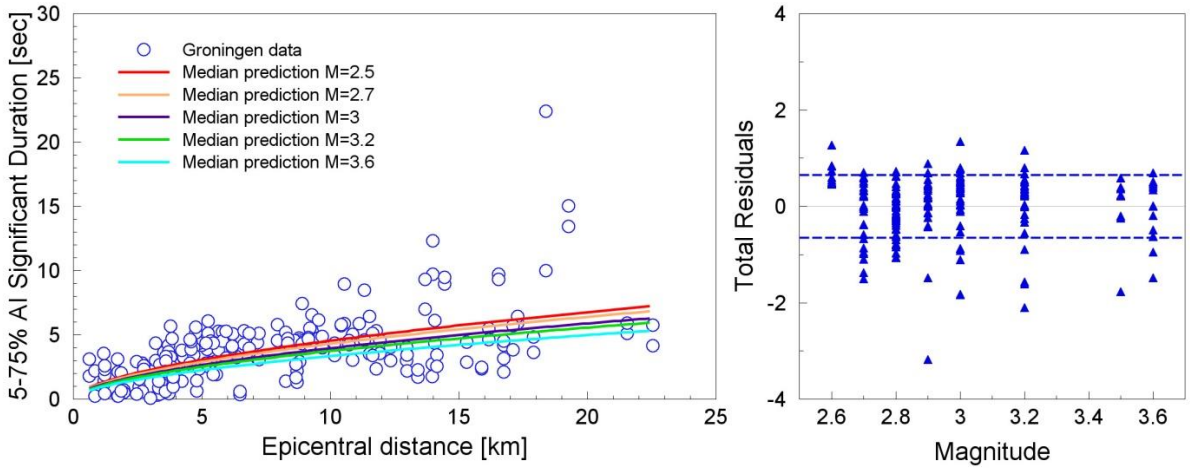

Figure 12.20. Groningen data, median prediction according to model #2 and total residuals of Groningen durations with respect to magnitude for the same model.

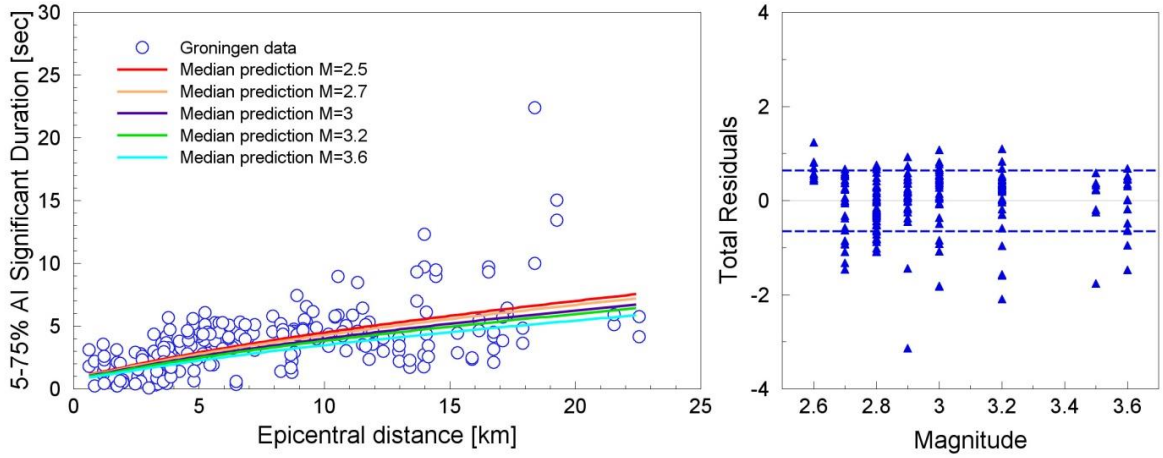

Figure 12.21. Groningen data, median prediction according to model #3 and total residuals of Groningen durations with respect to magnitude for the same model.

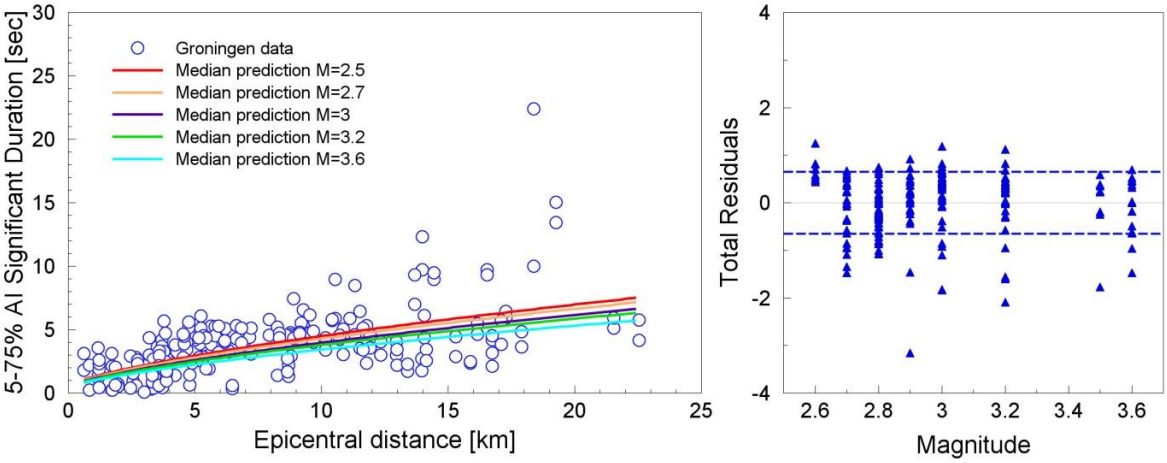

Figure 12.22. Groningen data, median prediction according to model #4 and total residuals of Groningen durations with respect to magnitude for the same model.

The above figures highlight two important aspects. The first is that the different regression models provide very similar predictions (model #3 has a slightly smaller standard deviation, but the differences among these models are very small) while the second, and more important, aspect is that the Groningen data show a very weak magnitude-dependence and opposite to what is usually expected, that is, durations increase with decreasing magnitudes.

Figure 12.23 shows the distance scaling of the Kempton & Stewart (2006) model and the path scaling function (model #3) considered earlier in this section. It is to note how for the Kempton & Stewart (2006) model, the slope in the region where there are observations is very different to what is suggested by the data. Hence, the path scaling function (model #3) represents a valid option to adjust such differences.

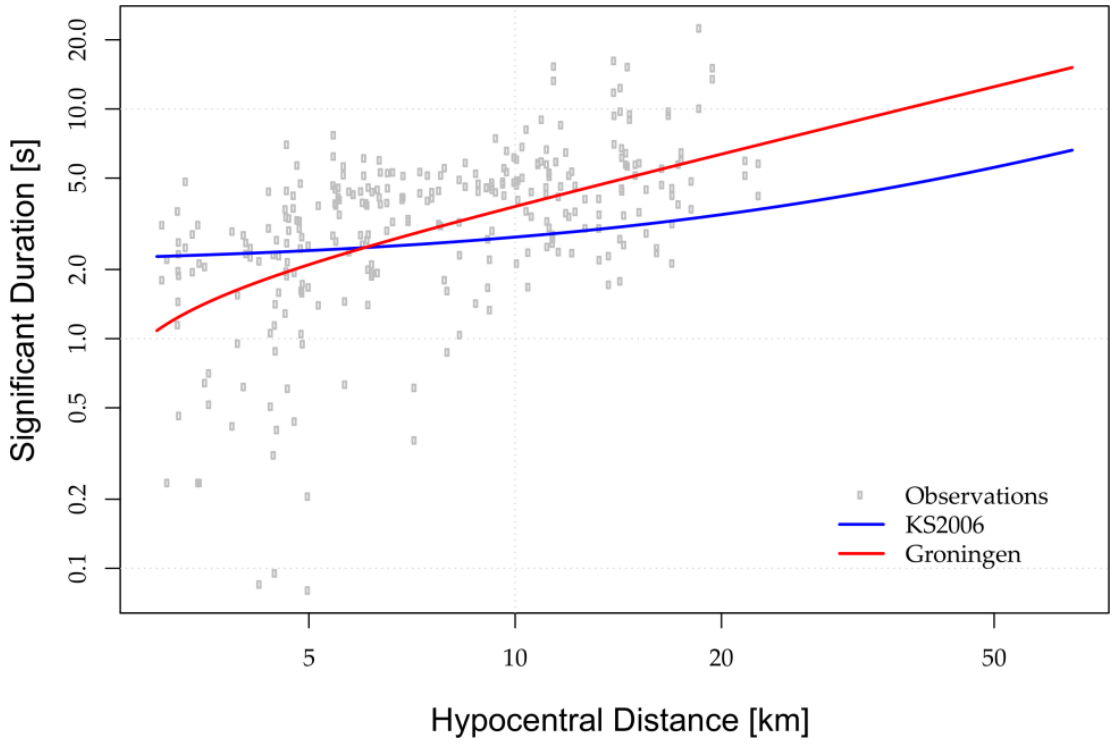

Figure 12.23. Comparison of the distance scaling of the Kempton & Stewart (2006) model and the Groningen data.

In addition, it is possible to observe some potential breaks in distance scaling consistent with those identified in the analysis of the Fourier and response spectral amplitudes if a segmented distance scaling model is fitted (Figure 12.24). However, the same figure also shows that there is a significant degree of dispersion within the data.

As already stated in section 12.2, the functional form for the Kempton & Stewart (2006) model is based upon Eq.(12.20), where the first term in the square brackets represents the source scaling (M_0 is the seismic moment while $\Delta\sigma$ represents the stress drop), the second term (c_2R_{rup}) reflects path scaling, and the final term, $f_2(S)$, represents shallow site effects.

$$\ln(D_{S5-75}) = \ln\left[\frac{\left(\frac{M_0}{\Delta\sigma}\right)^{1/3}}{4.9\cdot 10^6\,\beta} + c_2 R_{rup} + f_2(S)\right] \qquad (12.20)$$

Further terms are added to this base functional form to account for the effects of sediment depth and rupture directivity.

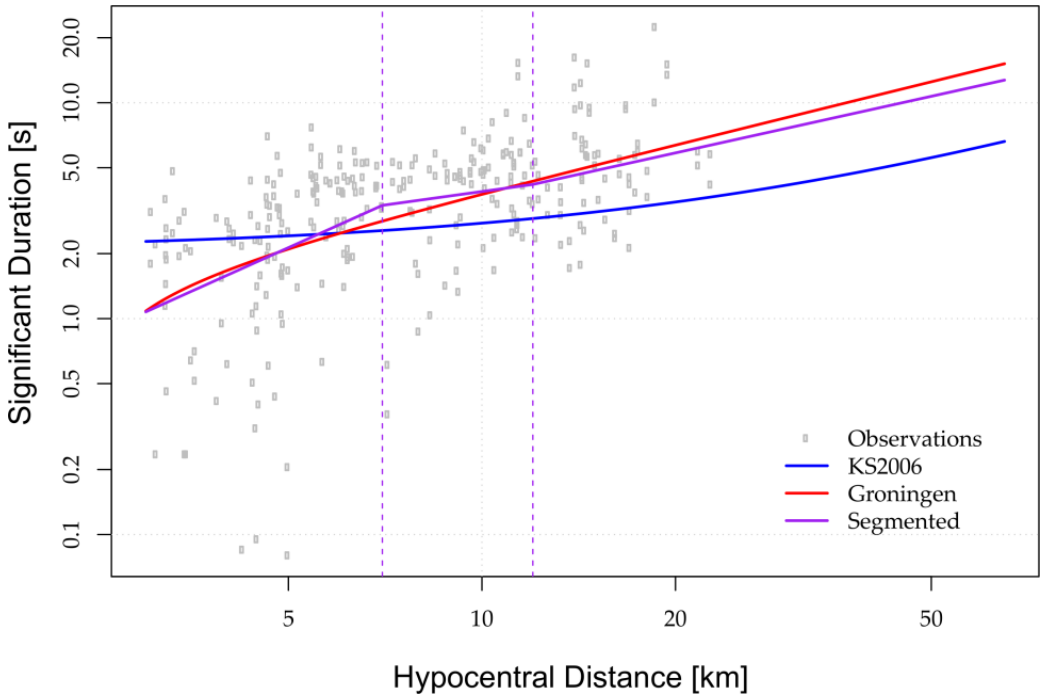

Figure 12.24. Comparison of distance scaling of Kempton & Stewart (2006) and the Groningen data, including a fit obtained using a segmented distance scaling.

It is important to note that the model is (conceptually) parameterized in terms of the stress drop $\Delta\sigma$ directly. That said, for $D_{S5\text{-}75}$, Kempton & Stewart (2006) find the best fit value for the stress drop of 411 bar, which is far higher than the expected value for the dataset used by the authors (typically, stress drop estimates for this database fall in the range 80-100 bar).

In particular, the Kempton & Stewart (2006) function is based upon the idea that the source scaling varies inversely with the corner frequency of a Brune spectrum and this is the first term inside the square brackets in Eq.(12.20). This first term, taken independently of the distance and site scaling, predicts a linear scaling of the logarithmic significant duration with magnitude. Therefore, any change in the value of the stress drop (or of the crustal velocity near the source, β) results in a shift up or down of the predicted logarithmic duration. This curve always remains linear when this term is considered in isolation.

However, when the Kempton & Stewart (2006) model is pushed to low values of magnitude the scaling does not actually stay linear. The reason for this can be appreciated from inspection of Eq.(12.20). In the case that the magnitude decreases, the seismic moment also decreases. For sufficiently small magnitude events, the first term in the square brackets in Eq.(12.20) becomes small in comparison with the contribution of the other terms related to distance and site scaling:

$$\ln(D_{S5-75}) \xrightarrow{M_0 \to 0} \ln(c_2 R_{rup} + f_2(S)) \qquad (12.21)$$

In order to observe how the Kempton & Stewart (2006) model predicts the Groningen data, a similar exercise to what was performed for the development of the V1 GMPE has been performed. In the first instance, however, the interest lies in understanding the source scaling of duration down to small magnitudes. For this reason model predictions for the limiting case of $R_{rup} = R_{hyp} = 3$ km will be compared.

In order to transform the observed data, the Groningen-specific path scaling options defined in Table 12.3 have been considered. As already noted, the optimal distance scaling model that was found among other similar alternative options was model #3, written again in Eq.(12.22):

$$\ln(D_{S5-75}) = b_1 + b_2 M + b_3 \ln(\sqrt{R_{epi}^{\ 2} + b_4}) \qquad (12.22)$$

To adjust the observed data to a reference distance of $R_{epi} = 0$km, we use this function to subtract the expected path effects from the data based upon their observed epicentral distances, and then add back in the corresponding effects for an epicentral distance of zero. This operation to shift the observed data back to the smallest possible epicentral distance is shown in Eq.(12.23).

$$\ln(D_{S5-75}(R_{epi} = 0)) = \ln[D_{S5-75}(R_{epi})] + b_3 \ln(b_4) - b_3 \ln(\sqrt{R_{epi}^{\ 2} + b_4}) \qquad (12.23)$$

In Figure 12.25 the predictions of the Kempton & Stewart (2006) model (for the three different types of basin effects available but always using $Z_{1.5} = 600$ m) are compared to the adjusted durations ($D_{S5\text{-}75}(R_{epi} = 0$ km) denoted by black dots). This comparison suggests that the Kempton & Stewart (2006) model is a very good candidate, which corroborates the findings of the V1 GMPE Report (Bommer *et al.*, 2015a), although here the basin effects predicted using DBL or 'ALL' options appear preferable to those using CBL.

A particularly useful feature of this model is that, in principle, adjustments can be made by interpreting the stress drop parameter as being an actual stress drop. This means that by treating a particular Kempton & Stewart (2006) coefficient as being equivalent to the stress drop, predictions can be made for any desired alternative value of stress drop. An example of this is shown in Figure 12.26 in which modified predictions for a stress drop of 30 bar have been provided. It is worth noting that this adjustment has no impact for small magnitude events, but becomes significant for the larger events.

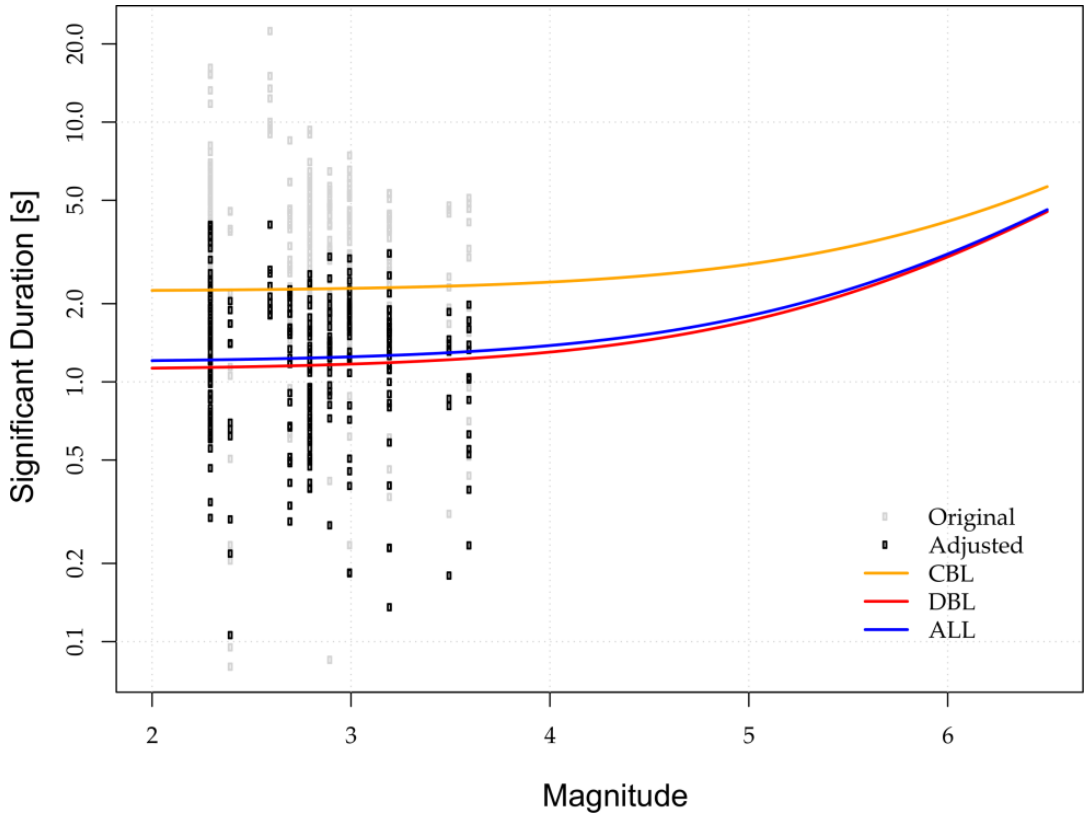

Figure 12.25. Comparison of Kempton & Stewart (2006) fit to adjusted Groningen observations.

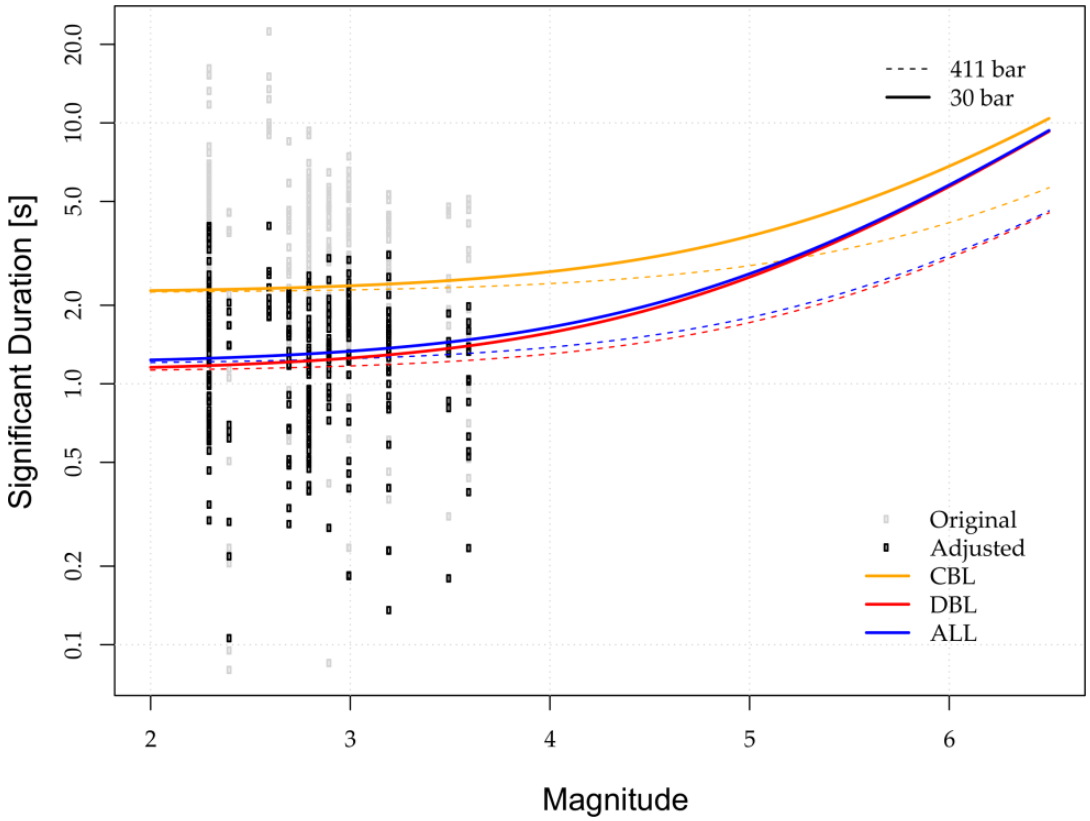

Figure 12.26. Comparison of the Kempton & Stewart (2006) model adjusted for an alternative value of stress drop, with adjusted Groningen observations.

However, from numerous other studies there is reason to assume that the stress drop for moderate events using the same dataset as that used by Kempton & Stewart (2006) should be closer to 80-100 bar rather than ≈ 400 bar. Therefore, while it is conceptually easy to make the adjustment, it is not clear how the resulting predictions actually reflect the stress drop levels that we are interested in.

12.4 Exploration of model options

On the basis of the exploration of residuals in Section 12.2 as well the investigations undertaken and presented in the report for the V1 duration model (Bommer *et al.*, 2015a), the Kempton & Stewart (2006) model appeared to perform reasonably well in terms of its magnitude scaling but deficiencies were noted in terms of its distance scaling (Section 12.3).

However, the functional form adopted by Kempton & Stewart (2006) was able to achieve this relatively good performance without targeting the small magnitude range during their model development. That is, the nonlinear scaling for very small magnitude events was not achieved by design.

One of the features of the Kempton & Stewart (2006) model that makes it worthy of consideration for the V2 duration model is that the underlying functional form is based upon conceptual arguments that allow one to understand how the effects of stress drop should influence predicted durations. Given that it is desirable to develop a duration model that can account for differences in stress drop, this feature is potentially very useful. However as already said in Section 12.2, the model of Kempton & Stewart (2006) has, since the release of the V1 duration model (Bommer *et al.*, 2015a), been superseded by the new model of Afshari & Stewart (2015).

Much of the underlying concepts that underpin the Kempton & Stewart (2006) model are retained for the Afshari & Stewart (2015) model, but there are some notable exceptions. For the latter model the approach of including site effects (both shallow and deep) as additive contributions to the source duration has been abandoned and they are now included as multiplicative terms. This modelling approach makes more physical sense, but has the side effect of making the theoretical scaling of the source durations inconsistent with what is observed in Groningen.

However, the Afshari & Stewart (2015) model avoids this issue that would present itself for small magnitude events by fixing the level of source duration to be constant for magnitudes below a particular threshold of $\mathbf{M}_1 = 5.35$. The basis of this modelling decision was investigations of inferred magnitude dependence of stress drop from the database that they considered.

Figure 12.27 compares the source scaling (durations are predicted for an epicentral distance of zero kilometres, and observed durations are mapped to this distance by applying the proposed distance scaling model presented in Section 12.3) for the Kempton & Stewart (2006) and Afshari & Stewart (2015) models.

The predictions are made assuming that R_{hyp} is equivalent to R_{rup} for these very small events and a V_{S30} = 200 m/s is considered. For the deep site effects, the Kempton & Stewart (2006) model is implemented with the 'ALL' case (*i.e.*, not 'CBL' or 'DBL') and the depth to the V_S 1500 m/s horizon is assumed to be 600 m, as adopted for the V1 duration model investigations. For the Afshari & Stewart (2015) model, the sediment depth differential $\delta_{z1} = z_1 - \mu_{z1}(V_{S30})$ has been calculated considering that the depth to the V_S = 1000 m/s horizon is set to be the expected value for California (Eq.(12.24)).

$$\ln(\mu_{z1}) = \frac{-7.15}{4}\ln\left(\frac{V_{S30}^4 + 570.94^4}{1360^4 + 570.94^4}\right) - \ln(1000) \qquad (12.24)$$

From this figure it can be appreciated that the general magnitude scaling over the range from **M** 5.0-7.0 is very similar for the two models. However, it is also clear that the Afshari & Stewart (2015) model shows strong breaks in scaling at particular magnitudes ($\mathbf{M}_1$ = 5.35 and **M** = 7.15) and these breaks reflect modelling choices made by these developers.

As there is no magnitude scaling below $\mathbf{M}_1$ for the Afshari & Stewart (2015) model (which is consistent with the Groningen data), but the predictions are clearly biased high, an obvious option is to effectively lower the value of $\mathbf{M}_1$ present in their model so that a good agreement is obtained with the observed data. This approach is shown conceptually in Figure 12.28 where the effect of using various different values of $\mathbf{M}_1$ is shown.

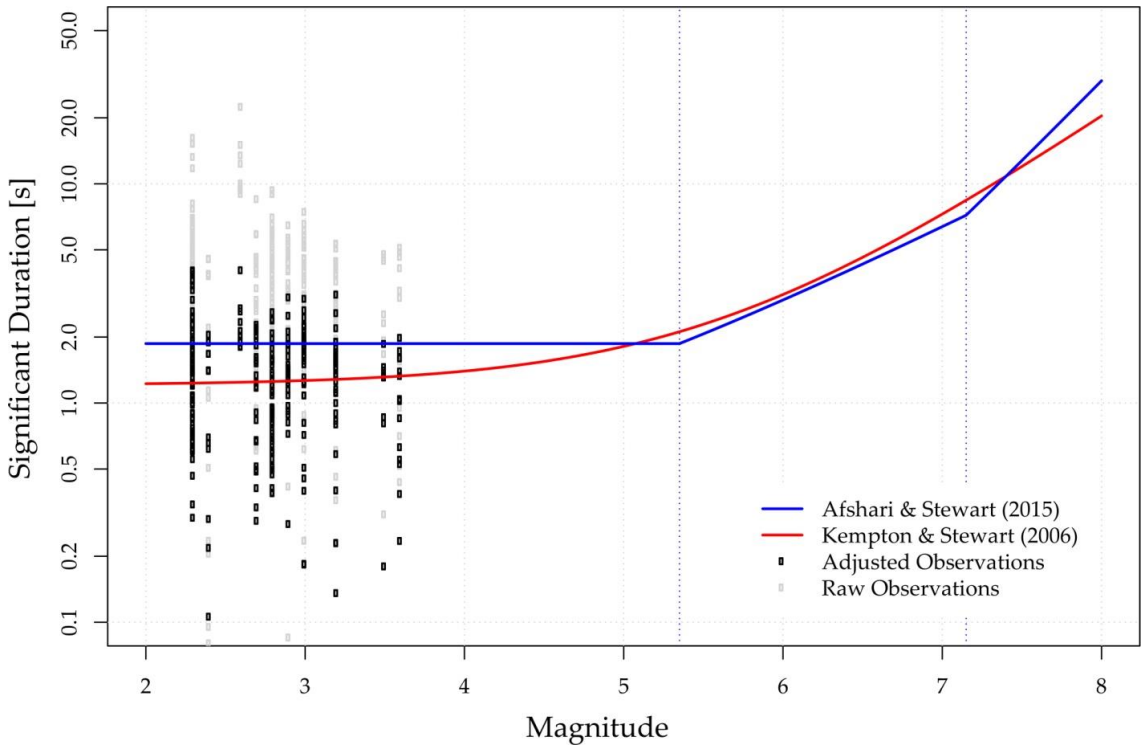

Figure 12.27. Comparison of the source scaling of the Kempton & Stewart (2006) and Afshari & Stewart (2015) duration models.

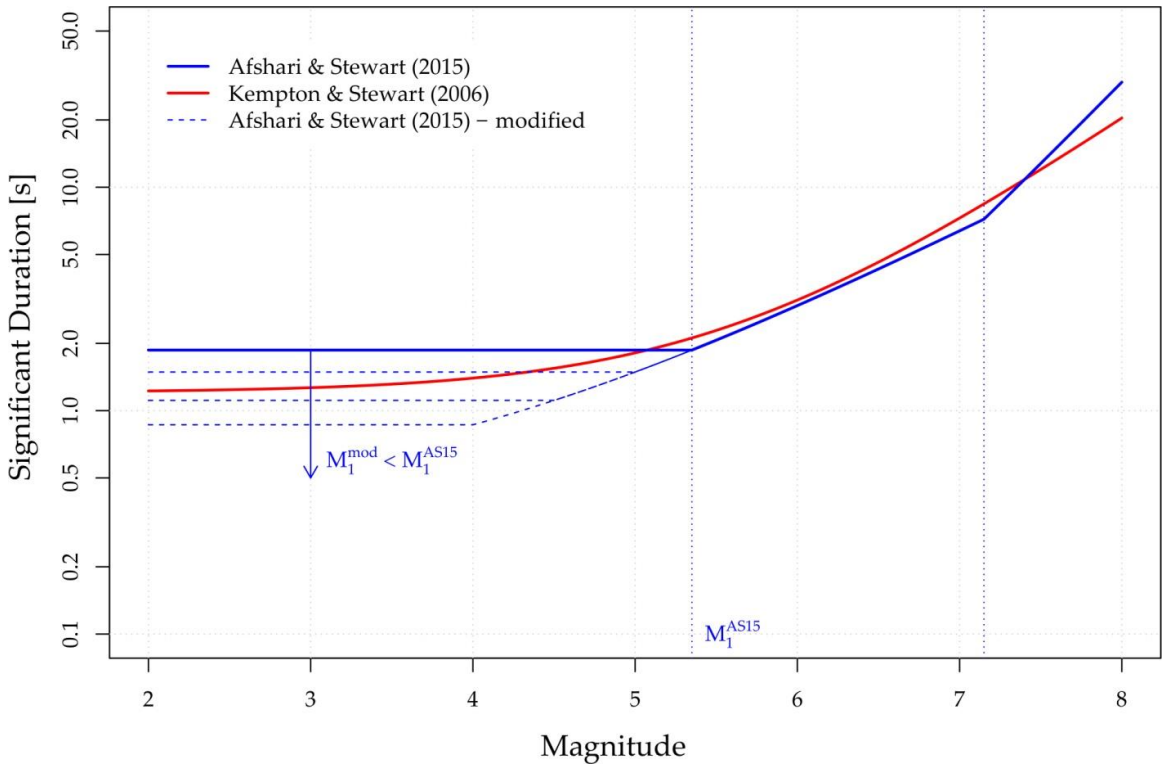

Figure 12.28. Comparison of the source scaling of the Kempton & Stewart (2006) and Afshari & Stewart (2015) duration models with adjustments made to the AS2015 model at small magnitudes.

Clearly, this approach enables one to retain the features of the magnitude scaling for moderate to large events but to have a good agreement with the Groningen durations at the same time. In terms of a model adjustment, this effect is very straightforward to achieve.

However, while the source scaling of the new Afshari & Stewart (2015) model is relatively straightforward to adjust, the distance scaling, like that of the Kempton & Stewart (2006) model, remains inconsistent with the scaling observed in Groningen.

In the previous section, a number of alternative distance scaling functions were considered to represent the Groningen observations. These models were all developed in terms of the epicentral distance to ensure consistency with the model for the response spectral ordinates. However, when showing the distance scaling of the Kempton & Stewart (2006) and Afshari & Stewart (2015) models, it is more natural to plot the scaling with respect to hypocentral distance given that these models adopt the rupture distance metric (which tends to be equivalent to hypocentral distance for small magnitude events).

The scaling of these models with respect to hypocentral distance is shown in Figure 12.29. Also shown in this figure are two Groningen-specific models, the red curve corresponds to the optimal functional form found in Section 12.3 of this report and has distance scaling expressed in Eq.(12.25).

$$\ln(D_{S5-75}) \propto c_2 \ln(\sqrt{R^2 + c_3}) \qquad (12.25)$$

In the same figure an additional segmented distance scaling model is shown in purple. This purple curve has distance scaling that can be represented by Eq.(12.26) where R in this particular case is hypocentral distance and the r_a and r_b values are taken as being 7 and 12km respectively. These values are consistent with breaks in scaling observed in the numerical waveform modelling and from the Fourier spectral inversions undertaken for the development of the spectral amplitude GMPE.

$$\ln(D_{S5-75}) \propto \begin{cases} c_4 \ln(R) & R \le r_a \\ c_4 \ln(R) + c_{4a} \ln\left(\frac{R}{r_a}\right) & r_a < R \le r_b \\ c_4 \ln(R) + c_{4a} \ln\left(\frac{R}{r_a}\right) + c_{4b} \ln\left(\frac{R}{r_b}\right) & R > r_b \end{cases} \quad (12.26)$$

The main information given by this comparison is that both the segmented distance scaling and the continuous distance scaling are very similar to each other. In addition, the general rate of increase in durations for larger distances is very comparable to the rates suggested by the Afshari & Stewart (2015) and Kempton & Stewart (2006) models. However, the amplitudes are clearly very different and these latter models clearly under-predict the durations over a significant range of importance for the hazard and risk model. Note that the predictions presented here are for a magnitude of 2.8.

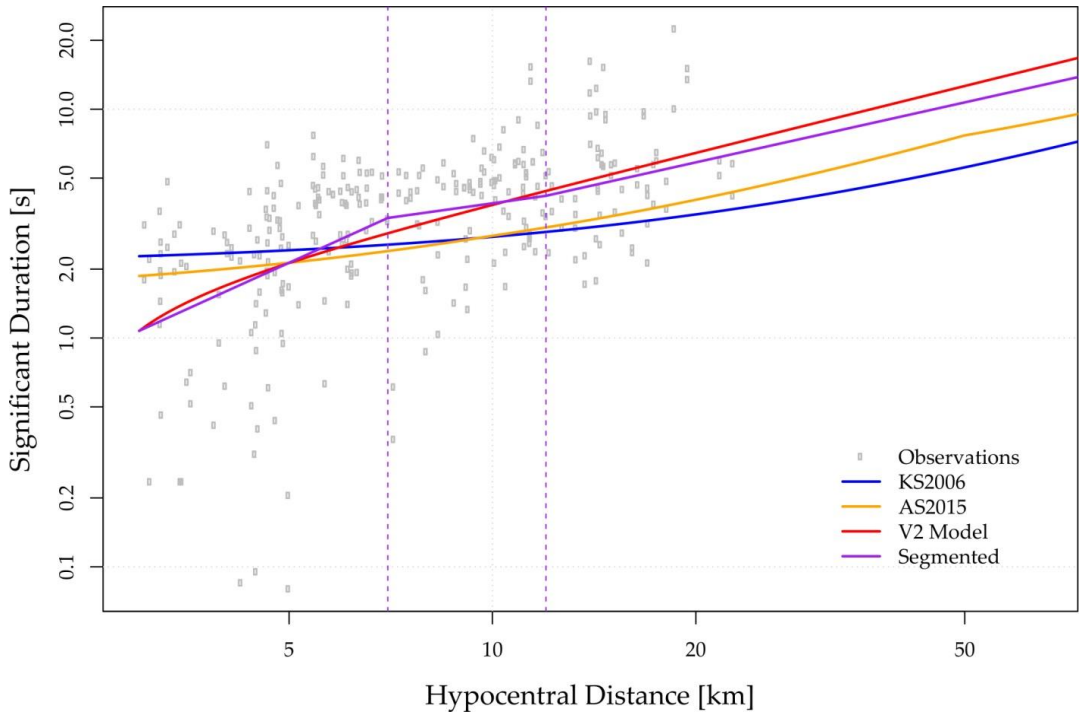

Figure 12.29. Comparison of the path scaling of the Kempton & Stewart (2006) and Afshari & Stewart (2015) duration models with adjustments made to the AS2015 model at small magnitudes.

Interestingly, when this same comparison is performed in terms of epicentral distance the strength of the segmentation is greatly reduced (Figure 12.30). Note that in this case all of the other models are simply plotted by converting the distance metric into epicentral distance (the V2 Model is simply implemented using its native epicentral distance, while the Kempton & Stewart (2006) and Afshari & Stewart (2015) models have their 'native' hypocentral distance values converted to epicentral distance assuming a 3 km focal depth), but the segmented distance scaling model is a new model that is found by regression using epicentral distance as a distance metric instead of hypocentral distance.

It may be noted that the complete functional form of the V2 model will be provided in the next section and that here the V2 model just makes use of the optimal distance scaling found from the previous section coupled with the adjusted source model where the adjustments are based upon the approach just mentioned in this section of adjusting $\mathbf{M}_1$.

For epicentral distance the data do not support a strong segmentation and over the region where there are the most data the two Groningen-specific models are extremely close to each other. It can also be noted that the large distance scaling (in terms of the slopes of the distance scaling) are closer for the V2 Model and the Afshari & Stewart (2015) model than the other cases. For these reasons, the V2 Model distance scaling, without segmentation, is adopted hereafter.

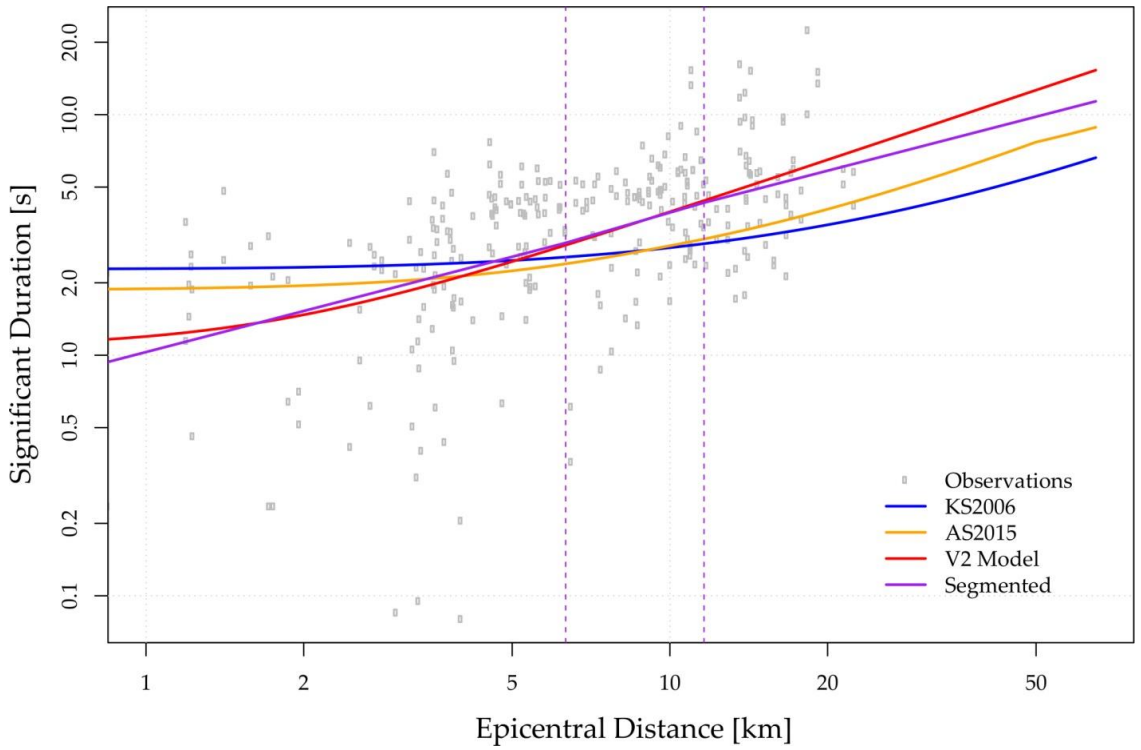

Figure 12.30. Comparison of the path scaling of the Kempton & Stewart (2006) and Afshari & Stewart (2015) duration models with adjustments made to the AS2015 model at small magnitudes.

Both the Kempton & Stewart (2006) and Afshari & Stewart (2015) models have an explicit dependence upon the average shear-wave velocity over the uppermost 30m. It is not reasonable to assess the performance of these terms for the Groningen data as the records are all made over a very narrow range of this variable. For this reason, the site response terms of the most recent Afshari & Stewart (2015) are assumed to be most appropriate for the V2 model.

One remaining issue that exists is how to deal with developing alternative models to reflect differing assumptions about stress drop. Although the Afshari & Stewart (2015) model shares the same conceptual arguments as the Kempton & Stewart (2006) model in terms of how stress drop effects durations, the latter model had a magnitude independent stress drop term while the Afshari & Stewart (2015) model has very strong magnitude dependence.

Moreover, in the Kempton & Stewart (2006) case it is very straightforward to make adjustments to account for stress drop as it is possible to simply replace the particular parameter that reflects stress drop by an alternative value, and this value adjusts the scaling over all magnitudes. However, this is not possible for the more recent Afshari & Stewart (2015) model.

However, it has previously been noted that the actual stress drops that are implied by the model coefficients for both the Kempton & Stewart (2006) and Afshari & Stewart (2015) cases are not in any way consistent with what is typically expected from studies of spectral amplitudes using the same or similar datasets. Therefore, for the purposes of reflecting the differences in stress drop the particular parameters of the two models are not interpreted as reflecting absolute values of the stress drop, but relative differences in the stress drop are assumed to manifest themselves in a meaningful way.

For this reason, in order to develop prediction equations for alternative stress drops the fundamental assumption is made that the 100 bar stress drop level, that is the upper bound considered for Groningen, reflects typical shallow crustal earthquakes and is thus representative of the implicit values of stress drop encapsulated within the Kempton & Stewart (2006) and Afshari & Stewart (2015) models. Therefore, even though the apparent stress drop of the former model is 411 bar, it is assumed that this model is really reflecting 100 bar stress drop levels.

As a result, in order to obtain predictions for a 10 bar or 30 bar case the implicit stress drop parameter is adjusted in the two models by the appropriate ratio (411 bar becomes 30/100 x 411 for the 30 bar case and 411 becomes 10/100 x 411 for the 10 bar case). The advantage of this approach is that it can be applied in the same manner to the magnitude dependent stress drop function adopted by Afshari & Stewart (2015); that is, their stress drops are simply multiplied as a function of magnitude by the same constant ratios for all magnitudes.

To see the effect of these adjustments Figure 12.31 shows how the base models can be adjusted to reflect lower levels of stress drop. Note that the original Afshari & Stewart (2015) model is shown in orange while the blue lines show the final developed model for the V2 durations that is fully detailed in the following section.

Figure 12.31 shows that very similar changes to the large-magnitude duration levels occur for both the Kempton & Stewart (2006) and Afshari & Stewart (2015) models. The differences between the two models really arise over the range **M** 4-5.5 where the former model is actually controlled by the presence of site effects rather than source effects.

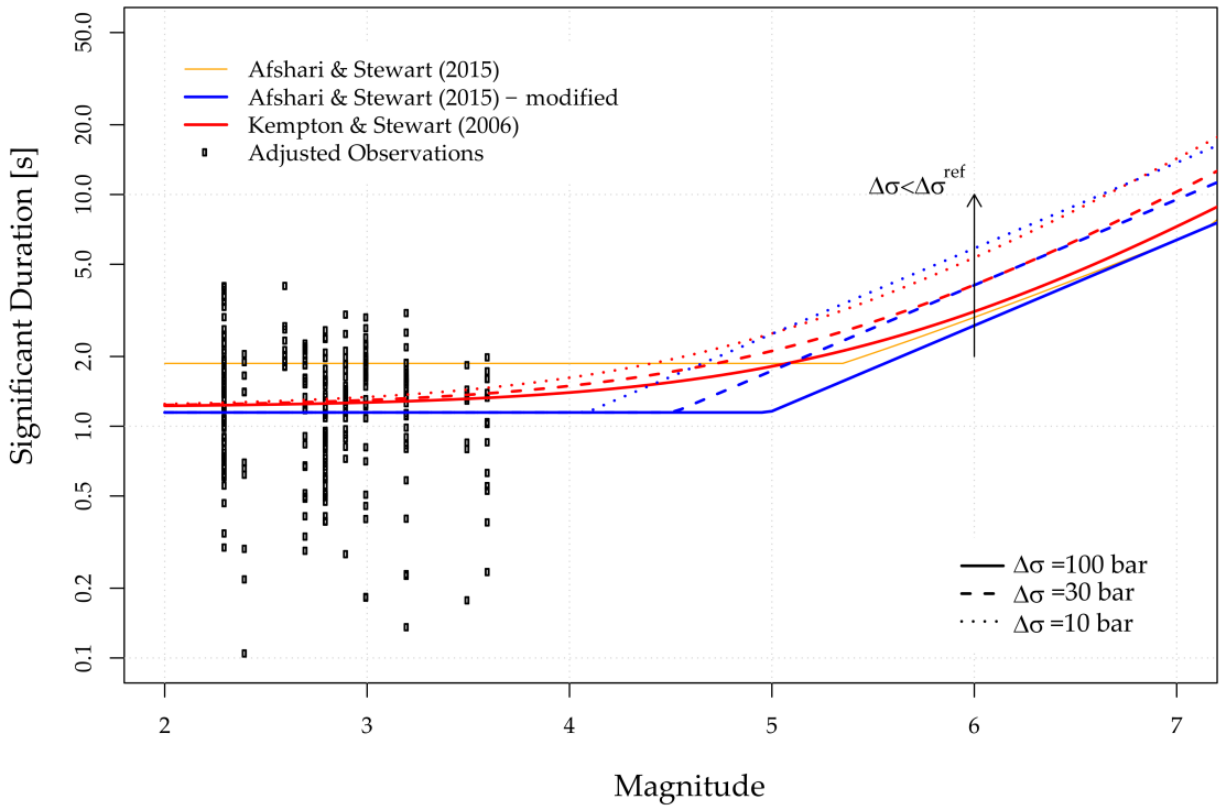

Figure 12.31. Comparison of the source scaling of the Kempton & Stewart (2006) and Afshari & Stewart (2015) duration models with adjustments made to reflect different levels of stress drop. Note that the modified AS2015 model (*blue lines*) is the final adjusted model with the small magnitude plateau also changed.

12.5. Development of the Adjusted Functional Form

Following the exploration of adjustment options, the proposed approach to develop the final V2 GMPE for duration is as follows:

1. Use the source scaling implied by the latest Afshari & Stewart (2015) model;
2. Make adjustments to this source scaling so that it reaches down to the small-magnitude plateau implied by the Groningen data;
3. Adjust the model so that the scaling of the source effects can reflect different levels of stress drop;
4. Use the Groningen-specific path scaling;
5. Retain the site response scaling of the Afshari & Stewart (2015) model, but ignore the deep soil terms (which have negligible effect even for very extreme combinations of $V_{S,0}$ and $Z_{1.0}$).

As already investigated in Section 12.2, the functional form of the Afshari & Stewart (2015) model can be expressed as in Eq.(12.27) with the terms F_E, F_P, and F_S reflecting source, path and site terms, respectively.

$$\ln(D_{S5-75}) = \ln[F_E(M, sof) + F_p(R_{rup})] + F_S(V_{S30}, \delta z_1) \tag{12.27}$$

The source scaling in the Afshari & Stewart (2015) model is defined as follows (Eq.(12.28)).

$$F_E(M, sof) = \begin{cases} 1/f_c & M > M_1 \\ b_0(sof) & M \le M_1 \end{cases} \tag{12.28}$$

In this expression, the corner frequency is defined as:

$$f_c = 4.9 \times 10^6 \beta \left(\frac{\Delta\sigma}{M_0} \right)^{1/3} \tag{12.29}$$

with

$$M_0 = 10^{1.5M + 16.05} \tag{12.30}$$

and β = 3.2 km/s. The stress parameter is defined as a function of magnitude as:

$$\Delta\sigma = \exp[b_1(sof) + b_2(M - M^*)] \tag{12.31}$$

It is worth noting that their full model has another break in scaling beyond a higher magnitude $\mathbf{M}_2$, but this break occurs at magnitudes beyond the range of interest for Groningen. The plateau level is controlled by a combination of b_0 which varies with style of faulting, and also the F_S term that is present even for zero distance.

Note also that the limiting magnitude for the source scaling $\mathbf{M}_1$ is defined as 5.35 for the 5-75% significant duration and that this causes the model to predict flat response for magnitudes below this level. The fact that the stress parameter is strongly magnitude dependent dictates that the slope of the source scaling with respect to magnitude is flatter than if predicted using simple $1/f_c$ considerations.

The overall magnitude scaling from this model can be found from comparing the magnitude dependence of the seismic moment with that for the stress drop. Note that for magnitudes values above $\mathbf{M}_1$ we can write:

$$F_E = \frac{1}{4.9 \cdot 10^6 \beta} \left(\frac{\Delta\sigma}{M_0} \right)^{-1/3} \tag{12.32}$$

and we can write the expression for the seismic moment as an exponential function as:

$$M_0 = \exp(\ln(10)(1.5M + 16.05) \quad (12.33)$$

Therefore, combining Eq.(12.31-33) it results that:

$$F_E = \frac{1}{4.9 \cdot 10^6 \beta} \exp\left[-\frac{1}{3}[b_1(sof) - b_2 M^* - 16.05\ln(10)] - \frac{1}{3}[b_2 - 1.5\ln(10)]M \right] \quad (12.34)$$

As previously discussed, to obtain alternative models that reflect differing levels of stress drop the assumption must be that the considered 100 bar case represents motions of a tectonic nature. Therefore, it is expected that the considered 100 bar stress drop would produce motions that are comparable to those used to develop the Afshari & Stewart (2015) model for large magnitude events. It is not possible to simply insert a new value for stress drop as these authors find their stress parameter to be strongly magnitude dependent. However, some analogous scaling can be applied.

Assuming that the 100 bar case is equivalent to their native stress drop level (and ignoring the issues associated with the β values being different) the source duration can be scaled by an amount that reflects the changes in the stress drop moving from 100 to 30 bar, etc. Therefore, we can define a stress drop scaling factor as in Eq.(12.35).

$$\gamma = \frac{\Delta\sigma_\chi}{\Delta\sigma_{AS}} = \frac{\Delta\sigma_\chi}{\Delta\sigma_{100}} \quad (12.35)$$

Hence, the expression for source duration can be written as in Eq.(12.36).

$$F_E = \frac{\gamma^{\frac{-1}{3}}}{4.9 \cdot 10^6 \beta} \exp\left[-\frac{1}{3}[b_1(sof) - b_2 M^* - 16.05\ln(10)] - \frac{1}{3}[b_2 - 1.5\ln(10)]M \right] \quad (12.36)$$

For implementation purposes the style-of-faulting can be treated as being ‘unknown’ and this allows the value of b_1 to be set at $b_1 = 5.576$, the value of b_2 is $b_2 = 0.9011$ and **M***=6. The value of β is kept fixed at the same level that was used in their original model of 3.2 km/s.

However, if an adjustment was attempted for this source velocity then the source durations for the larger events become greater than those of Afshari & Stewart (2015) by a factor of 1.6 at the larger magnitudes. Furthermore, the issue of how to relate different levels of stress drop with appropriate levels of β is not easy to resolve given that large magnitude events are very unlikely to stay contained at 3 km depth.

In order to ensure that this model matches the Groningen data, the value of $\mathbf{M}_1$ is allowed to vary in order to optimise the fit to the source-corrected observations. A random effects regression analysis is then performed in order to solve for the appropriate value of b_0, which

turns out to be b_0 = 1.0. This random effects regression is basically just performed on the distance-adjusted Groningen data (*i.e.*, we assume that the V2 distance scaling can be found independently, which is reasonable) and we then map all observations back to a distance of zero epicentral distance. The optimal value of b_0 is then found from a regression model illustrated in Eq.(12.37).

$$\ln(D_{S5-75}^{adj}(R_{epi}=0)) = b_0^{'} + \eta_t + \varepsilon_{ij} \tag{12.37}$$

In the above equation, the parameter is actually b'_0 rather than b_0 because the observed Groningen motions already contain the effects of site response. Therefore, to find the appropriate value of b_0 for the source scaling the effects of the site response implied by a typical level of V_{S30} = 200 m/s must be removed for all observations.

12.6. Version 2 GMPE for duration

According to the considerations and assumptions made in the previous section, the overall final model can be written as in Eq.(12.38).

$$\ln(D_{S5-75}) = \ln[F_E(M,\Delta\sigma) + F_P(R_{epi})] + F_S(V_{S30}) \tag{12.38}$$

In particular, the first term (the source term) can be evaluated as in Eq.(12.39) (where $\gamma = \Delta\sigma/100$).

$$F_E = \max[0.014374\gamma^{\frac{-1}{3}}\exp(0.85093M), 1.0] \tag{12.39}$$

The path scaling is defined as in Eq.(12.40).

$$F_P = 0.72985\ln(\sqrt{R_{epi}^2 + 1.7060^2}) - 0.38985 \tag{12.40}$$

The site scaling is simply defined as in Eq.(12.41), that is in the same way as Afshari & Stewart (2015) but ignoring the sediment depth terms (which suggest incredibly weak scaling anyway). In the equation, V_1 = 600 m/s and V_{ref} = 368.2 m/s.

$$F_S = -0.2246\ln\left(\frac{\min(V_{S30}, V_1)}{V_{ref}}\right) \tag{12.41}$$

Figures 12.32-34 show the median predictions from the adjusted Afshari & Stewart (2015) model with respect to magnitude, distance and shear wave velocities.

The inter-event standard deviation of the proposed model is a relatively low (τ = 0.2) and the intra-event standard deviation is ϕ = 0.6136. It is worth noting that the regressions that have

been performed to obtain these variance components are based upon the individual components and not the geometric mean. Given that some quite significant component-to-component differences in duration can be observed, the geometric mean values may be quite a lot lower than these values when compared to typical adjustments made for spectral amplitude variances.

Figure 12.35 shows the residuals of Groningen durations with respect to the adjusted Afshari & Stewart (2015) model. Results show a good agreement between the Groningen data and the adjusted model even if some issues still exist at short distances (probably due to the component-to-component differences observed in the Groningen data). Figures 12.36-12.38 show the comparison between the adjusted Afshari & Stewart (2015) model and the V1 model (*i.e.*, the Kempton & Stewart (2006) model assuming a CBL basin model and considering a basin depth of 600 m) with respect to magnitude, distance and accounting for different V_{S30} values respectively. In particular in these figures, solid lines refer to the adjusted Afshari & Stewart (2015) model while the dashed lines to the V1 model.

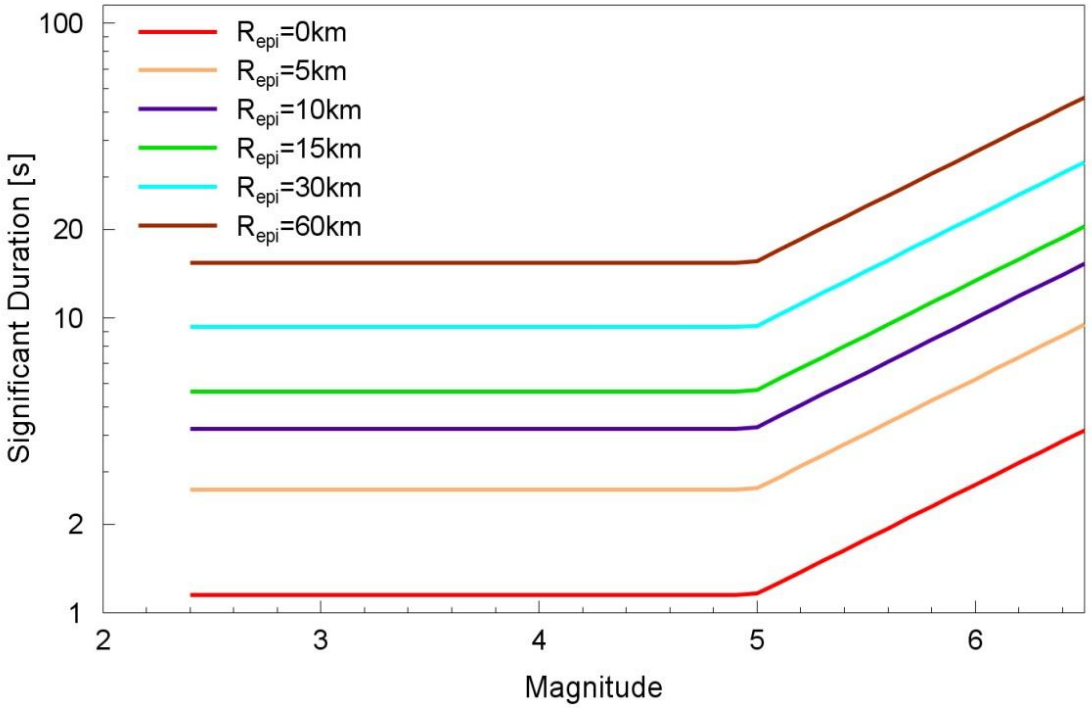

Figure 12.32. Median predictions from the adjusted Afshari & Stewart (2015) model with respect to magnitude for different epicentral distances. V_{S30} is set equal to 200 m/s.

Finally, Figure 12.39 shows the comparison between the adjusted Afshari & Stewart (2015) model (in the right-hand panel) and the V1 GMPE (in the left-hand panel) in terms of between-event (upper plots) and within-event residuals of Groningen durations with respect to epicentral distance (central panel) and V_{S30} (lower panel). Results show that the adjusted Afshari & Stewart (2015) model provides a better fit to the Groningen data in comparison to the V1 model, especially for the smallest magnitudes, therefore it is selected for use in the Version 2 risk model.

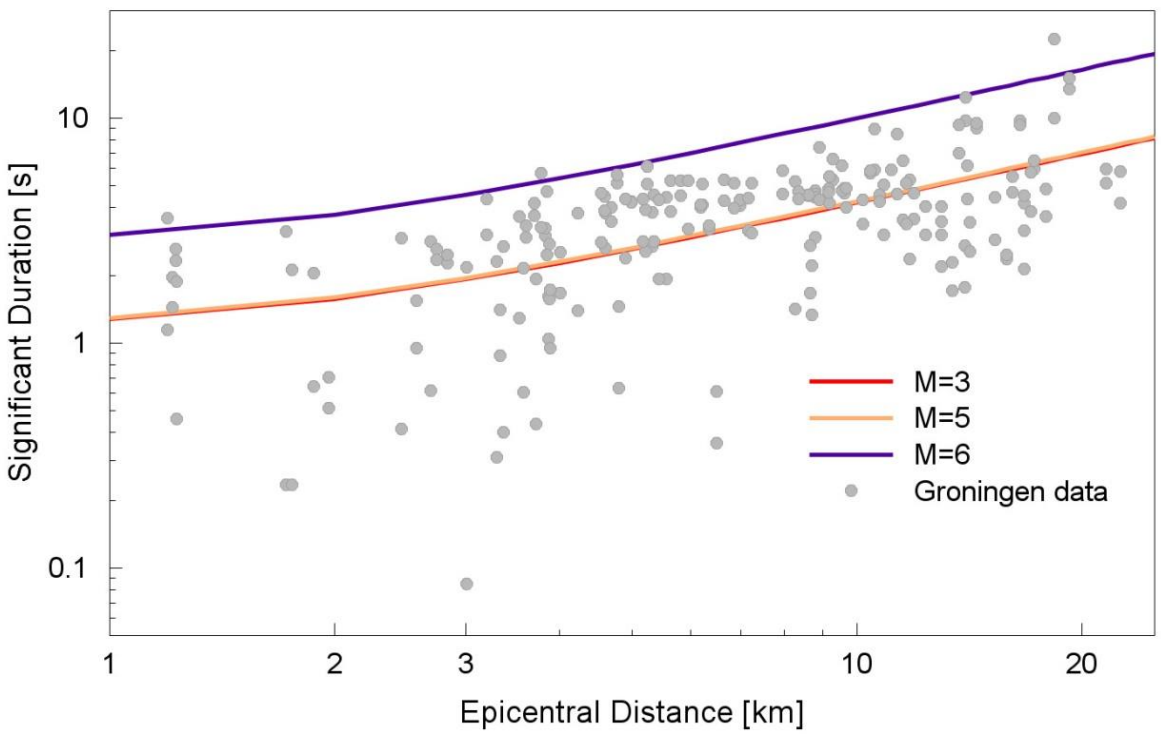

Figure 12.33. Groningen data and median predictions from the adjusted Afshari & Stewart (2015) model with respect to epicentral distances for different magnitude values. V_{S30} is set equal to 200 m/s.

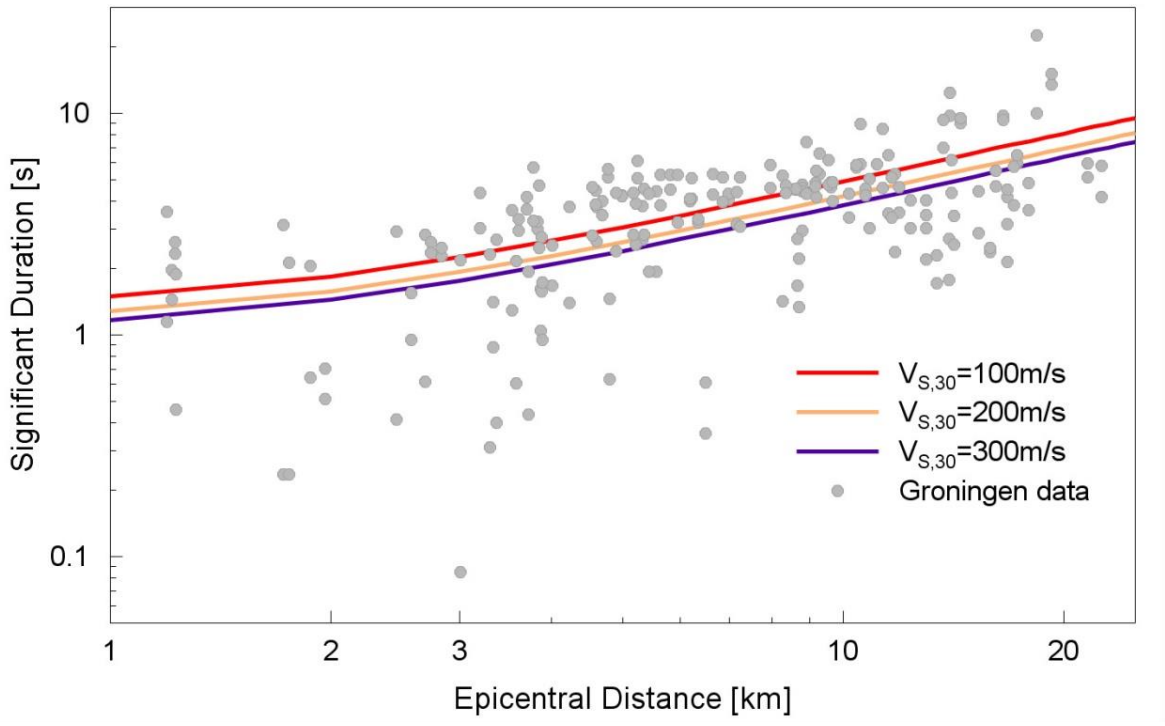

Figure 12.34. Groningen data and median predictions from the adjusted Afshari & Stewart (2015) model with respect to epicentral distances considering different V_{S30} values.

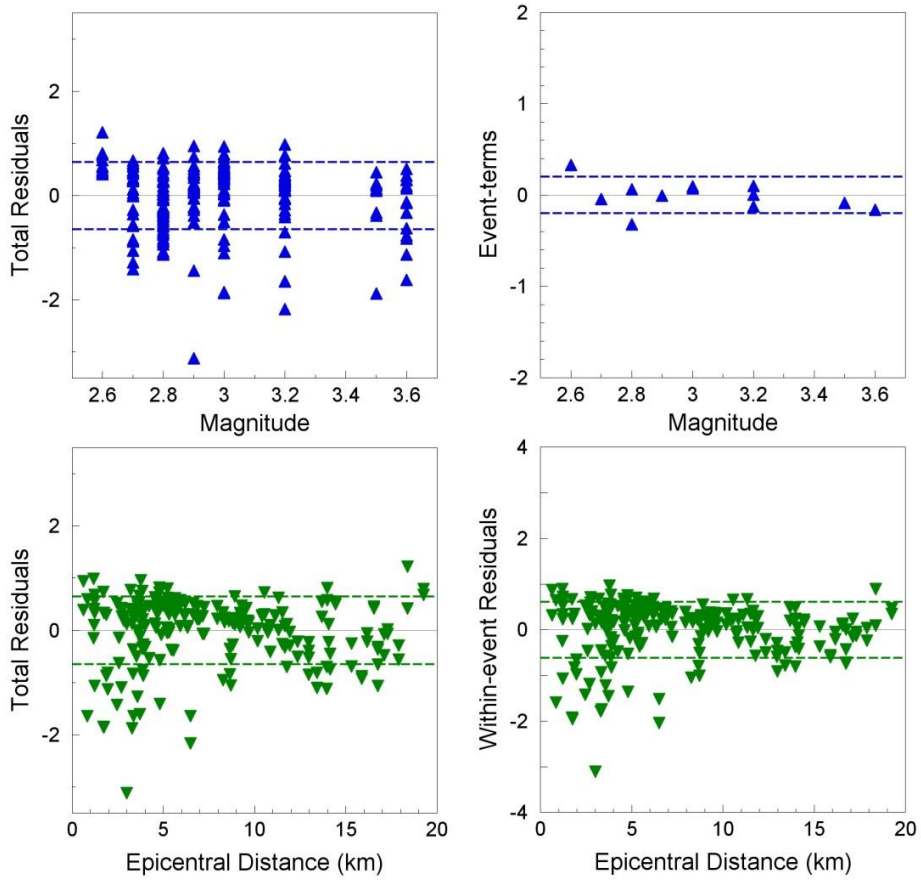

Figure 12.35. Total (*left*), between-event (*upper right*) and within-event (*lower right*) residuals of $D_{S5\text{-}75}$ of Groningen records with respect to the adjusted Afshari & Stewart (2015) model. Dashed lines correspond to the total sigma (*left*) and the inter- and intra-event standard deviations (*right*).

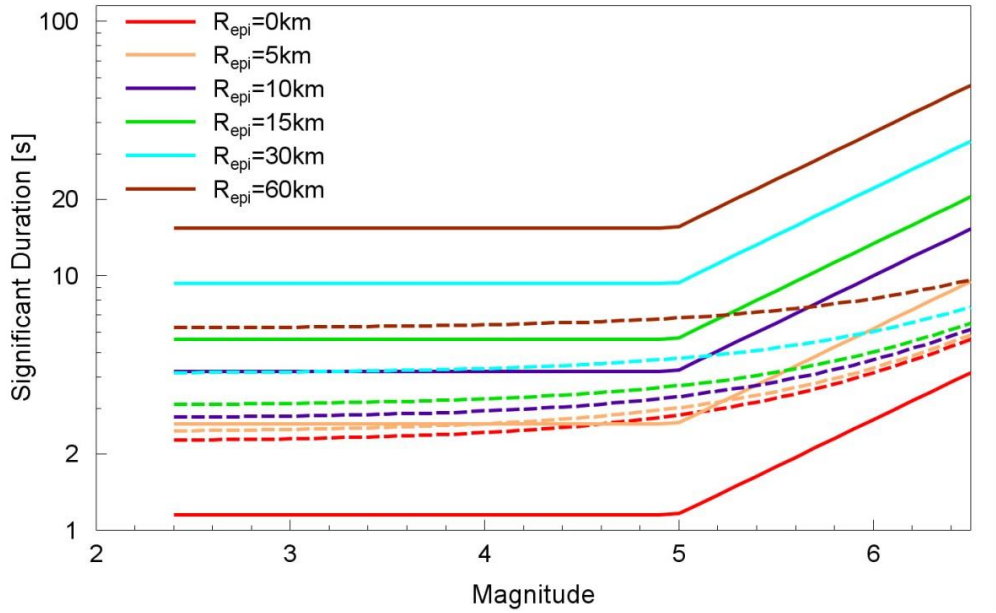

Figure 12.36. Groningen data and comparison between the median predictions from adjusted Afshari & Stewart (2015) model (solid lines) and the V1 model (*i.e.*, the Kempton & Stewart, 2006, model assuming a CBL basin model and considering a basin depth of 600 m) with respect to magnitude.

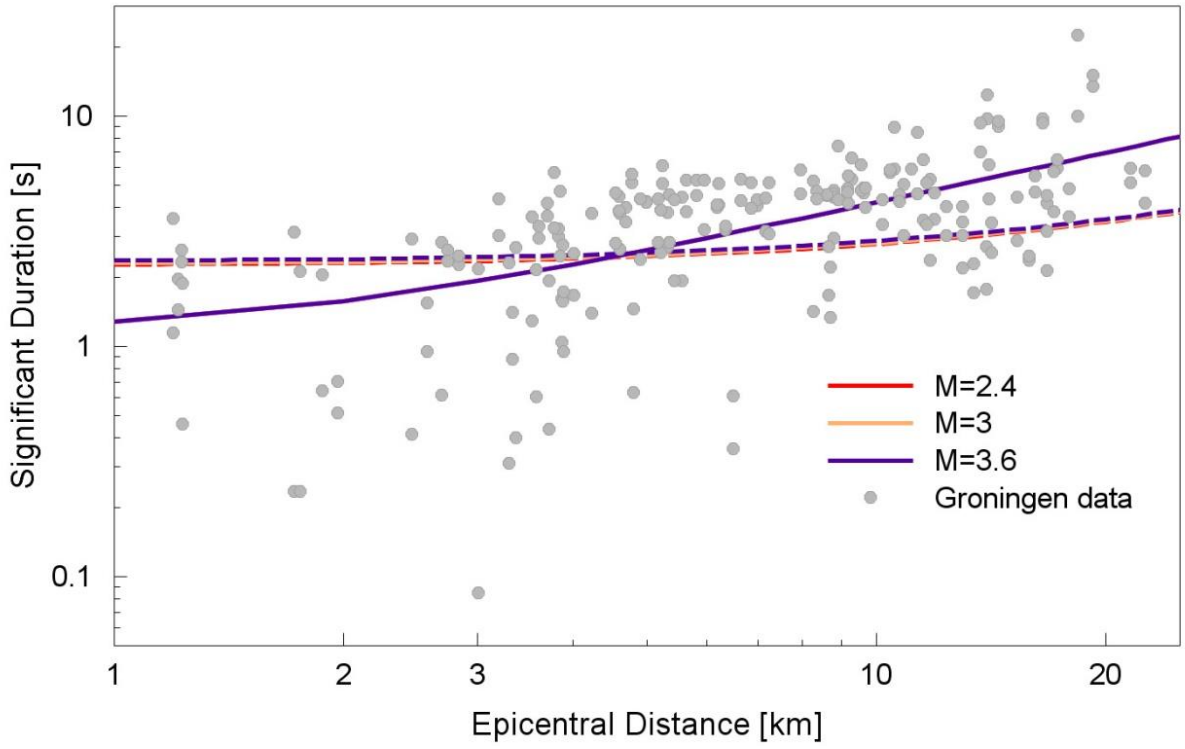

Figure 12.37. Groningen data and comparison between the median predictions from the adjusted Afshari & Stewart (2015) model (solid lines) and the V1 model (*i.e.*, the Kempton & Stewart (2006) model assuming a CBL basin model and considering a basin depth of 600 m) shown in dashed lines with respect to epicentral distance for different magnitude values.

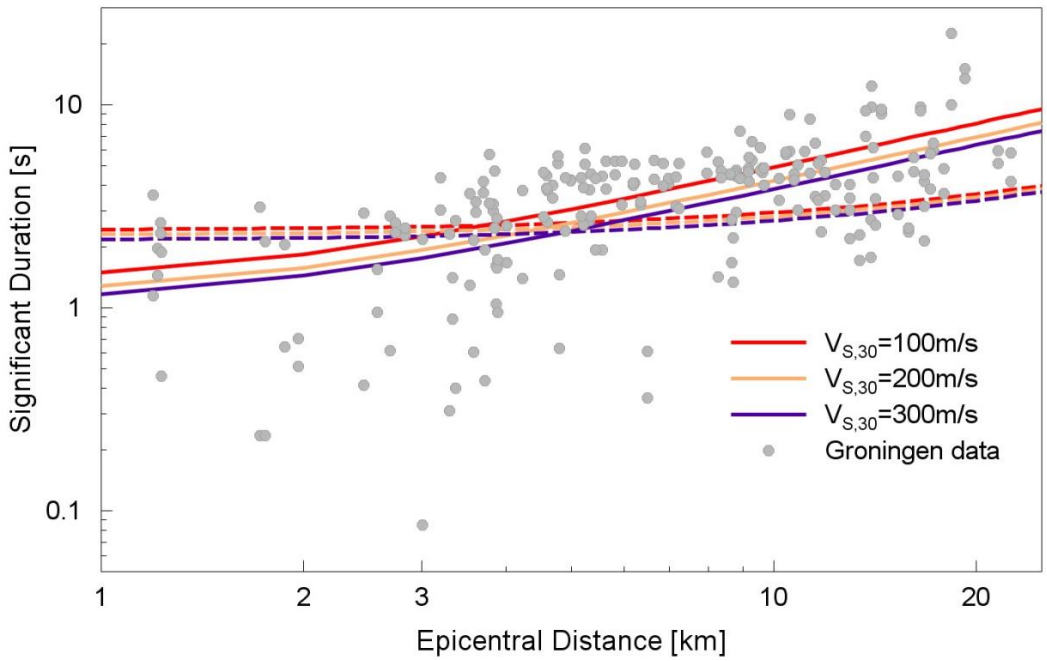

Figure 12.38. Groningen data and comparison between the median predictions from the adjusted Afshari & Stewart (2015) model (solid lines) and the V1 model shown using dashed lines with respect to epicentral distance for different V_{S30}.

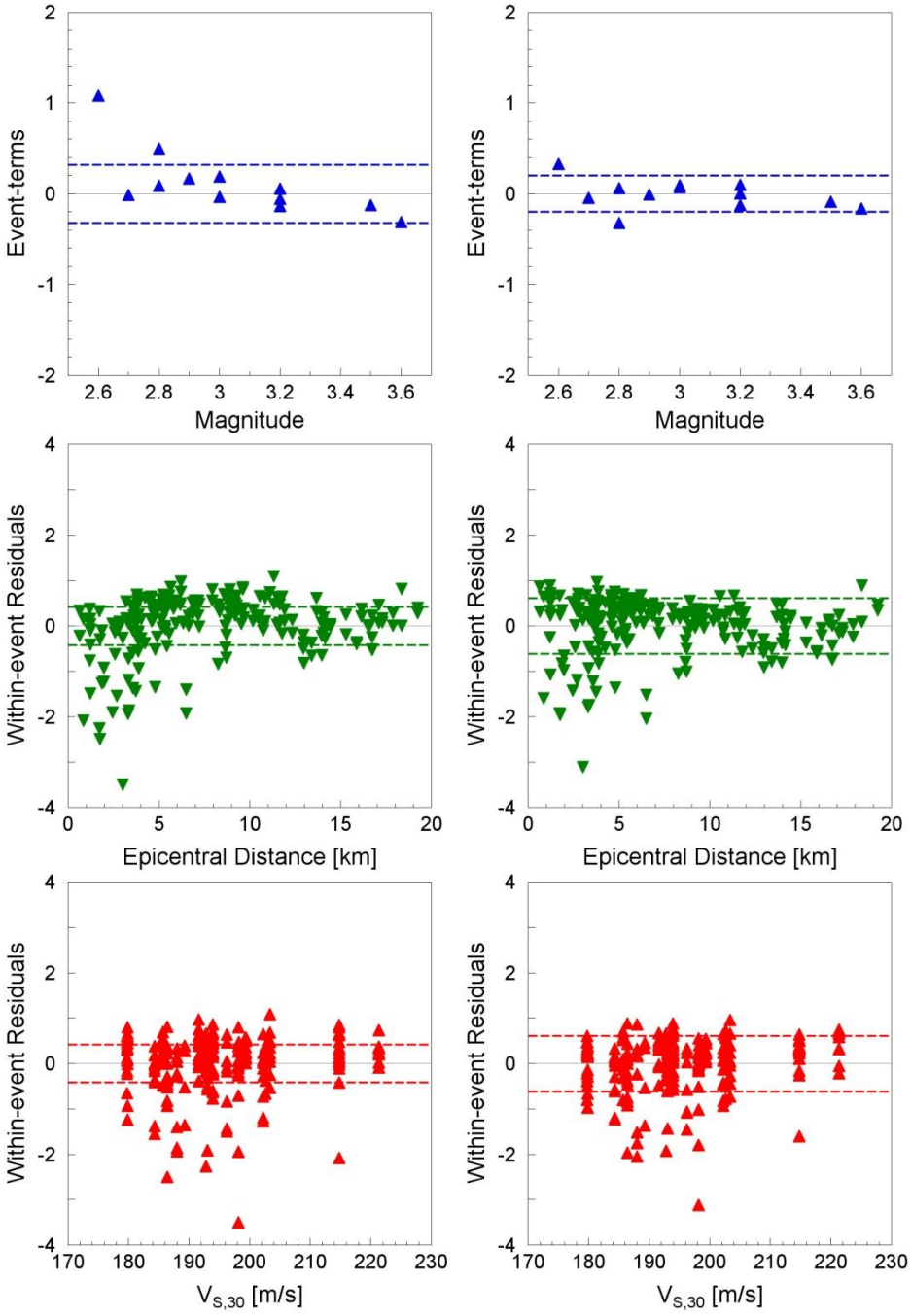

Figure 12.39. *Left*: Between-event (*upper*) and within-event (*central and lower*) residuals of the Groningen durations with respect to the V1 GMPE (*left)* and the adjusted Afshari &Stewart (2015) model (*right*). Dashed lines are inter- and intra-event standard deviations.

For completeness, Figure 12.40 shows the predictions from the three branches of the duration model—for the same three stress drops underlying the three branches of the GMPE for spectral accelerations—as a function of magnitude and distance. This figure shows that the influence of stress drop on the predicted durations is appreciable, particularly in the critical range of magnitudes from **M** 4 to 5 that contribute strongly to hazard and risk estimates for the Groningen field.

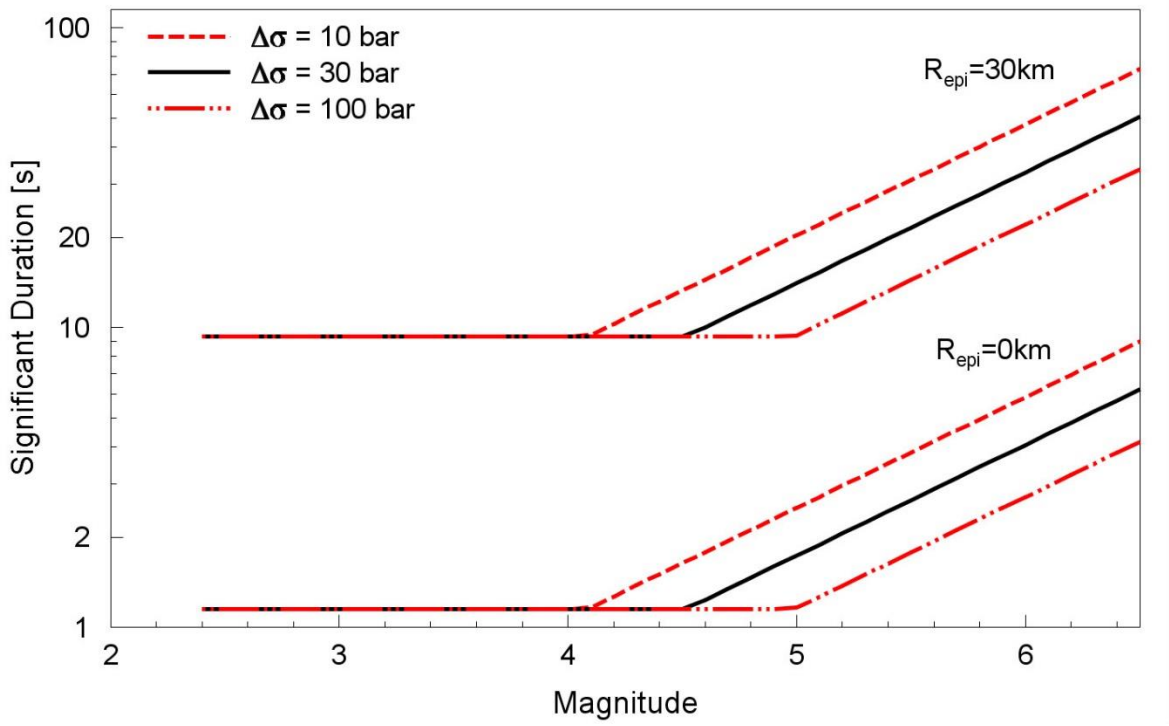

Figure 12.40. Median predictions from the three branches of the duration model as a function of magnitude and distance

12.7. Correlation of residuals of duration and accelerations

An important aspect of including duration in the risk assessment is to account for the inverse correlation between the duration of the shaking and the amplitude of the acceleration. For modelling purposes, however, what is needed is not the general correlation of duration and acceleration, but rather the correlation of the residuals with respect to the predicted median values of the two parameters. In particular, as the Kempton & Stewart (2006) model already provided a broad agreement with the Bradley (2011) model over the period range considered (Bommer *et al.*, 2015a), as illustrated in Figure 12.41. For this reason, the Bradley (2011) model is used to account for the correlation between the $D_{S5\text{-}75}$ and Sa(T) pending the derivation of a Groningen-specific model to accompany the final ground-motion model. Correlation coefficients (ρ) according to the Bradley (2011) model for the 16 periods of interest are reported in Table 12.4.

Table 12.4. Correlation coefficients according to the Bradley (2011) model.

T [s]	**0.01**	**0.1**	**0.2**	**0.3**	**0.4**	**0.5**	**0.6**	**0.7**	**0.85**	**1**	**1.5**	**2**	**2.5**	**3**	**4**	**5**
ρ	-0.45	-0.39	-0.39	-0.39	-0.33	-0.28	-0.24	-0.21	-0.17	-0.13	-0.05	-0.01	0.02	0.05	0.09	0.12

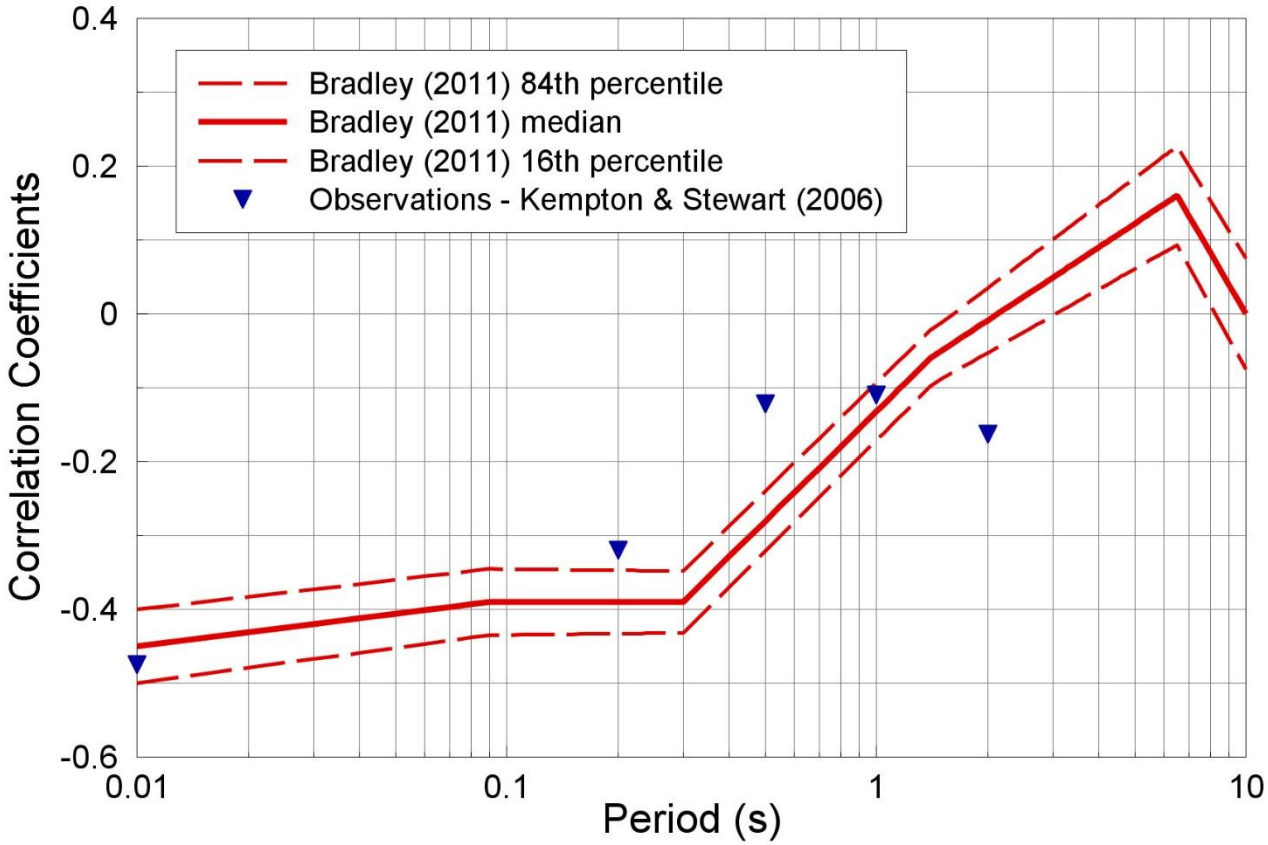

Figure 12.41. Correlation coefficients between the $D_{S5\text{-}75}$ and Sa(T) according to the Bradley (2011) model compared with the coefficients calculated for the Groningen data using the V1 models (Bommer *et al*., 2015a)

13. REFINEMENTS and IMPROVEMENTS of the GMPEs

The models presented in this report are the latest snapshot in the ongoing development of ground-motion predictions equations for the seismic hazard and risk assessments for the Groningen gas field that will underpin the 2016 Winningsplan. The evolution of the equations to date was briefly summarised in Section 1.2. In the coming months, the final version—Version 3, or V3—of the ground-motion prediction model will be produced. Whereas there were fundamental changes to the form of the model in the progress from V0 to V1 to V2, it is now expected that the V3 model will maintain the basic structure of the V2 model but include a number of refinements. The purpose of this closing chapter is to briefly outline some of the key tasks that will be undertaken towards this refinement and improvement of the current model, and some of the enhancements that are expected before the model is finalised ahead of the final seismic hazard and risk calculations for the Winningsplan 2016.

13.1. Expansion of the ground-motion database

Prior to deriving the V3 models, the ground-motion database for the Groningen field will be expanded to incorporate additional recordings that have become available or that may be obtained in next few weeks. Any significant earthquake (**M** ≥ 2.5) in the field is now likely to generate an appreciable number of recordings in view of the much denser network now in operation: in addition to the 18 permanent accelerograph stations, 58 newly-installed accelerographs (co-located with 200-m boreholes instrumented with geophones) are streaming data to KNMI; an additional 12 such installations are planned. An additional 10 recordings have been retrieved from three earlier earthquakes with magnitudes of M_L 2.6, 2.8 and 3.0, and a further 44 recordings were obtained during the Hellum M_L 3.1 earthquake that occurred to the south of the centre of the field on 30 September 2015; the resulting magnitude-distance distribution of the expanded database is shown in Figure 13.1.

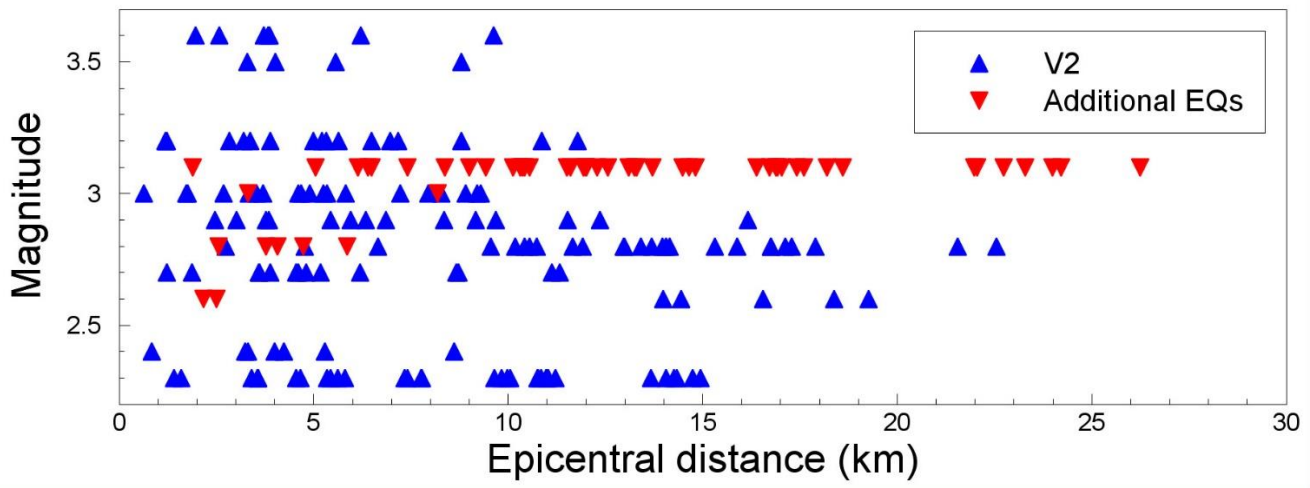

Figure 13.1. Magnitude-distance distribution resulting from combining the V2 database with more recent acquisitions

The impact of the expanded networks in terms of higher yields of recordings is well illustrated by the Hellum earthquake (Figure 13.2). Any earthquake of similar magnitude close to the centre of the field can be expected to yield similar numbers of recordings. While this undoubtedly provides considerable enrichment of the ground-motion database, it is also the case that to make optimal use of these recordings, V_S measurements will ultimately be required at all of the recording locations (see Section 13.2).

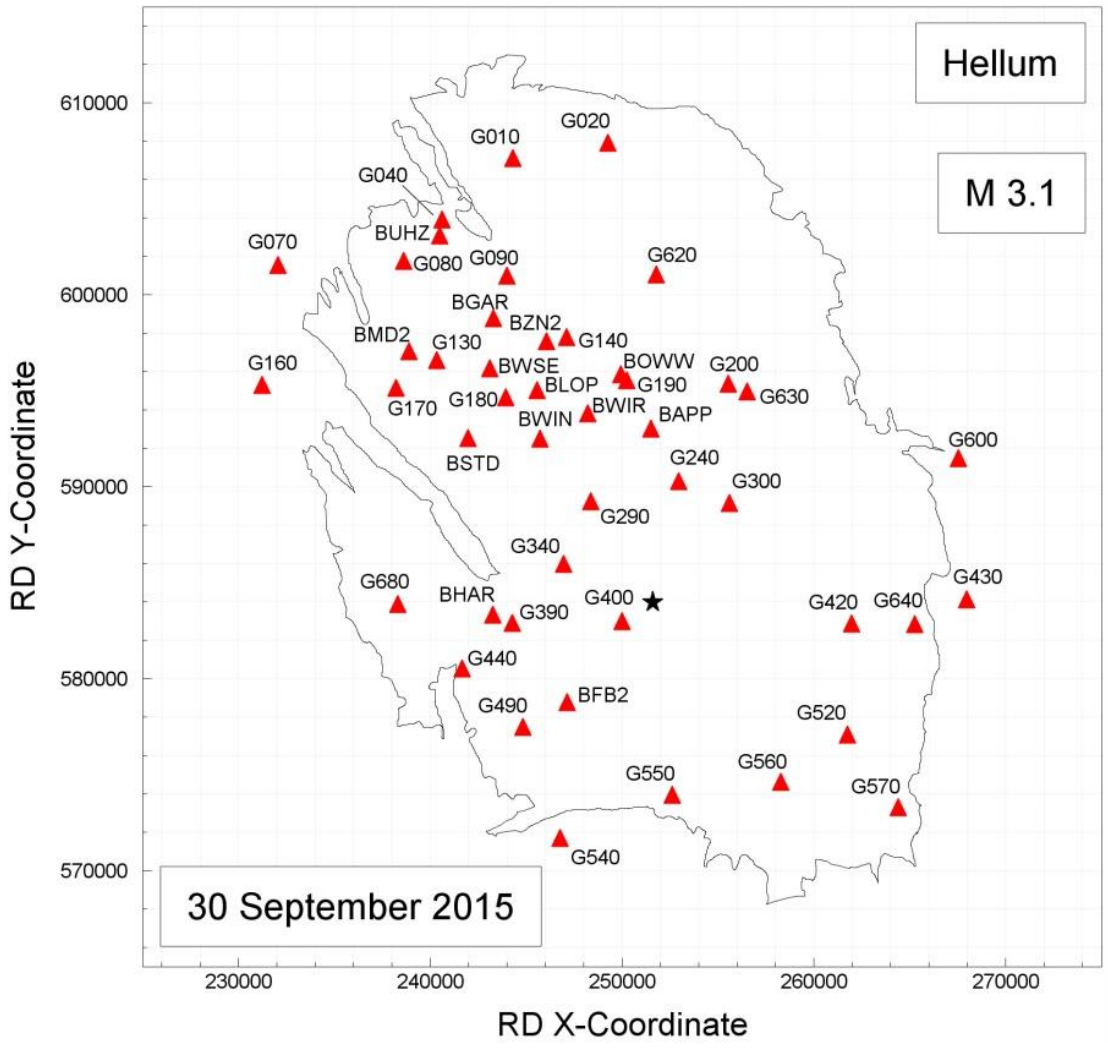

Figure 13.2. Location of accelerograph stations (*red triangles*) that recorded the Hellum earthquake, the epicentre of which is shown by the black star; station codes starting with B are part of the KNMI permanent network, those with G are newly-installed instruments co-located with the 200 m geophone boreholes

As discussed briefly in Section 3.1, there are also two other accelerograph networks in the field: those operated at NAM facilities for triggering safe shut-down and the instruments installed by TNO on behalf of NAM in private houses and public buildings throughout the region of the gas field. Work has now begun in collaboration with both TNO (Erik Langius and Carine van Bentum) and NAM (Kees Tanis) to explore the incorporation of the recordings from the latter network into the database. Given the density of the TNO network—with many more than 200 accelerographs installed—the potential impact on the database is very

considerable, notwithstanding that there are no plans in place currently to extend the V_S measurements to these locations (in addition to which there is the additional complication that Dutch privacy law renders confidential the identity and location of the private houses hosting the instruments). The issue that needs to be addressed, however, before these records can be used in the derivation of the V3 GMPEs is the degree to which they have been influenced by their unusual installation (Figure 13.3). Some of the instruments are attached directly to the floor of a building or even to the foundation beam (Figure 13.4) but others are sufficiently removed from the ground to be potentially recording structural response.

Figure 13.3. Examples of installation details of the TNO accelerographs; the lower left-hand image shows an instrument on the wall of the basement

Figure 13.4. Examples of TNO accelerographs installed in directly contact with the floor

The steps to be followed are to first identify those instruments attached directly to the floor of the buildings in which they are housed, which will be accepted as valid recordings of ground motions. For all other instruments, careful consideration will be given to the precise location of the accelerograph, and those attached to foundation beams, for example (Figure 13.5) are likely to be deemed acceptable as well, provided that the attachment of the bracket to the wall is very secure. For others, analyses will be carried out both of the frequency characteristics of the records (since any structural response should appear as a continuous signal within the time-history) and also comparing the general trend of the TNO records with those from the other networks, starting with the 30 September 2015 Hellum event (Figure 13.2).

Figure 13.5. Examples of TNO accelerographs attached to foundation beams

Structural analyses of the buildings housing the instruments are unlikely to be sufficiently accurate to determine the degree of building response in those accelerographs a few centimetres removed from the floor. However, an experiment is being designed whereby at some 10-15 of the stations, carefully chosen to sample both the building types and the

instrument locations within the building, a second accelerograph will be installed at ground level, either within the building or on a concrete slab immediately outside. These co-located instruments will be preferentially installed near the centre of the field to increase the possibility of triggering by earthquakes, since the value of the experiment will lie in the comparison of records from the two instruments.

13.2. Use of measured V_S profiles at the recording stations

As noted in Section 4.4, plans were put in place at an early stage to conduct direct measurements of the VS profiles at the 18 permanent KNMI accelerogaph stations. There were a number of delays in beginning this work primarily due to access and permit issues, but thanks to the efforts of Eddy Kuperus and Eddie Siemerink of NAM is was finally possible to conduct the surveys at all 18 stations. Regrettably, it was not always possible to perform the measurements directly adjacent to the location of the instrument (Figure 13.6) but due attention was given to selecting test locations on the same geological formations as the station and, where possible, CPTs were performed at both the survey location and closer to the instrument to confirm the degree of similarity.

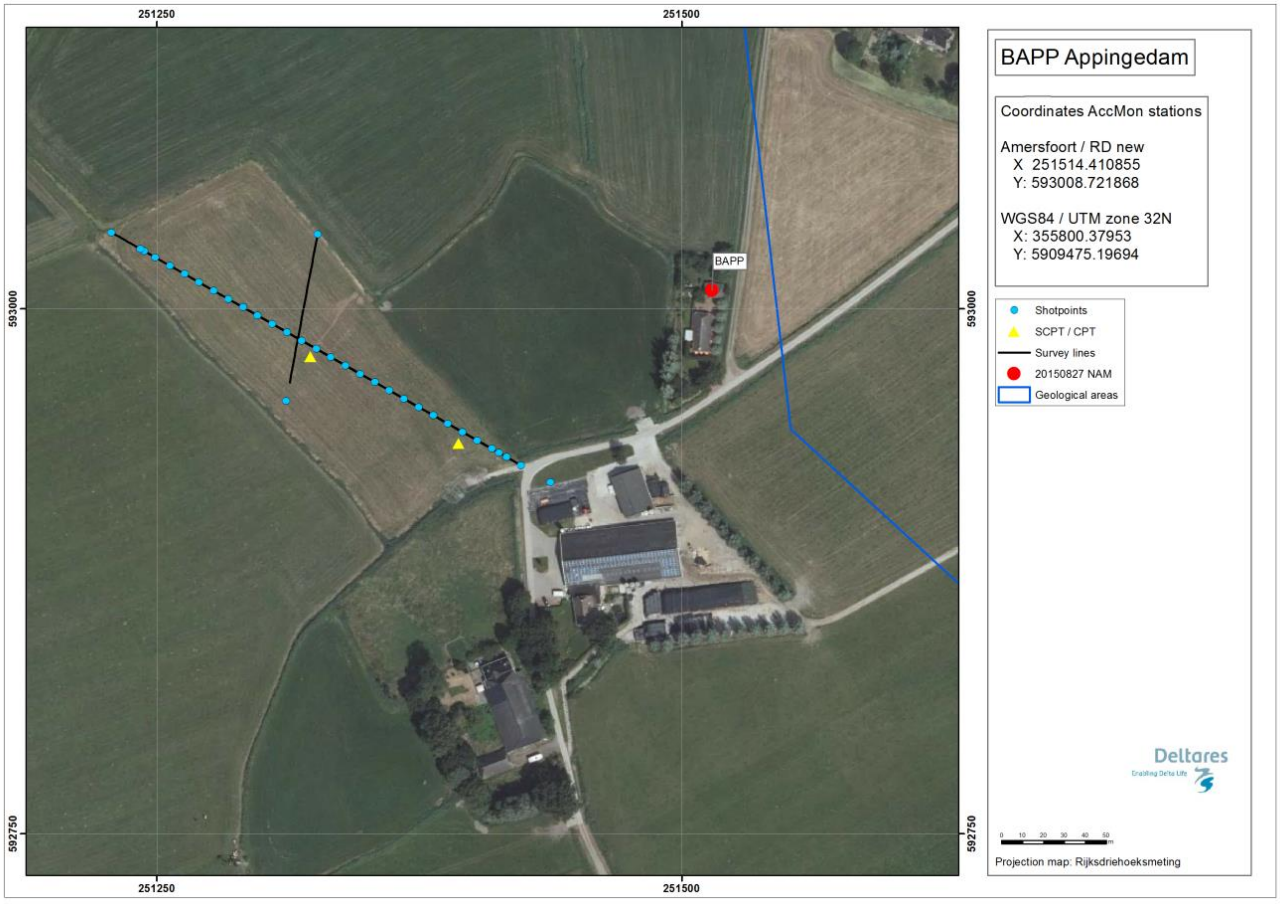

Figure 13.6. Location of seismic CPT and active and passive MASW arrays with respect to the BAPP accelerograph station (*red circle*); the scale bar is 50 metres (de Kleine *et al*., 2015)

The tests were coordinated by Deltares and the endeavour was led by Marco de Kleine, with support from Ger de Lange, Marios Karoulis and Rik Noorlandt. Some of the tests were performed by sub-contractors engaged by Deltares. The work was carried out between July and September 2015 in two phases, the first focusing on four of the stations and using a wide range of measurement techniques, including PS suspension logging and cross-hole measurements. The former was judged, by contractors Robertson Geologging, to be unreliable in these very soft deposits. At these and all other locations, seismic CPT and both active and passive MASW measurements were performed. The results were analysed and interpreted both by Deltares and by Antonio di Matteo and Ewoud van Dedem at Shell for the MASW, and the final V_S profiles will be made available in the near future.

The first step in the process will be to compare both the V_S profile at each station and the range of possible profiles as inferred from the different measurements with the profiles developed in Section 4.2. The transfer functions at the stations will then be re-calculated using the new profiles and these used to transform the surface FAS to the NU_B horizon, before repeating the inversions. The measure V_S profiles will also be used to calculate linear site amplification functions at the station locations and these will be compared with the range of amplification factors assigned to the host zone of each recording station.

13.3. Use of borehole recordings

The 70 new accelerographs being installed by NAM—and subsequently operated by KNMI—are all co-located with 200 metre deep boreholes installed with geophones at 50 m intervals. Although only weak motions have been recorded to date and notwithstanding the fact that the shallowest instrument below the surface accelerograph is at 50 metres, the recordings potentially offer a unique opportunity for exploring the validity of the amplification factors derived for the field. Clearly exact agreement between the linear portion of the zonal amplification factor and the empirical amplification factors is not expected—not least because the deepest geophone is at 200 m whereas the reference rock horizon for the site amplification functions is at about 350 m—but they should lie within a certain confidence limit on the amplification factors.

There are several challenges, however, that might place limits on the value of this exercise. The geophones—which are 4.5 Hz instruments with pre-amplifiers to boost the low-frequency response down to about 1 Hz—record velocity and therefore the time-series need to be differentiated to obtain accelerations, although with a sampling rate of 250 Hz this should be reliable. More significant is the high-gain set on the instruments which means that they are likely to clip under more intense motions.

13.4. New duration definition and consistent duration predictions

As noted in Section 12.1, the definition adopted for measuring the duration of the Groningen ground motions is the significant duration based on the accumulation of 5% to 75% of the total Arias intensity, $D_{S5\text{-}75}$. This may not be the most suitable measure to capture the duration

characteristics of the Groningen motions, for which reason alternative definitions might be explored. Several considerations need to be kept in mind, however, for an entirely consistent treatment of duration across all elements of the hazard and risk modelling:

- The duration must be predictable, which was one of the motivations for choosing the $D_{S5\text{-}75}$ definition since it allowed use of existing predictive models.
- A consistent duration prediction should be included in all stages of the work, including the signal durations used in the stochastic simulations for response spectral ordinates. For the V2 simulations, the predictive model of Boore & Thompson (2014) was used, which predicts a duration intended to be equivalent to the $D_{S5\text{-}75}$ definition and is defined as twice the duration $D_{S20\text{-}80}$. Figure 13.7 compares these two duration measures for the Groningen recordings.
- The definition of duration adopted also needs to be appropriate to the characterisation of the fragility functions.

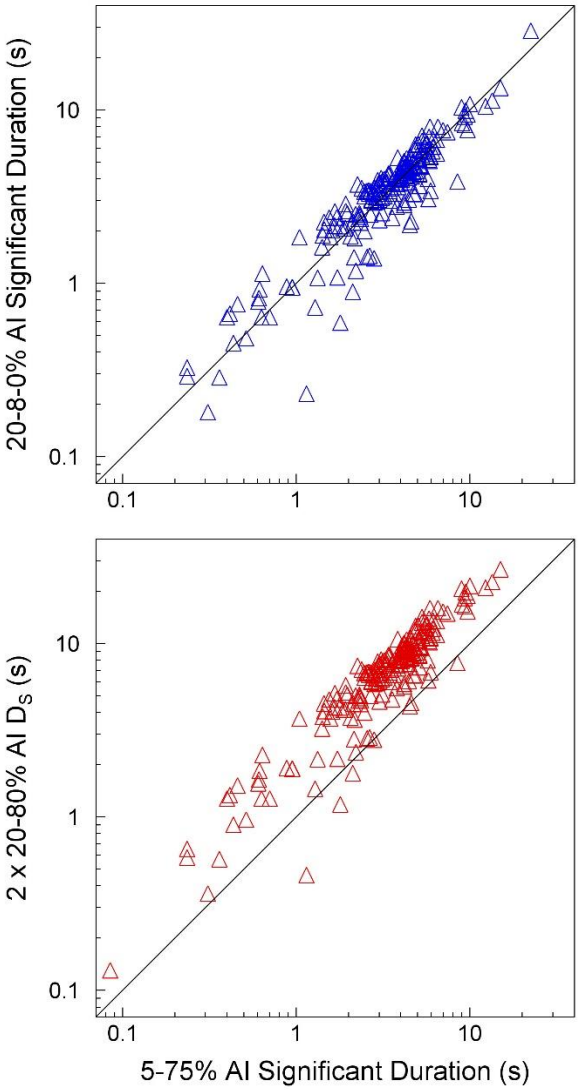

Figure 13.7. Correlations of duration definitions for individual components of recordings from earthquakes of magnitude ≥ 2.5 in the Groningen field

13.5. Summary of sensitivity analyses and potential refinements

The V2 GMPEs provide coherent and reliable predictions of spectral accelerations and durations in the Groningen study area that serve the current needs of both the seismic hazard assessments and the risk estimations. However, it is also clearly the case that this model can be improved and refined, and herein we list several ideas for additional work to be conducted in the few remaining months prior to delivery of the V3 hazard and risk model that will underpin the 2016 Winningsplan.

The list of ideas presented herein is probably not exhaustive since new insights will no doubt arise as the work progresses and as additional feedback on the V2 model is received from various parties. At the same time, this is a list of potential improvements rather than a definitive plan or inventory of firm commitments since the final scope of work will depend upon the available time. Moreover, the work will be guided by the needs of the fragility development programme and the risk analyses, as well as by identification of those elements of the model for which refinements potentially offer the greatest benefits in terms of reduced uncertainties and more reliable predictions.

The current ideas regarding enhancement and improvement of the V2 models are listed below under the headings of parameters to be predicted, the equations for the NU_B horizon, and the site response model.

Ground-motion parameters

Apart from the refined definition of duration discussed in the previous section, the V3 GMPEs are also likely to provide more predictions of response spectral accelerations. One motivation for this is that horizontal accelerations are required at a greater number of short oscillator periods—in the ranger from 0.01 to 0.2 seconds—in order for the application of V/H ratios to lead to reliable vertical spectral shapes. The other target periods may be extended or modified to accommodate the most recent results from the structural modelling team and their insights regarding representative vibration periods of the Groningen building typologies.

The preliminary V/H ratio model presented in Section 11.4 will clearly be re-visited. Although no trends in the V/H ratios from the Groningen data were observed with respect to magnitude or distance, explorations will be made for any consistent patterns at individual stations indicating possible site effects. Additionally, the possible application of the implied V/H ratios from the emerging NGA-West2 GMPEs for vertical components of motion (*e.g.*, Bozorgnia & Campbell, 2015) will also be explored for their potential application or adjustment o Groningen.

Another requirement that has been indicated for the fragility development is predictions of the response spectral accelerations at damping ratios other than 5% of critical. This need could be addressed in one of a number of ways, the most cumbersome being to derive suites of GMPEs—at the NU_B horizon but using the same site amplification factors—for spectral accelerations at multiple levels of damping; interpolations could be used for intermediate

values. Alternatively, we could derive predictive equations for scaling factors to be applied to transform the 5%-damped ordinates to other levels. It is known that such factors are dependent on the duration of the motion (Bommer & Mendis, 2005) and this can be captured by predictions conditioned on duration directly (*e.g*., Stafford *et al*., 2008) or else on the parameters that in turn control duration, such as magnitude, distance and site classification (*e.g.,* Akkar *et al*., 2014b).

Another ground-motion parameter for which predictions are now required is peak ground velocity, PGV, which has been requested by those conducting seismic stability analyses for dikes in the Groningen region. The current indication is that the PGV predictions will only be required at the NU_B reference rock horizon since detailed site-specific response calculations will be performed as part of those assessments.

GMPEs for motions at the NU_B horizon

Figure 13.8 shows, for each response spectrum in the GMPE database—including the additional small-magnitude events (Section 3.3)—the residual misfit as a function of oscillator period using the NU_B stochastic simulation model in addition to the site-specific NU_B to surface amplification functions. The bias apparent in the GMPE (Section 6.5, Figure 6.51) is also apparent in these simulations and it is therefore clear that the source of the bias lies at the simulation stage rather than, for example, the parametric form of the GMPE.

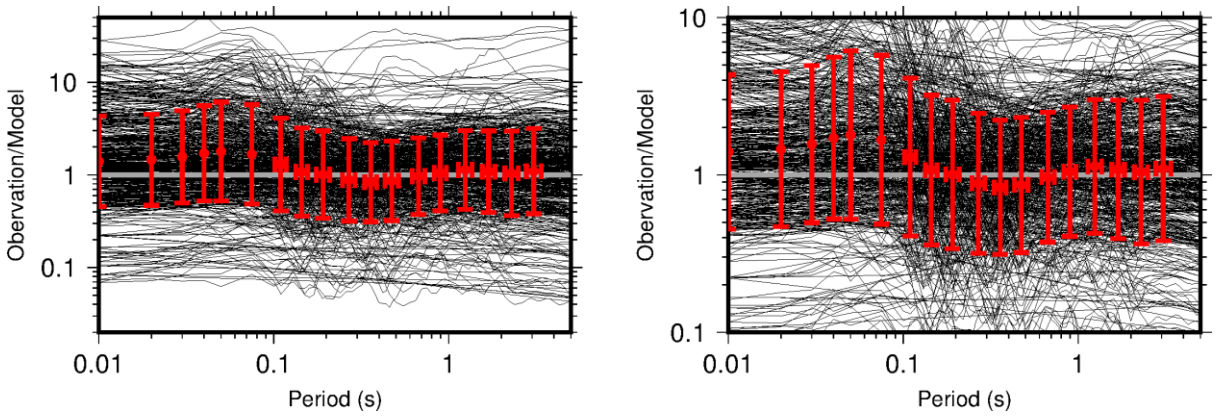

Figure 13.8. residual misfit between the NU_B simulations plus NU_B to surface amplification and the full V2 database (including additional small magnitude events and without selection for usable period). The same figure is plotted using an enlarged scale in the right panel.

A question posed by this comparison is the source of the bias introduced in the V2 model. One source might lie in the simplicity of the model – with a single stress-parametre, Q, NU_B amplification function and κ0 (although this is the same as in the V1 model). In order to investigate this we use the record/event-specific stress-parametre and κ (comprising Q and κ0 effects) obtained from the original spectral inversions (Section 5). We obtain—as we would expect—a significantly less biased model misfit (Figure 13.9). Including only the

records from the V1 database, we see little bias at all and significantly reduced scatter (Figure 13.10).

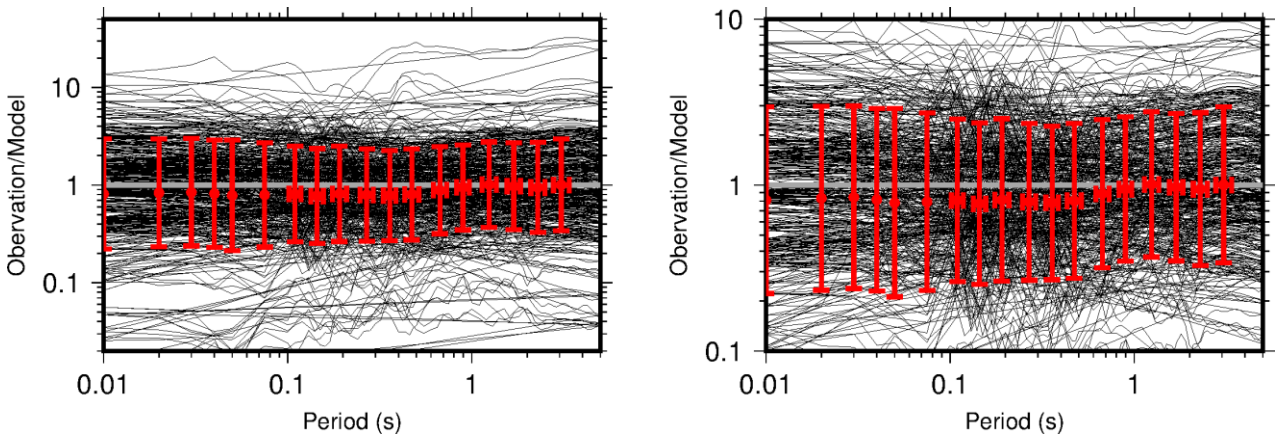

Figure 13.9. residual misfit between the simulations – modified to use stress parameter and κ directly inverted from the corresponding FAS – and the full database.

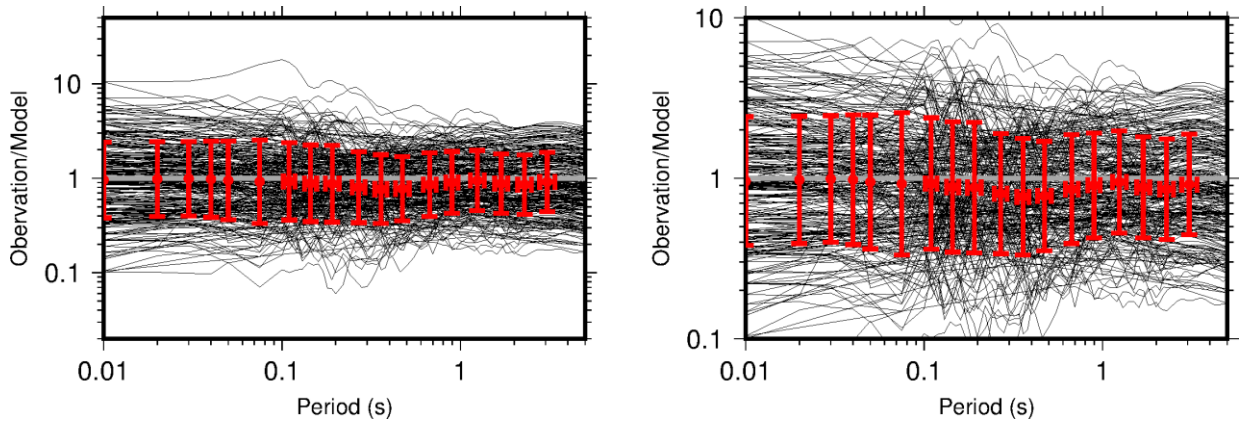

Figure 13.10. Residual misfit between the simulations – modified to use stress parameter and κ directly inverted from the corresponding FAS – and the V1 database.

Using event specific stress-parameters does not help in the case of unknown source (*i.e.*, the forward simulation problem). However, one issue might be that the events have a somewhat bi-modal distribution of stress-parameter (see Figure 5.3). It is, for instance, notable that the majority of new events are low-magnitude, low stress-parameter. Although it has so far been avoided due to what was foreseen as unjustified complexity (given the few data points) future revisions may investigate using a magnitude dependent stress-parameter.

There is also scope for improving the model through additional use of the full waveform simulations. Building on from the full waveform modelling (FWM) undertaken to inform the development of the geometrical spreading model (Section 5.3), we aim to further investigate wave-propagation effects in Groningen. A systematic feature observed in the residual misfit of the GMPE to the recorded data is that at short periods (e.*g.*, 0.01 – 0.2 s) a distance trend is still apparent. The residuals suggest that for short period motions the decay rate in the first few kilometres is faster than currently modelled (despite using the tri-linear model), and that

relatively sharp changes in the rate of decay are observed at around 7 km. The fact that this only appears at short periods is contrary to usual models of geometrical spreading – which assume frequency independent effects. However, recent work using regional data has shown that the apparent geometrical spreading rate may be frequency dependent (Atkinson & Boore, 2014). Atkinson & Boore (2014) suggested that their observation may have been due to a trade off with anelastic attenuation function, which was calibrated at regional distances. Initial testing using the 3D Groningen model has indicated, however, that even in elastic media the apparent rate of geometrical decay is strongly dependent on the analysis frequency (Figure 13.11). We plan to investigate this feature and—where possible—integrate it into the stochastic simulations and GMPE.

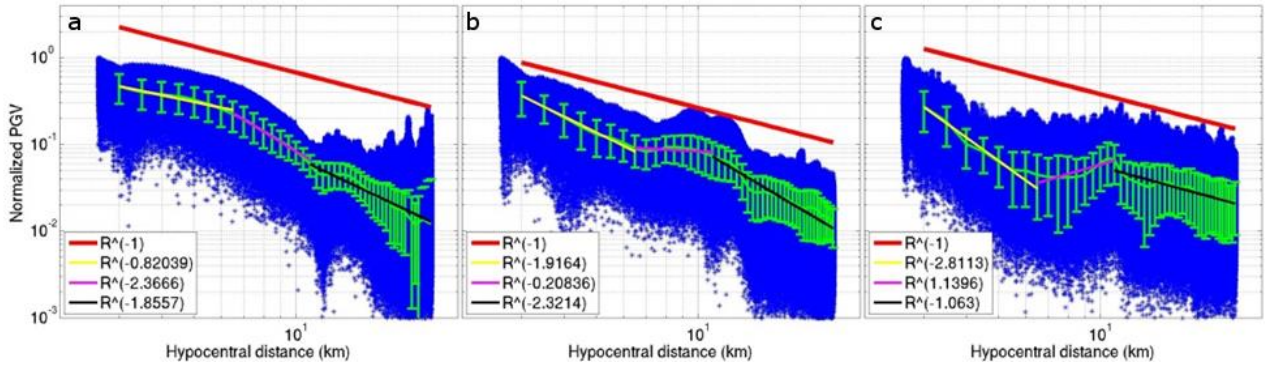

Figure 13.11. Geometric mean horizontal component FAS of simulated waveforms versus hypocentral distance at (a) 0.5 Hz, (b) 2 Hz and (c) 8 Hz. Binned mean values are indicated every 500m. Individual best-fit slopes are shown along with 1/R for reference.

There is also scope for the re-visiting the branches of the NU_B ground-motion model and their assigned weights, since the V2 model essentially retained the basic formulation of the V1 model. With the expanded ground-motion database now being used, including many more recordings from smaller events (**M** < 2.5), we consider it possible that the lower stress drop estimates may well be the result of the high kappa values at these soft soil sites masking the true corner frequencies. The lowest branch of the logic-tree may, therefore, be modified or even removed. The weights on the other branches would then need re-adjustment and this may be partly informed by comparisons with other models and/or other datasets, particularly those related to shallow induced seismicity. A difficulty, as was noted in the V1 model derivation (Bommer *et al*., 2015a), of using recordings of tectonic earthquakes to make such inferences is that adjustments need to be made not only for site conditions but also for focal depth, accounting for both the shorter travel path to the surface and the reduced stress drop expected for such shallow events. NGA-West models such as those of Campbell & Bozorgnia (2014), which include hypocentral depth as a scaling parameter for the effect of source embedment within the crust, may be useful in this regard.

Another issue that does need to still be address is the assumed equivalence of local and moment magnitudes in the Groningen field. While this is not a critical issue is some regards, as discussed in Section 2.1, because of the internal consistency of the hazard model in terms

of the seismicity catalogue and the derivation of the GMPEs, it is the case that the extrapolation of the GMPEs to larger magnitudes using stochastic simulations is based on seismic moments. Therefore, it is important to ascertain not necessarily that the scales are equivalent—although this does have a theoretical basis over the magnitude range for which the extrapolations are being made (Deichmann, 2006)—but that the relationship between the two is linear. The adaptation of existing GMPEs for V/H spectral ratios and for duration, as well as the use of other to derive corrections to the within-event variability (Section 10.3), all do depend on the validity of the currently assumed equivalence.

Site response model

The single most significant change in the evolution from the V1 to V2 models was the development of the field zonation for non-linear site amplification factors for motions at the reference rock horizon. While we are confident that the site amplification model is essentially correct and its incorporation represents a major improvement to the ground-motion prediction model for induced earthquakes in Groningen, there is also significant scope for exploring this element of the model for improvements and refinements. Since there are so many potential activities that fall under this heading, they are presented herein simply as bullet points grouped under general topics but without elaboration.

- Geological model:
    - Shallow part (Surface to NAP-50 m): final GeoTOP version instead of beta version
    - Shallow part: better representation of *wierden* (dwelling mounds)
    - Shallow part: better representation of anthropogenic top layers of sand
    - Deeper part: include interpretation of 70 borehole logs to 200 m depth, e.g. for better definition of location and composition of geological systems such as Peelo channels

- V_S model:
    - Use of measured V_S to approx. NAP-30 m at recording stations.
    - New Groningen specific V_S relations based on enlarged dataset of SCPTs and relation between SCPT and CPT from Groningen database. Introduce depth-dependency in Groningen-specific Vs models.
    - Improvement of V_S transition between GeoTOP and MEIDAS using improved geological model.
    - V_S information to 200 m depth at the 70 vertical array locations (fieldwork and interpretation of recorded earthquake signals needed)
    - Introduce a Groningen-specific Vs spatial correlation model (for vertical spatial correlation).
    - Uncertainties in V_S in the look-up table may be too low. They are lower than the minimum recommended for sites with measurements per the SPID document.

- Validate the MEIDAS model, wherever possible, with new data from the V_S profiling at the recording stations.
- Uncertainties in the MEIDAS velocities should be larger outside the region of coverage of the model
- Uncertainty in V_S below MEIDAS are based on errors in the measured V_S at a single well. This is conceptually wrong, since what we want to capture is epistemic uncertainty for sites with no measurements, not potential measurement uncertainty at the few sites with measurements.

- Shear degradation and damping curves:
  - Improved lookup table of geomechanical parameters OCR and I_p, based on database of laboratory measurements (to be built) or new laboratory measurements (to be measured).
  - Determination of shear degradation and damping curves for Groningen peats (to be measured in the laboratory).
  - Use Menq's (2003) curves for sands. For this, we need better estimates of coefficient of uniformity (Cu) for the field.
  - Use equation from Cetin & Ozcan (2009) in place of Equation (7.14)
  - Interpret damping from geophone recordings in 200 m boreholes
  - Check effect of using vertical stress or mean effective stress for determination of the shear modulus degradation curves (NB: the presently available curves and expression are derived from test results on isotropically consolidated samples, so at samples where the vertical stress and the mean effective stress are the same)
  - Include in the look-up table additional information from the CPT profiles. This should include cone friction (fs) and soil behaviour type index(Ic). This information would be useful to guide the selection of parameters used to evaluate MRD curves (like PI).
  - Consider using a larger D_{min}. Could base this on: a) vertical array data compiled recently (Stewart, personal communication), b) Q vs. V_S correlations from the literature, c) kappa constraints from the records and from an estimates of kappa for NU_B, d) information from the vertical arrays.
  - Considering capping damping at values around 20 to 30%.
  - Consider alternative correlations for undrained strength for peats, including correlations that are not based on CPT but are simply based on normalized strengths.

- Randomisations and Zonation
  - Sensitivity analysis for parameters that were fixed in V2: Darendeli curves, OCR, I_p, unit weight, V_S for NAP-50 m.
  - Use median AF for each voxel stacks to re-draw the zonation map.
  - Explore automated zonation algorithms.
  - As a validation/verification exercise, we can compare the site amplification model parameters (f_1, f_2, f_3) for each of the geologic/geotechnical zones in the study region with those of V_{S30}-based global model like Stewart & Seyhan

(2014). This will be useful to see if trends are consistent with what has been found elsewhere.
    - Evaluate if the very large strains observed in the site response runs to get AF for the zones are leading to unusual values of strains.
    - Consider randomization of the soil types within each voxel.
    - Re-evaluate AF when the predicted values are outside a 3 standard deviation band.

- Computation of AF factors
    - Ignore the effect of very soft surface layers (as done for recording stations)

- Kappa
    - Link the observed kappa0s at the recording stations to the zones where the recording stations are located. This could just modify the AF functions for zones with recording stations

- Sigma model
    - Single-station phi (ϕ_{SS}) at long periods could be lower than the 0.45 value used.

- Validation
    - Validate results STRATA calculations with results of measured acceleration records in boreholes (*e.g.*, using Hellum earthquake of 30 September 2015).
    - Check whether the positive biases in EQL analyses vs non-linear analyses and RVT versus time series analyses inferred from the literature apply to Groningen profiles
    - For sites with a reasonable number of recordings (about 4 or more), partition within-event residuals to compute the site terms. Plot those terms together with the site amp model for that zone. If there is a dip in the site term where the model has a bump, then this can indicate over-prediction of the amplification at that frequency. If the site terms are flat, then the modelling approach is validated.
    - Check H/V from records in the field and see if they match predicted resonant frequencies.
    - Use the station amplification functions predicted by Ben as an intermediate step in his analysis to see if the predictions of amplification at the stations are correct.

REFERENCES

Abercrombie, R.E. & P.C. Leary (1993). Source parametres of small earthquakes recorded at 2.5 km depth, Cajon Pass, southern California: implications for earthquake scaling. *Geophysical Research Letters* **20**, 1511-1514.

Abrahamson, N.A. & R.R. Youngs (1992). A stable algorithm for regression analyses using the random effects model. . *Bulletin of the Seismological Society of America* **82**(1), 505-510.

Afshari, K. & J.P. Stewart (2015). Physically parametrized prediction equations for significant duration in active crustal regions, *under review for Earthquake Spectra.*

Akkar, S. & J.J. Bommer (2006). Influence of long-period filter cut-off on elastic spectral displacements. *Earthquake Engineering & Structural Dynamics* **35**(9), 1145-1165.

Akkar, S., M.A. Sandıkkaya & J.J. Bommer (2014a). Empirical ground-motion models for point- and extended-source crustal earthquake scenarios in Europe and the Middle East. *Bulletin of Earthquake Engineering* **12**(1), 359-387. *Erratum*: **12**(1), 389-390.

Akkar, S., M.A. Sandıkkaya & B.Ö, Ay (2014b). Compatible ground-motion prediction equations for damping scaling factors and vertical-to-horizontal spectral amplitude ratios for the broader European region. *Bulletin of Earthquake Engineering* **12**(1), 517-547.

Al Atik, L., N.A. Abrahamson, J.J. Bommer, F. Scherbaum, F. Cotton & N. Kuehn (2010). The variability of ground-motion prediction models and its components. *Seismological Research Letters* **81**(5), 783-793.

Ancheta, R.D., R.B. Darragh, J.P. Stewart, E. Seyhan, W.J. Silva, B.S.-J. Chiou, K.E. Wooddell, R.W. Graves, A.R. Kottke, D.M. Boore, T. Kishida & J.L. Donahue (2014). NGA-West2 database. *Earthquake Spectra* **30**(3), 989-1005.

Anderson, J.G. & J.N. Brune (1999). Probabilistic seismic hazard assessment without the ergodic assumption. *Seismological Research Letters* **70**, 19-28.

Anderson, J.G. & S.E. Hough (1984). A model for the shape of the Fourier amplitude spectrum of acceleration at high frequencies. *Bulletin of the Seismological Society of America* **74**, 1969-1993.

Andrus, R.D., N.P. Mohanan, P. Piratheepan, B.S. Ellis, & T.L. Holzer, (2007). Predicting shear-wave velocity from cone penetration resistance. *Proceedings of the 4th International Conference on Earthquake Geotechnical Engineering*, Thessaloniki, Greece, 25-28.

Assimaki D. & W. Li (2012). Site- and ground motion-dependent nonlinear effects in seismological model predictions. *Soil Dynamics & Earthquake Engineering* **32**(1), 143–151.

Atkinson, G.M. (2006). Single-station sigma. *Bulletin of the Seismological Society of America* **96**, 446-455.

Atkinson, G.M. (2015). Ground-motion prediction equation for small-to-moderate events at short hypocentral distances, with application to induced-seismicity hazards. *Bulletin of the Seismological Society of America* **105**(2A), 981-992.

Atkinson, G.M. & D.M. Boore (2014). The attenuation of Fourier amplitudes for rock sites in eastern North America. *Bulletin of the Seismological Society of America* **104**, 513--528.

Baker, J.W. & C.A. Cornell (2006a). Which spectral acceleration are you using? *Earthquake Spectra* **22**(2), 293-312.

Baker, J.W. & C.A. Cornell (2006b). Spectral shape, epsilon and record selection. *Earthquake Engineering & Structural Dynamics* **35**, 1077–1095.

Bal, I.E, J.J. Bommer, P.J. Stafford, H. Crowley & R. Pinho (2010). The influence of geographical resolution of urban exposure data in an earthquake loss model for Istanbul. *Earthquake Spectra* **26**(3), 619-634.

Baltay, A.S. & T.C. Hanks (2014). Understanding the magnitude dependence of PGA and PGV in NGA-West 2 data. *Bulletin of the Seismological Society of America* **104**(6), 2851-2865.

Bazzurro, P. & C.A. Cornell (2004a). Ground-motion amplification in nonlinear soil sites with uncertain properties. *Bulletin of the Seismological Society of America* **94**, 2090-2109.

Bazzurro, P. & C.A. Cornell (2004b). Nonlinear soil-site effects in probabilistic seismic hazard analysis. *Bulletin of the Seismological Society of America* **94**(6), 2110-2123.

Benjamin, J. R. & A. Cornell, A. (1970). *Probability, statistics, and decision for civil engineers*. McGraw-Hill, New York.

Bommer, J. J. & S. Akkar (2012). Consistent source-to-site distance metrics in ground-motion prediction equations and seismic source models for PSHA. *Earthquake Spectra* **28**(1), 1-15.

Bommer, J.J., S. Akkar & S. Drouet (2012). Extending ground-motion prediction equations for spectral ordinates to higher response frequencies. *Bulletin of Earthquake Engineering* **10**(2), 379-399.

Bommer, J.J., S. Akkar & Ö. Kale (2011). A model for vertical-to-horizontal response spectral ratios for Europe and the Middle East. *Bulletin of the Seismological Society of America* **101**(4), 1783-1806.

Bommer, J.J., S.J. Bourne, H. Crowley, B. Edwards, P. Kruiver, S. Oates & A. Rodriguez-Marek (2015b). *Seismic design loads for the Groningen Forum*. A report prepared for NAM, version 3, 26 June 2015, 88 pp.

Bommer, J.J., K.J. Coppersmith, R.T. Coppersmith, K.L. Hanson, A. Mangongolo, J. Neveling, E.M. Rathje, A. Rodriguez-Marek, F. Scherbaum, R. Shelembe, P.J. Stafford & F.O. Strasser (2015c). A SSHAC Level 3 probabilistic seismic hazard analysis for a new-build nuclear site in South Africa. *Earthquake Spectra* **31**(2), 661-698.

Bommer J. & B. Dost (2014). *Version 0 ground-motion prediction equations*. 16 June 2014, 17 pp.

Bommer, J.J., B. Dost, B. Edwards, P.J. Stafford, J. van Elk, D. Doornhof & M. Ntinalexis (2016). Developing an application-specific ground-motion model for induced seismicity. *Bulletin of the Seismological Society of America* **106**(1), *in press*.

Bommer, J.J., J. Douglas, F. Scherbaum, F. Cotton, H. Bungum & D. Fäh (2010). On the selection of ground-motion prediction equations for seismic hazard analysis. *Seismological Research Letters* **81**(5), 794-801.

Bommer, J.J., G. Magenes, J. Hancock & P. Penazzo (2004). The influence of strong-motion duration on the seismic response of masonry structures. *Bulletin of Earthquake Engineering* **2**(1), 1-26.

Bommer, J.J. & A. Martinez-Pereira (1999). The effective duration of earthquake strong motion. *Journal of Earthquake Engineering* **3**(2), 127-172.

Bommer, J.J. & R. Mendis (2005). Scaling of displacement spectral ordinates with damping ratios. *Earthquake Engineering & Structural Dynamics* **34**(2), 145-165.

Bommer, J.J., R. Pinho & H. Crowley (2005). Using displacement-based earthquake loss assessment in the selection of seismic code design levels. *Proceeding of ICOSSAR'05 (International Conference on Structural Safety and Reliability),* Rome, 3567-3574.

Bommer, J.J., P.J. Stafford & J.E. Alarcón (2009). Empirical equations for the prediction of the significant, bracketed and uniform duration of earthquake ground motion. *Bulletin of the Seismological Society of America* **99**(6), 3217-3233.

Bommer, J.J., P.J. Stafford, B. Edwards, B. Dost & M. Ntinalexis (2015a). *Development of version 1 GMPEs for response spectral accelerations and for strong-motion durations*. Version 2, 21 June 2015, 304 pp.

Boore, D.M. (2005a). *SMSIM – Fortran programs for simulating ground motions from earthquakes: Version 2.3—A revision of OFR 96-80*. US Geological Survey Open-File Report 00-509, 55 pp.

Boore, D.M. (2005b). Erratum: Equations for estimating horizontal response spectra and peak acceleration from western north American earthquakes: A summary of recent work, by D.M. Boore, W.B. Joyner and T.E. Fumal. *Seismological Research Letters* **76**(3), 368-369.

Boore, D. M. & W. B. Joyner (1984). A note on the use of random vibration theory to predict peak amplitudes of transient signals. *Bulletin of the Seismological Society of America* **74**(5), 2035–2039.

Boore, D. M. & E. M. Thompson (2012). Empirical improvements for estimating earthquake response spectra with random vibration theory. *Bulletin of the Seismological Society of America* **102**(2), 761–772.

Boore, D.M. & E.M. Thompson (2014). Path durations for use in the stochastic-method simulations of ground motions. *Bulletin of the Seismological Society of America* **104**(5), 2541-2552.

Boore, D.M. (2010). Orientation-independent, nongeometric-mean measures of seismic intensity from two horizontal components of motion. *Bulletin of the Seismological Society of America* **100**(4), 1830-1835.

Boore, D.M. & J.J. Bommer (2005). Processing strong-motion accelerograms: needs, options and consequences. *Soil Dynamics & Earthquake Engineering* **25**(2), 93-115.

Boore, D.M., J.F. Gibbs, W.B. Joyner, J.C. Tinsley & D.J. Ponti (2003). Estimated ground motion from the 1994 Northridge, California, earthquake at the site of the Interstate 10 and La Cienega Boulevard bridge collapse, West Los Angeles, California. *Bulletin of the Seismological Society of America* **93**(6), 2737-2751.

Boore, D.M. & E.M. Thompson (2014). Path durations for use in the stochastic-method simulations of ground motions. *Bulletin of the Seismological Society of America* **104**(5), 2541-2552.

Boore, D.M., Watson-Lamprey, J. & Abrahamson, N.A. (2006). Orientation-independent measures of ground motion. *Bulletin of the Seismological Society of America* **94**(4A), 1502-1511.

Boulanger, R.W., R. Arulnathan, L.F. Harder, R.A. Torres & M.W. Driller (1997). *Dynamic properties of Sherman Island peat*. Report UCD/CGM-97/01, Department of Civil & Environmental Engineering, University of Californina, Davis, California.

Bourne, S.J., S.J. Oates, J. van Elk & D. Doornhof (2014). A seismological model for earthquakes induced by fluid extraction from a subsurface reservoir. *Journal of Geophysical Research Solid Earth* **119**, doi: 10.1002/201JB011663.

Bourne, S.J., S.J. Oates, J.J. Bommer, B. Dost, J. van Elk & D. Doornhof (2015). A Monte Carlo method for probabilistic hazard assessment of induced seismicity due to conventional natural gas production. *Bulletin of the Seismological Society of America* **105**(3), 1721-1738.

Bozorgnia, Y. & K.W. Campbell (2015). Vertical ground motion model for PGA, PGV, and linear response spectra using the NGA-West2 database. *Earthquake Spectra*, doi: http://dx.doi.org/10.1193/072814EQS121M

Bradley, B.A. (2011). Correlation of significant duration with amplitude and cumulative intensity measures and its use in ground motion selection. *Journal of Earthquake Engineering* **15**(6), 809-832.

Brune, J.N. (1970). Tectonic stress and the spectra of seismic shear waves from earthquakes. *Journal of Geophysical Research* **75**(26), 4997-5009. Correction (1971), **76**(20), 5002.

Campbell, K.W. & Y. Bozorgnia (2003). Updated near-source ground-motion (attenuation) relations for the horizontal and vertical components of peak ground acceleration and acceleration response spectra. *Bulletin of the Seismological Society of America* **93**(1), 314-331.

Campbell, K.W. & Y. Bozorgnia (2007). *Campbell-Bozorgnia NGA Ground Motion Relations for the Geometric Mean Horizontal Component of Peak and Spectral Ground Motion Parameters.* PEER Report 2007/02, Pacific Earthquake Engineering Research Center, University of California at Berkeley, 240 pp.

Campbell, K.W. & Y. Bozorgnia (2014). NGA-West2 ground motion model for the average horizontal components of PGA, PGV, and 5%-damped elastic pseudo-acceleration response spectra. *Earthquake Spectra* **30**(3), 1087-1115.

Chandramohan, R., J.W. Baker & G.G. Deierlein (2015). Quantifying the influence of ground motion duration on structural collapse capacity using spectrally equivalent records. *Earthquake Spectra*, doi: http://dx.doi.org/10.1193/122813EQS298MR2

Chiou, B.S.-J. & R.R. Youngs (2008). An NGA model for the average horizontal component of peak ground motion and response spectra. *Earthquake Spectra* **24**(1), 173-215.

Chopra, A.K. (2007). *Dynamics of Structures: Theory and Applications to Earthquake Engineering*. Prentice Hall, Upper Saddle River, New Jersey, third edition.

Clark, D., A. McPherson, T. Allen & M. De Kool (2014). Coseismic surface deformation caused by the 23 March 2012 M_W 5.4 Ernabella (Pukatja) earthquake, central Australia: implications for fault scaling relations in cratonic settings. *Bulletin of the Seismological Society of America* **104**, 24-39.

Cotton, F., R. Archuleta & M. Causse (2013). What is sigma of the stress drop? *Seismological Research Letters* **84**(1), 42-48.

Crowley, H., V. Silva, I.E. Bal & R. Pinho (2012). Calibration of seismic design codes using loss estimation. *Proceedings of 15th World Conference on Earthquake Engineering*, Lisbon, Portugal, Paper no. 4891.

Crowley, H., P.J. Stafford & J.J. Bommer (2008). Can earthquake loss models be validated using field observations? *Journal of Earthquake Engineering* **12**(7), 1078-1104.

Darendeli, M. (2001). *Development of a new family of normalized modulus reduction and material damping curves*. Ph.D. Thesis, Dept. of Civil Eng., University of Texas, Austin, TX.

Deichmann, N. (2006). Local magnitude: a moment revisited. *Bulletin of the Seismological Society of America* **96**, 1267-1277.

de Kleine, M., R. Noorlandt, G. der Lange & M. Karaoulis (2015). *V_S measurements at KNMI accelerograph stations*. Deltares Report 1210624-000, draft.

Douglas, J. & P. Jousset (2011). Modeling the difference in ground-motion magnitude-scaling in small and large earthquakes. *Seismological Research Letters* **82**(4), 504-508.

Dost, B., B. Edwards & J.J. Bommer (2015). *Local and moment magnitudes in the Groningen field*. Unpublished draft report.

Edwards, B., D. Fäh & D. Giardini (2011). Attenuation of seismic shear wave energy in Switzerland. *Geophysical Journal International* **185**, 967-984.

Edwards, B., A. Rietbrock, J. J. Bommer & B. Baptie (2008). The acquisition of source, path, and site effects from micro-earthquake recordings using *q* tomography: Application to the United Kingdom. *Bulletin of the Seismological Society of America* **98**, 1915-1935.

Ernst, F. (2013). Modal Elastic Inversion. *75th EAGE Conference and Exhibition*, London.

Eshelby, J. D. (1957). The determination of the elastic field of an ellipsoidal inclusion, and related problems. *Proceedings of the Royal Society of London: Series-A* **241**, 376-396.

Esposito, S. & I. Iervolino (2011). PGA and PGV spatial correlation models based on European multievent datasets. *Bulletin of the Seismological Society of America* **101**(5), 2532-2541.

Esposito, S. & I. Iervolino (2012). Spatial correlation of spectral acceleration in European data. *Bulletin of the Seismological Society of America* **102**(6), 2781-2788.

Goda, K. & G.M. Atkinson (2010). Intraevent spatial correlation of ground-motion parametres using SK-net data. *Bulletin of the Seismological Society of America* **100**(6), 3055-3067.

Graizer, V. (2014). Comment on “Comparison of time series and random vibration theory site-response methods” by Albert R. Kottke and Ellen M. Rathje. *Bulletin of the Seismological Society of America* **104**(1), 540-546.

Gülerce, Z. & N.A. Abrahamson (2011). Site-specific design spectra for vertical ground motion. *Earthquake Spectra* **27**(4), 1023-1047.

Hanks, T.C. & H. Kanamori (1979). Moment magnitude scale. *Journal of Geophysical Research* **84**, 2348-2350.

Hashash, Y.M.A., D.R. Groholski & C. Phillips (2010). Recent advances in nonlinear site response analysis. *Proceedings of the 5th International Conference on Recent Advances in Geotechnical Earthquake Engineering and Soil Dynamics and Symposium in honor of Prof. Idriss*, May 24-29 San Diego, California.

Hashash, Y.M.A., M.I. Musgrove, J.A. Harmon, D.R. Groholski, C.A. Phillips & D. Park (2015). *User Manual for DEEPSOIL 6.0.*, 116 pp.

Hashash, Y.M.A. & D. Park (2002). Viscous damping formulation and high frequency motion propagation in nonlinear site response analysis. *Soil Dynamics & Earthquake Engineering*, **22**(7), 611–624.

Iervolino, I., G. Manfredi & E. Cosenza (2006). Ground motion duration effects on nonlinear seismic response. *Earthquake Engineering & Structural Dynamics* **35**(1), 21-38.

Jayaram, N. & J.W. Baker (2009). Correlation model for spatially distributed ground motion intensities. *Earthquake Engineering & Structural Dynamics* **38**(15), 1687-1708.

Kaklamanos J., B.A. Bradley, E.M. Thompson & L.G. Baise (2013). Critical parameters affecting bias and variability in site-response analyses using KiK-net downhole array data. *Bulletin of the Seismological Society of America* **103**(3), 1733-1749.

Kaklamanos, J., L.G. Baise, E.M. Thompson & L. Dorfmann (2015). Comparison of 1D linear, equivalent-linear, and nonlinear site response models at six KiK-net validation sites. *Soil Dynamics & Earthquake Engineering* **69**, 207-219.

Kallioglou, P., T. Tika, G. Koninis, S. Papadopoulos & K. Pitilakis (2009). Shear modulus and damping ratio of organic soils. *Geotechnical and Geological Engineering* **27**(2), 217-235.

Kempton, J.J. & J.P. Stewart (2006). Prediction equations for significant duration of earthquake ground motions considering site and near-source effects. *Earthquake Spectra* **22**(4), 985-1013.

Kim, B. & Y.M.A. Hashash (2013). Site response analysis using downhole array recordings during the March 2011 Tohoku-Oki earthquake and the effect of long-duration ground motions. *Earthquake Spectra* **29**, 37-54.

Kim B., Y.M.A. Hashash, A. Kottke, D. Assimaki, W. Li, E.M. Rathje, K.W. Campbell, W.J. Silva & J.P. Stewart (2013). A predictive model for the relative differences between nonlinear and equivalent-linear site response analyses. *Transactions, SMiRT-22*, Division IV, San Francisco, CA.

Kim, B., Y.M.A. Hashash, J.P. Stewart, E.M. Rathje, J.A. Harmon, M.I. Musgrove, K.W. Campbell & W.J. Silva (2015,). Relative differences between nonlinear and equivalent-linear 1D site response analyses, submitted to *Earthquake Spectra*.

Kishida, T., R.W. Boulanger, N.A. Abrahamson, M.W. Driller & T.M. Wehling (2009a). Site effects for the Sacramento-San Joaquin delta. *Earthquake Spectra* **25**(2), 301-322.

Kishida, T., R.W. Boulanger, N.A. Abrahamson, T.W. Wehling & M.W. Driller (2009b). Regression models for dynamic properties of highly organic soils. *Journal of Geotechnical and Geoenvironmental Engineering* **135**(4), 533-543.

Konno, K. & T. Ohmachi (1998). Ground-motion characteristics estimated from spectral ratio between horizontal and vertical components of microtremor. *Bulletin of the Seismological Society of America* **88**, 228–241.

Kottke, A.R. & E.M. Rathje (2013). Comparisons of time series and random-vibration theory site-response methods. *Bulletin of the Seismological Society of America* **103**(3), 2111-2127.

Kottke, A. (2010). *A Comparison of Seismic Site Response Methods*. Ph.D. Thesis, Dept. of Civil Eng., University of Texas, Austin, TX.

Kottke, A.R. & E.M. Rathje (2008). *Technical Manual for Strata*. PEER Report 2008/10, Pacific Earthquake Engineering Research Center, University of California at Berkeley, February, 84 pp.

Kramer, S.L. (1996). *Dynamic response of peat*. Washington State Department of Transportation, Report WA-RD 412.2, November 1996, 55 pp.

Kramer S.L. (2000). Dynamic response of Mercer Slough peat. *Journal of Geotechnical and Geoenvironmental Engineering* **126**(6), 504-510.

Kramer, S. L. & S. B. Paulsen (2004). Practical use of geotechnical site response models. *Proceedings of the International Workshop on Uncertainties in Nonlinear Soil Properties and their Impact on Modeling Dynamic Soil Response*, University of California, Berkeley.

Kruiver, P.P., G. de Lange, A. Wiersma, P. Meijers, M. Korff, J. Peeters, J. Stafleu, R. Harting, R. Dambrink, F. Busschers, J. Gunnink (2015). *Geological schematisation of the shallow subsurface of Groningen - For site response to earthquakes for the Groningen gas field*. Deltares Report No. 1209862-005-GEO-0004-v5-r, 16 March 2015.

Kwok A.O.L., J.P. Stewart & Y.M.A Hashash (2008). Nonlinear ground-response analysis of Turkey Flat shallow stiff-soil site to strong ground motion. *Bulletin of the Seismological Society of America* **98**(1), 331-343.

Lee, J. & R.A. Green (2014). An empirical significant duration relationship for stable continental regions. *Bulletin of Earthquake Engineering* **12**(1), 217-235.

Lefebvre, G., & D. LeBoeuf (1987). Rate effects and cyclic loading of sensitive clays. *Journal of Geotechnical Engineering* **113**(5), 476-489.

Leonard, M. (2014). Self-consistent earthquake fault-scaling relations: Update and extension to stable continental strike-slip faults. *Bulletin of the Seismological Society of America* **104**(6), 2953-2965.

Li W. & D. Assimaki (2010). Site and ground motion dependent parametric uncertainty of nonlinear site response analyses in earthquake simulations. *Bulletin of the Seismological Society of America* **100**(3), 954-968

Li, X.S., Z. Wang, & C.K. Shen (1992). *SUMDES: a nonlinear procedure for response analysis of horizontally-layered sites subjected to multidirectional earthquake loading*, User's Manual, Department of Civil Engineering, University of California, Davis.

Lin, P.-S., B.S.-J. Chiou, N.A. Abrahamson, M. Walling, C.-T. Lee & C.-T. Cheng (2011). Repeatable source, site, and path effects on the standard deviation for empirical ground-motion prediction models. *Bulletin of the Seismological Society of America* **101**, 2281-2295.

Liu, L. & S. Pezeshk (1999). An improvement on the estimation of pseudoresponse spectral velocity using RVT method. *Bulletin of the Seismological Society of America* **89**, 1384-1389.

Lunne, T., P.K. Robertson, & J.J.M. Powell (1997). *Cone Penetration Testing in Geotechnical Practice.* EF Spon/Blackie Academic, Routledge Publishers, London, 312 pp.

Matasovic, N. (2006). *D-MOD_2: a computer program for seismic response analysis of horizontally layered soil deposits, earthfill dams, and solid waste landfills*, User's Manual, GeoMotions, LLC, Lacey, Washington.

Matasovic, N. & Y. Hashash (2012). *NCHRP428: Practices and procedures for site-specific evaluations of earthquake ground motions* (A synthesis of highway practice). National Cooperative Highway Research Program, Transportation Research Board: 78 pages. Washington, D.C.

Matasovic, N. & M. Vucetic (1993). Cyclic characterization of liquefiable sands. *ASCE Journal of Geotechnical Engineering* **119**(11), 1805-1822.

McKenna, F. & G. L. Fenves (2001). *The OpenSees command language manual*, version 1.2. Pacific Earthquake Engineering Research Center, University of California at Berkeley, available at http://opensees. berkeley.edu.

NCHRP (2012). *Practices and Procedures for Site-Specific Evaluations of Earthquake Ground Motions*, Synthesis 428 (N. Matasovic and Y.M.A. Hashash). National Cooperative Highway Research Program, Transportation Research Board, Washington D.C.

NEN (2015). *Assessment of buildings in case of erection, reconstruction and disapproval - Basic rules for seismic actions; Induced earthquakes*. Draft NPR 9998, Nederlands Normalisatie-instituut, Delft.

Ntinalexis, M., B. Polidoro, J.J. Bommer & B. Edwards (2015a). *Selection of processing procedures for the accelerograph recordings of induced seismicity in Groningen*. Report prepared for NAM, 24 August 2015, 169 pp.

Ntinalexis, M., J.J. Bommer & B. Dost (2015b). *Ground-motion records from the Groningen field from the KNMI accelerograph network: database for V2 GMPE development*. Report prepared for NAM, 27 August 2015, 649 pp.

Papaspiliou M., S. Kontoe & J.J. Bommer (2012). An exploration of incorporating site response into PSHA-part II: Sensitivity of hazard estimates to Site Response Approaches. *Journal of Soil Dynamics & Earthquake Engineering* **42**, 316–330.

Pehlivan M. (2013). *Incorporating site response analysis and associated uncertainties into the seismic hazard assessment of nuclear facilities*. Ph.D. Thesis, Dept. of Civil Eng., University of Texas, Austin, TX.

Pehlivan, M., E.M. Rathje & R.B. Gilbert (2012). Incorporating site-specific site response analysis into PSHA. *Second International Conference on Performance-Based Design in Earthquake Geotechnical Engineering*, Taormina, Italy.

Phillips, C. & Y. Hashash (2009). Damping formulation for non-linear 1D site response analyses. *Soil Dynamics & Earthquake Engineering* **29**, 1143–1158.

Pyke, R.M. (1979). Nonlinear soil models for irregular cyclic loadings. *ASCE Journal of Geotechnical Engineering* **105**(GT6), 715–726.

Rathje, E.M. & A.R. Kottke (2011). Relative differences between equivalent-linear and nonlinear site response methods. *Proceedings of 5th International Conference on Earthquake Geotechnical Engineering*, Santiago, Chile.

Rathje, E.M. & M.C. Ozbey (2006). Site-specific validation of random vibration theory-based seismic site response analysis. *ASCE Journal of Geotechnical & Geoenvironmental Engineering* **132**(7), 911–922.

Rathje, E.M. & A.R. Kottke (2014). Reply to “Comment on ‘Comparison of Time Series and Random-Vibration Theory Site-Response Methods’ by V. Graizer”. *Bulletin of the Seismological Society of America* **104**(1), 547–550.

Rathje E.M., A.R. Kottke & W.L. Trent (2010). Influence of input motion and site property variabilities on seismic site response analysis. *Journal of Geotechnical and Geoenvironmental Engineering* **136**(4), 607-619.

Régnier, J., H. Cadet, L.F. Bonilla, E. Bertrand & J.-F. Semblat (2013). Assessing nonlinear behavior of soils in seismic site response: Statistical analysis on KiK-net strong-motion data. *Bulletin of the Seismological Society of America* **103**(3), 1750–1770.

Robertson, P.K. (1990). Soil classification using the cone penetration test. *Canadian Geotechnical Journal* **27**(1), 151-158.

Rodriguez-Marek, A., F. Cotton, N.A. Abrahamson, S. Akkar, L. Al Atik, B. Edwards, G.A. Montalva & H. Dawood (2013). A model for single-station standard deviation using data from various tectonic regions, *Bulletin of the Seismological Society of America* **103**, 3149-3163.

Rodriguez-Marek, A., G.A. Montalva, F. Cotton & F. Bonilla (2011). Analysis of single-station standard deviation using the KiK-net data. *Bulletin of the Seismological Society of America* **101**, 1242-1258.

Rodriguez-Marek, A., E.M. Rathje, J.J. Bommer, F. Scherbaum & P.J. Stafford (2014). Application of single-station sigma and site response characterization in a probabilistic seismic hazard analysis for a new nuclear site. *Bulletin of the Seismological Society of America* **104**(4), 1601-1619.

Sandıkkaya, M.A., S. Akkar & P.-Y. Bard (2013). A nonlinear site-amplification model for the next pan-European ground-motion prediction equations. *Bulletin of the Seismological Society of America* **103**(1), 19-32.

Scherbaum, F. (1990). Combined inversion for the three-dimensional q structure and source parametres using microearthquake spectra. *Journal of Geophysical Research: Solid* Earth **95**, 12423-12438

Seed, H.B. & I.M. Idriss (1970). Analysis of ground motions at Union Bay, Seattle, during earthquakes and distant nuclear blasts. *Bulletin Seismological Society of America* **60**(1), 135-136.

Skempton, A. W. & D.J. Henkel (1953). The post-glacial clays of the Thames Estuary at Tilbury and Shellhaven. *Proceedings of the 3rd International Conference on Soil Mechanics and Foundation Engineering* **1**, 302-308.

Sorensen, K. K., & N. Okkels (2013). Correlation between drained shear strength and plasticity index of undisturbed overconsolidated clays. *Proceedings of the 18th International Conference on Soil Mechanics and Geotechnical Engineering*, Paris, France, 423-428.

Stafford, P.J. (2014). Source-scaling relationships for the simulation of rupture geometry within probabilistic seismic-hazard analysis. *Bulletin of the Seismological Society of America* **104**(4), 1620-1634.

Stafford, P.J., R. Mendis & J.J. Bommer (2008). The dependence of spectral damping ratios on duration and number of cycles. *ASCE Journal of Structural Engineering* **134**(8)*,* 1364-1373.

Stewart, J.P., K. Afshari & Y.M.A. Hashash (2014). *Guidelines for Performing Hazard-Consistent One-Dimensional Ground Response Analysis for Ground Motion Prediction.* PEER Report 2014/16, Pacific Earthquake Engineering Research Center, University of California, Berkeley, CA.

Stewart, J.P., D.M. Boore, E. Seyhan & G.M. Atkinson (2015). NGA-West2 equations for predicting vertical-component PGA, PGV, and 5%-damped PSA from shallow crustal earthquakes. *Earthquake Spectra,* doi: http://dx.doi.org/10.1193/072114EQS116M

Stewart J.P., A.O. Kwok, Y.M.A. Hashash, N. Matasovic, R. Pyke, Z. Wang & Z. Yang (2008). *Benchmarking of nonlinear geotechnical ground response analysis procedures.* PEER Report No. 2008/04, Pacific Earthquake Engineering Research Center, University of California, Berkeley, CA.

Stewart, J.P. & A.O. Kwok (2008). Nonlinear seismic ground response analysis: code usage protocols and verification against vertical array data. *Geotechnical Engineering and Soil Dynamics IV*, May 18-22, 2008, Sacramento, CA. *ASCE Geotechnical Special Publication* **181**, D. Zeng, M.T. Manzari, and D.R. Hiltunen (eds.), 24 pages (electronic file).

Stokoe, K. H., J.A. Bay, B.L. Rosenbald, S.K. Hwang & M.R. Twede (1994). *In situ seismic and dynamic laboratory measurements of geotechnical materials at Queensboro Bridge and Roosevelt Island*. Geotech. Engineering Report GR 94-5, Civil Engineering Department, University of Texas at Austin, Texas.

Strasser, F.O., N.A. Abrahamson & J.J. Bommer (2009). Sigma: issues, insights, and challenges. *Seismological Research Letters* **80**(1), 40-56.

Tokimatsu, K. & T. Sekiguchi (2006a). Effects of nonlinear dynamic soil properties on strong Motions at Ojiya K-Net and JMA Stations during 2004 Mid Niigata Prefecture Earthquake. *Proceedings of the 8th U.S. National Conference on Earthquake Engineering*, San Francisco, California, USA, April 18-22.

Tokimatsu, K & T. Sekiguchi (2006b). Effects of nonlinear properties of surface soils on strong ground motions recorded in Ojiya during 2004 mid Niigata Prefecture earthquake. *Soils and Foundations* **46**(6), 765-775.

Tokimatsu, K. & T. Sekiguchi (2007). Effects of Dynamic Properties of Peat on Strong Ground Motions during 2004 Mid Niigata Prefecture Earthquake. *4th International Conference on Earthquake Geotechnical Engineering* June 25-28, Paper No. 1531.

Toro, G. (1995). *Probabilistic models of site velocity profiles for generic and site-specific ground motion amplification studies*. Department of Nuclear Energy Brookhaven National Laboratory, Upton, New York.

Trifunac, M.D. & A.G. Brady (1975). A study on duration of earthquake ground motion. *Bulletin of the Seismological Society of America* **65**, 581-626.

Vanmarcke, E.H. & S.P. Lai, (1980). Strong-motion duration of earthquakes. *Bulletin of the Seismological Society of America* **70**, 1293- 1307.

Villani, M. & N.A. Abrahamson (2015). Repeatable path and site effects on the ground-motion sigma based on empirical data from southern California and simulated waveforms from the CyberShake platform. *Bulletin of the Seismological Society of America* **105**(5), 2681-2695.

Wang, M. & T. Takada (2005). Macrospatial correlation model of seismic ground motions. *Earthquake Spectra* **21**(4), 1137-1156.

Wassing, B.B.T., D. Malers, R.S. Westerhoff, J.H.A. Bosch, & H.J.T. Weerts (2003). *Seismisch hazard van geïnduceerde aardbevingen - Rapportage fase 1*, TNO Geological Survey of the Netherlands report NITG-03-185-C-def, 77 pp.

Wehling, T.M., R.W. Boulanger, L.F. Harder & M.W. Driller (2001). *Dynamic Properties of Sherman Island Peat: Phase II Study*. Department of Civil & Environmental Engineering, College of Engineering, University of California at Davis. Report No. UCD/CGM-01/05, March 2001, 130 pp.

Wehling, T.M., R.W. Boulanger, R. Arulnathan, L.F. Harder, & M.W. Driller (2003). Nonlinear dynamic properties of a fibrous organic soil. *Journal of Geotechnical and Geoenvironmental Engineering* **129**(10), 929-939.

Wells, D. L. & K. J. Coppersmith (1994). New empirical relationships among magnitude, rupture length, rupture width, rupture area, and surface displacement. *Bulletin of the Seismological Society of America* **84**, 974-1002.

Yee, E., J.P. Stewart & K. Tokimatsu (2013). Elastic and large-strain nonlinear seismic site response from analysis of vertical array recordings*. Journal of Geotechnical and Geoenvironmental Engineering*, **139(10)**, 1789-1801.

Yenier, E. & G.M. Atkinson (2014). Equivalent point-source modeling of moderate-to-large magnitude earthquakes and associated ground-motion saturation effects. *Bulletin of the Seismological Society of America* **104**(3), 1458-1478.

Youngs, R.R. (2004). *Software validation report for SHAKE04*, Geomatrix Consultants, Oakland, California.

Zwanenburg, C. (2005). *The influence of anisotropy on the consolidation behaviour of peat*, Ph.D thesis Delft University of Technology, October 2005.

APPENDIX I

Kappa determinations for recording stations

The plots on the following pages show the application of the Anderson & Hough (1984) technique for the estimation of kappa, using the FAS beyond 10 Hz or 15 Hz depending on **M** (10 Hz for 2.5-2.7 and 15 Hz for ≥ 2.8; no fits were made for recordings from events smaller than M 2.5). The station and earthquake date are identified on each plot.

In each plot, the black line is the FAS of the signal, the red line the noise FAS, and the blue line the kappa model; the vertical dashed green lines represent the fitting limits.

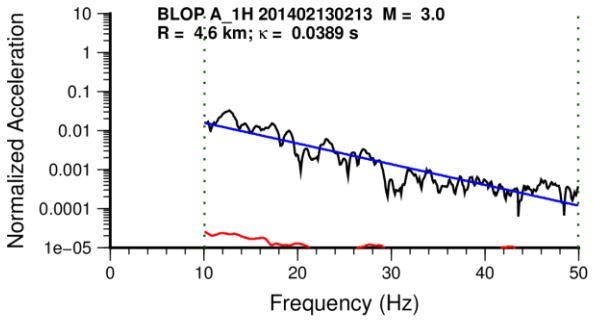
BLOP A_1H 201402130213 M = 3.0
R = 4.6 km; κ = 0.0389 s
Normalized Acceleration
Frequency (Hz)

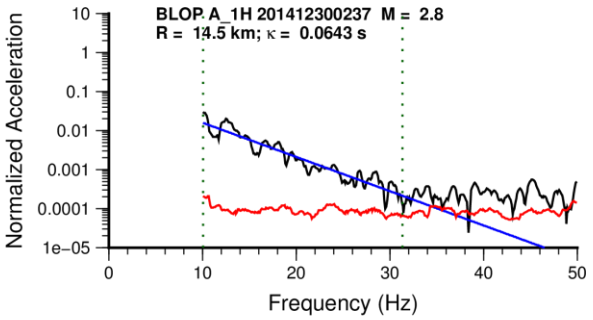
BLOP A_1H 201412300237 M = 2.8
R = 14.5 km; κ = 0.0643 s
Normalized Acceleration
Frequency (Hz)

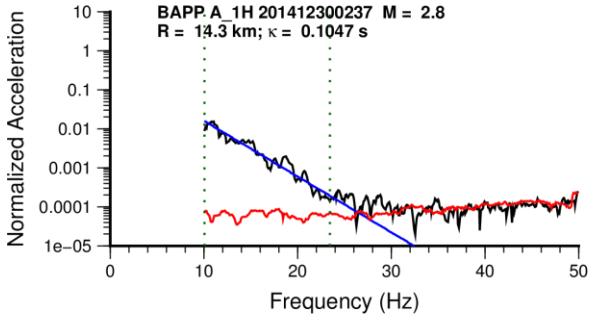
BAPP A_1H 201412300237 M = 2.8
R = 14.3 km; κ = 0.1047 s
Normalized Acceleration
Frequency (Hz)

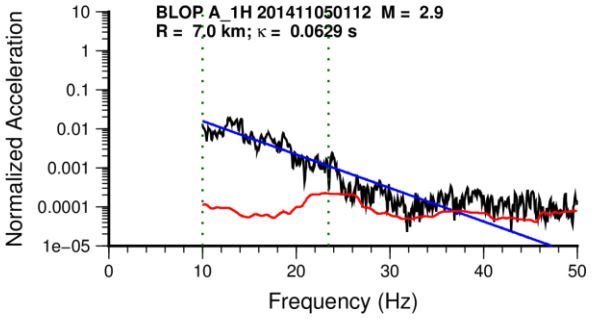
BLOP A_1H 201411050112 M = 2.9
R = 7.0 km; κ = 0.0629 s
Normalized Acceleration
Frequency (Hz)

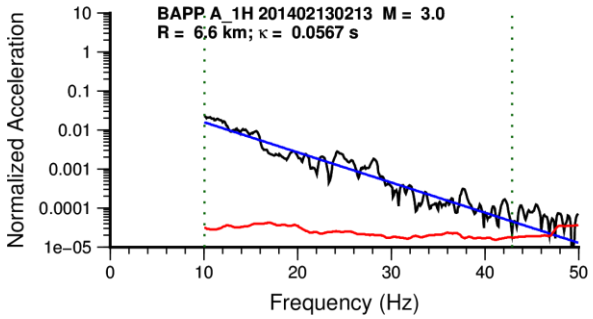
BAPP A_1H 201402130213 M = 3.0
R = 6.6 km; κ = 0.0567 s
Normalized Acceleration
Frequency (Hz)

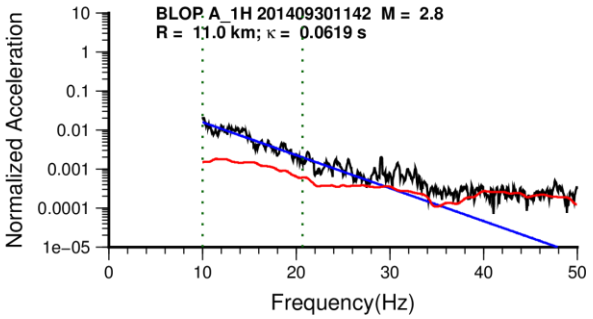
BLOP A_1H 201409301142 M = 2.8
R = 11.0 km; κ = 0.0619 s
Normalized Acceleration
Frequency(Hz)

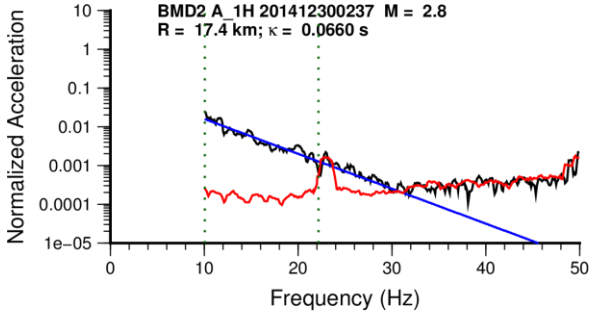
BMD2 A_1H 201412300237 M = 2.8
R = 17.4 km; κ = 0.0660 s
Normalized Acceleration
Frequency (Hz)

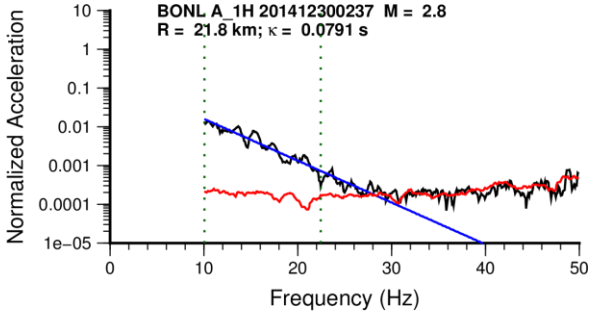
BONL A_1H 201412300237 M = 2.8
R = 21.8 km; κ = 0.0791 s
Normalized Acceleration
Frequency (Hz)

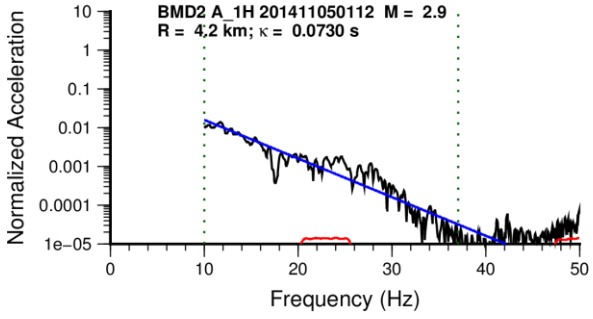
BMD2 A_1H 201411050112 M = 2.9
R = 4.2 km; κ = 0.0730 s
Normalized Acceleration
Frequency (Hz)

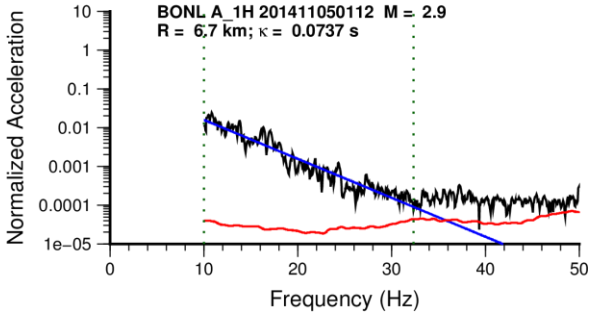
BONL A_1H 201411050112 M = 2.9
R = 6.7 km; κ = 0.0737 s
Normalized Acceleration
Frequency (Hz)

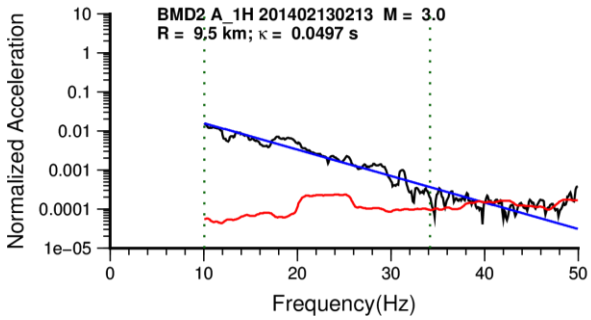
BMD2 A_1H 201402130213 M = 3.0
R = 9.5 km; κ = 0.0497 s
Normalized Acceleration
Frequency(Hz)

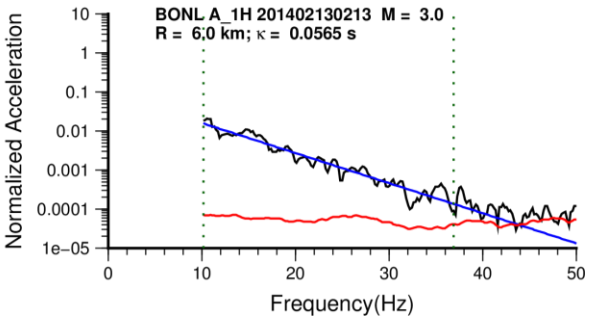
BONL A_1H 201402130213 M = 3.0
R = 6.0 km; κ = 0.0565 s
Normalized Acceleration
Frequency(Hz)

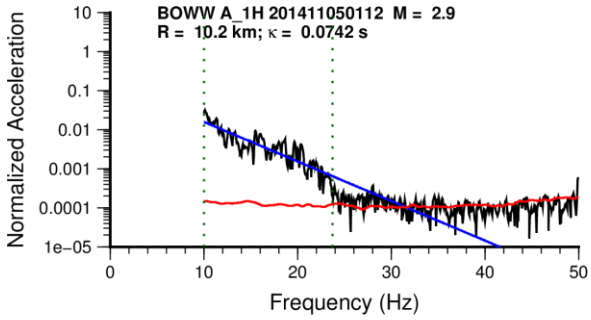
BOWW A_1H 201411050112 M = 2.9
R = 10.2 km; κ = 0.0742 s
Normalized Acceleration
Frequency (Hz)

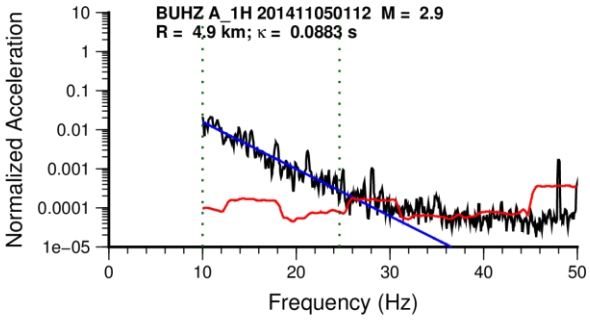
BUHZ A_1H 201411050112 M = 2.9
R = 4.9 km; κ = 0.0883 s
Normalized Acceleration
Frequency (Hz)

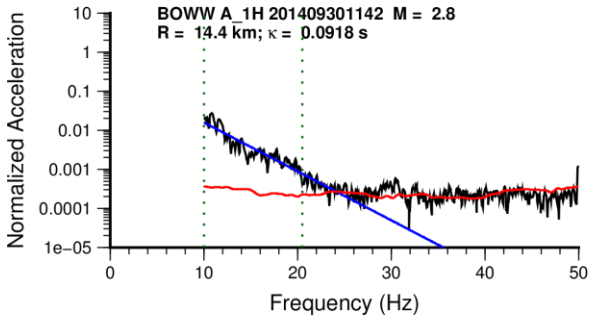
BOWW A_1H 201409301142 M = 2.8
R = 14.4 km; κ = 0.0918 s
Normalized Acceleration
Frequency (Hz)

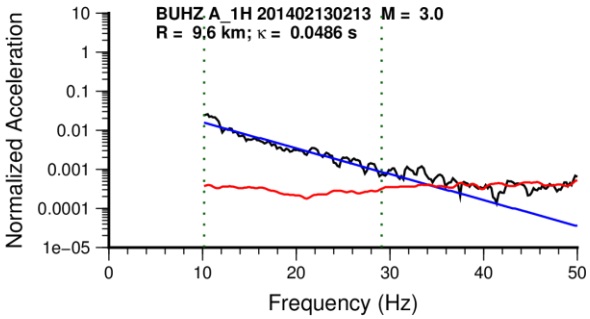
BUHZ A_1H 201402130213 M = 3.0
R = 9.6 km; κ = 0.0486 s
Normalized Acceleration
Frequency (Hz)

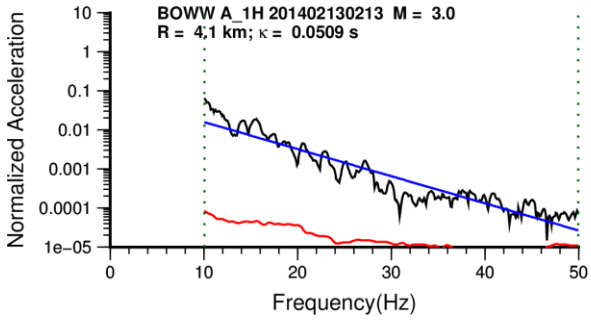
BOWW A_1H 201402130213 M = 3.0
R = 4.1 km; κ = 0.0509 s
Normalized Acceleration
Frequency(Hz)

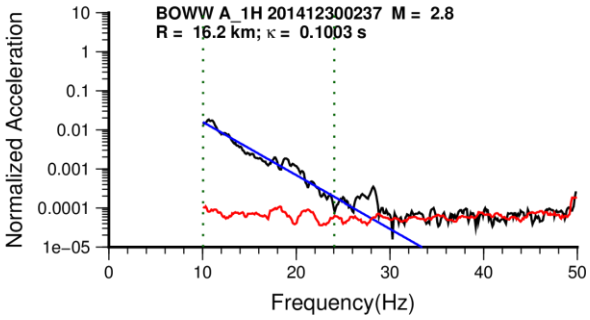
BOWW A_1H 201412300237 M = 2.8
R = 16.2 km; κ = 0.1003 s
Normalized Acceleration
Frequency(Hz)

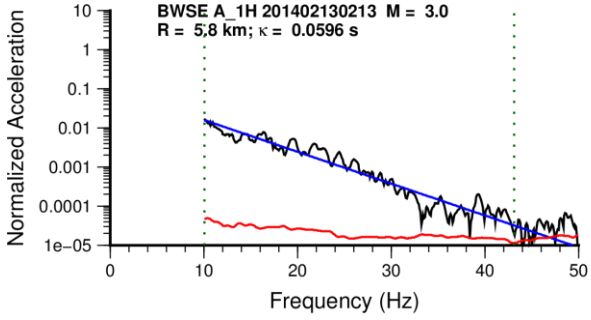
BWSE A_1H 201402130213 M = 3.0
R = 5.8 km; κ = 0.0596 s
Normalized Acceleration
Frequency (Hz)

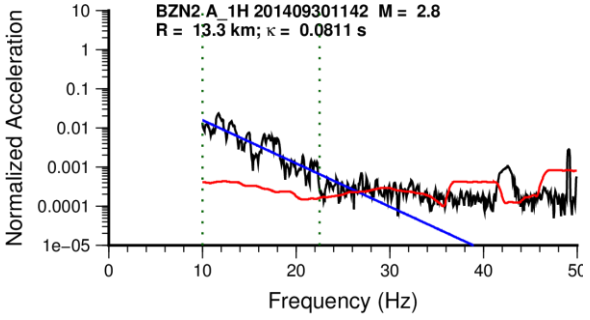
BZN2 A_1H 201409301142 M = 2.8
R = 13.3 km; κ = 0.0811 s
Normalized Acceleration
Frequency (Hz)

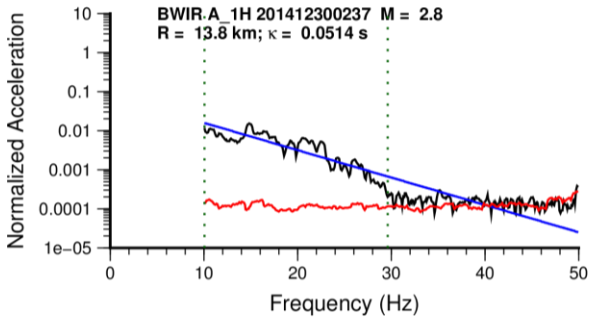
BWIR.A_1H 201412300237 M = 2.8
R = 13.8 km; κ = 0.0514 s
Normalized Acceleration
Frequency (Hz)

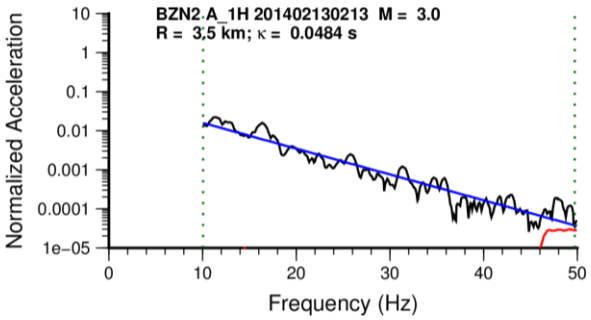
BZN2.A_1H 201402130213 M = 3.0
R = 3.5 km; κ = 0.0484 s
Normalized Acceleration
Frequency (Hz)

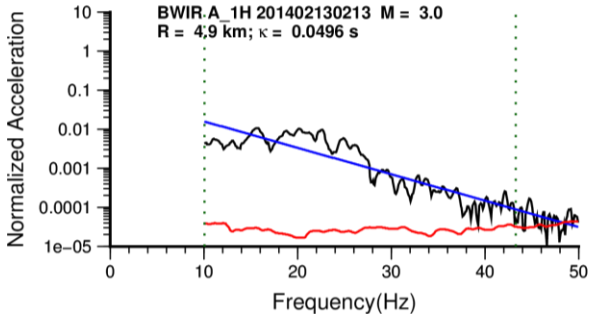
BWIR.A_1H 201402130213 M = 3.0
R = 4.9 km; κ = 0.0496 s
Normalized Acceleration
Frequency(Hz)

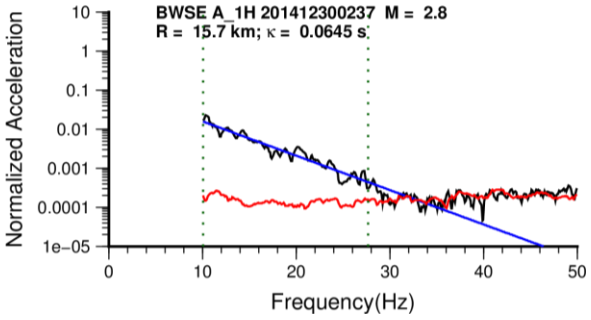
BWSE.A_1H 201412300237 M = 2.8
R = 15.7 km; κ = 0.0645 s
Normalized Acceleration
Frequency(Hz)

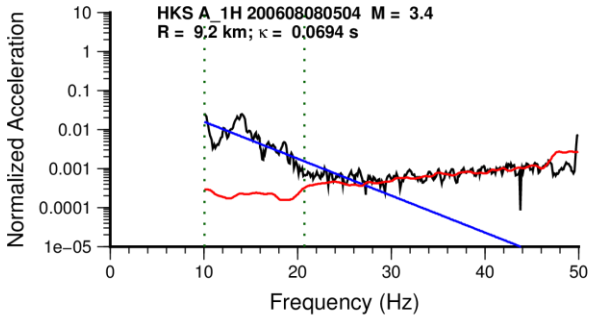
HKS.A_1H 200608080504 M = 3.4
R = 9.2 km; κ = 0.0694 s
Normalized Acceleration
Frequency (Hz)

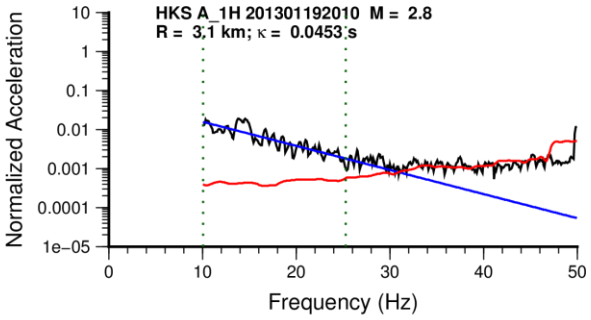
HKS.A_1H 201301192010 M = 2.8
R = 3.1 km; κ = 0.0453 s
Normalized Acceleration
Frequency (Hz)

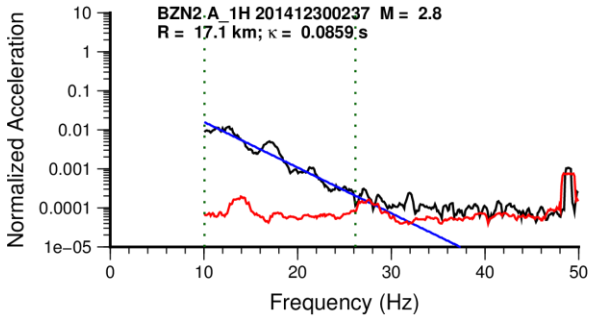
BZN2.A_1H 201412300237 M = 2.8
R = 17.1 km; κ = 0.0859 s
Normalized Acceleration
Frequency (Hz)

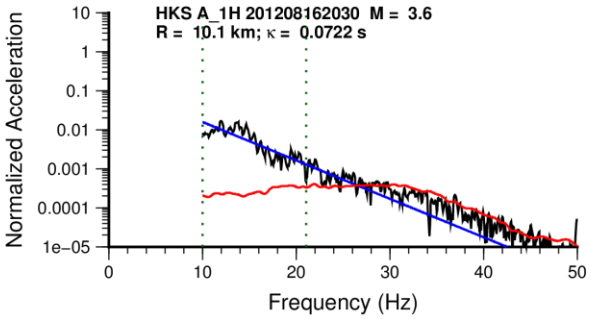
HKS.A_1H 201208162030 M = 3.6
R = 10.1 km; κ = 0.0722 s
Normalized Acceleration
Frequency (Hz)

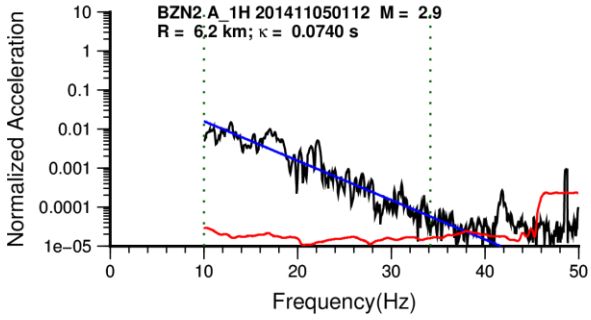
BZN2.A_1H 201411050112 M = 2.9
R = 6.2 km; κ = 0.0740 s
Normalized Acceleration
Frequency(Hz)

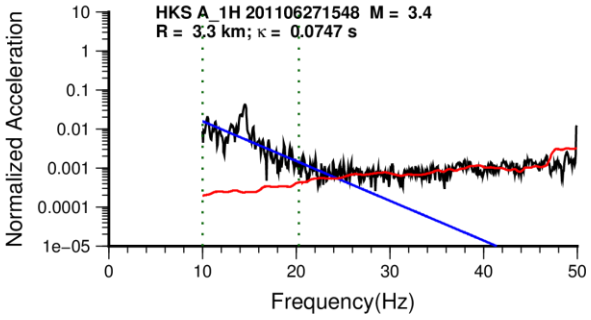
HKS.A_1H 201106271548 M = 3.4
R = 3.3 km; κ = 0.0747 s
Normalized Acceleration
Frequency(Hz)

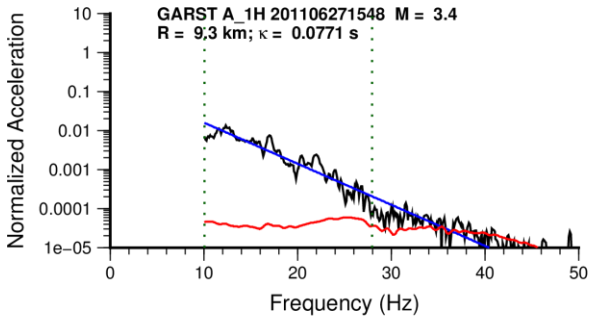
GARST A_1H 201106271548 M = 3.4
R = 9.3 km; κ = 0.0771 s
Normalized Acceleration
Frequency (Hz)

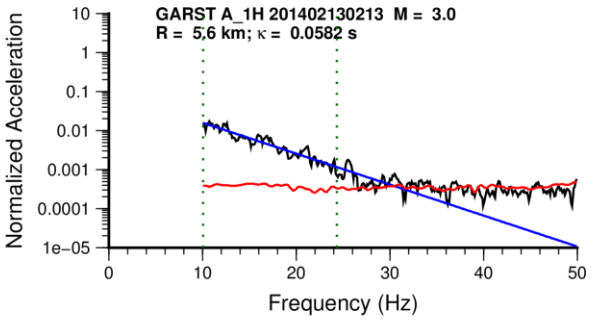
GARST A_1H 201402130213 M = 3.0
R = 5.6 km; κ = 0.0582 s
Normalized Acceleration
Frequency (Hz)

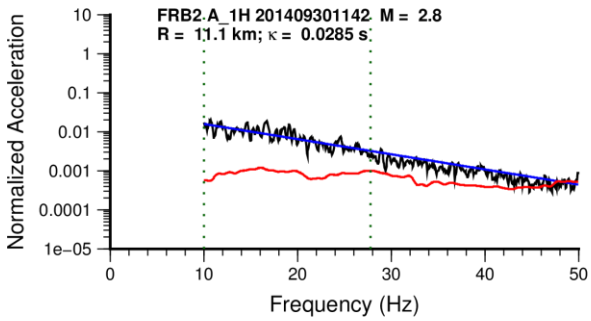
FRB2 A_1H 201409301142 M = 2.8
R = 11.1 km; κ = 0.0285 s
Normalized Acceleration
Frequency (Hz)

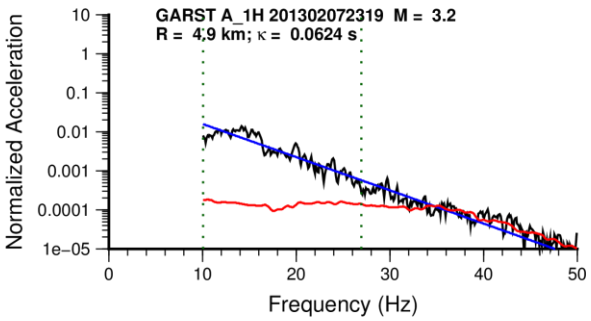
GARST A_1H 201302072319 M = 3.2
R = 4.9 km; κ = 0.0624 s
Normalized Acceleration
Frequency (Hz)

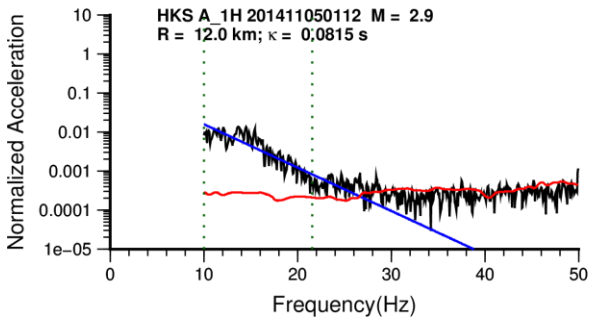
HKS A_1H 201411050112 M = 2.9
R = 12.0 km; κ = 0.0815 s
Normalized Acceleration
Frequency(Hz)

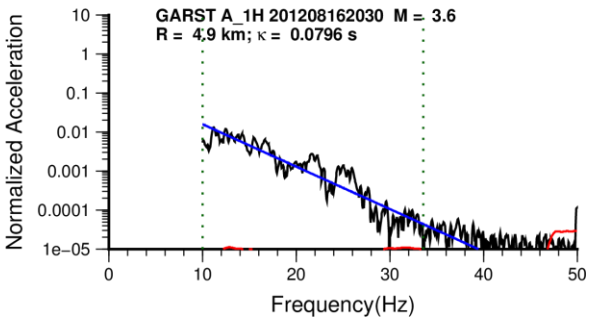
GARST A_1H 201208162030 M = 3.6
R = 4.9 km; κ = 0.0796 s
Normalized Acceleration
Frequency(Hz)

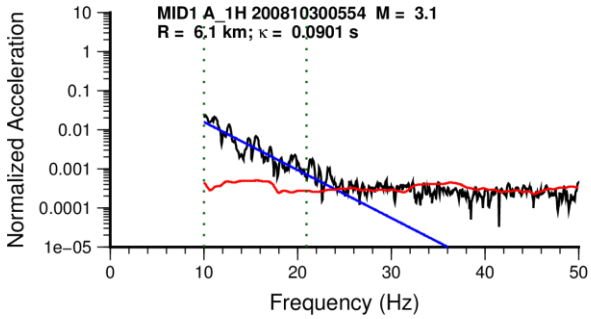
MID1 A_1H 200810300554 M = 3.1
R = 6.1 km; κ = 0.0901 s
Normalized Acceleration
Frequency (Hz)

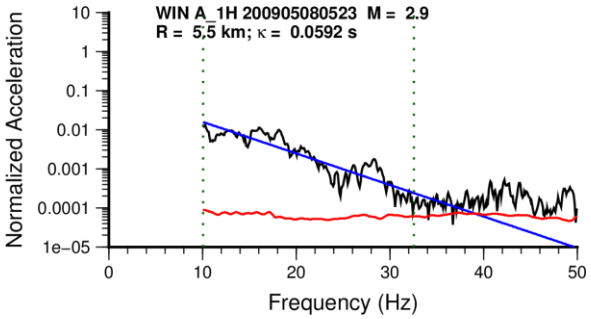
WIN A_1H 200905080523 M = 2.9
R = 5.5 km; κ = 0.0592 s
Normalized Acceleration
Frequency (Hz)

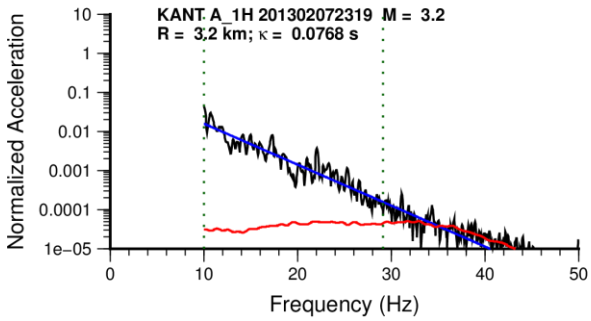
KANT A_1H 201302072319 M = 3.2
R = 3.2 km; κ = 0.0768 s
Normalized Acceleration
Frequency (Hz)

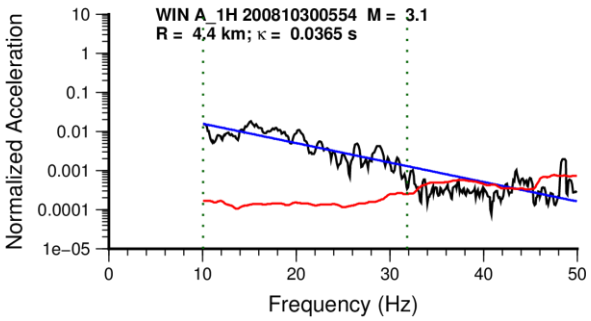
WIN A_1H 200810300554 M = 3.1
R = 4.4 km; κ = 0.0365 s
Normalized Acceleration
Frequency (Hz)

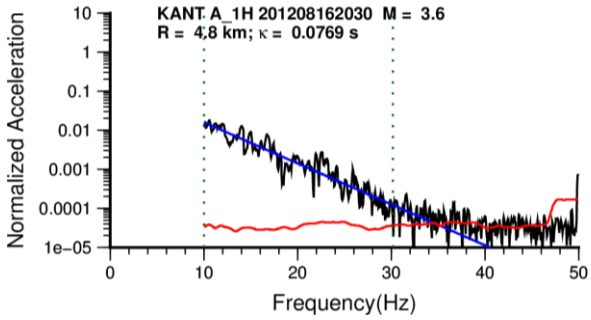
KANT A_1H 201208162030 M = 3.6
R = 4.8 km; κ = 0.0769 s
Normalized Acceleration
Frequency(Hz)

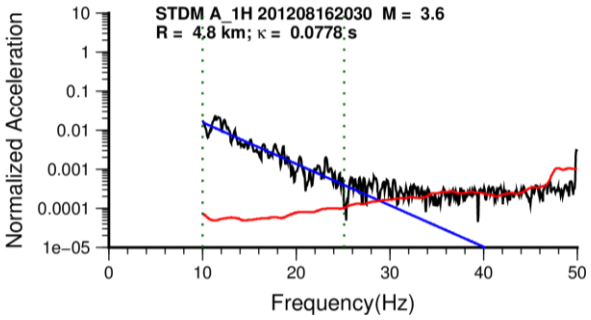
STDM A_1H 201208162030 M = 3.6
R = 4.8 km; κ = 0.0778 s
Normalized Acceleration
Frequency(Hz)

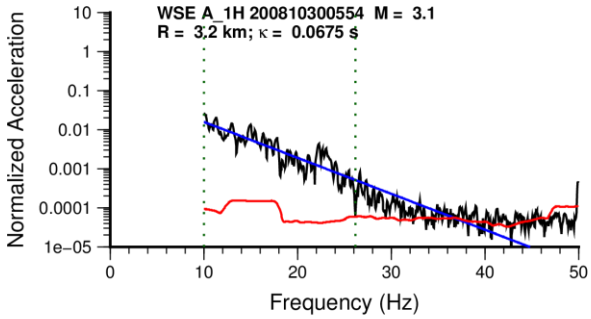
WSE A_1H 200810300554 M = 3.1
R = 3.2 km; κ = 0.0675 s
Normalized Acceleration
Frequency (Hz)

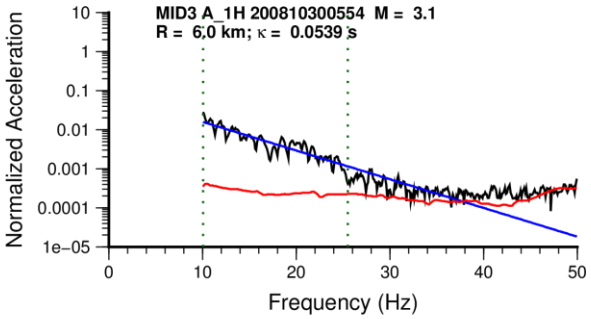
MID3 A_1H 200810300554 M = 3.1
R = 6.0 km; κ = 0.0539 s
Normalized Acceleration
Frequency (Hz)

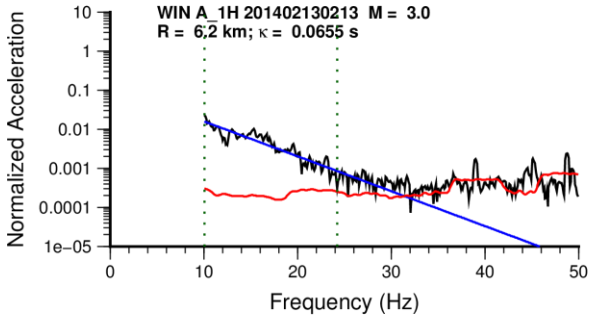
WIN A_1H 201402130213 M = 3.0
R = 6.2 km; κ = 0.0655 s
Normalized Acceleration
Frequency (Hz)

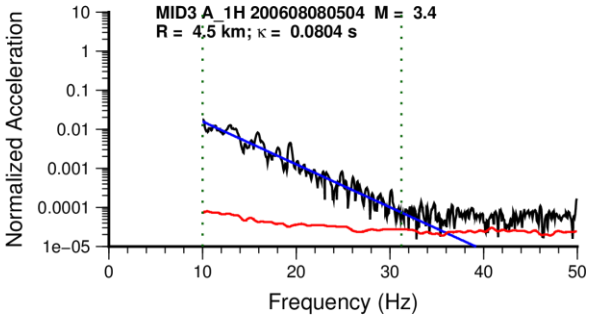
MID3 A_1H 200608080504 M = 3.4
R = 4.5 km; κ = 0.0804 s
Normalized Acceleration
Frequency (Hz)

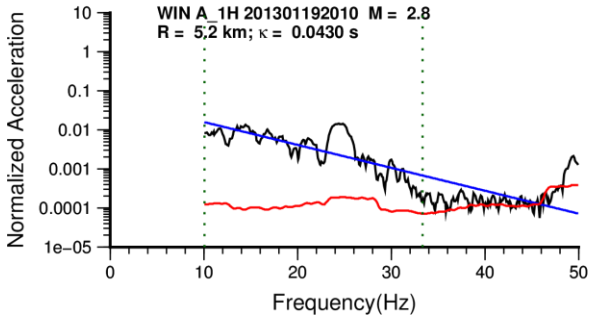
WIN A_1H 201301192010 M = 2.8
R = 5.2 km; κ = 0.0430 s
Normalized Acceleration
Frequency(Hz)

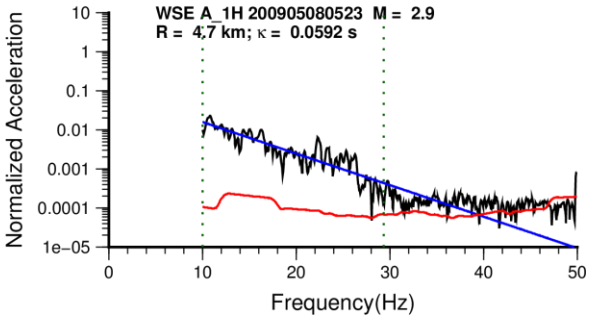
WSE A_1H 200905080523 M = 2.9
R = 4.7 km; κ = 0.0592 s
Normalized Acceleration
Frequency(Hz)

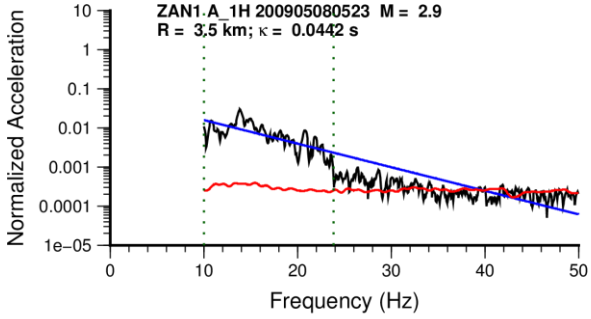
ZAN1 A_1H 200905080523 M = 2.9
R = 3.5 km; κ = 0.0442 s
Normalized Acceleration
Frequency (Hz)

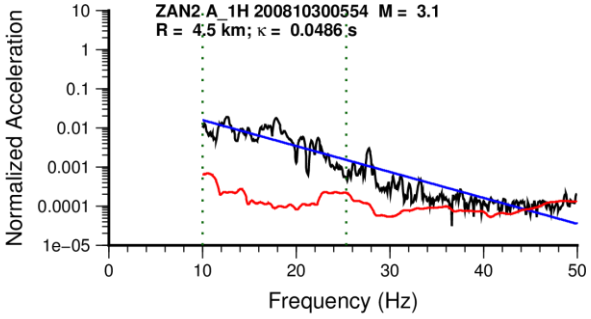
ZAN2 A_1H 200810300554 M = 3.1
R = 4.5 km; κ = 0.0486 s
Normalized Acceleration
Frequency (Hz)

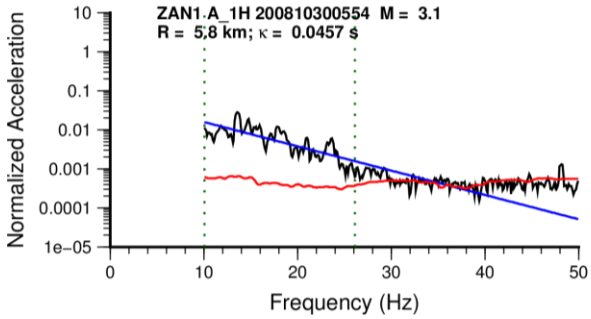
ZAN1.A_1H 200810300554 M = 3.1
R = 5.8 km; κ = 0.0457 s
Normalized Acceleration
Frequency (Hz)

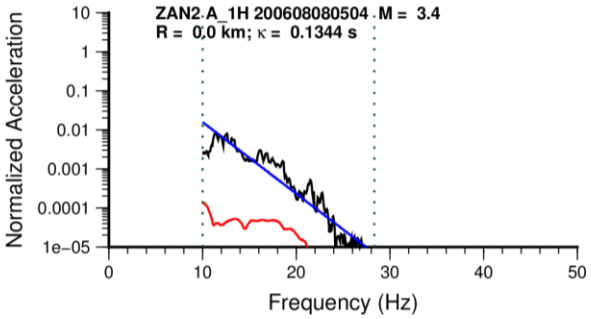
ZAN2.A_1H 200608080504 M = 3.4
R = 0.0 km; κ = 0.1344 s
Normalized Acceleration
Frequency (Hz)

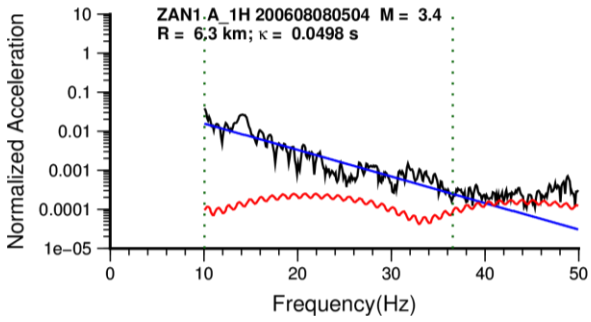
ZAN1.A_1H 200608080504 M = 3.4
R = 6.3 km; κ = 0.0498 s
Normalized Acceleration
Frequency(Hz)

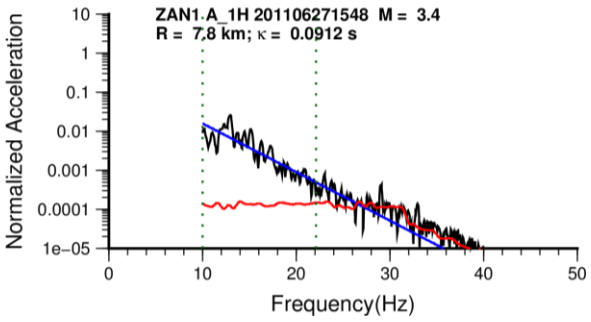
ZAN1.A_1H 201106271548 M = 3.4
R = 7.8 km; κ = 0.0912 s
Normalized Acceleration
Frequency(Hz)

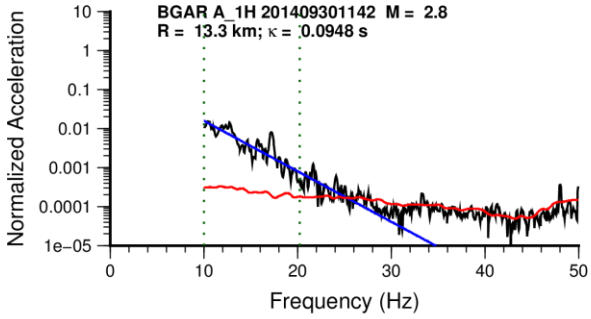
BGAR A_1H 201409301142 M = 2.8
R = 13.3 km; κ = 0.0948 s
Normalized Acceleration
Frequency (Hz)

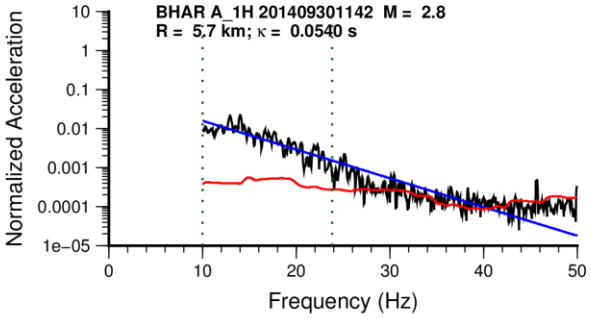
BHAR A_1H 201409301142 M = 2.8
R = 5.7 km; κ = 0.0540 s
Normalized Acceleration
Frequency (Hz)

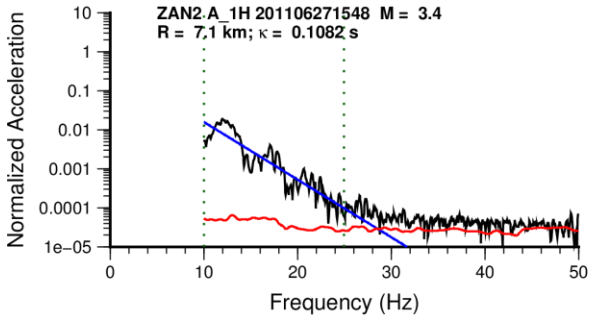
ZAN2.A_1H 201106271548 M = 3.4
R = 7.1 km; κ = 0.1082 s
Normalized Acceleration
Frequency (Hz)

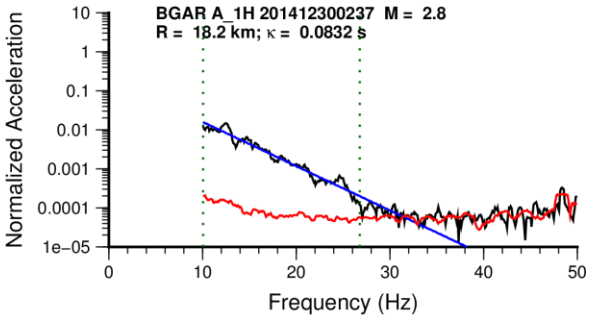
BGAR A_1H 201412300237 M = 2.8
R = 18.2 km; κ = 0.0832 s
Normalized Acceleration
Frequency (Hz)

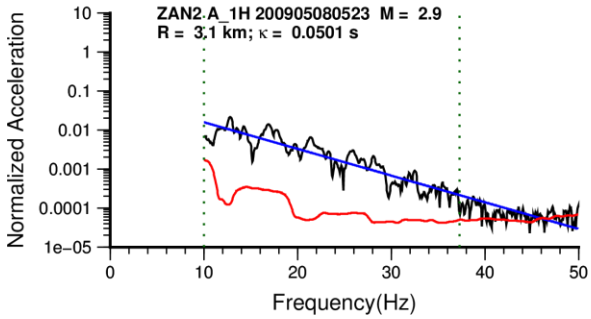
ZAN2.A_1H 200905080523 M = 2.9
R = 3.1 km; κ = 0.0501 s
Normalized Acceleration
Frequency(Hz)

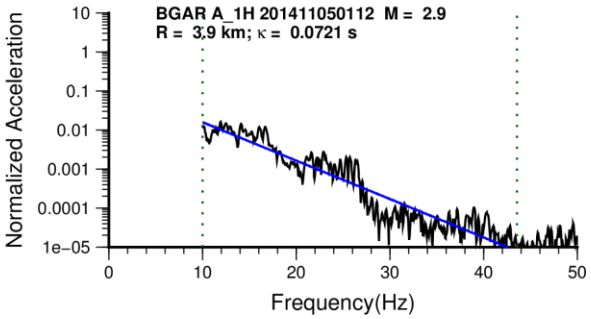
BGAR A_1H 201411050112 M = 2.9
R = 3.9 km; κ = 0.0721 s
Normalized Acceleration
Frequency(Hz)

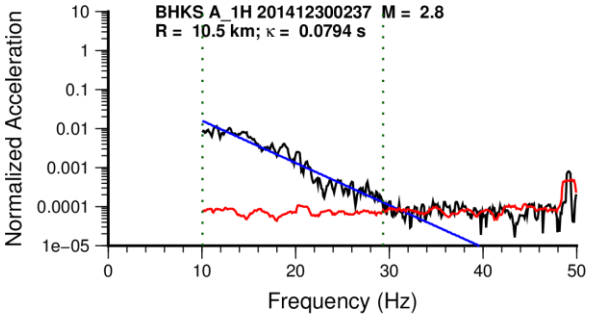
BHKS A_1H 201412300237 M = 2.8
R = 10.5 km; κ = 0.0794 s
Normalized Acceleration
Frequency (Hz)

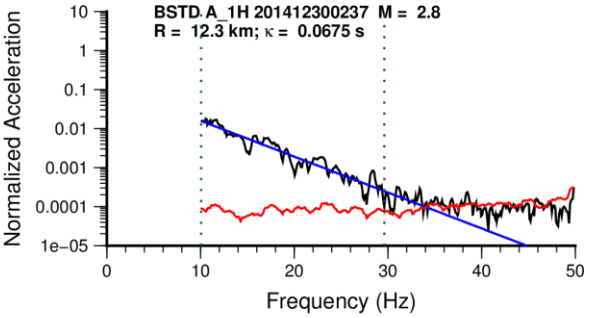
BSTD A_1H 201412300237 M = 2.8
R = 12.3 km; κ = 0.0675 s
Normalized Acceleration
Frequency (Hz)

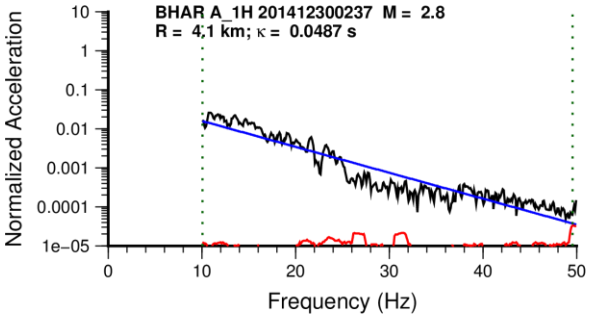
BHAR A_1H 201412300237 M = 2.8
R = 4.1 km; κ = 0.0487 s
Normalized Acceleration
Frequency (Hz)

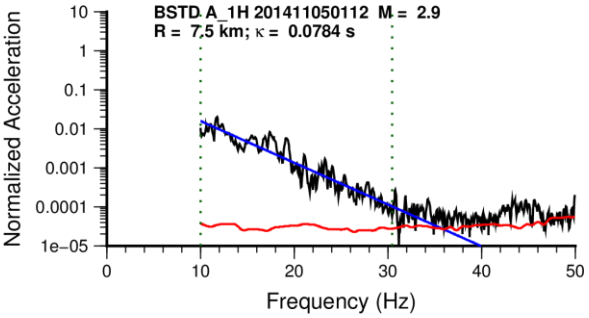
BSTD A_1H 201411050112 M = 2.9
R = 7.5 km; κ = 0.0784 s
Normalized Acceleration
Frequency (Hz)

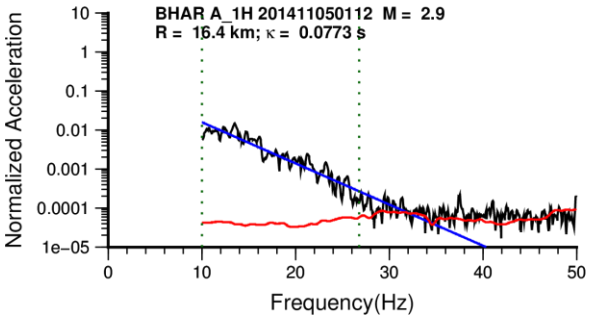
BHAR A_1H 201411050112 M = 2.9
R = 16.4 km; κ = 0.0773 s
Normalized Acceleration
Frequency(Hz)

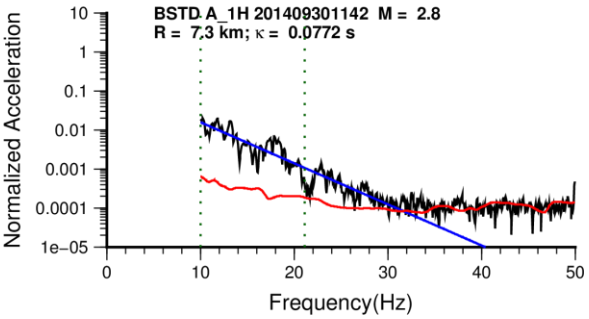
BSTD A_1H 201409301142 M = 2.8
R = 7.3 km; κ = 0.0772 s
Normalized Acceleration
Frequency(Hz)

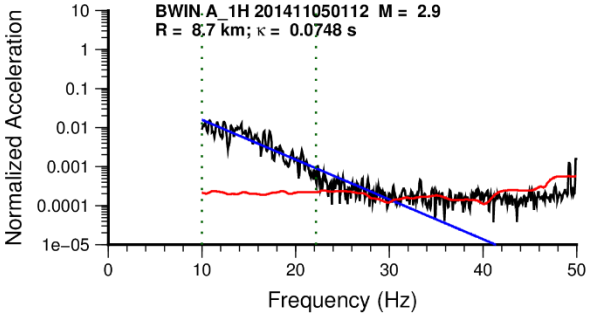
BWIN A_1H 201411050112 M = 2.9
R = 8.7 km; κ = 0.0748 s
Normalized Acceleration
Frequency (Hz)

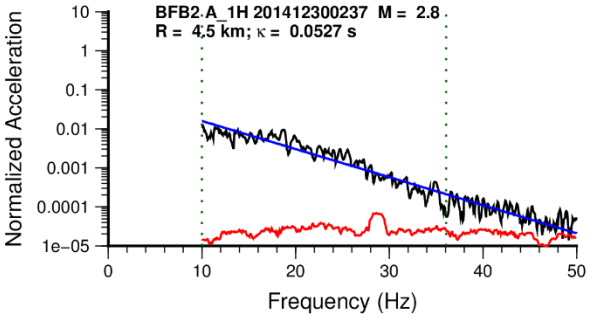
BFB2 A_1H 201412300237 M = 2.8
R = 4.5 km; κ = 0.0527 s
Normalized Acceleration
Frequency (Hz)

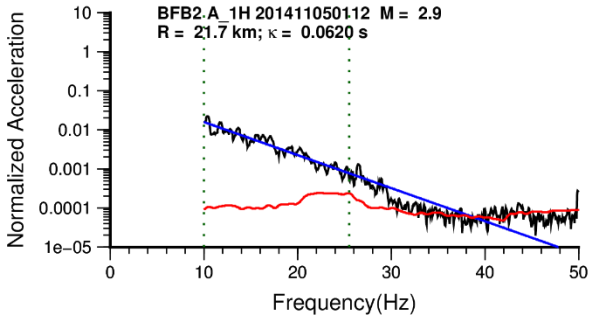
BFB2 A_1H 201411050112 M = 2.9
R = 21.7 km; κ = 0.0620 s
Normalized Acceleration
Frequency(Hz)

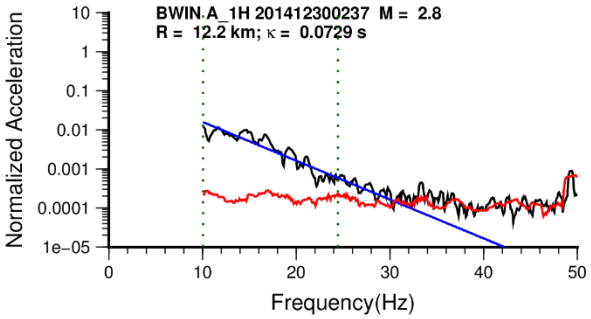
BWIN A_1H 201412300237 M = 2.8
R = 12.2 km; κ = 0.0729 s
Normalized Acceleration
Frequency(Hz)

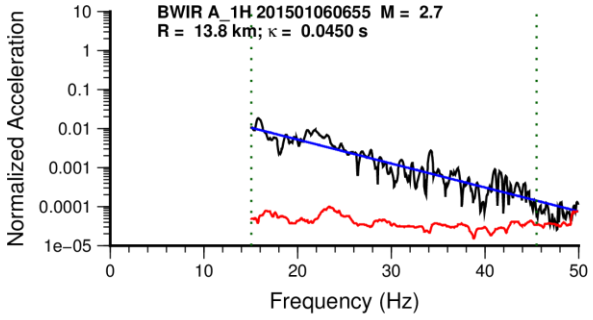
BWIR A_1H 201501060655 M = 2.7
R = 13.8 km; κ = 0.0450 s
Normalized Acceleration
Frequency (Hz)

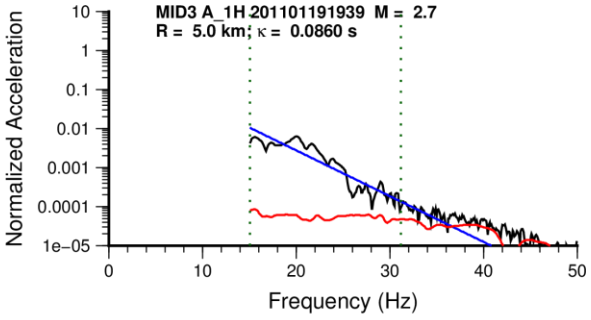
MID3 A_1H 201101191939 M = 2.7
R = 5.0 km; κ = 0.0860 s
Normalized Acceleration
Frequency (Hz)

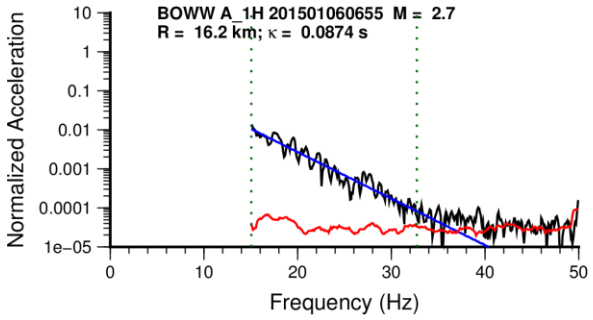
BOWW A_1H 201501060655 M = 2.7
R = 16.2 km; κ = 0.0874 s
Normalized Acceleration
Frequency (Hz)

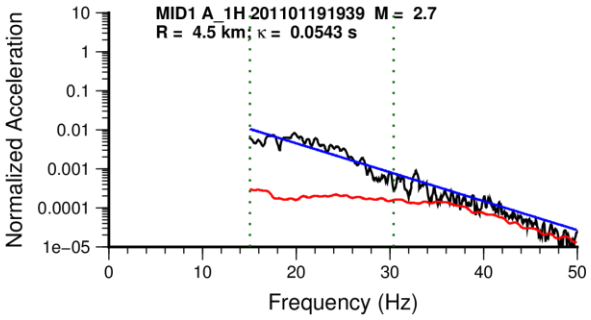
MID1 A_1H 201101191939 M = 2.7
R = 4.5 km; κ = 0.0543 s
Normalized Acceleration
Frequency (Hz)

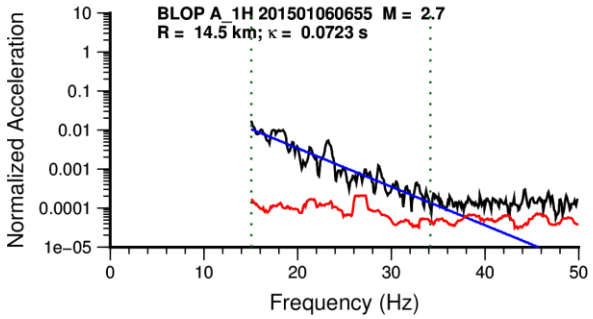
BLOP A_1H 201501060655 M = 2.7
R = 14.5 km; κ = 0.0723 s
Normalized Acceleration
Frequency (Hz)

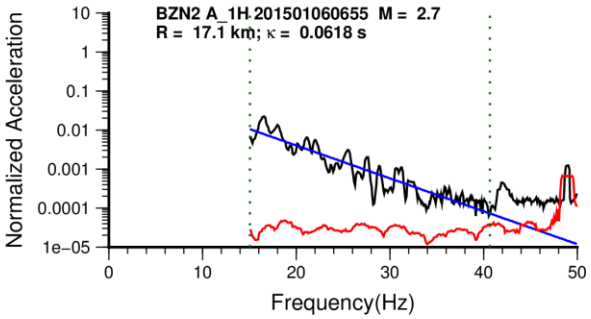
BZN2 A_1H 201501060655 M = 2.7
R = 17.1 km; κ = 0.0618 s
Normalized Acceleration
Frequency(Hz)

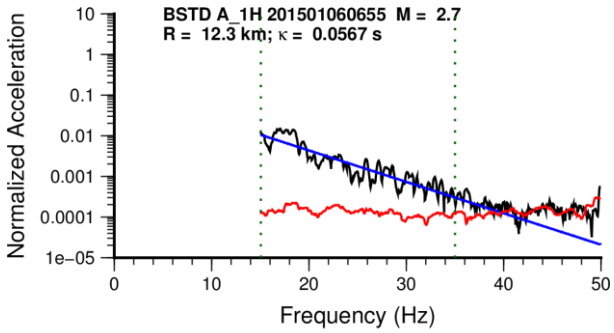
BSTD A_1H 201501060655 M = 2.7
R = 12.3 km; κ = 0.0567 s
Normalized Acceleration
Frequency (Hz)

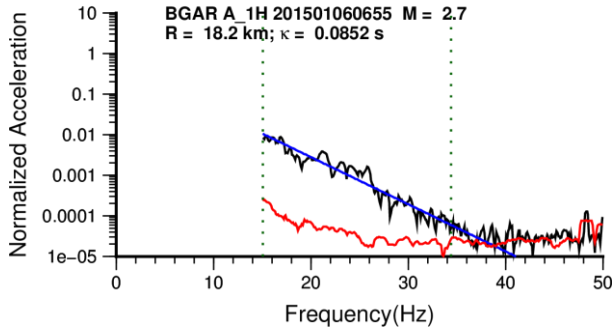
BGAR A_1H 201501060655 M = 2.7
R = 18.2 km; κ = 0.0852 s
Normalized Acceleration
Frequency(Hz)

APPENDIX II

Station V_S, density and damping profiles

In the following pages, plots are shown for profiles of VS, unit weight and damping for each of the recording stations, as generated from the field-wide velocity model and the Deltares look-up tables. For each station, the full profile down to the NU_B horizon is shown, together with an additional plot of the top 50 m in order to provide images with greater resolution for the uppermost part of the profile that is likely to have the largest influence on the site response characteristics.

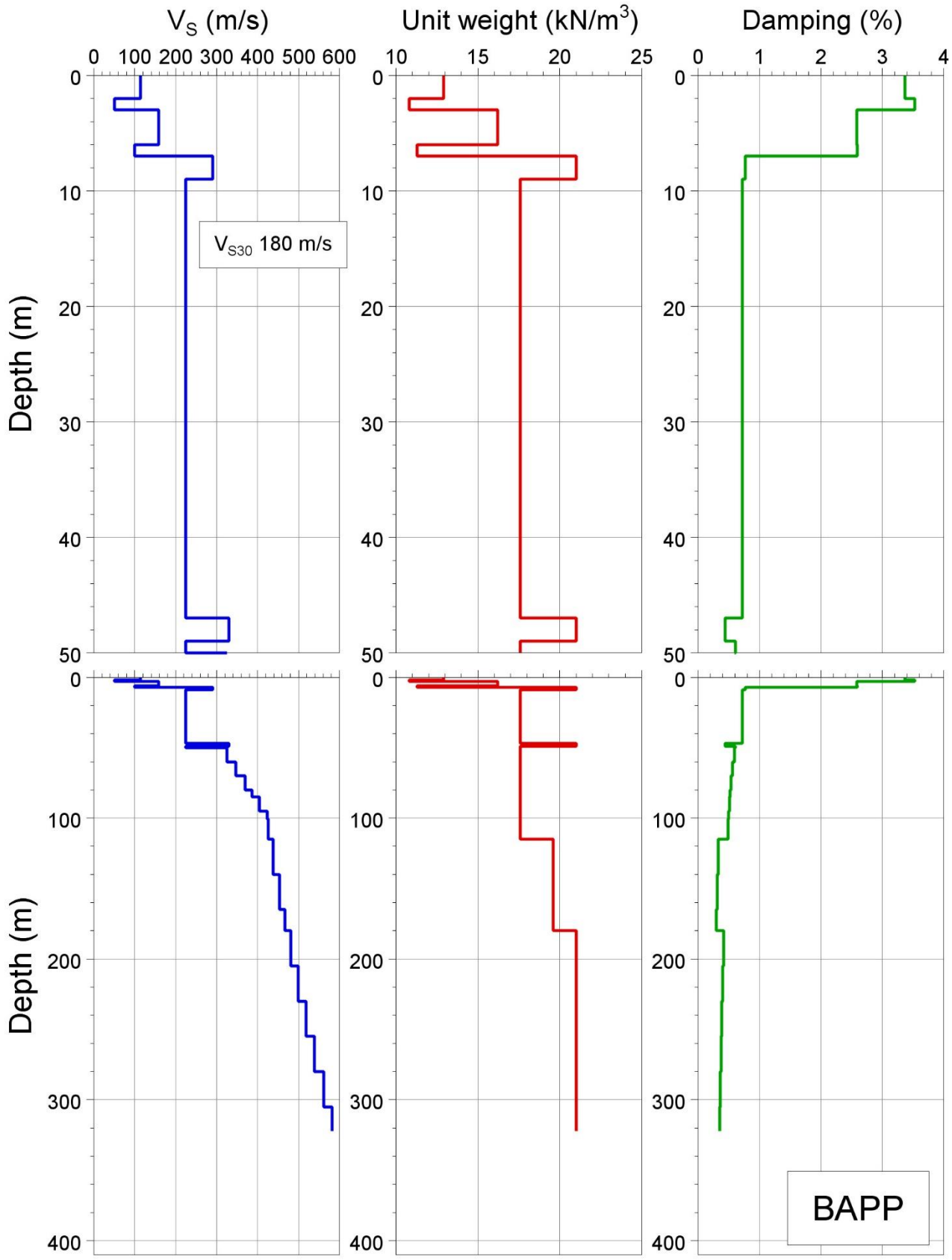
V_S (m/s)
Unit weight (kN/m^3)
Damping (%)
V_{S30} 180 m/s
Depth (m)
BAPP

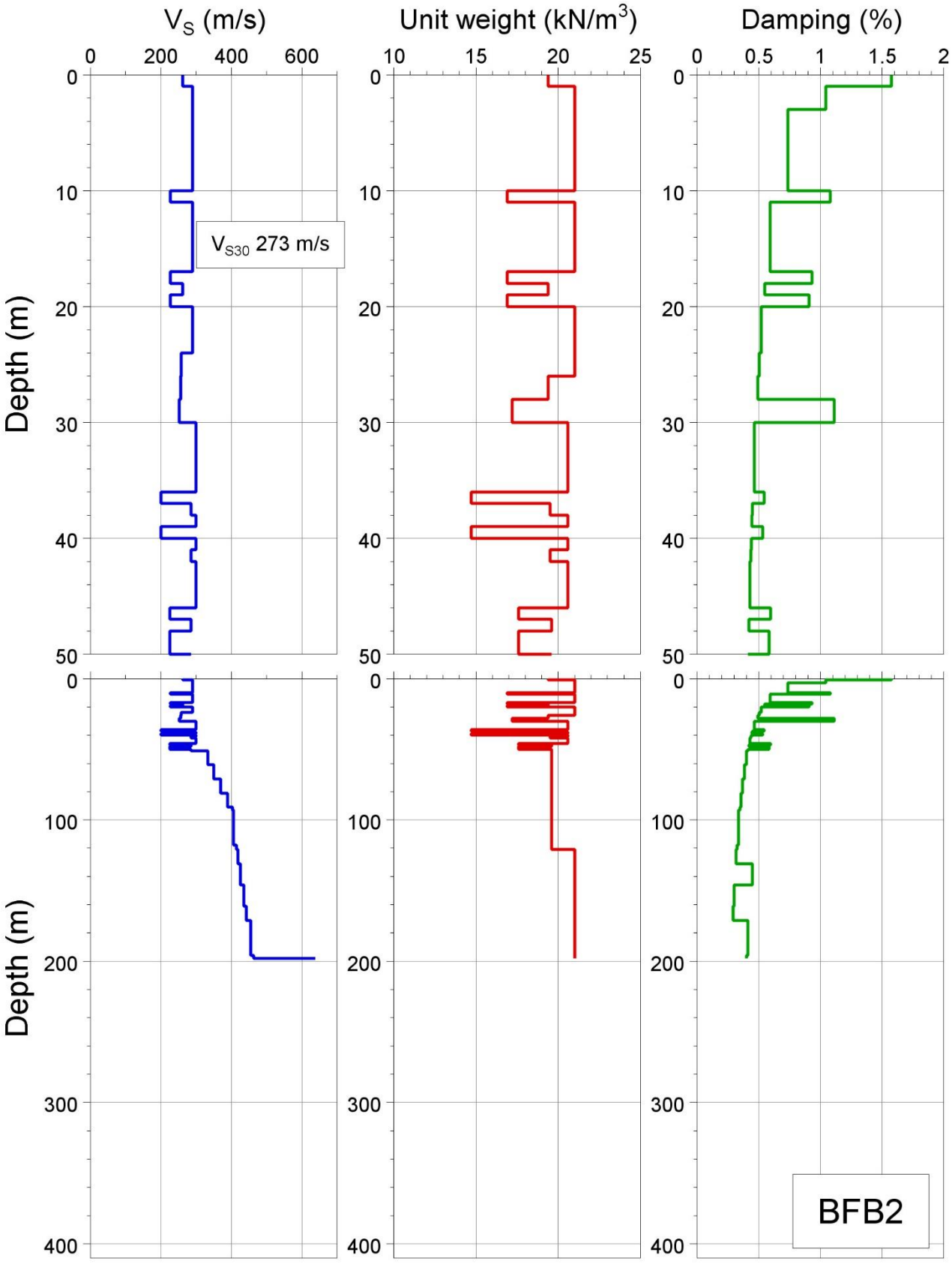
V_S (m/s)
Unit weight (kN/m^3)
Damping (%)
V_{S30} 273 m/s
Depth (m)
Depth (m)
BFB2

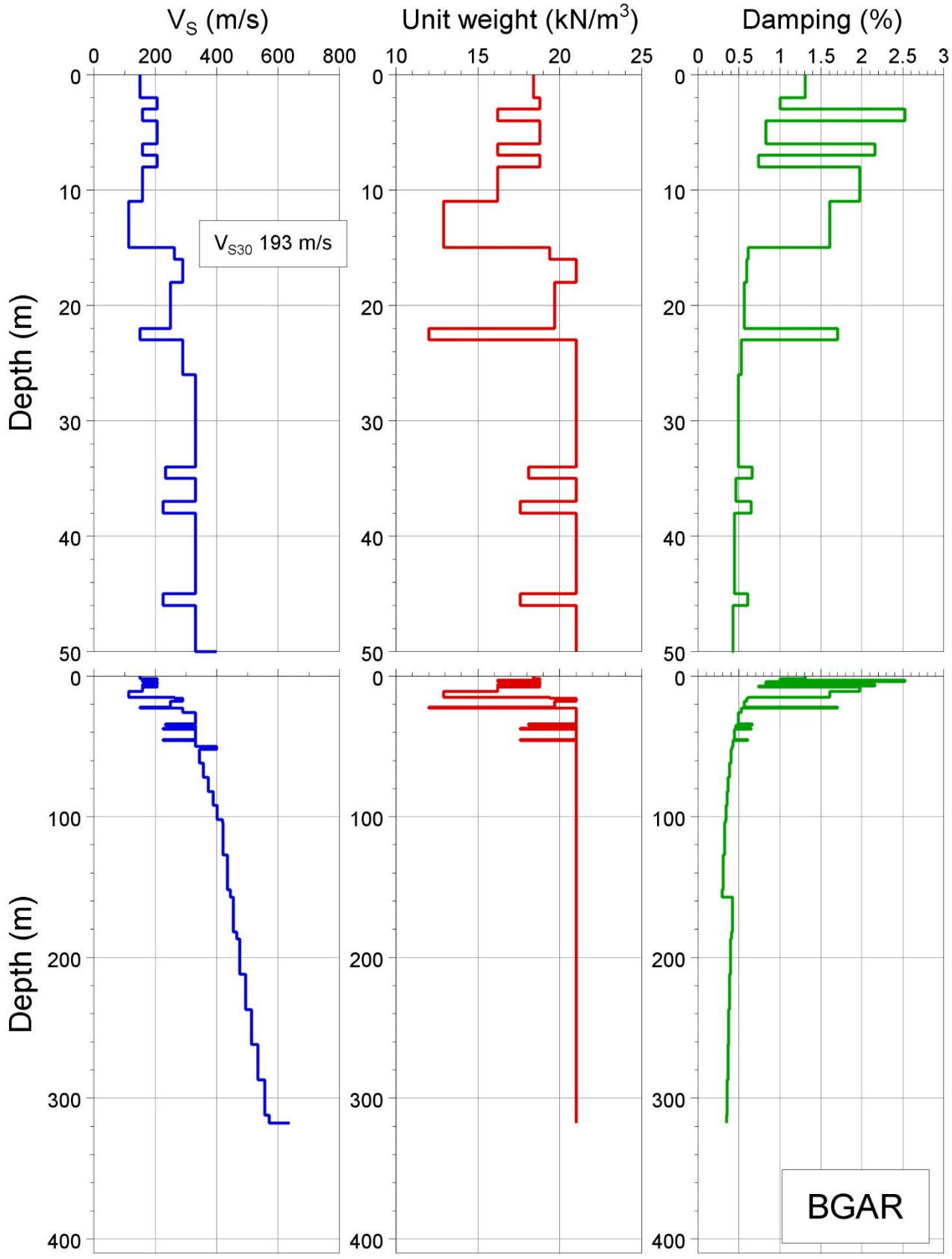
V_S (m/s)
Unit weight (kN/m^3)
Damping (%)
0 200 400 600 800
10 15 20 25
0 0.5 1 1.5 2 2.5 3
Depth (m)
V_{S30} 193 m/s
0 10 20 30 40 50
0 100 200 300 400
BGAR

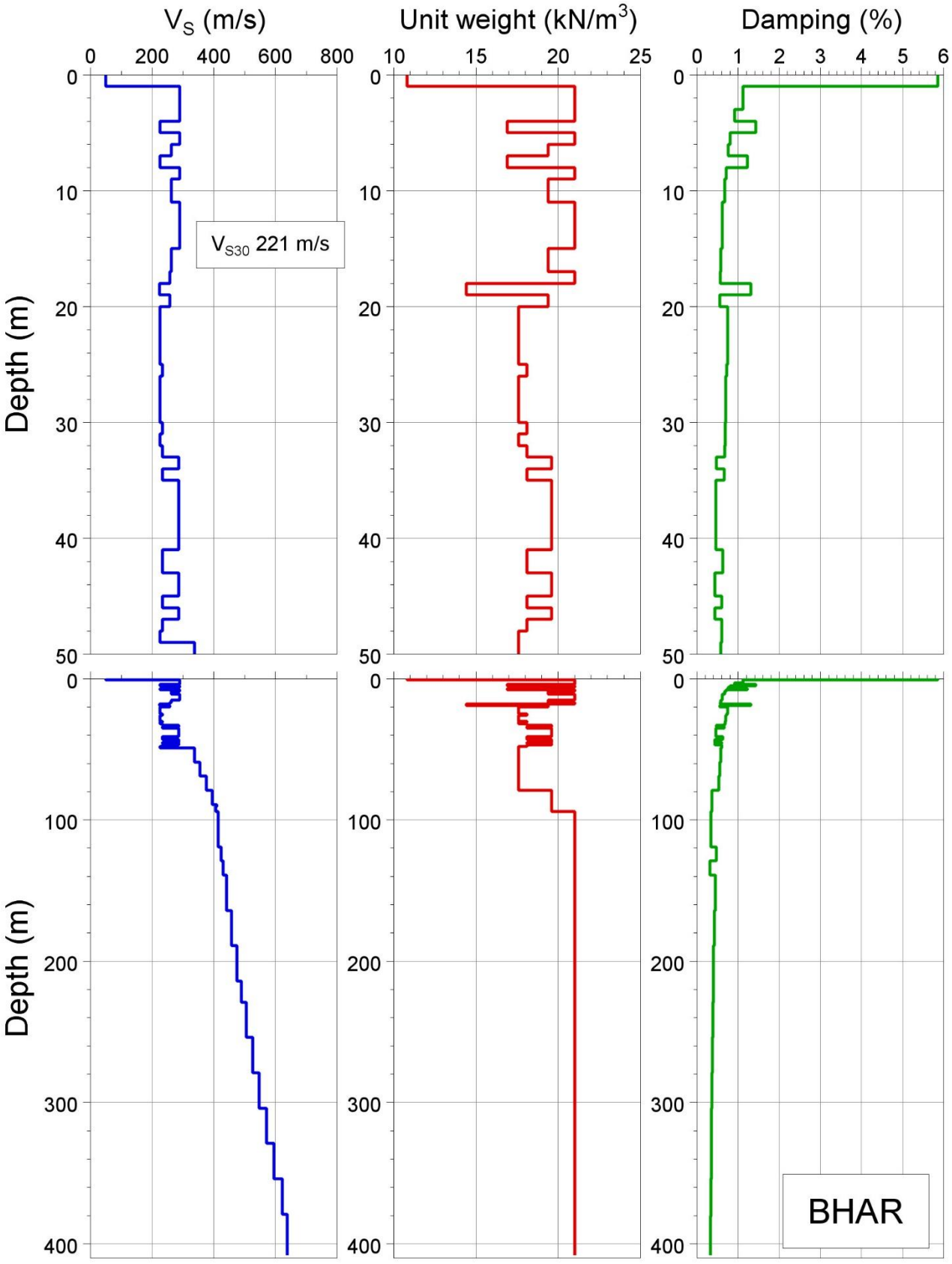
V_S (m/s)
Unit weight (kN/m^3)
Damping (%)
V_{S30} 221 m/s
Depth (m)
Depth (m)
BHAR

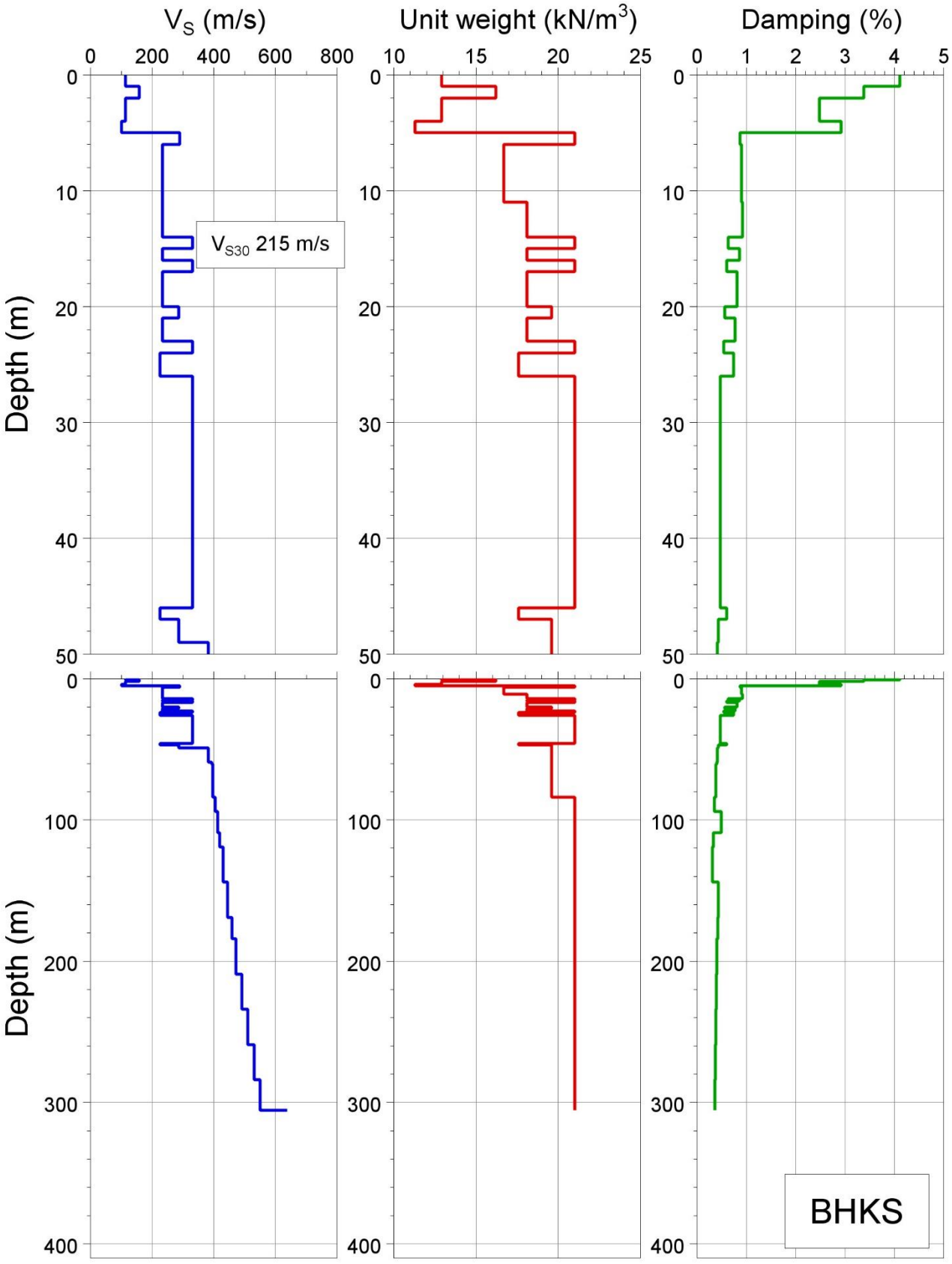
V_S (m/s)
Unit weight (kN/m^3)
Damping (%)
V_{S30} 215 m/s
Depth (m)
Depth (m)
BHKS

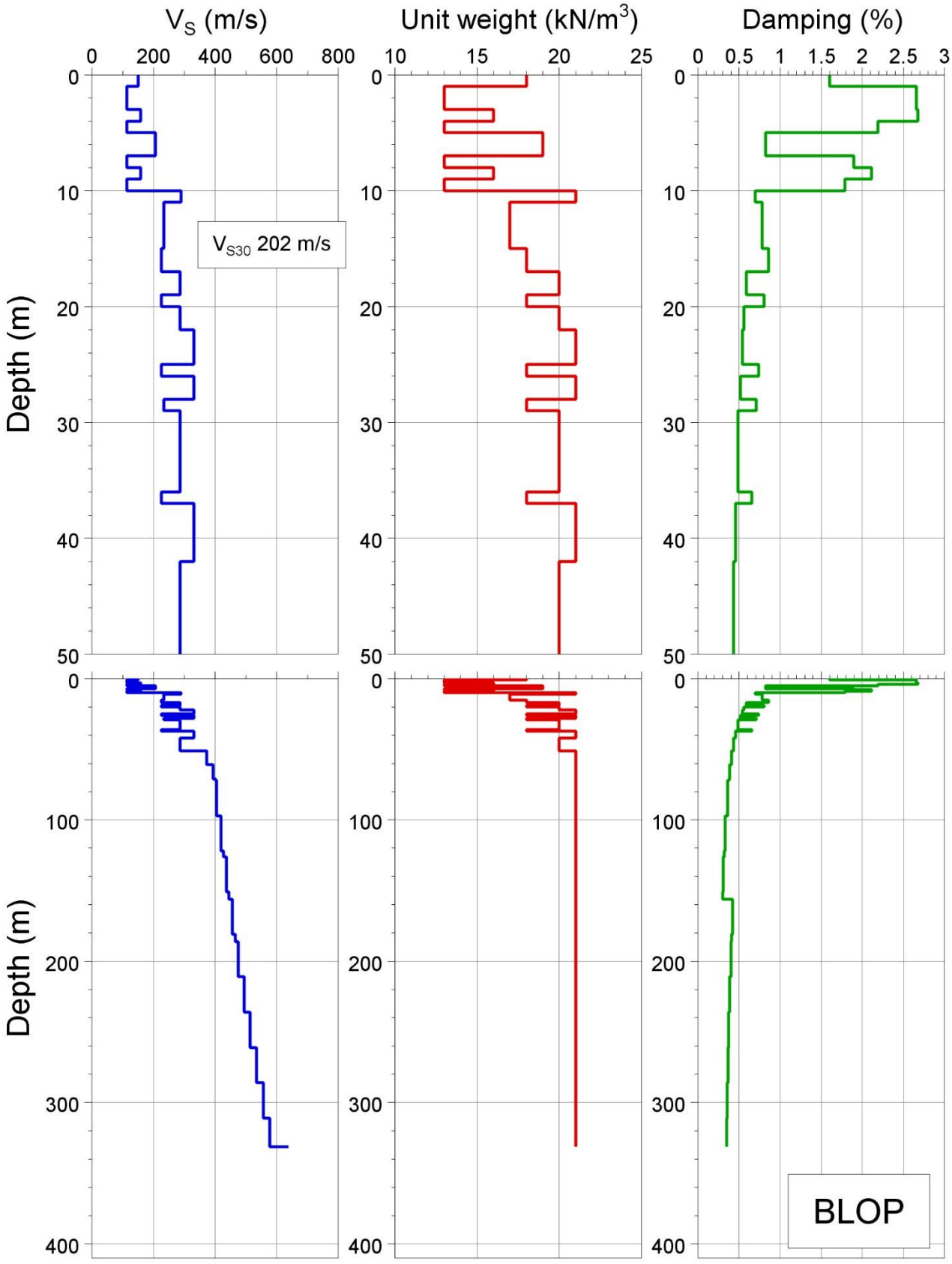
V_S (m/s)
Unit weight (kN/m^3)
Damping (%)
V_{S30} 202 m/s
Depth (m)
Depth (m)
BLOP

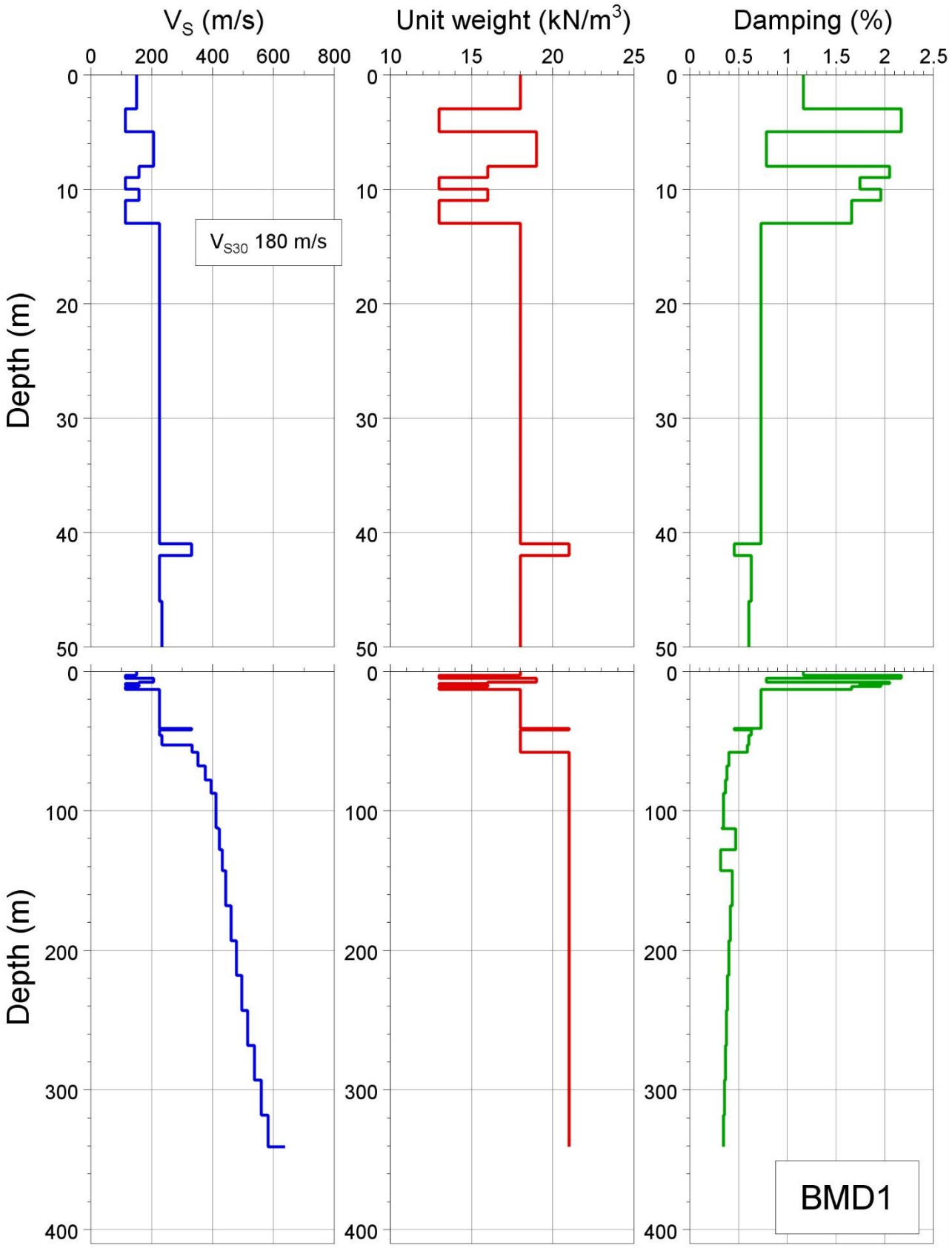
V_S (m/s)
Unit weight (kN/m^3)
Damping (%)
V_{S30} 180 m/s
Depth (m)
Depth (m)
BMD1

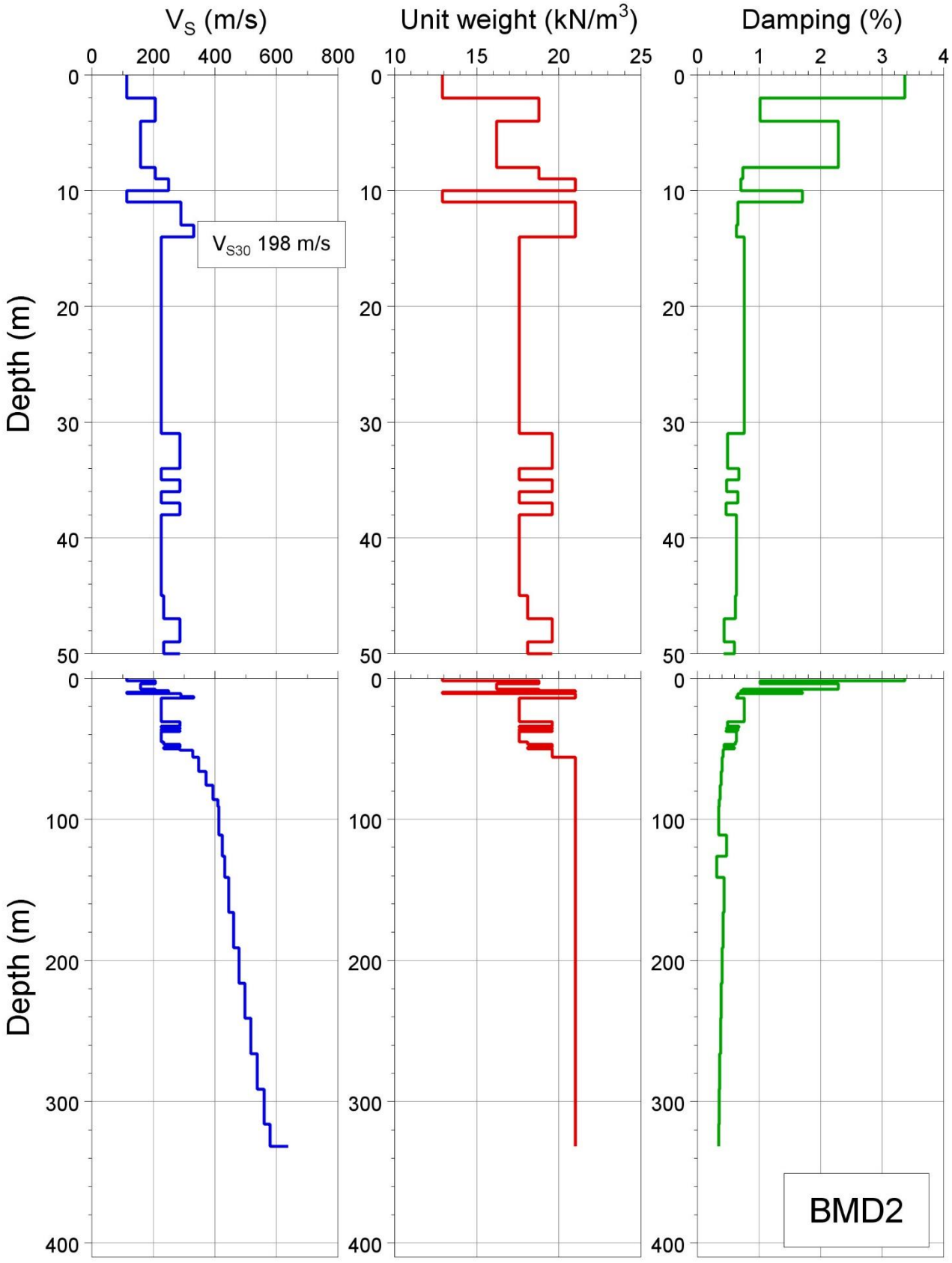
V_S (m/s)
Unit weight (kN/m^3)
Damping (%)
V_{S30} 198 m/s
Depth (m)
BMD2

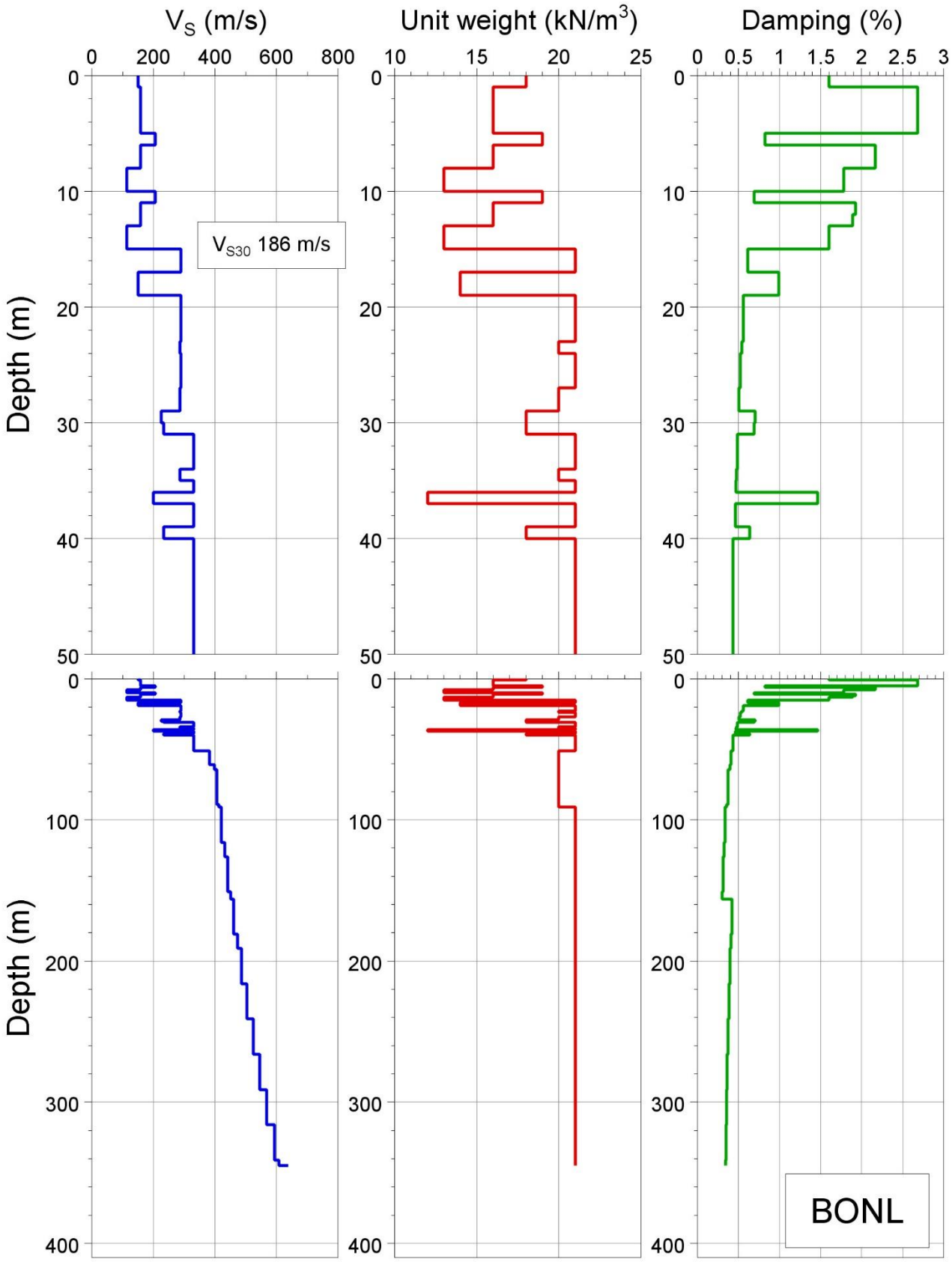
V_S (m/s)
Unit weight (kN/m^3)
Damping (%)
V_{S30} 186 m/s
Depth (m)
Depth (m)
BONL

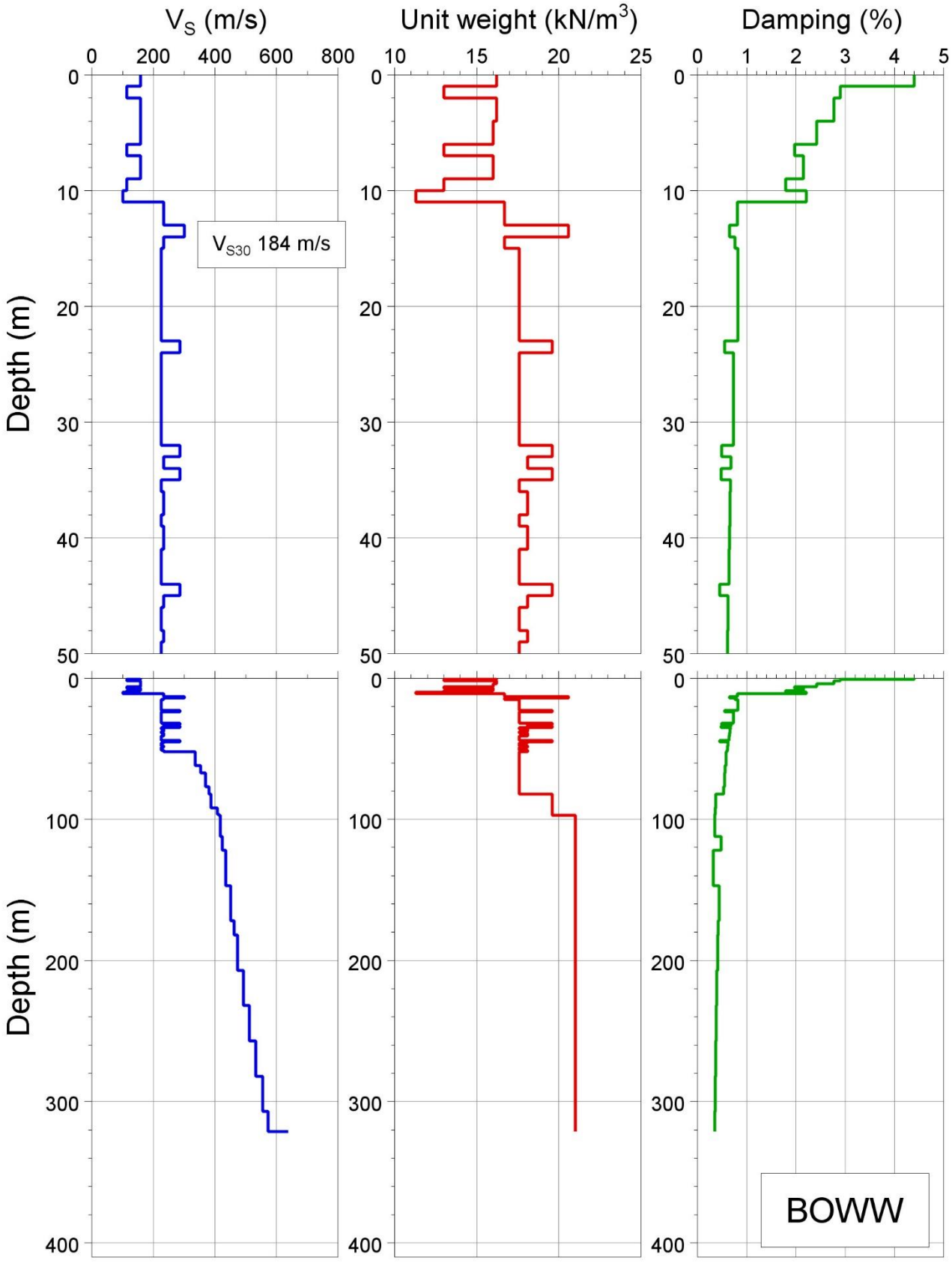
V_S (m/s)
Unit weight (kN/m^3)
Damping (%)
V_{S30} 184 m/s
Depth (m)
Depth (m)
BOWW

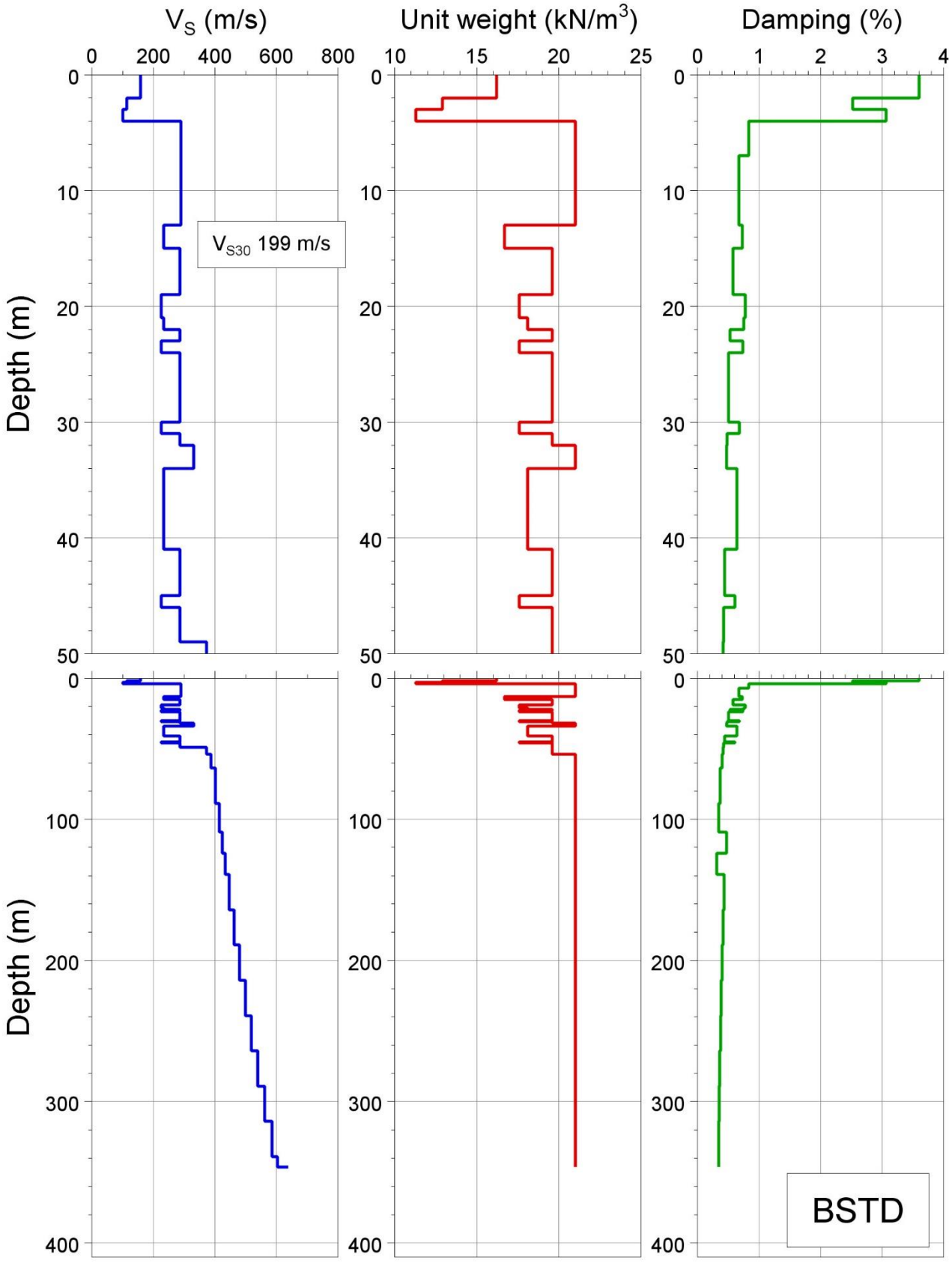
V_S (m/s)
Unit weight (kN/m^3)
Damping (%)
V_{S30} 199 m/s
Depth (m)
Depth (m)
BSTD

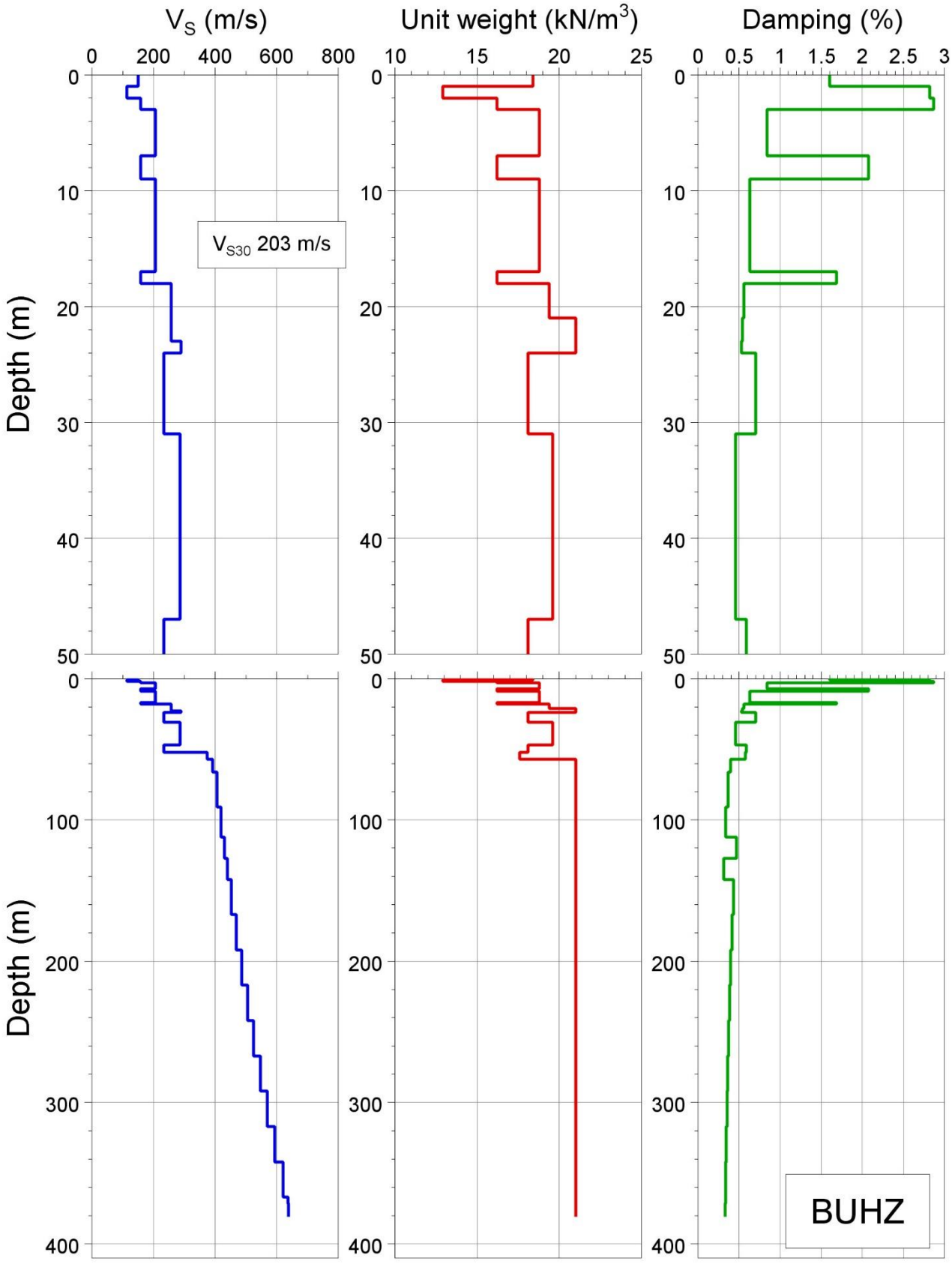
V_S (m/s)
Unit weight (kN/m^3)
Damping (%)
V_{S30} 203 m/s
Depth (m)
BUHZ

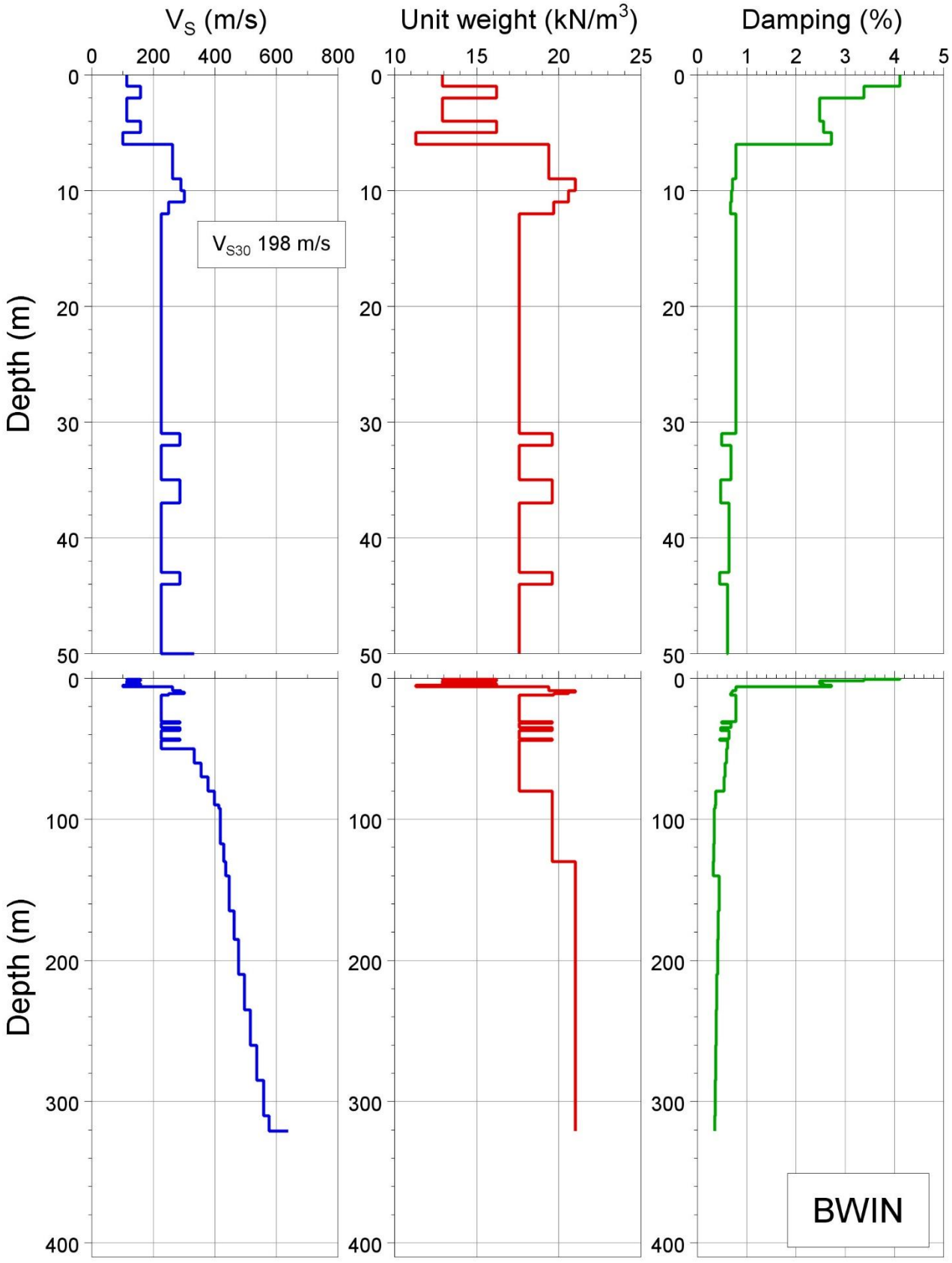
V_S (m/s)
Unit weight (kN/m^3)
Damping (%)
V_{S30} 198 m/s
Depth (m)
Depth (m)
BWIN

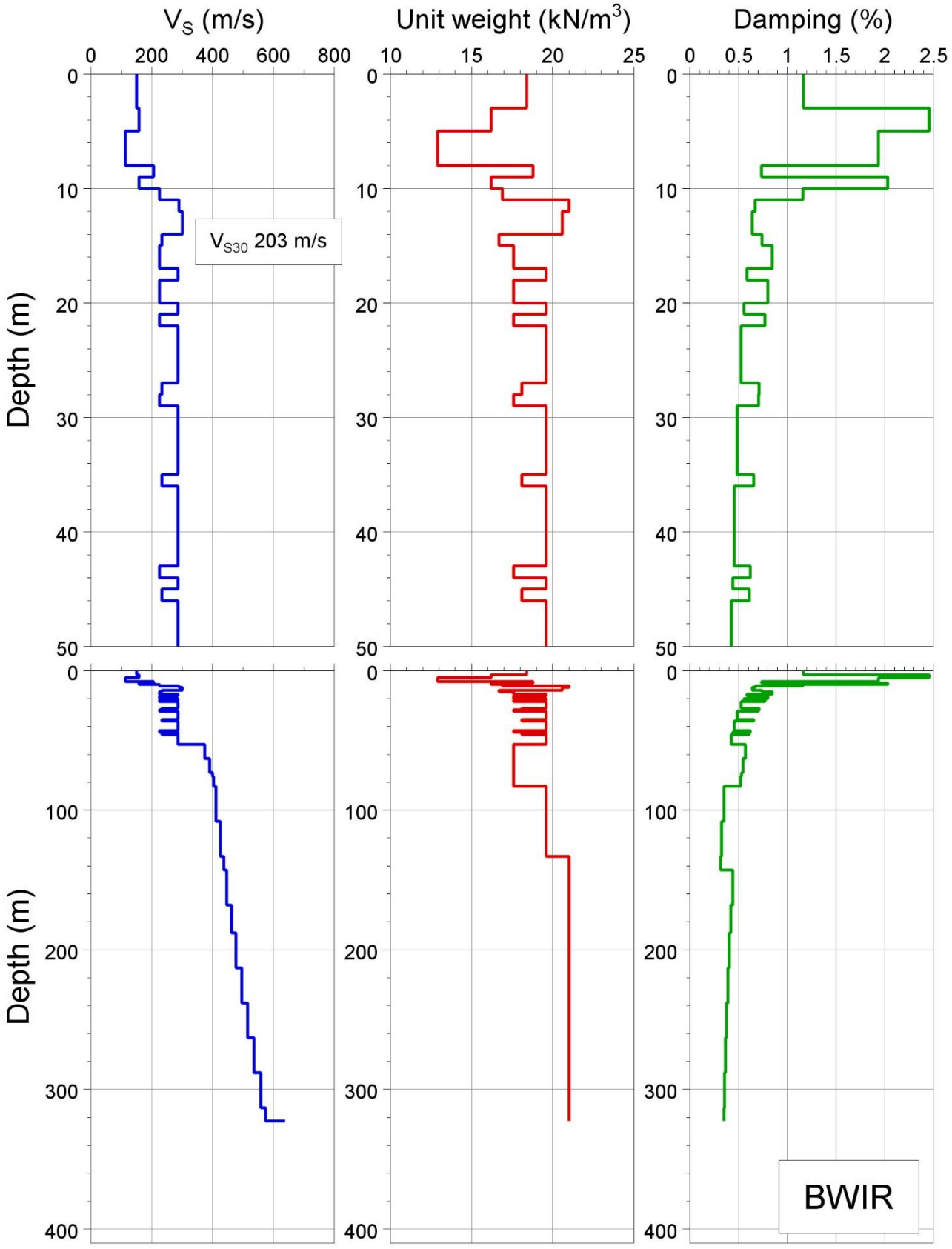
V_S (m/s)
Unit weight (kN/m^3)
Damping (%)
V_{S30} 203 m/s
Depth (m)
Depth (m)
BWIR

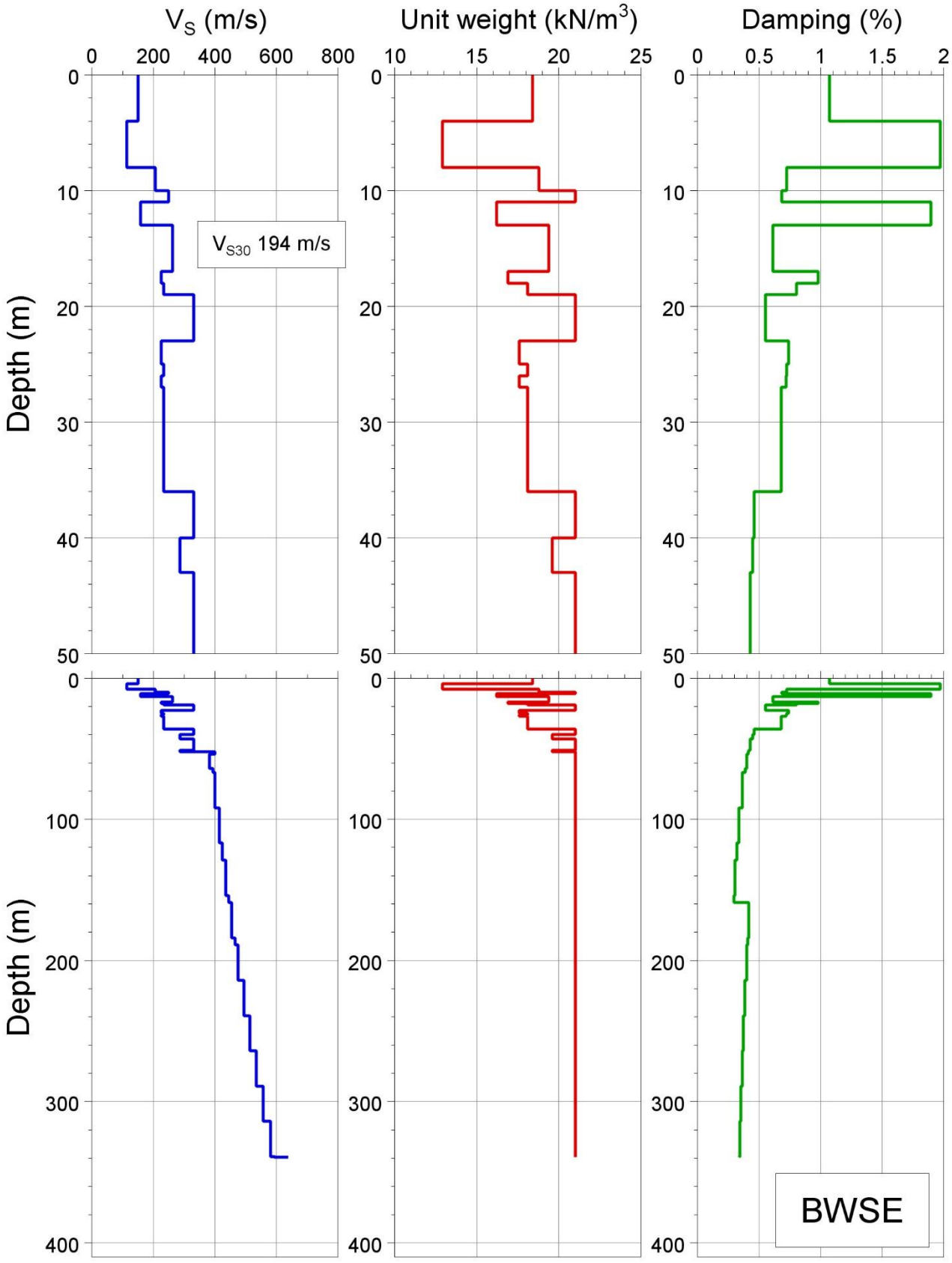
V_S (m/s)
Unit weight (kN/m^3)
Damping (%)
V_{S30} 194 m/s
Depth (m)
Depth (m)
BWSE

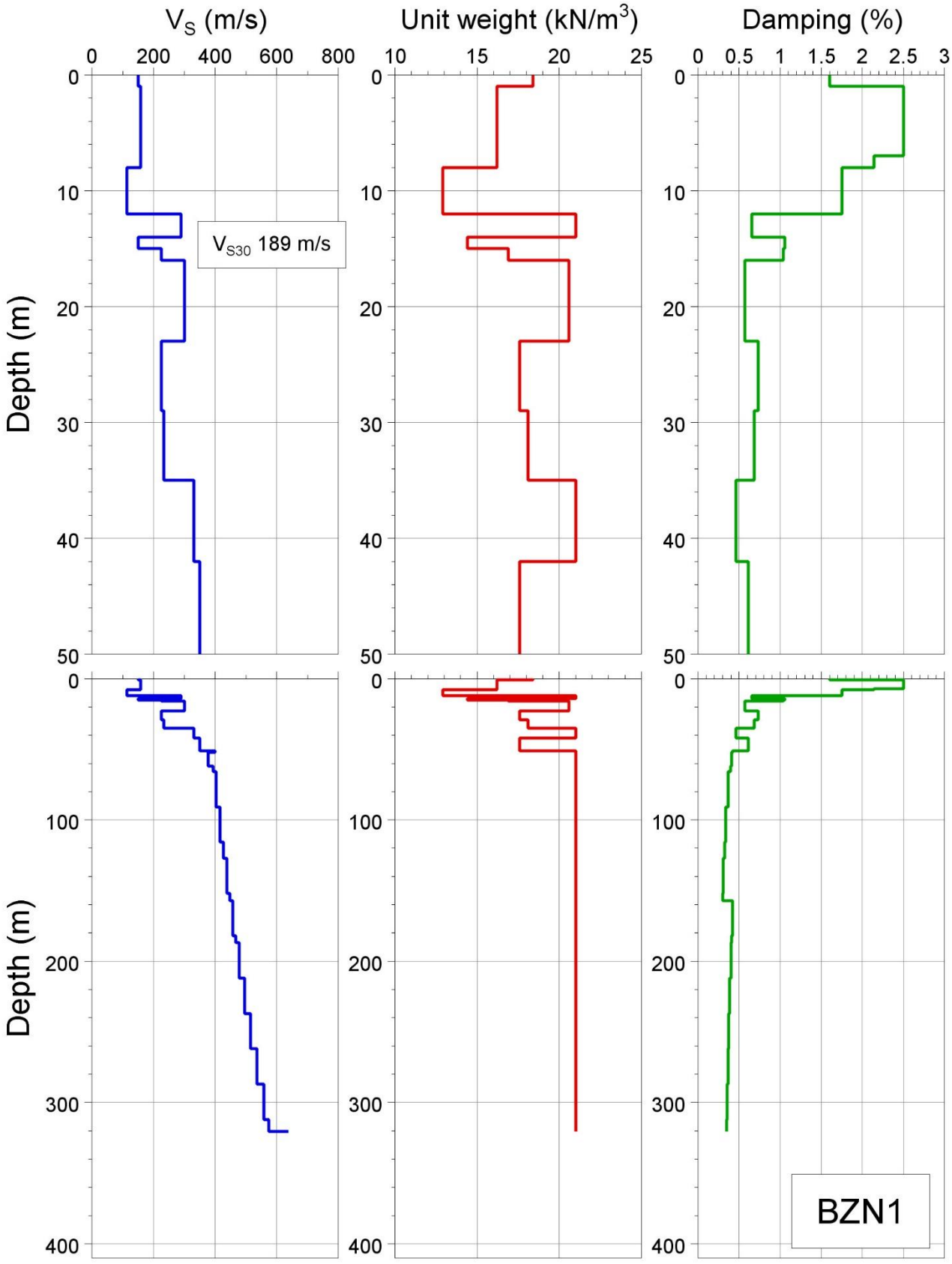
V_S (m/s)
Unit weight (kN/m^3)
Damping (%)
V_{S30} 189 m/s
Depth (m)
Depth (m)
BZN1

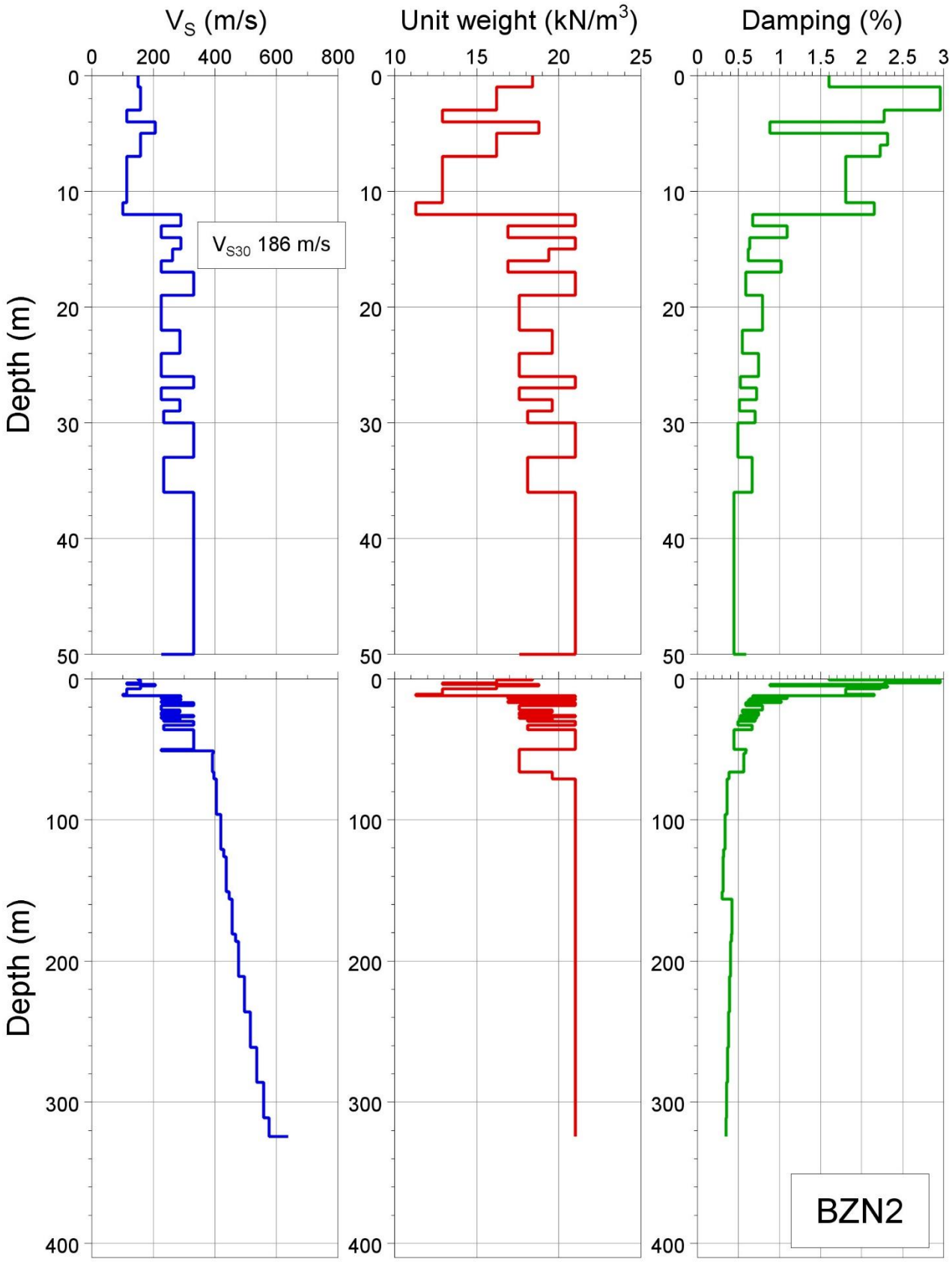
V_S (m/s)
Unit weight (kN/m^3)
Damping (%)
0 200 400 600 800
10 15 20 25
0 0.5 1 1.5 2 2.5 3
V_{S30} 186 m/s
Depth (m)
0 10 20 30 40 50
0 100 200 300 400
BZN2

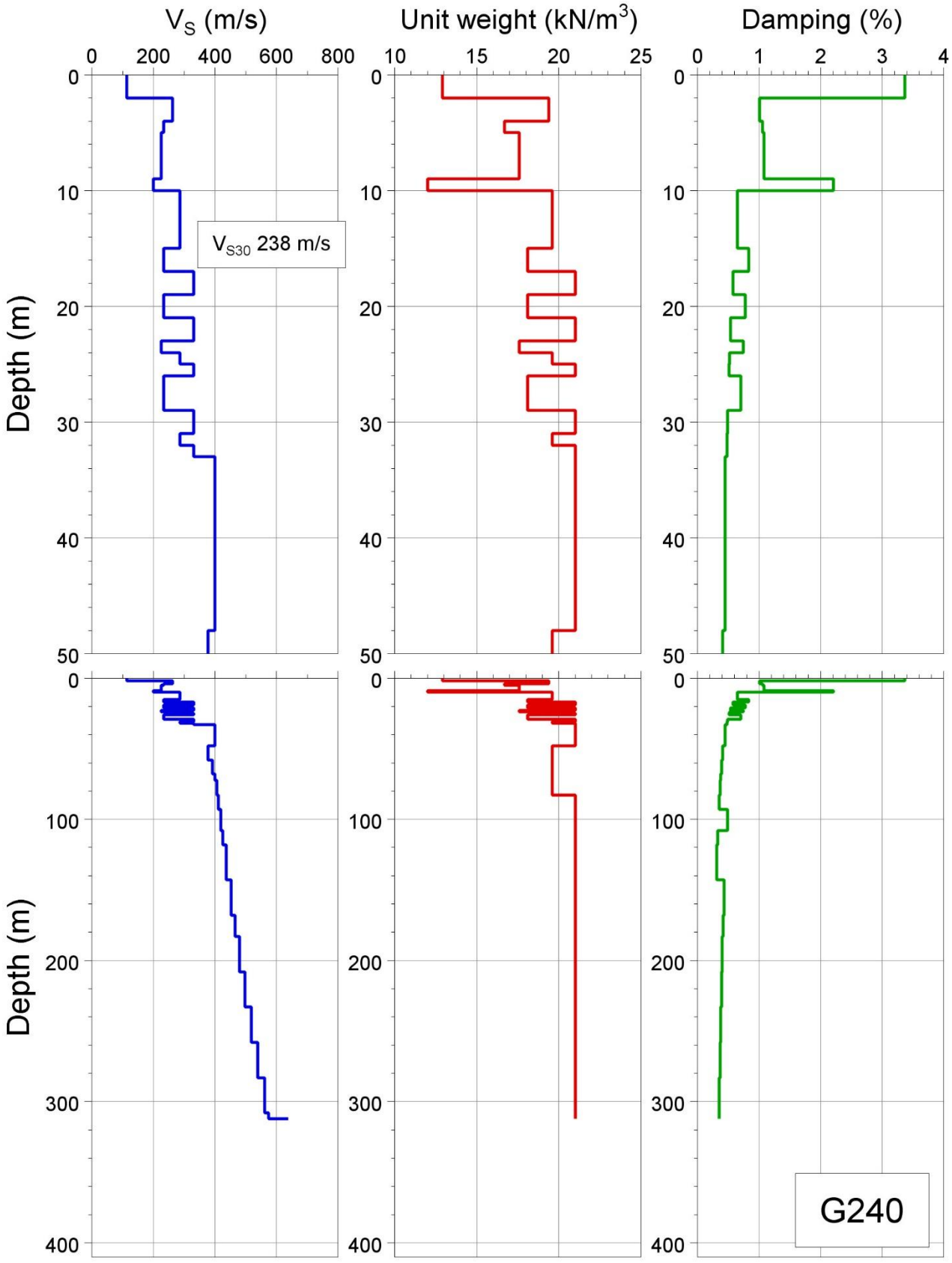
V_S (m/s)
Unit weight (kN/m^3)
Damping (%)
V_{S30} 238 m/s
Depth (m)
G240

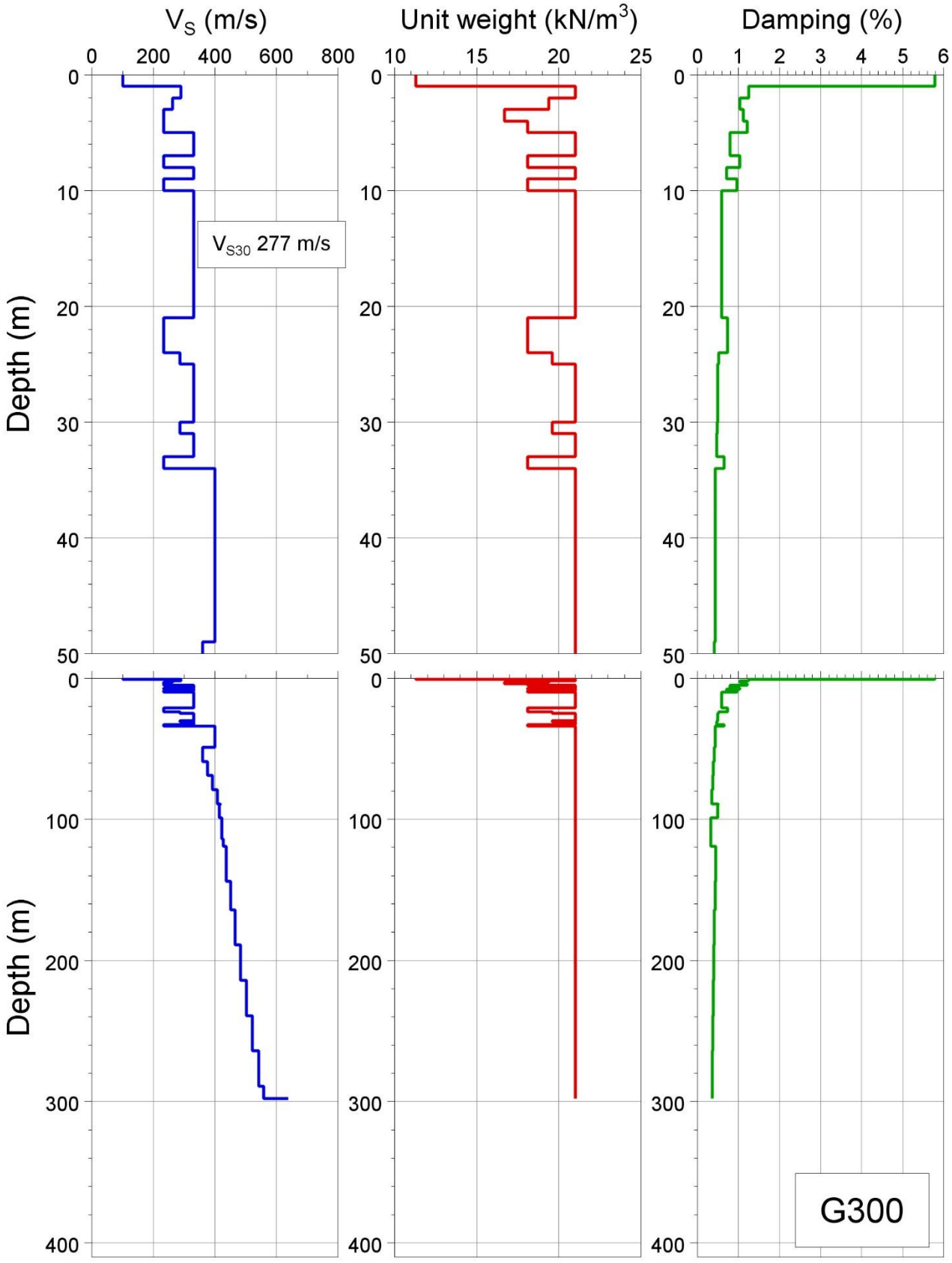
V_S (m/s)
Unit weight (kN/m^3)
Damping (%)
V_{S30} 277 m/s
Depth (m)
Depth (m)
G300

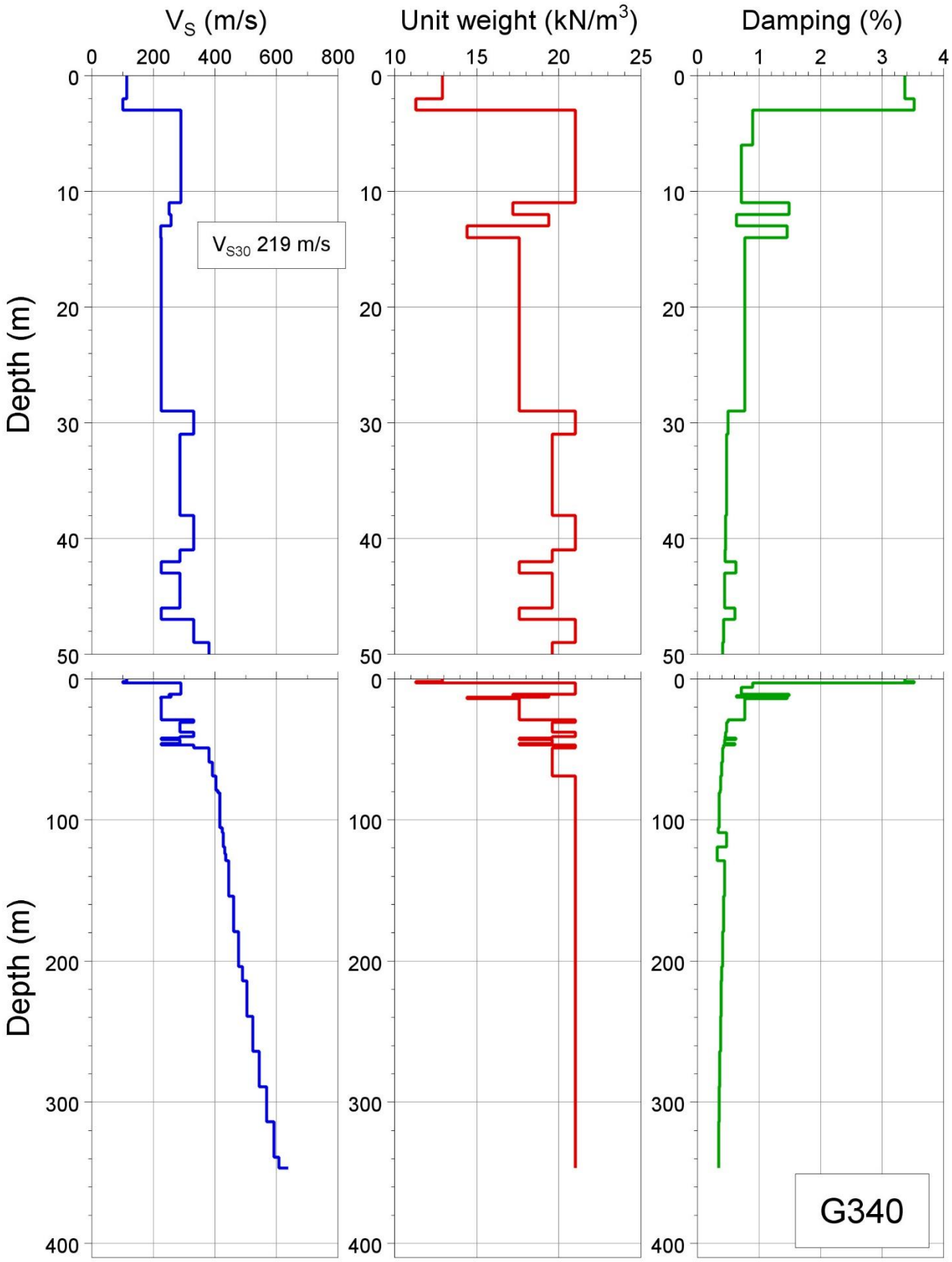
V_S (m/s)
Unit weight (kN/m^3)
Damping (%)
V_{S30} 219 m/s
Depth (m)
Depth (m)
G340

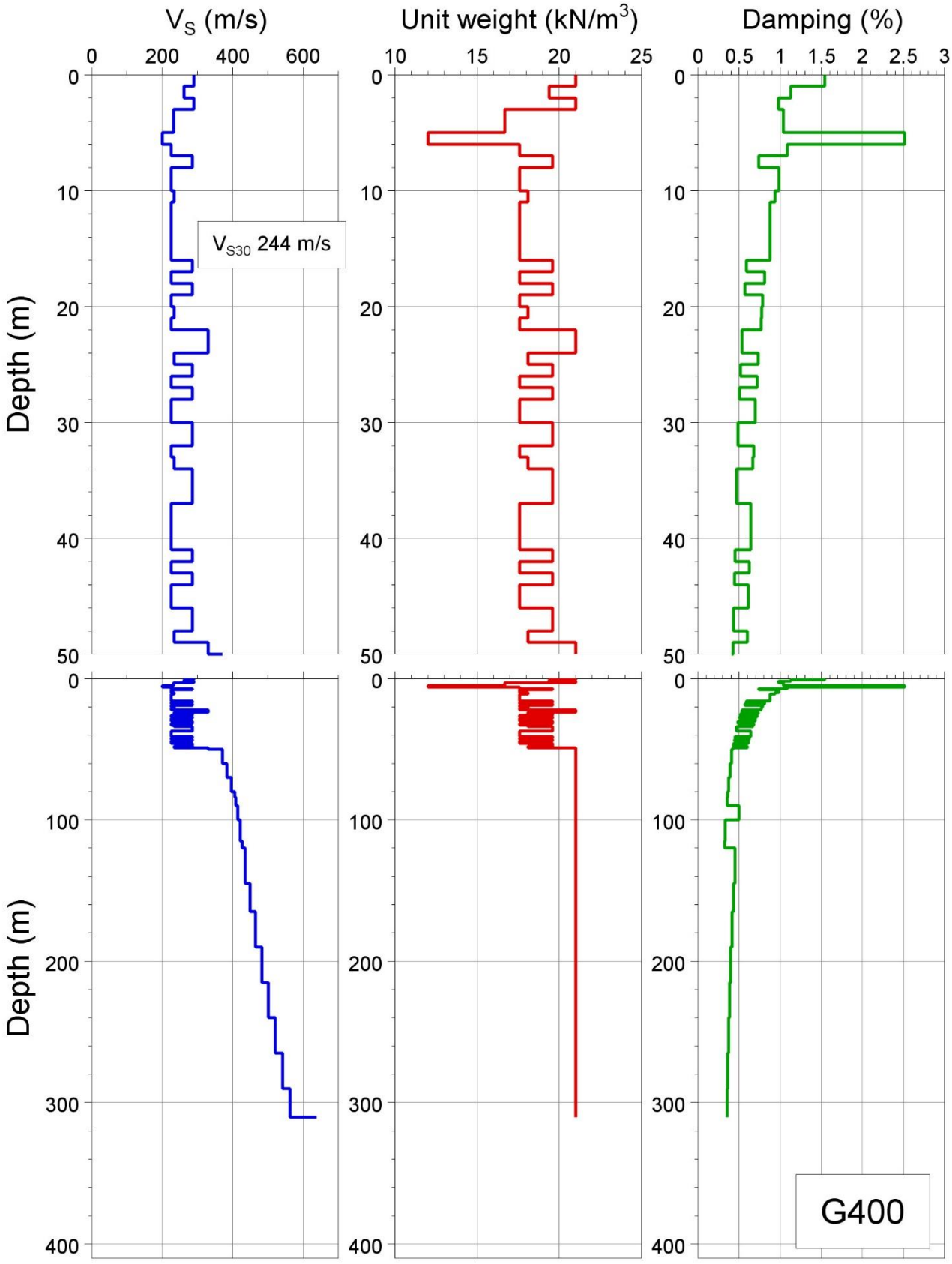
V_S (m/s)
Unit weight (kN/m^3)
Damping (%)
Depth (m)
V_{S30} 244 m/s
G400

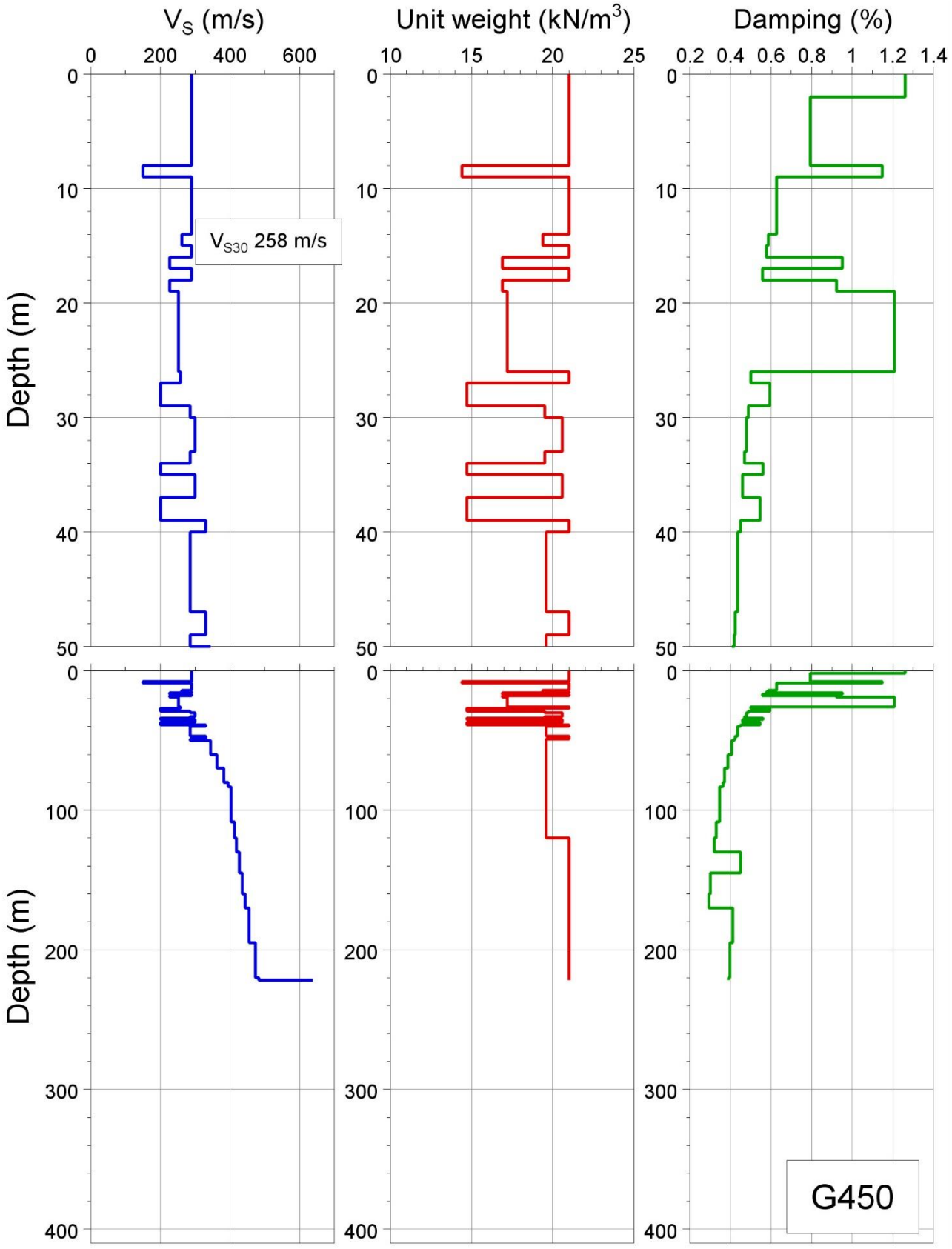
V_S (m/s)
Unit weight (kN/m^3)
Damping (%)
V_{S30} 258 m/s
Depth (m)
G450

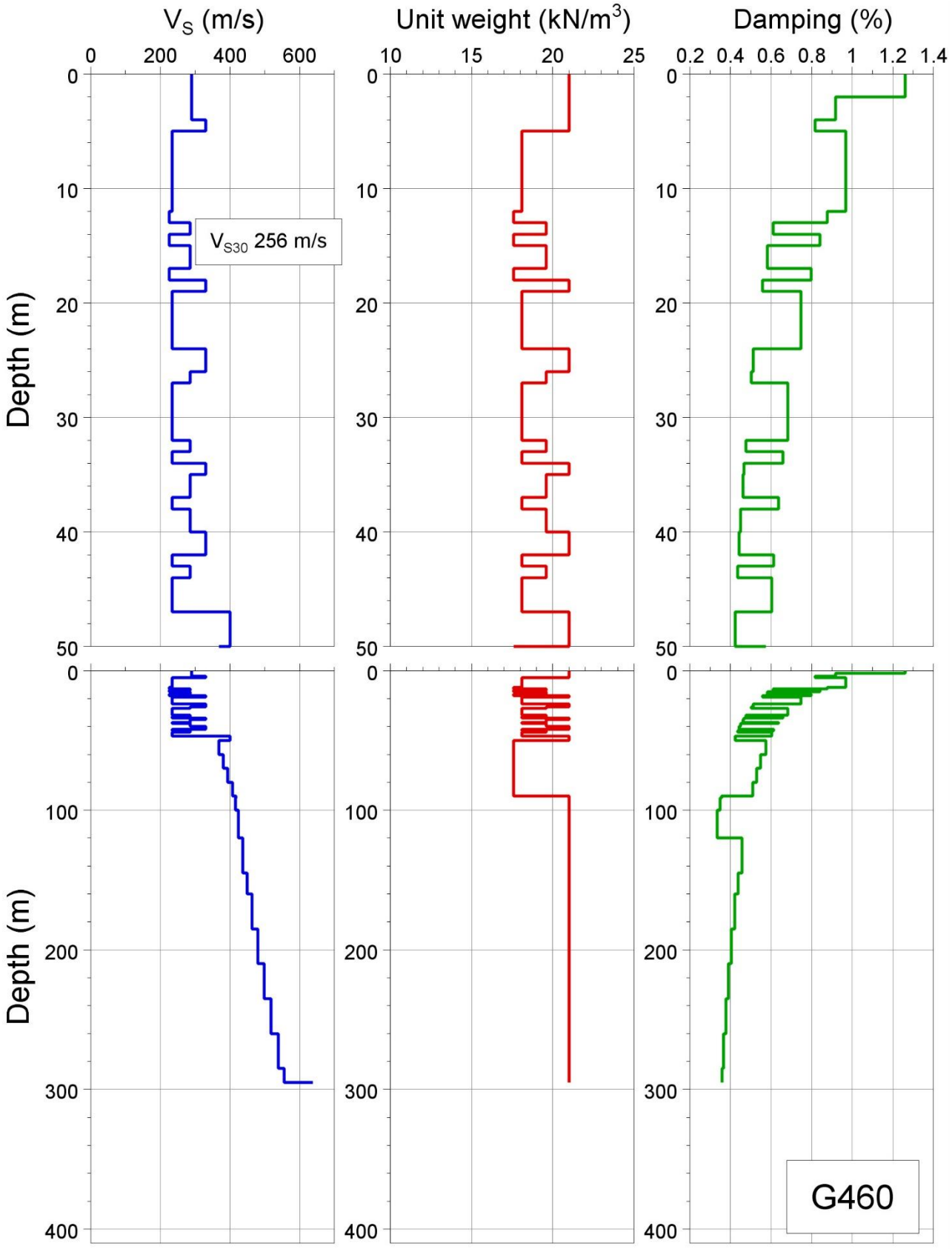
V_S (m/s)
Unit weight (kN/m^3)
Damping (%)
V_{S30} 256 m/s
Depth (m)
G460

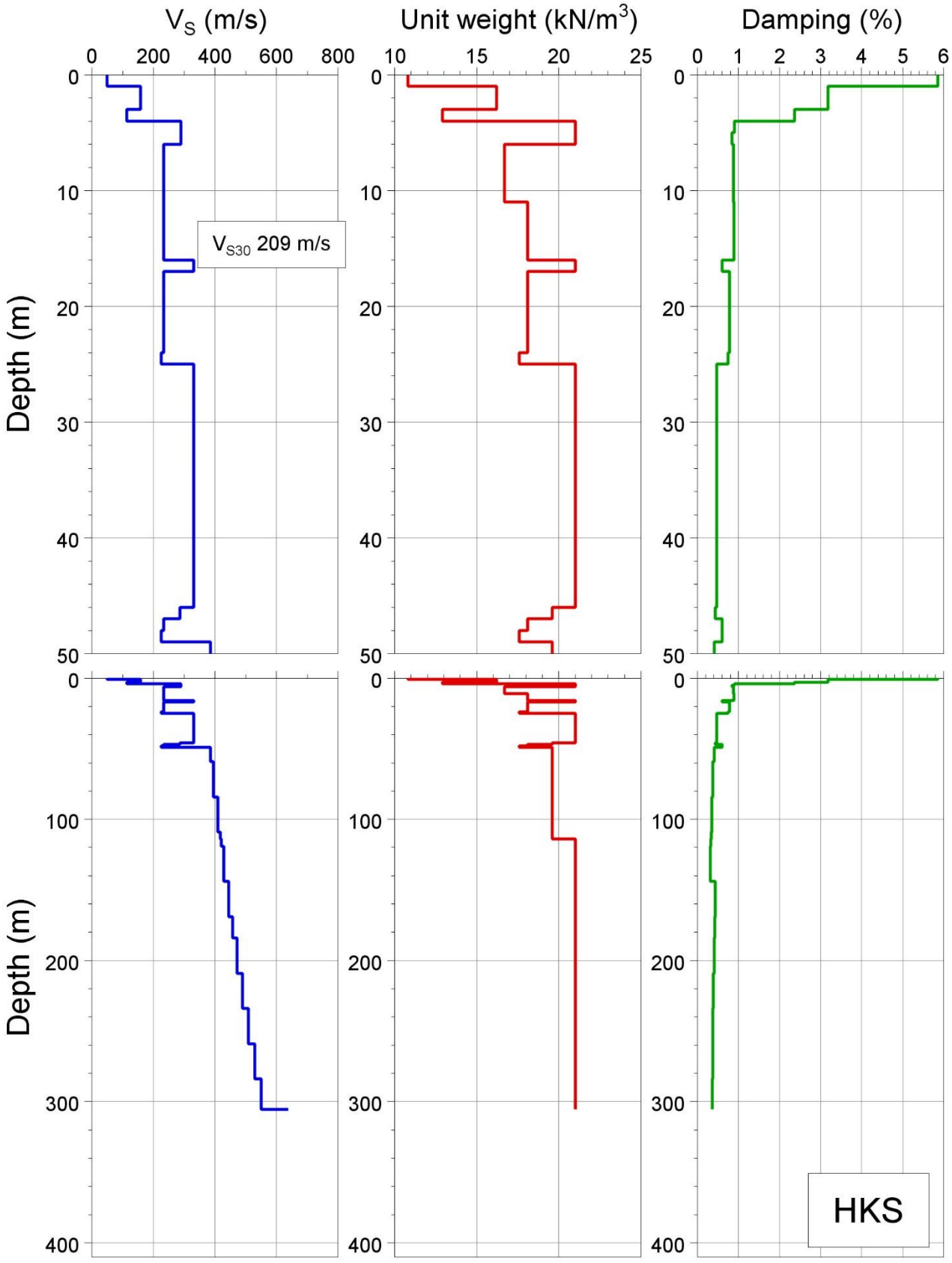
V_S (m/s)
Unit weight (kN/m^3)
Damping (%)
Depth (m)
V_{S30} 209 m/s
HKS

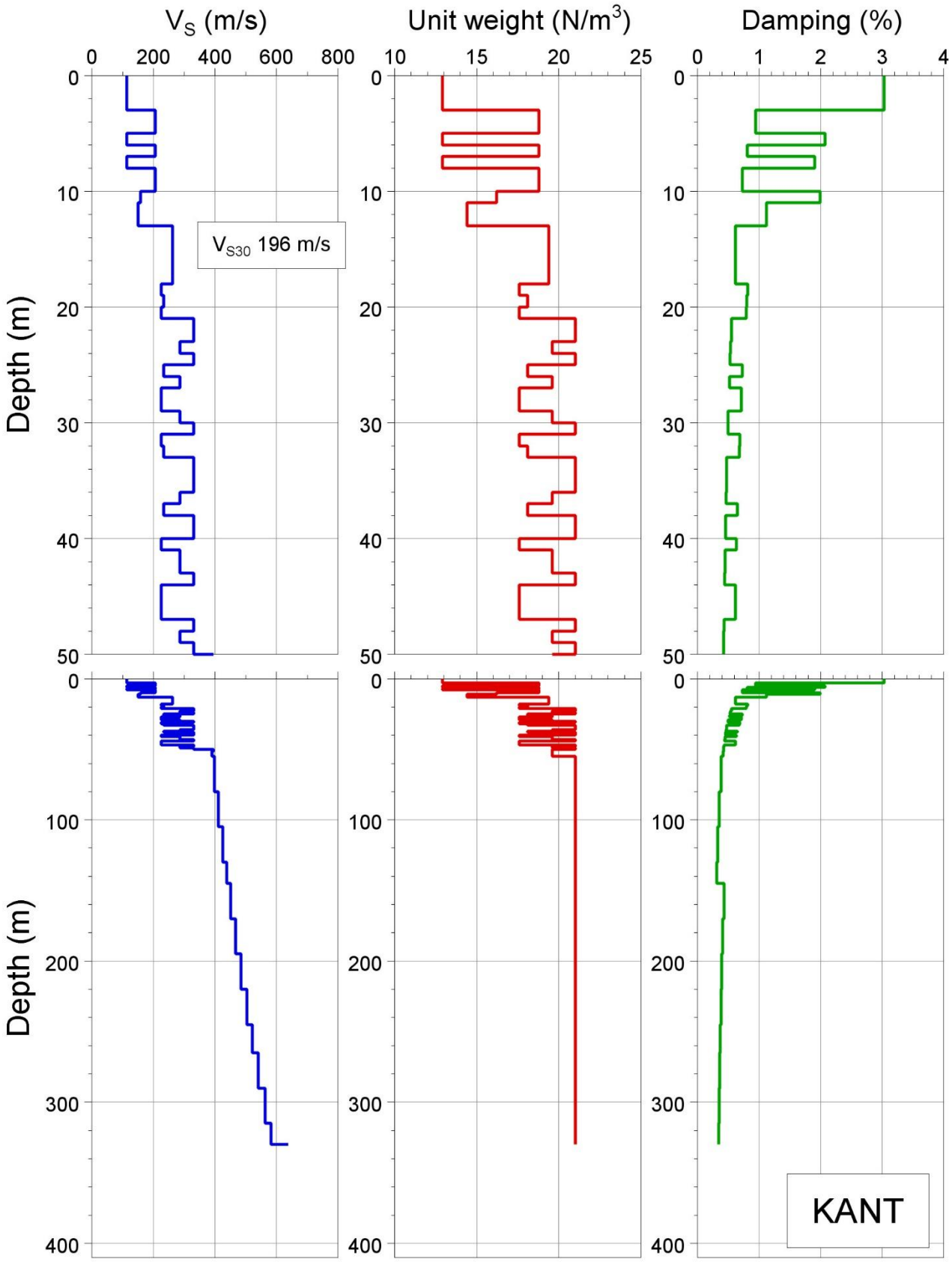
V_S (m/s)
Unit weight (N/m^3)
Damping (%)
V_{S30} 196 m/s
Depth (m)
Depth (m)
KANT

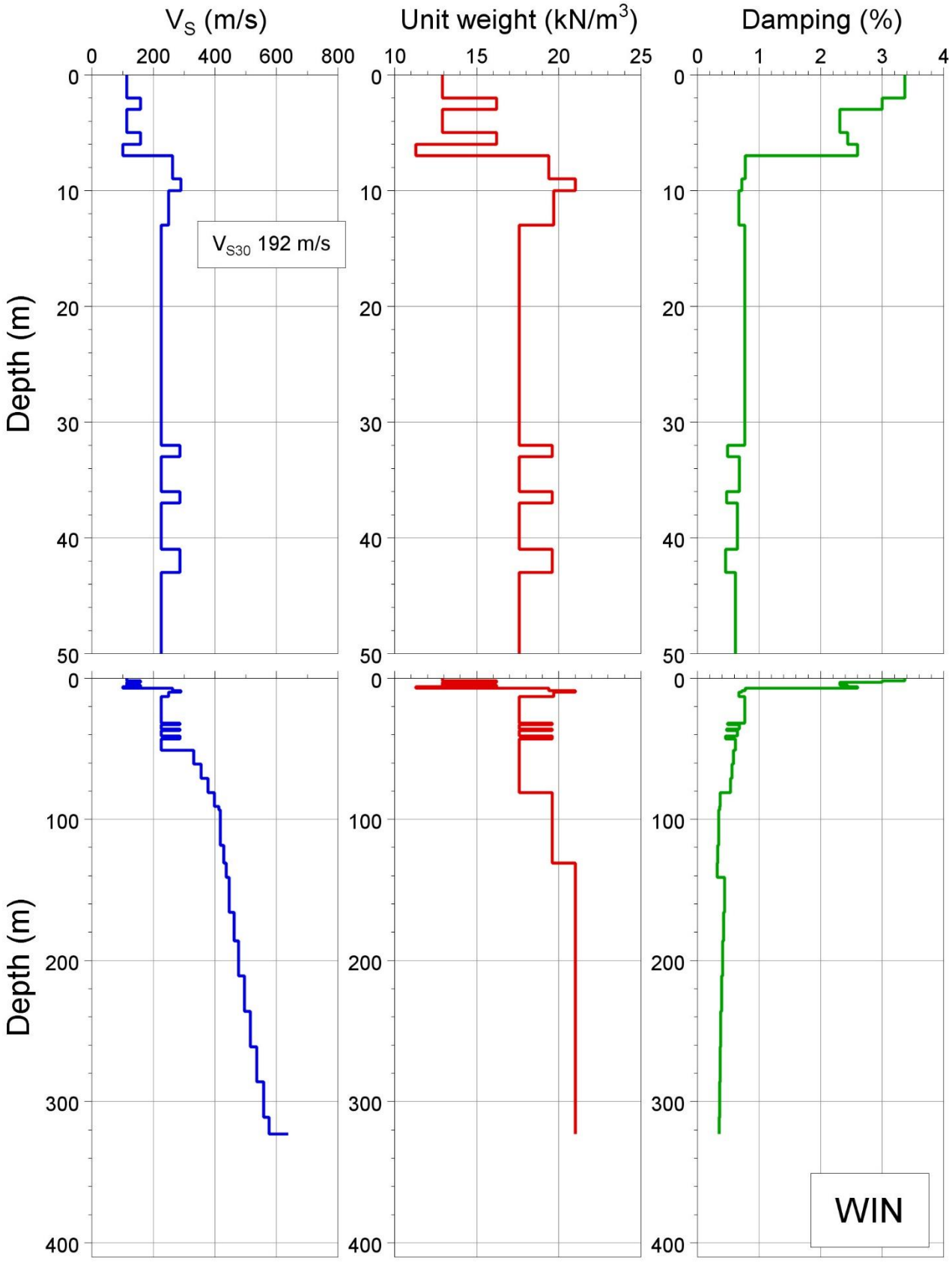
V_S (m/s)
Unit weight (kN/m^3)
Damping (%)
V_{S30} 192 m/s
Depth (m)
Depth (m)
WIN

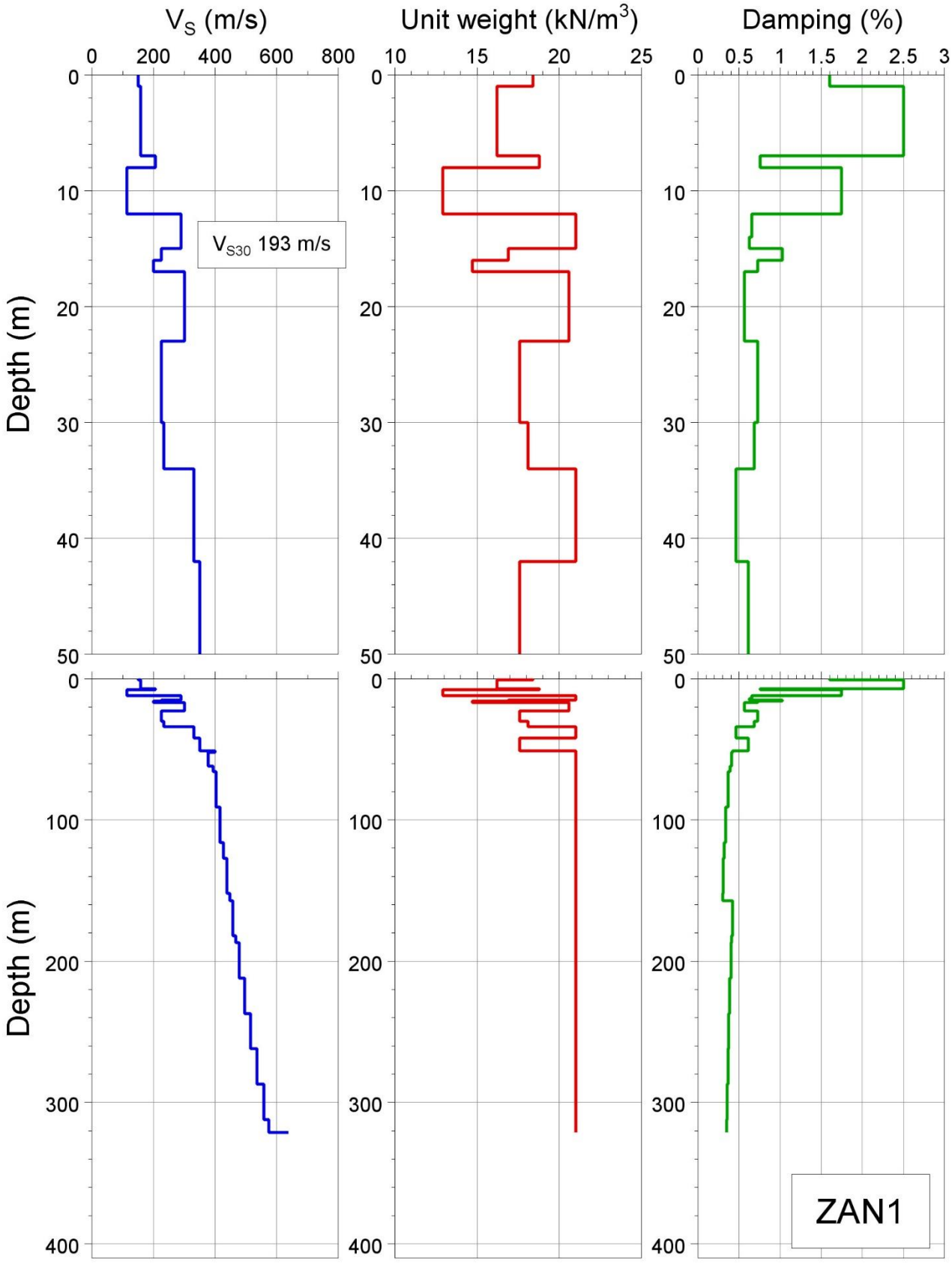
V_S (m/s)
Unit weight (kN/m^3)
Damping (%)
Depth (m)
V_{S30} 193 m/s
ZAN1

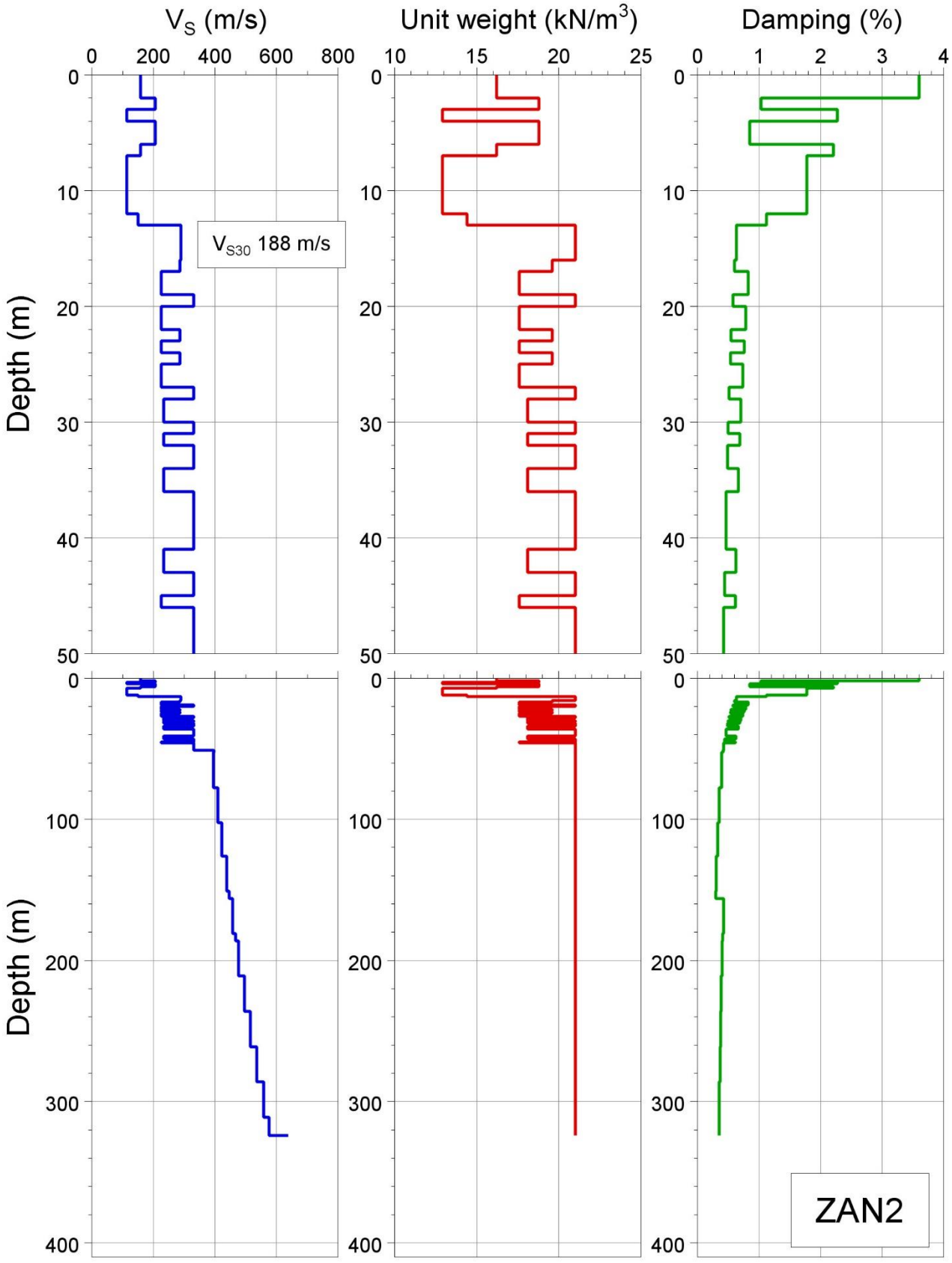
V_S (m/s)
Unit weight (kN/m^3)
Damping (%)
V_{S30} 188 m/s
Depth (m)
Depth (m)
ZAN2

APPENDIX III

Transfer functions for recording stations

In the following pages plots of the Transfer Functions—in terms of Fourier Amplitude Spectra (FAS) of accelerations—are presented for the recording stations, as calculated using the profiles shown in Appendix II. In each case, the blue line shows the smoothed Transfer Function and the red circles the target frequencies for the simulations of FAS, as listed in Table 1.2. In some of the plots there is also green line, which represents the Transfer Function as calculated excluding surface or near-surface peat layers.

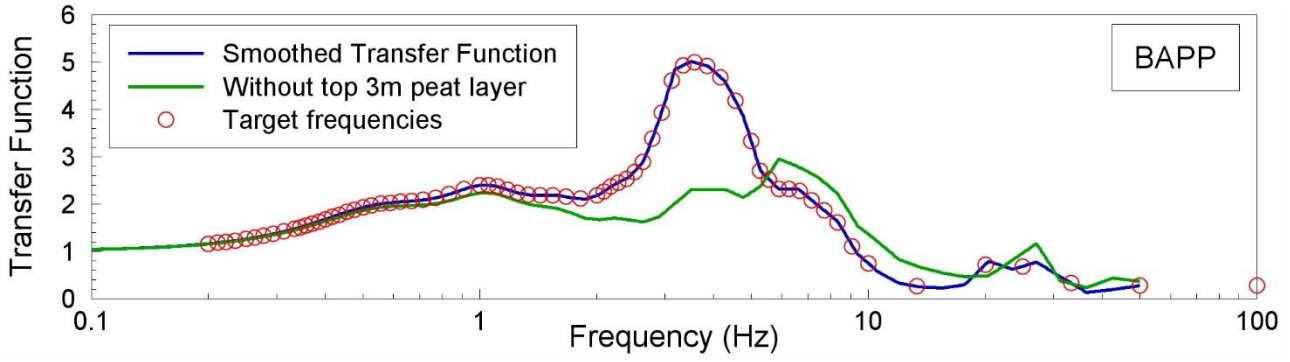
Smoothed Transfer Function
Without top 3m peat layer
Target frequencies
BAPP
Transfer Function
Frequency (Hz)
0
1
2
3
4
5
6
0.1
1
10
100

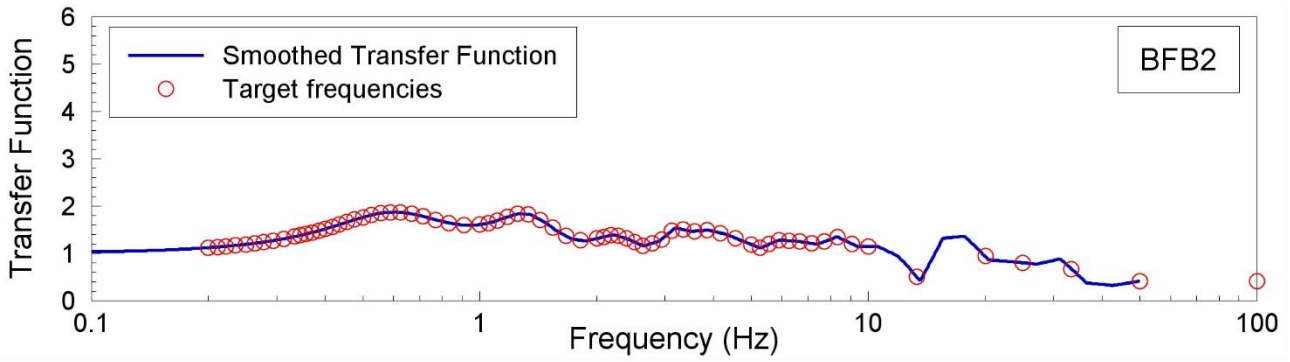
Smoothed Transfer Function
Target frequencies
BFB2
Transfer Function
Frequency (Hz)
0
1
2
3
4
5
6
0.1
1
10
100

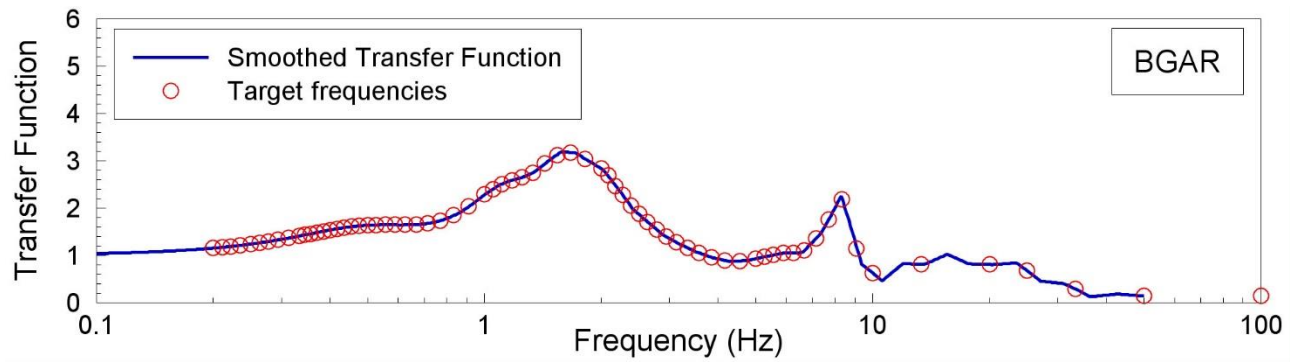
Smoothed Transfer Function
Target frequencies
BGAR
Transfer Function
Frequency (Hz)
0
1
2
3
4
5
6
0.1
1
10
100

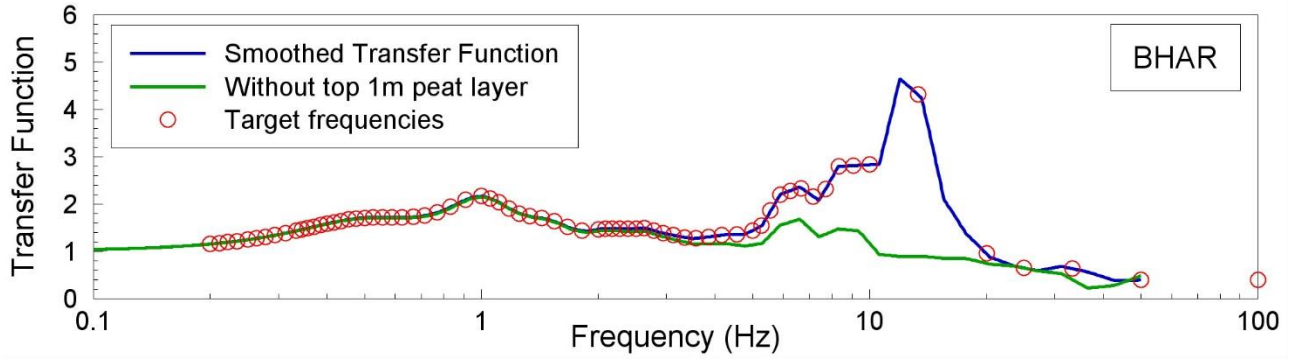
Smoothed Transfer Function
Without top 1m peat layer
Target frequencies
BHAR
Transfer Function
Frequency (Hz)
0
1
2
3
4
5
6
0.1
1
10
100

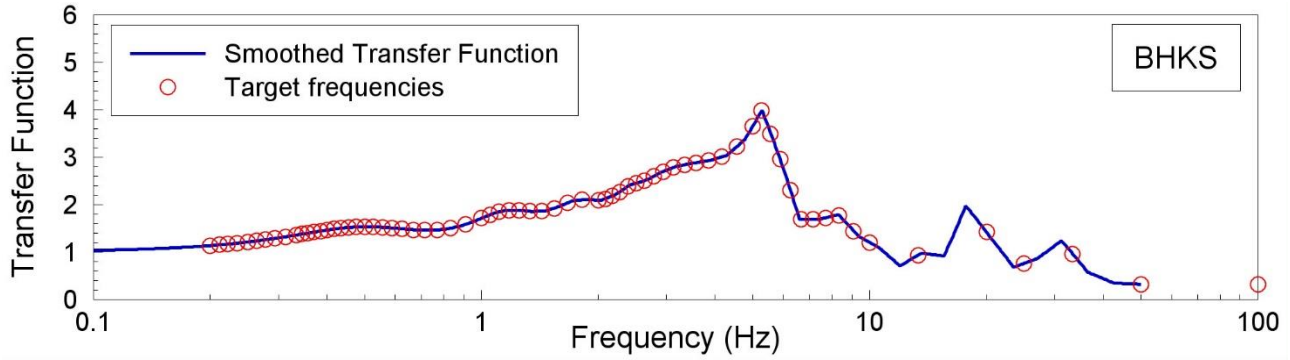
Smoothed Transfer Function
Target frequencies
BHKS
Transfer Function
Frequency (Hz)
0
1
2
3
4
5
6
0.1
1
10
100

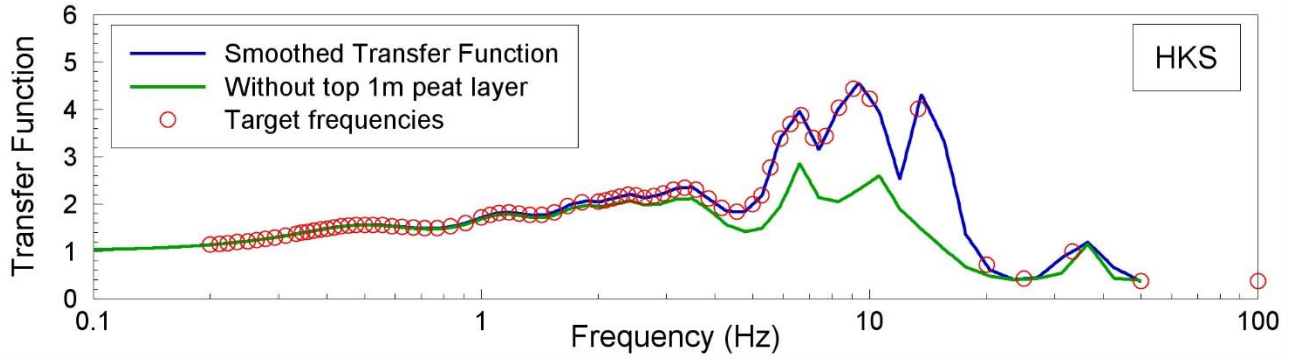
Smoothed Transfer Function
Without top 1m peat layer
Target frequencies
HKS
Transfer Function
Frequency (Hz)
0
1
2
3
4
5
6
0.1
1
10
100

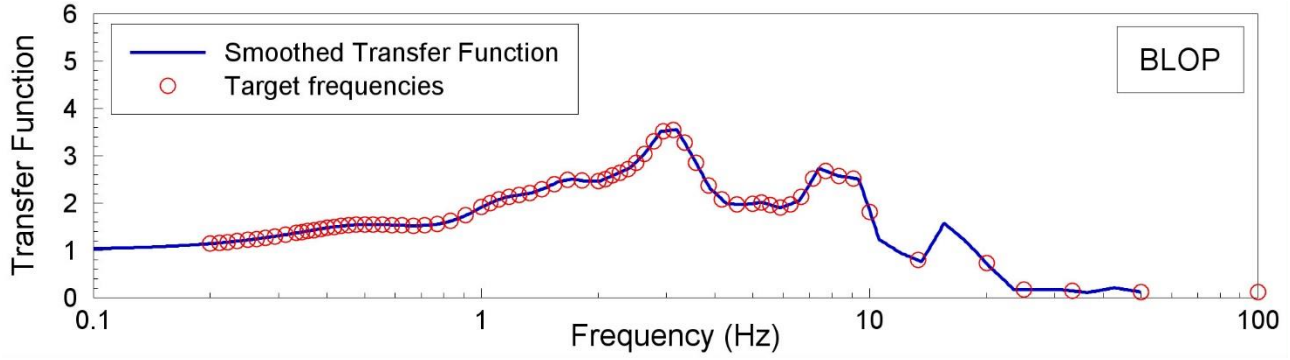
Smoothed Transfer Function
Target frequencies
BLOP
Transfer Function
Frequency (Hz)
0
1
2
3
4
5
6
0.1
1
10
100

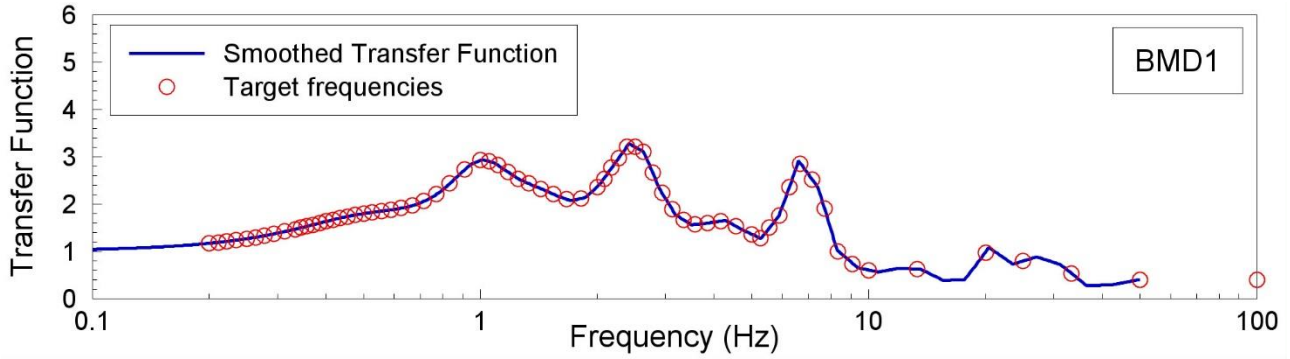
Smoothed Transfer Function
Target frequencies
BMD1
Transfer Function
Frequency (Hz)
0
1
2
3
4
5
6
0.1
1
10
100

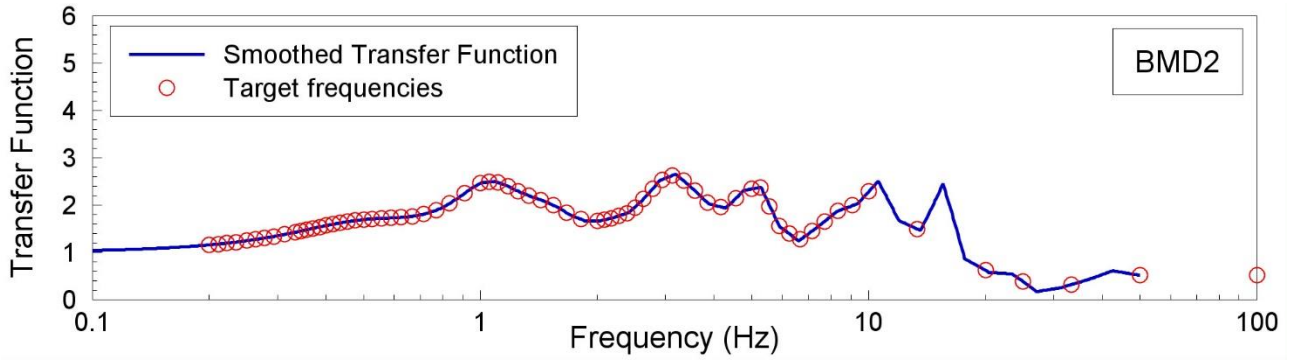
Smoothed Transfer Function
Target frequencies
BMD2
Transfer Function
Frequency (Hz)
0
1
2
3
4
5
6
0.1
1
10
100

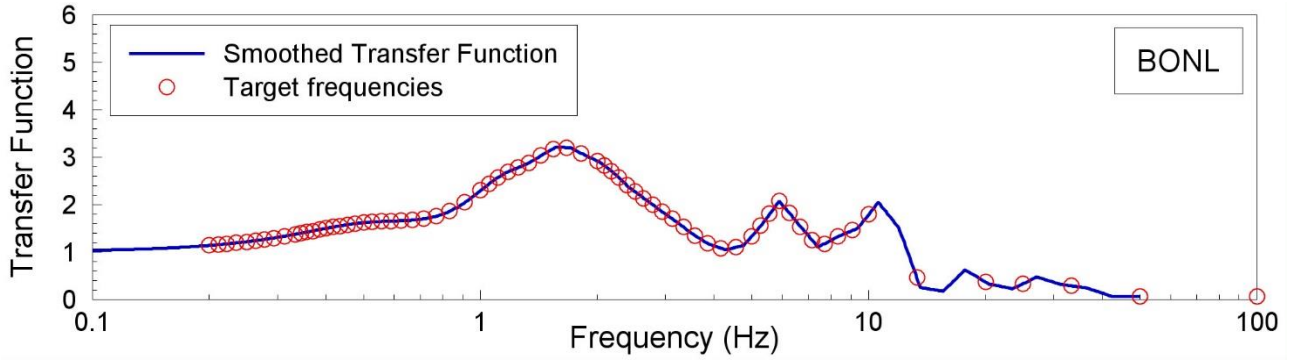
Smoothed Transfer Function
Target frequencies
BONL
Transfer Function
Frequency (Hz)
0
1
2
3
4
5
6
0.1
1
10
100

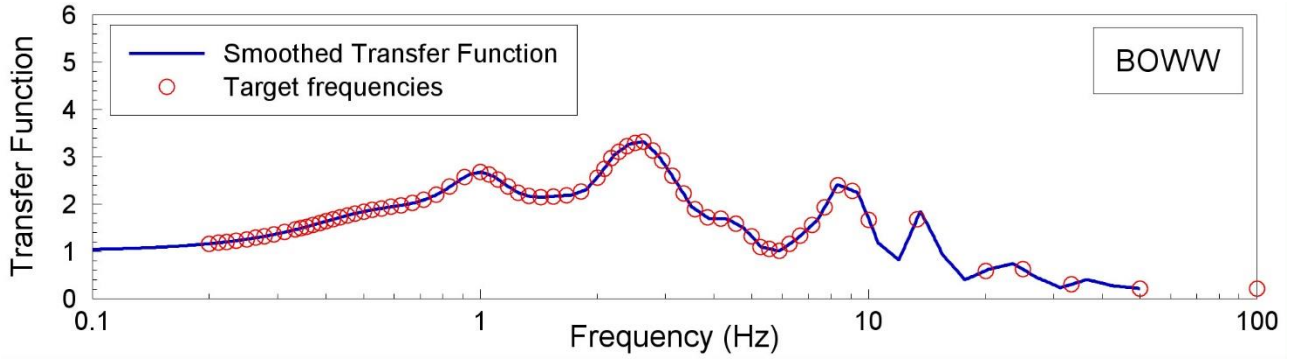
Smoothed Transfer Function
Target frequencies
BOWW
Transfer Function
Frequency (Hz)
0
1
2
3
4
5
6
0.1
1
10
100

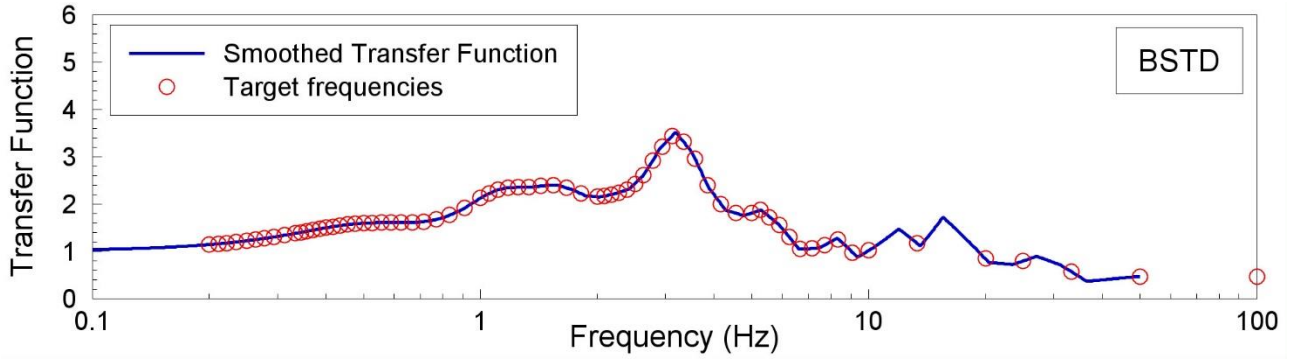
Smoothed Transfer Function
Target frequencies
BSTD
Transfer Function
Frequency (Hz)
0
1
2
3
4
5
6
0.1
1
10
100

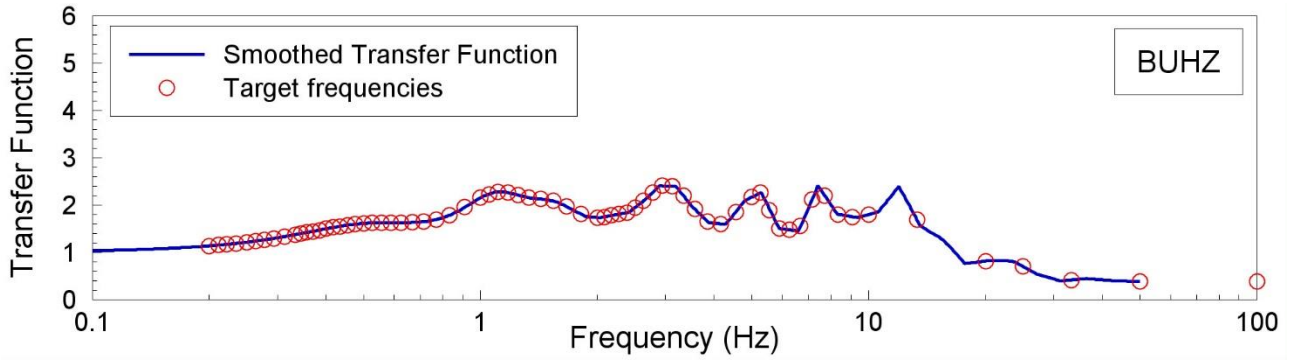
Smoothed Transfer Function
Target frequencies
BUHZ
Transfer Function
Frequency (Hz)
0
1
2
3
4
5
6
0.1
1
10
100

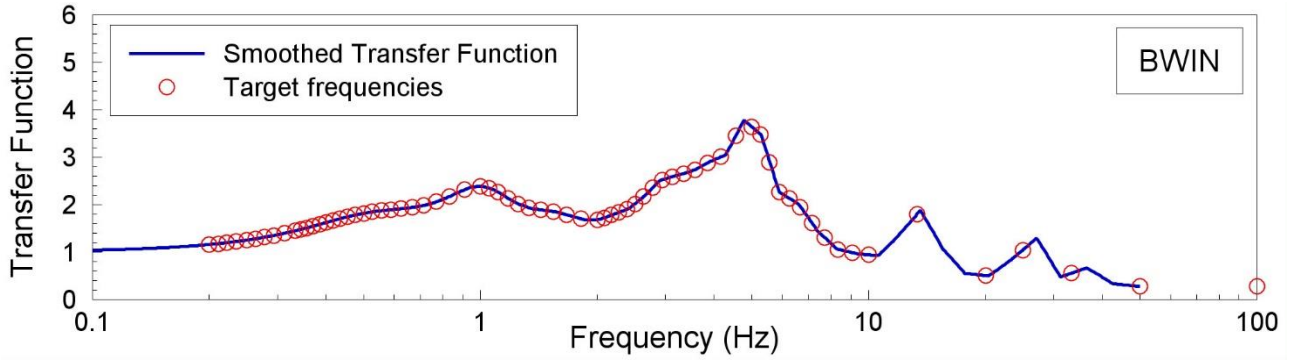
Smoothed Transfer Function
Target frequencies
BWIN
Transfer Function
Frequency (Hz)
0
1
2
3
4
5
6
0.1
1
10
100

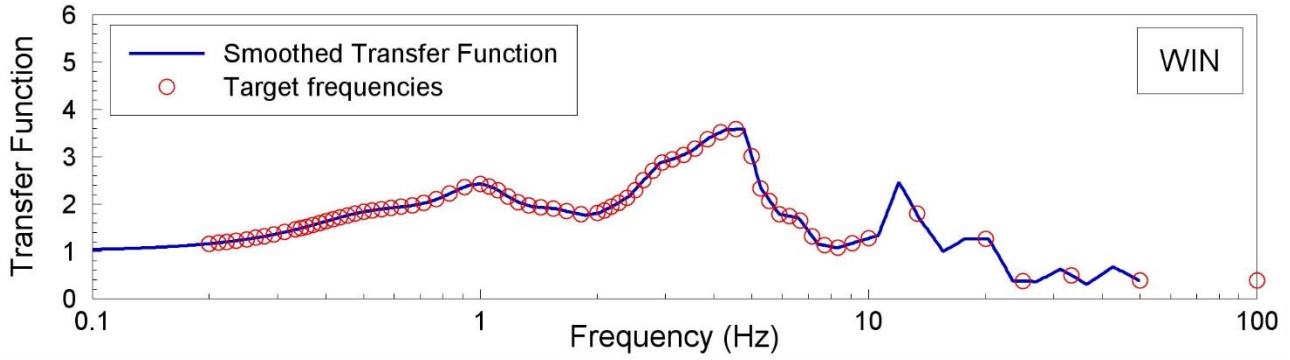
Smoothed Transfer Function
Target frequencies
WIN
Transfer Function
Frequency (Hz)
0
1
2
3
4
5
6
0.1
1
10
100

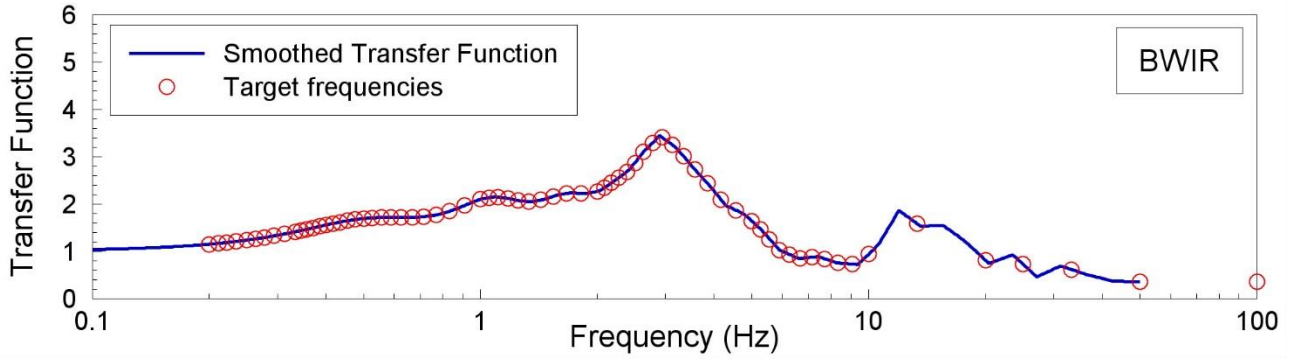
Smoothed Transfer Function
Target frequencies
BWIR
Transfer Function
Frequency (Hz)
0
1
2
3
4
5
6
0.1
1
10
100

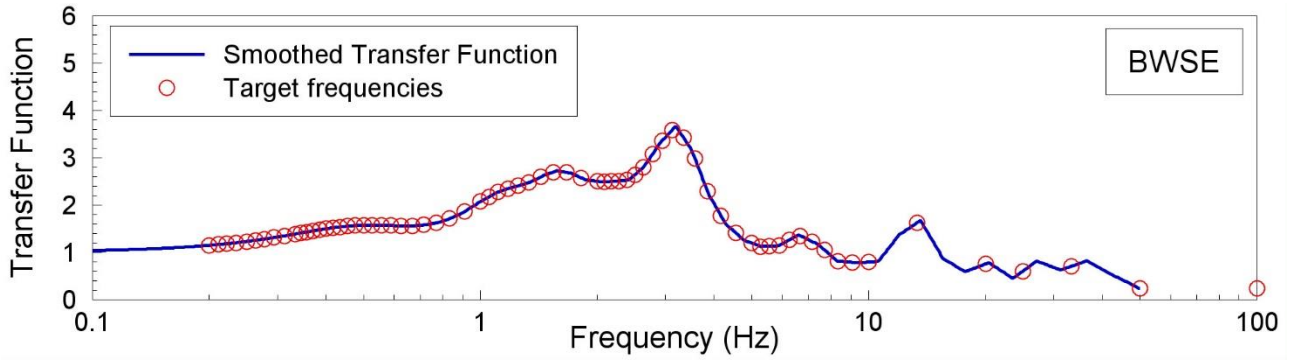
Smoothed Transfer Function
Target frequencies
BWSE
Transfer Function
Frequency (Hz)
0
1
2
3
4
5
6
0.1
1
10
100

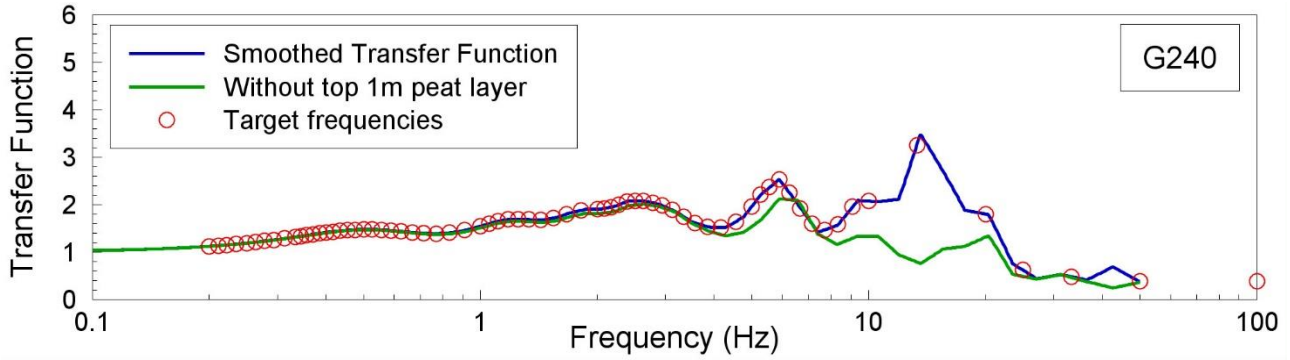
Smoothed Transfer Function
Without top 1m peat layer
Target frequencies
G240
Transfer Function
Frequency (Hz)
0
1
2
3
4
5
6
0.1
1
10
100

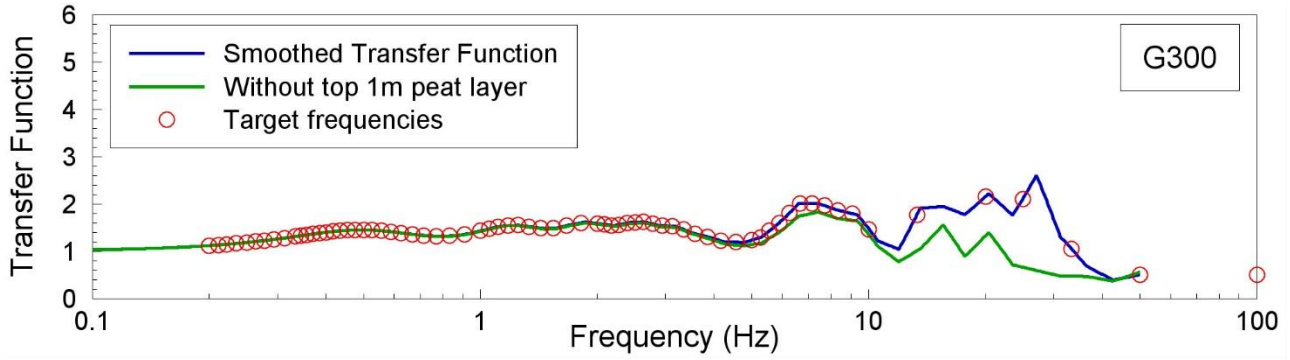
Smoothed Transfer Function
Without top 1m peat layer
Target frequencies
G300
Transfer Function
Frequency (Hz)
0
1
2
3
4
5
6
0.1
1
10
100

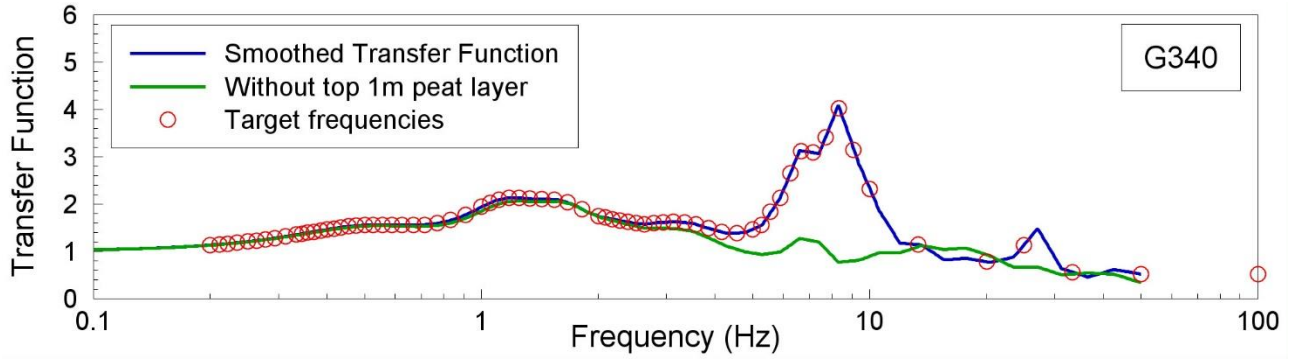
Smoothed Transfer Function
Without top 1m peat layer
Target frequencies
G340
Transfer Function
Frequency (Hz)
0
1
2
3
4
5
6
0.1
1
10
100

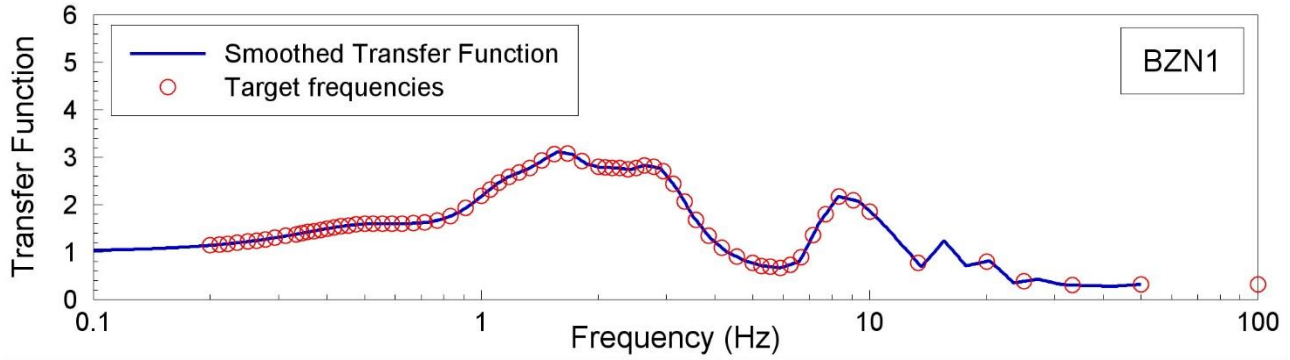
Smoothed Transfer Function
Target frequencies
BZN1
Transfer Function
Frequency (Hz)
0
1
2
3
4
5
6
0.1
1
10
100

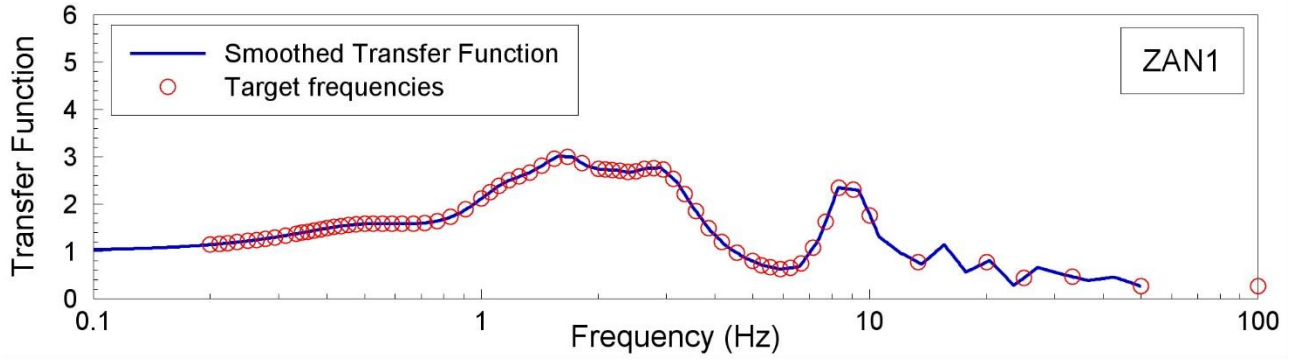
Smoothed Transfer Function
Target frequencies
ZAN1
Transfer Function
Frequency (Hz)
0
1
2
3
4
5
6
0.1
1
10
100

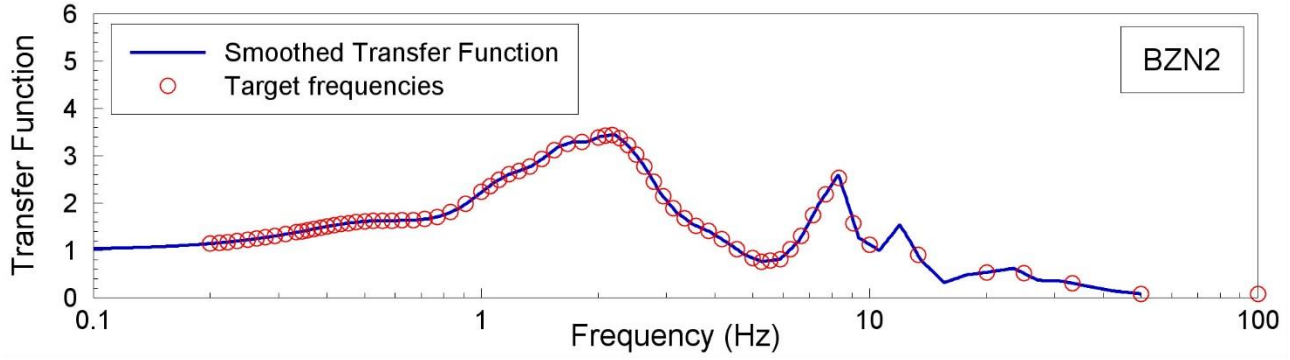
Smoothed Transfer Function
Target frequencies
BZN2
Transfer Function
Frequency (Hz)
0
1
2
3
4
5
6
0.1
1
10
100

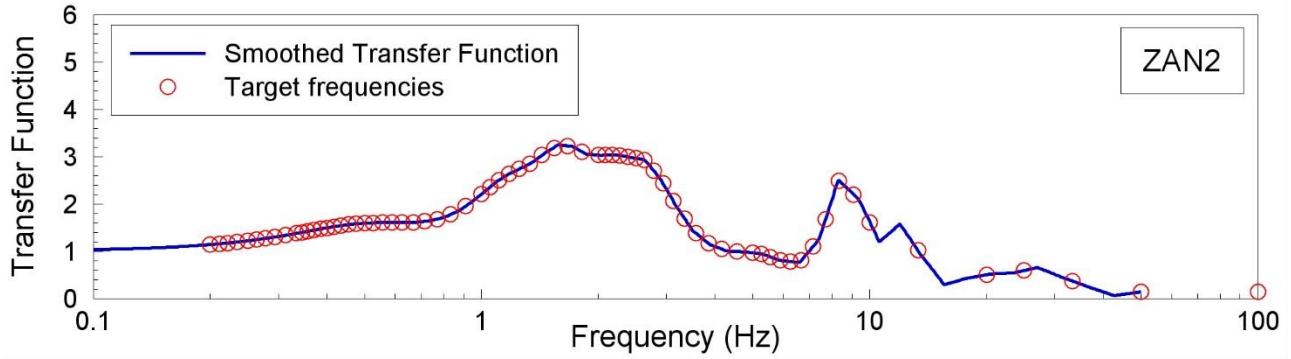
Smoothed Transfer Function
Target frequencies
ZAN2
Transfer Function
Frequency (Hz)
0
1
2
3
4
5
6
0.1
1
10
100

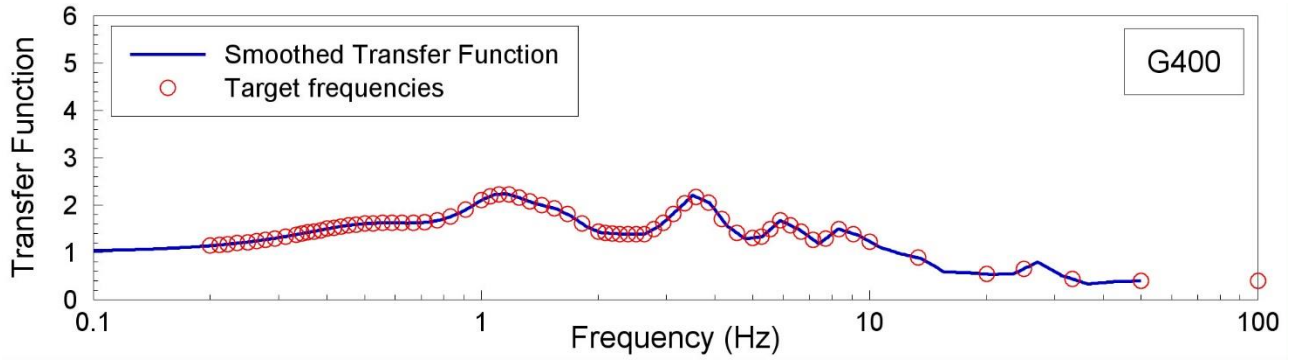
Smoothed Transfer Function
Target frequencies
G400
Transfer Function
Frequency (Hz)
0
1
2
3
4
5
6
0.1
1
10
100

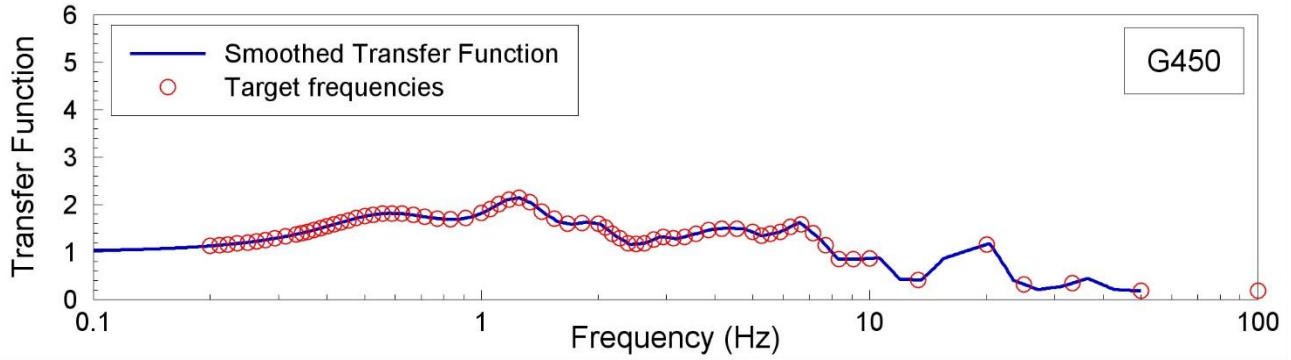
Smoothed Transfer Function
Target frequencies
G450
Transfer Function
Frequency (Hz)
0
1
2
3
4
5
6
0.1
1
10
100

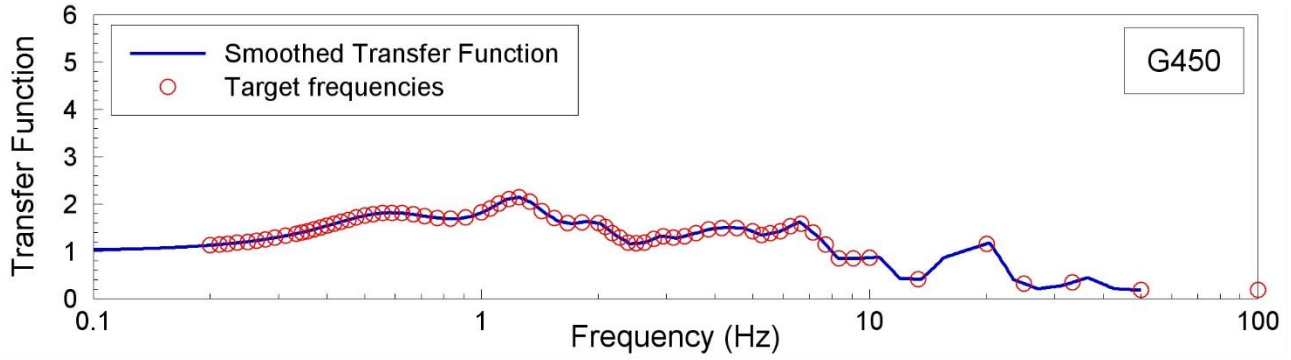
Smoothed Transfer Function
Target frequencies
G450
Transfer Function
Frequency (Hz)
0
1
2
3
4
5
6
0.1
1
10
100

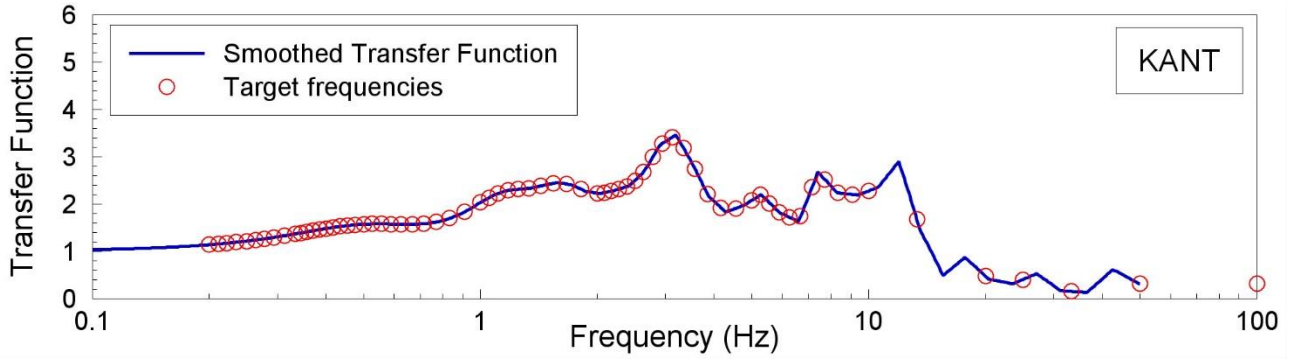
Smoothed Transfer Function
Target frequencies
KANT
Transfer Function
Frequency (Hz)
0
1
2
3
4
5
6
0.1
1
10
100

APPENDIX IV

Linear amplification functions for Sa(T) at recording stations

The following pages show plots of the linear amplification functions for response spectral ordinates calculated for the recording stations. On each plot, the 16 target response periods are indicated by circles. As for the transfer functions in Appendix III, in those cases where the uppermost peat layers are ignored in the calculation of the site amplification functions, the original and modified results are both shown.

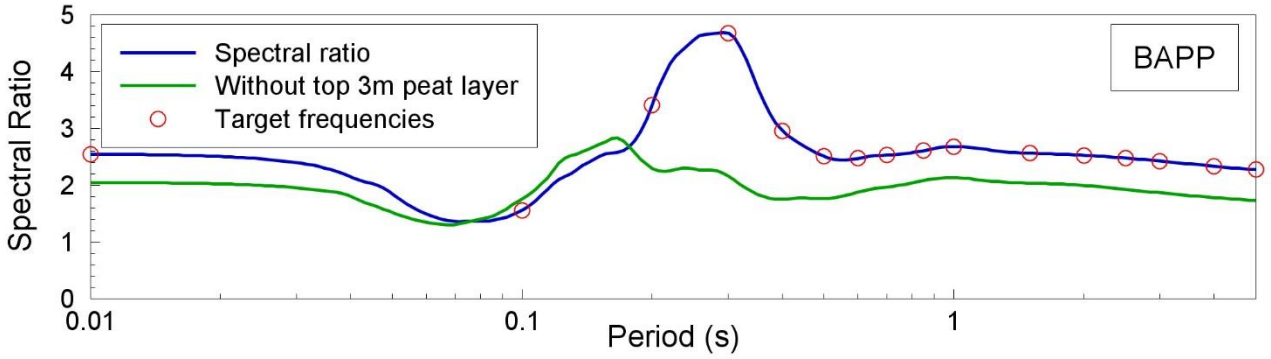
Spectral ratio
Without top 3m peat layer
Target frequencies
BAPP
Spectral Ratio
Period (s)
0.01
0.1
1
0
1
2
3
4
5

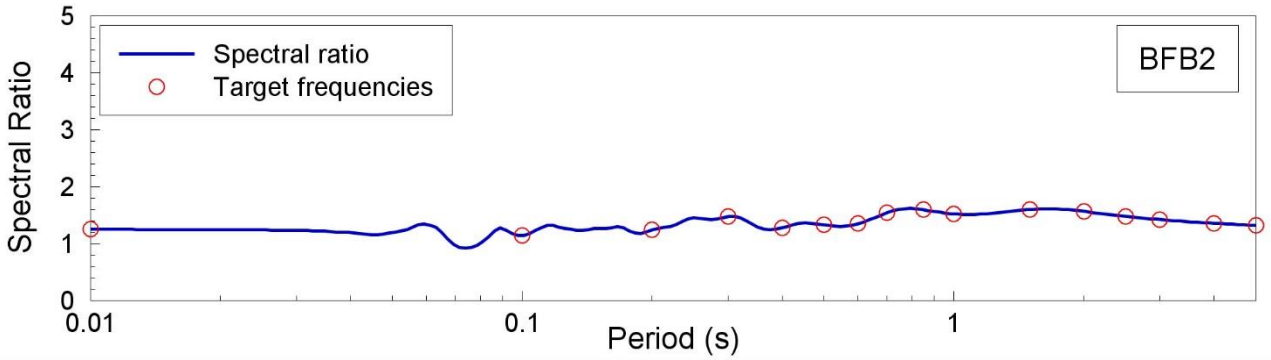
Spectral ratio
Target frequencies
BFB2
Spectral Ratio
Period (s)
0.01
0.1
1
0
1
2
3
4
5

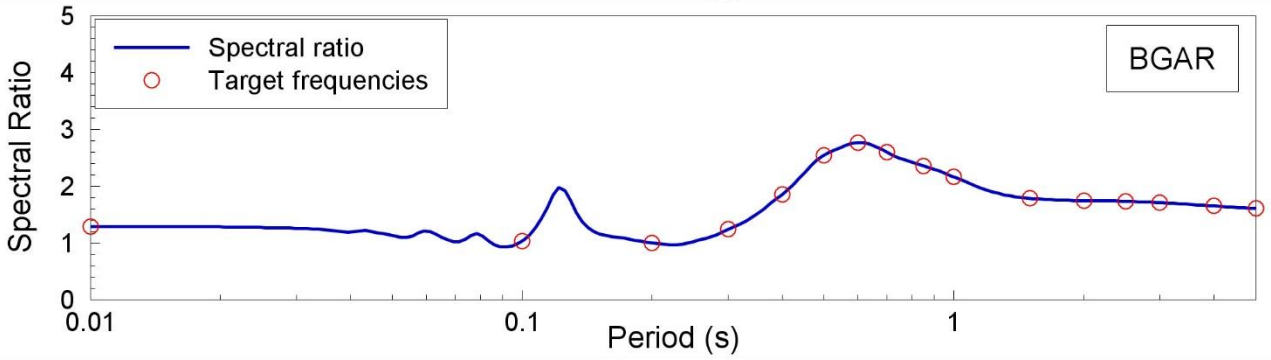
Spectral ratio
Target frequencies
BGAR
Spectral Ratio
Period (s)
0.01
0.1
1
0
1
2
3
4
5

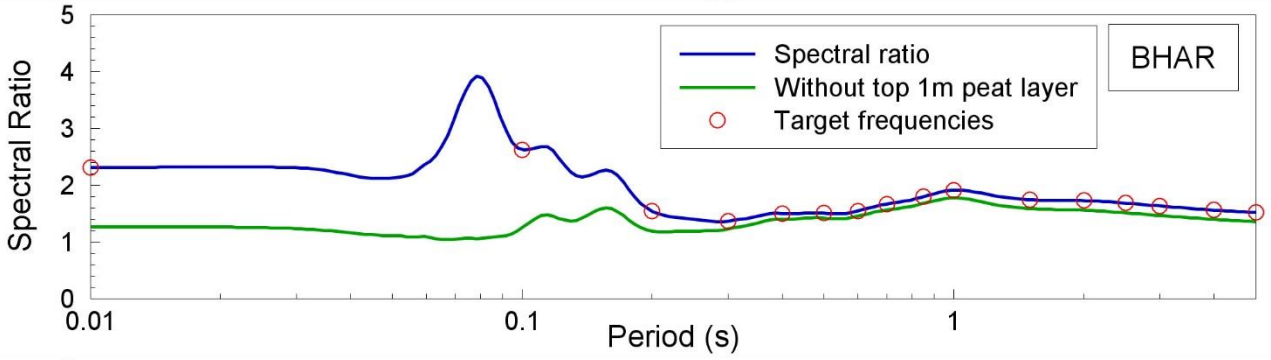
Spectral ratio
Without top 1m peat layer
Target frequencies
BHAR
Spectral Ratio
Period (s)
0.01
0.1
1
0
1
2
3
4
5

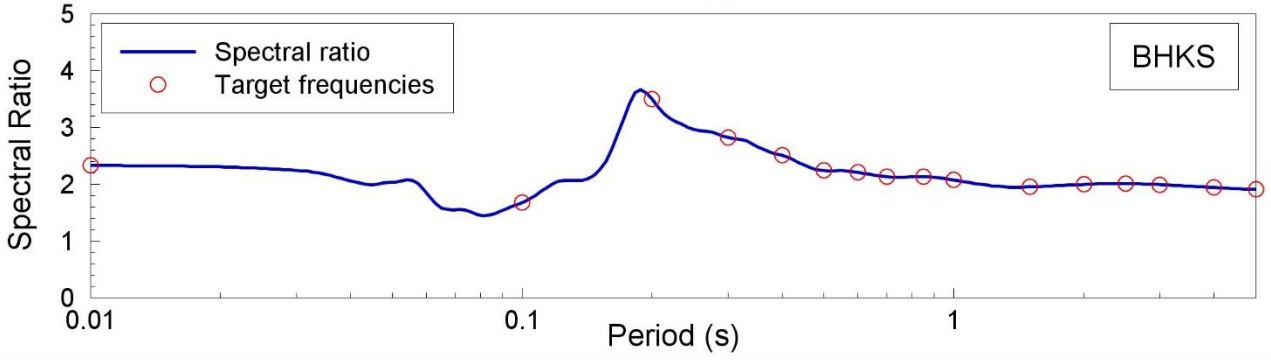
Spectral ratio
Target frequencies
BHKS
Spectral Ratio
Period (s)
0.01
0.1
1
0
1
2
3
4
5

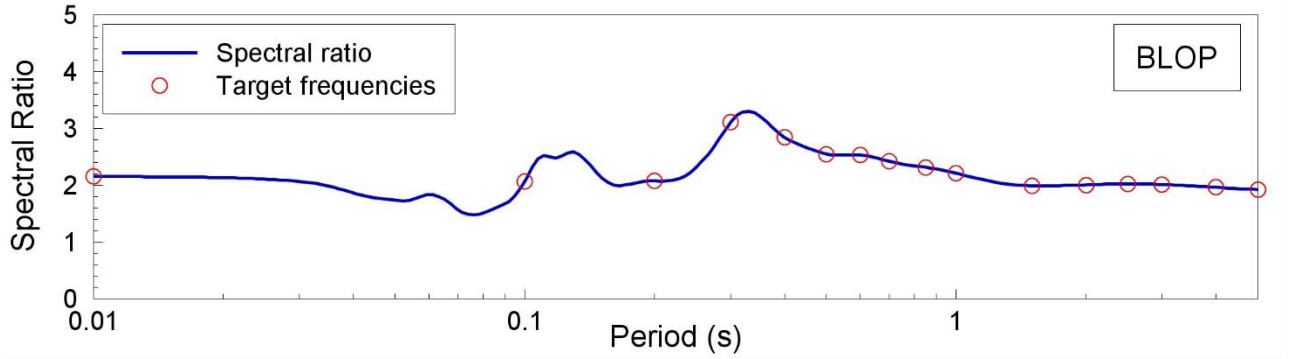
Spectral ratio
Target frequencies
BLOP
Spectral Ratio
Period (s)
0.01
0.1
1
0
1
2
3
4
5

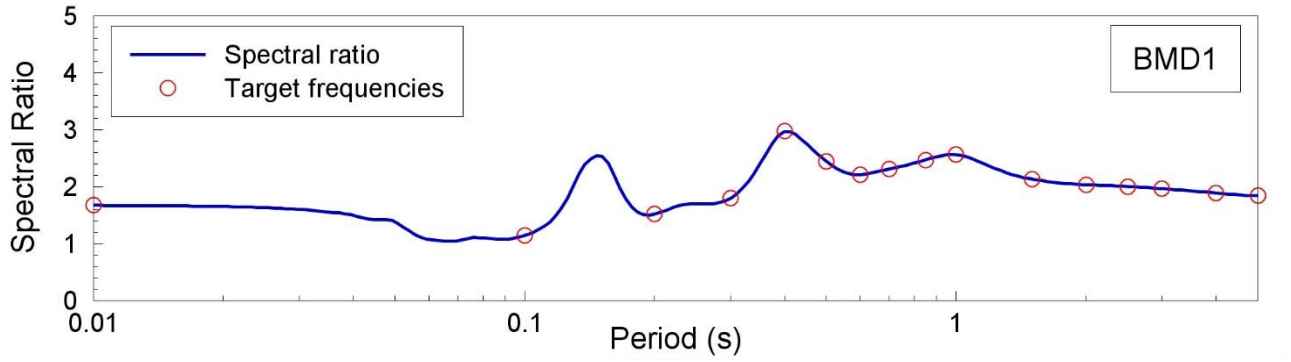
Spectral ratio
Target frequencies
BMD1
Spectral Ratio
Period (s)
0.01
0.1
1
0
1
2
3
4
5

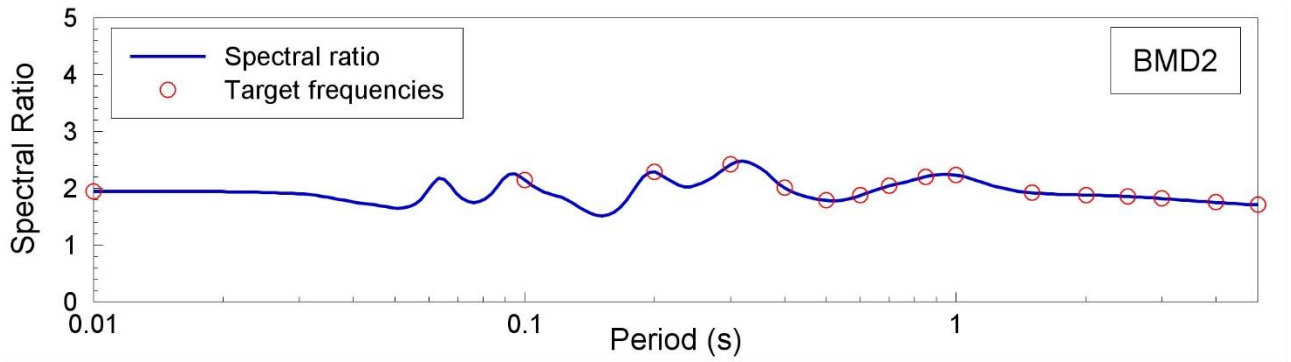
Spectral ratio
Target frequencies
BMD2
Spectral Ratio
Period (s)
0.01
0.1
1
0
1
2
3
4
5

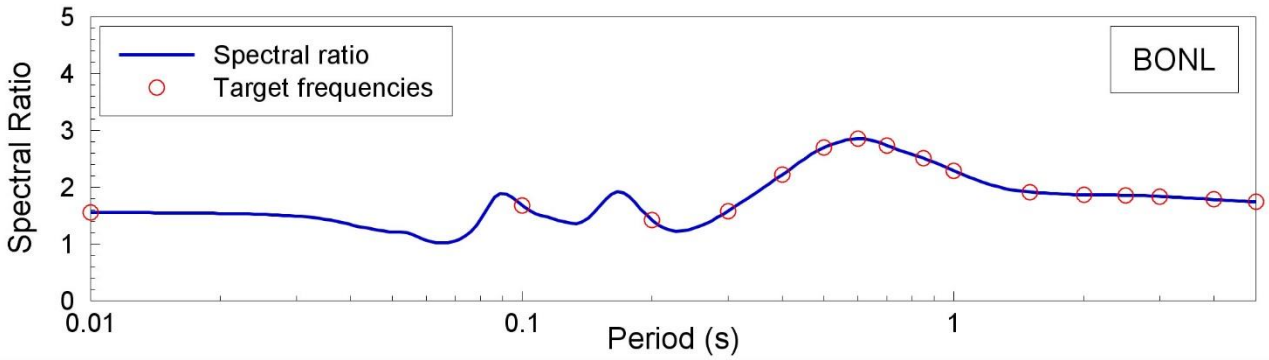
Spectral ratio
Target frequencies
BONL
Spectral Ratio
Period (s)
0.01
0.1
1
0
1
2
3
4
5

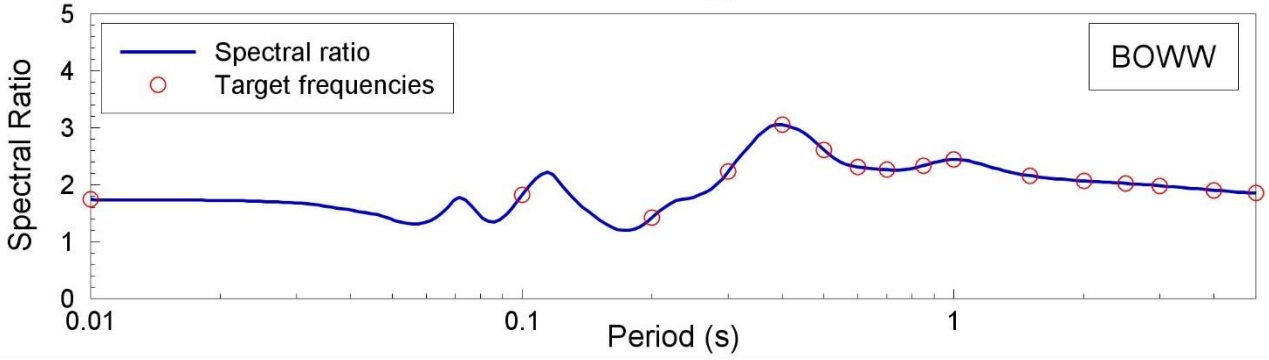
Spectral ratio
Target frequencies
BOWW
Spectral Ratio
Period (s)
0.01
0.1
1
0
1
2
3
4
5

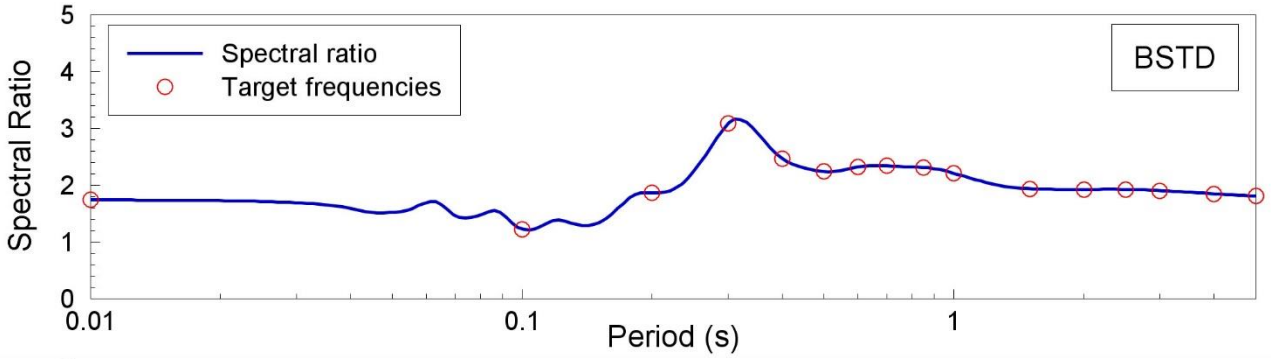
Spectral ratio
Target frequencies
BSTD
Spectral Ratio
Period (s)
0.01
0.1
1
0
1
2
3
4
5

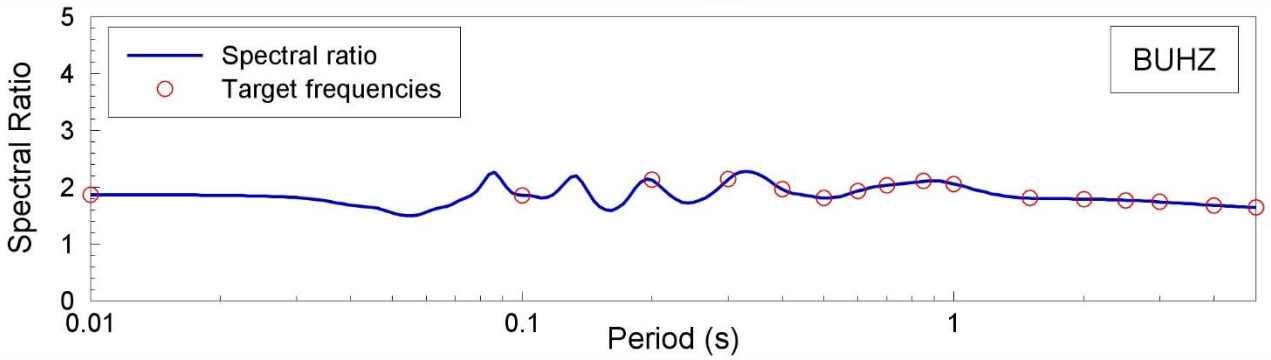
Spectral ratio
Target frequencies
BUHZ
Spectral Ratio
Period (s)
0.01
0.1
1
0
1
2
3
4
5

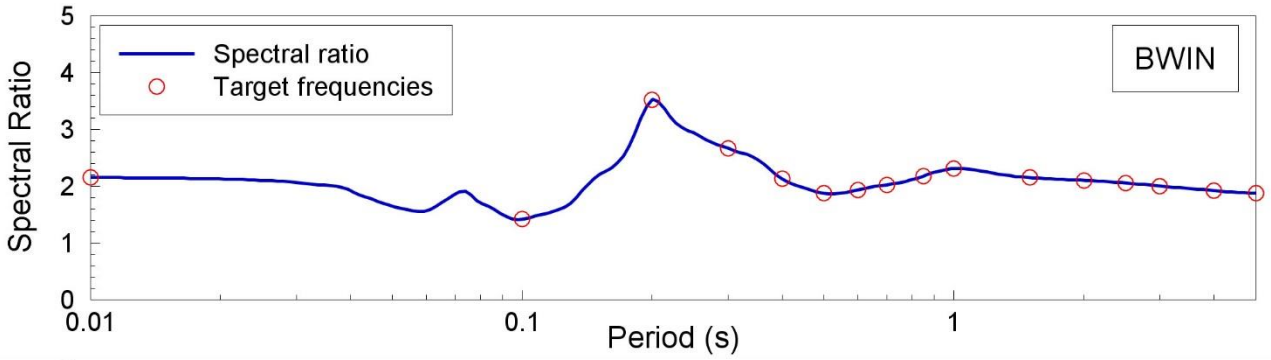
Spectral ratio
Target frequencies
BWIN
Spectral Ratio
Period (s)
0.01
0.1
1
0
1
2
3
4
5

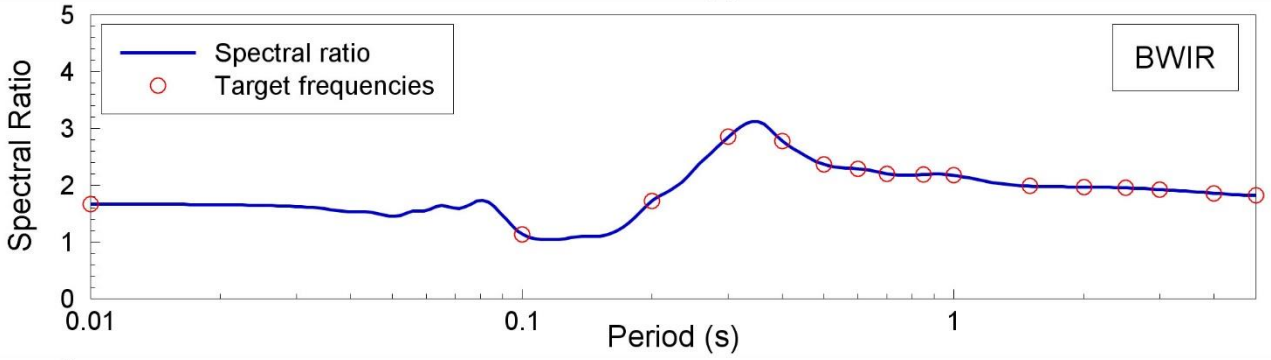
Spectral ratio
Target frequencies
BWIR
Spectral Ratio
Period (s)
0.01
0.1
1
0
1
2
3
4
5

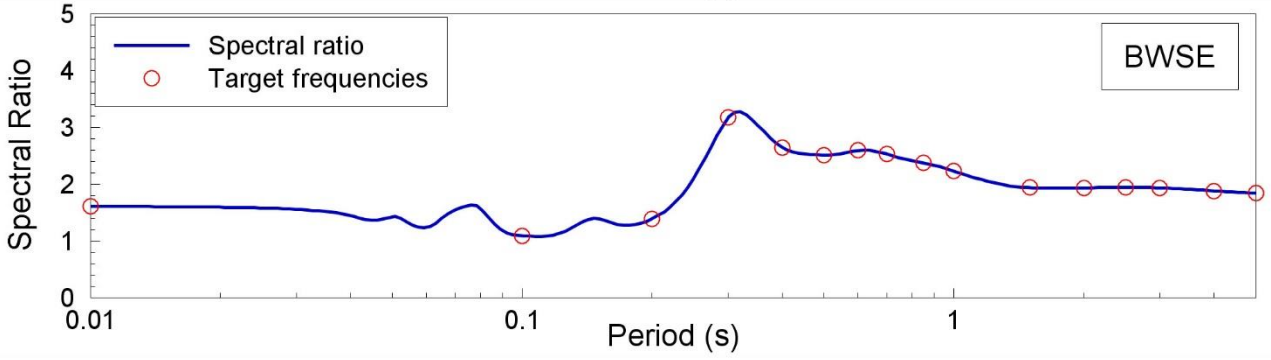
Spectral ratio
Target frequencies
BWSE
Spectral Ratio
Period (s)
0.01
0.1
1
0
1
2
3
4
5

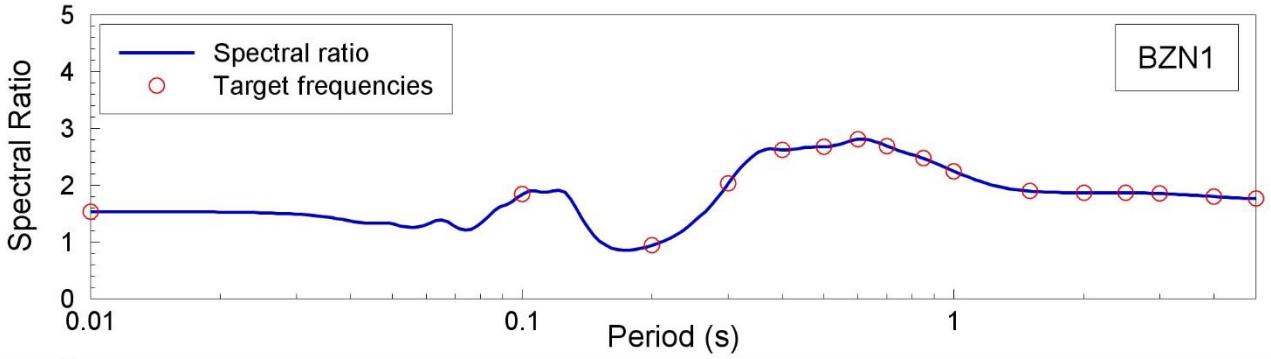
Spectral ratio
Target frequencies
BZN1
Spectral Ratio
Period (s)
0.01
0.1
1
0
1
2
3
4
5

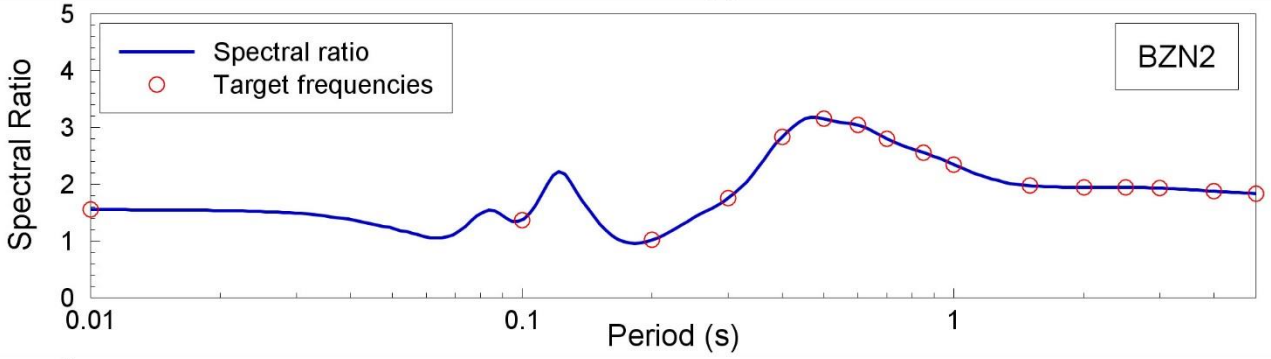
Spectral ratio
Target frequencies
BZN2
Spectral Ratio
Period (s)
0.01
0.1
1
0
1
2
3
4
5

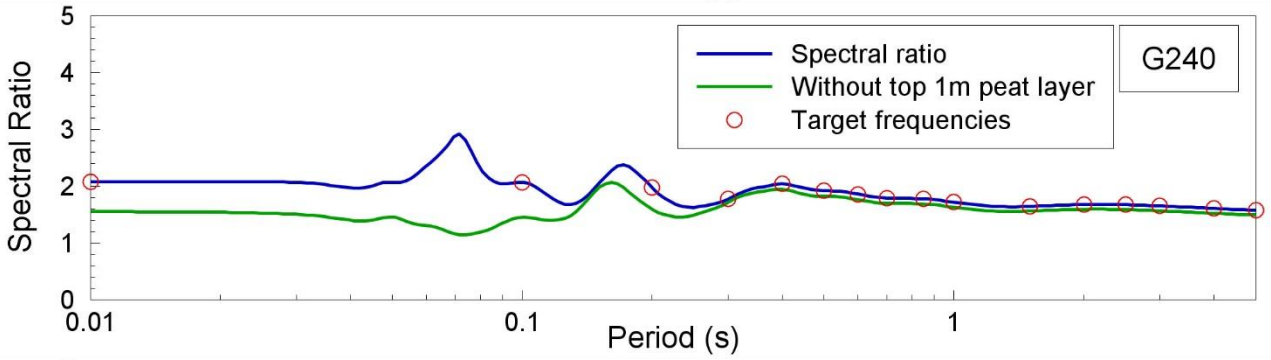
Spectral ratio
Without top 1m peat layer
Target frequencies
G240
Spectral Ratio
Period (s)
0.01
0.1
1
0
1
2
3
4
5

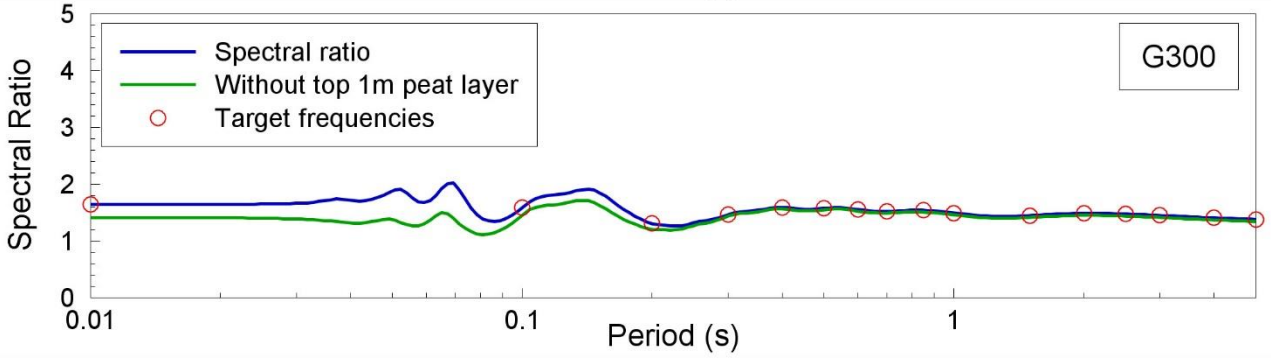
Spectral ratio
Without top 1m peat layer
Target frequencies
G300
Spectral Ratio
Period (s)
0.01
0.1
1
0
1
2
3
4
5

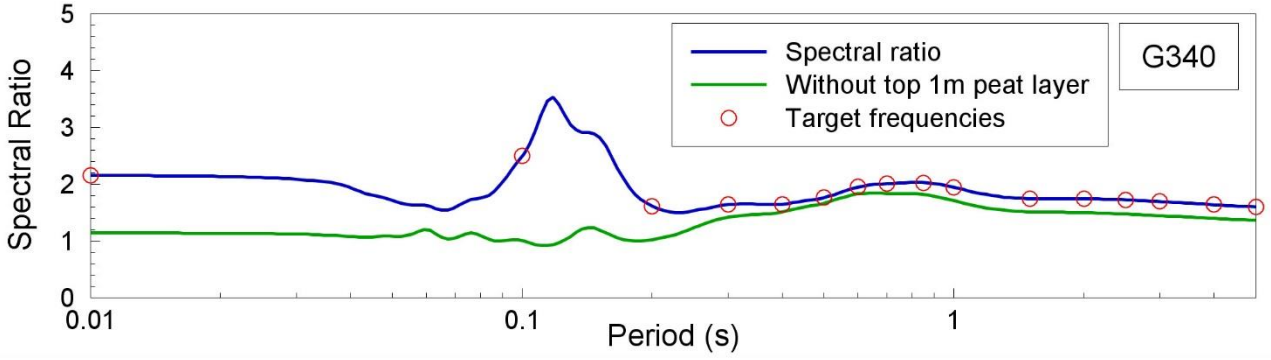
Spectral ratio
Without top 1m peat layer
Target frequencies
G340
Spectral Ratio
Period (s)
0.01
0.1
1
0
1
2
3
4
5

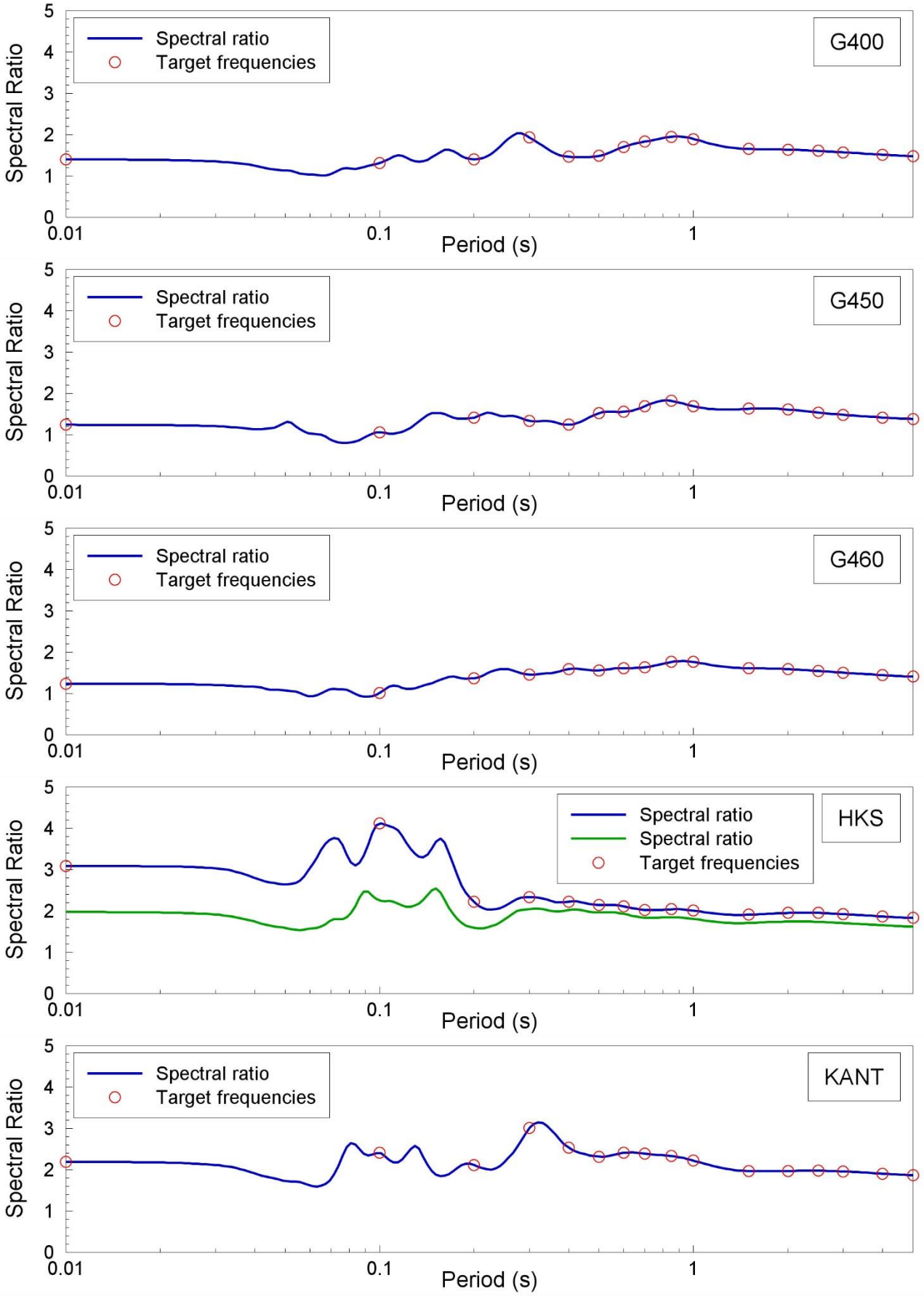
Spectral ratio
Target frequencies
G400
Spectral Ratio
Period (s)
0.01
0.1
1
0
1
2
3
4
5
Spectral ratio
Target frequencies
G450
Spectral Ratio
Period (s)
Spectral ratio
Target frequencies
G460
Spectral Ratio
Period (s)
Spectral ratio
Spectral ratio
Target frequencies
HKS
Spectral Ratio
Period (s)
Spectral ratio
Target frequencies
KANT
Spectral Ratio
Period (s)

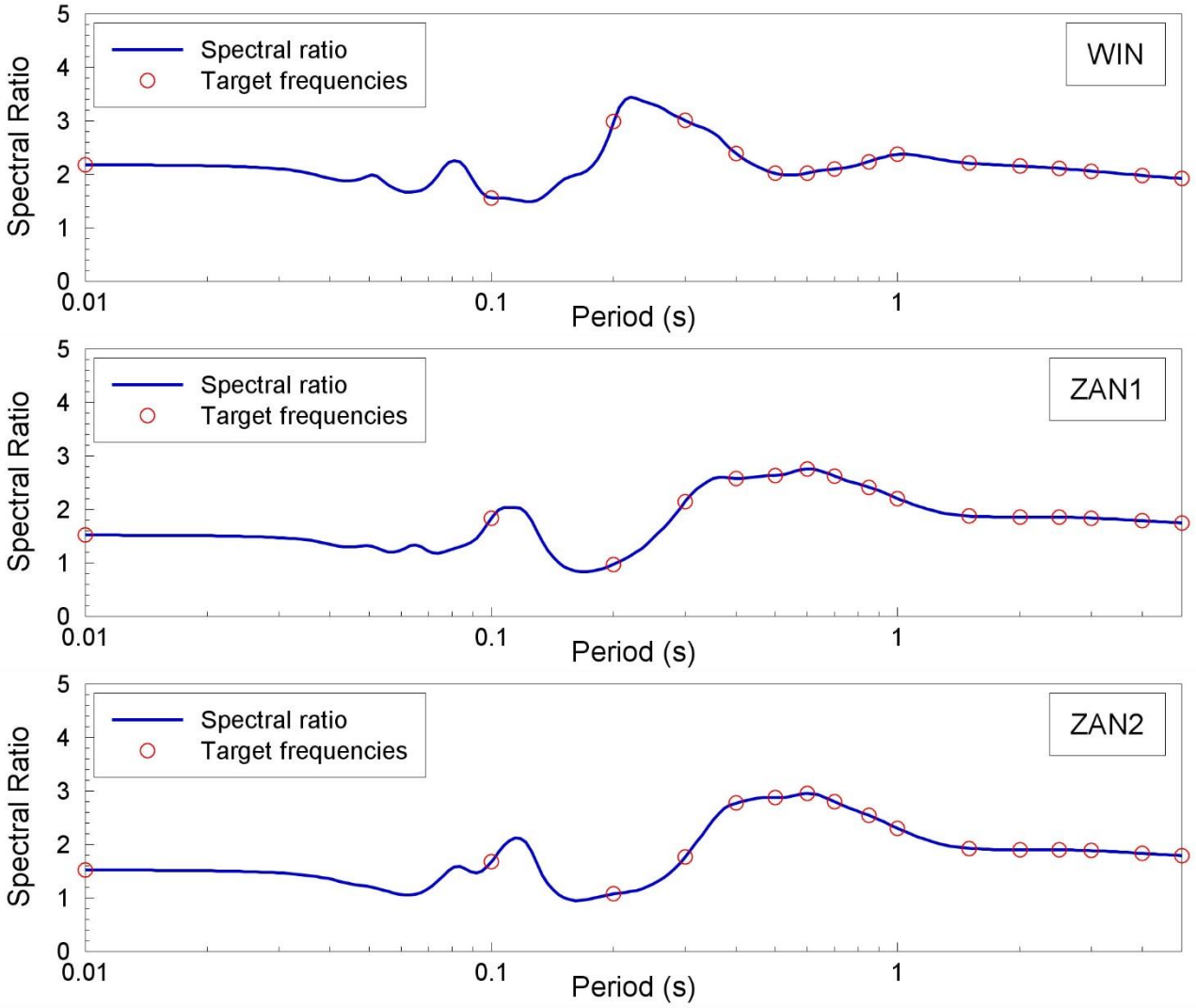
Spectral ratio
Target frequencies
WIN
Spectral Ratio
Period (s)
0.01
0.1
1
0
1
2
3
4
5
Spectral ratio
Target frequencies
ZAN1
Spectral Ratio
Period (s)
Spectral ratio
Target frequencies
ZAN2
Spectral Ratio
Period (s)

APPENDIX V

Spectral fits for corner frequency and stress drop

In the following pages plots are shown of the fit of the theoretical Brune spectrum to spectra of the surface recordings in the Groningen field. Each fit is made with event-specific source terms, path terms and NU_B level site-specific terms, together with influence of the Transfer Functions from the NU_B horizon to the surface (as presented in Appendix III). The station code and the date of the earthquake are given in the legend of each plot.

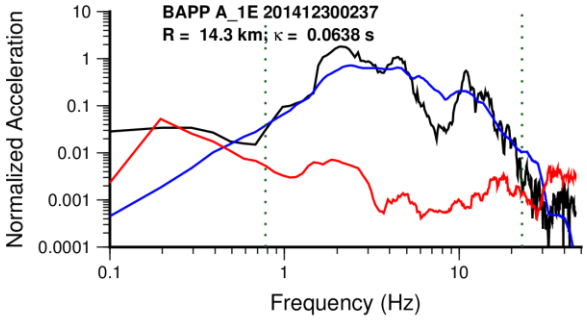
BAPP A_1E 201412300237
R = 14.3 km; κ = 0.0638 s
Normalized Acceleration
Frequency (Hz)

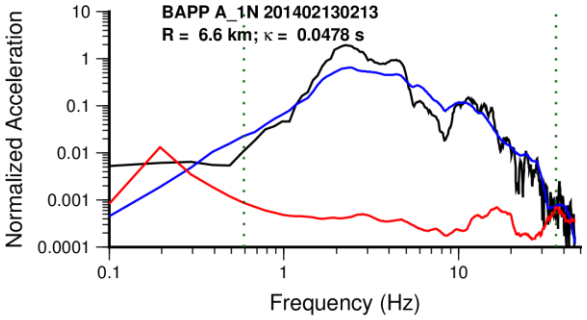
BAPP A_1N 201402130213
R = 6.6 km; κ = 0.0478 s
Normalized Acceleration
Frequency (Hz)

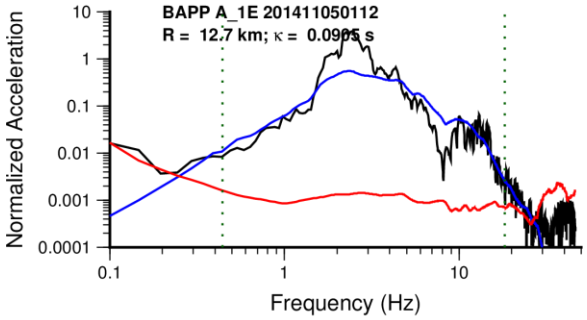
BAPP A_1E 201411050112
R = 12.7 km; κ = 0.0905 s
Normalized Acceleration
Frequency (Hz)

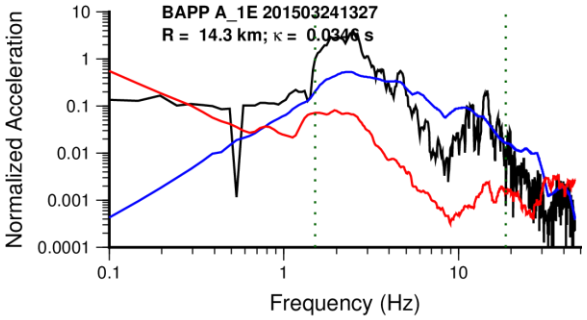
BAPP A_1E 201503241327
R = 14.3 km; κ = 0.0346 s
Normalized Acceleration
Frequency (Hz)

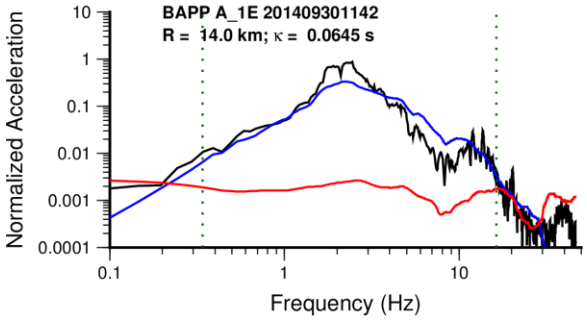
BAPP A_1E 201409301142
R = 14.0 km; κ = 0.0645 s
Normalized Acceleration
Frequency (Hz)

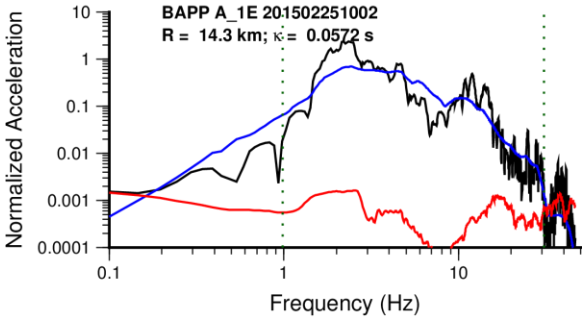
BAPP A_1E 201502251002
R = 14.3 km; κ = 0.0572 s
Normalized Acceleration
Frequency (Hz)

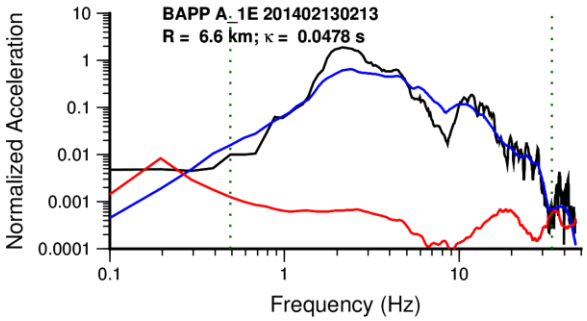
BAPP A_1E 201402130213
R = 6.6 km; κ = 0.0478 s
Normalized Acceleration
Frequency (Hz)

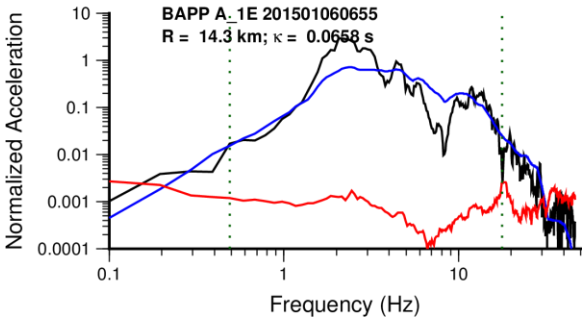
BAPP A_1E 201501060655
R = 14.3 km; κ = 0.0658 s
Normalized Acceleration
Frequency (Hz)

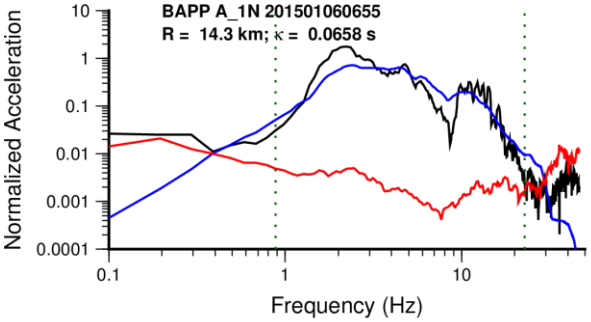
BAPP A_1N 201501060655
R = 14.3 km; κ = 0.0658 s
Normalized Acceleration
Frequency (Hz)

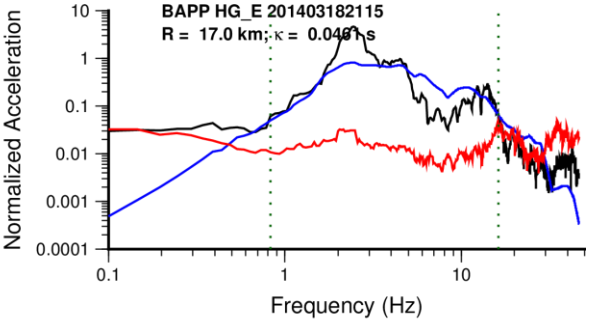
BAPP HG_E 201403182115
R = 17.0 km; κ = 0.0461 s
Normalized Acceleration
Frequency (Hz)

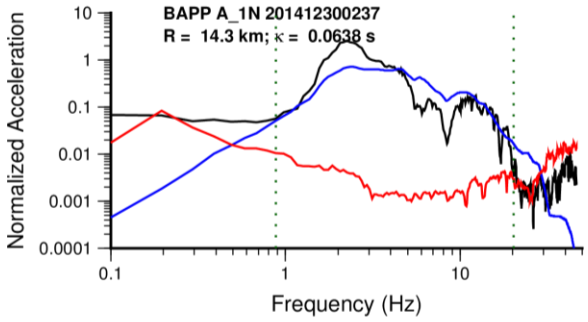
BAPP A_1N 201412300237
R = 14.3 km; κ = 0.0638 s
Normalized Acceleration
Frequency (Hz)

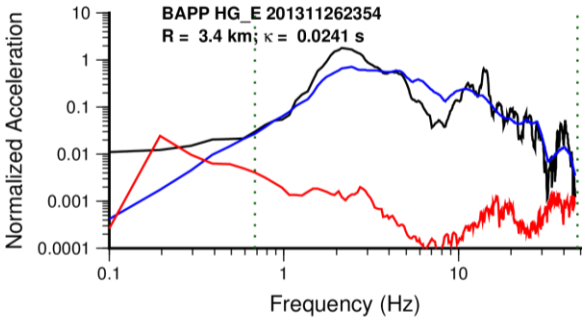
BAPP HG_E 201311262354
R = 3.4 km; κ = 0.0241 s
Normalized Acceleration
Frequency (Hz)

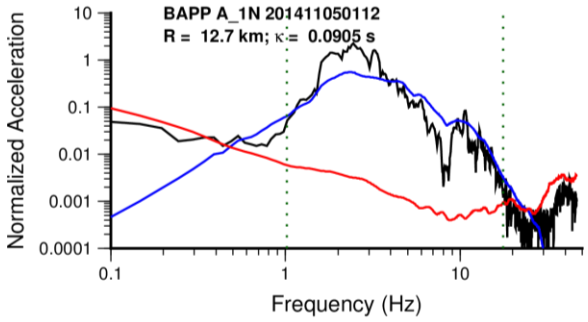
BAPP A_1N 201411050112
R = 12.7 km; κ = 0.0905 s
Normalized Acceleration
Frequency (Hz)

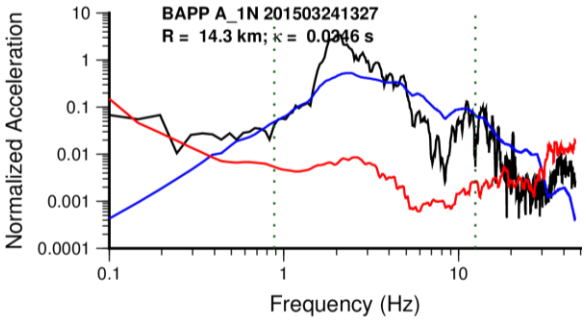
BAPP A_1N 201503241327
R = 14.3 km; κ = 0.0346 s
Normalized Acceleration
Frequency (Hz)

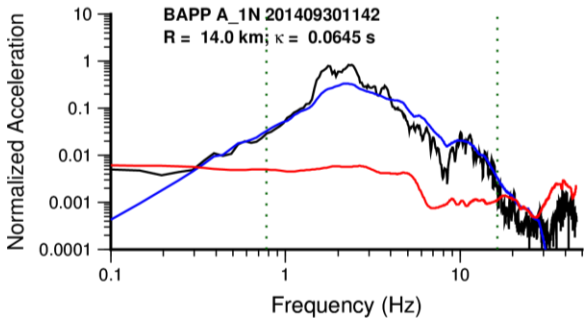
BAPP A_1N 201409301142
R = 14.0 km; κ = 0.0645 s
Normalized Acceleration
Frequency (Hz)

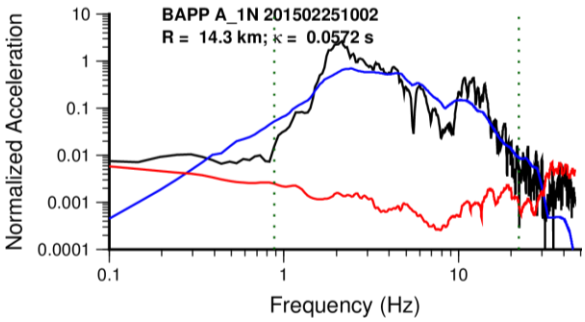
BAPP A_1N 201502251002
R = 14.3 km; κ = 0.0572 s
Normalized Acceleration
Frequency (Hz)

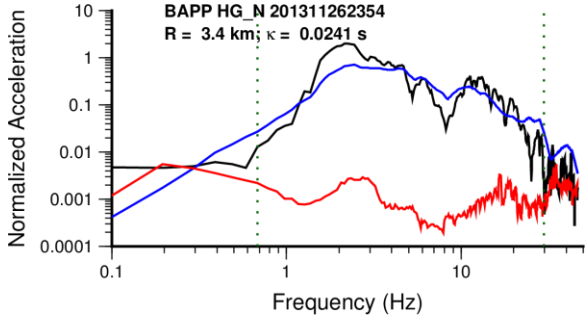
BAPP HG_N 201311262354
R = 3.4 km; κ = 0.0241 s
Normalized Acceleration
Frequency (Hz)

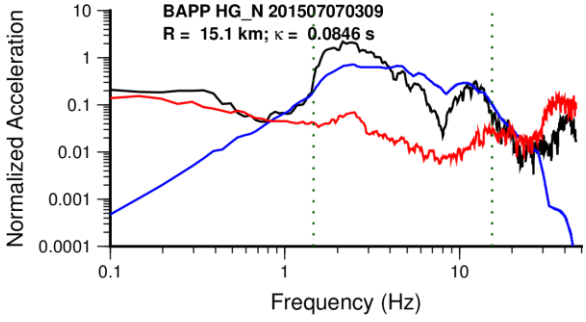
BAPP HG_N 201507070309
R = 15.1 km; κ = 0.0846 s
Normalized Acceleration
Frequency (Hz)

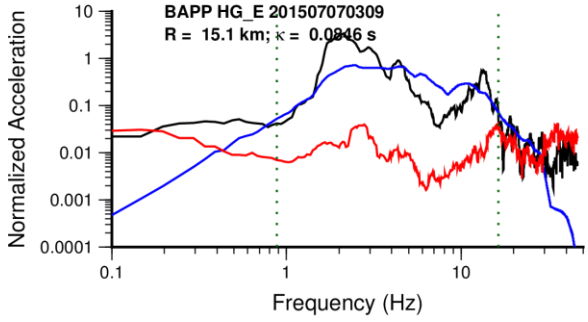
BAPP HG_E 201507070309
R = 15.1 km; κ = 0.0846 s
Normalized Acceleration
Frequency (Hz)

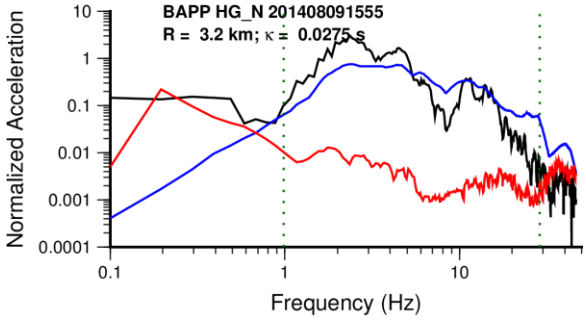
BAPP HG_N 201408091555
R = 3.2 km; κ = 0.0275 s
Normalized Acceleration
Frequency (Hz)

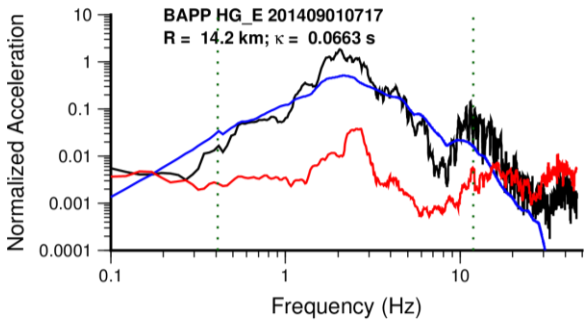
BAPP HG_E 201409010717
R = 14.2 km; κ = 0.0663 s
Normalized Acceleration
Frequency (Hz)

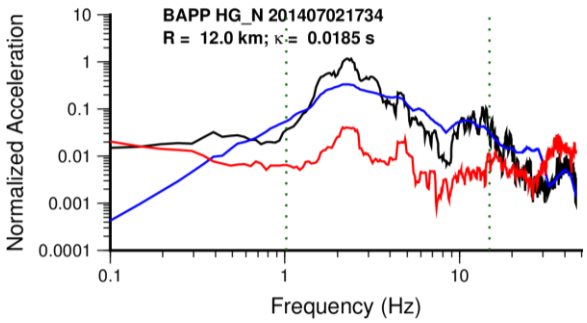
BAPP HG_N 201407021734
R = 12.0 km; κ = 0.0185 s
Normalized Acceleration
Frequency (Hz)

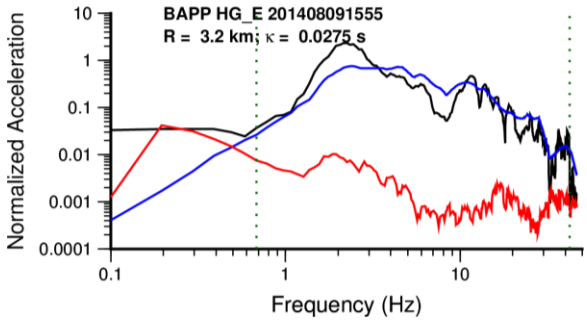
BAPP HG_E 201408091555
R = 3.2 km; κ = 0.0275 s
Normalized Acceleration
Frequency (Hz)

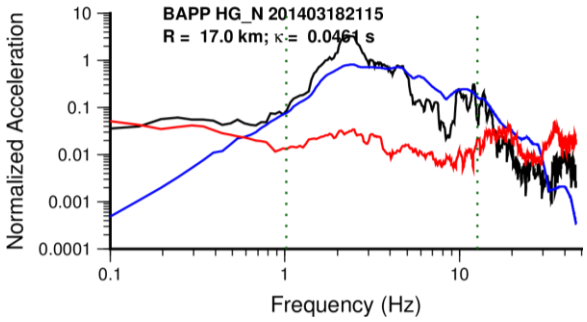
BAPP HG_N 201403182115
R = 17.0 km; κ = 0.0461 s
Normalized Acceleration
Frequency (Hz)

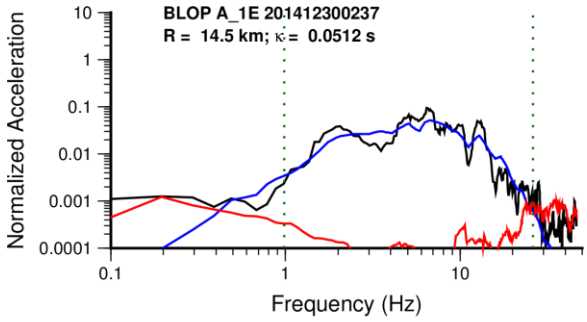
BLOP A_1E 201412300237
R = 14.5 km; κ = 0.0512 s
Normalized Acceleration
Frequency (Hz)

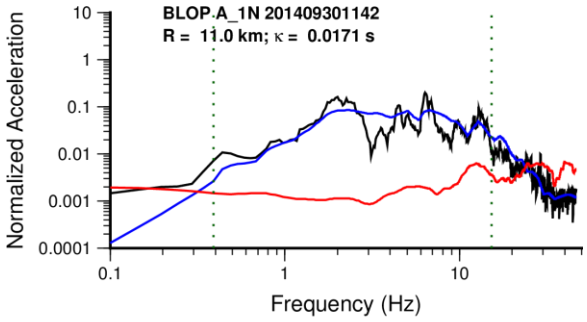
BLOP A_1N 201409301142
R = 11.0 km; κ = 0.0171 s
Normalized Acceleration
Frequency (Hz)

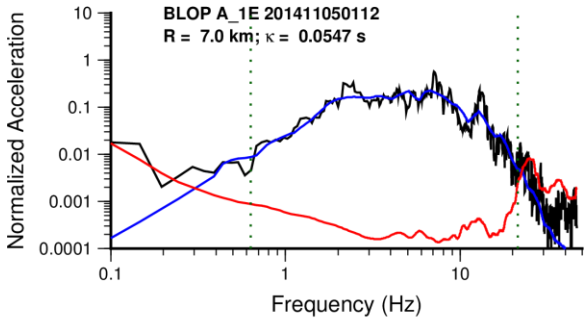
BLOP A_1E 201411050112
R = 7.0 km; κ = 0.0547 s
Normalized Acceleration
Frequency (Hz)

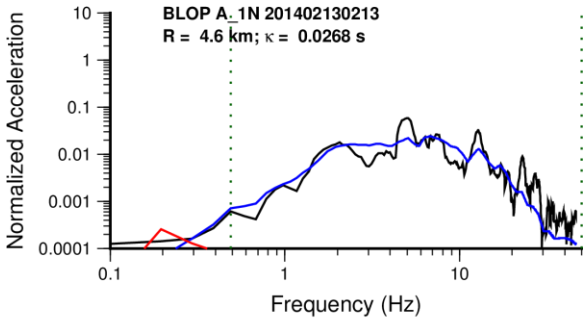
BLOP A_1N 201402130213
R = 4.6 km; κ = 0.0268 s
Normalized Acceleration
Frequency (Hz)

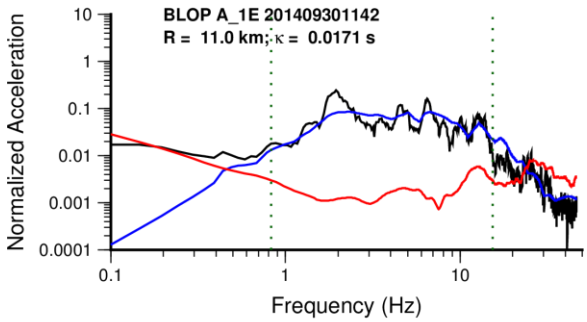
BLOP A_1E 201409301142
R = 11.0 km; κ = 0.0171 s
Normalized Acceleration
Frequency (Hz)

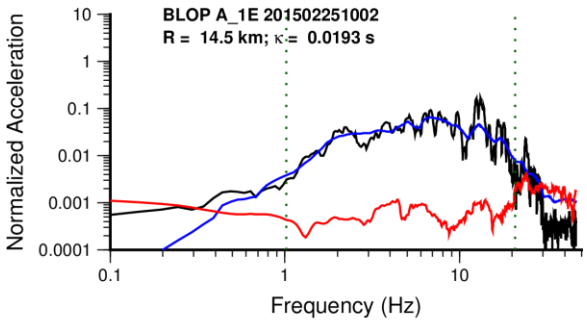
BLOP A_1E 201502251002
R = 14.5 km; κ = 0.0193 s
Normalized Acceleration
Frequency (Hz)

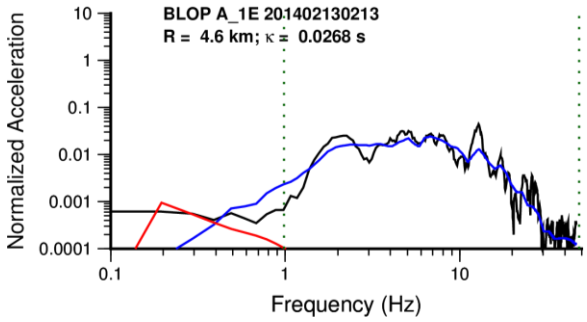
BLOP A_1E 201402130213
R = 4.6 km; κ = 0.0268 s
Normalized Acceleration
Frequency (Hz)

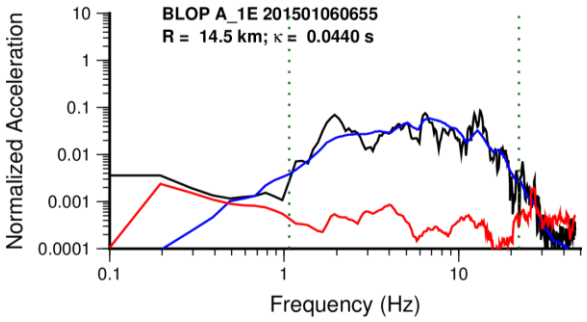
BLOP A_1E 201501060655
R = 14.5 km; κ = 0.0440 s
Normalized Acceleration
Frequency (Hz)

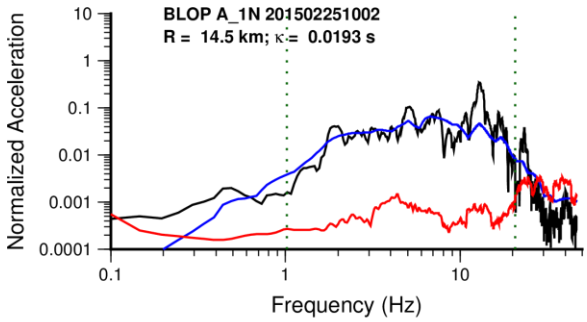
BLOP A_1N 201502251002
R = 14.5 km; κ = 0.0193 s
Normalized Acceleration
Frequency (Hz)

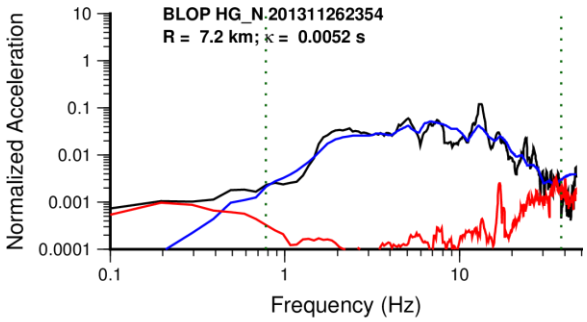
BLOP HG_N 201311262354
R = 7.2 km; κ = 0.0052 s
Normalized Acceleration
Frequency (Hz)

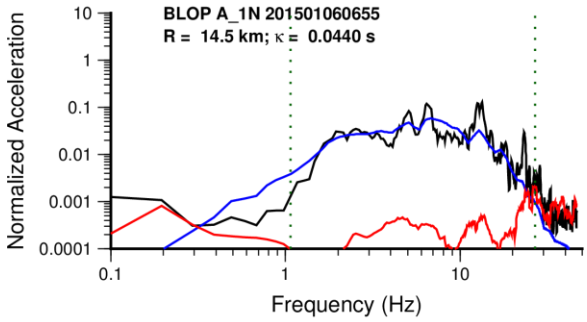
BLOP A_1N 201501060655
R = 14.5 km; κ = 0.0440 s
Normalized Acceleration
Frequency (Hz)

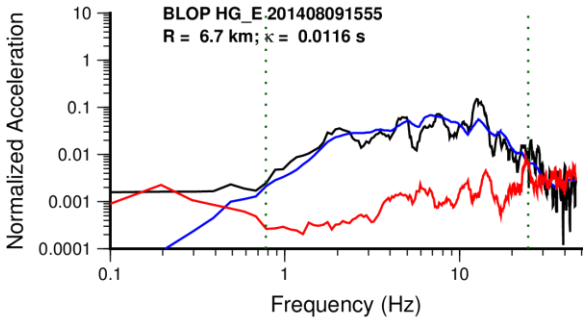
BLOP HG_E 201408091555
R = 6.7 km; κ = 0.0116 s
Normalized Acceleration
Frequency (Hz)

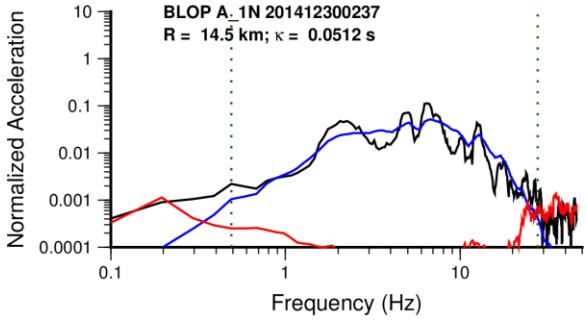
BLOP A_1N 201412300237
R = 14.5 km; κ = 0.0512 s
Normalized Acceleration
Frequency (Hz)

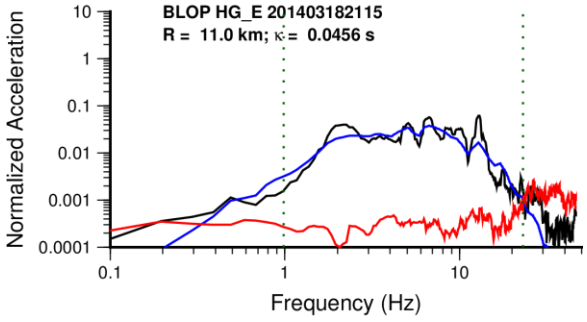
BLOP HG_E 201403182115
R = 11.0 km; κ = 0.0456 s
Normalized Acceleration
Frequency (Hz)

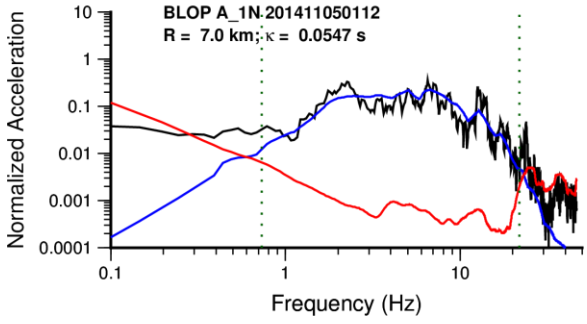
BLOP A_1N 201411050112
R = 7.0 km; κ = 0.0547 s
Normalized Acceleration
Frequency (Hz)

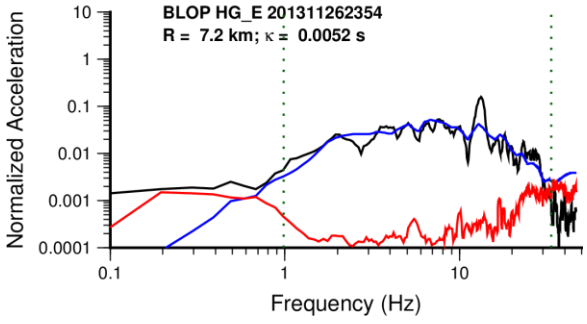
BLOP HG_E 201311262354
R = 7.2 km; κ = 0.0052 s
Normalized Acceleration
Frequency (Hz)

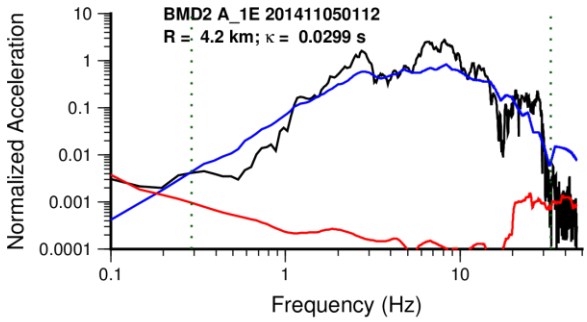
BMD2 A_1E 201411050112
R = 4.2 km; κ = 0.0299 s
Normalized Acceleration
Frequency (Hz)

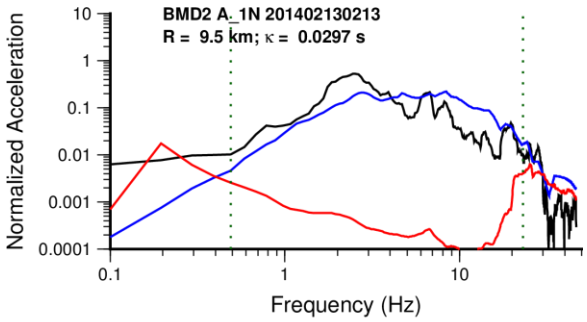
BMD2 A_1N 201402130213
R = 9.5 km; κ = 0.0297 s
Normalized Acceleration
Frequency (Hz)

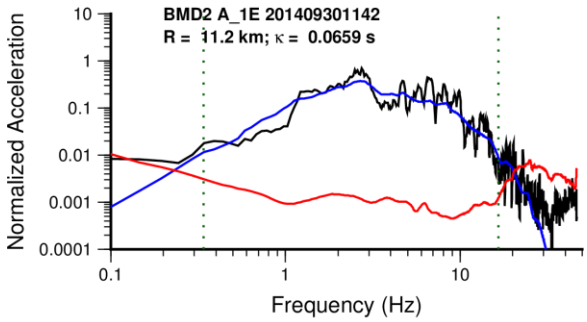
BMD2 A_1E 201409301142
R = 11.2 km; κ = 0.0659 s
Normalized Acceleration
Frequency (Hz)

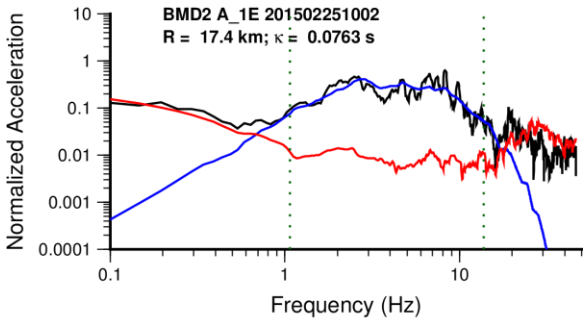
BMD2 A_1E 201502251002
R = 17.4 km; κ = 0.0763 s
Normalized Acceleration
Frequency (Hz)

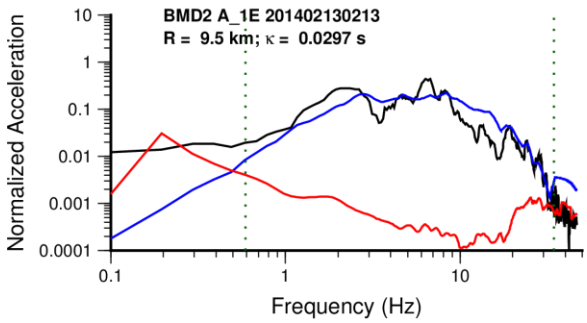
BMD2 A_1E 201402130213
R = 9.5 km; κ = 0.0297 s
Normalized Acceleration
Frequency (Hz)

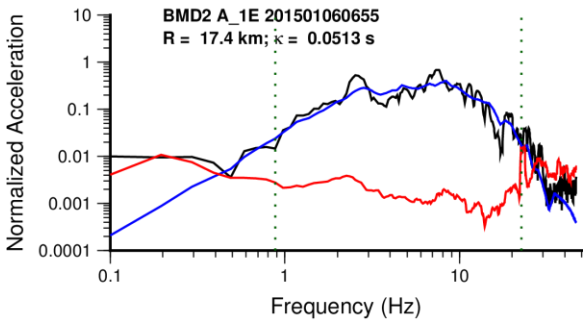
BMD2 A_1E 201501060655
R = 17.4 km; κ = 0.0513 s
Normalized Acceleration
Frequency (Hz)

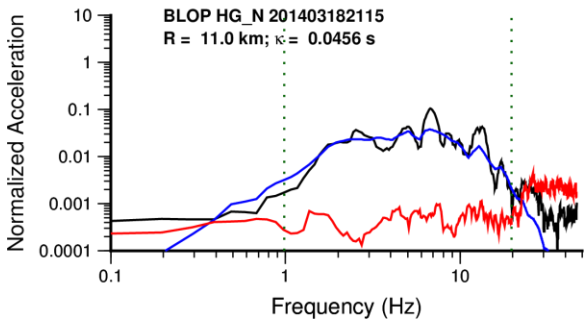
BLOP HG_N 201403182115
R = 11.0 km; κ = 0.0456 s
Normalized Acceleration
Frequency (Hz)

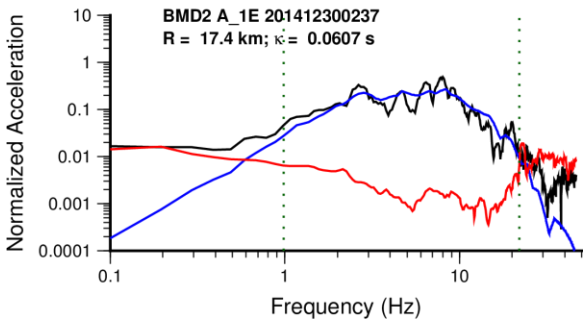
BMD2 A_1E 201412300237
R = 17.4 km; κ = 0.0607 s
Normalized Acceleration
Frequency (Hz)

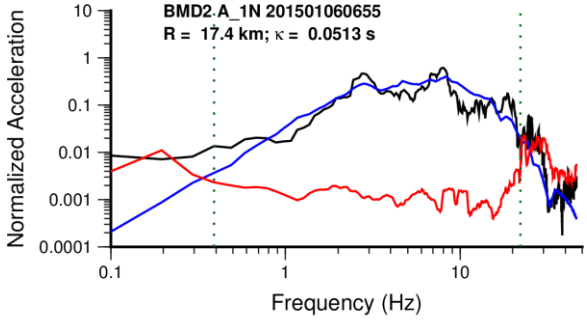
BMD2 A_1N 201501060655
R = 17.4 km; κ = 0.0513 s
Normalized Acceleration
Frequency (Hz)

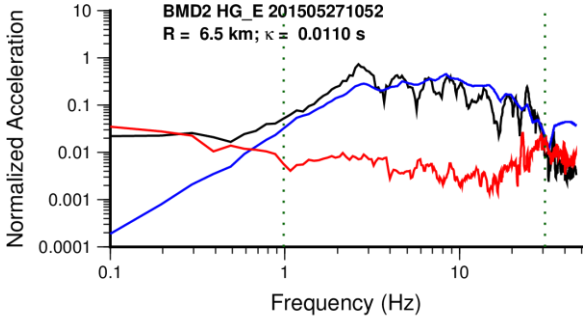
BMD2 HG_E 201505271052
R = 6.5 km; κ = 0.0110 s
Normalized Acceleration
Frequency (Hz)

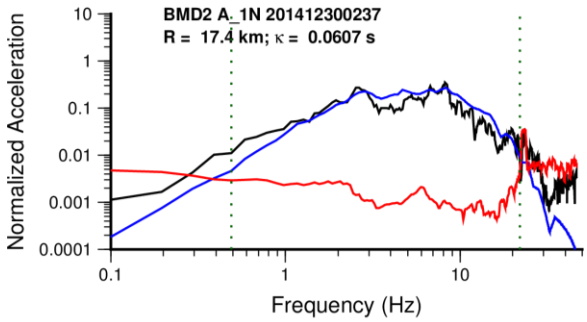
BMD2 A_1N 201412300237
R = 17.4 km; κ = 0.0607 s
Normalized Acceleration
Frequency (Hz)

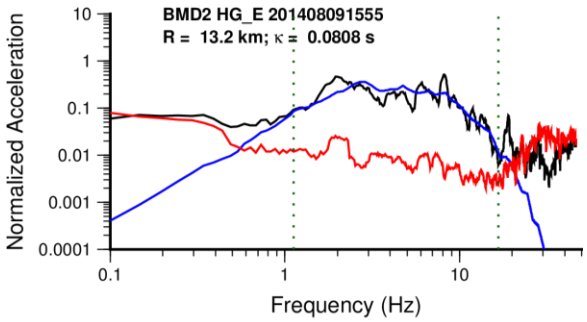
BMD2 HG_E 201408091555
R = 13.2 km; κ = 0.0808 s
Normalized Acceleration
Frequency (Hz)

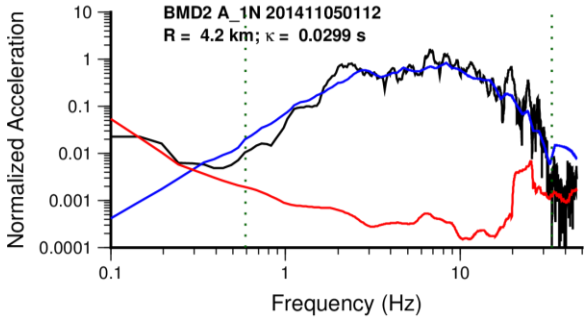
BMD2 A_1N 201411050112
R = 4.2 km; κ = 0.0299 s
Normalized Acceleration
Frequency (Hz)

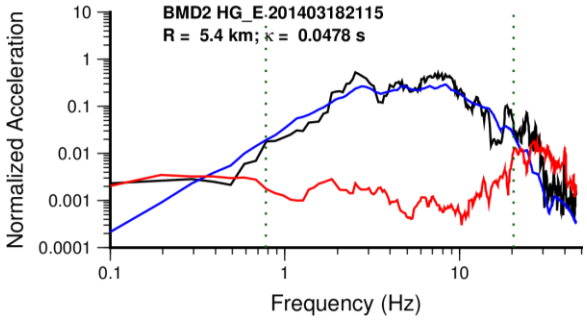
BMD2 HG_E 201403182115
R = 5.4 km; κ = 0.0478 s
Normalized Acceleration
Frequency (Hz)

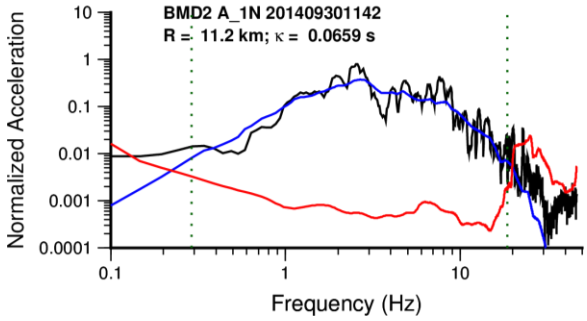
BMD2 A_1N 201409301142
R = 11.2 km; κ = 0.0659 s
Normalized Acceleration
Frequency (Hz)

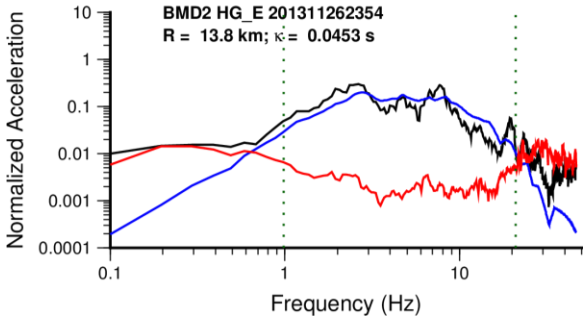
BMD2 HG_E 201311262354
R = 13.8 km; κ = 0.0453 s
Normalized Acceleration
Frequency (Hz)

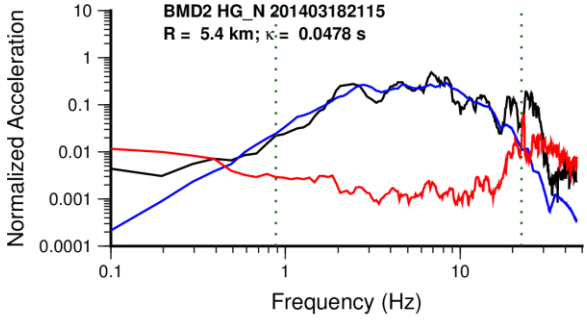
BMD2 HG_N 201403182115
R = 5.4 km; κ = 0.0478 s
Normalized Acceleration
Frequency (Hz)

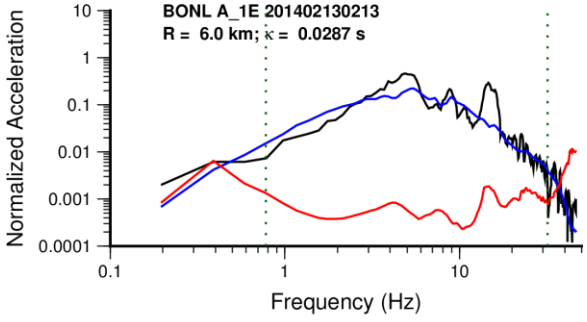
BONL A_1E 201402130213
R = 6.0 km; κ = 0.0287 s
Normalized Acceleration
Frequency (Hz)

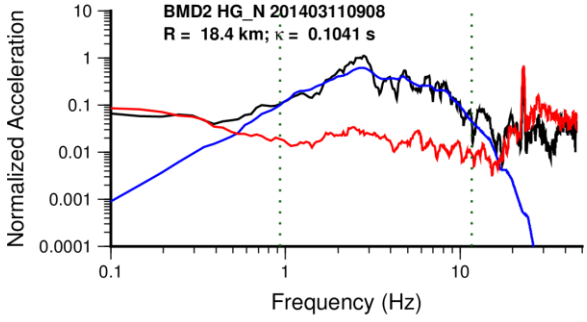
BMD2 HG_N 201403110908
R = 18.4 km; κ = 0.1041 s
Normalized Acceleration
Frequency (Hz)

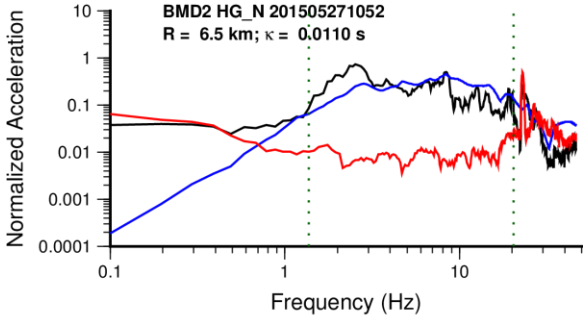
BMD2 HG_N 201505271052
R = 6.5 km; κ = 0.0110 s
Normalized Acceleration
Frequency (Hz)

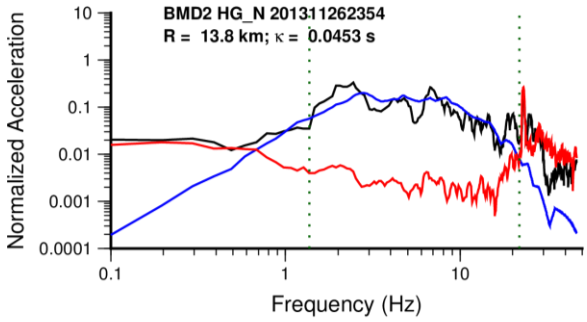
BMD2 HG_N 201311262354
R = 13.8 km; κ = 0.0453 s
Normalized Acceleration
Frequency (Hz)

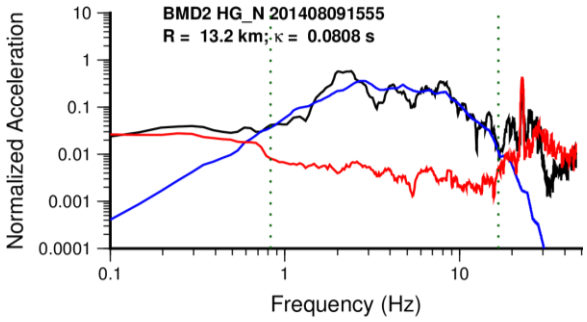
BMD2 HG_N 201408091555
R = 13.2 km; κ = 0.0808 s
Normalized Acceleration
Frequency (Hz)

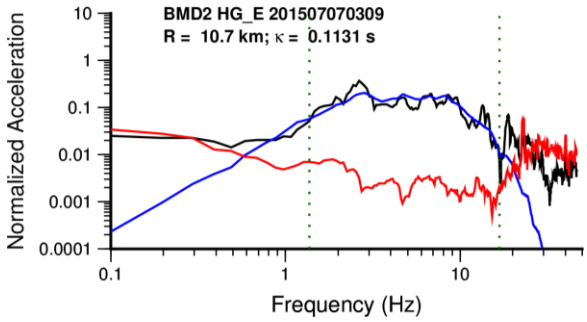
BMD2 HG_E 201507070309
R = 10.7 km; κ = 0.1131 s
Normalized Acceleration
Frequency (Hz)

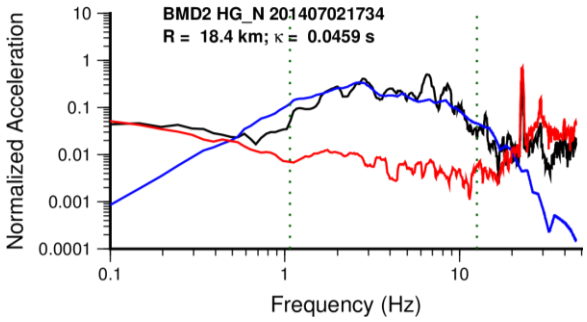
BMD2 HG_N 201407021734
R = 18.4 km; κ = 0.0459 s
Normalized Acceleration
Frequency (Hz)

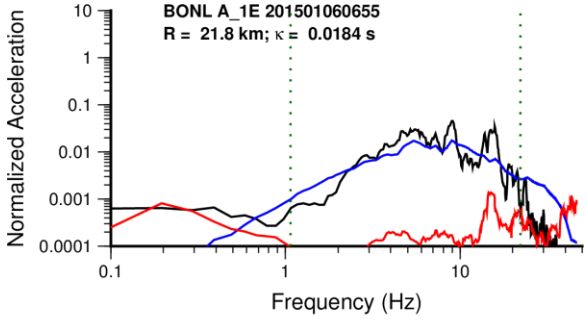
BONL A_1E 201501060655
R = 21.8 km; κ = 0.0184 s
Normalized Acceleration
Frequency (Hz)

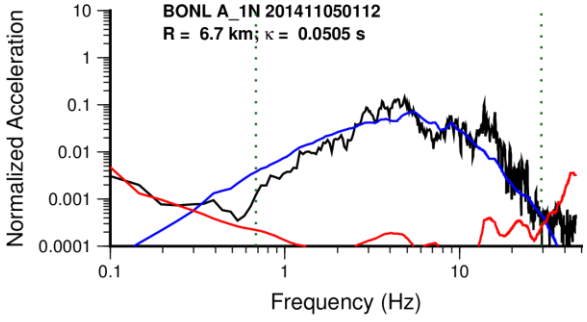
BONL A_1N 201411050112
R = 6.7 km; κ = 0.0505 s
Normalized Acceleration
Frequency (Hz)

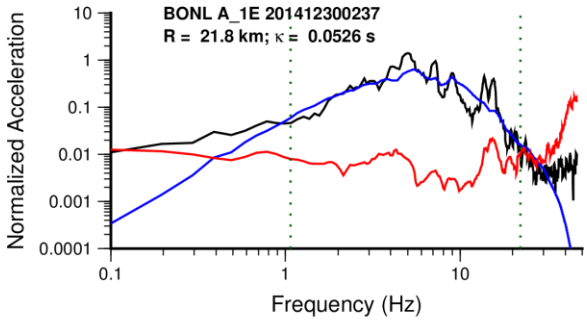
BONL A_1E 201412300237
R = 21.8 km; κ = 0.0526 s
Normalized Acceleration
Frequency (Hz)

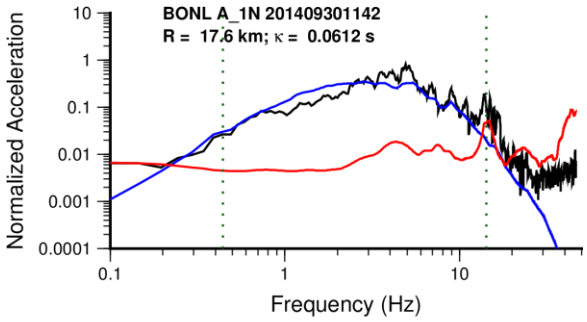
BONL A_1N 201409301142
R = 17.6 km; κ = 0.0612 s
Normalized Acceleration
Frequency (Hz)

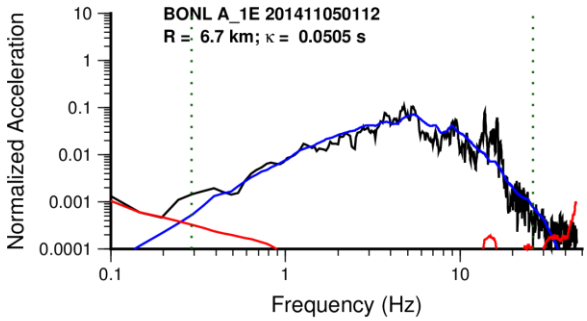
BONL A_1E 201411050112
R = 6.7 km; κ = 0.0505 s
Normalized Acceleration
Frequency (Hz)

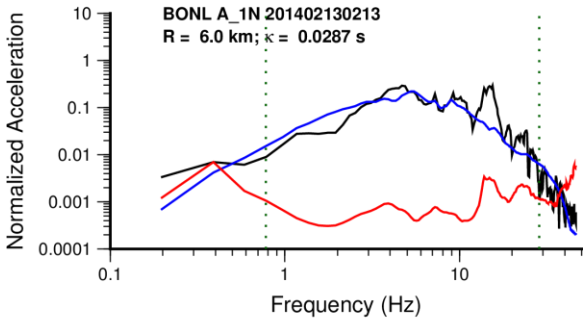
BONL A_1N 201402130213
R = 6.0 km; κ = 0.0287 s
Normalized Acceleration
Frequency (Hz)

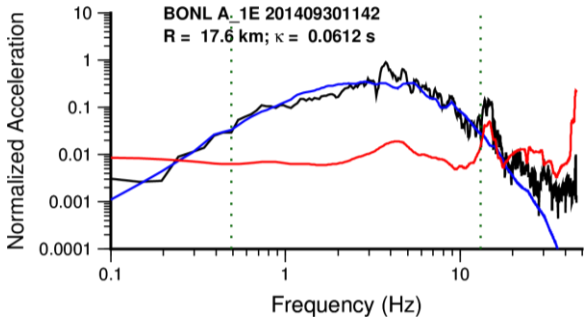
BONL A_1E 201409301142
R = 17.6 km; κ = 0.0612 s
Normalized Acceleration
Frequency (Hz)

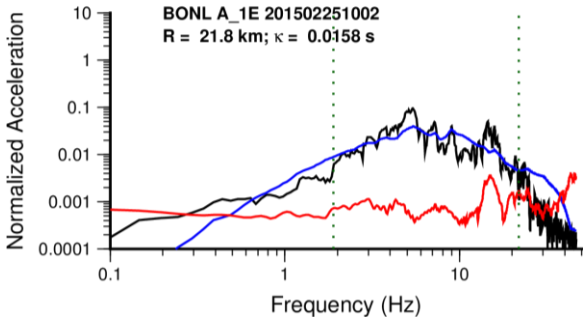
BONL A_1E 201502251002
R = 21.8 km; κ = 0.0158 s
Normalized Acceleration
Frequency (Hz)

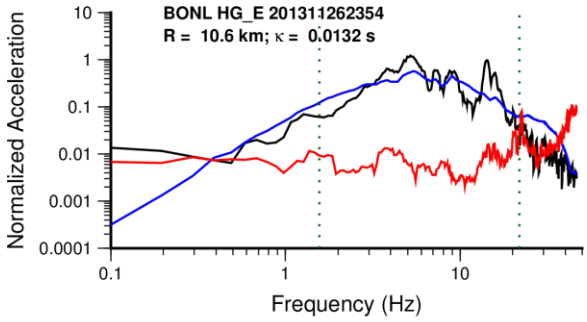
BONL HG_E 201311262354
R = 10.6 km; κ = 0.0132 s
Normalized Acceleration
Frequency (Hz)

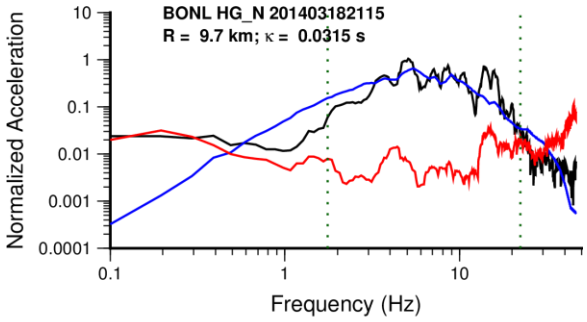
BONL HG_N 201403182115
R = 9.7 km; κ = 0.0315 s
Normalized Acceleration
Frequency (Hz)

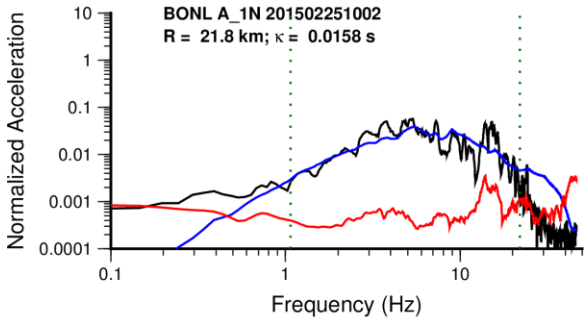
BONL A_1N 201502251002
R = 21.8 km; κ = 0.0158 s
Normalized Acceleration
Frequency (Hz)

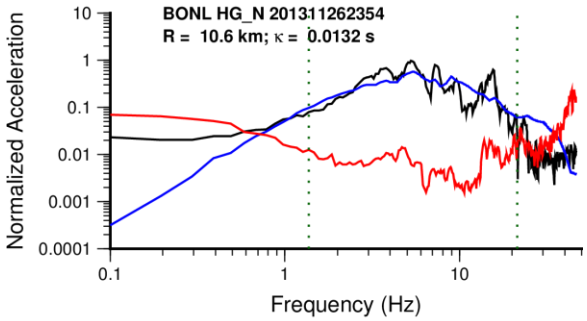
BONL HG_N 201311262354
R = 10.6 km; κ = 0.0132 s
Normalized Acceleration
Frequency (Hz)

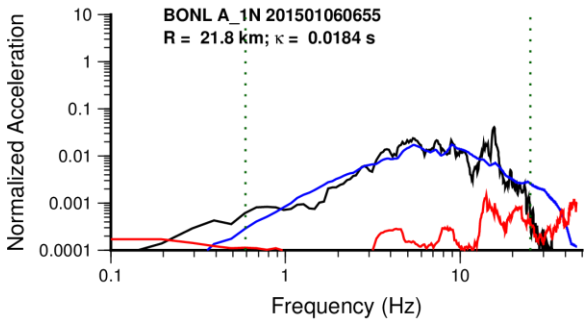
BONL A_1N 201501060655
R = 21.8 km; κ = 0.0184 s
Normalized Acceleration
Frequency (Hz)

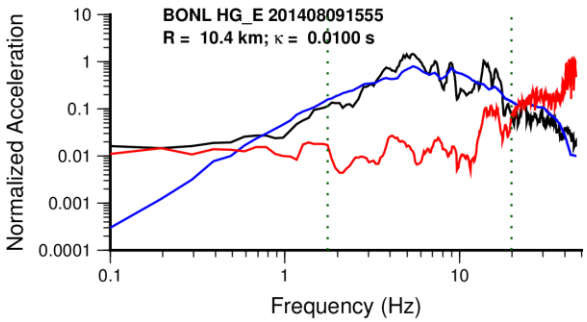
BONL HG_E 201408091555
R = 10.4 km; κ = 0.0100 s
Normalized Acceleration
Frequency (Hz)

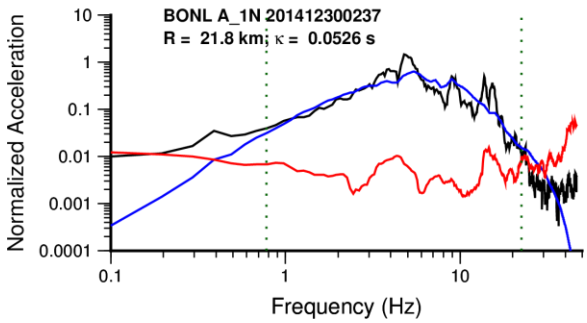
BONL A_1N 201412300237
R = 21.8 km; κ = 0.0526 s
Normalized Acceleration
Frequency (Hz)

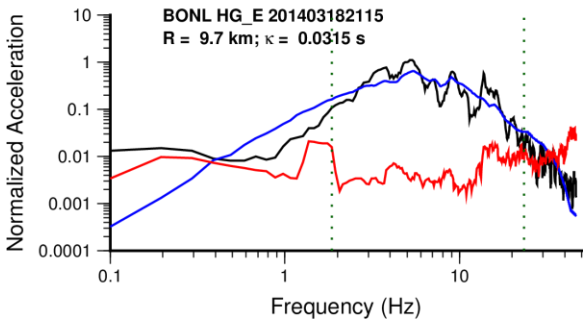
BONL HG_E 201403182115
R = 9.7 km; κ = 0.0315 s
Normalized Acceleration
Frequency (Hz)

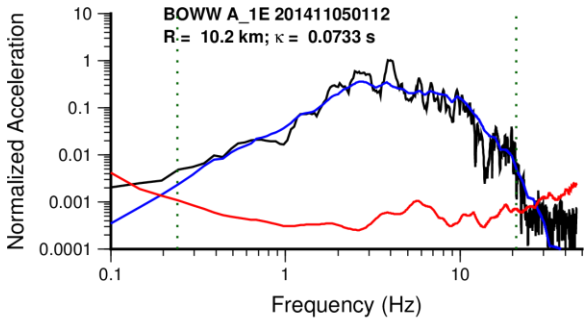
BOWW A_1E 201411050112
R = 10.2 km; κ = 0.0733 s
Normalized Acceleration
Frequency (Hz)

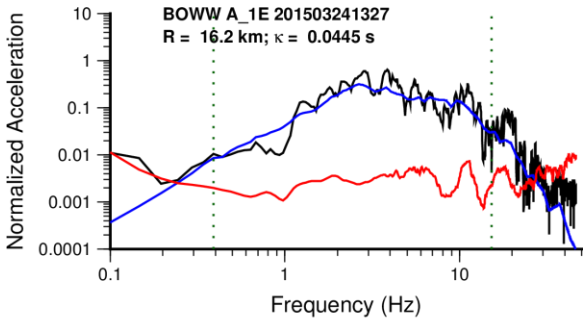
BOWW A_1E 201503241327
R = 16.2 km; κ = 0.0445 s
Normalized Acceleration
Frequency (Hz)

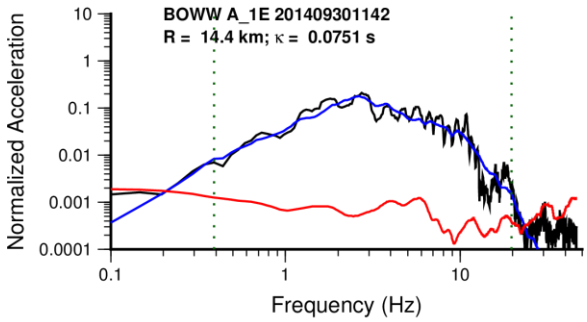
BOWW A_1E 201409301142
R = 14.4 km; κ = 0.0751 s
Normalized Acceleration
Frequency (Hz)

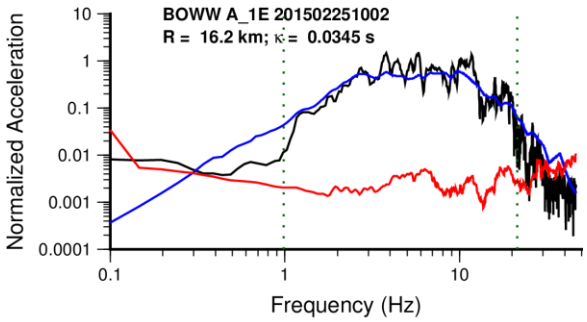
BOWW A_1E 201502251002
R = 16.2 km; κ = 0.0345 s
Normalized Acceleration
Frequency (Hz)

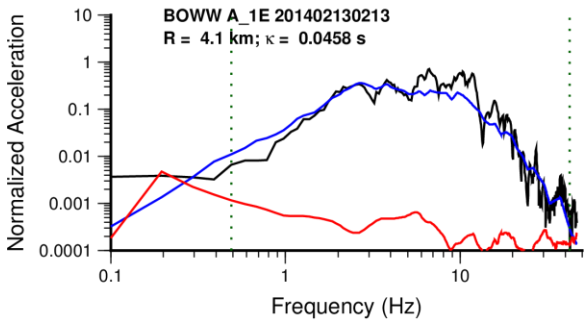
BOWW A_1E 201402130213
R = 4.1 km; κ = 0.0458 s
Normalized Acceleration
Frequency (Hz)

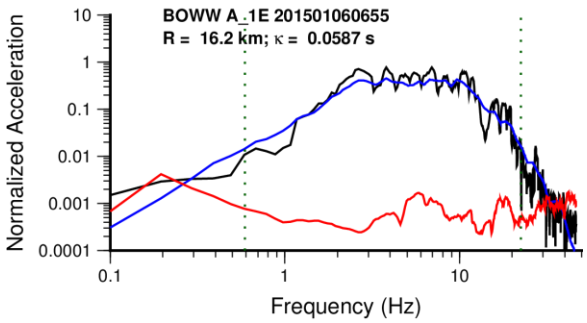
BOWW A_1E 201501060655
R = 16.2 km; κ = 0.0587 s
Normalized Acceleration
Frequency (Hz)

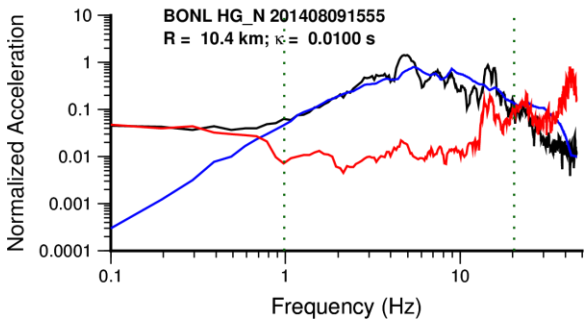
BONL HG_N 201408091555
R = 10.4 km; κ = 0.0100 s
Normalized Acceleration
Frequency (Hz)

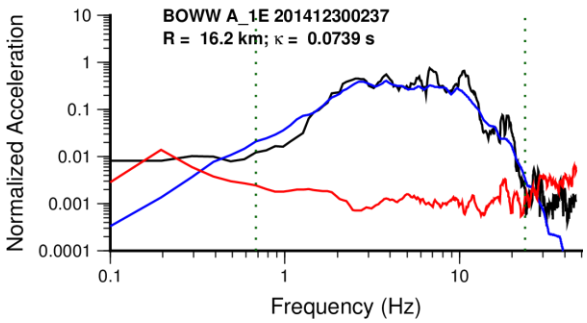
BOWW A_1E 201412300237
R = 16.2 km; κ = 0.0739 s
Normalized Acceleration
Frequency (Hz)

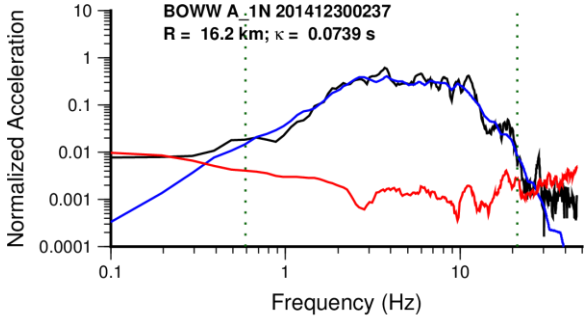
BOWW A_1N 201412300237
R = 16.2 km; κ = 0.0739 s
Normalized Acceleration
Frequency (Hz)

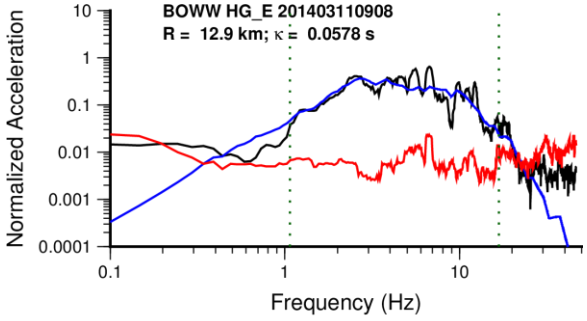
BOWW HG_E 201403110908
R = 12.9 km; κ = 0.0578 s
Normalized Acceleration
Frequency (Hz)

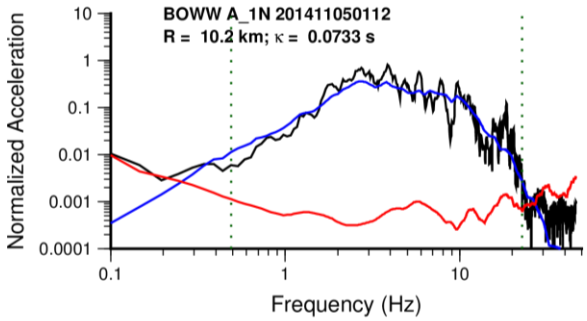
BOWW A_1N 201411050112
R = 10.2 km; κ = 0.0733 s
Normalized Acceleration
Frequency (Hz)

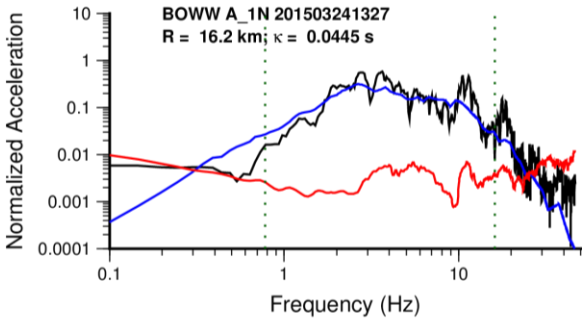
BOWW A_1N 201503241327
R = 16.2 km; κ = 0.0445 s
Normalized Acceleration
Frequency (Hz)

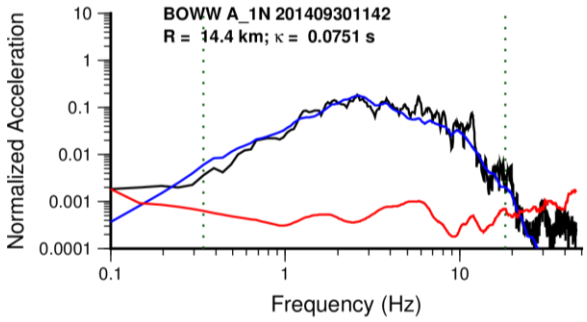
BOWW A_1N 201409301142
R = 14.4 km; κ = 0.0751 s
Normalized Acceleration
Frequency (Hz)

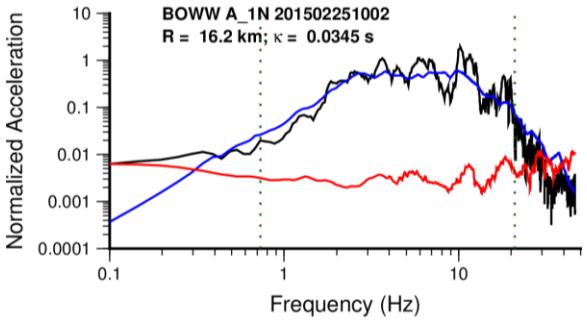
BOWW A_1N 201502251002
R = 16.2 km; κ = 0.0345 s
Normalized Acceleration
Frequency (Hz)

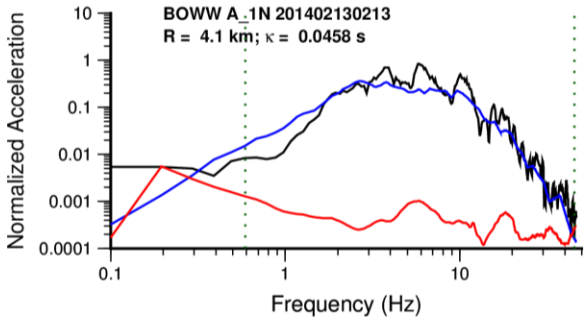
BOWW A_1N 201402130213
R = 4.1 km; κ = 0.0458 s
Normalized Acceleration
Frequency (Hz)

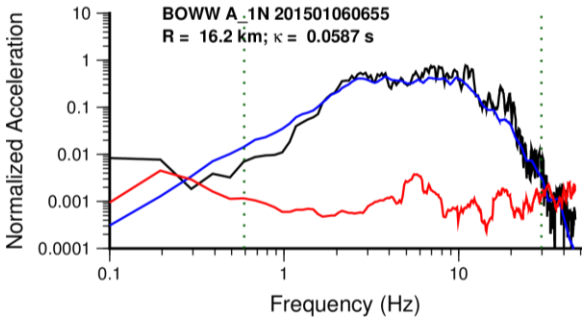
BOWW A_1N 201501060655
R = 16.2 km; κ = 0.0587 s
Normalized Acceleration
Frequency (Hz)

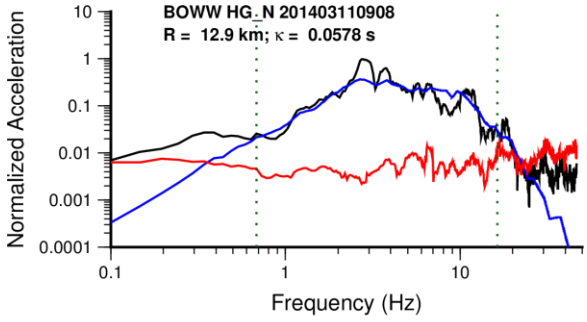
BOWW HG_N 201403110908
R = 12.9 km; κ = 0.0578 s
Normalized Acceleration
Frequency (Hz)

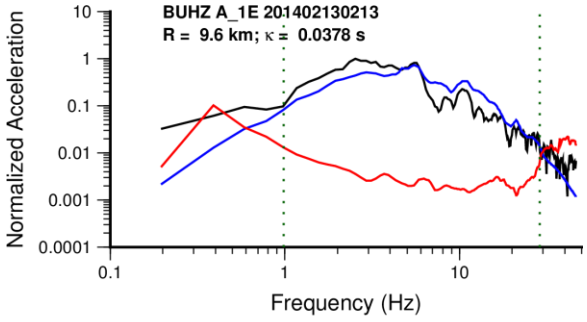
BUHZ A_1E 201402130213
R = 9.6 km; κ = 0.0378 s
Normalized Acceleration
Frequency (Hz)

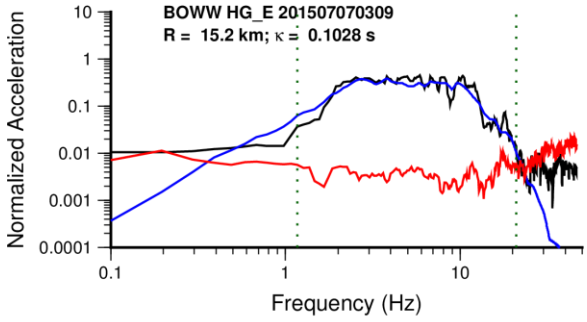
BOWW HG_E 201507070309
R = 15.2 km; κ = 0.1028 s
Normalized Acceleration
Frequency (Hz)

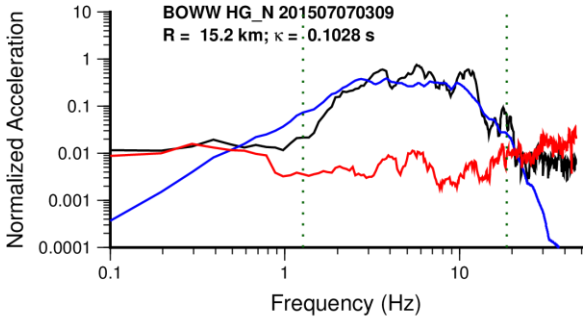
BOWW HG_N 201507070309
R = 15.2 km; κ = 0.1028 s
Normalized Acceleration
Frequency (Hz)

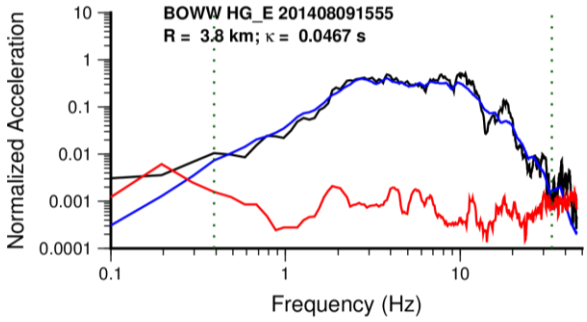
BOWW HG_E 201408091555
R = 3.8 km; κ = 0.0467 s
Normalized Acceleration
Frequency (Hz)

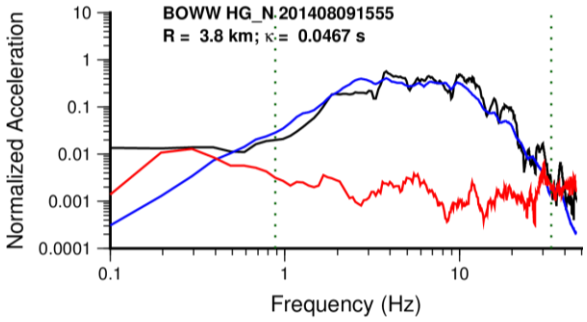
BOWW HG_N 201408091555
R = 3.8 km; κ = 0.0467 s
Normalized Acceleration
Frequency (Hz)

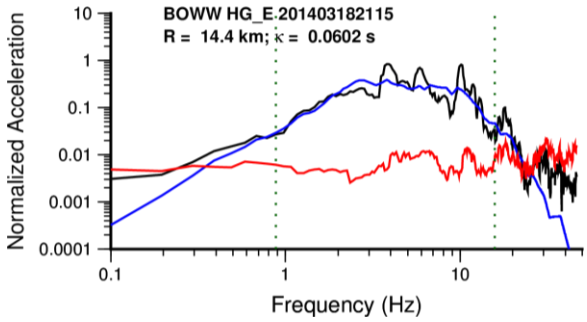
BOWW HG_E 201403182115
R = 14.4 km; κ = 0.0602 s
Normalized Acceleration
Frequency (Hz)

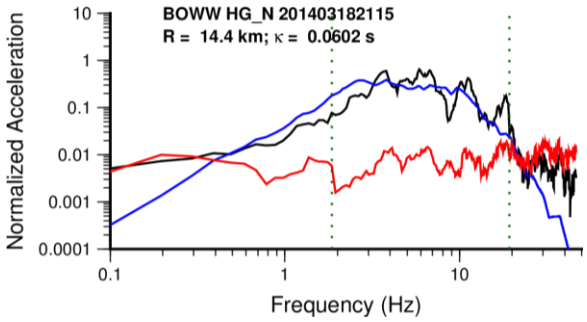
BOWW HG_N 201403182115
R = 14.4 km; κ = 0.0602 s
Normalized Acceleration
Frequency (Hz)

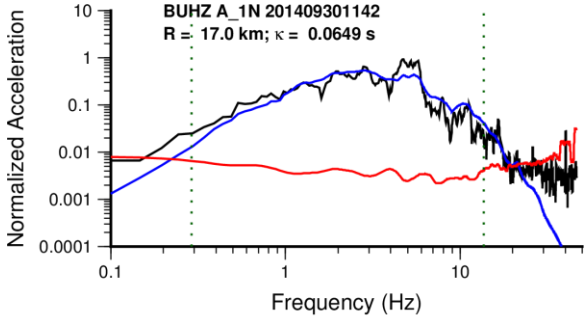
BUHZ A_1N 201409301142
R = 17.0 km; κ = 0.0649 s
Normalized Acceleration
Frequency (Hz)

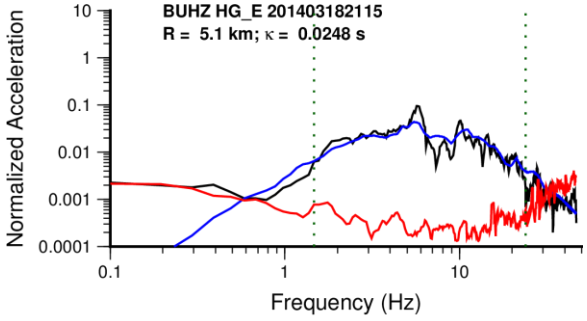
BUHZ HG_E 201403182115
R = 5.1 km; κ = 0.0248 s
Normalized Acceleration
Frequency (Hz)

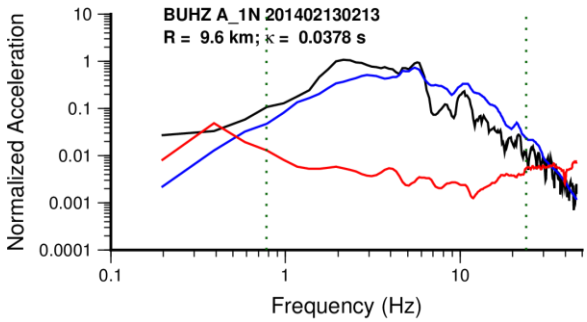
BUHZ A_1N 201402130213
R = 9.6 km; κ = 0.0378 s
Normalized Acceleration
Frequency (Hz)

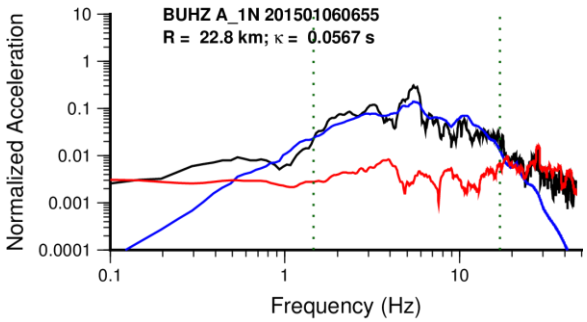
BUHZ A_1N 201501060655
R = 22.8 km; κ = 0.0567 s
Normalized Acceleration
Frequency (Hz)

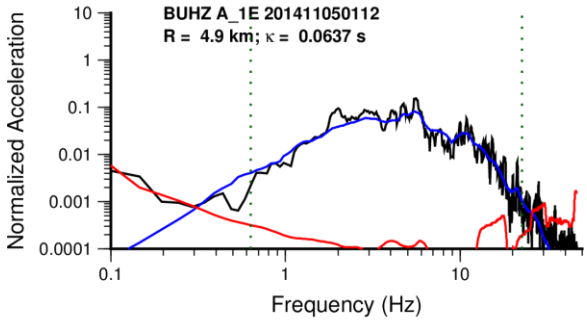
BUHZ A_1E 201411050112
R = 4.9 km; κ = 0.0637 s
Normalized Acceleration
Frequency (Hz)

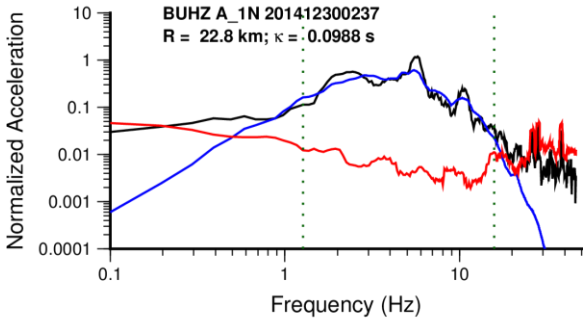
BUHZ A_1N 201412300237
R = 22.8 km; κ = 0.0988 s
Normalized Acceleration
Frequency (Hz)

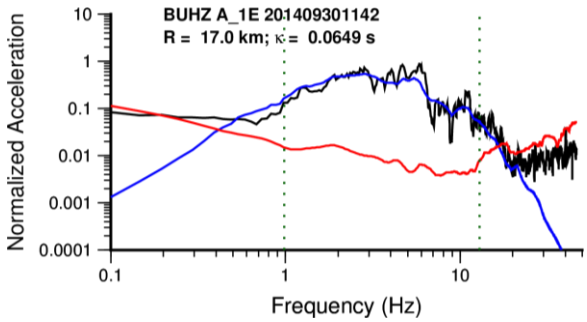
BUHZ A_1E 201409301142
R = 17.0 km; κ = 0.0649 s
Normalized Acceleration
Frequency (Hz)

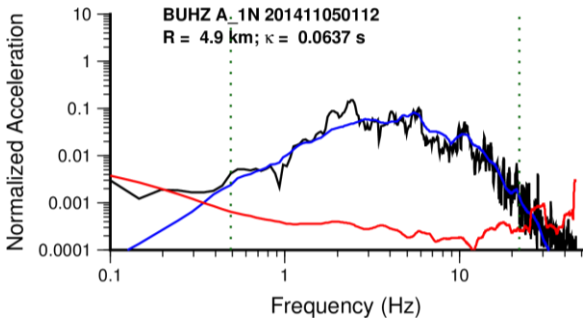
BUHZ A_1N 201411050112
R = 4.9 km; κ = 0.0637 s
Normalized Acceleration
Frequency (Hz)

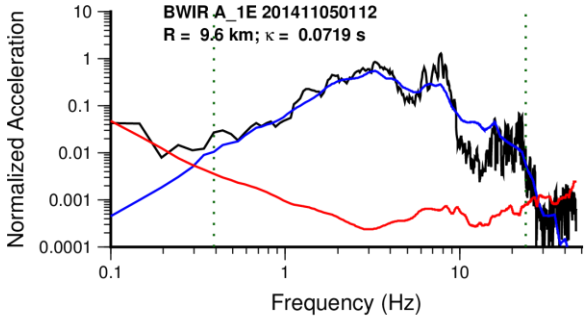
BWIR A_1E 201411050112
R = 9.6 km; κ = 0.0719 s
Normalized Acceleration
Frequency (Hz)

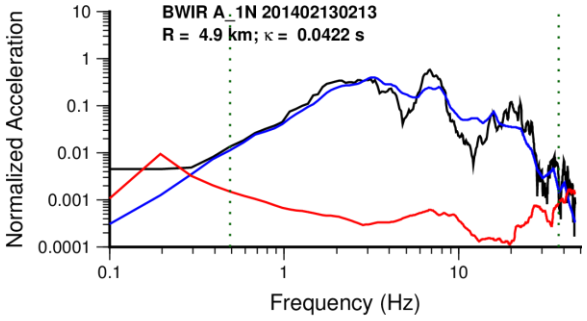
BWIR A_1N 201402130213
R = 4.9 km; κ = 0.0422 s
Normalized Acceleration
Frequency (Hz)

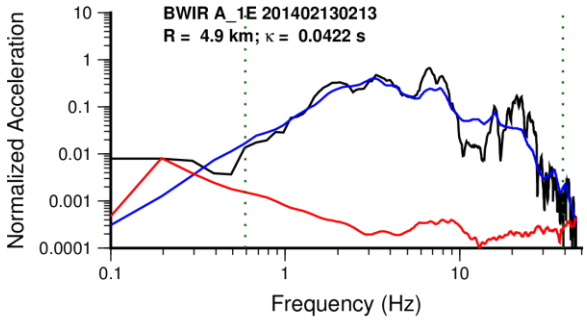
BWIR A_1E 201402130213
R = 4.9 km; κ = 0.0422 s
Normalized Acceleration
Frequency (Hz)

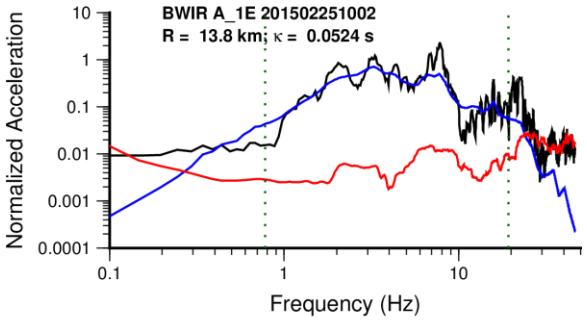
BWIR A_1E 201502251002
R = 13.8 km; κ = 0.0524 s
Normalized Acceleration
Frequency (Hz)

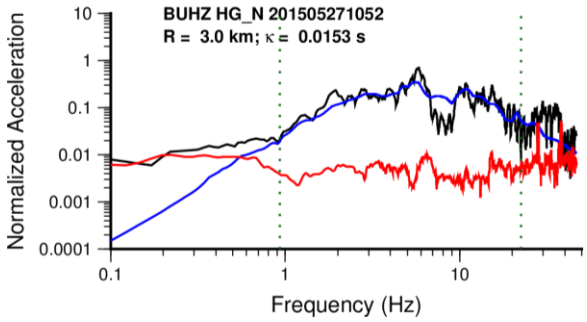
BUHZ HG_N 201505271052
R = 3.0 km; κ = 0.0153 s
Normalized Acceleration
Frequency (Hz)

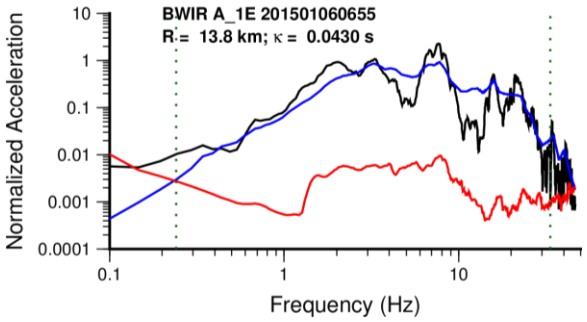
BWIR A_1E 201501060655
R = 13.8 km; κ = 0.0430 s
Normalized Acceleration
Frequency (Hz)

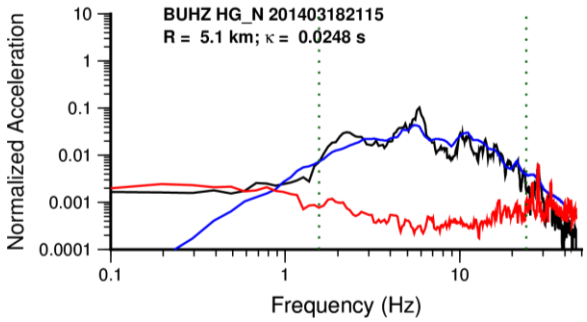
BUHZ HG_N 201403182115
R = 5.1 km; κ = 0.0248 s
Normalized Acceleration
Frequency (Hz)

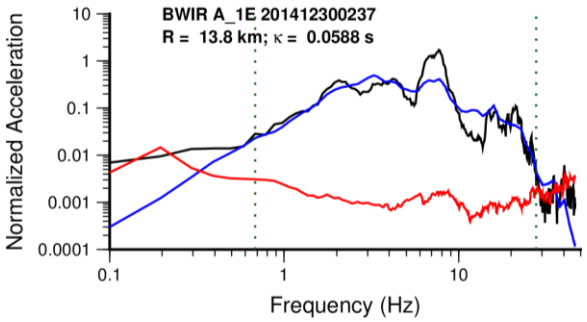
BWIR A_1E 201412300237
R = 13.8 km; κ = 0.0588 s
Normalized Acceleration
Frequency (Hz)

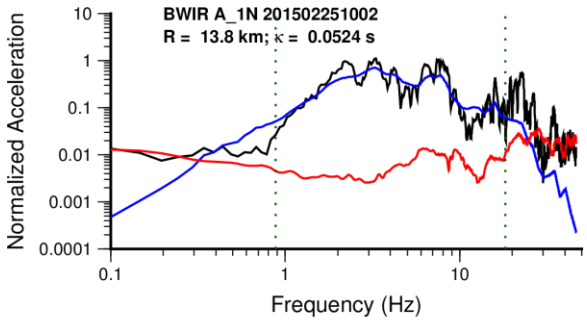
BWIR A_1N 201502251002
R = 13.8 km; κ = 0.0524 s
Normalized Acceleration
Frequency (Hz)

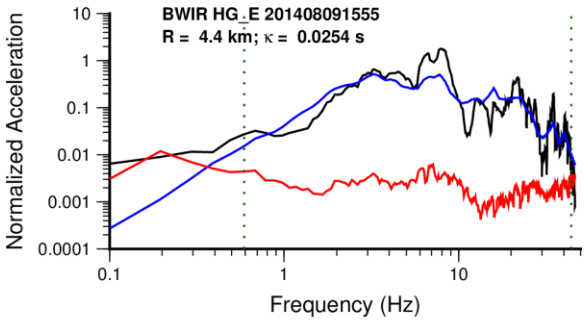
BWIR HG_E 201408091555
R = 4.4 km; κ = 0.0254 s
Normalized Acceleration
Frequency (Hz)

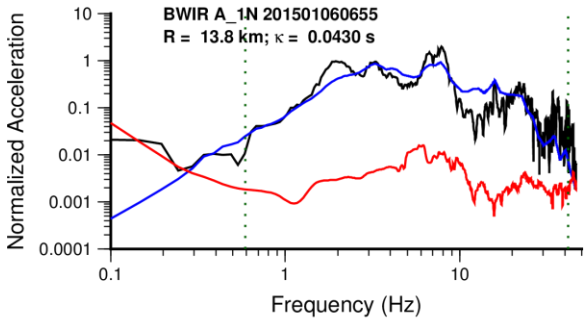
BWIR A_1N 201501060655
R = 13.8 km; κ = 0.0430 s
Normalized Acceleration
Frequency (Hz)

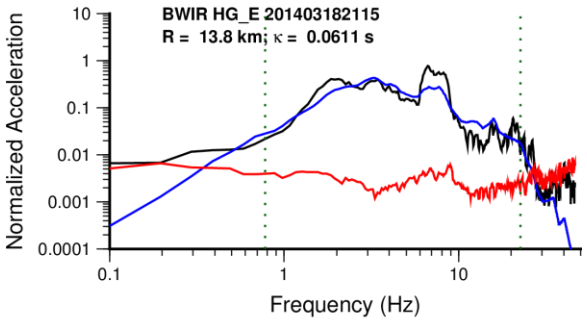
BWIR HG_E 201403182115
R = 13.8 km; κ = 0.0611 s
Normalized Acceleration
Frequency (Hz)

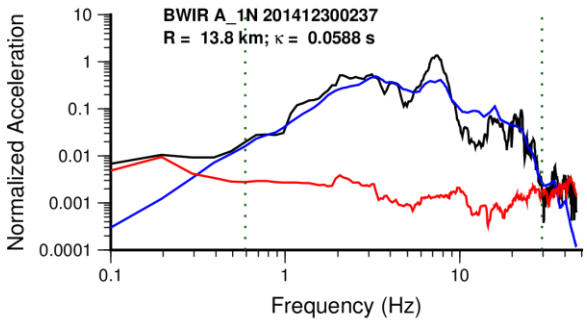
BWIR A_1N 201412300237
R = 13.8 km; κ = 0.0588 s
Normalized Acceleration
Frequency (Hz)

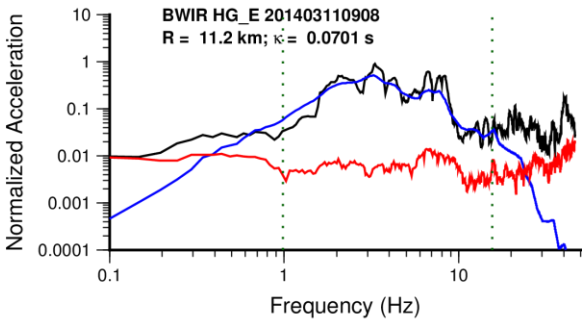
BWIR HG_E 201403110908
R = 11.2 km; κ = 0.0701 s
Normalized Acceleration
Frequency (Hz)

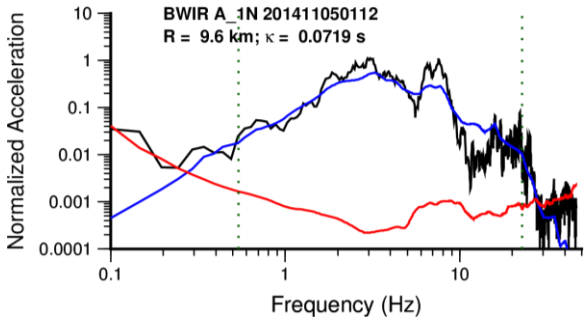
BWIR A_1N 201411050112
R = 9.6 km; κ = 0.0719 s
Normalized Acceleration
Frequency (Hz)

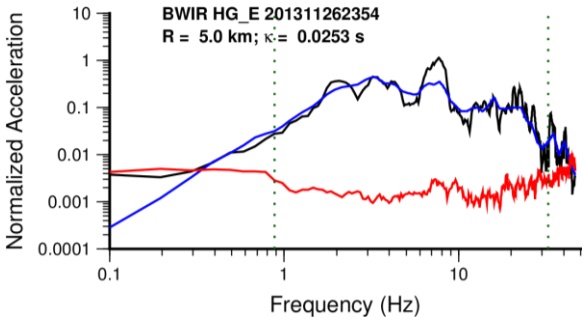
BWIR HG_E 201311262354
R = 5.0 km; κ = 0.0253 s
Normalized Acceleration
Frequency (Hz)

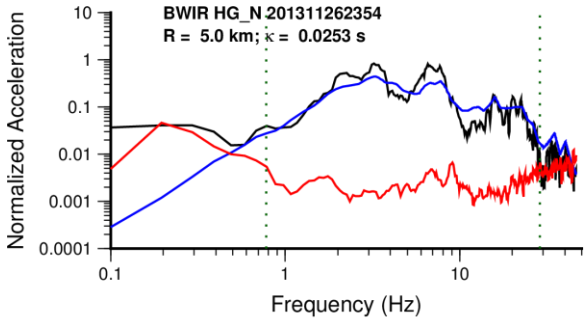
BWIR HG_N 201311262354
R = 5.0 km; κ = 0.0253 s
Normalized Acceleration
Frequency (Hz)

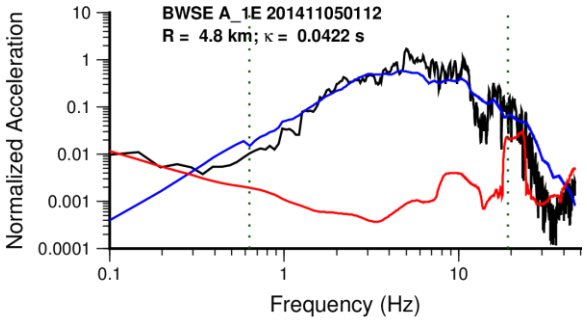
BWSE A_1E 201411050112
R = 4.8 km; κ = 0.0422 s
Normalized Acceleration
Frequency (Hz)

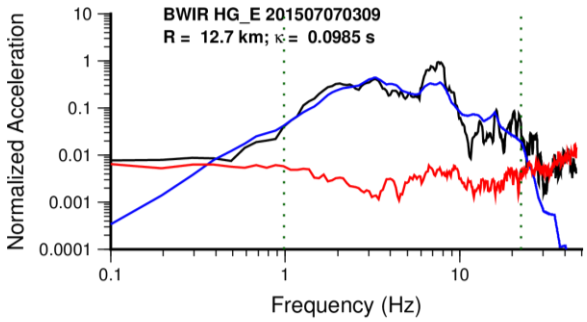
BWIR HG_E 201507070309
R = 12.7 km; κ = 0.0985 s
Normalized Acceleration
Frequency (Hz)

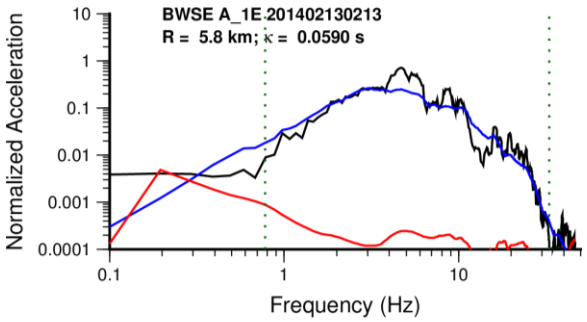
BWSE A_1E 201402130213
R = 5.8 km; κ = 0.0590 s
Normalized Acceleration
Frequency (Hz)

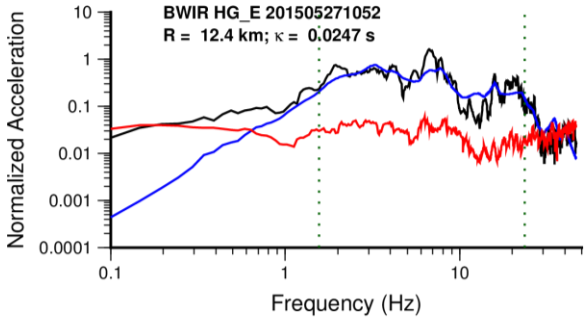
BWIR HG_E 201505271052
R = 12.4 km; κ = 0.0247 s
Normalized Acceleration
Frequency (Hz)

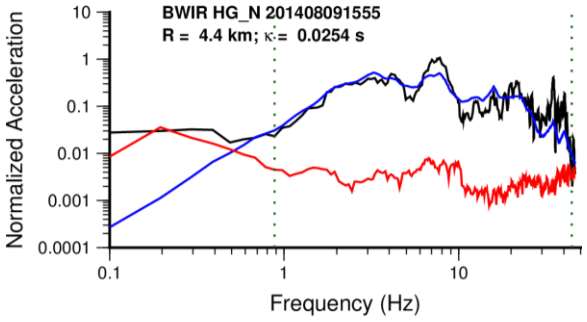
BWIR HG_N 201408091555
R = 4.4 km; κ = 0.0254 s
Normalized Acceleration
Frequency (Hz)

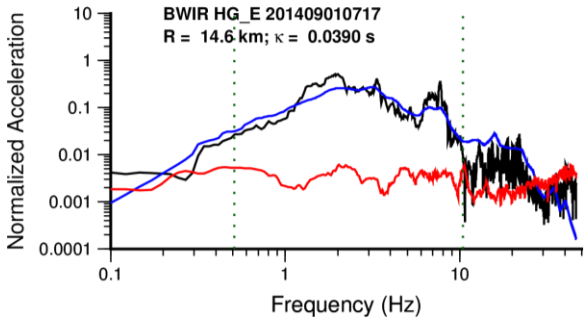
BWIR HG_E 201409010717
R = 14.6 km; κ = 0.0390 s
Normalized Acceleration
Frequency (Hz)

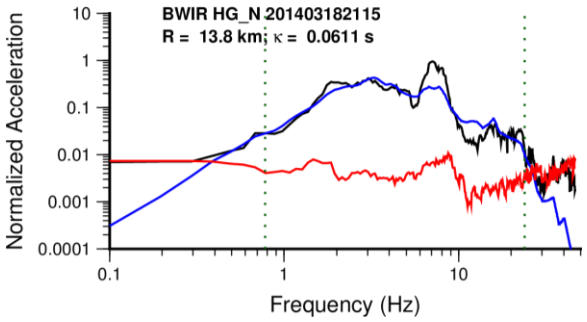
BWIR HG_N 201403182115
R = 13.8 km; κ = 0.0611 s
Normalized Acceleration
Frequency (Hz)

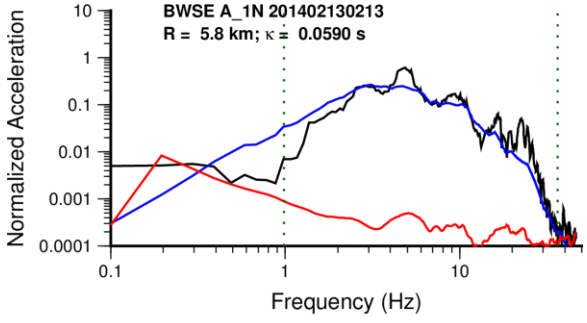
BWSE A_1N 201402130213
R = 5.8 km; κ = 0.0590 s
Normalized Acceleration
Frequency (Hz)

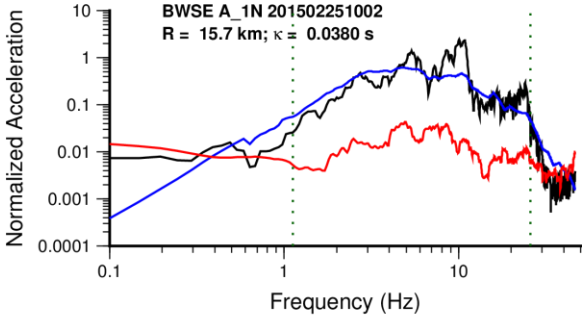
BWSE A_1N 201502251002
R = 15.7 km; κ = 0.0380 s
Normalized Acceleration
Frequency (Hz)

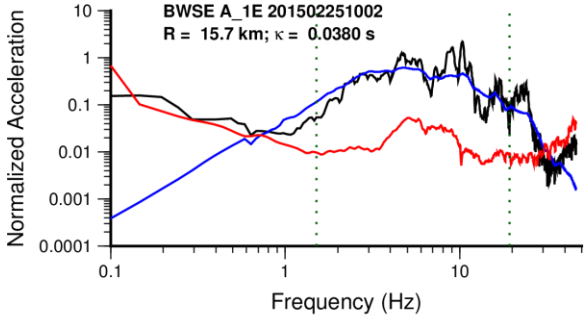
BWSE A_1E 201502251002
R = 15.7 km; κ = 0.0380 s
Normalized Acceleration
Frequency (Hz)

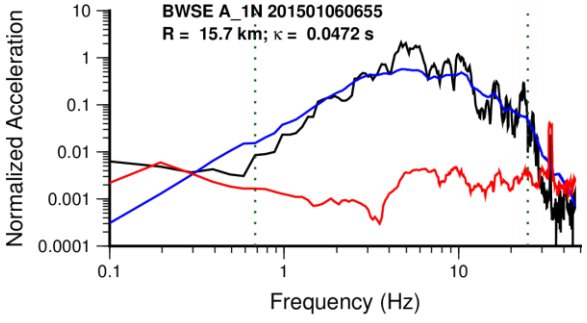
BWSE A_1N 201501060655
R = 15.7 km; κ = 0.0472 s
Normalized Acceleration
Frequency (Hz)

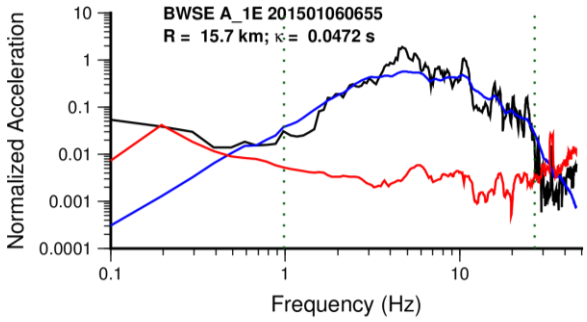
BWSE A_1E 201501060655
R = 15.7 km; κ = 0.0472 s
Normalized Acceleration
Frequency (Hz)

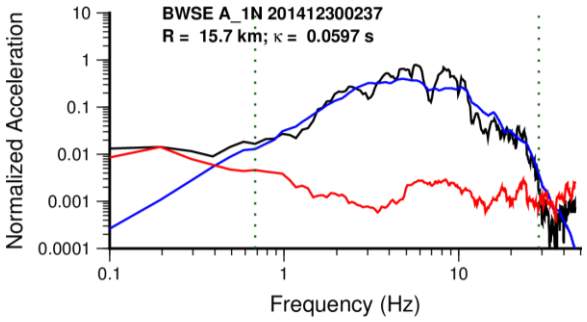
BWSE A_1N 201412300237
R = 15.7 km; κ = 0.0597 s
Normalized Acceleration
Frequency (Hz)

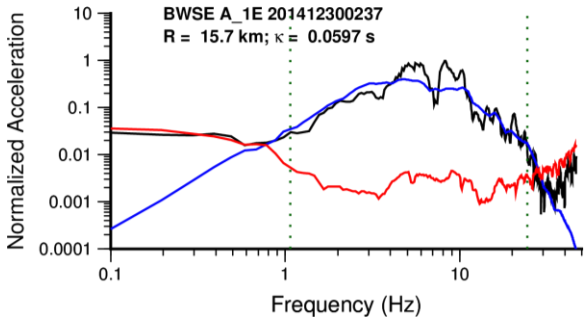
BWSE A_1E 201412300237
R = 15.7 km; κ = 0.0597 s
Normalized Acceleration
Frequency (Hz)

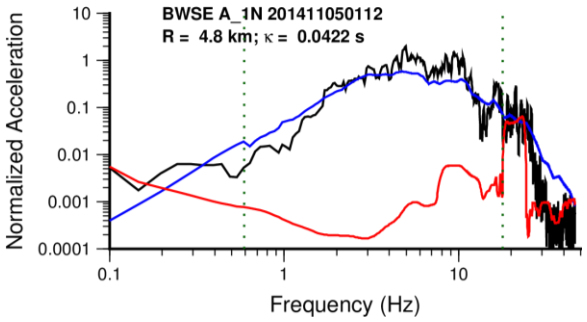
BWSE A_1N 201411050112
R = 4.8 km; κ = 0.0422 s
Normalized Acceleration
Frequency (Hz)

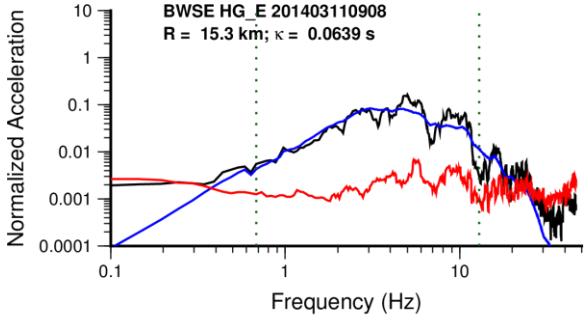
BWSE HG_E 201403110908
R = 15.3 km; κ = 0.0639 s
Normalized Acceleration
Frequency (Hz)

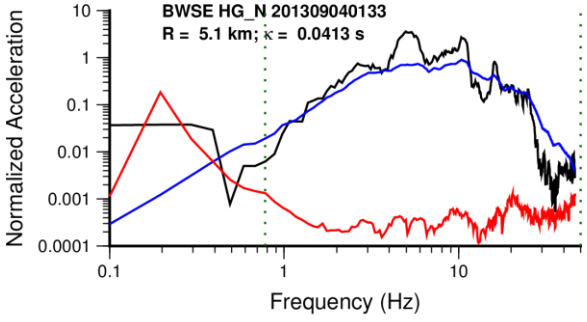
BWSE HG_N 201309040133
R = 5.1 km; κ = 0.0413 s
Normalized Acceleration
Frequency (Hz)

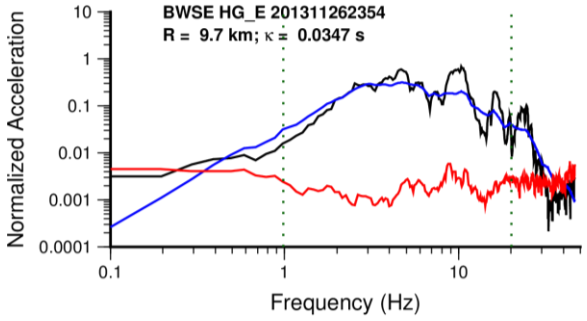
BWSE HG_E 201311262354
R = 9.7 km; κ = 0.0347 s
Normalized Acceleration
Frequency (Hz)

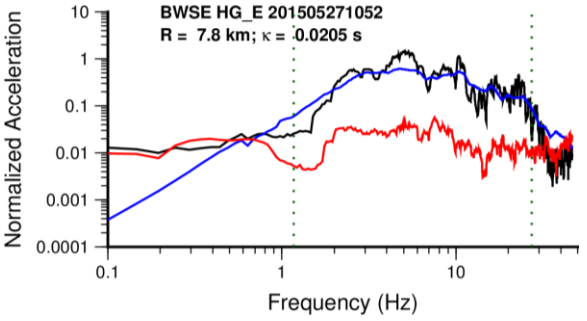
BWSE HG_E 201505271052
R = 7.8 km; κ = 0.0205 s
Normalized Acceleration
Frequency (Hz)

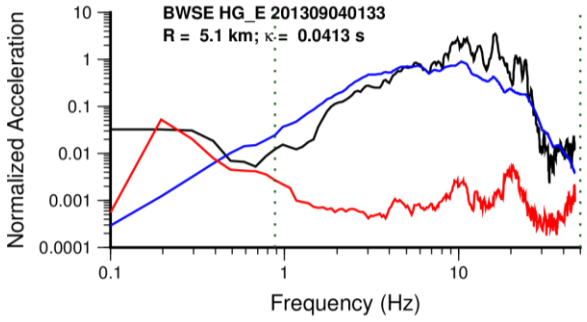
BWSE HG_E 201309040133
R = 5.1 km; κ = 0.0413 s
Normalized Acceleration
Frequency (Hz)

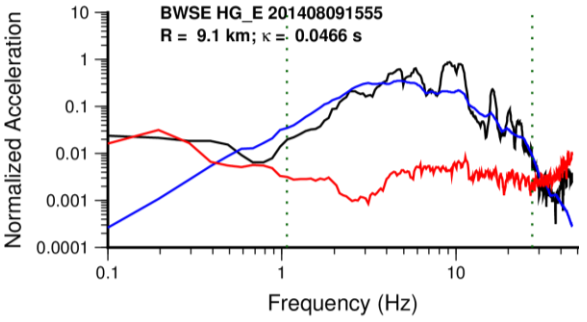
BWSE HG_E 201408091555
R = 9.1 km; κ = 0.0466 s
Normalized Acceleration
Frequency (Hz)

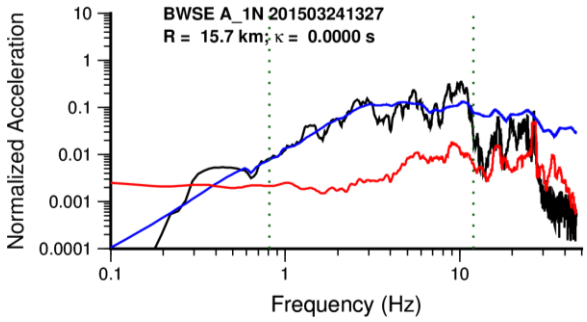
BWSE A_1N 201503241327
R = 15.7 km; κ = 0.0000 s
Normalized Acceleration
Frequency (Hz)

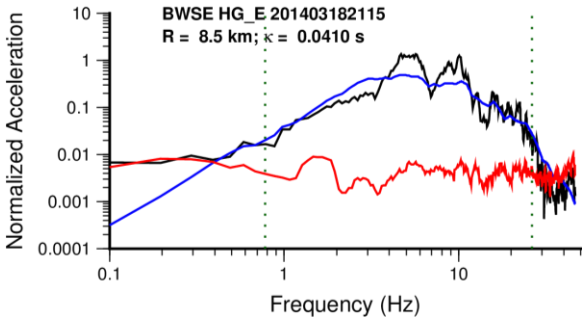
BWSE HG_E 201403182115
R = 8.5 km; κ = 0.0410 s
Normalized Acceleration
Frequency (Hz)

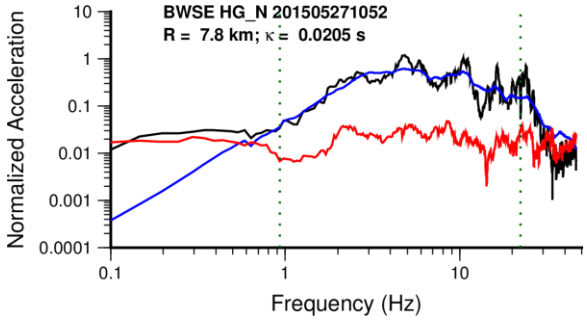
BWSE HG_N 201505271052
R = 7.8 km; κ = 0.0205 s
Normalized Acceleration
Frequency (Hz)

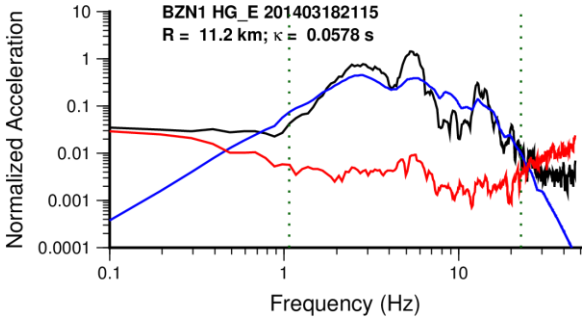
BZN1 HG_E 201403182115
R = 11.2 km; κ = 0.0578 s
Normalized Acceleration
Frequency (Hz)

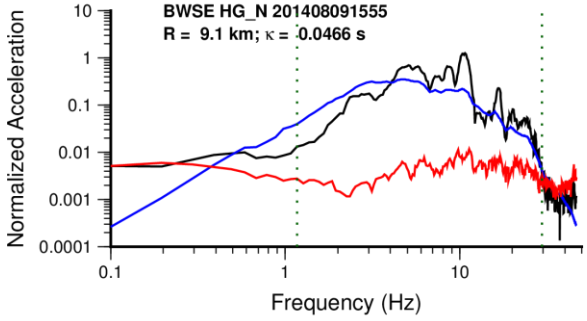
BWSE HG_N 201408091555
R = 9.1 km; κ = 0.0466 s
Normalized Acceleration
Frequency (Hz)

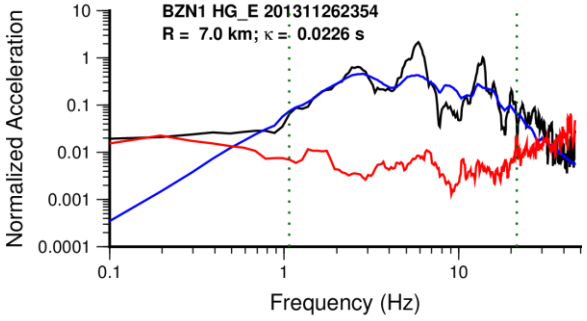
BZN1 HG_E 201311262354
R = 7.0 km; κ = 0.0226 s
Normalized Acceleration
Frequency (Hz)

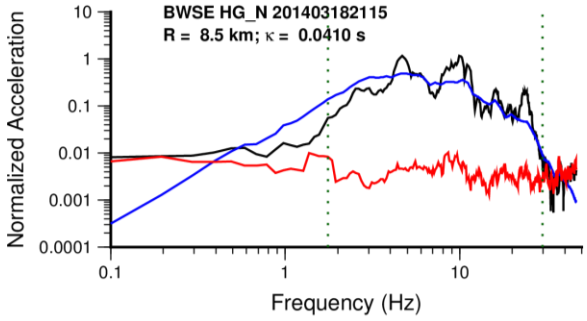
BWSE HG_N 201403182115
R = 8.5 km; κ = 0.0410 s
Normalized Acceleration
Frequency (Hz)

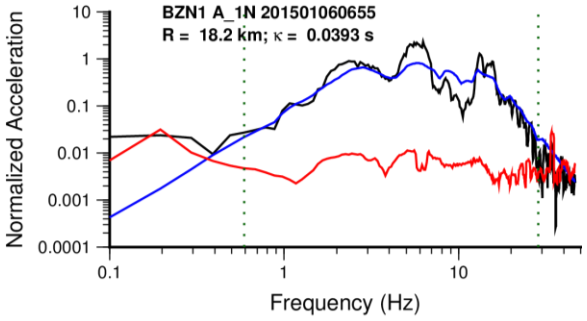
BZN1 A_1N 201501060655
R = 18.2 km; κ = 0.0393 s
Normalized Acceleration
Frequency (Hz)

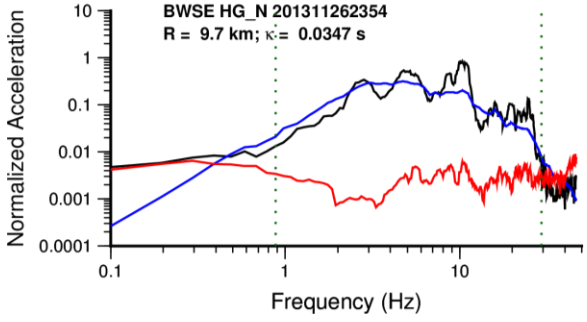
BWSE HG_N 201311262354
R = 9.7 km; κ = 0.0347 s
Normalized Acceleration
Frequency (Hz)

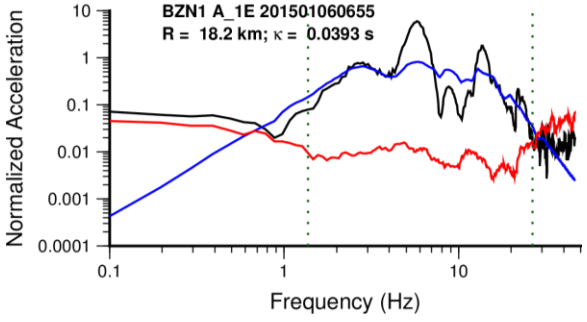
BZN1 A_1E 201501060655
R = 18.2 km; κ = 0.0393 s
Normalized Acceleration
Frequency (Hz)

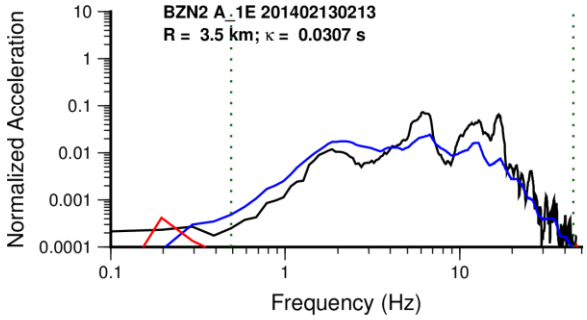
BZN2 A_1E 201402130213
R = 3.5 km; κ = 0.0307 s
Normalized Acceleration
Frequency (Hz)

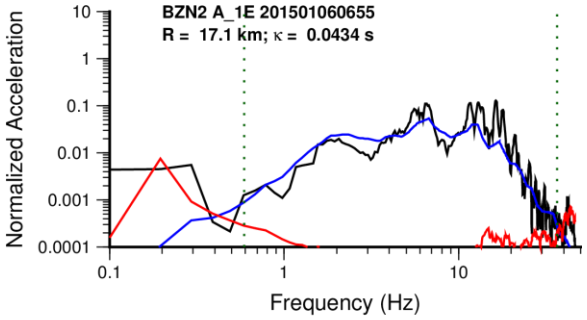
BZN2 A_1E 201501060655
R = 17.1 km; κ = 0.0434 s
Normalized Acceleration
Frequency (Hz)

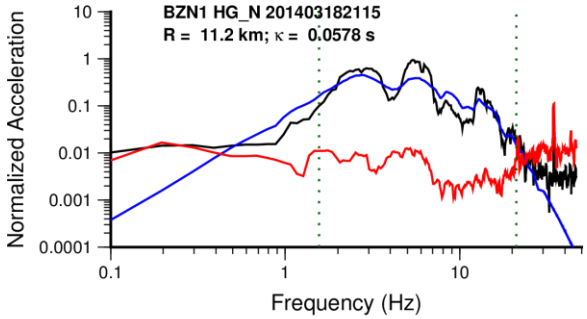
BZN1 HG_N 201403182115
R = 11.2 km; κ = 0.0578 s
Normalized Acceleration
Frequency (Hz)

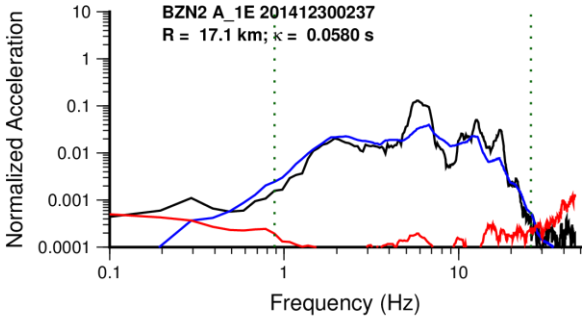
BZN2 A_1E 201412300237
R = 17.1 km; κ = 0.0580 s
Normalized Acceleration
Frequency (Hz)

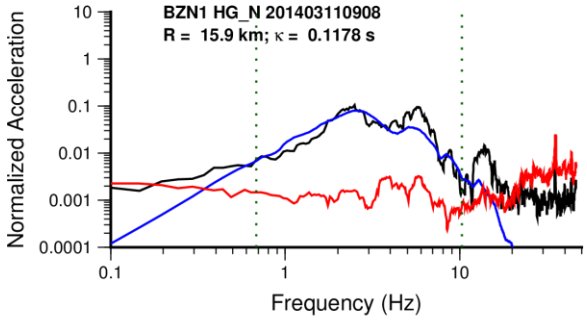
BZN1 HG_N 201403110908
R = 15.9 km; κ = 0.1178 s
Normalized Acceleration
Frequency (Hz)

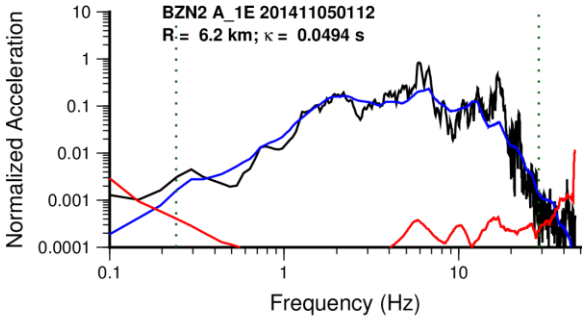
BZN2 A_1E 201411050112
R = 6.2 km; κ = 0.0494 s
Normalized Acceleration
Frequency (Hz)

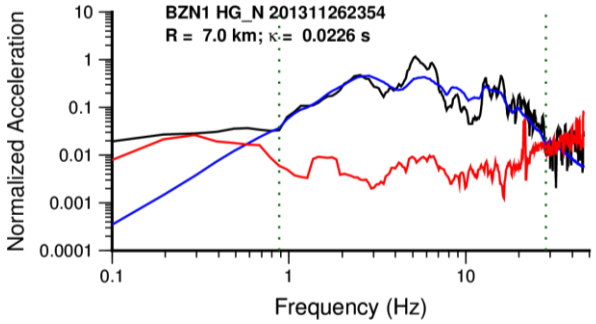
BZN1 HG_N 201311262354
R = 7.0 km; κ = 0.0226 s
Normalized Acceleration
Frequency (Hz)

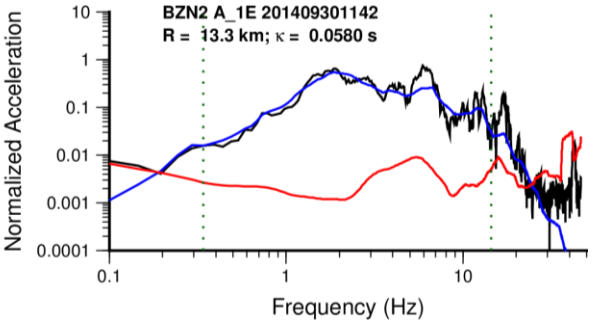
BZN2 A_1E 201409301142
R = 13.3 km; κ = 0.0580 s
Normalized Acceleration
Frequency (Hz)

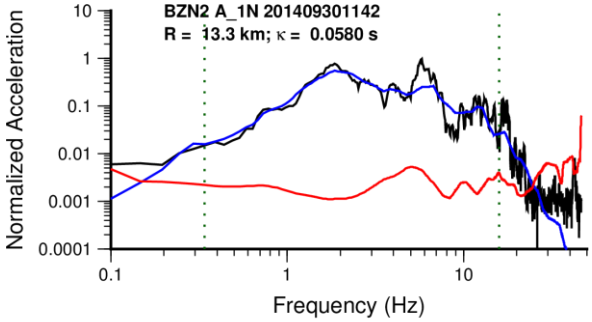
BZN2 A_1N 201409301142
R = 13.3 km; κ = 0.0580 s
Normalized Acceleration
Frequency (Hz)

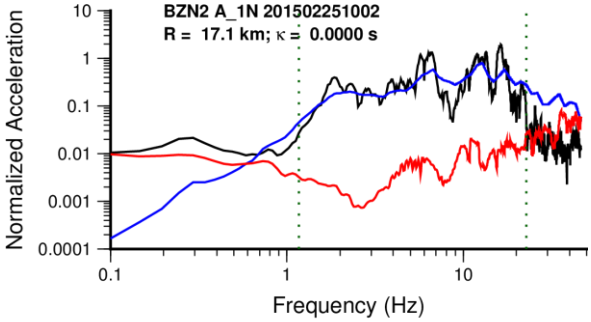
BZN2 A_1N 201502251002
R = 17.1 km; κ = 0.0000 s
Normalized Acceleration
Frequency (Hz)

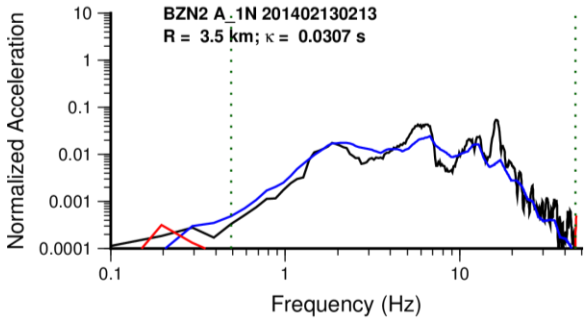
BZN2 A_1N 201402130213
R = 3.5 km; κ = 0.0307 s
Normalized Acceleration
Frequency (Hz)

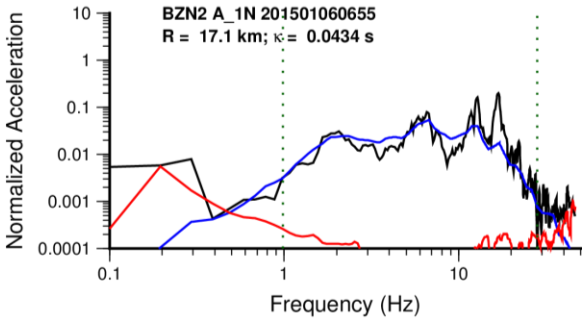
BZN2 A_1N 201501060655
R = 17.1 km; κ = 0.0434 s
Normalized Acceleration
Frequency (Hz)

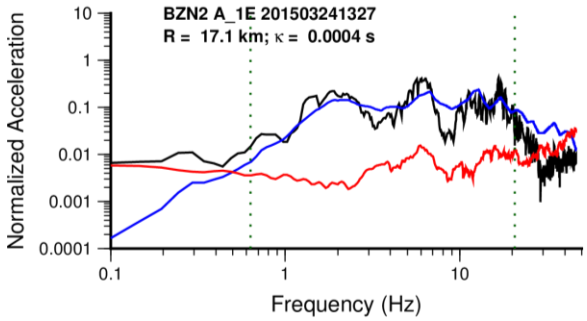
BZN2 A_1E 201503241327
R = 17.1 km; κ = 0.0004 s
Normalized Acceleration
Frequency (Hz)

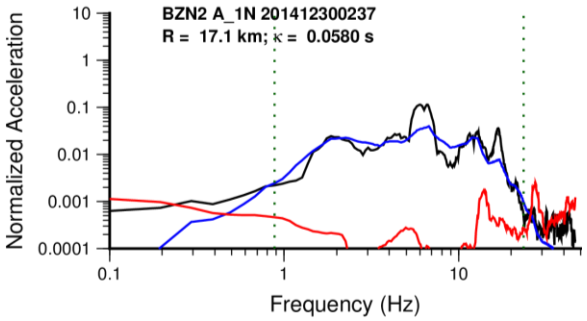
BZN2 A_1N 201412300237
R = 17.1 km; κ = 0.0580 s
Normalized Acceleration
Frequency (Hz)

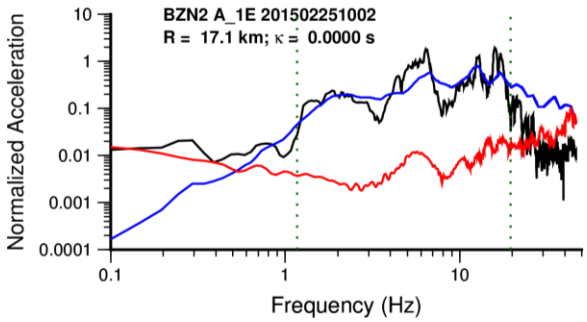
BZN2 A_1E 201502251002
R = 17.1 km; κ = 0.0000 s
Normalized Acceleration
Frequency (Hz)

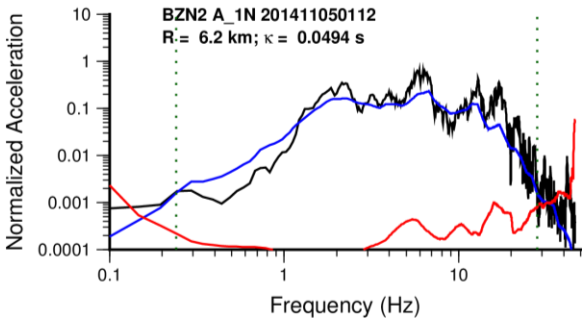
BZN2 A_1N 201411050112
R = 6.2 km; κ = 0.0494 s
Normalized Acceleration
Frequency (Hz)

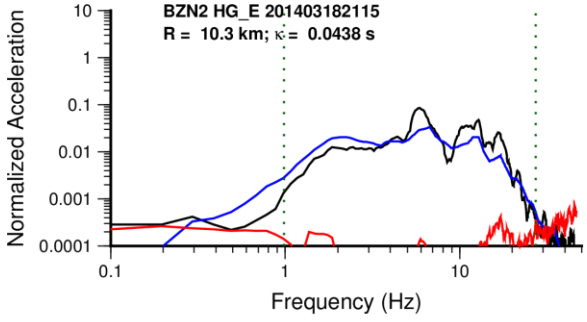
BZN2 HG_E 201403182115
R = 10.3 km; κ = 0.0438 s
Normalized Acceleration
Frequency (Hz)

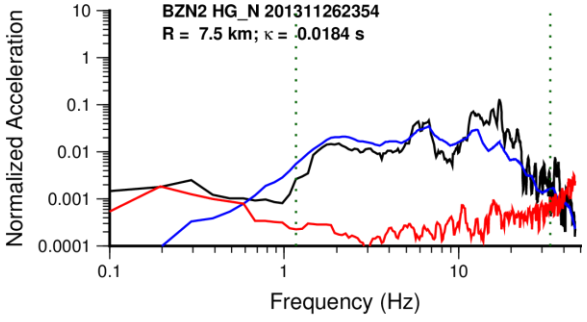
BZN2 HG_N 201311262354
R = 7.5 km; κ = 0.0184 s
Normalized Acceleration
Frequency (Hz)

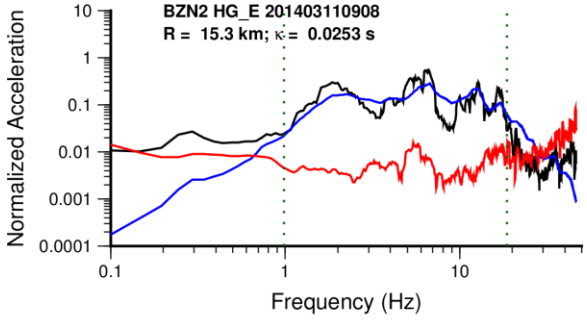
BZN2 HG_E 201403110908
R = 15.3 km; κ = 0.0253 s
Normalized Acceleration
Frequency (Hz)

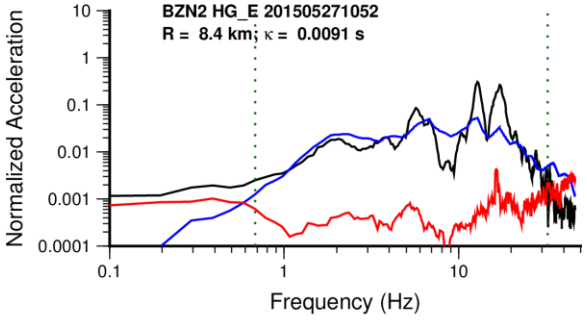
BZN2 HG_E 201505271052
R = 8.4 km; κ = 0.0091 s
Normalized Acceleration
Frequency (Hz)

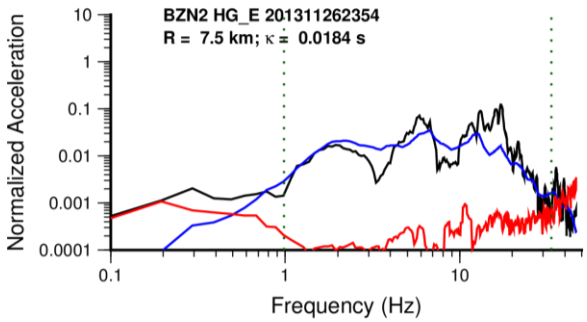
BZN2 HG_E 201311262354
R = 7.5 km; κ = 0.0184 s
Normalized Acceleration
Frequency (Hz)

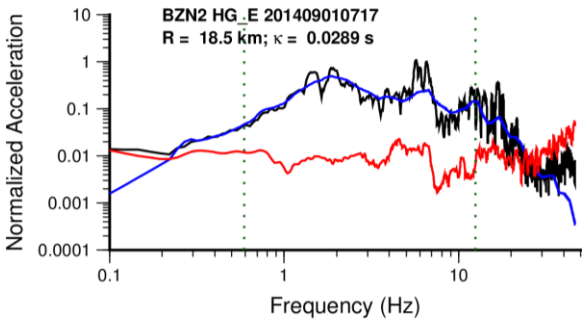
BZN2 HG_E 201409010717
R = 18.5 km; κ = 0.0289 s
Normalized Acceleration
Frequency (Hz)

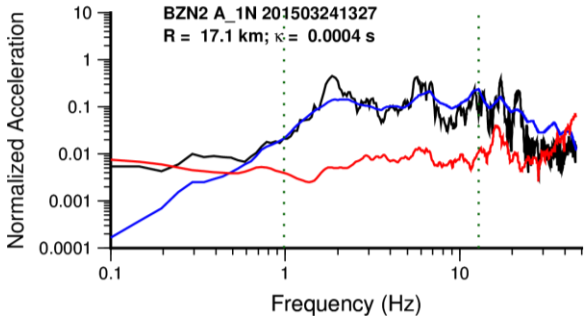
BZN2 A_1N 201503241327
R = 17.1 km; κ = 0.0004 s
Normalized Acceleration
Frequency (Hz)

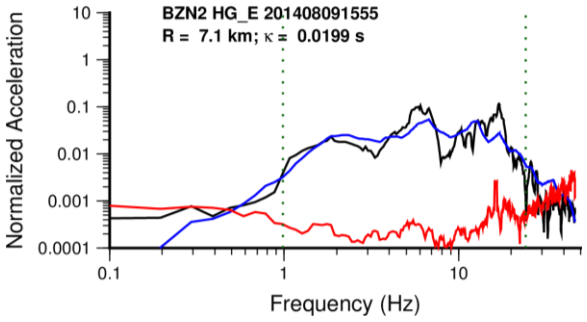
BZN2 HG_E 201408091555
R = 7.1 km; κ = 0.0199 s
Normalized Acceleration
Frequency (Hz)

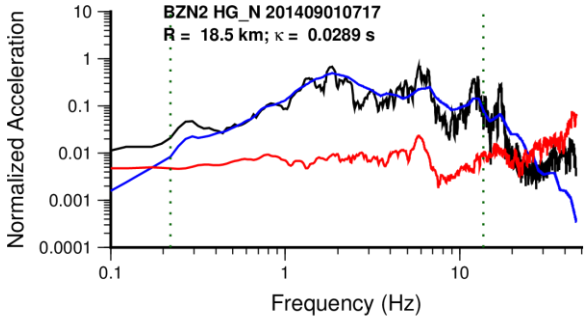
BZN2 HG_N 201409010717
R = 18.5 km; κ = 0.0289 s
Normalized Acceleration
Frequency (Hz)

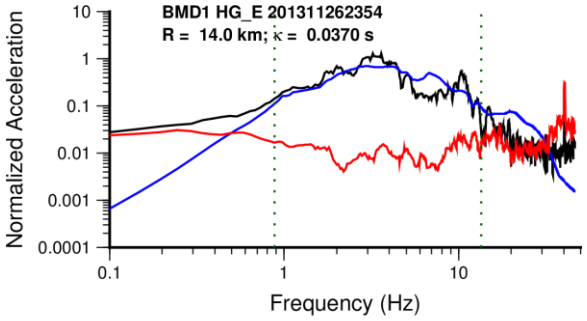
BMD1 HG_E 201311262354
R = 14.0 km; κ = 0.0370 s
Normalized Acceleration
Frequency (Hz)

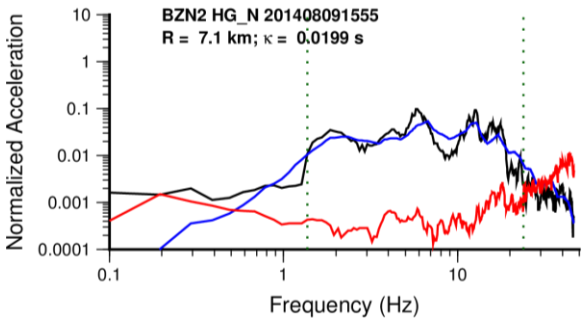
BZN2 HG_N 201408091555
R = 7.1 km; κ = 0.0199 s
Normalized Acceleration
Frequency (Hz)

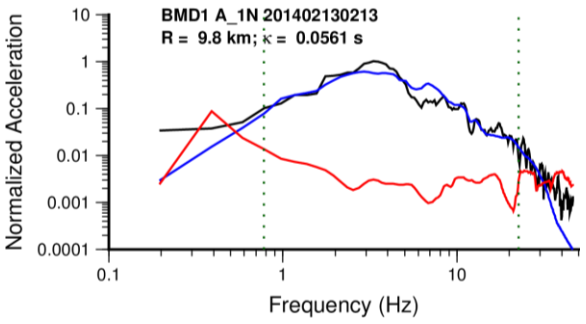
BMD1 A_1N 201402130213
R = 9.8 km; κ = 0.0561 s
Normalized Acceleration
Frequency (Hz)

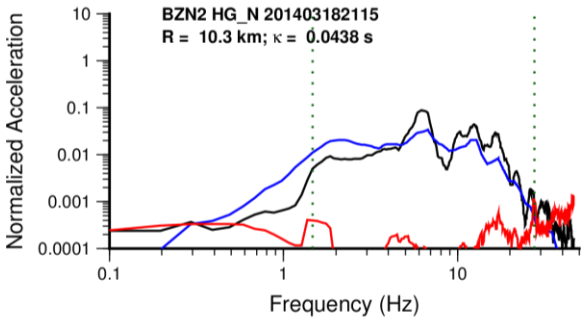
BZN2 HG_N 201403182115
R = 10.3 km; κ = 0.0438 s
Normalized Acceleration
Frequency (Hz)

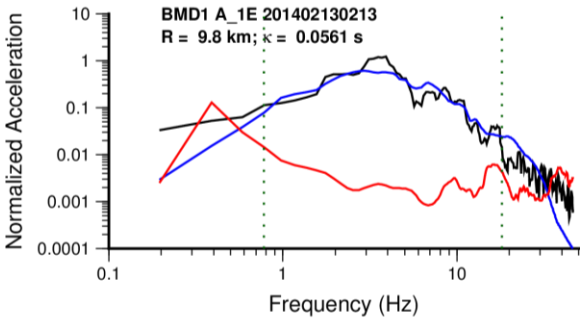
BMD1 A_1E 201402130213
R = 9.8 km; κ = 0.0561 s
Normalized Acceleration
Frequency (Hz)

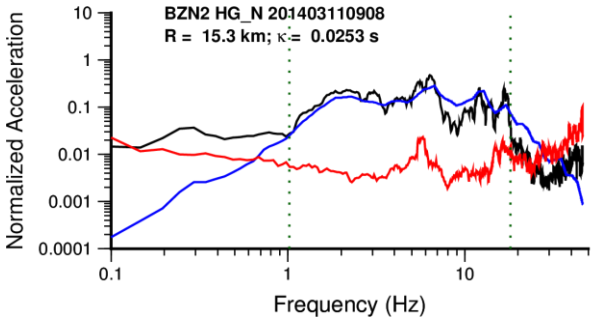
BZN2 HG_N 201403110908
R = 15.3 km; κ = 0.0253 s
Normalized Acceleration
Frequency (Hz)

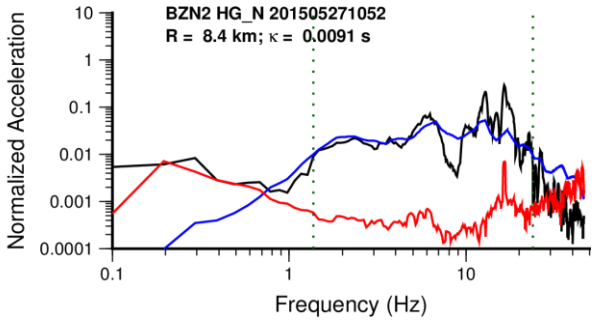
BZN2 HG_N 201505271052
R = 8.4 km; κ = 0.0091 s
Normalized Acceleration
Frequency (Hz)

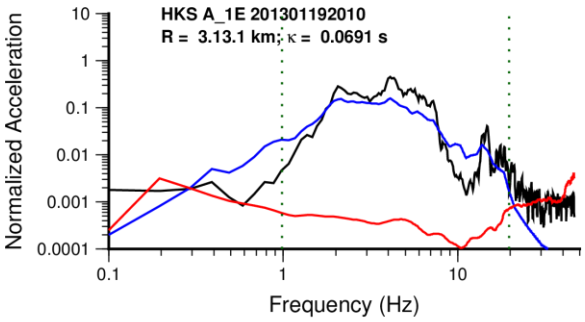
HKS A_1E 201301192010
R = 3.13.1 km; κ = 0.0691 s
Normalized Acceleration
Frequency (Hz)

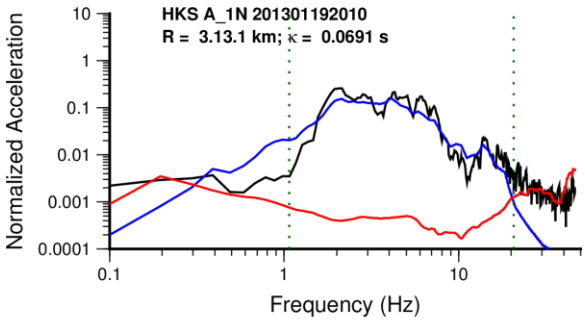
HKS A_1N 201301192010
R = 3.13.1 km; κ = 0.0691 s
Normalized Acceleration
Frequency (Hz)

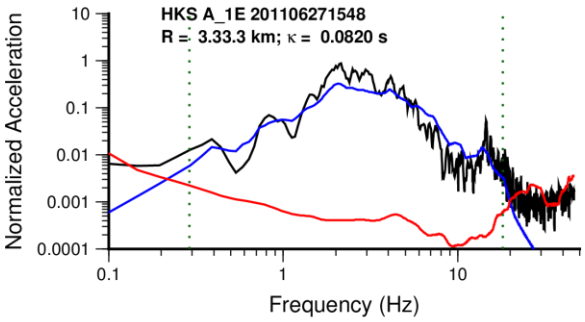
HKS A_1E 201106271548
R = 3.33.3 km; κ = 0.0820 s
Normalized Acceleration
Frequency (Hz)

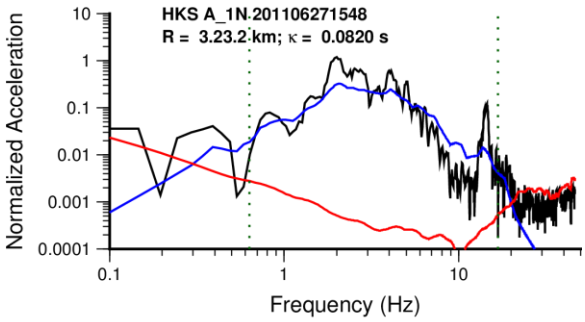
HKS A_1N 201106271548
R = 3.23.2 km; κ = 0.0820 s
Normalized Acceleration
Frequency (Hz)

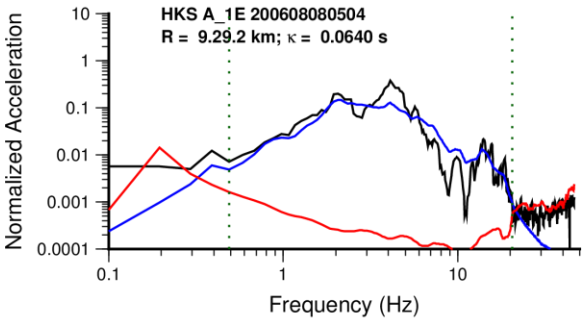
HKS A_1E 200608080504
R = 9.29.2 km; κ = 0.0640 s
Normalized Acceleration
Frequency (Hz)

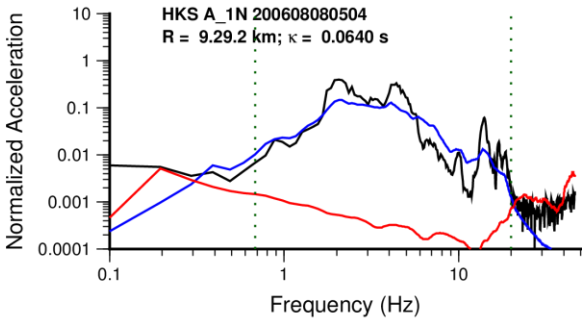
HKS A_1N 200608080504
R = 9.29.2 km; κ = 0.0640 s
Normalized Acceleration
Frequency (Hz)

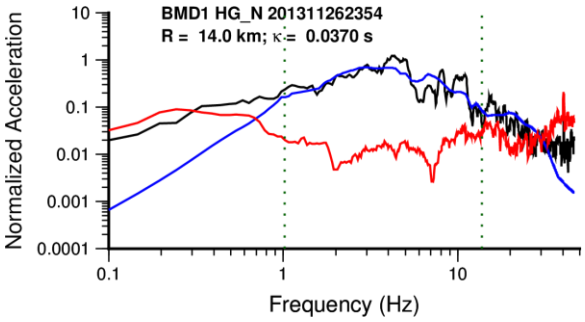
BMD1 HG_N 201311262354
R = 14.0 km; κ = 0.0370 s
Normalized Acceleration
Frequency (Hz)

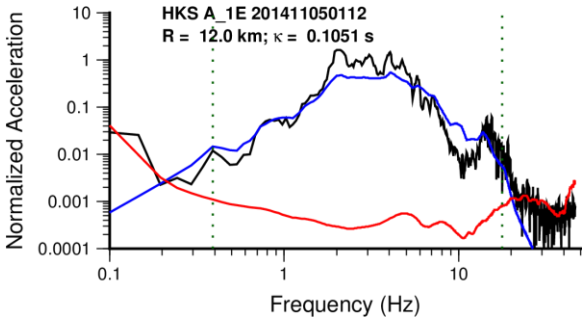
HKS A_1E 201411050112
R = 12.0 km; κ = 0.1051 s
Normalized Acceleration
Frequency (Hz)

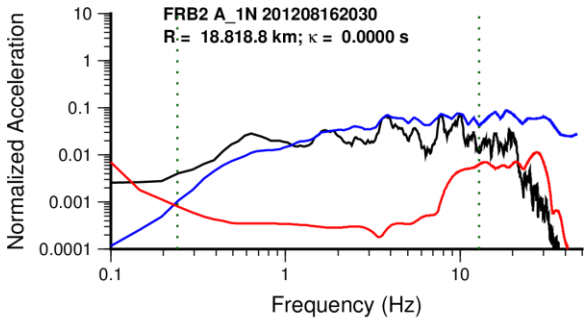
FRB2 A_1N 201208162030
R = 18.818.8 km; κ = 0.0000 s
Normalized Acceleration
Frequency (Hz)

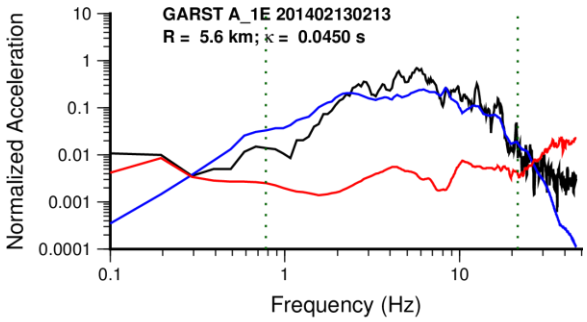
GARST A_1E 201402130213
R = 5.6 km; κ = 0.0450 s
Normalized Acceleration
Frequency (Hz)

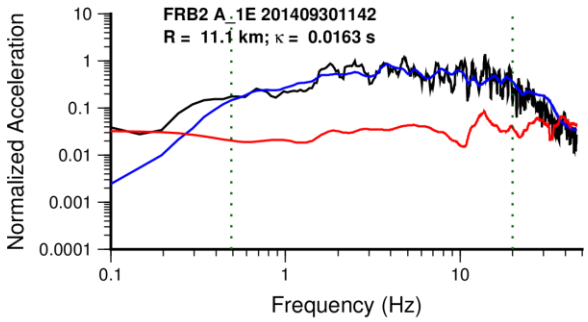
FRB2 A_1E 201409301142
R = 11.1 km; κ = 0.0163 s
Normalized Acceleration
Frequency (Hz)

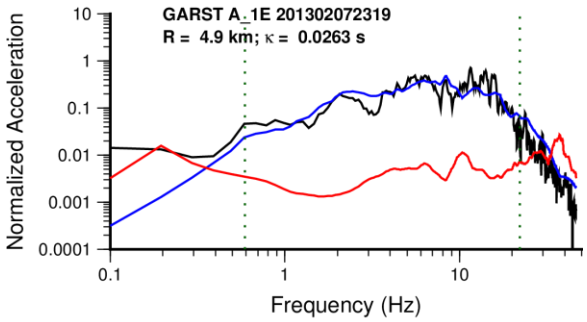
GARST A_1E 201302072319
R = 4.9 km; κ = 0.0263 s
Normalized Acceleration
Frequency (Hz)

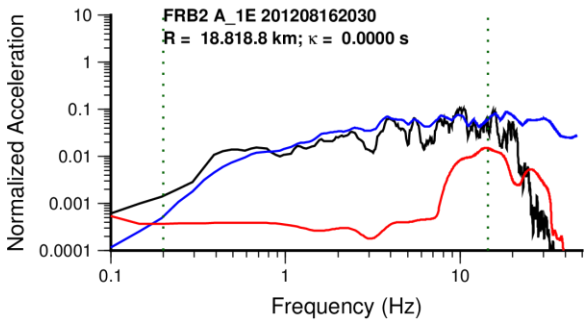
FRB2 A_1E 201208162030
R = 18.818.8 km; κ = 0.0000 s
Normalized Acceleration
Frequency (Hz)

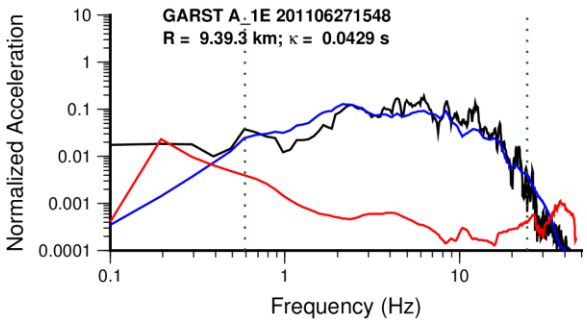
GARST A_1E 201106271548
R = 9.39.3 km; κ = 0.0429 s
Normalized Acceleration
Frequency (Hz)

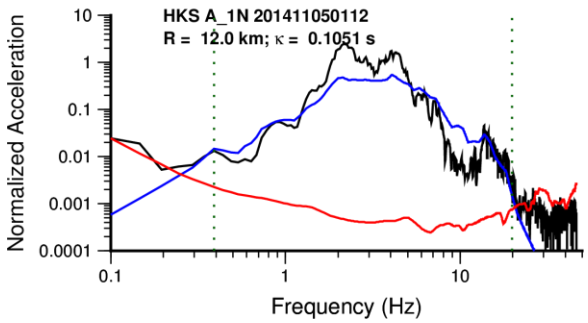
HKS A_1N 201411050112
R = 12.0 km; κ = 0.1051 s
Normalized Acceleration
Frequency (Hz)

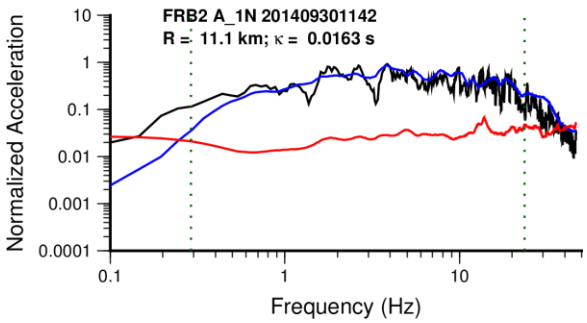
FRB2 A_1N 201409301142
R = 11.1 km; κ = 0.0163 s
Normalized Acceleration
Frequency (Hz)

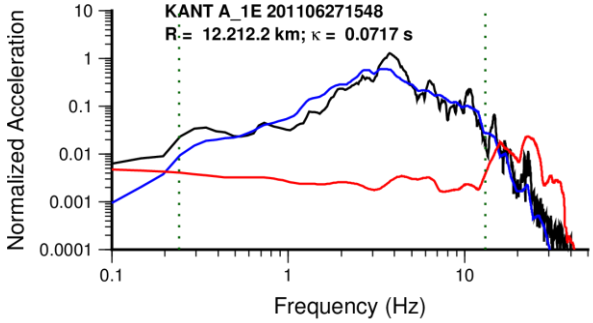
KANT A_1E 201106271548
R = 12.212.2 km; κ = 0.0717 s
Normalized Acceleration
Frequency (Hz)

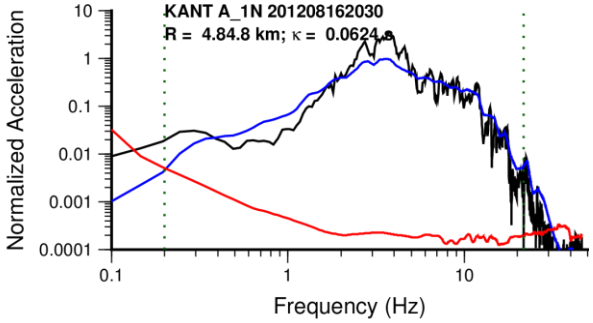
KANT A_1N 201208162030
R = 4.84.8 km; κ = 0.0624 s
Normalized Acceleration
Frequency (Hz)

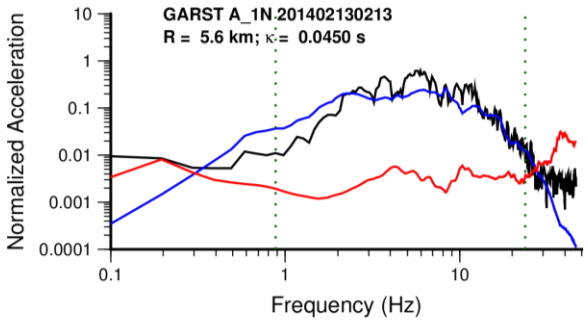
GARST A_1N 201402130213
R = 5.6 km; κ = 0.0450 s
Normalized Acceleration
Frequency (Hz)

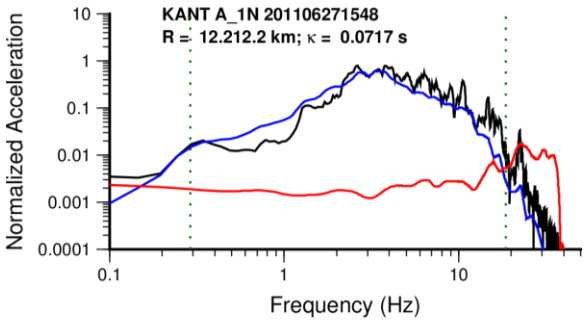
KANT A_1N 201106271548
R = 12.212.2 km; κ = 0.0717 s
Normalized Acceleration
Frequency (Hz)

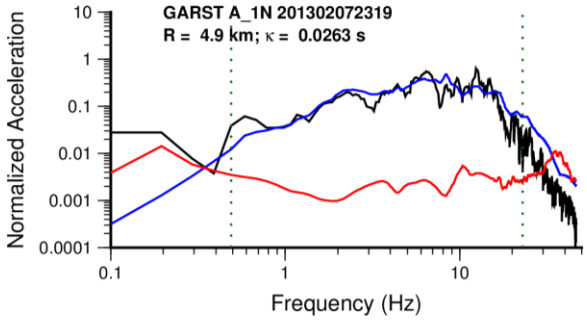
GARST A_1N 201302072319
R = 4.9 km; κ = 0.0263 s
Normalized Acceleration
Frequency (Hz)

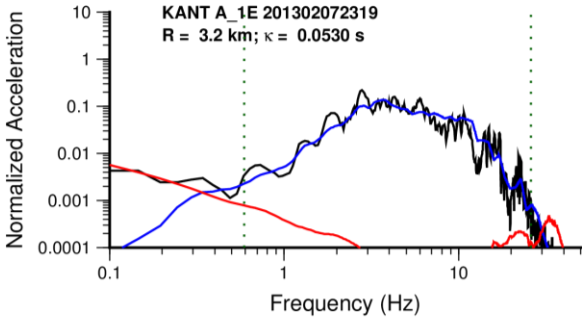
KANT A_1E 201302072319
R = 3.2 km; κ = 0.0530 s
Normalized Acceleration
Frequency (Hz)

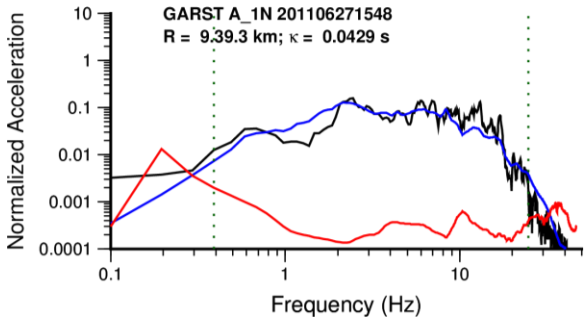
GARST A_1N 201106271548
R = 9.39.3 km; κ = 0.0429 s
Normalized Acceleration
Frequency (Hz)

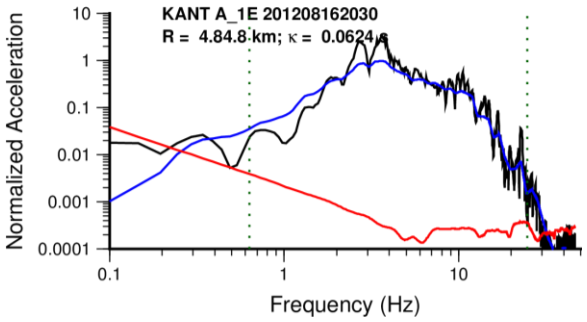
KANT A_1E 201208162030
R = 4.84.8 km; κ = 0.0624 s
Normalized Acceleration
Frequency (Hz)

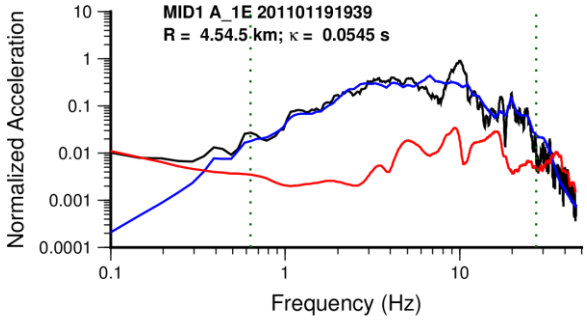
MID1 A_1E 201101191939
R = 4.54.5 km; κ = 0.0545 s
Normalized Acceleration
Frequency (Hz)

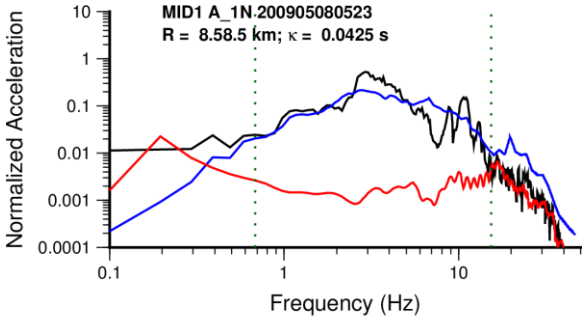
MID1 A_1N 200905080523
R = 8.58.5 km; κ = 0.0425 s
Normalized Acceleration
Frequency (Hz)

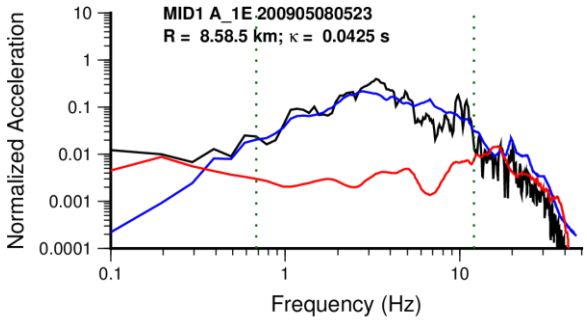
MID1 A_1E 200905080523
R = 8.58.5 km; κ = 0.0425 s
Normalized Acceleration
Frequency (Hz)

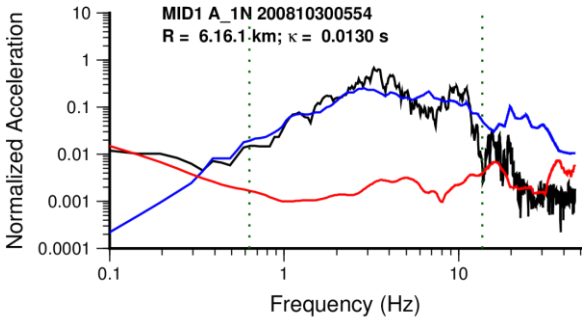
MID1 A_1N 200810300554
R = 6.16.1 km; κ = 0.0130 s
Normalized Acceleration
Frequency (Hz)

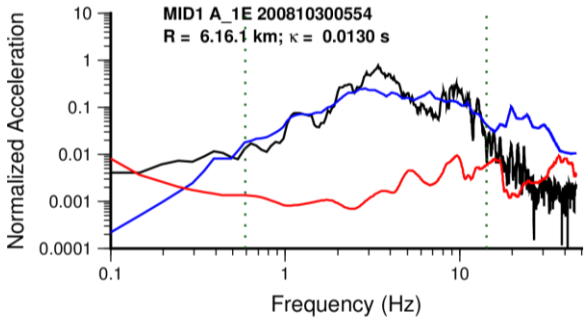
MID1 A_1E 200810300554
R = 6.16.1 km; κ = 0.0130 s
Normalized Acceleration
Frequency (Hz)

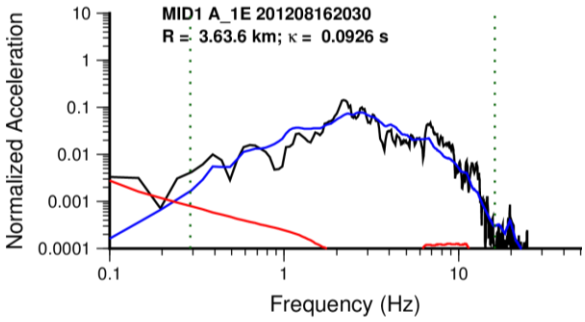
MID1 A_1E 201208162030
R = 3.63.6 km; κ = 0.0926 s
Normalized Acceleration
Frequency (Hz)

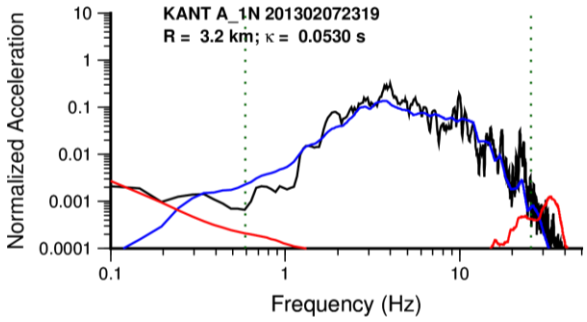
KANT A_1N 201302072319
R = 3.2 km; κ = 0.0530 s
Normalized Acceleration
Frequency (Hz)

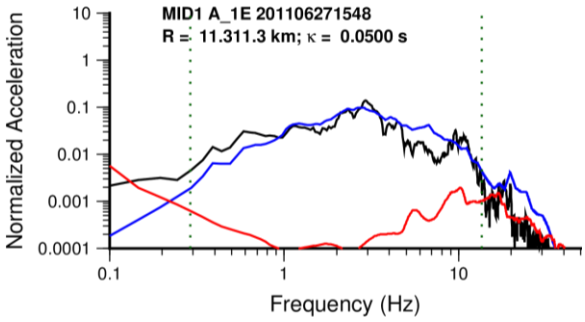
MID1 A_1E 201106271548
R = 11.311.3 km; κ = 0.0500 s
Normalized Acceleration
Frequency (Hz)

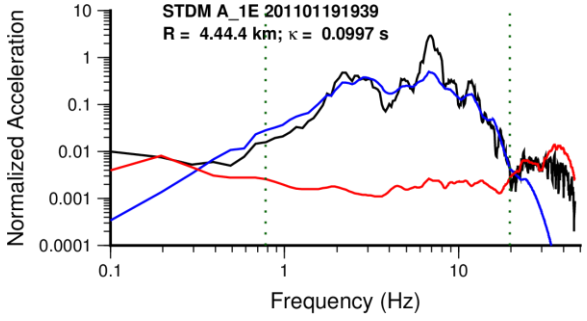
STDM A_1E 201101191939
R = 4.44.4 km; κ = 0.0997 s
Normalized Acceleration
Frequency (Hz)

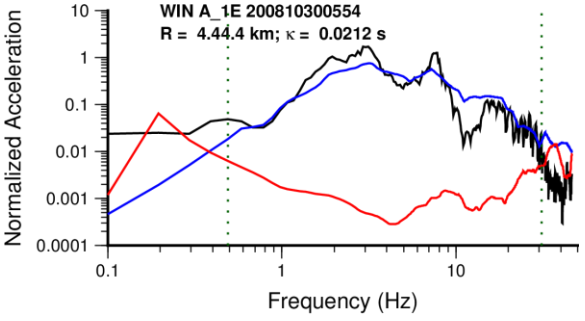
WIN A_1E 200810300554
R = 4.44.4 km; κ = 0.0212 s
Normalized Acceleration
Frequency (Hz)

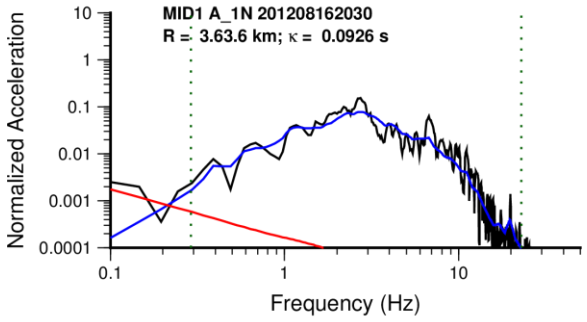
MID1 A_1N 201208162030
R = 3.63.6 km; κ = 0.0926 s
Normalized Acceleration
Frequency (Hz)

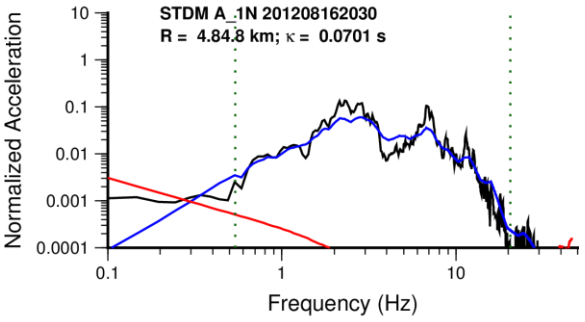
STDM A_1N 201208162030
R = 4.84.8 km; κ = 0.0701 s
Normalized Acceleration
Frequency (Hz)

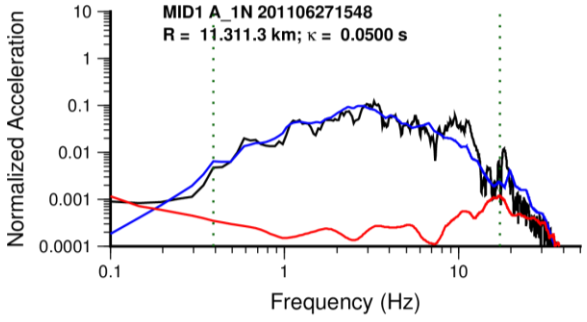
MID1 A_1N 201106271548
R = 11.311.3 km; κ = 0.0500 s
Normalized Acceleration
Frequency (Hz)

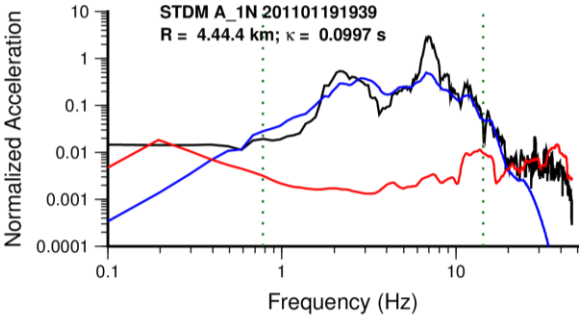
STDM A_1N 201101191939
R = 4.44.4 km; κ = 0.0997 s
Normalized Acceleration
Frequency (Hz)

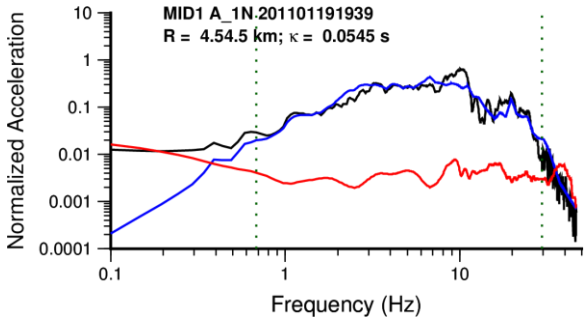
MID1 A_1N 201101191939
R = 4.54.5 km; κ = 0.0545 s
Normalized Acceleration
Frequency (Hz)

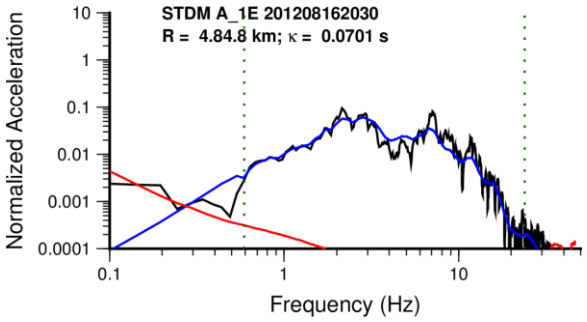
STDM A_1E 201208162030
R = 4.84.8 km; κ = 0.0701 s
Normalized Acceleration
Frequency (Hz)

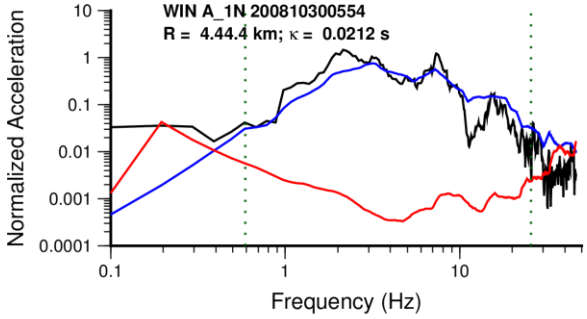
WIN A_1N 200810300554
R = 4.44.4 km; κ = 0.0212 s
Normalized Acceleration
Frequency (Hz)

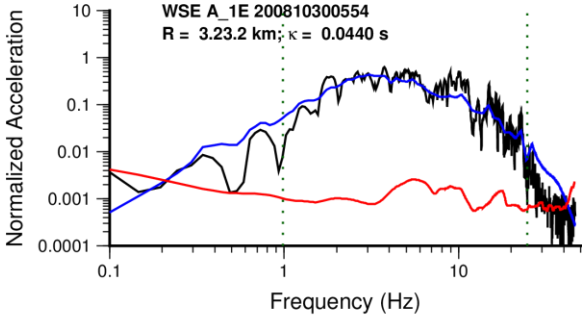
WSE A_1E 200810300554
R = 3.23.2 km; κ = 0.0440 s
Normalized Acceleration
Frequency (Hz)

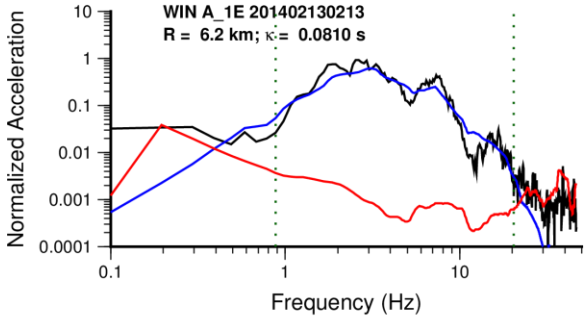
WIN A_1E 201402130213
R = 6.2 km; κ = 0.0810 s
Normalized Acceleration
Frequency (Hz)

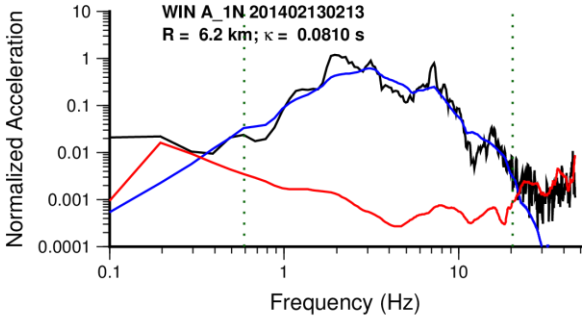
WIN A_1N 201402130213
R = 6.2 km; κ = 0.0810 s
Normalized Acceleration
Frequency (Hz)

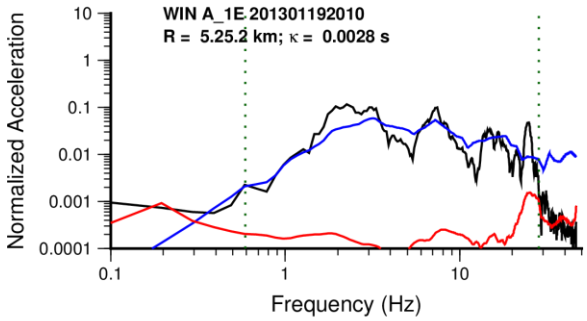
WIN A_1E 201301192010
R = 5.25.2 km; κ = 0.0028 s
Normalized Acceleration
Frequency (Hz)

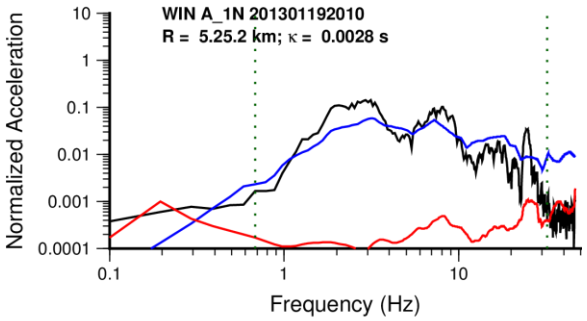
WIN A_1N 201301192010
R = 5.25.2 km; κ = 0.0028 s
Normalized Acceleration
Frequency (Hz)

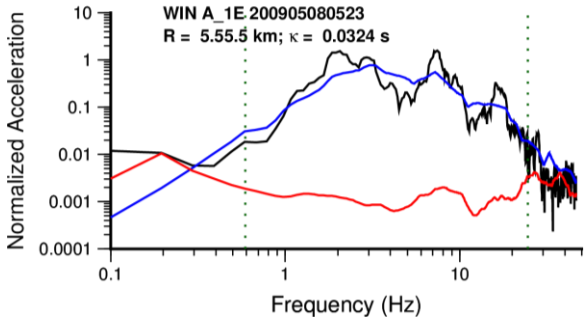
WIN A_1E 200905080523
R = 5.55.5 km; κ = 0.0324 s
Normalized Acceleration
Frequency (Hz)

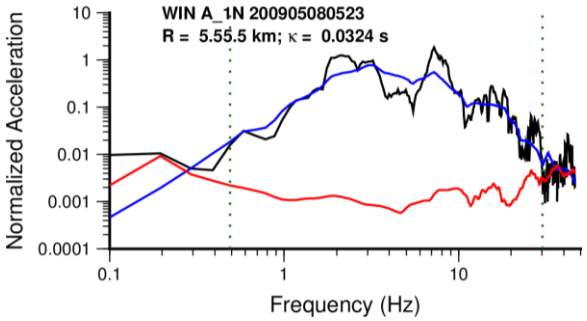
WIN A_1N 200905080523
R = 5.55.5 km; κ = 0.0324 s
Normalized Acceleration
Frequency (Hz)

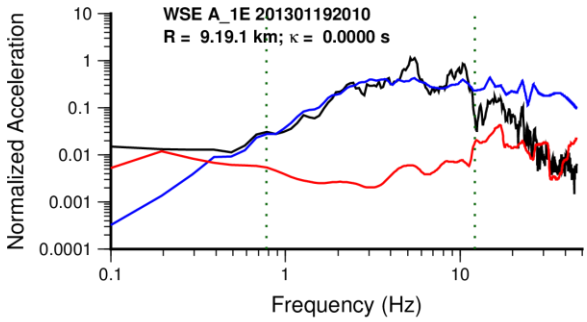
WSE A_1E 201301192010
R = 9.19.1 km; κ = 0.0000 s
Normalized Acceleration
Frequency (Hz)

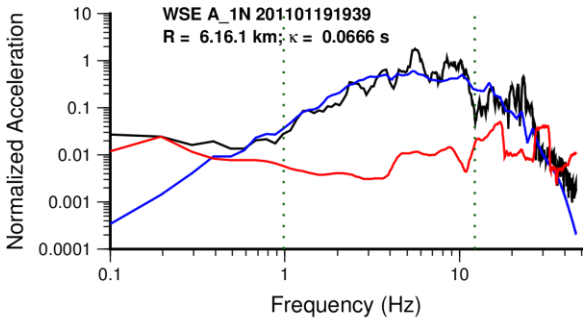
WSE A_1N 201101191939
R = 6.16.1 km; κ = 0.0666 s
Normalized Acceleration
Frequency (Hz)

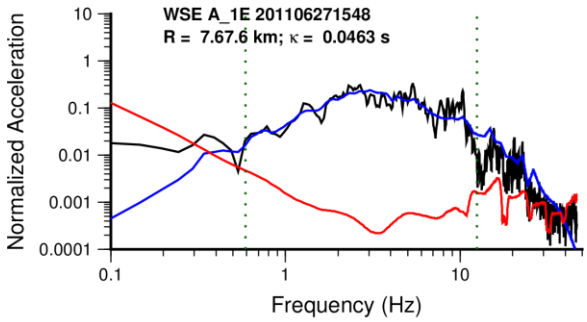
WSE A_1E 201106271548
R = 7.67.6 km; κ = 0.0463 s
Normalized Acceleration
Frequency (Hz)

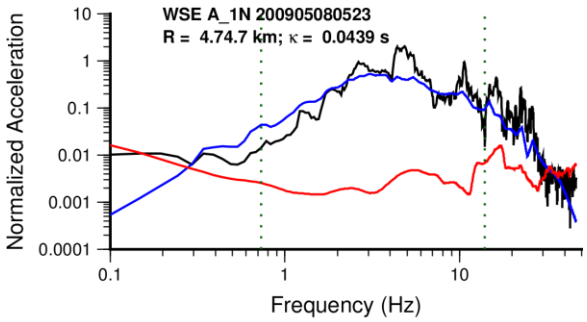
WSE A_1N 200905080523
R = 4.74.7 km; κ = 0.0439 s
Normalized Acceleration
Frequency (Hz)

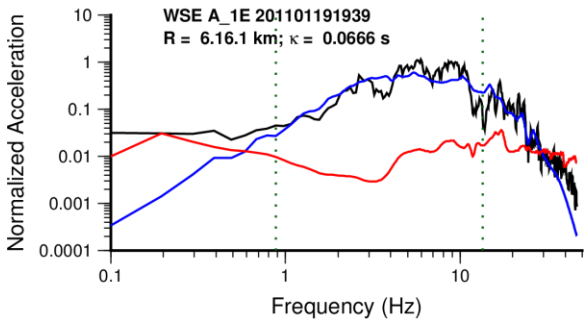
WSE A_1E 201101191939
R = 6.16.1 km; κ = 0.0666 s
Normalized Acceleration
Frequency (Hz)

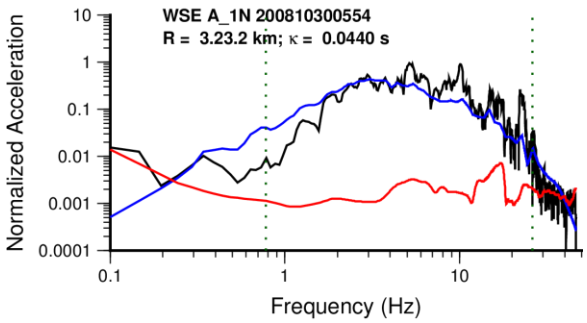
WSE A_1N 200810300554
R = 3.23.2 km; κ = 0.0440 s
Normalized Acceleration
Frequency (Hz)

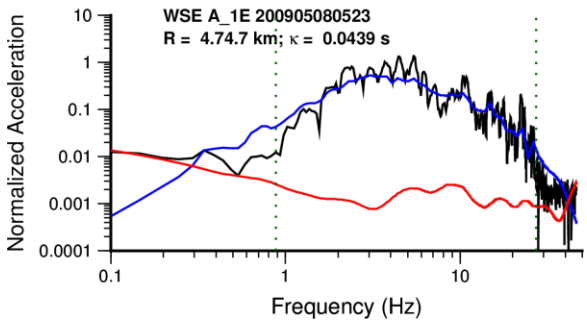
WSE A_1E 200905080523
R = 4.74.7 km; κ = 0.0439 s
Normalized Acceleration
Frequency (Hz)

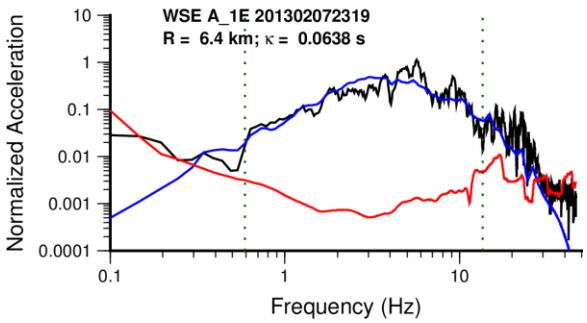
WSE A_1E 201302072319
R = 6.4 km; κ = 0.0638 s
Normalized Acceleration
Frequency (Hz)

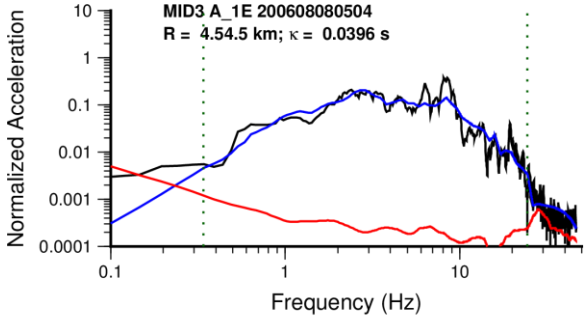
MID3 A_1E 200608080504
R = 4.54.5 km; κ = 0.0396 s
Normalized Acceleration
Frequency (Hz)

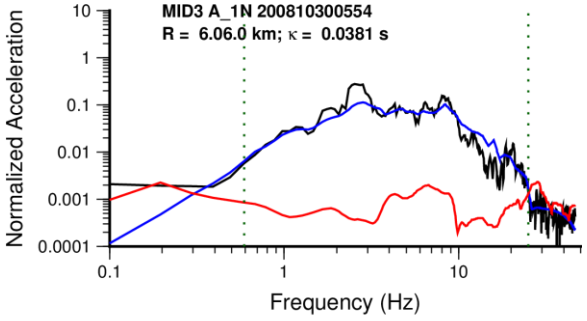
MID3 A_1N 200810300554
R = 6.06.0 km; κ = 0.0381 s
Normalized Acceleration
Frequency (Hz)

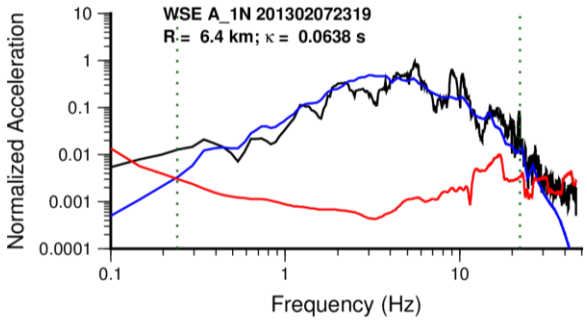
WSE A_1N 201302072319
R = 6.4 km; κ = 0.0638 s
Normalized Acceleration
Frequency (Hz)

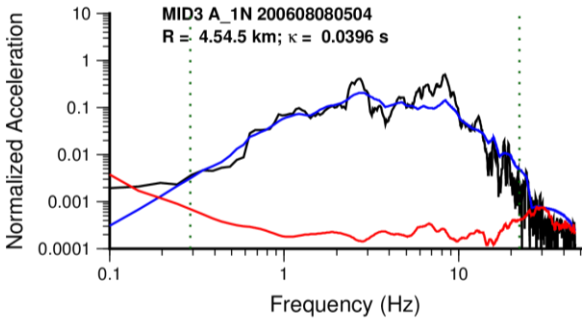
MID3 A_1N 200608080504
R = 4.54.5 km; κ = 0.0396 s
Normalized Acceleration
Frequency (Hz)

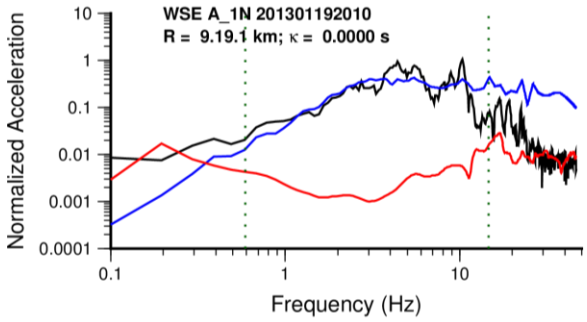
WSE A_1N 201301192010
R = 9.19.1 km; κ = 0.0000 s
Normalized Acceleration
Frequency (Hz)

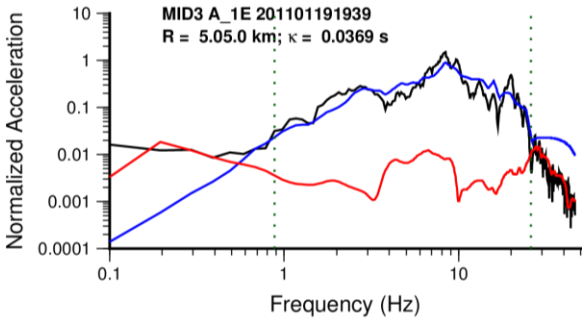
MID3 A_1E 201101191939
R = 5.05.0 km; κ = 0.0369 s
Normalized Acceleration
Frequency (Hz)

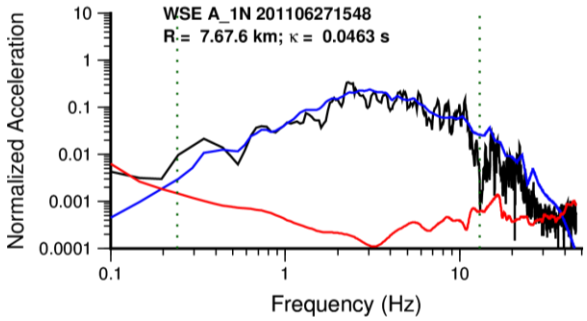
WSE A_1N 201106271548
R = 7.67.6 km; κ = 0.0463 s
Normalized Acceleration
Frequency (Hz)

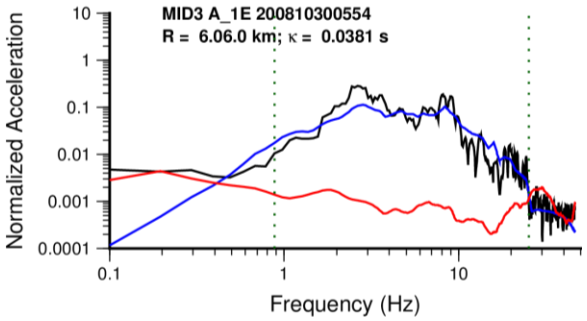
MID3 A_1E 200810300554
R = 6.06.0 km; κ = 0.0381 s
Normalized Acceleration
Frequency (Hz)

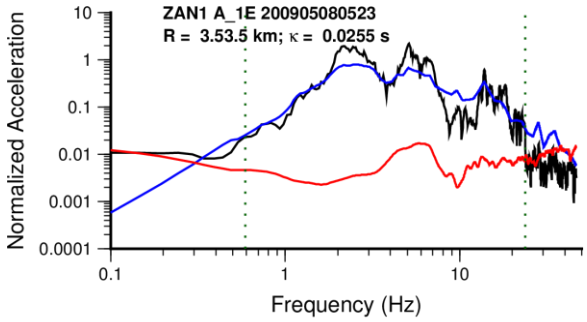
ZAN1 A_1E 200905080523
R = 3.53.5 km; κ = 0.0255 s
Normalized Acceleration
Frequency (Hz)

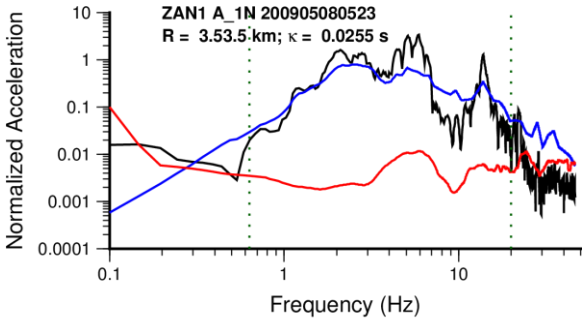
ZAN1 A_1N 200905080523
R = 3.53.5 km; κ = 0.0255 s
Normalized Acceleration
Frequency (Hz)

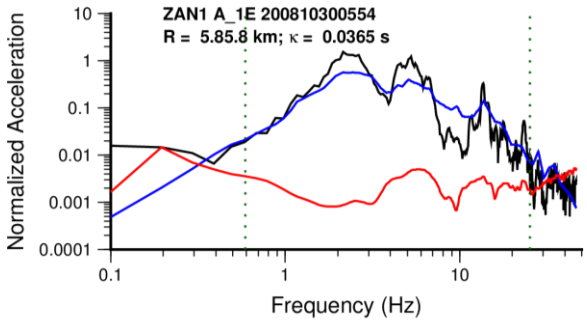
ZAN1 A_1E 200810300554
R = 5.85.8 km; κ = 0.0365 s
Normalized Acceleration
Frequency (Hz)

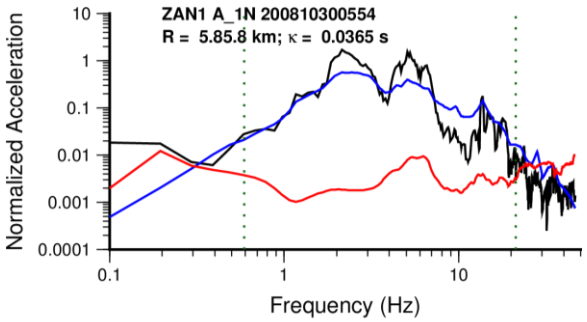
ZAN1 A_1N 200810300554
R = 5.85.8 km; κ = 0.0365 s
Normalized Acceleration
Frequency (Hz)

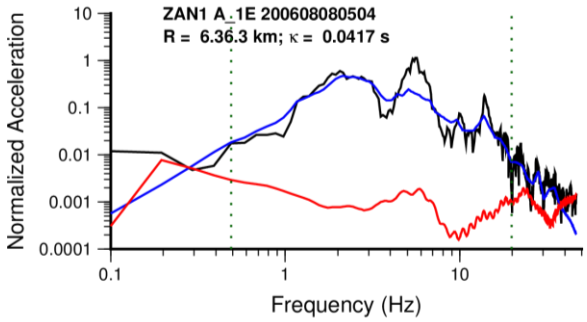
ZAN1 A_1E 200608080504
R = 6.36.3 km; κ = 0.0417 s
Normalized Acceleration
Frequency (Hz)

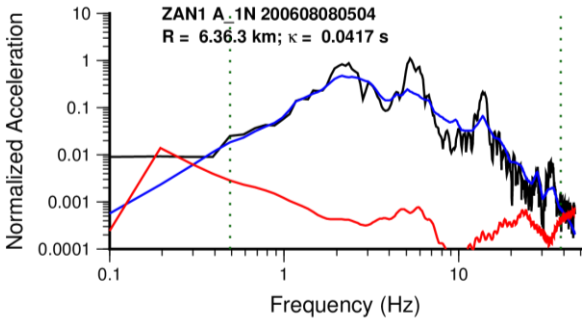
ZAN1 A_1N 200608080504
R = 6.36.3 km; κ = 0.0417 s
Normalized Acceleration
Frequency (Hz)

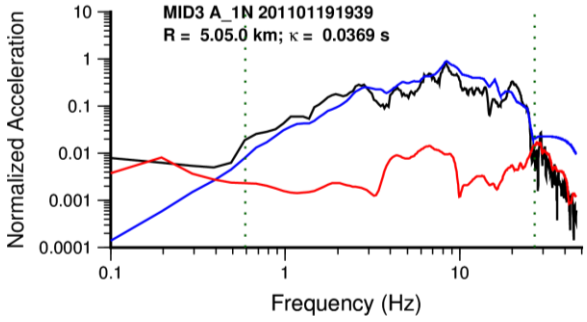
MID3 A_1N 201101191939
R = 5.05.0 km; κ = 0.0369 s
Normalized Acceleration
Frequency (Hz)

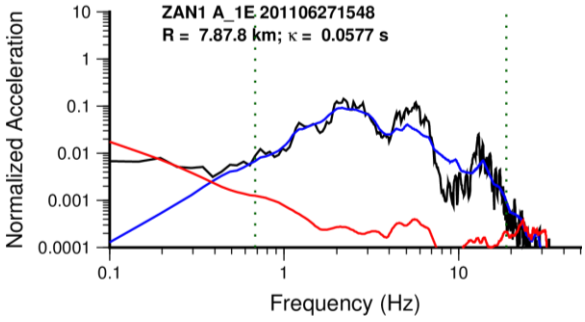
ZAN1 A_1E 201106271548
R = 7.87.8 km; κ = 0.0577 s
Normalized Acceleration
Frequency (Hz)

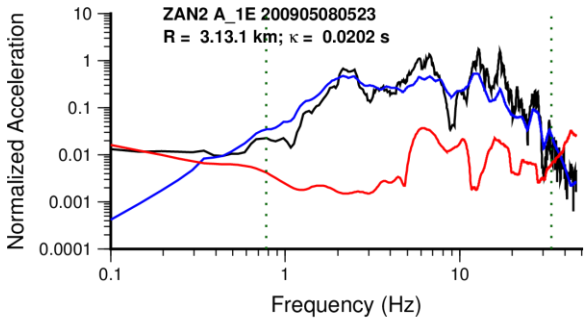
ZAN2 A_1E 200905080523
R = 3.13.1 km; κ = 0.0202 s
Normalized Acceleration
Frequency (Hz)

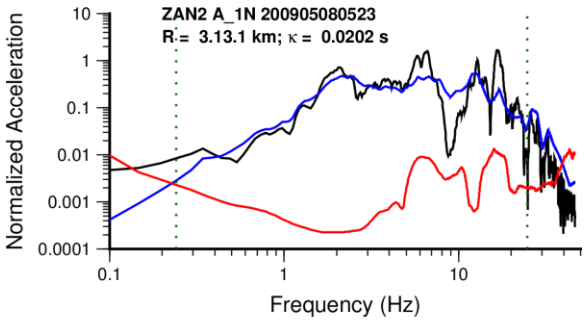
ZAN2 A_1N 200905080523
R = 3.13.1 km; κ = 0.0202 s
Normalized Acceleration
Frequency (Hz)

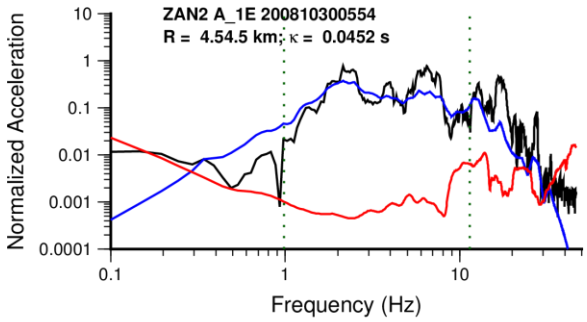
ZAN2 A_1E 200810300554
R = 4.54.5 km; κ = 0.0452 s
Normalized Acceleration
Frequency (Hz)

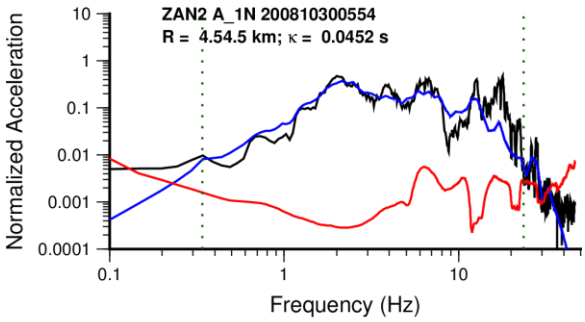
ZAN2 A_1N 200810300554
R = 4.54.5 km; κ = 0.0452 s
Normalized Acceleration
Frequency (Hz)

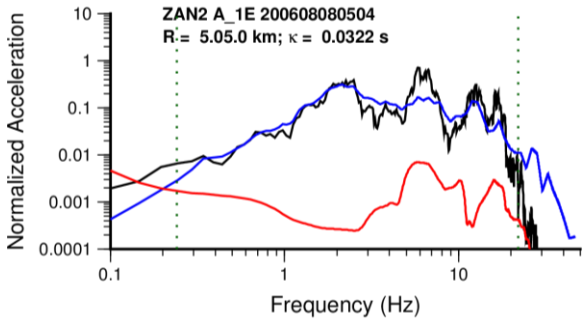
ZAN2 A_1E 200608080504
R = 5.05.0 km; κ = 0.0322 s
Normalized Acceleration
Frequency (Hz)

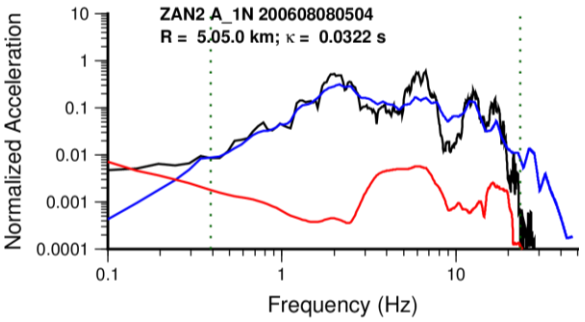
ZAN2 A_1N 200608080504
R = 5.05.0 km; κ = 0.0322 s
Normalized Acceleration
Frequency (Hz)

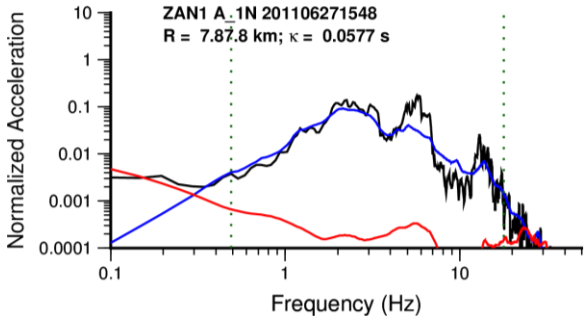
ZAN1 A_1N 201106271548
R = 7.87.8 km; κ = 0.0577 s
Normalized Acceleration
Frequency (Hz)

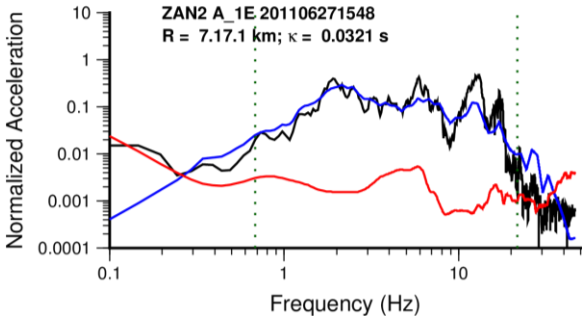
ZAN2 A_1E 201106271548
R = 7.17.1 km; κ = 0.0321 s
Normalized Acceleration
Frequency (Hz)

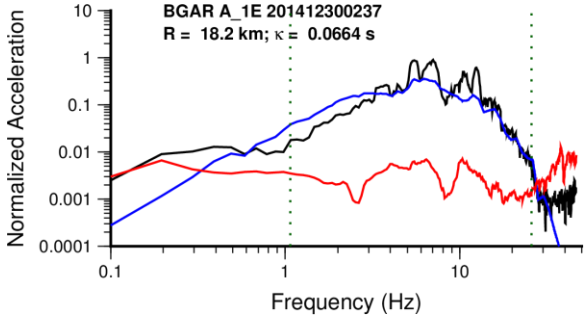
BGAR A_1E 201412300237
R = 18.2 km; κ = 0.0664 s
Normalized Acceleration
Frequency (Hz)

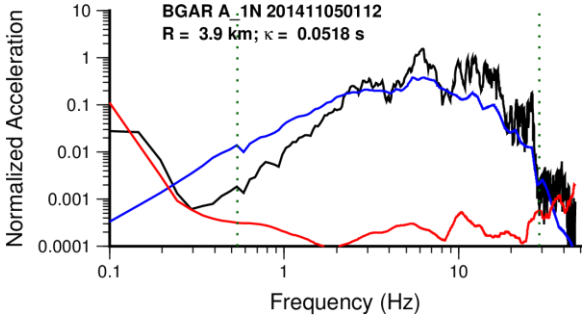
BGAR A_1N 201411050112
R = 3.9 km; κ = 0.0518 s
Normalized Acceleration
Frequency (Hz)

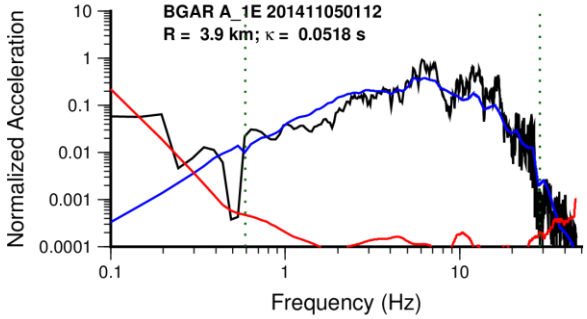
BGAR A_1E 201411050112
R = 3.9 km; κ = 0.0518 s
Normalized Acceleration
Frequency (Hz)

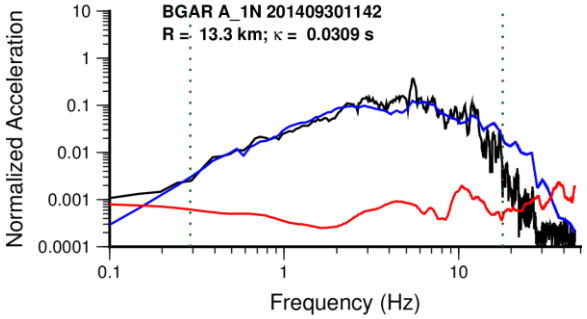
BGAR A_1N 201409301142
R = 13.3 km; κ = 0.0309 s
Normalized Acceleration
Frequency (Hz)

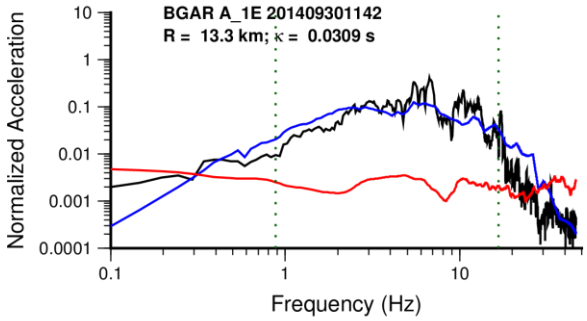
BGAR A_1E 201409301142
R = 13.3 km; κ = 0.0309 s
Normalized Acceleration
Frequency (Hz)

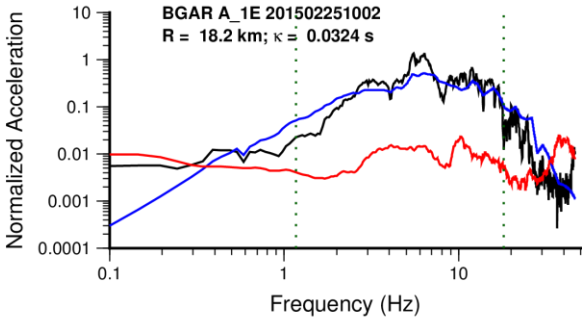
BGAR A_1E 201502251002
R = 18.2 km; κ = 0.0324 s
Normalized Acceleration
Frequency (Hz)

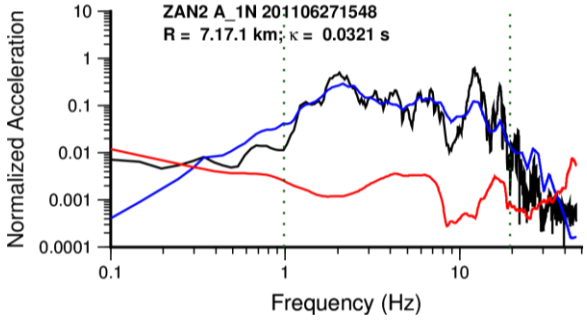
ZAN2 A_1N 201106271548
R = 7.17.1 km; κ = 0.0321 s
Normalized Acceleration
Frequency (Hz)

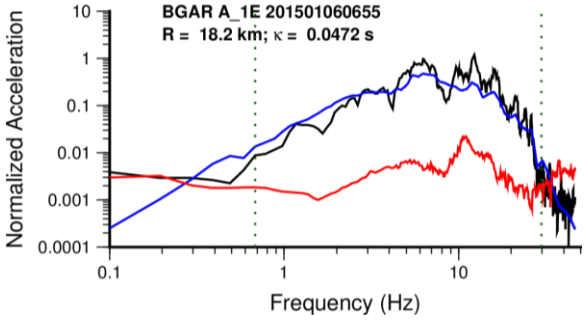
BGAR A_1E 201501060655
R = 18.2 km; κ = 0.0472 s
Normalized Acceleration
Frequency (Hz)

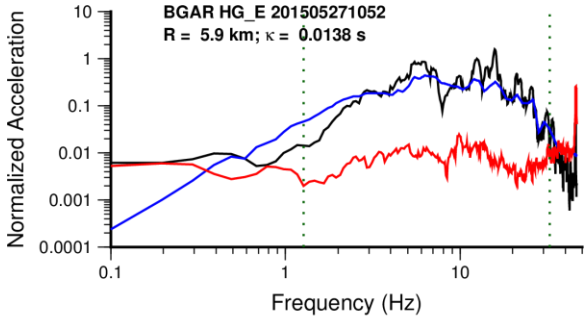
BGAR HG_E 201505271052
R = 5.9 km; κ = 0.0138 s
Normalized Acceleration
Frequency (Hz)

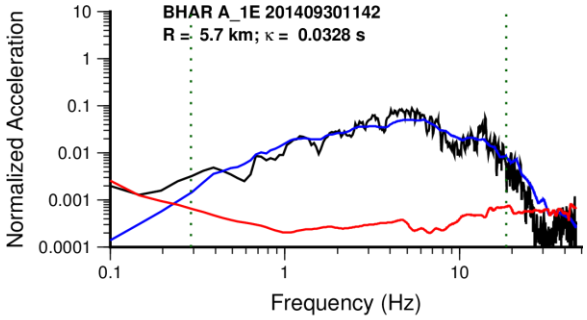
BHAR A_1E 201409301142
R = 5.7 km; κ = 0.0328 s
Normalized Acceleration
Frequency (Hz)

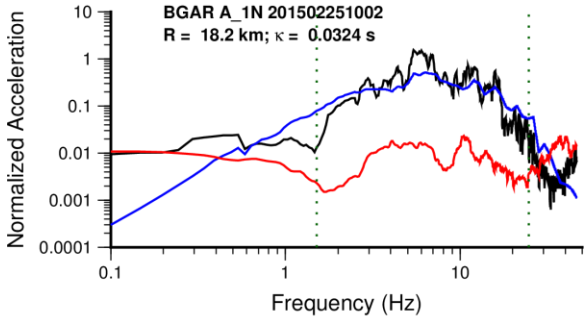
BGAR A_1N 201502251002
R = 18.2 km; κ = 0.0324 s
Normalized Acceleration
Frequency (Hz)

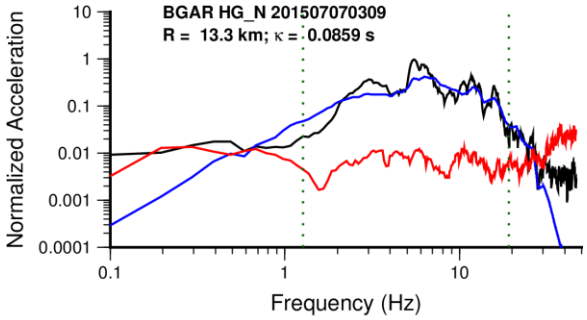
BGAR HG_N 201507070309
R = 13.3 km; κ = 0.0859 s
Normalized Acceleration
Frequency (Hz)

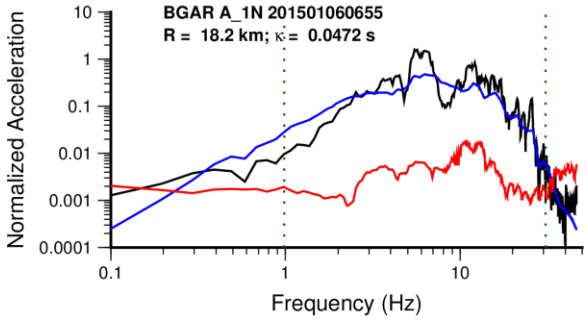
BGAR A_1N 201501060655
R = 18.2 km; κ = 0.0472 s
Normalized Acceleration
Frequency (Hz)

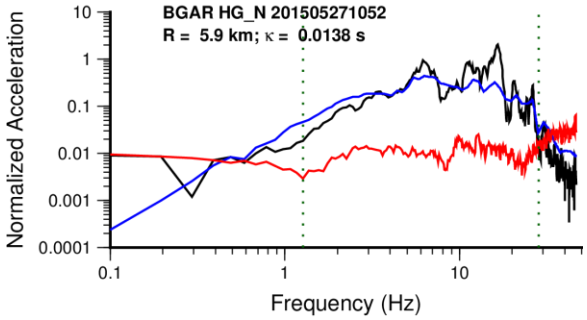
BGAR HG_N 201505271052
R = 5.9 km; κ = 0.0138 s
Normalized Acceleration
Frequency (Hz)

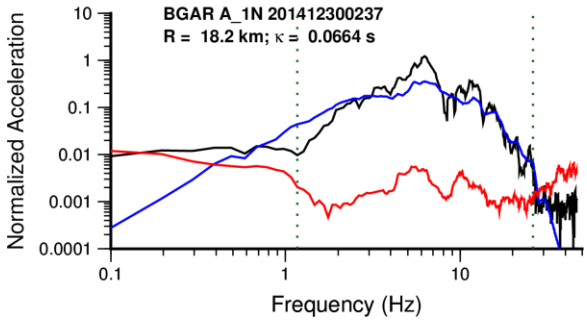
BGAR A_1N 201412300237
R = 18.2 km; κ = 0.0664 s
Normalized Acceleration
Frequency (Hz)

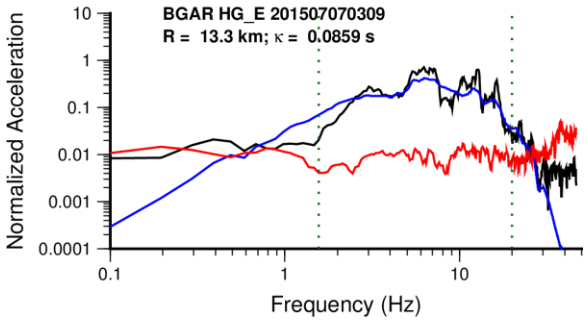
BGAR HG_E 201507070309
R = 13.3 km; κ = 0.0859 s
Normalized Acceleration
Frequency (Hz)

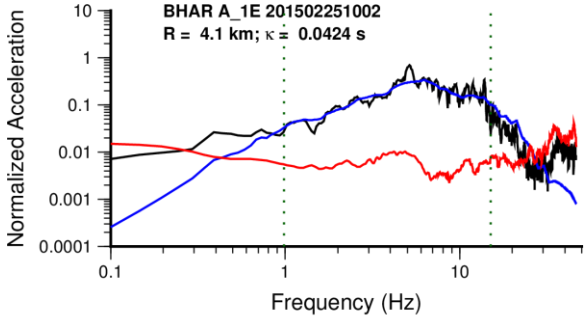
BHAR A_1E 201502251002
R = 4.1 km; κ = 0.0424 s
Normalized Acceleration
Frequency (Hz)

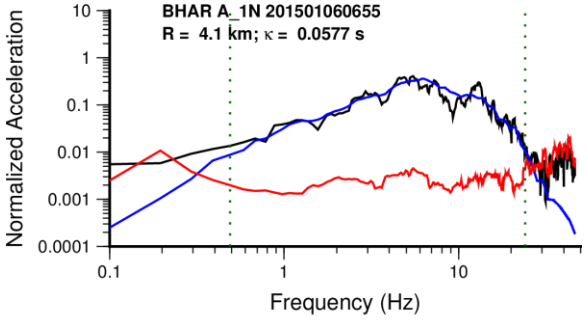
BHAR A_1N 201501060655
R = 4.1 km; κ = 0.0577 s
Normalized Acceleration
Frequency (Hz)

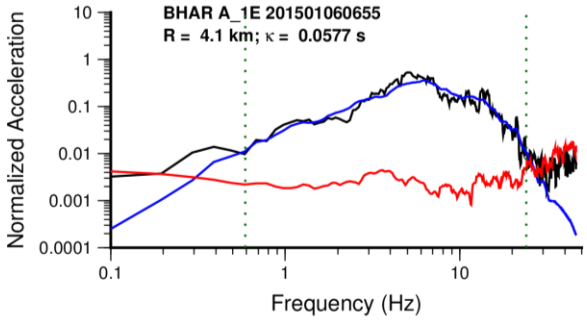
BHAR A_1E 201501060655
R = 4.1 km; κ = 0.0577 s
Normalized Acceleration
Frequency (Hz)

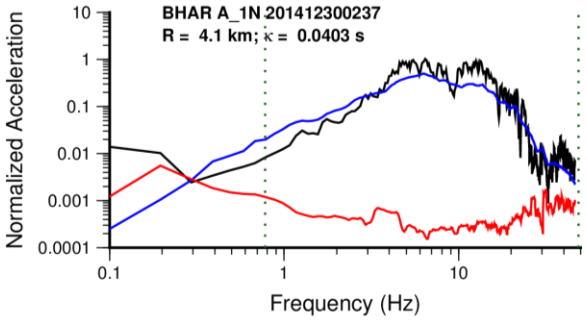
BHAR A_1N 201412300237
R = 4.1 km; κ = 0.0403 s
Normalized Acceleration
Frequency (Hz)

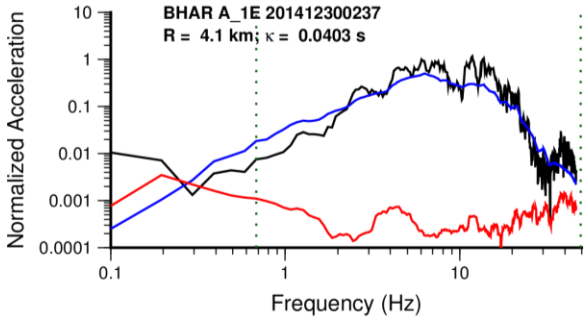
BHAR A_1E 201412300237
R = 4.1 km; κ = 0.0403 s
Normalized Acceleration
Frequency (Hz)

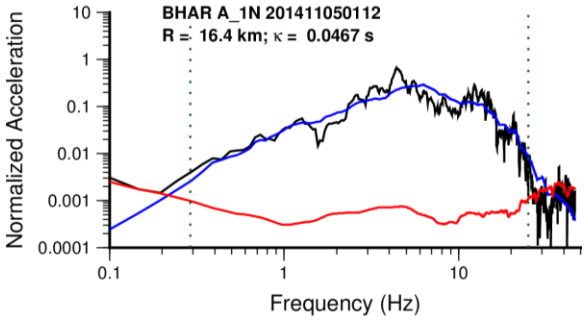
BHAR A_1N 201411050112
R = 16.4 km; κ = 0.0467 s
Normalized Acceleration
Frequency (Hz)

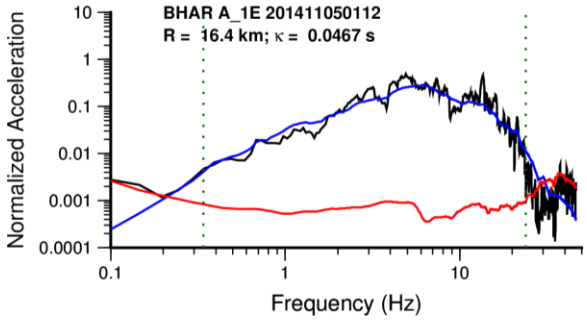
BHAR A_1E 201411050112
R = 16.4 km; κ = 0.0467 s
Normalized Acceleration
Frequency (Hz)

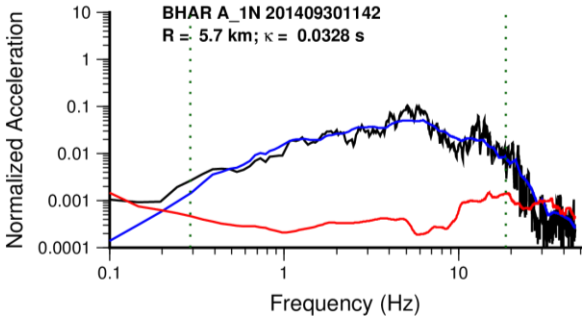
BHAR A_1N 201409301142
R = 5.7 km; κ = 0.0328 s
Normalized Acceleration
Frequency (Hz)

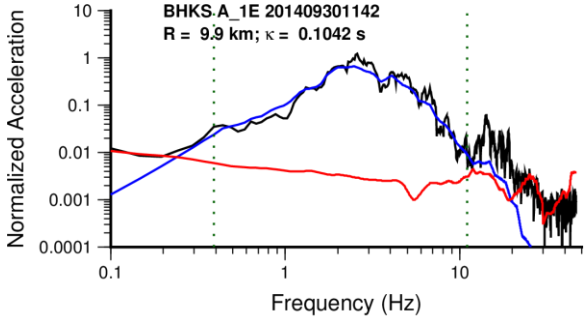
BHKS A_1E 201409301142
R = 9.9 km; κ = 0.1042 s
Normalized Acceleration
Frequency (Hz)

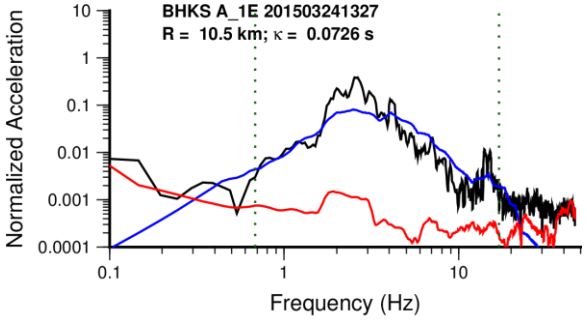
BHKS A_1E 201503241327
R = 10.5 km; κ = 0.0726 s
Normalized Acceleration
Frequency (Hz)

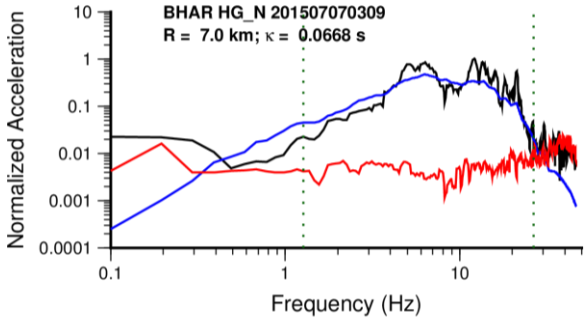
BHAR HG_N 201507070309
R = 7.0 km; κ = 0.0668 s
Normalized Acceleration
Frequency (Hz)

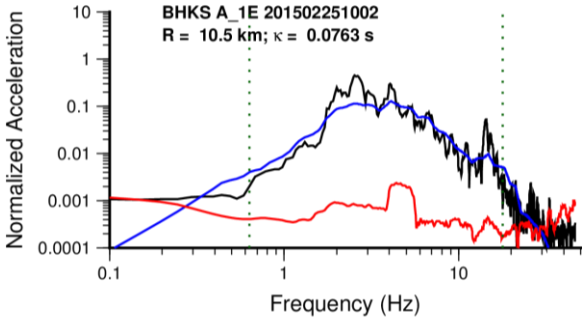
BHKS A_1E 201502251002
R = 10.5 km; κ = 0.0763 s
Normalized Acceleration
Frequency (Hz)

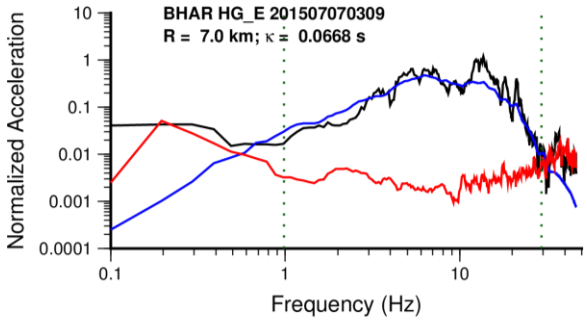
BHAR HG_E 201507070309
R = 7.0 km; κ = 0.0668 s
Normalized Acceleration
Frequency (Hz)

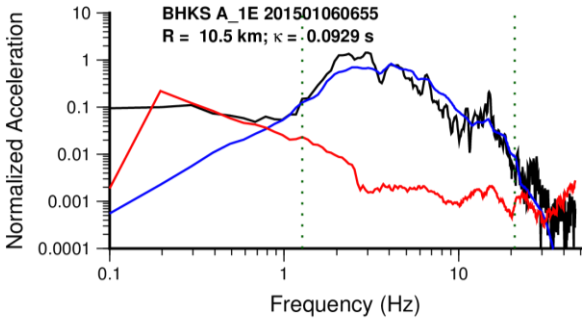
BHKS A_1E 201501060655
R = 10.5 km; κ = 0.0929 s
Normalized Acceleration
Frequency (Hz)

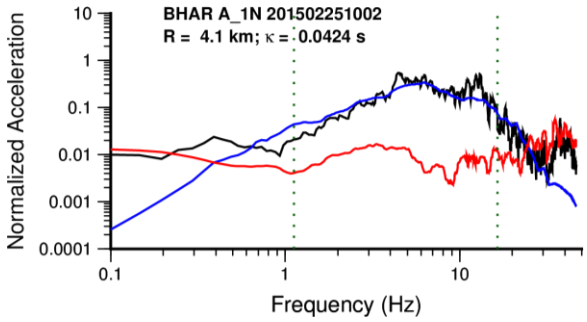
BHAR A_1N 201502251002
R = 4.1 km; κ = 0.0424 s
Normalized Acceleration
Frequency (Hz)

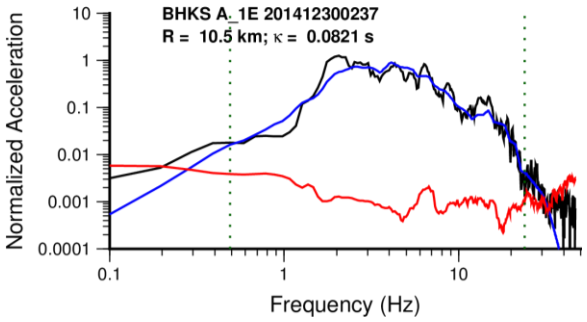
BHKS A_1E 201412300237
R = 10.5 km; κ = 0.0821 s
Normalized Acceleration
Frequency (Hz)

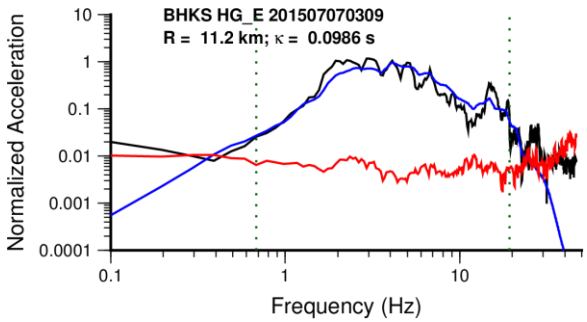
BHKS HG_E 201507070309
R = 11.2 km; κ = 0.0986 s
Normalized Acceleration
Frequency (Hz)

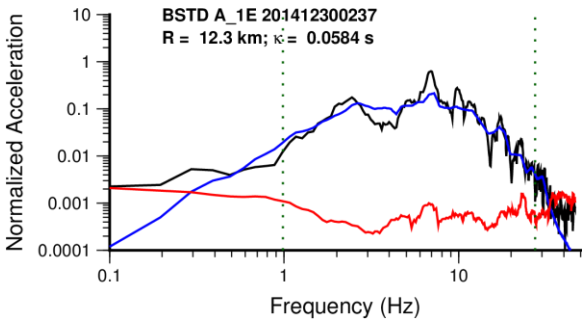
BSTD A_1E 201412300237
R = 12.3 km; κ = 0.0584 s
Normalized Acceleration
Frequency (Hz)

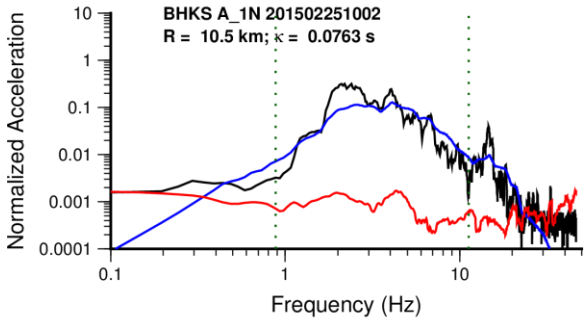
BHKS A_1N 201502251002
R = 10.5 km; κ = 0.0763 s
Normalized Acceleration
Frequency (Hz)

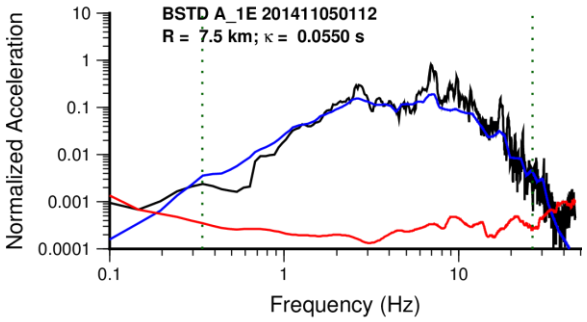
BSTD A_1E 201411050112
R = 7.5 km; κ = 0.0550 s
Normalized Acceleration
Frequency (Hz)

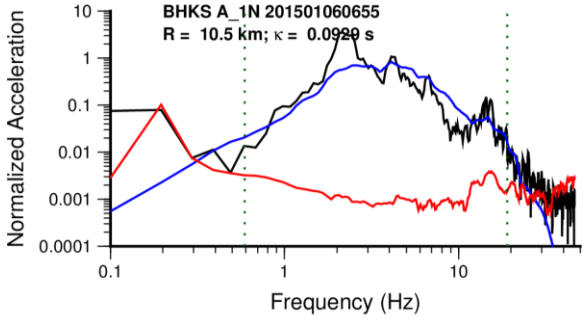
BHKS A_1N 201501060655
R = 10.5 km; κ = 0.0920 s
Normalized Acceleration
Frequency (Hz)

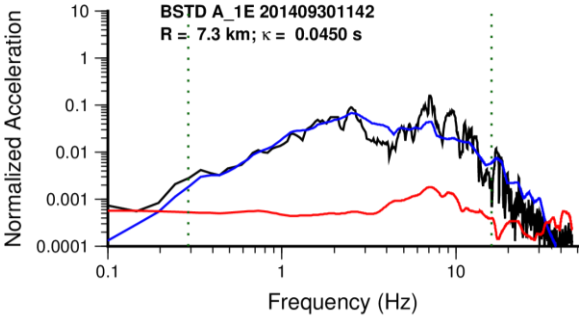
BSTD A_1E 201409301142
R = 7.3 km; κ = 0.0450 s
Normalized Acceleration
Frequency (Hz)

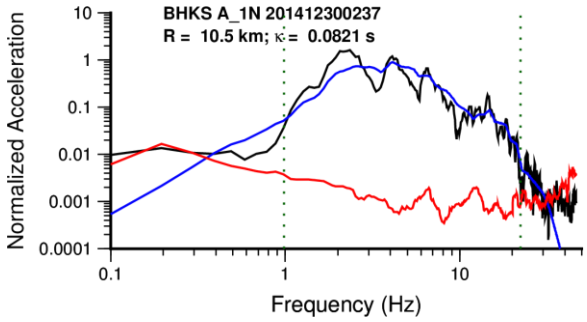
BHKS A_1N 201412300237
R = 10.5 km; κ = 0.0821 s
Normalized Acceleration
Frequency (Hz)

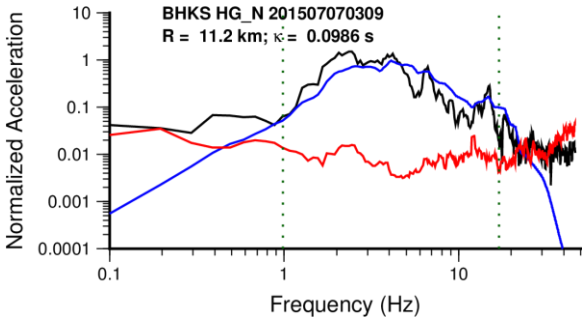
BHKS HG_N 201507070309
R = 11.2 km; κ = 0.0986 s
Normalized Acceleration
Frequency (Hz)

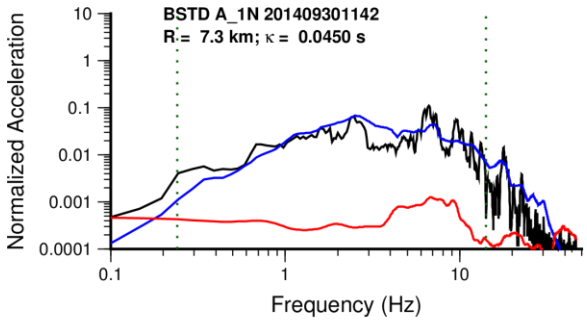
BSTD A_1N 201409301142
R = 7.3 km; κ = 0.0450 s
Normalized Acceleration
Frequency (Hz)

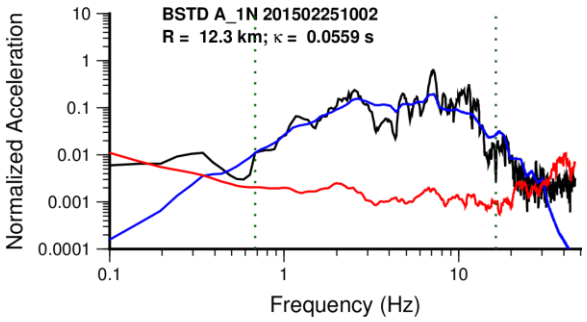
BSTD A_1N 201502251002
R = 12.3 km; κ = 0.0559 s
Normalized Acceleration
Frequency (Hz)

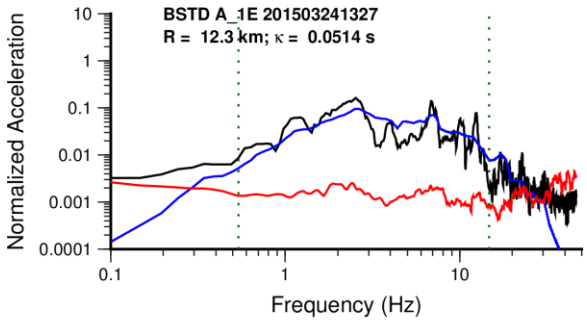
BSTD A_1E 201503241327
R = 12.3 km; κ = 0.0514 s
Normalized Acceleration
Frequency (Hz)

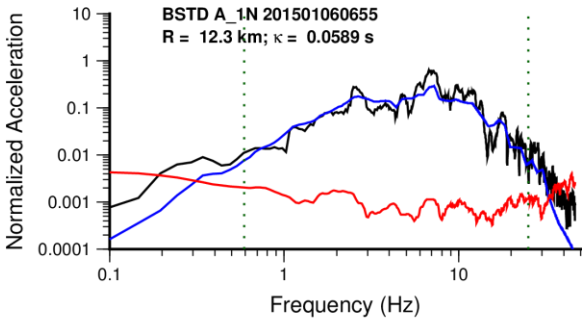
BSTD A_1N 201501060655
R = 12.3 km; κ = 0.0589 s
Normalized Acceleration
Frequency (Hz)

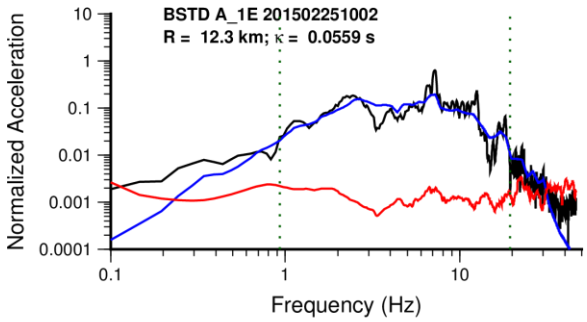
BSTD A_1E 201502251002
R = 12.3 km; κ = 0.0559 s
Normalized Acceleration
Frequency (Hz)

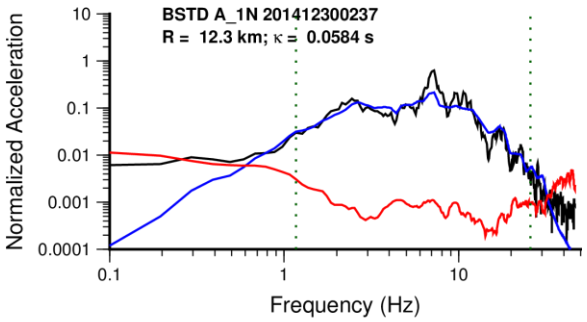
BSTD A_1N 201412300237
R = 12.3 km; κ = 0.0584 s
Normalized Acceleration
Frequency (Hz)

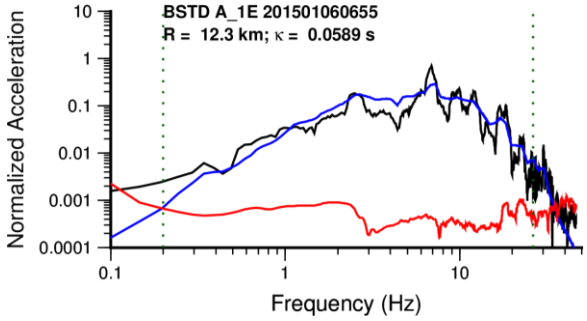
BSTD A_1E 201501060655
R = 12.3 km; κ = 0.0589 s
Normalized Acceleration
Frequency (Hz)

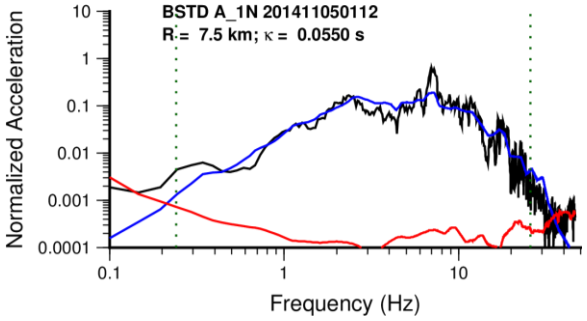
BSTD A_1N 201411050112
R = 7.5 km; κ = 0.0550 s
Normalized Acceleration
Frequency (Hz)

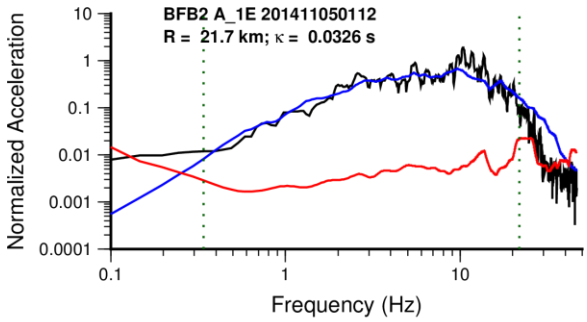
BFB2 A_1E 201411050112
R = 21.7 km; κ = 0.0326 s
Normalized Acceleration
Frequency (Hz)

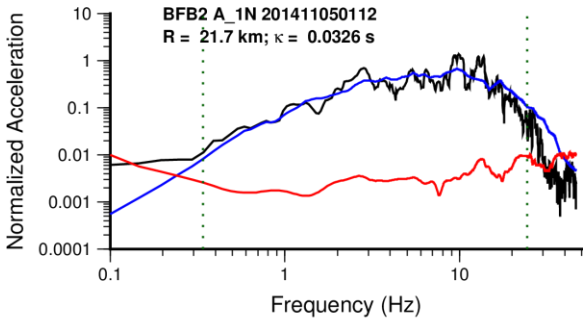
BFB2 A_1N 201411050112
R = 21.7 km; κ = 0.0326 s
Normalized Acceleration
Frequency (Hz)

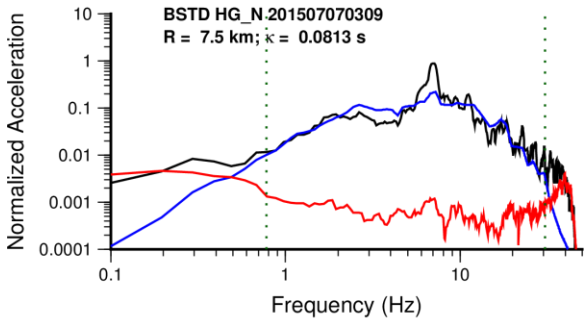
BSTD HG_N 201507070309
R = 7.5 km; κ = 0.0813 s
Normalized Acceleration
Frequency (Hz)

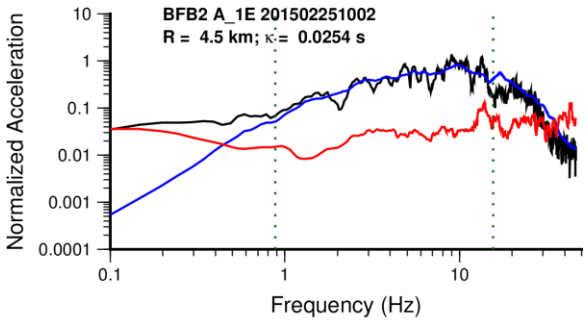
BFB2 A_1E 201502251002
R = 4.5 km; κ = 0.0254 s
Normalized Acceleration
Frequency (Hz)

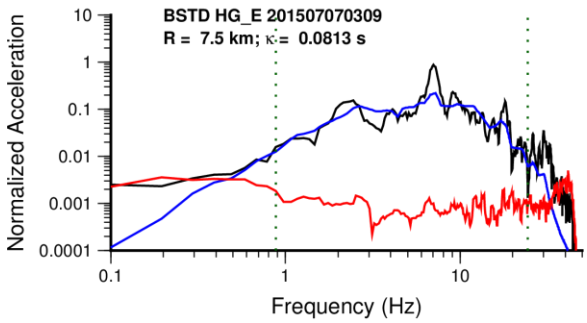
BSTD HG_E 201507070309
R = 7.5 km; κ = 0.0813 s
Normalized Acceleration
Frequency (Hz)

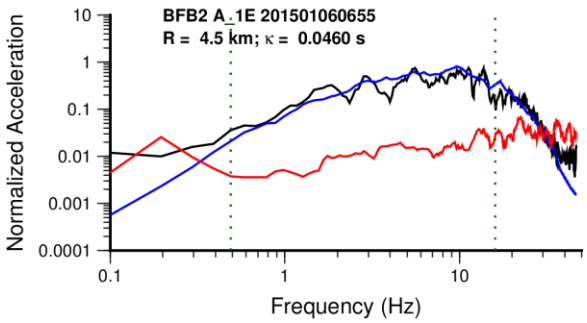
BFB2 A_1E 201501060655
R = 4.5 km; κ = 0.0460 s
Normalized Acceleration
Frequency (Hz)

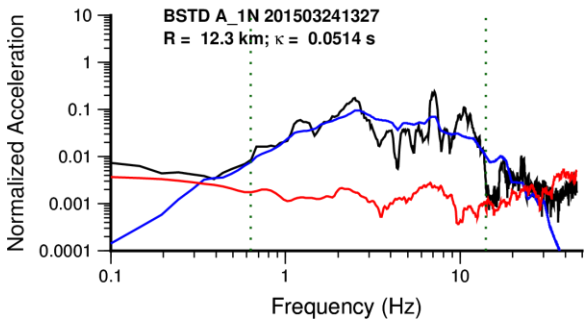
BSTD A_1N 201503241327
R = 12.3 km; κ = 0.0514 s
Normalized Acceleration
Frequency (Hz)

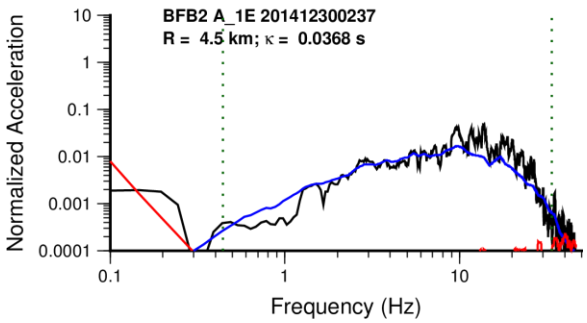
BFB2 A_1E 201412300237
R = 4.5 km; κ = 0.0368 s
Normalized Acceleration
Frequency (Hz)

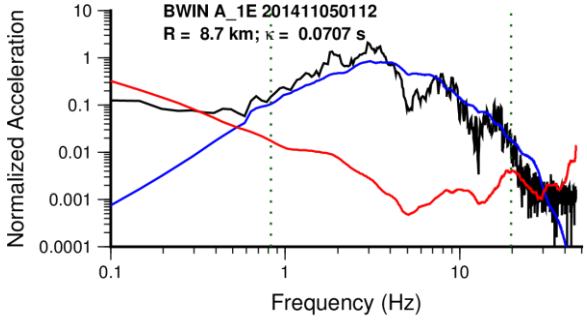
BWIN A_1E 201411050112
R = 8.7 km; κ = 0.0707 s
Normalized Acceleration
Frequency (Hz)

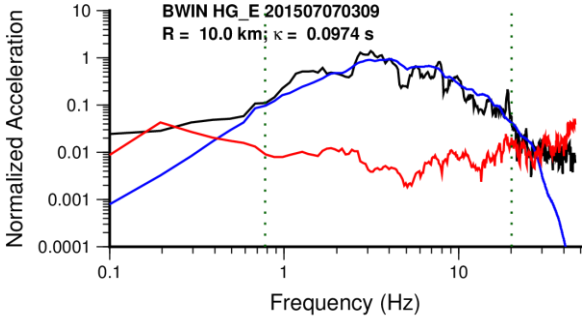
BWIN HG_E 201507070309
R = 10.0 km; κ = 0.0974 s
Normalized Acceleration
Frequency (Hz)

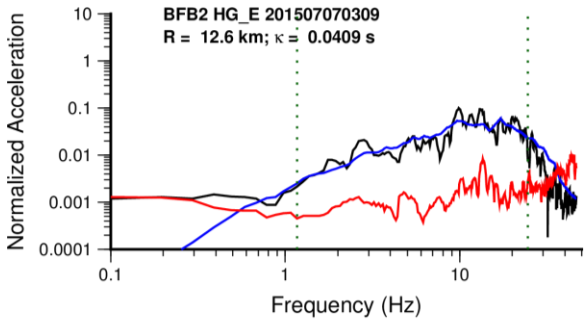
BFB2 HG_E 201507070309
R = 12.6 km; κ = 0.0409 s
Normalized Acceleration
Frequency (Hz)

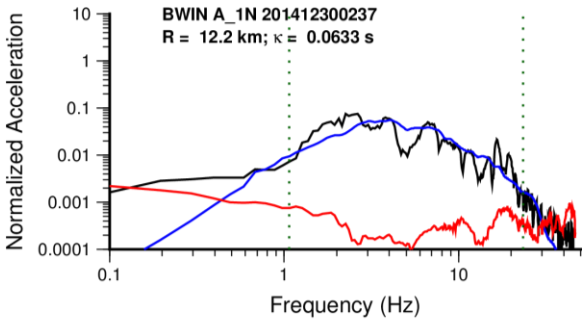
BWIN A_1N 201412300237
R = 12.2 km; κ = 0.0633 s
Normalized Acceleration
Frequency (Hz)

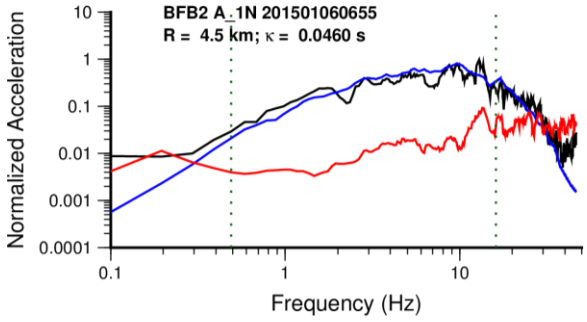
BFB2 A_1N 201501060655
R = 4.5 km; κ = 0.0460 s
Normalized Acceleration
Frequency (Hz)

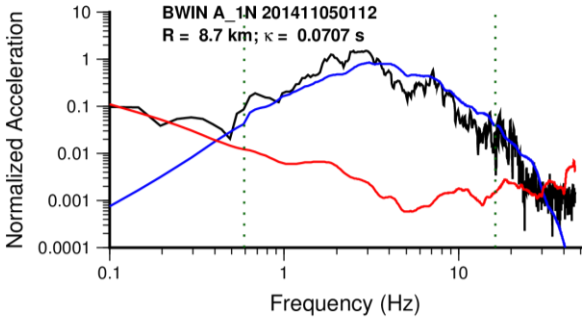
BWIN A_1N 201411050112
R = 8.7 km; κ = 0.0707 s
Normalized Acceleration
Frequency (Hz)

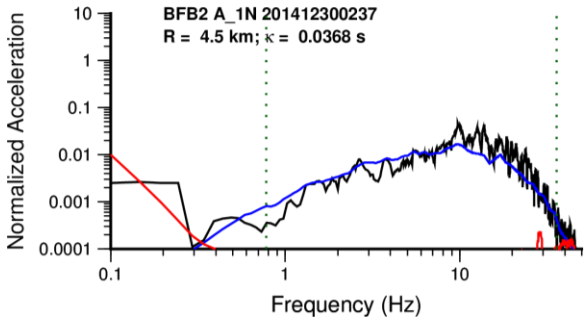
BFB2 A_1N 201412300237
R = 4.5 km; κ = 0.0368 s
Normalized Acceleration
Frequency (Hz)

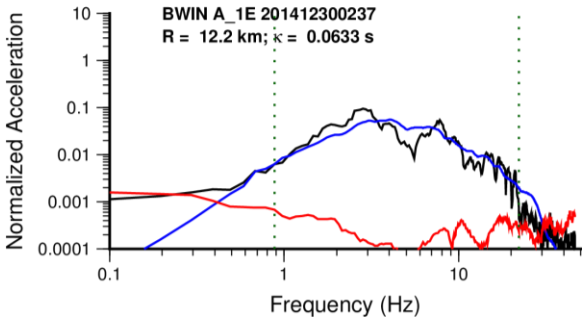
BWIN A_1E 201412300237
R = 12.2 km; κ = 0.0633 s
Normalized Acceleration
Frequency (Hz)

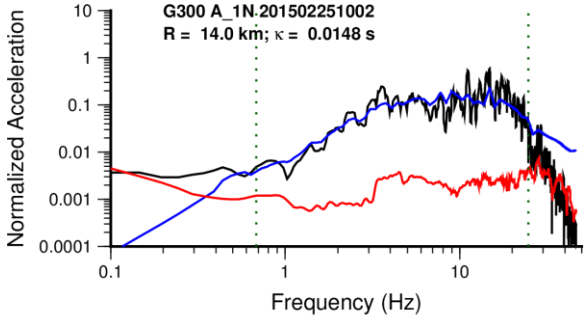
G300 A_1N 201502251002
R = 14.0 km; κ = 0.0148 s
Normalized Acceleration
Frequency (Hz)

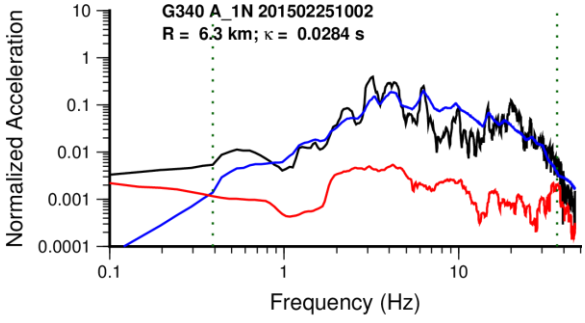
G340 A_1N 201502251002
R = 6.3 km; κ = 0.0284 s
Normalized Acceleration
Frequency (Hz)

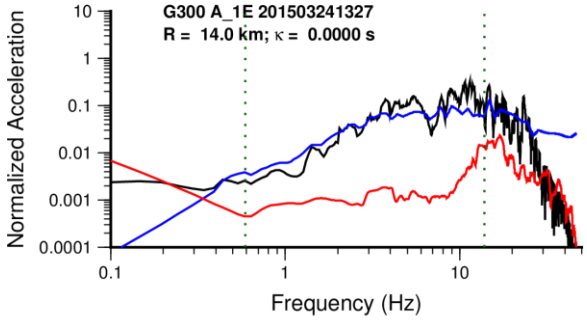
G300 A_1E 201503241327
R = 14.0 km; κ = 0.0000 s
Normalized Acceleration
Frequency (Hz)

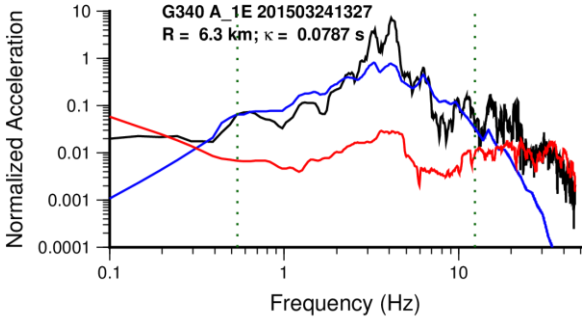
G340 A_1E 201503241327
R = 6.3 km; κ = 0.0787 s
Normalized Acceleration
Frequency (Hz)

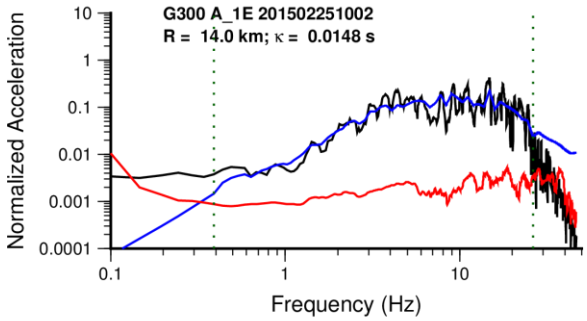
G300 A_1E 201502251002
R = 14.0 km; κ = 0.0148 s
Normalized Acceleration
Frequency (Hz)

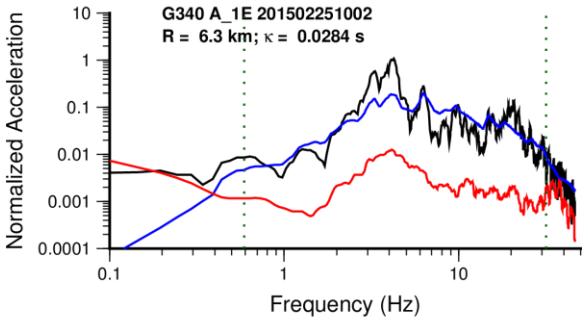
G340 A_1E 201502251002
R = 6.3 km; κ = 0.0284 s
Normalized Acceleration
Frequency (Hz)

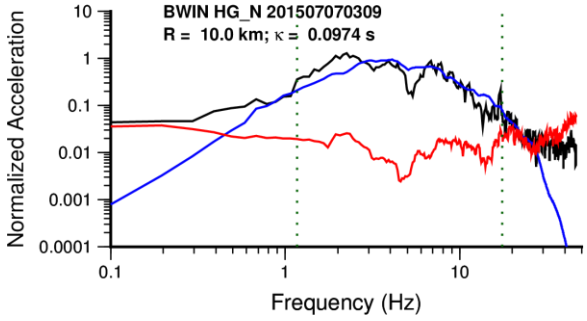
BWIN HG_N 201507070309
R = 10.0 km; κ = 0.0974 s
Normalized Acceleration
Frequency (Hz)

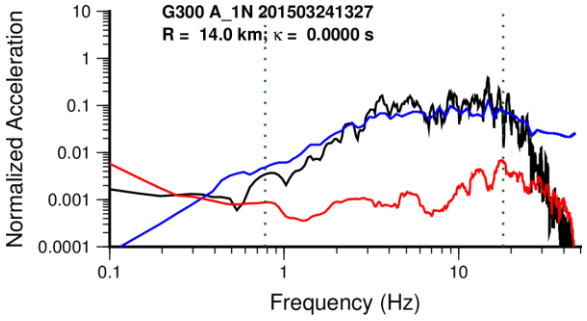
G300 A_1N 201503241327
R = 14.0 km; κ = 0.0000 s
Normalized Acceleration
Frequency (Hz)

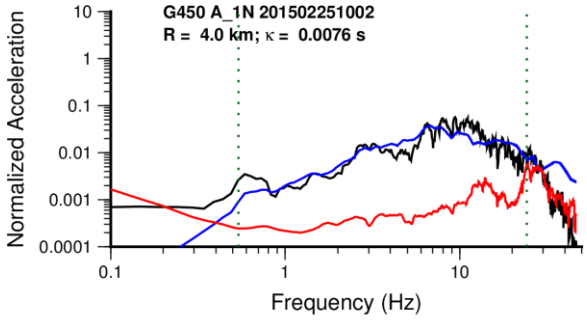
G450 A_1N 201502251002
R = 4.0 km; κ = 0.0076 s
Normalized Acceleration
Frequency (Hz)

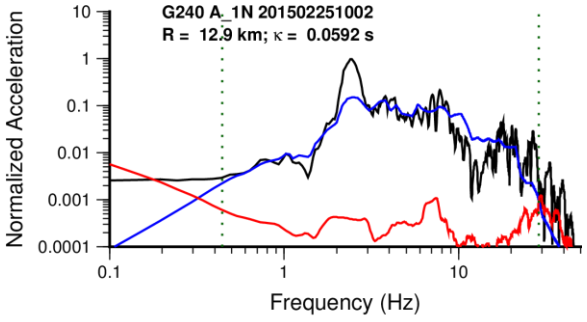
G240 A_1N 201502251002
R = 12.9 km; κ = 0.0592 s
Normalized Acceleration
Frequency (Hz)

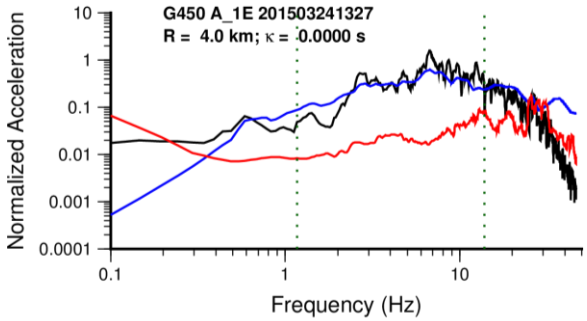
G450 A_1E 201503241327
R = 4.0 km; κ = 0.0000 s
Normalized Acceleration
Frequency (Hz)

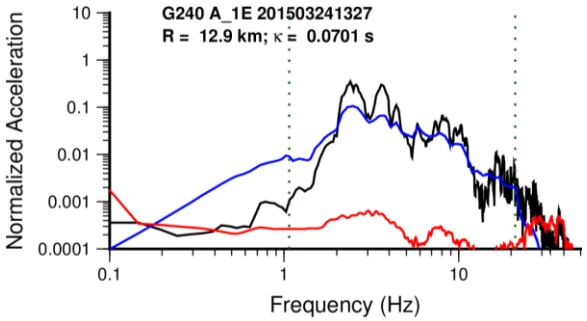
G240 A_1E 201503241327
R = 12.9 km; κ = 0.0701 s
Normalized Acceleration
Frequency (Hz)

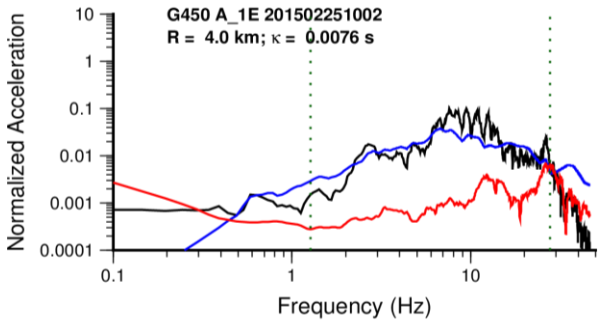
G450 A_1E 201502251002
R = 4.0 km; κ = 0.0076 s
Normalized Acceleration
Frequency (Hz)

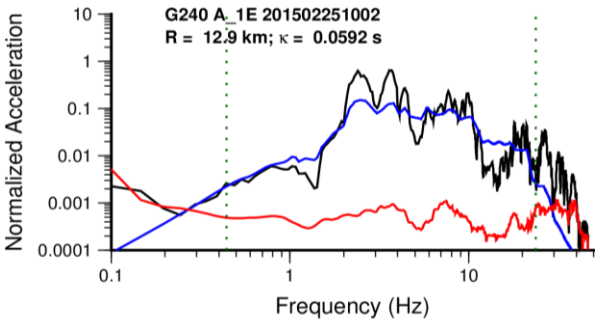
G240 A_1E 201502251002
R = 12.9 km; κ = 0.0592 s
Normalized Acceleration
Frequency (Hz)

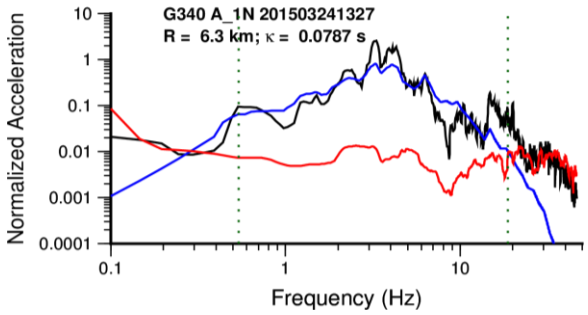
G340 A_1N 201503241327
R = 6.3 km; κ = 0.0787 s
Normalized Acceleration
Frequency (Hz)

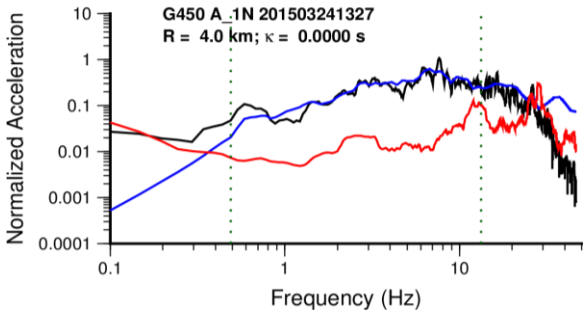
G450 A_1N 201503241327
R = 4.0 km; κ = 0.0000 s
Normalized Acceleration
Frequency (Hz)

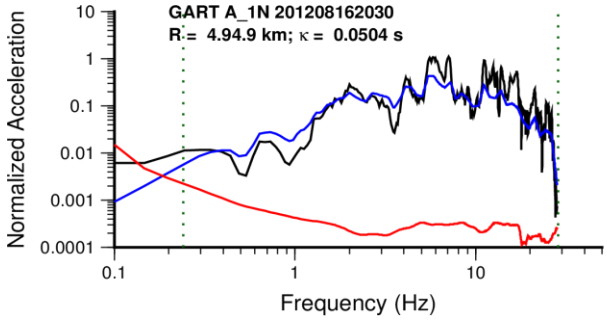
GART A_1N 201208162030
R = 4.94.9 km; κ = 0.0504 s
Normalized Acceleration
Frequency (Hz)

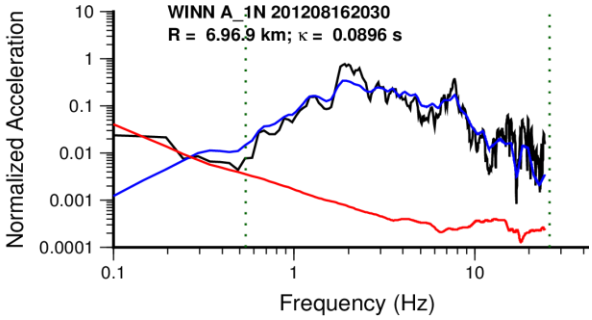
WINN A_1N 201208162030
R = 6.96.9 km; κ = 0.0896 s
Normalized Acceleration
Frequency (Hz)

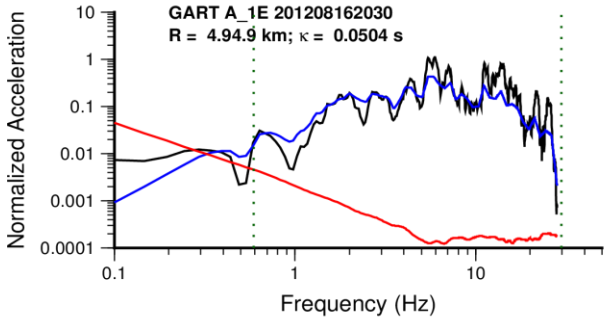
GART A_1E 201208162030
R = 4.94.9 km; κ = 0.0504 s
Normalized Acceleration
Frequency (Hz)

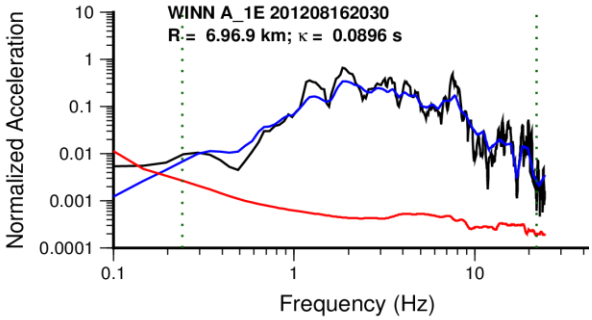
WINN A_1E 201208162030
R = 6.96.9 km; κ = 0.0896 s
Normalized Acceleration
Frequency (Hz)

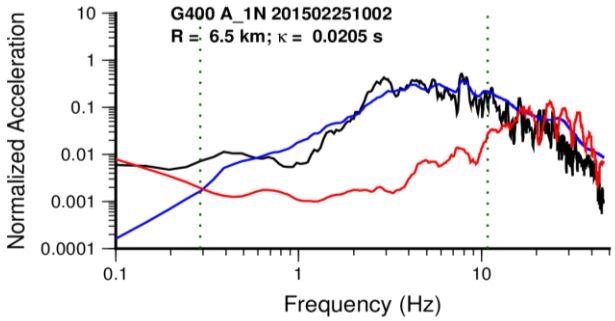
G400 A_1N 201502251002
R = 6.5 km; κ = 0.0205 s
Normalized Acceleration
Frequency (Hz)

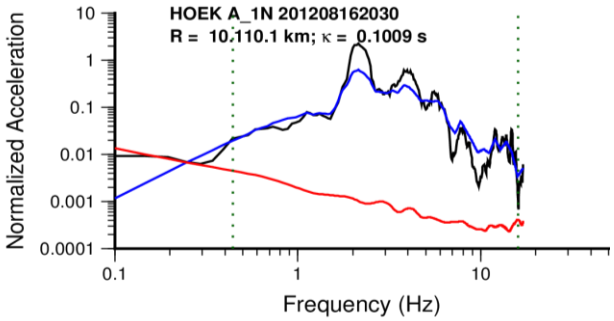
HOEK A_1N 201208162030
R = 10.110.1 km; κ = 0.1009 s
Normalized Acceleration
Frequency (Hz)

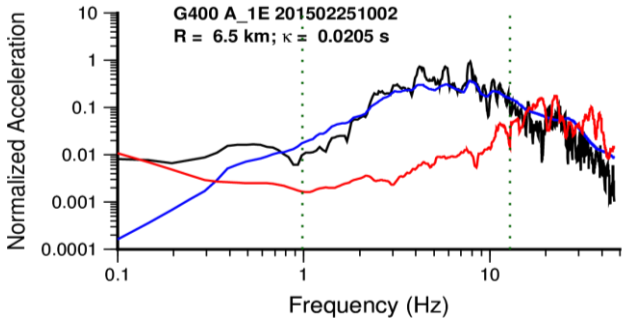
G400 A_1E 201502251002
R = 6.5 km; κ = 0.0205 s
Normalized Acceleration
Frequency (Hz)

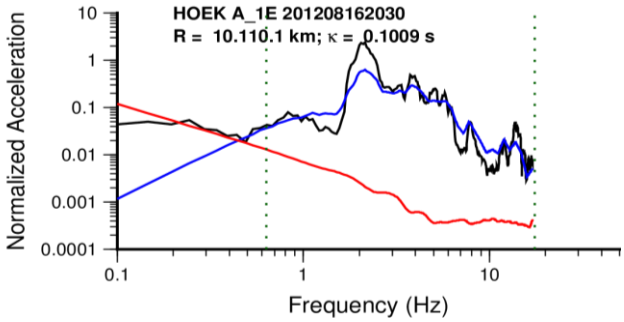
HOEK A_1E 201208162030
R = 10.110.1 km; κ = 0.1009 s
Normalized Acceleration
Frequency (Hz)